

*marine drugs*

# Marine Drug Research in China

## Selected Papers from the 15-NASMD Conference

---

Edited by

Xuefeng Zhou, Xiaowei Luo and Yonghong Liu

Printed Edition of the Special Issue Published in *Marine Drugs*

**Marine Drug Research in China:  
Selected Papers from the 15-NASMD  
Conference**



# Marine Drug Research in China: Selected Papers from the 15-NASMD Conference

Editors

Xuefeng Zhou

Xiaowei Luo

Yonghong Liu

MDPI • Basel • Beijing • Wuhan • Barcelona • Belgrade • Manchester • Tokyo • Cluj • Tianjin



*Editors*

Xuefeng Zhou  
Chinese Academy of Sciences  
China

Xiaowei Luo  
Guangxi University of  
Chinese Medicine  
China

Yonghong Liu  
Guangxi University of  
Chinese Medicine  
China

*Editorial Office*

MDPI  
St. Alban-Anlage 66  
4052 Basel, Switzerland

This is a reprint of articles from the Special Issue published online in the open access journal *Marine Drugs* (ISSN 1660-3397) (available at: [https://www.mdpi.com/journal/marinedrugs/special\\_issues/Marine\\_Drugs\\_Research\\_in\\_China\\_15-NASMD](https://www.mdpi.com/journal/marinedrugs/special_issues/Marine_Drugs_Research_in_China_15-NASMD)).

For citation purposes, cite each article independently as indicated on the article page online and as indicated below:

LastName, A.A.; LastName, B.B.; LastName, C.C. Article Title. *Journal Name* **Year**, *Volume Number*, Page Range.

**ISBN 978-3-0365-4569-1 (Hbk)**

**ISBN 978-3-0365-4570-7 (PDF)**

© 2022 by the authors. Articles in this book are Open Access and distributed under the Creative Commons Attribution (CC BY) license, which allows users to download, copy and build upon published articles, as long as the author and publisher are properly credited, which ensures maximum dissemination and a wider impact of our publications.

The book as a whole is distributed by MDPI under the terms and conditions of the Creative Commons license CC BY-NC-ND.

# Contents

|   |     |
|---|-----|
| About the Editors . . . . .   | ix  |
| Preface to "Marine Drug Research in China: Selected Papers from the 15-NASMD Conference" . . . . .  | xi  |
| <b>Shuang-Yi Zhang, Guo-Xu Zhao, Shi-Kun Suo, Yu-Mei Wang, Chang-Feng Chi and Bin Wang</b><br>Purification, Identification, Activity Evaluation, and Stability of Antioxidant Peptides from<br>Alcalase Hydrolysate of Antarctic Krill ( <i>Euphausia superba</i> ) Proteins<br>Reprinted from: <i>Mar. Drugs</i> <b>2021</b> , <i>19</i> , 347, doi:10.3390/md19060347 . . . . .   | 1   |
| <b>Fan Mao, Yongbo Bao, Nai-Kei Wong, Minwei Huang, Kunna Liu, Xiangyu Zhang,<br/>Zhuo Yang, Wenjie Yi, Xiao Shu, Zhiming Xiang, Ziniu Yu and Yang Zhang</b><br>Large-Scale Plasma Peptidomic Profiling Reveals a Novel, Nontoxic, <i>Crassostrea</i><br><i>hongkongensis</i> -Derived Antimicrobial Peptide against Foodborne Pathogens<br>Reprinted from: <i>Mar. Drugs</i> <b>2021</b> , <i>19</i> , 420, doi:10.3390/md19080420 . . . . . | 19  |
| <b>Kunlong Li, Ziqi Su, Yongli Gao, Xiuping Lin, Xiaoyan Pang, Bin Yang, Huaming Tao,<br/>Xiaowei Luo, Yonghong Liu and Xuefeng Zhou</b><br>Cytotoxic Minor Piericidin Derivatives from the Actinomycete Strain <i>Streptomyces psammoticus</i><br>SCSIO NS126<br>Reprinted from: <i>Mar. Drugs</i> <b>2021</b> , <i>19</i> , 428, doi:10.3390/md19080428 . . . . .   | 35  |
| <b>Hui Lei, Xiaoxu Bi, Xiuping Lin, Jianglian She, Xiaowei Luo, Hong Niu, Dan Zhang and<br/>Bin Yang</b><br>Heterocornols from the Sponge-Derived Fungus <i>Pestalotiopsis heterocornis</i> with<br>Anti-Inflammatory Activity<br>Reprinted from: <i>Mar. Drugs</i> <b>2021</b> , <i>19</i> , 585, doi:10.3390/md19110585 . . . . .   | 49  |
| <b>Jieyi Long, Yaqi Chen, Weihao Chen, Junfeng Wang, Xuefeng Zhou, Bin Yang and<br/>Yonghong Liu</b><br>Cyclic Peptides from the Soft Coral-Derived Fungus <i>Aspergillus sclerotiorum</i> SCSIO 41031<br>Reprinted from: <i>Mar. Drugs</i> <b>2021</b> , <i>19</i> , 701, doi:10.3390/md19120701 . . . . .   | 63  |
| <b>Jia-Rong Hou, Yan-Hong Wang, Ying-Nan Zhong, Tong-Tong Che, Yang Hu, Jie Bao and<br/>Ning Meng</b><br>Protective Effect of Flavonoids from a Deep-Sea-Derived <i>Arthrimum</i> sp. against<br>ox-LDL-Induced Oxidative Injury through Activating the AKT/Nrf2/HO-1 Pathway in<br>Vascular Endothelial Cells<br>Reprinted from: <i>Mar. Drugs</i> <b>2021</b> , <i>19</i> , 712, doi:10.3390/md19120712 . . . . .                           | 75  |
| <b>Liang Wu, Chun-Lan Xie, Xian-Wen Yang and Gang Chen</b><br>Pharmacokinetics and Metabolism Study of Deep-Sea-Derived Butyrolactone I in Rats by<br>UHPLC-MS/MS and UHPLC-Q-TOF-MS<br>Reprinted from: <i>Mar. Drugs</i> <b>2022</b> , <i>20</i> , 11, doi:10.3390/md20010011 . . . . .  | 89  |
| <b>Wei Chen, Kaixiong Ye, Xiaoji Zhu, Huihui Zhang, Ranran Si, Jianing Chen, Zijun Chen,<br/>Kaili Song, Zhicheng Yu and Bingnan Han</b><br>Actinomycin X2, an Antimicrobial Depsipeptide from Marine-Derived <i>Streptomyces</i><br><i>cyaneofuscatus</i> Applied as a Good Natural Dye for Silk Fabric<br>Reprinted from: <i>Mar. Drugs</i> <b>2022</b> , <i>20</i> , 16, doi:10.3390/md20010016 . . . . .                                  | 103 |

|  |     |
|--|-----|
| <b>Lianxiang Luo, Ai Zhong, Qu Wang and Tongyu Zheng</b><br>Structure-Based Pharmacophore Modeling, Virtual Screening, Molecular Docking, ADMET, and Molecular Dynamics (MD) Simulation of Potential Inhibitors of PD-L1 from the Library of Marine Natural Products<br>Reprinted from: <i>Mar. Drugs</i> <b>2022</b> , <i>20</i> , 29, doi:10.3390/md20010029 . . . . .   | 121 |
| <b>Senhua Chen, Heng Guo, Minghua Jiang, Qilin Wu, Jing Li, Hongjie Shen and Lan Liu</b><br>Mono- and Dimeric Xanthonones with Anti-Glioma and Anti-Inflammatory Activities from the Ascidian-Derived Fungus <i>Diaporthe</i> sp. SYSU-MS4722<br>Reprinted from: <i>Mar. Drugs</i> <b>2022</b> , <i>20</i> , 51, doi:10.3390/md20010051 . . . . .  | 139 |
| <b>Shu Jiang, Cui-Ping Jiang, Pei Cao, Yong-Hong Liu, Cheng-Hai Gao and Xiang-Xi Yi</b><br>Sonneradon A Extends Lifespan of <i>Caenorhabditis elegans</i> by Modulating Mitochondrial and IIS Signaling Pathways<br>Reprinted from: <i>Mar. Drugs</i> <b>2022</b> , <i>20</i> , 59, doi:10.3390/md20010059 . . . . .   | 153 |
| <b>Xia-Yu Chen, Qi Zeng, Yu-Chan Chen, Wei-Mao Zhong, Yao Xiang, Jun-Feng Wang, Xue-Feng Shi, Wei-Min Zhang, Si Zhang and Fa-Zuo Wang</b><br>Chevalones H–M: Six New $\alpha$ -Pyrone Meroterpenoids from the Gorgonian Coral-Derived Fungus <i>Aspergillus hiratsukae</i> SCSIO 7S2001<br>Reprinted from: <i>Mar. Drugs</i> <b>2022</b> , <i>20</i> , 71, doi:10.3390/md20010071 . . . . .                                  | 167 |
| <b>Cheng-Mei Liu, Fei-Hua Yao, Xin-Hua Lu, Xue-Xia Zhang, Lian-Xiang Luo, Xiao Liang and Shu-Hua Qi</b><br>Isoquinoline Alkaloids as Protein Tyrosine Phosphatase Inhibitors from a Deep-Sea-Derived Fungus <i>Aspergillus puniceus</i><br>Reprinted from: <i>Mar. Drugs</i> <b>2022</b> , <i>20</i> , 78, doi:10.3390/md20010078 . . . . .  | 179 |
| <b>Rong Chao, Gulab Said, Qun Zhang, Yue-Xuan Qi, Jie Hu, Cai-Juan Zheng, Ji-Yong Zheng, Chang-Lun Shao, Guang-Ying Chen and Mei-Yan Wei</b><br>Design, Semisynthesis, Insecticidal and Antibacterial Activities of a Series of Marine-Derived Geodin Derivatives and Their Preliminary Structure–Activity Relationships<br>Reprinted from: <i>Mar. Drugs</i> <b>2022</b> , <i>20</i> , 82, doi:10.3390/md20020082 . . . . . | 195 |
| <b>Chunlei Li, Sirui Zhang, Jianhua Zhu, Weijuan Huang, Yuanyuan Luo, Hui Shi, Dongbo Yu, Ligu Chen, Liyan Song and Rongmin Yu</b><br>A Novel Peptide Derived from <i>Arca inflata</i> Induces Apoptosis in Colorectal Cancer Cells through Mitochondria and the p38 MAPK Pathway<br>Reprinted from: <i>Mar. Drugs</i> <b>2022</b> , <i>20</i> , 110, doi:10.3390/md20020110 . . . . .                                       | 213 |
| <b>Xuewei Xia, Jun Liu, Li Huang, Xiaoyong Zhang, Yunqin Deng, Fengming Li, Zhiyuan Liu and Riming Huang</b><br>Molecular Details of Actinomycin D-Treated MRSA Revealed via High-Dimensional Data<br>Reprinted from: <i>Mar. Drugs</i> <b>2022</b> , <i>20</i> , 114, doi:10.3390/md20020114 . . . . .  | 231 |
| <b>Mengyu Sun, Dongdong Zhou, Jingwan Wu, Jing Zhou and Jing Xu</b><br>Sdy-1 Executes Antitumor Activity in HepG2 and HeLa Cancer Cells by Inhibiting the Wnt/ $\beta$ -Catenin Signaling Pathway<br>Reprinted from: <i>Mar. Drugs</i> <b>2022</b> , <i>20</i> , 125, doi:10.3390/md20020125 . . . . .   | 247 |
| <b>Qian Wu, Yimin Chang, Qian Che, Dehai Li, Guojian Zhang and Tianjiao Zhu</b><br>Citrobenzofuran D–F and Phomenone A–B: Five Novel Sesquiterpenoids from the Mangrove-Derived Fungus <i>Penicillium</i> sp. HDN13-494<br>Reprinted from: <i>Mar. Drugs</i> <b>2022</b> , <i>20</i> , 137, doi:10.3390/md20020137 . . . . .   | 265 |

|   |     |
|---|-----|
| <b>Meng-Juan Xu, Lin-Jing Zhong, Jun-Kun Chen, Qing Bu and Lin-Fu Liang</b><br>Secondary Metabolites from Marine Sponges of the Genus <i>Oceanapia</i> : Chemistry and Biological Activities<br>Reprinted from: <i>Mar. Drugs</i> <b>2022</b> , <i>20</i> , 144, doi:10.3390/md20020144 . . . . .   | 275 |
| <b>Daichun Li, Xiaojian Liao, Shenghui Zhong, Bingxin Zhao and Shihai Xu</b><br>Synthesis of Marine Cyclopeptide Galaxamide Analogues as Potential Anticancer Agents<br>Reprinted from: <i>Mar. Drugs</i> <b>2022</b> , <i>20</i> , 158, doi:10.3390/md20030158 . . . . .   | 291 |
| <b>Shuo-Lei Zheng, Qian-Bin Luo, Shi-Kun Suo, Yu-Qin Zhao, Chang-Feng Chi and Bin Wang</b><br>Preparation, Identification, Molecular Docking Study and Protective Function on HUVECs of Novel ACE Inhibitory Peptides from Protein Hydrolysate of Skipjack Tuna Muscle<br>Reprinted from: <i>Mar. Drugs</i> <b>2022</b> , <i>20</i> , 176, doi:10.3390/md20030176 . . . . .                                 | 303 |
| <b>Ying Wang, Xiao-Ming Li, Sui-Qun Yang, Fan-Zhong Zhang, Bin-Gui Wang, Hong-Lei Li and Ling-Hong Meng</b><br>Sesquiterpene and Sorbicillinoid Glycosides from the Endophytic Fungus <i>Trichoderma longibrachiatum</i> EN-586 Derived from the Marine Red Alga <i>Laurencia obtusa</i><br>Reprinted from: <i>Mar. Drugs</i> <b>2022</b> , <i>20</i> , 177, doi:10.3390/md20030177 . . . . .               | 325 |
| <b>Yanting Zhang, Zhichao Li, Bingyao Huang, Kai Liu, Shuai Peng, Xinming Liu, Chenghai Gao, Yonghong Liu, Yanhui Tan and Xiaowei Luo</b><br>Anti-Osteoclastogenic and Antibacterial Effects of Chlorinated Polyketides from the Beibu Gulf Coral-Derived Fungus <i>Aspergillus unguis</i> GXIMD 02505<br>Reprinted from: <i>Mar. Drugs</i> <b>2022</b> , <i>20</i> , 178, doi:10.3390/md20030178 . . . . . | 337 |
| <b>Xia Wei, Fang-Ting Wang, Mei-Xia Si-Tu, Hao Fan, Jin-Shan Hu, Hao Yang, Shan-Yue Guan, Lin-Kun An and Cui-Xian Zhang</b><br>Pyranodipyran Derivatives with Tyrosyl DNA Phosphodiesterase 1 Inhibitory Activities and Fluorescent Properties from <i>Aspergillus</i> sp. EGF 15-0-3<br>Reprinted from: <i>Mar. Drugs</i> <b>2022</b> , <i>20</i> , 211, doi:10.3390/md20030211 . . . . .                  | 349 |
| <b>Qingyun Peng, Weihao Chen, Xiuping Lin, Jiao Xiao, Yonghong Liu and Xuefeng Zhou</b><br>Butenolides from the Coral-Derived Fungus <i>Aspergillus terreus</i> SCSIO41404<br>Reprinted from: <i>Mar. Drugs</i> <b>2022</b> , <i>20</i> , 212, doi:10.3390/md20030212 . . . . .   | 365 |
| <b>Jiena Ye, Jiawen Zheng, Xiaoxiao Tian, Baogui Xu, Falei Yuan, Bin Wang, Zuisu Yang and Fangfang Huang</b><br>Fucoxanthin Attenuates Free Fatty Acid-Induced Nonalcoholic Fatty Liver Disease by Regulating Lipid Metabolism/Oxidative Stress/Inflammation via the AMPK/Nrf2/TLR4 Signaling Pathway<br>Reprinted from: <i>Mar. Drugs</i> <b>2022</b> , <i>20</i> , 225, doi:10.3390/md20040225 . . . . .  | 377 |
| <b>Lizhi Gong, Yuzhen Wu, Xiaohan Qiu, Xiujuan Xin, Faliang An and Miaomiao Guo</b><br>Adsorption Characteristics and Enrichment of Emodin from Marine-Derived <i>Aspergillus flavipes</i> HN4-13 Extract by Macroporous Resin XAD-16<br>Reprinted from: <i>Mar. Drugs</i> <b>2022</b> , <i>20</i> , 231, doi:10.3390/md20040231 . . . . .  | 391 |
| <b>Xinya Xu, Yanhui Tan, Chenghai Gao, Kai Liu, Zhenzhou Tang, Chunju Lu, Haiyan Li, Xiaoyong Zhang and Yonghong Liu</b><br>New 3-Acyl Tetramic Acid Derivatives from the Deep-Sea-Derived Fungus <i>Lecanicillium fusisporum</i><br>Reprinted from: <i>Mar. Drugs</i> <b>2022</b> , <i>20</i> , 255, doi:10.3390/md20040255 . . . . .  | 405 |



|   |            |
|---|------------|
| <b>Zhihui Ma, Zhiyou Yang, Xinyue Feng, Jiahang Deng, Chuantong He, Rui Li, Yuntao Zhao, Yuewei Ge, Yongping Zhang, Cai Song and Saiyi Zhong</b><br>The Emerging Evidence for a Protective Role of Fucoidan from <i>Laminaria japonica</i> in Chronic Kidney Disease-Triggered Cognitive Dysfunction<br>Reprinted from: <i>Mar. Drugs</i> <b>2022</b> , <i>20</i> , 258, doi:10.3390/md20040258 . . . . . | <b>417</b> |
| <b>Ziqi Su, Kunlong Li, Xiaowei Luo, Yongyan Zhu, Shao-Yu Mai, Quanhong Zhu, Bin Yang, Xuefeng Zhou and Huaming Tao</b><br>Aromatic Acids and Leucine Derivatives Produced from the Deep-Sea Actinomycetes <i>Streptomyces chumphonensis</i> SCSIO15079 with Antihyperlipidemic Activities<br>Reprinted from: <i>Mar. Drugs</i> <b>2022</b> , <i>20</i> , 259, doi:10.3390/md20040259 . . . . .           | <b>435</b> |
| <b>Dongjin Pan, Bingyao Huang, Yuman Gan, Chenghai Gao, Yonghong Liu and Zhenzhou Tang</b><br>Phycocyanin Ameliorates Colitis-Associated Colorectal Cancer by Regulating the Gut Microbiota and the IL-17 Signaling Pathway<br>Reprinted from: <i>Mar. Drugs</i> <b>2022</b> , <i>20</i> , 260, doi:10.3390/md20040260 . . . . .  | <b>447</b> |
| <b>Shufen He, Peishan Li, Jingxuan Wang, Yanzhu Zhang, Hongmei Lu, Liufei Shi, Tao Huang, Weiyang Zhang, Lijian Ding, Shan He and Liwei Liu</b><br>Discovery of New Secondary Metabolites from Marine Bacteria <i>Hahella</i> Based on an Omics Strategy<br>Reprinted from: <i>Mar. Drugs</i> <b>2022</b> , <i>20</i> , 269, doi:10.3390/md20040269 . . . . .   | <b>461</b> |
| <b>Lianxiang Luo, Qu Wang and Yinglin Liao</b><br>The Inhibitors of CDK4/6 from a Library of Marine Compound Database: A Pharmacophore, ADMET, Molecular Docking and Molecular Dynamics Study<br>Reprinted from: <i>Mar. Drugs</i> <b>2022</b> , <i>20</i> , 319, doi:10.3390/md20050319 . . . . .  | <b>477</b> |

## About the Editors

### Xuefeng Zhou

Xuefeng Zhou. PhD, studied pharmaceutics in Tongji Medical College, Huazhong University of Science and Technology (Wuhan, China) from 1999 to 2003, and earned his Bachelor of Science. From 2003 to 2008, he continued his studies and research on natural products and pharmacology in Tongji Medical College, and earned his PhD degree. In June 2008, he joined the research group of Prof. Dr. Yonghong Liu as a research assistant and associate professor in the South China Sea Institute of Oceanology (SCSIO), Chinese Academy of Sciences (Guangzhou, China). From June 2014 to June 2015, he joined the William Fenical's Lab as a visiting scholar, in Scripps Institution of Oceanography, University of California at San Diego. Since 2018, he has held the position of professor in SCSIO. His research interests include the chemistry of marine natural products, optimization and mechanism study of lead compounds for marine drugs.

### Xiaowei Luo

Xiaowei Luo. PhD, obtained his BS degree from the Southern Medical University (Guangzhou, China), and further earned his PhD degree from the University of Chinese Academy of Sciences (Beijing, China)/South China Sea Institute of Oceanology, Chinese Academy of Sciences (Guangzhou, China) under the guidance of Prof. Dr. Yonghong Liu. He joined the Institute of Marine Drugs, Guangxi University of Chinese Medicine (Nanning, China) as a research assistant in June 2019 and has been an associate professor since December 2021. His current research focuses on the discovery, optimization, and mechanism study of novel lead compounds from marine microorganisms.

### Yonghong Liu

Yonghong Liu. PhD, obtained his BS and MS degrees from the Changchun College of Traditional Chinese Medicine, China, and his PhD degree from the Pusan National University, Korea, where he studied the isolation, structure elucidation and structure–activity relationships of biological active marine natural products under the guidance of Prof. Dr. Jee H. Jung. He conducted his postdoctoral research with Nobutoshi Murakami at Osaka University, Japan and Pedro Abreu at the New University of Lisbon, Portugal, before returning to China to become a senior scientist at the South China Sea Institute of Oceanology, Chinese Academy of Sciences. His research interests include the isolation, structural elucidation, and synthesis of biologically active secondary metabolites from marine organisms. His group has obtained more than 2000 natural products from marine organisms.



# Preface to “Marine Drug Research in China: Selected Papers from the 15-NASMD Conference”

As a grand event in the field of marine drugs, the 15th National Annual Conference and 2021 International Symposium on Marine Drugs (15-NASMD), sponsored by the Professional Committee of Marine Drugs of the Chinese Pharmaceutical Association and organized by the Institute of Marine Drugs, Guangxi University of Chinese Medicine, was held in Nanning, China, on the 12th-15th November 2021. The marine environment harbors a vast number of abundant species, which are the source of a wide array of structurally diverse bioactive secondary metabolites. Over 36,000 marine natural products have been reported to date, and approximately 1500 new marine natural products have been isolated per year over the last five years. Notably, marine microorganisms (especially marine fungi) have gradually been found to be prolific and predominant sources of novel bioactive secondary metabolites in recent years. In the new era, marine drug research in China has made various significant achievements, playing an important role in the international marine drug research fields, and is realizing the leap from basic research to industrialization. The Beibu Gulf, located in the north of the South China Sea and the south of Guangxi Zhuang Autonomous Region, represents an underexplored reservoir of diverse marine microbial species of potential interest in the discovery of novel lead compounds.

The Special Issue “15-NASMD” of the journal *Marine Drugs* covers this whole field, from the discovery of structurally new and bioactive natural products (including biomacromolecules), from marine macro-/micro-organisms, to the pharmacodynamics, pharmacokinetics, metabolisms, and mechanisms of marine-derived lead compounds, both in vitro and in vivo, along with the synthesis and/or structural optimization of marine-derived lead compounds and their structure–activity relationships. Taken together, this Special Issue not only provides inspiration for the discovery of marine-derived novel bioactive compounds, but also sheds light on the further research and development of marine candidate drugs.

**Xuefeng Zhou, Xiaowei Luo, and Yonghong Liu**  
*Editors*



## Article

# Purification, Identification, Activity Evaluation, and Stability of Antioxidant Peptides from Alcalase Hydrolysate of Antarctic Krill (*Euphausia superba*) Proteins

Shuang-Yi Zhang <sup>1</sup>, Guo-Xu Zhao <sup>1</sup>, Shi-Kun Suo <sup>1</sup>, Yu-Mei Wang <sup>1</sup>, Chang-Feng Chi <sup>2,\*</sup> and Bin Wang <sup>2,\*</sup>

<sup>1</sup> Zhejiang Provincial Engineering Technology Research Center of Marine Biomedical Products, School of Food and Pharmacy, Zhejiang Ocean University, Zhoushan 316022, China; zsydoubleone@outlook.com (S.-Y.Z.); xuzhao1109@sina.com (G.-X.Z.); 13275896859@163.com (S.-K.S.); Wangyumei731@163.com (Y.-M.W.)

<sup>2</sup> National and Provincial Joint Laboratory of Exploration and Utilization of Marine Aquatic Genetic Resources, National Engineering Research Center of Marine Facilities Aquaculture, School of Marine Science and Technology, Zhejiang Ocean University, Zhoushan 316022, China

\* Correspondence: chichangfeng@hotmail.com (C.-F.C.); wangbin4159@hotmail.com (B.W.); Tel./Fax: +86-580-255-4818 (C.-F.C.); +86-580-255-4781 (B.W.)

**Abstract:** For utilizing the largest source of marine proteins, Antarctic krill (*Euphausia superba*) proteins were defatted and hydrolyzed separately using pepsin, alcalase, papain, trypsin, and nestrage, and alcalase hydrolysate (EPAH) showed the highest DPPH radical (DPPH·) and hydroxyl radical (HO·) scavenging activity among five hydrolysates. Using ultrafiltration and chromatography methods, fifteen antioxidant peptides were purified from EPAH and identified as Asn-Gln-Met (NQM), Trp-Phe-Pro-Met (WFPM), Gln-Asn-Pro-Thr (QNPT), Tyr-Met-Asn-Phe (YMNF), Ser-Gly-Pro-Ala (SGPA), Ser-Leu-Pro-Tyr (SLPY), Gln-Tyr-Pro-Pro-Met-Gln-Tyr (QYPPMQY), Glu-Tyr-Glu-Ala (EYEA), Asn-Trp-Asp-Asp-Met-Arg-Ile-Val-Ala-Val (NWDDMRIVAV), Trp-Asp-Asp-Met-Glu-Arg-Leu-Val-Met-Ile (WDDMERLVMII), Asn-Trp-Asp-Asp-Met-Glu-Pro-Ser-Phe (NWD-DMEPSF), Asn-Gly-Pro-Asp-Pro-Arg-Pro-Ser-Gln-Gln (NGPDPFPSQQ), Ala-Phe-Leu-Trp-Asn (AFLWA), Asn-Val-Pro-Asp-Met (NVPDM), and Thr-Phe-Pro-Ile-Tyr-Asp-Tyr-Pro-Gln (TFPIYDPQ), respectively, using a protein sequencer and ESI/MS. Among fifteen antioxidant peptides, SLPY, QYPPMQY and EYEA showed the highest scavenging activities on DPPH· (EC<sub>50</sub> values of 1.18 ± 0.036, 1.547 ± 0.150, and 1.372 ± 0.274 mg/mL, respectively), HO· (EC<sub>50</sub> values of 0.826 ± 0.027, 1.022 ± 0.058, and 0.946 ± 0.011 mg/mL, respectively), and superoxide anion radical (EC<sub>50</sub> values of 0.789 ± 0.079, 0.913 ± 0.007, and 0.793 ± 0.056 mg/mL, respectively). Moreover, SLPY, QYPPMQY and EYEA showed strong reducing power, protective capability against H<sub>2</sub>O<sub>2</sub>-damaged plasmid DNA, and lipid peroxidation inhibition ability. Furthermore, SLPY, QYPPMQY, and EYEA had high stability under temperatures lower than 80 °C, pH values ranged from 6–8, and simulated GI digestion for 180 min. The results showed that fifteen antioxidant peptides from alcalase hydrolysate of Antarctic krill proteins, especially SLPY, QYPPMQY and EYEA, might serve as effective antioxidant agents applied in food and health products.

**Keywords:** Antarctic krill (*Euphausia superba*); peptide; antioxidant activity; stability

**Citation:** Zhang, S.-Y.; Zhao, G.-X.; Suo, S.-K.; Wang, Y.-M.; Chi, C.-F.; Wang, B. Purification, Identification, Activity Evaluation, and Stability of Antioxidant Peptides from Alcalase Hydrolysate of Antarctic Krill (*Euphausia superba*) Proteins. *Mar. Drugs* **2021**, *19*, 347. <https://doi.org/10.3390/md19060347>

Academic Editors: Yonghong Liu and Xuefeng Zhou

Received: 25 May 2021

Accepted: 15 June 2021

Published: 17 June 2021

**Publisher's Note:** MDPI stays neutral with regard to jurisdictional claims in published maps and institutional affiliations.



**Copyright:** © 2021 by the authors. Licensee MDPI, Basel, Switzerland. This article is an open access article distributed under the terms and conditions of the Creative Commons Attribution (CC BY) license (<https://creativecommons.org/licenses/by/4.0/>).

## 1. Introduction

Antarctic krill (*Euphausia superba*) is a crucial marine biological resource distributed in the Antarctic Ocean [1,2]. Its total biomass is up to 6.5–10 million tons and has been thought as the largest underexploited resource of the ocean [3,4]. Presently, Antarctic krill is thought as an abundant and high-quality resource for various food and health-care products because some bioactive substances, including oil, peptides and protein, astaxanthin, and chitin, have been prepared from Antarctic krill (*E. superba*) and its processing by-products [5–10].

Bioactive peptides are composed of 2 to 20 amino acid residues and released from their parent proteins using different methods of hydrolysis, including enzymatic hydroly-

ysis, chemical hydrolysis, and biological fermentation [11–13]. Beyond the recognized nutritional value, bioactive peptides exhibited various biological functions, including hypolipidemic [14], hypotensive [15], anticoagulant [16], anticancer [17,18], and antimicrobial activities [19]. Among the most studied bioactive peptides, antioxidant peptides derived from marine living resources and their processing by-products, such as yellowfin tuna (*Thunnus albacares*) skin [20], monkfish muscle [21,22], red tilapia (*Oreochromis* sp.) scale [23], miiuy croaker swim bladder [24], Skipjack tuna bone and head [25,26], and mackerel muscle [13], exhibit excellent capacity for inhibiting lipid peroxidation and scavenging reactive oxide species (ROS). EDIVCW and YWDAW from the protein hydrolysate of monkfish muscle showed strong radical scavenging activity and equivalent capability on controlling lipid peroxidation with glutathione (GSH). Moreover, EDIVCW and YWDAW showed positive protective function on H<sub>2</sub>O<sub>2</sub>-damaged HepG2 through increasing the activity of antioxidant enzymes (superoxide dismutase and glutathione peroxidase) and decreasing the contents of ROS and malondialdehyde (MDA) [22]. Similarly, the antioxidant hexapeptide of FPYLRH from the swim bladder hydrolysate of miiuy croaker (*Miichthys miiuy*) could improve the viability of H<sub>2</sub>O<sub>2</sub>-damaged HUVECs through increasing the activity of intracellular antioxidant enzymes and lowering the levels of ROS, MDA, and nitric oxide [24]. ICRD and LCGEC from the roe protein hydrolysate of skipjack tuna (*Katsuwonus pelamis*) could decrease the apoptosis of HaCaT cells induced by ultraviolet-B treatment and altered Keap1/Nrf2-ARE pathway transcription [27]. EDYGA from soft-shelled turtles was confirmed as the most potent ARE-luciferase inducer because it could increase the Nrf2 level through down-regulating Keap1 [28]. Therefore, antioxidant peptides derived from marine resource have drawn worldwide attention due to its huge potential applied in drugs, health-care products, as well as for food industries of quality control [11,29].

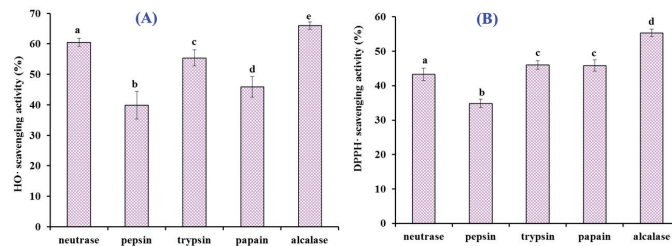
As the most abundant marine biological resource, the utilization of Antarctic krill proteins has been continuously studied, and bioactive peptides from Antarctic krill proteins, including angiotensin converting enzyme (ACE) inhibitory peptides, high Fisher value oligopeptides, anti-osteoporotic peptides, metallic element chelating peptides, and dipeptidyl peptidase IV (DPP-IV) inhibitory peptides, have gathered considerable attention because of their significant bioactive activities [2,4,8,30,31]. Wang et al. (2019) prepared peptides through hydrolyzing Antarctic krill using neutral proteinase and the peptides could down-regulate the expression of hypoxia-inducible factor-2 $\alpha$  and its downstream genes to ameliorate the cartilage degeneration of the medial meniscus mouse model [8]. Zhao et al. (2019) isolated eight ACE inhibiting peptides from the trypsin hydrolysate of Antarctic krill protein and the tripeptide of FAS could adjust the contents of nitric oxide and endothelin-1 of HUVEC and correct the endothelial cell dysfunction [32]. KVEPLP, PAL, and IPA from the hydrolysate of Antarctic krill protein using animal proteolytic enzymes could be used to manage hypertension and diabetes because of their strong DPP-IV and/or ACE inhibitory activity [6,33]. Xia et al. (2015) and Han et al. (2018) reported that treatment with phosphorylated peptides from Antarctic krill could significantly prevent the decrease in bone mass and improve porous bone structures and biochemical characteristics of ovariectomized Sprague Dawley rats [30,34]. Hou et al. (2018) and Sun et al. (2021) found that trypsin hydrolysate of Antarctic krill protein and VLGYIQIR could be applied as a novel calcium and zinc supplement [2,31]. Equally, antioxidant peptides from Antarctic krill protein are rarely reported. Then, this study was mainly to isolate and characterize antioxidant peptides from protein hydrolysates of Antarctic krill. Moreover, the antioxidant activity and stability of isolated antioxidant peptides were systematically investigated.

## 2. Results and Discussion

### 2.1. Preparation of Protein Hydrolysates of Antarctic Krill and Their Radical Scavenging Activities

The specificity of protease determines its hydrolysis site, thus significantly affecting the degree of hydrolysis and biological activity of protein hydrolysate [4,35,36]. Therefore, defatted Antarctic krill powder was separately hydrolyzed with alcalase, trypsin, neutrase, pepsin, and papain, and the radical scavenging activity of five protein hydrolysates is

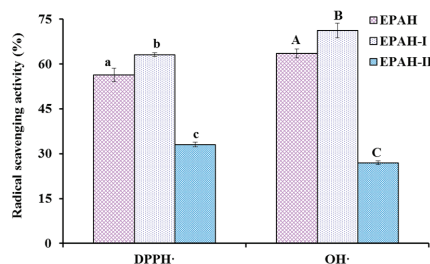
shown in Figure 1. At the concentration of 5.0 mg/mL, the HO· and DPPH· scavenging ratios of alcalase hydrolysate were  $65.99 \pm 1.22\%$  and  $55.32 \pm 1.08\%$ , respectively, which were significantly higher than those of trypsin, neutrase, pepsin, and papain hydrolysates ( $p < 0.05$ ). Alcalase is an endo-protease of the serine type and can degrade most amide bonds of protein molecules, and is usually as a tool enzyme to prepare antioxidant peptides from marine protein resources, such as croceine croaker muscle [37], bluefin tuna heads [38], and swim bladders of miiuy croaker [39]. Therefore, the alcalase hydrolysate (named EPAH) of Antarctic krill proteins was selected for further study.



**Figure 1.** HO· (A) and DPPH· (B) scavenging activities of enzymatic hydrolysates of Antarctic krill (*E. superba*) proteins at the concentration of 5.0 mg/mL. All the results were triplicates of mean  $\pm$  SD. <sup>a–e</sup> Columns with the same superscripts indicate no significant difference ( $p > 0.05$ ).

## 2.2. Preparation of Antioxidant Peptides from EPAH

Using the MW cut-off membrane of 3.5 kDa, EPAH was divided into two peptide fractions including EPAH-I (MW < 3.5 kDa) and EPAH-II (MW > 3.5 kDa), and their antioxidant activity is presented in Figure 2. At the concentration of 5.0 mg/mL, HO· and DPPH· scavenging activities of EPAH-I were  $71.17 \pm 1.52\%$  and  $63.09 \pm 2.40\%$ , respectively, which were significantly higher than those of EPAH ( $65.99 \pm 1.22\%$  and  $55.32 \pm 1.08\%$ ) and EPAH-II ( $27.01 \pm 0.59\%$  and  $33.05 \pm 0.76\%$ ) ( $p < 0.05$ ). MW is considered to be one of the main factors affecting the antioxidant activity [11,37]. Li et al. (2013) and Chi et al. (2016) reported that the antioxidant capacities, including radical scavenging activity and reducing power of collagen hydrolysates from cartilages, were negatively correlated with the logarithm of their average MWs [40,41]. Therefore, EPAH-I with smaller MW showing high radical scavenging activity was in line with these previous reports.

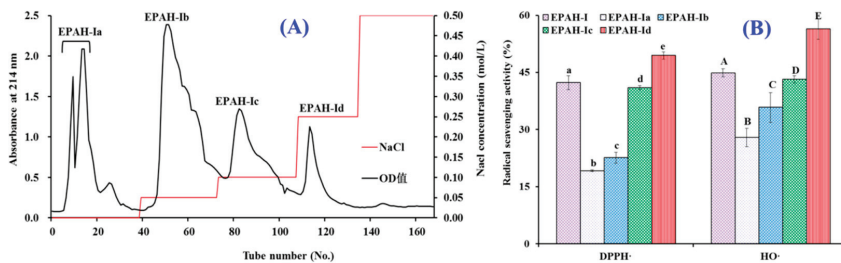


**Figure 2.** HO· and DPPH· scavenging activity (%) of alcalase hydrolysate and its two fractions from Antarctic krill (*E. superba*) proteins at the concentration of 5.0 mg/mL. All the results were triplicates of mean  $\pm$  SD. <sup>a–c or A–C</sup> Columns with the same superscripts of this type indicate no significant difference ( $p > 0.05$ ).

To obtain the sub-fractions with higher antioxidant activity, EPAH-I was fractionated by DEAE-52 cellulose anion-exchange chromatography and separated into four fractions (EPAH-Ia to EPAH-Id) (Figure 3A). EPAH-Ia, EPAH-Ib, EPAH-Ic, and EPAH-Id were eluted out by deionized water, with 0.1, 0.25, and 0.5 M NaCl, respectively. At the concentration of 2.0 mg/mL, the scavenging activities of EPAH-Id on HO· and DPPH· were  $56.38 \pm 2.67\%$

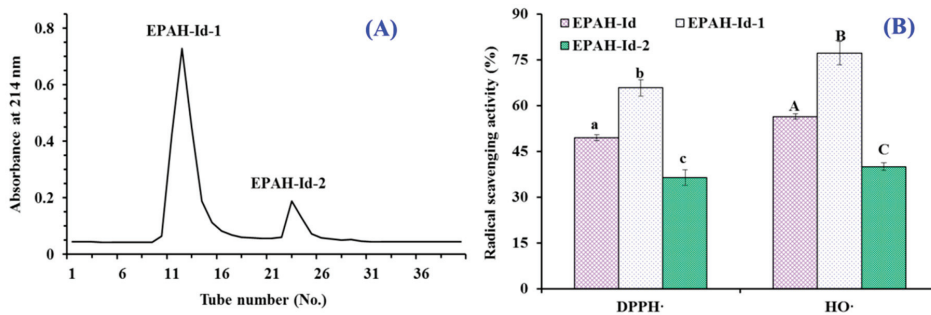


and  $49.43 \pm 0.94\%$ , which were significantly higher than those of EPAH-I, EPAH-Ia, EPAH-Ib, and EPAH-Ic (Figure 3B). Anion-exchange chromatography is a method that separates compounds based on their charges using an ion-exchange resin containing positively charged groups [39,42]. Peptides with hydrophobic amino acid and/or basic residues, such as Leu, Ala, and Pro, are thought to have strong antioxidant activities and are usually isolated from protein hydrolysates using anion exchange resins [43,44]. Therefore, the present data indicated that EPAH-Id might contain high antioxidant amino acid residues and was chosen for further study.



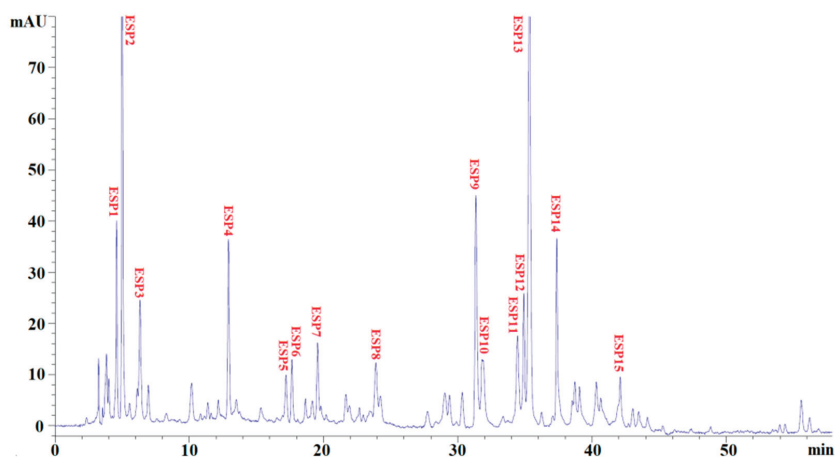
**Figure 3.** DEAE-52 cellulose chromatographic diagram (A) of EPAH-I and radical scavenging activity of EPAH-I and its four fractions (EPAH-Ia to EPAH-Id) at 2.0 mg/mL (B). All the results were triplicates of mean  $\pm$  SD. <sup>a-e</sup> or <sup>A-E</sup> Columns with the same superscripts of this type indicate no significant difference ( $p > 0.05$ ).

Subsequently, EPAH-Id was separated by Sephadex G-25 gel chromatography on the basis of molecular size and two peptide fractions (EPAH-Id-1 and EPAH-Id-2) were prepared according to their chromatographic curves at 214 nm (Figure 4A). Figure 4B indicates that the HO· ( $77.17 \pm 3.8\%$ ) and DPPH· ( $65.77 \pm 0.83\%$ ) scavenging abilities of EPAH-Id-1 at the concentration of 2.0 mg/mL were significantly higher than those of EPAH-Id and EPAH-Id-2 ( $p < 0.05$ ).



**Figure 4.** Sephadex G-25 chromatographic diagram (A) of EPAH-Id and the radical scavenging activity of EPAH-Id and its two fractions (EPAH-Id-1 and EPAH-Id-2) at 2.0 mg/mL (B). All the results were triplicates of mean  $\pm$  SD. <sup>a-c</sup> or <sup>A-C</sup> Values with same superscripts of this type indicate no significant difference ( $p > 0.05$ ).

Using the ultrafiltration and open column chromatography methods, the subfraction of EPAH-Id-1 with high HO· and DPPH· scavenging activity was finally separated using RP-HPLC with a linear gradient of acetonitrile and its peptide profile at 214 nm, presented in Figure 5. Fifteen antioxidant peptides with retention times of 4.46 min (ESP1), 4.92 min (ESP2), 6.21 min (ESP3), 13.01 min (ESP4), 17.19 min (ESP5), 17.78 min (ESP6), 19.65 min (ESP7), 23.84 min (ESP8), 31.41 min (ESP9), 31.93 min (ESP10), 34.46 min (ESP11), 34.97 min (ESP12), 35.34 min (ESP13), 37.38 min (ESP14), and 42.17 min (ESP15), respectively, were isolated, collected and lyophilized (Table 1).



**Figure 5.** Elution profile of EPAH-Id-1 purified using RP-HPLC on a Zorbax SB C-18 column (4.6 mm × 250 mm) from 0 to 60 min at 214 nm.

**Table 1.** Retention time, amino acid sequences, and MWs of fifteen antioxidant peptides (ESP1 to ESP15) from alcalase hydrolysate of Antarctic krill (*E. superba*) proteins.

|       | Retention Time (min) | Amino Acid Sequence | Theoretical MW/Determined MW (Da) |
|-------|----------------------|---------------------|-----------------------------------|
| ESP1  | 4.46                 | NQM                 | 391.44/391.50                     |
| ESP2  | 4.92                 | WFPM                | 579.71/580.03                     |
| ESP3  | 6.21                 | QNPT                | 458.47/458.50                     |
| ESP4  | 13.01                | YMNF                | 573.66/573.50                     |
| ESP5  | 17.19                | SGPA                | 330.34/330.15                     |
| ESP6  | 17.78                | SLPY                | 478.54/478.80                     |
| ESP7  | 19.65                | QYPPMQY             | 926.05/926.00                     |
| ESP8  | 23.84                | EYEA                | 510.49/510.60                     |
| ESP9  | 31.41                | NWDDMRIVAV          | 1218.38/1218.40                   |
| ESP10 | 31.93                | WDDMERLVMI          | 1307.54/1307.40                   |
| ESP11 | 34.46                | NWDDMEPSF           | 1140.18/1140.30                   |
| ESP12 | 34.97                | NGPDPFPSQQ          | 1094.14/1094.21                   |
| ESP13 | 35.34                | AFLWA               | 649.74/650.10                     |
| ESP14 | 37.38                | NVPDM               | 574.65/574.60                     |
| ESP15 | 42.17                | TFPIYDPQ            | 1143.24/1143.30                   |

### 2.3. Identification of Antioxidant Peptides (ESP1 to ESP15) from EPAH-Id-1

Fifteen antioxidant peptides from EPAH-Id-1 (ESP1 to ESP15) underwent massive preparation through repeated RP-HPLC isolation, and their amino acid sequences and MWs were measured using a protein sequencer and ESI-MS. As shown in Table 1, their amino acid sequences were identified as Asn-Gln-Met (NQM, ESP1), Trp-Phe-Pro-Met (WFPM, ESP2), Gln-Asn-Pro-Thr (QNPT, ESP3), Tyr-Met-Asn-Phe (YMNF, ESP4), Ser-Gly-Pro-Ala (SGPA, ESP5), Ser-Leu-Pro-Tyr (SLPY, ESP6), Gln-Tyr-Pro-Pro-Met-Gln-Tyr (QYPPMQY, ESP7), Glu-Tyr-Glu-Ala (EYEA, ESP8), Asn-Trp-Asp-Asp-Met-Arg-Ile-Val-Ala-Val (NWDDMRIVAV, ESP9), Trp-Asp-Asp-Met-Glu-Arg-Leu-Val-Met-Ile (WDDMERLVMI, ESP10), Asn-Trp-Asp-Asp-Met-Glu-Pro-Ser-Phe (NWDDMEPSF, ESP11), Asn-Gly-Pro-Asp-Pro-Arg-Pro-Ser-Gln-Gln (NGPDPFPSQQ, ESP12), Ala-Phe-Leu-Trp-Asn (AFLWA, ESP13), Asn-Val-Pro-Asp-Met (NVPDM, ESP14), and Thr-Phe-Pro-Ile-Tyr-Asp-Tyr-Pro-Gln (TFPIYDPQ, ESP15), and their determined MWs using ESI-MS were well in line with their theoretical MWs (Table 1).

#### 2.4. Antioxidant Activity of Antioxidant Peptides (ESP1 to ESP15)

For evaluating the antioxidant activities of isolated antioxidant peptides (ESP1 to ESP15), assays of radical scavenging, protective activity against radical-induced DNA damage, lipid peroxidation inhibition and reducing power were carried out, and GSH was employed as the positive control. The EC<sub>50</sub> values of fifteen antioxidant peptides (ESP1 to ESP15) on HO·, DPPH·, and O<sub>2</sub><sup>-</sup>· are shown in Table 2.

**Table 2.** EC<sub>50</sub> values of fifteen antioxidant peptides (ESP1 to ESP15) from alcalase hydrolysate of Antarctic krill (*E. superba*) proteins on HO·, DPPH·, and O<sub>2</sub><sup>-</sup>·, respectively.

|                  | Amino Acid Sequence | EC <sub>50</sub> (mg/mL)     |                                |                               |
|------------------|---------------------|------------------------------|--------------------------------|-------------------------------|
|                  |                     | HO·                          | DPPH·                          | O <sub>2</sub> <sup>-</sup> · |
| ESP1             | NQM                 | 1.425 ± 0.067 <sup>a</sup>   | 1.695 ± 0.033 <sup>a,e,i</sup> | 1.796 ± 0.029 <sup>a</sup>    |
| ESP2             | WFFPM               | 1.751 ± 0.075 <sup>b</sup>   | 5.364 ± 0.337 <sup>b</sup>     | 2.746 ± 0.302 <sup>b</sup>    |
| ESP3             | QNPT                | 1.931 ± 0.031 <sup>c,h</sup> | 7.193 ± 0.460 <sup>c</sup>     | 2.933 ± 0.075 <sup>c</sup>    |
| ESP4             | YMNF                | 1.443 ± 0.066 <sup>a,j</sup> | 1.672 ± 0.044 <sup>a,e,i</sup> | 1.136 ± 0.063 <sup>d</sup>    |
| ESP5             | SGPA                | 2.362 ± 0.021 <sup>d</sup>   | 4.135 ± 0.192 <sup>d</sup>     | 1.863 ± 0.104 <sup>a,e</sup>  |
| ESP6             | SLPY                | 0.826 ± 0.027 <sup>e</sup>   | 1.181 ± 0.036 <sup>e</sup>     | 0.789 ± 0.079 <sup>f</sup>    |
| ESP7             | QYPPMQY             | 1.022 ± 0.058 <sup>f</sup>   | 1.547 ± 0.150 <sup>a,e</sup>   | 0.913 ± 0.007 <sup>f</sup>    |
| ESP8             | EYEA                | 0.946 ± 0.011 <sup>e,f</sup> | 1.372 ± 0.274 <sup>a,e</sup>   | 0.793 ± 0.056 <sup>f</sup>    |
| ESP9             | NWDDMRIVAV          | 2.612 ± 0.013 <sup>g</sup>   | 6.192 ± 0.192 <sup>f</sup>     | 3.756 ± 0.025 <sup>g</sup>    |
| ESP10            | WDDMERLVM           | 1.953 ± 0.042 <sup>h</sup>   | 4.719 ± 0.163 <sup>g</sup>     | 1.996 ± 0.011 <sup>e</sup>    |
| ESP11            | NWDDMEPSF           | 2.598 ± 0.036 <sup>g</sup>   | 3.029 ± 0.077 <sup>h</sup>     | 1.862 ± 0.094 <sup>a,e</sup>  |
| ESP12            | NGPDPRPSQQ          | 2.742 ± 0.105 <sup>i</sup>   | 7.054 ± 0.460 <sup>c</sup>     | 2.031 ± 0.011 <sup>e</sup>    |
| ESP13            | AFLWA               | 1.527 ± 0.080 <sup>j,k</sup> | 2.029 ± 0.092 <sup>i</sup>     | 1.162 ± 0.036 <sup>d</sup>    |
| ESP14            | NVPDM               | 1.839 ± 0.032 <sup>b,c</sup> | 4.876 ± 0.145 <sup>g</sup>     | 2.916 ± 0.153 <sup>c</sup>    |
| ESP15            | TFPIYDPQ            | 1.549 ± 0.072 <sup>k</sup>   | 2.135 ± 0.106 <sup>i</sup>     | 1.252 ± 0.051 <sup>d</sup>    |
| Positive control | GSH                 | 0.492 ± 0.063 <sup>l</sup>   | 0.073 ± 0.021 <sup>j</sup>     | 0.250 ± 0.023 <sup>h</sup>    |

All the results were triplicates of mean ± SD. <sup>a-l</sup> Values with same superscripts indicate no significant difference of different peptide on same radicals ( $p > 0.05$ ).

##### 2.4.1. Radical Scavenging Activity of Antioxidant Peptides (ESP1 to ESP15)

In the organism, HO· can oxidize and damage most of the macromolecules due to its high reactivity characteristic. Therefore, looking for natural antioxidant peptides with high HO· scavenging ability is key for discovering new antioxidants. Table 2 shows that EC<sub>50</sub> values of ESP6, ESP7, and ESP8 on HO· were 0.826 ± 0.027, 1.022 ± 0.058, and 0.946 ± 0.011 mg/mL, respectively, which were significantly lower than those of the other twelve antioxidant peptides ( $p < 0.05$ ), but there were significantly higher than that of GSH ( $p < 0.05$ ). In addition, EC<sub>50</sub> values of ESP6, ESP7, and ESP8 were also lower than those of antioxidant peptides from miiuy croaker swim bladders (2.31 ± 0.12, 2.35 ± 0.22, 2.45 ± 0.25, and 2.85 ± 0.19 mg/mL for FTGMD, GFYAA, FSGLR, and VPDD, respectively) [39], weatherfish loach (PSYV: 2.64 mg/mL) [45], skate cartilages (IVAGPQ: 5.03 mg/mL) [18], and heads of bluefin leatherjacket (WEGPK: 5.567 mg/mL) [42]. However, EC<sub>50</sub> values of ESP6, ESP7, and ESP8 were also higher than those of antioxidant peptides from blue mussel (YPPAK: 0.228 mg/mL) [36], miiuy croaker swim bladders (FPYLRH: 0.68 ± 0.05 mg/mL) [39], *Sphyrna lewini* muscle (0.15 and 0.24 mg/mL for WDR and PYFNK, respectively) [46], and giant squid protein (0.123 and 0.078 mg/mL for NGPLQAGQPGER and FDSGPAGVL, respectively) [47,48]. The present finding indicated that the antioxidant peptides from Antarctic krill proteins, especially ESP6, ESP7, and ESP8, could efficiently scavenge HO· to decrease or clear off the damage induced by HO· in biological systems.

Table 2 indicates that ESP6 with EC<sub>50</sub> value of 1.18 ± 0.036 mg/mL exhibited the strongest DPPH· scavenging ability among fifteen antioxidant peptides (ESP1 to ESP15), but the EC<sub>50</sub> value of ESP6 was not significantly different to those of ESP1 (1.695 ± 0.033 mg/mL), ESP4 (1.672 ± 0.044 mg/mL), ESP7 (1.547 ± 0.150 mg/mL), and ESP8 (1.372 ± 0.274 mg/mL),

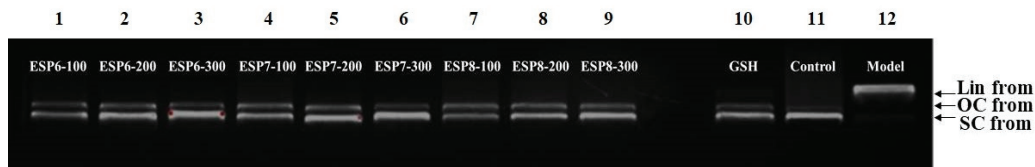
but significantly lower than those of other ten isolated antioxidant peptides ( $p < 0.05$ ). Moreover, the  $EC_{50}$  values of ESP1, ESP4, ESP6, ESP7, and ESP8 were less than those of antioxidant peptides from *Mytilus edulis* (YPPAK: 2.62 mg/mL) [36], weather loach (PSYV: 17.0 mg/mL) [45], *Sphyrna lewini* muscle (3.63 and 4.11 mg/mL for WDR and PYFNK, respectively) [46], and red stingray cartilages (4.01, 4.61, and 3.69 mg/mL for IEEEEQ, VPR, LEEEE, respectively) [49]. However, the  $EC_{50}$  values of ESP1, ESP4, ESP6, ESP7, and ESP8 were higher than those of antioxidant peptides from monkfish muscle (0.39, 0.62, and 0.51 mg/mL for EDIVCW, MEPVW, and YWDAW, respectively) [22], scales of croceine croaker (0.675 and 0.283 mg/mL for GPAGPAG and GFPSPG, respectively) [36], and miiuy croaker swim bladders ( $0.51 \pm 0.03$  and  $0.78 \pm 0.05$  mg/mL for FPYLRH and GIEWA, respectively) [39]. These results indicated that the antioxidant peptides of ESP1, ESP4, ESP6, ESP7, and ESP8 had strong ability to inhibit DPPH· reaction.

Table 2 showed that the  $EC_{50}$  values of ESP6, ESP7, and ESP8 on  $O_2^- \cdot$  were  $0.789 \pm 0.079$ ,  $0.913 \pm 0.007$ , and  $0.793 \pm 0.056$  mg/mL, respectively, which indicated that their  $O_2^- \cdot$  scavenging ability was significantly stronger than those of other twelve antioxidant peptides ( $p < 0.05$ ). However, no significant difference was found among the  $EC_{50}$  values of ESP6, ESP7, and ESP8 ( $p > 0.05$ ). In addition, the  $EC_{50}$  values of ESP6, ESP7, and ESP8 were lower than those of antioxidant peptides from *Raja porosa* cartilage (1.61, 1.66, and 1.82 mg/mL for FIMGPY, GPAGDY, and IVAGPQ, respectively) [18], monkfish muscle (MEPVW: 0.94 mg/mL) [22], croceine croaker muscle (MILMR: 0.993 mg/mL) [37], swim bladders of miiuy croaker ( $3.04 \pm 0.27$ ,  $3.61 \pm 0.25$ ,  $3.03 \pm 0.19$ ,  $3.35 \pm 0.20$ , and  $4.11 \pm 0.31$  mg/mL for FTGMD, YLPYA, GFYAA, FSGLR, and VPDDD, respectively) [39] and muscle (YFLWP: 3.08 mg/mL) [50]. However, The  $EC_{50}$  values of ESP6, ESP7, and ESP8 were higher than those of antioxidant peptides from blue mussel (YPPAK: 0.072 mg/mL) [36], *Sphyrna lewini* muscle (0.09 and 0.11 mg/mL for WDR and PYFNK, respectively) [46], and skipjack tuna heads (0.56, 0.38, and 0.71 mg/mL for WMFDW, WMGPY, and EMGPA, respectively) [25]. In organisms,  $O_2^- \cdot$  can be transformed into the highly reactive HO· and toxic peroxy radicals, which will cause injury to some key biomolecules and further induce oxidative stress. Finally, oxidative stress causes the dysfunction of the organisms, and those influences have been strongly associated with the occurrence and evolution of some chronic diseases [17]. Therefore, ESP6, ESP7, and ESP8 might take on a major responsibility in clearing off  $O_2^- \cdot$  damage in biological systems.

#### 2.4.2. Protective Activity of ESP6, ESP7, and ESP8 against $H_2O_2$ -Damaged Plasmid DNA

DNA damage caused by superfluous ROS in organism is a key point in these ROS-induced degenerative processes, such as premature aging, neurodegenerative and cardiovascular diseases [24,51]. Then, the protective effects of ESP6, ESP7, and ESP8 against  $H_2O_2$ -damaged plasmid DNA (pBR322DNA) were measured and the results are shown in Figure 6. Under normal conditions, the supercoiled (SC) form is the main structure of plasmid DNA (pBR322 DNA) (Figure 6, lane 11). However, a relaxed open circular (OC) form will be generated when one of the phosphodiester chains of pBR322 DNA is split. Moreover, the linear (LIN) double-stranded DNA molecule is produced when second cleavage is near the first breakage. In the assay, HO· was generated from the chemical reaction of  $FeSO_4$  and  $H_2O_2$ , and it further cut off the DNA strands and converted the SC form into the OC form and LIN form structures [24,51,52]. Lane 12 in Figure 6 showed that the SC form of plasmid DNA (pBR322 DNA) was mainly converted into LIN form, which indicated that excessive HO· generated in the reaction broke the double strand of pBR322 DNA. As shown in Figure 6 (lane 1 to lane 9), the contents of the SC form of pBR322 DNA was obviously higher than that of the model group (Figure 6, lane 11). In addition, the contents of the SC form of pBR322 DNA in ESP6, ESP7, and ESP8 groups showed a significant concentration–effect relationship. In the high-dose groups, ESP6, ESP7, and ESP8 achieved similar protective effects to that of the positive control group (Figure 6, lane 10). These data indicated that ESP6, ESP7, and ESP8 have significant protective ability on

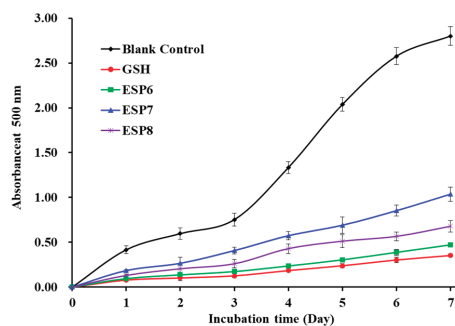
plasmid DNA (pBR322 DNA). These results were also in line with the finding in Table 2 that ESP6, ESP7, and ESP8 could effectively scavenge HO $\cdot$  to protect biomolecules.



**Figure 6.** The protective effects of ESP6, ESP7, and ESP8 on the H<sub>2</sub>O<sub>2</sub>-damaged plasmid DNA (pBR322DNA). Lane 1, DNA + FeSO<sub>4</sub> + H<sub>2</sub>O<sub>2</sub> + ESP6 (100 μM); Lane 2, DNA + FeSO<sub>4</sub> + H<sub>2</sub>O<sub>2</sub> + ESP6 (200 μM); Lane 3, DNA + FeSO<sub>4</sub> + H<sub>2</sub>O<sub>2</sub> + ESP6 (300 μM); Lane 4, DNA + FeSO<sub>4</sub> + H<sub>2</sub>O<sub>2</sub> + ESP7 (100 μM); Lane 5, DNA + FeSO<sub>4</sub> + H<sub>2</sub>O<sub>2</sub> + ESP7 (200 μM); Lane 6, DNA + FeSO<sub>4</sub> + H<sub>2</sub>O<sub>2</sub> + ESP7 (300 μM); Lane 7, DNA + FeSO<sub>4</sub> + H<sub>2</sub>O<sub>2</sub> + ESP8 (100 μM); Lane 8, DNA + FeSO<sub>4</sub> + H<sub>2</sub>O<sub>2</sub> + ESP8 (200 μM); Lane 9, DNA + FeSO<sub>4</sub> + H<sub>2</sub>O<sub>2</sub> + ESP8 (300 μM); Lane 10, DNA + FeSO<sub>4</sub> + H<sub>2</sub>O<sub>2</sub> + GSH (200 μM); Lane 11, the native pBR322DNA; Lane 12, pBR322DNA + FeSO<sub>4</sub> + H<sub>2</sub>O<sub>2</sub>.

#### 2.4.3. Lipid Peroxidation Inhibition Assay of ESP6, ESP7, and ESP8

Lipid peroxidation is a key factor of the aging process and pathophysiology of many chronic diseases [42]. In addition, lipid peroxidation can change food properties, including nutrition, texture, flavor, color, and luster, to give rise to food deterioration. In the linoleic acid system, the lipid peroxidation inhibition abilities of ESP6, ESP7, and ESP8 were measured and the lower absorbance at 500 nm illustrates higher antioxidant ability [25]. Figure 7 indicates the absorbance value of the blank control group was significantly higher than those of antioxidant peptides (ESP6, ESP7, and ESP8) groups, which indicated that ESP6, ESP7, ESP8, and GSH can effectively control the peroxidation reaction when they were incubated with linoleic acid for 7 days. Furthermore, the absorbance values of the ESP6 group were lower than those of ESP7 and ESP8 groups. Then, ESP6, ESP7, and ESP8 could serve as the natural antioxidant agents to control lipid oxidation in organisms and fat-rich foods.

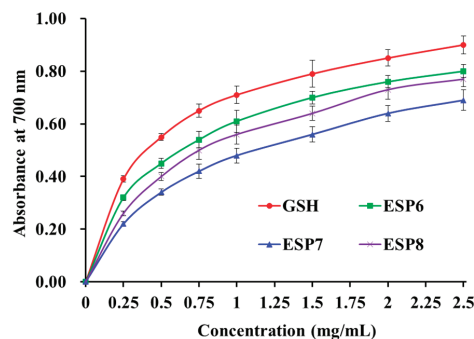


**Figure 7.** Lipid peroxidation inhibition capability of ESP6, ESP7, and ESP8 from the alcalase hydrolysate of Antarctic krill (*E. superba*) proteins. All the results were triplicates of mean  $\pm$  SD.

#### 2.4.4. Reducing Power of ESP6, ESP7, and ESP8

As presented in Figure 8, the reducing power of ESP6, ESP7, and ESP8 showed a certain dose–effect relationship when their concentrations were decreased from 0 to 2.5 mg/mL. The result illustrated that ESP6 had a higher reducing capacity to convert Fe<sup>3+</sup>/ferricyanide complex into the ferrous form than ESP7 and ESP8. However, the reducing power of ESP6, ESP7, and ESP8 was less than that of GSH. The reducing power is considered to be an important indicator of the potential activity of antioxidant peptides in reduction reactions, which can be used to evaluate their abilities to provide hydrogen and/or electrons [41,50].

The present results suggested that ESP6, ESP7, and ESP8 could serve as electron donors to reduce the oxidized intermediates in lipid peroxidation reactions of organisms.



**Figure 8.** The reducing power of ESP6, ESP7, and ESP8 from the alcalase hydrolysate of Antarctic krill (*E. superba*) proteins. All the results were triplicates of mean  $\pm$  SD.

Antioxidant peptides have been prepared from different food protein resources. Molecular size is believed to play an essential role in their activities [11]. Antioxidant peptides with smaller molecules can be more accessible to free radicals to control the cycle of lipid peroxidation [11,53]. Moreover, molecular size is an important constraint for antioxidant peptides striding over the blood–brain barrier to exert their pharmacological activities in living organisms [54]. Therefore, ESP6, ESP7, and ESP8 could be easily close to the free radical to play their functions, because they were oligopeptides with MWs of 478.80, 926.00, and 510.90 Da, respectively (Table 1).

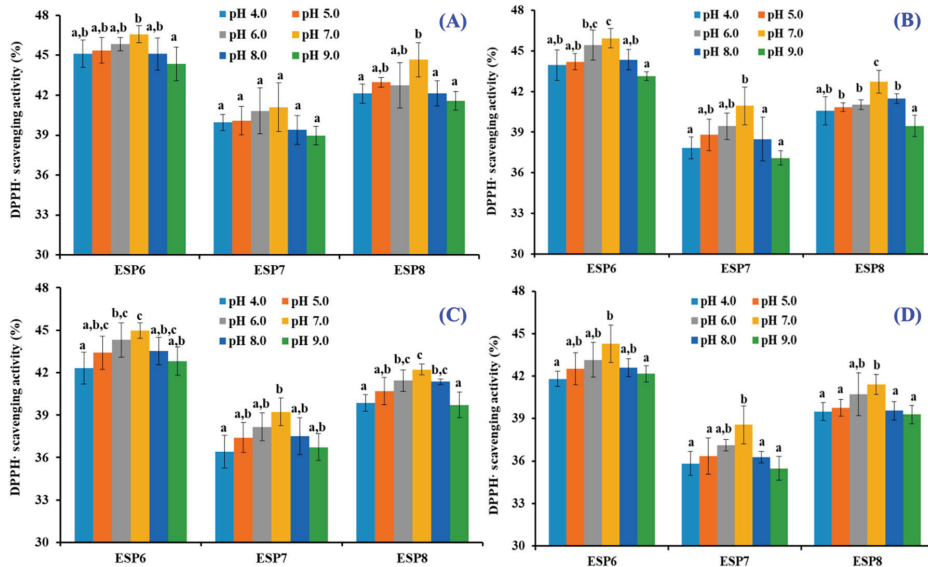
Amino acid composition, including species, sequence and spatial structure, is another key factor thought to be involved in the bioactivities of antioxidant peptides [11]. Hydrophobic and aromatic amino acids, such as Leu, Pro, Tyr, Phe, Ala, and Met, have an important impact on the activity of antioxidant peptides because those amino acids could raise the antioxidant activities through improving the lipid solubility and combination with radical species of antioxidant peptides [11,21]. Rajapakse et al. (2005) and Gulçin (2007) reported that Leu showed the highest antioxidant activity among the amino acids [55,56]. Chen et al. (2020) speculated that Leu and Thr contribute to the highest activity of IL-GATIDNSK from defatted round scad [57]. Yang et al. (2019) reported that Ala, Ile, and Val in GADIVA, and Ala and Ile in GAEGFIF could assist them in a conducive manner to combine with target radicals [26]. Wu et al. (2018) reported that Met residue contributed greatly to the inhibition of free-radical chain reactions of PMRGGGGYHY because it could form a sulfoxide structure, which acted as a reactive site to clear oxidants [58]. Therefore, Leu, Met, and Ala should play a key role in the antioxidant activity of ESP6, ESP7, and ESP8, respectively.

Wong et al. (2020) reported that Pro could serve as a proton/hydrogen donor to play its antioxidant role [59]. In addition, Pro could increase the flexibility of bioactive peptides, and the low ionization potential of its pyrrolidine ring could quench singlet oxygen [53]. Therefore, Pro presented in ESP6 and ESP7 are important for their bioactivities. Tyr residues could remove free radicals and provide protons to electron-deficient radicals to change them into more stable phenoxy radicals, which could inhibit the peroxidizing serial reaction induced by ROS during the scavenging process [60,61]. Wu et al. (2018) and Sheih et al. (2009) reported that Tyr could act as hydrogen donors to play an important role in antioxidant activity, because it could remove free radicals and change them into more stable phenoxy radicals, which inhibited the propagation of the radical-mediated peroxidizing chain reaction [58,61]. Guo et al. (2009) reported that antioxidant peptides with Tyr residues (YDY, RY, YEEN, KY, YEG, YD, YY, and RYN) showed high antioxidant ability [62]. Then, Tyr is contributed to the bioactivity of ESP6, ESP7, and ESP8.

In the lipid and aqueous solutions of oxidation, the ratio of hydrophilic/hydrophobic amino acids in antioxidant peptides can significantly affect their solubility and biological activity [21,63]. Therefore, the hydrophobic amino acids were critical for their protective response in lipid peroxidation by eliminating the free radicals derived from lipids in a heterogeneous lipid phase [64]. Gly residue can maintain the strong flexibility of the polypeptide skeleton and act as single hydrogen donor to neutralize ROS [25,65]. Hydrophilic amino acids including Glu, Gln, and Lys in EVGK and RCLQ have a positive influence on their  $\text{Fe}^{2+}$  chelating ability [65]. Asp, Glu, and Gln were found to show remarkable influence on the antioxidant abilities of NYDGSTDYGLQINSR and LDEPDPLI [66,67]. Therefore, Ser, Gln, and Glu are also contribute to the radical-scavenging, lipid peroxidation inhibitory, and reducing power ability of ESP6, SP7, and ESP8, respectively.

### 2.5. Effects of pH, Thermal, and Simulated GI Digestion Treatments on the Stability of ESP6, ESP7, and ESP8

Figure 9 indicates that the DPPH· scavenging activity of ESP6, ESP7, and ESP8 treated with designated pH values has the same varying tendency. Under neutral conditions, ESP6, ESP7, and ESP8 showed the highest activity. In addition, it could be found that the DPPH· scavenging activity of ESP6, ESP7, and ESP8 decreased gradually with the time from 0 to 180 min. Except 30 min, DPPH· scavenging activity of ESP6, ESP7, and ESP8 subjected to pH 7.0 treatment was significantly higher than those of ESP6, ESP7, and ESP8 subjected to pH 4.0 and 9.0 treatments. The results indicated that high acid and alkali treatments had significant negative effects on the antioxidant activity of ESP6, ESP7, and ESP8. Table 3 shows that the reduced proportion of ESP6 treated for 180 min at different pH values was smaller than those of ESP7 and ESP8, which indicated that the pH stability of ESP6 was higher than those of ESP7 and ESP8.



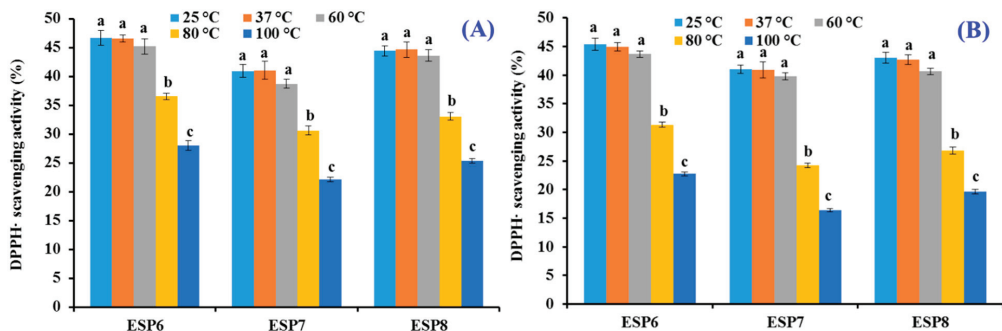
**Figure 9.** DPPH· scavenging activity of ESP6, ESP7, and ESP8 subjected to different pH treatments for 30 min (A), 60 min (B), 120 min (C), and 180 min (D), respectively. All the results were triplicates of mean  $\pm$  SD. <sup>a-c</sup> values with same letters indicate no significant difference of same peptide subjected to different pH treatments ( $p > 0.05$ ).

**Table 3.** Reduced proportion of DPPH· scavenging activity of ESP6, ESP6, and ESP8 subjected to different pH treatments for 180 min.

|      | Reduced Proportion of DPPH· Scavenging Activity (%) |             |             |             |             |             |
|------|---|-------------|-------------|-------------|-------------|-------------|
|      | pH 4.0  | pH 5.0      | pH 6.0      | pH 7.0      | pH 8.0      | pH 9.0      |
| ESP6 | 5.76 ± 0.06   | 5.06 ± 0.55 | 4.42 ± 0.73 | 3.29 ± 0.77 | 4.99 ± 0.58 | 5.41 ± 0.95 |
| ESP7 | 6.95 ± 0.65   | 6.44 ± 0.79 | 5.65 ± 1.33 | 4.22 ± 1.34 | 6.49 ± 1.21 | 7.29 ± 0.99 |
| ESP8 | 6.99 ± 6.72   | 6.72 ± 0.87 | 5.74 ± 1.36 | 5.05 ± 0.89 | 6.92 ± 0.99 | 7.19 ± 0.52 |

Data are expressed as mean ± SD ( $n = 3$ ).

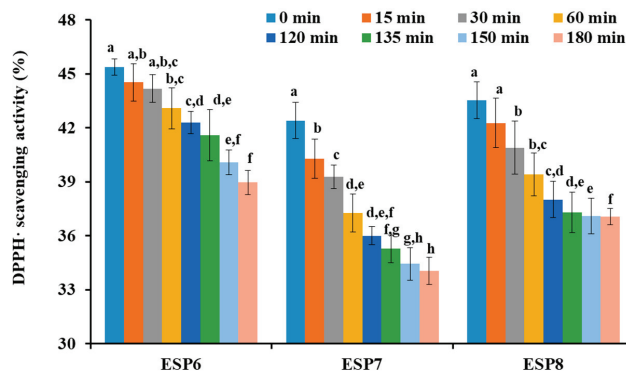
As shown in Figure 10, different temperature treatments could greatly affect the DPPH· scavenging activities of ESP6, ESP7, and ESP8. The DPPH· scavenging activities of ESP6, ESP7, and ESP8 at 25, 37, and 60 °C for 30 and 60 min were significantly different from those treated at 80 and 100 °C for 30 and 60 min, respectively ( $p < 0.05$ ). In addition, there was no significant difference of the DPPH· scavenging activities of ESP6, ESP7, and ESP8 at 25, 37, and 60 °C for 30 and 60 min ( $p > 0.05$ ). In addition, the DPPH· scavenging activities of ESP6, ESP7, and ESP8 decreased by 51.42 ± 2.76%, 60.26 ± 3.51%, and 56.01 ± 1.98%, respectively, at 100 °C when the time was ranged from 0 min to 60 min. Those data suggested that ESP6 was more tolerant to high temperatures compared with ESP7 and ESP8.



**Figure 10.** DPPH· scavenging activity of ESP6, ESP7, and ESP8 subjected to different thermal treatments for 30 min (A) and 60 min (B). All the results were triplicates of mean ± SD. <sup>a-c</sup> Values with same letters indicate no significant difference of same peptide subjected to different temperature treatments ( $p > 0.05$ ).

In response to simulated GI digestion, the DPPH· scavenging ratios of ESP6, ESP7, and ESP8 are shown in Figure 11. The data indicated that DPPH· scavenging activities of ESP6, ESP7, and ESP8 at the concentration of 1.0 mg/mL were decreased gradually with the treating time ranged from 0 to 180 min. The DPPH· scavenging activities of ESP6, ESP7, and ESP8 before simulated GI digestion (ESP6: 45.39 ± 0.46%; ESP7: 42.41 ± 1.01%; ESP8: 43.54 ± 1.02%) were significantly ( $p < 0.05$ ) lower than those obtained after simulated GI digestion (ESP6: 38.97 ± 0.67%; ESP7: 34.05 ± 0.74%; ESP8: 37.06 ± 0.45%). Furthermore, the DPPH· scavenging ratios of ESP6, ESP7, and ESP8 decreased by 6.41 ± 0.96%, 8.36 ± 0.59%, and 6.48 ± 1.03%, respectively, which suggested that ESP6 has stronger stability than ESP7 and ESP8 when they were treated with simulated GI digests.





**Figure 11.** DPPH-scavenging activity of ESP6, ESP7, and ESP8 subjected to simulated GI digestion treatments from 0 to 180 min. All the results were triplicates of mean  $\pm$  SD. <sup>a-h</sup> Values with same letters indicate no significant difference of same sample at different time ( $p > 0.05$ ).

The pH and thermal stability of antioxidant peptides are key properties for their applications in food and health products, and tolerance property on simulated GI digestion treatments can help to assess the rate of metabolism and timeliness of antioxidant peptides in vivo [25,52,68,69]. The previous literature indicated that WAFAPA and MYPGLA with 25–100 °C or pH 3–11 treatments show high stability [59], but ATSHH treated with 50–90 °C and strong acids and bases will decrease its partial DPPH-scavenging activity [70]. Zhang et al. (2019) found that the HO $\cdot$  scavenging activity of WMFDW, WMGPY, and EMGPA could be significantly influenced under high temperature (>60 °C) and strong acid and alkali conditions [25]. The present results indicated that ESP6 (SLPY), ESP7 (QYPPMQY), and ESP8 (EYEA) had similar thermal and pH stability to ATSHH, WMFDW, WMGPY, and EMGPA because their activity was significantly decreased under high temperature (>60 °C) and strong acid and alkali conditions. In addition, the stability of ESP6 (SLPY) was higher than those of ESP7 (QYPPMQY) and ESP8 (EYEA) under thermal, pH, and simulated GI digestion treatments.

### 3. Materials and Methods

#### 3.1. Materials

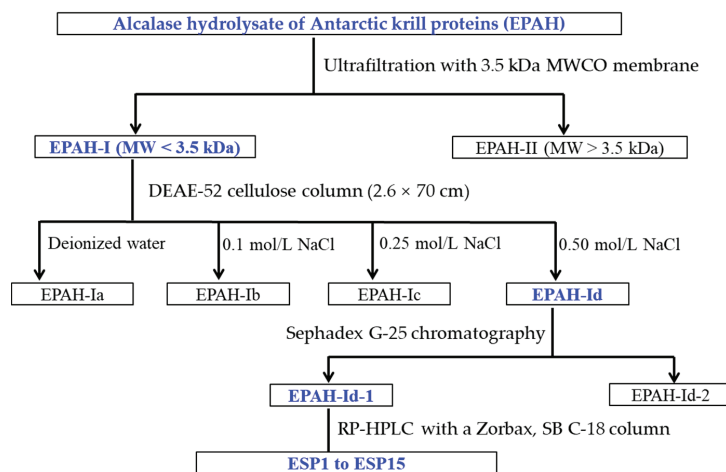
Antarctic krill (*E. superba*) powder was kindly provided by Zhejiang Hailisheng Biotechnology Co. Ltd. (Zhoushan, China). Trypsin, papain, trifluoroacetic acid, 2,2-Diphenyl-1-picrylhydrazyl (DPPH), phosphate buffered saline, Sephadex G-25, and pepsin, were purchased from Sigma-Aldrich (Shanghai) Trading Co., Ltd. (Shanghai, China). Neutrase was purchased from Imperial Jade Biotechnology, Co. Ltd. (Yinchuan, China). Alcalase was purchased from Novozymes Biotechnology Co., Ltd. (Tianjin, China). Diethylaminoethyl (DEAE)-52 cellulose anion exchange resin was purchased from Nanjing Jiancheng Bioengineering Co., Ltd. (Nanjing, China). Acetonitrile was bought from Thermo Fisher Scientific (Shanghai) Co., Ltd. (Shanghai, China).

#### 3.2. Preparation of Protein Hydrolysate of Antarctic Krill (EPAH)

The Antarctic krill powder was defatted according to our previous method with a light modification [4]. Subsequently, the defatted shrimp powder was dissolved in 0.05 M phosphate buffer with a solid/liquid ratio of 1:30, and the mixed solutions were treated for 6 h separately using pepsin (pH 2.0, 37 °C), alcalase (pH 8.5, 50 °C), papain (pH 6.0, 50 °C), neutrase (pH 7.0, 60 °C), and trypsin (pH 8.0, 40 °C) with total dosage of enzyme of 2.0% ( $w/w$ ). After hydrolysis reaction, five hydrolysates were kept in a boiling water bath for 15 min to inactivate enzymes and centrifuged at  $4000 \times g$  for 15 min. The supernatants of five hydrolysates were concentrated, lyophilized and kept in a  $-20$  °C refrigerator. In addition, alcalase hydrolysate was named EPAH.

### 3.3. Preparation of Antioxidant Peptides from Alcalase Hydrolysate (EPAH) of Antarctic Krill Proteins

Antioxidant peptides were purified from EPAH by the ultrafiltration and chromatographic process (Figure 12).



**Figure 12.** The flow chart of purifying antioxidant peptides from alcalase hydrolysate (EPAH) of Antarctic krill (*E. superba*) proteins.

EPAH was ultrafiltrated by 3.5 kDa molecular weight (MW) cut-off membrane, and two peptide fractions of EPAH-I (MW < 3.5 kDa) and EPAH-II (MW > 3.5 kDa) were prepared.

EPAH-I solution (6 mL, 50.0 mg/mL) was loaded onto a DEAE-52 cellulose column (2.6 × 70 cm) pre-equilibrated with deionized water, and eluted with deionized water, and a 0.10, 0.25, and 0.50 M NaCl solution, respectively. The flow rate of eluent was set as 3.0 mL/min and monitored at 214 nm. Four fractions (EPAH-Ia to EPAH-Id) were collected according to chromatogram map.

An amount of 5 mL of EPAH-Id solution (50.0 mg/mL) was injected into the Sephadex G-25 chromatographic column (2.6 cm × 120 cm) and eluted using ultrapure water. The eluent with a flow rate of 0.6 mL/min was collected every 3 min and two components, named EPAH-Id-1 and EPAH-Id-2, were isolated according to the chromatographic curve of EPAH-Id at 214 nm.

EPAH-Id-1 was further separated by the Agilent 1200 HPLC system (Agilent Ltd., Santa Clara, CA, USA) on a Zorbax, SB C-18 column (4.6 × 250 mm, 5 μm) using a linear gradient of acetonitrile (0–100% in 0–60 min) in 0.05% trifluoroacetic acid. The elution solution with a flow rate of 0.8 mL/min was monitored at 214 nm. Finally, fifteen antioxidant peptides (ESP1 to ESP15) were isolated from EPAH-Id-1 on their chromatographic peaks, lyophilized, and kept in a −20 °C refrigerator.

### 3.4. Identification of Antioxidant Peptides (ESP1 to ESP15) from EPAH-Id-1

The Applied Biosystems 494 protein sequencer (Perkin Elmer/Applied Biosystems Inc., Foster City, CA, USA) was employed to analyze the N-terminal amino acid sequences of fifteen antioxidant peptides (ESP1 to ESP15), and the Q-TOF mass spectrometer (MS) (Micromass, Waters, Milford, MA, USA) with an electrospray ionization (ESI) source were applied to measure the MWs of fifteen antioxidant peptides (ESP1 to ESP15).

### 3.5. Antioxidant Activities of Antioxidant Peptides (ESP1 to ESP15)

The scavenging assays of DPPH radical (DPPH·), superoxide anion radical ( $O_2^{\cdot-}$ ), and hydroxyl radical (HO·) were determined on the previous method [35,36], and the  $EC_{50}$  values of antioxidant peptides (ESP1 to ESP15) on DPPH·, HO·, and  $O_2^{\cdot-}$  were defined as the sample concentration induced half of the decrease in the initial radical contents. The assays of reducing power and lipid peroxidation inhibition were performed according to the methods described by Zhang et al. (2019) [25], and GSH was used as the positive control in all antioxidant assays.

### 3.6. Stability Characteristics of ESP6, ESP7, and ESP8 against the Treatments of Heat, pH, and Simulated Gastrointestinal (GI) Digestion

The pH stability and thermostability of ESP6, ESP7, and ESP8 were analyzed in accordance with the previous method with a light modification [25]. In short, effects of acid and alkali treatments at pH values of 5, 6, 7, 8, or 9 were employed to estimate the acid and alkali stability characteristics of ESP6, ESP7, and ESP8 at 25 °C, and the analyzed time was set to 30, 60, 120, and 180 min.

The thermostability of ESP6, ESP7, and ESP8 at 25, 37, 60, 80, or 100 °C was analyzed in water bath, and the analyzed time was set to 30 and 60 min.

The influence of simulate GI digestion on the stability of ESP6, ESP7, and ESP8 was evaluated by the two-stage digestion model [26]. In short, ESP6, ESP7, and ESP8 were separately treated with pepsin for 120 min and pancreatin for 60 min.

The DPPH· scavenging ratio (%) of ESP6, ESP7, and ESP8 at 1.0 mg/mL were measured at the set time to analyze their stability.

### 3.7. Statistical Analysis

The experiment data were represented as the mean  $\pm$  standard deviation (SD,  $n = 3$ ). An ANOVA test using SPSS 19.0 (SPSS Corporation, Chicago, IL, USA) was employed to analyze the means of each treatment, and Duncan's multiple range test was applied to analyze the significant differences among the different groups ( $p < 0.05$ ).

## 4. Conclusions

In summary, the purification, identification, activity evaluation and stability of antioxidant peptides from alcalase hydrolysate of Antarctic krill (*E. superba*) proteins were systematically studied, and fifteen antioxidant peptides were purified from alcalase hydrolysate and identified as NQM, WFPM, QNPT, YMNE, SGPA, SLPY, QYPPMQY, EYEA, NWDDMRIVAV, WDDMERLVMI, NWDDMEPSE, NGPDRPSQQ, AFLWA, NVPDM, and TFPIYDPQ, respectively. Among them, SLPY, QYPPMQY and EYEA showed high radical scavenging activities,  $H_2O_2$ -damaged plasmid DNA protective effects, reducing power, and lipid peroxidation inhibition ability. In addition, SLPY, QYPPMQY, and EYEA had high stability under temperatures lower than 80 °C, pH values ranged from 6–8, and simulated GI digestion for 180 min. The present results provided support for SLPY, QYPPMQY and EYEA to serve as effective antioxidant agents used in health-promoting food products. The antioxidant mechanism in vivo models and the clinical efficacy of SLPY, QYPPMQY and EYEA have been researched in our lab.

**Author Contributions:** S.-Y.Z. and G.-X.Z.: conceptualization, data curation, formal analysis, investigation, methodology, validation, writing—original draft. G.-X.Z. and S.-K.S.: conceptualization, data curation, formal analysis, investigation, methodology, validation. Y.-M.W.: conceptualization, data curation, formal analysis, investigation, methodology, validation, writing—original draft. C.-F.C.: funding acquisition, resources, supervision, writing—review and editing. B.W.: conceptualization, funding acquisition, resources, supervision, writing—review and editing. All authors have read and agreed to the published version of the manuscript.

**Funding:** This work was funded by the National Natural Science Foundation of China (No. 82073764) and Ten-thousand Talents Plan of Zhejiang Province (No. 2019R52026).

**Institutional Review Board Statement:** Not applicable.

**Informed Consent Statement:** Not applicable.

**Data Availability Statement:** Data are contained within the article.

**Conflicts of Interest:** The authors declare no competing financial interest.

## Abbreviations

ROS, reactive oxide species; EDIVCW, Glu-Asp-Ile-Val-Cys-Trp; YWDAW, Tyr-Trp-Asp-Ala-Trp; GSH, glutathione; FPYLRH, Phe-Pro-Tyr-Leu-Arg-His; HUVECs, human umbilical vein endothelial cells; MDA, malondialdehyde; ICRD, Ile-Cys-Arg-Asp; LCGEC, Leu-Cys-Gly-Glu-Cys; Keap1, Kelch-like ECH-associating protein 1; Nrf2, nuclear factor erythroid 2-related factor 2; ARE, antioxidant response element; EDYGA, Glu-Asp-Tyr-Gly-Ala; DPP-IV, dipeptidyl peptidase IV; ACE, angiotensin converting enzyme; FAS, Phe-Ala-Ser; KVEPLP, Lys-Val-Glu-Pro-Lys-Pro; PAL, Pro-Ala-Lys; IPA, Ile-Pro-Ala; VLGYIQIR, Val-Lys-Gly-Tyr-Ile-Gln-Ile-Arg; DEAE, diethylaminoethyl; DPPH, 2,2-Diphenyl-1-picrylhydrazyl; EPAH, the alcalase hydrolysate of *Euphausia superba* proteins; MW, molecular weight; ESL, electrospray ionization; MS, mass spectrometer; DPPH·, DPPH radical; HO·, hydroxyl radical; O<sub>2</sub><sup>-</sup>, superoxide anion radical; GI, Gastrointestinal; FTGMD, Phe-Thr-Gly-Met-Asp; GFYAA, Gly-Phe-Tyr-Ala-Ala; FSGLR, Phe-Ser-Gly-Leu-Arg; VPDD, Val-Pro-Asp-Asp; PSYV, Pro-Ser-Tyr-Val; IVAGPQ, Ile-Val-Ala-Gly-Pro-Gln; WEGPK, Trp-Gly-Pro-Lys; YPPAK, Tyr-Pro-Ala-Lys; WDR, Trp-Asp-Arg; NGPLQAGQPGER, Asn-Gly-Pro-Leu-Gln-Ala-Gly-Gln-Pro-Gly-Glu-Arg; PYFNK, Pro-Tyr-Phe-Asn-Lys; FDSGPAGVL, Phe-Asp-Ser-Gly-Pro-Ala-Gly-Val-Leu; IEEEEQ, Ile-Glu-Glu-Glu-Gln; VPR, Val-Pro-Arg; LEEEEE, Leu-Glu-Glu-Glu-Glu; MEPVW, Met-Glu-Pro-Val-Trp; GPAGPAG, Gly-Pro-Ala-Gly-Pro-Ala-Gly; GFPSG, Gly-Phe-Pro-Ser-Gly; FPYLRH, Phe-Pro-Tyr-Leu-Arg-His; GIEWA, Gly-Ile-Glu-Trp-Ala; FIMGPY, Phe-Ile-Met-Gly-Pro-Tyr; GPAGDY, Gly-Pro-Ala-Gly-Asp-Tyr; MILMR, Met-Ile-Leu-Met-Arg; YLPYA, Tyr-Leu-Pro-Tyr-Ala; YFLWP, Tyr-Phe-Leu-Trp-Pro; WMFDW, Trp-Met-Phe-Asp-Trp; WMGPY, Trp-Met-Gly-Pro-Tyr; EMGPA, Glu-Met-Gly-Pro-Ala; ILGATIDNSK, Ile-Leu-Gly-Ala-Thr-Ile-Asp-Asn-Ser-Lys; GADIVA, Gly-Ala-Asp-Ile-Val-Ala; GAEG-FIF, Gly-Sla-Glu-Gly-Phe-Ile-Phe; PMRGGGGYHY, Pro-Met-Arg-Gly-Gly-Gly-Gly-Tyr-His-Tyr; YDY, Tyr-Asp-Tyr; RY, Arg-Tyr; YEEN, Tyr-Glu-Glu-Asn; KY, Lys-Tyr; YEG, Tyr-Glu-Gly; YD, Tyr-Asp.

## References

- Nicol, S.; Foster, J.; Kawaguchi, S. The fishery for Antarctic krill—Recent developments. *Fish Fish* **2011**, *13*, 30–40. [\[CrossRef\]](#)
- Sun, R.; Liu, X.; Yu, Y.; Miao, J.; Leng, K.; Gao, H. Preparation process optimization, structural characterization and in vitro digestion stability analysis of Antarctic krill (*Euphausia superba*) peptides zinc chelate. *Food Chem.* **2021**, *340*, 128056. [\[CrossRef\]](#)
- Chu, F.; Wang, D.; Liu, T.; Han, H.; Yu, Y.; Yang, Q. An optimized cocktail of chitinolytic enzymes to produce N, N'-diacetylchitobiose and N-acetyl-d-glucosamine from defatted krill by-products. *Int. J. Biol. Macromol.* **2019**, *133*, 1029–1034. [\[CrossRef\]](#) [\[PubMed\]](#)
- Lan, C.; Zhao, Y.Q.; Li, X.R.; Wang, B. High Fischer ratio oligopeptides determination from Antarctic krill: Preparation, peptides profiles, and in vitro antioxidant activity. *J. Food Biochem.* **2019**, *43*, e12827. [\[CrossRef\]](#) [\[PubMed\]](#)
- Hatanaka, A.; Miyahara, H.; Suzuki, K.I.; Sato, S. Isolation and identification of antihypertensive peptides from antarctic krill tail meat hydrolysate. *J. Food Sci.* **2009**, *74*, H116–H120. [\[CrossRef\]](#) [\[PubMed\]](#)
- Ji, W.; Zhang, C.; Ji, H. Purification, identification and molecular mechanism of two dipeptidyl peptidase IV (DPP-IV) inhibitory peptides from Antarctic krill (*Euphausia superba*) protein hydrolysate. *J. Chromatogr. B* **2017**, *1064*, 56–61. [\[CrossRef\]](#)
- Choi, J.Y.; Jang, J.S.; Son, D.J.; Im, H.S.; Kim, J.Y.; Park, J.E.; Choi, W.R.; Han, S.B.; Hong, J.T. Antarctic krill oil diet protects against lipopolysaccharide-induced oxidative stress, neuroinflammation and cognitive impairment. *Int. J. Mol. Sci.* **2017**, *18*, 2554. [\[CrossRef\]](#) [\[PubMed\]](#)
- Wang, K.; Li, Y.; Dai, Y.; Han, L.; Zhu, Y.; Xue, C.; Wang, P.; Wang, J. Peptides from Antarctic Krill (*Euphausia superba*) Improve Osteoarthritis via Inhibiting HIF-2 $\alpha$ -Mediated Death Receptor Apoptosis and Metabolism Regulation in Osteoarthritic Mice. *J. Agric. Food Chem.* **2019**, *67*, 3125–3133. [\[CrossRef\]](#)
- Yu, Y.; Liu, X.; Miao, J.; Leng, K. Chitin from Antarctic krill shell: Eco-preparation, detection, and characterization. *Int. J. Biol. Macromol.* **2020**, *164*, 4125–4137. [\[CrossRef\]](#)
- Zhou, X.; Xiang, X.; Zhou, Y.; Zhou, T.; Deng, S.; Zheng, B.; Zheng, P. Protective effects of Antarctic krill oil in dextran sulfate sodium-induced ulcerative colitis mice. *J. Funct. Foods* **2021**, *79*, 104394. [\[CrossRef\]](#)

11. Sila, A.; Bougatef, A. Antioxidant peptides from marine by-products: Isolation, identification and application in food systems. A review. *J. Funct. Foods* **2016**, *21*, 10–26. [[CrossRef](#)]
12. Chai, T.T.; Law, Y.C.; Wong, F.C.; Kim, S.K. Enzyme-Assisted Discovery of Antioxidant Peptides from Edible Marine Invertebrates: A Review. *Mar. Drugs* **2017**, *15*, 42. [[CrossRef](#)] [[PubMed](#)]
13. Bashir, K.M.I.; Sohn, J.H.; Kim, J.S.; Choi, J.S. Identification and characterization of novel antioxidant peptides from mackerel (*Scomber japonicus*) muscle protein hydrolysates. *Food Chem.* **2020**, *323*, 126809. [[CrossRef](#)]
14. Wang, Y.M.; Pan, X.; He, Y.; Chi, C.F.; Wang, B. Hypolipidemic activities of two pentapeptides (VIAPW and IRWWW) from miiuy croaker (*Miichthys miiuy*) muscle on lipid accumulation in HepG2 cells through regulation of AMPK pathway. *Appl. Sci.* **2020**, *10*, 817. [[CrossRef](#)]
15. Manikkam, V.; Vasiljevic, T.; Donkor, O.N.; Mathai, M.L. A review of potential marine-derived hypotensive and anti-obesity peptides. *Crit. Rev. Food Sci. Nutr.* **2016**, *56*, 92–112. [[CrossRef](#)]
16. Tu, M.; Liu, H.; Cheng, S.; Mao, F.; Chen, H.; Fan, F.; Lu, W.; Du, M. Identification and characterization of a novel casein anticoagulant peptide derived from in vivo digestion. *Food Funct.* **2019**, *10*, 2552–2559. [[CrossRef](#)]
17. Chi, C.F.; Hu, F.Y.; Wang, B.; Li, T.; Ding, G.F. Antioxidant and anticancer peptides from protein hydrolysate of blood clam (*Tegillarca granosa*) muscle. *J. Funct. Foods* **2015**, *15*, 301–313. [[CrossRef](#)]
18. Pan, X.; Zhao, Y.Q.; Hu, F.Y.; Chi, C.F.; Wang, B. Anticancer activity of a hexapeptide from skate (*Raja porosa*) cartilage protein hydrolysate in HeLa cells. *Mar. Drugs* **2016**, *14*, 153. [[CrossRef](#)]
19. Sila, A.; Nedjar-Aroume, N.; Hedhili, K.; Chataigné, G.; Balti, R.; Nasri, M.; Dhulster, P.; Bougatef, A. Antibacterial peptides from barbel muscle protein hydrolysates: Activity against some pathogenic bacteria. *LWT* **2014**, *55*, 183–188. [[CrossRef](#)]
20. Nurilmala, M.; Hizbullah, H.H.; Karnia, E.; Kusumaningtyas, E.; Ochiai, Y. Characterization and antioxidant activity of collagen, gelatin, and the derived peptides from yellowfin tuna (*Thunnus albacares*) Skin. *Mar. Drugs* **2020**, *18*, 98. [[CrossRef](#)]
21. Chi, C.F.; Wang, B.; Wang, Y.M.; Deng, S.G.; Ma, J.Y. Isolation and characterization of three antioxidant pentapeptides from protein hydrolysate of monkfish (*Lophius litulon*) muscle. *Food Res. Int.* **2014**, *55*, 222–228. [[CrossRef](#)]
22. Hu, X.M.; Wang, Y.M.; Zhao, Y.Q.; Chi, C.F.; Wang, B. Antioxidant peptides from the protein hydrolysate of monkfish (*Lophius litulon*) muscle: Purification, identification, and cytoprotective function on HepG2 cells damage by H<sub>2</sub>O<sub>2</sub>. *Mar. Drugs* **2020**, *18*, 153. [[CrossRef](#)]
23. Sierra, L.; Fan, H.; Zapata, J.; Wu, J. Antioxidant peptides derived from hydrolysates of red tilapia (*Oreochromis* sp.) scale. *LWT* **2021**, *146*, 111631. [[CrossRef](#)]
24. Cai, S.Y.; Wang, Y.M.; Zhao, Y.Q.; Chi, C.F.; Wang, B. Cytoprotective effect of antioxidant pentapeptides from the protein hydrolysate of swim bladders of miiuy croaker (*Miichthys miiuy*) against H<sub>2</sub>O<sub>2</sub>-mediated human umbilical vein endothelial cell (HUVEC) injury. *Int. J. Mol. Sci.* **2019**, *20*, 5425. [[CrossRef](#)] [[PubMed](#)]
25. Zhang, L.; Zhao, G.X.; Zhao, Y.Q.; Qiu, Y.T.; Chi, C.F.; Wang, B. Identification and active evaluation of antioxidant peptides from protein hydrolysates of skipjack tuna (*Katsuwonus pelamis*) head. *Antioxidants* **2019**, *8*, 318. [[CrossRef](#)] [[PubMed](#)]
26. Yang, X.R.; Zhao, Y.Q.; Qiu, Y.T.; Chi, C.F.; Wang, B. Preparation and characterization of gelatin and antioxidant peptides from gelatin hydrolysate of skipjack tuna (*Katsuwonus pelamis*) bone stimulated by in vitro gastrointestinal digestion. *Mar. Drugs* **2019**, *17*, 78. [[CrossRef](#)]
27. Han, J.; Huang, Z.; Tang, S.; Lu, C.; Wan, H.; Zhou, J.; Li, Y.; Ming, T.; Jim Wang, Z.; Su, X. The novel peptides ICRD and LCGEC screened from tuna roe show antioxidative activity via Keap1/Nrf2-ARE pathway regulation and gut microbiota modulation. *Food Chem.* **2020**, *327*, 127094. [[CrossRef](#)]
28. Wang, N.; Wang, W.; Sadiq, F.A.; Wang, S.; Caiqin, L.; Jianchang, J. Involvement of Nrf2 and Keap1 in the activation of antioxidant responsive element (ARE) by chemopreventive agent peptides from soft-shelled turtle. *Process. Biochem.* **2020**, *92*, 174–181. [[CrossRef](#)]
29. Venkatesan, J.; Anil, S.; Kim, S.K.; Shim, M.S. Marine fish proteins and peptides for cosmeceuticals: A review. *Mar. Drugs* **2017**, *15*, 143. [[CrossRef](#)]
30. Han, L.; Mao, X.; Wang, K.; Li, Y.; Zhao, M.; Wang, J.; Xue, C. Phosphorylated peptides from Antarctic krill (*Euphausia superba*) ameliorated osteoporosis by activation of osteogenesis-related MAPKs and PI3K/AKT/GSK-3 $\beta$  pathways in dexamethasone-treated mice. *J. Funct. Foods* **2018**, *47*, 447–456. [[CrossRef](#)]
31. Hou, H.; Wang, S.; Zhu, X.; Li, Q.; Fan, Y.; Cheng, D.; Li, B. A novel calcium-binding peptide from Antarctic krill protein hydrolysates and identification of binding sites of calcium-peptide complex. *Food Chem.* **2018**, *243*, 389–395. [[CrossRef](#)] [[PubMed](#)]
32. Zhao, Y.Q.; Zhang, L.; Tao, J.; Chi, C.F.; Wang, B. Eight antihypertensive peptides from the protein hydrolysate of Antarctic krill (*Euphausia superba*): Isolation, identification, and activity evaluation on human umbilical vein endothelial cells (HUVECs). *Food Res. Int.* **2019**, *121*, 197–204. [[CrossRef](#)]
33. Ji, W.; Zhang, C.; Ji, H. Two novel bioactive peptides from Antarctic krill with dual angiotensin converting enzyme and dipeptidyl peptidase IV inhibitory activities. *J. Food Sci.* **2017**, *82*, 1742–1749. [[CrossRef](#)] [[PubMed](#)]
34. Xia, G.; Zhao, Y.; Yu, Z.; Tian, Y.; Wang, Y.; Wang, S.; Wang, J.; Xue, C. Phosphorylated peptides from Antarctic krill (*Euphausia superba*) prevent estrogen deficiency induced osteoporosis by inhibiting bone resorption in ovariectomized rats. *J. Agric. Food Chem.* **2015**, *63*, 9550–9557. [[CrossRef](#)] [[PubMed](#)]
35. Jiang, H.; Tong, T.; Sun, J.; Xu, Y.; Zhao, Z.; Liao, D. Purification and characterization of antioxidative peptides from round scad (*Decapterus maruadi*) muscle protein hydrolysate. *Food Chem.* **2014**, *154*, 158–163. [[CrossRef](#)] [[PubMed](#)]

36. Wang, B.; Li, L.; Chi, C.F.; Ma, J.H.; Luo, H.Y.; Xu, Y.F. Purification and Characterization of a novel antioxidant peptide derived from blue mussel (*Mytilus edulis*) protein hydrolysate. *Food Chem.* **2013**, *138*, 1713–1719. [[CrossRef](#)] [[PubMed](#)]
37. Chi, C.F.; Hu, F.Y.; Wang, B.; Ren, X.J.; Deng, S.G.; Wu, C.W. Purification and characterization of three antioxidant peptides from protein hydrolysate of croceine croaker (*Pseudosciaena crocea*) muscle. *Food Chem.* **2015**, *168*, 662–667. [[CrossRef](#)]
38. Bougatef, A.; Balti, R.; Haddar, A.; Jellouli, K.; Souissi, N.; Nasri, M. Antioxidant and functional properties of protein hydrolysates of bluefin tuna (*Thunnus thynnus*) heads as influenced by the extent of enzymatic hydrolysis. *Biotechnol. Bioproc. Eng.* **2012**, *17*, 841–852. [[CrossRef](#)]
39. Zhao, W.H.; Luo, Q.B.; Pan, X.; Chi, C.F.; Sun, K.L.; Wang, B. Preparation, identification, and activity evaluation of ten antioxidant peptides from protein hydrolysate of swim bladders of miyu croaker (*Miichthys miyu*). *J. Funct. Foods* **2018**, *47*, 503–511. [[CrossRef](#)]
40. Chi, C.; Hu, F.; Li, Z.; Wang, B.; Luo, H. Influence of different hydrolysis processes by trypsin on the physicochemical, antioxidant, and functional properties of collagen hydrolysates from *Sphyrna lewini*, *Dasyatis akjei*, and *Raja porosa*. *J. Aquat. Food Prod. Technol.* **2016**, *25*, 616–632. [[CrossRef](#)]
41. Li, Z.; Wang, B.; Chi, C.; Luo, H.; Gong, Y.; Ding, G. Influence of average molecular weight on antioxidant and functional properties of collagen hydrolysates from *Sphyrna lewini*, *Dasyatis akjei* and *Raja porosa*. *Food Res. Int.* **2013**, *51*, 283–293. [[CrossRef](#)]
42. Chi, C.F.; Wang, B.; Wang, Y.M.; Zhang, B.; Deng, S.G. Isolation and characterization of three antioxidant peptides from protein hydrolysate of bluefin leatherjacket (*Navodon septentrionalis*) heads. *J. Funct. Foods* **2015**, *12*, 1–10. [[CrossRef](#)]
43. Chang, S.K.; Ismail, A.; Yanagita, T.; Esa, N.M.; Baharuldin, M.T.H. Antioxidant peptides purified and identified from the oil palm (*Elaeis guineensis* Jacq.) kernel protein hydrolysate. *J. Funct. Foods* **2015**, *14*, 63–75. [[CrossRef](#)]
44. Chi, C.F.; Wang, B.; Hu, F.Y.; Wang, Y.M.; Zhang, B.; Deng, S.G.; Wu, C.W. Purification and identification of three novel antioxidant peptides from protein hydrolysate of bluefin leatherjacket (*Navodon septentrionalis*) skin. *Food Res. Int.* **2015**, *73*, 124–129. [[CrossRef](#)]
45. You, L.; Zhao, M.; Regenstein, J.M.; Ren, J. Purification and identification of antioxidative peptides from loach (*Misgurnus anguillicaudatus*) protein hydrolysate by consecutive chromatography and electrospray ionization mass spectrometry. *Food Res. Int.* **2010**, *43*, 1167–1173. [[CrossRef](#)]
46. Wang, B.; Li, Z.R.; Chi, C.F.; Zhang, Q.H.; Luo, H.Y. Preparation and evaluation of antioxidant peptides from ethanol-soluble proteins hydrolysate of *Sphyrna lewini* muscle. *Peptides* **2012**, *36*, 240–250. [[CrossRef](#)]
47. Mendis, E.; Rajapakse, N.; Kim, S.K. Antioxidant properties of a radical-scavenging peptide purified from enzymatically prepared fish skin gelatin hydrolysate. *J. Agric. Food Chem.* **2005**, *53*, 581–587. [[CrossRef](#)] [[PubMed](#)]
48. Rajapakse, N.; Mendis, E.; Byun, H.G.; Kim, S.K. Purification and in vitro antioxidative effects of giant squid muscle peptides on free radical-mediated oxidative systems. *J. Nutr. Biochem.* **2005**, *16*, 562–569. [[CrossRef](#)] [[PubMed](#)]
49. Pan, X.Y.; Wang, Y.M.; Li, L.; Chi, C.F.; Wang, B. Four antioxidant peptides from protein hydrolysate of red stingray (*Dasyatis akjei*) cartilages: Isolation, identification, and in vitro activity evaluation. *Mar. Drugs* **2019**, *17*, 263. [[CrossRef](#)]
50. He, Y.; Pan, X.; Chi, C.F.; Sun, K.L.; Wang, B. Ten new pentapeptides from protein hydrolysate of miyu croaker (*Miichthys miyu*) muscle: Preparation, identification, and antioxidant activity evaluation. *LWT* **2019**, *105*, 1–8. [[CrossRef](#)]
51. Zhao, Y.Q.; Zeng, L.; Yang, Z.S.; Huang, F.F.; Ding, G.F.; Wang, B. Anti-fatigue effect by peptide fraction from protein hydrolysate of croceine croaker (*Pseudosciaena crocea*) swim bladder through inhibiting the oxidative reactions including DNA damage. *Mar. Drugs* **2016**, *14*, 221. [[CrossRef](#)] [[PubMed](#)]
52. Yang, X.R.; Zhang, L.; Zhao, Y.Q.; Chi, C.F.; Wang, B. Purification and characterization of antioxidant peptides derived from protein hydrolysate of the marine bivalve mollusk *Tergillarca granosa*. *Mar. Drugs* **2019**, *17*, 251. [[CrossRef](#)]
53. Wen, C.; Zhang, J.; Zhang, H.; Duan, Y.; Ma, H. Plant protein-derived antioxidant peptides: Isolation, identification, mechanism of action and application in food systems: A review. *Trends Food Sci. Technol.* **2020**, *105*, 308–322. [[CrossRef](#)]
54. Deane, R.; Du Yan, S.; Submamaryan, R.K.; LaRue, B.; Jovanovic, S.; Hogg, E.; Welch, D.; Manness, L.; Lin, C.; Yu, J.; et al. RAGE mediates amyloid-beta peptide transport across the blood-brain barrier and accumulation in brain. *Nat. Med.* **2003**, *9*, 907–913. [[CrossRef](#)] [[PubMed](#)]
55. Rajapakse, N.; Mendis, E.; Jung, W.K.; Je, J.Y.; Kim, S.K. Purification of a radical scavenging peptide from fermented mussel sauce and its antioxidant properties. *Food Res. Int.* **2005**, *38*, 175–182. [[CrossRef](#)]
56. Gulcin, I. Comparison of in vitro antioxidant and antiradical activities of L-tyrosine and L-Dopa. *Amino Acids* **2007**, *32*, 431–438. [[CrossRef](#)] [[PubMed](#)]
57. Chen, H.; Wang, S.; Zhou, A.; Miao, J.; Liu, J.; Benjakul, S. A novel antioxidant peptide purified from defatted round scad (*Decapterus maruadii*) protein hydrolysate extends lifespan in *Caenorhabditis elegans*. *J. Funct. Foods* **2020**, *68*, 103907. [[CrossRef](#)]
58. Wu, R.; Wu, C.; Liu, D.; Yang, X.; Huang, J.; Zhang, J.; Liao, B.; He, H. Antioxidant and antifreezing peptides from salmon collagen hydrolysate prepared by bacterial extracellular protease. *Food Chem.* **2018**, *248*, 346–352. [[CrossRef](#)]
59. Wong, F.C.; Xiao, J.; Ong, M.G.-L.; Pang, M.J.; Wong, S.J.; The, L.K.; Chai, T.T. Identification and characterization of antioxidant peptides from hydrolysate of blue-spotted stingray and their stability against thermal, pH and simulated gastrointestinal digestion treatments. *Food Chem.* **2019**, *271*, 614–622. [[CrossRef](#)]
60. Orsini Delgado, M.C.; Nardo, A.; Pavlovic, M.; Rogniaux, H.; Añón, M.C.; Tironi, V.A. Identification and characterization of antioxidant peptides obtained by gastrointestinal digestion of amaranth proteins. *Food Chem.* **2016**, *197*, 1160–1167. [[CrossRef](#)]
61. Sheih, I.C.; Wu, T.K.; Fang, T.J. Antioxidant properties of a new antioxidative peptide from algae protein waste hydrolysate in different oxidation systems. *Bioresour. Technol.* **2009**, *100*, 3419–3425. [[CrossRef](#)]

62. Guo, H.; Kouzuma, Y.; Yonekura, M. Structures and properties of antioxidative peptides derived from royal jelly protein. *Food Chem.* **2009**, *113*, 238–245. [[CrossRef](#)]
63. Klompong, V.; Benjakul, S.; Kantachote, D.; Shahidi, F. Antioxidative activity and functional properties of protein hydrolysate of yellow stripe trevally (*Selaroides leptolepis*) as influenced by the degree of hydrolysis and enzyme type. *Food Chem.* **2007**, *102*, 1317–1327. [[CrossRef](#)]
64. Udenigwe, C.C.; Aluko, R.E. Chemometric analysis of the amino acid requirements of antioxidant food protein hydrolysates. *Int. J. Mol. Sci.* **2011**, *12*, 3148–3161. [[CrossRef](#)] [[PubMed](#)]
65. Yang, J.; Huang, J.; Dong, X.; Zhang, Y.; Zhou, X.; Huang, M.; Zhou, G. Purification and identification of antioxidant peptides from duck plasma proteins. *Food Chem.* **2020**, *319*, 126534. [[CrossRef](#)] [[PubMed](#)]
66. Memarpoor-Yazdi, M.; Asoodeh, A.; Chamani, J. A novel antioxidant and antimicrobial peptide from hen egg white lysozyme hydrolysates. *J. Funct. Foods* **2012**, *4*, 278–286. [[CrossRef](#)]
67. Zhu, C.Z.; Zhang, W.G.; Zhou, G.H.; Xu, X.L.; Kang, Z.L.; Yin, Y. Isolation and identification of antioxidant peptides from Jinhua ham. *J. Agric. Food Chem.* **2013**, *61*, 1265–1271. [[CrossRef](#)]
68. Sun, L.; Zhang, Y.; Zhuang, Y. Antiphotobleaching effect and purification of an antioxidant peptide from tilapia (*Oreochromis niloticus*) gelatin peptides. *J. Funct. Foods* **2013**, *5*, 154–162. [[CrossRef](#)]
69. Ahn, C.B.; Cho, Y.S.; Je, J.Y. Purification and anti-inflammatory action of tripeptide from salmon pectoral fin byproduct protein hydrolysate. *Food Chem.* **2015**, *168*, 151–156. [[CrossRef](#)]
70. Jang, H.L.; Liceaga, A.M.; Yoon, K.Y. Purification, characterisation and stability of an antioxidant peptide derived from sandfish (*Arctoscopus japonicus*) protein hydrolysates. *J. Funct. Foods* **2016**, *20*, 433–442. [[CrossRef](#)]

## Article

# Large-Scale Plasma Peptidomic Profiling Reveals a Novel, Nontoxic, *Crassostrea hongkongensis*-Derived Antimicrobial Peptide against Foodborne Pathogens

Fan Mao<sup>1,2,†</sup>, Yongbo Bao<sup>3,†</sup>, Nai-Kei Wong<sup>1,4,†</sup>, Minwei Huang<sup>1,2</sup>, Kunna Liu<sup>1,2</sup>, Xiangyu Zhang<sup>1,2</sup>, Zhuo Yang<sup>1,2</sup>, Wenjie Yi<sup>1,2</sup>, Xiao Shu<sup>1,2</sup>, Zhiming Xiang<sup>1,2</sup>, Ziniu Yu<sup>1,2,\*</sup> and Yang Zhang<sup>1,2,\*</sup>

- <sup>1</sup> CAS Key Laboratory of Tropical Marine Bio-Resources and Ecology and Guangdong Provincial Key Laboratory of Applied Marine Biology, South China Sea Institute of Oceanology, Innovation Academy of South China Sea Ecology and Environmental Engineering, Chinese Academy of Sciences, Guangzhou 510301, China; maofan@scsio.ac.cn (F.M.); wongnk@stu.edu.cn (N.-K.W.); mwhuang@scsio.ac.cn (M.H.); liukunna18@mails.ucas.ac.cn (K.L.); zhangxiangyu17@mails.ucas.ac.cn (X.Z.); yangzhuo19@mails.ucas.ac.cn (Z.Y.); yiwjenjie20@mails.ucas.ac.cn (W.Y.); xiaoshu@scsio.ac.cn (X.S.); zhimingxiang@scsio.ac.cn (Z.X.)
- <sup>2</sup> Southern Marine Science and Engineering Guangdong Laboratory (Guangzhou), Guangzhou 510301, China
- <sup>3</sup> Zhejiang Key Laboratory of Aquatic Germplasm Resources, College of Biological and Environmental Sciences, Zhejiang Wanli University, Ningbo 315100, China; baoyongbo@zww.edu.cn
- <sup>4</sup> Department of Pharmacology, Medical College, Shantou University, Shantou 515063, China
- \* Correspondence: carlzyu@scsio.ac.cn (Z.Y.); yzhang@scsio.ac.cn (Y.Z.); Tel.: +86-20-8910-2507 (Z.Y. & Y.Z.)
- † These authors contributed equally to this work.

**Citation:** Mao, F.; Bao, Y.; Wong, N.-K.; Huang, M.; Liu, K.; Zhang, X.; Yang, Z.; Yi, W.; Shu, X.; Xiang, Z.; et al. Large-Scale Plasma Peptidomic Profiling Reveals a Novel, Nontoxic, *Crassostrea hongkongensis*-Derived Antimicrobial Peptide against Foodborne Pathogens. *Mar. Drugs* **2021**, *19*, 420. <https://doi.org/10.3390/md19080420>

Academic Editors: Yonghong Liu and Xuefeng Zhou

Received: 6 July 2021

Accepted: 22 July 2021

Published: 26 July 2021

**Publisher's Note:** MDPI stays neutral with regard to jurisdictional claims in published maps and institutional affiliations.



**Copyright:** © 2021 by the authors. Licensee MDPI, Basel, Switzerland. This article is an open access article distributed under the terms and conditions of the Creative Commons Attribution (CC BY) license (<https://creativecommons.org/licenses/by/4.0/>).

**Abstract:** Antimicrobial peptides are a fundamental component of mollusks' defense systems, though they remain a thinly investigated subject. Here, infection by *Vibrio parahaemolyticus* triggered a significant increase in antimicrobial activity in oyster plasma. By using PBS-challenged oysters as a control, plasma peptides from immunologically challenged oysters were subjected to peptidomic profiling and in silico data mining to identify bioactive peptides. Thirty-five identified plasma peptides were up-regulated post infection, among which, six up-regulated peptides (URPs) showed a relatively high positive charge. URP20 was validated with significant antibacterial activity. Virtually, URP20 triggered aggregation of bacterial cells, accompanied by their membrane permeabilization. Interestingly, URP20 was found to be active against Gram-positive and Gram-negative foodborne pathogens as well as *Candida albicans*, with no cytotoxicity to mammalian cells and mice. Our study provides the first large-scale plasma peptidomic dataset that identifies novel bioactive peptides in marine mollusks. Further exploration of peptide diversity in marine invertebrates should prove a fruitful pursuit for designing novel AMPs with broad applications.

**Keywords:** oyster; plasma; peptidome; antimicrobial peptides; cytotoxicity

## 1. Introduction

Overconsumption of antibiotics has led to the rapid emergence and dissemination of antimicrobial resistance in multidrug-resistant pathogens against virtually all classes of existing antimicrobials [1], which threatens to jeopardize the sustainable development of clinical medicine, animal husbandry, aquaculture, and the food industry [2,3]. Meanwhile, rising public needs for safe, fresh, minimally processed, and naturally sourced foods have posed challenges on food security worldwide, and urged research on innovative antimicrobials [4]. Antimicrobial peptides (AMPs) are key effector molecules in host innate defenses in both vertebrates and invertebrates; cationic AMPs possess broad-spectrum activities against microorganisms [5] and have been increasingly recognized as templates for developing alternative antimicrobials to combat multidrug-resistant superbugs [6]. An extensive body of literature has been devoted to investigating AMPs' structures and



modes of action [7], with an emerging focus on potential antimicrobial constituents of food products [8].

To date, over 3200 AMPs from various kingdoms (11% from plants, 11% from bacteria, 0.6% from fungi, 74% from animals), along with a more modest inventory of synthetic peptides, have been described. Among those from natural sources, only 2% of the peptides were identified from mollusks [9]. Mollusks are the second largest phylum of invertebrate animals, comprising 23% of all named marine organisms. These sessile marine organisms lack adaptive immunity, and instead depend heavily on the innate immune system including cell-mediated and humoral components for recognition and elimination of invading microbes [10]. Antimicrobial peptides constitute one of the most important components of the innate immunity in mollusks that provides protection against pathogenic microorganisms [11]. While mollusks are increasingly being appreciated as a rich, accessible source of AMPs, only AMPs from mussels have been studied in detail, which include mussel defensins, mytilins, myticins, and mytimycin [12–16]. Moreover, previous works have focused on the purification and characterization of defensins in other mollusk species, such as oyster defensin from gill extracts of the American oyster (*Crassostrea virginica*) [17], the Pacific oyster (*Crassostrea gigas*) [18], and two defensins from *H. discus discus* [19], whereas the pharmaceutical potential of AMPs from marine mollusks remains scarcely explored. Given that innate immune defenses via AMPs prove sufficient to contain microbial infections in mollusks, it seems logical that at least some of such immune components could act as efficient and potent inhibitors of microbial growth [20]. In applied contexts, despite that mollusk AMPs have been characterized in limited species, some have shown great potential as antiviral agents [21].

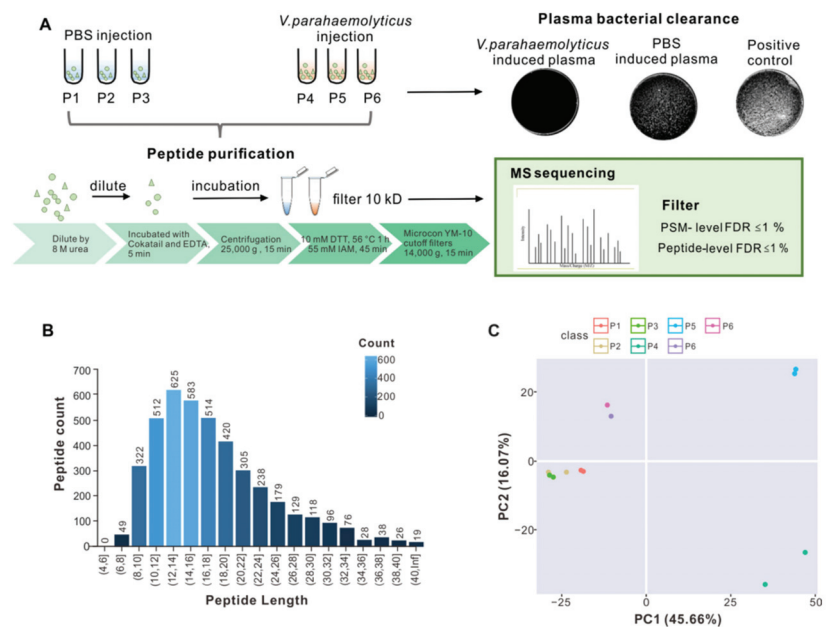
The Hong Kong oyster (*Crassostrea hongkongensis*) is a commercially and nutritionally valuable mollusk species in aquaculture, and is endemic to coasts of the South China Sea. As filter feeders dwelling in intertidal zones, oysters are prone to infections. The haemolymph is a circulating body fluid found in invertebrates, which serves as an immune tissue functionally analogous to the blood of vertebrates [22]. It is primarily composed of haemolymph cells (hemocytes) and the haemolymph plasma. During infections, a variety of specialized proteins are secreted via exocytosis from hemocytes into the plasma, for mounting humoral responses [23]. In our study, we observed that activated plasma from haemolymph following bacterial challenge exhibited great inhibitory activity against *Vibrio parahaemolyticus* growth, suggesting the existence of abundant antimicrobial components in the plasma, presumably including endogenous peptides with potential antimicrobial activity. Thus far, only a very small number of plasma-derived AMPs from marine mollusks have been studied [9]. In addition, due to the complexity of the origins and composition of plasma components in mollusks, it has been relatively difficult to directly purify and identify any endogenous peptides from the plasma. Therefore, it is highly desirable to develop a novel methodological platform for distinguishing plasma peptides from interfering species that occur in high concentration, such as proteins, lipids, and salts, in the marine mollusk *C. hongkongensis*.

Here, we utilized a mass spectrometry approach as a fundamental tool for profiling and analyzing plasma peptidome in conjunction with peptide isolation and enrichment to improve the workflow of detecting endogenous peptides from *C. hongkongensis* plasma. Candidates of plasma peptidome based on extracts from the bacterially challenged control groups were identified and subsequently subjected to antimicrobial susceptibility assays to further validate potential AMPs in the plasma. We also assessed the cytotoxicity of identified plasma peptides to mammalian cells and in laboratory mice. Thus, we hypothesized that it would be possible to develop potential AMPs from oyster plasma, and provided evidence supporting its applications as potentially relevant to anti-infective treatment, food preservatives, cosmetics, and agricultural uses.

## 2. Results

### 2.1. Large-Scale Peptidome Applied to Oyster Plasma

Oyster plasma contains various soluble factors secreted by hemocytes and other cells, which were separated from the haemolymph and collected for antibacterial activity assays. Plasma was collected after *V. parahaemolyticus* injection, with PBS injection being set as a control. Plasma of the *V. parahaemolyticus* challenged group was markedly more bactericidal than that of the PBS-treated control, as shown in Figure 1A (upper right panel), suggesting that bacterial challenge rapidly stimulated the expression of bactericidal factors, while the positive control (incubation with LB agar liquid medium for 2 h) contained more *V. parahaemolyticus* cells.



**Figure 1.** Collection of oyster plasmas for isolation and identification of bactericidal peptides. (A) Oysters were treated with *V. parahaemolyticus* or PBS by injection or for 24 h, followed by plasma collection. Bactericidal effects were assessed by incubating (*V. parahaemolyticus* versus PBS-treated) plasmas and LB (positive control) with *V. parahaemolyticus*, whose colony-forming units (CFUs) were subsequently visualized and enumerated in LB agar plates. Peptides of interest were purified from the plasma via indicated steps and subjected to analysis by LC-MS/MS. (B) Lengths of the identified peptides in each sample. The names of the samples are shown on the horizontal axis, and the number of polypeptides on the vertical axis. (C) Principal component analysis (PCA) score plot of the plasma samples. Colors mark for different samples.

In addition to reported plasma proteins such as lectin [24], other novel antibacterial effector proteins may exist. Peptidomics was herein employed to identify new bioactive peptides with antibacterial activity from plasma based on liquid chromatography and tandem mass spectrometry. To apply large-scale peptidomics to oyster plasma proteins, oyster plasma was extracted from the *V. parahaemolyticus* challenged group (P4, P5, P6) and PBS-treated control (P1, P2, P3). Figure 1A summarized the workflow of the technical processes, which includes peptide purification, peptide filtering, and MS sequencing. To exclude larger protein fragments, these were removed by molecular-weight cutoff (10 kD) spin filters, before MS sequencing of the resultant peptide samples was performed. Peptides were identified by using the MaxQuant integrated Andromeda engine, with filtering at

PM-level FDR  $\leq 1\%$ , and further filtering at peptide-level FDR  $\leq 1\%$  to obtain significant identification results.

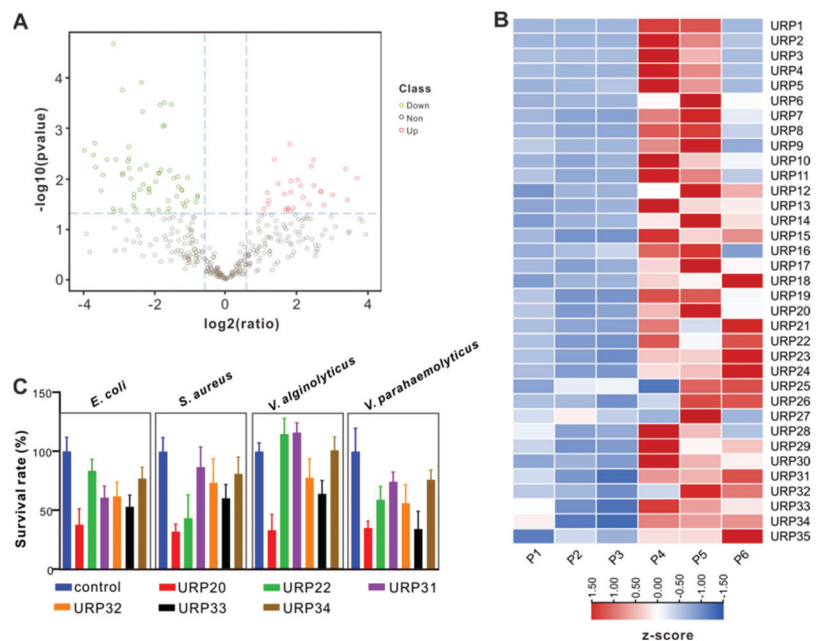
### 2.2. Peptide Identification and Informatics Analysis

Each sample in the bacteria-challenged group and PBS-treated control was divided into two sub-samples, respectively, for performing technical repetition. The total spectral count ranged around 617,210 in all the samples, and 39,000 were identified (Table S1). As this study focused mainly on peptides, large proteins ( $>10$  kD) were filtered out manually. Most of the fragments had peptide lengths of 8 to 34 amino acids. Only a few fragments were shorter than 8 amino acids or longer than 34 amino acids (Figure 1B). Then, principal component analysis (PCA) was performed on the subset of identified peptide in each sample, showing that the samples in control group (P1, P2, and P3) formed together and the samples in infection group (P4, P5, and P6) formed in distinct groups, illustrating the individual difference post infection.

### 2.3. Comparative Analysis on Peptide Expression and General Function

The resulting peptidomes were analyzed, which shows that fewer peptides in the PBS-treated plasma were identified than in the case of bacteria-challenged plasma (Figure S1). A considerable fraction of the peptides was derived from intracellular proteins likely arising from tissue damage under bacterial infection, and was thus not assumed to constitute bioactive peptide. Then, comparative analysis on peptide expression following *V. alginolyticus* infection and PBS infection was performed to elucidate positive active peptides during infection. Differentially expressed peptides (DEPs) were analyzed by comparing peptide abundance in the *V. alginolyticus* infection group with the PBS infection group. In Figure 2A, we use a volcano plot to summarize the magnitude, significance and variability in *V. alginolyticus* infection group. Thirty-five identified peptides indicate an ascending trend in peptide expression, whereas 67 peptides were down-regulated during *V. alginolyticus* infection. Significant protein expression in this study was defined as a *p* value of less than 0.05, with fold changes greater than 1.4 and below 0.7. To illustrate this, the peptide expression level of 35 up-regulated peptides (URPs) is exhibited in Figure 2B.

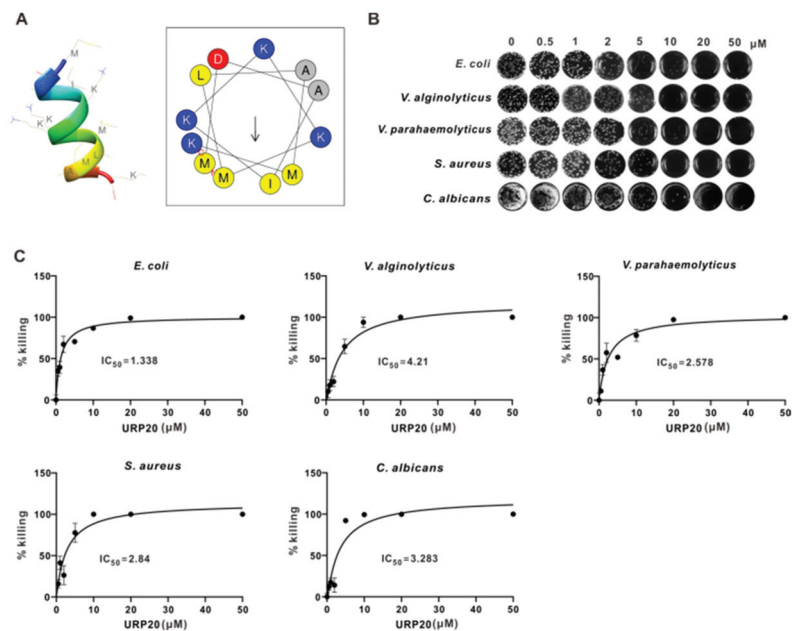
To facilitate screening of up-regulated peptides (URPs) with antimicrobial potential, the URPs were submitted to the HeliQuest website for prediction on general physicochemical features, in terms of hydrophobicity, hydrophobic moment, and net charge (*z*) (Table S2). Consequently, a total of six up-regulated peptides (URP20, URP22, URP31, URP32, URP33, and URP34) were selected for chemical synthesis, since they possessed a positive charge  $\geq +2$ . Then, synthetic peptides were applied for antibacterial activity assay to evaluate their biological activities. We found that URP20 exhibited remarkable inhibitory activity on all bacterial cells tested, in comparison with five other up-regulated peptides (Figure 2C). Furthermore, URP20 showed a medium degree of hydrophobicity (0.25667), compared to peptides with higher hydrophobicity (URP14, 0.601; URP15, 0.629) or lower hydrophobicity (URP17,  $-0.134$ ), as shown in Table S2. In addition, URP20 has a net charge of +3, which may favor its binding to cell membranes.



**Figure 2.** Comparative analysis of the identified peptides. (A) Volcano plots show the relationship between fold-changes and significance for vibrio infection group vs control group. The y-axis shows the  $-\log_{10}(p\text{-values})$  and the x-axis shows the difference in expression as measured in  $\log_2$  (fold change). (B) Heatmaps of gene expression levels of the differentially expressed peptides (DEPs). Peptide expression levels were normalized by z-score normalization method. (C) Bactericidal effects of potential antimicrobial peptides (net charge  $\geq 2$  in up-regulated peptides) at  $5 \mu\text{M}$  on the growth of *E. coli*, *V. alginolyticus*, *V. parahaemolyticus*, and *S. aureus*. Bacterial cells were treated with an equal amount of PBS as a control group. Bactericidal effects were assessed by counting bacterial CFUs on LB agar plates, which were then expressed as percent survival rate relative to that of the control group. Data are presented as means  $\pm$  SD.

#### 2.4. URP20 Showed Broad-Spectrum Antimicrobial Activity against Bacteria and Fungi

To establish the antimicrobial mode of action of URP20, MICs and MBCs were analyzed, along with its peptide structure and helical wheel projection. The peptide structure was predicted on the PEP-FOLD server, which confirmed the formation of  $\alpha$ -helix. As shown in Table S2, URP20 is a positively charged peptide. The helical wheel projection of URP20 (Figure 3A) indicates where the positively charged amino acids, namely lysines (in blue), are localized. Hydrophobic residues (grey and yellow) are situated on different sides of the wheel, giving rise to a hydrophobic moment (arrow) in the URP20 molecule. Based on this, it is anticipated that URP20 could embed itself in phospholipid membranes with its positive charges pointing outside and its hydrophobic elements facing the hydrophobic core of the membrane.



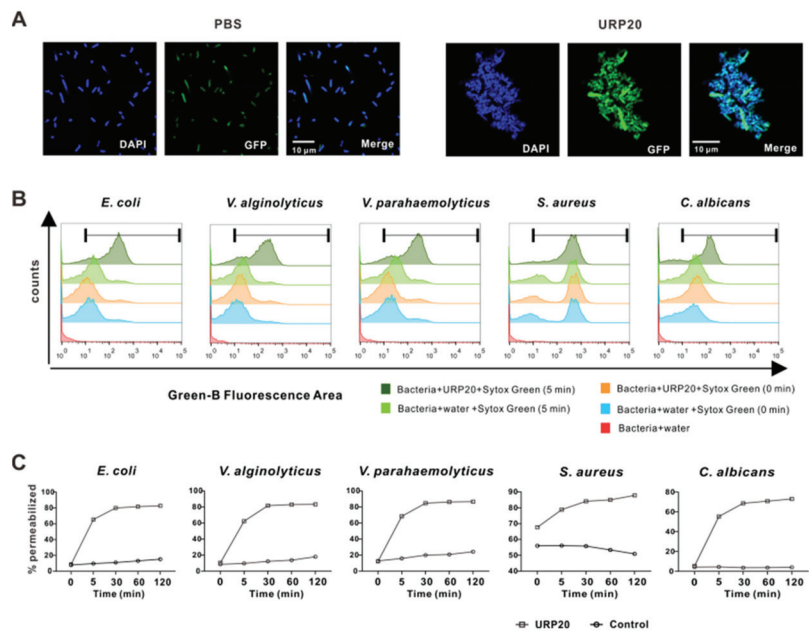
**Figure 3.** Antimicrobial activity of URP20. (A) Peptide structure and helical wheel projection of URP20. Peptide structure was predicted by the PEP-FOLD server. Amino acids are indicated by abbreviations. The peptide helical wheel was predicted on the HeliQuest website. The amino acid composition is indicated by one-letter symbols, namely, Lys (K), Met (M), Leu (L), Ile (I), Ala (A), and Asp (D). Group coloring key: yellow and grey represent nonpolar and hydrophobic amino acids; blue represents basic and charged amino acid; red represents acidic amino acids. The amino acids in red color mark the N- and C-termini of the peptide. An arrow represents the hydrophobic moment. (B) Antimicrobial activity of URP20 at various concentrations against Gram-negative bacteria (*E. coli*, *V. alginolyticus*, and *V. parahaemolyticus*), Gram-positive bacteria (*S. aureus*), and fungi (*C. albicans*). (C) MIC and MBC were calculated based on statistical data on URP20-dependent killing efficiency in the microbial samples. Data are expressed as a percentage of killing (mean  $\pm$  SD) relative to that of the control group. IC<sub>50</sub> values are also indicated. Tests were performed in triplicates.

Antimicrobial susceptibilities of *E. coli*, *V. alginolyticus*, *V. parahaemolyticus*, *S. aureus*, and *C. albicans* toward URP20 were tested. The results (Figure 3B,C) show that URP20 exerted obvious but differential inhibitory effects on the growth of several bacteria. At low concentrations (0.5  $\mu\text{M}$ ), URP20 was not inhibitory to bacterial growth. Minimum inhibitory concentrations (MICs) for Gram-negative bacteria (*E. coli*, *V. alginolyticus*, *V. parahaemolyticus*) ranged from 1 to 10  $\mu\text{M}$  (MIC<sub>50</sub> = 1.338  $\mu\text{M}$ , 4.21  $\mu\text{M}$ , 2.572  $\mu\text{M}$ , respectively), and corresponding minimum bactericidal concentrations (MBCs) ranged from 10 to 20  $\mu\text{M}$ . MICs for Gram-positive bacteria (*S. aureus*) were 1  $\mu\text{M}$ –5  $\mu\text{M}$  (MIC<sub>50</sub> = 2.84  $\mu\text{M}$ ), and corresponding MBCs were 5  $\mu\text{M}$ –10  $\mu\text{M}$ . The MICs for the fungi (*C. albicans*) ranged from 1  $\mu\text{M}$  to 10  $\mu\text{M}$  (MIC<sub>50</sub> = 3.283  $\mu\text{M}$ ), and corresponding MBCs ranged from 10 to 20  $\mu\text{M}$ . According to statistical results (Figure 3C), 0.5  $\mu\text{M}$  of URP20 also had some inhibitory effects on the growth of bacteria.

### 2.5. URP20 Triggered Aggregation of Bacterial Cells, Accompanied by Microbial Membrane Permeabilization

In order to elucidate the antimicrobial mode of action of URP20, we proceeded to observe URP20-treated *E. coli* in confocal fluorescence microscopy (Figure 4A). Bacterial cells were found to adhere to each other in the presence of URP20 (10  $\mu\text{M}$ ), while the blank

control *E. coli* without peptide treatment showed a dispersed and uniform distribution in the bright field, suggesting that URP20 triggered aggregation of the bacterial cells.

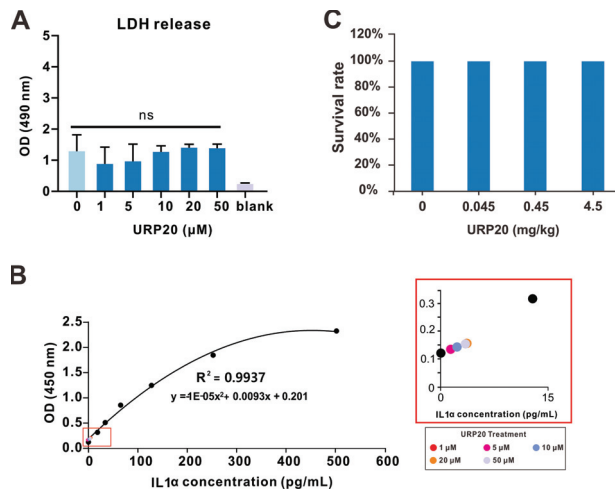


**Figure 4.** Antimicrobial mechanisms of URP20. (A) URP20 triggered aggregation of bacterial cells. Confocal microscopy images were acquired after URP20 challenge (10 min) of bacteria (*E. coli*). DNA was stained with DAPI (blue), and GFP-labelled bacteria emitted green fluorescence. In the control group, URP20 was replaced by an equal amount of PBS. (B) Permeabilization efficiency of URP20 after 5 min peptide incubation in bacterial or fungi cells. Membrane permeabilization of bacterial or fungal cells was measured by the Sytox Green assay. Bacterial or fungal cells were exposed to URP20 (20 μM) or an equal amount of water (control). (C) Time-lapse study on the effects on URP20 on membrane permeabilization in bacterial or fungal cells. Bacterial or fungal cells were exposed to URP20 (20 μM) or an equal amount of water (control, white circles) at indicated time points (0, 5, 30, 60, and 120 min).

We reasoned that detrimental modifications of the microbial cell surface may occur upon URP20 challenge. We thus focused our subsequent study on the effects of URP20 on microbial membrane permeabilization. SYTOX Green stain is a green-fluorescent nuclear and chromosome counterstain that is impermeant to living cells but can penetrate membranes of dead cells, making it a useful indicator of dead cells within a population. As membrane porosity increases, microbial DNA is stained by internalized SYTOX Green, which accumulates at different levels of fluorescence intensity in flow cytometry. Figure 4B shows the extent of damage to microbial cell membranes by URP20 (at MIC for 5 min). Remarkably, URP20 incubation sharply increased the fluorescence density by 50%, whereas fluorescence density was low in the group without URP20 incubation (5 min) and there was nearly no fluorescence in the group without URP20 incubation and SYTOX Green staining (microbial group added with water only). Then, time-dependent incubation of URP20 and microbial cells were performed (Figure 4C), which shows that membrane permeabilization progressed over time. For example, after URP20 incubation for 30 min, membrane permeabilization of *E. coli*, *V. alginolyticus*, *V. parahaemolyticus*, and *C. albicans* became stable, while that of *S. aureus* occurred more gradually. The results indicate time-dependent damage of URP20 to microbial cells membranes.

### 2.6. URP20 Was Not Cytotoxic to Mammalian Cells or Laboratory Mice

Since AMPs may exert toxic effects on host cells, we set out to assess any potential toxicity of URP20 to mammalian cells *in vivo* or to laboratory mice. *In vitro*, URP20 elicited negligible LDH release in HEK293T cells (Figure 5A), with minor effects seen in the induction of a proinflammatory response (reflected by IL1 $\alpha$  levels) in murine J774.1 cells (Figure 5B) across a broad range of concentrations of up to 50  $\mu$ M, compared to the control group (no peptides).



**Figure 5.** *In vitro* and *in vivo* toxicity of URP20. (A) HEK293T cells were treated with URP20 in different concentrations (0, 1, 5, 10, 20, 50  $\mu$ M) for 24 h. Cell death was quantified by measuring lactic dehydrogenase (LDH) release. Data represent means  $\pm$  SD of optical densities from three independent experiments. Blank: wells with no medium and cells. (B) Standard curve of IL1 $\alpha$  concentration was established, as displayed in the left panel. Murine J774.1 cells were treated with URP20 at different concentrations (1, 5, 10, 20, 50  $\mu$ M) for 24 h, followed by detection of IL1 $\alpha$  levels by ELISA, as shown in the right panel. Colored dots represent IL1 $\alpha$  response corresponding to different URP20 concentrations in treatment. (C) C57BL/6 mice were treated with URP20 at indicated concentrations (0, 0.045, 0.45, and 4.5 mg/kg) by intratracheal (i.t.) instillation and subsequently euthanized at 24 h after determination of mobility. Survive rate is displayed above.

To further assess any toxic effects of URP20 *in vivo*, we tested this in C57BL/6 mice (20 g in weight) by intratracheal (i.t.) instillation of the compound at up to 4.5 mg/kg. The URP20 treatment resulted in no fatalities and appeared to be well tolerated by observation of apparent effects in physical traits such as mobility (Figure 5C), which likewise suggests no toxicity to the host *in vivo*.

### 3. Discussion

In this study, we presented a novel approach to the extraction of plasma peptides, empowered by mass spectrometric identification and bioinformatics analysis to tease out potential antimicrobial peptides. To our knowledge, ours is the first comprehensive large-scale plasma peptidomic dataset that describes a large number of endogenous peptides from marine mollusk plasma, based on mass spectrometry. Similar peptidomic analysis was performed in Freshwater Mollusk *Pomacea poeyana*, revealing promising antimicrobial candidates [25]. In this study, low-abundance endogenous peptides were enriched by filtering with an ultrafiltration tube with a 10 kD filter membrane from a highly complex plasma environment with proteins of large heterogeneity in sizes and charges. This threshold was established for the generally accepted size of AMPs [26]. Thereafter, MS detection

was performed with an emphasis on in depth peptide identification. Additional functional characterization of endogenous peptides by bioinformatics was employed to decipher their biological meanings.

Interestingly, plasma from bacteria-challenged oysters showed significantly higher bactericidal activity, implying an increased expression level of antimicrobial components in bacteria-challenged samples. It is clear that some peptides occurred as degradation products from endogenous proteins, due to immunologically induced tissue damage and proteolysis [27]. Previously, it has been demonstrated that some bioactive peptides are well-defined peptides from specific proteolytic degradation of larger proteins [28,29]. For example, histone-derived AMP, known as Abhisin, is an endogenous AMP derived from the *N*-terminal region of histone H2A in disk abalone, with typical antimicrobial peptide characteristics [30]. In addition, another type of endogenous peptides is encoded by DNA coding sequences, such as short reading frames (sORF) [31] and non-coding RNA (ncRNA) [32]. Therefore, it is relatively challenging to develop novel bioactive peptides plainly on the basis of their biological sources. Thus, the analytical strategy and procedural framework used in our study have been proven robust for high-throughput identification of bioactive peptides.

AMPs are regarded as promising candidates for novel food preservatives in industrial and pharmaceutical applications, due to their relative safety and broad-spectrum antimicrobial activity. Here, we mainly focused on the antimicrobial activity of identified plasma peptides, but not the origin of the peptides, to reduce the peptidomic complexity. Antimicrobial activity of these peptides varied in different bacteria strains, and only URP20-selected plasma peptides showed strong antimicrobial activity. While AMPs are characterized by a wide antimicrobial spectrum, several previous works described specificity of some AMPs toward certain bacterial species. For example, the mussel defensins, MGDs, mytilins, and myticins have shown greater antibacterial activity against Gram-positive than against Gram-negative bacteria [15]. Generally, AMPs target membranes and directly kill microbes by disruptive forces of electrostatic and hydrophobic interactions [33]. Nevertheless, there has been no unifying principles on the actual modes of bacterial killing by AMPs to different species, resulting in limited understanding on the diversity of antimicrobial activity.

It has been proposed that biophysical determinants of antimicrobial activity include small size, cationicity, and amphipathicity [34]. In this study, URP20 was a plasma peptide identified with potent anti-bacterial and anti-fungal activity. It displayed robust and broad-spectrum antimicrobial activity, which reflected its amino acid composition. Among them, lysine (K), leucine (L), and isoleucine (I) helps to effectively form antimicrobial peptides. The positively charged lysine (K) can bind to negatively charged bacterial components, allowing an AMP to be more tightly attached to a membrane surface. Lysine (K), along with alanine (A), is known for boosting antimicrobial activity [35]. Leucine (L) and isoleucine (I) provide hydrophobic groups to bind bilayers with high affinity, thereby disrupting lipid vesicles and bacterial membranes [36]. Most of the antimicrobial peptides are positively charged alkaline peptides, which interact with anionic substances to increase local osmolality, disrupt cell membranes, and eventually induce cell death [37]. URP20 showed a significant ability to damage to cell membranes of Gram-negative and Gram-positive bacteria and fungi, which suggests a broad spectrum of antimicrobial activity against a microbes. Indeed, major bacterial pathogens that cause foodborne infections include *Staphylococcus aureus*, *Escherichia coli*, *Vibrio cholera*, among others [38]. The robust and broad-spectrum antimicrobial activity of URP20 allowed it to target *Vibrio* spp., *E. coli*, and *S. aureus*, raising the possibility of its use as a potential preservative to extend the shelf-life of food products. Additionally, *Candida albicans* is a fungal species of the human microbiota with the ability to asymptotically colonize many parts of the body [39]. Although few mollusk AMPs have been tested for antifungal activities, the antimicrobial activity of URP20 against *Candida albicans* seen in this study points to potential of mollusk peptides as lead compounds for developing antifungal agents. In



addition, we also showed that, within the range of bactericidal concentrations, URP20 was not cytotoxic or proinflammatory toward mammalian cells and mice, which lends further support to its safe use as naturally occurring antibacterial agents.

Overall, antimicrobial peptides are a promising new class of naturally sourced components as alternative food preservatives [8,40]. Selective cytotoxicity of cationic AMPs against a broad spectrum of human cancer cells supports their exploration as novel antitumor agents, which may avoid the disadvantages of conventional chemotherapy. Marine invertebrates have been increasingly appreciated as a rich source of novel and AMPs [20]. The development of a large-scale plasma peptidomic strategy has patently facilitated biological characterization and in silico mining of novel marine AMPs. Collectively, we believe that future analysis on peptide diversity in marine invertebrates will inspire new designs of functionally attractive AMPs for biotechnological applications.

#### 4. Materials and Methods

##### 4.1. Oyster Collection

Hong Kong oysters, *Crassostrea hongkongensis* (two-year old individuals with an average 100 mm shell length), were obtained from oyster culture facilities in Zhanjiang, Guangdong Province, China, and maintained at 22–25 °C in tanks with re-circulating seawater before experiments. The oysters were fed twice a daily with *Tetraselmis suecica* and *Isochrysis galbana*, during acclimation (two weeks) prior to study.

##### 4.2. Bacterial Challenge and Plasma Collection

To investigate bactericidal effects of plasma components, 100 oysters were randomly assigned into 2 groups and placed in 2 tanks: the bacterial challenge and control groups. For the experimental group, oysters were challenged by injecting 100 µL *Vibrio parahaemolyticus* ( $1 \times 10^8$  CFU/mL) suspended in phosphate buffer saline (PBS) into the adductor muscle. For the control group, an equal volume of PBS was injected. At 24 h post-challenge, hemolymph was collected from the pericardial cavity through the adductor muscle and immediately centrifuged ( $700 \times g$  for 10 min at 4 °C) to separate the plasma from hemocytes. Every three samples (ten oyster/sample) oysters in one sample were randomly collected in each group after injection (P1, P2, P3 for PBS injection group; P4, P5, P6 for *V. parahaemolyticus* injection group).

##### 4.3. Bacterial Clearance Assay

Twenty microliters of the plasma from individual samples were mixed and incubated with 20 µL *V. parahaemolyticus* ( $1 \times 10^6$  CFU/mL) at 37 °C for 2 h. Equal amounts of PBS and LB agar liquid medium were determined as the negative control and positive control. After two hours of incubation, 10 µL of the mixture was drawn as an inoculum for agar plating. Enumeration of survivors' colonies (CFU) was performed on LB (Luria-Bertani) agar plates in triplicates.

##### 4.4. Peptide Purification

Appropriate amounts of the samples were taken and centrifuged at a high speed of  $20,000 \times g$  for 10 min to remove impurities such as precipitation. The supernatant was placed on ice and diluted with 8 M urea to a final concentration of 10 µg/µL, followed by incubation in the presence of 1 × protease cocktail and 2 mM EDTA for 5 min. Then, DTT (dithiothreitol) was added to a final concentration of 10 mM, followed by incubation for 1 h at 56 °C, and a final concentration of 55 mM IAM (iodoacetamide) was added to the mixture in a darkroom, followed by further incubation for 45 min at room temperature. Next, equal amounts of proteins in each sample were filtered in ultrafiltration tubes with a 10 kD filter membrane and centrifuged in a volume of 400 µL at a time at  $14,000 \times g$  for 15 min. The resultant filtrates were collected, which were then further purified by a C18 solid-phase extraction column (following a standard protocol involving activation, balance, sample loading, washing, and elution). The eluent was cold-frozen and drained.

The drained polypeptides were re-dissolved by 0.1% FA (Formic acid) of an appropriate volume, and their trace amounts were detected by MALDI-TOF mass spectrometry (MS) for quality control, followed by analysis by LC-MS/MS (Thermo Q-Exactive).

#### 4.5. MS Sequencing

LC-MS/MS analysis was performed on an UltiMate 3000 UHPLC (Thermo Scientific, Waltham, MA, USA), a prominence nano-HPLC system (Shimadzu, Tokyo, Japan) coupled with Q-Exactive (Thermo Fisher Scientific, Waltham, MA, USA). The peptides were re-dissolved and loaded on trap column (30  $\mu\text{m}$   $\times$  5 mm,  $\mu$ -Precolumn, Thermo Scientific, Waltham, MA, USA) with buffer A (2% ACN, 0.1% FA) in 5 min, followed by a 55 min gradient: from 5% B (98% ACN, 0.1% FA) to 25% B in 40 min, to 35% B in 5 min, to 80% B in 2 min, to 80% B for 2 min, dropped to 5% within 0.5 min and then kept at 5% B for 5.5 min at a flow rate of 300 nL/min. The sample was then separated and transferred to the mass spectrometry system.

After liquid-phase separation, peptides were ionized by a nanoESI source and then transferred to a Q-Exactive tandem mass spectrometer (Thermo Fisher Scientific, San Jose, CA, USA) for data-dependent acquisition (DDA) mode detection. The main parameters used were: ion source voltage set to 1.6 kV, and the scanning range of primary mass spectrometry to 350–1600  $m/z$ ; resolution set to 70,000; and an initial  $m/z$  of secondary mass spectrometry fixed as 100, at a resolution of 17,500. The parent ion screening conditions for secondary fragmentation were: charge, 2+ to 7+; and peak strength of the parent ion, > 10,000 and ranks in the first 20. Ion fragmentation mode was HCD, and fragmentation ions were detected in Orbitrap. The dynamic exclusion time was set to 15 s. The mass spectrometry proteomics data have been deposited to the ProteomeXchange Consortium via the PRIDE partner repository with the dataset identifier PXD025247.

#### 4.6. Peptide Identification and Bioinformatics Analysis

The raw MS/MS data were converted to MGF files and searched against the protein sequences from the genome database of *Crassostrea hongkongensis* [41], using MaxQuant 1.5.3.30. The parameters were set as follows: no enzyme selected; fixed modifications of carbamidomethyl (C); variable modification of oxidation (M); acetyl (protein N-term); 4.5 ppm ppm of precursor mass tolerance; 20 ppm of fragment ion tolerances; used match-between-runs (using default parameters); minimal peptide length, 7; and maximal peptide length, 45. The credible peptide identifications were obtained with FDR < 0.01 at both peptide spectrum matches (PSMs) and peptide levels. The identified peptides were applied to gene Ontology (GO) annotation by Blast2GO (version 5.2).

#### 4.7. Prediction on Antimicrobial Activity

Physicochemical properties of up-regulated peptides (URPs) were subjected to analysis by HeliQuest (<https://heliquest.ipmc.cnrs.fr/>, 2020-07-29), with regard to hydrophobicity, hydrophobic moment, and net charge ( $z$ ).

#### 4.8. Antimicrobial Susceptibility Assay

Candidate antimicrobial peptides was synthesized by Bankpeptide (Hefei, Anhui, China). For testing antimicrobial activities of the peptides, suspensions (about  $10^6$ – $10^7$  CFU/mL) of *Escherichia coli* DH5 $\alpha$ , *Vibrio alginolyticus* ZJ51, *Vibrio parahaemolyticus* E151, *Staphylococcus aureus* ATCC 29213, and *Candida albicans* ATCC 96901 were first prepared. The candidate antimicrobial peptides (5  $\mu\text{M}$ ) were separately incubated with the microbial suspensions for 1 h. Subsequently, a sample was taken as an inoculum for agar plating. CFUs (colony forming units) were enumerated on LB (for bacteria) and peptone (for *C. albicans*) agar plates following overnight culture for 16 h at 37  $^\circ\text{C}$ . A control group was set up by adding equal amounts of PBS. Antimicrobial susceptibilities were determined as a percentage of survival compared to that of the control group, and expressed as means  $\pm$  SD. All tests were performed in triplicates and repeat for three times.

#### 4.9. Determination of Minimum Inhibitory Concentrations (MICs) and Minimum Bactericidal Concentrations (MBCs) of URP20

For antibacterial and antifungal assays, MICs and MBCs were determined by plating bacterial/fungal cells on LB or peptone agar plates following incubation with different concentrations of URP20 (0, 0.5, 1, 2, 5, 10, 20, and 50  $\mu\text{M}$ ). Bacterial or fungal cells harvested from overnight cultures were washed three times to remove all traces of culture media and adjusted to a density of  $10^5$ – $10^6$  CFU/mL in sterile PBS before exposure to URP20. The bacterial or fungal suspensions were then incubated with or without peptides in PBS for 2 h at 37 °C. Subsequently, 10 microliters of the mixture from each sample were serially diluted in 1000  $\mu\text{L}$  PBS, from which a 10  $\mu\text{L}$  inoculum was plated in LB agar plates in a 12 well plate for overnight culture, followed by imaging and bacterial or fungus colony counts. Data were analyzed using GraphPad Prism (8.0) software and expressed as a percentage (means  $\pm$  SD) of killing compared to that of the control group. All tests were performed in triplicates and repeated for three times.

#### 4.10. Confocal Imaging of URP20 Triggered Assembly of the Bacterial Cells

Following overnight culture, bacteria (*E. coli* DH5 $\alpha$ ) were washed three times to remove all traces of culture medium and adjusted to a density of  $10^7$  CFU/mL in sterile PBS before exposure to URP20. *E. coli* DH5 $\alpha$  cells were transformed with a pFPV25.1 plasmid, which enabled them to emit green fluorescence (GFP). After 10 min exposure to URP20, the bacterial cells were washed three times, placed in confocal dishes, and fixed for 10 min in cold paraformaldehyde (4%). Then, cells were stained for DNA for 10 min with 0.25  $\mu\text{g}/\text{mL}$  DAPI (4, 6-diamidino-2-phenylindole). Finally, images were acquired with a Leica LP8X confocal fluorescence microscope.

#### 4.11. Membrane Permeabilization Assay

Bacterial and fungal cells harvested from overnight cultures were washed and resuspended at a density of  $10^9$  CFU/mL in PBS, before being incubated with 1  $\mu\text{M}$  Sytox green (Invitrogen, Waltham, MA, USA). Cells (100  $\mu\text{L}$ ) were then exposed to URP20 (20  $\mu\text{M}$ ) for different durations of time (0, 5, 30, 60, and 120 min), followed by washing three times with PBS. Cells were then subjected to flow cytometry to assess the extent of membrane permeabilization. For the untreated control group, PBS was added to replace the URP20, and the corresponding sample was subjected to flow cytometry, after incubation periods of 0, 5, 30, 60, and 120 min. The cells with no Sytox green and peptide were set as a blank control. Fluorescence intensity was measured at indicated time points. Permeabilization efficiency was determined by the percentage of cells emitting fluorescence.

#### 4.12. Cytotoxicity Assay

Potential cytotoxicity of URP20 was assessed through measurement of the release of lactate dehydrogenase (LDH) in the HEK293T cells, purchased from Guangzhou Cellcook Biotech Co.,Ltd. (Guangzhou, China). First, the cells were cultured overnight in DMEM (10% FBS, 1% penicillin-streptomycin solution) and then exposed to URP20 (0–50  $\mu\text{M}$ ) for another 24 h incubation under serum-free conditions. Then, cell viability was assessed by measuring the release of LDH with a commercial lactate dehydrogenase assay kit (ab102526; Abcam, Cambridge, UK).

Mouse J774.1 cells, purchased from Guangzhou Cellcook Biotech Co.,Ltd., were cultured overnight in DMEM (10% FBS, 1% penicillin-streptomycin solution) and allowed to attach. Then, cells were incubated with fresh medium, and treated with the peptide at different concentrations (1, 5, 10, 20, 50  $\mu\text{M}$ ) for another 24 h. Subsequently, cytokine levels were measured using an IL1 $\alpha$  ELISA kit (PI561; Beyotime, Haimen, China).

#### 4.13. In Vivo Toxicity in Mice

Animal experiments were carried out at the Guangdong Laboratory Animals Monitoring Institute, approved and reviewed by Institutional Animal Care and Use Committee of

the institute. Wide-type C57BL/6J mice with an average weight of 20 g were anesthetized by isoflurane inhalation and instilled intratracheally with different doses (0, 0.045, 0.45, 4.5 mg/kg) of URP20 in PBS (50 µL) and again 6 h later. Control mice were instilled with an equal amount of PBS without peptide. Survival of the mice was monitored over a period of 24 h after secondary instillation. Statistical analyses on the data were carried out by using GraphPad Prism software.

**Supplementary Materials:** The following are available online at <https://www.mdpi.com/article/10.3390/md19080420/s1>, Table S1. An overview of the peptide identification in each sample; Table S2. Physicochemical properties of up-regulated peptides (URPs); Figure S1 Abundances of identified peptides in each sample.

**Author Contributions:** Conceptualization, Y.Z. and Z.Y. (Ziniu Yu); methodology, F.M.; software, F.M.; validation, F.M., M.H. and K.L.; formal analysis, Z.Y. (Zhuo Yan), Z.X. and W.Y.; investigation, F.M. and Y.B.; resources, X.Z. and X.S.; data curation, F.M.; writing—original draft preparation, F.M.; writing—review and editing, Y.Z. and N.-K.W.; visualization, F.M.; supervision, Y.Z. and Z.Y. (Ziniu Yu); project administration, N.-K.W. and Y.B.; funding acquisition, F.M., Y.B., Y.Z. and Z.Y. (Ziniu Yu). All authors have read and agreed to the published version of the manuscript.

**Funding:** This research was funded by grants from the National Science Foundation of China (No. 32073002, 31902404), Key Special Project for Introduced Talents Team of Southern Marine Science and Engineering Guangdong Laboratory (Guangzhou) (GML2019ZD0407), Natural Science Foundation of Guangdong Province (2020A1515011533), the China Agricultural Research System (No. CARS-49), the Demonstration Project for Innovative Development of Marine Economy (NBHY-2017-S4), the Zhejiang Provincial Top Key Discipline (KF2020009), Institution of South China Sea Ecology and Environmental Engineering, Chinese Academy of Sciences (ISEE2018PY01, ISEE2018PY03, ISEE2018ZD01), and Science and Technology Planning Project of Guangdong Province, China (2017B030314052, 201707010177).

**Institutional Review Board Statement:** The study was conducted according to the guidelines of the Declaration of Helsinki, and approved and reviewed by Institutional Animal Care and Use Committee of Guangdong Laboratory Animal Monitoring Institute (No. 20201104039, approved on 4 November 2020).

**Informed Consent Statement:** Not applicable.

**Data Availability Statement:** The mass spectrometry proteomics data have been deposited to the ProteomeXchange Consortium via the PRIDE partner repository with the dataset identifier PXD025247 (<https://www.ebi.ac.uk/pride/archive/projects/PXD025247>).

**Acknowledgments:** We are deeply grateful to our lab members and collaborators, who have provided us with able assistance or valuable advice at all stages of this study.

**Conflicts of Interest:** The authors declare no conflict of interest.

## References

1. Alos, J.I. Antibiotic resistance: A global crisis. *Enferm. Infect. Microbiol. Clin.* **2015**, *33*, 692–699. [[CrossRef](#)]
2. Martin, M.J.; Thottathil, S.E.; Newman, T.B. Antibiotics Overuse in Animal Agriculture: A Call to Action for Health Care Providers. *Am. J. Public Health* **2015**, *105*, 2409–2410. [[CrossRef](#)] [[PubMed](#)]
3. Capita, R.; Alonso-Calleja, C. Antibiotic-resistant bacteria: A challenge for the food industry. *Crit. Rev. Food Sci. Nutr.* **2013**, *53*, 11–48. [[CrossRef](#)]
4. Sierra, J.M.; Fuste, E.; Rabanal, F.; Vinuesa, T.; Vinas, M. An overview of antimicrobial peptides and the latest advances in their development. *Expert Opin. Biol. Ther.* **2017**, *17*, 663–676. [[CrossRef](#)] [[PubMed](#)]
5. Hancock, R.E.; Diamond, G. The role of cationic antimicrobial peptides in innate host defences. *Trends Microbiol.* **2000**, *8*, 402–410. [[CrossRef](#)]
6. Mishra, B.; Reiling, S.; Zarena, D.; Wang, G.S. Host defense antimicrobial peptides as antibiotics: Design and application strategies. *Curr. Opin. Chem. Biol.* **2017**, *38*, 87–96. [[CrossRef](#)]
7. Lee, T.H.; Hall, K.N.; Aguilar, M.I. Antimicrobial Peptide Structure and Mechanism of Action: A Focus on the Role of Membrane Structure. *Curr. Top. Med. Chem.* **2016**, *16*, 25–39. [[CrossRef](#)]
8. Rai, M.; Pandit, R.; Gaikwad, S.; Kovics, G. Antimicrobial peptides as natural bio-preservative to enhance the shelf-life of food. *J. Food Sci. Tech.* **2016**, *53*, 3381–3394. [[CrossRef](#)] [[PubMed](#)]

9. Wang, G.S.; Li, X.; Wang, Z. APD3: The antimicrobial peptide database as a tool for research and education. *Nucleic Acids Res.* **2016**, *44*, D1087–D1093. [[CrossRef](#)]
10. Gerdol, M.; Gomez-Chiarri, M.; Castillo, M.G.; Figueras, A.; Fiorito, G.; Moreira, R.; Novoa, B.; Pallavicini, A.; Ponte, G.; Roubledakis, K.; et al. Immunity in Molluscs: Recognition and Effector Mechanisms, with a Focus on Bivalvia. In *Advances in Comparative Immunology*; Cooper, E., Ed.; Springer: Cham, Switzerland, 2018; pp. 225–341.
11. De Zoysa, M. *Antimicrobial Peptides in Marine Mollusks and Their Potential Applications*; John Wiley & Sons Ltd.: Hoboken, NJ, USA, 2013; pp. 695–707.
12. Mitta, G.; Vandenbulcke, F.; Hubert, F.; Roch, P. Mussel defensins are synthesised and processed in granulocytes then released into the plasma after bacterial challenge. *J. Cell Sci.* **1999**, *112*, 4233–4242. [[CrossRef](#)]
13. Mitta, G.; Vandenbulcke, F.; Roch, P. Original involvement of antimicrobial peptides in mussel innate immunity. *FEBS Lett.* **2000**, *486*, 185–190. [[CrossRef](#)]
14. Mitta, G.; Hubert, F.; Noel, T.; Roch, P. Myticin, a novel cysteine-rich antimicrobial peptide isolated from haemocytes and plasma of the mussel *Mytilus galloprovincialis*. *Eur. J. Biochem.* **1999**, *265*, 71–78. [[CrossRef](#)]
15. Mitta, G.; Vandenbulcke, F.; Hubert, F.; Salzet, M.; Roch, P. Involvement of mytilins in mussel antimicrobial defense. *J. Biol. Chem.* **2000**, *275*, 12954–12962. [[CrossRef](#)]
16. Mitta, G.; Vandenbulcke, F.; Noel, T.; Romestand, B.; Beauvillain, J.C.; Salzet, M.; Roch, P. Differential distribution and defence involvement of antimicrobial peptides in mussel. *J. Cell Sci.* **2000**, *113*, 2759–2769. [[CrossRef](#)]
17. Seo, J.K.; Crawford, J.M.; Stone, K.L.; Noga, E.J. Purification of a novel arthropod defensin from the American oyster, *Crassostrea virginica*. *Biochem. Biophys. Res. Commun.* **2005**, *338*, 1998–2004. [[CrossRef](#)]
18. Schmitt, P.; Wilmes, M.; Pugniere, M.; Aumelas, A.; Bachere, E.; Sahl, H.G.; Schneider, T.; Destoumieux-Garzon, D. Insight into Invertebrate Defensin Mechanism of Action oyster defensins inhibit peptidoglycan biosynthesis by binding to lipid II. *J. Biol. Chem.* **2010**, *285*, 29208–29216. [[CrossRef](#)] [[PubMed](#)]
19. De Zoysa, M.; Whang, I.; Lee, Y.; Lee, S.; Lee, J.S.; Lee, J. Defensin from disk abalone *Haliotis discus discus*: Molecular cloning, sequence characterization and immune response against bacterial infection. *Fish Shellfish Immunol.* **2010**, *28*, 261–266. [[CrossRef](#)]
20. Sperstad, S.V.; Haug, T.; Blencke, H.M.; Styrvoid, O.B.; Li, C.; Stensvag, K. Antimicrobial peptides from marine invertebrates: Challenges and perspectives in marine antimicrobial peptide discovery. *Biotechnol. Adv.* **2011**, *29*, 519–530. [[CrossRef](#)] [[PubMed](#)]
21. Roch, P.; Yang, Y.; Toubiana, M.; Aumelas, A. NMR structure of mussel mytilin, and antiviral-antibacterial activities of derived synthetic peptides. *Dev. Comp. Immunol.* **2008**, *32*, 227–238. [[CrossRef](#)] [[PubMed](#)]
22. Campos, A.; Apraiz, I.; da Fonseca, R.R.; Cristobal, S. Shotgun analysis of the marine mussel *Mytilus edulis* hemolymph proteome and mapping the innate immunity elements. *Proteomics* **2015**, *15*, 4021–4029. [[CrossRef](#)]
23. Soderhall, K.; Cerenius, L. Role of the prophenoloxidase-activating system in invertebrate immunity. *Curr. Opin. Immunol.* **1998**, *10*, 23–28. [[CrossRef](#)]
24. Breitenbach Barroso Coelho, L.C.; Marcelino Dos Santos Silva, P.; Felix de Oliveira, W.; de Moura, M.C.; Viana Pontual, E.; Soares Gomes, F.; Guedes Paiva, P.M.; Napoleao, T.H.; Dos Santos Correia, M.T. Lectins as antimicrobial agents. *J. Appl. Microbiol.* **2018**, *125*, 1238–1252. [[CrossRef](#)] [[PubMed](#)]
25. Gonzalez Garcia, M.; Rodriguez, A.; Alba, A.; Vazquez, A.A.; Morales Vicente, F.E.; Perez-Erviti, J.; Spellerberg, B.; Stenger, S.; Grieshober, M.; Conzelmann, C.; et al. New Antibacterial Peptides from the Freshwater Mollusk *Pomacea poeyana* (Pilsbry, 1927). *Biomolecules* **2020**, *10*, 1473. [[CrossRef](#)] [[PubMed](#)]
26. Joerger, R.D. Alternatives to antibiotics: Bacteriocins, antimicrobial peptides and bacteriophages. *Poult. Sci.* **2003**, *82*, 640–647. [[CrossRef](#)]
27. Carrillo, J.L.M.; Rodríguez, F.P.C.; Coronado, O.G.; García, M.A.M.; Cordero, J.F.C. Physiology and Pathology of Innate Immune Response Against Pathogens. In *Physiology and Pathology of Immunology*; Rezaei, N., Ed.; IntechOpen: London, UK, 2017.
28. Bohle, L.A.; Brede, D.A.; Diep, D.B.; Holo, H.; Nes, I.F. Specific degradation of the mucus adhesion-promoting protein (MapA) of *Lactobacillus reuteri* to an antimicrobial peptide. *Appl. Environ. Microbiol.* **2010**, *76*, 7306–7309. [[CrossRef](#)]
29. Rubinsztein, D.C. The roles of intracellular protein-degradation pathways in neurodegeneration. *Nature* **2006**, *443*, 780–786. [[CrossRef](#)]
30. De Zoysa, M.; Nikapitiya, C.; Whang, I.; Lee, J.S.; Lee, J. Abhisin: A potential antimicrobial peptide derived from histone H2A of disk abalone (*Haliotis discus discus*). *Fish Shellfish Immunol.* **2009**, *27*, 639–646. [[CrossRef](#)]
31. Andrews, S.J.; Rothnagel, J.A. Emerging evidence for functional peptides encoded by short open reading frames. *Nat. Rev. Genet.* **2014**, *15*, 193–204. [[CrossRef](#)]
32. Zhu, S.; Wang, J.; He, Y.; Meng, N.; Yan, G.R. Peptides/Proteins Encoded by Non-coding RNA: A Novel Resource Bank for Drug Targets and Biomarkers. *Front. Pharmacol.* **2018**, *9*, 1295. [[CrossRef](#)]
33. Lai, Y.P.; Gallo, R.L. AMPed up immunity: How antimicrobial peptides have multiple roles in immune defense. *Trends Immunol.* **2009**, *30*, 131–141. [[CrossRef](#)]
34. Yount, N.Y.; Bayer, A.S.; Xiong, Y.Q.; Yeaman, M.R. Advances in antimicrobial peptide immunobiology. *Biopolymers* **2006**, *84*, 435–458. [[CrossRef](#)]
35. Taniguchi, M.; Takahashi, N.; Takayanagi, T.; Ikeda, A.; Ishiyama, Y.; Saitoh, E.; Kato, T.; Ochiai, A.; Tanaka, T. Effect of substituting arginine and lysine with alanine on antimicrobial activity and the mechanism of action of a cationic dodecapeptide (CL(14-25)), a partial sequence of cyanate lyase from rice. *Biopolymers* **2014**, *102*, 58–68. [[CrossRef](#)]

36. Saint Jean, K.D.; Henderson, K.D.; Chrom, C.L.; Abiuso, L.E.; Renn, L.M.; Caputo, G.A. Effects of Hydrophobic Amino Acid Substitutions on Antimicrobial Peptide Behavior. *Probiotics Antimicrob. Proteins* **2018**, *10*, 408–419. [[CrossRef](#)]
37. Brogden, K.A. Antimicrobial peptides: Pore formers or metabolic inhibitors in bacteria? *Nat. Rev. Microbiol.* **2005**, *3*, 238–250. [[CrossRef](#)]
38. Kirk, M.D.; Pires, S.M.; Black, R.E.; Caipo, M.; Crump, J.A.; Devleeschauwer, B.; Dopfer, D.; Fazil, A.; Fischer-Walker, C.L.; Hald, T.; et al. World Health Organization Estimates of the Global and Regional Disease Burden of 22 Foodborne Bacterial, Protozoal, and Viral Diseases, 2010: A Data Synthesis. *PLoS Med.* **2015**, *12*, e1001921.
39. Nobile, C.J.; Johnson, A.D. *Candida albicans* Biofilms and Human Disease. *Annu. Rev. Microbiol.* **2015**, *69*, 71–92. [[CrossRef](#)]
40. Palmieri, G.; Balestrieri, M.; Proroga, Y.T.; Falcigno, L.; Facchiano, A.; Riccio, A.; Capuano, F.; Marrone, R.; Neglia, G.; Anastasio, A. New antimicrobial peptides against foodborne pathogens: From in silico design to experimental evidence. *Food Chem.* **2016**, *211*, 546–554. [[CrossRef](#)]
41. Zhang, Y.; Mao, F.; Xiao, S.; Yu, H.; Xiang, Z.; Xu, F.; Li, J.; Wang, L.; Xiong, Y.; Chen, M.; et al. Comparative genomics reveals evolutionary drivers of sessile life and left-right shell asymmetry in bivalves. *bioRxiv* **2021**.



## Article

# Cytotoxic Minor Piericidin Derivatives from the Actinomycete Strain *Streptomyces psammoticus* SCSIO NS126

Kunlong Li <sup>1,2,3</sup>, Ziqi Su <sup>4</sup>, Yongli Gao <sup>2,5</sup>, Xiuping Lin <sup>1</sup>, Xiaoyan Pang <sup>1</sup>, Bin Yang <sup>1,2</sup>, Huaming Tao <sup>4</sup>, Xiaowei Luo <sup>6,\*</sup>, Yonghong Liu <sup>1,2,3,6,\*</sup> and Xuefeng Zhou <sup>1,2,\*</sup>

- <sup>1</sup> CAS Key Laboratory of Tropical Marine Bio-Resources and Ecology, Guangdong Key Laboratory of Marine Materia Medica, South China Sea Institute of Oceanology, Chinese Academy of Sciences, Guangzhou 510301, China; likunlong16@mailsucas.ac.cn (K.L.); xiupinglin@hotmail.com (X.L.); xypang@scsio.ac.cn (X.P.); yangbin@scsio.ac.cn (B.Y.)
- <sup>2</sup> Southern Marine Science and Engineering Guangdong Laboratory (Guangzhou), Guangzhou 511458, China; yongligao@scsio.ac.cn
- <sup>3</sup> College of Earth and Planetary Sciences, University of Chinese Academy of Sciences, Beijing 100049, China
- <sup>4</sup> School of Traditional Chinese Medicine, Southern Medical University, Guangzhou 510515, China; ziqisli@163.com (Z.S.); taohm@smu.edu.cn (H.T.)
- <sup>5</sup> Institutional Center for Shared Technologies and Facilities, South China Sea Institute of Oceanology, Chinese Academy of Sciences, Guangzhou 510301, China
- <sup>6</sup> Institute of Marine Drugs, Guangxi University of Chinese Medicine, Nanning 530200, China
- \* Correspondence: luoxiaowei1991@126.com (X.L.); yonghongliu@scsio.ac.cn (Y.L.); xfzhou@scsio.ac.cn (X.Z.); Tel.: +86-020-89023174 (X.Z.)

**Citation:** Li, K.; Su, Z.; Gao, Y.; Lin, X.; Pang, X.; Yang, B.; Tao, H.; Luo, X.; Liu, Y.; Zhou, X. Cytotoxic Minor Piericidin Derivatives from the Actinomycete Strain *Streptomyces psammoticus* SCSIO NS126. *Mar. Drugs* **2021**, *19*, 428. <https://doi.org/10.3390/md19080428>

Academic Editor: Vassilios Roussis

Received: 7 July 2021

Accepted: 26 July 2021

Published: 28 July 2021

**Publisher's Note:** MDPI stays neutral with regard to jurisdictional claims in published maps and institutional affiliations.



**Copyright:** © 2021 by the authors. Licensee MDPI, Basel, Switzerland. This article is an open access article distributed under the terms and conditions of the Creative Commons Attribution (CC BY) license (<https://creativecommons.org/licenses/by/4.0/>).

**Abstract:** The mangrove-sediment-derived actinomycete strain *Streptomyces psammoticus* SCSIO NS126 was found to have productive piericidin metabolites featuring anti-renal cell carcinoma activities. In this study, in order to explore more diverse piericidin derivatives, and therefore to discover superior anti-tumor lead compounds, the NS126 strain was further fermented at a 300-L scale under optimized fermentation conditions. As a result, eight new minor piericidin derivatives (piericidins L-R (1–7) and 11-demethyl-gluco-piericidin A (8)) were obtained, along with gluco-piericidin B (9). The new structures including absolute configurations were determined by spectroscopic methods coupled with experimental and calculated electronic circular dichroism. We also proposed plausible biosynthetic pathways for these unusual post-modified piericidins. Compounds **1** and **6** showed selective cytotoxic activities against OS-RC-2 cells, and **2–5** exhibited potent cytotoxicity against HL-60 cells, with IC<sub>50</sub> values lower than 0.1 μM. The new piericidin glycoside **8** was cytotoxic against ACHN, HL-60 and K562, with IC<sub>50</sub> values of 2.3, 1.3 and 5.5 μM, respectively. The ability to arrest the cell cycle and cell apoptosis effects induced by **1** and **6** in OS-RC-2 cells, **2** in HL-60 cells, and **8** in ACHN cells were then further investigated. This study enriched the structural diversity of piericidin derivatives and confirmed that piericidins deserve further investigations as promising anti-tumor agents.

**Keywords:** actinomycete; piericidins; absolute configuration; cytotoxicity

## 1. Introduction

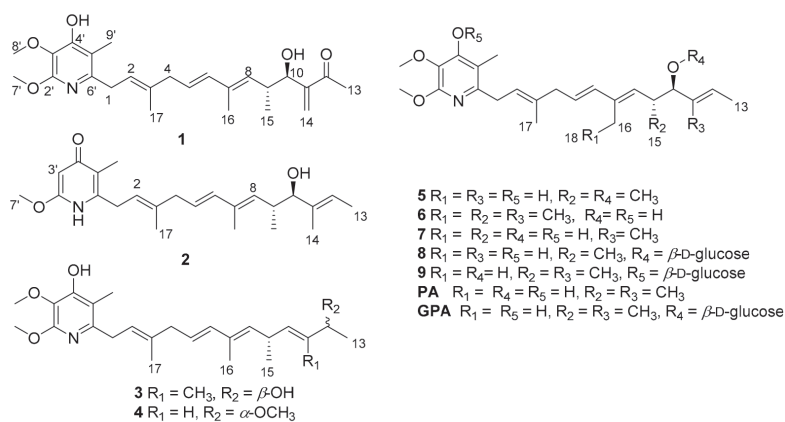
Actinomycetes from terrestrial sources have been studied and screened since the 1950s, yielding many important anti-infective and anti-cancer drugs. At the same time, actinomycetes isolated from the marine environment, especially *Streptomyces* strains, have yielded several promising drug candidates, and have received considerable attention in recent years [1–3]. Piericidins, which are produced by actinomycetes isolated from soil, insects and marine samples, are known as NADH:ubiquinone oxidoreductase inhibitors and antitumor agents [4].

Recently, some biologically significant piericidins were discovered in two mangrove-sediment-derived *Streptomyces* strains by our group [5–7]. In a culture extract of the strain



*Streptomyces psammoticus* SCSIO NS126, twenty-seven natural piericidins were isolated and found to have notable anti-renal cell carcinoma (RCC) activities. Our previous studies also revealed that piericidins could conceivably provide a novel scaffold for the further development of potent and mechanistically novel anti-RCC agents [5,6]. It was previously shown that external pH plays an important role in regulating the secondary metabolites of microorganisms [8]. At times, the influence of pH was found to be greater than that of carbon and nitrogen nutrition in the cultivation of bacteria [9]. In recent years, bacteria capable of growing under acidic conditions have attracted the interest of scientists due to their structurally novel secondary metabolites featuring compelling biological activities [10]. Researchers have demonstrated that mangrove-sediment microbial communities are highly correlated with environmental factors such as salinity, pH and nutrient bioavailability [11].

In order to explore more diverse piericidin derivatives, and therefore to discover better anti-tumor lead compounds, we sought to optimize the fermentation conditions of the mangrove-sediment-derived NS126 strain by adjusting the pH and choosing the culture time, as well as engaging in large-scale fermentation (300 L). In addition to the isolation and accumulation of the reported active piericidins, nine other piericidin compounds (1–9) were obtained (Figure 1), including eight new piericidins (1–8) in trace amounts (about 1–3 mg), as well as a known glucopiericidin B (9) that was first discovered in this strain. Herein, we report the isolation, structural elucidation and bioactivities of these compounds.



**Figure 1.** Structures of compounds 1–9, PA and GPA.

## 2. Results

In the fermentation condition screening tests, the secondary metabolites of the NS126 strain fermented at pH 4 showed greater chemical diversity (Figure S82). Moreover, after culturing for 30 h (pH 4), the strain was able to produce a large quantity of the main piericidin metabolites (Figure S83), piericidin A (PA) and glucopiericidin A (GPA) (Figure 1) [6]. At the same time, the extract also showed a variety of chemicals in its composition (Figure S84). Strain NS126 was further fermented at a 300 L scale under optimized fermentation conditions (pH 4, cultured for 30 h). About 1200 mg PA and 680 mg GPA were isolated and purified in order to further evaluate their pharmacological and pharmacokinetic/toxicokinetic properties [5]. In addition to the accumulation of the reported active piericidins, eight other new piericidins (1–8) were obtained in trace amounts (about 1–3 mg), as well as a known glucopiericidin B (9) that was discovered first in this strain [12] (Figure 1).

Compound **1** was isolated as a pale yellow oil. The HRESIMS ( $m/z$  430.2583  $[M + H]^+$ ) data suggested the molecular formula of  $C_{25}H_{35}NO_5$ , revealing nine degrees of unsaturation. The IR spectrum exhibited absorption bands for the pyridine ring (1585, 1500 and  $802\text{ cm}^{-1}$ ) and one carbonyl group ( $1670\text{ cm}^{-1}$ ). The NMR spectra showed signals for seven methyls (including two oxygenated ones), three methylenes (including one terminal olefinic carbon), six methines (including four olefinic ones) and nine aromatic/olefinic carbons. A comparison of the pyridine ring's  $^1\text{H}$  and  $^{13}\text{C}$  NMR data (Tables 1 and 2) with those of the PA indicated that they share a similar skeleton [13]. However, a set of signals at H<sub>2</sub>-14 ( $\delta_{\text{H}}$  6.21;  $\delta_{\text{H}}$  6.02), C-11 ( $\delta_{\text{C}}$  152.0) and C-12 ( $\delta_{\text{C}}$  201.8) (Tables 1 and 2), which was not present in the  $^1\text{H}$  and  $^{13}\text{C}$  NMR spectra of PA, was observed in the spectrum of **1**. Through the analysis of the HMBC spectrum, the  $\alpha$ ,  $\beta$ -unsaturated carbonyl moiety ( $\text{CH}_2=\text{C}-\text{C}=\text{O}$ ) was confirmed by the HMBC correlations from H<sub>2</sub>-14 to C-10/C-11/C-12, H<sub>3</sub>-13 to C-11/C-14 and H-10 to C-12 (Figure 2). In this way, the planar structure of **1**, named piericidin L (**1**), was identified, as shown in Figure 1. Piericidin L is the first piericidin analogue possessing a terminal-olefinic-bond moiety conjugated with the carbonyl moiety [6].

Table 1.  $^1\text{H}$  NMR data of **1**–**8** (700 MHz,  $\delta$  in ppm).

| Pos. | 1 <sup>a</sup>        | 2 <sup>a</sup> | 3 <sup>a</sup> | 4 <sup>b</sup>         | 5 <sup>b</sup> | 6 <sup>c</sup>       | 7 <sup>a</sup> | 8 <sup>a</sup>        |
|------|-----------------------|----------------|----------------|------------------------|----------------|----------------------|----------------|-----------------------|
| 1    | 3.39 (d, 6.9)         | 3.36 (d, 6.9)  | 3.42 (d, 6.9)  | 3.37 (d, 6.9)          | 3.37 (d, 6.9)  | 3.25 (d, 6.9)        | 3.35 (d, 6.9)  | 3.48 (d, 6.9)         |
| 2    | 5.28 (t, 6.9)         | 5.18 (t, 6.9)  | 5.27 (t, 6.9)  | 5.41 (t, 6.9)          | 5.40 (d, 6.9)  | 5.30 (t, 6.9)        | 5.31 (t, 6.9)  | 5.26 (t, 6.9)         |
| 4    | 2.76 (d, 7.1)         | 2.79 (d, 6.9)  | 2.77 (d, 7.0)  | 2.78 (d, 6.9)          | 2.78 (d, 6.7)  | 2.72 (d, 6.8)        | 2.76 (d, 6.9)  | 2.80 (d, 7.1)         |
| 5    | 5.45 (m)              | 5.50 (m)       | 5.53(m)        | 5.57 (m)               | 5.52 (m)       | 5.48 (m)             | 5.53 (m)       | 5.55 (m)              |
| 6    | 6.02<br>(d,15.8)      | 6.08 (d, 5.5)  | 6.02 (d, 6.2)  | 6.05 (d,<br>15.8)      | 6.07 (d, 6.0)  | 5.86 (d, 5.7)        | 6.03(d,15.5)   | 6.08 (d, 6.1)         |
| 8    | 5.26 (d,<br>10.4)     | 5.30 (d, 9.2)  | 5.22 (d, 9.2)  | 5.20 (d, 9.1)          | 5.26 (d, 9.4)  | 5.19 (d, 9.7)        | 5.30 (t, 6.7)  | 5.30 (d, 9.5)         |
| 9    | 2.75 (m)              | 2.64 (m)       | 3.42 (m)       | 3.18 (m)               | 2.63 (m)       | 2.50 (m)             | 2.35 (m)       | 2.83 (m)              |
| 10   | 4.52 (d, 4.0)         | 3.69 (d, 8.2)  | 5.26 (d, 9.0)  | 5.53 (m)               | 3.31 (m)       | 3.59 (d, 7.1)        | 3.96 (t, 7.0)  | 4.00 (d, 8.0)         |
| 11   |                       |                |                | 5.27(m)                | 5.26 (m)       |                      |                | 5.52 (m)              |
| 12   |                       | 5.44 (q, 6.8)  | 4.11 (q, 6.9)  | 3.65 (m)               | 5.60 (m)       | 5.32 (q, 6.4)        | 5.44 (q, 5.9)  | 5.65 (m)              |
| 13   | 2.30 (s)              | 1.62 (d, 6.8)  | 1.20 (d, 6.9)  | 1.21 (dd,<br>2.1, 6.3) | 1.73 (d, 6.7)  | 1.54 (d, 6.6)        | 1.60 (d, 5.4)  | 1.71 (d, 6.4)         |
| 14   | 6.21 (s);<br>6.01 (s) | 1.60 (s)       | 1.65 (d, 1.3)  | 3.23 (s)               | 3.22 (s)       | 1.50 (s)             | 1.60 (s)       |                       |
| 15   | 1.03 (d, 6.9)         | 0.81 (d, 6.9)  | 1.01 (d, 6.8)  | 1.08 (t, 6.3)          | 0.93 (d, 6.9)  | 0.77 (d, 6.8)        |                | 1.02 (d, 6.9)         |
| 16   | 1.57 (s)              | 1.74 (s)       | 1.74 (s)       | 1.74 (s)               | 1.72 (s)       | 2.17(m);<br>2.12 (m) | 1.71 (s)       | 1.75 (s)              |
| 17   | 1.74 (s)              | 1.74 (s)       | 1.74 (s)       | 1.75 (s)               | 1.74 (s)       | 1.70 (s)             | 1.73 (s)       | 1.78 (s)              |
| 18   |                       |                |                |                        |                | 0.93 (t, 7.4)        |                |                       |
| 3'   |                       | 5.88 (s)       |                |                        |                |                      |                |                       |
| 7'   | 3.96 (s)              | 3.86 (s)       | 4.00 (s)       | 3.95 (s)               | 3.95 (s)       | 3.77 (s)             | 3.90 (s)       | 4.09 (s)              |
| 8'   | 3.76 (s)              |                | 3.77 (s)       | 3.86 (s)               | 3.86 (s)       | 3.61 (s)             | 3.74 (s)       | 3.81 (s)              |
| 9'   | 2.06 (s)              | 1.96 (s)       | 2.07 (s)       | 2.09 (s)               | 2.09 (s)       | 1.95 (s)             | 2.04 (s)       | 2.11 (s)              |
| 1''  |                       |                |                |                        |                |                      |                | 4.33 (d, 7.8)         |
| 2''  |                       |                |                |                        |                |                      |                | 3.20 (m)              |
| 3''  |                       |                |                |                        |                |                      |                | 3.36(m)               |
| 4''  |                       |                |                |                        |                |                      |                | 3.66(m)               |
| 5''  |                       |                |                |                        |                |                      |                | 3.20 (m)              |
| 6''  |                       |                |                |                        |                |                      |                | 3.65 (m);<br>3.78 (m) |

<sup>a</sup> Data measured in CD<sub>3</sub>OD. <sup>b</sup> Data measured in CDCl<sub>3</sub>. <sup>c</sup> Data measured in DMSO-*d*<sub>6</sub>.

Table 2.  $^{13}\text{C}$  NMR data of 1–8 (175 MHz,  $\delta$  in ppm).

| Pos. | 1 <sup>a</sup>         | 2 <sup>a</sup>        | 3 <sup>a</sup>        | 4 <sup>b</sup>        | 5 <sup>b</sup>        | 6 <sup>c</sup>        | 7 <sup>a</sup>        | 8 <sup>a</sup>        |
|------|------------------------|-----------------------|-----------------------|-----------------------|-----------------------|-----------------------|-----------------------|-----------------------|
| 1    | 34.8, CH <sub>2</sub>  | 32.3, CH <sub>2</sub> | 34.1, CH <sub>2</sub> | 34.6, CH <sub>2</sub> | 34.6, CH <sub>2</sub> | 34.2, CH <sub>2</sub> | 34.9, CH <sub>2</sub> | 33.4, CH <sub>2</sub> |
| 2    | 122.9, CH              | 121.0, CH             | 122.2, CH             | 122.2, CH             | 122.1, CH             | 122.2, CH             | 123.4, CH             | 121.5, CH             |
| 3    | 136.7, C               | 138.4, C              | 137.1, C              | 135.1, C              | 135.2, C              | 133.9, C              | 135.9, C              | 137.9, CH             |
| 4    | 43.9, CH <sub>2</sub>  | 43.9, CH <sub>2</sub> | 43.9, CH <sub>2</sub> | 43.3, CH <sub>2</sub> | 43.3, CH <sub>2</sub> | 42.4, CH <sub>2</sub> | 44.0, CH <sub>2</sub> | 43.9, CH <sub>2</sub> |
| 5    | 126.4, CH              | 125.7, CH             | 126.3, CH             | 126.2, CH             | 125.6, CH             | 124.2, CH             | 126.5, CH             | 126.2, CH             |
| 6    | 137.6, CH              | 138.1, CH             | 137.6, CH             | 136.0, CH             | 136.4, CH             | 134.5, CH             | 137.4, CH             | 137.8, CH             |
| 7    | 135.2, C               | 134.8, C              | 132.7, C              | 133.0, C              | 133.5, C              | 138.1, C              | 135.9, C              | 134.6, C              |
| 8    | 132.9, CH              | 135.8, CH             | 136.6, CH             | 134.4, CH             | 133.6, CH             | 134.6, CH             | 127.8, CH             | 134.4, CH             |
| 9    | 38.4, CH               | 37.6, CH              | 32.6, CH              | 35.2, CH              | 37.6, CH              | 36.1, CH              | 34.9, CH <sub>2</sub> | 38.1, CH              |
| 10   | 73.7, CH               | 83.7, CH              | 130.3, CH             | 137.1, CH             | 86.8, CH              | 80.4, CH              | 78.5, CH              | 86.1, CH              |
| 11   | 152.0, C               | 136.6, C              | 138.0, CH             | 129.8, CH             | 129.9, CH             | 137.8, C              | 138.7, C              | 131.5, CH             |
| 12   | 201.8, C               | 122.8, CH             | 73.9, CH              | 78.2, CH              | 129.9, CH             | 119.4, CH             | 121.5, CH             | 129.4, CH             |
| 13   | 26.5, CH <sub>3</sub>  | 13.1, CH <sub>3</sub> | 22.0, CH <sub>3</sub> | 21.6, CH <sub>3</sub> | 17.9, CH <sub>3</sub> | 12.8, CH <sub>3</sub> | 13.1, CH <sub>3</sub> | 18.0, CH <sub>3</sub> |
| 14   | 126.8, CH <sub>2</sub> | 11.1, CH <sub>3</sub> | 11.8, CH <sub>3</sub> | 55.8, CH <sub>3</sub> | 56.3, CH <sub>3</sub> | 11.4, CH <sub>3</sub> | 11.1, CH <sub>3</sub> | -                     |
| 15   | 18.5, CH <sub>3</sub>  | 18.1, CH <sub>3</sub> | 21.8, CH <sub>3</sub> | 21.0, CH <sub>3</sub> | 16.8, CH <sub>3</sub> | 18.3, CH <sub>3</sub> | -                     | 16.4, CH <sub>3</sub> |
| 16   | 13.0, CH <sub>3</sub>  | 13.1, CH <sub>3</sub> | 12.9, CH <sub>3</sub> | 12.8, CH <sub>3</sub> | 13.0, CH <sub>3</sub> | 19.7, CH <sub>2</sub> | 12.9, CH <sub>3</sub> | 13.0, CH <sub>3</sub> |
| 17   | 16.7, CH <sub>3</sub>  | 16.7, CH <sub>3</sub> | 16.7, CH <sub>3</sub> | 16.8, CH <sub>3</sub> | 16.8, CH <sub>3</sub> | 16.5, CH <sub>3</sub> | 16.6, CH <sub>3</sub> | 16.7, CH <sub>3</sub> |
| 18   | -                      | -                     | -                     | -                     | -                     | 13.8, CH <sub>3</sub> | -                     | -                     |
| 2'   | 155.9, C               | 161.8, C              | 155.8, C              | 153.7, C              | 153.6, C              | 154.3, C              | 156.1, C              | 155.7, C              |
| 3'   | 130.6, C               | 92.8, CH              | 131.2, C              | 127.9, C              | 127.9, C              | 128.5, C              | 130.1, C              | 131.5, C              |
| 4'   | 158.5, C               | 179.1, C              | 159.8, C              | 154.1, C              | 154.1, C              | 157.1, C              | 157.2, C              | 161.6, C              |
| 5'   | 115.2, C               | 117.6, C              | 115.9, C              | 112.1, C              | 112.1, C              | 112.9, C              | 114.8, C              | 116.8, C              |
| 6'   | 151.2, C               | 149.8, C              | 150.5, C              | 151.0, C              | 151.1, C              | 148.9, C              | 151.7, C              | 149.9, C              |
| 7'   | 54.4, CH <sub>3</sub>  | 56.1, CH <sub>3</sub> | 55.7, CH <sub>3</sub> | 53.2, CH <sub>3</sub> | 53.2, CH <sub>3</sub> | 52.3, CH <sub>3</sub> | 53.7, CH <sub>3</sub> | 57.3, CH <sub>3</sub> |
| 8'   | 61.0, CH <sub>3</sub>  | -                     | 61.2, CH <sub>3</sub> | 60.8, CH <sub>3</sub> | 60.8, CH <sub>3</sub> | 59.7, CH <sub>3</sub> | 60.8, CH <sub>3</sub> | 61.4, CH <sub>3</sub> |
| 9'   | 10.8, CH <sub>3</sub>  | 10.3, CH <sub>3</sub> | 10.7, CH <sub>3</sub> | 10.6, CH <sub>3</sub> | 10.6, CH <sub>3</sub> | 10.6, CH <sub>3</sub> | 10.8, CH <sub>3</sub> | 10.7, CH <sub>3</sub> |
| 1''  | -                      | -                     | -                     | -                     | -                     | -                     | -                     | 103.3, CH             |
| 2''  | -                      | -                     | -                     | -                     | -                     | -                     | -                     | 75.5, CH              |
| 3''  | -                      | -                     | -                     | -                     | -                     | -                     | -                     | 78.3, CH              |
| 4''  | -                      | -                     | -                     | -                     | -                     | -                     | -                     | 71.6, CH              |
| 5''  | -                      | -                     | -                     | -                     | -                     | -                     | -                     | 77.9, CH              |
| 6''  | -                      | -                     | -                     | -                     | -                     | -                     | -                     | 62.7, CH <sub>2</sub> |

<sup>a</sup> Data measured in CD<sub>3</sub>OD. <sup>b</sup> Data measured in CDCl<sub>3</sub>. <sup>c</sup> Data measured in DMSO-*d*<sub>6</sub>.

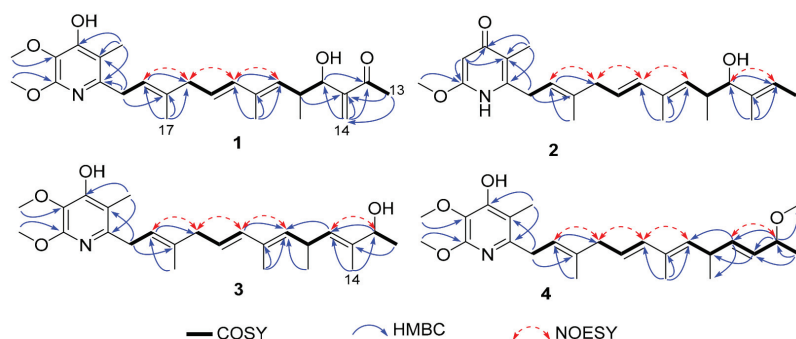


Figure 2. Key COSY, HMBC and NOESY correlations in 1–4.

Compound 2 was obtained as a brown oil, and it exhibited a molecular formula of C<sub>24</sub>H<sub>35</sub>NO<sub>3</sub> via the (+)-HRESIMS ion at  $m/z$  386.2696 [M + H]<sup>+</sup>. The NMR signals of 2 resembled those of Mer-A2026 B, except for the presence of another carbonyl group at C-4' ( $\delta_{\text{C}}$  179.1), which was confirmed by the HMBC correlations of H-3' with C-2'/C-4'/C-5', and those of H<sub>3</sub>-9' with C-4'/C-5' (Figure 2) [14]. In this way, the planar structure of 2 was

established (Figure 1) and named piericidin N (2), which is the third piericidin aglycone found to consist of a pyridone structure [15,16].

Compound 3 was isolated as a pale yellow oil. The (+)-HRESIMS data ( $m/z$  438.2614  $[M + Na]^+$ ) indicated that this compound possessed the same molecular formula as PA— $C_{25}H_{37}NO_4$ . A comparison of the  $^1H$  and  $^{13}C$  NMR data for 3 and PA suggested that 3 was an analogue of PA, with a pyridine, four double bonds, and two hydroxyl groups (Tables 1 and 2) [13]. However, the locations of C-10 ( $\delta_C$  130.3) and C-12 ( $\delta_C$  73.9) changed, as determined by the  $^1H$ - $^1H$  COSY signals of two isolated proton-spin systems of H-8/H-9/H-10 ( $\delta_H$  5.26) and H-12 ( $\delta_H$  4.11)/H<sub>3</sub>-13, together with the HMBC correlations of H-10 with C-8/C-9, H<sub>3</sub>-13 with C-11/C-12, H<sub>3</sub>-14 with C-10/C-12, and H<sub>3</sub>-15 with C-8/C-9/C-10 (Figure 2). In this way, the planar structure of 3 was determined and named piericidin Q (3), as shown in Figure 1.

Compound 4 was determined to have the same molecular formula as 3. A comparison of the  $^1H$  and  $^{13}C$  NMR spectra of 4 with those of 3 showed many similarities, except for the elimination of 11-CH<sub>3</sub> and the methylation of 12-OH (Tables 1 and 2), which were confirmed by the  $^1H$ - $^1H$  COSY correlations of H-8/H-9/H-10/H-11/H-12/H-13, as well as the HMBC correlations of H-10 to C-8/C-9, H-11 to C-9, H-12 to C-11/C-12, and H<sub>3</sub>-14 to C-12 (Figure 2). Compound 4 was named piericidin O (4), as shown in Figure 1. Both 3 and 4 are the first-discovered piericidin analogues with changes in C-10 and C-12, representing novel post-modification piericidins.

Compound 5 displayed a hydrogen adduct ion at  $m/z$  416.2808  $[M + H]^+$  in its (+)-HRESIMS data, which determined the molecular formula of  $C_{25}H_{37}NO_4$ . The analysis of the  $^1H$  and  $^{13}C$  NMR data indicated that 5 was structurally close to 11-demethylpiericidin A, except that 10-OH was changed to a methoxyl group in 5 [6]. The above data were supported by the HMBC correlations of H<sub>3</sub>-14 with C-10 and H-10 with C-8/C-15/C-12, as well as the  $^1H$ - $^1H$  COSY correlations of H-8/H-9/H-10/H-11/H-12/H-13. The ultimate planar structure of 5, piericidin P (5), is shown in Figure 1.

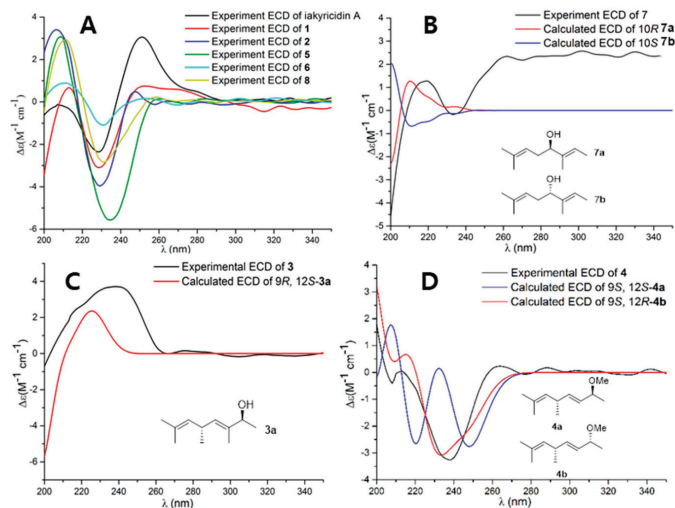
Compounds 6 and 7 were both isolated as a faint yellow oil, and their molecular formulae were established as  $C_{26}H_{39}NO_4$  and  $C_{24}H_{35}NO_4$ , according to the HRESIMS data ( $m/z$  430.2955  $[M + H]^+$ ) and ( $m/z$  402.2640  $[M + H]^+$ ), respectively. A comparison of their  $^1H$  and  $^{13}C$  NMR data with those of PA indicated that both 6 and 7 shared a similar PA skeleton (Tables 1 and 2) [13]. For 6, the only change was the replacement of 7-CH<sub>3</sub> in the PA with ethyl (16-CH<sub>2</sub>, 18-CH<sub>3</sub>), which was corroborated by the HMBC correlations from H<sub>3</sub>-18 to C-7 and H<sub>2</sub>-16 to C-6/C-7/C-8, as well as the  $^1H$ - $^1H$  COSY correlations of H<sub>3</sub>-18/H<sub>2</sub>-16. Similarly, the only difference in 7 was the disappearance of 9-CH<sub>3</sub> in PA, which was confirmed by the  $^1H$ - $^1H$  COSY correlations (H-8/H<sub>2</sub>-9/H-10) and HMBC correlations (H<sub>2</sub>-9 to C-7/C-11). The planar structures of 6 and 7, named piericidins M (6) and R (7), were ultimately determined as shown in Figure 1.

Compound 8 was obtained as a pale yellow oil with a molecular formula of  $C_{30}H_{45}NO_9$ , as determined by (+)-HRESIMS ( $m/z$  564.3162  $[M + H]^+$ ). The  $^1H$  and  $^{13}C$  NMR data were similar to those of glucopiericidin A, except for the absence of 11-CH<sub>3</sub> (Tables 1 and 2), which was confirmed by the HMBC correlations of H-10 with C-8/C-15/C-12 and the  $^1H$ - $^1H$  COSY correlations of H-8/H-9/H-10/H-11/H-12/H-13 [12]. The connection between the hexose unit and C-10 was established by the HMBC correlation of the anomeric proton H-1" ( $\delta_H$  4.33) with C-10 ( $\delta_C$  86.1). After the acidic hydrolysis of 8, D-glucose was identified by reversed-phase HPLC (26.78 min). The coupling constant of the anomeric proton at  $\delta_H$  4.33 ( $J = 7.8$  Hz) indicated it to be a  $\beta$ -glucoside [17]. The planar structure of 8 was thus established as 11-demethyl-glucopiericidin A (8), as shown in Figure 1.

The geometries of the olefins in compounds 1–8 were all deduced to be *E*, based on the NOESY correlations of H-2/H<sub>2</sub>-4, H<sub>2</sub>-4/H-6, H-6/H-8 and H-10/H-12 (Figure 2).

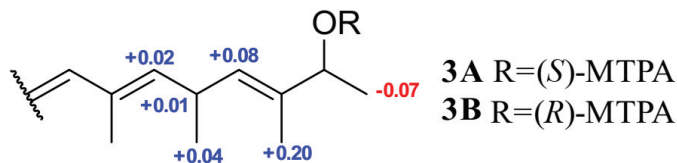
Considering a biosynthetic point of view, the nearly identical experimental ECD curves between compounds 1–2, 5–6, 8 and the reported iakyricidin A revealed the shared 9*R* and 10*R* configurations in the five compounds (Figure 3A) [7]. Moreover, the Boltzmann-weighted ECD spectra of the truncated model 10*R*-7a gave the best agreement with the

experimental ECD spectrum of **7** (Figure 3B) and facilitated the determination of the 10*R* absolute configuration of **7**, which was consistent with that of the biosynthetic piericidin analogues [18].



**Figure 3.** (A) Experimental ECD spectra of **1–2**, **5–6**, **8**, and iakyrigidin A. (B) Experimental ECD spectra of **7**, and the calculated ECD spectra of truncated models **7a/7b**. (C) Experimental ECD spectra of **3**, and the calculated ECD spectrum of truncated model **3a**. (D) Experimental ECD spectra of **4**, and the calculated ECD spectra of truncated models **4a/4b**.

Mosher's method was employed to determine the absolute configurations of C-12 in **3**. The treatment of **3** with (*R*)- and (*S*)-MTPA-Cl yielded (*S*)- and (*R*)-MTPA ester derivatives, respectively. The calculation of the  $^1\text{H NMR } \Delta\delta_{S-R}$  values for the *mono*-MTPA esters of **3** established the 12*S* configuration (Figure 4) [7]. Moreover, given that **3** was a post-modified derivative of PA, the absolute configuration of C-9 was inferred as *R*, which was supported by the similarity between the calculated ECD spectrum of truncated models 9*R* and 12*S*-**3a** and the experimental ECD of **3**, as shown in Figure 3C. Finally, the absolute configurations of **3** were assigned as (9*R*, 12*S*) [18].

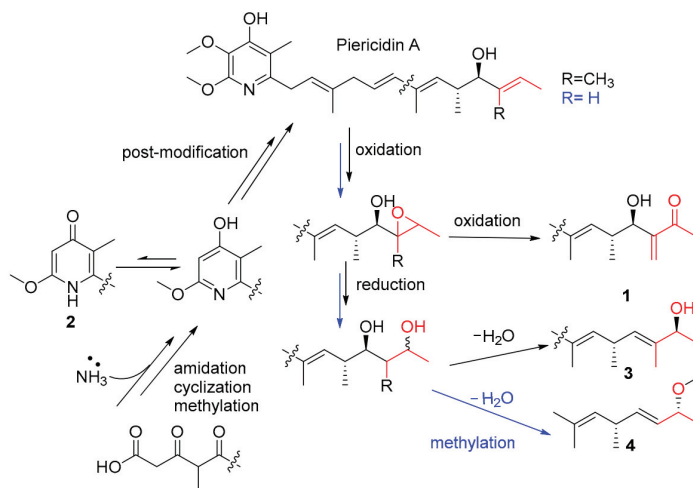


**Figure 4.**  $\Delta\delta_{\text{H}}$  values ( $\delta_{\text{S}} - \delta_{\text{R}}$ , in ppm) for **3A** and **3B**.

From a biosynthetic point of view, and considering **4** as post-modified piericidin, the absolute configuration of C-9 was determined as *S*. Due to the opposite cotton effect that occurred at 240 nm between **3** and **4**, the absolute configuration of C-12 in **4** was inferred to be *R*. Furthermore, the ECD spectra of the truncated models 12*R*\*-**4a/4b** were calculated in order to determine the absolute configurations. The results indicated that the experimental ECD spectra exhibited similar cotton effects to those of the spectra calculated for 12*R*-**4b**, as shown in Figure 3D [18]. Accordingly, the absolute configuration of **4** was established as (9*S*, 12*R*).

The known glucopiericidin B (9) was identified by the comparison of its  $^1\text{H}$  and  $^{13}\text{C}$  NMR data with the literature data [12]. This is the first time that glucopiericidin B (9) was obtained from this strain.

In the biosynthetic pathways, piericidins originate from a modular polyketide synthase (PKS) pathway [16,19]. Compounds 1, 3 and 4 represented three unusual post-modified piericidins, all of which might be biogenetically derived from the main metabolite, PA/11-demethylpiericidin A. Compound 1 was formed from PA through two-step oxidation. Compounds 3 and 4 were derived from PA/11-demethylpiericidin A through oxidation, hydrogenation reduction, dehydration and methylation (Scheme 1). Compounds 6 and 7 were much more likely to be biogenetically derived from the main metabolite, piericidin A, by infrequent methylation on C-16 (for 6) or demethylation on C-15 (for 7). Unlike the previously reported compounds of this strain, the plausible post-PKS modification steps have never been reported in the corresponding positions of piericidins. Some authors reported special piericidin analogues with branched-chain C–C cyclization [7] and 13-dimethoxy and C-2/C-3 epoxy rings [6,16]; these rare analogues indicated several plausible special post-PKS modifications in piericidin biosynthesis.



**Scheme 1.** Plausible biogenetic pathways.

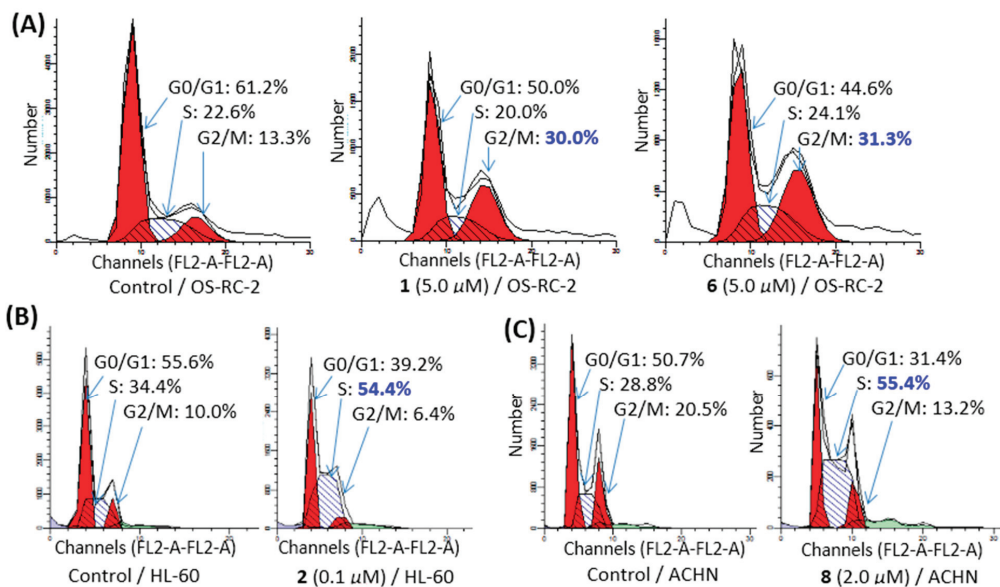
Due to the previously discovered potential of piericidins in treating RCC [6], eight new piericidins were evaluated for their antiproliferative activities against three human renal cancer cell lines—ACHN, 786-O, and OS-RC-2—together with three human leukemia cell lines: HL-60, K-562 and MOLT-4. As presented in Table 3, piericidins L (1) and M (6) showed selective anti-proliferative activities against OS-RC-2 cells, with  $\text{IC}_{50}$  values of 2.2 and 4.5  $\mu\text{M}$ , respectively. Compounds 2–5 exhibited strong inhibition against HL-60 cells, with  $\text{IC}_{50}$  values lower than 0.1  $\mu\text{M}$ . The new piericidin glycoside, 11-demethylglucopiericidin A (8), displayed significant cytotoxicities against ACHN, HL-60 and K562, with  $\text{IC}_{50}$  values of 2.3, 1.3 and 5.5  $\mu\text{M}$ , respectively.

**Table 3.** Cytotoxic activities of 1–8 against six cancer cells (IC<sub>50</sub> μM)<sup>a</sup>.

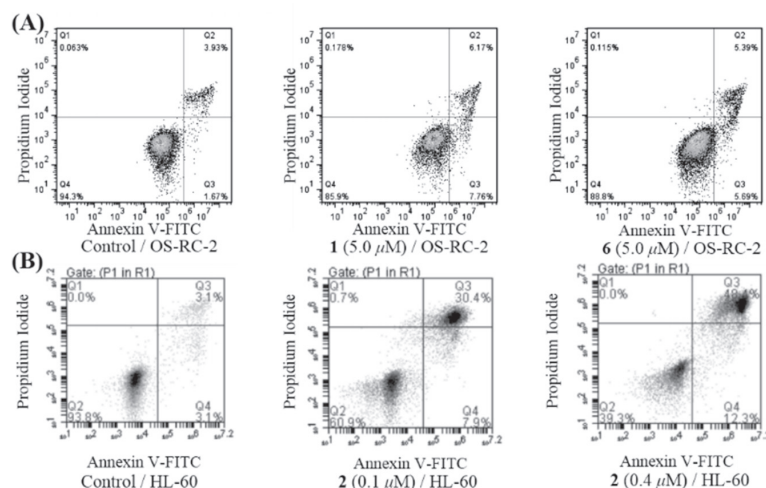
| No.             | ACHN        | 786-O      | OS-RC-2    | HL-60       | K562       | MOLT-4   |
|-----------------|-------------|------------|------------|-------------|------------|----------|
| 1               | >50         | >50        | 2.2 ± 0.21 | 12 ± 1.02   | >50        | >50      |
| 2               | >50         | >50        | 42.9 ± 5.3 | 0.08 ± 0.01 | >50        | /        |
| 3               | >50         | >50        | >50        | 0.08 ± 0.01 | >50        | /        |
| 4               | >50         | >50        | >50        | 0.08 ± 0.01 | >50        | /        |
| 5               | >50         | >50        | >50        | 0.1 ± 0.01  | >50        | /        |
| 6               | >50         | >50        | 4.5 ± 0.37 | 9.8 ± 0.52  | >50        | >50      |
| 7               | >50         | >50        | 15 ± 1.3   | >50         | >50        | >50      |
| 8               | 2.3 ± 0.32  | 12.0 ± 1.2 | 28.7 ± 3.2 | 1.3 ± 0.14  | 5.5 ± 0.69 | /        |
| PA <sup>b</sup> | 0.40 ± 0.02 | 30 ± 3.2   | 5.2 ± 0.67 | 8.5 ± 0.86  | 2.4 ± 0.28 | 25 ± 2.6 |

<sup>a</sup> Mean ± SD (n = 5). IC<sub>50</sub> was calculated using concentrations of 50, 10, 2, 0.4, 0.08 μM. <sup>b</sup> PA was used as a positive control.

Due to the compounds' selective activities against cancer cells [7], we further investigated the abilities of 1 and 6, 2, and 8 to arrest the cell cycle and induce cell apoptosis effects in OS-RC-2 cells, HL-60 cells and ACHN cells, respectively. In order to determine whether an alteration of the cell cycle occurred after treatment with these compounds, the DNA content of the treated cells was measured by flow cytometry. The results indicated that 1 and 6 (with concentrations of 5 μM for both) could arrest the cell cycle during the G2/M phase in OS-RC-2 cells (Figure 5A), while 2 (0.1 μM, Figure 5B) and 8 (2 μM, Figure 5C) could arrest the cell cycle during the S phase in HL-60 and ACHN cells. The apoptotic cells induced by 1, 2, or 6 were quantified by flow cytometry using Annexin V (AV)-FITC/propidium iodide (PI) double staining. The results showed that 1 and 6 (both 5 μM) could induced apoptosis after a 24 h treatment of OS-RC-2 cells (Figure 6A), while 2 (0.1 and 0.4 μM) could induce apoptosis after a 72 h treatment of HL-60 cells (Figure 6B).



**Figure 5.** (A) 1- and 6-arrested cell cycle progression during the G2/M phase in OS-RC-2 cells; (B) 2-arrested cell cycle progression during the S phase in HL-60 cells; (C) 8-arrested cell cycle progression during the S phase in ACHN cells.



**Figure 6.** (A) 1- and 6-induced apoptosis in OS-RC-2 cells; the OS-RC-2 cells were treated with 1 or 6 (5 μM) for 24 h. (B) 2-induced apoptosis in HL-60 cells; the HL-60 cells were treated with 2 (0.1 and 0.4 μM) for 72 h.

### 3. Discussion

According to our previous review, 40 natural piericidin derivatives were reported before 2016, including 11 piericidin glycosides [4]. In order to explore the natural piericidin compounds from Actinomycetes, our group performed chemical dereplication using high-performance liquid chromatography/mass spectrometry (HPLC/MS) to screen the strains with piericidins in marine (including mangrove-derived) *Streptomyces* strains [6]. The HPLC/MS analysis uncovered abundant and diverse piericidins in two actinomycete strains, *S. iakyrus* SCSIO NS104 and *S. psammoticus* SCSIO NS126, isolated from a mangrove sediment sample collected from the Pearl River estuary in the South China Sea. The chemical investigation of the NS104 and NS126 strains revealed 34 natural piericidins, including 21 new compounds [6,7]. These two actinomycete strains, especially NS126, have made important contributions and provided both new and diverse natural piericidin derivatives. Although the recent literature showed that biosynthesis provides a novel way to produce piericidin derivatives [20], the optimization of the fermentation conditions of the target strain remains the most effective way to obtain target compounds with similar structures. In this paper, the NS126 strain was further optimized and subjected to a 300 L fermenter, which resulted in the isolation of eight unusual post-modified piericidin derivatives (1–8) in trace amounts under acidic conditions. The bioassay showed the carbonyl-containing piericidin L (1) with selective cytotoxic activities, which was similar to the previous reported carbonyl-containing piericidin analog iakyracidin A [7]. It is suggested that a carbonylated branched chain could greatly enhance the cytotoxicity of the piericidin analogs. The new piericidin glycoside 8 has a broad spectrum of cytotoxic activity, and it also confirmed that piericidin glycosides possess the potential for further development as antitumor agents [5,6]. This study advances our comprehensive understanding of the structural diversity and cytotoxicity of actinomycete-derived piericidin compounds.

### 4. Materials and Methods

#### 4.1. General Experimental Procedures

The optical rotations were achieved using a PerkinElmer MPC 500 (Waltham) polarimeter. The UV spectra were recorded on a Shimadzu UV-2600 PC spectrometer (Shimadzu). The ECD spectra were measured using a Chirascan circular dichroism spectrometer (Applied Photophysics). The IR spectra were measured on an IR Affinity-1 spectrometer



(Shimadzu, Beijing, China). The NMR spectra were obtained on a Bruker Avance spectrometer (Bruker) operating at 700 MHz for  $^1\text{H}$  NMR and 175 MHz for  $^{13}\text{C}$  NMR, using tetramethylsilane as an internal standard. The HRESIMS spectra were collected on a Bruker mix TOF-QII mass spectrometer (Bruker). The TLC and column chromatography (CC) were performed on plates pre-coated with GF254 silica gel (10–40  $\mu\text{m}$ ) and over silica gel (200–300 mesh) (Qingdao Marine Chemical Factory) and a Sephadex LH-20 (Amersham Biosciences), respectively. All of the solvents employed were of analytical grade (Tianjin Fuyu Chemical and Industry Factory). The semipreparative HPLC was performed on an HPLC (Hitachi-L2130, diode array detector, Hitachi L-2455, Tokyo, Japan) using a Phenomenex ODS column (250 mm  $\times$  10.0 mm i.d., 5  $\mu\text{m}$ ; Phenomenex, Torrance, CA, USA). The artificial sea salt was a commercial product (Guangzhou Haili Aquarium Technology Company, Guangzhou, China).

#### 4.2. Collection of THE Information on, and Cultivation of, the NS126 Strain

The information on the NS126 strain was reported in our previous study [6]. A few cell-loops of the strains were inoculated into a 1000 mL Erlenmeyer flask containing 100 mL seed medium (mannitol 1 g, soya peptone 0.5 g, soya-bean oil 0.125 g,  $\text{K}_2\text{HPO}_3$  0.02 g, pH 7.0 and 50 mL distilled water) and then cultivated on a rotary shaker at 180 rpm, 28  $^\circ\text{C}$ , for 24 h as the seed culture. Then, 300 mL seed culture was inoculated into a 10 L fermenter containing 6 L seed medium at 180 rpm, 28  $^\circ\text{C}$ , for 24 h. The fermentation conditions, pH (pH 4, pH 7 and pH 10) and culture time (18 h, 24 h, 30 h, 33 h, 36 h and 42 h), were screened. Lastly, the entire seed culture was transferred to a 300 L fermenter containing 200 L media (cotton seed meal, 2.5 g; soluble starch, 1 g; glucose, 1 g; yeast extract, 0.3 g;  $\text{CaCO}_3$ , 0.5 g, and 100 mL distilled water, pH 4). After cultivation at 180 rpm, 28  $^\circ\text{C}$ , for 30 h, the bacterial culture broth was centrifuged at 3500 rpm to obtain mycelium. Then, the mycelium was broken using an ultrasonic treatment apparatus for 15 min and extracted three times with an equal volume of ethyl acetate. The organic extract was then concentrated under a vacuum to provide the crude extract (138.5 g).

#### 4.3. Isolation and Purification

The EtOAc extract (120 g) was subjected to silica gel vacuum liquid chromatography using a step-gradient elution of petroleum ether (PE)– $\text{CH}_2\text{Cl}_2$  (1:0, 2:1, 0:1),  $\text{CH}_2\text{Cl}_2$ –MeOH (200:1, 100:1, 50:1, 30:1, 0:1), to yield eight fractions according to the TLC profiles (Frs.B1–B10). From Frs.B3, compounds **1** (1.1 mg,  $t_{\text{R}}$  = 41 min), **2** (2.5 mg,  $t_{\text{R}}$  = 32 min), **3** (2.0 mg,  $t_{\text{R}}$  = 45 min), **4** (0.9 mg,  $t_{\text{R}}$  = 48 min), **5** (2.1 mg,  $t_{\text{R}}$  = 43 min) and **9** (1.05 mg,  $t_{\text{R}}$  = 30 min) were further purified through a Sephadex LH-20 with  $\text{CH}_2\text{Cl}_2$ /MeOH (1:1, *v/v*) and semipreparative HPLC (80% MeOH/ $\text{H}_2\text{O}$ , 2 mL/min, 230 nm). Frs.B4 was separated into four subfractions (Frs.B4-1–4-4) using ODS silica gel chromatography via elution with MeCN/ $\text{H}_2\text{O}$  (5–100%). Frs.B4-2 was directly separated via semipreparative HPLC (80% MeOH/ $\text{H}_2\text{O}$ , 2 mL/min, 230 nm) to yield **6** (1.01 mg,  $t_{\text{R}}$  = 34 min), **7** (0.93 mg,  $t_{\text{R}}$  = 37 min) and **8** (2.0 mg,  $t_{\text{R}}$  = 37 min).

Piericidin L (**1**): pale yellow oil;  $[\alpha]_{\text{D}}^{25} + 3.1$  (c 0.10, MeOH); UV (MeOH)  $\lambda_{\text{max}}$  (log  $\epsilon$ ) 200 (3.14), 226 (2.93) and 268 (2.37) nm; IR (film)  $\nu_{\text{max}}$  3377, 2920, 1670, 1585, 1411, 1190, 1124, 1045, 972, 721, 667 and 600  $\text{cm}^{-1}$ ; CD (0.33 mg/mL, MeOH)  $\lambda_{\text{max}}$  ( $\Delta\epsilon$ ) 201 (–2.69), 220 (+0.30), 235 (–1.23) and 267 (+0.27) nm;  $^1\text{H}$  and  $^{13}\text{C}$  NMR (see Tables 1 and 2); and (+)-HR-ESIMS *m/z* 430.2583,  $[\text{M} + \text{H}]^+$  (calculated for  $\text{C}_{25}\text{H}_{36}\text{NO}_5$  430.2588).

Piericidin N (**2**): brown oil;  $[\alpha]_{\text{D}}^{25} + 2.5$  (c 0.10, MeOH); UV (MeOH)  $\lambda_{\text{max}}$  (log  $\epsilon$ ) 211 (3.20), 223 (3.28), 227 (3.25) and 238 (3.30) nm; IR (film)  $\nu_{\text{max}}$  3273, 2926, 1606, 1541, 1506, 1456, 1373, 1232, 1192 and 827  $\text{cm}^{-1}$ ; CD (0.33 mg/mL, MeOH)  $\lambda_{\text{max}}$  ( $\Delta\epsilon$ ) 211 (+1.04), 239 (–1.37) and 254 (+0.21) nm;  $^1\text{H}$  and  $^{13}\text{C}$  NMR (see Tables 1 and 2); and (+)-HR-ESIMS *m/z* 386.2696,  $[\text{M} + \text{H}]^+$  (calculated for  $\text{C}_{24}\text{H}_{36}\text{NO}_3$  386.2690).

Piericidin Q (**3**): pale yellow oil;  $[\alpha]_{\text{D}}^{25} + 3.7$  (c 0.10, MeOH); UV (MeOH)  $\lambda_{\text{max}}$  (log  $\epsilon$ ) 219 (2.86) and 240 (3.01) nm; IR (film)  $\nu_{\text{max}}$  3369, 2926, 2854, 1699, 1587, 1558, 1471, 1141, 1126, 1035, 964, 800 and 725  $\text{cm}^{-1}$ ; CD (0.33 mg/mL, MeOH)  $\lambda_{\text{max}}$  ( $\Delta\epsilon$ ) 240 (+1.40) nm;  $^1\text{H}$

and  $^{13}\text{C}$  NMR (see Tables 1 and 2); and (+)-HR-ESIMS  $m/z$  438.2614,  $[\text{M} + \text{Na}]^+$  (calculated for  $\text{C}_{25}\text{H}_{37}\text{NNaO}_4$  438.2615).

Piericidin O (4): pale yellow oil;  $[\alpha]_{\text{D}}^{25} + 1.0$  (c 0.10, MeOH); UV (MeOH)  $\lambda_{\text{max}}$  (log  $\epsilon$ ) 218 (2.85), 236 (2.95) and 263 (2.19) nm; IR (film)  $\nu_{\text{max}}$  3346, 2927, 1653, 1558, 1506, 1417 and 1035  $\text{cm}^{-1}$ ; CD (0.33 mg/mL, MeOH)  $\lambda_{\text{max}}$  ( $\Delta\epsilon$ ) 205 (−0.21), 210 (+0.07) and 237 (−1.28) nm;  $^1\text{H}$  and  $^{13}\text{C}$  NMR (see Tables 1 and 2); and (+)-HR-ESIMS  $m/z$  416.2799,  $[\text{M} + \text{H}]^+$  (calculated for  $\text{C}_{25}\text{H}_{38}\text{NO}_4$  416.2795).

Piericidin P (5): pale yellow oil;  $[\alpha]_{\text{D}}^{25} + 3.5$  (c 0.10, MeOH); UV (MeOH)  $\lambda_{\text{max}}$  (log  $\epsilon$ ) 217 (3.31), 235 (3.30) and 260 (1.47) nm; IR (film)  $\nu_{\text{max}}$  3365, 2926, 2852, 1589, 1471, 1192, 1126, 1091, 1045 and 972  $\text{cm}^{-1}$ ; CD (0.33 mg/mL, MeOH)  $\lambda_{\text{max}}$  ( $\Delta\epsilon$ ) 210 (+1.43), 235 (−2.14) nm;  $^1\text{H}$  and  $^{13}\text{C}$  NMR (see Tables 1 and 2); and (+)-HR-ESIMS  $m/z$  416.2799,  $[\text{M} + \text{H}]^+$  (calculated for  $\text{C}_{25}\text{H}_{38}\text{NO}_4$  416.2795).

Piericidin M (6): pale yellow oil;  $[\alpha]_{\text{D}}^{25} + 2.4$  (c 0.08, MeOH); UV (MeOH)  $\lambda_{\text{max}}$  (log  $\epsilon$ ) 200 (3.35), 219 (3.01), 232 (3.09) and 266 (2.39) nm; IR (film)  $\nu_{\text{max}}$  3381, 2920, 1471, 1456, 1412, 1190, 1124, 1026, 966, 825, 775 and 669  $\text{cm}^{-1}$ ; CD (0.33 mg/mL, MeOH)  $\lambda_{\text{max}}$  ( $\Delta\epsilon$ ) 206 (+1.01), 213 (+2.85), 232 (−3.17) and 253 (+0.43) nm;  $^1\text{H}$  and  $^{13}\text{C}$  NMR (see Tables 1 and 2); and (+)-HR-ESIMS  $m/z$  430.2955,  $[\text{M} + \text{H}]^+$  (calculated for  $\text{C}_{26}\text{H}_{40}\text{NO}_4$  430.2952).

Piericidin R (7): pale yellow oil;  $[\alpha]_{\text{D}}^{25} + 4.5$  (c 0.09, MeOH); UV (MeOH)  $\lambda_{\text{max}}$  (log  $\epsilon$ ) 201 (3.12), 217 (2.89), 232 (2.98) and 268 (2.23) nm; IR (film)  $\nu_{\text{max}}$  3360, 2922, 1585, 1472, 1412, 1190, 1124, 1043, 964, 773, 660 and 600  $\text{cm}^{-1}$ ; CD (0.33 mg/mL, MeOH)  $\lambda_{\text{max}}$  ( $\Delta\epsilon$ ) 218 (−3.02), 235 (−7.33) and 260 (−0.49) nm;  $^1\text{H}$  and  $^{13}\text{C}$  NMR (see Tables 1 and 2); and (+)-HR-ESIMS  $m/z$  402.2640,  $[\text{M} + \text{H}]^+$  (calculated for  $\text{C}_{24}\text{H}_{36}\text{NO}_4$  402.2639).

11-demethyl-glucopiericidin A (8): pale yellow oil;  $[\alpha]_{\text{D}}^{25} + 1.6$  (c 0.10, MeOH); UV (MeOH)  $\lambda_{\text{max}}$  (log  $\epsilon$ ) 200 (3.55), 217 (3.28), 237 (3.43), 260 (2.55) and 268 (2.60) nm; IR (film)  $\nu_{\text{max}}$  3390, 2929, 1683, 1653, 1558, 1506, 1456, 1417, 1126, 1076 and 1039  $\text{cm}^{-1}$ ; CD (0.33 mg/mL, MeOH)  $\lambda_{\text{max}}$  ( $\Delta\epsilon$ ) 200 (+0.02), 215 (+1.67) and 234 (−1.50) nm;  $^1\text{H}$  and  $^{13}\text{C}$  NMR (see Tables 1 and 2); and (+)-HR-ESIMS  $m/z$  564.3162,  $[\text{M} + \text{H}]^+$  (calculated for  $\text{C}_{30}\text{H}_{46}\text{NO}_9$  564.3167).

#### 4.4. Mono-MTPA Esters of Piericidin Q (3)

Piericidin Q (3, 0.6 mg) was dissolved in freshly distilled dry pyridine (2 mL) with dry crystals of dimethylaminopyridine (DMAP 0.3 mg). The treatment with (*R*)-MTPA-Cl at 28 °C yielded the *S*-MTPA ester after 16 h. The reaction mixture was purified by semipreparative HPLC (95%  $\text{CH}_3\text{CN}$  in  $\text{H}_2\text{O}$ ) to produce the *S*-MTPA ester (3A) after 30 min. The *R*-MTPA ester (3B) was prepared with *S*-MTPA-Cl in the same manner. The  $\Delta\delta_{S-R}$  values for the mono-*S*- and *R*-MTPA esters of piericidin Q were recorded in ppm in  $\text{CD}_3\text{OD}$  (Table S7).

#### 4.5. Acid Hydrolysis of 11-Demethyl-Glucopiericidin A (8)

The 11-Demethyl-glucopiericidin A (8, 1 mg) was refluxed with 2.0 M HCl (2 mL) for 6 h at 80 °C. The reaction mixture was then evaporated to dryness and diluted with  $\text{H}_2\text{O}$  (2 mL). After extraction with EtOAc (3 × 2 mL), the aqueous layer was concentrated and heated with L-Cysteine Methyl Ester Hydrochloride (3 mg) in pyridine (1 mL) at 60 °C for 1 h. Then, *o*-Tolyl isothiocyanate (0.4 mL) was added to the reaction mixture, which was subsequently stirred at 60 °C for 1 h. The sugar (*D*-glucose) standard was derivatized using L-Cysteine Methyl Ester Hydrochloride and *o*-Tolyl isothiocyanate in the same manner. The reaction mixtures were analyzed using reversed-phase HPLC under the following conditions: a YMC-Pack ODS-A column (250 × 4.6 mm, 5  $\mu\text{m}$ ), a UV detector, the  $\text{CH}_3\text{CN}/\text{H}_2\text{O}$  mobile phase (20/80, *v/v*, 0.08% TFA), a detection wavelength of 250 nm, and a 0.8 mL/min flow rate. Comparing the retention times with those of the derivative of an authentic sample of *D*-glucose (retention time: 26.97 min, Figure S81) confirmed the *D*-configuration of the glucose.

#### 4.6. ECD Calculation

The relative configurations of **3**, **4** and **7** were subjected to random conformational searches using the Spartan'14 software with the MMFF method [21]. The conformers with a Boltzmann population of over 5% (relative energy within 6 kcal/mol) were chosen for the ECD calculations using the Gaussian 09 software [22], and the stable conformers were initially optimized at the B3LYP/6-31+G(d,p) level in MeOH using the CPCM model. The overall theoretical calculation of ECD was achieved in MeOH using time-dependent density functional theory at the B3LYP/6-31+G(d,p) level for the stable conformers of **3**, **4**, and **7**. The rotatory strengths were calculated for a total of 30 excited states. The ECD spectra of the different conformers were generated using SpecDis 1.6 (University of Würzburg) and Prism 5.0 (GraphPad Software Inc., San Diego, CA, USA) software, with a half-bandwidth of 0.3–0.4 eV, according to the Boltzmann-calculated contribution of each conformer after UV correction.

#### 4.7. Cell Culture and Cytotoxic Bioassay

HL-60, K-562, MOLT-4, ACHN, OS-RC-2 and 786-O cells were purchased from Shanghai Cell Bank, Chinese Academy of Sciences. The ACHN cells were grown and maintained in an MEM medium with 10% FBS, while the other cells were grown in a RPMI1640 medium with 10% FBS. The cell viability was determined using a CCK-8 (Dojindo) assay [23]. The cells were seeded at a density of 400 to 800 cells/well in 384-well plates, and were then treated with various concentrations (50, 10, 2, 0.4 and 0.08  $\mu\text{M}$ ) of compounds or a solvent control. After 72 h of incubation, the CCK-8 reagent was added, and the absorbance of the triplicate tests was measured at 450 nm using an Envision 2104 multi-label reader (Perkin Elmer). The dose–response curves were plotted in order to determine the  $\text{IC}_{50}$  using Prism 5.0 (GraphPad Software Inc.).

#### 4.8. Cell Cycle and Apoptosis Assay

The cell cycle arrests by **1** and **6** in OS-RC-2 cells, by **2** in HL-60 cells, and by **8** in ACHN cells were analyzed via PI DNA staining using flow cytometry [23,24]. In summary, the cells were treated with compounds under suitable concentrations (5  $\mu\text{M}$  for **1** and **6**; 0.1 and 0.4  $\mu\text{M}$  for **2**; 2  $\mu\text{M}$  for **8**) for 24, 48 and 72 h. After the treatment, the cells were harvested, prepared and fixed overnight. The fixed cells were then harvested, washed, re-suspended, and finally stained with PI (Sigma-Aldrich). The cell-cycle distribution was studied using an Accuri C6 (BD) flow cytometer. The cell apoptosis was analyzed using a FITC annexin V apoptosis detection kit (BD), according to the manufacturer's protocol [24]. The cells were treated with the compounds under suitable concentrations (5  $\mu\text{M}$  for **1** and **6**; 0.1 and 0.4  $\mu\text{M}$  for **2**; 2  $\mu\text{M}$  for **8**) for 24, 48 and 72 h, stained with annexin V-FITC and PI solution, examined, and analyzed quantitatively using an Accuri C6 (BD) flow cytometer.

### 5. Conclusions

In this study, eight new minor piericidin derivatives were obtained from the sediment-derived actinomycete strain *Streptomyces psammoticus* SCSIO NS126, which was fermented at a 300-L scale under optimized fermentation conditions. The new structures including absolute configurations were determined by spectroscopic methods coupled with experimental and calculated ECD. The plausible biosynthetic pathways for these unusual post-modified piericidins were also proposed. Most of the derivatives showed obvious cytotoxic activities against several cancer cells. It is suggested that some unusual post-modified piericidins, such as carbonyl-containing piericidin, possess selective anti-tumor potential. This study increases our knowledge on the structural diversity and cytotoxicity of actinomycete-derived piericidin compounds, and confirms that piericidins deserve further investigations as promising anti-tumor agents.

**Supplementary Materials:** The following are available online at <https://www.mdpi.com/article/10.3390/md19080428/s1>. Figures S1–S3: The optimized conformers and equilibrium populations of **3a**, **4a/4b**, and **7a/7b**; Figures S4–S80: 1D and 2D NMR for compounds **1–9**; Figure S81: The HPLC results for D-glucose and **8** via acidic hydrolysis; Figures S82–S84: The HPLC analysis of crude extracts under different fermentation conditions; Tables S1–S6: Energies of **3a**, **4a/4b**, and **7a/7b** in ECD calculations; Table S7:  $^1\text{H}$  NMR Data of **3A/3B**.

**Author Contributions:** Conceptualization, Y.L. and X.Z.; data curation, K.L. and Z.S.; funding acquisition, Y.L. and X.Z.; investigation, K.L., X.P., B.Y., H.T. and X.L. (Xiaowei Luo); methodology, K.L., Z.S., Y.G. and X.L. (Xiuping Lin); project administration, Y.L. and X.Z. All authors have read and agreed to the published version of the manuscript.

**Funding:** This work was supported by grants from the National Key Research and Development Program of China (2019YFC0312503), the Marine Economy Development Project of Guangdong Province (GDNRC2021052), the Key Special Project for Introduced Talents Team of Southern Marine Science and Engineering Guangdong Laboratory (Guangzhou) (GML2019ZD0406), the National Natural Science Foundation of China (U20A20101, 81973235, 21977102), K.C.Wong Education Foundation (GJTD-2020-12), the Guangdong Local Innovation Team Program (2019BT02Y262), and the Guangdong Basic and Applied Basic Research Foundation (2019B151502042). We are grateful to the analytical facilities (Z. Xiao, A. Sun, X. Zheng, and Y. Zhang) at SCSIO.

**Institutional Review Board Statement:** Not applicable.

**Informed Consent Statement:** Not applicable.

**Conflicts of Interest:** The authors declare no conflict of interest.

## References

- Carroll, A.R.; Copp, B.R.; Davis, R.A.; Keyzers, R.A.; Prinsep, M.R. Marine natural products. *Nat. Prod. Rep.* **2020**, *37*, 175–223. [[CrossRef](#)] [[PubMed](#)]
- Jagannathan, S.V.; Manemann, E.M.; Rowe, S.E.; Callender, M.C.; Soto, W. Marine actinomycetes, new sources of biotechnological products. *Mar. Drugs* **2021**, *19*, 365. [[CrossRef](#)] [[PubMed](#)]
- Wang, Y.-N.; Meng, L.-H.; Wang, B.-G. Progress in research on bioactive secondary metabolites from deep-sea derived microorganisms. *Mar. Drugs* **2020**, *18*, 614. [[CrossRef](#)] [[PubMed](#)]
- Zhou, X.; Fenical, W. The unique chemistry and biology of the piericidins. *J. Antibiot.* **2016**, *69*, 582–593. [[CrossRef](#)] [[PubMed](#)]
- Liang, Z.; Chen, Y.; Gu, T.; She, J.; Dai, F.; Jiang, H.; Zhan, Z.; Li, K.; Liu, Y.; Zhou, X.; et al. LXR-mediated regulation of marine-derived piericidins aggravates high cholesterol diet-induced cholesterol metabolism disorder in mice. *J. Med. Chem.* **2021**, *64*, 9943–9959. [[CrossRef](#)]
- Zhou, X.; Liang, Z.; Li, K.; Fang, W.; Tian, Y.; Luo, X.; Chen, Y.; Zhan, Z.; Zhang, T.; Liao, S.; et al. Exploring the natural piericidins as anti-renal cell carcinoma agents targeting Peroxiredoxin 1. *J. Med. Chem.* **2019**, *62*, 7058–7069. [[CrossRef](#)]
- Li, K.; Liang, Z.; Chen, W.; Luo, X.; Fang, W.; Liao, S.; Lin, X.; Yang, B.; Wang, J.; Tang, L.; et al. Iakyracidins A-D, antiproliferative piericidin analogues bearing a carbonyl group or cyclic skeleton from *Streptomyces iakyrus* SCSIO NS104. *J. Org. Chem.* **2019**, *84*, 12626–12631. [[CrossRef](#)]
- Espeso, E.A.; Tilburn, J.; Arst, H.N.; Penalva, M.A. pH regulation is a major determinant in expression of a fungal penicillin biosynthetic gene. *Embo. J.* **1993**, *12*, 3947–3956. [[CrossRef](#)]
- Haneburger, I.; Eichinger, A.; Skerra, A.; Jung, K. New insights into the signaling mechanism of the pH-responsive, membrane-integrated transcriptional activator CadC of *Escherichia coli*. *J. Biol. Chem.* **2011**, *286*, 10681–10689. [[CrossRef](#)]
- Wilson, Z.E.; Brimble, M.A. Molecules derived from the extremes of life. *Nat. Prod. Rep.* **2009**, *26*, 44–71. [[CrossRef](#)]
- Lin, X.; Hetharua, B.; Lin, L.; Xu, H.; Zheng, T.; He, Z.; Tian, Y. Mangrove sediment microbiome: Adaptive microbial assemblages and their routed biogeochemical processes in Yunxiao mangrove national nature reserve, China. *Microb. Ecol.* **2019**, *78*, 57–69. [[CrossRef](#)]
- Matsumoto, M.; Mogi, K.I.; Nagaoka, K.; Ishizeki, S.; Kawahara, R.; Nakashima, T. New piericidin glucosides, glucopiericidin A and glucopiericidin B. *J. Antibiot.* **1987**, *40*, 149–156. [[CrossRef](#)]
- Lipshutz, B.H.; Amorelli, B. Total synthesis of piericidin A1. Application of a modified negishi carboalumination-nickel-catalyzed cross-coupling. *J. Am. Chem. Soc.* **2009**, *131*, 1396–1397. [[CrossRef](#)]
- Kominato, K.; Watanabe, Y.; Hirano, S.I.; Kioka, T.; Tone, H. Mer-A2026A and B, novel piericidins with vasodilating effect. II. Physicochemical properties and chemical structures. *J. Antibiot.* **1995**, *48*, 103–105. [[CrossRef](#)]
- Ueda, J.; Togashi, T.; Matukura, S.; Nagai, A.; Nakashima, T.; Komaki, H.; Anzai, K.; Harayama, S.; Doi, T.; Takahashi, T. A novel nuclear export inhibitor JBIR-02, a new piericidin discovered from *Streptomyces* sp. ML55. *J. Antibiot.* **2007**, *60*, 459–462. [[CrossRef](#)]
- Chen, Y.L.; Zhang, W.J.; Zhu, Y.G.; Zhang, Q.B.; Tian, X.P.; Zhang, S.; Zhang, C.S. Elucidating hydroxylation and methylation steps tailoring piericidin A1 biosynthesis. *Org. Lett.* **2014**, *16*, 736–739. [[CrossRef](#)]

17. Ye, X.S.; He, J.; Cheng, Y.C.; Zhang, L.; Qiao, H.Y.; Pan, X.G.; Zhang, J.; Liu, S.N.; Zhang, W.K.; Xu, J.K. Cornusides A-O, bioactive iridoid glucoside dimers from the fruit of *Cornus officinalis*. *J. Nat. Prod.* **2017**, *80*, 3103–3111. [[CrossRef](#)]
18. Han, X.N.; Liu, Z.Z.; Zhang, Z.Z.; Zhang, X.M.; Zhu, T.T.; Gu, Q.Q.; Li, W.L.; Che, Q.; Li, D.H. Geranylpyrrol A and piericidin F from *Streptomyces* sp CHQ-64 Delta rdmF. *J. Nat. Prod.* **2017**, *80*, 1684–1687. [[CrossRef](#)]
19. Liu, Q.; Yao, F.; Chooi, Y.H.; Kang, Q.J.; Xu, W.; Li, Y.R.; Shao, Y.C.; Shi, Y.F.; Deng, Z.X.; Tang, Y.; et al. Elucidation of piericidin A1 biosynthetic locus revealed a thioesterase-dependent mechanism of  $\alpha$ -pyridone ring formation. *Chem. Biol.* **2012**, *19*, 243–253. [[CrossRef](#)]
20. Liu, Z.; Xiao, F.; Cai, S.; Liu, C.; Li, H.; Wu, T.; Jiang, Y.; Wang, X.; Che, Q.; Zhu, T.; et al. Effective generation of glucosylpiericidins with selective cytotoxicities and insights into their biosynthesis. *Appl. Environ. Microbiol.* **2021**, *87*, e00294. [[CrossRef](#)]
21. Yang, B.; Tao, H.; Lin, X.; Wang, J.; Liao, S.; Dong, J.; Zhou, X.; Liu, Y. Prenylated indole alkaloids and chromone derivatives from the fungus *Penicillium* sp SCS10041218. *Tetrahedron* **2018**, *74*, 77–82. [[CrossRef](#)]
22. Frisch, M.J.; Trucks, G.W.; Schlegel, H.B.; Scuseria, G.E.; Robb, M.A.; Cheeseman, J.R.; Scalmani, G.; Barone, V.; Mennucci, B.; Petersson, G.A.; et al. *Gaussian 09, Revision x.x*; Gaussian Inc.: Wallingford, CT, USA, 2009.
23. Tan, Y.; Yang, B.; Lin, X.; Luo, X.; Pang, X.; Tang, L.; Liu, Y.; Li, X.; Zhou, X. Nitrobenzoyl sesquiterpenoids with cytotoxic activities from a marine-derived *Aspergillus ochraceus* fungus. *J. Nat. Prod.* **2018**, *81*, 92–97. [[CrossRef](#)]
24. Luo, X.; Lin, X.; Tao, H.; Wang, J.; Li, J.; Yang, B.; Zhou, X.; Liu, Y. Isochromophilones A–F, cytotoxic chloroazaphilones from the marine mangrove endophytic fungus *diaporthe* sp. SCSIO 41011. *J. Nat. Prod.* **2018**, *81*, 934–941. [[CrossRef](#)]

Article

# Heterocornols from the Sponge-Derived Fungus *Pestalotiopsis heterocornis* with Anti-Inflammatory Activity

Hui Lei <sup>1</sup>, Xiaoxu Bi <sup>2</sup>, Xiuping Lin <sup>3</sup>, Jianglian She <sup>3</sup>, Xiaowei Luo <sup>4</sup>, Hong Niu <sup>1</sup>, Dan Zhang <sup>1</sup> and Bin Yang <sup>3,\*</sup>

<sup>1</sup> School of Pharmacy, Southwest Medical University, Luzhou 646000, China; huilei@swmu.edu.cn (H.L.); dawn123454@swmu.edu.cn (H.N.); zhangdan@swmu.edu.cn (D.Z.)

<sup>2</sup> College of Agriculture and Life Sciences, Kunming University, Kunming 650241, China; bxx2797@163.com

<sup>3</sup> CAS Key Laboratory of Tropical Marine Bio-Resources and Ecology, Guangdong Key Laboratory of Marine Materia Medica, South China Sea Institute of Oceanology, Chinese Academy of Sciences, Guangzhou 510301, China; xiupinglin@scsio.ac.cn (X.L.); shejianglian20@mailsucas.ac.cn (J.S.)

<sup>4</sup> Institute of Marine Drugs, Guangxi University of Chinese Medicine, Nanning 530200, China; luoxw@gxctcmu.edu.cn

\* Correspondence: yangbin@scsio.ac.cn; Tel.: +86-020-89023174

**Abstract:** One strain-many compounds (OSMAC) manipulation of the sponge-derived fungus *Pestalotiopsis heterocornis* XWS03F09 resulted in the production of new secondary metabolites. The chemical study of the fermentation, cultivated on 3% artificial sea salt in the rice media, led to the isolation of twelve compounds, including eight new polyketide derivatives, heterocornols Q–X (1–8), one new ceramide (9), and three known analogues (10–12). The structures and absolute configurations of the new compounds were elucidated by spectroscopic data and calculated ECD analysis. Heterocornols Q (1) and R (2) are novel 6/5/7/5 tetracyclic polyketide derivatives featuring dihydroisobenzofuran and benzo-fused dioxabicyclo [4.2.1] nonane system, which might be derived from the acetyl-CoA by epoxidation, polyene cyclization, and rearrangement to form the core skeleton. Compound 12 showed moderate or weak antimicrobial activities against with MIC values ranging from 25 to 100 µg/mL. Heterocornols T and X (7 and 8) could inhibit the production of LPS-induced NO significantly, comparable to dexamethasone. Further Western blotting analysis showed 7 and 8 markedly suppressed the iNOS protein expression in LPS-induced RAW 264.7 cells in a dose-dependent manner. The result showed that 7 and 8 might serve as potential leads for development of anti-inflammatory activity.

**Citation:** Lei, H.; Bi, X.; Lin, X.; She, J.; Luo, X.; Niu, H.; Zhang, D.; Yang, B. Heterocornols from the Sponge-Derived Fungus *Pestalotiopsis heterocornis* with Anti-Inflammatory Activity. *Mar. Drugs* **2021**, *19*, 585. <https://doi.org/10.3390/md19110585>

Academic Editors: Bill J. Baker and Micha Ilan

Received: 23 August 2021

Accepted: 15 October 2021

Published: 20 October 2021

**Publisher's Note:** MDPI stays neutral with regard to jurisdictional claims in published maps and institutional affiliations.



**Copyright:** © 2021 by the authors. Licensee MDPI, Basel, Switzerland. This article is an open access article distributed under the terms and conditions of the Creative Commons Attribution (CC BY) license (<https://creativecommons.org/licenses/by/4.0/>).

**Keywords:** *Pestalotiopsis heterocornis*; heterocornols; anti-inflammatory activity; sponge-derived fungus

## 1. Introduction

During the past several decades, marine-derived fungi are recognized as an important source of novel drug leads. However, most of their biosynthetic gene clusters are silent under laboratory conditions fungi, whereas only a fraction of gene clusters have been transcribed. In order to enlarge the diversity of metabolites, different strategies such as the one strain-many compounds (OSMAC) strategy [1–5], epigenetic modification [6–8], and genome mining have been devoted to activating the silent gene clusters [9–13]. Among them, the OSMAC strategy represents a simple strategy involving the systematic alteration of culture conditions.

Our previous investigation on the marine sponge-derived fungus *Pestalotiopsis heterocornis* XWS03F09 has resulted in the discovery of heterocornols A–P [14,15], pestaloisocoumarins A and B, isopolisin B, and pestalotioli A [16]. For exploring the chemical diversity of microorganisms using the OSMAC strategy, we reinvestigated the secondary metabolites of the strain XWS03F09, with additional 3% artificial sea salt to solid rice medium. Further chemical exploration resulted in the isolation of eight new polyketide derivatives, heterocornols Q–X (1–8), and one new ceramide (9), together with three known analogues,

pestalone (10) [17], and pestalachlorides A and B (11 and 12) [18]. The isolated compounds (1–9 and 12) were evaluated for the cytotoxic, antimicrobial, and anti-inflammatory activities in vitro. Here, we report the details of the isolation, structure elucidation, and biological activities of these compounds.

## 2. Results and Discussion

The fermentation of the fungus *P. heterocornis* XWS03F09 in the rice media was cultivated for 36 days, made up separately with different culture conditions (0, 1%, 3%, 5% artificial sea salt to solid rice medium), and then was extracted with EtOAc three times. The resulting extracts were analyzed by HPLC. The HPLC-UV profiles of the secondary metabolites indicated that they possessed almost the same metabolites, but with dramatic differences in their major constituents (Figure S56). As the concentration of artificial sea salt in the rice media increased, the strain stopped the production of some metabolites. The strain produced some new metabolites with 3% salinity compared with the previous fermentation. The chemical study of the fermentation, cultivated on 3% artificial sea salt in the rice media, yielded twelve metabolites, including eight new polyketide derivatives, heterocornols Q–X (1–8), and one new ceramide (9) (Figure 1).

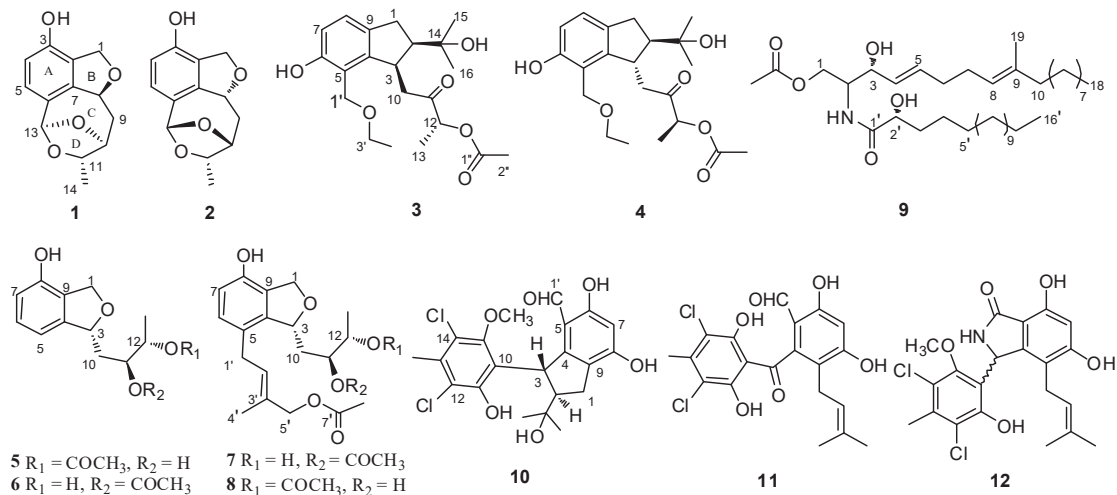


Figure 1. Structures of compounds 1–12.

Compound 1 was isolated as a white amorphous solid, and its molecular formula was established as  $\text{C}_{13}\text{H}_{14}\text{O}_4$  on the basis of HRESIMS at  $m/z$  257.0783  $[\text{M} + \text{Na}]^+$  (Figure S1). The  $^1\text{H}$  NMR spectrum (Table 1 and Figure S2) of 1 displayed resonances attributed to two aromatic protons at  $\delta_{\text{H}}$  7.01 (d,  $J = 7.9$  Hz), and 6.58 (d,  $J = 7.9$  Hz) belonging to a 1,2,3,4-tetrasubstituted benzene, one methyl [ $\delta_{\text{H}}$  1.30 (d,  $J = 6.2$  Hz)], one dioxygenated methine ( $\delta_{\text{H}}$  5.96, s), three oxygenated methines [ $\delta_{\text{H}}$  5.50 (dd,  $J = 8.3$ , 2.5 Hz), 4.34 (t,  $J = 2.5$  Hz), and  $\delta_{\text{H}}$  4.61 (q,  $J = 6.0$  Hz)], one oxygenated methylene [ $\delta_{\text{H}}$  5.12 (dd,  $J = 12.1$ , 2.5 Hz), 4.96 (dd,  $J = 12.1$ , 2.7 Hz)], one methylene [ $\delta_{\text{H}}$  2.32 (dt,  $J = 13.5$ , 4.7 Hz), and 1.94 (ddd,  $J = 13.5$ , 11.3, 2.8 Hz)]. The  $^{13}\text{C}$  NMR and DEPT spectra (Figures S3 and S4) of 1 displayed 13 carbon signals corresponding to one methyl, two methylenes, six methines including two olefinic carbons, four oxygenated carbons, and four quaternary carbons. The NMR features of 1 were very similar to those of vaccinol P [19], indicating that 1 was a polyketide derivative structurally related to vaccinol P. The major difference was the presence of an eight-membered carbon ring in 1, instead of the C-8 a side chain in vaccinol P, which was supported by the additional HMBC correlations from H-13 ( $\delta_{\text{H}}$  5.96) to C-11 ( $\delta_{\text{C}}$  81.4), C-10 ( $\delta_{\text{C}}$  77.3), C-5 ( $\delta_{\text{C}}$  127.1), C-6 ( $\delta_{\text{C}}$  129.4), and C-7 ( $\delta_{\text{C}}$  143.7), from H-11 ( $\delta_{\text{H}}$  4.34) to

C-13 ( $\delta_C$  106.4), C-14 ( $\delta_C$  21.1), together with the COSY correlations H-8/H-9/H-10/H-11/H-14 (Figure 2, Figures S5 and S6). Furthermore, the HMBC correlations between H-1 ( $\delta_H$  4.96/5.12) and C-3 ( $\delta_C$  153.4), C-7 ( $\delta_C$  143.7), C-8 ( $\delta_C$  82.6), and C-2 ( $\delta_C$  127.4) indicated that a five-membered carbon ring was fused with ring B through C-2 and C-7. The HMBC correlations from H-11 ( $\delta_H$  4.34) to C-13 ( $\delta_C$  106.4), C-14 ( $\delta_C$  21.1), from H-9 ( $\delta_H$  2.32/1.94) to C-7 ( $\delta_C$  143.7), C-8 ( $\delta_C$  82.6), and C-10 ( $\delta_C$  77.3) indicated that the C-11 of the vicinal diol side chain was connected with C-13 through an O-bridged hemiketal moiety to form an eight-membered ring, which fused to both rings A and B sharing the same joined carbon C-7 and established a tricyclic 6/5/8 skeleton. Benzene ring A, five-membered ring B, and eight-membered ring accounted for six degrees of unsaturation, and the remaining ones thus required **1** to be tetracyclic. Furthermore, the HMBC correlations between H-10 ( $\delta_H$  4.61) and C-13 ( $\delta_C$  106.4), C-8 ( $\delta_C$  82.6). The different chemical shifts of C-10 ( $\delta_C$  77.3), C-11 ( $\delta_C$  81.4), and C-13 ( $\delta_C$  106.4) indicated that the eight-membered carbon ring was divided into rings C and D. Therefore, **1** was identified to be a 6/5/7/5 tetracyclic polyketide derivative featuring a novel carbon skeleton with a dihydroisobenzofuran and benzo-fused dioxabicyclo [4.2.1] nonane system. The relative configuration of **1** was determined by analyzing the NOESY correlations (Figure 3, Figure S7). The NOESY spectrum of **1** revealed cross-peaks from H-8 to H-11 and from H-10 to H<sub>3</sub>-14, which, together with the lack of a correlation from H-10 to H-11, led to the determination of the relative configuration of **1** as 8*S*,10*S*,11*S*,13*R*. The ECD calculations of **1** were also carried out to determine the absolute configuration. The result showed that the calculated spectrum of (8*S*,10*S*,11*S*,13*R*)-**1** agreed with the experimental one, indicating the absolute configuration of **1** to be 8*S*,10*S*,11*S*,13*R* (Figure 4). Thus, the structure of **1** was determined and named heterocornol Q (**1**).

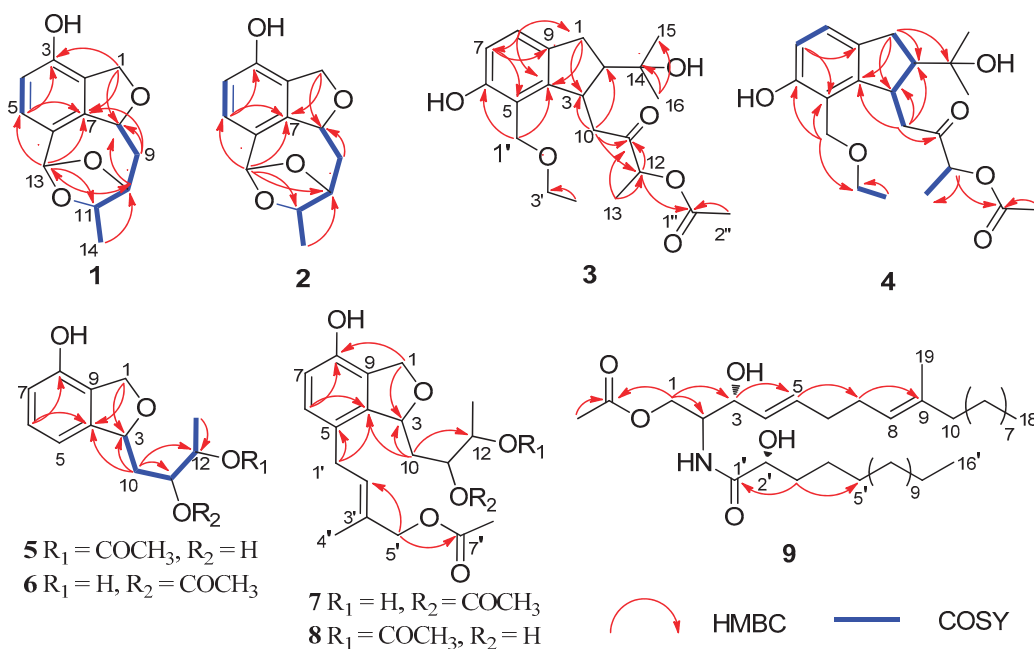
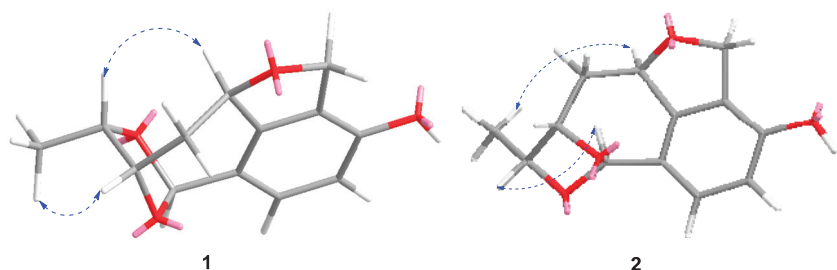
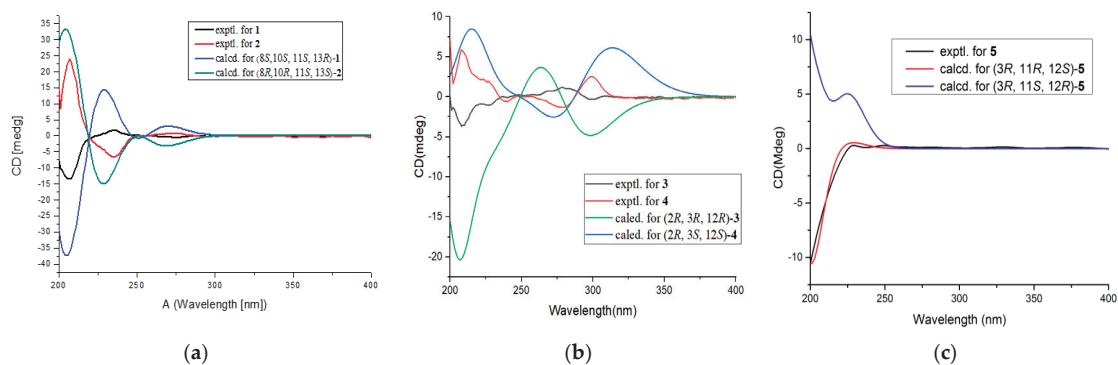


Figure 2. COSY and key HMBC correlations of **1**–**9**.



**Table 1.**  $^1\text{H}$  NMR (500 MHz) data for 1–4 in  $\text{CD}_3\text{OD}$ .

| No. | 1                          |  | 2                          |  | 3                          |   | 4                          |                                       |
|-----|----------------------------|--|----------------------------|--|----------------------------|---|----------------------------|---------------------------------------|
|     | $\delta_{\text{C}}$ , Type | $\delta_{\text{H}}$ (J in Hz)  | $\delta_{\text{C}}$ , Type | $\delta_{\text{H}}$ (J in Hz)  | $\delta_{\text{C}}$ , Type | $\delta_{\text{H}}$ (J in Hz)                 | $\delta_{\text{C}}$ , Type | $\delta_{\text{H}}$ (J in Hz)         |
| 1   | 72.4, $\text{CH}_2$        | 5.12, dd (12.1, 2.5)<br>4.96, dd (12.1, 2.7)                         | 72.1, $\text{CH}_2$        | 5.11, dd (12.0, 2.2)<br>4.93, dd (12.0, 3.2)                               | 31.7, $\text{CH}_2$        | 2.81, d (16.4)<br>3.07, dd (16.4, 8.5)        | 31.7, CH                   | 2.83, d (8.3)<br>3.10, dd (16.3, 8.3) |
| 2   | 127.4, C                   |  | 127.8, C                   |  | 55.6, CH                   | 2.05, m                                       | 55.5, CH                   | 2.00, m                               |
| 3   | 153.4, C                   |  | 153.5, C                   |  | 40.8, CH                   | 3.75, dd (10.6, 2.3)                          | 40.9, CH                   | 3.76, dd (10.6, 2.8)                  |
| 4   | 113.8, CH                  | 6.58, d (7.9)  | 113.7, CH                  | 6.58, d (7.9)  | 147.4, C                   |   | 147.2, C                   |                                       |
| 5   | 127.1, CH                  | 7.01, d (7.9)  | 126.8, CH                  | 7.01, d (7.9)  | 119.1, C                   |   | 119.1, C                   |                                       |
| 6   | 129.4, C                   |  | 129.2, C                   |  | 154.8, C                   |   | 154.8, C                   | 6.63, d (8.0)                         |
| 7   | 143.7, C                   |  | 143.7, C                   |  | 114.0, CH                  | 6.63, d (8.1)                                 | 114.0, CH                  | 6.94, d (8.0)                         |
| 8   | 82.6, CH                   | 5.50, dd (8.3, 2.5)  | 82.5, CH                   | 5.71, ddt (10.9, 5.6, 2.6)   | 124.2, CH                  | 6.93, d (8.1)                                 | 124.2, CH                  | 2.79, m                               |
| 9   | 39.4, $\text{CH}_2$        | 2.32, dt (13.5, 4.7)<br>1.94, ddd (13.5, 11.3, 2.8)<br>4.61, q (6.0) | 35.8, $\text{CH}_2$        | 2.32, ddd (14.8, 5.6, 2.5)<br>1.97, ddd (14.8, 11.2, 4.5)<br>4.40, q (3.9) | 44.2, $\text{CH}_2$        | 2.74, dd (16.2, 10.7)<br>3.01, dd (16.2, 2.4) | 43.9, $\text{CH}_2$        | 2.79, m<br>2.90, d (2.8)              |
| 10  | 77.3, CH                   | 4.61, q (6.0)  | 77.3, CH                   | 4.40, q (3.9)  | 208.1, C                   |   | 208.0, C                   |                                       |
| 11  | 81.4, CH                   | 4.34, t (2.5)  | 78.5, CH                   | 4.28, dd (6.6, 4.4)  | 74.7, CH                   | 5.08, q (7.2)                                 | 75.1, CH                   | 5.06, q (7.1)                         |
| 12  | 106.4, CH                  | 5.96, s  | 105.3, CH                  | 5.82, s  | 14.8, $\text{CH}_3$        | 1.39, d (7.2)                                 | 14.9, $\text{CH}_3$        | 1.39, d (7.1)                         |
| 13  | 21.1, $\text{CH}_3$        | 1.30, d (6.2)  | 13.0, $\text{CH}_3$        | 1.51, d (6.6)  | 72.6, C                    |   | 72.5, C                    |                                       |
| 15  |                            |  |                            |  | 25.3, $\text{CH}_3$        | 0.91, s                                       | 25.3, $\text{CH}_3$        | 0.91, s                               |
| 16  |                            |  |                            |  | 25.7, $\text{CH}_3$        | 1.05, s                                       | 25.7, $\text{CH}_3$        | 1.05, s                               |
| 17  |                            |  |                            |  | 64.3, $\text{CH}_2$        | 4.48, d (10.6)<br>4.60, d (10.6)              | 64.3, $\text{CH}_2$        | 4.48, d (10.6)<br>4.60, d (10.6)      |
| 3'  |                            |  |                            |  | 65.5, $\text{CH}_2$        | 3.57, d (7.0)                                 | 65.4, $\text{CH}_2$        | 3.56, dd (7.1, 3.5)                   |
| 4'  |                            |  |                            |  | 14.1, $\text{CH}_3$        | 1.20, d (7.0)                                 | 14.1, $\text{CH}_3$        | 1.19, d (6.7)                         |
| AcO |                            |  |                            |  | 170.7, C                   |   | 170.7, C                   |                                       |
|     |                            |  |                            |  | 19.1, $\text{CH}_3$        | 2.09, s                                       | 19.2, $\text{CH}_3$        | 2.10, s                               |

**Figure 3.** Key NOESY correlations of compounds 1 and 2.**Figure 4.** Comparison between calculated and experimental ECD spectra of 1–5. (a) for 1 and 2; (b) for 3 and 4; (c) for 5.

Compound **2** was isolated as a white amorphous solid, and possessed the same molecular formula  $\text{C}_{13}\text{H}_{14}\text{O}_4$  as that of **1**, based upon its HRESIMS at  $m/z$  233.0806  $[\text{M} - \text{H}]^-$  and  $^{13}\text{C}$  NMR data (Figure S8). The high resemblances of the 1D and 2D NMR data (Table 1 and Figures S9–S14) of **1** and **2**, indicating that both compounds had the same

planar structures [20]. Compared with **1**, the main difference occurred at the configuration at C-8, C-10, C-11, and C-13, which was proved by the carbon chemical shifts of C-8 ( $\Delta\delta_C$   $-0.1$  ppm), C-10 ( $\Delta\delta_C$   $0.0$  ppm), C-11 ( $\Delta\delta_C$   $-4.1$  ppm), C-13 ( $\Delta\delta_C$   $-1.1$  ppm), and C-14 ( $\Delta\delta_C$   $-8.1$  ppm). The NOESY correlations of H-8/H<sub>3</sub>-14 (Figures 3 and S14) along with the NOESY correlations for H-13/H-11 revealed that H-8 and H<sub>3</sub>-14 were positioned on the opposite face relative to H-10 and H-11. On the basis of the above evidence and the presumed biosynthetic pathway, we suggest that the relative configuration of **2** was assigned as 8*R*, 10*R*, 11*S*, 13*S*. This assignment was further confirmed by the calculated ECD spectrum of (8*R*, 10*R*, 11*S*, 13*S*)-**2**, the result of which showed good accordance with the experimental one (Figure 4). Thus, the structure of **2** was determined and named heterocornol R (**2**).

Compound **3** was isolated as a white amorphous solid, and the molecular formula was determined to be C<sub>21</sub>H<sub>30</sub>O<sub>6</sub> by HRESIMS, giving a molecular ion peak at *m/z* 401.1955 [M + Na]<sup>+</sup>, indicating seven degrees of unsaturation (Figure S15). The <sup>1</sup>H NMR spectrum (Figure S16) revealed characteristic signals for two aromatic protons of a 1,2,3,4-tetrasubstituted benzene [ $\delta_H$  6.93 (d, *J* = 8.1 Hz) and 6.63 (d, *J* = 8.1 Hz)], and five methyl groups [ $\delta_H$  2.09 (s), 1.39 (d, *J* = 7.2 Hz), 1.2 (d, *J* = 7.0 Hz), 1.05 (s), and 0.91 (s)]. <sup>1</sup>H and <sup>13</sup>C NMR spectroscopic data of **3** (Figures S17 and S18) revealed that it possessed the similar structural characteristics with pestalachloride E [21], a chlorinated benzophenone derivative obtained from a marine fungal *pestalotiopsis* sp. The major difference was that one aldehyde group at C-5 and dichloro-substituted phenol at C-3 in pestalachloride E was replaced by one ethoxyethane (C-5) and ethyl ketone side chain (C-3) in **3**, respectively. This was further confirmed by the HMBC correlations from H-1' ( $\delta_H$  4.60) to C-4 ( $\delta_C$  147.4), C-6 ( $\delta_C$  154.8), C-5 ( $\delta_C$  119.1), and C-3' ( $\delta_C$  65.5), from H-10 ( $\delta_H$  3.01) to C-3 ( $\delta_C$  40.8), C-2 ( $\delta_C$  55.6), and C-4 ( $\delta_C$  147.4), together with the COSY correlations H-1/H-2/H-3/H-10 and H-7/H-8. HMBC correlations between H-8 ( $\delta_H$  6.93) and C-1 ( $\delta_C$  31.7), C-7 ( $\delta_C$  114.0), and C-4 ( $\delta_C$  147.4) and between H-13 ( $\delta_H$  1.39) and C-11 ( $\delta_C$  208.1), C-12 ( $\delta_C$  74.7) and between H-16 ( $\delta_H$  1.05) and C-14 ( $\delta_C$  72.6), C-2 ( $\delta_C$  55.6), and C-15 ( $\delta_C$  25.3) reconfirmed that the hydroxyl was located at C-14. The planar structure of **3** was confirmed by HSQC, COSY, and HMBC experiments (Figures 2, S19 and S20).

Compound **4** was isolated as a white amorphous solid and had the same molecular formula, C<sub>21</sub>H<sub>30</sub>O<sub>6</sub>, as **3** by HRESIMS data (Figure S21). Detailed analyses of its NMR spectroscopic features implied that **3** and **4** had the same planar structures. Analysis of the 2D NMR spectra confirmed the structure of **4** (Figures 2 and S22–S27).

Unfortunately, in the NOESY spectrum, NOE interactions could not be used to determine the different stereoscopic relationship between **3** and **4**. The apparent difference between **3** and **4** are the opposite Cotton effects (Figure 4) and the opposite optical rotations. To further assign the absolute configuration of **3** and **4**, ECD calculations were performed (Figures 4, S28 and S29). According to the literature [22,23], the ECD band between 260 and 285 nm is allied with the <sup>1</sup>L<sub>b</sub> transition of the aromatic chromophore. The region of the spectrum from 260 to 285 is diagnostic of the configuration of aromatic compounds. The experimental ECD spectrum for compound **3** displays positive Cotton effects at 278 nm and negative effects at 208 and 300 nm. The calculated ECD spectra for **3** with an *R* configuration at C-12 showed a negative Cotton effect between 280 and 320 nm. The CD spectrum of **4** showed negative (229 and 240 nm) and positive (300 and 208 nm) Cotton effects, indicating that the C-12 of **4** was represented as *S*. As a result, the calculated ECD curve for 2*R*, 3*R*, 12*R*-**3** was the best match with **3**, and 2*R*, 3*S*, 12*S*-**4** was the best match with **4** (Figures 4 and S30–S35).

The molecular formula of **5** was assigned to be C<sub>14</sub>H<sub>18</sub>O<sub>5</sub> on the basis of the HRESIMS ion at *m/z* 289.1047 [M + Na]<sup>+</sup> and <sup>13</sup>C NMR data (Figure S36). The <sup>1</sup>H and <sup>13</sup>C NMR data of **5** (Figures S37–S39) were similar to those of vaccinol O [19]. The major difference was due to the presence of signals of the acetyl moiety ( $\delta_H$  2.04,  $\delta_C$  172.5, and 21.2) in **5**, instead of the carbonyl group in vaccinol O. In addition, signals for an isopentyl unit were absent in the NMR spectra of **5** (Tables 2 and 3), which was confirmed by COSY and HMBC experiments

(Figures S40–S42). In addition, the CD spectrum of **5** exhibited a negative Cotton effect at 204 nm in accordance with that of vaccinol O [19], which allowed assignment of the 3*R* absolute configuration (Figure 4). The coupling constant  $J_{H-11/H-12} = 4.2$  Hz revealed that the relative configurations of C-11 and C-12 in **5** were suggested as an *erythro* [24]. In order to discriminate between (11*R*, 12*S*)-**5** and (11*S*, 12*R*)-**5**, the electronic circular dichroism (ECD) spectrum of **5** was calculated and compared with the experimental spectra. As a result, the calculated spectrum of (11*R*, 12*S*)-**5** matched well with the experimental data (Figure 4), indicating absolute configuration of **5**, to be 3*R*, 11*R*, 12*S*.

Table 2. <sup>1</sup>H NMR (500 MHz) data for **5–9**.

| No.    | 5 <sup>a</sup>   | 6 <sup>a</sup>   | 7 <sup>a</sup>                                    | 8 <sup>a</sup>                         | 9 <sup>b</sup>                             |
|--------|--|--|---|--|--|
|        | $\delta_H$ (f in Hz)   | $\delta_H$ (f in Hz)   | $\delta_H$ (f in Hz)                              | $\delta_H$ (f in Hz)                   | $\delta_H$ (f in Hz)                       |
| 1      | 5.06, dd (12.0, 2.7)<br>4.97, d (12.0)   | 5.04, dd (12.3, 2.8)<br>4.97, dd (12.3)                      | 5.10, dd (12.0, 3.1)<br>4.94, d (12.0)            | 5.08, dd (12.1, 2.7)<br>4.98, d (12.1) | 4.32, dt (8.1, 4.0)<br>4.19, dt (8.1, 3.8) |
| 2      |  |  |   |  | 4.21, m                                    |
| 3      | 5.39, d (9.9)  | 5.18, dd (10.0, 2.1)   | 5.43, brd (9.0)                                   | 5.55, brd (9.0)                        | 4.20, brs                                  |
| 4      |  |  |   |  | 5.49, dd (15.4, 6.4)                       |
| 5      | 6.67, d (7.7)  | 6.67, d (7.8)  |   |  | 5.77, dt (15.4, 6.4)                       |
| 6      | 7.11, t (7.7)  | 7.11, t (7.8)  | 6.88, d (8.1)                                     | 6.87, d (8.1)                          | 2.08, m                                    |
| 7      | 6.66, d (7.7)  | 6.66, d (7.8)  | 6.60, d (8.1)                                     | 6.60, d (8.1)                          |  |
| 8      |  |  |   |  | 5.08, d (6.4)                              |
| 10     | 1.84, ddd (14.3, 10.3, 2.3)<br>1.71, ddd (14.3, 10.0, 2.5)<br>3.93, ddd (10.3, 4.2, 2.5) | 2.08, m<br>1.86, dt (4.5, 2.5)<br>3.93, ddd (10.2, 4.5, 2.3) | 1.84, dd (6.7, 4.3)<br>5.03, ddd (10.0, 4.3, 2.0) | 2.13, m<br>5.04, ddd (10.0, 4.7, 2.6)  | 1.24, m<br>1.26, m                         |
| 11     | 4.85, m  | 5.05, m  | 4.87, dd (6.5, 4.3)                               | 4.89, dd (6.4, 4.7)                    | 1.32, m                                    |
| 13     | 1.21, d (6.5)  | 1.13, d (6.5)  | 1.12, s   | 1.23, s                                | 1.32, m                                    |
| 1      |  |  | 3.25, m   | 3.36, m                                |  |
| 2      |  |  | 5.54, t (7.0)                                     | 5.45, t (6.5)                          | 4.11, dt (8.1, 3.8)                        |
| 3      |  |  |   |  | 1.61, m, 1.81, m                           |
| 4      |  |  | 2.03, s   | 2.06, s                                | 1.42, m                                    |
| 5      |  |  | 4.48, s   | 4.69, s                                | 1.26, m                                    |
| 11-OAc |  | 2.09, s  | 1.61, s   |  | 1.34, m                                    |
| 12-OAc | 2.04, s  |  |   | 1.62, s                                |  |
| 5-OAc  |  |  | 2.02, s   | 2.04, s                                |  |
| 1-OAc  |  |  |   |  | 2.06, m                                    |
| 14–17  |  |  |   |  | 1.24–1.42                                  |
| 18     |  |  |   |  | 0.88, t (7.0)                              |
| 19     |  |  |   |  | 1.58, brs                                  |

<sup>a</sup> NMR data for compounds **5–8** in CD<sub>3</sub>OD, <sup>b</sup> NMR data for compound **9** in CDCl<sub>3</sub> ( $\delta$  in ppm and *J* in Hz).

Compound **6** had the same molecular formula as **5**, which was established by their HRESIMS together with the <sup>13</sup>C NMR data (Figure S43). Its <sup>1</sup>H and <sup>13</sup>C NMR data (Tables 2 and 3, Figures S44 and S45) closely resembled those of **5**, except for an acetyl moiety at C-12 ( $\delta_C$  75.3) in **5** and C-11 ( $\delta_C$  76.2) in **6**. Compared with **5**, chemical shift of C-10 ( $\delta_C$  37.1), C-11 ( $\delta_C$  69.7), C-12 ( $\delta_C$  76.2), and C-13 ( $\delta_C$  18.4) of **6** were shifted upfield ( $\Delta$ 3.3 ppm,  $\Delta$ 5.6 ppm) and downfield ( $\Delta$ 5.2 ppm,  $\Delta$ 3.3 ppm), respectively. The planar structure of **6** was confirmed by HSQC, COSY, and HMBC experiments (Figures 2, S46 and S47). The shared biogenesis and similar chemical shifts and coupling constants of **6** and **5** suggested the **6** had the same relative configurations for C-3, C-11, and C-12 as those of **5**. In addition, compound **6** showed the similar specific rotation ( $[\alpha]_D^{25} -2.5$  (*c* 0.1, MeOH)) to that of **5** ( $[\alpha]_D^{25} -2.4$  (*c* 0.20, MeOH)), which indicated compound **6** had the same configuration. Given that both **5** and **6** were isolated from the same strain, the absolute configuration of **6** was deduced as 3*R*, 11*R*, 12*S*.

The molecular formula of **7** and **8** were assigned as C<sub>21</sub>H<sub>28</sub>O<sub>7</sub>, by analysis of their HRESIMS and <sup>13</sup>C NMR data (Figures S48 and S53). Their NMR spectroscopic features implied that **7** and **8** were a pair of regioisomers. Moreover, the 1D NMR data of **7** and **8** were similar to those of **5** (Figures S49–S51 and S54–S56). The only difference was due to the presence of signals of the additional isopentyl unit and acetyl moiety in **8**. Thus, it suggested that **8** was a derivative of **5**, which was confirmed by the HMBC correlation from H-1' ( $\delta_H$  3.36) to C-4 ( $\delta_C$  141.8), C-6 ( $\delta_C$  130.3), C-5 ( $\delta_C$  126.0), and C-3' ( $\delta_C$  132.4), from H-5' ( $\delta_H$  4.69) to C-4' ( $\delta_C$  21.6), C-2' ( $\delta_C$  129.7), and 5'-OAc ( $\delta_C$  172.8). Compared with **7**, the only difference was that **7** had an acetyl group at C-11, while **8** had an acetyl group at C-12, which was confirmed by the HMBC correlations of H-12 ( $\delta_H$  4.89) with C-10 ( $\delta_C$  35.0),

C-13 ( $\delta_C$  15.0), and 12-OAc ( $\delta_C$  171.4) in **8** (Figure 2, Figures S52 and S57). Comparison of the analogous chemical shifts and coupling constants between **5** and **8**, and between **6** and **7**, together with biogenetic considerations based on their coisolation [19,25], we suggest that the absolute configuration of **7** and **8** to have 3*R*, 11*R*, 12*S* configurations, which are the same as those of **5**.

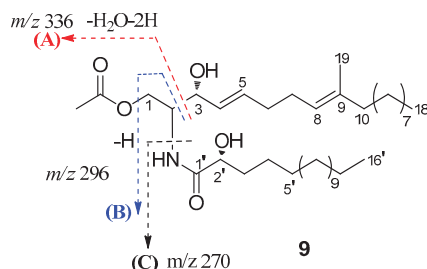
**Table 3.**  $^{13}\text{C}$  NMR (125 MHz) data for **5–9**.

|        | 5 <sup>a</sup>                    | 6 <sup>a</sup>                    | 7 <sup>a</sup>                    | 8 <sup>a</sup>                    | 9 <sup>b</sup>                    |
|--------|-----------------------------------|-----------------------------------|-----------------------------------|-----------------------------------|-----------------------------------|
| No.    | $\delta_C$ , Type                 | $\delta_C$ , Type                 | $\delta_C$ , Type                 | $\delta_C$ , Type                 | $\delta_C$ , Type                 |
| 1      | 71.4, CH <sub>2</sub>             | 71.6, CH <sub>2</sub>             | 72.8, CH <sub>2</sub>             | 70.0, CH <sub>2</sub>             | 62.9, CH <sub>2</sub>             |
| 2      |                                   |                                   |                                   |                                   | 53.0, CH                          |
| 3      | 82.2, CH                          | 82.2, CH                          | 84.1, CH                          | 83.2, CH                          | 73.0, CH                          |
| 4      | 145.4, C                          | 145.1, C                          | 142.8, C                          | 141.8, C                          | 128.2, CH                         |
| 5      | 113.0, CH                         | 113.0, CH                         | 126.0, C                          | 126.0, C                          | 134.4, CH                         |
| 6      | 130.2, CH                         | 130.3, CH                         | 130.7, CH                         | 130.3, CH                         | 31.9, CH <sub>2</sub>             |
| 7      | 114.9, CH                         | 115.0, CH                         | 115.6, C                          | 115.2, CH                         | 27.5, CH <sub>2</sub>             |
| 8      | 152.9, C                          | 153.0, C                          | 151.3, C                          | 151.3, C                          | 123.1, CH                         |
| 9      | 126.1, C                          | 126.3, C                          | 126.1, C                          | 126.5, C                          | 136.2, C                          |
| 10     | 40.4, CH <sub>2</sub>             | 37.1, CH <sub>2</sub>             | 38.9, CH <sub>2</sub>             | 35.0, CH <sub>2</sub>             | 39.7, CH <sub>2</sub>             |
| 11     | 71.0, CH                          | 69.7, CH                          | 74.7, CH                          | 72.4, CH                          | 28.0, CH <sub>2</sub>             |
| 12     | 75.3, CH                          | 76.2, CH                          | 71.5, CH                          | 74.7, CH                          | 29.4, CH <sub>2</sub>             |
| 13     | 15.1, CH <sub>3</sub>             | 18.4, CH <sub>3</sub>             | 15.0, CH <sub>3</sub>             | 15.0, CH <sub>3</sub>             | 29.4, CH <sub>2</sub>             |
| 1      |                                   |                                   | 31.3, CH <sub>2</sub>             | 31.2, CH <sub>2</sub>             | 174.6, C                          |
| 2      |                                   |                                   | 128.7, CH                         | 129.7, CH                         | 72.2, CH                          |
| 3      |                                   |                                   | 132.5, C                          | 132.4, C                          | 34.9, CH <sub>2</sub>             |
| 4      |                                   |                                   | 21.2, CH <sub>3</sub>             | 21.6, CH <sub>3</sub>             | 25.0, CH <sub>2</sub>             |
| 5      |                                   |                                   | 70.9, CH <sub>2</sub>             | 64.7, CH <sub>3</sub>             | 28.0, CH <sub>2</sub>             |
| 6~15   |                                   |                                   |                                   |                                   | 29.7~31.9                         |
| 16     |                                   |                                   |                                   |                                   | 14.1, CH <sub>3</sub>             |
| 11-AcO |                                   |                                   | 172.4, C<br>20.8, CH <sub>3</sub> |                                   |                                   |
| 12-AcO | 172.5, C<br>21.2, CH <sub>3</sub> | 172.7, C<br>21.1, CH <sub>3</sub> |                                   | 171.4, C<br>20.8, CH <sub>3</sub> |                                   |
| 5-AcO  |                                   |                                   | 172.8, C<br>21.2, CH <sub>3</sub> | 172.8, C<br>20.8, CH <sub>3</sub> |                                   |
| 1-AcO  |                                   |                                   |                                   |                                   | 171.3, C<br>20.9, CH <sub>3</sub> |
| 14~17  |                                   |                                   |                                   |                                   | 22.7~31.9,<br>CH <sub>2</sub>     |
| 18     |                                   |                                   |                                   |                                   | 14.1, CH <sub>3</sub>             |
| 19     |                                   |                                   |                                   |                                   | 16.0, CH <sub>3</sub>             |

<sup>a</sup> NMR data for compounds **5–8** in CD<sub>3</sub>OD, <sup>b</sup> NMR data for compound **9** in CDCl<sub>3</sub> ( $\delta$  in ppm and *J* in Hz).

Compound **9**, an amorphous powder, possessed a molecular formula of C<sub>37</sub>H<sub>69</sub>NO<sub>5</sub> based on its  $^{13}\text{C}$  NMR data and HRESIMS *m/z* 608.5251 [M + H]<sup>+</sup> (Figures S58 and S59). The  $^1\text{H}$  NMR (Table 2 and Figure S60) spectrum of **9** exhibited an amide proton [ $\delta_{\text{H}}$  6.91 (NH, d, *J* = 8.0 Hz)], two disubstituted olefinic protons [ $\delta_{\text{H}}$  5.77 (1H, dt, *J* = 15.4, 6.4 Hz) and  $\delta_{\text{H}}$  5.49 (1H, dt, *J* = 15.4, 6.4 Hz)], a trisubstituted olefinic proton [ $\delta_{\text{H}}$  5.08 (1H, d, *J* = 6.4 Hz)], one oxygenated methylene [ $\delta_{\text{H}}$  4.32 (1H, dt, *J* = 8.1, 4.0 Hz) and  $\delta_{\text{H}}$  4.19 (1H, dt, *J* = 8.1, 3.8 Hz)], two oxygenated methine [ $\delta_{\text{H}}$  4.20 (1H, brs) and  $\delta_{\text{H}}$  4.11 (1H, dt, *J* = 8.1, 3.8 Hz)], aliphatic methylenes ( $\delta_{\text{H}}$  1.24~1.42). Additionally, resonances for three methyl groups, including an olefinic methyl group ( $\delta_{\text{H}}$  1.58, brs) and two terminal methyl groups [ $\delta_{\text{H}}$  0.88 (6H, t, *J* = 7.0 Hz)], were observed. Analysis of the  $^{13}\text{C}$  NMR data and HSQC spectra (Figures S61 and S62) revealed the existence of characteristic signals resonances including an amide carbonyl at  $\delta_C$  173.9, methine carbons at  $\delta_C$  53.0, and aliphatic carbons at  $\delta_C$  22.7~29.7. Detailed analysis of these aforementioned data of **9** suggested it was very similar to those of the previously reported ceramide compound [24], (2*S*, 2'*R*, 3*R*, 4*E*, 8*E*)-*N*-2'-Hydroxyhexadecanoyl-2-amino-9-methyl-4, 8-octadecadiene-1,3-diol. The major

differences are the presence of an additional acetyl group of protons ( $\delta_{\text{H}}$  2.05, 20.9, and 171.3) in **9**, indicating that **9** was a 1-O-acetyl derivative of ceramide compound. Combined with the 2D NMR spectra data, an acetyl group was suggested at C-1 in **9**, which was further confirmed by the HMBC correlation of H-1 ( $\delta_{\text{H}}$  4.32 and 4.19) with C-2 ( $\delta_{\text{C}}$  53.0), C-3 ( $\delta_{\text{C}}$  73.0), and C-1'' ( $\delta_{\text{C}}$  171.3) (Figures 2 and S63). Furthermore, based on the  $J$  values for H-4 ( $\delta_{\text{H}}$  5.49, dd,  $J = 15.4, 6.4$  Hz), the geometries of the double bonds for H-4/H-5 was *trans*. Compared to the NMR data from (2*S*, 2'*R*, 3*R*, 4*E*, 8*E*)-*N*-2'-Hydroxyhexadecanoyl-2-amino-9-methyl-4,8-octadecadiene-1,3-diol [26,27], the chemical shift value of the olefinic methyl group at C-9 ( $\delta_{\text{C}}$  16.0) in compound **9** suggests that the double bond at C-8 is *E* geometry. The length of the fatty acid was determined by the characteristic peaks at  $m/z$  253, 296, 314, 336 in the EI-MS (Figures 5 and S59) [28]. According to the literature [29] and our NMR data, the chemical shift of C-3 and C-2' in ceramide compound were almost superimposed with configuration of C-3 and C-2'. Comparing the coupling constant of H-2 and H-3, and  $^{13}\text{C}$  NMR data of the synthetic (2*S*, 2'*R*, 3*R*, 4*E*, 8*E*)-*N*-2'-Hydroxyhexadecanoyl-2-amino-9-methyl-4,8-octadecadiene-1,3-diol, the configuration of **9** was deduced. Thus, **9** was determined and named pestalotiopsisamide.

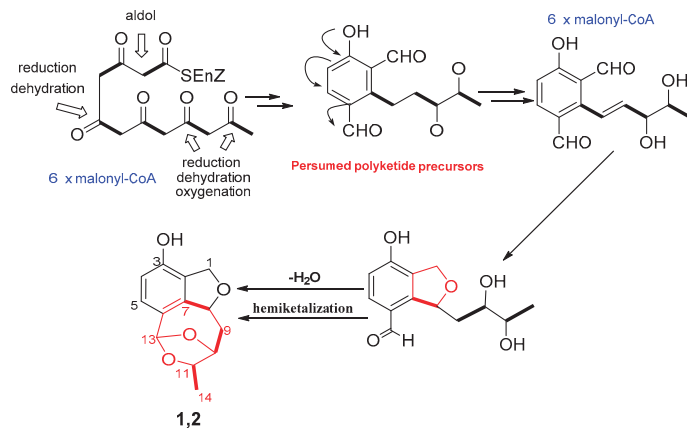


**Figure 5.** Observed key mass fragments of ceramide **9**.

Polyketides are common biosynthetic precursor in the process of synthesizing aromatics and macrolides in microorganisms. Compounds **1–8** were formed via different polyketide precursors by polyketide synthases. Presumed polyketide precursors are considered to be biogenetically derived from acetyl-CoA by reduction, dehydration, oxygenation, and cyclization to form the core skeleton. Next, presumed polyketide precursors underwent reduction to form a vicinal diol (an intermediate), which could generate a dihydroisobenzofuran through reduction and dehydration. Finally, the dihydroisobenzofuran undergoes dehydration and nucleophilic addition to yield **1** or **2** (Scheme 1), featuring a novel 6/5/7/5 tetracyclic polyketide derivatives.

The isolated compounds (**1–9** and **12**) were evaluated for their cytotoxic activities against four human cancer cell lines (Hela, A549, HCT-8, A2780) via MTT assay. However, none of them showed obvious cytotoxicities. They were also tested with their antimicrobial activities against three bacteria and one fungi using a micro broth dilution method (Table 4). Only compound **12** showed antibacterial activities against Gram-positive bacteria *Staphylococcus aureus* and *Bacillus subtilis* and Gram-negative bacteria *Escherichia coli*, with MIC values ranging from 25 to 50  $\mu\text{g}/\text{mL}$ . Moreover, **12** also exhibited weak antifungal activities against *Candida albicans* with MIC values 100  $\mu\text{g}/\text{mL}$ .

Anti-inflammatory *in vitro* screening tests revealed that **7** and **8** could inhibit the production of LPS-induced NO in RAW 264.7 cells significantly (Figure 6A,B) with no cytotoxicity, comparable to the positive drug dexamethasone (DXM, 33  $\mu\text{M}$ ). Further Western blotting analysis showed **7** and **8** markedly suppressed the iNOS protein expression in LPS-induced RAW 264.7 cells in a concentration-dependent manner (Figure 6C,D). The result showed that the two new polyketide derivatives, heterocornols T and X (**7** and **8**), might serve as potential leads for development of anti-inflammatory activity.



Scheme 1. Plausible Biosynthetic Pathway of compounds 1 and 2.

Table 4. Antibacterial activity of the compounds (MIC, µg/mL).

| Strains  | <i>S. aureus</i>  | <i>B. subtilis</i> | <i>E. coli</i>    | <i>C. albicans</i> |
|----------|-------------------|--------------------|-------------------|--------------------|
| 12       | 50                | 25                 | 25                | 100                |
| Positive | 0.25 <sup>a</sup> | 0.13 <sup>a</sup>  | 0.13 <sup>a</sup> | 1.0 <sup>b</sup>   |

<sup>a</sup> Ciprofloxacin; <sup>b</sup> Amphotericin.

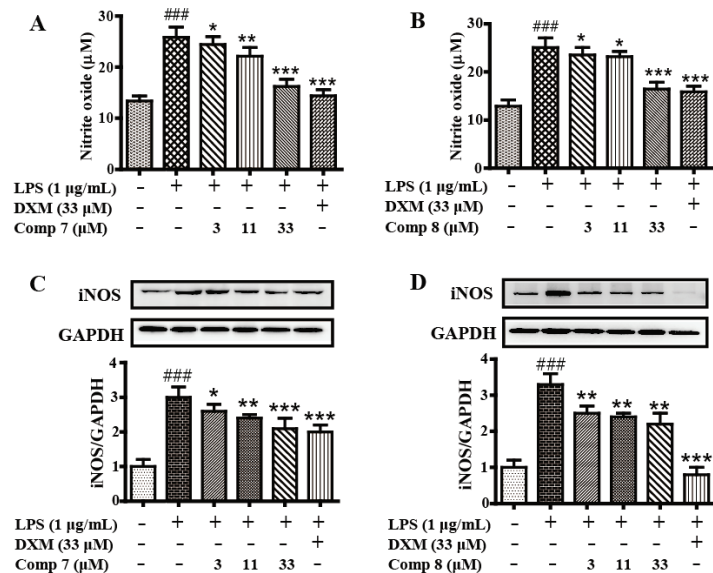


Figure 6. The anti-inflammatory activity of compounds 7 and 8. Cells were pretreated with both compounds 7 and 8 differently concentrations (0, 3, 11, 33 µM) and DXM (33 µM) for 2 h, then stimulated with or without LPS (1 µg/mL) for 24 h. The culture medium was collected to detect the concentrations of nitrite with Griess agent (A,B). Protein levels of iNOS were evaluated by Western blot (C,D). The data represent the means ± S.E. of three independent experiments. (###  $p < 0.001$  was compared to control. \*  $p < 0.05$ , \*\*  $p < 0.01$ , \*\*\*  $p < 0.001$  compared to LPS group).

### 3. Materials and Methods

#### 3.1. General Experimental Procedures

Optical rotations were determined using an AntonPaar MCP500 polarimeter. UV spectra were measured with a Shimadzu UV-2600 PC spectrometer. IR spectra were recorded on a Shimadzu IR Affinity-1 spectrometer with KBr pellets. 1D and 2D NMR spectra were collected on a Bruker DRX-500 spectrometer,  $\delta$  in ppm rel. to TMS,  $J$  in Hz. HRESIMS were performed using a Bruker maXis TOF-Q mass spectrometer (Bruker, Daltonics, Billerica, MA, USA). Silica gel (100–200 mesh, 200–300 mesh, Qingdao Marine Chemical Ltd., Qingdao, China), Sephadex LH-20 (GE Healthcare Bio-sciences AB, Uppsala, Sweden), YMC\*GEL ODS-A (S-50  $\mu$ m, 12 nm) (YMC Co., Ltd., Kyoto, Japan) were used for column chromatography. Semipreparative HPLC was performed using an ODS column (YMC-ODS-A, 250  $\times$  10 mm, 5  $\mu$ m). CD spectra were measured on a Biologic MOS-450 spectra polarimeter (Biologic Science, Claix, France). ECD spectra were measured with a Chirascan circular dichroism spectrometer (Applied Photophysics). MTT and antimicrobial assays were analyzed using a microplate reader (BioTek Synergy H1, BioTek Instruments, Inc., Winooski, VT, USA).

#### 3.2. Fungal Material

The fungal strain XWS03F09 was isolated from the sponge *Phakellia fusca*, which was collected from the Xisha Islands of China in 2012. It was identified as *Pestalotiopsis heterocornis* XWS03F09 by analysis of its ITS region of the rDNA as described, which has been deposited in the GenBank database (accession no. JN943628.1). A voucher specimen (No. XWS03F09) was deposited in the School of Pharmacy, Southwest Medical University, Luzhou, Sichuan, China.

#### 3.3. Fermentation, Extraction, and Isolation

The fungal strain *Pestalotiopsis heterocornis* XWS03F09 was grown at 28 °C without shaking for 36 days in 1000 mL conical flasks containing solid rice medium (each flask contained 200 g of rice, 6 g of artificial sea salt; 200 mL of distilled water, boiled in an autoclave for 20 min at 121 °C). The total of fermented rice cultures was extracted with EtOAc three times to afford 165 g of crude extract (Figure S64).

The extract was subjected to silica gel column chromatography eluting with a gradient CH<sub>2</sub>Cl<sub>2</sub>-MeOH (30:1–0:100) to give 9 fractions based on TLC properties. Fraction 3 was separated by silica gel column chromatography eluting with petroleum ether-EtOAc (6:1) to give seven subfractions (Frs. 3.1–3.7). Fr. 3.2 was subjected to Sephadex LH-20 chromatography (MeOH) to afford three subfractions (Frs. 3.2.1–3.2.3). Frs. 3.2.2 was purified by semipreparative HPLC (70% MeOH/H<sub>2</sub>O) to afford **1** (7.0 mg) and **2** (3.0 mg). Fr. 3.3 was subjected to Sephadex LH-20 chromatography to produce four subfractions (Frs. 3.3.1–3.3.4). Fr. 3.3.2 was separated by ODS column chromatography eluting with MeOH-H<sub>2</sub>O (60%) to yield **5** (7.0 mg). Fr. 3.4 was subjected to a Sephadex LH-20 column (MeOH) and purified by preparative TLC to give **9** (4.0 mg). Fraction 4 was isolated by column chromatography on silica gel eluting with petroleum ether-EtOAc (4:1–0:1) to yield five subfractions (Frs. 4.1–4.5). Fr. 4.1 was separated by semipreparative HPLC (60% MeOH/H<sub>2</sub>O) to produce **3** (3.5 mg) and **4** (8.0 mg). Fr. 4.2 was separated by a Sephadex LH-20 column eluting with MeOH to yield three subfractions (Frs. 4.2.1–4.2.3). Fr. 4.2.3 was separated by repeated column chromatography and further purification with semipreparative HPLC (60% MeOH/H<sub>2</sub>O) to give **10** (2.0 mg), **11** (1.0 mg). Fr. 4.3 was subjected to silica gel column chromatography eluting with a CH<sub>2</sub>Cl<sub>2</sub>-Acetone to yield five subfractions (Frs. 4.3.1–4.3.5). Fr. 4.3.3 was purified by semipreparative HPLC (55% MeOH/H<sub>2</sub>O) to afford **12** (7.0 mg). Fraction 5 was subjected to silica gel column chromatography eluting with CH<sub>2</sub>Cl<sub>2</sub>-Acetone (3:1) to yield five subfractions (Frs. 5.1–5.5). Fr. 5.3 was separated over an ODS column eluting with a gradient of MeOH and H<sub>2</sub>O and further purified by semipreparative HPLC with MeOH-H<sub>2</sub>O (40:60) to afford **7** (4.0 mg) and **8** (4.0 mg). Fr. 5.3 was fractionated on Sephadex LH-20 (MeOH) to provide four subfractions (Fr. 5.3.1–5.3.4).

Fr. 5.3.2 was repeatedly purified using semipreparative HPLC with MeOH-H<sub>2</sub>O to give 6 (20.0 mg).

*Heterocornol Q (1)*: white amorphous solid;  $[\alpha]_{\text{D}}^{25} - 5.1$  (c 0.4, MeOH); UV (MeOH)  $\lambda_{\text{max}}$  (log  $\epsilon$ ) 280 (2.64), 271 (2.66), 226 (3.33), 208 (3.74) nm; CD (MeOH)  $\lambda_{\text{max}}$  ( $\Delta\epsilon$ ) 206 (−3.19), 235 (0.39), IR (film)  $\nu_{\text{max}}$  3360, 2916, 1612, 1550, 1373, 1290, 1199, 1105, 1053, 927, cm<sup>−1</sup>; <sup>1</sup>H NMR and <sup>13</sup>C NMR data, see Table 1; HRESIMS  $m/z$  257.0783 [M + Na]<sup>+</sup> (calculated for C<sub>13</sub>H<sub>14</sub>NaO<sub>4</sub>, 257.0790).

*Heterocornol R (2)*: white amorphous solid;  $[\alpha]_{\text{D}}^{25} + 46.6$  (c 0.1, MeOH); UV (MeOH)  $\lambda_{\text{max}}$  (log  $\epsilon$ ) 280 (3.66), 271 (2.67), 223 (4.32), 212 (4.47) nm; CD (MeOH)  $\lambda_{\text{max}}$  ( $\Delta\epsilon$ ) 207 (5.68), 236 (−1.57), IR (film)  $\nu_{\text{max}}$  3340, 2916, 1612, 1506, 1377, 1290, 1197, 1161, 1080, 1051, 1014, 927 cm<sup>−1</sup>; <sup>1</sup>H NMR and <sup>13</sup>C NMR data, see Table 1; HRESIMS at  $m/z$  233.0806 [M − H]<sup>−</sup> (calculated for C<sub>13</sub>H<sub>13</sub>O<sub>4</sub>, 233.0814).

*Heterocornol S (3)*: white amorphous solid;  $[\alpha]_{\text{D}}^{25} - 1.4$  (c 0.2, MeOH); UV (MeOH)  $\lambda_{\text{max}}$  (log  $\epsilon$ ) 287 (3.36), 206 (4.18) nm; CD (MeOH)  $\lambda_{\text{max}}$  ( $\Delta\epsilon$ ) 208 (−1.41), 278 (0.45), 300 (−0.12), IR (film)  $\nu_{\text{max}}$  3331, 3298, 2972, 2930, 2852, 1717, 1636, 1456, 1373, 1240, 1076, 1018, 667 cm<sup>−1</sup>; <sup>1</sup>H NMR and <sup>13</sup>C NMR data, see Table 1; HRESIMS  $m/z$  401.1955 [M + Na]<sup>+</sup> (calculated for C<sub>21</sub>H<sub>30</sub>NaO<sub>6</sub>, 401.1940).

*Heterocornol T (4)*: white amorphous solid;  $[\alpha]_{\text{D}}^{25} + 1.9$  (c 0.2, MeOH); UV (MeOH)  $\lambda_{\text{max}}$  (log  $\epsilon$ ) 287 (3.43), 206 (4.21) nm; CD (MeOH)  $\lambda_{\text{max}}$  ( $\Delta\epsilon$ ) 208 (2.25), 240 (−0.24), 279 (−0.50), 299 (0.96), IR (film)  $\nu_{\text{max}}$  3323, 3244, 2968, 2862, 1717, 1647, 1603, 1456, 1373, 1240, 1188, 1151, 1081, 1041, 815 cm<sup>−1</sup>; <sup>1</sup>H NMR and <sup>13</sup>C NMR data, see Table 1; HRESIMS  $m/z$  401.1937 [M+Na]<sup>+</sup> (calculated for C<sub>21</sub>H<sub>30</sub>NaO<sub>6</sub>, 401.1940).

*Heterocornol U (5)*: white amorphous solid;  $[\alpha]_{\text{D}}^{25} - 2.4$  (c 0.20, MeOH); UV (MeOH)  $\lambda_{\text{max}}$  (log  $\epsilon$ ) 276 (3.58), 269 (3.59), 218 (4.35) nm; CD (300  $\mu\text{g}/\text{mL}$ ); CD (MeOH)  $\lambda_{\text{max}}$  ( $\Delta\epsilon$ ) 200 (−2.85), 250 (0.08), IR (film)  $\nu_{\text{max}}$  3404, 3335, 2938, 1713, 1599, 1470, 1373, 1254, 1151, 1022, 1007, 835 cm<sup>−1</sup>; <sup>1</sup>H NMR and <sup>13</sup>C NMR data, see Tables 2 and 3; HRESIMS  $m/z$  289.1047 [M + Na]<sup>+</sup> (calculated for C<sub>14</sub>H<sub>18</sub>NaO<sub>5</sub>, 289.1052).

*Heterocornol V (6)*: white amorphous solid;  $[\alpha]_{\text{D}}^{25} - 2.5$  (c 0.1, MeOH); UV (MeOH)  $\lambda_{\text{max}}$  (log  $\epsilon$ ) 276 (3.72), 269 (3.73), 220 (4.51) nm; IR (film)  $\nu_{\text{max}}$  3414, 2972, 2934, 1732, 1653, 1602, 1498, 1456, 1373, 1240, 1028 cm<sup>−1</sup>; <sup>1</sup>H NMR and <sup>13</sup>C NMR data, see Tables 2 and 3; HRESIMS  $m/z$  289.1046 [M + Na]<sup>+</sup> (calculated for C<sub>14</sub>H<sub>18</sub>NaO<sub>5</sub>, 289.1052).

*Heterocornols W (7)*: white amorphous solid;  $[\alpha]_{\text{D}}^{25} - 10.0$  (c 0.2, MeOH); UV (MeOH)  $\lambda_{\text{max}}$  (log  $\epsilon$ ) 273.8 (3.62), 213 (4.40) nm; IR (film)  $\nu_{\text{max}}$  3414, 2940, 2870, 1732, 1717, 1640, 1456, 1373, 1149, 1024 cm<sup>−1</sup>; <sup>1</sup>H NMR and <sup>13</sup>C NMR data, see Tables 2 and 3; HRESIMS  $m/z$  415.1755 [M + Na]<sup>+</sup> (calculated for C<sub>21</sub>H<sub>28</sub>NaO<sub>7</sub>, 415.1733).

*Heterocornol X (8)*: white amorphous solid;  $[\alpha]_{\text{D}}^{25} - 14.6$  (c 0.1, MeOH); UV (MeOH)  $\lambda_{\text{max}}$  (log  $\epsilon$ ) 272 (3.78), 208 (4.60) nm; IR (film)  $\nu_{\text{max}}$  3414, 2941, 2870, 1732, 1716, 1650, 1490, 1485, 1373, 1240, 1026 cm<sup>−1</sup>; <sup>1</sup>H NMR and <sup>13</sup>C NMR data, see Tables 2 and 3; HRESIMS  $m/z$  415.1745 [M + Na]<sup>+</sup> (calculated for C<sub>21</sub>H<sub>28</sub>NaO<sub>7</sub>, 415.1733).

(2*S*, 2'*R*, 3*R*, 4*E*, 8*E*)-*N*-2'-Hydroxyhexadecanoyl-2-amino-9-methyl-4, 8-octadecadiene-yl acetate (9): amorphous powder;  $[\alpha]_{\text{D}}^{25} + 13.0$  (c 0.1 MeOH); <sup>1</sup>H NMR and <sup>13</sup>C NMR data, see Tables 2 and 3; HRESIMS  $m/z$  608.5251 [M + H]<sup>+</sup> (calculated for C<sub>37</sub>H<sub>70</sub>NO<sub>5</sub>, 608.5254).

### 3.4. ECD Calculations

The calculations of new compounds were performed by using the TDDFT method as carried out using the Gaussian 09 program [30]. Conformational analysis was initially conducted by using the Spartan'14 software. Conformers with a Boltzmann distribution over 5% (the relative energy within 6 kcal/mol) were chosen for ECD calculations at the B3LYP/6-311+G(d,p) level. The ECD spectra of different conformers were generated using the program SpecDis by applying a Gaussian band shape with a 0.30 eV width, according to the Boltzmann-calculated contribution after UV correction.



### 3.5. Cell Culture and Cytotoxicity Assay

The hela, A549, HCT-8, A2780, and RAW 264.7 cells were cultured in DMEM medium with 10% FBS, 2 mM glutamine, 100 U/mL of penicillin, and 100 µg/mL of streptomycin at 37 °C under 5% CO<sub>2</sub> atmosphere. The cytotoxicities of **1–9** and **12** against five cell lines, including hela, A549, HCT-8, A2780, and RAW 264.7, were evaluated by the MTT method described in the literature [31].

### 3.6. Antimicrobial Assay

A micro broth dilution assay as previously reported [32] was used to evaluate the MICs of **1–9** and **12** against three bacteria (*Staphylococcus aureus* ATCC 25923, *Bacillus subtilis* ATCC 6633, *Escherichia coli* ATCC 25922), and one fungi (*Candida albicans* MYA-2867). The MIC was defined as the lowest concentration of the antimicrobial agent that completely inhibited visual growth of an organism. Ciprofloxacin and amphotericin B (Sigma Inc.) were used as positive controls against bacteria and fungi, respectively.

### 3.7. Determination of Nitric Oxide Production

The RAW 264.7 cells seeded at  $1 \times 10^6$  cell/well in six-well plates. After 24 h, the cells pretreated with compounds **7** (0, 3, 11, 33 µM), **8** (0, 3, 11, 33 µM), and dexamethasone (DXM, 33 µM) for 2 h, and then stimulated with LPS (1 µg/mL) for 24 h. The supernatant was collected for detecting the NO production with the Griess method.

### 3.8. Western Blot Analysis

The RAW 264.7 cells were pretreated with compounds **7** (0, 3, 11, 33 µM), **8** (0, 3, 11, 33 µM), and DXM (33 µM) for 2 h, and then stimulated with LPS (1 µg/mL) for 24 h. Total protein was extracted via RIPA (Beyotime, Beijing, China) and the concentration measured by BCA protein assay kit (Beyotime, Beijing, China). The (40 µg) protein was separated with 10% SDS-PAGE and transferred onto PVDF membrane (Millipore, Billerica, MA, USA), which was blocked for 1 h with 5% non-fat milk in TBS at room temperature. Then, the membrane was incubated with primary antibody overnight, then washed three times with TBST and incubated with horseradish peroxidase conjugated secondary antibody for 1 h at room temperature, washed three times with TBST and visualized by CEL (Millipore). GAPDH served as an internal control. Band pattern was analyzed with Fluor Chem FC3 system (ProteinSimple, San Francisco, CA, USA).

### 3.9. Data Analysis

The data were expressed as the mean ± S.E. of at least three independent experiments. The statistical significance of the differences between the means was determined either using Student's t-test or one-way analysis of variance where appropriate. If the means were found to be significantly different, multiple pairwise comparisons were carried out by Tukey's post hoc test. The threshold value for acceptance of difference was 5% ( $p \leq 0.05$ ).

## 4. Conclusions

Eight new polyketide derivatives, heterocornols Q–X (**1–8**), one new ceramide (**9**), and three known analogues (**10–12**) were isolated from the sponge-derived fungus *Pestalotiopsis heterocornis* XWS03F09. The structures and absolute configurations of the new compounds were elucidated by spectroscopic data and calculated by ECD analysis. Compound **12** displayed growth inhibition towards *S. aureus*, *B. subtilis*, and *E. coli*, with MIC values ranging from 25 to 100 µg/mL. Heterocornols T and X (**7** and **8**) could inhibit the production of LPS-induced NO significantly, comparable to dexamethasone. The result showed that **7** and **8** might serve as potential leads for development of anti-inflammatory activity.

**Supplementary Materials:** The following are available online at <https://www.mdpi.com/article/10.3390/md19110585/s1>, Figures S1–S64: <sup>1</sup>H, <sup>13</sup>C, HSQC, HMBC, COSY, NOESY, IR, and HRESIMS spectra of the new compounds **1–9**.

**Author Contributions:** H.L. performed the extraction, isolation and identification, and prepared manuscript. X.L. (Xiuping Lin) contributed to the collection, isolation, and identification of the fungal strain. X.B., H.N. and D.Z. contributed to this work by bioassay experiments. X.L. (Xiaowei Luo) and J.S. accomplished the ECD calculation. B.Y. performed the elucidation of structures and revised the manuscript. All authors have read and agreed to the published version of the manuscript.

**Funding:** This work was funded by the Open Project of Sichuan Industrial Institute of Antibiotics, Chengdu University (ARRLKF20-04), Applied Basic Research Fund of Luzhou municipal government-Southwest Medical University (2018LZXNYD-ZK13), Project of Southwest Medical University (2017-ZRQN-093), Special Funds for Promoting Economic Development (Marine Economic Development) of Guangdong Province (No. [2020]039), Guangdong Local Innovation Team Program (2019BT02Y262), and Guangdong Basic and Applied Basic Research Foundation (2019B151502042).

**Institutional Review Board Statement:** Not applicable.

**Data Availability Statement:** The data presented in this study are available in the main text and the Supplementary Materials of this article.

**Conflicts of Interest:** The authors declare no conflict of interest.

## References

1. Yoon, V.; Nodwell, J.R. Activating secondary metabolism with stress and chemicals. *J. Ind. Microbiol. Biotechnol.* **2014**, *41*, 415–424. [[CrossRef](#)]
2. Bode, H.B.; Bethe, B.; Höfs, R.; Zeeck, A. Big effects from small changes: Possible ways to explore nature's chemical diversity. *ChemBioChem* **2002**, *3*, 619–627. [[CrossRef](#)]
3. Wang, W.J.; Li, D.Y.; Li, Y.C.; Hua, H.M.; Ma, E.L.; Li, Z.L. Caryophyllene sesquiterpenes from the marine-derived fungus *Ascotricha* sp. ZJ-M-5 by the one strain–many compounds strategy. *J. Nat. Prod.* **2014**, *77*, 1367–1371. [[CrossRef](#)]
4. Rateb, M.E.; Houssen, W.E.; Harrison, W.T.A.; Deng, H.; Okoro, C.K.; Asenjo, J.A.; Andrews, B.A.; Bull, A.T.; Goodfellow, M.; Ebel, R.; et al. Diverse metabolic profiles of a streptomyces strain isolated from a hyper-arid environment. *J. Nat. Prod.* **2011**, *74*, 1965–1971. [[CrossRef](#)] [[PubMed](#)]
5. Paranagama, P.A.; Wijeratne, E.M.K.; Gunatilaka, A.A.L. Uncovering biosynthetic potential of plant-associated fungi: Effect of culture conditions on metabolite production by *paraphaeosphaeria* quadrisepata and *chaetomium* chiversii (1). *J. Nat. Prod.* **2007**, *70*, 1939–1945. [[CrossRef](#)]
6. Wang, X.R.; Filho, J.G.S.; Hoover, A.R.; King, J.B.; Ellis, T.K.; Powell, D.R.; Cichewicz, R.H. Chemical epigenetics alters the secondary metabolite composition of guttate excreted by an atlantic-forest-soil-derived *Penicillium citreonigrum*. *J. Nat. Prod.* **2010**, *73*, 942–948. [[CrossRef](#)] [[PubMed](#)]
7. Sun, K.L.; Zhu, G.L.; Hao, J.J.; Wang, Y.; Zhu, W.M. Chemical-epigenetic method to enhance the chemodiversity of the marine algicolous fungus, *Aspergillus terreus* OUCMDZ-2739. *Tetrahedron* **2018**, *74*, 83–87. [[CrossRef](#)]
8. Akone, S.H.; Mandi, A.; Kurtan, T.; Hartmann, R.; Lin, W.H.; Daletos, G.; Proksch, P. Inducing secondary metabolite production by the endophytic fungus *Chaetomium* sp. through fungal–bacterial co-culture and epigenetic modification. *Tetrahedron* **2016**, *72*, 6340–6347. [[CrossRef](#)]
9. Han, J.Y.; Zhang, J.Y.; Song, Z.J.; Zhu, G.L.; Liu, M.M.; Dai, H.Q.; Hsiang, T.; Liu, X.T.; Zhang, L.X.; Quinn, R.J.; et al. Genome-based mining of new antimicrobial meroterpenoids from the phytopathogenic fungus *Bipolaris sorokiniana* strain 11134. *Appl. Microbiol. Biotechnol.* **2020**, *104*, 3835–3846. [[CrossRef](#)]
10. Challis, G.L. Genome mining for novel natural product discovery. *J. Med. Chem.* **2008**, *51*, 2618–2628. [[CrossRef](#)]
11. Ziemert, N.; Alanjary, M.; Weber, T. The evolution of genome mining in microbes—A review. *Nat. Prod. Rep.* **2016**, *33*, 988–1005. [[CrossRef](#)]
12. Helfrich, E.J.N.; Reite, S.; Piel, J. Recent advances in genome-based polyketide discovery. *Curr. Opin. Biotechnol.* **2014**, *29*, 107–115. [[CrossRef](#)]
13. Nett, M.; Ikeda, H.; Moore, B.S. Genomic basis for natural product biosynthetic diversity in the actinomycetes. *Nat. Prod. Rep.* **2009**, *26*, 1362–1384. [[CrossRef](#)]
14. Lei, H.; Lin, X.P.; Han, L.; Ma, J.; Dong, K.L.; Wang, X.B.; Mu, Y.; Liu, Y.H.; Huang, X.S. Polyketide derivatives from a marine-sponge-associated fungus *Pestalotiopsis heterocornis*. *Phytochemistry* **2017**, *142*, 51–59. [[CrossRef](#)]
15. Lei, H.; Lei, J.; Zhou, X.F.; Hu, M.; Niu, H.; Song, C.; Chen, S.W.; Liu, Y.H.; Zhang, D. Cytotoxic polyketides from the marine sponge-derived fungus *pestalotiopsis heterocornis* XWS03F09. *Molecules* **2019**, *24*, 2655. [[CrossRef](#)] [[PubMed](#)]
16. Lei, H.; Lin, X.P.; Han, L.; Ma, J.; Ma, Q.J.; Zhong, J.L.; Liu, Y.H.; Sun, T.M.; Wang, J.H.; Huang, X.S. New metabolites and bioactive chlorinated benzophenone derivatives produced by a marine-derived fungus *Pestalotiopsis heterocornis*. *Mar. Drugs* **2017**, *15*, 69. [[CrossRef](#)] [[PubMed](#)]
17. Cueto, M.; Jensen, P.R.; Kauffman, C.; Fenical, W.; Lobkovsky, E.; Clardy, J. Pestalone, a new antibiotic produced by a marine fungus in response to bacterial challenge. *J. Nat. Prod.* **2001**, *64*, 1444–1446. [[CrossRef](#)] [[PubMed](#)]

18. Li, E.; Jiang, L.H.; Guo, L.D.; Zhang, H.; Che, Y.S. Pestalochlorides A-C, antifungal metabolites from the plant endophytic fungus *Pestalotiopsis adusta*. *Bioorg. Med. Chem.* **2008**, *16*, 7894–7899. [[CrossRef](#)]
19. Wang, J.F.; Liang, R.; Liao, S.R.; Yang, B.; Tu, Z.C.; Lin, X.P.; Wang, B.G.; Liu, Y.H. Vaccinols J–S, ten new salicyloid derivatives from the marine mangrove-derived endophytic fungus *Pestalotiopsis vaccinii*. *Fitoterapia* **2017**, *120*, 164–170. [[CrossRef](#)]
20. Höller, U.; Gloer, J.B.; Wicklow, D.T. Biologically active polyketide metabolites from an undetermined fungicolous hyphomycete resembling *Cladosporium*. *J. Nat. Prod.* **2002**, *65*, 876–882. [[CrossRef](#)]
21. Xing, Q.; Gan, L.S.; Mou, X.F.; Wang, W.; Wang, C.Y.; Wei, M.Y.; Shao, C.L. Isolation, resolution and biological evaluation of pestalochlorides E and F containing both point and axial chirality. *RSC Adv.* **2016**, *6*, 22653–22658. [[CrossRef](#)]
22. Pescitelli, G.; Bruhn, T. Good computational practice in the assignment of absolute configurations by TDDFT calculations of ECD spectra. *Chirality* **2016**, *28*, 466–474. [[CrossRef](#)]
23. Kurtan, T.; Antus, S.; Pescitelli, G. *Comprehensive Chiroptical Spectroscopy*; Berova, N., Polavarapu, P.L., Nakanishi, K., Woody, R.W., Eds.; Wiley: Hoboken, NJ, USA, 2012; Volume 2, pp. 73–114.
24. Chen, X.W.; Li, C.W.; Cui, C.B.; Hua, W.; Zhu, T.J.; Gu, Q.Q. Nine new and five known polyketides derived from a deep sea-sourced *Aspergillus* sp. 16-02-1. *Mar. Drugs* **2014**, *12*, 3116–3137. [[CrossRef](#)] [[PubMed](#)]
25. Xia, M.W.; Cui, C.B.; Li, C.W.; Wu, C.J. Three new and eleven known unusual C25 steroids: Activated production of silent metabolites in a marine-derived fungus by chemical mutagenesis strategy using diethyl sulphate. *Mar. Drugs* **2014**, *12*, 1545–1568. [[CrossRef](#)]
26. Yaoita, Y.; Kohata, R.; Kakuda, R.; Machida, K.; Kikuchi, M. Ceramide constituents from five mushrooms. *Chem. Pharm. Bull.* **2002**, *50*, 681–684. [[CrossRef](#)] [[PubMed](#)]
27. García, M.O.; Rodríguez, A.D. Palominin, a novel furanosesterterpene from a Caribbean sponge *Iricinia* sp. *Tetrahedron* **1990**, *46*, 1119–1124. [[CrossRef](#)]
28. Yaoita, Y.; Satoh, Y.; Kikuchi, M. A new ceramide from *Ramaria botrytis* (Pers.) Ricken. *J. Nat. Med.* **2007**, *61*, 205–207. [[CrossRef](#)]
29. Kwon, H.C.; Kim, K.R.; Zee, S.D.; Cho, S.Y.; Lee, K.R. A new indolinepeptide from *Paecilomyces* sp. J300. *Arch. Pharm. Res.* **2004**, *27*, 604–609. [[CrossRef](#)]
30. Frisch, M.J.; Trucks, G.W.; Schlegel, H.B.; Scuseria, G.E.; Robb, M.A.; Cheeseman, J.R. *Gaussian 09, Revision D.01*; Gaussian, Inc.: Wallingford, CT, USA, 2013.
31. Jin, Y.; Aobulikasimu, N.; Zhang, Z.G.; Liu, C.B.; Cao, B.X.; Lin, B.; Guan, P.P.; Mu, Y.; Jiang, Y.; Han, L.; et al. Amycolasporins and dibenzoyls from lichen-associated *Amycolatopsis hippodromi* and their antibacterial and antiinflammatory activities. *J. Nat. Prod.* **2020**, *83*, 3545–3553. [[CrossRef](#)]
32. Ding, N.; Jiang, Y.; Han, L.; Chen, X.; Ma, J.; Qu, X.; Mu, Y.; Liu, J.; Li, L.; Jiang, C.; et al. Bafilomycins and odoriferous sesquiterpenoids from *Streptomyces albolongus* isolated from *Elephas maximus* feces. *J. Nat. Prod.* **2016**, *79*, 799–805. [[CrossRef](#)]

## Article

# Cyclic Peptides from the Soft Coral-Derived Fungus *Aspergillus sclerotiorum* SCSIO 41031

Jieyi Long <sup>1,2</sup>, Yaqi Chen <sup>3</sup>, Weihao Chen <sup>1,2</sup>, Junfeng Wang <sup>1</sup>, Xuefeng Zhou <sup>1</sup>, Bin Yang <sup>1,\*</sup> and Yonghong Liu <sup>1,2,\*</sup>

<sup>1</sup> CAS Key Laboratory of Tropical Marine Bio-Resources and Ecology, Guangdong Key Laboratory of Marine Materia Medica, South China Sea Institute of Oceanology, Chinese Academy of Sciences, Guangzhou 510301, China; longjieyi17@mailsucas.ac.cn (J.L.); chenweihao17@mailsucas.ac.cn (W.C.); wangjunfeng@scsio.ac.cn (J.W.); xfzhou@scsio.ac.cn (X.Z.)

<sup>2</sup> College of Earth and Planetary Sciences, University of Chinese Academy of Sciences, Beijing 100049, China

<sup>3</sup> State Key Laboratory of Chemical Oncogenomics, Key Laboratory of Chemical Genomics, Peking University Shenzhen Graduate School, Shenzhen 518055, China; chenyaq0316@pku.edu.cn

\* Correspondence: yangbin@scsio.ac.cn (B.Y.); yonghongliu@scsio.ac.cn (Y.L.)

**Abstract:** Three novel cyclic hexapeptides, sclerotides C–E (1–3), and a new lipodepsipeptide, scopularide I (4), together with a known cyclic hexapeptide sclerotide A (5), were isolated from fermented rice cultures of a soft coral-derived fungus: *Aspergillus sclerotiorum* SCSIO 41031. The structures of the new peptides were determined by 1D and 2D NMR spectroscopic analysis, Marfey's method, ESIMS/MS analysis, and single crystal X-ray diffraction analysis. Scopularide I (4) exhibited acetylcholinesterase inhibitory activity with an IC<sub>50</sub> value of 15.6 μM, and weak cytotoxicity against the human nasopharyngeal carcinoma cell line HONE-EBV with IC<sub>50</sub> value of 10.1 μM.

**Keywords:** sclerotides; lipodepsipeptide; *Aspergillus sclerotiorum*; nasopharyngeal carcinoma; AChE inhibitory

**Citation:** Long, J.; Chen, Y.; Chen, W.; Wang, J.; Zhou, X.; Yang, B.; Liu, Y. Cyclic Peptides from the Soft Coral-Derived Fungus *Aspergillus sclerotiorum* SCSIO 41031. *Mar. Drugs* **2021**, *19*, 701. <https://doi.org/10.3390/md19120701>

Academic Editor: Claudiu T. Supuran

Received: 24 November 2021

Accepted: 7 December 2021

Published: 10 December 2021

**Publisher's Note:** MDPI stays neutral with regard to jurisdictional claims in published maps and institutional affiliations.

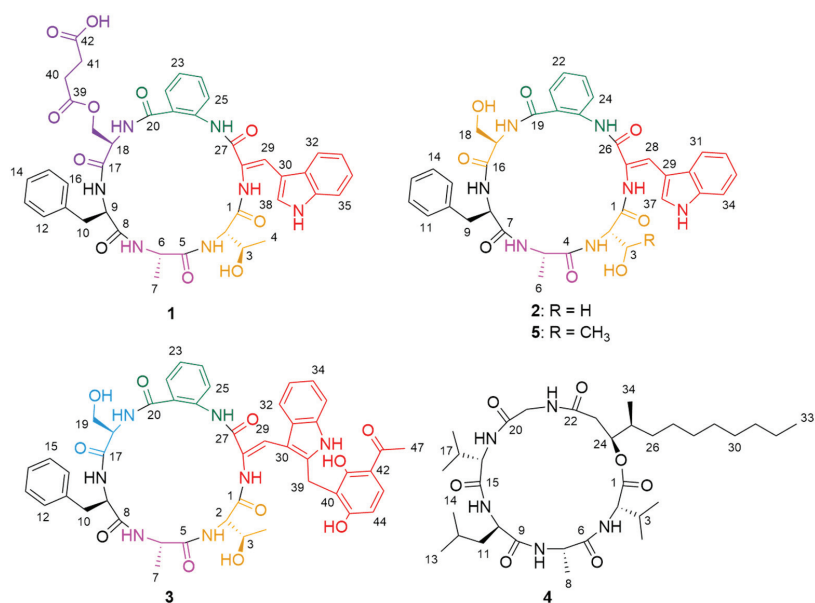


**Copyright:** © 2021 by the authors. Licensee MDPI, Basel, Switzerland. This article is an open access article distributed under the terms and conditions of the Creative Commons Attribution (CC BY) license (<https://creativecommons.org/licenses/by/4.0/>).

## 1. Introduction

Marine microorganisms are generally considered to be a significant new chemical resource of secondary metabolites [1,2]. These organisms thrive in the hostile and competitive oceanic environment and produce a variety of chemically diverse and biologically active compounds [3–5], which have attracted great attention in biomedical research [6,7]. As a class of important metabolites from marine microorganisms, cyclic peptides generally possess a scarce molecular skeleton. Representatives include lucentamycins [8] and marthiapeptide A [9] from marine actinomycetes, sclerotiotides A–K [10], JBIR-15 [11], maribasins [12] and sclerotides A and B [13] from marine fungi. Of these representatives, sclerotides present a unique hexapeptide containing both anthranilic acid and dehydroamino acid residues, which are rarely reported in nature.

In our ongoing studies discovering structurally novel and bioactive natural hybrid peptides from soft coral-derived fungi [14], three novel cyclic hexapeptides, sclerotides C–E (1–3) and a new lipodepsipeptide scopularide I (4), along with a known cyclic hexapeptide, sclerotide A (5) [13], were obtained from *Aspergillus sclerotiorum* SCSIO 41031 (Figure 1). Herein we report the isolation, structure elucidation, and biological activities of these new cyclic peptides.



**Figure 1.** Structures of compounds 1–5.

## 2. Results

### 2.1. Structure Elucidate

Sclerotide C (**1**) was isolated as a yellow crystal. The HRESIMS spectrum showed an ion peak at  $m/z$  810.3062  $[M + H]^+$ , corresponding to the molecular formula  $C_{41}H_{43}N_7O_{11}$ , which required 24 degrees of unsaturation. Analysis of NMR spectra revealed six exchangeable amide NH protons ( $\delta_H$  7.33, 8.43, 8.74, 8.79, 8.98, 10.89) and six correlated carbonyls ( $\delta_C$  163.5, 168.8, 169.3, 170.3, 171.5, 172.1, 172.6), indicating **1** was a hexapeptide. A careful analysis of the NMR data (Table 1), including HSQC, COSY, and HMBC, indicated that sclerotide C (**1**) possessed similar primary structure to sclerotide A (**5**), with the difference of four additional carbons. With respect to sclerotide A, two additional methylene groups ( $\delta_{H/C}$  2.45/28.6, C-40;  $\delta_{H/C}$  2.45/28.6, C-41) and two carbonyls ( $\delta_C$  172.1, C-39;  $\delta_C$  173.4, C-42) were easily detected from the 1D NMR and HSQC data. Moreover, the connection between C-19 and C-39 was inferred by HMBC correlations from H-19 to C-39. The downfield shifts exhibited by the Ser-NH proton ( $\delta_H$  8.98 in **1** vs. 8.62 in **5**), H-18 ( $\delta_H$  4.51 in **1** vs. 4.23 in **5**), H-19 ( $\delta_H$  4.26 and 4.31 in **1** vs. 3.70 in **5**), and C-19 ( $\delta_C$  63.0 in **1** vs. 60.9 in **5**), were all compatible with the presence of the butanedioic acid serine ester (BASE) residue in **1**. The above results revealed that compound **1** was constructed with six amino acid residues, including new esterified serine derivatives (BASE) and five known amino acids, anthranilic acid (AA), dehydrotryptophan ( $\Delta$ -Trp), Thr, Ala, and Phe. The connectivity between the residues of **1** was established by the key HMBC correlations (Figure 2) from NH ( $\delta_H$  8.79) of  $\Delta$ -Trp to C-1 ( $\delta_C$  170.3) of Thr, NH ( $\delta_H$  7.33) of Thr to C-5 ( $\delta_C$  172.6) of Ala, NH ( $\delta_H$  8.74) of Ala to C-8 ( $\delta_C$  171.5) of Phe, NH ( $\delta_H$  8.43) of Phe to C-17 ( $\delta_C$  168.8) of BASE, NH ( $\delta_H$  8.98) of BASE to C-20 ( $\delta_C$  169.3) of AA, and NH ( $\delta_H$  10.89) of AA to C-27 ( $\delta_C$  163.5) of  $\Delta$ -Trp. Thus, the constitution of **1** was assigned as *cyclo* (Thr-Ala-Phe-BASE-AA- $\Delta$ -Trp). The downfield chemical shift of H-29 ( $\delta_H$  7.96) implied *Z*-configuration of  $\Delta^{28,29}$  in **1**, as detailed in previous research [13].

Table 1. <sup>1</sup>H and <sup>13</sup>C NMR data for 1 and 2 (700, 175 MHz, DMSO-*d*<sub>6</sub>, TMS, δ ppm).

| Sclerotide C (1) |                |                          | Sclerotide D (2) |                |                           |                      |
|------------------|----------------|--------------------------|------------------|----------------|---------------------------|----------------------|
| Position         | δ <sub>C</sub> | δ <sub>H</sub> (J in Hz) | Position         | δ <sub>C</sub> | δ <sub>H</sub> (J in Hz)  |                      |
| Thr              | 1              | 170.3                    | Ser              | 1              | 169.7                     |                      |
|                  | 2              | 59.0                     |                  | 2              | 56.8                      | 4.55, td (7.2, 4.2)  |
|                  | 3              | 65.5                     |                  | 3              | 60.7                      | 4.04, dd (11.2, 8.7) |
|                  | 4              | 20.8                     |                  |                |                           | 3.96, dd (11.3, 4.3) |
| Ala              | NH             | 7.33, d (8.4)            | Ala              | NH             | 7.13, d (8.1)             |                      |
|                  | 5              | 172.6                    |                  | 4              | 172.5                     |                      |
|                  | 6              | 49.6                     |                  | 5              | 49.2                      | 4.25, m              |
| Phe              | 7              | 16.7                     | 6                | 16.3           | 1.25, d (7.3)             |                      |
|                  | NH             | 8.74, d (6.1)            | NH               |                | 8.62, d (6.5)             |                      |
|                  | 8              | 171.5                    | Phe              | 7              | 171.8                     |                      |
| 9                | 54.4           | 8                        |                  | 54.5           | 4.53, "q" like (7.6)      |                      |
| 10               | 35.6           | 9                        |                  | 35.1           | 2.93, dd (14.0, 7.3)      |                      |
| BASE             |                | 2.93, dd (14.1, 7.1)     |                  |                | 2.88, dd (14.0, 7.9)      |                      |
|                  | 11             | 137.6                    | 10               | 137.5          |                           |                      |
|                  | 12             | 129.0                    | 11               | 129.0          | 7.20, d (7.2)             |                      |
|                  | 13             | 128.1                    | 12               | 128.1          | 7.23, m                   |                      |
|                  | 14             | 126.3                    | 13               | 126.2          | 7.17, m                   |                      |
|                  | 15             | 128.1                    | 14               | 128.1          | 7.23, m                   |                      |
|                  | 16             | 129.0                    | 15               | 129.0          | 7.20, d (7.2)             |                      |
|                  | NH             |                          | NH               |                | 8.26, d (7.0)             |                      |
|                  | 17             | 168.8                    | Ser              | 16             | 170.8                     |                      |
|                  | 18             | 54.4                     |                  | 17             | 59.2                      | 4.18, q (5.8)        |
|                  | 19             | 63.0                     |                  | 18             | 60.8                      | 3.70, d (5.7)        |
| AA               |                | 4.51, td (7.2, 4.2)      |                  |                | 8.65, d (5.5)             |                      |
|                  |                | 4.26, dd (11.3, 7.9)     |                  |                |                           |                      |
|                  |                | 4.31, m                  |                  |                |                           |                      |
|                  | 39             | 172.1                    | NH               |                |                           |                      |
|                  | 40             | 28.6                     |                  |                |                           |                      |
| Δ-Trp            | 41             | 28.6                     |                  |                |                           |                      |
|                  | 42             | 173.4                    |                  |                |                           |                      |
|                  | NH             |                          |                  |                |                           |                      |
|                  | 20             | 169.3                    | AA               | 19             | 169.5                     |                      |
|                  | 21             | 122.0                    |                  | 20             | 119.6                     |                      |
|                  | 22             | 129.2                    |                  | 21             | 129.1                     | 7.96, dd (8.1, 1.1)  |
|                  | 23             | 122.7                    |                  | 22             | 122.2                     | 7.20, m              |
| 24               | 132.2          | 23                       |                  | 132.6          | 7.59, ddd (8.4, 6.6, 1.0) |                      |
| 25               | 121.0          | 24                       |                  | 119.6          | 8.79, d (8.3)             |                      |
| 26               | 138.6          | 25                       |                  | 139.7          |                           |                      |
| NH               |                |                          |                  | 11.75, s       |                           |                      |
| 27               | 163.5          | Δ-Trp                    | 26               | 163.4          |                           |                      |
| 28               | 122.2          |                          | 27               | 121.8          |                           |                      |
| 29               | 125.9          |                          | 28               | 126.3          | 7.97, s                   |                      |
| 30               | 108.6          |                          | 29               | 108.7          |                           |                      |
| 31               | 127.4          |                          | 30               | 127.4          |                           |                      |
| 32               | 117.7          |                          | 31               | 117.7          | 7.76, d (7.7)             |                      |
| 33               | 120.4          |                          | 32               | 120.4          | 7.16, m                   |                      |
| 34               | 122.0          |                          | 33               | 122.2          | 7.20, m                   |                      |
| 35               | 112.0          |                          | 34               | 111.9          | 7.42, d (7.9)             |                      |
| 36               | 135.5          |                          | 35               | 135.5          |                           |                      |
| 37-NH            |                |                          |                  |                | 11.97, d (2.0)            |                      |
| 38               | 128.7          | 36-NH                    | 37               | 128.7          | 8.03, d (2.8)             |                      |
| NH               |                |                          | NH               |                | 8.82, s                   |                      |

<sup>a</sup> Ovl: overlapped or multiplet with other signals.

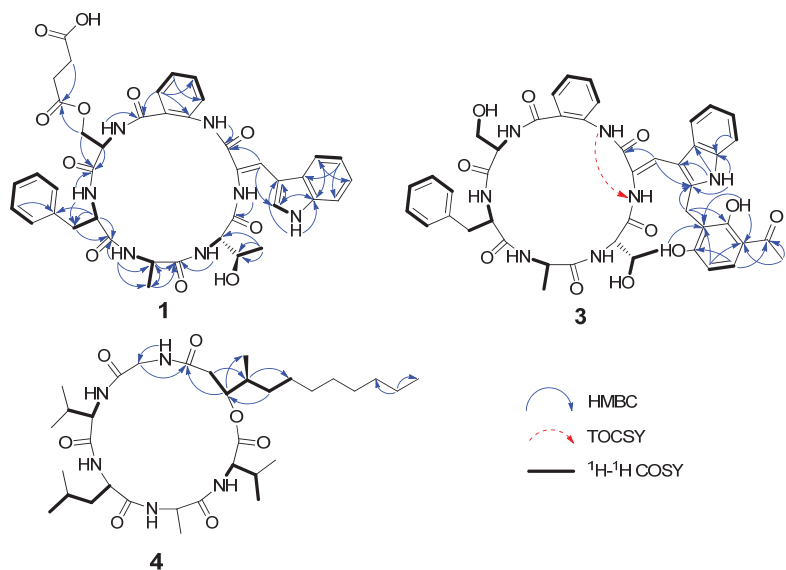


Figure 2. Key HMBC,  $^1\text{H}-^1\text{H}$  COSY, and TOCSY correlations for 1, 3 and 4.

Compound 1 was crystallized in a MeOH/H<sub>2</sub>O (10:1) mixture. The planar structure of 1 was further confirmed by X-ray diffraction analysis with Flack parameter 0.04(13) (Figure 3), and the unambiguous assignments of the absolute configuration as L-Thr, L-Ala, D-Phe, and D-Ser derivatives (BASE) were established. Thus, the structure of compound 1 was determined as *cyclo* (L-Thr-L-Ala-D-Phe-D-BASE-AA-Z- $\Delta$ -Trp).

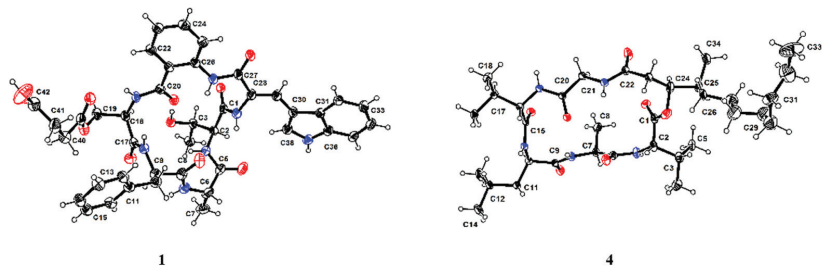


Figure 3. ORTEP drawing of compounds 1 and 4.

The molecular formula of sclerotide D (2) was determined as C<sub>36</sub>H<sub>37</sub>N<sub>7</sub>O<sub>8</sub> based on HRESIMS data ( $m/z$  696.2772 [M + H]<sup>+</sup>). Comparison of its NMR data with those of 5 indicated that 2 and 5 possessed the same carbon framework. The difference between 2 and 5 was that the threonine residue of 5 was replaced by a serine residue in the same position, which was in agreement with the 14 mass units difference. These were further confirmed by the  $^1\text{H}-^1\text{H}$  COSY correlations (H-2/H-3) and the HMBC correlations (from H-3 to C-1 and C-2). Furthermore, the ECD spectra (Figure 4) of 2 were similar to those of 1 and 5. The absolute configurations of the amino acid residues were identified as L-Ser, L-Ala, D-Phe, and D-Ser, respectively, by Marfey's method and HPLC analysis (Supplementary Figure S44). Thus, the structure of 2 was finally established to be *cyclo* (L-Ser-L-Ala-D-Phe-D-Ser-AA-Z- $\Delta$ -Trp).

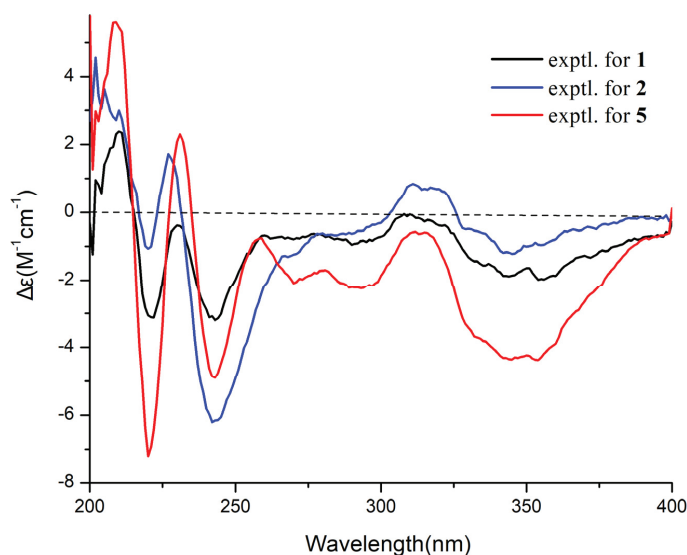


Figure 4. Experimental ECD spectra of compounds 1, 2, and 5.

Sclerotide E (**3**) was isolated as a yellow, amorphous powder and had a molecular formula of  $C_{46}H_{47}N_7O_{11}$  deduced from HRESIMS data ( $m/z$  874.3401  $[M + H]^+$ ), which required 27 degrees of unsaturation. The  $^1H$  and  $^{13}C$  NMR data of **3** (Table 2) showed similarity to those of **1**, **2**, and **5**, and the obvious differences between **3** and **5** was the additional presence of one methylene ( $\delta_{H/C}$  4.05/19.8,  $CH_2$ -39), six olefins (two oxygenated) ( $\delta_C$  110.9, C-40; 162.4, C-41; 111.5, C-42; 162.8, C-45,  $\delta_{H/C}$  7.75/131.9, CH-43; 6.53/107.5, CH-44), and a ketone carbonyl carbon ( $\delta_C$  203.3, C-46), which suggested the presence of a tetra-substituted acetophenone group. The suggestion was proved by the  $^1H$ - $^1H$  COSY correlation between H-43 ( $\delta_H$  7.75) and H-44 ( $\delta_H$  6.53), together with the HMBC correlations (Figure 2) from H-39 to C-40, C-45, and C-41, from H-43 to C-45 and C-46, H-44 to C-40 and C-42, from  $CH_3$ -47 to C-42 and C-46. The missing signal at  $\delta_H$  8.03 for  $\Delta$ -Trp and the HMBC correlations of H-39 to C-38 revealed that the additional unit was attached to  $\Delta$ -Trp at C-38. The suggested sequence was further confirmed by the ESIMS/MS spectrum of **3** (Figure 5). Consequently, the unusual amino acid residue was identified as 2-(3-acetyl-2,6-dihydroxyphenyl)- $N$ - $\Delta$ -acetyltryptamine (ADPAT). The downfield chemical shift of H-29 ( $\delta_H$  7.87) implied  $Z$ -configuration of  $\Delta^{28,29}$  in **3** referred to **1**.

The connectivity between the residues of **3** was also established by the key HMBC correlations illustrated in Figure 2 and the ESIMS/MS spectrum (Figure 5). These results revealed that compound **3** consisted of *cyclo* (Thr-Ala-Phe-Ser-AA-ADPAT). Marfey's method was employed to determine the absolute configurations of **3**, which were assigned as L-Thr, L-Ala, D-Phe, and D-Ser. Thus, the structure of **3** was established as *cyclo* [L-Thr-L-Ala-D-Phe-D-Ser-AA- $Z$ -ADPAT].

Compound **4** was isolated as a colorless crystal, and HRESIMS data ( $m/z$  652.4669  $[M + H]^+$ ) supported a molecular formula of  $C_{34}H_{61}N_5O_7$ , accounting for 7 degrees of unsaturation. The  $^1H$  and  $^{13}C$  NMR data (Table 2) showed typical peptide characteristic signals: five amide NH protons ( $\delta_H$  8.65, 8.07, 8.00, 7.90, 7.42) and six ester/amide-type carbonyls ( $\delta_C$  169.1-171.9), revealing that the structure of **4** was similar to that of scopularide D [15]. Careful comparisons of the 1D and 2D NMR data between **4** and scopularide D showed that overall they were similar, but there was a slight difference which was the additional presence of one high-field methylene and the absence of a methyl attached at the long-chain fatty acid, which was in agreement with the 14 mass units difference. These were further confirmed by the  $^1H$ - $^1H$  COSY correlations (H-23/H-24/H-25/H-26/H-27)



and the HMBC correlation (from H-25 to C-27). The complete structure for **4**, including absolute configurations, was confirmed by single crystal X-ray analysis (CCDC 1816072) using Cu K $\alpha$  radiation with Flack parameter of 0.05(12), which allowed the assignments of amino acid residues as L-Val, L-Ala, D-Leu, and L-Val, and gave the configurations for (2*S*,25*S*)-24-hydroxyl-25-methylauric acid (HMLA) lipid residue (Figure 5).

## 2.2. Bioassays

The isolated compounds (**1–5**) were evaluated for the antimicrobial, anti-inflammatory, cytotoxic, and enzyme inhibitory activities *in vitro*. Compounds **1–5** did not exhibit any growth inhibition when tested against methicillin-resistant bacteria *Staphylococcus aureus*, *Staphylococcus aureus*, *Escherichia coli*, *Enterococcus faecalis*, *Pseudomonas aeruginosa*, and *Vibrio alginolyticus* or fungus *Curvularia australiensis*, *Colletotrichum acutatum*, *Fusarium oxysporum*, *Colletotrichum asianum*, and *Pyricularia oryza* in microbroth dilution assays. Likewise, **1–5** showed no inhibitory activities against lipopolysaccharide-induced nitric oxide (NO) in RAW 264.7 cells at the concentration of 10.0  $\mu$ M. In addition, the cytotoxicity against nine cancer cell lines (HL-60, K562, MOLT-4, ACHN, 786-O, OS-RC-2, THP-1, HONE1, and HONE1-EBV) were also tested. Only **4** exhibited cytotoxic toward human nasopharyngeal carcinoma (NPC) cell lines (HONE1 and HONE1-EBV) with IC<sub>50</sub> values of 13.0 and 10.1  $\mu$ M, respectively. Moreover, **4** showed moderate inhibition against acetylcholinesterase, with an IC<sub>50</sub> value of 15.6  $\mu$ M.

## 2.3. Molecular Docking

In order to gain an insight into the molecular interactions between compounds **1–5** and AChE, the crystal structure of the torpedo californica acetylcholinesterase enzyme (PDB ID: 2CMF) [16] was used as the receptor, and it was subjected to an *in silico* molecular docking analysis with **1–5**, using the induced-fit module in the Schrödinger software suite. As a result, compound **4** fit comfortably into the binding pocket for alkylene-linked tacrine dimers with similar binding positions. In the 2D binding model (Figure 6B), the alkyl chain of **4** formed hydrophobic interaction with the active-site residues TRP84, ASP72, TRY70, and TRP279, and the NH of Gly formed a hydrogen bond with the active site residue TYR334. Compounds **1–3** and **5** were not beneficial for binding to AChE.

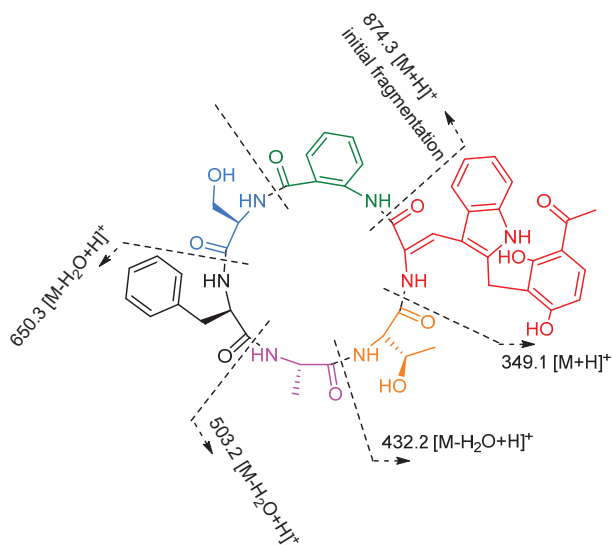
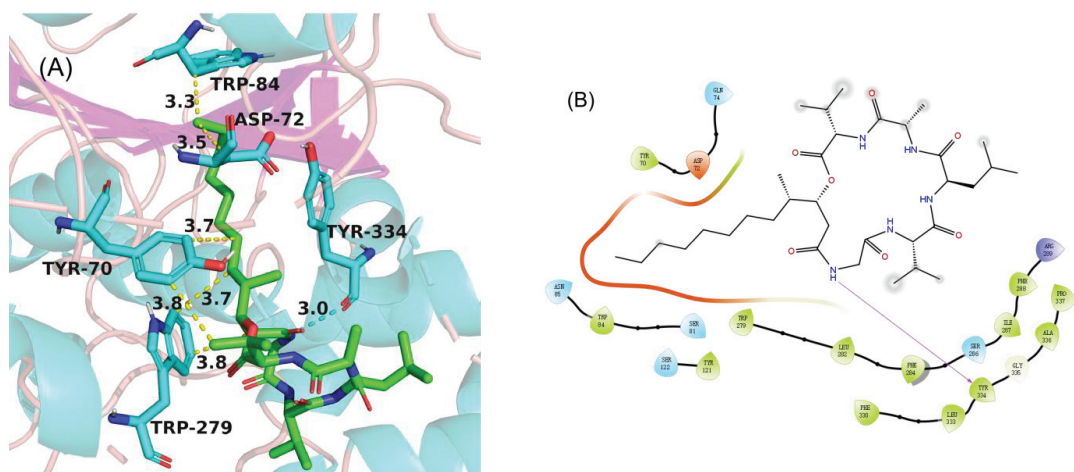


Figure 5. (+)-HRESIMS/MS fragments of compound **3**.

**Table 2.**  $^1\text{H}$  and  $^{13}\text{C}$  NMR data for **3** and **4** (700, 175 MHz, DMSO- $d_6$ , TMS,  $\delta$  ppm).

| Position | Sclerotides E (3)   |                               | Position | Scopularide I (4)   |                               |
|----------|---------------------|-------------------------------|----------|---------------------|-------------------------------|
|          | $\delta_{\text{C}}$ | $\delta_{\text{H}}$ (J in Hz) |          | $\delta_{\text{C}}$ | $\delta_{\text{H}}$ (J in Hz) |
| Thr      | 1                   | 169.6                         | Val      | 1                   | 170.8                         |
|          | 2                   | 57.5                          |          | 2                   | 57.7                          |
|          | 3                   | 66.2                          |          | 3                   | 29.6                          |
|          | 4                   | 19.9                          |          | 4                   | 18.8                          |
| 3-OH     |                     |                               | 5        | 17.4                |                               |
|          | NH                  | 7.32, d (8.6)                 | NH       |                     | 7.42, br s                    |
| Ala      | 5                   | 171.9                         | Ala      | 6                   | 171.9                         |
|          | 6                   | 48.1                          |          | 7                   | 48.0                          |
|          | 7                   | 16.6                          |          | 8                   | 17.5                          |
| NH       |                     | 8.39, d (8.5)                 | NH       |                     | 8.00, d (7.8)                 |
|          | 8                   | 170.3                         | Leu      | 9                   | 171.4                         |
| 9        | 54.4                | 10                            |          | 51.9                |                               |
| Phe      | 10                  | 35.6                          | 11       | 38.7                |                               |
|          |                     |                               | 12       | 24.2                |                               |
|          | 11                  | 137.6                         | 13       | 23.0                |                               |
|          | 12                  | 129.1                         | 14       | 21.0                |                               |
|          | 13                  | 128.1                         | NH       |                     | 8.65, d (6.6)                 |
|          | 14                  | 126.3                         | Val      | 15                  | 171.7                         |
|          | 15                  | 128.1                         |          | 16                  | 58.8                          |
|          | 16                  | 129.1                         | 17       | 29.5                |                               |
| NH       |                     | 8.31, d (7.8)                 | 18       | 19.0                |                               |
|          | 17                  | 170.8                         | 19       | 19.1                |                               |
| Ser      | 18                  | 57.8                          | NH       |                     | 8.07, d (7.6)                 |
|          | 19                  | 61.1                          | Gly      | 20                  | 169.1                         |
| 19-OH    |                     | 21                            |          | 42.0                |                               |
| NH       |                     | 8.31, d (7.8)                 | NH       |                     | 4.08, ovl <sup>a</sup>        |
|          | 20                  | 168.1                         |          |                     | 3.45, dd (17.1, 3.7)          |
| AA       | 21                  | 123.1                         | HMLA     | 22                  | 169.9                         |
|          | 22                  | 129.7                         |          | 23                  | 37.5                          |
|          | 23                  | 129.2                         |          |                     | 2.53, dd (15.6, 9.6)          |
|          | 24                  | 132.1                         | 24       | 75.5                | 2.24, m                       |
|          | 25                  | 122.2                         | 25       | 36.3                | 4.91, ddd (9.4, 3.8, 2.3)     |
|          | 26                  | 138.3                         | 26       | 31.6                | 1.67, m                       |
| NH       |                     | 10.86, br s                   |          |                     | 1.36, m                       |
|          | 27                  | 164.2                         | 27       | 26.6                | 1.02, m                       |
| ADPAT    | 28                  | 123.2                         |          |                     | 1.28, ovl <sup>a</sup>        |
|          | 29                  | 126.2                         | 28       | 28.7                | 1.18, ovl <sup>a</sup>        |
|          | 30                  | 106.8                         | 29       | 28.9                | 1.23, ovl <sup>a</sup>        |
|          | 31                  | 125.3                         | 30       | 29.3                | 1.23, ovl <sup>a</sup>        |
|          | 32                  | 120.7                         | 31       | 31.3                | 1.23, ovl <sup>a</sup>        |
|          | 33                  | 120.9                         | 32       | 22.1                | 1.27, ovl <sup>a</sup>        |
|          | 34                  | 120.1                         | 33       | 14.0                | 0.85, s                       |
|          | 35                  | 112.6                         | 34       | 14.8                | 0.83, ovl <sup>a</sup>        |
|          | 36                  | 135.9                         |          |                     |                               |
| 37-NH    |                     | 10.78, s                      |          |                     |                               |
|          | 38                  | 141.6                         |          |                     |                               |
| NH       |                     | 9.32, s                       |          |                     |                               |
|          | 39                  | 19.8                          |          |                     | 4.05, d (14.7)                |
|          | 40                  | 110.9                         |          |                     |                               |
|          | 41                  | 162.4                         |          |                     |                               |
| 41-OH    |                     | 13.27, s                      |          |                     |                               |
|          | 42                  | 111.5                         |          |                     |                               |
|          | 43                  | 131.9                         |          |                     | 7.75, d (8.9)                 |
|          | 44                  | 107.5                         |          |                     | 6.53, d (8.8)                 |
|          | 45                  | 162.8                         |          |                     |                               |
| 45-OH    |                     | 11.01, s                      |          |                     |                               |
|          | 46                  | 203.3                         |          |                     |                               |
|          | 47                  | 26.1                          |          |                     | 2.54, s                       |

<sup>a</sup> Ovl: overlapped or multiplet with other signals.



**Figure 6.** Molecular docking of **4** with AChE (PDB code: 2CMF). The binding sites of the molecule **4** (A) with the AChE protein. The 2D interaction details of the predicted binding mode of **4** (B) with the AChE.

### 3. Materials and Methods General Experimental Procedures

#### 3.1. General Experimental Procedures

Optical rotations were measured with an MCP 500 automatic polarimeter (Anton, Graz, Austria) with MeOH as a solvent. UVECD spectra were measured with a Chirascan circular dichroism spectrometer (Applied Photophysics Ltd., Surrey, UK).  $^1\text{H}$ ,  $^{13}\text{C}$  NMR, DEPT, and 2D-NMR spectra were recorded on the Avance-700 spectrometer (Bruker, Billerica, MA, USA). HRESIMS and ESIMS spectra data were recorded on a MaXis quadrupole-time-of-flight mass spectrometer and an amaZon SL ion trap mass spectrometer (Bruker), respectively. X-ray diffraction intensity data were collected on a CrysAlis PRO CCD area detector diffractometer with graphite-monochromated Cu  $K\alpha$  radiation ( $\lambda = 1.54178 \text{ \AA}$ ). Thin layer chromatography (TLC) and column chromatography (CC) were performed on plates precoated with silica gel GF 254 (10–40  $\mu\text{m}$ ) and over silica gel (200–300 mesh) (Qingdao Marine Chemical Factory, Qingdao, China). All solvents used were of analytical grade (Tianjin Fuyu Chemical and Industry Factory, Tianjin, China). HPLC was carried out on a Hitachi Primaide with a YMC ODS Series column (YMC-Pack ODS-A, YMC Co. Ltd., 250  $\times$  10 mm i.d., S-5  $\mu\text{m}$ , 12.0 nm, 2.0 mL/min, Kyoto, Japan) or an Angilent 1260 S3 HPLC apparatus using an ODS column (YMC-pack ODS-A, 250  $\times$  4.6 mm, S-5  $\mu\text{m}$ , 12 nm, 1.0 mL/min).

#### 3.2. Fungal Material

The fungal strain SCSIO 41031 was isolated from a soft coral, which was collected in Beihai, Guangxi Province, China. The isolate was stored on Müller Hinton broth (MB) agar (malt extract 15.0 g, artificial sea salt 10.0 g, and agar 15.0 g) slants at 4.0  $^\circ\text{C}$ , and a voucher specimen was deposited in the CAS Key Laboratory of Tropical Marine Bio-Resources and Ecology, South China Sea Institute of Oceanology, Chinese Academy of Sciences, Guangzhou, China. Based on sequencing of the ITS region, the fungal strain SCSIO 41031 was identified as *Aspergillus sclerotiorum* with 100% similarity (GenBank no. KC478520.1).

#### 3.3. Fermentation and Extraction

The strain *Aspergillus sclerotiorum* SCSIO 41031 was cultured on MB-agar plates at 25.0  $^\circ\text{C}$  for 7 days. The seed medium (malt extract 15.0 g and artificial sea salt 10.0 g in 1.0 L tap  $\text{H}_2\text{O}$ , pH 7.4–7.8) was inoculated with strain SCSIO 41031 and incubated at 25.0  $^\circ\text{C}$  for 3 days on a rotating shaker (180 rpm). Then, a large-scale fermentation of fungal

SCSIO 41031 was incubated for 30 days at room temperature in 1 L × 30 conical flasks with solid rice medium (each flask contained 200.0 g rice, 2.5 g artificial sea salt, and 250 mL H<sub>2</sub>O). The whole fermented cultures were overlaid and extracted with EtOAc three times to afford a brown extract (109 g).

### 3.4. Isolation and Purification

The EtOAc extract was subjected to vacuum liquid chromatography (VLC) on a silica gel column eluting with a CH<sub>2</sub>Cl<sub>2</sub> and MeOH mixed solvent system in a step gradient (100:0–0:1, V/V) to gain nine fractions according to TLC profiles. Fr.7 (7.3 g) was divided into four parts (Frs.7-1–7-4) by ODS silica gel chromatography eluting with MeOH/H<sub>2</sub>O (10–100%). Fr.7-3 (1.3 g) was further purified by HPLC (42% CH<sub>3</sub>CN/H<sub>2</sub>O, 2 mL/min) to yield **5** (320.3 mg, *t<sub>R</sub>* 18.5 min) and a subfraction (Fr.7-3-1, 12.2 mg, *t<sub>R</sub>* 23.1 min). Moreover, Fr.7-3-1 was further purified by semipreparative HPLC (59% MeOH/H<sub>2</sub>O, 2 mL/min) to offer **1** (3.6 mg, *t<sub>R</sub>* 26.2min) and **3** (2.1 mg, *t<sub>R</sub>* 28.4 min), respectively. Fr.8 was separated by semipreparative HPLC (90% MeOH/H<sub>2</sub>O, 2 mL/min) to offer **4** (200.1 mg, *t<sub>R</sub>* 13.5 min). Additionally, Fr.9 was divided into three subfractions (Frs. 9-1–9-3) by ODS silica gel eluting with MeOH/H<sub>2</sub>O (10–100%). Fr.9-3 was separated by semipreparative HPLC (40% CH<sub>3</sub>CN/H<sub>2</sub>O, 2 mL/min) to offer **2** (7.4 mg, *t<sub>R</sub>* 19.2 min).

Sclerotide C (**1**): yellow crystal;  $[\alpha]_D^{25} - 88$  (*c* 0.06, MeOH); UV (MeOH)  $\lambda_{\max}$  (log  $\epsilon$ ) 200 (4.71), 220 (4.45), 275 (3.99), 358 (4.18) nm; IR (film)  $\nu_{\max}$  3325, 2926, 2358, 2331, 1683, 1541, 1456, 1207, 1141, 802, 725, 669 cm<sup>-1</sup>; <sup>1</sup>H and <sup>13</sup>C NMR data, Table 1; HRESIMS *m/z* 810.3062 [M + H]<sup>+</sup> (calculated for C<sub>41</sub>H<sub>44</sub>N<sub>7</sub>O<sub>11</sub>, 810.3093), 832.2875 [M + Na]<sup>+</sup> (calculated for C<sub>41</sub>H<sub>43</sub>N<sub>7</sub>NaO<sub>11</sub>, 832.2913).

Sclerotide D (**2**): yellow solid;  $[\alpha]_D^{25} - 13$  (*c* 0.09, MeOH); UV (MeOH)  $\lambda_{\max}$  (log  $\epsilon$ ) 200 (4.68), 220 (4.50), 275 (3.97), 358 (4.20) nm; IR (film)  $\nu_{\max}$  3298, 2929, 2854, 2362, 2330, 1681, 1521, 1456, 1236, 1203, 1139, 1049, 748, 669 cm<sup>-1</sup>; <sup>1</sup>H and <sup>13</sup>C NMR data, Table 1; HRESIMS *m/z* 696.2772 [M + H]<sup>+</sup> (calculated for C<sub>36</sub>H<sub>38</sub>N<sub>7</sub>O<sub>8</sub>, 696.2776), 718.2591 [M + Na]<sup>+</sup> (calculated for C<sub>36</sub>H<sub>37</sub>N<sub>7</sub>NaO<sub>8</sub>, 718.2596).

Sclerotide E (**3**): yellow solid;  $[\alpha]_D^{25} - 15$  (*c* 0.08, MeOH); UV (MeOH)  $\lambda_{\max}$  (log  $\epsilon$ ) 200 (4.85), 280 (4.21), 352 (4.02) nm; IR (film)  $\nu_{\max}$  3313, 2924, 2852, 2362, 2330, 1670, 1541, 1436, 1280, 1203, 1138, 842, 802, 723 cm<sup>-1</sup>; <sup>1</sup>H and <sup>13</sup>C NMR data, Table 1; HRESIMS *m/z* 874.3401 [M + H]<sup>+</sup> (calculated for C<sub>46</sub>H<sub>48</sub>N<sub>7</sub>O<sub>11</sub>, 874.3406), 896.3210 [M + Na]<sup>+</sup> (calculated for C<sub>46</sub>H<sub>47</sub>N<sub>7</sub>NaO<sub>11</sub>, 896.3226).

Scopularide I (**4**): colorless needle crystal;  $[\alpha]_D^{25} - 8$  (*c* 0.13, MeOH); UV (MeOH)  $\lambda_{\max}$  (log  $\epsilon$ ) 200 (4.22) nm; IR (film)  $\nu_{\max}$  3311, 2956, 2924, 2358, 2324, 1635, 1521, 1192, 1026 cm<sup>-1</sup>; <sup>1</sup>H and <sup>13</sup>C NMR data, Table 1; HRESIMS *m/z* 652.4669 [M + H]<sup>+</sup> (calculated for C<sub>34</sub>H<sub>62</sub>N<sub>5</sub>O<sub>7</sub>, 652.4644), 674.4478 [M + Na]<sup>+</sup> (calculated for C<sub>34</sub>H<sub>61</sub>N<sub>5</sub>NaO<sub>7</sub>, 674.4463).

### 3.5. Marfey's Analysis of **2** and **3**

Compounds **2** (1.0 mg) and **3** (1.0 mg) were hydrolyzed in 1.0 mL of 6 N HCl and heated at 110 °C for 18 h. The solution was evaporated to dryness after cooled, and the hydrolysate was added: 100.0  $\mu$ L of H<sub>2</sub>O, 100.0  $\mu$ L of 1% FDAA (Marfey's reagent, 1-fluoro-2,4-dinitrophenyl-5-L-alanine amide) in acetone, and 20.0  $\mu$ L of 1 M NaHCO<sub>3</sub>. The mixture was kept at 40 °C for 1 h, and the reaction was quenched by adding 20.0  $\mu$ L of 1 M HCl [14]. The dried mixture was dissolved in MeOH and HPLC analyses performed on an Agilent Technologies 1200 Infinity system (column: YMC-Pack ODS-A column, 250 × 4.6 mm I.D., S-5  $\mu$ m, 12 nm; mobile phase: CH<sub>3</sub>CN/H<sub>2</sub>O (0.03% TFA in H<sub>2</sub>O), linear gradients started with 15% CH<sub>3</sub>CN and finished with 60% CH<sub>3</sub>CN in 40 min; 100% CH<sub>3</sub>CN from 40 min to 50 min, flow rate was 1 mL/min, with UV detection at an absorbance of 340 nm). The standard amino acids were derived with FDAA in the same process. The retention times of these standard amino acids were as follows: FDAA, *t<sub>R</sub>* 22.8 min, d/l-Phe, *t<sub>R</sub>* 33.5/30.8 min; d/l-Ala, *t<sub>R</sub>* 22.8/20.9 min; d/l-Thr, *t<sub>R</sub>* 20.1/17.1 min; d/l-Ser, *t<sub>R</sub>* 16.4/16.1 min. The retention times of amino acids in hydrolysate of **2** were 16.1, 16.4, 20.9, and 33.5 min, respectively. Comparison of these retention times confirmed that the amino

acids in **2** were L-Ser, D-Ser, L-Ala, D-Phe (Supplementary Figure S44). The retention times of amino acids in hydrolysate of **3** were 16.4, 17.1, 20.9, and 33.5 min, respectively, which were confirmed as <sub>d</sub>-Ser, <sub>l</sub>-Thr, <sub>l</sub>-Ala, and <sub>d</sub>-Phe (Supplementary Figure S44).

### 3.6. X-ray Crystallographic Analysis

Sclerotide C (**1**) was crystallized from the mixture of methanol and H<sub>2</sub>O (10:1) to give yellow crystals. The crystal data was as follows: monoclinic, space group P2<sub>1</sub>2<sub>1</sub>2<sub>1</sub> with  $a = 10.5314(2)\text{\AA}$ ,  $b = 12.7668(3)\text{\AA}$ ,  $c = 30.3494(8)\text{\AA}$ ,  $V = 4080.55(16)\text{\AA}^3$ ,  $Z = 4$ ,  $D_{\text{calc}} = 1.318\text{g/cm}^3$ ,  $R = 0.0706$ ,  $wR_2 = 0.1661$ . The absolute configuration was determined on the basis of a Flack parameter of 0.04(13). Crystallographic data (excluding structure factors) for structure **1** in this paper were deposited with the Cambridge Crystallographic Data Centre as supplementary publication number CCDC 2026267. Copies of the data can be obtained, free of charge, on application to CCDC, 12 Union Road, Cambridge CB21EZ, UK (fax: +44-(0)-1223-336033 or e-mail: deposit@ccdc.cam.ac.uk).

Scopularide I (**4**) was crystallized from the mixture of methanol and H<sub>2</sub>O (10:1) to give colorless crystals. The crystal data was as follows: monoclinic, space group C2 with  $a = 25.7630(3)\text{\AA}$ ,  $b = 9.31313(9)\text{\AA}$ ,  $c = 17.4956(2)\text{\AA}$ ,  $V = 3998.24(8)\text{\AA}^3$ ,  $Z = 4$ ,  $D_{\text{calc}} = 1.143\text{g/cm}^3$ ,  $R = 0.0920$ ,  $wR_2 = 0.2540$ . The absolute configuration was determined on the basis of a Flack parameter of -0.03(12). Crystallographic data (excluding structure factors) for structure **4** in this paper were deposited with the Cambridge Crystallographic Data Centre as supplementary publication number CCDC 2026265. Copies of the data can be obtained, free of charge, on application to CCDC, 12 Union Road, Cambridge CB21EZ, UK (fax: +44-(0)-1223-336033 or e-mail: deposit@ccdc.cam.ac.uk).

### 3.7. Bioactivity Assay

The AChE inhibition activity was measured based on the modified Ellman's method [17]. Tacrine was used as positive drug. The inhibition rates of AChE were calculated using Origin 8.0 software.

Antibacterial activities against methicillin-resistant *Staphylococcus aureus*, *Staphylococcus aureus*, *Escherichia coli*, *Enterococcus faecalis*, *Pseudomonas aeruginosa*, and *Vibrio alginolyticus* and antifungal activities against *Curvularia australiensis*, *Colletotrichum acutatum*, *Fusarium oxysporum*, *Colletotrichum asianum*, and *Pyricularia oryza* were tested using a modification of the broth microdilution method [18].

The obtained compounds (**4** and **5**) were evaluated for their cytotoxic activities against three cancer cell lines, THP-1, HONE1, and HONE1-EBV. The THP-1, HONE1, and HONE1-EBV cell lines were obtained from Sun Yat-sen University Cancer Center. The cytotoxic activity was determined by the CCK-8 (Dojindo) method [19]. Briefly, THP-1, HONE1, and HONE1-EBV cells were cultured in DMEM media supplemented with 10% phosphate-buffered saline (FBS), respectively. The cells were seeded at a density of 400 to 800 cells/well in 384-well plates and then incubated with the compounds in a gradient concentration (50.0, 10.0, 2.0, 0.4, and 0.08  $\mu\text{M}$ ) or with a solvent control for 72 h, followed by the addition of CCK-8 reagent. The OD value of each well was measured at 450 nm using a SpectraMax M5 Microplate Reader (Molecular Devices). Sorafenib functioned as the positive control. Dose–response curves were plotted to determine IC<sub>50</sub> based upon the average values of three parallel experiments using Prism 5.0.

### 3.8. Molecular Docking Analysis

The molecular docking analysis with the structure of AChE (PDB code: 2CMF) [16] was conducted according to the procedure described previously [20].

## 4. Conclusions

In summary, the chemical investigation of the soft coral-derived fungus *Aspergillus sclerotiorum* SCSIO 41031 has led to four new compounds—three cyclic hexapeptides (**1–3**), and a new lipodepsipeptide (**4**). Their structures, including their absolute configurations,

were determined by comprehensive spectroscopic methods and X-ray crystallographic analysis together with Marfey's method. The folding of the peptide backbone remains to be studied. The in vitro bioassay and in silico docking study revealed compound **4** to be a potential anti-nasopharyngeal cancer drug and a moderate AChE inhibitor.

**Supplementary Materials:** The following are available online at <https://www.mdpi.com/article/10.3390/md19120701/s1>, Figures S1–S43: <sup>1</sup>H NMR, <sup>13</sup>C NMR, DEPT, HSQC, HMBC, COSY, ROESY, TOESY, UV, HRESIMS, and CD spectra of compounds 1–4. Figure S44–S45: HPLC analysis of FDAA derivatives of standard amino acids and FDAA derivatives of compound 2 and 3. Figure S46 and Table S1: data of compound 4 against AChE. Figure S47 and Table S2: data of compound 4 against HONE1-EBV and HONE1.

**Author Contributions:** Conceptualization, B.Y. and Y.L.; formal analysis, Y.C., W.C. and J.W.; investigation, J.L.; methodology, J.W. and X.Z.; project administration, W.C. and J.L.; resources, B.Y.; writing—original draft, J.L.; writing—review and editing, B.Y. and Y.L. All authors have read and agreed to the published version of the manuscript.

**Funding:** This study was supported by grants from the Finance Science and Technology Project of Hainan Province (ZDKJ202018), Key Special Project for Introduced Talents Team of Southern Marine Science and Engineering Guangdong Laboratory (Guangzhou) (GML2019ZD0406), National Natural Science Foundation of China (21977102, 81973235), Institution of South China Sea Ecology and Environmental Engineering, Chinese Academy of Sciences (No. ISEE2021PY05), Special Funds for Promoting Economic Development (Marine Economic Development) of Guangdong Province (No. [2020]039), and Guangdong Local Innovation Team Program (2019BT02Y262).

**Informed Consent Statement:** Not applicable.

**Acknowledgments:** We would like to thank Seik Weng Ng for the X-ray crystallographic data analysis and we are grateful to the analytical facilities (Z. Xiao, A. Sun, Y. Zhang et al.) at SCSIO.

**Conflicts of Interest:** The authors declare no conflict of interest. The funders had no role in the design of the study; in the collection, analysis, or interpretation of data; in the writing of the manuscript; or in the decision to publish the results.

## References

- Carroll, A.R.; Copp, B.R.; Davis, R.A.; Keyzers, R.A.; Prinsep, M.R. Marine Natural Products. *Nat. Prod. Rep.* **2021**, *38*, 362–413. [[CrossRef](#)] [[PubMed](#)]
- Darcel, L.; Das, S.; Bonnard, I.; Banaigs, B.; Inguibert, N. Thirtieth Anniversary of the Discovery of Laxaphycins. Intriguing Peptides Keeping a Part of Their Mystery. *Mar. Drugs* **2021**, *19*, 473. [[CrossRef](#)] [[PubMed](#)]
- Li, J.; Tao, H.; Lei, X.; Zhang, H.; Zhou, X.; Liu, Y.; Li, Y.; Yang, B. Arthriniosteroids A–D, Four New Steroids from the Soft Coral-Derived Fungus *Simplicillium lanosoniveum* SCSIO41212. *Steroids* **2021**, *171*, 108831. [[CrossRef](#)] [[PubMed](#)]
- Niu, S.; Liu, D.; Shao, Z.; Huang, J.; Fan, A.; Lin, W. Chlorinated Metabolites with Antibacterial Activities from a Deep-Sea-Derived *Spiromastix* Fungus. *RSC Adv.* **2021**, *11*, 29661–29667. [[CrossRef](#)]
- Zhang, H.; Lei, X.-X.; Shao, S.; Zhou, X.; Li, Y.; Yang, B. Azaphilones and Meroterpenoids from the Soft Coral-Derived Fungus *Penicillium glabrum* Glmu003. *Chem. Biodivers.* **2021**, *18*, e2100663. [[CrossRef](#)] [[PubMed](#)]
- Dayanidhi, D.L.; Thomas, B.C.; Osterberg, J.S.; Vuong, M.; Vargas, G.; Kwartler, S.K.; Schmaltz, E.; Dunphy-Daly, M.M.; Schultz, T.F.; Rittschof, D.; et al. Exploring the Diversity of the Marine Environment for New Anti-Cancer Compounds. *Front. Mar. Sci.* **2021**, *7*, 4766. [[CrossRef](#)]
- Esposito, R.; Ruocco, N.; Viel, T.; Federico, S.; Zupo, V.; Costantini, M. Sponges and Their Symbionts as a Source of Valuable Compounds in Cosmeceutical Field. *Mar. Drugs* **2021**, *19*, 444. [[CrossRef](#)] [[PubMed](#)]
- Cho, J.Y.; Williams, P.G.; Kwon, H.C.; Jensen, P.R.; Fenical, W. Lucentamycins A–D, Cytotoxic Peptides from the Marine-Derived Actinomycete *Nocardioopsis lucentensis*. *J. Nat. Prod.* **2007**, *70*, 1321–1328. [[CrossRef](#)] [[PubMed](#)]
- Zhou, X.; Huang, H.; Chen, Y.; Tan, J.; Song, Y.; Zou, J.; Tian, X.; Hua, Y.; Ju, J.; Marthiapeptide, A. An Anti-Infective and Cytotoxic Polythiazole Cyclopeptide from a 60 L Scale Fermentation of the Deep Sea-Derived *Marinactinospora Thermotolerans* SCSIO 00652. *J. Nat. Prod.* **2012**, *75*, 2251–2255. [[CrossRef](#)] [[PubMed](#)]
- Zheng, J.; Xu, Z.; Wang, Y.; Hong, K.; Liu, P.; Zhu, W. Cyclic Tripeptides from the Halotolerant Fungus *Aspergillus sclerotiorum* PT06–1. *J. Nat. Prod.* **2010**, *73*, 1133–1137. [[CrossRef](#)] [[PubMed](#)]
- Motohashi, K.; Inaba, S.; Takagi, M.; Shin-Ya, K. JBIR-15, a New Aspochracin Derivative, Isolated from a Sponge-Derived Fungus, *Aspergillus sclerotiorum* Huber Sp080903f04. *Biosci. Biotechnol. Biochem.* **2009**, *73*, 1898–1900. [[CrossRef](#)] [[PubMed](#)]
- Yao, F.-H.; Liang, X.; Cheng, X.; Ling, J.; Dong, J.-D.; Qi, S.-H. Antifungal peptides from the marine gorgonian-associated fungus *Aspergillus* sp. SCSIO41501. *Phytochemistry* **2021**, *192*, 112967. [[CrossRef](#)] [[PubMed](#)]

13. Zheng, J.; Zhu, H.; Hong, K.; Wang, Y.; Liu, P.; Wang, X.; Peng, X.; Zhu, W. Novel cyclic hexapeptides from marine-derived fungus, *Aspergillus sclerotiorum* PT06–1. *Org. Lett.* **2009**, *11*, 5262–5265. [[CrossRef](#)] [[PubMed](#)]
14. Dai, Y.; Lin, Y.; Pang, X.; Luo, X.; Salendra, L.; Wang, J.; Zhou, X.; Lu, Y.; Yang, B.; Liu, Y. Peptides from the soft coral-associated fungus *Simplicillium* sp. SCSIO41209. *Phytochemistry* **2018**, *154*, 56–62. [[CrossRef](#)] [[PubMed](#)]
15. Elbanna, A.H.; Khalil, Z.G.; Bernhardt, P.V.; Capon, R.J. Scopularides revisited: Molecular networking guided exploration of lipopeptides in Australian marine fish gastrointestinal tract-derived fungi. *Mar. Drugs* **2019**, *17*, 475. [[CrossRef](#)] [[PubMed](#)]
16. Rydberg, E.H.; Brumshtein, B.; Greenblatt, H.M.; Wong, D.M.; Shaya, D.; Williams, L.D.; Carlier, P.R.; Pang, Y.-P.; Silman, I.; Sussman, J.L. Complexes of alkylene-linked tacrine dimers with torpedo californica acetylcholinesterase: Binding of bis5-tacrine produces a dramatic rearrangement in the active-site gorge. *J. Med. Chem.* **2006**, *49*, 5491–5500. [[CrossRef](#)] [[PubMed](#)]
17. Ellman, G.L.; Courtney, K.D.; Andres, V.; Feather-Stone, R.M. A new and rapid colorimetric determination of acetylcholinesterase activity. *Biochem. Pharmacol.* **1961**, *7*, 88–95. [[CrossRef](#)]
18. Soliseptide, A. A cyclic hexapeptide possessing piperazic acid groups from *Streptomyces solisilvae* HNM30702. *Org. Lett.* **2018**, *20*, 1371–1374.
19. Sang, B.H.; Shin, Y.J.; Hyon, J.Y.; Wee, W.R. Cytotoxicity of Voriconazole on Cultured Human Corneal Endothelial Cells. *Antimicrob. Agents. Chemother.* **2011**, *55*, 4519–4523.
20. Dai, Y.; Li, K.; She, J.; Zeng, Y.; Wang, H.; Liao, S.; Lin, X.; Yang, B.; Wang, J.; Tao, H.; et al. Lipopeptide Epimers and a Phthalide Glycerol Ether with AChE Inhibitory Activities from the Marine-Derived Fungus *Cochliobolus lunatus* SCSIO41401. *Mar. Drugs* **2020**, *18*, 547. [[CrossRef](#)] [[PubMed](#)]

Article

# Protective Effect of Flavonoids from a Deep-Sea-Derived *Arthrinium* sp. against ox-LDL-Induced Oxidative Injury through Activating the AKT/Nrf2/HO-1 Pathway in Vascular Endothelial Cells

Jia-Rong Hou <sup>†</sup>, Yan-Hong Wang <sup>†</sup>, Ying-Nan Zhong, Tong-Tong Che, Yang Hu, Jie Bao <sup>\*</sup> and Ning Meng <sup>\*</sup>

Department of Biotechnology, School of Biological Science and Technology, University of Jinan, Jinan 250022, China; jiaronghou@163.com (J.-R.H.); wangyanhong1203@163.com (Y.-H.W.); zhongyingnan98@163.com (Y.-N.Z.); mls\_chett@ujn.edu.cn (T.-T.C.); huyang922@163.com (Y.H.)

<sup>\*</sup> Correspondence: bio\_bao@ujn.edu.cn (J.B.); mls\_mengn@ujn.edu.cn (N.M.)

<sup>†</sup> These authors contributed equally to this work.

**Abstract:** Oxidized low-density lipoprotein (ox-LDL)-induced oxidative injury in vascular endothelial cells is crucial for the progression of cardiovascular diseases, including atherosclerosis. Several flavonoids have been shown cardiovascular protective effects. Recently, our research group confirmed that the novel flavonoids isolated from the deep-sea-derived fungus *Arthrinium* sp., 2,3,4,6,8-pentahydroxy-1-methylxanthone (compound 1) and arthone C (compound 2) effectively scavenged ROS in vitro. In this study, we further investigated whether these compounds could protect against ox-LDL-induced oxidative injury in endothelial cells and the underlying mechanisms. Our results showed that compounds 1 and 2 inhibited ox-LDL-induced apoptosis and adhesion factors expression in human umbilical vein vascular endothelial cells (HUVECs). Mechanistic studies showed that these compounds significantly inhibited the ROS level increase and the NF- $\kappa$ B nuclear translocation induced by ox-LDL. Moreover, compounds 1 and 2 activated the Nrf2 to transfer into nuclei and increased the expression of its downstream antioxidant gene HO-1 by inducing the phosphorylation of AKT in HUVECs. Importantly, the AKT inhibitor MK-2206 2HCl or knockdown of Nrf2 by RNA interference attenuated the inhibition effects of these compounds on ox-LDL-induced apoptosis in HUVECs. Meanwhile, knockdown of Nrf2 abolished the effects of the compounds on ox-LDL-induced ROS level increase and the translocation of NF- $\kappa$ B to nuclei. Collectively, the data showed that compounds 1 and 2 protected endothelial cells against ox-LDL-induced oxidative stress through activating the AKT/Nrf2/HO-1 pathway. Our study provides new strategies for the design of lead compounds for related cardiovascular diseases treatment.

**Keywords:** vascular endothelial cell; flavonoid; oxidized low-density lipoprotein; Nrf2; apoptosis

**Citation:** Hou, J.-R.; Wang, Y.-H.; Zhong, Y.-N.; Che, T.-T.; Hu, Y.; Bao, J.; Meng, N. Protective Effect of Flavonoids from a Deep-Sea-Derived *Arthrinium* sp. against ox-LDL-Induced Oxidative Injury through Activating the AKT/Nrf2/HO-1 Pathway in Vascular Endothelial Cells. *Mar. Drugs* **2021**, *19*, 712. <https://doi.org/10.3390/md19120712>

Academic Editors: Yonghong Liu and Xuefeng Zhou

Received: 2 December 2021

Accepted: 13 December 2021

Published: 18 December 2021

**Publisher's Note:** MDPI stays neutral with regard to jurisdictional claims in published maps and institutional affiliations.



**Copyright:** © 2021 by the authors. Licensee MDPI, Basel, Switzerland. This article is an open access article distributed under the terms and conditions of the Creative Commons Attribution (CC BY) license (<https://creativecommons.org/licenses/by/4.0/>).

## 1. Introduction

Atherosclerotic (AS) is a multifactorial inflammatory disease characterized by lipid deposition in the vessel wall, which seriously threatens human health [1,2]. Studies have shown that vascular endothelial injury is a key event in the occurrence and development of atherosclerosis [3,4]. Endothelial injury is characterized by vascular endothelial cell death, accompanied by a vascular inflammatory reaction, vascular wall morphological changes, and eventually triggers cardiovascular events [5]. Moreover, some factors are related to vascular endothelial cell injury, and oxidative stress is an important reason for atherosclerosis. It is reported that reactive oxygen species (ROS) can cause vascular endothelial cell dysfunction and damage to vascular wall cells [6]. As a main risk factor of atherosclerosis, hypercholesterolemia triggers the deposition of oxidized low-density lipoprotein (ox-LDL) under the intima in vascular walls [7,8]. Moreover, ox-LDL induces reactive oxygen species (ROS) overproduction, adhesion molecule release, and endothelial



cell injury [9–11]. Therefore, protecting endothelial cells against ox-LDL-induced oxidative stress may be an effective strategy for the prevention and treatment of atherosclerosis. Drugs that preserve endothelial cells' function during oxidative stress are urgently needed.

Marine fungi are a great natural source of lead compounds in drug discovery as they are rich in a great diversity of chemical molecules with unique structural features that exhibit various types of biological activities [12–15]. Flavonoids are well-known antioxidants and have been used as dietary supplements [16]. Recently, our research group isolated flavonoids from the deep-sea-derived fungus *Arthrinium* sp. UJNMF0008 and confirmed that 2,3,4,6,8-pentahydroxy-1-methylxanthone (compound 1) and arthone C (compound 2) had antioxidant activity in vitro [17]. Compounds 1 and 2 belong to xanthone compounds of flavonoids, and compound 2 was a new compound reported firstly by our research group [17]. It is well known that the xanthone compounds, mainly isolated from plants, microorganisms, lichens, and synthesis, have extensive biological activities, including antioxidants. For example, Johanis Wairata et al. isolated four xanthone compounds with strong antioxidant activity from *Garcinia forbesii* [18]. Tran et al. isolated Garcinoxanthone U, garcinone E, and 1,3,6,7-tetrahydroxyxanthone with DPPH scavenging activity from *Garcinia mangostana* [19]. Moreover, recent studies have shown that marine and terrestrial endophytic fungi are also an important mine of xanthone compounds, and more than 90 xanthone compounds have been reported from marine fungi [20]. For example, Wu et al. isolated 12 xanthenes with ABTS scavenging activity from the metabolites of the deep-sea fungus *Aspergillus versicolor*. Importantly, it is reported that synthetic 1,3,5,6-tetrahydroxyxanthone protected endothelial cells from ox-LDL-induced adhesion of monocytes to endothelial cells [21]. Demethylbellidifolin, a major component of *Swertia davidi*, inhibited the adhesion of monocytes to endothelial cells by reducing the levels of tumor necrosis factor- $\alpha$  and endogenous nitric oxide synthase inhibitors [22]. Additionally, mangiferin has been shown to alleviate ox-LDL-induced VEC dysfunction [23]. These researches suggested that xanthone compounds may serve as protective agents for vascular endothelial cells. However, few marine-derived xanthenes have been studied in vascular endothelial cells. In the present study, we further investigated whether compounds 1 and 2 could protect against ox-LDL-induced vascular endothelial cell injury and explored its potential actions on oxidative signaling events.

## 2. Results

### 2.1. The Compounds 1 and 2 Inhibited ox-LDL-Induced HUVEC Apoptosis and Adhesion Factors Expression

Chemical structures of compounds 1 and 2 are shown in Figure 1. To assess the effects of compounds on ox-LDL-induced injury, we pretreated HUVECs with compounds 1 and 2 at different concentrations and stimulated the cells with 50  $\mu\text{g}/\text{mL}$  ox-LDL for 6 h. Then, hoechst33258 staining was performed to detect nuclear DNA condensation and fragmentation, characteristics of apoptosis. We found that in the ox-LDL-treated groups, about 60–80% cells with nuclear condensation and fragmentation, while after the compounds 1 and 2 treatment, the percentage of apoptosis cells significantly decreased to around 20–40%. Results from the TUNEL assay showed that compounds 1 and 2 significantly reduced the number of TUNEL-positive cells (Figure 2A,C). The results of the Hoechst 33258 staining assay and TUNEL staining assay revealed that compounds 1 and 2 have protective effects on ox-LDL-induced HUVEC apoptosis.

To further explore the anti-apoptosis effect of compounds 1 and 2, the expression of apoptosis-related proteins was detected by Western blotting. As presented in Figure 2B, the level of pro-apoptotic protein Bax decreased significantly, while that of anti-apoptotic protein Bcl-2 increased significantly in HUVECs after treatment with compounds 1 and 2. These results confirmed that the compounds 1 and 2 had protective effects on ox-LDL-induced HUVEC apoptosis.

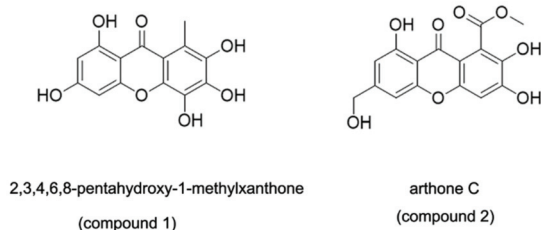


Figure 1. Chemical structures of compounds 1 and 2.

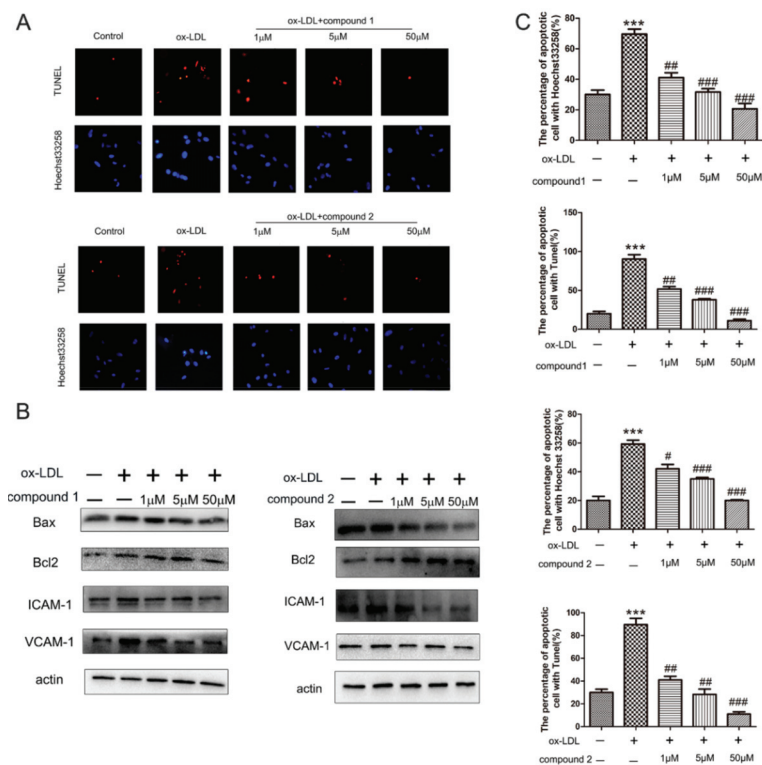
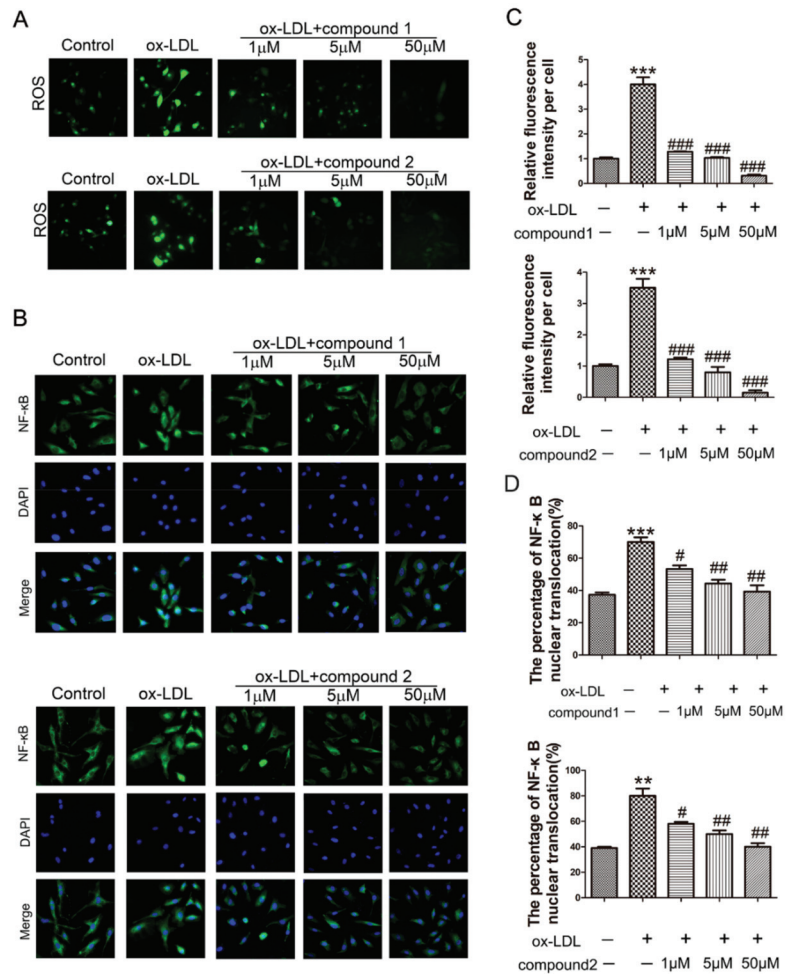


Figure 2. Effects of compounds 1 and 2 on ox-LDL-induced apoptosis and adhesion factors expression in HUVECs. HUVECs were treated with 50 μg/mL ox-LDL, 50 μg/mL ox-LDL and 1–50 μM compound 1 or 2 for 6 h (A) Nuclear fragmentation of cells by Hoechst 33258 and TUNEL staining (10×). (B) Western blot analysis of Bax, Bcl-2, VCAM-1, and ICAM-1 protein levels. (C) Bar chart showing quantification of HUVEC apoptosis percentage according to Hoechst 33258 and TUNEL staining. \*\*\*  $p < 0.001$  vs. Control, #  $p < 0.05$ , ##  $p < 0.01$ , ###  $p < 0.001$  vs. ox-LDL,  $n = 3$ .

Next, we determined whether compounds 1 and 2 could inhibit the expression of endothelial adhesion molecules. The results of Western blot demonstrated that the protein level of VCAM-1 and ICAM-1 decreased after treatment with the compounds 1 and 2, confirming that the compounds 1 and 2 inhibited ox-LDL-induced adhesion molecules expression in VECs (Figure 2B).

## 2.2. The Compounds 1 and 2 Significantly Inhibited the Accumulation of ROS and the Activation of NF- $\kappa$ B in HUVECs

The effect of compounds 1 and 2 on ROS production in HUVECs was determined by using the DCFH-DA probe. Compared with the ox-LDL-treated group, the ROS levels were significantly reduced after the addition of compounds 1 and 2 (Figure 3A,C).



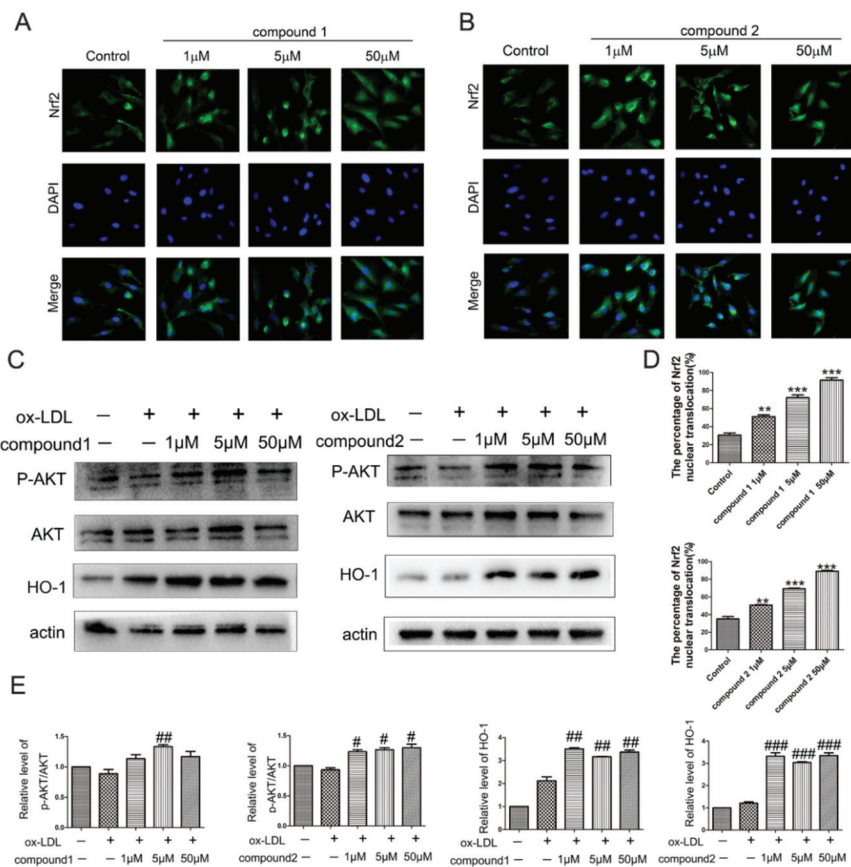
**Figure 3.** Compounds 1 and 2 inhibited the increased ROS level and NF- $\kappa$ B nuclear translocation induced by ox-LDL. HUVECs were treated with 50  $\mu$ g/mL ox-LDL, 50  $\mu$ g/mL ox-LDL and 1–50  $\mu$ M compound 1 or 2 for 6 h. (A) The intracellular ROS level was examined by DCFH probe. (B) Fluorescent micrographs of NF- $\kappa$ B location in HUVECs. (C) The quantification of intracellular ROS level. (D) Bars showed the percentage of NF- $\kappa$ B nuclear translocation. \*\*  $p < 0.01$ , \*\*\*  $p < 0.001$  vs. control, #  $p < 0.05$ , ##  $p < 0.01$ , ###  $p < 0.001$  vs. ox-LDL,  $n = 3$ .

It is reported that the accumulation of ROS could promote NF- $\kappa$ B translocation into the nuclei and subsequently induce the expression of ICAM-1 and VCAM-1 [24]. Therefore, immunofluorescence staining was used to explore whether compounds 1 and 2 affect the location of NF- $\kappa$ B in ox-LDL-activated VECs. The results showed that NF- $\kappa$ B translocated

into the nuclei after the cells were treated with ox-LDL, and this was dramatically inhibited by compounds 1 and 2 (Figure 3B,D).

### 2.3. The Compounds 1 and 2 Activated AKT/Nrf2/HO-1 Antioxidant Pathway

The transcriptional factor nuclear factor-(erythroid-derived 2)-like 2 factor (Nrf2) plays a major role in cellular antioxidant responses. It has been reported that cytoprotective gene heme oxygenase 1 (HO-1) is induced by Nrf2 nuclear translocation [25]. To elucidate the molecular mechanism of the protective effect of compounds 1 and 2 against ox-LDL-induced oxidative damage in HUVECs, we explored whether the compounds affect Nrf2/HO-1 pathway. By immunofluorescence staining, we found that the compounds 1 and 2 activated Nrf2 nuclear translocations in HUVECs (Figure 4A,B,D). Moreover, compared with the ox-LDL control group, the expression of HO-1 was significantly increased after the addition of compound 1 or 2 (Figure 4C,E).

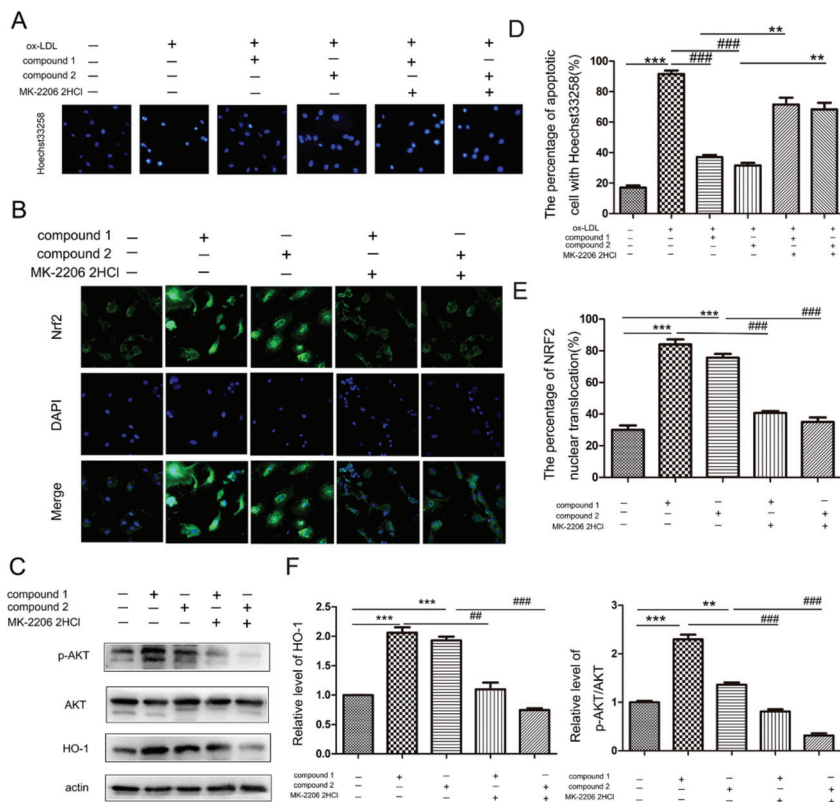


**Figure 4.** Effects of compounds 1 and 2 on AKT/Nrf2/HO-1 signaling pathway in HUVECs. (A,B) HUVECs were treated with 1–50  $\mu$ M compound 1 or 2 for 6 h, fluorescent micrographs of Nrf2 location in HUVECs. (C) HUVECs were treated with 50  $\mu$ g/mL ox-LDL, 50  $\mu$ g/mL ox-LDL and 1–50  $\mu$ M compound 1 or 2 for 6 h. The protein levels of phosphorylation AKT (pAKT) and HO-1 were examined by Western blot analysis. (D) Bars showed the percentage of Nrf2 nuclear translocation in (A,B). (E) Densitometry results of pAKT/AKT and HO-1 protein levels in panel (C). \*\*  $p < 0.01$ , \*\*\*  $p < 0.001$  vs. Control, #  $p < 0.05$ , ##  $p < 0.01$ , ###  $p < 0.001$  vs. ox-LDL,  $n = 3$ .

In addition, it has been reported that AKT is the upstream gene of Nrf2. We further analyzed whether the compounds affect the phosphorylation of AKT. The results of Western blot demonstrated that the compounds 1 and 2 treatment increased the protein levels of pAKT (Figure 4C,E). Therefore, these results suggested that compounds 1 and 2 activated AKT/Nrf2/HO-1 antioxidant pathway.

2.4. Compounds 1 and 2 Protected VECs and Mediated Nrf2 Activation through AKT

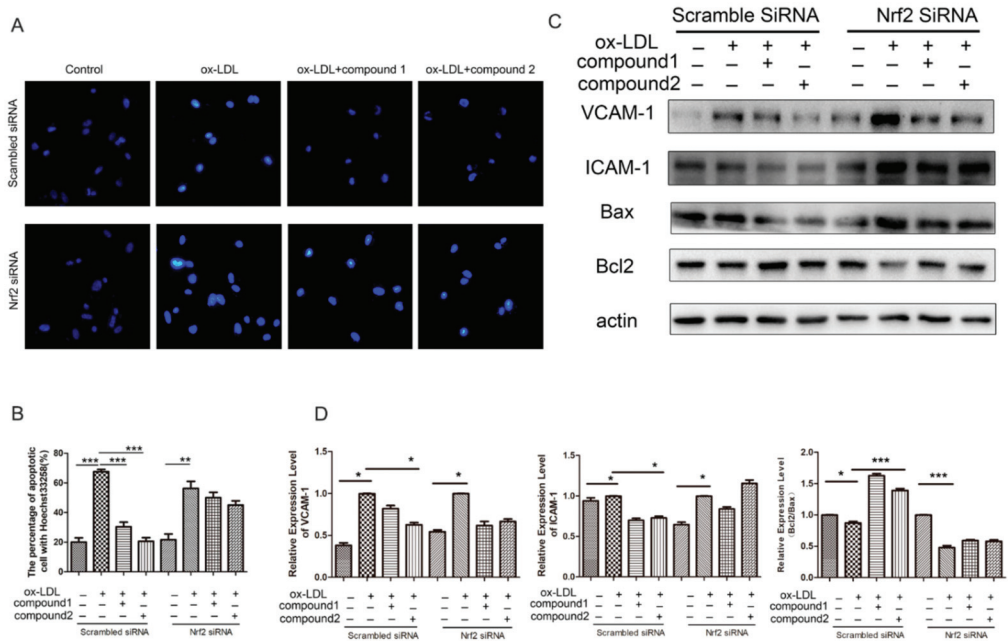
Furthermore, MK-2206 2HCl (a specific inhibitor of AKT) was used to confirm whether the compounds protect VECs and mediate Nrf2 activation through AKT. The results of Hoechst33258 staining showed that MK-2206 2HCl blocked the anti-apoptosis effects of compounds in ox-LDL-stimulated HUVECs (Figure 5A,D). Importantly, compounds 1 and 2 neither activate Nrf2 into nuclei nor increase the HO-1 protein level in the presence of MK-2206 2HCl, suggesting these compounds activated Nrf2/HO-1 through AKT (Figure 5B,C,E,F).



**Figure 5.** Inhibition of AKT abolished the effects of compounds 1 and 2 on ox-LDL-induced apoptosis and Nrf2/HO-1 activation. (A) HUVECs were pretreated with 5 μM MK-2206 2HCl for 1 h and treated with 50 μg/mL ox-LDL, 50 μg/mL ox-LDL and 50 μM compound 1 or 2 for 6 h. Nuclear fragmentation of cells by Hoechst 33258 staining. (B,C) HUVECs were pretreated with 5 μM MK-2206 2HCl for 1 h and treated with 50 μM compound 1 or 2 for 6 h. Fluorescent micrographs of Nrf2 location in HUVECs (B), Western blot analysis of HO-1 protein levels and phosphorylation levels of AKT (pAKT) (C). (D) Bar chart showing quantification of HUVEC apoptosis percentage according to Hoechst 33258 staining. (E) Quantitative analysis of Nrf2 nuclear translocation in panel (B). (F) Densitometry analysis of pAKT/ACT and HO-1 protein levels in panel (C). \*\*  $p < 0.01$ , \*\*\*  $p < 0.001$ , ##  $p < 0.01$ , ###  $p < 0.001$  between the two values,  $n = 3$ .

2.5. Knockdown of Nrf2 Abolished the Inhibition Effects of Compounds on ox-LDL-Induced Apoptosis and Adhesion Factor Expression

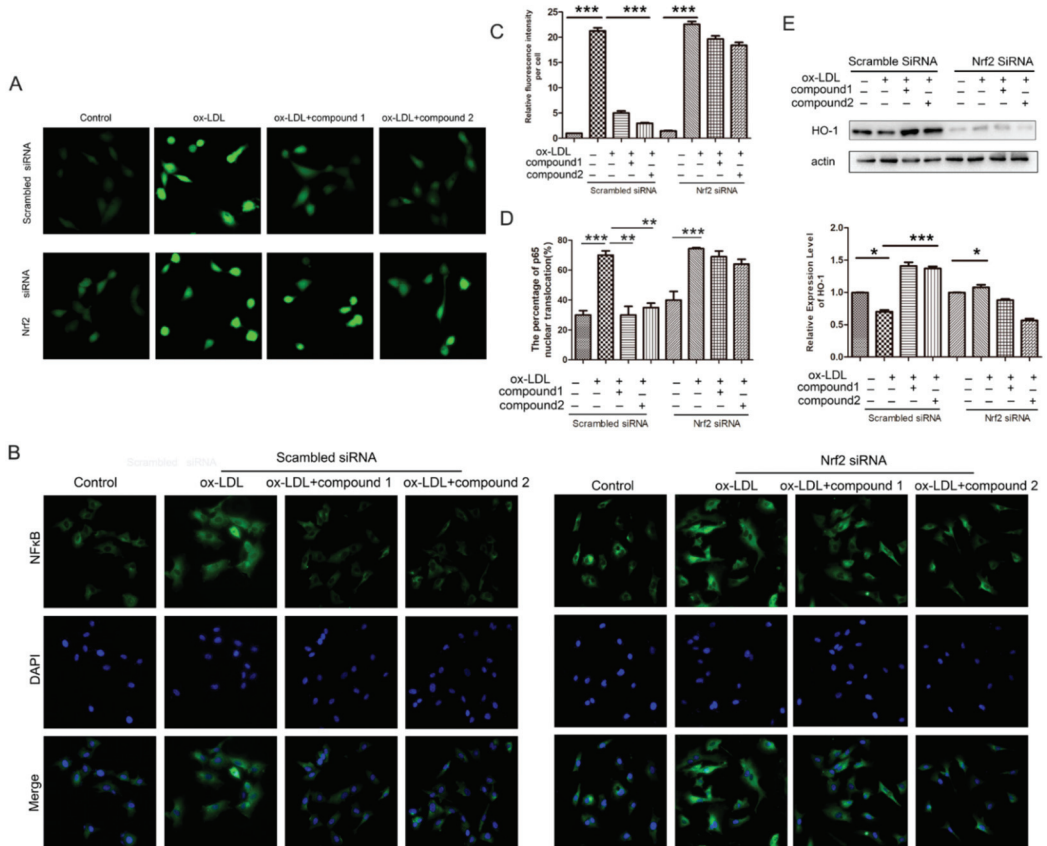
To further determine whether the protection of the compounds on VECs is Nrf2-dependent, we knocked down the Nrf2 expression using RNA interference. In cells treated with nonsilencing (scramble) siRNA, compounds 1 and 2 inhibited ox-LDL-induced VEC apoptosis, whereas, in Nrf2-knockdown cells, the effect of the compounds was suppressed (Figure 6A,B). Western blot analysis revealed that the effects of compounds 1 and 2 on ICAM-1, VCAM-1, BAX, and Bcl2 protein levels were inhibited by knockdown of Nrf2 (Figure 6C,D). Therefore, our results suggested that compounds protected endothelial cells from ox-LDL-induced injury via activating Nrf2 anti-oxidation pathway.



**Figure 6.** Compounds 1 and 2 protected against ox-LDL-induced injury via Nrf2 in HUVECs. HUVECs were treated with 40 nM Nrf2 siRNA or scramble siRNA for 48 h and stimulated with 50 µg/mL ox-LDL, 50 µg/mL ox-LDL, and 50 µM compound 1 or 2 up to 6 h. (A) Nuclear fragmentation of cells by Hoechst 33258 staining (10×). (B) Quantitative analysis of HUVEC apoptosis percentage according to Hoechst 33258 staining. (C) Western blot analysis of Bax, Bcl2, VCAM-1, and ICAM-1 protein levels. (D) Densitometry analysis of VCAM-1, ICAM-1, and Bcl2/Bax protein levels in panel (C). \*  $p < 0.05$ , \*\*  $p < 0.01$ , \*\*\*  $p < 0.001$  between the two values,  $n = 3$ .

2.6. Knockdown of the Nrf2 Suppressed the Effects of the Compounds 1 and 2 on the Increased ROS Level and the NF-κB Nuclear Translocation Induced by ox-LDL in HUVECs

Additionally, we examined the effects of the compounds on ROS level and NF-κB nuclear translocation in which Nrf2 was knocked down. The results showed that compounds 1 and 2 did not inhibit ox-LDL-induced increase in ROS level and NF-κB nuclear translocation when the VECs were knockdown of Nrf2, confirming these compounds inhibited ox-LDL-induced oxidative stress through Nrf2 (Figure 7).



**Figure 7.** Knockdown of Nrf2 suppressed the inhibitory effects of compounds 1 and 2 on the accumulation of ROS and the activation of NF-κB induced by ox-LDL in HUVECs. HUVECs were treated with 40 nM Nrf2 siRNA or scramble siRNA for 48 h and stimulated with 50 μg/mL ox-LDL, 50 μg/mL ox-LDL, and 50 μM compound 1 or 2 up to 6 h. (A) The intracellular ROS level was examined by DCHF probe. (B) Fluorescent micrographs showed the location of NF-κB in HUVECs. (C) Quantitative analysis of intracellular ROS in panel (A). (D) Quantitative analysis of NF-κB nuclear translocation percentage in panel (B). (E) Western blot analysis of HO-1 protein level, bar graph showed the HO-1 protein level compared with β-actin. \*  $p < 0.05$ , \*\*  $p < 0.01$ , \*\*\*  $p < 0.001$ , between the two values,  $n = 3$ .

### 3. Discussion

In this study, we demonstrated that xanthone compounds of flavonoids from deep-sea-derived *Arthrinium* sp. compounds 1 and 2 exhibited protective effects on ox-LDL-stimulated vascular endothelial cells via activating AKT/Nrf2/HO-1 anti-oxidative signal pathway.

Endothelial cell injury is believed to be the initial step in the atherosclerosis process [26]. A series of studies have indicated that ox-LDL, a main risk factor of atherosclerosis, contributes to endothelium injury by inducing endothelial cell oxidative stress [27]. Therefore, inhibition of endothelial cell oxidative injury by chemical small molecules is an effective strategy for the treatment of atherosclerosis. Recently, a series of new flavonoids were isolated from a marine-derived fungus *Arthrinium* sp. by our research group [17]. It is known that flavonoids are potentially involved in cardiovascular prevention, mainly by decreasing oxidative stress [28]. Our previous studies have shown that among these marine-derived flavonoids, compounds 1 and 2 exhibited potent antioxidant properties

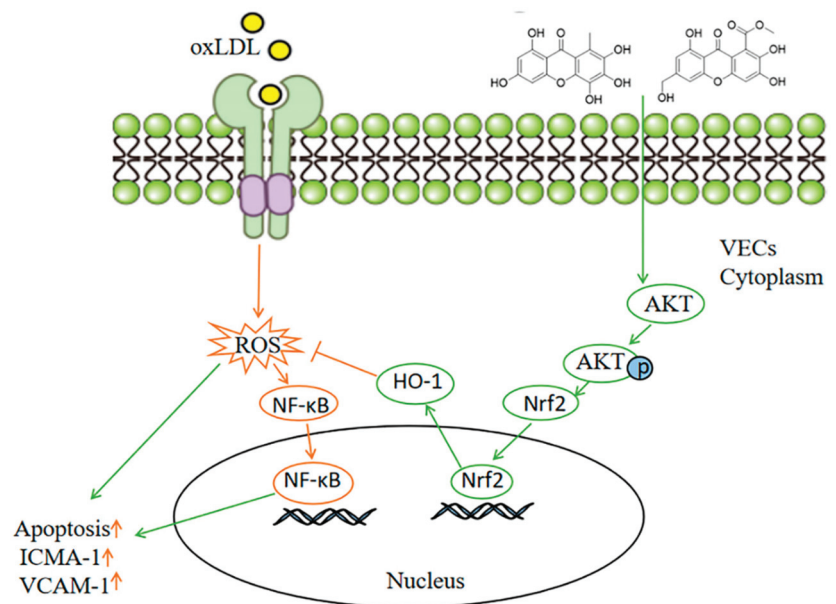
with DPPH and ABTS radical scavenging activities in vitro [17]. Compounds **1** and **2** belong to xanthone compounds of flavonoids. Interestingly, some research has demonstrated that xanthone compounds, such as synthetic 1,3,5,6-tetrahydroxyxanthone, demethylbellidifolin, and mangiferin exhibited protective effects in VECs [22,23,29]. However, marine-derived xanthenes protect vascular endothelial cells from ox-LDL-induced injury toward atherosclerosis are limited. Here, we further explored the effects of compounds **1** and **2** on ox-LDL-stimulated HUVECs. The results revealed that compounds **1** and **2** significantly inhibited ox-LDL-induced apoptosis and the increase in ICMA-1 and VCAM-1 protein levels.

Through the DPPH scavenging activity test of 30 xanthone compounds by Xican Li, it is speculated that the structure of hydroquinone or catechol plays an important role in the antioxidant activity of these compounds, which is consistent with our previous reports that compounds **1** and **2** possess the structure of hydroquinone [30]. Moreover, it is reported that ROS accumulation induced by ox-LDL promotes NF- $\kappa$ B translocation into the nuclei and subsequently induces endothelial cell injury [31]. In this study, our results confirmed that compounds **1** and **2** significantly inhibited the accumulation of ROS and the activation of NF- $\kappa$ B in HUVECs, suggesting that these two compounds may protect endothelial cells through antioxidant pathways.

Nrf2 is an important transcription factor that regulates the cellular oxidative stress response. Nrf2 promotes the transcription of various downstream antioxidant genes, including hemeoxygenase-1 (HO-1) [32]. It has been shown that Nrf2 activators decreased the probability of developing atherosclerotic lesions by decreasing oxidative stress [33]. Moreover, some xanthone compounds exert cell-protective effects by activating Nrf2 [34]. For example, euxanthone activated Nrf2 and protected ox-LDL-induced endothelial cell injury [35]. Mangiferin inhibited doxorubicin-induced VEC apoptosis via the Nrf2/HO-1 signaling pathway [36]. Therefore, we detected whether compounds **1** and **2** protect VECs against ox-LDL-induced oxidative damage by affecting Nrf2/HO-1 pathway and found that these compounds activated Nrf2 to translocate into nuclei and increased HO-1 protein level. Importantly, knockdown of Nrf2 by siRNA inhibited the antioxidant and protective effects of the compounds on the endothelium. These results revealed that compounds **1** and **2** exhibited antioxidant stress and protective effects by activating Nrf2 in VECs. In addition, it has been reported that Nrf2 activation is regulated by AKT, and inhibition of Akt attenuates Nrf2 activation [37,38]. We found that compounds **1** and **2** increased the phosphorylation level of AKT. However, inhibition of AKT activity significantly inhibited Nrf2 activation and the protective effect of the compounds on vascular endothelial cells, indicating these compounds mediated Nrf2 antioxidant pathway through AKT.

In summary, our results revealed two novel flavonoids from deep-sea-derived fungus *Arthrinium* sp., which named compounds **1** and **2** significantly inhibited ox-LDL-induced VEC apoptosis and adhesion factors expression. Mechanism studies further elucidated that the compounds **1** and **2** activated AKT/Nrf2/HO-1 signaling pathways and further inhibited ox-LDL-induced ROS overproduction and NF- $\kappa$ B activation (Figure 8). Therefore, our study provides a possible therapeutic avenue for the treatment of atherosclerosis.





**Figure 8.** Scheme summarizing the mechanism for inhibition effects of compounds 1 and 2 on ox-LDL-induced VEC injury. Ox-LDL induces ROS generation and activates NF- $\kappa$ B nuclear translocation, which leads to VEC apoptosis and adhesion molecule expression. Compounds 1 and 2 activate Nrf2 nuclear translocation by inducing AKT phosphorylation. The nuclear Nrf2 facilitates the expression of HO-1, which inhibits cellular ROS production and NF- $\kappa$ B activation induced by ox-LDL.

#### 4. Materials and Methods

##### 4.1. Reagents

Medium M199 and bovine serum were obtained from Gibco Co. (Carlsbad, CA, USA). Protein was extracted from cells using radio immunoprecipitation assay (RIPA) lysis buffer (Dingguo Changsheng Biotechnology Co., Ltd., Beijing, China). The primary antibodies anti-Bcl-2, anti-Bax, anti-HO-1, anti-ICAM-1, anti-VCAM-1, anti-phospho-AKT, and anti-AKT were acquired from Proteintech Group, Inc. (Chicago, IL, USA). The peroxidase-conjugated secondary antibodies were obtained from Dingguo Changsheng Biotechnology Co., Ltd. (Beijing, China).

##### 4.2. Cell Culture

HUVECs were obtained from ScienCell (San Diego, CA, USA) and cultured on gelatin-coated plastic dishes in M199 medium with 20% (*v/v*) bovine serum and 10 IU/mL fibroblast growth factor 2. HUVECs were maintained at 37 °C under humidified conditions and 5% CO<sub>2</sub>. Morphologic changes of HUVECs were observed by inverted phase-contrast microscopy (ZEISS, Primovert, Germany).

##### 4.3. Immunofluorescence Assay

After treatment, the culture medium was removed by washing with PBS. Then, HUVECs were fixed with 4% paraformaldehyde and blocked with PBS containing 3% goat serum for 20 min at room temperature. After blocking, cells were incubated with p65 or Nrf2 primary antibody (1/100) at 4 °C overnight. After three rinses in 0.1 M PBS, cells were treated with corresponding fluorescence-labeled secondary antibodies (1/200) in a humid chamber at 37 °C for 1 h. After washing with PBS, the immunofluorescence was examined by an inverted fluorescent microscope (Leica, Wiesbaden, Germany).

#### 4.4. Western Blot Analysis

Protein was extracted from HUVECs using radio immunoprecipitation assay (RIPA) lysis buffer (Dingguo Changsheng Biotechnology Co., Ltd., Beijing, China). The protein concentration was determined using BCA Protein Assay kits (Beyotime, Shenzhen, Guangdong, China). Equal amounts of protein lysates (15 µg per lane) underwent 15% SDS-PAGE, and separated proteins were transferred to PVDF membranes (Millipore, Madison, WI, USA). The membranes were blocked at room temperature for 1.5 h in 5% non-fat dry milk diluted with TBST to reduce non-specific binding. The membranes were incubated overnight at 4 °C with primary antibodies. After washing with TBST three times, membranes were incubated with HRP-conjugated secondary antibody (Dingguo Changsheng Biotechnology Co., Ltd., Beijing, China) for 1.5 h at room temperature. Immune complexes were detected by enhanced chemiluminescence (Millipore Corporation, Billerica, MA, USA). Integrated densities of bands were quantified by Image J software.

#### 4.5. TUNEL Staining

TUNEL staining was performed according to the manufacturer's protocol using In Situ Cell Death Detection Kit, TMR red (Roche, Switzerland, France). DAPI staining reagent (Beyotime, China) was used to stain nuclei. Briefly, after all treatments, HUVECs were fixed with 1% buffered formaldehyde for 30 min and subsequently permeabilized with 0.25% Triton X-100 in 0.1% sodium citrate for five minutes. Then, the fixed cells were stained using fluorescein-conjugated TUNEL. The TUNEL-positive cells were observed under a fluorescence microscope (LEICA, Germany). Eight visual fields were selected from each group to calculate the proportion of TUNEL-positive cells.

#### 4.6. Hoechst33258 Staining for Apoptosis

After treatment, HUVECs were washed twice with PBS. Then, HUVECs were stained with 10 mg/mL Hoechst 33258 (Dingguo Changsheng Biotechnology Co., Ltd., DH163) at 37 °C for 15 min and washed with PBS three times. At last, the cells were photographed under a fluorescence microscope (LEICA DMi8, Wiesbaden, Germany). The nuclear condensation and fragmentation of cells were used as indicators of apoptotic cells.

#### 4.7. Intracellular ROS Assay

The levels of intracellular ROS were detected using the fluorescent probe 2',7'-dichlorodihydrofluorescein (DCFH, Invitrogen, Carlsbad, CA, USA). After treatment, cells were incubated with DCFH-DA (10 mM) for 30 min at 37 °C in 5% CO<sub>2</sub> and washed with PBS three times. The cellular fluorescence was monitored under a fluorescence microscope (LEICA DMi8, Wiesbaden, Germany). The amount of ROS was quantified as the relative fluorescence intensity of DCF per cell within the sight area.

#### 4.8. Transient Transfection and RNA Interference

HUVECs at 60–70% confluence were transfected with Nrf2 or scrambled siRNA using a Lippo2000 transfection reagent according to the manufacturer's protocol (Invitrogen, Waltham, MA, USA). After incubation for 6 h, the transfection medium was removed and replaced with fresh normal growth medium for 24–48 h.

#### 4.9. Statistical Analysis

Data are presented as mean ± SEM. Images were processed by use of Graphpad Prism 5 (GraphPad Software, La Jolla, CA, USA) and Adobe Photoshop (Adobe, San Jose, CA, USA). At least three independent replications were performed. One-way ANOVA combined with Bonferroni post-hoc tests were used to determine the significance between different groups.  $p < 0.05$  was considered statistically significant.

**Author Contributions:** Conceptualization, N.M. and J.B.; methodology, J.-R.H. and Y.-H.W.; validation, J.-R.H. and Y.-H.W.; formal analysis, J.-R.H.; investigation, Y.-N.Z. and Y.H.; data curation,

J.-R.H. and Y.-H.W.; writing—original draft preparation, J.-R.H. and N.M.; writing—review and editing, J.B. and N.M.; visualization, Y.-N.Z. and T.-T.C.; supervision, N.M.; project administration, N.M. and J.B. All authors have read and agreed to the published version of the manuscript.

**Funding:** This research work was financially supported by the National Natural Science Foundation of China (no. 31671214), Natural Science Foundation of Shandong Province (nos. ZR2020YQ52, ZR2020MD091, ZR2019PC051), Project of Shandong Province Higher Educational Youth Innovation Science and Technology Program (2020KJE006), the Science and Technology Project of University of Jinan (no. XKY1517), and the Open Fund of Joint LMB, LMM, and LAMB (LMB20201007).

**Institutional Review Board Statement:** Not applicable.

**Informed Consent Statement:** Not applicable.

**Data Availability Statement:** The data presented in this study are publicly available.

**Conflicts of Interest:** The authors declare no conflict of interest.

## References

1. Wang, P.; Xiu, C.H.; Wang, L.F. The relationship between carotid atherosclerosis and cardiovascular disease. *Chin. J. Atheroscler.* **2014**, *22*, 1175–1178.
2. Chen, Y.; Li, D.; Xu, Y. Essential oils from fructose A. zerumbet protect human aortic endothelial cells from apoptosis induced by Ox-LDL in vitro. *Evid. Complement. Alternat. Med.* **2014**, *14*, 956824.
3. Santoro, M.M.; Samuel, T.; Mitchell, T. Birc2 (clap1) regulates endothelial cell integrity and blood vessel homeostasis. *Nat. Genet.* **2017**, *39*, 1397–1402. [[CrossRef](#)] [[PubMed](#)]
4. Kumar, S.; Kim, C.W.; Simmons, R.D.; Jo, H. Role of flow-sensitive microRNAs in endothelial dysfunction and atherosclerosis: Mechanosensitive atheromiRs. *Arterioscler. Thromb. Vasc. Biol.* **2014**, *34*, 2206–2216. [[CrossRef](#)] [[PubMed](#)]
5. Zhang, Y.; Qin, W.; Zhang, L. MicroRNA-26a prevents endothelial cell apoptosis by directly targeting TRPC6 in the setting of atherosclerosis. *Sci. Rep.* **2015**, *5*, 9401. [[CrossRef](#)] [[PubMed](#)]
6. Incalza, M.A.; D’Oria, R.; Natalicchio, A.; Perrini, S.; Laviola, L.; Giorgino, F. Oxidative stress and reactive oxygen species in endothelial dysfunction associated with cardiovascular and metabolic diseases. *Vasc. Pharmacol.* **2018**, *100*, 1–19. [[CrossRef](#)]
7. Rafieian-Kopaei, M.; Setorki, M.; Doudi, M.; Baradaran, A.; Nasri, H. Atherosclerosis: Process, indicators, risk factors and new hopes. *Int. J. Prev. Med.* **2014**, *5*, 927.
8. Suciur, C.F.; Prete, M.; Ruscitti, P.; Favoino, E.; Giacomelli, R.; Perosa, F. Oxidized low density lipoproteins: The bridge between atherosclerosis and autoimmunity. Possible implications in accelerated atherosclerosis and for immune intervention in autoimmune rheumatic disorders. *Autoimmun. Rev.* **2018**, *17*, 366–375. [[CrossRef](#)]
9. Bao, M.H.; Li, J.M.; Zhou, Q.L.; Li, G.Y.; Zeng, J.; Zhao, J.; Zhang, Y.W. Effects of miR-590 on ox-LDL-induced endothelial cell apoptosis: Roles of p53 and NF-κB. *Mol. Med. Rep.* **2016**, *13*, 867–873. [[CrossRef](#)]
10. Yao, J.; Zou, Z.; Wang, X.; Ji, X.; Yang, J. Pinoresinol Diglucoside Alleviates ox-LDL-Induced Dysfunction in Human Umbilical Vein Endothelial Cells. *Evid.-Based Complement. Altern. Med.* **2016**, *2016*, 3124519. [[CrossRef](#)]
11. Kattoor, A.J.; Kanuri, S.H.; Mehta, J.L. Role of Ox-LDL and LOX-1 in Atherogenesis. *Curr. Med. Chem.* **2019**, *26*, 1693–1700. [[CrossRef](#)] [[PubMed](#)]
12. Wang, K.W.; Ding, P. New Bioactive Metabolites from the Marine-derived Fungi *Aspergillus*. *Mini Rev. Med. Chem.* **2018**, *18*, 1072–1094. [[CrossRef](#)]
13. Jiang, M.; Wu, Z.; Guo, H.; Liu, L.; Chen, S. A Review of Terpenes from Marine-Derived Fungi: 2015–2019. *Mar. Drugs* **2020**, *18*, 321. [[CrossRef](#)] [[PubMed](#)]
14. Xu, J.; Yi, M.; Ding, L.; He, S. A Review of Anti-Inflammatory Compounds from Marine Fungi, 2000–2018. *Mar. Drugs* **2019**, *17*, 636. [[CrossRef](#)]
15. Willems, T.; De Mol, M.L.; De Bruycker, A.; De Maeseineire, S.L.; Soetaert, W.K. Alkaloids from Marine Fungi: Promising Antimicrobials. *Antibiotics* **2020**, *9*, 340. [[CrossRef](#)]
16. Middleton, E., Jr.; Kandaswami, C.; Theoharides, T.C. The effects of plant flavonoids on mammalian cells: Implications for inflammation, heart disease, and cancer. *Pharmacol. Rev.* **2000**, *52*, 673–751.
17. Bao, J.; He, F.; Yu, J.H.; Zhai, H.; Cheng, Z.Q.; Jiang, C.S.; Zhang, Y.; Zhang, Y.; Zhang, X.; Chen, G.; et al. New Chromones from a Marine-Derived Fungus, *Arthrinium* sp., and Their Biological Activity. *Molecules* **2018**, *23*, 1982. [[CrossRef](#)] [[PubMed](#)]
18. Wairata, J.; Sukandar, E.R.; Fadlan, A.; Purnomo, A.S.; Taher, M.; Ersam, T. Evaluation of the Antioxidant, Antidiabetic, and Antiplasmodial Activities of Xanthones Isolated from *Garcinia forbesii* and their in silico Studies. *Biomedicines* **2021**, *9*, 1380. [[CrossRef](#)]
19. Tran, T.H.; Nguyen, V.T.; Le, H.T.; Nguyen, H.M.; Tran, T.H.; Do Thi, T.; Nguyen, X.C.; Ha, M.T. Garcinoxanthones SV, new xanthone derivatives from the pericarps of *Garcinia mangostana* together with their cytotoxic and antioxidant activities. *Fitoterapia* **2021**, *151*, 104880. [[CrossRef](#)]

20. Khattab, A.R.; Farag, M.A. Marine and terrestrial endophytic fungi: A mine of bioactive xanthone compounds, recent progress, limitations, and novel applications. *Crit. Rev. Biotechnol.* **2021**, *15*, 1–28. [[CrossRef](#)]
21. Wu, Z.H.; Liu, D.; Xu, Y.; Chen, J.L.; Lin, W.H. Antioxidant xanthenes and anthraquinones isolated from a marine-derived fungus *Aspergillus versicolor*. *Chin. J. Nat. Med.* **2018**, *16*, 219–224. [[CrossRef](#)]
22. Jiang, D.J.; Hu, G.Y.; Jiang, J.L.; Xiang, H.L.; Deng, H.W.; Li, Y.J. Relationship between protective effect of xanthone on endothelial cells and endogenous nitric oxide synthase inhibitors. *Bioorg. Med. Chem.* **2003**, *11*, 5171–5177. [[CrossRef](#)]
23. Jiang, F.; Zhang, D.L.; Jia, M.; Hao, W.H.; Li, Y.J. Mangiferin inhibits high-fat diet induced vascular injury via regulation of PTEN/AKT/eNOS pathway. *J. Pharmacol. Sci.* **2018**, *137*, 265–273. [[CrossRef](#)]
24. Wang, Z.; Liu, B.; Zhu, J.; Wang, D.; Wang, Y. Nicotine-mediated autophagy of vascular smooth muscle cell accelerates atherosclerosis via nAChRs/ROS/NF- $\kappa$ B signaling pathway. *Atherosclerosis* **2019**, *284*, 1–10. [[CrossRef](#)] [[PubMed](#)]
25. Loboda, A.; Damulewicz, M.; Pyza, E.; Jozkowicz, A.; Dulak, J. Role of Nrf2/HO-1 system in development, oxidative stress response and diseases: An evolutionarily conserved mechanism. *Cell Mol. Life Sci.* **2016**, *73*, 3221–3247. [[CrossRef](#)]
26. Wang, R.; Wang, M.; Ye, J.; Sun, G.; Sun, X. Mechanism overview and target mining of atherosclerosis: Endothelial cell injury in atherosclerosis is regulated by glycolysis (Review). *Int. J. Mol. Med.* **2021**, *47*, 65–76. [[CrossRef](#)] [[PubMed](#)]
27. Pirillo, A.; Norata, G.D.; Catapano, A.L. LOX-1, ox-LDL, and atherosclerosis. *Mediat. Inflamm.* **2013**, *2013*, 152786. [[CrossRef](#)] [[PubMed](#)]
28. Grassi, D.; Desideri, G.; Ferri, C. Flavonoids: Antioxidants against atherosclerosis. *Nutrients* **2010**, *2*, 889–902. [[CrossRef](#)]
29. Jiang, D.J.; Jiang, J.L.; Tan, G.S.; Huang, Z.Z.; Deng, H.W.; Li, Y.J. Demethylbellidifolin inhibits adhesion of monocytes to endothelial cells via reduction of tumor necrosis factor alpha and endogenous nitric oxide synthase inhibitor level. *Planta Med.* **2003**, *69*, 1150–1152.
30. Jin, Z.Q.; Chen, X. A simple reproducible model of free radical-injured isolated heart induced by 1,1-diphenyl-2-picryl-hydrazyl (DPPH). *J. Pharm. Toxicol. Methods* **1998**, *39*, 63–70. [[CrossRef](#)]
31. Cominacini, L.; Garbin, U.; Pasini, A.F.; Davoli, A.; Campagnola, M.; Pastorino, A.M.; Gaviraghi, G.; Lo Cascio, V. Oxidized low-density lipoprotein increases the production of intracellular reactive oxygen species in endothelial cells: Inhibitory effect of lacidipine. *J. Hypertens.* **1998**, *16 Pt 2*, 1913–1919. [[CrossRef](#)] [[PubMed](#)]
32. Saha, S.; Buttari, B.; Panieri, E.; Profumo, E.; Saso, L. An Overview of Nrf2 Signaling Pathway and Its Role in Inflammation. *Molecules* **2020**, *25*, 5474. [[CrossRef](#)] [[PubMed](#)]
33. Juurlink, B.H. Dietary Nrf2 activators inhibit atherogenic processes. *Atherosclerosis* **2012**, *225*, 29–33. [[CrossRef](#)] [[PubMed](#)]
34. Tanaka, M.; Kishimoto, Y.; Sasaki, M.; Sato, A.; Kamiya, T.; Kondo, K.; Iida, K. *Terminalia bellirica* (Gaertn.) Roxb. Extract and Gallic Acid Attenuate LPS-Induced Inflammation and Oxidative Stress via MAPK/NF- $\kappa$ B and AKT/AMPK/Nrf2 Pathways. *Oxid. Med. Cell. Longev.* **2018**, *2018*, 9364364. [[CrossRef](#)]
35. Li, S.; Sun, Y.; Han, Z.; Bu, X.; Yu, W.; Wang, J. Retraction notice to “Cytoprotective effects of euxanthone against ox-LDL-induced endothelial cell injury is mediated via Nrf2. *Life Sci.* **2019**, *223*, 174–184. [[CrossRef](#)] [[PubMed](#)]
36. Ismail, M.B.; Rajendran, P.; AbuZahra, H.M.; Veeraghavan, V.P. Mangiferin Inhibits Apoptosis in Doxorubicin-Induced Vascular Endothelial Cells via the Nrf2 Signaling Pathway. *Int. J. Mol. Sci.* **2021**, *22*, 4259. [[CrossRef](#)]
37. Zhuang, Y.; Wu, H.; Wang, X.; He, J.; He, S.; Yin, Y. Resveratrol Attenuates Oxidative Stress-Induced Intestinal Barrier Injury through PI3K/Akt-Mediated Nrf2 Signaling Pathway. *Oxid. Med. Cell. Longev.* **2019**, *2019*, 7591840. [[CrossRef](#)] [[PubMed](#)]
38. Nakaso, K.; Yano, H.; Fukuhara, Y.; Takeshima, T.; Wada-Isoe, K.; Nakashima, K. PI3K is a key molecule in the Nrf2-mediated regulation of antioxidative proteins by hemin in human neuroblastoma cells. *FEBS Lett.* **2003**, *546*, 181–184. [[CrossRef](#)]



## Article

# Pharmacokinetics and Metabolism Study of Deep-Sea-Derived Butyrolactone I in Rats by UHPLC–MS/MS and UHPLC–Q-TOF-MS

Liang Wu <sup>1</sup>, Chun-Lan Xie <sup>2</sup>, Xian-Wen Yang <sup>2,\*</sup> and Gang Chen <sup>1,\*</sup>

<sup>1</sup> Department of Pharmaceutical Analysis, School of Pharmacy, Fudan University, Shanghai 201203, China; yhdhospital@163.com

<sup>2</sup> Key Laboratory of Marine Biogenetic Resources, Third Institute of Oceanography, Ministry of Natural Resources, 184 Daxue Road, Xiamen 361005, China; xiechunlanxx@163.com

\* Correspondence: yangxianwen@tio.org.cn (X.-W.Y.); hncy\_educ@163.com (G.C.); Tel.: +86-592-219-5319 (X.-W.Y.); +86-21-51980168 (G.C.)

**Abstract:** Butyrolactone I (BTL-I) is a butanolide isolated from the deep-sea-derived fungus, *Aspergillus* sp. It provides a potential new target for the prevention and treatment of food allergies. This study aimed to investigate the metabolic and pharmacokinetic profile of BTL-I in rats. The metabolic profiles were obtained by UHPLC–Q-TOF-MS. As a result, eleven metabolites were structurally identified, and the proposed metabolic pathways of BTL-I were characterized. The main metabolites were the oxidative and glucuronidative metabolites. In addition, a sensitive UHPLC–MS/MS method was established for the quantitation of BTL-I in rat plasma (LOQ = 2 ng/mL). The method was fully validated and successfully applied to the pharmacokinetic study of BTL-I in rats after oral administration or intravenous administration. The oral bioavailability was calculated as 6.29%, and the maximum plasma concentrations were  $9.85 \pm 1.54$  ng/mL and  $17.97 \pm 1.36$  ng/mL for intravenous and intragastric dosing groups, respectively.

**Keywords:** butyrolactone I; food allergy; metabolism; pharmacokinetics

**Citation:** Wu, L.; Xie, C.-L.; Yang, X.-W.; Chen, G.

Pharmacokinetics and Metabolism Study of Deep-Sea-Derived Butyrolactone I in Rats by UHPLC–MS/MS and UHPLC–Q-TOF-MS. *Mar. Drugs* **2022**, *20*, 11. <https://doi.org/10.3390/md20010011>

Academic Editors: Yonghong Liu and Xuefeng Zhou

Received: 11 November 2021

Accepted: 20 December 2021

Published: 22 December 2021

**Publisher's Note:** MDPI stays neutral with regard to jurisdictional claims in published maps and institutional affiliations.



**Copyright:** © 2021 by the authors. Licensee MDPI, Basel, Switzerland. This article is an open access article distributed under the terms and conditions of the Creative Commons Attribution (CC BY) license (<https://creativecommons.org/licenses/by/4.0/>).

## 1. Introduction

Food allergies are an immune-mediated adverse reaction to food [1,2]. Food allergies to cow's milk and eggs have become prevalent among young children over the past 20 years [3,4]. Currently, the only effective way to prevent allergic reactions to food is to strictly avoid the allergen of concern, and the recognized treatment for severe allergic reactions is epinephrine [5]. Consequently, providing improved therapeutic options has become an important avenue in food allergy research. The exploitation of small-molecule inhibitors is one important research direction for anti-food allergy studies, due to their diverse chemical structures [6]. There is certain evidence from human and animal studies that basophils and mast cells are key effector cells that contribute to allergic reactions to foods [7]. It has been reported that several compounds from marine microorganisms could partially inhibit degranulation in IgE-mediated mast cell responses [8,9].

Butyrolactone I (BTL-I) is a butanolide first reported in 1997 [10]. It showed an anti-neuroinflammatory effect on lipopolysaccharide (LPS)-induced microglia cells by inhibiting the phosphorylation of p65 and IκB [11]. Moreover, BTL-I could inhibit cyclin-dependent kinases (CDK), including CDK1 and CDK5 [12,13]. In a previous study, we obtained this compound from a deep-sea-derived *Aspergillus* sp. We found that it exhibited significant anti-food allergic activities in vitro and in vivo [14]. Therefore, BTL-I has additive or synergistic therapeutic potential in diseases with multi-factorial etiologies, and provides a potential new insight to the prevention and treatment of food allergy diseases [15].

Although the activities were studied extensively, the pharmacokinetics and metabolism of BTL-I remain unknown. Pharmacokinetics and metabolism are significantly important in

the drug discovery and development processes, not only for supporting toxicity but also for optimizing the drug candidate [16]. Pharmacokinetics are useful for obtaining information to help understand the molecular basis of pharmacological activity, for treatment scheme selection, and for more effective drug application [17]. Therefore, it was meaningful to obtain the pharmacokinetic and metabolism profiles of the drug, to better comprehend how effective it could be. Previous studies have investigated the metabolism of BTL-I in rat urine and feces [18], in which ten phase I metabolites in rat feces were isolated and identified. However, the metabolites distributed in rat blood and bile were unknown.

In the present study, a rapid and sensitive LC–MS/MS method was developed and validated for the determination of BTL-I in rat plasma. A reliable method was subsequently applied to investigate the pharmacokinetic behaviors of BTL-I in rats after intravenous and oral administration. Moreover, the metabolism of BTL-I *in vivo* was investigated using an ultra-high-performance liquid chromatography–quadrupole time-of-flight mass spectrometry (UHPLC–Q–TOF–MS) method.

## 2. Results and Discussion

### 2.1. Metabolism Study of BTL in Rats

#### 2.1.1. Fragmentation of BTL-I Standard

BTL-I was eluted at 13.88 min under the current chromatographic condition. The MS<sup>2</sup> fragmentation pattern of BTL-I was studied for a better understanding of the MS<sup>2</sup> fragmentation patterns of the metabolites. In positive ion mode, BTL-I showed a protonated molecular ion  $[M + H]^+$  at  $m/z$  425.1598 ( $C_{24}H_{25}O_7^+$ ). The MS<sup>2</sup> fragmentation of the parent ion showed three predominant fragment ions at  $m/z$  393.1333 ( $C_{23}H_{21}O_6^+$ ),  $m/z$  331.1353 ( $C_{23}H_{19}O_{33}^+$ ),  $m/z$  175.1131 ( $C_{12}H_{15}O^+$ ). One minor ion at  $m/z$  275.0715 ( $C_{18}H_{11}O_{33}^+$ ) was also observed. The proposed fragmentation pathways are shown in Figure 1. These fragment ions can be used as characteristic ions for the identification of metabolites.

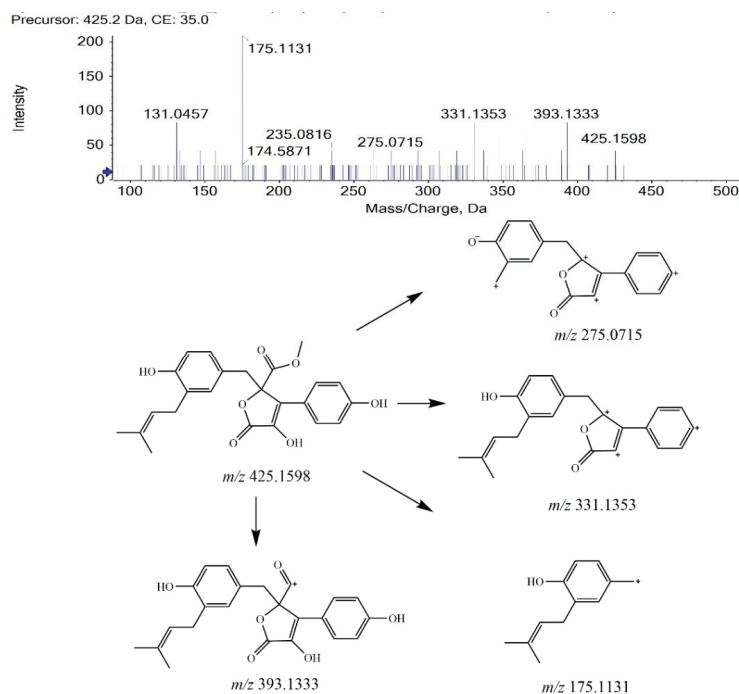
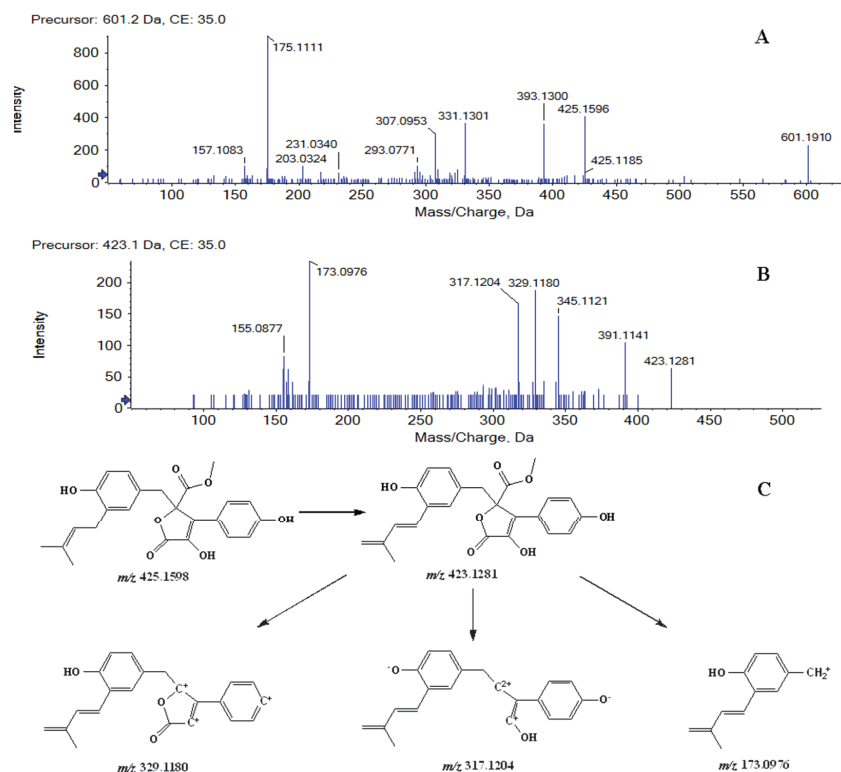


Figure 1. MS<sup>2</sup> spectrum of BTL-I and its fragmentation pathways.

### 2.1.2. Analysis of BTL-I Metabolites

By comparison with the blank samples, precursor ions uniquely found in BTL-I dosed samples were considered as potential metabolites, and then used for subsequent MS<sup>2</sup> analysis. Eleven potential metabolites were observed and structurally identified based on their MS and MS<sup>2</sup> spectra.

Metabolites M1 and M2 were detected at 11.08, 11.87 min, respectively. In positive ion mode, both of them showed the protonated molecular ion [M + H]<sup>+</sup> at *m/z* 601.1910 (−0.7 ppm, element composition C<sub>30</sub>H<sub>33</sub>O<sub>13</sub><sup>+</sup>), 176 *m/z* units higher than that of BTL-I, suggesting that they were glucuronide conjugates of BTL-I. The MS<sup>2</sup> fragmentation (Figure 2A) showed fragment ions at *m/z* 425.1596, 393.1300, 331.1301, 175.1111. Therefore, Metabolites M1 and M2 were identified as the glucuronide conjugates of BTL-I.



**Figure 2.** MS<sup>2</sup> spectrum of M1, M2 (A), and M3, M4, M5, M6 (B), along with the fragmentation pathway of M3, M4, M5, M6 (C).

Metabolites M3, M4, M5 and M6 were eluted at 8.42, 9.19, 10.82, 11.63 min, respectively. All of them showed the protonated molecule [M + H]<sup>+</sup> at *m/z* 423.1440 (−1.0 ppm, element composition C<sub>24</sub>H<sub>23</sub>O<sub>7</sub><sup>+</sup>), 2 *m/z* units lower than that of BTL-I. In the product ion scan (Figure 2B), product ions at *m/z* 391.1141, 345.1099, 329.1180, 317.1204 and 173.0976 were observed. The proposed fragmentation pathway was shown in Figure 2C. Therefore, metabolites M3, M4, M5 and M6 were tentatively identified as the dehydrogenate metabolites of BTL-I.

Metabolite M7 was eluted at the retention time of 11.17 min. It showed a protonated molecule [M + H]<sup>+</sup> at *m/z* 443.1698 (−1.8 ppm, element composition C<sub>24</sub>H<sub>27</sub>O<sub>8</sub><sup>+</sup>), 18 *m/z* units higher than that of BTL-I. Therefore, M7 was thought to be conjugated with water.



The retention times of metabolites M8 and M9 were 9.38, and 11.71 min, respectively. Both of them showed the same protonated molecule  $[M + H]^+$  at  $m/z$  411.1443 ( $-0.2$  ppm, element composition  $C_{23}H_{23}O_7^+$ ). In the product ion scan of M8 (Figure S3A), product ions at  $m/z$  275.0743 and 175.1133 were observed. In the product ion scan of M9 (Figure S3B), product ions at  $m/z$  393.1261, 331.1387, 275.0768 and 175.1133 were observed. Therefore, metabolites M8 and M9 were identified as the demethylation metabolites of BTL-I. The demethylation site of M9 was thought to be the methyl of ester linkage.

Metabolite M10 was eluted at 13.03 min. It showed the protonated molecule  $[M + H]^+$  at  $m/z$  441.1525 ( $-5.4$  ppm, element composition  $C_{24}H_{25}O_8^+$ ), 16  $m/z$  units higher than that of BTL-I. At the further product ion scan (Figure S4), product ion at  $m/z$  363.1112 was observed. Therefore, metabolite M10 was identified as an oxidate metabolite of BTL-I. According to the previous study [18], M10 was supposed as 7''S-hydroxy-9''-ene-butyrolactone I or 7''R-hydroxy-9''-ene-butyrolactone I.

Metabolite M11 was eluted at 11.96 min. It showed the protonated molecule  $[M+H]^+$  at  $m/z$  457.1506 (1.8 ppm, element composition  $C_{24}H_{25}O_9^+$ ), 16  $m/z$  units higher than that of M10. Therefore, metabolite M11 was identified as a dioxidation metabolite of BTL-I. According to the previous study [18], M11 was supposed as 7''S,8''R-dihydroxy-aspernolide E or 7''R, 8''S-dihydroxy-aspernolide E.

### 2.1.3. Metabolic Profiling of BTL-I in Rats

According to the metabolite profiles, the proposed metabolic pathways were predicted, as shown in Figure 3. The elemental compositions, observed and calculated masses, mass errors, and characteristic fragment ions of the proposed metabolites, are summarized in Table 1. The extraction ion chromatographies of the metabolites in rat bile and feces are shown in Figure 4.

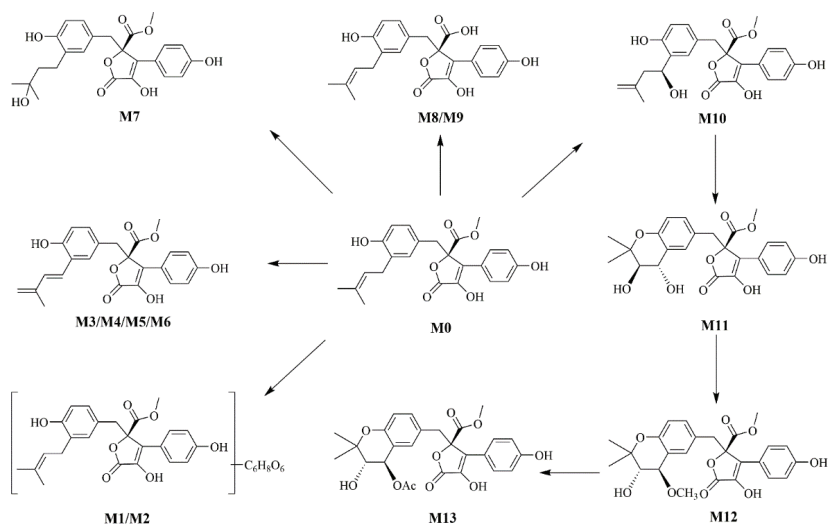
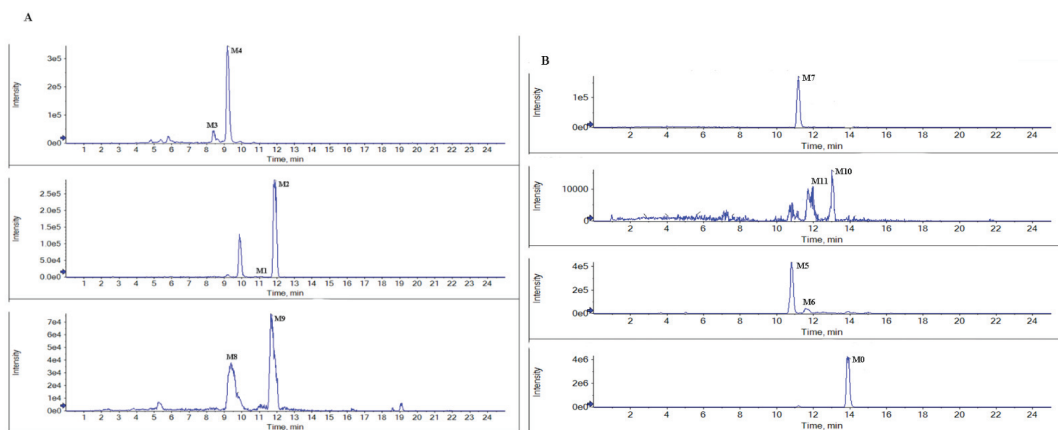


Figure 3. The proposed metabolic pathways of BTL-I in rats.

**Table 1.** Mass spectral data of BTL-I (M0) and its metabolites (M1–M11). U, urine; F, feces; B, bile.

|     | $t_R$ | Measured $m/z$ | Calculated $m/z$ | Formula              | Product ions   | Error (ppm) | Source |
|-----|-------|----------------|------------------|----------------------|--|-------------|--------|
| M0  | 13.87 | 425.1598       | 425.1600         | $C_{24}H_{25}O_7$    | 393.1306,<br>331.1369,<br>275.0701,<br>175.1124              | −0.5        | B F    |
| M1  | 11.08 | 601.1906       | 601.1910         | $C_{30}H_{33}O_{13}$ | 425.1596,<br>393.1300,<br>331.1301,<br>175.1111              | −0.7        | B U    |
| M2  | 11.87 | 601.1906       | 601.1910         | $C_{30}H_{33}O_{13}$ | 425.1606,<br>393.1301,<br>331.1334,<br>175.1115              | −0.7        | B      |
| M3  | 8.42  | 423.1440       | 423.1444         | $C_{24}H_{23}O_7$    | 391.1141,<br>345.1099,<br>329.1217,<br>317.1183,<br>173.0970 | −1.0        | B      |
| M4  | 9.19  | 423.1440       | 423.1444         | $C_{24}H_{23}O_7$    | 391.1141,<br>345.1121,<br>329.1180,<br>317.1204,<br>173.0976 | −1.0        | B      |
| M5  | 10.82 | 423.1440       | 423.1444         | $C_{24}H_{23}O_7$    | 345.1134,<br>329.1214,<br>275.0971,<br>173.0961              | −1.0        | F      |
| M6  | 11.63 | 423.1440       | 423.1444         | $C_{24}H_{23}O_7$    | 345.1134,<br>329.1214,<br>275.0971,<br>173.0961              | −1.0        | F      |
| M7  | 11.17 | 443.1698       | 443.1706         | $C_{24}H_{27}O_8$    | 349.0429   | −1.8        | F      |
| M8  | 9.38  | 411.1443       | 411.1444         | $C_{23}H_{23}O_7$    | 275.0743,<br>175.1098  | −0.2        | B      |
| M9  | 11.71 | 411.1443       | 411.1444         | $C_{23}H_{23}O_7$    | 393.1261,<br>331.1387,<br>275.0768,<br>175.1133              | −0.2        | B      |
| M10 | 13.03 | 441.1525       | 441.1549         | $C_{24}H_{25}O_8$    | 363.1112   | −5.4        | F      |
| M11 | 11.96 | 457.1506       | 457.1498         | $C_{24}H_{25}O_9$    | 363.1112   | 1.8         | F      |

BTL-I was detected in the bile and feces after oral dosing compared with the blank samples. Among the eleven metabolites identified, there was only a trace of the prototype compound detected in plasma and urine after intragastric dosing. Among the metabolites, six metabolites including M1, M2, M3, M4, M8, M9 were detected in the bile samples, and the most abundant metabolites were M2 and M4. Metabolites M5, M6, M7, M10, M11 were detected in the feces, and the most abundant metabolite was M5 and M7. It was thought that BTL-I was poorly absorbed into plasma after oral administration. The absorbed BTL-I was quickly excreted into bile, and metabolized to the metabolites. The result was in agreement with the reported literature [18].



**Figure 4.** Representative extraction ion chromatograms of the metabolites in rat bile (A), and feces (B) after the oral administration of BTL-I.

## 2.2. Pharmacokinetic Study

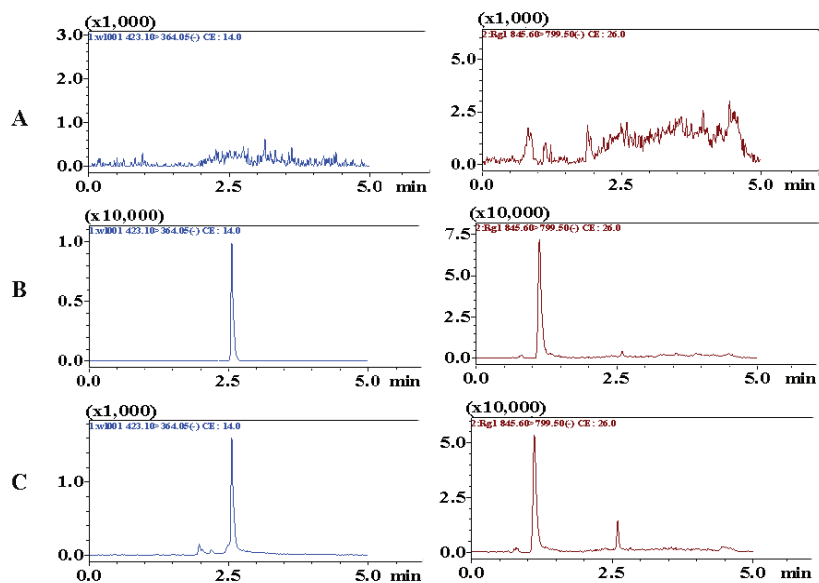
### 2.2.1. Method Development

The LC-MS/MS conditions, including parent-product ion transitions and source parameters, were further investigated for analyzing BTL-I and the internal standard (IS), ginsenoside Rg1. Although the response of BTL-I was more sensitive in positive ion mode than that in negative ion mode, the signal was more stable in negative ion mode than that in positive ion mode. In addition, BTL-I could easily form other adduct molecular ions in positive ion mode, for example, adding sodium. Therefore, negative ion mode was adopted for the quantitation of BTL-I in plasma. BTL-I showed the parent ion  $[M - H]^-$  at  $m/z$  423.1, and IS showed the parent ion  $[M - H]^-$  at  $m/z$  845.6. In product ion scan mode, BTL-I and IS showed product ions at  $m/z$  364.1 and 799.5, respectively. Therefore,  $m/z$  423.1–364.1 for BTL-I, and  $m/z$  845.6–799.5 for IS were applied as MRM transitions. Then, collision energies and other source parameters were optimized to obtain higher sensitivity.

To obtain the satisfactory shape of the chromatographic peak and retention times, different aqueous phases, including water, 0.1% FA in water, and 5 mM ammonium acetate in water, were compared. The response of BTL-I using 0.1% FA in water was higher than that of the other aqueous phases. Therefore, acetonitrile and 0.1% FA in water were selected as the mobile phase.

### 2.2.2. Method Validation

Chromatograms including blank plasma samples, blank samples spiked with analytes, and plasma samples collected after administration, were obtained to assess specificity. As shown in Figure 5, the retention times of BTL-I and IS were 2.51 and 1.22 min, respectively. No interference or co-eluting peaks were observed at the retention times of analytes. The method showed good linearity over the range of 2–500 ng/mL, with a regression coefficient ( $r$ ) of 0.9956. The LLOQ was 2 ng/mL and the LOD was 0.5 ng/mL, which suggested that the method was sensitive enough to determine BTL-I in rat plasma.



**Figure 5.** Representative MRM chromatograms of BTL-I (2.51 min) and IS (1.22 min) in (A) blank rat plasma, (B) blank rat plasma spiked with BTL-I at LLOQ (2 ng/mL) and IS, (C) rat plasma samples collected after intragastric administration.

Intra- and inter-precision and accuracy were summarized in Table 2. The results suggested that the concentration of BTL-I in rat plasma could be accurately and precisely measured by the current assay.

**Table 2.** Precision and accuracy of BTL-I in rat plasma ( $n = 6$ ).

| Concentration (ng/mL) | Intra-Day             |               | Inter-Day             |              |
|-----------------------|-----------------------|---------------|-----------------------|--------------|
|                       | Precision (R.S.D., %) | Accuracy      | Precision (R.S.D., %) | Accuracy     |
| 2                     | 2.95                  | 87.95 ± 5.62  | 7.25                  | 86.45 ± 7.33 |
| 5                     | 3.87                  | 101.23 ± 4.06 | 6.41                  | 91.52 ± 6.31 |
| 200                   | 1.23                  | 91.44 ± 2.95  | 5.12                  | 90.89 ± 4.88 |
| 400                   | 3.18                  | 96.83 ± 3.33  | 4.14                  | 92.77 ± 5.36 |

The results of the extraction recovery and matrix effect were listed in Table 3. The recovery was over the range of 72.37% to 79.84%. The values of the matrix effect were greater than 85%, indicating that the matrix effect could be ignored.

**Table 3.** Extraction recovery and matrix effect of BTL-I in rat plasma ( $n = 6$ ).

|     | Nominal Conc. (ng/mL) | Matrix Effect (%) | Extraction Recovery (%) |
|-----|-----------------------|-------------------|-------------------------|
| BTL | 5                     | 86.13 ± 6.33      | 75.09 ± 4.29            |
|     | 200                   | 88.29 ± 5.14      | 72.37 ± 7.22            |
|     | 400                   | 92.14 ± 3.19      | 79.84 ± 6.15            |
| IS  | 20                    | 85.12 ± 4.47      | 80.17 ± 5.09            |

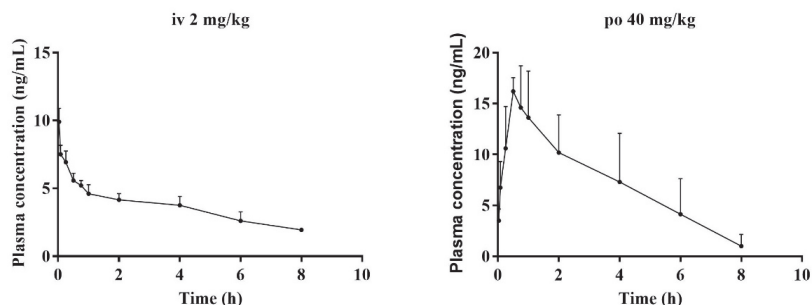
The stability results of BTL-I under different conditions were listed in Table 4. The data demonstrated that BTL-I was stable during the sample collection, preparation and analysis process. Bias (%) ranging of 4.2 % to 5.1 % in incurred sample stability assay further confirmed the good stability of BTL-I and its metabolites in rat plasma.

**Table 4.** Stability of BTL-I under different storage conditions ( $n = 6$ ).

| Stability                   | Nominal Concentrations (ng/mL) | Measured Concentrations (ng/mL) | Accuracy R.E. (%) | R.S.D. (%) |
|-----------------------------|--------------------------------|---------------------------------|-------------------|------------|
| Short term                  | 5                              | 4.82 ± 0.33                     | 96.36 ± 6.67      | 6.85       |
|                             | 200                            | 189.71 ± 11.15                  | 94.86 ± 5.58      | 5.87       |
|                             | 400                            | 405.27 ± 18.51                  | 101.32 ± 4.63     | 4.57       |
| Long term                   | 5                              | 4.78 ± 0.21                     | 95.86 ± 4.27      | 4.39       |
|                             | 200                            | 190.71 ± 13.14                  | 95.36 ± 6.57      | 6.89       |
|                             | 400                            | 411.27 ± 12.44                  | 102.82 ± 3.11     | 3.02       |
| Post-preparative            | 5                              | 5.19 ± 0.42                     | 103.80 ± 8.09     | 7.50       |
|                             | 200                            | 197.51 ± 12.49                  | 98.76 ± 7.38      | 7.45       |
|                             | 400                            | 401.39 ± 23.84                  | 100.35 ± 5.88     | 5.91       |
| Freezing and thawing cycles | 5                              | 5.07 ± 0.32                     | 101.50 ± 6.40     | 6.50       |
|                             | 200                            | 195.51 ± 21.49                  | 97.76 ± 10.75     | 10.45      |
|                             | 400                            | 403.29 ± 18.89                  | 100.83 ± 4.72     | 5.11       |

### 2.2.3. Pharmacokinetic Study

After validation, the method was further applied to study the pharmacokinetic properties of BTL-I in rats after intravenous and oral administration. No obvious abnormalities in the rats' general conditions were observed. There was no significant increase or decrease in the activity of the rats. The concentrations of BTL-I in rat plasma versus time profiles were depicted in Figure 6, and the pharmacokinetic parameters were listed in Table 5.

**Figure 6.** Mean plasma concentration–time curves of BTL-I in rats, after intravenous (2 mg/kg) and intragastric (40 mg/kg) administrations ( $n = 5$ ).**Table 5.** Pharmacokinetic parameters of BTL-I in rat plasma after oral (40 mg/kg) and intravenous (2 mg/kg) administration ( $n = 5$ ).

|                    | Unit                 | Intravenous      | Oral              |
|--------------------|----------------------|------------------|-------------------|
| AUC <sub>0-t</sub> | ng <sup>2</sup> h/mL | 45.13 ± 3.96     | 57.93 ± 26.11     |
| AUC <sub>0-∞</sub> | ng <sup>2</sup> h/mL | 48.09 ± 6.68     | 60.5 ± 26.85      |
| T <sub>max</sub>   | h                    |                  | 0.69 ± 0.24       |
| C <sub>max</sub>   | ng/mL                |                  | 17.97 ± 1.36      |
| Cl                 | L/h/kg               | 272.11 ± 66.64   | 292.64 ± 171.51   |
| Vd                 | L/kg                 | 1375.46 ± 328.31 | 5730.25 ± 2415.75 |
| MRT                | h                    | 5.68 ± 1.48      | 2.88 ± 0.55       |
| T <sub>1/2</sub>   | h                    | 1.36 ± 0.25      | 1.23 ± 0.22       |
| F                  | %                    |                  | 6.29              |

After intravenous administration (2 mg/kg), the concentration of BTL-I at the first time point was extremely low (19.85 ± 1.54 ng/mL). The value of the apparent volume of distribution (Vd) was 1375.46 ± 328.31 L/kg, suggesting that BTL-I was mainly distributed in the organs. BTL-I was quickly eliminated from the plasma, with a T<sub>1/2</sub> value

of  $1.36 \pm 0.25$  h. After oral administration, BTL-I was rapidly absorbed into plasma and detected at 5 min after oral administration. BTL-I reached the peak at  $0.69 \pm 0.24$  h, with a  $C_{\max}$  value of  $17.97 \pm 1.36$   $\mu\text{g/L}$ . BTL-I was quickly eliminated from the plasma, with a  $T_{1/2}$  value of  $1.23 \pm 0.22$  h. The  $\text{AUC}_{0-\infty}$  after oral administration and intravenous administration were  $60.5 \pm 26.85$   $\text{ng}^*\text{h/mL}$  and  $48.09 \pm 6.68$   $\text{ng}^*\text{h/mL}$ , respectively. The oral absolute bioavailability was calculated as 6.29%. According to the current result, the metabolites with a high abundance in tissue deserve further study.

### 3. Materials and Methods

#### 3.1. Chemicals and Reagents

BTL-I was isolated from a deep-sea-derived fungus and identified by Dr. Chunlan Xie in the Third Institute of Oceanography, Ministry of Natural Resources, as previously reported [14]. The chemical structure was confirmed by nuclear magnetic resonance (NMR) spectroscopy (Figures S1 and S2). The purity was above 98%, as determined by HPLC. Ginsenoside Rg1 was purchased from Shanghai R&D Centre for Standardization of Chinese Medicines (Shanghai, China). HPLC grade of acetonitrile and MeOH were purchased from Fisher Scientific Co. (Santa Clara, CA, USA). Ultra-high purified water was prepared using a Milli-Q water-purification system (Millipore Co., Billerica, MA, USA). The other chemicals were purchased from Sinopharm chemical reagent Co., Ltd. (Shanghai, China).

#### 3.2. Animals, Drug Administration and Sampling

Male Sprague-Dawley rats (230–250 g) were provided by SLEK Laboratory Animal Co., Ltd. (Shanghai, China). The animals were housed in an environmentally controlled breeding room for 7 days, and fed with standard laboratory food and water ad libitum, except for a fasting period 12 h prior to experiment. The animal experiments were approved by the Animal Ethics Committee of Shanghai University of Traditional Chinese Medicine (No: PZSHUTCM20107008).

For pharmacokinetic study, 12 rats were randomly assigned into two groups ( $n = 6$ ). BTL-I (2 mg/mL) was dissolved in 5% dimethylsulfoxide, 5% tween-80 and 90% saline. Animals were administered with BTL-I intravenously (2 mg/kg) and orally (40 mg/kg). Venous blood samples were collected into heparinized tubes from the tail at pre-dose and pre-defined times (2 (intravenous only), 5, 15, 30 min and 1, 2, 4, 6, 8, 24 h) after administration. The plasma sample was harvested by centrifuging blood at  $4000 \times g$  for 10 min, and then stored at  $-20$  °C until further preparation.

For the metabolism study, 12 rats were randomly divided into four groups ( $n = 3$ ): plasma, urine, bile and feces groups. Animals were administered with BTL-I orally (50 mg/kg). Blank blood samples were collected before administration and the collected blood samples, at different time points (0.25, 0.5, 1, 2, 4, 8 h), were pooled in equal volumes. The pooled blood samples were centrifuged at  $4000 \times g$  for 10 min to obtain the plasma samples. Urine, bile and feces samples were collected 4 h pre-dose and 0–24 h post-dose. All the samples were stored at  $-20$  °C prior to analysis.

#### 3.3. Sample Preparation

##### 3.3.1. Sample Pretreatment

For pharmacokinetic study, 150  $\mu\text{L}$  methanol-containing IS (100 ng/mL) was added to a portion of 50  $\mu\text{L}$  plasma samples. The mixture was vortexed for 30 s and centrifuged at 13,000 rpm for 10 min to precipitate the proteins. A 150  $\mu\text{L}$  aliquot of the supernatant was mixed with an equal volume of water. After vortexed for 30 s, 5  $\mu\text{L}$  aliquot was analyzed by LC-MS/MS.

For the metabolism study, samples were prepared by protein precipitation to enrich the concentrations of metabolites. 4 mL MeOH was added to 1 mL plasma/1 mL urine/1 mL bile sample in tubes, and then vortexed for 2 min. After that, the mixture was centrifuged at 13,000 rpm for 10 min. The supernatant was transferred to a new tube and evaporated to dryness under a stream of nitrogen at room temperature. The residue was reconstituted by

200  $\mu$ L 50% methanol. Afterwards, it was vortexed for 30 s and centrifuged at 13,000 rpm for 10 min; then, 5  $\mu$ L of the supernatant was analyzed by UHPLC–Q–TOF–MS system. Feces sample (100 mg) was homogenized in 4 folds volumes of saline, the homogenate was extracted with 900  $\mu$ L of methanol, vortexed for 1 min, and centrifuged at 13,000 rpm for 10 min. The supernatant was transferred to a clean tube and evaporated to dryness under a stream of nitrogen. The residue was reconstituted by 200  $\mu$ L 50% methanol, vortexed for 30 s and centrifuged at 13,000 rpm for 10 min. Then 5  $\mu$ L of the supernatant was analyzed by the UHPLC–Q–TOF–MS system.

### 3.3.2. Preparation of Standard Curve and Quality Control (QC) Samples

BTL-I standard was weighed accurately and dissolved in DMSO to prepare stock solution (1 mg/mL). Different concentrations of working solutions (2, 10, 20, 100, 250, 500 ng/mL) were prepared by serial diluting the stock solution with MeOH. The QC samples were prepared similarly to the calibration standard samples with concentration levels of 5, 50, and 400 ng/mL for the low, medium, and high levels, respectively. A working solution of IS at the concentration of 100 ng/mL was prepared in the same manner.

### 3.4. Instrument and LC–MS Conditions

#### 3.4.1. LC–MS/MS Condition

For the pharmacokinetic study, the LC–MS/MS instruments were composed of a Shimadzu LC system equipped with SIL-30AC autosampler LC-30AC binary pump, a CTO-20AC column oven, and a 8050 triple quadrupole mass spectrometer, coupled with an electrospray ionization source. The chromatographic separation was conducted on an ACQUITY UPLC HSS T3 column (100  $\times$  2.1 mm, 1.8  $\mu$ m) with the column temperature was at 40  $^{\circ}$ C. The mobile phases were composed of 0.1% formic acid aqueous solution (A), and acetonitrile (B). The gradient elution was set as follows: 0–0.5 min, 5% B; 0.5–1 min, 5–80% B; 1–3 min, 80% B; 3–5 min, 5% B. The flow rate was set at 0.4 mL/min and the injection volume was set at 5  $\mu$ L.

Source parameters were optimized as follows: interface temperature, 300  $^{\circ}$ C; capillary voltage, 500 V; gas flow, 10 L/min; nebulizer gas, 3 L/min. The multiple reaction monitoring (MRM) mode was selected for quantitative analysis in negative ion mode. The precursor-to-product ion transitions were  $m/z$  423.1–364.1 for BTL-I and  $m/z$  845.6–799.5 for IS.

#### 3.4.2. UHPLC–Q–TOF–MS Condition

For the metabolic profiling study, a Shimadzu 3000 UHPLC system combined with an AB SCIEX 5600 QTOF mass spectrometer (AB Sciex) was applied for the analysis of the metabolites. The chromatographic separation was performed on an ACQUITY UPLC HSS T3 column (100  $\times$  2.1 mm; 1.8  $\mu$ m). The mobile phase consisted of water containing 0.1% formic acid (A), and acetonitrile (B), at a flow rate of 0.4 mL/min. The gradient elution was set as follows: 5–20% B at 0–4 min; 20–40% B at 4–10 min; 40–60% B at 10–15 min; 60–80% B at 15–16 min; 80–95% B at 16–18 min; 95% B at 18–20 min, and finally 5% B at 20–25 min. The injection volume was 2  $\mu$ L. The ESI source parameters were set as follows: spray voltage, 3.0 kV; capillary temperature, 300  $^{\circ}$ C; sheath gas, 40 arb; auxiliary gas, 10 arb; S-Lens voltage, 50 V. The data was acquired over the range of  $m/z$  100–1000 Da.

### 3.5. Method Validation

The method validation was operated according to the Bioanalytical method validation guidance for industry, issued by the United States Food and Drug Administration (FDA). The items of validation included selectivity, carry-over, linearity, precision and accuracy, matrix effect, extraction recovery, and stability.

### 3.5.1. Selectivity and Carry-Over Effect

The selectivity of the method was evaluated by analyzing blank plasma samples from six different individuals, blank plasma spiked with BTL-I and IS, as well as the plasma samples obtained after oral administration.

The carry-over effect was assessed by analyzing two processed, blank plasma samples after the highest concentration point of the calibration curve. The response in the blank sample should be less than 20% of LLOQ for BTL-I and 5% for IS.

### 3.5.2. Linearity and Lowest Limit of Quantitation (LLOQ)

A standard curve was plotted using the ratio of BTL-I peak area/IS peak area against sample concentrations, including six different concentrations. The linearity of the method was assessed by the standard curve. The LLOQ was defined as the concentration at which the ratio of signal to noise was not less than 10.

### 3.5.3. Precision and Accuracy

The precision was expressed as relative standard deviation (RSD%) and the accuracy was relative error (RE%). The intra- and inter-day precision and accuracy were assessed by calculating the LLOQ and QC samples (2, 5, 50, 400 ng/mL) in six replicates on the same day and on three consecutive days, respectively. As required, variation should not exceed 15% for both precision and accuracy.

### 3.5.4. Matrix Effect and Extraction Recovery

The matrix effect and extraction recovery were evaluated by the peak area ratio of BTL-I to IS at three QC levels. The specific evaluating processes were as follows: matrix effect was evaluated by peak area ratio (A) of BTL-I to IS, dissolved in the supernatant of the processed blank plasma, compared with the corresponding peak area ratio (B) of BTL-I to IS, in the pure water at three QC levels. The ratio of A to C was used to evaluate the extraction recovery, where C represented the peak area ratio of BTL-I to IS dissolved in the spiked blank plasma.

### 3.5.5. Stability

The stability of the QC samples was investigated by analyzing the samples under four storage conditions, including being kept at room temperature for 8 h, being stored at  $-20\text{ }^{\circ}\text{C}$  for 15 days, being kept at  $4\text{ }^{\circ}\text{C}$  for 24 h, and being subjected to three freeze–thaw cycles. As required, RSD should not exceed 15%.

## 3.6. Data Analysis

The UHPLC–MS/MS data was acquired and processed using Labsolutions<sup>TM</sup> software (Shimadzu, Japan). The pharmacokinetic parameters, including the area under the concentration–time curve (AUC), clearance (Cl), volume of distribution (Vd), mean residence time (MRT), peak concentration ( $C_{\max}$ ), the time at the peak concentration ( $T_{\max}$ ) and the elimination of half-lives ( $T_{1/2}$ ), were calculated using the PK Solutions 2.0<sup>TM</sup> (Summit Research Services, USA) by a non-compartmental model. The absolute bioavailability was calculated based on the equation:  $F(\%) = (\text{AUC}_{\text{p.o.}} \times \text{Dose}_{\text{i.v.}}) / (\text{AUC}_{\text{i.v.}} \times \text{Dose}_{\text{p.o.}}) \times 100\%$ .

Raw UHPLC–Q-TOF-MS data files were acquired by Analyst software (Version 2.3.1, AB sciex, CA, USA) and imported into Peakview (Version 1.6, AB sciex, CA, USA) software to identify the metabolites of BTL-I. For comprehensive profiling, the whole process was divided into automatic prediction and manual validation. In the step of automatic prediction, the high resolution mass spectrometry data was obtained by inputting the chemical formula and its metabolic intermediates with the ionization set as  $[\text{M} + \text{H}]^+$  or  $[\text{M} + \text{Na}]^+$  and  $[\text{M} - \text{H}]^-$  or  $[\text{M} + \text{HCOO}]^-$ . Then, candidate metabolites were predicted by the software based on the typical metabolic reactions of templates. The step of manual validation was achieved by extracting ion chromatograms to screen candidate metabolites



with the mass tolerance set to 5 ppm. Moreover, MS<sup>2</sup> fragment ions were extracted for the structural confirmation of candidate metabolites.

#### 4. Conclusions

In the present study, *in vivo* pharmacokinetics and the metabolism of BTL-I were investigated. A total of eleven metabolites were detected in rats by UHPLC–Q-TOF-MS. The major metabolic pathways were oxidative and glucuronide conjugation. In the pharmacokinetic study, BTL-I was quickly eliminated from the plasma. The oral bioavailability was approximately 6.29%. The information gained in this study was helpful for us to understand the pharmacological actions of the drug.

**Supplementary Materials:** The following are available online at <https://www.mdpi.com/article/10.3390/md20010011/s1>, Figures S1–S4: <sup>1</sup>H, <sup>13</sup>C, HSQC, and HMBC NMR spectra of BTL-I.

**Author Contributions:** Project coordination and design, G.C. and X.-W.Y.; isolation and purification of the compound C.-L.X.; experiment conduction, data analysis, writing—original draft preparation, writing—review and editing, L.W.; critical revision of the publication was performed by all authors. All authors have read and agreed to the published version of the manuscript.

**Funding:** This study was financially supported by the National Natural Science Foundation of China (21877022), the Medicine-Engineering Cooperation Project of Fudan University (YG2021-015), and Yiwu Research Institute of, Fudan University (21-492).

**Institutional Review Board Statement:** The study was conducted according to the guidelines of Helsinki, and approved by the Institutional Review Board of Animal Ethics Committee of Shanghai University of Traditional Chinese Medicine (No: PZSHUTCM20107008).

**Data Availability Statement:** Data available on request due to restrictions e.g., privacy or ethical.

**Conflicts of Interest:** The authors declare no conflict of interest.

#### References

1. Eggesbo, M.; Botten, G.; Halvorsen, R.; Magnus, P. The prevalence of allergy to egg: A population-based study in young children. *Allergy* **2001**, *56*, 403–411. [[CrossRef](#)] [[PubMed](#)]
2. Bochner, B.S.; Rothenberg, M.E.; Boyce, J.A.; Finkelman, F. Advances in mechanisms of allergy and clinical immunology in 2012. *J. Allergy Clin. Immunol.* **2013**, *131*, 661–667. [[CrossRef](#)] [[PubMed](#)]
3. Karam, M.; Scherzer, R.; Ogbogu, P.U.; Green, T.D.; Greenhawt, M. Food allergy prevalence, knowledge, and behavioral trends among college students—A 6-year comparison. *J. Allergy Clin. Immunol. Pract.* **2017**, *5*, 504–506. [[CrossRef](#)] [[PubMed](#)]
4. Nwaru, B.I.; Hickstein, L.; Panesar, S.S.; Roberts, G.; Muraro, A.; Sheikh, A. Prevalence of common food allergies in Europe: A systematic review and meta-analysis. *Allergy* **2014**, *69*, 992–1007. [[CrossRef](#)] [[PubMed](#)]
5. Freeland, D.M.H.; Manohar, M.; Andorf, S.; Hobson, B.D.; Zhang, W.; Nadeau, K.C. Oral immunotherapy for food allergy. *Semin. Immunol.* **2017**, *30*, 36–44. [[CrossRef](#)] [[PubMed](#)]
6. Carroll, A.R.; Copp, B.R.; Davis, R.A.; Keyzers, R.A.; Prinsep, M.R. Marine natural products. *Nat. Prod. Rep.* **2021**, *38*, 362–413. [[CrossRef](#)] [[PubMed](#)]
7. Reber, L.L.; Marichal, T.; Mukai, K.; Kita, Y.; Tokuoka, S.M.; Roers, A.; Hartmann, K.; Karasuyama, H.; Nadeau, K.C.; Tsai, M.; et al. Selective ablation of mast cells or basophils reduces peanut-induced anaphylaxis in mice. *J. Allergy Clin. Immunol.* **2013**, *132*, 881–888. [[CrossRef](#)] [[PubMed](#)]
8. Gao, Y.Y.; Liu, Q.M.; Liu, B.; Xie, C.L.; Cao, M.J.; Yang, X.W.; Liu, G.M. Inhibitory activities of compounds from the marine actinomycete *Williamsia* sp. MCCC 1A11233 variant on IgE-mediated mast cells and passive cutaneous anaphylaxis. *J. Agric. Food Chem.* **2017**, *65*, 10749–10756. [[CrossRef](#)] [[PubMed](#)]
9. Xing, C.P.; Chen, D.; Xie, C.L.; Liu, Q.; Zhong, T.H.; Shao, Z.; Liu, G.; Luo, L.Z.; Yang, X.W. Anti-food allergic compounds from *Penicillium griseofulvum* MCCC 3A00225, a deep-sea-derived fungus. *Mar. Drugs* **2021**, *19*, 224. [[CrossRef](#)] [[PubMed](#)]
10. Kiriyama, N.; Nitta, K.; Sakaguchi, Y.; Taguchi, Y.; Yamamoto, Y. Studies on the metabolic products of *Aspergillus terreus*. III. Metabolites of the strain IFO 8835. (1). *Chem. Pharm. Bull.* **1977**, *25*, 2593–2601. [[CrossRef](#)]
11. Zhang, Y.Y.; Zhang, Y.; Yao, Y.B.; Lei, X.L.; Qian, Z.J. Butyrolactone-I from coral-derived fungus *Aspergillus terreus* attenuates neuro-inflammatory response via suppression of NF-κB pathway in BV-2 cells. *Mar. Drugs* **2018**, *16*, 202. [[CrossRef](#)] [[PubMed](#)]
12. Hosoi, T.; Uchiyama, M.; Okumura, E.; Saito, T.; Ishiguro, K.; Uchida, T.; Okuyama, A.; Kishimoto, T.; Hisanaga, S. Evidence for cdk5 as a major activity phosphorylating tau protein in porcine brain extract. *J. Biochem.* **1995**, *117*, 741–749. [[CrossRef](#)] [[PubMed](#)]
13. Kitagawa, M.; Higashi, H.; Suzuki-Takahashi, I.; Segawa, K.; Hanks, S.K.; Taya, Y.; Nishimura, S.; Okuyama, A. Phosphorylation of E2F-1 by cyclin A-cdk2. *Oncogene* **1995**, *10*, 229–236. [[PubMed](#)]

14. Liu, Q.M.; Xie, C.L.; Gao, Y.Y.; Liu, B.; Lin, W.X.; Liu, H.; Cao, M.J.; Su, W.J.; Yang, X.W.; Liu, G.M. Deep-sea-derived butyrolactone I suppresses ovalbumin-induced anaphylaxis by regulating mast cell function in a murine model. *J. Agric. Food Chem.* **2018**, *66*, 5581–5592. [[CrossRef](#)] [[PubMed](#)]
15. Ahn, S.; Jang, D.M.; Park, S.C.; An, S.; Shin, J.; Han, B.W.; Noh, M. Cyclin-dependent kinase 5 inhibitor butyrolactone I elicits a partial agonist activity of peroxisome proliferator-activated receptor  $\gamma$ . *Biomolecules* **2020**, *10*, 275. [[CrossRef](#)] [[PubMed](#)]
16. He, C.; Wan, H. Drug metabolism and metabolite safety assessment in drug discovery and development. *Expert. Opin. Drug Metab. Toxicol.* **2018**, *14*, 1071–1085. [[CrossRef](#)] [[PubMed](#)]
17. Shikov, A.N.; Flisyuk, E.V.; Obluchinskaya, E.D.; Pozharitskaya, O.N. Pharmacokinetics of Marine-Derived Drugs. *Mar. Drugs* **2020**, *18*, 557. [[CrossRef](#)]
18. An, X.; Feng, B.M.; Chen, G.; Chen, S.F.; Bai, J.; Hua, H.M.; Wang, H.F.; Pei, Y.H. Isolation and identification of phase I metabolites of butyrolactone I in rats. *Xenobiotica* **2017**, *47*, 236–244. [[CrossRef](#)] [[PubMed](#)]



## Article

# Actinomycin X2, an Antimicrobial Depsipeptide from Marine-Derived *Streptomyces cyaneofuscatus* Applied as a Good Natural Dye for Silk Fabric

Wei Chen <sup>1</sup>, Kaixiong Ye <sup>1</sup>, Xiaoji Zhu <sup>2</sup>, Huihui Zhang <sup>1</sup>, Ranran Si <sup>3</sup>, Jianing Chen <sup>1</sup>, Zijun Chen <sup>1</sup>, Kaili Song <sup>2,4</sup>, Zhicheng Yu <sup>2,4</sup> and Bingnan Han <sup>2,\*</sup>

<sup>1</sup> Department of Development Technology of Marine Resources, College of Life Sciences and Medicine, Zhejiang Sci-Tech University, Hangzhou 310018, China; 201920201070@mails.zstu.edu.cn (W.C.); kaixiongye@163.com (K.Y.); huihuizhang09@163.com (H.Z.); 202020801006@mails.zstu.edu.cn (J.C.); 202020801010@mails.zstu.edu.cn (Z.C.)

<sup>2</sup> Engineering Research Center for Eco-Dyeing & Finishing of Textiles, Zhejiang Sci-Tech University, Hangzhou 310018, China; 201920302006@mails.zstu.edu.cn (X.Z.); kailisong@zstu.edu.cn (K.S.); yuzhicheng8@aliyun.com (Z.Y.)

<sup>3</sup> School of Materials Science and Engineering, Zhejiang Sci-Tech University, Hangzhou 310018, China; Siranran95@163.com

<sup>4</sup> Key Laboratory of Advanced Textile Materials and Manufacturing Technology, Ministry of Education, Zhejiang Sci-Tech University, Hangzhou 310018, China

\* Correspondence: hanbingnan@zstu.edu.cn; Tel.: +18057133438

**Citation:** Chen, W.; Ye, K.; Zhu, X.; Zhang, H.; Si, R.; Chen, J.; Chen, Z.; Song, K.; Yu, Z.; Han, B. Actinomycin X2, an Antimicrobial Depsipeptide from Marine-Derived *Streptomyces cyaneofuscatus* Applied as a Good Natural Dye for Silk Fabric. *Mar. Drugs* **2022**, *20*, 16. <https://doi.org/10.3390/md20010016>

Academic Editors: Yonghong Liu and Xuefeng Zhou

Received: 7 December 2021

Accepted: 20 December 2021

Published: 23 December 2021

**Publisher's Note:** MDPI stays neutral with regard to jurisdictional claims in published maps and institutional affiliations.



**Copyright:** © 2021 by the authors. Licensee MDPI, Basel, Switzerland. This article is an open access article distributed under the terms and conditions of the Creative Commons Attribution (CC BY) license (<https://creativecommons.org/licenses/by/4.0/>).

**Abstract:** Actinomycins as clinical medicine have been extensively studied, while few investigations were conducted to discover the feasibility of actinomycins as antimicrobial natural dye contributing to the medical value of the functional fabrics. This study was focused on the application of actinomycin X2 (Ac.X2), a peptide pigment cultured from marine-derived *Streptomyces cyaneofuscatus*, in the dyeing and finishing of silk fabric. The dyeing potential of Ac.X2 with silk vs. cotton fabrics was assessed. As a result, the silk fabric exhibited greater uptake and color fastness with Ac.X2. Through Fourier transform infrared spectroscopy (FT-IR), scanning electron microscopy (SEM), and X-ray diffraction (XRD) analyses, some changes of chemical property for the dyed fabric and Ac.X2 were studied. The silk fabric dyed with Ac.X2 exhibited good UV protection ability. The antibacterial properties of dyed and finished silk were also evaluated, which exhibited over 90% antibacterial activity even after 20 washing cycles. In addition, the brine shrimp assay was conducted to evaluate the general toxicity of the tested fabric, and the results indicated that the dyed silk fabrics had a good biological safety property.

**Keywords:** actinomycin X2; microbial pigments; dyeing; silk; antibacterial properties

## 1. Introduction

Natural pigments, a surprisingly indispensable part of human life, play an important role in the food, cosmetic, medical treatment, and textile industries [1–3]. Since the early 20th century, a number of active natural pigments have been identified from marine sources, such as marine invertebrates, algae, and microbes. The major categories of these pigments can be divided by chemical structures, either as carotenoids, indole derivatives (quinones and violacein), alkaloids (prodiginines and tambjamins), polyenes, macrolides, peptides, or terpenoids [4–10]. Many of these pigments have a variety of biological activities, including antibacterial, antioxidant, and anti-inflammatory [11–13].

During the last few decades, a range of synthetic functional chemicals such as triclosan, metallic salts, quaternary ammonium-based products, etc. [14–17], have been developed and widely used as finishing agents for making antimicrobial silk fabric. However, these products are known to have significant limitations, such as toxic side effects, skin irritation, and effluent problems [18]. Many nature dyes with antimicrobial activity have been applied

to silk textiles such as indigoids, prodigiosins, curcumins, and tannins [19–21]. However, most of these natural dyes applied to dyeing and finishing of silk fabrics are characterized by poor wash fastness, poor stability, and less sustainable use of bio-resources [22–24].

Actinomycetes, as a rich source of various secondary metabolites, have drawn more and more attention in the field of biomedicine and biotechnology [25–27]. Actinomycins, a class of cyclic depsipeptides, featured a phenoxazinone chromophore. Apart from their variety of biological properties, including antibacterial, antiviral, and antitumor effects [28–31], they are characterized by bright orange-yellow color pigments. During the last few years, the interest in actinomycins as clinical medicine has been gradually increased [32–35], while few investigations were conducted to discover the feasibility of actinomycins as antimicrobial natural dye contributing to the medical value of the functional fabrics.

In this study, a strain of *Streptomyces cyaneofuscatus* isolated from the cyanobacterium *Lyngbya* sp. collected from Nanji Island, China, was cultured and its main secondary metabolite actinomycin X2 was chemically and biologically characterized. This investigation was focused on the dyeing potential of Ac.X2 as a bio-colorant for silk fabric by assessing of dyeing performance of silk vs. cotton fibers. Through FT-IR, SEM, and XRD analysis, some changes of functional group with silk fabric and Ac.X2 were also studied. Finally, the antibacterial potential, UV protection ability, and the toxicity of the dyed silk fabrics were also evaluated. The outcome of this study has supported that Ac.X2 could be applied as an active natural dye for silk fabric contributing to the excellent wash fastness, strong stability as well as great antibacterial properties of the dyed silk.

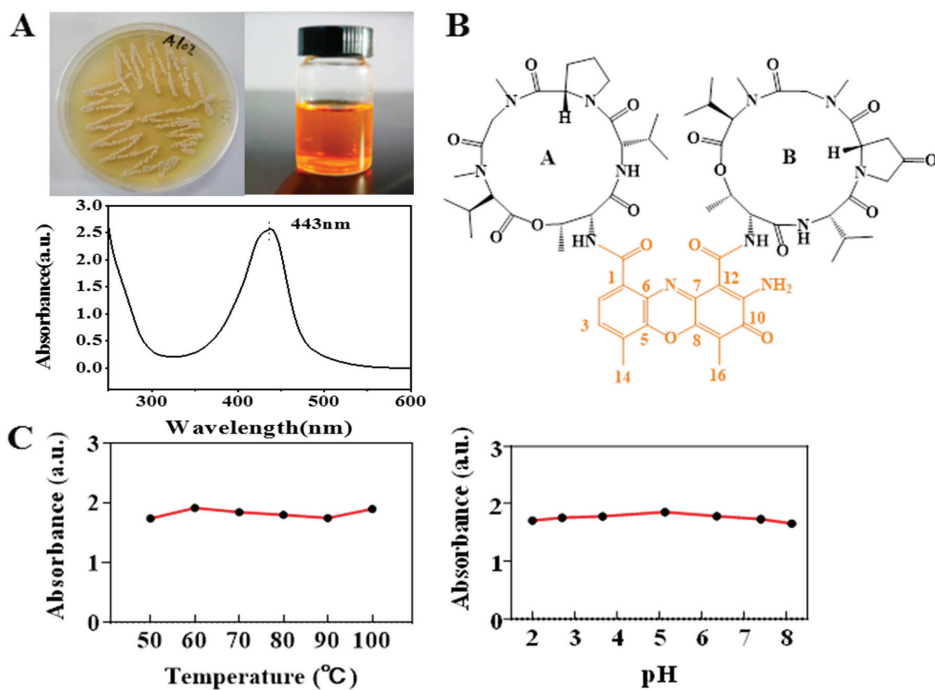
## 2. Results and Discussion

### 2.1. Isolation and Identification of Pigment-Producing Actinomycetes

Actinomycetes are well known for the production of chemically and biologically diverse secondary metabolites, such as antibiotics and pigments. A strain of actinomycete producing bright orange-yellow pigment was recently isolated from marine cyanobacteria collected from Nanji Island, China. The neighbor-joining phylogenetic tree (Figure S1), based on 16S rRNA gene sequences, revealed that strain fell within the clade comprising the type strains of species of the genus *Streptomyces*, clustering coherently with the type strain of *Streptomyces cyaneofuscatus* with a sequence similarity of 99.6%. Based on both morphological and molecular characteristics, this strain was identified as *Streptomyces cyaneofuscatus* and deposited at the China General Microbiological Culture Collection Center (CGMCC) with the accession number.

### 2.2. Fermentation and Characterization of Actinomycin X2

This strain was cultured for 7 days (pH 7.0, temperature 28 °C, rotate speed 160 rpm) in a 500 mL Erlenmeyer flask containing 200 mL ISP4 medium. A total of 200 mL fermentation broth was extracted by ethyl acetate and obtained crude orange-yellow pigment (Figure 1A). The extraction of the culture filtrates produced yields of crude pigment at  $98.21 \pm 2.68$  mg/L with a total fermentation broth of 2 L. Through a preparative liquid chromatography, a pure orange-yellow pigment as the only major component was obtained. It was estimated that the ethyl acetate extract consists of 19.7% of pure actinomycin. This pigment was analyzed by high-resolution mass spectrometry presenting the molecular weight  $m/z$  1269.6173 ( $[M + H]^+$ , calcd:1269.62) (Figure S2). Combining  $^1\text{H}$  NMR and  $^{13}\text{C}$  NMR analysis (Figure S3), in comparison with the previously reported data [36], the structure of this pigment was confirmed to be actinomycin X2 (Ac.X2) (Figure 1B), displaying a maximum UV absorption peak at 443 nm (Figure 1A). Ac.X2 exhibited excellent thermal stability, acid and alkali resistance (Figure 1C). The antibacterial test of Ac.X2 using the paper diffusion method showed a strong inhibition effect with inhibition zones of 20 mm on *Staphylococcus aureus* [36] with a weak effect on *Escherichia coli*. (Figure S4).



**Figure 1.** (A) The colony grew on G1 agar at 28 °C for 14 days; crude pigment of the liquid culture; The UV-visible spectra of actinomycin X2. (B) Structure of Ac.X2. (C) Temperature and pH stability of Ac.X2.

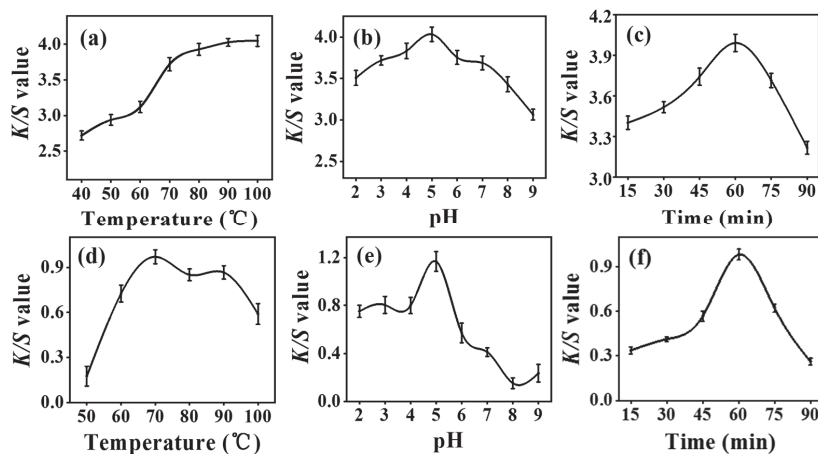
### 2.3. Characterization of Dyed Textile

#### 2.3.1. Optimization of Dyeing Conditions

The exploration of optimal dyeing conditions of temperature, pH, and time was based on the method of the one-factor-at-a-time optimization technique (O.F.T.) evaluated by reflectance spectroscopy ( $K/S$ ) [37]. The results of dyeing temperature optimization of silk fabric indicated that the color strength increased consistently with increasing temperature from 40 to 100 °C (Figure 2a). In contrast, the color strength of dyed cotton fabric tended to decrease after reaching the maximum at 70 °C (Figure 2d). It can be attributed to that the high temperature leading to the damage of the cellulose molecule [38]. The results of dyeing pH optimization exhibited that both silk and cotton fabric achieved the highest  $K/S$  value at pH 5 (Figure 2b,e). The results of dyeing time optimization showed that both silk and cotton fabric reached the maximum color strength when the dyeing process lasted for 60 min, and the  $K/S$  value decreased in contrast with further increase in dyeing time (Figure 2c,f). Overall, the silk fabric presented greater color strength dyed with Ac.X2 than the cotton fabric under each optimized condition.



#### 2.3.2. Color Characteristics of Dyed Fabrics

The corresponding color strengths (expressed by  $K/S$  value) and the CIELAB color coordinates were listed for silk fabric vs. cotton fabric (Tables 1 and S1). As for the colors, it indicated that the values of the coordinates  $a^*$  and  $b^*$  were higher for the dyed silk fabric, suggesting that dyed silk fabrics obtained more red and yellow character [39]. The color difference ( $\Delta E^*$ ) between the dyed fabrics exhibited that the dyed silk fabric had a better building-up capability than the cotton toward the nature dye Ac.X2. Overall, the silk fabric presented a much better uptake value of Ac.X2 with exhaustion (85.43%) compared to the value of 20.76% for the cotton fabric.



**Figure 2.** Effect of dyeing temperature on  $K/S$  value of (a) dyed silk; (d) dyed cotton. Effect of dye bath pH on  $K/S$  value of (b) dyed silk; (e) dyed cotton. Effect of dyeing time on  $K/S$  value of (c) dyed silk; (f) dyed cotton.

**Table 1.** Color strength, colorimetric parameters, and color difference ( $\Delta E^*$ ) of o.w.f 1%-dyed fabric samples under previous dyeing process.

| Fabric Sample | Apparent Color  | $K/S$ Value | $L^*$  | $a^*$ | $b^*$ | $\Delta E^*$ | Percentage Exhaustion (%) |
|---------------|---|-------------|--------|-------|-------|--------------|---------------------------|
| Silk          |   | 4.0740      | −15.57 | 14.41 | 55.36 | 64.10        | 85.43%                    |
| Cotton        |  | 1.1094      | −10.58 | 10.46 | 38.51 | 50.44        | 20.76%                    |

$K/S$ : Color strength,  $L^*$ : lightness,  $a^*$ : (+value = red, −value = green)  $b^*$ : (+value = yellow, −value = blue).




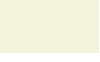
As seen in Table 2, the color shades of dyed silk showed a slight decline after 5 laundering cycles, whereas cotton fabrics had poor color retention. Moreover, it was also noted that the  $\Delta K/S$  of cotton changed obviously after 5 laundering cycles but silk fabrics showed little difference, which implicated that the silk fabric might have a much stronger molecular interaction with Ac.X2 compared to the cotton fabric. Further, an N, N-Dimethylformamide (DMF) stripping study was performed to determine the interacting strength of Ac.X2 with silk vs. cotton fabrics. The dyed silk fabric withstood the treatment of DMF much stronger than the dyed cotton, which displayed by the  $\Delta K/S$  values in Table 2. This result suggested that intermolecular covalent bonding may occur during the dyeing process of Ac.X2 with silk fabric [24,40].

### 2.3.3. Fourier Transform Infrared Spectroscopy (FT-IR) Analysis

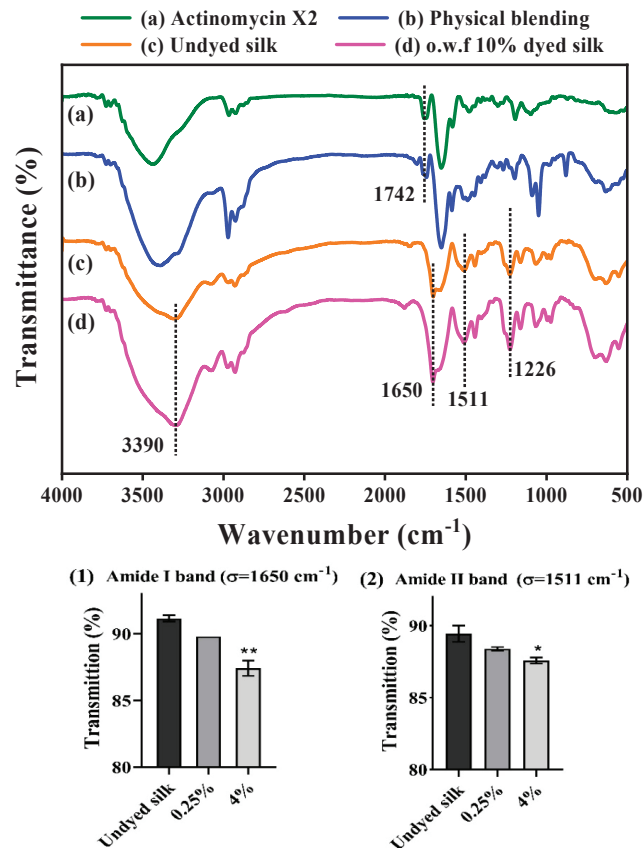
The structural functionalization of the dyed silk in comparison to the undyed silk and Ac.X2 was analyzed by the FT-IR technique (Figure 3). The FT-IR analysis of the Ac.X2 and physical blending material revealed the appearance of an absorption band at  $1742\text{ cm}^{-1}$ , characteristic of the C=O ester stretch band [41], but this band was not observed in the spectra of the dyed silk fabrics, which implicated that the ester functionalization of Ac.X2 did not exist in the dyed silk fabrics. The absorption spectra of the undyed silk and the dyed silk with o.w.f 10% Ac.X2 exhibited a similar vibration pattern, in which a major peak at  $3279\text{ cm}^{-1}$ , assigned to the -N-H stretching vibration, C=O (amide I band indicative of  $\beta$ -sheet) at  $1650\text{ cm}^{-1}$  and N-H deformation (amide II band indicative of  $\beta$ -sheet) at

1511  $\text{cm}^{-1}$  were observed in both dyed and undyed silk fabrics [42–44]. However, the absorption intensity of the above characteristic signals of peptide functionalities increased in the dyed sample compared to the undyed silk fabric (Figure 3(1,2)).

**Table 2.** Ac.X2-dyed silk and cotton experienced DMF extraction and after 5 times laundering, respectively.

| Fabric | After 5 Times Laundering  |           | $\Delta K/S$ | After DMF Extraction  |           | $\Delta K/S$ |
|--------|---|-----------|--------------|---|-----------|--------------|
|        | A.C.  | K/S Value |              | A.C.  | K/S Value |              |
| Silk   |  | 3.7444    | −0.3296      |  | 3.7529    | −0.3211      |
| Cotton |  | 0.0464    | −1.063       |  | 0.0689    | −1.0405      |

A.C. = Apparent color.



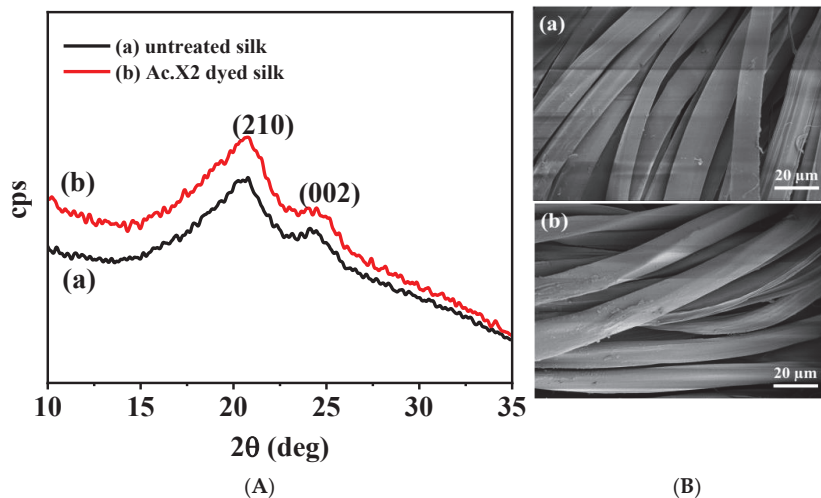
**Figure 3.** FT-IR images of (a) actinomycin X2, (Ac.X2), (b) physical blending, (c) undyed silk, (d) o.w.f 10%-dyed silk fabric. Transmittance of (1) amide I band, (2) amide II band. \*  $p < 0.05$ , \*\*  $p < 0.01$ .

### 2.3.4. X-ray Diffraction (XRD) Analysis and Scanning Electron Microscopy (SEM) Analysis

XRD analysis of Ac.X2-dyed silk and untreated silk was carried out for the purpose of determining the change in the secondary structure of silk [45], as shown in Figure 4A.



The similar diffraction patterns of the  $2\theta$  angles were observed in the dyed and undyed silk fabrics, in which two obvious crystalline peaks characteristics of the protein  $\beta$ -sheet structure, were labeled by the (210) and (002) planes at  $2\theta$  of  $19.4^\circ$  and  $24.2^\circ$ , appeared, respectively [46,47]. As the results, it also suggested that the dyeing process of Ac.X2 mainly occurred in the amorphous area of the silk fiber rather than the crystalline area.



**Figure 4.** (A) XRD patterns of undyed and o.w.f 10% Ac.X2-dyed silk fabrics. (B) SEM images (1000X), (a) undyed silk fabric, (b) Ac.X2-dyed silk fabric.







The effect of the coloration process on the silk fabric morphology was examined by SEM micrograph. As shown in Figure 4B, both dyed and undyed silk fabrics were observed to be smooth, uniform, and free from roughness with no particle deposition and surface irregularity in morphology. Therefore, it might implicate the penetration of the Ac.X2 into the fiber structure rather than a surface deposition, resulting in strong fastness properties of the dyed silk fabric.

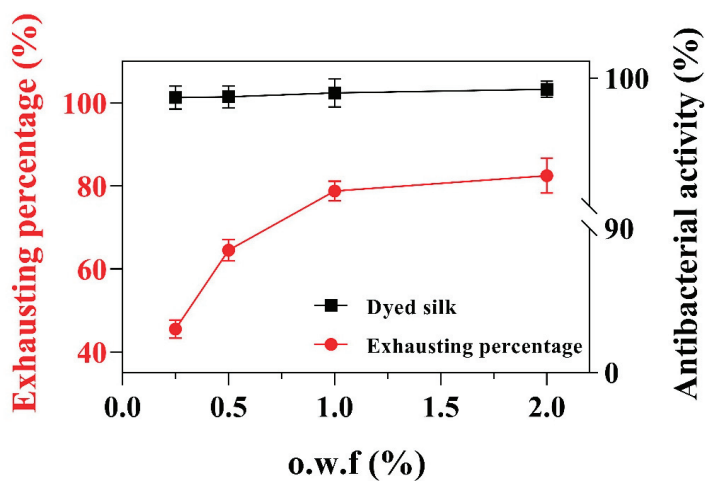
## 2.4. Fastness and Functional Finishing Properties of the Silk Fabrics Dyed with Ac.X2

### 2.4.1. Color Strength Associated with Dye Concentration

To further explore the dyeing performance of Ac.X2 on the silk fabric associated with their antibacterial activities, six different dye concentrations of Ac.X2 (o.w.f 0.1%–4%) were evaluated. As seen in Table 3, the color strength of dyed silk fabrics was increased with dye concentration in a reasonably good manner. From the colorimetric data ( $a^*/b^*$  plots) depicted in Table 3, it can be seen that the yellow shade from Ac.X2 produced varying color saturation with increasing  $a^*$  and  $b^*$  values due to the improving adsorption of dyed silk fabric, and their shades present reddish-yellow had a little shift toward red-coordinate in the yellow-red zone of color space. The adsorption quantity increased with increasing initial concentration, but the color depth of dyed silk had little augmentation when its initial concentration exceeded 1% o.w.f (Figure 5). These results are consistent with those reported by Zhou et al. [48], who stated that the uptake of *Rheum emodi* by silk displayed the extent of exhaustion over 40%, but no increase in its adsorption when the concentration exceeded 4% o.w.f.

**Table 3.** The effect of dye concentration on color characteristics of dyed silk fabric.

| o.w.f. | Apparent Color  | K/S Value | $L^*$  | $a^*$ | $b^*$ |
|--------|---|-----------|--------|-------|-------|
| 0.1    |  | 0.3657    | −5.17  | 0.66  | 24.85 |
| 0.25   |  | 0.6665    | −6.07  | 0.82  | 28.86 |
| 0.5    |  | 1.1644    | −8.51  | 2.26  | 35.37 |
| 1      |  | 4.0740    | −15.57 | 14.41 | 55.36 |
| 2      |  | 5.3555    | −16.37 | 18.37 | 57.4  |
| 4      |  | 5.8977    | −20.71 | 18.7  | 57.62 |



**Figure 5.** UPF (bars) and UVA transmittance (black dots) for undyed and different dye concentrations of Ac.X2-dyed silk fabrics. Bars are means of three measurements. Horizontal black line represents the UVA transmittance threshold established by the European standard for sun protective clothing (\*\*  $p < 0.01$ ).

#### 2.4.2. Color Fastness

Silk fabrics are subjected to frequent washing, rubbing, and perspiring during their usage. Table 4 shows the color fastness (wash, rub, and perspiration fastness) results of the o.w.f 1% Ac.X2-dyed silk fabrics under the optimum dyeing process. The fastness ratings on a gray scale ranging from 1 to 5 were evaluated (1 for bad, 2 for fairly good, 3 for good, 4 for very good, and 5 for excellent results). The grade of color change to wash was “very good”

(4), and the color staining to the wash of the dyed silk fabrics was rated as “excellent” (5). As shown in Table 4, the perspiration and rub fastness of silk fabric dyed in the optimum condition were considered good to excellent range, quite satisfactory for industrial-scale dyeing, with a general rating of 4–5 on a gray scale. Owing to the absence of direct affinity between most natural dyes and fibers, many environment-unfriendly mordants (e.g., alum, copper sulfate, and ferrous sulfate) are needed to help to obtain good fastness for natural dyes with fabrics [42,49,50]. However, Ac.X2 exhibited excellent fastness to silk without using mordant, which may indicate good potential for industrial application.

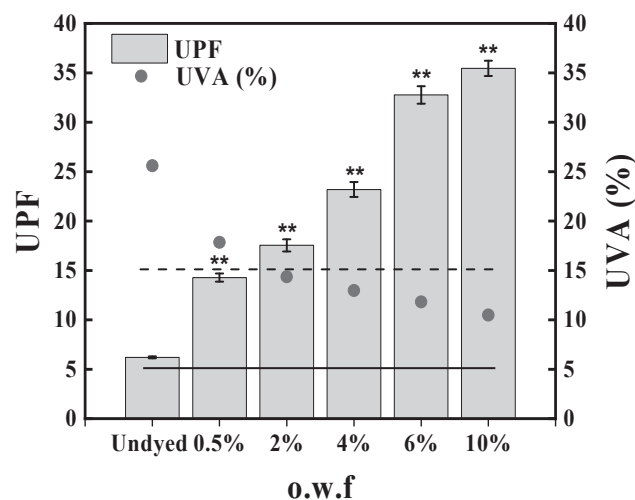
**Table 4.** Fastness properties of silk fabrics dyed with Ac.X2.

| Wash Fastness |      |      | Rub Fastness |     | Perspiration Fastness |      |      |        |      |      |
|---------------|------|------|--------------|-----|-----------------------|------|------|--------|------|------|
|               |      |      |              |     | Acid                  |      |      | Alkali |      |      |
| c.c.          | s.s. | s.c. | Dry          | Wet | c.c.                  | s.s. | s.c. | c.c.   | s.s. | s.c. |
| 4             | 5    | 5    | 4–5          | 4   | 4–5                   | 3–4  | 4    | 4–5    | 3–4  | 4    |

c.c. = color change s.s. = color staining of silk s.c. = color staining of cotton.

#### 2.4.3. UV Protection Performance

In order to avoid or limit the health risks such as sunburn, premature aging, allergies, and skin cancers, it is important to reduce UV ray exposure with clothing made of protective materials. UV protection levels of silk fabric samples dyed with different dye concentrations are presented in Figure 6. As regards the UPF, the dyed silk fabric over 0.5% o.w.f reaches values corresponding to the good protection category in the undyed fabrics. However, silk fabrics dyed with Ac.X2 showed a poor protection level for UVA transmittance with values below 5% (Figure 6). This is the threshold above which photosensitive skin disorders, such as chronic actinic dermatitis and solar urticaria, can be aggravated according to the European standard for sun protective clothing and also the Chinese National standard GB/T18830-2009 [51,52]. Silk fabrics dyed with baicalin extract dye and curcumin also exhibited good UPF values, which can be classified as a ‘very good’ scale [20]. Similar results were found for marigold extract dye, honeysuckle extracts, and Chinese tallow leaves extract on wool fabrics, and chitosan mordanted green tea dye on cotton fabrics [53–55]. In this perspective, it can be concluded that dyed fabrics are more protective than undyed ones and the protection level rises with the increase in dye concentration.

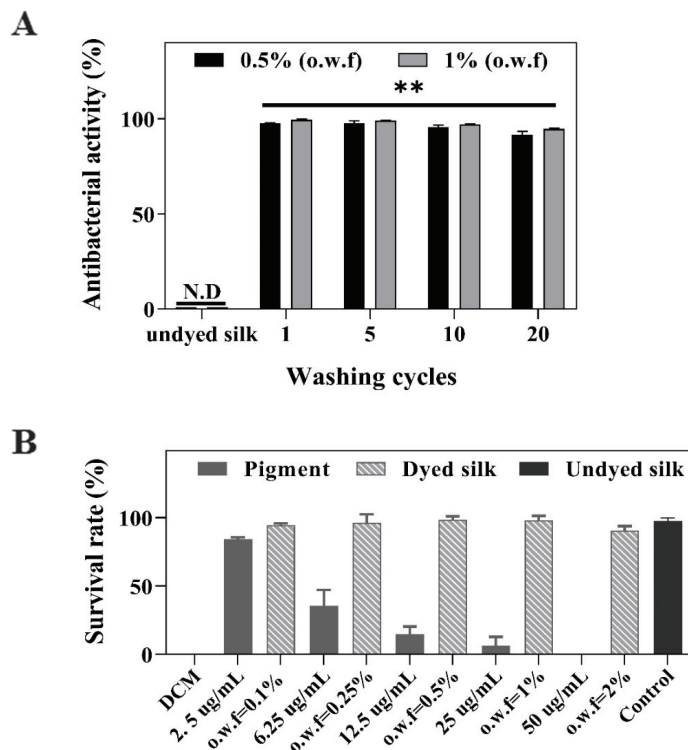


**Figure 6.** Antibacterial activity and exhausting percentage of different o.w.f-dyed silk against *Staphylococcus aureus* tested by GB/T 20944.3-2008 method.

#### 2.4.4. Antibacterial Activity and Toxicity of Brine Shrimp

Silk fabrics are especially susceptible to microbial growth with poor antibacterial activity, and Ac.X2 has been investigated to have good antibacterial potential. Thus, two methods of AATCC 100-2012 (Figure S7) and GB/T 20944.3-2008 (Figure 5) were used to evaluate the antibacterial properties accomplished by the dyed silk fabrics. The results indicated that both methods exerted high antibacterial activity over 95% against *S. aureus* of the 0.25–2% o.w.f processed fabrics. The adsorption of Ac.X2 on silk fabrics is an alternative way to introduce the antibacterial functionality of marine pigment for their use in protective clothing and medical textiles.

The bacteriostasis rate of the 0.5% (o.w.f)- and 1% (o.w.f)-dyed silk after long washing cycles test was presented in Figure 7A, and all samples exhibited over 90% antibacterial activity even after 20 washing cycles. The results suggested that the Ac.X2-dyed fabrics had durable antibacterial properties compared to the undyed silk, which indicates the application of Ac.X2 in silk fabric solves the limitations in terms of efficacy and durability of natural antimicrobial agents [6]. The investigation of brine shrimp toxicity was also conducted to explore the primary safety of dyed silk fabrics. The lethality assay of brine shrimp *A. salina* was developed by Vanhaecke et al. [56], which was suggested to evaluate the toxicity of compounds [57–59]. It showed that the pigment concentration negatively correlated with the survival rate of *A. salina*. In contrast, *A. salina* still had a high survival rate in the same amount of pigment dyed with silk fabrics groups (Figure 7B). It may implicate that the safety of the dyed fabric was almost equivalent to the normal fabric.



**Figure 7.** (A) Antibacterial activity of o.w.f 0.5%- and o.w.f 1%-dyed silk samples against *Staphylococcus aureus* tested by GB/T 20944.3-2008 method after repeated laundering. (\*\*  $p < 0.01$ ), N.D = No detect (B) The survival rate of *A. salina* with different pigment concentrations and the same amount of Ac.X2-dyed silk.

The public's mature demand in recent times boomed the silk textile industry for the use of natural colorants, while the synthetic colorants with high dye exhaustion over 80% [60] have even been withdrawn from external usage due to its apparent hazards. On the other hand, the pigments such as *Terminalia catappa*, *Vaccinium Corymbosum* L. derived from raw plant materials are known to have low absorption (10%) vs. Ac.X2 (85.43%) in the silk fabric dyeing process and poor color fastness range 1–2 compared to microbial pigment Ac.X2 with the color fastness range of 4–5 [61,62]. More importantly, some natural pigments such as *Carthamus tinctorius* L. had little antibacterial activity of 29% against *S. aureus* in the absence of synthetic functional chemicals, even though the AgNPs-treated fabrics dyed with caffeic acid was highly durable as more than 90% inhibition after 10 washing cycles [63], Ac.X2 has good antibacterial activity over 90% against *S. aureus* at the low concentration of 0.5% without any additional finishing agents.

### 3. Materials and Methods

#### 3.1. Textile Material

The crepe de Chine silk fabric (warp and weft count, 23 dtex/2; warp density 54 threads/cm, weft density 41 threads/cm; 70 g/m<sup>2</sup> weight), the scoured and bleached cotton (warp 180 dtex, weft 180 dtex; warp density 93 yarns per inch, weft density 41 yarns per inch; 240 g/m<sup>2</sup> weight), were obtained from a local ordinary mill (High Fashion Co., Ltd., Hangzhou, China).

#### 3.2. Strain Isolation

Actinomycetes producing yellow pigment were isolated from cyanobacteria (Lyngbya species) collected from the shore of Nanji Island, China. Weighed 1 g of fresh cyanobacteria and cut it into small pieces (5 mm length). The cut samples were mixed with 10 mL ddH<sub>2</sub>O and diluted 10-fold to the concentration of 10<sup>-1</sup>, 10<sup>-2</sup>, 10<sup>-3</sup>, respectively. Using Gauze's No. 1 (G1) agar medium as selective medium consisting of soluble starch 2.0%, KNO<sub>3</sub> 0.1%, K<sub>2</sub>HPO<sub>4</sub> 0.05%, MgSO<sub>4</sub>·7H<sub>2</sub>O 0.05%, NaCl 0.05%, FeSO<sub>4</sub>·7H<sub>2</sub>O 0.001%, sea salt 2.0%. Plates were incubated at 28 °C for 7 days [64].

#### 3.3. Identification of Pigment-Producing Actinomycetes

##### 3.3.1. Morphological Studies

The pigment-producing strain was cultured on G1 at 28 °C for 14 days. Colony characteristics, including shape, size, and pigment-producing time were recorded. The morphological characteristics of spores and mycelia were observed by a light microscope (Nikon ECLIPSE E100, TKY, Japan).

##### 3.3.2. Molecular Studies

Genomic DNA of pigment-producing bacteria was extracted by a bacterial DNA kit (Beijing Biomed Gene Technology Co., Ltd., Beijing, China). Universal primers 27F and 1492R were used to amplify the 16S rDNA. Polymerase chain reaction (PCR) was performed in 25 µL reaction containing 0.5 µL DNA template, 0.5 µL of each forward and reverse primers, 12.5 µL 2× Mix (CoWin Biosciences, Jiangsu, China) and 11 µL deionized water, and the following conditions: initial denaturation at 94 °C for 5 min, 30 cycles of denaturation (94 °C, 1 min), annealing (55 °C, 1 min), and elongation (72 °C, 1 min 15 s), and final elongation at 72 °C for 10 min. BLAST of the NCBI database was used to carry out multiple sequence alignment. The phylogenetic tree of pigment-producing bacteria was constructed by the neighbor-joining method of MEGA 5.0.

##### 3.4. Extraction and Purification of Pigment

Single colonies growing in G1 agar medium were transferred to a 250 mL Erlenmeyer flask containing 50 mL of seed medium (with the same ingredients as G1) and incubated at 28 °C and 160 rpm for 8 days. Transfer 1 mL of seed solution to a 500 mL Erlenmeyer flask containing 200 mL ISP4 medium (10 g/L soluble starch, 1 g/L MgSO<sub>4</sub>·7H<sub>2</sub>O, 2 g/L peptone,

1 mg/L  $\text{FeSO}_4 \cdot 7\text{H}_2\text{O}$ , 1 g/L  $\text{K}_2\text{HPO}_4$ , 1 g/L NaCl, 2 g/L  $\text{CaCO}_3$ , 1 mg/L  $\text{MnCl}_2 \cdot 7\text{H}_2\text{O}$ , 1 mg/L  $\text{ZnSO}_4 \cdot 7\text{H}_2\text{O}$ , 20 g/L sea salt, pH = 7.2–7.4) and fermented for 7 days at 28 °C and 160 rpm. After the fermentation, the fermentation broth was centrifuged (8000 rpm at 4 °C) for 10 min by an ultrafast centrifuge (BIORIDGE TG16, Shanghai, China) to collect the supernatant. Extract with ethyl acetate:fermentation broth = 1:1 volume ratio. Repeat this step three times. The extraction solution was reduced to concentrate at room temperatures, and the pigment extract was obtained. The crude pigment extract was dissolved in methanol and filtered through a membrane of 0.22  $\mu\text{m}$ . The pigment was purified by HPLC with a column of YMC-Pack ODS-A (250  $\times$  20 nm), using 75% acetonitrile as a mobile phase.

### 3.5. Characterization of Pigment

#### 3.5.1. Temperature Stability

Take 6 tubes of 5 mL 1 mg/mL solution of pigment methanol, respectively. Place the test tube in a water bath pot and heat it at 50, 60, 70, 80, 90, and 100 °C for 10 min and then cool it to room temperature. Under the maximum absorption wavelength of 443 nm, the absorbance of methanol solution was measured by spectrophotometer (MAPADA UV-1800PC) with methanol as the reference solution, and the color change was observed.

#### 3.5.2. pH Stability

The pH values were adjusted to 2, 3, 4, 5, 6, 7, and 8 by 1 M HCl and 1 M NaOH, respectively. Under the maximum absorption wavelength of 443 nm, the absorbance of methanol solution was measured by ultraviolet spectrophotometer with methanol as the reference solution, and the color change was observed.

#### 3.5.3. Antimicrobial Activity

The antimicrobial activity of pigment against *Staphylococcus aureus* (*S. aureus*, ATCC 6538, Gram-positive) and *Escherichia coli* (*E. coli*, ATCC 8739, Gram-negative) bacteria was determined by paper disk diffusion assay. The pigment was prepared into a solution of 0.1 mg/mL with dimethyl sulfoxide (DMSO). Five microliters of pigment were added to the filter paper of Luria-Bertani medium (LB), and two microliters of DMSO were used as the negative control. The LB medium was cultured in a 37 °C incubator for 24 h, and the diameter of the inhibition zone was measured.

### 3.6. Textile Dyeing

The dyeing effect of pigment on silk and cotton fabrics was evaluated. Prepare 4  $\times$  10 cm of two kinds of each fabric and record the weight, according to 1% o.w.f (on the weight of fiber) to prepare the corresponding pigment. According to the pigment/dispersing agent NNO (2-Naphthalenesulfonic acid) (Aladdin, Shanghai, China) = 2/1 mixed to fully grind, material to liquor ratio (MLR) 1:30.  $\text{CH}_3\text{COOH}$  and NaOH were used for adjustment of the dyebath pH to the initial values. The dyeing process was carried out in a dyeing apparatus equipped with two 500 mL steel beakers. The optimal dyeing conditions of Ac.X2 natural dye onto silk and cotton fabric were investigated with simple water bath dyeing conditions under continuous manual stirring by optimizing dyeing variables including pH (2–9), temperature (40–100 °C), and time (15–90 min) using one-factor-at-a-time (OFT) optimization technique by reflectance spectroscopy (*K/S*). After dyeing, rinse the samples with distilled water at 40 °C for 20 times and dry them. The fabric with the best dyeing effect was selected for further experiments.

### 3.7. Measurement

#### 3.7.1. Fourier Transform Infrared Spectroscopy (FT-IR) Analysis

The FT-IR spectra of the untreated and Ac.X2-dyed silk fabrics were recorded using an FT-IR spectrometer (Nicolet iS20, MA, USA) with a resolution of 4  $\text{cm}^{-1}$  by recording

32 scans in % transmittance mode in the range of 500–4000  $\text{cm}^{-1}$ . The samples were prepared by using a KBr-disk.

### 3.7.2. X-ray Diffraction (XRD) Analysis

XRD measurement of the untreated and Ac.X2-dyed silk samples was carried out on a Bruker D8 ADVANCE in the  $2\theta$  angle ranging from  $10^\circ$  to  $35^\circ$  with  $0.09^\circ$  step interval. The generator voltage was kept at 40 kV, and the generator current was 40 mA. The sample in the form of chopped fibers was prepared and placed on the stub.

### 3.7.3. Scanning Electron Microscopy (SEM)

Morphological investigations on silk fabric samples colored with the actinomycin X2 for comparison with a reference silk fabric were carried out by a SU 8010 SEM, at an acceleration voltage of 30 kV, 50 pA of the current probe, and 30 mm working distance. The samples were mounted on aluminum specimen stubs with conductive plastic. Samples were sputter-coated with a 20–30 nm thick gold layer in rarefied argon, using a sputter coater, using a current intensity of 15 mA, for 2 min.

## 3.8. Characterization of the Dyed Samples

### 3.8.1. The Influence of Dye Concentration on the Dyeing Effect

In previous experiments, the pigment showed the best dyeing effect on the silk fabric. In this experiment, silk fabric was dyed with 5 different o.w.f (0.1%, 0.2%, 0.5%, 1%, 2%, and 4%) under optimum dyeing condition.

### 3.8.2. Color Characteristics

The color strength ( $K/S$  value) and CIE  $L^*$ ,  $a^*$ ,  $b^*$  of dyed fabrics were measured by a Datacolor 600 spectrophotometer under illuminant D65, by a  $10^\circ$  standard observer. Each sample was folded twice so as to provide a thickness of four layers. The reflectance ( $R$ ) values were converted to corresponding color strength values using Kubelka–Munk Equation (1). The CIE system was a specialized color system designed by International Commission on illumination.  $L^*$  presents a lightness value (a higher lightness value represents a lower color yield);  $a^*$  presents redness-greenness (+value = red, –value = green);  $b^*$  presents yellowness-blueness (+value = yellow, –value = blue) [50,65,66]. The exhausting percentage of dyed silk and cotton was obtained according to Equation (2), which was used to characterize the dye uptake after the dyeing process.

$$K/S = (1 - R^2) / 2R \quad (1)$$

where  $K$ ,  $R$ , and  $S$  are the adsorption coefficient, reflectance of dyed fabric, and the scattering coefficient, respectively.

$$\text{Exhausting percentage (\%)} = (A_1 - A_0) / A_1 \times 100\% \quad (2)$$

where  $A_1$  and  $A_0$  are the absorbances of dye liquor at 443 nm before and after the dyeing process.

### 3.8.3. Color Fastness Testing

The washing color fastness of dyed silk fabrics was evaluated according to the standard GB/T3921-2008 by washing the samples for 30 min at  $40^\circ\text{C}$  with 0.2% ( $w/v$ ) standard detergent. Dry and wet rub fastness was tested using the standard of GB/T3920-2008. The perspiration fastness was tested on the basis of GB/T3922-2013.

### 3.8.4. UV Protection Performance

The UV protection factor (UPF) of undyed silk and different dye concentration dyed silk was determined on three fabric samples ( $2 \times 2 \text{ cm}^2$ ). Each sample was taken from the center of the fabric, fixed on a common slide frame, and placed in a UV-2000F Textiles

UV Factor Tester (Labsphere company, NES, USA) equipped with an integrating sphere to measure both direct and diffuse transmitted light. Each sample was positioned at right angles to the light beams. Transmission measurements were made in the 290–400 nm range with a 1 nm step.

### 3.8.5. Antibacterial Activity

The antibacterial experiment of dyed silk and after washing samples was carried out according to the American Association of Textile Chemists and Colorists AATCC 100-2012 and the antibacterial standard for textiles (GB/T 20944.3-2008). *Staphylococcus aureus* (ATCC6538) was selected as a test strain.

In the AATCC 100-2012 experiment, the test samples were inoculated with a suitable concentration of bacteria, transferred to a constant temperature incubator at 37 °C for 12 h, and then neutralized with 0.03 mol/L PBS buffer solution for 1 min. Dilute to a suitable concentration by 10 times dilution. Transfer 1 mL of the diluted solution to a clean plate, and about 15 mL of NB agar medium was irrigated. After the agar was cooled and solidified, the plates were placed in a constant temperature incubator at 37 °C for 48 h. The plates with appropriate colony density were counted, and the inhibition rate was calculated according to Equation (3):

$$R (\%) = (A - B) / A \times 100\% \quad (3)$$

where R is the bacterial inhibition rate (%) and A and B are the number of bacterial colonies from undyed silk and dyed silk, respectively.

In the GB/T 20944.3-2008 experiment, small pieces of fabric sample (2 × 2 cm) were introduced into 5 mL 0.03 mol/L PBS, which contained  $1 \times 10^5$  CFU/mL bacteria, followed by shaking incubation at 37 °C for 24 h. The medium was diluted 10 times with 0.03 mol/L PBS to a suitable multiple. Transfer 1 mL of the diluted solution to a clean plate, and about 15 mL of NB agar medium was irrigated. After the agar was cooled and solidified, the plates were placed in a constant temperature incubator at 37 °C for 48 h. The plates with appropriate colony density were counted, and the inhibition rate was calculated according to Equation (3), too. Data were treated by one-way analysis of variance (ANOVA) and multiple comparisons analyses. Statistically significant values were the ones having  $p < 0.05$ .

### 3.8.6. Brine Shrimp Toxicity Assay

The lethality assay of brine shrimp *Artemia salina* (*A. salina*) was developed by previous studies, which had been suggested to evaluate the toxicity of compounds. Commercially available *A. salina* or brine shrimp cysts were purchased and cultivated in 3.2% of saline water. Before cultivation, the saline was aerated, and then cysts were kept at room temperature for 24 h. For toxicity screening, hatched larvae were collected and introduced in saline water. Add 0.9% saline water and approximately the same number of larvae 30 per well to make a 12-wells test culture plate. Ac.X2 with 2.5 µg/mL, 6.25 µg/mL, 12.5 µg/mL, 25 µg/mL and 1 × 1 cm dyed silk fabrics (o.w.f = 0.1%, 0.25%, 0.5%, 1%, 2%) were added to the test culture plate, while the equal volume of dimethyl sulfoxide (DMSO) (Aladdin, Shanghai, China) and dichloromethane (Aladdin, Shanghai, China) were added as blank control test and positive control separately. After 24 h at 25 °C, the percent of survival of *A. salina* was calculated.

This study has demonstrated for the first time the application of actinomycin X2 (Ac.X2), a peptide orange-yellow pigment as a natural dye from marine microorganisms. By using OFT, a series of dyeing experiments was performed, and dyeing parameters were optimized, and it displayed fantastic dyeing performance with silk fabric owing to the high dye uptake percentage (85.43%) and satisfactory color fastness. The dyed silk fabric characterized by FT-IR, XRD, and SEM analysis may indicate some chemical reaction occurring under the dyeing condition. In addition, it was illustrated in this research that Ac.X2-dyed silk fabrics exerted good UV protection ability and high antibacterial activity over 95–99% against *S. aureus*, and it still had remarkable antibacterial activity (over 90%)



after 20 times repeated laundering compared to other natural dye. Furthermore, brine shrimp toxicity results indicated that Ac.X2-dyed silk exhibited similar biological safety as regular silk. With the enhanced awareness of eco-safety, Ac.X2 as the marine source of natural pigment is an interesting route and offers opportunities for potential bio-based value.

**Supplementary Materials:** The following are available online at <https://www.mdpi.com/article/10.3390/md20010016/s1>, Figure S1: Neighbor-joining phylogenetic tree of strain A102 based on the 16S rRNA gene sequence generated by Mega5.0, Numbers on branch nodes are bootstrap values (expressed as percentage of 1000 replications). Figure S2: HPLC and MS data of pigment. Figure S3: <sup>13</sup>C-NMR and <sup>1</sup>H-NMR (at 400 MHz in CDCl<sub>3</sub>) profiles of the pigment. Figure S4: Antimicrobial activity of the pigment to two microorganisms. Figure S5: Pigment absorbance standard curve. Figure S6: Effects of liquid medium on (A) different liquid medium; (B) nitrogen source; (C) carbon source; (D) pH. Figure S7: Bacteriostatic rates of different o.w.f silk tested by AATCC 100-2012 method. Figure S8: The images of plates of different o.w.f dyed silk against *Staphylococcus aureus* tested by AATCC 100-2012 method. Figure S9: The images of plates of different o.w.f dyed silk against *Staphylococcus aureus* tested by GB/T 20944.3-2008 method. Figure S10: Antibacterial activity of (A) dyed o.w.f 0.5% and (B) o.w.f 1% silk sample against *Staphylococcus aureus* tested by GB/T 20944.3-2008 method after different washing times. Table S1: Antibacterial activity of dyed o.w.f 0.5% and o.w.f 1% silk sample against *Staphylococcus aureus* tested by GB/T 20944.3-2008 method after different washing cycles.

**Author Contributions:** Writing—original draft preparation, W.C., K.Y., X.Z., H.Z., R.S., J.C., Z.C., K.S., Z.Y. and B.H.; writing—review and editing, W.C. and B.H.; funding acquisition, B.H. All authors have read and agreed to the published version of the manuscript.

**Funding:** National Natural Science Foundation of China: (81973233); the Key Research and Development Program of Zhejiang Province, China (2021C02062); National life science competition for College Students (65122); Scientific Research Foundation of Zhejiang Sci-Tech University: (17042058-Y); Special Program for Research and Development of Zhejiang Sci-Tech University (2019Y009).

**Acknowledgments:** The authors thank the reviewers whose comments and suggestions helped improve this manuscript and gratefully acknowledge the College of Life Sciences and Medicines, Zhejiang Sci-Tech University.

**Conflicts of Interest:** The authors declare no conflict of interest.

## References

1. Chattopadhyay, P.; Chatterjee, S.; Sen, S.K. Biotechnological potential of natural food grade biocolorants. *Afr. J. Biotechnol.* **2008**, *7*, 2972–2985.
2. Durán, M.; Ponezi, A.N.; Faljoni-Alario, A.; Teixeira, M.F.S.; Justo, G.Z.; Durán, N. Potential applications of violacein: A microbial pigment. *Med. Chem. Res.* **2012**, *21*, 1524–1532. [[CrossRef](#)]
3. Salian, A.; Dutta, S.; Mandal, S. A roadmap to UV-protective natural resources: Classification, characteristics, and applications. *Mater. Chem. Front.* **2021**, *5*, 7696–7723.
4. Yusuf, M.; Shabbir, M.; Mohammad, F. Natural Colorants: Historical, Processing and Sustainable Prospects. *Nat. Prod. Bioprospecting* **2017**, *7*, 123–145. [[CrossRef](#)] [[PubMed](#)]
5. Soliev, A.B.; Hosokawa, K.; Enomoto, K. Bioactive Pigments from Marine Bacteria: Applications and Physiological Roles. *Evid.-Based Complement. Altern. Med.* **2011**, *2011*, 670349. [[CrossRef](#)] [[PubMed](#)]
6. Mansour, R. Natural dyes and pigments: Extraction and applications. In *Handbook of Renewable Materials for Coloration and Finishing*; John Wiley & Sons: Hoboken, NJ, USA, 2018; pp. 75–102.
7. Rao, A.S.; Deka, S.P.; More, S.S.; Nair, A.; More, V.S.; Ananthjaraju, K.S. A Comprehensive Review on Different Microbial-Derived Pigments and Their Multipurpose Activities. In *Microbial Polymers: Applications and Ecological Perspectives*; Vaishnav, A., Choudhary, D.K., Eds.; Springer: Singapore, 2021; pp. 479–519.
8. Durán, N.; Teixeira, M.F.; De Conti, R.; Esposito, E. Ecological-friendly pigments from fungi. *Crit. Rev. Food Sci. Nutr.* **2002**, *42*, 53–66. [[CrossRef](#)]
9. Amal, A.; Abeer, K.; Samia, H.; El-Nasser, A.; Nadia, H. Selection of Pigment (Melanin) production in *Streptomyces* and their application in Printing and Dyeing of Wool Fabrics. *Res. J. Chem. Sci.* **2011**, *1*, 22–28.

10. Yusoff, W.; Mohamad, S.; Ahmad, W. Fastness Properties and Color Analysis of Natural Colorants from Actinomycetes Isolates on Silk Fabric. In Proceedings of the International Colloquium in Textile Engineering, Fashion, Apparel and Design 2014 (ICTEFAD 2014); Springer: Singapore, 2014.
11. Aubourg, S.P.; Torres-Arreola, W.; Trigo, M.; Ezquerro-Brauer, J.M. Partial characterization of jumbo squid skin pigment extract and its antioxidant potential in a marine oil system. *Eur. J. Lipid Sci. Technol.* **2016**, *118*, 1293–1304. [[CrossRef](#)]
12. Tawiah, B.; Badoo, W.; Fu, S. Advances in the Development of Antimicrobial Agents for Textiles: The Quest for Natural Products. Review. *Fibres Text. East. Eur.* **2016**, *24*, 3–136. [[CrossRef](#)]
13. Srilekha, V.; Krishna, G.; Seshasrinivas, V.; Charya, M.A.S. Antibacterial and anti-inflammatory activities of marine *Brevibacterium* sp. *Res. Pharm. Sci.* **2017**, *12*, 283. [[CrossRef](#)] [[PubMed](#)]
14. McBain, A.J.; Ledder, R.G.; Moore, L.E.; Catrenich, C.E.; Gilbert, P. Effects of quaternary-ammonium-based formulations on bacterial community dynamics and antimicrobial susceptibility. *Appl. Environ. Microbiol.* **2004**, *70*, 3449–3456. [[CrossRef](#)]
15. Dastjerdi, R.; Montazer, M. A review on the application of inorganic nano-structured materials in the modification of textiles: Focus on anti-microbial properties. *Colloids Surf. B Biointerfaces* **2010**, *79*, 5–18. [[CrossRef](#)] [[PubMed](#)]
16. Purwar, R.; Joshi, M. Recent Developments in Antimicrobial Finishing of Textiles: A Review. *Aatcc Rev.* **2004**, *4*, 2–26.
17. Simoncic, B.; Tomsic, B. Structures of novel antimicrobial agents for textiles—a review. *Text. Res. J.* **2010**, *80*, 1721–1737. [[CrossRef](#)]
18. Lee, D.G. Removal of a synthetic broad-spectrum antimicrobial agent, triclosan, in wastewater treatment systems: A short review. *Environ. Eng. Res.* **2015**, *20*, 111–120. [[CrossRef](#)]
19. Mamo, M.; Mengesha, A.; Upadhyay, R.; Dekebo, A. Studies on antimicrobial and dyeing potentials of some new oxazolidinone derivatives. *J. Pharm. Res.* **2012**, *5*, 5543–5548.
20. Zhou, Y.; Tang, R.-C. Modification of curcumin with a reactive UV absorber and its dyeing and functional properties for silk. *Dye. Pigment* **2016**, *134*, 203–211. [[CrossRef](#)]
21. Shah, S.S.; Shah, S.S.; Iqbal, A.; Ahmed, S.; Khan, W.M.; Hussain, S.; Li, Z. Phytochemical screening and antimicrobial activities of red silk cotton tree (*Bombax ceiba* L.). *Pak. J. Pharm. Sci.* **2018**, *31*, 947.
22. Mahesh, S.; Manjunatha, A.; Reddy, V.; Kumar, G. Studies on Antimicrobial Textile Finish Using Certain Plant Natural Products. In Proceedings of the International Conference on Advances in Biotechnology and Pharmaceutical Sciences (ICABPS'2011), Bangkok, Thailand, 23–24 December 2011.
23. Hussain, A.I.; Anwar, F.; Chatha, S.A.; Latif, S.; Sherazi, S.T.; Ahmad, A.; Worthington, J.; Sarker, S.D. Chemical composition and bioactivity studies of the essential oils from two *Thymus* species from the Pakistani flora. *LWT-Food Sci. Technol.* **2013**, *50*, 185–192. [[CrossRef](#)]
24. Teli, M.; Pandit, P. Application of *Sterculia foetida* fruit shell waste biomolecules on silk for aesthetic and wellness properties. *Fibers Polym.* **2018**, *19*, 41–54. [[CrossRef](#)]
25. Chandrakar, S.; Gupta, A.K. Actinomycin-producing endophytic *Streptomyces parvulus* associated with root of *aloe vera* and optimization of conditions for antibiotic production. *Probiotics Antimicrob. Proteins* **2019**, *11*, 1055–1069. [[CrossRef](#)] [[PubMed](#)]
26. Jensen, P.R.; Mincer, T.J.; Williams, P.G.; Fenical, W. Marine actinomycete diversity and natural product discovery. *Antonie Van Leeuwenhoek* **2005**, *87*, 43–48. [[CrossRef](#)]
27. Lam, K.S. Discovery of novel metabolites from marine actinomycetes. *Curr. Opin. Microbiol.* **2006**, *9*, 245–251. [[CrossRef](#)] [[PubMed](#)]
28. Weaver, M.S.; Navid, F.; Huppmann, A.; Meany, H.; Angiolillo, A. Vincristine and dactinomycin in infantile myofibromatosis with a review of treatment options. *J. Pediatric Hematol. Oncol.* **2015**, *37*, 237–241. [[CrossRef](#)]
29. Xiong, Z.-Q.; Zhang, Z.-P.; Li, J.-H.; Wei, S.-J.; Tu, G.-Q. Characterization of *Streptomyces padanus* JAU4234, a producer of actinomycin X<sub>2</sub>, fungichromin, and a new polyene macrolide antibiotic. *Appl. Environ. Microbiol.* **2012**, *78*, 589–592. [[CrossRef](#)] [[PubMed](#)]
30. Sharma, M.; Manhas, R.K. Purification and characterization of actinomycins from *Streptomyces* strain M7 active against methicillin resistant *Staphylococcus aureus* and vancomycin resistant *Enterococcus*. *BMC Microbiol.* **2019**, *19*, 44. [[CrossRef](#)]
31. Wang, D.; Wang, C.; Gui, P.; Liu, H.; Khalaf, S.M.; Elsayed, E.A.; Wadaan, M.A.; Hozzein, W.N.; Zhu, W. Identification, bioactivity, and productivity of actinomycins from the marine-derived *Streptomyces heliomycini*. *Front. Microbiol.* **2017**, *8*, 1147. [[CrossRef](#)]
32. Kleeff, J.; Kornmann, M.; Sawhney, H.; Korc, M. Actinomycin D induces apoptosis and inhibits growth of pancreatic cancer cells. *Int. J. Cancer* **2000**, *86*, 399–407. [[CrossRef](#)]
33. Green, R.; Howell, M.; Khalil, R.; Nair, R.; Yan, J.; Foran, E.; Katiri, S.; Banerjee, J.; Singh, M.; Bharadwaj, S.; et al. Actinomycin D and Telmisartan Combination Targets Lung Cancer Stem Cells Through the Wnt/Beta Catenin Pathway. *Sci. Rep.* **2019**, *9*, 18177. [[CrossRef](#)]
34. Chen, Z.; Ou, P.; Liu, L.; Jin, X. Anti-MRSA activity of actinomycin X<sub>2</sub> and collismycin a produced by *Streptomyces globisporus* WA5-2-37 from the intestinal tract of American cockroach (*Periplaneta americana*). *Front. Microbiol.* **2020**, *11*, 555. [[CrossRef](#)]
35. Herbrink, A.; Corretto, E.; Chroňáková, A.; Langhansová, H.; Petrášková, P.; Hrdý, J.; Čihák, M.; Křišťůfek, V.; Bobek, J.; Petříček, M. A human lung-associated *streptomyces* sp. TR1341 produces various secondary metabolites responsible for virulence, cytotoxicity and modulation of immune response. *Front. Microbiol.* **2020**, *10*, 3028. [[CrossRef](#)]

36. Qureshi, K.A.; Bholay, A.D.; Rai, P.K.; Mohammed, H.A.; Khan, R.A.; Azam, F.; Jaremko, M.; Emwas, A.-H.; Stefanowicz, P.; Waliczek, M.; et al. Isolation, characterization, anti-MRSA evaluation, and in-silico multi-target anti-microbial validations of actinomycin X2 and actinomycin D produced by novel *Streptomyces smyrnaeus* UKAQ\_23. *Sci. Rep.* **2021**, *11*, 14539. [[CrossRef](#)] [[PubMed](#)]
37. Zhou, Q.; Rather, L.J.; Ali, A.; Wang, W.; Zhang, Y.; Haque, Q.M.R.; Li, Q. Environmental friendly bioactive finishing of wool textiles using the tannin-rich extracts of Chinese tallow (*Sapium sebiferum* L.) waste/fallen leaves. *Dye. Pigment* **2020**, *176*, 108230. [[CrossRef](#)]
38. Ren, Y.; Gong, J.; Fu, R.; Zhang, J.; Fang, K.; Liu, X. Antibacterial dyeing of silk with prodigiosins suspension produced by liquid fermentation. *J. Clean. Prod.* **2018**, *201*, 648–656. [[CrossRef](#)]
39. dos Santos Silva, P.M.; Fiaschitello, T.R.; de Queiroz, R.S.; Freeman, H.S.; da Costa, S.A.; Leo, P.; Montemor, A.F.; da Costa, S.M. Natural dye from *Croton urucurana* Baill. bark: Extraction, physicochemical characterization, textile dyeing and color fastness properties. *Dye. Pigment* **2020**, *173*, 107953. [[CrossRef](#)]
40. Teli, M.; Pandian, S.; Vyas, U. Simultaneous acid dyeing and resin finishing of cotton fabrics. *Indian J. Fibre Text. Res.* **1990**, *15*, 18–22.
41. de Mesquita, J.P.; Donnici, C.L.; Teixeira, I.F.; Pereira, F.V. Bio-based nanocomposites obtained through covalent linkage between chitosan and cellulose nanocrystals. *Carbohydr. Polym.* **2012**, *90*, 210–217. [[CrossRef](#)]
42. Chatsuwan, N.; Puechkamut, Y.; Pinsirodom, P. Characterization, Functionality and Antioxidant Activity of Water-Soluble Proteins Extracted from *Bombyx mori* Linn. *Curr. Appl. Sci. Technol.* **2018**, *18*, 83–96.
43. Ahmed, H.E.; Darwish, S.S. Effect of museum conditions on historical dyed silk fabric with madder dye. *J. Polym. Environ.* **2012**, *20*, 596–606. [[CrossRef](#)]
44. Cui, W.; Liu, X.; Shen, X.; Peng, X.; Xu, W. Dyeing Properties of Silk Super Fine Powder. *Res. J. Text. Appar.* **2008**, *12*, 23–29. [[CrossRef](#)]
45. Kamalha, E.; Zheng, Y.S.; Zeng, Y.C.; Fredrick, M.N. FTIR and WAXD study of regenerated silk fibroin. *Adv. Mater. Res.* **2013**, *677*, 211–215. [[CrossRef](#)]
46. Lu, Q.; Hu, X.; Wang, X.; Kluge, J.A.; Lu, S.; Cebe, P.; Kaplan, D.L. Water-insoluble silk films with silk I structure. *Acta Biomater.* **2010**, *6*, 1380–1387. [[CrossRef](#)] [[PubMed](#)]
47. Drummy, L.F.; Farmer, B.; Naik, R.R. Correlation of the  $\beta$ -sheet crystal size in silk fibers with the protein amino acid sequence. *Soft Matter* **2007**, *3*, 877–882. [[CrossRef](#)] [[PubMed](#)]
48. Zhou, Y.; Zhang, J.; Tang, R.-C.; Zhang, J. Simultaneous dyeing and functionalization of silk with three natural yellow dyes. *Ind. Crop. Prod.* **2015**, *64*, 224–232. [[CrossRef](#)]
49. Ahmad, W.A.; Ahmad, W.Y.W.; Zakaria, Z.A.; Yusof, N.Z. Application of bacterial pigments as colorant. In *Application of Bacterial Pigments as Colorant*; Springer: Berlin/Heidelberg, Germany, 2012; pp. 57–74.
50. Gong, K.; Pan, Y.; Rather, L.J.; Wang, W.; Zhou, Q.; Zhang, T.; Li, Q. Natural pigment during flora leaf senescence and its application in dyeing and UV protection finish of silk and wool—A case study of Cinnamomum Camphora. *Dye. Pigment* **2019**, *166*, 114–121. [[CrossRef](#)]
51. Grifoni, D.; Bacci, L.; Lonardo, S.D.; Pinelli, P.; Scardigli, A.; Camilli, F.; Sabatini, F.; Zipoli, G.; Romani, A. UV protective properties of cotton and flax fabrics dyed with multifunctional plant extracts. *Dye. Pigment* **2014**, *105*, 89–96. [[CrossRef](#)]
52. Wang, L.; Wang, N.; Jia, S.; Zhou, Q. Research on dyeing and ultraviolet protection of silk fabric using vegetable dyes extracted from *Flos Sophorae*. *Text. Res. J.* **2009**, *79*, 1402–1409. [[CrossRef](#)]
53. Shabbir, M.; Rather, L.J.; Mohammad, F. Economically viable UV-protective and antioxidant finishing of wool fabric dyed with *Tagetes erecta* flower extract: Valorization of marigold. *Ind. Crop. Prod.* **2018**, *119*, 277–282. [[CrossRef](#)]
54. Sun, S.-S.; Tang, R.-C. Adsorption and UV Protection Properties of the Extract from Honeysuckle onto Wool. *Ind. Eng. Chem. Res.* **2011**, *50*, 4217–4224. [[CrossRef](#)]
55. Kim, S.-h. Dyeing characteristics and UV protection property of green tea dyed cotton fabrics. *Fibers Polym.* **2006**, *7*, 255–261. [[CrossRef](#)]
56. Vanhaecke, P.; Persoone, G.; Claus, C.; Sorgeloos, P. Proposal for a short-term toxicity test with *Artemia* nauplii. *Ecotoxicol. Environ. Saf.* **1981**, *5*, 382–387. [[CrossRef](#)]
57. Lopes, V.R.; Fernández, N.; Martins, R.F.; Vasconcelos, V. Primary Screening of the Bioactivity of Brackishwater Cyanobacteria: Toxicity of Crude Extracts to *Artemia salina* Larvae and *Paracentrotus lividus* Embryos. *Mar. Drugs* **2010**, *8*, 471–482. [[CrossRef](#)] [[PubMed](#)]
58. Moshafi, M.H.; Fariba, S.; Gholam-Reza, D.; Alieh, A. Bioassay Screening of the Essential Oil and Various Extracts of Fruits of *Heracleum persicum* Desf. and Rhizomes of *Zingiber officinale* Rosc. using Brine Shrimp Cytotoxicity Assay. *Iran. J. Pharm. Res.* **2009**, *8*, 59–63.
59. Manilal, A.; Sujith, S.; Kiran, G.S.; Selvin, J.; Shakir, C. Cytotoxic Potentials of Red Alga, *Laurencia brandenii* Collected from the Indian Coast. *Glob. J. Pharmacol.* **2009**, *3*, 90–94.
60. Cai, J.; Jiang, H.; Chen, W.; Cui, Z. Design, synthesis, characterization of water-soluble indophenine dyes and their application for dyeing of wool, silk and nylon fabrics. *Dye. Pigment* **2020**, *179*, 108385. [[CrossRef](#)]
61. Prusty, A.K.; Das, T.; Nayak, A.; Das, N.B. Colourimetric analysis and antimicrobial study of natural dyes and dyed silk. *J. Clean. Prod.* **2010**, *18*, 1750–1756. [[CrossRef](#)]

62. Kiliç, M.; Koçak, D.; Canbolat, Ş.; Dayioğlu, H.; Merdan, N.; Filiz, A. Investigation of the Effect of the Dyeing Method on the Dyeing Properties of Wool Fabrics Dyed with Natural Dyes Extracted from *Vaccinium corymbosum* L. *Marmara Fen Bilim. Derg.* **2015**, *27*, 78–82. [[CrossRef](#)]
63. Shahid, M.; Cheng, X.-W.; Tang, R.-C.; Chen, G. Silk functionalization by caffeic acid assisted in-situ generation of silver nanoparticles. *Dye. Pigment* **2017**, *137*, 277–283. [[CrossRef](#)]
64. Shirling, E.T.; Gottlieb, D. Methods for characterization of *Streptomyces* species. *Int. J. Syst. Evol. Microbiol.* **1966**, *16*, 313–340. [[CrossRef](#)]
65. Rather, L.J.; Azam, M.; Shabbir, M.; Bukhari, M.N.; Shahid, M.; Khan, M.A.; Haque, Q.M.R.; Mohammad, F. Antimicrobial and fluorescence finishing of woolen yarn with *Terminalia arjuna* natural dye as an ecofriendly substitute to synthetic antibacterial agents. *RSC Adv.* **2016**, *6*, 39080–39094. [[CrossRef](#)]
66. Rather, L.J.; Akhter, S.; Padder, R.A.; Hassan, Q.P.; Hussain, M.; Khan, M.A.; Mohammad, F. Colorful and semi durable antioxidant finish of woolen yarn with tannin rich extract of *Acacia nilotica* natural dye. *Dye. Pigment* **2017**, *139*, 812–819. [[CrossRef](#)]



## Article

# Structure-Based Pharmacophore Modeling, Virtual Screening, Molecular Docking, ADMET, and Molecular Dynamics (MD) Simulation of Potential Inhibitors of PD-L1 from the Library of Marine Natural Products

Lianxiang Luo <sup>1,2,3,\*</sup>, Ai Zhong <sup>4</sup>, Qu Wang <sup>4</sup> and Tongyu Zheng <sup>4</sup><sup>1</sup> The Marine Biomedical Research Institute, Guangdong Medical University, Zhanjiang 524023, China<sup>2</sup> The Marine Biomedical Research Institute of Guangdong Zhanjiang, Zhanjiang 524023, China<sup>3</sup> Southern Marine Science and Engineering Guangdong Laboratory (Zhanjiang), Zhanjiang 524023, China<sup>4</sup> The First Clinical College, Guangdong Medical University, Zhanjiang 524023, China;

zhongai@gdmu.edu.cn (A.Z.); wang15728276376@hotmail.com (Q.W.); dzheng@gdmu.edu.com (T.Z.)

\* Correspondence: luolianxiang321@gdmu.edu.cn

**Citation:** Luo, L.; Zhong, A.; Wang, Q.; Zheng, T. Structure-Based Pharmacophore Modeling, Virtual Screening, Molecular Docking, ADMET, and Molecular Dynamics (MD) Simulation of Potential Inhibitors of PD-L1 from the Library of Marine Natural Products. *Mar. Drugs* **2022**, *20*, 29. <https://doi.org/10.3390/md20010029>

Academic Editors: Yonghong Liu and Xuefeng Zhou

Received: 7 December 2021

Accepted: 23 December 2021

Published: 25 December 2021

**Publisher's Note:** MDPI stays neutral with regard to jurisdictional claims in published maps and institutional affiliations.



**Copyright:** © 2021 by the authors. Licensee MDPI, Basel, Switzerland. This article is an open access article distributed under the terms and conditions of the Creative Commons Attribution (CC BY) license (<https://creativecommons.org/licenses/by/4.0/>).

**Abstract:** Background: In the past decade, several antibodies directed against the PD-1/PD-L1 interaction have been approved. However, therapeutic antibodies also exhibit some shortcomings. Using small molecules to regulate the PD-1/PD-L1 pathway may be another way to mobilize the immune system to fight cancer. Method: 52,765 marine natural products were screened against PD-L1 (PDBID: 6R3K). To identify natural compounds, a structure-based pharmacophore model was generated, following by virtual screening and molecular docking. Then, the absorption, distribution, metabolism, and excretion (ADME) test was carried out to select the most suitable compounds. Finally, molecular dynamics simulation was also performed to validate the binding property of the top compound. Results: Initially, 12 small marine molecules were screened based on the pharmacophore model. Then, two compounds were selected for further evaluation based on the molecular docking scores. After ADME and toxicity studies, molecule 51320 was selected for further verification. By molecular dynamics analysis, molecule 51320 maintains a stable conformation with the target protein, so it has the chance to become an inhibitor of PD-L1. Conclusions: Through structure-based pharmacophore modeling, virtual screening, molecular docking, ADMET approaches, and molecular dynamics (MD) simulation, the marine natural compound 51320 can be used as a small molecule inhibitor of PD-L1.

**Keywords:** PD-L1; virtual screening; pharmacophore modeling; ADME; molecular dynamics

## 1. Introduction

Blocking the interaction of PD-1/PD-L1 and PD-1/PD-L1 pathway modulators has shown unprecedented clinical efficacy in a variety of tumor models [1–4]. Existing studies have shown that the programmed cell death protein 1 (PD-1)/programmed cell death ligand 1 (PD-L1) signaling pathway can induce tumor-specific T cell apoptosis by inhibiting T cell activation [5]. It plays a role in immune escape and immune suppression under pathological conditions such as inflammation [6–11].

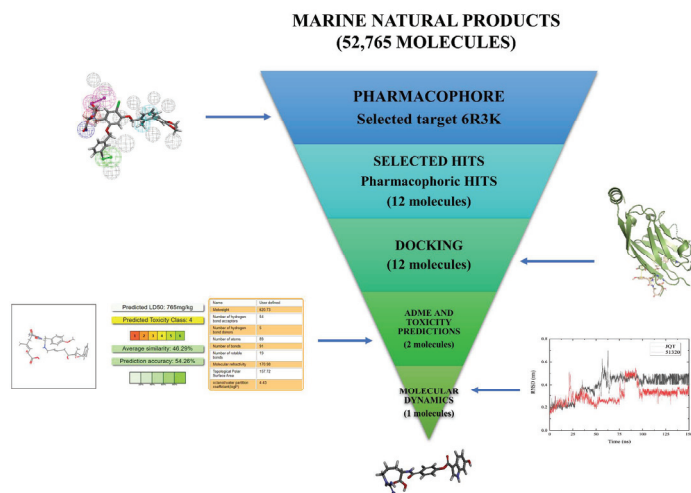
Because PD-L1 is highly expressed in a variety of tumor cells, after PD-L1 binds to PD-1, T cell activation is inhibited, and T cells are in a state of immune tolerance [12]. At this time, the immune system cannot kill the cancer cells, and tumor immune escape occurs [13]. Therefore, this type of inhibitor has a wide range of tumors, especially for tumors with high PD-L1 expression, and the response rate is higher.

Therefore, a targeted inhibitor designed for PD-L1 can cut off the signal pathway and activate T cells [14]. Therefore, its immune tolerance is relieved, T cells are mobilized to kill tumors, and tumor treatment is realized. Anti-PD-L1 monoclonal antibody is one of

the most important drugs for lung cancer immunotherapy [15]. However, therapeutic antibodies also show some disadvantages. For example, tumor penetration rate is low, it is difficult to overcome physiological barriers, and there is a lack of oral bioavailability, high manufacturing cost, inaccessibility to intracellular targets, and immune-related adverse events (irAE) [16]. Using small molecules to regulate the PD-1/PD-L1 pathway may be another way to mobilize the immune system to fight cancer. In 2015, Zak et al. reported the crystal structure of the hPD-1/hD-L1 complex, which is generally considered to provide important receptor-ligand interactions, and they are reasonable structure-based drugs on the surface of PD-L1 Design (SBDD), which provides several major active sites [17]. In recent years, several small molecule drugs that can bind to PD-L1 and inhibit the interaction of PD-1/L1 have been discovered [18,19]. Therefore, it is of great significance to generate simple, stable, and efficient PD-L1 small molecule inhibitors.

Due to its special ecological environment, the ocean contains rich natural products. With the development of terrestrial resources, the marine environment provides a new field for research. By the end of 2020, it is estimated that more than 29,000 marine natural products have been found, and marine natural products have also received increasing attention from scientists [20]. It has been found that marine natural products have different structural characteristics from terrestrial natural products with various biological activities such as antifungal, antiviral, anti-parasitic, anti-tumor, and anti-inflammatory [21,22]. Natural products are the best choice as a source of new drugs [23], and marine organisms are thus considered as the latest source of bioactive natural products related to terrestrial plants and non-marine microorganisms [24]. We have collected three marine natural product databases: Marine Natural Product Database (MNPD) [25], Seaweed Metabolite Database (SWMD) [26], and Comprehensive Marine Natural Product Database (CMNPD) [27]. In this study, 52,765 kinds of marine natural products were virtually screened by targeting PD-L1. In order to predict a variety of marine natural products that may inhibit PD-L1. We hope to provide new options for the development of new anti-tumor drugs.

Structure-based pharmacophore modeling, virtual screening, molecular docking, ADMET approaches, and molecular dynamics (MD) simulation were performed on a library of marine natural products to find the novel compounds against PD-L1, which are demonstrated as Figure 1.



**Figure 1.** The virtual screening workflow (VSW) used in this work for the identification of hit molecules targeting PD-L1. A workflow overview of pharmacophore modeling, virtual screening, molecular docking, absorption, distribution, metabolism, elimination, and toxicity (ADMET) approaches, and MD simulation.

## 2. Results

### 2.1. Structure-Based Pharmacophore Modeling and Virtual Screening

#### 2.1.1. Pharmacophore Model Establishment

Pharmacophore describes the three-dimensional arrangement of basic spatial and electronic characteristics to achieve the best combination of ligands and macromolecules. The main application area of the pharmacophore model is database search. By searching the compound database through the pharmacophore model, it is possible to find biologically active compounds with specific targets, and to find new chemical entities with similar biological activities and different skeleton structures. Depending on the available target or known ligand information, the design of the pharmacophore model can be structure-based or ligand-based [28–30]. In this study, the available PD-L1 information of its small molecule inhibitors was used to construct the structure-based pharmacophore model. Hence, the 7 pharmacophore models containing the feature set were generated (Table 1) [31–35]. Among the generated models, 6R3K composed of DHHHNP chemical characteristics with the highest selectivity score (16.25) was selected as the best model.

**Table 1.** Ranking of pharmacophore models.

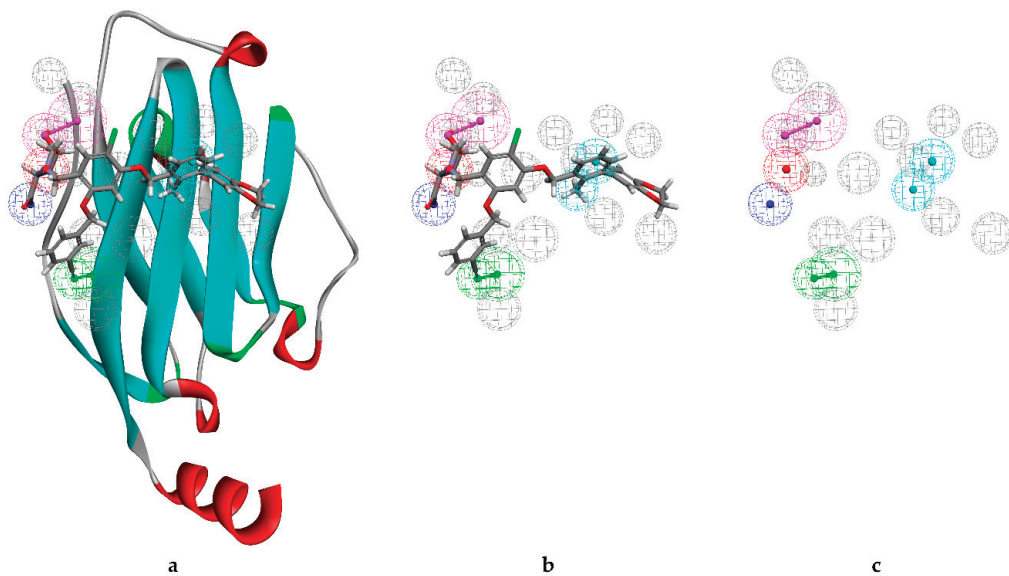
| Compound | Number of Features | Feature Set | Selectivity Score | References |
|----------|--------------------|-------------|-------------------|------------|
| 6R3K     | 6                  | DHHHNP      | 16.25             | [31]       |
| 5NIU     | 6                  | DDHHHP      | 15.635            | [32]       |
| 5N2F     | 6                  | AAHHNP      | 12.936            | [33]       |
| 5N2D     | 6                  | AHHHPR      | 12.848            | [33]       |
| 5J89     | 5                  | HHHHP       | 11.196            | [17]       |
| 6NM8     | 6                  | HHHHHP      | 10.996            | [34]       |
| 5J8O     | 6                  | HHHHHR      | 9.2594            | [35]       |

Therefore, the structure-based pharmacophore model was constructed based on PD-L1 (6R3K) and small molecule JQT (Figure 1). Ten pharmacophore models were generated. According to careful selection, we applied ligand 8 as the pharmacophore model for screening. DS software was used to generate key chemical features based on the pharmacophore model and co-crystallized ligand JQT and pharmacophore ligand 08 in Figure 2b. The total number of pharmacophores is 8. Two of them are hydrophobic, two hydrogen bond acceptors, two hydrogen bond donors, one positively charged ion center, and one negatively charged ion center (Figure 2c).

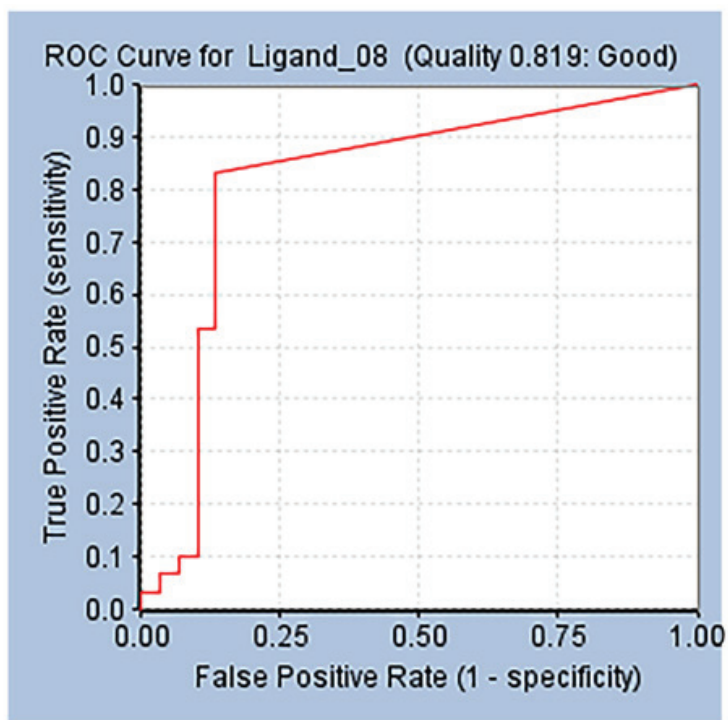
#### 2.1.2. Pharmacophore Model Validation

Verification is necessary to obtain true pharmacophore analysis and to evaluate the quality of molecular models [36]. Before database screening, the structure-based pharmacophore model established in this study was verified to verify whether the pharmacophore has a good ability to distinguish between active and inactive molecules. Receiver operating characteristic curve (ROC curve for short) is also known as sensitivity curve. The ROC curve graph is a curve reflecting the relationship between sensitivity and specificity. The X axis of the abscissa is 1-specificity, also known as false positive rate (false positive rate), the closer the X axis is to zero, the higher the accuracy rate; the Y axis of ordinate is called sensitivity, also known as true positive rate (sensitivity), the larger the Y-axis, the better the accuracy. According to the curve position, the whole graph is divided into two parts. The area under the curve is called AUC (area under curve), which is used to indicate the accuracy of prediction. The higher the AUC value, the larger the area under the curve, indicating the prediction, the higher the accuracy rate. The closer the curve is to the upper left corner (the smaller the X, the larger the Y), the higher the prediction accuracy rate [37]. In our verification process, the AUC (area under the ROC curve) at 1% threshold is 0.819 (Figure 3), which proves that our model has ability to distinguish between truly active substances and decoy compounds.





**Figure 2.** The overall pharmacophore model generated during the study. (a) PD-L1 crystal (PDB ID:6R3K) with the co-crystallized ligand JQT and pharmacophore interaction map; (b) co-crystallized ligand JQT and pharmacophore ligand 08; (c) pharmacophore ligand 08.



**Figure 3.** Receiver operating characteristic (ROC) curve of Ligand\_08.

### 2.1.3. Virtual Screening Based on Pharmacophore

A marine natural product library containing a total of 52,765 compounds was used for virtual screening based on pharmacophores against the generated pharmacophore models. A total of 12 compounds that meet the characteristics of all pharmacophores were generated. Compounds labeled HIT were retrieved and stored for further evaluation.

### 2.2. Molecular Docking

Molecular docking is an important part of the drug design process. This study aims to evaluate the binding ability of HITS compounds to the target PD-L1 protein. According to the previously obtained binding sites, a receptor grid with  $X = -7.1$ ,  $Y = 59.3$ , and  $Z = -19.5$  was prepared.

AutoDock was used to dock a specific number of drugs with PD-L1, and evaluate its binding ability, which is in line with the characteristics of the pharmacophore model. Among them, the binding affinity of compound 37080 and compound 51320 are  $-6.5$  kcal/mol and  $-6.3$  kcal/mol (Table 2), and their binding affinity is better than that of the PD-L1 inhibitor used in the process of generating the main pharmacophore model ( $-6.2$  kcal/mol). The interaction of compound 37080 in the docking complex is shown in Figure 4a,b, and the interaction of compound 51320 is shown in the Figure 4c,d. In compound 51320 with good docking performance, it can be observed that the compound forms a hydrogen bond with Ala121, the oxygen atom interacts with the residue Asp122, and there is an ionic interaction with the residue ASP122 (Figure 4d). More importantly, the Pi-Pi interaction established between residue Ile54 and the compound and the Pi-Sigma interaction between residue Tyr123 and the compound also played a key role in ligand-receptor binding. Obviously, the rich interaction types between compound 51320 and the protein allow the best docking results between them. It can be seen from the interaction analysis that the docking result is reliable and the selected compound can be further analyzed.

**Table 2.** Molecular docking results of JQT and 12 selected ligands from the library of marine natural products.

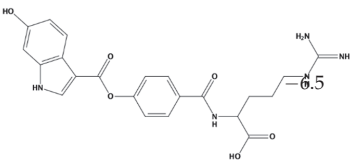
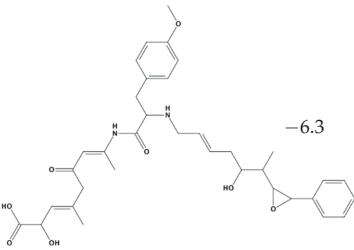
| Molecules | 2D Structure  | Binding Affinity (kcal/mol) | Formula              |
|-----------|---|-----------------------------|----------------------|
| 37080     |  | -6.5                        | $C_{22}H_{23}N_5O_6$ |
| 51320     |  | -6.3                        | $C_{35}H_{44}N_2O_8$ |

Table 2. Cont.

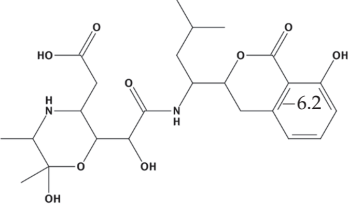
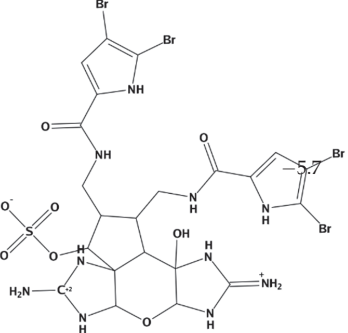
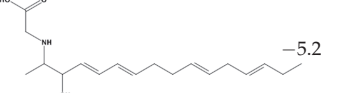
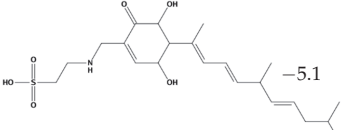
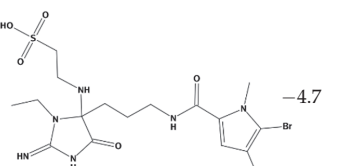
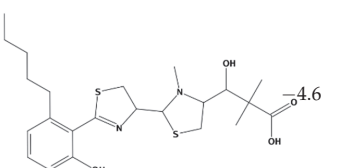
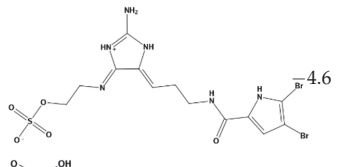
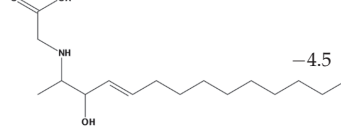
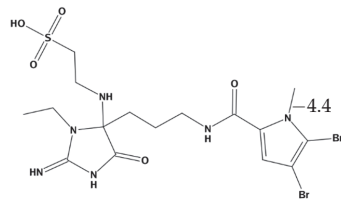
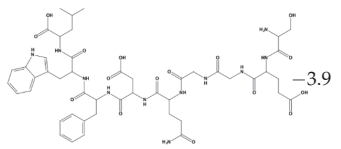
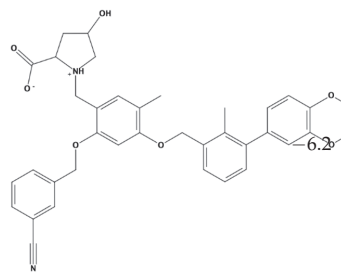
| Molecules | 2D Structure  | Binding Affinity (kcal/mol) | Formula                      |
|-----------|---|-----------------------------|------------------------------|
| 37113     |    | -6.2                        | $C_{24}H_{34}N_2O_9$         |
| 38010     |    | -5.7                        | $C_{22}H_{25}Br_4N_{10}O_8S$ |
| 41160     |    | -5.2                        | $C_{18}H_{29}NO_3$           |
| 32979     |  | -5.1                        | $C_{22}H_{35}NO_6S$          |
| 35432     |  | -4.7                        | $C_{16}H_{24}Br_2N_6O_5S$    |
| 21793     |  | -4.6                        | $C_{23}H_{34}N_2O_4S_2$      |

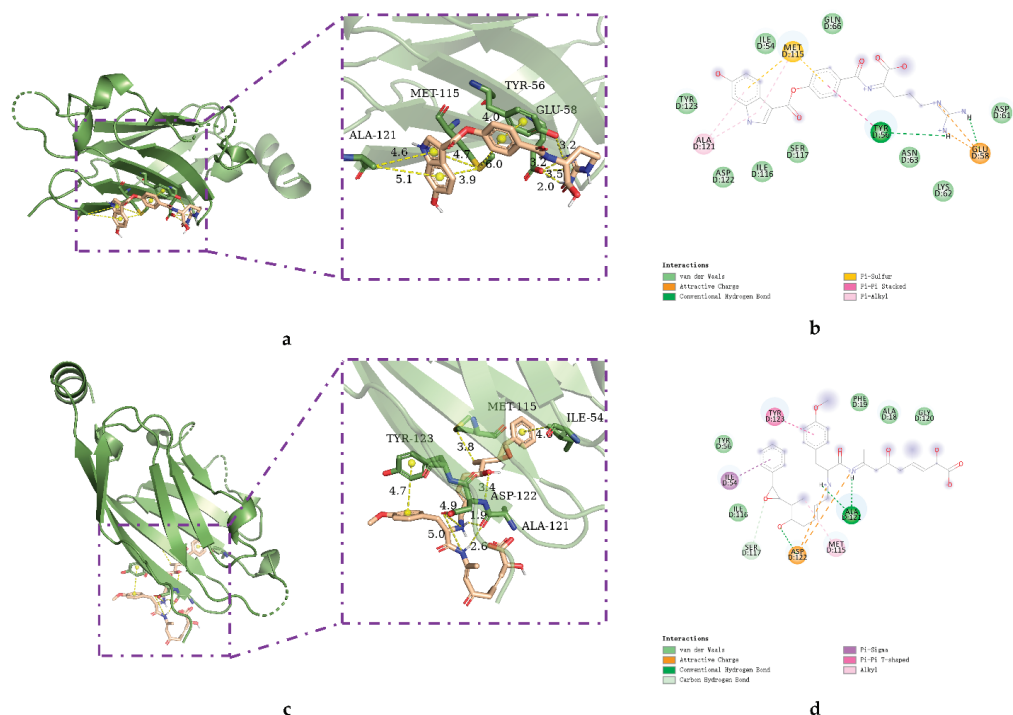
Table 2. Cont.

| Molecules | 2D Structure   | Binding Affinity (kcal/mol) | Formula   |
|-----------|--|-----------------------------|---|
| 23671     |   | -4.6                        | C <sub>13</sub> H <sub>16</sub> Br <sub>2</sub> N <sub>6</sub> O <sub>5</sub> S |
| 41159     |   | -4.5                        | C <sub>16</sub> H <sub>31</sub> NO <sub>3</sub>                                 |
| 35433     |   | -4.4                        | C <sub>16</sub> H <sub>24</sub> Br <sub>2</sub> N <sub>6</sub> O <sub>5</sub> S |
| 50094     |   | -3.9                        | C <sub>47</sub> H <sub>63</sub> N <sub>11</sub> O <sub>16</sub>                 |
| JQT       |  | -6.2                        | C <sub>36</sub> H <sub>33</sub> ClN <sub>2</sub> O <sub>7</sub>                 |

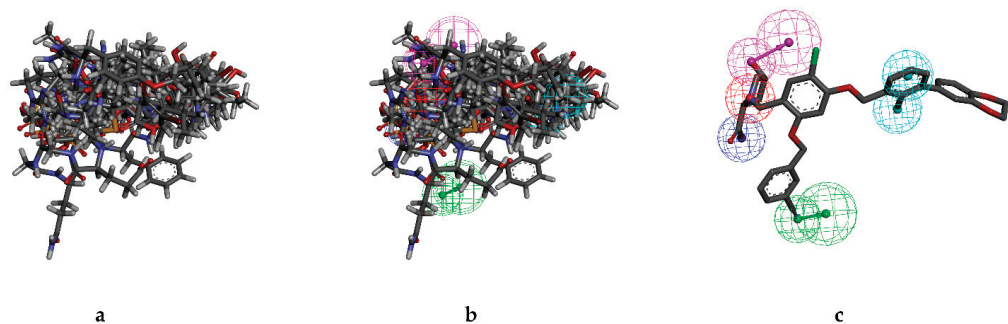
### 2.3. Analysis of Pharmacophore Characteristics

The pharmacophore characteristics of compounds play an important role in the molecular recognition process of targeted biological macromolecules. The pharmacophore of a compound can be described according to the characteristics of H, AR, HBA or HBD, PI, and NI. This helps to identify and design new drugs for the treatment of selected diseases.

These features retain the necessary geometric arrangement of atoms required to produce a specific biological reaction. Therefore, the characteristics of the pharmacophore we generated were analyzed. As shown in Figure 5a, the overlap of the ligand and pharmacophore characteristics shows that the selected compound should be effective for our target protein. Superimposition of the top12 hit compounds on to the pharmacophore model was shown in Figure 5b and superimposition of JQT on to the pharmacophore model was shown in Figure 5c.



**Figure 4.** Interaction between the protein–ligand complex. (a) Three-dimensional binding mode of the 37080 and protein complex; (b) two-dimensional binding mode of the 37080 and protein complex; (c) three-dimensional binding mode of the 51320 and protein complex; (d) two-dimensional binding mode of the 51320 and protein complex.



**Figure 5.** Structure-based pharmacophore. (a) Aligned ligands. (b) Selected ligands superimposed to the simplified pharmacophore model. (c) Ligand JQT superimposed to the simplified pharmacophore model.

#### 2.4. ADME and Toxicity Test ADME Properties Analysis

Swiss-ADME is a website (<https://www.swissadme.ch>, accessed on 9 October 2021) which allows the user to draw their respective ligand or drug molecule or include SMILES data from PubChem and provides parameters such as lipophilicity (iLOGP, XLOGP3, WLOGP, MLOGP, SILICOS-IT, Log P0/w), water solubility Log S (ESOL, Ali, SILICOS-IT), drug-likeness rules (Lipinski, Ghose, Veber, Egan, and Muegge), and Medicinal Chemistry

(PAINS, Brenk, Lead-likeness, Synthetic accessibility) [38]. The ADME prediction study of the designed compounds demonstrated Table 3. The Swiss-ADME section gives a physicochemical property of possible oral drug candidates according to five different rules determined by Lipinski, Ghose, Veber, Egan, and Muegge [39–42]. The reference value of Log S for moderately soluble and highly soluble molecules ranged from  $-4$  to  $-6$  and  $-2$  to  $-4$ , respectively. According to the results, all molecules are classified as moderately soluble and highly soluble. All these parameters infer that 51320 is close to a drug-like molecule.

**Table 3.** ADME properties of JQT and selected ligands from the library of marine natural products.

| Molecule | MW      | Rotatable Bonds | H-bond Acceptors | H-bond Donors | ESOL Log S | TPSA   | WLOGP   | GI Absorption | log Kp (cm/s) |
|----------|---------|-----------------|------------------|---------------|------------|--------|---------|---------------|---------------|
| 37080    | 453.45  | 12              | 7                | 7             | $-3.18$    | 190.62 | 1.54    | 0.78          | Low           |
| 51320    | 620.73  | 19              | 9                | 5             | $-3.82$    | 157.72 | 3.33    | 0.99          | Low           |
| 37113    | 494.53  | 9               | 10               | 6             | $-1.91$    | 174.65 | $-0.09$ | 0.04          | Low           |
| 38010    | 909.18  | 10              | 8                | 11            | $-5.32$    | 271.15 | $-2.38$ | 0.43          | Low           |
| 41160    | 307.43  | 12              | 4                | 3             | $-1.6$     | 69.56  | 3.22    | 0.35          | High          |
| 32979    | 441.58  | 11              | 7                | 4             | $-2.04$    | 132.31 | 3.13    | 1.28          | High          |
| 35432    | 572.27  | 11              | 7                | 5             | $-2$       | 165    | 0.94    | 0.31          | Low           |
| 21793    | 466.66  | 9               | 6                | 3             | $-3.74$    | 143.96 | 3.07    | 2.18          | Low           |
| 23671    | 528.18  | 9               | 6                | 5             | $-3.99$    | 166.6  | 1.06    | $-0.33$       | Low           |
| 41159    | 285.42  | 13              | 4                | 3             | $-2.01$    | 69.56  | 3.11    | 0.14          | High          |
| 35433    | 572.27  | 11              | 7                | 5             | $-2$       | 165    | 0.94    | 0.31          | Low           |
| 50094    | 1038.07 | 40              | 17               | 15            | $-0.68$    | 449.83 | $-3.85$ | $-4.93$       | Low           |
| JQT      | 641.11  | 10              | 9                | 2             | $-5.81$    | 121.48 | 5.30    | 2.64          | Low           |

### 2.5. Toxicity Analysis

In order to better select lead compounds, the measurement of toxicity within silicon is an important step before the candidate drug goes into clinical trials. Calculation-based electronic toxicity measurement is widely used because of its accuracy and accessibility. It can provide information on any synthetic or natural compound. In order to determine the toxicity and adverse effects of the two selected compounds, we used the freely available testing tool ProTox-II server [43]. The software evaluates several toxicological parameters, such as acute toxicity, liver toxicity, cytotoxicity, carcinogenicity, mutagenicity, and immunotoxicity, and is based on the predicted median lethal dose (LD50) (in mg/kg body weight) (Table 4). According to the ProTox-II server, compound 51320 belongs to 4 types of toxicity, with LD 50 of 300–2000 mg/kg, which is harmful when administered orally. Compound JQT belongs to grade 4 toxicity, and its LD 50 value is 800 mg/kg. However, it was active in cytotoxicity. Combined with the ADME results, 51320 is closer to drug-like molecules than JQT. Subsequently, MD simulations were performed on 51320 molecules and JQT.

### 2.6. Structure-Based Pharmacophore Modeling and Virtual Screening

MD simulations are used to explore the binding stability of the protein–ligand docking complex. MD simulations also provide information about molecular interactions within a reference time or provide valuable assessments in explaining drug resistance [44,45]. In this paper, MD simulation methods are used to analyze the docking file of a complex of a natural compound and PD-L1 protein to determine the stability and intermolecular interaction between the protein and the molecule within a 100 ns time interval. The trajectory of MD is extracted, and the simulation results of protein–ligand (P-L) interaction mapping based on RMSD and RMSF are described. The results show that compound 51320 is stable.

**Table 4.** List of toxicity properties (organ toxicity, toxicity endpoints, Tox21-nuclear receptor signaling pathways, Tox21-stress response pathway) of the selected 2 compounds.

| Endpoint                                  | Target                                   | JQT      | 51320    |
|---|--|----------|----------|
| Organ toxicity                            | Hepatotoxicity                           | Inactive | Inactive |
| Toxicity end points                       | Carcinogenicity                          | Inactive | Inactive |
|   | Immunotoxicity                           | Inactive | Inactive |
|   | Mutagenicity                             | Inactive | Inactive |
|   | Cytotoxicity                             | Active   | Inactive |
|   | LD50 (mg/kg)                             | 800      | 765      |
|   | Toxicity class                           | 4        | 4        |
| Tox21-nuclear receptor signaling pathways | Aryl hydrocarbon receptor (AhR)          | Inactive | Inactive |
|   | Androgen receptor (AR)                   | Inactive | Inactive |
| Tox21-stress response pathways            | Heat shock factor response element (HSE) | Inactive | Inactive |

### 2.6.1. RMSD Analysis

In order to obtain the equilibrium time of each simulated protein ligand complex during the MD simulation, the root mean square deviation (RMSD) of the backbone was calculated. RMSD diagrams are commonly used to evaluate the time required for the system to reach structural equilibrium and estimate the duration of running simulations. RMSD is an important parameter for estimating changes or changes in molecular conformation. Due to the sudden change of structural conditions, the RMSD value of the analog complex including the reference suddenly increased, which is related to the protein crystallization method. The latter effect is expected, because in the crystal structure, the protein is rigid, and when it is solvated in the water tank, it resumes its dynamic motion.

The complex system with a time frame  $x$  should have an RMSD that can be calculated from the following Equation (1).

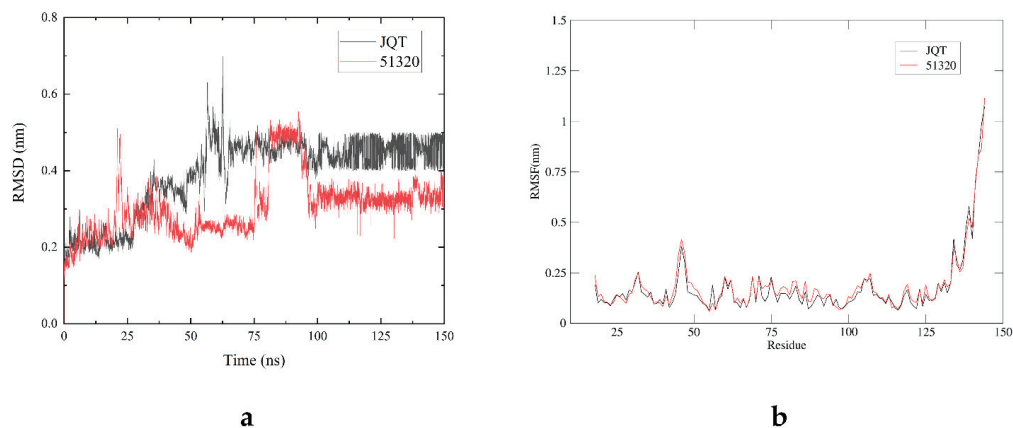
$$RMSD_x = \sqrt{\frac{1}{N} \sum_{i=1}^N (r'_i(t_x) - r_i(t_{ref}))^2} \quad (1)$$

Here, the  $RMSD_x$  is the calculation of RMSD for the specific number of frames,  $N$  is the number of selected atoms,  $t_{ref}$  is the reference or mentioned time, and  $r'$  is the selected atom in the frame  $x$  after super imposing on the reference frame,  $t_x$  is the recording intervals.

As shown in Figure 6a, the RMSD of selected compounds 51320 and JQT were analyzed to determine whether the system has been balanced. The system of compound 51320 was in equilibrium after 105 ns, and finally stabilized at 0.33 nm, which reflected the good stability of the whole system to some extent. In addition, the docking score of the compound was  $-6.3$  kcal/mol. The JQT system was in equilibrium after 100 ns, but finally stabilized at 0.45 nm, and the score of the JQT complex was  $-6.2$  kcal/mol. Overall, both systems could be in equilibrium after 150 ns simulation, and the stability of the two systems was good. Compound 51320 had better system stability.

### 2.6.2. RMSF Analysis

In order to determine the deviation of the ligand from the initial posture and the degree of movement of protein residues, the root mean square fluctuation (RMSF) values of all sampled conformations during the 30 ns simulation were also calculated. RMSF fluctuates greatly, indicating that the residue is unstable, otherwise the residue is stable. The RMSF for residue  $i$  was calculated from the following Equation (2).



**Figure 6.** Root mean square deviation (RMSD) and root mean square fluctuation (RMSF) plots of JQT complex (black), 51320 (red). (a) RMSD values extracted from protein fit ligand of the protein–ligand docked complexes. RMSD plot of JQT complex (black), 51320 (red); (b) the RMSF graph of all complexes along with protein during 100 ns MD simulation. RMSF plot of JQT complex (black), 51320 (red).

$$RMSF_i = \sqrt{\frac{1}{T} \sum_{t=1}^T \langle (r'_i(t) - r_i(t_{ref}))^2 \rangle} \quad (2)$$

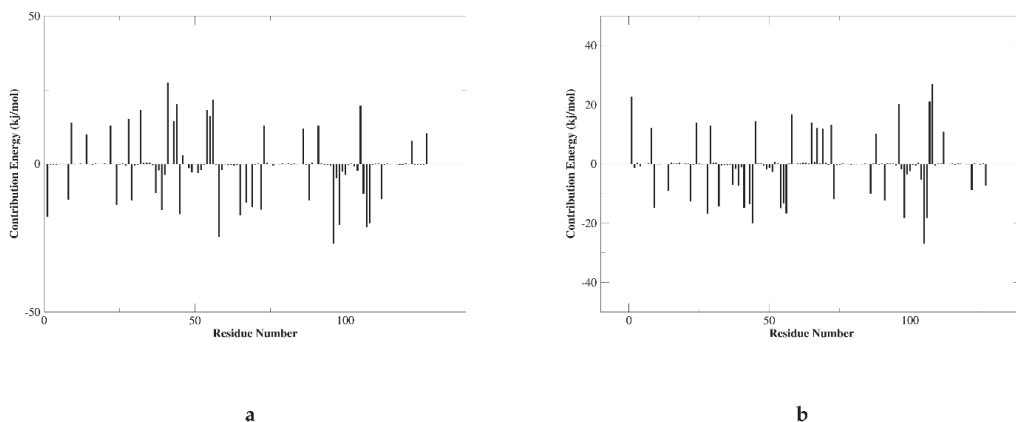
where  $T$  is the overall trajectory time,  $r_i$  is the residue location,  $t_{ref}$  is the reference time,  $r'$  is the location of atoms in residue  $i$  after aligned on the reference, and the angle brackets  $\langle \rangle$  are the average of the square distance.

The RMSF of two compounds was analyzed to measure the displacement of specific atoms during the simulation. In Figure 6b, the final image results of the two systems basically overlap between 0.05 and 1.25 nm, while RMSF values of docking pocket and residue generating interaction force are both lower than 0.25 nm, which to some extent indicates that the flexibility of the two systems is low, and the overall effect of compound binding is better.

### 2.7. MM/GBSA Analysis

Molecular mechanics Poisson–Boltzmann surface area (MM/PBSA) is an effective and reliable method for calculating the free energy of binding of small inhibitors to their protein targets. Another important indicator that considers the potential affinity of a ligand to its target is the free energy of binding calculated using MM-PBSA and MD. In general, complexes with lower binding free energy can be considered more stable, and their ligands are expected to have higher activity and potency. We summarize the interaction energy and binding free energy of the two complexes in Figure 7a,b, respectively. The MM/GBSA of the complex system is calculated from a single trajectory collected from the respective 100 ns simulation (Table 5). The analysis of the contribution of each energy term shows that the electrostatic interaction of 51320 (−179.032 kJ/mol) (Figure 8b) is much stronger than the corresponding term of JQT (Figure 8a) and PD-L1 (12.196 kJ/mol). Therefore, the compounds screened will be able to maintain a lasting interaction with the desired protein. The quantitative information on the contribution of each amino acid residue to energy is very helpful for a better understanding of the binding mechanism of inhibitor molecules. The analysis of the selected compounds in Figure 8 revealed that MET-115, TYR-56, and ILE-54 have high energy contributions in JQT and 51320. It can be seen from the above results that the selected compound can maintain long-term interaction with the binding site of the PD-L1 protein, resulting in the inhibition of the target protein.

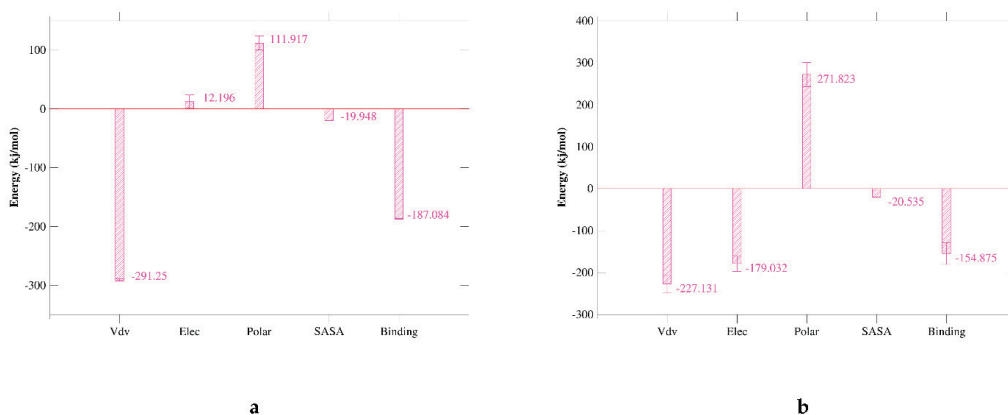




**Figure 7.** Residue wise decomposition of binding free energies obtained from the MMPBSA analyses. (a) JQT; (b) 51320.

**Table 5.** Binding energy of binding for the protein complexed with ligands JQT, 51320.

| Criteria                        | JQT                  | 51320                 |
|---------------------------------|----------------------|-----------------------|
| Van der Waal energy (kJ/mol)    | $-291.250 \pm 1.797$ | $-227.131 \pm 21.896$ |
| Electrostatic energy (kJ/mol)   | $12.196 \pm 11.229$  | $-179.032 \pm 18.056$ |
| Polar solvation energy (kJ/mol) | $111.917 \pm 12.103$ | $271.823 \pm 28.866$  |
| SASA energy (kJ/mol)            | $-19.948 \pm 0.176$  | $-20.535 \pm 0.727$   |
| Binding energy (kJ/mol)         | $-187.084 \pm 0.748$ | $-154.875 \pm 25.470$ |



**Figure 8.** Binding energy of binding for the protein complexed with ligands JQT, 51320. (a) JQT; (b) 51320.

### 3. Discussion

In recent years, anti PD-L1 monoclonal antibodies have also shown positive reactions in clinical trials of various malignant tumors. However, antibody drugs have some shortcomings, such as immunogenicity problems and poor tumor tissue permeability, resulting in a low overall response rate of PD-1/PD-L1 antibody drugs [29]. At present, small molecule inhibitors based on PD-1/PD-L1 are gradually recovering. Marine natural

products are closely related to the fields of drug discovery and molecular biology, and have always attracted the attention of the scientific community. Therefore, our research aims to use marine natural products to perform virtual screening of PD-L1 detection sites.

In this study, we collected 7 structures of PD-L1 with low molecular mass inhibitor by reading the literature. A structure-based pharmacophore model was constructed by using DS 4.5, and 6R3K with the highest selection score was selected. The pharmacophore model constructed by the complex was used to screen the marine natural product database. The pharmacophore model is validated by the active compound, and the AUC under the ROC curve indicates that the model has good distinguishing ability. The validated pharmacophore model was used in the virtual screening process. A total of 12 compounds were retrieved for hits and further screened by molecular docking methods. According to the molecular docking score, the first two compounds with a better binding score than the original ligand JQT (−6.2 kcal/mol) were selected for further verification.

We conducted interaction analysis from the perspective of molecular docking. The rich interaction types between compound 513320 and protein can be seen, the docking result is reliable, and the selected conformation can be further analyzed. In addition, quantum mechanics/molecular mechanics (QM/MM) calculations can be performed on the complex to select conformations from docking simulations [46]. After years of development and calibration, QM/MM hybrid method has become an indispensable tool to study the dynamics of a variety of chemical and biochemical processes. For example, an article uses a molecular docking method combining quantum mechanics and molecular mechanics (QM/MM) to determine the resuscitation pathway of inhibited AChE [47]. Another article studied the reaction mechanism between oxime and *Mm*AChE, using the sequential QM/docking (MM) method [48]. QM/MM is mostly used to characterize and study the transition state and activation energy of enzyme reactions. The conformation calculated by this method describes the surrounding environment in more detail. However, the calculation becomes more complicated and not easy to control. We selected the conformation by analyzing the interaction between molecules and combining scores, which not only pays attention to the binding mode but also has scores for reference. However, the influence of the environment is not considered, and some compounds will change the docking conformation due to environmental changes. All in all, it is better to use QM/MM for the selection of the molecular conformation of the enzyme's active target. It is more visual and convenient to use molecular interaction force to choose the conformation of other molecules. In the future, further QM/MM research on PD-L1 and molecules can be carried out for better selection of molecular conformations.

The two selected compounds 51320 and 37080 have been evaluated based on ADME characteristics, and the 51320 showed good ADME characteristics. Compound 37080 violates Lipinski's Five Rules, so this compound was skipped for further evaluation. Compounds with good ADME properties were further evaluated for toxicity properties to measure harmful effects on humans or animals. Toxicity analysis found that the selected compound 51320 has very low toxicity and JQT has cytotoxicity. Our selected compound 51320 has no cytotoxicity and is better than JQT.

The MD simulation method identifies the stability of the compound to the protein binding site. The 150 ns simulation trajectory was searched and analyzed based on RMSD and RMSF to confirm the stability of the compound and protein binding site. In addition, the MM/GBSA calculated from a single trajectory found a high  $\Delta G$  binding value, indicating that the selected protein-ligand complex has long-term simulation stability.

All in all, marine natural products provide a lot of information for the discovery of new drugs. Through virtual screening, small-molecule inhibitors of PD-L1 were efficiently identified from more than 52,000 marine natural products. The expansion and further optimization of the screening range can finally identify useful immunomodulators to help improve public health.

## 4. Materials and Methods

### 4.1. Structure-Based Pharmacophore Modeling and Virtual Screening

#### 4.1.1. Complex-Based Pharmacophore Modeling

Our first goal in this project was to collect as much information as possible about PD-L1 as an inhibitor target. Through a literature search, we downloaded 7 PD-L1 compounds and small molecule inhibitors from the PDB. Discovery Studio 4.5 was used to establish a pharmacophore model based on the compound (Table 1). The pharmacophore model with the highest score was used to screen the compound.

#### 4.1.2. Pharmacophore Model Validation

In the modeling process, the receiver operating characteristic (ROC) curve analysis and verification method built in DS 4.5 was used. Pharmacophore validation helps to assess the potential properties of active and inactive compounds, usually derived from specific protein-ligand interactions. A total of 90 active antagonists obtained from patent and literature searches were used to validate the pharmacophore model, which is composed of 60 active compounds and 30 inactive compounds. Then, the generated pharmacophore was verified by using the verification option in the receptor ligand pharmacophore generation protocol implemented in DS 4.5. From the area under the ROC curve (AUC), we can judge whether a pharmacophore has successfully selected active ingredients and removed inactive ingredients [49,50]. The area under the ROC curve (AUC) is  $0 \leq A \leq 1$ . When  $A > 0.5$ , the closer A is to 1, the higher the diagnostic accuracy. When  $A = 0.5$ , the diagnosis does not work at all. When  $A < 0.5$ , it does not meet the actual situation.

#### 4.1.3. Virtual Screening Based on Pharmacophore

The marine small molecule databases (MND, SWMD, CMNPD) were screened according to the characteristics of the pharmacophore. DS 4.5 created and acquired 3D models in the case of protein-ligand interactions. These compounds were directly transferred to the database list for rapid virtual screening based on pharmacophore characteristics. According to the pharmacophore matching score, the fitted hit compounds were ranked and further verified. Of the 20 molecules obtained, a total of 12 hits were selected after careful visual inspection.

### 4.2. ADME and Toxicity Test

#### 4.2.1. ADME

ADME is important to analyze the pharmacodynamics of the proposed molecule which could be used as a drug. The Swiss ADME server (<http://www.swissadme.ch/>, accessed on 9 October 2021) was used to evaluate the selected ligands which were harvested from PubChem, which was done on the basis canonical SMILES [38]. The ADME properties of the chosen compounds were calculated. The major ADME-associated parameters such as pharmacokinetic properties and the solubility of the drug were considered. The values of the observed properties are presented in Table 3.

#### 4.2.2. Toxicity Test

Calculation-based methods have made it possible to obtain a safety profile of the desired compound to measure toxicity through computer methods. ProTox-II ([http://tox-new.charite.de/protox\\_II/](http://tox-new.charite.de/protox_II/), accessed on 9 October 2021) server was used to determine the toxic effects of the two selected compounds [51]. The ProTox-II server predicts the median lethal dose (LD50), organ toxicity (hepatotoxicity), and toxicological endpoint (immunotoxicity and cytotoxicity) of the query molecule.

### 4.3. MD Simulation

In order to further verify the results obtained, the second docking program CDOCKER on DS 4.5 was adopted. The results were evaluated based on the interaction energy of CDOCKER, and a higher interaction energy of CDOCKER meant greater beneficial binding.

After docking, the compound with the highest binding energy for each target is simulated by MD simulation to check the stability of the compound in the binding pocket. Then, GROMACS 2019.1 software package [52], gromos54a7atb.ff force field and single point charge (SPC216) model was used for molecular dynamics simulation of the 150 ns. In order to ensure the total charge neutrality of the simulated system, a corresponding number of sodium ions was added to replace the water molecules in the three systems to produce a solvent box of appropriate size. Then, periodic boundary conditions (PBC) [53] were applied in the three directions of the system. Using the gromos54a7\_atb force field, the force field parameters of the entire atom can be obtained from the ATB website (<http://atb.uq.edu.au/>, accessed on 9 October 2021). A first pass (EM) was conducted to minimize the energy of 50,000 steps of the entire system at 300 K, then through MD simulation with location constraints, through NVT collection (constant particle number, volume and temperature), and finally through NPT collection (constant particle number, pressure, and temperature) [53]. In addition, we balanced enzymes, ligand molecules, and solvents.

#### 4.4. MM/GBSA

Improved MM-PBSA or Molecular Mechanics–Poisson Boltzmann Surface Area is an opensource software used to calculate the free energy of binding between the receptor and the inhibitor. As a scoring function, MM-PBSA has been used in the calculation method of drug design [54]. In this study, MM-PBSA was used to determine the binding free energy of JQT and molecule 51320, respectively.

The following Equation (3) describes the binding free energy:

$$G_{binding} = G_{complex} - (G_{protein} + G_{ligand}) \quad (3)$$

The free energy of protein-inhibitor complex is represented by  $G_{Complex}$ , the free energy of protein in solvent is represented by  $G_{protein}$ , and the free energy of inhibitor in solvent is represented by  $G_{ligand}$ .

## 5. Conclusions

PD-L1 has become a therapeutic target for many malignant tumors. In this study, a structure-based pharmacophore model was generated using the crystal structure of PD-L1 (6R3K) and the combined small molecule inhibitor JQT. These were used for virtual screening of a marine natural product database. Molecular docking, ADME analysis, and toxicity studies were performed on the obtained compounds. Subsequently, the molecule 51320 was selected for molecular dynamics simulation and MM/GBSA methods, revealing that 51320 is a potential small molecule inhibitor that helps inhibit PD-L1. The small molecule can be further evaluated through different laboratory-based experimental techniques to help determine the activity of the compound, thereby providing an alternative to immunotherapy.

**Author Contributions:** L.L. conceived and designed the study; A.Z., Q.W. and T.Z. contributed to the acquisition, analysis, and interpretation of data; L.L. and A.Z. wrote the manuscript; L.L. reviewed the paper and provided comments; and all authors reviewed the manuscript. All authors have read and agreed to the published version of the manuscript.

**Funding:** This project was supported by Administration of Traditional Chinese Medicine of Guangdong Province (20201180); Administration of Traditional Chinese Medicine of Guangdong Province (20211223); Science and Technology Special Project of Zhanjiang (2019A01009); Basic and Applied Basic Research Program of Guangdong Province (2019A1515110201); Program of Department of Natural Resources of Guangdong Province (GDNRC [2020]038 and [2021]53); Discipline Construction Project of Guangdong Medical University (4SG21004G).

**Institutional Review Board Statement:** Not applicable.

**Informed Consent Statement:** Not applicable.

**Data Availability Statement:** The data used to support the findings of this study are included within the article.

**Conflicts of Interest:** The authors declare that they have no known competing financial interest or personal relationships that could have appeared to influence the work reported in this paper.

## References

- Gong, J.; Chehrizi-Raffle, A.; Reddi, S.; Salgia, R. Development of PD-1 and PD-L1 inhibitors as a form of cancer immunotherapy: A comprehensive review of registration trials and future considerations. *J. Immunother. Cancer* **2018**, *6*, 8. [CrossRef]
- Webb, E.S.; Peng, L.; Baleiro, R.; Lemoine, N.R.; Ming, Y.; Wang, Y.J. Immune checkpoint inhibitors in cancer therapy. *J. Biomed. Res.* **2018**, *32*, 317–326. [PubMed]
- Ferrara, R.; Mezquita, L.; Texier, M.; Lahmar, J.; Audigier-Valette, C.; Tessonier, L.; Mazieres, J.; Zalcman, G.; Brosseau, S.; Le Moulec, S.; et al. Hyperprogressive Disease in Patients with Advanced Non-Small Cell Lung Cancer Treated with PD-1/PD-L1 Inhibitors or with Single-Agent Chemotherapy. *JAMA Oncol.* **2018**, *4*, 1543–1552. [CrossRef]
- Nishijima, T.F.; Shachar, S.S.; Nyrop, K.A.; Muss, H.B. Safety and Tolerability of PD-1/PD-L1 Inhibitors Compared with Chemotherapy in Patients with Advanced Cancer: A Meta-Analysis. *Oncologist* **2017**, *22*, 470–479. [CrossRef]
- Mühlbauer, M.; Fleck, M.; Schütz, C.; Weiss, T.; Froh, M.; Blank, C.; Schölmerich, J.; Hellerbrand, C. PD-L1 is induced in hepatocytes by viral infection and by interferon- $\alpha$  and - $\gamma$  and mediates T cell apoptosis. *J. Hepatol.* **2006**, *45*, 520–528. [CrossRef] [PubMed]
- Alsaab, H.O.; Sau, S.; Alzhrani, R.; Tatiparti, K.; Bhise, K.; Kashaw, S.K.; Iyer, A.K. PD-1 and PD-L1 Checkpoint Signaling Inhibition for Cancer Immunotherapy: Mechanism, Combinations, and Clinical Outcome. *Front. Pharmacol.* **2017**, *8*, 561. [CrossRef] [PubMed]
- Bari, S.; Muzaffar, J.; Chan, A.; Jain, S.R.; Haider, A.M.; Adams Curry, M.; Hostler, C.J. Outcomes of Programmed Cell Death Protein 1 (PD-1) and Programmed Death-Ligand 1 (PD-L1) Inhibitor Therapy in HIV Patients with Advanced Cancer. *J. Oncol.* **2019**, *2019*, 1–5. [CrossRef]
- Cimadamore, A.; Massari, F.; Santoni, M.; Lopez-Beltran, A.; Cheng, L.; Scarpelli, M.; Montironi, R.; Moch, H. PD1 and PD-L1 Inhibitors for the Treatment of Kidney Cancer: The Role of PD-L1 Assay. *Curr. Drug Targets* **2020**, *21*, 1664–1671. [CrossRef]
- Sun, J.; Zheng, Y.; Mamun, M.A.A.; Li, X.; Chen, X.; Gao, Y. Research progress of PD-1/PD-L1 immunotherapy in gastrointestinal tumors. *Biomed. Pharmacother.* **2020**, *129*, 110504. [CrossRef]
- Seetharamu, N.; Preehagul, I.; Sullivan, K. New PD-L1 inhibitors in non-small cell lung cancer—Impact of atezolizumab. *Lung Cancer Targets Ther.* **2017**, *8*, 67–78. [CrossRef]
- Kumar, R.; Collins, D.; Dolly, S.; McDonald, F.; O'Brien, M.E.R.; Yap, T.A. Targeting the PD-1/PD-L1 axis in non-small cell lung cancer. *Curr. Probl. Cancer* **2017**, *41*, 111–124. [CrossRef]
- Cha, J.H.; Chan, L.C.; Li, C.W.; Hsu, J.L.; Hung, M.C. Mechanisms Controlling PD-L1 Expression in Cancer. *Mol. Cell* **2019**, *76*, 359–370. [CrossRef]
- Jiang, X.; Wang, J.; Deng, X.; Xiong, F.; Ge, J.; Xiang, B.; Wu, X.; Ma, J.; Zhou, M.; Li, X.; et al. Role of the tumor microenvironment in PD-L1/PD-1-mediated tumor immune escape. *Mol. Cancer* **2019**, *18*, 10. [CrossRef] [PubMed]
- Kumagai, S.; Togashi, Y.; Kamada, T.; Sugiyama, E.; Nishinakamura, H.; Takeuchi, Y.; Vitaly, K.; Itahashi, K.; Maeda, Y.; Matsui, S.; et al. The PD-1 expression balance between effector and regulatory T cells predicts the clinical efficacy of PD-1 blockade therapies. *Nat. Immunol.* **2020**, *21*, 1346–1358. [CrossRef] [PubMed]
- Park, J.E.; Kim, S.E.; Keam, B.; Park, H.R.; Kim, S.; Kim, M.; Kim, T.M.; Doh, J.; Kim, D.W.; Heo, D.S. Anti-tumor effects of NK cells and anti-PD-L1 antibody with antibody-dependent cellular cytotoxicity in PD-L1-positive cancer cell lines. *J. Immunother. Cancer* **2020**, *8*, e000873. [CrossRef]
- Delaney, N.; Michot, J.-M.; Comont, T.; Kramkimel, N.; Lazarovici, J.; Dupont, R.; Champiat, S.; Chahine, C.; Robert, C.; Herbaux, C.; et al. Haematological immune-related adverse events induced by anti-PD-1 or anti-PD-L1 immunotherapy: A descriptive observational study. *Lancet Haematol.* **2019**, *6*, e48–e57. [CrossRef]
- Zak, K.M.; Grudnik, P.; Guzik, K.; Zieba, B.J.; Musielak, B.; Dömling, A.; Dubin, G.; Holak, T.A. Structural basis for small molecule targeting of the programmed death ligand 1 (PD-L1). *Oncotarget* **2016**, *7*, 30323. [CrossRef]
- Fang, W.; Zhang, J.; Hong, S.; Zhan, J.; Zhang, L.J.O. EBV-driven LMP1 and IFN- $\gamma$  up-regulate PD-L1 in nasopharyngeal carcinoma: Implications for oncotargeted therapy. *Oncotarget* **2014**, *5*, 12189. [CrossRef]
- Lim, S.-O.; Li, C.-W.; Xia, W.; Cha, J.-H.; Chan, L.-C.; Wu, Y.; Chang, S.-S.; Lin, W.-C.; Hsu, J.-M.; Hsu, Y.-H.; et al. Deubiquitination and Stabilization of PD-L1 by CSN5. *Cancer Cell* **2016**, *30*, 925–939. [CrossRef]
- Carroll, A.R.; Copp, B.R.; Davis, R.A.; Keyzers, R.A.; Prinsep, M.R. Marine natural products. *Nat. Prod. Rep.* **2021**, *38*, 362–413. [CrossRef]
- Villa, F.A.; Gerwick, L. Marine natural product drug discovery: Leads for treatment of inflammation, cancer, infections, and neurological disorders. *Immunopharmacol. Immunotoxicol.* **2010**, *32*, 228–237. [CrossRef]
- Abdelmohsen, U.R.; Balasubramanian, S.; Oelschlaeger, T.A.; Grkovic, T.; Pham, N.B.; Quinn, R.J.; Hentschel, U. Potential of marine natural products against drug-resistant fungal, viral, and parasitic infections. *Lancet Infect. Dis.* **2017**, *17*, e30–e41. [CrossRef]

23. Newman, D.J.; Cragg, G.M. Natural Products as Sources of New Drugs over the Nearly Four Decades from 01/1981 to 09/2019. *J. Nat. Prod.* **2020**, *83*, 770–803. [[CrossRef](#)] [[PubMed](#)]
24. Jiménez, C. Marine Natural Products in Medicinal Chemistry. *ACS Med. Chem. Lett.* **2018**, *9*, 959–961. [[CrossRef](#)] [[PubMed](#)]
25. Blunt, J.W.; Copp, B.R.; Hu, W.P.; Munro, M.H.; Northcote, P.T.; Prinsep, M.R. Marine natural products. *Nat. Prod. Rep.* **2008**, *25*, 35–94. [[CrossRef](#)] [[PubMed](#)]
26. Davis, G.D.J.; Vasanthi, A.H.R. Seaweed metabolite database (SWMD): A database of natural compounds from marine algae. *Bioinformation* **2011**, *5*, 361. [[CrossRef](#)]
27. Lyu, C.; Chen, T.; Qiang, B.; Liu, N.; Wang, H.; Zhang, L.; Liu, Z. CMNPD: A comprehensive marine natural products database towards facilitating drug discovery from the ocean. *Nucleic Acids Res.* **2020**, *49*, D509–D515. [[CrossRef](#)]
28. Muneer, I.; ul Qamar, M.T.; Tusleem, K.; Abdul Rauf, S.; Hussain, H.M.J.; Siddiqi, A.R. Discovery of selective inhibitors for cyclic AMP response element-binding protein: A combined ligand and structure-based resources pipeline. *Anti-Cancer Drugs* **2019**, *30*, 363–373. [[CrossRef](#)]
29. Ul Qamar, M.T.; Kiran, S.; Ashfaq, U.A.; Javed, M.R.; Anwar, F.; Ali, M.A.; Gilani, A.u.H. Discovery of novel dengue NS2B/NS3 protease inhibitors using pharmacophore modeling and molecular docking based virtual screening of the zinc database. *Int. J. Pharmacol.* **2016**, *12*, 621–632.
30. Kaserer, T.; Beck, K.R.; Akram, M.; Odermatt, A.; Schuster, D.J.M. Pharmacophore models and pharmacophore-based virtual screening: Concepts and applications exemplified on hydroxysteroid dehydrogenases. *Molecules* **2015**, *20*, 22799–22832. [[CrossRef](#)]
31. Muszjak, D.; Surmiak, E.; Plewska, J.; Magiera-Mularz, K.; Holak, T. Terphenyl-based Small-Molecule Inhibitors of Programmed Cell Death-1/Programmed Death-Ligand 1 Protein–Protein Interaction. *J. Med. Chem.* **2021**, *64*, 15. [[CrossRef](#)] [[PubMed](#)]
32. Skalniak, L.; Zak, K.M.; Guzik, K.; Magiera, K.; Musielak, B.; Pachota, M.; Szelazek, B.; Kocik, J.; Grudnik, P.; Tomala, M.; et al. Small-molecule inhibitors of PD-1/PD-L1 immune checkpoint alleviate the PD-L1-induced exhaustion of T-cells. *Oncotarget* **2017**, *8*, 72167–72181. [[CrossRef](#)] [[PubMed](#)]
33. Guzik, K.; Zak, K.M.; Grudnik, P.; Magiera, K.; Musielak, B.; Törner, R.; Skalniak, L.; Dömling, A.; Dubin, G.; Holak, T.A. Small-Molecule Inhibitors of the Programmed Cell Death-1/Programmed Death-Ligand 1 (PD-1/PD-L1) Interaction via Transiently Induced Protein States and Dimerization of PD-L1. *J. Med. Chem.* **2017**, *60*, 5857–5867. [[CrossRef](#)]
34. Perry, E.; Mills, J.J.; Zhao, B.; Wang, F.; Sun, Q.; Christov, P.P.; Tarr, J.C.; Rietz, T.A.; Olejniczak, E.T.; Lee, T.; et al. Fragment-based screening of programmed death ligand 1 (PD-L1). *Bioorganic Med. Chem. Lett.* **2019**, *29*, 786–790. [[CrossRef](#)] [[PubMed](#)]
35. Amaral, M.; Kokh, D.B.; Bomke, J.; Wegener, A.; Buchstaller, H.P.; Eggenweiler, H.M.; Matias, P.; Sirrenberg, C.; Wade, R.C.; Frech, M.J.N.C. Protein conformational flexibility modulates kinetics and thermodynamics of drug binding. *Nat. Commun.* **2017**, *8*, 2276. [[CrossRef](#)]
36. Temml, V.; Garscha, U.; Romp, E.; Schubert, G.; Gerstmeier, J.; Kutil, Z.; Matuszczak, B.; Waltenberger, B.; Stuppner, H.; Werz, O.J.S.R. Discovery of the first dual inhibitor of the 5-lipoxygenase-activating protein and soluble epoxide hydrolase using pharmacophore-based virtual screening. *Sci. Rep.* **2017**, *7*, 42751. [[CrossRef](#)]
37. Tai, W.; Tao, L.; Yuan, H.; Wang, F.; Liu, H.; Lu, S.; Leng, Y.; Zhang, W.; Jiang, Y.; Chen, Y. Pharmacophore modeling and virtual screening studies to identify new c-Met inhibitors. *J. Mol. Model.* **2012**, *18*, 3087–3100. [[CrossRef](#)]
38. Antoinette Daina, O.M.; Zoete, V. SwissADME: A free web tool to evaluate pharmacokinetics, drug-likeness and medicinal chemistry friendliness of small molecules. *Sci. Rep.* **2017**, *7*, 42717. [[CrossRef](#)]
39. Baldwin, J.J. Prediction of drug absorption using multivariate statistics. *J. Med. Chem.* **2000**, *43*, 3867–3877.
40. Ghose, A.K.; Viswanadhan, V.N.; Wendoloski, J.J. A Knowledge-Based Approach in Designing Combinatorial or Medicinal Chemistry Libraries for Drug Discovery. 1. A Qualitative and Quantitative Characterization of Known Drug Databases. *J. Comb. Chem.* **1999**, *1*, 55–68. [[CrossRef](#)]
41. Lipinski, C.A.; Lombardo, F.; Dominy, B.W.; Feeney, P.J. Experimental and computational approaches to estimate solubility and permeability in drug discovery and development settings. *Adv. Drug Deliv. Rev.* **1997**, *23*, 3–25. [[CrossRef](#)]
42. Muegge, I.; Heald, S.L.; Brittelli, D. Simple Selection Criteria for Drug-like Chemical Matter. *J. Med. Chem.* **2001**, *44*, 1841–1846. [[CrossRef](#)]
43. Banerjee, P.; Eckert, A.O.; Schrey, A.K.; Preissner, R. ProTox-II: A webserver for the prediction of toxicity of chemicals. *Nucleic Acids Res.* **2018**, *46*, W257–W263. [[CrossRef](#)]
44. El-Hasab, E.M.; El-Bastawissy, E.E.; El-Moselhy, T.F. Identification of potential inhibitors for HCV NS3 genotype 4a by combining protein–ligand interaction fingerprint, 3D pharmacophore, docking, and dynamic simulation. *J. Biomol. Struct. Dyn.* **2018**, *36*, 1713–1727. [[CrossRef](#)]
45. Alamri, M.A.; Qamar, M.T.U.; Mirza, M.U.; Bhadane, R.; Alqahtania, S.M.; Muneer, I.; Froeyen, M.; Salo-Ahen, O.M.H. Pharmacoinformatics and molecular dynamics simulation studies reveal potential covalent and FDA-approved inhibitors of SARS-CoV-2 main protease 3CLpro. *J. Biomol. Struct. Dyn.* **2020**, *39*, 4936–4948. [[CrossRef](#)] [[PubMed](#)]
46. Ryde, U. QM/MM Calculations on Proteins. *Methods Enzymol.* **2016**, *577*, 119–158. [[CrossRef](#)]
47. Kuca, K.; Musilek, K.; Jun, D.; Zdarova-Karasova, J.; Nepovimova, E.; Soukup, O.; Hrabanova, M.; Mikler, J.; Franca, T.C.C.; Da Cunha, E.F.F.; et al. A newly developed oxime K203 is the most effective reactivator of tabun-inhibited acetylcholinesterase. *BMC Pharm. Toxicol.* **2018**, *19*, 8. [[CrossRef](#)] [[PubMed](#)]

48. Ramalho, T.C.; Cunha, E.F.F.D.; Castro, A.A.D.; Pereira, A.F.; de Lima, W.E.A. Flexibility in the Molecular Design of Acetylcholinesterase Reactivators: Probing Representative Conformations by Chemometric Techniques and Docking/QM Calculations. *Lett. Drug Des. Discov.* **2016**, *13*, 360–371.
49. Kirchmair, J.; Markt, P.; Distinto, S.; Wolber, G.; Langer, T. Evaluation of the performance of 3D virtual screening protocols: RMSD comparisons, enrichment assessments, and decoy selection—What can we learn from earlier mistakes? *J. Comput.-Aided Mol. Des.* **2008**, *22*, 213–228. [[CrossRef](#)] [[PubMed](#)]
50. Pin, J.P.; Bertrand, O.; Triballeau, N.; Brabet, I.; Acher, F. Virtual screening workflow development guided by the “receiver operating characteristic” curve approach. Application to high-throughput docking on metabotropic glutamate receptor subtype 4. *J. Med. Chem.* **2005**, *48*, 2534–2547.
51. Drwal, M.N.; Priyanka, B.; Mathias, D.; Wettig, M.R.; Robert, R. ProTox: A web server for the in silico prediction of rodent oral toxicity. *Nucleic Acids Res.* **2014**, *42*, W53. [[CrossRef](#)] [[PubMed](#)]
52. Abraham, M.J.; Murtola, T.; Schulz, R.; Páll, S.; Smith, J.C.; Hess, B.; Lindahl, E. GROMACS: High performance molecular simulations through multi-level parallelism from laptops to supercomputers. *SoftwareX* **2015**, *1–2*, 19–25. [[CrossRef](#)]
53. Mark, P.; Nilsson, L. Structure and Dynamics of the TIP3P, SPC, and SPC/E Water Models at 298 K. *J. Phys. Chem. A* **2001**, *105*, 9954–9960. [[CrossRef](#)]
54. Kumari, R.; Kumar, R.; Lynn, A.; Open Source Drug Discovery Consortium. g\_mmpbsa—A GROMACS tool for high-throughput MM-PBSA calculations. *J. Chem. Inf. Model.* **2014**, *54*, 1951–1962. [[CrossRef](#)] [[PubMed](#)]

## Article

# Mono- and Dimeric Xanthenes with Anti-Glioma and Anti-Inflammatory Activities from the Ascidian-Derived Fungus *Diaporthe* sp. SYSU-MS4722

Senhua Chen<sup>1,2</sup>, Heng Guo<sup>1,2</sup>, Minghua Jiang<sup>1,2</sup>, Qilin Wu<sup>1,2</sup>, Jing Li<sup>1,2</sup>, Hongjie Shen<sup>1,2,\*</sup> and Lan Liu<sup>1,2,3,4,\*</sup>

<sup>1</sup> School of Marine Sciences, Sun Yat-sen University, Zhuhai 519082, China; chensenh@mail.sysu.edu.cn (S.C.); guoh59@mail2.sysu.edu.cn (H.G.); jiangmh23@mail2.sysu.edu.cn (M.J.); wuqlin3@mail2.sysu.edu.cn (Q.W.); lijing356@mail.sysu.edu.cn (J.L.)

<sup>2</sup> Southern Laboratory of Ocean Science and Engineering, Zhuhai 519082, China

<sup>3</sup> Guangdong Provincial Key Laboratory of Marine Resources and Coastal Engineering, Zhuhai 519082, China

<sup>4</sup> Pearl River Estuary Marine Ecosystem Research Station, Ministry of Education, Zhuhai 519082, China

\* Correspondence: shenhj5@mail2.sysu.edu.cn (H.S.); cesllan@mail.sysu.edu.cn (L.L.)

**Abstract:** Seven new xanthenes, diaporthones A–G (1–7), together with 13 known analogues, including five mono- (8–14) and six dimeric xanthenes (15–20), were obtained from the ascidian-derived fungus *Diaporthe* sp. SYSU-MS4722. Their planar structures were established by extensive spectroscopic analyses, including 1D and 2D NMR and high-resolution mass spectrometry (HR-ESIMS). The absolute configurations of 1–7 were clearly identified by X-ray crystallographic analysis and calculation of the ECD Spectra. Compounds 15–20 showed significant anti-inflammatory activity with IC<sub>50</sub> values between 6.3 and 8.0 μM. In addition, dimeric xanthenes (15–20) showed selective cytotoxicity against T98G cell lines with IC<sub>50</sub> values ranging from 19.5 to 78.0 μM.

**Keywords:** xanthenes; ascidian-derived fungus; *Diaporthe* sp.; anti-glioma activity

**Citation:** Chen, S.; Guo, H.; Jiang, M.; Wu, Q.; Li, J.; Shen, H.; Liu, L. Mono- and Dimeric Xanthenes with Anti-Glioma and Anti-Inflammatory Activities from the Ascidian-Derived Fungus *Diaporthe* sp. SYSU-MS4722. *Mar. Drugs* **2022**, *20*, 51. <https://doi.org/10.3390/md20010051>

Academic Editors: Xuefeng Zhou and Yonghong Liu

Received: 5 December 2021

Accepted: 4 January 2022

Published: 5 January 2022

**Publisher's Note:** MDPI stays neutral with regard to jurisdictional claims in published maps and institutional affiliations.



**Copyright:** © 2022 by the authors. Licensee MDPI, Basel, Switzerland. This article is an open access article distributed under the terms and conditions of the Creative Commons Attribution (CC BY) license (<https://creativecommons.org/licenses/by/4.0/>).

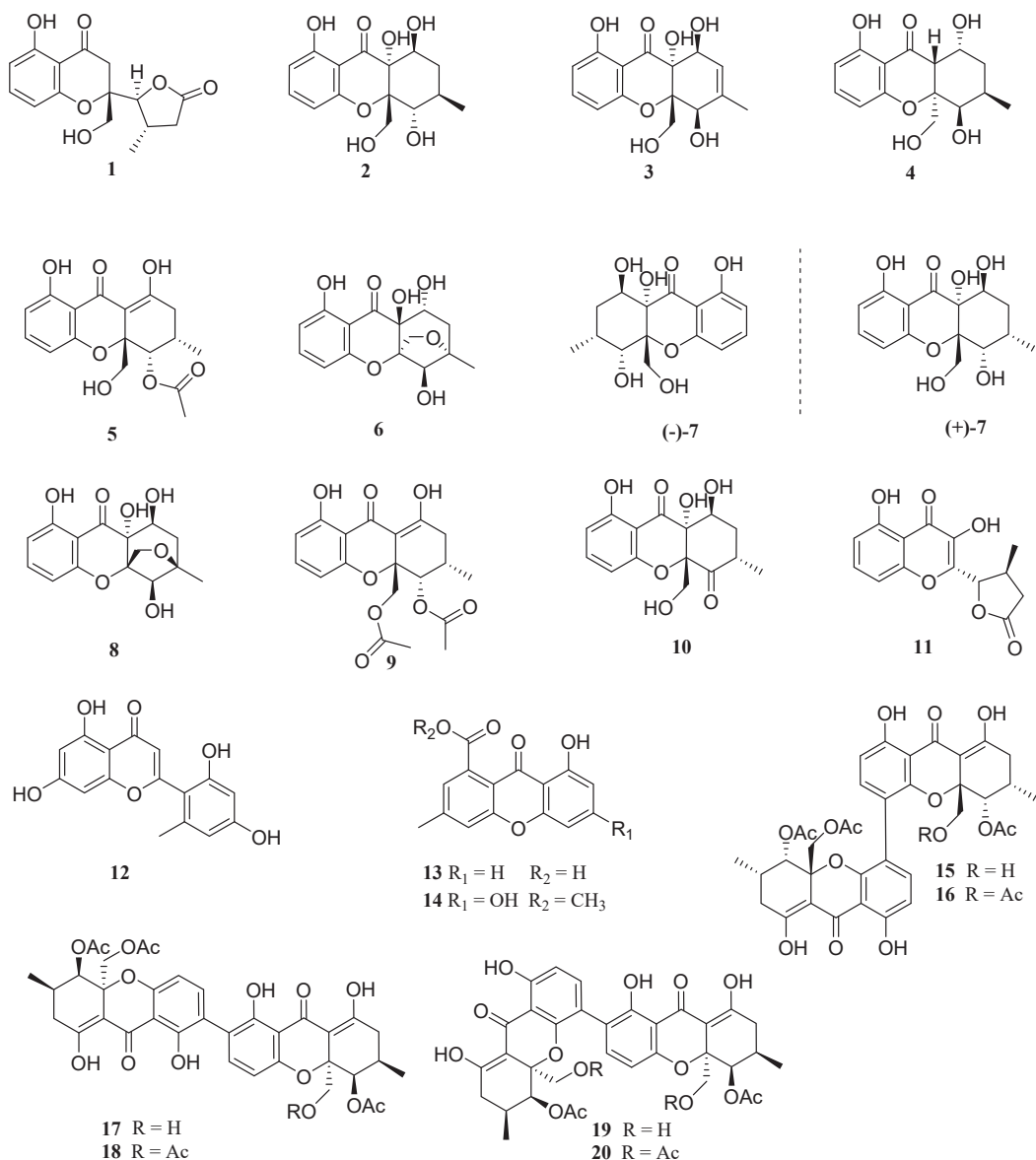
## 1. Introduction

Glioma is a fatal disease of the central nervous system having an incidence rate of 3.20 per 100,000 people [1–3]. Due to limitations of the blood–brain barrier, only four drugs, including lomustine, carmustine, temozolomide, and bevacizumab, have been approved by FDA to treat glioma in the past four decades [4,5]. Temozolomide (TMZ) as the first-line therapy drug is used for the treatment of glioma; however, at least 50% of TMZ-treated patients and more than 90% of recurrent gliomas show no response to TMZ [6,7]. Thus, it is an urgent need to find more anti-glioma agents for the treatment of glioma. In recent years, anti-glioma molecules of marine origin have attracted many scientific research institutes or pharmaceutical companies' attention. For example, marizomib (salinosporamide A) received orphan drug designation for glioblastoma in the United States [8,9], which was discovered from the marine actinomycete *Salinispora tropica* [10] and *Salinispora Arenicola* [11] and is an irreversible proteasome inhibitor with a nanomolar range IC<sub>50</sub> value [11]. Depatuxizumab vedotin was an antibody–drug conjugate (ADC) in phase 3 trials to treat newly diagnosed glioblastoma with EGFR amplification [8], which was developed from pentapeptide dolastatin 10 that was produced from the sea hare *Dolabella Auricularia* [12].

In the past five years, our research group has focused on the bioactive secondary metabolites of ascidian-derived fungi collected from the South China Sea [5,13–16]. A marine-derived fungus *Diaporthe* sp. SYSU-MS4722 was isolated from the South China Sea, whose EtOAc extract of a fermentation broth showed moderate anti-glioma activity. A subsequent chemical investigation led to the isolation of seven new polyketides, diaporthones A–G (1–7), together with 13 known analogues, including five mono- (8–14) and



six dimeric xanthenes (15–20) (Figure 1). Dimeric xanthenes (15–20) revealed selective cytotoxicity against T98G cell lines with  $IC_{50}$  values ranging from 19.5 to 78.0  $\mu$ M.



**Figure 1.** Chemical structures of compounds 1–20.

## 2. Results and Discussion

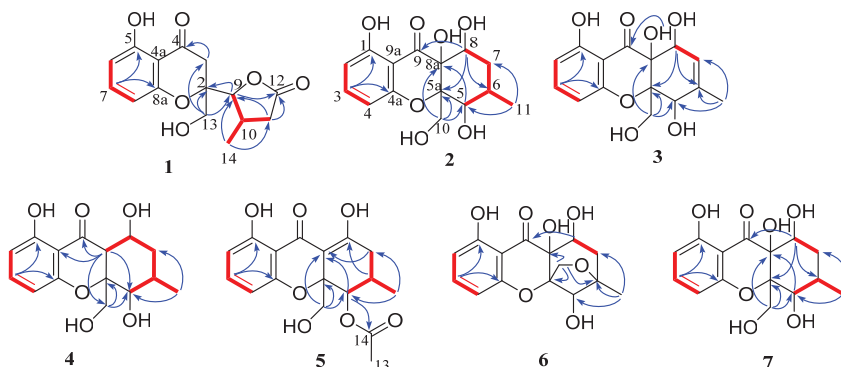
The EtOAc extract of marine-derived fungus *Diaporthe* sp. SYSU-MS4722 was performed on the repeated silica gel and Sephadex LH-20 column chromatography, followed by semipreparative HPLC to afford seven new xanthenes, diaporthones A–H (1–7) along with 13 known analogues including seven mono- (8–14) and six dimeric xanthenes (15–20).

Diaporthone A (**1**) was obtained as yellow crystal, and its molecular formula was established as  $C_{15}H_{16}O_6$  by the negative HRESIMS ions at  $m/z$  291.0869  $[M - H]^-$  (calculated for  $C_{15}H_{15}O_6$ , 291.0874) (Figure S1), indicating eight degrees of unsaturation. The  $^1H$  NMR (Table 1) displayed three aromatic protons ( $\delta_H$  6.40 (1H, d,  $J = 8.3$  Hz); 6.43 (H,  $J = 8.3$  Hz); 7.38 (1H, t,  $J = 8.3$  Hz)) owing to a 1,2,3-trisubstituted benzene ring, two methines ( $\delta_H$  4.39 (1H, d,  $J = 4.2$  Hz); 2.85 (H, m)), two methylenes ( $\delta_H$  2.22 (1H, dd,  $J = 8.9, 21.6$  Hz), 2.86 (1H, m); 3.76 (2H, s),  $\delta_H$  2.98 (2H, br s)), and one methyl ( $\delta_H$  1.20 (3H, d,  $J = 6.6$  Hz)). The  $^{13}C$  NMR showed the presence of 15 carbons, which were assigned with the help of an HMBC experiment. Except for signals ( $\delta_C$  161.4, 159.4, 138.1, 108.7, 107.2, 106.9) attributed to one aromatic ring, the other carbons were identified as one conjugated carbonyl ( $\delta_C$  196.8), one ester carbonyl ( $\delta_C$  177.3), and remaining six  $sp^3$  hybridized carbons.  $^1H$  and  $^{13}C$  NMR data (Table 1) suggested that **1** belonged to a chromone derivative containing a  $\gamma$ -lactone moiety.

**Table 1.**  $^1H$  (600 MHz) and  $^{13}C$  (150 MHz) NMR spectroscopic data of **1** in  $CD_3OD$ .

| No. | <b>1</b>          |                                | No. | <b>1</b>          |                                |
|-----|-------------------|--------------------------------|-----|-------------------|--------------------------------|
|     | $\delta_C$ , Type | $\delta_H$ , Mult ( $J$ in Hz) |     | $\delta_C$ , Type | $\delta_H$ , Mult ( $J$ in Hz) |
| 2   | 83.2, C           |                                | 8a  | 159.4, C          |                                |
| 3   | 36.7, $CH_2$      | 2.98, br s                     | 9   | 87.1, CH          | 4.39, d (4.2)                  |
| 4   | 196.8, C          |                                | 10  | 29.6, CH          | 2.85, m                        |
| 4a  | 107.2, C          |                                | 11  | 35.9, $CH_2$      | 2.22, dd (21.6, 8.9)           |
| 5   | 161.4, C          |                                |     |                   | 2.85, m                        |
| 6   | 106.9, CH         | 6.40, d (8.3)                  | 12  | 177.3, C          |                                |
| 7   | 138.1, CH         | 7.36, t (8.3)                  | 13  | 61.5, $CH_2$      | 3.76, s                        |
| 8   | 108.7, CH         | 6.43, d (8.3)                  | 14  | 19.4, $CH_3$      | 1.21, d (6.6)                  |

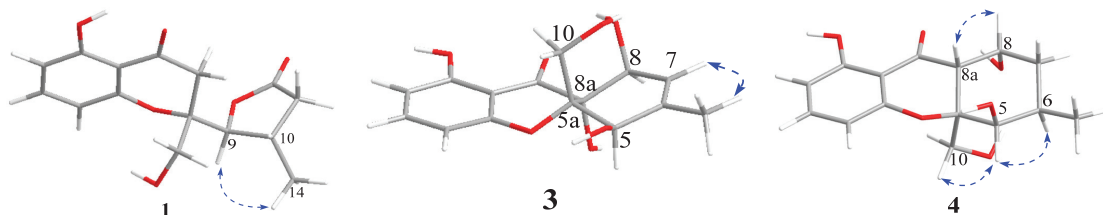
The planar structure of **1** was identified based on the extensive 2D NMR ( $^1H$ - $^1H$  COSY, HSQC, and HMBC) (Figures S2–S7) spectroscopic data (Figure 2). The HMBC correlations from H-7 to C-5 and C-8a, from H-8 to C-4a, from H-13 to C-2 and C-3, and  $^1H$ - $^1H$  COSY of H-6/H-7/H-8, as well as the NMR chemical shifts, complete a 4-hydroxylchromone skeleton with a hydroxymethyl group at C-2. The  $\gamma$ -lactone moiety with a methyl group was assigned by HMBC correlations from H-9 to ester carbonyl C-12, from H-11 to C-9 and C-12, from H-14 to C-9, C-10 and C-11, and the  $^1H$ - $^1H$  COSY correlations of H-9/H-10/H-11 and H-10/H-14. The  $\gamma$ -lactone moiety was finally linked to C-2 of the chromone skeleton, supported by HMBC correlations from H-13 to C-9 and H-9 to C-2.



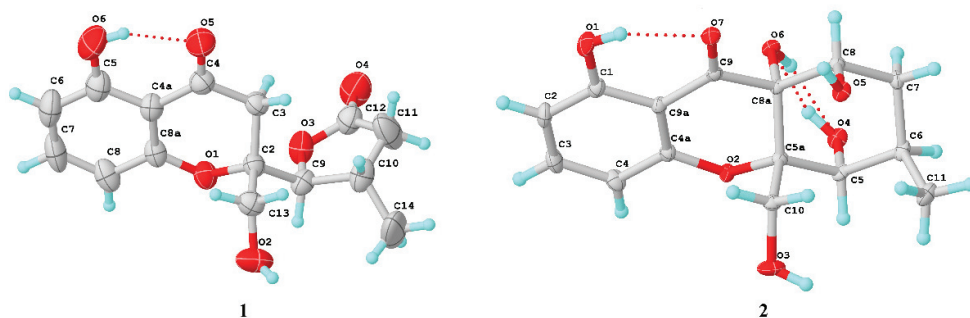
**Figure 2.** Key  $^1H$ - $^1H$  COSY (red line) and HMBC (blue arrow) correlations of compounds **1**–**7**.

The NOESY spectrum of **1** showed a correlation from H-9 to H-14, indicating that H-9 and H-14 were on the same side of the  $\gamma$ -lactone (Figure 3). The X-ray structure (Figure 4)

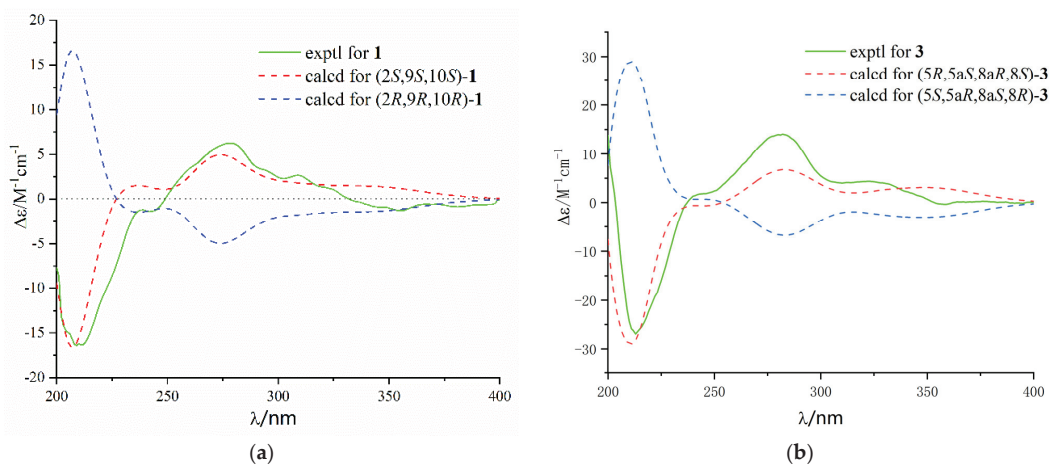
showed that the protons H-13 and H-9 were located on the close position of the axis of rotation C2–C9, indicating that the relative configuration of **1** was  $2S^*$ ,  $9S^*$ , and  $10S^*$ . In addition, the ECD spectrum of  $(2S, 9S, 10S)$ -**1** calculated by a quantum chemical method at the [B3LYP/6-311 + G(2d,p)] was in good agreement with that of the experimental one (Figure 5). Thus, the absolute configuration of **1** was identified as  $2S, 9S$ , and  $10S$ .



**Figure 3.** Key NOE (blue dash arrow) correlations of compounds **1**, **3**, and **4** (3D structures were generated by minimizing the energy using a molecular mechanics (MM2) computation by Chem3D).



**Figure 4.** X-ray crystallographic analysis of **1** and **2**.



**Figure 5.** Experimental and predicted ECD spectra of **1** (a) and **3** (b) in MeOH.

It can be seen that the proton H<sub>2</sub>-3 of **1** was the  $\alpha$ -H atom of ketone with weak acid, whose  $\alpha$ -hydrogen exchange ( $\alpha$ -deuterodeprotonation reaction) could be found in CD<sub>3</sub>OD. The signal of H<sub>2</sub>-3 was observed as a weak and small peak, and the integrals were

much less than two in the  $^1\text{H}$  NMR spectrum. The natural product with the  $\alpha$ -H atom of ketone moiety would be better for acquiring the NMR data under the deuterated solvents without exchangeable deuterium.

Diaporthone B (**2**) was obtained as yellow crystal, and its molecular formula was established as  $\text{C}_{15}\text{H}_{18}\text{O}_7$  by the negative HRESIMS ions at  $m/z$  309.0976  $[\text{M} - \text{H}]^-$  (calculated for  $\text{C}_{15}\text{H}_{17}\text{O}_7$ , 309.0980), indicating eight degrees of unsaturation. The  $^1\text{H}$  NMR (Figure S10) displayed three aromatic protons ( $\delta_{\text{H}}$  6.44 (1H, dd,  $J = 8.2, 0.9$  Hz); 6.55 (H, d,  $J = 8.2$  Hz); 7.39 (1H, t,  $J = 8.3$  Hz)), three methines ( $\delta_{\text{H}}$  4.44 (1H, t,  $J = 4.2$  Hz); 4.29 (1H, m); 2.34 (1H, m)), two methylenes ( $\delta_{\text{H}}$  1.57 (1H, dd,  $J = 14.5, 2.8$  Hz); 2.43 (1H, m); 3.83 (1H, d,  $J = 13.5$  Hz); 4.28 (1H, s)), and one methyl ( $\delta_{\text{H}}$  1.32 (3H, d,  $J = 7.8$  Hz)). The  $^{13}\text{C}$  NMR showed the presence of 15 carbons corresponding to seven  $\text{sp}^2$  hybrid carbons including one ketone carbonyl ( $\delta_{\text{C}}$  196.4) for xanthone characteristic and eight  $\text{sp}^3$  hybrid carbons. The planar structure of **2** was identified by  $^1\text{H}$ - $^1\text{H}$  COSY, HSQC, and HMBC spectroscopic data (Figure 2). The HMBC correlations from H-10 to C-5a and C-8a, from H-3 to C-1 and C-4a, and  $^1\text{H}$ - $^1\text{H}$  COSY of H-2/H-3/H-4, as well as the NMR chemical shifts, suggested the presence of a hydroxylchromone skeleton with a hydroxymethyl group at C-5a and a hydroxyl at C-8a. The remaining ring was assigned to be 4-hydroxyl-5-methyl cyclohexenol on the basis of  $^1\text{H}$ - $^1\text{H}$  COSY of H-6/H-7/H-8/H-9 and H-6/H-11, and key HMBC correlations from H-8 to C-9 and C-5a, H-5 to C-8a. Finally, the structure and absolute configuration (5*S*, 5*aS*, 6*R*, 8*aR*, 8*S*) were distinctly demonstrated by X-ray crystallographic analysis (Figure 4) from Cu  $\text{K}\alpha$  data with a Flack parameter of  $-0.01(14)$  [17] and a Hooft parameter of 0.06(7) [18].

Diaporthone C (**3**) was obtained as a colorless oil, whose molecular formula was determined as  $\text{C}_{15}\text{H}_{16}\text{O}_7$  on the basis of negative-ion HRESIMS ( $m/z$  307.0820  $[\text{M} - \text{H}]^-$ , calculated for  $\text{C}_{15}\text{H}_{15}\text{O}_7$ , 307.0823). Detailed analysis of its NMR spectroscopic data (Table 2) suggested that **3** was similar to **2** belonging to the xanthone class, except for the presence of an additional double bond ( $\delta_{\text{C}}$  140.1 and 122.1;  $\delta_{\text{H}}$  5.60) in **3**. The key HMBC correlations from methyl protons H-11 to olefinic carbons C-6 and C-7 were allowed to assign the location of the double bond in **3**. The gross structure of **3** was identified by the 2D NMR spectroscopy (Figure 2). NOE correlations of H-5 with H-10 and H-10 with H-8 were not observed, and the relative configuration of compound **3** should be 5*R*\*, 5*aS*\*, 8*aR*\*, and 8*S*\* (Figure 3). The predicted ECD curve of **3** matched well with the experimental one (Figure 5). Hence, the absolute configuration of **3** was identified as 5*R*, 5*aS*, 8*aR*, and 8*S*.

Diaporthone D (**4**) was obtained as a colorless oil, and its molecular formula  $\text{C}_{15}\text{H}_{19}\text{O}_6$  was identified by the positive HRESIMS ion at HRESIMS  $m/z$  295.1169  $[\text{M} + \text{H}]^+$  (calculated for  $\text{C}_{15}\text{H}_{19}\text{O}_6$ , 295.1176). Comparison of the  $^1\text{H}$  and  $^{13}\text{C}$  NMR data (Table 1) of **4** with those of **2** suggested that **4** possessed the same xanthone framework, except for one of the hydroxyl groups (8*a*-OH) in **2** being replaced by a proton in **4**. The  $^1\text{H}$ - $^1\text{H}$  COSY of H-8 and H-8a and HMBC correlations from H-8a to C-9 and C-10 assigned the position of the proton H-8, in accordance with the proton having double peaks at 2.48 ppm (Figures S26–S31). The gross structure of **4** was identified by the 2D NMR spectroscopy (Figure 2). The coupling constant value of  $J_{8,8a} = 4.5$  Hz and NOE correlation of H-8a with H-8 indicated that the orientation of H-8 and H-8a was the same face of cyclohexane (Figure 3). The coupling constant value of  $J_{5,6} = 2.1$  Hz and NOE correlation of H-5 with H-6 and H-10 suggested that H-5, H-6, and H-10 were on the same side. The relative configuration of compound **4** was assigned as 5*R*\*, 5*aR*\*, 6*R*\*, 8*aR*\*, and 8*R*\*. The absolute configuration of **4** was assigned by comparing the experimental and calculated ECD spectra, and the calculated ECD spectrum was agreed with that of the experimental one (Figure 6). Therefore, the absolute configuration of **4** was assigned as 5*R*, 5*aR*, 6*R*, 8*aR*, and 8*R*.

Table 2.  $^1\text{H}$  (400 MHz) and  $^{13}\text{C}$  (100 MHz) NMR spectroscopic data of 2–4.

| No.   | 2 <sup>a</sup>             |                                      | 3 <sup>b</sup>             |                                      | 4 <sup>a</sup>             |                                      |
|-------|----------------------------|--------------------------------------|----------------------------|--------------------------------------|----------------------------|--------------------------------------|
|       | $\delta_{\text{C}}$ , Type | $\delta_{\text{H}}$ , Mult (J in Hz) | $\delta_{\text{C}}$ , Type | $\delta_{\text{H}}$ , Mult (J in Hz) | $\delta_{\text{C}}$ , Type | $\delta_{\text{H}}$ , Mult (J in Hz) |
| 1     | 163.4, C                   |                                      | 163.1, C                   |                                      | 162.5, C                   |                                      |
| 2     | 109.7, CH                  | 6.44, dd (8.2, 0.9)                  | 108.8, CH                  | 6.36, d (8.7)                        | 109.2, CH                  | 6.41, dd (8.3, 1.0)                  |
| 3     | 139.0, CH                  | 7.39, t (8.3)                        | 138.6, CH                  | 7.36, t (8.3)                        | 138.8, CH                  | 7.34, t (8.3)                        |
| 4     | 109.6, CH                  | 6.55, d (8.2)                        | 108.2, CH                  | 6.39, d (8.8)                        | 109.2, CH                  | 6.41, dd (8.3, 1.0)                  |
| 4a    | 159.8, C                   |                                      | 160.9, C                   |                                      | 161.1, C                   |                                      |
| 5     | 75.3, CH                   | 4.29, m                              | 73.9, CH                   | 4.74, d (6.3)                        | 71.6, CH                   | 3.90, d (2.1)                        |
| 5a    | 76.2, C                    |                                      | 74.3, C                    |                                      | 83.5, C                    |                                      |
| 6     | 36.2, CH                   | 2.34, m                              | 140.1, C                   |                                      | 26.4, CH                   | 2.43, m                              |
| 7     | 29.9, CH <sub>2</sub>      | 1.57, dt (14.8, 2.8)<br>2.43, m      | 122.1, CH                  | 5.60, dt (4.6, 1.8)                  | 34.9, CH <sub>2</sub>      | 1.53, m<br>1.84, m                   |
| 8     | 69.6, CH                   | 4.44, t (3.6)                        | 68.0, CH                   | 4.61, t (5.0)                        | 69.4, CH                   | 4.23, dt (4.7, 2.6)                  |
| 8a    | 85.0, C                    |                                      | 86.9, C                    |                                      | 48.5, CH                   | 2.48, d (4.5)                        |
| 9     | 196.4, C                   |                                      | 197.3, C                   |                                      | 202.4, C                   |                                      |
| 9a    | 108.6, C                   |                                      | 108.3, C                   |                                      | 111.3, C                   |                                      |
| 10    | 60.5, CH <sub>2</sub>      | 3.83, d (13.5)<br>4.28, m            | 64.3, CH <sub>2</sub>      | 4.09, m                              | 63.2, CH <sub>2</sub>      | 3.72, d (12.0)<br>3.81, d (12.0)     |
| 11    | 20.7, CH <sub>3</sub>      | 1.32, d (7.8)                        | 19.3, CH <sub>3</sub>      | 1.84, d (1.4)                        | 18.0, CH <sub>3</sub>      | 1.06, d (7.0)                        |
| 1-OH  |                            |                                      |                            | 11.26, s                             |                            |                                      |
| 5-OH  |                            |                                      |                            | 4.84, d (6.6)                        |                            |                                      |
| 8-OH  |                            |                                      |                            | 4.69, d (5.1)                        |                            |                                      |
| 8a-OH |                            |                                      |                            | 5.43, s                              |                            |                                      |
| 10-OH |                            |                                      |                            | 3.80, d (5.1)                        |                            |                                      |

<sup>a</sup> Spectra were recorded in CD<sub>3</sub>OD; <sup>b</sup> Spectra were recorded in acetone-*d*<sub>6</sub>.

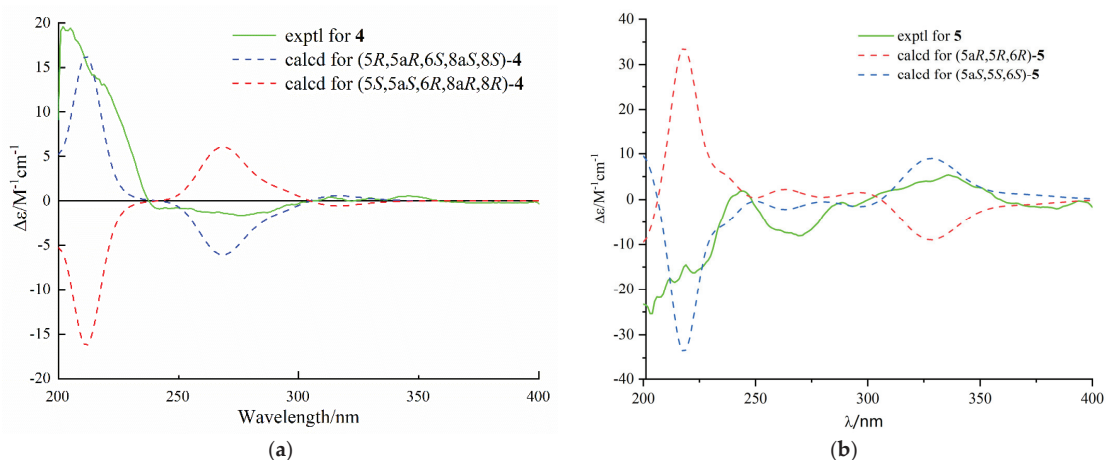


Figure 6. Experimental and predicted ECD spectra of 4 (a) and 5 (b) in MeOH.

Diaporthone E (5) was obtained as a colorless oil. The negative HRESIMS  $m/z$  333.0975  $[\text{M} - \text{H}]^-$  (calculated for C<sub>17</sub>H<sub>17</sub>O<sub>7</sub>, 333.0980) suggested the molecular formula of 5 was C<sub>17</sub>H<sub>18</sub>O<sub>7</sub> with four degrees of unsaturation. The 1D and 2D NMR data (Figures S34–S39) indicated that compound 5 shared the same xanthone skeleton as penexanthone B (9). The only difference between them was that compound 5 was the absence of an additional acetyl group (10-Ac) compared to 6. Compound 5 was a precursor of biosynthesis of 12-deacetylphomoxanthone A (15), and there is reason to believe that they share the same absolute configuration of 5*S*, 5*aS*, and 6*S*. The predicted ECD spectrum of (5*S*, 5*aS*, 6*S*)-5

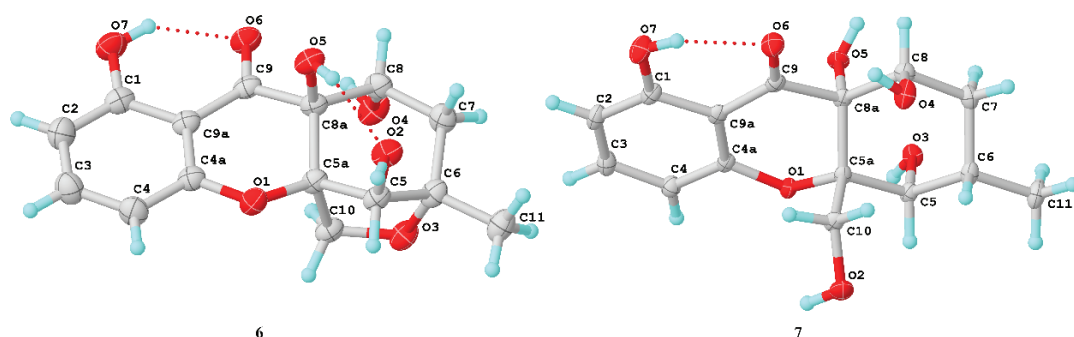
showed well fit with that of the experimental one (Figure 6). Thus, compound 5 was identified as de-10-acetylpenexanthone B.

Diaporthone F (6) was obtained as a yellow crystal and had the same molecular formula ( $C_{15}H_{16}O_7$ ) as 8 established by the HR-ESIMS ions at  $m/z$  307.0828  $[M - H]^-$  (calculated for  $C_{15}H_{15}O_7$ , 307.0823). Compound 6 shared the same planar structure as phomoxanthone G (8), which was further identified by  $^1H$ - $^1H$  COSY, HSQC, and HMBC spectroscopies (Figures S42–S47). Detailed analysis of their NMR (Table 3), diaporthone F (6) and phomoxanthone G should be a pair of epimers. The structure of 6 (Figure 7) and configuration (5*R*, 5*aR*, 6*S*, 8*aS*, 8*R*) were identified by X-ray crystallographic analysis from Cu K $\alpha$  data with a Flack parameter of -0.13(15) [17] and a Hooft parameter of 0.16(9).

**Table 3.**  $^1H$  (400 MHz) and  $^{13}C$  (100 MHz) NMR spectroscopic data of 5–7.

| No. | 5 <sup>a</sup>        |                             | 6 <sup>a</sup>        |  | 7 <sup>b</sup>        |                              |
|-----|-----------------------|-----------------------------|-----------------------|--|-----------------------|------------------------------|
|     | $\delta_C$ , Type     | $\delta_H$ , Mult (J in Hz) | $\delta_C$ , Type     | $\delta_H$ , Mult (J in Hz)              | $\delta_C$ , type     | $\delta_H$ , Mult (J in Hz)  |
| 1   | 162.0, C              |                             | 164.4, C              |  | 163.4, C              |                              |
| 2   | 108.1, CH             | 6.42, d (8.2)               | 108.5, CH             | 6.52, d (8.2)                            | 109.7, CH             | 6.48, dd, (8.3, 0.9)         |
| 3   | 138.2, CH             | 7.31, t (8.3)               | 139.0, CH             | 7.45, t (8.3)                            | 139.0, CH             | 7.43, t, (8.3)               |
| 4   | 110.5, CH             | 6.52, d (8.3)               | 110.9, CH             | 6.54, d (8.2)                            | 109.7, CH             | 6.59, dd, (8.3, 0.9)         |
| 4a  | 157.6, C              |                             | 161.2, C              |  | 160.2, C              |                              |
| 5   | 70.3, CH              | 5.72, s                     | 80.5, CH              | 4.22, s                                  | 74.5, CH              | 4.28, m                      |
| 5a  | 82.4, C               |                             | 78.1, C               |  | 76.3, C               |                              |
| 6   | 27.8, CH              | 2.39, m                     | 82.9, C               |  | 29.2, CH              | 2.25, m                      |
| 7   | 33.5, CH <sub>2</sub> | 2.43, m                     | 36.9, CH <sub>2</sub> | 1.80, dt (15.2, 0.8)2.39, dd (15.2, 5.4) | 31.9, CH <sub>2</sub> | 2.25, m2.06, m               |
| 8   | 178.1, C              |                             | 71.1, CH              | 4.47, dd (5.3, 0.9)                      | 68.5, CH              | 4.40, t, (2.9)               |
| 8a  | 101.0, C              |                             | 81.9, C               |  | 85.4, C               |                              |
| 9   | 187.7, C              |                             | 195.6, C              |  | 196.2, C              |                              |
| 9a  | 106.7, C              | 3.51, d (13.2)              | 107.5, C              |  | 108.6, C              |                              |
| 10  | 65.6, CH <sub>2</sub> | 4.03, d (13.2)              | 67.9, CH <sub>2</sub> | 4.38, d (8.1)3.65, d (8.1)               | 60.4, CH <sub>2</sub> | 4.26, d (13.4)3.78, d (13.4) |
| 11  | 17.7, CH <sub>3</sub> | 1.06, d (5.5)               | 23.9, CH <sub>3</sub> | 1.33, s                                  | 18.1, CH <sub>3</sub> | 1.12, d (6.7)                |
| 12  | 170.8, C              |                             |                       |  |                       |                              |
| 13  | 21.0, CH <sub>3</sub> | 2.09, s                     |                       |  |                       |                              |
| 14  | 162.0, C              |                             |                       |  |                       |                              |

<sup>a</sup> Spectra were recorded in CDCl<sub>3</sub>; <sup>b</sup> Spectra were recorded in CD<sub>3</sub>OD.



**Figure 7.** X-ray crystallographic analysis of 6 and 7.

Compound 7 was obtained as a yellow crystal and had the molecular formula  $C_{15}H_{18}O_7$ , which was established by the HR-ESIMS ions at  $m/z$  309.0978  $[M - H]^-$  (calculated for  $C_{15}H_{17}O_7$ , 309.0979). The structure of 7 was clearly identified by X-ray crystallographic analysis (Figure 6), whose relative and planar structure was the same as

that of phaseolorin D [19]. In detail, the X-ray structure was the monoclinic space group  $P2_1/c$  (Figure 7), which was different from that of phaseolorin D ((+)-7) with the triclinic space group. It suggested that compound 7 should be an enantiomer in the solid crystals (Figure 8), which showed an excellent fit with the result of no signal of CD spectrum and no optical activity sign in methanol. Subsequently, the chiral HPLC was used for purification of ( $\pm$ )-7, and the two enantiomers, (+)-7 ( $t_R = 28.7$  min) and (–)-7 ( $t_R = 31.5$  min) were purified, respectively, and showed opposite Cotton effects in their CD spectra and opposite optical rotations (Figure 9). The calculated ECD curve of (5*R*, 5*aR*, 6*R*, 8*aS*, 8*R*)-7 was comparable to the experimental one of (–)-7, resulting in that the absolute configuration of (–)-7 was 5*R*, 5*aR*, 6*R*, 8*aS*, 8*R*. Compounds 2 and ( $\pm$ )-7 were epimers derived from the same precursor, chrysophanol, and a possible biogenetic pathway for 2 and ( $\pm$ )-7 was proposed, as shown in Figure S62 (supplementary material). Compounds 2, 3, and (+)-7 showed a very similar ECD spectrum with a strong and negative Cotton effect (CE) at 209 nm and two negative CEs at approximately 281 and 326 nm (Figure S63, Supplementary Material), while (–)-7 revealed opposite Cotton effects. The negative Cotton effect (CE) at 209 nm should be derived from the  $n-\pi^*$  transition of the chromone chromophore with the absolute configuration of 5*aS* and 8*aR*.

The other known compounds were identified as phaseolorin D (+)-7 [19], Phomoxanthone G (8) [20], penexanthone B (9) [21], phaseolorin E (10) [19], phomoxanthone F (11) [20], penimethavone A (12) [22], monodictyxanthone (13) [23], methyl 6,8-dihydroxy-3-methyl-9-oxo-9*H*-xanthene-1-carboxylate (14) [24], 12-deacetylphomoxanthone A (15) [25], phomoxanthone A (16) [26], dicerandrol B (17) [27], dicerandrol C (18) [27], phomoxanthone B (19) [26] and deacetylphomoxanthone B (20) [28] by comparing their spectroscopic data with those reported in the literature.

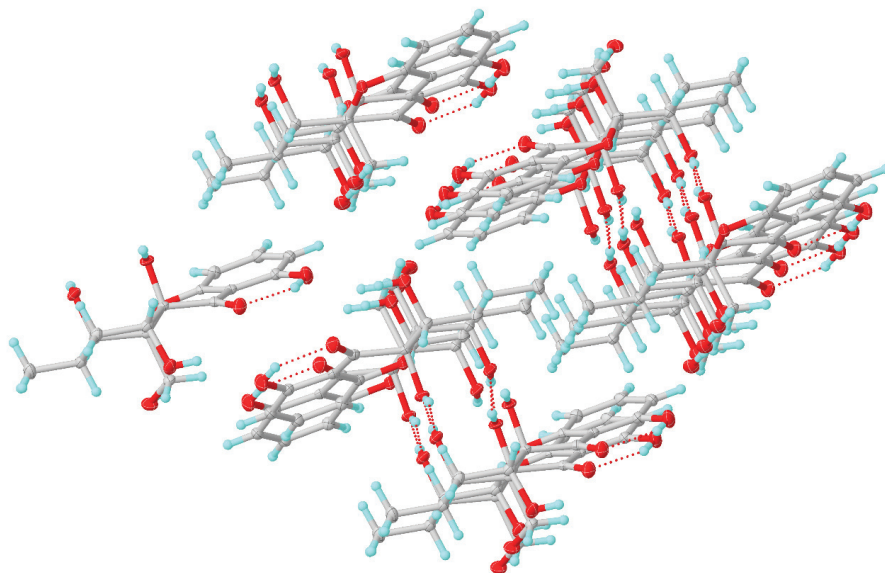
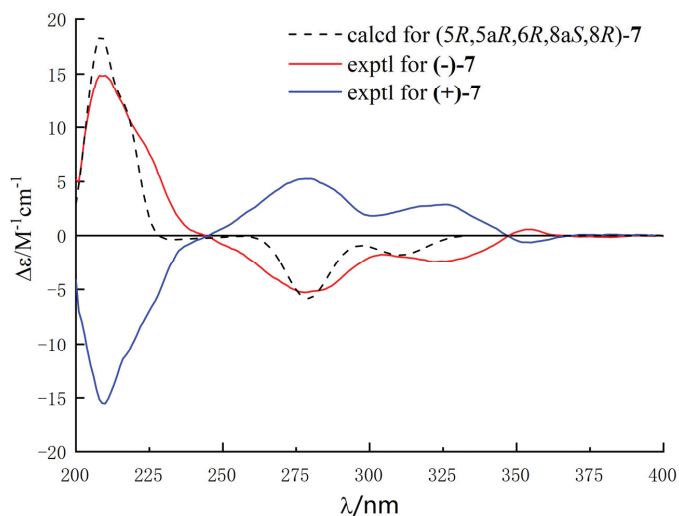


Figure 8. Molecular packing properties of 7.



**Figure 9.** Experimental and predicted ECD spectra of (+)- and (-)-7 (in MeOH).

All isolates were evaluated for anti-glioma using T98G, U87MG, and U251 human cell lines with temozolomide as the positive control. Only dimeric xanthenes (**15–20**) exhibited promising growth-inhibitory effects on the T98G cell line with  $IC_{50}$  values between 19.5 to 78.0  $\mu\text{M}$  (Table 4). Additionally, all monomeric xanthenes (**1–14**) displayed weak or no cytotoxicity against T98G, U87MG, and U251 human cell lines. The result suggested that the dimeric skeleton of xanthenes played an important role in anti-glioma activity.

**Table 4.** Anti-glioma activity against T98G, U87MG, and U251 human cell lines and inhibition of NO production in LPS-induced RAW264.7 cells of compounds **11** and **14–20**.

| Compounds    | T98G ( $IC_{50}$ , $\mu\text{M}$ ) | U87MG ( $IC_{50}$ , $\mu\text{M}$ ) | U251 ( $IC_{50}$ , $\mu\text{M}$ ) | Inhibition of NO Production, $IC_{50}$ ( $\mu\text{M}$ ) |
|--------------|------------------------------------|-------------------------------------|------------------------------------|--|
| <b>11</b>    | >100                               | >100                                | >100                               | 41.4   |
| <b>14</b>    | >100                               | >100                                | >100                               | 32.2   |
| <b>15</b>    | 23.8                               | >100                                | >100                               | 6.3  |
| <b>16</b>    | 19.5                               | >100                                | >100                               | 7.5  |
| <b>17</b>    | 57.6                               | >100                                | >100                               | 6.3  |
| <b>18</b>    | 34.6                               | >100                                | >100                               | 7.6  |
| <b>19</b>    | 74.1                               | >100                                | >100                               | 8.0  |
| <b>20</b>    | 78.2                               | >100                                | >100                               | 7.8  |
| Temozolomide | 151                                | 203                                 | 189                                | -  |
| Indomethacin | -                                  | -                                   | -                                  | 35.8   |

All compounds (**1–20**) were also tested for the inhibition of nitric oxide (NO) production in RAW264.7 cells activated by lipopolysaccharide. Compounds **15–20** showed strong inhibition of NO with  $IC_{50}$  values between 6.3 and 8.0  $\mu\text{M}$ , compared to the positive control indomethacin, whose  $IC_{50}$  value was 35.8  $\mu\text{M}$  (Table 4). Compounds **11** and **14** exhibited considerable anti-inflammatory activity with  $IC_{50}$  values of 41.4 and 32.2  $\mu\text{M}$ , respectively. However, the other compounds do not have effects on anti-inflammatory activity ( $IC_{50} > 50 \mu\text{M}$ ).



### 3. Materials and Methods

#### 3.1. General Experimental Procedures

Optical rotations were recorded on an MCP-200 polarimeter (Anton Paar, Graz, Austria) with MeOH as solvent at 25 °C. UV spectra were measured on a Blue Star A spectrophotometer. IR data were carried out on a Fourier transformation infrared spectrometer coupled with an EQUINOX 55 infrared microscope (Bruker, Rheinstetten, Germany). A Bruker Avance 400 MHz spectrometer (Bruker, Karlsruhe, Germany) was used for 1D and 2D NMR spectra test with TMS as an internal standard. ESIMS and HRESIMS data were measured on an ACQUITY QDA (Waters Corporation, Milford, MA, USA) and an LTQ-Orbitrap LC-MS spectrometer (Thermo Corporation, Waltham, MA, USA), respectively. A Shimadzu Essentia LC-16 was used for HPLC preparative separations by a Welch-Ultimate XB-C18 column (250 × 21.2 mm, 5 µM, 12 nm, Welch Materials, Inc., Shanghai, China) an ACE-5-C18-AR, ACE-5-CN-ES and ACE-C18-PFP column (250 × 10 mm, 5 µM, 12 nm, FLM Advanced Chromatography Technologies Ltd., Guangzhou, China). Column chromatography (CC) was performed on silica gel (200–300 mesh, Qingdao Marine Chemical Inc., Qingdao, China) and Sephadex LH-20 (Amersham Biosciences, Uppsala, Sweden).

#### 3.2. Fungal Material

The experimental strain SYSU-MS4722 was isolated from the ascidian *Styela plicata* that was obtained by Professor Lan Liu from the Bay of Da'ao, Shenzhen City, Guangdong, Province, China, in April 2016. The standard protocol [29] was used for the isolation of fungus. The molecular biological protocol that included DNA amplification and sequencing of the ITS region was used for fungal identification. The sequence data of the fungal strain have been deposited at GenBank with accession no. OK623372. A BLAST search result suggested that the sequence was most similar (100%) to the sequence of *Diaporthe* sp. NFIF-2-6 (compared to MW202988.1).

#### 3.3. Extraction and Isolation

The strain *Diaporthe* sp. SYSU-MS4722 was fermented on a solid medium in a 1 L culture flask (containing 50 g of rice and 50 mL of H<sub>2</sub>O with 3% sea salt) with a total of 120 flasks incubating at room temperature for 30 days. The solid fermentation was extracted with MeOH four times to afford a crude extract, and then the crude was dissolved in H<sub>2</sub>O and continuously was extracted four times with EtOAc. The EtOAc extract (42 g) was subjected to a silica gel column eluting with gradient petroleum ether/EtOAc (from 8:2 to 0:1) to obtain six fractions (A–F).

Fr.A was fractionated on a Sephadex LH-20 column with MeOH/CH<sub>2</sub>Cl<sub>2</sub> (50:50) to afford three fractions (Fr.A.1 to Fr.A.3). Fr.A.3 was further purified by RP-HPLC (MeOH/H<sub>2</sub>O, 80:20 flow rate 2 mL/min, ACE-C18-PFP column 10 × 250 mm, 5 µM) to give **5** (5.0 mg) and **9** (11.0 mg). Fr.B was fractionated on a Sephadex LH-20 column with CH<sub>2</sub>Cl<sub>2</sub>/MeOH to provide four subfractions (Fr.B.1 to Fr.B.4). Fr.B.1 was further subjected to silica gel chromatography eluting with CH<sub>2</sub>Cl<sub>2</sub>/MeOH (99:1) to afford **11** (2.0 mg). Fr.B.2 was further purified by silica gel chromatography and RP-HPLC (MeOH/H<sub>2</sub>O, 75:25 flow rate 2 mL/min, ACE-C18-PFP column 10 × 250 mm, 5 µM) to obtain **13** (6.0 mg), **16** (2.0 mg), and **19** (3.0 mg). Fr.B.3 was further fractionated on a silica gel column and RP-HPLC to give **18** (14.0 mg) and **20** (12.0 mg). Fr.B.4 was subjected to a silica gel column with CH<sub>2</sub>Cl<sub>2</sub>/MeOH (98:2) and then purified by RP-HPLC with MeOH/H<sub>2</sub>O (70:30) to give **1** (2 mg), **15** (5.0 mg), and **17** (7.0 mg). Fr.C was applied to a silica gel column eluting with CH<sub>2</sub>Cl<sub>2</sub>/MeOH (97:3) to afford five fractions (Fr.C.4.1 to Fr.C.4.5). Fr.C.4.2 was further purified by silica gel column to give **4** (8.0 mg). Fr.C.4.4 was subjected to silica gel chromatography to afford **8** (9.1 mg) and subfraction (Fr.C.4.4.2). Fr.C.4.4.2 was further purified by RP-HPLC (MeOH/H<sub>2</sub>O, 65:35 flow rate 2 mL/min, ACE-C18-PFP column 10 × 250 mm, 5 µM) to give **2** (5.0 mg, *t*<sub>R</sub> = 11.2 min), **7** (2.0 mg, *t*<sub>R</sub> = 12.1 min), and **10** (11.0 mg, *t*<sub>R</sub> = 14.0). Fr.C.4.5 was further fractionated on a silica gel column and RP-HPLC to afford **3** (4.0 mg), **mboxtextbf12** (10.0 mg), and **14** (9.0 mg).

**Compound 1:** C<sub>15</sub>H<sub>16</sub>O<sub>6</sub>; Yellow crystal; [α]<sub>D</sub>20 (c 0.01, MeOH) +41.2; UV (MeOH) λ<sub>max</sub> (log ε) 270 (3.91) nm; CD (MeOH) λ<sub>max</sub> (Δε) 212 (−2.66), 243 (+1.49) nm; IR (neat) ν<sub>max</sub> 3458, 2976, 1786, 1653, 1468, 1234, 1065 cm<sup>−1</sup>; HR-ESIMS *m/z* 291.0869 [M − H]<sup>−</sup> (calculated for C<sub>15</sub>H<sub>15</sub>O<sub>6</sub>, 291.0874).

**Compound 2:** C<sub>15</sub>H<sub>18</sub>O<sub>7</sub>; Colorless crystal; [α]<sub>D</sub>20 (c 0.01, MeOH) +38.6; UV (MeOH) λ<sub>max</sub> (log ε) 208 (4.10), 277 (3.85) nm; CD (MeOH) λ<sub>max</sub> (Δε) 209 (−28.85), 281 (+10.75), 326 (+6.41) nm; IR (neat) ν<sub>max</sub> 3446, 2952, 1633, 1610, 1456, 1225, 1028 cm<sup>−1</sup>; HR-ESIMS *m/z* 309.0976 [M − H]<sup>−</sup> (calculated for C<sub>15</sub>H<sub>17</sub>O<sub>7</sub>, 309.0980).

**Compound 3:** C<sub>15</sub>H<sub>16</sub>O<sub>7</sub>; Colorless crystal; [α]<sub>D</sub>20 (c 0.02, MeOH) +32.4; UV (MeOH) λ<sub>max</sub> (log ε) 205 (4.03), 278 (3.87) nm; CD (MeOH) λ<sub>max</sub> (Δε) 212 (−17.55), 282 (+9.36), 323 (+2.89) nm; IR (neat) ν<sub>max</sub> 3402, 2962, 1641, 1583, 1468, 1213, 1043 cm<sup>−1</sup>; HR-ESIMS *m/z* 307.0820 [M − H]<sup>−</sup> (calculated for C<sub>15</sub>H<sub>15</sub>O<sub>7</sub>, 307.0823).

**Compound 4:** C<sub>15</sub>H<sub>18</sub>O<sub>6</sub>; Colorless powder; [α]<sub>D</sub>20 (c 0.02, MeOH) +13.4; UV (MeOH) λ<sub>max</sub> (log ε) 207 (4.20), 276 (3.52) nm; CD (MeOH) λ<sub>max</sub> (Δε) 202 (+24.71), 219 (+12.97) nm; IR (neat) ν<sub>max</sub> 3454, 2970, 1722, 1643, 1456, 1363, 1232, 1045 cm<sup>−1</sup>; HR-ESIMS *m/z* 295.1169 [M + H]<sup>+</sup> (calculated for C<sub>15</sub>H<sub>19</sub>O<sub>6</sub>, 295.1176).

**Compound 5:** C<sub>17</sub>H<sub>18</sub>O<sub>7</sub>; Colorless powder; [α]<sub>D</sub>20 (c 0.01, MeOH) +9.2; UV (MeOH) λ<sub>max</sub> (log ε) 224 (3.75), 254(3.50) nm; CD (MeOH) λ<sub>max</sub> (Δε) 243 (+0.44), 235 (+1.32) nm; IR (neat) ν<sub>max</sub> 3438, 2935, 2871, 1745, 1616, 1468, 1238, 1055 cm<sup>−1</sup>; HR-ESIMS *m/z* 333.0975 [M-H]<sup>−</sup> (calculated for C<sub>17</sub>H<sub>17</sub>O<sub>7</sub>, 333.0980).

**Compound 6:** C<sub>15</sub>H<sub>16</sub>O<sub>7</sub>; Colorless crystal; [α]<sub>D</sub>20 (c 0.02, MeOH) −175; UV (MeOH) λ<sub>max</sub> (log ε) 208 (4.05), 278(3.78), 356 (3.30) nm; IR (neat) ν<sub>max</sub> 3367, 1630, 1459, 1222, 1033, 813 cm<sup>−1</sup>; HR-ESIMS *m/z* 307.08278 [M − H]<sup>−</sup> (calculated for C<sub>15</sub>H<sub>15</sub>O<sub>7</sub>, 307.08233).

**Compound 7:** C<sub>15</sub>H<sub>18</sub>O<sub>7</sub>; Colorless crystal; UV (MeOH) λ<sub>max</sub> (log ε) 209 (4.15), 279(3.78), 353 (3.30) nm; IR (neat) ν<sub>max</sub> 3499, 3289, 2936, 1648, 1629, 1461, 1224, 1022, 811, 694 cm<sup>−1</sup>; HR-ESIMS *m/z* 309.0978 [M − H]<sup>−</sup> (calculated for C<sub>15</sub>H<sub>19</sub>O<sub>7</sub>, 309.0979).

(+)-(7): [α]<sub>D</sub>20 (c 0.0035, MeOH) +73.4; ECD (MeOH) λ<sub>max</sub> (Δε): 209 (−16.8), 279 (+5.6), 327 (+2.8) nm.

(−)-(7): [α]<sub>D</sub>20 (c 0.0011, MeOH) −79.2; ECD (MeOH) λ<sub>max</sub> (Δε): 209 (+15.4), 279 (−5.1), 327 (+2.5) nm.

### 3.4. X-ray Crystallographic Analysis

The crystals of compounds **1**, **2**, **6**, and **7** were obtained on the base of the vapor diffusion method. All single-crystal X-ray diffraction data were collected on a Rigaku Oxford diffractometer with Cu-Kα radiation (λ = 1.54178 Å). The structures were solved by direct methods using SHELXS-97 and refined full-matrix least-squares difference Fourier techniques using Olex2-1.2. All hydrogen atoms bonded to carbons were added at the geometrically ideal positions by the “ride on” method. All crystallographic data of **1**, **2**, **6**, and **7** have been deposited with the Cambridge Crystallographic Data Centre. Copies of the data can be obtained, free of charge, on application to the Director, CCDC, 12 Union Road, Cambridge CB2 1EZ, UK (fax: 44-(0)1223-336033, or e-mail: deposit@ccdc.cam.ac.uk).

**Compound 1:** C<sub>15</sub>H<sub>16</sub>O<sub>6</sub> (*M<sub>r</sub>* = 291.09 g/mol), orthorhombic, space group P2<sub>1</sub>2<sub>1</sub>2<sub>1</sub>, *a* = 5.4585(4) Å, *b* = 11.5804(10) Å, *c* = 22.0066(14) Å, α = 90°, β = 90°, γ = 90°, *V* = 1391.07(18) Å<sup>3</sup>, *Z* = 4, *T* = 249.99(10) K, μ(Cu Kα) = 0.915 mm<sup>−1</sup>, *D<sub>calc</sub>* = 1.3955 g/cm<sup>3</sup>, 5334 reflections measured, 2742 unique (*R<sub>int</sub>* = 0.0538, *R<sub>sigma</sub>* = 0.0628), which were used in all calculations. The final *R<sub>1</sub>* was 0.0557 (*I* > = 2*σ*(*I*)) and *wR<sub>2</sub>* was 0.1503. The Flack parameter was 0.0(3), and the Hooft parameter was −0.2(3). Goodness of fit on *F*<sup>2</sup> was 1.048. CCDC 2116967.

**Compound 2:** C<sub>15</sub>H<sub>18</sub>O<sub>7</sub> (*M<sub>r</sub>* = 310.31 g/mol), monoclinic, space group P2<sub>1</sub>, *a* = 10.1547(4) Å, *b* = 7.1459(2) Å, *c* = 10.3653(4) Å, α = 90°, β = 116.414(4)°, γ = 90°, *V* = 673.63(5) Å<sup>3</sup>, *Z* = 2, Crystal size 0.35 × 0.3 × 0.25 mm<sup>3</sup>, *T* = 150.00(10) K, μ(Cu Kα) = 1.036 mm<sup>−1</sup>, *D<sub>calc</sub>* = 1.530 g/cm<sup>3</sup>, 4665 reflections measured, 2621 unique (*R<sub>int</sub>* = 0.0268, *R<sub>sigma</sub>* = 0.0298), which were used in all calculations. The final *R<sub>1</sub>* was 0.0359 (*I* > = 2*σ*(*I*)) and *wR<sub>2</sub>* was 0.0986. The Flack parameter was −0.01(14), and the Hooft parameter was 0.06(7). Goodness of fit on *F*<sup>2</sup> was 1.044. CCDC 2116970.

**Compound 6:** C<sub>15</sub>H<sub>16</sub>O<sub>7</sub> (*Mr* = 308.29 g/mol): monoclinic, space group P2<sub>1</sub>, *a* = 8.0807(2) Å, *b* = 10.5548(2) Å, *c* = 8.3669(2) Å,  $\alpha = 90^\circ$ ,  $\beta = 93.743(2)^\circ$ ,  $\gamma = 90^\circ$ , *V* = 712.09(3) Å<sup>3</sup>, *Z* = 2, Crystal size 0.25 × 0.2 × 0.02 mm<sup>3</sup>, *T* = 149.98(10) K,  $\mu(\text{CuK}\alpha) = 0.055 \text{ mm}^{-1}$ , *D*<sub>calc</sub> = 0.068 g/cm<sup>3</sup>, 6306 reflections measured, 2765 unique (*R*<sub>int</sub> = 0.0384, *R*<sub>sigma</sub> = 0.0323), which were used in all calculations. The final *R*<sub>1</sub> was 0.0402 (*I* > 2σ(*I*)) and *wR*<sub>2</sub> was 0.1178. The Flack parameter was 0.13(15), and the Hooft parameter was 0.16(9). Goodness of fit on *F*<sup>2</sup> was 1.069. CCDC 2116974.

**Compound 7:** C<sub>15</sub>H<sub>18</sub>O<sub>7</sub> (*Mr* = 310.30 g/mol): monoclinic, space group P2<sub>1</sub>/c, *a* = 11.3702(3) Å, *b* = 7.30602(17) Å, *c* = 16.9135(5) Å,  $\alpha = 90^\circ$ ,  $\beta = 108.413(3)^\circ$ ,  $\gamma = 90^\circ$ , *V* = 1333.09(7) Å<sup>3</sup>, *Z* = 4, Crystal size 0.3 × 0.25 × 0.08 mm<sup>3</sup>, *T* = 150.00(10) K,  $\mu(\text{Cu K}\alpha) = 1.047 \text{ mm}^{-1}$ , *D*<sub>calc</sub> = 1.5460 g/cm<sup>3</sup>, 3935 reflections measured, 2546 unique (*R*<sub>int</sub> = 0.0295, *R*<sub>sigma</sub> = 0.0370), which were used in all calculations. The final *R*<sub>1</sub> was 0.0520 (*I* > 2σ(*I*)) and *wR*<sub>2</sub> was 0.1591. Goodness of fit on *F*<sup>2</sup> was 1.058. CCDC 2116976.

### 3.5. Calculation of the ECD Spectra

Merck molecular force field (MMFF) and DFT/TD-DFT calculations were carried out with the Spartan'14 software package (Wavefunction Inc., Irvine, CA, USA) and the Gaussian 09 program, respectively. MMFF conformational search generated low-energy conformers within a 10 kcal·mol<sup>−1</sup> energy window and optimized using PM6 semi-empirical optimizations. Then, each conformer was optimized with HF/6-31G(d) method in Gaussian09. Further optimization was performed at the b3lyp/6-311g\*\* level. The frequency was calculated at the same level to confirm each optimized conformer with the true minimum and to estimate their relative thermal free energies ( $\Delta G$ ) at 298.15 K. The optimized conformers were continually used for the ECD calculations in methanol, which were carried out with Gaussian09 (b3lyp/6-311g\*\*). Solvent effects were taken into account by using the polarizable continuum model (PCM). The ECD data were generated by the program SpecDis using a Gaussian band shape with 0.30 eV exponential half-width from dipole-length dipolar and rotational strengths, and the final ECD spectrum was drawn by Origin 2018. All calculations were performed by Tianhe-2 of the National Super Computer Center in Guangzhou.

### 3.6. Anti-Glioma Activity

The human glioma cell lines, T98G, U87MG, and U251, were purchased from the Cell Bank of the Chinese Academy of Sciences. Cells were cultured in Dulbecco's Modified Eagle's Medium (DMEM, Gibco, Carlsbad, CA, USA), containing 10% fetal bovine serum (FBS), 100 IU/mL penicillin, 100 µg/mL streptomycin (all from Gibco, Carlsbad, CA, USA) in a cell incubator with 5% CO<sub>2</sub> at 37 °C.

Cell proliferation was analyzed by MTT according to the manufacturer's instructions. Briefly, T98G, U87MG, and U251 were digested and seeded at 1 × 10<sup>3</sup> cells/well in 96-well plates and cultured in 100 µL medium overnight. The cells were treated by tested compounds with gradient concentrations for 48 h. At each indicated time point, MTT solution (10 µL/well) was added and then incubated at 37 °C for 2 h. The optical density (OD) at 450 nm was recorded by a microplate reader (Multiskan GO, Thermo Scientific, Waltham, MA, USA). Each experiment was performed three times.

### 3.7. Anti-Inflammatory Activity

RAW 264.7 cells were seeded in 96-well plates at a density of 5 × 10<sup>5</sup> cells/mL. After 12 h, the cells were treated with 1 µg/mL of LPS and tested samples, followed by additional incubation for 24 h at 37 °C. MTT stock solution (2 mg/mL) was added to wells for a total reaction volume of 100 µL. After 4 h incubation, the supernatants were aspirated. The formazan crystals in each well were dissolved in DMSO (100 µL), and the absorbance was measured with the wavelength of 490 nm by a microplate reader (Multiskan GO, Thermo Scientific). The data were expressed as mean percentages of the viable cells compared to the respective control. After pre-incubation of RAW 264.7 cells (1.5 × 10<sup>5</sup> cells/mL)

with 1 µg/mL LPS and samples at 37 °C for 24 h, the quantity of nitrite accumulated in the culture medium was measured as an indicator of NO production. Briefly, cell culture medium (50 µL) was added with Griess reagent (100 µL) and incubated at room temperature for 10 min. The absorbance was measured by a microplate reader (Multiskan GO, Thermo Scientific, Waltham, MA, USA) at 540 nm wavelength.

#### 4. Conclusions

The chemical investigation of the ascidian-derived fungus *Diaporthe* sp. SYSU-MS4722 afforded seven new polyketides, diaporthones A–G (1–7), together with 13 known analogues, including five mono- (8–14) and six dimeric xanthenes (15–20). The absolute configurations of 1–7 were identified by X-ray crystallographic analysis and Calculation of the ECD Spectra. Compounds 11 and 15–20 showed significant anti-inflammatory activity with inhibition of nitric oxide (NO) production in RAW264.7 cells activated by lipopolysaccharide with IC<sub>50</sub> values between 6.3 and 8.0 µM. At the same time, dimeric xanthenes (15–20) exhibited selectively growth-inhibitory effects on T98G cell lines with IC<sub>50</sub> values ranging from 19.5 to 78.0 µM.

**Supplementary Materials:** The following are available online at <https://www.mdpi.com/article/10.3390/md20010051/s1>, Figure S1: The HRESIMS spectrum of compound 1, Figures S2–S7: The 1D and 2D NMR (600 MHz) spectra of compound 1 in CD<sub>3</sub>OD, Figure S8: The IR spectrum of compound 1, Figure S9: The HRESIMS spectrum of compound 2, Figures S10–S15: The 1D and 2D NMR (400 MHz) spectra of compound 2 in CD<sub>3</sub>OD, Figure S16: The IR spectrum of compound 2, Figure S17: The HRESIMS spectrum of compound 3, Figures S18–S23: The 1D and 2D NMR (400 MHz) spectra of compound 3 in acetone-*d*<sub>6</sub>, Figure S24: The IR spectrum of compound 3, Figure S25: The HRESIMS spectrum of compound 4, Figures S26–S31: The 1D and 2D NMR (400MHz) spectra of compound 4 in CD<sub>3</sub>OD, Figure S32: The IR spectrum of compound 4, Figure S33: The HRESIMS spectrum of compound 5, Figures S34–S39: The 1D and 2D NMR (400 MHz) spectra of compound 5 in CD<sub>3</sub>OD, Figure S40: The IR spectrum of compound 5, Figure S41: The HRESIMS spectrum of compound 6, Figures S42–S47: The 1D and 2D NMR (400 MHz) spectra of compound 6 in CDCl<sub>3</sub>, Figure S48: The IR spectrum of compound 6, Figure S49: The HRESIMS spectrum of compound 7, Figures S50–S55: The 1D and 2D NMR (400MHz) spectra of compound 7 in CD<sub>3</sub>OD, Figure S56: The IR spectrum of compound 7.

**Author Contributions:** Conceptualization, S.C. and L.L.; methodology, S.C. and H.G.; validation, S.C., H.G., and H.S.; formal analysis, M.J.; investigation, S.C.; resources, L.L. and J.L.; data curation, Q.W.; writing—original draft preparation, S.C. and H.S. writing—review and editing, S.C.; project administration, S.C.; funding acquisition, S.C. and L.L. All authors have read and agreed to the published version of the manuscript.

**Funding:** This work was supported by the National Natural Science Foundation of China (Grant No. 41806155, U20A2001), Science and Technology Innovation Special Fund of Zhuhai City (Grant No. ZH22017003200020PWC), the Fundamental Research Funds for the Natural Science Foundation of Guangdong Province (Grant No. 2018A030310304), the National Key R&D Program of China (Grant No. 2019YFC0312501), the Key-Area Research, and Development Program of Guangdong Province (Grant No. 2020B1111030005).

**Acknowledgments:** We acknowledge S.G., Y.L., and L.F. of Test Center, Sun Yat-sen University to help us to finish the spectra test.

**Conflicts of Interest:** The author declare no conflict of interest.

#### References

1. Weller, M.; Wick, W.; Aldape, K.; Brada, M.; Berger, M.; Pfister, S.M.; Nishikawa, R.; Rosenthal, M.; Wen, P.Y.; Stupp, R.; et al. Glioma. *Nat. Revs. Dis. Primers* **2015**, *1*, 15017. [[CrossRef](#)]
2. Bray, F.; Ferlay, J.; Soerjomataram, I.; Siegel, R.L.; Torre, L.A.; Jemal, A. Global cancer statistics 2018: GLOBOCAN estimates of incidence and mortality worldwide for 36 cancers in 185 countries. *CA Cancer J. Clin.* **2018**, *68*, 394–424. [[CrossRef](#)] [[PubMed](#)]
3. Lapointe, S.; Perry, A.; Butowski, N.A. Primary brain tumours in adults. *Lancet* **2018**, *392*, 432–446. [[CrossRef](#)]

4. Zhao, P.; Wang, Y.; Kang, X.; Wu, A.; Yin, W.; Tang, Y.; Wang, J.; Zhang, M.; Duan, Y.; Huang, Y. Dual-targeting biomimetic delivery for anti-glioma activity via remodeling the tumor microenvironment and directing macrophage-mediated immunotherapy. *Chem. Sci.* **2018**, *9*, 2674–2689. [[CrossRef](#)]
5. Chen, S.; Shen, H.; Zhang, P.; Cheng, H.; Dai, X.; Liu, L. Anti-glioma trichobamide A with an unprecedented tetrahydro-5H-furo[2,3-b]pyrrol-5-one functionality from ascidian-derived fungus *Trichobotrys effuse* 4729. *Chem Commun.* **2019**, *55*, 1438–1441. [[CrossRef](#)]
6. Yan, Y.; Xu, Z.; Dai, S.; Qian, L.; Sun, L.; Gong, Z. Targeting autophagy to sensitive glioma to temozolomide treatment. *J. Exp. Clin. Cancer Res.* **2016**, *35*, 23. [[CrossRef](#)]
7. Chen, X.; Zhang, M.; Gan, H.; Wang, H.; Lee, J.H.; Fang, D.; Kitange, G.J.; He, L.; Hu, Z.; Parney, I.F.; et al. A novel enhancer regulates MGMT expression and promotes temozolomide resistance in glioblastoma. *Nat. Commun.* **2018**, *9*, 2949. [[CrossRef](#)]
8. Pereira, R.B.; Evdokimov, N.M.; Lefranc, F.; Valentão, P.; Kornienko, A.; Pereira, D.M.; Andrade, P.B.; Gomes, N.G.M. Marine-derived anticancer agents: Clinical benefits, innovative mechanisms, and new targets. *Mar. Drugs* **2019**, *17*, 329. [[CrossRef](#)]
9. Di, K.; Lloyd, G.K.; Abraham, V.; MacLaren, A.; Burrows, F.J.; Desjardins, A.; Trikha, M.; Bota, D.A. Marizomib activity as a single agent in malignant gliomas: Ability to cross the blood-brain barrier. *Neuro-Oncol.* **2016**, *18*, 840–848. [[CrossRef](#)]
10. Reed, K.A.; Manam, R.R.; Mitchell, S.S.; Xu, J.; Teisan, S.; Chao, T.H.; Deyanat-Yazdi, G.; Neuteboom, S.T.; Lam, K.S.; Potts, B.C. Salinosporamides D-J from the marine actinomycete *Salinispora tropica*, bromosalinosporamide, and thioester derivatives are potent inhibitors of the 20S proteasome. *J. Nat. Prod.* **2007**, *70*, 269–276. [[CrossRef](#)] [[PubMed](#)]
11. Feling, R.H.; Buchanan, G.O.; Mincer, T.J.; Kauffman, C.A.; Jensen, P.R.; Fenical, W. Salinosporamide A: A highly cytotoxic proteasome inhibitor from a novel microbial source, a marine bacterium of the new genus *salinispora*. *Angew. Chem. Int. Ed.* **2003**, *42*, 355–357. [[CrossRef](#)]
12. Senter, P.D.; Sievers, E.L. The discovery and development of brentuximab vedotin for use in relapsed Hodgkin lymphoma and systemic anaplastic large cell lymphoma. *Nat. Biotech.* **2012**, *30*, 631–637. [[CrossRef](#)] [[PubMed](#)]
13. Niaz, S.I.; Zhang, P.; Shen, H.; Li, J.; Chen, B.; Chen, S.; Liu, L.; He, J. Two new isochromane derivatives penisochromanes A and B from ascidian-derived fungus *Penicillium* sp. 4829. *Nat. Prod. Res.* **2019**, *33*, 1262–1268. [[CrossRef](#)]
14. Chen, S.; Jiang, M.; Chen, B.; Salanoi, J.; Niaz, S.I.; He, J.; Liu, L. Penicamide A, A Unique N,N'-Ketal Quinazolinone Alkaloid from Ascidian-Derived Fungus *Penicillium* sp. 4829. *Mar. Drugs* **2019**, *17*, 522. [[CrossRef](#)]
15. Chen, S.; Shen, H.; Deng, Y.; Guo, H.; Jiang, M.; Wu, Z.; Yin, H.; Liu, L. Rousssoelins A and B: Two phenols with antioxidant capacity from ascidian-derived fungus *Rousssoella siamensis* SYSU-MS4723. *Mar. Life Sci. Technol.* **2021**, *3*, 69–76. [[CrossRef](#)]
16. Jiang, M.; Wu, Z.; Wu, Q.; Yin, H.; Guo, H.; Yuan, S.; Liu, Z.; Chen, S.; Liu, L. Amphichoterpenoids A–C, unprecedented picoline-derived meroterpenoids from the ascidian-derived fungus *Amphichorda felina* SYSU-MS7908. *Chin. Chem. Lett.* **2021**, *32*, 1893–1896. [[CrossRef](#)]
17. Flack, H.D.; Bernardinelli, G. The use of X-ray crystallography to determine absolute configuration. *Chirality* **2008**, *20*, 681–690. [[CrossRef](#)]
18. Hooft, R.W.; Straver, L.H.; Spek, A.L. Determination of absolute structure using Bayesian statistics on Bijvoet differences. *J. Appl. Crystallogr.* **2008**, *41*, 96–103. [[CrossRef](#)] [[PubMed](#)]
19. Guo, H.; Liu, Z.-M.; Chen, Y.-C.; Tan, H.-B.; Li, S.-N.; Li, H.-H.; Gao, X.-X.; Liu, H.-X.; Zhang, W.-M.J.M.D. Chromone-derived polyketides from the deep-sea fungus *Diaporthe phaseolorum* FS431. *Mar. Drugs* **2019**, *17*, 182. [[CrossRef](#)]
20. Hu, H.-B.; Luo, Y.-F.; Wang, P.; Wang, W.-J.; Wu, J. Xanthone-derived polyketides from the Thai mangrove endophytic fungus *Phomopsis* sp. xy21. *Fitoterapia* **2018**, *131*, 265–271. [[CrossRef](#)] [[PubMed](#)]
21. Cao, S.; McMillin, D.W.; Tamayo, G.; Delmore, J.; Mitsiades, C.S.; Clardy, J. Inhibition of tumor cells interacting with stromal cells by xanthonones isolated from a Costa Rican *Penicillium* sp. *J. Nat. Prod.* **2012**, *75*, 793–797. [[CrossRef](#)]
22. Hou, X.-M.; Wang, C.-Y.; Gu, Y.-C.; Shao, C.-L. Penimethavone A, a flavone from a gorgonian-derived fungus *Penicillium chrysogenum*. *Nat. Prod. Res.* **2016**, *30*, 2274–2277. [[CrossRef](#)]
23. Krick, A.; Kehraus, S.; Gerhäuser, C.; Klimo, K.; Nieger, M.; Maier, A.; Fiebig, H.-H.; Atodiresei, I.; Raabe, G.; Fleischhauer, J.; et al. Potential cancer chemopreventive in Vitro activities of monomeric xanthone derivatives from the marine algaliculous fungus *Monodictys putredinis*. *J. Nat. Prod.* **2007**, *70*, 353–360. [[CrossRef](#)]
24. Jin, Y.; Qin, S.; Gao, H.; Zhu, G.; Wang, W.; Zhu, W.; Wang, Y. An anti-HBV anthraquinone from aciduric fungus *Penicillium* sp. OUCMDZ-4736 under low pH stress. *Extremophiles* **2018**, *22*, 39–45. [[CrossRef](#)] [[PubMed](#)]
25. Rönseberg, D.; Debbab, A.; Mändi, A.; Vasylyeva, V.; Böhrer, P.; Stork, B.; Engelke, L.; Hamacher, A.; Sawadogo, R.; Diederich, M.; et al. Pro-Apoptotic and Immunostimulatory tetrahydroxanthone dimers from the endophytic fungus *Phomopsis longicolla*. *J. Org. Chem.* **2013**, *78*, 12409–12425. [[CrossRef](#)] [[PubMed](#)]
26. Isaka, M.; Jaturapat, A.; Rukseree, K.; Danwisetkanjana, K.; Tanticharoen, M.; Thebtaranonth, Y. Phomoxanthonones A and B, novel xanthone dimers from the endophytic fungus *Phomopsis* species. *J. Nat. Prod.* **2001**, *64*, 1015–1018. [[CrossRef](#)]
27. Wagenaar, M.M.; Clardy, J. Dicerandrols, new antibiotic and cytotoxic dimers produced by the fungus *Phomopsis longicolla* Isolated from an endangered mint. *J. Nat. Prod.* **2001**, *64*, 1006–1009. [[CrossRef](#)]
28. Rukachaisirikul, V.; Sommart, U.; Phongpaichit, S.; Sakayaroj, J.; Kirtikara, K. Metabolites from the endophytic fungus *Phomopsis* sp. PSU-D15. *Phytochemistry* **2008**, *69*, 783–787. [[CrossRef](#)] [[PubMed](#)]
29. Kjer, J.; Debbab, A.; Aly, A.H.; Proksch, P. Methods for isolation of marine-derived endophytic fungi and their bioactive secondary products. *Nat. Protoc.* **2010**, *5*, 479–490. [[CrossRef](#)] [[PubMed](#)]

## Article

# Sonneradon A Extends Lifespan of *Caenorhabditis elegans* by Modulating Mitochondrial and IIS Signaling Pathways

Shu Jiang, Cui-Ping Jiang, Pei Cao, Yong-Hong Liu, Cheng-Hai Gao \* and Xiang-Xi Yi \*

Institute of Marine Drugs/School of Pharmaceutical Sciences, Guangxi University of Chinese Medicine, Nanning 530200, China; June.chiang@foxmail.com (S.J.); ping990120@foxmail.com (C.-P.J.); pcao@gxtcmu.edu.cn (P.C.); yonghongliu@scsio.ac.cn (Y.-H.L.)

\* Correspondence: gaoch@gxtcmu.edu.cn (C.-H.G.); yixiangxi2017@163.com (X.-X.Y.)

**Abstract:** Aging is related to the lowered overall functioning and increased risk for various age-related diseases in humans. Sonneradon A (SDA), a new compound first extracted from the edible fruits of mangrove *Sonneratia apetala*, showed remarkable antiaging activity. However, the role of SDA in antiaging remains unclear. In this article, we studied the function of SDA in antiaging by using the animal model *Caenorhabditis elegans*. Results showed that SDA inhibited production of reactive oxygen species (ROS) by 53%, and reduced the accumulation of aging markers such as lipids and lipofuscins. Moreover, SDA also enhanced the innate immune response to *Pseudomonas aeruginosa* infection. Genetic analysis of a series of mutants showed that SDA extended the lifespan of the mutants of *eat-2* and *glp-1*. Together, this effect may be related to the enhanced resistance to oxidative stress via mitochondrial and insulin/insulin-like growth factor-1 signaling (IIS) pathways. The results of this study provided new evidence for an antiaging effect of SDA in *C. elegans*, as well as insights into the implication of antiaging activity of SDA in higher organisms.

**Keywords:** antiaging; *Sonneratia apetala*; signaling pathway; *Caenorhabditis elegans*; mutants

**Citation:** Jiang, S.; Jiang, C.-P.; Cao, P.; Liu, Y.-H.; Gao, C.-H.; Yi, X.-X.

Sonneradon A Extends Lifespan of *Caenorhabditis elegans* by Modulating Mitochondrial and IIS Signaling Pathways. *Mar. Drugs* **2022**, *20*, 59. <https://doi.org/10.3390/md20010059>

Academic Editor: Marialuisa Menna

Received: 13 December 2021

Accepted: 4 January 2022

Published: 8 January 2022

**Publisher's Note:** MDPI stays neutral with regard to jurisdictional claims in published maps and institutional affiliations.



**Copyright:** © 2022 by the authors. Licensee MDPI, Basel, Switzerland. This article is an open access article distributed under the terms and conditions of the Creative Commons Attribution (CC BY) license (<https://creativecommons.org/licenses/by/4.0/>).

## 1. Introduction

*Caenorhabditis elegans* (*C. elegans*) is a powerful experimental system characterized by a short lifespan, the capability to self-reproductive, and ease of cultivation; it has a small and transparent body that is easy to observe, and thus it is commonly used to pre-screen compounds for the research of anticancer, antiaging, and lipid metabolism drugs, or for toxicity studies [1]. Since two-thirds of its genes are homologous to human-disease-related genes, *C. elegans* has been used as a model for studying aging and aging-related diseases [2]. In worms, aging can be detected by the attenuation of exercise and stress ability, cognitive ability, and pharyngeal pump, as well as the accumulation of autofluorescence.

Mangrove is a large group of various salt-tolerant woody trees or shrubs that lives along sheltered coastlines within the tropic or subtropic latitudes. Mangrove plants are usually categorized into two subgroups, true mangrove and semi-mangrove plants. *Sonneratia apetala*, belonging to the family Sonneratiaceae, is an excellent fast-growing true mangrove that is native to India, Bangladesh, Sri Lanka, and other South Asian and Southeast Asian countries [3]. In the 1990s, *S. apetala* was introduced from Sundarban, India to Guangdong, Guangxi and Hainan of China. The ripe edible fruits of *S. apetala* are rich in amino acids, anthocyanins, and other phenolic compounds [4]. In recent years, the search for new molecules with food-additive and nutraceutical applications from marine natural plant extracts has grown significantly. Fruit extracts of *S. apetala* have been found to have numerous beneficial effects on human health, such as antibacterial, antioxidant, and antihepatic lesion activities [4,5]. Studies have shown that acetone, ethanol, methanol, and water extracts from plant leaves and bark had antibacterial effects on *Staphylococcus aureus*, *Shigella flexneri*, *Bacillus licheniformis*, *Bacillus brevis*, *Vibrio cholerae*, *Pseudomonas aeruginosa*, *Bacillus epidermidis*, *Bacillus subtilis*, and *Escherichia coli* at the concentrations of

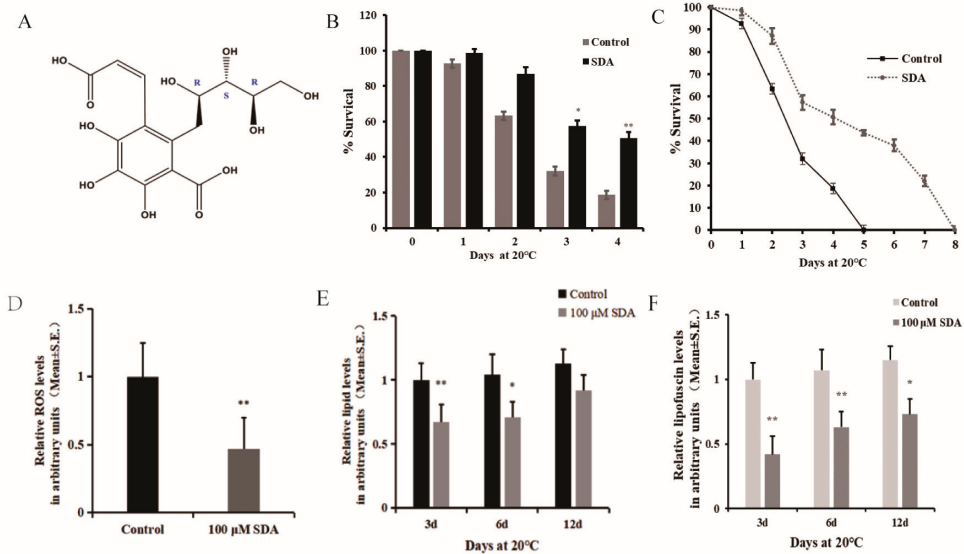
1.25–5.00 mg/mL [6]. Ethanol fruit extract (250 and 500 mg/kg, p.o.) showed a significant analgesic effect in an acetic-acid-induced writhing model of Swiss albino mice [7]. Some lupeol-derived chalcones extracted from *S. apetala* were found to reduce the levels of total cholesterol, phospholipids, and triacylglycerol in plasma of hyperlipidemia rats, and had antioxidant effects [8].

Sonneradon A (SDA, 1A) is a new compound that was extracted from the fruits of *S. apetala* firstly in our previous study [4]. It has been shown to extend the lifespan and healthspan of *C. elegans*. Further, the HSF-1 pathway might be a probable path for antiaging effects by molecular docking. However, the mechanism for its senescence-delaying effect in worms is still unclear. Thus, we studied the mechanisms involved in its bioactivities using the model animal *C. elegans* in this work. Herein, the purpose of this study was to assess the effects of SDA on ROS accumulation, as well as to investigate its effects on fat and autofluorescence accumulation and other indicators related to nematode aging comprehensively, and its underlying mechanism in *C. elegans*.

## 2. Results

### 2.1. Antioxidant Capacity of SDA in Wild-Type Worms

Studies have repeatedly shown that antioxidant activity is closely related to the longevity of many organisms [9]. Considering that SDA could increase *C. elegans* lifespan and healthspan, we performed an oxidative stress tolerance assay to determine whether the prosurvival effect of SDA was related to its antioxidant capacity for gaining mechanistic insight. The maximum survival time of the untreated model (control) worms exposed to paraquat oxidative was 5 d, which was extended to 8 d by treatment with 100  $\mu$ M SDA. On day 4; i.e., the day before the control group reached zero survival, the survival rate of the SDA group was 32% higher than that of the control group (Figure 1B,C).



**Figure 1.** Effect of SDA on oxidative stress in *C. elegans*: (A) structure of compound SDA; (B) survival time after exposure to paraquat-induced oxidative stress; (C) daily survival rate; (D) ROS levels; (E) relative lipids levels; (F) relative autofluorescence levels. The *p*-values were calculated using a two-tailed *t*-test. All data are expressed as mean  $\pm$  SEM, ( $n \geq 30$  per group). \*  $p < 0.05$ , \*\*  $p < 0.01$ .

Moreover, to further validate the link between survival and redox balance in this context, we determined the ROS levels induced by paraquat exposure. The effect of SDA on ROS levels in *C. elegans* under oxidative stress condition was measured using

2'<sup>7</sup>-dichlorofluorescein diacetate, and the results are shown in Figure 1D. The results showed that SDA significantly reduced the ROS levels by 53.27%.

*C. elegans* lack mammalian-specific adipocytes, but the neutral fats (triglycerides and cholesterol) stored in its intestinal and subcutaneous cells exist in the form of droplets, which is the main storage form of fat in nematodes. These lipid droplets can be expressed by the fat soluble dye Nile red [10,11]. We stained worms with Nile red to evaluate the effect of SDA on lipid deposition in *C. elegans*, and found that treatment with 100 µM SDA significantly reduced the fat accumulation of *C. elegans* on day 3 (33.0%) and day 6 (31.7%) compared to the control group ( $p < 0.01$ ) (Figure 1E). Moreover, the fluorescence intensity of lipids in worms gradually increased with the test time, and the lipid content of nematodes in the SDA group was 1.89% lower than that in the control group ( $p > 0.05$ ) on day 12.

Advanced glycation end products (AGEs) are considered a possible cause of aging [12]. Blue fluorescence in nematodes is a possible indicator of AGE accumulation, and *C. elegans* hermaphrodites can serve as a model for investigating the utility of antisenesescence interventions that act via the suppression of AGEs production [13]. To further assess the impacts of SDA on *C. elegans* of antiaging, we examined autofluorescence and found that 100 µM SDA treatment delayed the accumulation of autofluorescence as compared with the control group. After 100 µM SDA treatment, the accumulation of autofluorescence decreased by 58.1% compared with the control group on day 3, and the autofluorescence decreased by 44.0% and 41.7% on days 6 and 12, respectively (Figure 1F).

## 2.2. SDA Delay of the Progression of Aging-Related Diseases in *C. elegans* Models of Alzheimer's Disease (AD) and Upregulation of the Innate Immune Response

Since SDA could extend the lifespan and enhance the antioxidative stress ability of *C. elegans*, we next determined whether it could also ameliorate protein toxicity stress in worms and delay the progression of neurodegenerative diseases. Our results showed that 100 µM SDA could delay the temperature-induced paralysis of CL4176 worms (Figure 2A). After 31 h of culture at 25 °C, the Aβ gene of CL4176 worms in the SDA group was downregulated by 37.09% (Figure 2B), and the protein level decreased by 31.37% compared with the control group ( $p < 0.05$ ) (Figure 2C,D). These findings revealed that SDA has the potential to suppress the toxicity of amyloid plaque.

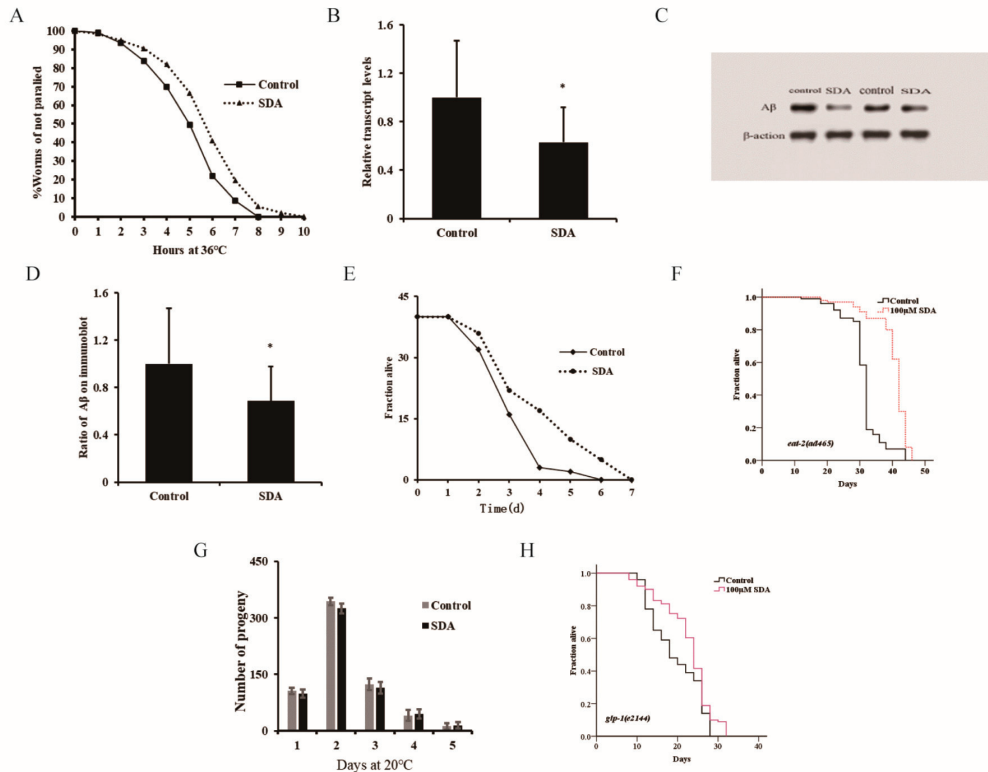
Many aromatic ring compounds have been shown to possess antioxidant and anti-inflammatory properties [4]. Aging is known to be associated with chronic inflammation, and increasing evidence supports the notion that the chronic inflammation plays a key role in the pathogenesis of several aging-associated diseases. Appropriate immunity is important for extending a healthy lifespan. In this study, we assessed the potential efficacy of SDA in enhancing the innate immune response to *P. aeruginosa* challenge and improving the lifespan of *C. elegans* under the infection condition (Figure 2E). We found that the lifespan of the SDA group was increased by 16.80% ( $p < 0.05$ ).

Pharyngeal pumping can regulate the food intake of *C. elegans*, and the change in bulb movement at the end of pharynx can cause dietary restriction (DR) effects. In addition, food intake reduction, which mimics DR in humans, has been shown to increase lifespan in animal studies [14]. Based on this, a lifespan experiment was conducted using the pumping-defective mutant *eat-2 (ad465) II* of *C. elegans* to determine whether SDA could exert its antiaging activity through DR. Results showed that the survival of nematodes was prolonged by 28.53% ( $p < 0.05$ ) after SDA treatment (Figure 2F), and the impairment of *eat-2* expression had no influence on the SDA-induced effects on the lifespan of wild-type worms. It was thus suggested that SDA may not play a role in delaying senescence through a DR mechanism.

The reproductive ability of *C. elegans* is directly related to the antiaging activity [3]. In the test for the reproductive capacity of SDA-administered nematode worms, we found that the number of eggs laid by nematodes was the largest on day 2 in both the control group and the SDA-administration group, reaching 344 and 325, respectively; there was no difference in the number of offspring larvae of nematodes between the two groups at



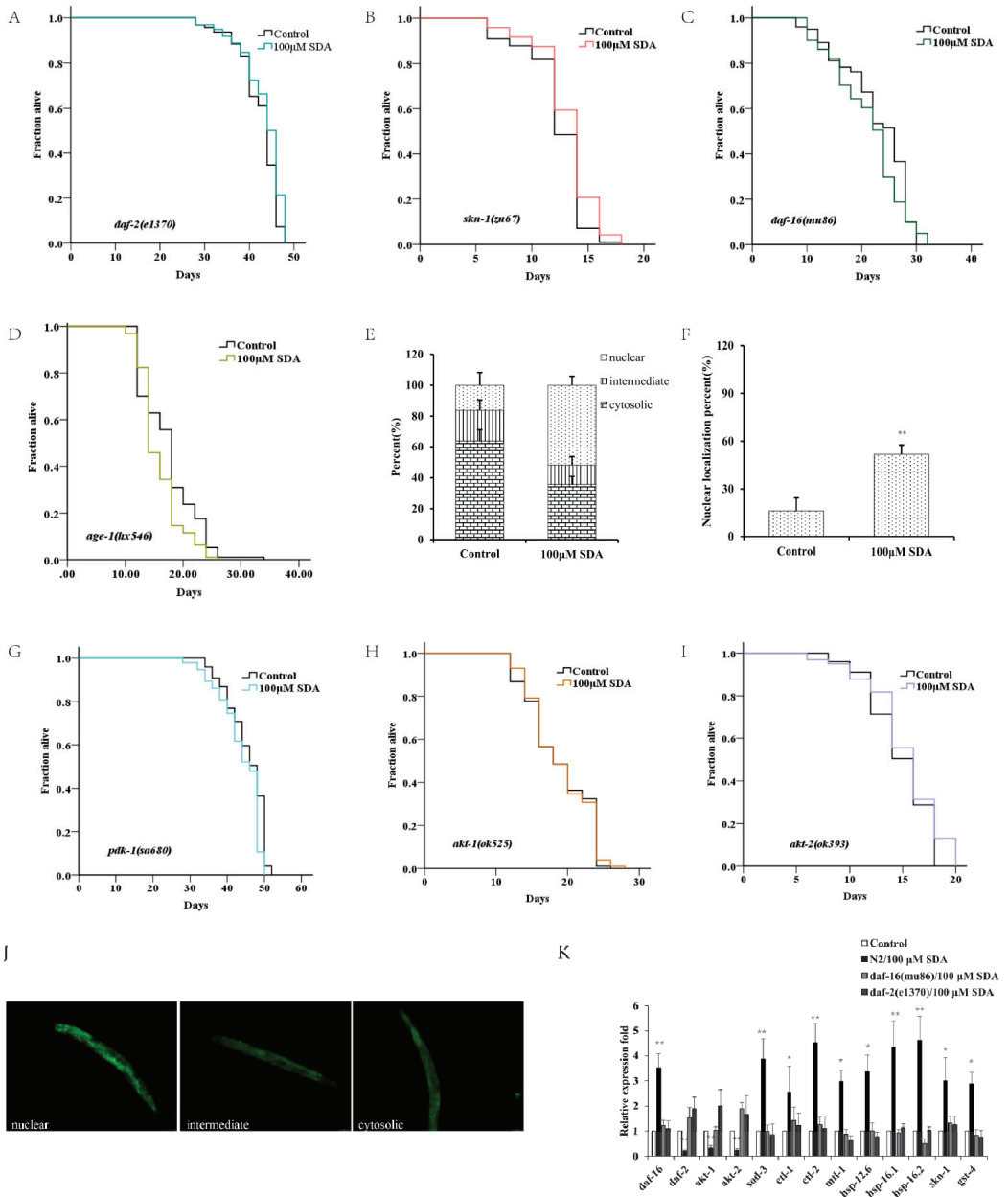
any time point tested, indicating that SDA treatment had no effect on the daily and total egg production of worms (Figure 2G). When we tested the lifespan of the reproductive-signal-related mutant *glp-1 (e2144) III*, we found that SDA could further extend the worms' lifespan (Figure 2H). These results suggested that an SDA-induced increase in the lifespan of *C. elegans* may not be related to the reproductive capacity of nematodes.



**Figure 2.** Paralysis rate of CL4176 elegans (A). A $\beta$  mRNA levels in *C. elegans* CL4176 (B). A $\beta$  protein levels in CL4176 worms (C). Ratio of A $\beta$  on immunoblot (D). Survival curves of wild-type N2 worms during *P. aeruginosa* infection (E). Survival curves of the *eat-2* mutant (F). Spawning capacity of *C. elegans* (n = 10) (G). Survival curves of the *glp-1* mutant (H). The p-values were calculated using a two-tailed t-test. All data are expressed as mean  $\pm$  SEM. \*  $p < 0.05$  compared to control.

### 2.3. Potential of SDA to Extend *C. elegans*' Lifespan through Insulin/Insulin-like Growth Factor-1 Signaling Pathways

The factor DAF-16/FOXO is the central regulator of longevity and oxidative stress tolerance, and the proteins encoded by *daf-16* target genes can protect cells from oxidative stress [15]. To determine how SDA affects lifespan extension and antioxidant stress in nematodes, we first examined expression of the transcription factor *daf-16* by TJ356 worms. The results showed that SDA did not further extend the lifespan of *skn-1* mutants (Figure 3B), suggesting that SDA may be partially dependent on DAF-16. Moreover, with SDA treatment, the DAF-16 accumulation (DAF-16::GFP) in the nucleus of TJ356 worms increased by 38.72% ( $p < 0.01$ ; Figure 3D,E,J).



**Figure 3.** Survival curves for the *daf-2* mutant (A). Survival curves for the *daf-16* mutant (B). Survival curves for *skn-1* mutants (C). Subcellular localization of DAF-16::GFP (D). Nuclear translocation of *daf-16* (E). Lifespan curves adjusted to Kaplan–Meier estimator for the mutants of *age-1* (F), *akt-1* (G), *akt-2* (H), and *pdk-1* (I). Images of the localization of DAF-16::GFP in worms (40×) (J). The mRNA level of genes in IIS pathways (K). The *p*-values were calculated using a two-tailed *t*-test. All data are expressed as mean ± SEM, (*n* ≥ 60). \* *p* < 0.05, \*\* *p* < 0.01 compared to control.

To determine whether SDA extended *C. elegans*' lifespan by regulating the DAF-16 activity, we measured expression levels of *mtl-1*, *ctl-1/2*, *sod-3*, *hsp-12.6*, *hsp-16.1*, and *hsp-16.2* of *daf-16*-targeted genes. The results showed that expression levels of these genes were significantly increased in wild-type N2 worms treated with 100  $\mu$ M SDA compared with the control group ( $p < 0.05$ ), but no such change was detected in *daf-16(mu86)* I. mutants (Figure 3K). Together, these results suggested that SDA may extend the lifespan of *C. elegans* by activating the DAF-16/FOXO pathway.

Like *daf-16*, the SKN-1/NRF2 is also a pivotal oxidative stress response transcription factor for worms. We analyzed the role of *skn-1* in the lifespan extension induced by SDA. SDA increased the maximum survival time of the mutant *skn-1(zu67)* IV. by 4.86% (Figure 3C). The mRNA level of *gst-4*, a target gene of *skn-1*, was also significantly increased (Figure 3K).

*Daf-16* has been known as an obligatory factor in the insulin/insulin-like growth factor-1 signaling (IIS) pathway. We conducted lifespan tests in *daf-2* mutants to determine whether SDA might interact with the factors in this pathway. The results showed that SDA did not further extend the lifespan of long-lived insulin-like receptor mutant *daf-2(e1370)* III. (Figure 3A). Moreover, SDA did not alter the expression level of *daf-16*-targeted genes in *daf-2* mutant worms (Figure 3K).

DAF-16 in the nucleus interacts with other factors in the IIS pathway known to play an important role in aging, such as *akt-1*, *akt-2*, *age-1* and *skn-1*. Therefore, we investigated the lifespan-extension effect of SDA on the mutants in the IIS pathway. The results showed that the mutants *akt-1(ok525)* V., *akt-2(ok393)* X., and *sgk-1(ok538)* X. diminished the effect of SDA on lifespan extension ( $p > 0.05$ ), which suggested that the effect of SDA on lifespan extension might be partially dependent on the *akt-1*, *akt-2*, and *sgk-1* genes. Therefore, we conducted a lifespan test on the loss-of-function mutant *pdk-1(sa680)* X., given that *pdk-1* regulates the activity of these three factors. Our results showed that SDA did not further extend the longevity of mutant *pdk-1(sa680)* X. Together, these results suggested that SDA may extend the lifespan of worms mainly through regulating IIS pathways.

### 3. Discussion

*S. apetala*, which is native to Bangladesh, is a member of a mangrove community that guards the coast, and plays an important role in maintaining the balance of the earth's ecosystem [4]. Studies have reported the bioactivity of *S. apetala* fruit extracts in rodent models using rats or mice. Recently *C. elegans* has emerged as a good model for mechanistic studies, given its numerous mutants available [16]. We found that SDA extended the lifespan of *C. elegans*, and this effect may be related to the enhanced resistance to oxidative stress via the mitochondrial and IIS pathways. To the best of our knowledge, this is the first study to demonstrate the antiaging activity and mechanism of compounds derived from *S. apetala* in *C. elegans*.

#### 3.1. SDA Reduces Free Radical Production and Enhances Nematode Immunity

Our previous studies have shown that 100  $\mu$ M SDA can prolong the lifespan of *C. elegans* and enhance their healthspan, while being resistant to heat stress [4]. To advance the research along this line, in the current study, we further investigated the mechanism underlying the antiaging effect of SDA in *C. elegans*.

With the advancement in age, the accumulation of autofluorescence is pathologically connected with various age-associated disorders. Intestinal fat is involved in energy metabolism, and therefore, the intestine is a main organ for the study of lipid metabolism [1]. In this study, we showed that strong red fluorescence occurred around the intestinal tract of *C. elegans* (Figure S2), which was consistent with the study by Alexandre et al. (2012). Advanced glycation end products (AGEs) were considered as a possible cause of aging [17]. Blue fluorescence in nematodes is a possible indicator of AGEs accumulation, and *C. elegans* hermaphrodites can serve as a model for investigating the utility of antisenesescence interventions that act via the suppression of AGEs production. In addition, Komura et al. showed

that blue autofluorescence was expected to be a better biomarker for tracing senescence [12]. CL4176 was genetically engineered to express a temperature-inducible human A $\beta$  protein in the body wall muscle of the worm. The A $\beta$  expression is muscle-directed by the use of the myo-3 promoter. When the strain was propagated at 15 °C, there was no expression of A $\beta$ , while upshifting the temperature to 25 °C induced the expression of human A $\beta$  protein, and the worms became paralyzed. The extent of paralysis reflected the toxicity caused by the expression of A $\beta$ .

The exact relationship among autofluorescence, senescence, and lifespan in the worm has remained unclear. Gerstbrein et al. reported that age pigments were valid reporters of the nematode healthspan [18], whereas Coburn et al. reported that blue fluorescence served as a death marker for several hours before and after death in *C. elegans* [19]. It has been suggested that the increases in blue autofluorescence over time observed in populations of aging *C. elegans* might reflect not the aging rate or health state of the population, but the fraction of dead or almost-dead individuals in the sample. To assess the utility of autofluorescence as a biomarker of senescence in *C. elegans*, Komura et al. measured the autofluorescence of individual nematodes using spectrofluorometry. The results showed that blue fluorescence in nematodes was a possible indicator of AGEs accumulation, and that *C. elegans* hermaphrodites can serve as a model for investigating the utility of anti-senescence interventions that act via the suppression of AGEs production. In addition, autofluorescence was expected to be a better biomarker for tracing senescence [13]. It has been reported that an increased level of intracellular ROS contributed to the aggregation of autofluorescence [20]. The free radical theory of aging is a widely accepted hypothesis that describes ROS as tremendously reactive molecules that contribute to aging and age-related manifestations [21]. Paraquat is a reagent commonly used to establish an oxidative stress model in nematodes, and it can induce a surge in reactive oxygen radicals in worms, resulting in cell degeneration and necrosis [3]. ROS is a byproduct of normal metabolism; however, its excessive and unbalanced production is known to cause deleterious cellular damage, leading to the oxidative damage of lipids and proteins, a prominent manifestation and mechanism of the aging process [22]. SDA exerts indirect antioxidant potential by the modulation of antioxidant defense systems.

Once the pathogenic bacteria are deposited in the intestine, they will invade the host cells and even kill nematodes through the process of infection. *C. elegans* usually responds to this situation by avoiding pathogens or activating its inducible innate immune system. *P. aeruginosa* infection is often secondary to immune damage from various causes. Due to its adaptability to genetic manipulation, susceptibility to many human and animal pathogens, and conservative immune signal transduction pathway, *C. elegans* has become a suitable model for studying the innate immunity of human and other animal hosts. *C. elegans* protects itself from disease-causing bacteria through its innate immune system [23]. We found that SDA enhanced tolerance to oxidative stress (Figure 1B,C) and reduced intracellular ROS levels (Figure 1D and Figure S1) in wild-type worms, supporting our hypothesis regarding the mitigated ROS-mediated lifespan extension. SDA also improved the innate immune response and resistance to bacterial infection. All these favorable effects of SDA may contribute to its longevity-promoting properties.

### 3.2. SDA Prolongs the Lifespan of *C. elegans* by Regulating Mitochondrial and IIS Signaling Pathways, but Not DR

To further investigate the working mechanism for SDA's antiaging effect in *C. elegans*, we analyzed several genetic factors that have been extensively studied for their involvement in regulating aging, DR, mitochondrial respiration signaling pathways, and IIS pathways in *C. elegans* [24].

DR is one of the most effective nondrug intervention methods for a broad variety of organisms, in addition to genetic editing [25–27]. There is a negative correlation between nematode lifespan and fecundity or brood size. In addition, longer lifespans are accompanied by lower reproductive rates [28]. However, contrary to what was expected, we observed

that in the treated worms, the number of larvae did not decrease as the reproduction time increased. These results suggested that SDA could not promote life extension in a similar way to DR (Figure 3G). Using SDA in the development of antiaging drugs will not impair the reproductive capacity of *C. elegans*.

The mechanism of mitochondrial senescence theory is that oxidative damage to mitochondrial DNA leads to the impairment of mitochondrial structure and function, affecting the energy supply of cells; thus, a series of senescence symptoms occurs [29]. We found that SDA inhibited paraquat-induced ROS production (Figure 1D). ROS is a group of natural byproducts mainly produced in mitochondria, and the lifespan of mitochondrial mutant strains has been shown to correlate with ROS-mediated signaling and oxidative stress. The *isp-1* and *clk-1* encoded a catalytic subunit of mitochondrial complex III and ubiquinone biosynthesis, respectively. Results suggested that the effect of SDA on the lifespan extension might be partially dependent on *isp-1* and *clk* genes. In short, SDA could extend the lifespan of *C. elegans* via mitochondrial respiration.

DAF-16/FOXO plays a central role in the regulation of development, aging, and stress resistance in *C. elegans* [30–32]. It has been shown that the excessive intake of sugar leads to increased insulin levels, which will further inhibit *daf-16* activity and ultimately shorten the lifespan [33,34]. Moreover, it regulates aging, stress resistance, and immunity in *C. elegans*. It has been reported that *daf-16* is responsible for the activation of major antioxidant machinery [35,36]. In the current study, we found that the lifespan-extension effect of SDA required *daf-16*. *Skn-1* activated enzymes that worked as radical scavengers and transferred glutathione [37]. *Skn-1* is located in the ASI neurons, in response to DR, or in the gut nuclei, in response to oxidative stress. Its accumulation in gut nuclei activates the phase 2 gene expression in response to stress, and is regulated by *sgk-1*, a serine/threonine kinase that can phosphorylate the *skn-1* transcription factor and modulate its nuclear localization [38]. The prolongation of nematode life by SDA may partly depend on the stress response molecule *skn-1*, which is also regulated by DAF-16 and IIS pathways. In *C. elegans*, the insulin-like receptor *daf-2* acts through PI3-kinase to activate the downstream of serine/threonine kinases *pdk-1*, *akt-1*, *akt-2*, and *sgk-1*, and subsequently regulates the *daf-16* activity [29]. Results showed an increase in the expression of *daf-2* (Figure 3K), which should have promoted a repression in the translocation of *daf-16* into the nuclei. In addition, nuclear translocation of *daf-16* in the fluorescent strain TJ356 was observed in worms treated with SDA (Figure 3I), distinctly. Our results showed that the *daf-16* mutant *daf-16(mu86)* totally suppressed the effects of SDA on lifespan extension and stress resistance, showing that the translocation of this transcription factor was essential to increase the lifespan of worms treated with SDA. The nuclear translocation of *daf-16* was a requisite for the transcriptional activation of target genes. We found that SDA did not further extend the lifespan of long-lived insulin-like receptor mutant *daf-2(e1370)* III., mutant *akt-1(ok525)* V., *akt-2(ok393)* X., *sgk-1(ok538)* X., or *pdk-1(sa680)* X., but increased the expression of pathway-related genes. Moreover, SDA impacted the related upstream and downstream factors of DAF-16 in the IIS pathway.

### 3.3. Key Points of Experimental Operation

ROS in *elegans* is a highly active and short-lived molecule. It is almost impossible to detect it in vivo directly in biological samples. ROS levels can be measured indirectly using reporter probes. These molecular probes were designed to be absorbed by cells and emit fluorescent signals after being oxidized by ROS. The transparency of *elegans* makes them particularly suitable for the use of these molecular probes, allowing site-specific visualization of ROS formation. This is a significant advantage over fruit flies and mice [39]. Like many other fluorescent probes, H2DCFDA is photoactive, so it is important to minimize exposure to light during treatment. When measuring ROS in *C. elegans* cells with H2DCFDA, we used the whole nematode for testing to prevent the cleaved nematode from releasing intracellular metal ions and increase its own ROS, which had an impact on

the results. Moreover, we measured the fluorescence intensity within 4 h after the start of the test to prevent H2DCFDA from easily diffusing into the cells.

As is known, ensuring the robustness of lifespan experiments can be challenging. Synchronization of cohorts is vital for *C. elegans* lifespan studies. In the lifespan experiment, we dissolved pregnant adults in bleach solution to euthanize the adults but not their eggs, so as to keep the lifespans of nematodes used in the experiment uniform. In lifespan studies, contaminations can be difficult to control, as old worms are likely to be killed if transferred repeatedly. Therefore, careful nematode-transfer techniques, aseptic techniques, and frequent inspection of inventory are necessary. The method we used to directly control the cell density was to measure the bacterial cell density by spectrophotometer with OP50 overnight in Luria–Bertani liquid medium at 37 °C, and then concentrate the raw material to the required cell density ( $OD_{600} = 0.6$ ) to keep the OP50 bacterial cell density consistent across plates and between experiments for the repeatability, and to prevent unexpected changes in food supply. Throughout the lifespan test, randomization and blinding also prevented other potential confounders. Any lifespan test required at least three independent, blind replications. Most importantly, when conducting nematode experiments, we recorded and reported as many details of relevant factors as possible in order to ensure the traceability and authenticity of the experimental results.

#### 4. Materials and Methods

##### 4.1. Reagents and *C. elegans* Strains

The SDA was obtained from the fruits of mangrove *S. apetala*, as we previously described [4]. All reagents were purchased from Beijing Solarbio Science & Technology Co., Ltd. (Beijing, China), and Nile Red and H2DCF-DA were obtained from Sigma-Aldrich Co., (St. Louis, MO, USA).

The Caenorhabditis Genetics Center (University of Minnesota, MN, USA) provided the *Escherichia coli* OP50 and *C. elegans* strains: CL4176 (*smg-1* (CC546) I; *dvIs27X*) and TJ356 (*DAF-16::GFP*(ZLS356)); DA465 (*eat-2(ad465)* II.); CF1903 (*glp-1(e2144)* III.); CB4876 (*clk-1(e2519)* III.); ZG31 (*hif-1(ia4)* V.); RB1206 (*rsk-1(ok1255)* III.); EU1 (*skn-1(zu67)* IV.); TJ1052 (*age-1(hx546)* II.); JT9609 (*pdk-1(sa680)*X.); RB759 (*akt-1(ok525)* V.); VC204 (*akt-2(ok393)* X.); VC345 (*sgk-1(ok538)* X.).

##### 4.2. *C. elegans* Culture

The strains used in this study were maintained on nematode growth media (NGM) plates at an appropriate temperature, as previously described [40]. The adult worms were dissolved in a bleach mixture (5 M NaOH, 10% NaClO) and then washed three times with M9 buffer. Next, the eggs were synchronized and transferred to the incubator to hatch into L1 larvae. Synchronized L1 larvae were cultured to L4 larvae for subsequent tests. SDA was dissolved in DMSO and diluted to the desired concentration prior to use. After the SDA solution was added to the NGM plate containing inactivated OP50 (65 °C for 30 min), the final DMSO concentration was 0.1%. The control group had the same solvent concentration as the SDA group [41].

##### 4.3. Lifespan Assays

Lifespan assays were performed as described in a previous report [35]. Briefly, at least 60 L4 larvae were transferred to fresh NGM plates on day 0 of the assay. *C. elegans* were transferred to fresh plates supplemented with 100 µM SDA or 0.1% DMSO (vehicle control) on every other day. Worms were considered dead when they failed to respond to touch with a platinum wire. Moreover, worms were censored if they crawled off the plate, displayed extruded internal organs, or died because of hatching progeny inside the uterus [42]. The entire lifespan assay was repeated in at least three independent experiments.

#### 4.4. Assay for Paraquat-Induced Oxidative Stress

For the oxidative stress test, synchronized L4 wild-type larvae were transferred to NGM plates containing 5 mM paraquat at 20 °C on the first day. On the following days, nematodes were monitored and scored as dead when they did not respond to touch with a platinum-wire picker.

#### 4.5. Measurement of Reactive Oxygen Species Production

To measure the reactive oxygen species (ROS) levels in *C. elegans*, at least 30 synchronized L4 wild-type larvae were cultured, and the procedure was the same as that for the oxidative stress resistance assay described above. After five days of feeding, worms were washed three times with M9 buffer to remove OP50 bacteria. Then, 50 µM H2DCF-DA (Sigma-Aldrich Co., St. Louis, MO, USA) was added to each NGM plate. After nematodes were incubated for 3 h at 20 °C, they were transferred onto microscope slides layered with 2% agar pads. The worms were anesthetized with 1% levamisole and then analyzed [43]. We quantified the fluorescence intensity at an excitation wavelength of 490 nm and an emission wavelength of 510–570 nm. We measured the fluorescence signal every hour and exported raw data. Blank-subtracted raw data (DCF fluorescence level) were normalized to those in untreated nematodes and were presented as mean standard deviation using Microsoft Office 2017 Excel software. A one-way ANOVA with a Tukey's post hoc test was carried out using SPSS Statistics 21 to analyze the statistical significance of differences.

#### 4.6. Lipid-Staining Assay by Nile Red

Nile red staining was conducted as described in a previous report [43]. First, OP50 bacteria in the original concentration of 0.5 mg/mL were diluted with the Nile red solution at a ratio of 1:250 (*v/v*). Then, at least 30 synchronized L1 larvae were transferred to the respective NGM plates and cultivated at 20 °C for 72 h. Thereafter, nematodes were transferred to three different plates according to different observation times (3/6/12 days). On the day of imaging, nematodes were fixed with 1% paraformaldehyde solution, stained with 1 mg/mL Nile red for 30 min under dark conditions, and washed three times with M9 buffer. The *elegans* with fixed Nile red staining were observed with a 40× objective lens under a Leica fluorescence microscope (DM4B), and 16-bit images were taken with a CCD camera (DFC7000T). Fluorescence intensity was defined using Image J (US National Institutes of Health, Bethesda, MD, USA).

#### 4.7. Autofluorescence Assay

After the incubations of synchronized L1 wild-type larvae in the presence or absence of 100 µM SDA for 72 h at 20 °C, worms were treated for 3/6/12 days and washed off using M9 buffer, and the anesthetized nematodes were transferred to microscope slides for observation. Each group, including at least 30 nematodes, was photographed, and the accumulation of fluorescent autofluorescence was analyzed as described in a previous work [44]. The *elegans* with fixed Nile red staining were observed with a 40× objective lens under a Leica fluorescence microscope (DM4B), and 16-bit images were taken with a CCD camera (DFC7000T; excitation/emission 358 nm/461 nm). The fluorescence intensity was calculated semiquantitatively using ImageJ, and represented in terms of normalized values of corrected total cell fluorescence (CTCF) (CTCF = integrated density (area of selected cell mean fluorescence of background readings)).

#### 4.8. Paralysis Assays

Adult CL4176 worms were transferred onto NGM plates to lay eggs. After 2 h, they were taken out and transferred to the medium added with SDA. After two days of culture at 16 °C, the worms were shifted to grow at 25 °C for 31 h, and then scoring was performed every hour. The worms were scored as “paralyzed” when they failed to respond to the stimulus after being gently touched with a platinum wire [2].

#### 4.9. *Pseudomonas Aeruginosa* Infection Assay

Synchronized L1 larvae were transferred onto NGM plates seeded with OP50 and cultured at 20 °C. The plates for infection assay were seeded with *P. aeruginosa* and cultured overnight before use. Synchronized L4 larvae were transferred onto NGM plates and seeded with the pathogen and cultured at 25 °C in the presence or absence of 100 µM SDA. The number of dead worms was scored every day.

#### 4.10. Reproduction

At least 10 synchronized L4 larvae were picked into NGM plates with SDA or without SDA, as described in the lifespan assay. Worms were transferred to the pretreated plates to lay eggs every day until the end of the fifth day of the experiment, and eggs were counted after incubation at 20 °C for 48 h [45].

#### 4.11. Intracellular Localization of DAF-16::GFP

The transgenic strains TJ356 were used to detect the intracellular localization of the GFP-tagged transcription factors. Synchronized L4 larvae were transferred to the prepared NGM plates with or without 100 µM SDA and maintained for 1 h at 20 °C. The control-group and the SDA-treatment-group worms were separately placed on a microscope slide and mixed with 1% levamisole, and the cellular localization of DAF-16::GFP was detected [46].

#### 4.12. RNA Extraction and Quantitative Polymerase Chain Reaction

About 2000 synchronized adult worms were transferred onto five NGM plates (6 cm diameter) with or without 100 µM SDA and cultured at 20 °C for 48 h. Total RNA was extracted using a RNAiso Plus (Takara Bio Inc., Dalian, China), and converted to cDNA using a high-capacity cDNA reverse transcription kit (Takara Bio Inc., Dalian, China). Quantitative reverse-transcriptase–polymerase chain reaction (qRT-PCR) was performed using a Power SYBR Green PCR Master Mix (Bio-Rad Laboratories, Inc., California, America) and the ABI 7500 system (Takara Bio Inc., Dalian, China). The relative expression levels of genes were determined using the 2<sup>−ΔΔCT</sup> method and normalized to the gene expression, and β-actin was used as an internal control. The *p*-values were calculated using a two-tailed *t*-test [47].

#### 4.13. Western Blot

CL4176 worms were treated with the same approach as in the paralysis assays. After the L4 nematodes were transferred to 25 °C and cultured for 31 h, the control group and SDA group CL4176 *C. elegans* were washed off from the plates using M9 buffer. The isolated proteins were analyzed via Western blotting [2,48]. The concentration of extracted protein was quantified with a Bioepitope Bicinchoninic Acid Protein Assay Kit. Equal amounts of protein were loaded onto Tris-Tricine gels. Proteins were transferred to polyvinylidene fluoride membranes (Solarbio, Beijing, China). The primary antibodies used for immunoblotting were anti-b-amyloid (Solarbio, Beijing, China) diluted 1:500 and anti-β-actin (Solarbio, Beijing, China) diluted 1:1000. The secondary antibodies used were horseradish peroxidase goat antimouse (Solarbio, Beijing, China) and horseradish peroxidase goat antirabbit (Solarbio, Beijing, China) diluted 1:5000. The proteins on the polyvinylidene fluoride membrane were detected with an enhanced chemiluminescence reagent (Solarbio, Beijing, China).

#### 4.14. Statistical Analysis

The statistical analysis and graphical presentation of data were performed using GraphPad Prism version 5. Analysis of variance and a nonpaired *t*-test were used to calculate statistical significance where applicable. Significant differences between the lifespan of treated and control worms were determined using the Kaplan–Meier survival assay, and *p*-values were calculated using the log-rank test. The results were plotted as mean ± standard error of the mean (SEM).



## 5. Conclusions

In this study, we demonstrated that SDA had antiaging activity in *C. elegans*. This effect could be mediated through modulating the mitochondrial and IIS pathways. Moreover, SDA had no effect on the reproductive ability of the worms treated, suggesting that it has potential in the development of antiaging drugs.

**Supplementary Materials:** The following are available online at <https://www.mdpi.com/article/10.3390/md20010059/s1>, Figure S1: Representative images of ROS; Figure S2: Representative images of relative lipid; Figure S3: Representative images of autofluorescence; Table S1: Primer sequences of genes used in experiment.

**Author Contributions:** Conceptualization, S.J., C.-P.J. and X.-X.Y.; methodology, X.-X.Y.; software, X.-X.Y.; validation, X.-X.Y.; formal analysis, S.J. and C.-P.J.; investigation, S.J. and C.-P.J.; resources, S.J. and C.-P.J.; data curation, S.J. and C.-P.J.; writing—original draft preparation, S.J., C.-P.J. and P.C.; writing—review and editing, S.J., C.-P.J. and P.C.; visualization, S.J., C.-P.J. and P.C.; supervision, Y.-H.L., C.-H.G. and X.-X.Y.; project administration, C.-H.G. and X.-X.Y.; funding acquisition, C.-H.G. and X.-X.Y. All authors have read and agreed to the published version of the manuscript.

**Funding:** This study was supported by the National Natural Science Fund (81903533), Guangxi Natural Science Foundation of China (2020GXNSFGA297002), Guangxi Natural Fund General Project (2018GXNSFAA281268), Special Fund for Bagui Scholars of Guangxi, Guangxi Key Laboratory of Efficacy Study on Chinese Materia Medica (No. 20-065-38), and the Program for Innovative Research Team of High Education and Outstanding Scholar in Guang Xi (2019-52).

**Data Availability Statement:** The data presented in this study are available upon request from the corresponding author.

**Acknowledgments:** We thank LetPub ([www.letpub.com](http://www.letpub.com)) (15 January 2021) for its linguistic assistance and scientific consultation during the preparation of this manuscript.

**Conflicts of Interest:** The authors declare no conflict of interest.

## References

- Barros, A.G.D.A.; Liu, J.; Lemieux, G.A.; Mullaney, B.C.; Ashrafi, K. Analyses of *C. elegans* Fat Metabolic Pathways. *Methods Cell Biol.* **2012**, *107*, 383–407. [[CrossRef](#)]
- Fei, T.; Fei, J.; Huang, F.; Xie, T.; Xu, J.; Zhou, Y.; Yang, P. The anti-aging and anti-oxidation effects of tea water extract in *Caenorhabditis elegans*. *Exp. Gerontol.* **2017**, *97*, 89–96. [[CrossRef](#)]
- Senchuk, M.M.; Dues, D.J.; Van Raamsdonk, J.M. Measuring Oxidative Stress in *Caenorhabditis elegans*: Paraquat and Juglone Sensitivity Assays. *Bio-Protocol* **2017**, *7*, e2086. [[CrossRef](#)] [[PubMed](#)]
- Yi, X.; Jiang, S.; Qin, M.; Liu, K.; Cao, P.; Chen, S.; Deng, J.; Gao, C. Compounds from the fruits of mangrove *Sonneratia apetala*: Isolation, molecular docking and antiaging effects using a *Caenorhabditis elegans* model. *Bioorganic Chem.* **2020**, *99*, 103813. [[CrossRef](#)]
- Liu, J.; Luo, D.; Wu, Y.; Gao, C.; Lin, G.; Chen, J.; Wu, X.; Zhang, Q.; Cai, J.; Su, Z. The Protective Effect of *Sonneratia apetala* Fruit Extract on Acetaminophen-Induced Liver Injury in Mice. *Evid.-Based Complement. Altern. Med.* **2019**, *2019*, 6919834. [[CrossRef](#)] [[PubMed](#)]
- Patra, J.K.; Das, S.K.; Thatoi, H. Phytochemical Profiling and Bioactivity of A Mangrove Plant, *Sonneratia apetala*, from Odisha Coast of India. *Chin. J. Integr. Med.* **2015**, *21*, 274–285. [[CrossRef](#)] [[PubMed](#)]
- Hossain, S.J.; Basar, M.H.; Rokeya, B.; Arif, K.M.T.; Sultana, M.S.; Rahman, M.H. Evaluation of antioxidant, antidiabetic and antibacterial activities of the fruit of *Sonneratia apetala* (Buch.-Ham.). *Orient. Pharm. Exp. Med.* **2013**, *13*, 95–102. [[CrossRef](#)]
- Srivastava, S.; Sonkar, R.; Mishra, S.K.; Tiwari, A.; Balramnavar, V.; Mir, S.; Bhatia, G.; Saxena, A.K.; Lakshmi, V. Erratum to: Antidyslipidemic and Antioxidant Effects of Novel Lupeol-Derived Chalcones. *Lipids* **2013**, *48*, 1017–1027. [[CrossRef](#)] [[PubMed](#)]
- Link, P.; Roth, K.; Sporer, F.; Wink, M. *Carlina acaulis* Exhibits Antioxidant Activity and Counteracts Abeta Toxicity in *Caenorhabditis elegans*. *Molecules* **2016**, *21*, 871. [[CrossRef](#)] [[PubMed](#)]
- Zhang, X.; Li, W.; Tang, Y.; Lin, C.; Cao, Y.; Chen, Y. Mechanism of pentagalloyl glucose in alleviating fat accumulation in *Caenorhabditis elegans*. *J. Agric. Food Chem.* **2019**, *67*, 14110–14120. [[CrossRef](#)]
- Shen, P.; Yue, Y.; Park, Y. A living model for obesity and aging research: *Caenorhabditis elegans*. *Crit. Rev. Food Sci. Nutr.* **2018**, *58*, 741–754. [[CrossRef](#)] [[PubMed](#)]
- Komura, T.; Yamanaka, M.; Nishimura, K.; Hara, K.; Nishikawa, Y. Autofluorescence as a noninvasive biomarker of senescence and advanced glycation end products in *Caenorhabditis elegans*. *NPJ Aging Mech. Dis.* **2021**, *7*, 12. [[CrossRef](#)]

13. Teuscher, A.C.; Ewald, C.Y. *Caenorhabditis elegans* Overcoming Autofluorescence to Assess GFP Expression During Normal Physiology and Aging in *Caenorhabditis elegans*. *Bio Protoc.* **2018**, *8*, e2940. [[CrossRef](#)]
14. Shintani, T.; Sakoguchi, H.; Yoshihara, A.; Izumori, K.; Sato, M. d-Allulose, a stereoisomer of d-fructose, extends *Caenorhabditis elegans* lifespan through a dietary restriction mechanism: A new candidate dietary restriction mimetic. *Biochem. Biophys. Res. Commun.* **2017**, *493*, 1528–1533. [[CrossRef](#)] [[PubMed](#)]
15. Tepper, R.G.; Ashraf, J.; Kaletsky, R.; Kleemann, G.; Murphy, C.T.; Bussemaker, H.J. PQM-1 Complements DAF-16 as a Key Transcriptional Regulator of DAF-2-Mediated Development and Longevity. *Cell* **2013**, *154*, 676–690. [[CrossRef](#)]
16. Matsunami, K. Frailty and *Caenorhabditis elegans* as a Benchmark Animal Model for Screening Drugs Including Natural Herbs. *Front. Nutr.* **2018**, *5*, 111. [[CrossRef](#)]
17. Zhi, L.; Yu, Y.; Li, X.; Wang, D. Molecular Control of Innate Immune Response to *Pseudomonas aeruginosa* Infection by Intestinal let-7 in *Caenorhabditis elegans*. *PLoS Pathog.* **2017**, *13*, e1006152. [[CrossRef](#)]
18. Gerstbrein, B.; Stamatas, G.; Kollias, N.; Driscoll, M. In vivo spectrofluorimetry reveals endogenous biomarkers that report healthspan and dietary restriction in *Caenorhabditis elegans*. *Aging Cell* **2005**, *4*, 127–137. [[CrossRef](#)] [[PubMed](#)]
19. Coburn, C.; Allman, E.; Mahanti, P.; Benedetto, A.; Cabreiro, F.; Pincus, Z.; Matthijssens, F.; Araiz, C.; Mandel, A.; Vlachos, M.; et al. Anthranilate Fluorescence Marks a Calcium-Propagated Necrotic Wave That Promotes Organismal Death in *C. elegans*. *PLoS Biol.* **2013**, *11*, e1001613. [[CrossRef](#)] [[PubMed](#)]
20. Sforzini, S.; Moore, M.N.; Mou, Z.; Boeri, M.; Banni, M.; Viarengo, A. Mode of action of Cr(VI) in immunocytes of earthworms: Implications for animal health. *Ecotoxicol. Environ. Saf.* **2017**, *138*, 298–308. [[CrossRef](#)] [[PubMed](#)]
21. Viña, J. The free radical theory of frailty: Mechanisms and opportunities for interventions to promote successful aging. *Free Radic. Biol. Med.* **2019**, *134*, 690–694. [[CrossRef](#)]
22. Kritsiligkou, P.; Rand, J.D.; Weids, A.J.; Wang, X.; Kershaw, C.; Grant, C.M. Endoplasmic reticulum (ER) stress-induced reactive oxygen species (ROS) are detrimental to the fitness of a thioredoxin reductase mutant. *J. Biol. Chem.* **2018**, *293*, 11984–11995. [[CrossRef](#)] [[PubMed](#)]
23. Nandakumar, R.; Tschisnarov, R.; Meissner, F.; Prabakaran, T.; Krissanaprasit, A.; Farahani, E.; Zhang, B.C.; Assil, S.; Martin, A.; Bertrams, W.; et al. Intracellular bacteria engage a STING-TBK1-MVB12b pathway to enable paracrine cGAS-STING signaling. *Nat. Microbiol.* **2019**, *4*, 701–713. [[CrossRef](#)] [[PubMed](#)]
24. Xu, C.; Liu, W.-B.; Zhang, D.-D.; Cao, X.-F.; Shi, H.-J.; Li, X.-F. Interactions between dietary carbohydrate and metformin: Implications on energy sensing, insulin signaling pathway, glycolipid metabolism and glucose tolerance in blunt snout bream *Megalobrama amblycephala*. *Aquaculture* **2018**, *483*, 183–195. [[CrossRef](#)]
25. Jia, K.; Levine, B. Autophagy is Required for Dietary Restriction-Mediated Life Span Extension in *C. elegans*. *Autophagy* **2007**, *3*, 597–599. [[CrossRef](#)] [[PubMed](#)]
26. Gelino, S.; Chang, J.T.; Kumsta, C.; She, X.; Davis, A.; Nguyen, C.; Panowski, S.; Hansen, M. Intestinal Autophagy Improves Healthspan and Longevity in *C. elegans* during Dietary Restriction. *PLoS Genet.* **2016**, *12*, e1006135.
27. Aparicio, R.; Hansen, M.; Walker, D.W.; Kumsta, C. The selective autophagy receptor SQSTM1/p62 improves lifespan and proteostasis in an evolutionarily conserved manner. *Autophagy* **2020**, *16*, 772–774. [[CrossRef](#)] [[PubMed](#)]
28. Galimov, E.R.; Gems, D. Shorter life and reduced fecundity can increase colony fitness in virtual *Caenorhabditis elegans*. *Aging Cell* **2020**, *19*, e13141. [[CrossRef](#)] [[PubMed](#)]
29. Zhu, Q.; Qu, Y.; Zhou, X.-G.; Chen, J.-N.; Luo, H.-R.; Wu, G.-S. A Dihydroflavonoid Naringin Extends the Lifespan of *C. elegans* and Delays the Progression of Aging-Related Diseases in PD/AD Models via DAF-16. *Oxidative Med. Cell. Longev.* **2020**, *2020*, 6069354. [[CrossRef](#)] [[PubMed](#)]
30. Bansal, A.; Kwon, E.-S.; Conte, D.; Liu, H.; Gilchrist, M.J.; MacNeil, L.T.; Tissenbaum, H.A. Transcriptional regulation of *Caenorhabditis elegans* FOXO/DAF-16 modulates lifespan. *Longev. Healthspan* **2014**, *3*, 5. [[CrossRef](#)]
31. Ewald, C.Y.; Marfil, V.; Li, C. Alzheimer-related protein APL-1 modulates lifespan through heterochronic gene regulation in *Caenorhabditis elegans*. *Aging Cell* **2016**, *15*, 1051–1062. [[CrossRef](#)]
32. Dhondt, I.; Petyuk, V.A.; Cai, H.; Vandemeulebroucke, L.; Vierstraete, A.; Smith, R.D.; Depuydt, G.; Braeckman, B.P. FOXO/DAF-16 Activation Slows Down Turnover of the Majority of Proteins in *C. elegans*. *Cell Rep.* **2016**, *16*, 3028–3040. [[CrossRef](#)]
33. Lee, S.J.; Murphy, C.T.; Kenyon, C. Glucose shortens the life span of *C. elegans* by downregulating DAF-16/FOXO activity and aquaporin gene expression. *Cell Metab.* **2009**, *10*, 379–391. [[CrossRef](#)]
34. Gerke, P.; Keshet, A.; Mertenskötter, A.; Paul, R.J. The JNK-Like MAPK KGB-1 of *Caenorhabditis elegans* Promotes Reproduction, Lifespan, and Gene Expressions for Protein Biosynthesis and Germline Homeostasis but Interferes with Hyperosmotic Stress Tolerance. *Cell. Physiol. Biochem.* **2014**, *34*, 1951–1973. [[CrossRef](#)] [[PubMed](#)]
35. Kim, S.-H.; Kim, B.-K.; Park, S.; Park, S.-K. Phosphatidylcholine Extends Lifespan via DAF-16 and Reduces Amyloid-Beta-Induced Toxicity in *Caenorhabditis elegans*. *Oxidative Med. Cell. Longev.* **2019**, *2019*, 2860642. [[CrossRef](#)] [[PubMed](#)]
36. Kim, B.-K.; Kim, S.-A.; Baek, S.-M.; Lee, E.Y.; Lee, E.S.; Chung, C.H.; Ahn, C.M.; Park, S.-K. Cur2004-8, a synthetic curcumin derivative, extends lifespan and modulates age-related physiological changes in *Caenorhabditis elegans*. *Drug Discov. Ther.* **2019**, *13*, 198–206. [[CrossRef](#)] [[PubMed](#)]
37. Tang, L.; Choe, K. Characterization of skn-1/wdr-23 phenotypes in *Caenorhabditis elegans*; pleiotrophy, aging, glutathione, and interactions with other longevity pathways. *Mech. Ageing Dev.* **2015**, *149*, 88–98. [[CrossRef](#)] [[PubMed](#)]

38. Song, B.; Zheng, B.; Li, T.; Liu, R.H. Raspberry extract ameliorates oxidative stress in *Caenorhabditis elegans* via the SKN-1/Nrf2 pathway. *J. Funct. Foods* **2020**, *70*, 103977. [[CrossRef](#)]
39. Labuschagne, C.F.; Brenkman, A.B. Current methods in quantifying ROS and oxidative damage in *Caenorhabditis elegans* and other model organism of aging. *Ageing Res. Rev.* **2013**, *12*, 918–930. [[CrossRef](#)]
40. Brenner, S. The genetics of *Caenorhabditis elegans*. *Genetics* **1974**, *77*, 71–94. [[CrossRef](#)]
41. Stuhr, N.L.; Curran, S.P. Bacterial diets differentially alter lifespan and healthspan trajectories in *C. elegans*. *Commun. Biol.* **2020**, *3*, 653. [[CrossRef](#)]
42. Zheng, S.; Liao, S.; Zou, Y.; Qu, Z.; Shen, W.; Shi, Y. Mulberry leaf polyphenols delay aging and regulate fat metabolism via the germline signaling pathway in *Caenorhabditis elegans*. *Age* **2014**, *36*, 9719. [[CrossRef](#)]
43. Meng, F.; Li, J.; Rao, Y.; Wang, W.; Fu, Y. A Chinese Herbal Formula, Gengnianchun, Ameliorates beta-Amyloid Peptide Toxicity in a *Caenorhabditis elegans* Model of Alzheimer's Disease. *Evid.-Based Complementary Altern. Med.* **2017**, *2017*, 7480980. [[CrossRef](#)]
44. Trivedi, S.; Pandey, R. 5'-Hydroxy-6, 7, 8, 3', 4'-pentamethoxyflavone extends longevity mediated by DR-induced autophagy and oxidative stress resistance in *C. elegans*. *Geroscience* **2021**, *43*, 759–772. [[CrossRef](#)]
45. Ogawa, T.; Kodera, Y.; Hirata, D.; Blackwell, T.K.; Mizunuma, M. Natural thioallyl compounds increase oxidative stress resistance and lifespan in *Caenorhabditis elegans* by modulating SKN-1/Nrf. *Sci. Rep.* **2016**, *6*, 21611. [[CrossRef](#)]
46. Fischer, N.; Büchter, C.; Koch, K.; Albert, S.; Csuk, R.; Wätjen, W. The resveratrol derivatives trans-3,5-dimethoxy-4-fluoro-4'-hydroxystilbene and trans-2,4',5-trihydroxystilbene decrease oxidative stress and prolong lifespan in *Caenorhabditis elegans*. *J. Pharm. Pharmacol.* **2016**, *69*, 73–81. [[CrossRef](#)]
47. Zheng, S.; Huang, X.; Xing, T.; Ding, A.; Wu, G.; Luo, H. Chlorogenic Acid Extends the Lifespan of *Caenorhabditis elegans* via Insulin/IGF-1 Signaling Pathway. *J. Gerontology. Ser. A Biol. Sci. Med. Sci.* **2017**, *72*, 464–472.
48. Rebolledo, D.L.; Aldunate, R.; Kohn, R.; Neira, I.; Minniti, A.N.; Inestrosa, N.C. Copper reduces Abeta oligomeric species and ameliorates neuromuscular synaptic defects in a *C. elegans* model of inclusion body myositis. *J. Neurosci.* **2011**, *31*, 10149–10158. [[CrossRef](#)] [[PubMed](#)]



## Article

# Chevalones H–M: Six New $\alpha$ -Pyrone Meroterpenoids from the Gorgonian Coral-Derived Fungus *Aspergillus hiratsukae* SCSIO 7S2001

Xia-Yu Chen <sup>1,2</sup>, Qi Zeng <sup>1,2</sup>, Yu-Chan Chen <sup>3</sup>, Wei-Mao Zhong <sup>1</sup>, Yao Xiang <sup>1,2</sup>, Jun-Feng Wang <sup>1</sup>, Xue-Feng Shi <sup>1</sup>, Wei-Min Zhang <sup>3</sup>, Si Zhang <sup>1</sup> and Fa-Zuo Wang <sup>1,\*</sup>

- <sup>1</sup> CAS Key Laboratory of Tropical Marine Bio-Resources and Ecology, Southern Marine Science and Engineering Guangdong Laboratory (Guangzhou), Guangdong Key Laboratory of Marine Materia Medica, RNAM Center for Marine Microbiology, South China Sea Institute of Oceanology, Chinese Academy of Sciences, 164 West Xingang Road, Guangzhou 510301, China; chenxiayu17@mailsucas.ac.cn (X.-Y.C.); 18489875310@163.com (Q.Z.); weimaozhong@hotmail.com (W.-M.Z.); xy920412@sina.cn (Y.X.); wangjunfeng@scsio.ac.cn (J.-F.W.); shixuefeng@scsio.ac.cn (X.-F.S.); zhsimcd@scsio.ac.cn (S.Z.)
- <sup>2</sup> University of Chinese Academy of Sciences, 19 Yuquan Road, Beijing 100049, China
- <sup>3</sup> State Key Laboratory of Applied Microbiology Southern China, Guangdong Provincial Key Laboratory of Microbial Culture Collection and Application, Institute of Microbiology, Guangdong Academy of Sciences, 100 Central Xianlie Road, Guangzhou 510070, China; chenyc@gdim.cn (Y.-C.C.); wmzhang@gdim.cn (W.-M.Z.)
- \* Correspondence: wangfazu@scsio.ac.cn

**Abstract:** Six new  $\alpha$ -pyrone meroterpenoid chevalones H–M (1–6), together with six known compounds (7–12), were isolated from the gorgonian coral-derived fungus *Aspergillus hiratsukae* SCSIO 7S2001 collected from Mischief Reef in the South China Sea. Their structures, including absolute configurations, were elucidated on the basis of spectroscopic analysis and X-ray diffraction data. Compounds 1–5 and 7 showed different degrees of antibacterial activity with MIC values of 6.25–100  $\mu\text{g}/\text{mL}$ . Compound 8 exhibited potent cytotoxicity against SF-268, MCF-7, and A549 cell lines with  $\text{IC}_{50}$  values of 12.75, 9.29, and 20.11  $\mu\text{M}$ , respectively.

**Keywords:** coral-derived fungi; *Aspergillus hiratsukae*; meroterpenoids; antibacterial activity; cytotoxic activity

**Citation:** Chen, X.-Y.; Zeng, Q.; Chen, Y.-C.; Zhong, W.-M.; Xiang, Y.; Wang, J.-F.; Shi, X.-F.; Zhang, W.-M.; Zhang, S.; Wang, F.-Z. Chevalones H–M: Six New  $\alpha$ -Pyrone Meroterpenoids from the Gorgonian Coral-Derived Fungus *Aspergillus hiratsukae* SCSIO 7S2001. *Mar. Drugs* **2022**, *20*, 71. <https://doi.org/10.3390/md20010071>

Academic Editor: Marialuisa Menna

Received: 11 December 2021

Accepted: 11 January 2022

Published: 14 January 2022

**Publisher's Note:** MDPI stays neutral with regard to jurisdictional claims in published maps and institutional affiliations.



**Copyright:** © 2022 by the authors. Licensee MDPI, Basel, Switzerland. This article is an open access article distributed under the terms and conditions of the Creative Commons Attribution (CC BY) license (<https://creativecommons.org/licenses/by/4.0/>).

## 1. Introduction

Chevalones are a class of meroterpenoids with multiple rings, polyketones and stereogenic structures. It is precisely because of this variable structure that they have a variety of biological activities. Chevalones A–D were first reported to be isolated from the soil-derived fungus *Eurotium chevalieri* and exhibited antimalarial activity, antimycobacterial activity and cytotoxicity against cancer cell lines [1]. On the other hand, chevalones were found to show synergistic effects, such as chevalone E, which enhanced the antibiotic oxacillin against methicillin-resistant *Staphylococcus aureus* [2,3], and potentiated the cytotoxic effect of doxorubicin in MDA-MB-231 breast cancer cells [4]. Chevalone C was found to show synergism with doxorubicin in A549 cells [5], and its acetylated analog also had certain cytotoxic activity against tumor cells [6]. In addition, chevalones F and G were both isolated by Paluka, but neither of them showed activity [7,8].

Recently, we conducted NMR data analysis on the pretreated crude extracts of marine-derived fungal secondary metabolites and found that the metabolites of the coral-derived fungus *Aspergillus hiratsukae* SCSIO 7S2001 contained NMR signals with high similarity to chevalone C [1]. After further investigation of secondary metabolites of the fungus *Aspergillus hiratsukae* SCSIO 7S2001, we isolated six new  $\alpha$ -pyrone meroterpenoid chevalones H–M (1–6), together with the six known compounds neoehinulin A (7) [9], echinuline

(8) [10], isorugulosuvine (9) [11], cyclo(L-Phe-L-Val) (10) [12], *trans*-cinnamic acid (11) [13], and *N*-phenethylacetamide (12) [14], by comparison with the reported literature data (Figure 1). Herein, we report the isolation, structural elucidation and bioactivities of these compounds.

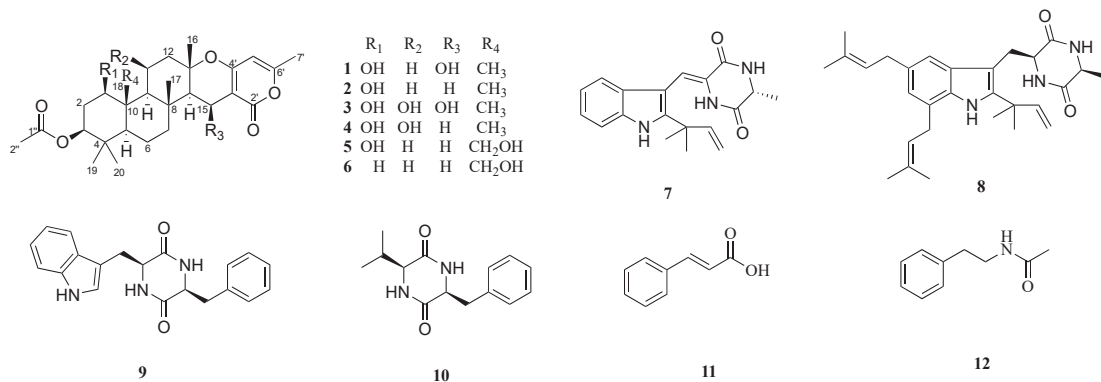


Figure 1. Chemical structures of compounds 1–12.

## 2. Results and Discussion

Compound **1** was obtained as colorless crystals, and its molecular formula was determined to be C<sub>28</sub>H<sub>40</sub>O<sub>7</sub> by HRESIMS (Figure S7) ion at  $m/z$  511.2673 [M + Na]<sup>+</sup> (calcd for C<sub>28</sub>H<sub>40</sub>O<sub>7</sub>Na, 511.2672), indicating nine degrees of unsaturation. The <sup>1</sup>H NMR spectrum (Table 1) revealed the presence of seven methyl proton signals at  $\delta_H$  0.85 (3H, s), 0.86 (3H, s), 0.95 (3H, s), 1.33 (3H, s), 1.57 (3H, s), 2.05 (3H, s), and 2.19 (3H, s) and 10 diastereotopic methylene proton signals  $\delta_H$  1.18–1.21 (1H, m), 1.58–1.60 (1H, m), 1.60–1.62 (1H, m), 1.64–1.66 (1H, m), 1.66–1.68 (1H, m), 1.69–1.72 (1H, m), 1.89 (1H,  $J = 12.3, 4.5$  Hz), 2.02 (1H,  $J = 11.9, 3.1$  Hz), 2.16–2.18 (1H, m), and 2.65–2.69 (1H, m), seven methine proton signals  $\delta_H$  0.76 (1H, dd,  $J = 12.1, 2.5$  Hz), 1.09 (1H, dd,  $J = 12.1, 2.4$  Hz), 1.42 (1H, d,  $J = 4.1$  Hz), 1.45 (1H, dd,  $J = 12.9, 4.7$  Hz), 3.54 (1H, dd,  $J = 11.4, 4.6$  Hz), 4.48 (1H, dd,  $J = 12.2, 4.4$  Hz), and 4.89 (1H, d,  $J = 4.0$  Hz), and the <sup>13</sup>C NMR and DEPT data (Table 1) of **1** showed the presence of 28 carbon resonances, including seven methyls, five methylenes, seven methines, and nine quaternary carbons (two carbonyl carbons, three olefinic carbons and four quaternary carbons), which revealed that its structure possessed great similarity to the known meroterpenoid chevalone B [1]. By comparing their spectroscopic data with published literature values, the main difference was the hydroxylation of C-1 and C-15, which was deduced by the carbon chemical shifts. The position of C-1 could be proven via a series of mutually coupled resonances H-1/H<sub>2</sub>-2/H-3, H-5/H-6/H-7, H-9/H-11/H-12 and H-15 and H-16 in the COSY spectrum, respectively, along with the HMBC correlation from H-3 to C-1'; C-15 was also proven by combining the COSY and HMBC in H-14/H-15 and H-15 to C-2' (Figure 2). The relative configuration of **1** was determined by NOESY correlations (Figure 3) of H-1/H-3, H-3/H-5, H-1/H-9, H-7/H-15, H-15/H-14, H-16/H-17 and H-17/H-18. Absolute configuration of **1** was confirmed by the experimental ECD of **1** (Figure 4) and single-crystal X-ray diffraction (Figure 5). Therefore, compound **1** was named chevalone H.

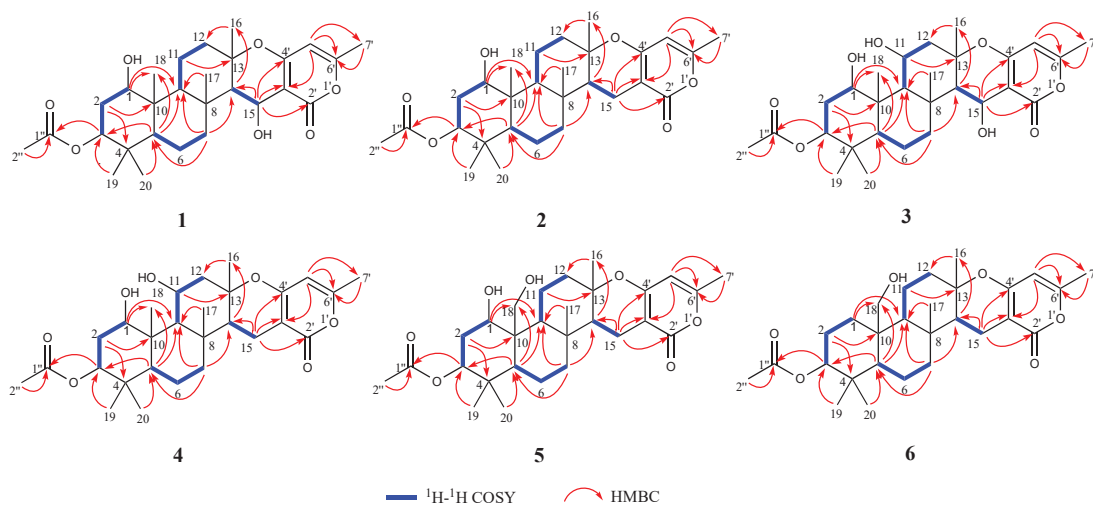


Figure 2. Key HMBC and COSY correlations of compounds 1–6.

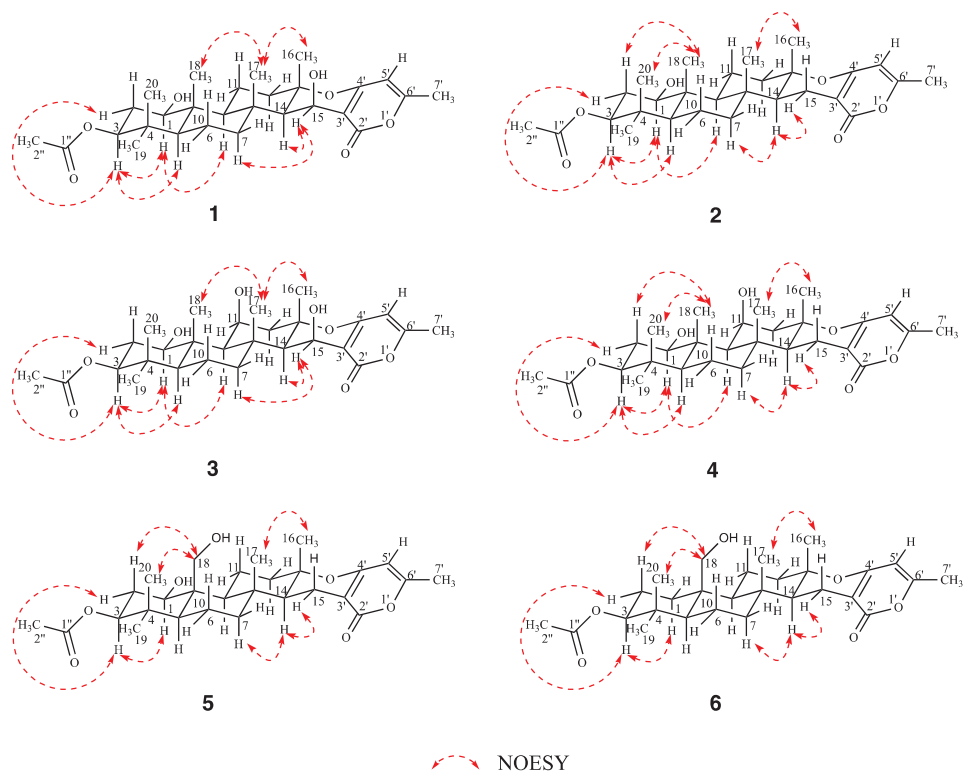


Figure 3. Key NOESY correlations of compounds 1–6.

Compound 2 was obtained as colorless crystals, and its molecular formula  $\text{C}_{28}\text{H}_{40}\text{O}_6$  was deduced from the HRESIMS  $m/z$  473.2907  $[\text{M} + \text{H}]^+$  (calcd for  $\text{C}_{28}\text{H}_{41}\text{O}_6$ , 473.2903), implying nine degrees of unsaturation. The  $^1\text{H}$  and  $^{13}\text{C}$  NMR spectra (Table 1) of 2 showed

a high similarity to those of **1**, except for the lack of a hydroxyl group at C-15 ( $\delta_C$  17.0), which was supported by the HMBC correlation from the methylene proton H<sub>2</sub>-15 to carbonyl carbon C-2'. The relative stereochemistry was determined by a combination of the coupling constant and analysis of the NOESY spectrum, which was similar to those of **1**. In addition, the experimental ECD of **2** displayed good agreement with the experimental ECD of **1** (Figure 4). Further configuration of **2** was proven by single-crystal X-ray diffraction experimental data (Figure 5). The absolute configuration of **2** was assigned as 1*R*,3*S*,5*S*,8*R*,9*S*,10*R*,13*S*,14*S*. On the basis of the above evidence, **2** was a new  $\alpha$ -pyrone meroterpenoid and named chevalone I.

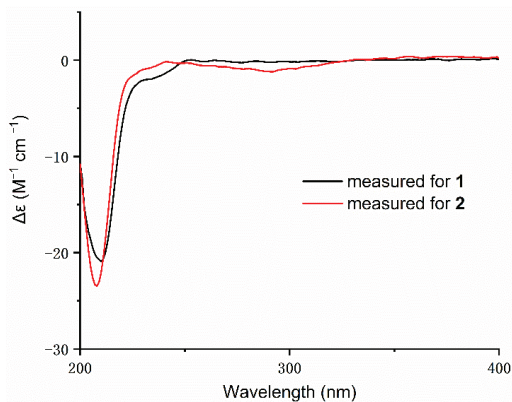


Figure 4. Experimental ECD spectra of compounds **1** and **2**.

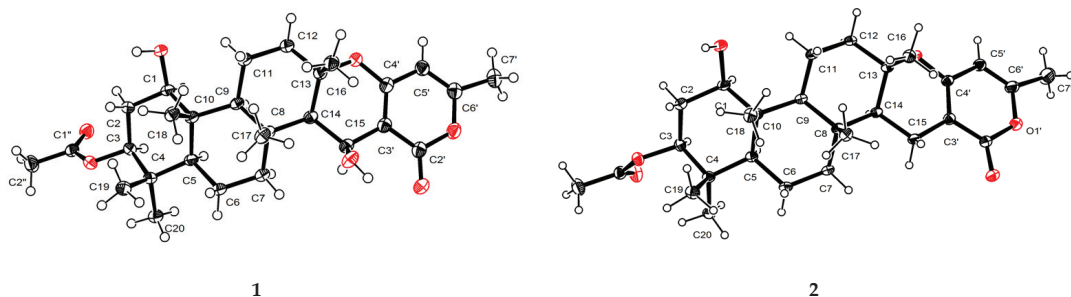


Figure 5. X-ray ORTEP diagram of compounds **1** and **2**.

Compound **3** was obtained as a white solid, and its molecular formula C<sub>28</sub>H<sub>40</sub>O<sub>8</sub> was deduced from the HRESIMS  $m/z$  527.2609 [M + Na]<sup>+</sup> (calcd for C<sub>28</sub>H<sub>40</sub>O<sub>8</sub>Na, 527.2621), implying nine degrees of unsaturation. The NMR spectra (Table 1) of **3** were similar to those of **1**, except for the presence of a secondary alcohol at C-11 ( $\delta_C$  70.0), which was supported by a series of COSY correlations between H-9/H-11/H-12. The relative stereochemistry was determined by a combination of the coupling constant and analysis of the NOESY spectrum, which was similar to those of **1**. The  $J$  values of 3.1 Hz for the coupling of H-9 to H-11 supported the axial position of H-11, indicating the *cis* ring junction. In addition, the experimental ECD of **3** displayed good agreement with the experimental ECD of **1** and **2** (Figure S73). The absolute configuration of **3** was assigned as 1*R*,3*S*,5*S*,8*R*,9*S*,10*S*,11*S*,13*S*,14*R*,15*S*. Thus, **3** was identified as a hydroxy derivative of **1** and named chevalone J.

**Table 1.**  $^1\text{H}$  NMR (700 MHz) and  $^{13}\text{C}$  NMR (176 MHz) data for compounds 1–3.

| NO. | 1 <sup>a</sup>           |                               | 2 <sup>a</sup>           |                               | 3 <sup>a</sup>           |                               |
|-----|--------------------------|-------------------------------|--------------------------|-------------------------------|--------------------------|-------------------------------|
|     | $\delta_{\text{C}}$ Type | $\delta_{\text{H}}$ (J in Hz) | $\delta_{\text{C}}$ Type | $\delta_{\text{H}}$ (J in Hz) | $\delta_{\text{C}}$ Type | $\delta_{\text{H}}$ (J in Hz) |
| 1   | 78.1 CH                  | 3.51 m                        | 77.7 CH                  | 3.54 dd (11.4, 4.6)           | 76.4 CH                  | 3.63 dd (11.2, 4.8)           |
| 2   | 34.5 CH <sub>2</sub>     | 1.69–1.72 m                   | 34.5 CH <sub>2</sub>     | 1.67–1.71 m                   | 33.5 CH <sub>2</sub>     | 1.93–1.95 m                   |
| 3   | 77.3 CH                  | 1.89 dt (12.3, 4.5)           | 77.2 CH                  | 1.90 dt (12.5, 4.4)           | 77.3 CH                  | 1.80–1.82 m                   |
| 4   | 37.9 C                   | 4.47 dd (12.2, 4.4)           | 37.9 C                   | 4.48 dd (12.2, 4.3)           | 37.7 C                   | 4.45 dd (12.3, 4.2)           |
| 5   | 53.3 CH                  | 0.74–0.78 m                   | 53.3 CH                  | 0.76 dd (12.1, 2.5)           | 54.4 CH                  | 0.80 dd (12.4, 2.4)           |
| 6   | 17.4 CH <sub>2</sub>     | 1.58–1.60 m                   | 17.6 CH <sub>2</sub>     | 1.56–1.58 m                   | 18.1 CH <sub>2</sub>     | 1.06–1.08 m                   |
|     |                          | 1.66–1.68 m                   |                          | 1.61–1.63 m                   |                          | 1.23–1.25 m                   |
| 7   | 40.5 CH <sub>2</sub>     | 1.18–1.21 m                   | 40.8 CH <sub>2</sub>     | 0.98–1.04 m                   | 42.0 CH <sub>2</sub>     | 1.18–1.20 m                   |
|     |                          | 2.16–2.18 m                   |                          | 1.85 dt (12.9, 3.4)           |                          | 2.15–2.17 m                   |
| 8   | 39.6 C                   |                               | 38.2 C                   |                               | 39.6 C                   |                               |
| 9   | 61.6 CH                  | 1.04 dd (11.7, 2.4)           | 61.1 CH                  | 1.10 dd (12.1, 2.4)           | 61.5 CH                  | 0.88 d (3.1)                  |
| 10  | 43.5 C                   |                               | 43.5 C                   |                               | 44.1 C                   |                               |
| 11  | 21.6 CH <sub>2</sub>     | 1.60–1.62 m                   | 21.4 CH <sub>2</sub>     | 1.43–1.45 m                   | 70.0 CH                  | 4.79 dt (5.4, 2.7)            |
|     |                          | 2.65–2.69 m                   |                          | 2.64–2.70 m                   |                          |                               |
| 12  | 41.8 CH <sub>2</sub>     | 1.64–1.66 m                   | 40.6 CH <sub>2</sub>     | 1.63–1.65 m                   | 48.7 CH <sub>2</sub>     | 1.87–1.89 m                   |
|     |                          | 2.02 dt (11.9, 3.1)           |                          | 2.00–2.04 m                   |                          | 2.28–2.30 m                   |
| 13  | 81.9 C                   |                               | 80.4 C                   |                               | 81.3 C                   |                               |
| 14  | 56.5 CH                  | 1.42 d (4.1)                  | 52.1 CH                  | 1.46 d (4.5)                  | 56.6 CH                  | 1.41 d (4.0)                  |
| 15  | 60.5 CH                  | 4.89 d (4.0)                  | 17.0 CH <sub>2</sub>     | 2.13 dd (16.7, 13.0)          | 60.2 CH <sub>2</sub>     | 4.95 d (4.0)                  |
|     |                          |                               |                          | 2.42 dd (16.7, 4.7)           |                          |                               |
| 16  | 22.1 CH <sub>3</sub>     | 1.57 s                        | 20.6 CH <sub>3</sub>     | 1.19 s                        | 23.1 CH <sub>3</sub>     | 1.77 s                        |
| 17  | 18.3 CH <sub>3</sub>     | 1.33 s                        | 16.4 CH <sub>3</sub>     | 0.90 s                        | 19.6 CH <sub>3</sub>     | 1.69 s                        |
| 18  | 12.4 CH <sub>3</sub>     | 0.95 s                        | 12.4 CH <sub>3</sub>     | 0.92 s                        | 14.9 CH <sub>3</sub>     | 1.29 s                        |
| 19  | 28.0 CH <sub>3</sub>     | 0.85 s                        | 27.9 CH <sub>3</sub>     | 0.84 s                        | 27.8 CH <sub>3</sub>     | 0.84 s                        |
| 20  | 16.2 CH <sub>3</sub>     | 0.86 s                        | 16.1 CH <sub>3</sub>     | 0.85 s                        | 16.0 CH <sub>3</sub>     | 0.88 s                        |
| 2'  | 165.6 C                  |                               | 165.6 C                  |                               | 165.6 C                  |                               |
| 3'  | 101.4 C                  |                               | 97.9 C                   |                               | 101.4 C                  |                               |
| 4'  | 163.4 C                  |                               | 163.5 C                  |                               | 163.0 C                  |                               |
| 5'  | 101.1 CH                 | 5.73 s                        | 100.8 CH                 | 5.68 s                        | 101.0 CH                 | 5.73 s                        |
| 6'  | 161.6 C                  |                               | 159.9 C                  |                               | 161.7 C                  |                               |
| 7'  | 20.0 CH <sub>3</sub>     | 2.19 s                        | 19.9 CH <sub>3</sub>     | 2.17 s                        | 20.0 CH <sub>3</sub>     | 2.19 s                        |
| 1'' | 171.0 C                  |                               | 171.0 C                  |                               | 171.0 C                  |                               |
| 2'' | 21.3 CH <sub>3</sub>     | 2.05 s                        | 21.3 CH <sub>3</sub>     | 2.05 s                        | 21.3 CH <sub>3</sub>     | 2.06 s                        |

<sup>a</sup> The solvent was CDCl<sub>3</sub>.

Compound **4** was obtained as a white solid, and its molecular formula C<sub>28</sub>H<sub>40</sub>O<sub>7</sub> was deduced from the HRESIMS  $m/z$  489.2857 [M + H]<sup>+</sup> (calcd for 489.2852), implying nine degrees of unsaturation. The NMR spectra (Table 2) of **4** indicated the same skeleton as **3**, except for the appearance of a methylene at C-15 ( $\delta_{\text{C}}$  17.2), which was deduced by the DEPT spectrum and HMBC correlation from H-15 to C-2'. The relative stereochemistry was determined by a combination of the coupling constant and analysis of the NOESY spectrum, which was similar to those of **3**. The  $J$  values of 2.9 Hz for the coupling of H-9 to H-11 supported the axial position of H-11, indicating the *cis* ring junction. In addition, the experimental ECD of **4** displayed good agreement with the experimental ECD of **1** and **2** (Figure S74). The absolute configuration of **4** was assigned as 1R,3S,5S,8R,9S,10R,11S,13S,14S. Thus, **4** was named chevalone K.

Compound **5** was obtained as a white solid, and its molecular formula C<sub>28</sub>H<sub>40</sub>O<sub>7</sub> was deduced from the HRESIMS  $m/z$  489.2839 [M + H]<sup>+</sup> (calcd for 489.2852), implying nine degrees of unsaturation. Comparison of the spectroscopic data of **5** and **2** showed that they share a similar chevalone skeleton, except that the NMR resonances at C-18 were replaced by hydroxymethyl groups ( $\delta_{\text{C}}$  63.5) (Table 2). The relative stereochemistry was determined by a combination of the coupling constant and analysis of the NOESY spectrum, which was similar to those of **2**. Similarly, the experimental ECD of **5** displayed good agreement with the experimental ECD of **1** and **2** (Figure S75), which also assigned its absolute configuration. On the basis of the above evidence, **5** was a new meroterpenoid and we named it chevalone L.

Compound **6** was obtained as a white solid, and its molecular formula C<sub>28</sub>H<sub>40</sub>O<sub>6</sub> was deduced from the HRESIMS  $m/z$  473.2892 [M+H]<sup>+</sup> (calcd for 473.2903), implying nine degrees of unsaturation. The  $^1\text{H}$  and  $^{13}\text{C}$  NMR spectra of **6** (Table 2) were similar to those of **5**, except for the lack of a hydroxyl group at C-1 ( $\delta_{\text{C}}$  63.5), which was deduced by the DEPT NMR and COSY correlation between H-1/H-2/H-3. The relative stereochemistry was determined by a combination of the coupling constant and analysis of the NOESY spectrum,



which was similar to those of **5**. In addition, the experimental ECD of **6** displayed good agreement with the experimental ECD of **1** and **2** (Figure S76). The absolute configuration of **6** was assigned as 3*S*,5*S*,8*R*,9*S*,10*R*,13*S*,14*S* and named chevalone M.

**Table 2.** <sup>1</sup>H NMR (700 MHz) and <sup>13</sup>C NMR (176 MHz) data for compounds 4–6.

| NO. | 4 <sup>a</sup>       |                                    | 5 <sup>b</sup>       |                                    | 6 <sup>b</sup>       |                                     |
|-----|----------------------|------------------------------------|----------------------|------------------------------------|----------------------|-------------------------------------|
|     | $\delta_C$ Type      | $\delta_H$ (J in Hz)               | $\delta_C$ Type      | $\delta_H$ (J in Hz)               | $\delta_C$ Type      | $\delta_H$ (J in Hz)                |
| 1   | 76.7 CH              | 3.59 dd (11.2, 4.9)                | 78.9 CH              | 3.82 dd (11.1, 5.1)                | 33.7 CH <sub>2</sub> | 1.73–1.75 m<br>0.93–0.95 m          |
| 2   | 34.0 CH <sub>2</sub> | 1.82–1.84 m<br>1.89 m              | 34.7 CH <sub>2</sub> | 1.95–1.98 m<br>1.98–2.00 m         | 24.7 CH <sub>2</sub> | 1.64–1.69 m                         |
| 3   | 79.0 CH              | 4.48 dd (12.3, 4.3)                | 77.2 CH              | 4.44 dd (12.1, 4.7)                | 82.4 CH              | 4.49 dd (11.8, 4.7)                 |
| 4   | 38.7 C               |                                    | 37.5 C               |                                    | 38.7 C               |                                     |
| 5   | 55.0 CH              | 0.91 dd (6.3, 1.8)                 | 53.8 CH              | 0.85–0.87 m                        | 57.3 CH              | 1.07–1.09 m                         |
| 6   | 19.2 CH <sub>2</sub> | 1.67–1.69 m<br>1.76 dd (12.8, 3.7) | 17.9 CH <sub>2</sub> | 1.53–1.55 m<br>1.61–1.63 m         | 18.6 CH <sub>2</sub> | 1.56–1.60 m<br>2.16 dd (16.6, 13.0) |
| 7   | 43.5 CH <sub>2</sub> | 1.09–1.12 m<br>1.80–1.82 m         | 41.8 CH <sub>2</sub> | 1.05–1.07 m<br>1.93 dt (13.0, 3.5) | 42.7 CH <sub>2</sub> | 1.14–1.18 m<br>1.89–1.94 m          |
| 8   | 39.0 C               |                                    | 38.4 C               |                                    | 38.6 C               |                                     |
| 9   | 61.6 CH              | 1.08 d (2.9)                       | 62.8 CH              | 1.18–1.20 m                        | 62.4 CH              | 1.06–1.07 m                         |
| 10  | 45.2 C               |                                    | 47.4 C               |                                    | 43.3 C               |                                     |
| 11  | 70.6 CH              | 4.84–4.86 m                        | 24.4 CH <sub>2</sub> | 2.04–2.06 m<br>2.68–2.70 m         | 22.8 CH <sub>2</sub> | 1.88–1.90 m                         |
| 12  | 47.9 CH <sub>2</sub> | 1.90–1.94 m<br>2.24–2.26 m         | 41.7 CH <sub>2</sub> | 1.51–1.53 m<br>2.00–2.02 m         | 42.6 CH <sub>2</sub> | 2.01–2.03 m<br>1.51–1.53 m          |
| 13  | 81.5 C               |                                    | 80.5 C               |                                    | 82.3 C               |                                     |
| 14  | 53.2 CH              | 1.56 dd (12.8, 4.7)                | 52.5 CH              | 1.44 dd (12.9, 4.8)                | 53.5 CH              | 1.50–1.51 m                         |
| 15  | 17.4 CH <sub>2</sub> | 2.40 dd (16.6, 4.8)                | 17.2 CH <sub>2</sub> | 2.16–2.18 m<br>2.43 dd (16.7, 4.8) | 17.8 CH <sub>2</sub> | 2.39 dd (16.7, 4.7)<br>1.28–1.32 m  |
| 16  | 22.0 CH <sub>3</sub> | 1.42 s                             | 20.1 CH <sub>3</sub> | 1.21 s                             | 20.6 CH <sub>3</sub> | 1.23 s                              |
| 17  | 18.2 CH <sub>3</sub> | 1.27 s                             | 15.5 CH <sub>3</sub> | 1.10 s                             | 16.1 CH <sub>3</sub> | 1.10 s                              |
| 18  | 15.3 CH <sub>3</sub> | 1.28 s                             | 63.5 CH <sub>2</sub> | 4.27 d (12.1)<br>3.90 d (12.2)     | 62.1 CH <sub>2</sub> | 3.85 d (12.0)<br>3.97 d (12.0)      |
| 19  | 28.0 CH <sub>3</sub> | 0.84 s                             | 28.2 CH <sub>3</sub> | 0.84 s                             | 29.1 CH <sub>3</sub> | 0.89 s                              |
| 20  | 16.3 CH <sub>3</sub> | 0.89 s                             | 16.2 CH <sub>3</sub> | 0.81 s                             | 17.3 CH <sub>3</sub> | 0.87 s                              |
| 2'  | 167.5 C              |                                    | 165.5 C              |                                    | 167.6 C              |                                     |
| 3'  | 98.7 C               |                                    | 97.8 C               |                                    | 98.7 C               |                                     |
| 4'  | 165.3 C              |                                    | 163.5 C              |                                    | 165.7 C              |                                     |
| 5'  | 102.1 CH             | 5.89 s                             | 100.8 CH             | 5.68 s                             | 102.1 CH             | 5.89 s                              |
| 6'  | 161.8 C              |                                    | 160.0 C              |                                    | 161.8 C              |                                     |
| 7'  | 19.5 CH <sub>3</sub> | 2.20 s                             | 19.9 CH <sub>3</sub> | 2.19 s                             | 19.5 CH <sub>3</sub> | 2.20 s                              |
| 1'' | 172.6 C              |                                    | 171.1 C              |                                    | 172.8 C              |                                     |
| 2'' | 21.0 CH <sub>3</sub> | 2.04 s                             | 21.3 CH <sub>3</sub> | 2.06 s                             | 21.1 CH <sub>3</sub> | 2.03 s                              |

<sup>a</sup> The solvent was CD<sub>3</sub>OD, <sup>b</sup> the solvent was CDCl<sub>3</sub>.

The antibacterial activity of compounds **1–12** against *M. lutea*, *K. pneumoniae*, methicillin-resistant *Staphylococcus aureus*, and *Streptococcus faecalis* was evaluated with the broth dilution assay [15], and ciprofloxacin was used as a positive control (Table 3). The MIC of compound **1** was 6.25 µg/mL for *M. lutea*, methicillin-resistant *Staphylococcus aureus*, and *Streptococcus faecalis*; that of compound **2** was 6.25 µg/mL for methicillin-resistant *Staphylococcus aureus*; that of compound **3** was 12.5 µg/mL for methicillin-resistant *Staphylococcus aureus*; that of compound **4** was 6.25 µg/mL for *K. pneumoniae*; that of compound **5** was 12.5 µg/mL for *M. lutea*, methicillin-resistant *Staphylococcus aureus*, and *Streptococcus faecalis*; and that of compound **7** was 12.5 µg/mL for *Streptococcus faecalis*.

**Table 3.** The antibacterial activities of compounds 1–12.

| Compounds | MIC (µg/mL)              |                              |  |                               |
|-----------|--------------------------|------------------------------|--|-------------------------------|
|           | <i>Micrococcus lutea</i> | <i>Klebsiella pneumoniae</i> | Methicillin-Resistant <i>Staphylococcus aureus</i> | <i>Streptococcus faecalis</i> |
| <b>1</b>  | 6.25                     | 50                           | 6.25   | 6.25                          |
| <b>2</b>  | 25                       | >100                         | 6.25   | 25                            |
| <b>3</b>  | 25                       | 25                           | 12.5   | >100                          |
| <b>4</b>  | >100                     | 6.25                         | 25   | 50                            |
| <b>5</b>  | 12.5                     | >100                         | 12.5   | 12.5                          |
| <b>6</b>  | >100                     | >100                         | >100   | >100                          |
| <b>7</b>  | >100                     | 50                           | >100   | 12.5                          |
| <b>8</b>  | >100                     | >100                         | >100   | >100                          |

Table 3. Cont.

| Compounds     | MIC ( $\mu\text{g/mL}$ ) |                              |  |                               |
|---------------|--------------------------|------------------------------|--|-------------------------------|
|               | <i>Micrococcus lutea</i> | <i>Klebsiella pneumoniae</i> | Methicillin-Resistant <i>Staphylococcus aureus</i> | <i>Streptococcus faecalis</i> |
| 9             | >100                     | >100                         | >100   | >100                          |
| 10            | >100                     | >100                         | >100   | >100                          |
| 11            | >100                     | >100                         | >100   | >100                          |
| 12            | >100                     | >100                         | >100   | >100                          |
| Ciprofloxacin | 0.25                     | 0.25                         | 0.50   | 0.50                          |

The cytotoxic activities of compounds 1–12 against SF-268, MCF-7, HepG-2, and A549 cell lines in vitro were evaluated with the SRB method [16], and adriamycin was used as a positive control (Table 4). Compounds 2 and 5 displayed weak cytotoxic activity against the SF-268, MCF-7, HepG-2, and A549 cell lines, and compound 8 displayed moderate cytotoxic activity against the SF-268, MCF-7, and A549 cell lines.

Table 4. Cytotoxic activity of compounds (1–12) against tumor cells.

| Compounds  | IC <sub>50</sub> ( $\mu\text{M}$ ) |                  |                   |                   |
|------------|------------------------------------|------------------|-------------------|-------------------|
|            | SF-268                             | MCF-7            | HepG-2            | A549              |
| 1          | >128                               | >128             | >128              | >128              |
| 2          | 65.64 $\pm$ 0.53                   | 91.69 $\pm$ 6.59 | 107.31 $\pm$ 9.83 | 84.54 $\pm$ 16.23 |
| 3          | >128                               | >128             | >128              | >128              |
| 4          | >128                               | >128             | >128              | >128              |
| 5          | 54.78 $\pm$ 3.18                   | 56.28 $\pm$ 2.05 | 58.54 $\pm$ 1.52  | 55.33 $\pm$ 1.60  |
| 6          | >128                               | >128             | >128              | >128              |
| 7          | >128                               | >128             | >128              | >128              |
| 8          | 12.75 $\pm$ 1.43                   | 9.29 $\pm$ 0.80  | >128              | 20.11 $\pm$ 2.31  |
| 9          | >128                               | >128             | >128              | >128              |
| 10         | >128                               | >128             | >128              | >128              |
| 11         | >128                               | >128             | >128              | >128              |
| 12         | >128                               | >128             | >128              | >128              |
| Adriamycin | 1.94 $\pm$ 0.01                    | 2.00 $\pm$ 0.04  | 2.16 $\pm$ 0.05   | 2.16 $\pm$ 0.07   |

Compound 2 exhibited weak cytotoxic activity to against cancer cells, and its IC<sub>50</sub> was 65.64–107.31  $\mu\text{M}$ . Compound 5 showed cytotoxic activity at 54.78–58.54  $\mu\text{M}$ . Compound 8 exhibited cytotoxic activity against the SF-268, MCF-7, and A549 cell lines with IC<sub>50</sub> values of 12.75  $\pm$  1.43, 9.29  $\pm$  0.80, and 20.11  $\pm$  2.31  $\mu\text{M}$ , respectively. Comparing the cytotoxic activity of compounds 2 and 5, 5 was slightly stronger than 2, indicating that the hydroxylation at methyl (C-18) of 5 is an advantage in terms of cytotoxic activity. Regarding compounds 7 and 8, 8 was significantly stronger than 7, which did not show significant activity under 100  $\mu\text{M}$ . This could indicate that prenylation in aromatic rings greatly contributes to cytotoxic activity, but the effect of double bond reduction on activity is unknown.

### 3. Materials and Methods

#### 3.1. General Experimental Procedures

<sup>1</sup>D and <sup>2</sup>D NMR spectra were recorded on an AVANCE III HD 700 (Temperature 298.0 K, Bruker, Billerica, MA, USA). Optical rotations were measured with an MCP 500 automatic polarimeter (Anton Paar, Graz, Austria) with CH<sub>3</sub>OH as the solvent. IR spectra were measured on an IR Affinity-1 spectrometer (Shimadzu, Kyoto, Japan). UV spectra were recorded on a UV-2600 spectrometer (Shimadzu, Tokyo, Japan). Circular dichroism spectra were measured by Chirascan circular dichroism spectrometer with the same concentration of UV measurement (Pathlength 10 mm, Applied Photophysics, Surrey, UK). HRESIMS spectra data were recorded on a MaXis quadrupole-time-of-flight mass spectrometer. Thin layer chromatography (TLC) was performed on plates precoated with silica gel GF254

(10–40  $\mu\text{m}$ ). Column chromatography (CC) was performed over silica gel (100–200 mesh and 200–300 mesh) (Qingdao Marine Chemical Factory, Qingdao, China) and ODS (50  $\mu\text{m}$ , YMC, Kyoto, Japan). High-performance liquid chromatography was performed on an Agilent 1260 HPLC equipped with a DAD detector using an ODS column (YMC-pack ODS-A, 250  $\times$  10 mm, 5  $\mu\text{m}$ , 3 mL/min). All solvents used in CC and HPLC were of analytical grade (Tianjin Damao Chemical Plant, Tianjin, China) and chromatographic grade (Oceanpak, Goteborg, Sweden), respectively.

### 3.2. Fungal Material

The fungal strain used in this investigation was isolated from gorgonian coral collected in the Mischief Reef of the South China Sea. It was identified as *Aspergillus hiratsukae* SCSIO 7S2001, according to a molecular biological protocol by DNA amplification and sequencing of the ITS region (deposited in GenBank, accession no. MN347034). A voucher strain (SCSIO 7S2001) was deposited in the RNAM Center for Marine Microbiology, South China Sea Institute of Oceanology, Chinese Academy of Sciences.

### 3.3. Fermentation and Extraction

The fungal strain *Aspergillus hiratsukae* SCSIO 7S2001 was cultured on PDA plates (potatoes 200.0 g, glucose 20.0 g, agar 15.0 g and sea salt 30.0 g in 1.0 L H<sub>2</sub>O) at 28 °C for 7 days. The seed medium (potatoes 200.0 g, glucose 20.0 g and sea salt 30.0 g in 1.0 L H<sub>2</sub>O) was inoculated with strain SCSIO 7S2001 and incubated at 28.0 °C for 3 days on a rotating shaker (180 rpm). Then, a large-scale fermentation of fungal SCSIO 7S2001 was incubated for 30 days at 28 °C in 245 conical flasks (each flask contained 80.0 g rice and 100.0 mL H<sub>2</sub>O with 3‰ salinity) with solid rice medium. The whole fermented cultures were soaked in CH<sub>3</sub>OH/H<sub>2</sub>O (*v/v*, 7:3) overnight and filtered through cheesecloth to obtain the filtrate, and the extraction was repeated three times. The extract was evaporated under reduced pressure to evaporate the filtrate until the solvent could not be distilled out or the solvent was distilled out slowly to obtain an aqueous solution. We added twice the amount of ethyl acetate for extraction to the aqueous solution to obtain an organic phase (EtOAc-H<sub>2</sub>O, 2:1), and repeated the extraction 3 times. Both organic phases were combined and concentrated under reduced pressure to give the whole crude extract (138 g).

### 3.4. Isolation and Purification

The extract was subjected to silica gel vacuum liquid chromatography (VLC) eluting with a gradient of CH<sub>3</sub>OH-CH<sub>2</sub>Cl<sub>2</sub> (0:1–1:0) to separate into four fractions. Fr.2 (5.8 g) was separated by a reverse-phase ODS silica gel column (CH<sub>3</sub>OH-H<sub>2</sub>O, 3:7–10:0) to obtain 10 fractions (Fr.2.1–2.10). Then, Fr.2.3 (75.8 mg) was purified by HPLC (CH<sub>3</sub>CN-H<sub>2</sub>O, 40:60) to yield **12** (42.9 mg, *t<sub>R</sub>* = 8.1 min). Fr.2.7 (157.6 mg) was purified by HPLC (CH<sub>3</sub>CN-H<sub>2</sub>O, 50:50) to yield Fr.2.7.1 (6.6 mg, *t<sub>R</sub>* = 26.9 min), F2.7.2 (7.8 mg, *t<sub>R</sub>* = 16.2 min), and **4** (6.6 mg, *t<sub>R</sub>* = 22.2 min). Fr.2.7.1 was recrystallized (EtOAc-N-hexane, 1:1) to yield **1** (5.8 mg). Fr.2.7.2 was recrystallized (EtOAc-N-hexane, 1:1) to yield **2** (5.8 mg). Fr.2.8 (139.2 mg) was purified by HPLC (CH<sub>3</sub>CN-H<sub>2</sub>O, 60:40) to yield **3** (26.4 mg, *t<sub>R</sub>* = 21.1 min), **5** (11.9 mg, *t<sub>R</sub>* = 15.5 min), and **6** (6.1 mg, *t<sub>R</sub>* = 17.9 min). Fr.2.10 (661.8 mg) was divided into two fractions by Sephadex LH-20 (CH<sub>3</sub>OH-CH<sub>2</sub>Cl<sub>2</sub> 1:1). Fr.2.10.1 was further purified by HPLC (CH<sub>3</sub>OH-H<sub>2</sub>O, 70:30) to yield **7** (5.7 mg, *t<sub>R</sub>* = 9.1 min). Fr.2.10.2 was further purified by HPLC (CH<sub>3</sub>OH-H<sub>2</sub>O, 90:10) to yield **8** (5.6 mg, *t<sub>R</sub>* = 12.1 min). Fr.3 was separated by a reverse-phase ODS silica gel column (CH<sub>3</sub>OH-H<sub>2</sub>O, 3:7–10:0) to obtain six fractions. Fr.3.3 was subjected to Sephadex LH-20 (CH<sub>3</sub>OH-CH<sub>2</sub>Cl<sub>2</sub>, 1:1) to obtain three fractions. Fr.3.3.1 was purified by HPLC (CH<sub>3</sub>CN-H<sub>2</sub>O, 30:70) to yield **9** (1.0 mg, *t<sub>R</sub>* = 17.3 min). Fr.3.3.2 was purified by HPLC (CH<sub>3</sub>CN-H<sub>2</sub>O, 20:80) to yield **10** (3.7 mg, *t<sub>R</sub>* = 27.0 min). Fr.3.3.3 was purified by HPLC (CH<sub>3</sub>CN-H<sub>2</sub>O, 32:68) to yield **11** (5.6 mg, *t<sub>R</sub>* = 13.3 min).

Chevalone H (**1**): white needle crystals.  $[\alpha]_D^{25} = -57.4^\circ$  (c 0.2, CH<sub>3</sub>OH). UV (c 0.5 mmol/L, CH<sub>3</sub>OH):  $\lambda_{\text{max}}$  (log  $\epsilon$ ) 205(4.39), 286(3.72) nm; IR (film)  $\nu_{\text{max}}$  3524, 2932, 2872, 1697, 1576,

1456, 1246, 1036  $\text{cm}^{-1}$ ; HR-ESIMS at  $m/z$  511.2673  $[\text{M} + \text{Na}]^+$ , calcd for  $\text{C}_{28}\text{H}_{41}\text{O}_8$ , 511.2666.  $^1\text{H}$  NMR ( $\text{CDCl}_3$ , 700 MHz) and  $^{13}\text{C}$  NMR ( $\text{CDCl}_3$ , 176 MHz) see Table 1.

Chevalone I (2): white needle crystals.  $[\alpha]_D^{25} = -74.8^\circ$  (c 0.2,  $\text{CH}_3\text{OH}$ ); UV (c 0.5 mmol/L,  $\text{CH}_3\text{OH}$ ):  $\lambda_{\text{max}}$  (log  $\epsilon$ ) 206(4.26), 286(3.73) nm; IR (film)  $\nu_{\text{max}}$  3429, 2936, 2864, 1697, 1653, 1578, 1449, 1387, 1237, 1031, 997  $\text{cm}^{-1}$ ; HRESIMS at  $m/z$  473.2907  $[\text{M} + \text{H}]^+$ , calcd for  $\text{C}_{28}\text{H}_{41}\text{O}_6$ , 473.2898.  $^1\text{H}$  NMR ( $\text{CDCl}_3$ , 700 MHz) and  $^{13}\text{C}$  NMR ( $\text{CDCl}_3$ , 176 MHz) see Table 1.

Chevalone J (3): white solid.  $[\alpha]_D^{25} = -6.6^\circ$  (c 0.2,  $\text{CH}_3\text{OH}$ ). UV (c 0.5 mmol/L,  $\text{CH}_3\text{OH}$ ):  $\lambda_{\text{max}}$  (log  $\epsilon$ ) 203(4.22), 286(3.56) nm. IR (film)  $\nu_{\text{max}}$  3366, 2936, 2857, 1697, 1653, 1541, 1456, 1024  $\text{cm}^{-1}$ . HR-ESIMS at  $m/z$  527.2609  $[\text{M} + \text{Na}]^+$ , calcd for  $\text{C}_{28}\text{H}_{40}\text{NaO}_8$ , 527.2615.  $^1\text{H}$  NMR ( $\text{CDCl}_3$ , 700 MHz) and  $^{13}\text{C}$  NMR ( $\text{CDCl}_3$ , 176 MHz) see Table 1.

Chevalone K (4): white solid.  $[\alpha]_D^{25} = -21.6^\circ$  (c 0.2,  $\text{CH}_3\text{OH}$ ). UV (c 0.5 mmol/L,  $\text{CH}_3\text{OH}$ ):  $\lambda_{\text{max}}$  (log  $\epsilon$ ) 205(4.32), 286(3.71) nm; IR (film)  $\nu_{\text{max}}$  3363, 2941, 1645, 1516, 1447, 1105,  $\text{cm}^{-1}$ ; HR-ESIMS  $m/z$  489.2857  $[\text{M} + \text{H}]^+$ , calcd for  $\text{C}_{28}\text{H}_{41}\text{O}_7$ , 489.2847.  $^1\text{H}$  NMR ( $\text{CD}_3\text{OD}$ , 700 MHz) and  $^{13}\text{C}$  NMR ( $\text{CD}_3\text{OD}$ , 176 MHz) see Table 2.

Chevalone L (5): white solid.  $[\alpha]_D^{25} = -35.6^\circ$  (c 0.2,  $\text{CH}_3\text{OH}$ ). UV (c 0.5 mmol/L,  $\text{CH}_3\text{OH}$ ):  $\lambda_{\text{max}}$  (log  $\epsilon$ ) 205(4.32), 286(3.71) nm; IR (film)  $\nu_{\text{max}}$  3362, 2928, 2851, 1697, 1653, 1576, 1506, 1238, 1026  $\text{cm}^{-1}$ ; HR-ESIMS at  $m/z$  489.2839  $[\text{M} + \text{H}]^+$ , calcd for  $\text{C}_{28}\text{H}_{41}\text{O}_7$ , 489.2847.  $^1\text{H}$  NMR ( $\text{CDCl}_3$ , 700 MHz) and  $^{13}\text{C}$  NMR ( $\text{CDCl}_3$ , 176 MHz) see Table 2.

Chevalone M (6): white solid.  $[\alpha]_D^{25} = -6.8^\circ$  (c 0.2,  $\text{CH}_3\text{OH}$ ). UV (c 0.5 mmol/L,  $\text{CH}_3\text{OH}$ ):  $\lambda_{\text{max}}$  (log  $\epsilon$ ) 205(4.32), 286(3.71) nm. IR (film)  $\nu_{\text{max}}$  3420, 2934, 1695, 1587, 1236, 1026; HR-ESIMS  $m/z$  473.2892  $[\text{M} + \text{H}]^+$ , calcd for  $\text{C}_{28}\text{H}_{41}\text{O}_6$ , 473.2898.  $^1\text{H}$  NMR ( $\text{CDCl}_3$ , 700 MHz) and  $^{13}\text{C}$  NMR ( $\text{CDCl}_3$ , 176 MHz) see Table 2.

### 3.5. Crystal Structure Analysis

Crystallographic data for the compounds chevalone H (1) and chevalone I (2) were collected on a Rigaku XtaLAB AFC12 single-crystal diffractometer using  $\text{Cu-K}\alpha$  radiation ( $\lambda = 0.71073$  Å) at 298(2) K. The structures of 1 and 2 were solved by direct methods (SHELXS97), expanded using difference Fourier techniques, and refined by full-matrix least-squares calculation [17]. The nonhydrogen atoms were refined anisotropically, and hydrogen atoms were fixed at calculated positions. Crystallographic data of compounds 1 and 2 have been deposited at the Cambridge Crystallographic Data Center under the reference numbers CCDC 1,989,730 and 1,989,731. Copies of the data could be obtained free of charge from the CCDC at [www.ccdc.cam.ac.uk](http://www.ccdc.cam.ac.uk) (accessed on 11 March 2020).

Crystal data for 1:  $\text{C}_{28}\text{H}_{40}\text{O}_7$ ,  $M = 488.27$  g/mol, orthorhombic, space group P212121,  $a = 10.74060(10)$  Å,  $b = 15.17330(10)$  Å,  $c = 36.9556(4)$  Å,  $V = 6022.67(10)$  Å<sup>3</sup>,  $Z = 4$ ,  $T = 105$  K,  $\mu$  ( $\text{Cu-K}\alpha$ ) =  $0.750$   $\text{mm}^{-1}$ ,  $D_{\text{calc}} = 1.271$   $\text{g}/\text{cm}^3$ , 32,806 reflections measured ( $7.538^\circ \leq \theta \leq 148.882^\circ$ ), 11,913 unique ( $R_{\text{int}} = 0.0284$ ,  $R_{\text{sigma}} = 0.0310$ ) which were used in all calculations. The final  $R_1$  was 0.0354 ( $I > 2\sigma(I)$ ), and  $wR_2$  was 0.0906 (all data). The goodness of fit on  $F_2$  was 1.053. Flack parameter = 0.03(4).

Crystal data for 2:  $\text{C}_{28}\text{H}_{40}\text{O}_6$ ,  $M = 472.29$  g/mol, orthorhombic, space group P212121,  $a = 5.99790(10)$  Å,  $b = 30.7241(6)$  Å,  $c = 13.2008(2)$  Å,  $V = 2432.64(7)$  Å<sup>3</sup>,  $Z = 4$ ,  $T = 105(8)$  K,  $\mu$  ( $\text{Cu-K}\alpha$ ) =  $0.718$   $\text{mm}^{-1}$ ,  $D_{\text{calc}} = 1.290$   $\text{g}/\text{cm}^3$ , 11,762 reflections measured ( $7.288^\circ \leq \theta \leq 148.656^\circ$ ), 4812 unique ( $R_{\text{int}} = 0.0348$ ,  $R_{\text{sigma}} = 0.0405$ ) which were used in all calculations. The final  $R_1$  was 0.0405 ( $I > 2\sigma(I)$ ), and  $wR_2$  was 0.1063 (all data). The goodness of fit on  $F_2$  was 1.099. Flack parameter =  $-0.02(10)$ .

### 3.6. Antibacterial Activity

The antibacterial activities were evaluated with the broth dilution assay [15]. Four bacterial strains (*Klebsiella pneumoniae* ATCC 13883, *Streptococcus faecalis* ATCC 29212, methicillin-resistant *Staphylococcus aureus* 01, and *Micrococcus lutea* 01) were used, and ciprofloxacin was used as a positive control.

### 3.7. Cytotoxicity Activity

Cytotoxicity against SF268 (human glioblastoma carcinoma), MCF-7 (breast cancer), HepG-2 (liver cancer) and A549 (lung cancer) cell lines was assayed by the sulforhodamine (SRB) method [16,18]. Adriamycin was used as a positive control possessing potent cytotoxic activity. IC<sub>50</sub> values were calculated with SPSS software using a nonlinear curve-fitting method. The cells of SF-268, MCF-7, HepG-2, and A549 were purchased from Stem Cell Bank, Chinese Academy of Sciences.

## 4. Conclusions

In this study, bioactive secondary metabolites were isolated from the gorgonian coral-derived fungus *Aspergillus hiratsukae* SCSIO 7S2001: six new  $\alpha$ -pyrone meroterpenoid chevalones H–M (1–6), together with six known compounds (7–12). The absolute configurations of the new compounds were deduced by combining the NOE spectrum, X-ray single crystal diffraction, and ECD spectra. Compounds 1–6 were a series of chevalone derivatives substituted by hydroxy groups based on the meroterpenoid skeleton. Furthermore, the presence of some impurity peaks in the spectral tests of compounds 3 and 6 was due to their low yields, which may be unnecessarily lost by further purification, and this did not affect their qualitative analysis.

Antimicrobial resistance is a global health and development threat and has become one of the most important public health threats facing humanity in the 21st century [19]. In this study, compounds 1–5 and 7 with bacterial inhibitory potential were screened. In terms of antitumor cell activity, compound 8 exhibited antitumor activity in different cancer cells.

Compound 11 has rarely been reported in marine fungi, and previous studies have shown that trans-cinnamic acid may be an environmentally friendly alternative therapeutic agent for bacterial infections in the aquaculture industry [20]. Compound 12 has been isolated from marine fungi but has not yet been found to have biological activity [21,22].

**Supplementary Materials:** The following are available online at <https://www.mdpi.com/article/10.3390/md20010071/s1>, Figures S1–S53: <sup>1</sup>H NMR, <sup>13</sup>C NMR, DEPT, HSQC, HMBC, COSY, IR, and HR-ESIMS spectra of compounds 1–6. Figures S54–S72: <sup>1</sup>H NMR, <sup>13</sup>C NMR spectra of compounds 7–12. Figures S73–S76: Experimental ECD spectra of compounds 1–6.

**Author Contributions:** X.-Y.C. performed the isolation, purification, characterization, and evaluation of the antibacterial activities of all the compounds, and prepared the manuscript; Q.Z. contributed to the isolation, purification, identification of the fungal strain and revised the manuscript; Y.-C.C. and W.-M.Z. (Wei-Min Zhang) contributed to the determination of cytotoxic activities; W.-M.Z. (Wei-Mao Zhong) and Y.X. contributed to the isolation of the compounds; J.-F.W., X.-F.S. and S.Z. contributed to the structural elucidation of the compounds and revised the manuscript; F.-Z.W. designed and supervised the research and revised the manuscript. All authors have read and agreed to the published version of the manuscript.

**Funding:** This work was financially supported by the Finance Science and Technology Project of Hainan Province (ZDKJ202018), the Key Special Project for Introduced Talents Team of Southern Marine Science and Engineering Guangdong Laboratory (Guangzhou) (GML2019ZD0401), the National Key Research and Development Program of China (2019YFC0312503), National Natural Science Foundation of China (41476136, 41890853, 41776169), Guangdong Provincial Special Fund for Marine Economic Development Project (Yue Natural Resources Contract No. [2020]042), and Guangdong Basic and Applied Basic Research Foundation (2021A1515011523).

**Institutional Review Board Statement:** Not applicable.

**Informed Consent Statement:** Not applicable.

**Data Availability Statement:** Data are contained within the article or Supplementary Material.

**Acknowledgments:** We gratefully acknowledge help from the equipment public service center (Xiao, Sun, Ma, Zhang, and Zheng) in SCSIO for measuring spectroscopic data and support from the Guangzhou Branch of the Supercomputing Center of Chinese Academy of Sciences. We also gratefully acknowledge help from Xiao-Yi Wei from South China Botanical Garden, Chinese Academy of Sciences for his suggestions on manuscript revision.

**Conflicts of Interest:** The authors declare no conflict of interest.

## References

- Kanokmedhakul, K.; Kanokmedhakul, S.; Suwannatrai, R.; Soyong, K.; Prabpai, S.; Kongsaree, P. Bioactive meroterpenoids and alkaloids from the fungus *Eurotium chevalieri*. *Tetrahedron* **2011**, *67*, 5461–5468. [\[CrossRef\]](#)
- Prompanya, C.; Dethoup, T.; Bessa, L.J.; Pinto, M.M.M.; Gales, L.; Costa, P.M.; Silva, A.M.S.; Kijjoa, A. New Isocoumarin Derivatives and Meroterpenoids from the Marine Sponge-Associated Fungus *Aspergillus similanensis* sp. nov. KUFA 0013. *Mar. Drugs* **2014**, *12*, 5160–5173. [\[CrossRef\]](#)
- Prata-Sena, M.; Ramos, A.A.; Buttachon, S.; Castro-Carvalho, B.; Marques, P.; Dethoup, T.; Kijjoa, A.; Rocha, E. Cytotoxic activity of Secondary Metabolites from Marine-derived Fungus *Neosartorya siamensis* in Human Cancer Cells. *Phytother Res.* **2016**, *30*, 1862–1871. [\[CrossRef\]](#)
- Wang, W.; Du, L.; Sheng, S.; Li, A.; Li, Y.; Cheng, G.; Li, G.; Sun, G.; Hu, Q.; Matsuda, Y. Genome mining for fungal polyketide-diterpenoid hybrids: Discovery of key terpene cyclases and multifunctional P450s for structural diversification. *Org. Chem. Front.* **2019**, *6*, 571–578. [\[CrossRef\]](#)
- Ramos, A.A.; Castro-Carvalho, B.; Prata-Sena, M.; Malhão, F.; Buttachon, S.; Dethoup, T.; Kijjoa, A.; Rocha, E. Can marine-derived fungus *Neosartorya siamensis* KUFA 0017 extract and its secondary metabolites enhance antitumor activity of doxorubicin? An in vitro survey unveils interactions against lung cancer cells. *Environ. Toxicol.* **2020**, *35*, 507–517. [\[CrossRef\]](#)
- Rajachan, O.; Kanokmedhakul, K.; Sanmanoch, W.; Boonlue, S.; Hannongbua, S.; Sarpapakorn, P.; Kanokmedhakul, S. Chevalone C analogues and globoscinic acid derivatives from the fungus *Neosartorya spinosa* KKU-1NK1. *Phytochemistry* **2016**, *132*, 68–75. [\[CrossRef\]](#)
- Paluka, J.; Kanokmedhakul, K.; Soyong, M.; Soyong, K.; Kanokmedhakul, S. Meroditerpene pyrone, tryptoquivaline and brasilamide derivatives from the fungus *Neosartorya pseudofischeri*. *Fitoterapia* **2019**, *137*, 104257. [\[CrossRef\]](#)
- Paluka, J.; Kanokmedhakul, K.; Soyong, M.; Soyong, K.; Yahuafai, J.; Siripong, P.; Kanokmedhakul, S. Meroterpenoid pyrones, alkaloid and bicyclic brasilamide from the fungus *Neosartorya Hiratsukae*. *Fitoterapia* **2020**, *142*, 104485. [\[CrossRef\]](#)
- Kuramochi, K.; Ohnishi, K.; Fujieda, S.; Nakajima, M.; Saitoh, Y.; Watanabe, N.; Takeuchi, T.; Nakazaki, A.; Sugawara, F.; Arai, T.; et al. Synthesis and Biological Activities of Neoechinulin A Derivatives: New Aspects of Structure–Activity Relationships for Neoechinulin A. *Chem. Pharm. Bull.* **2008**, *56*, 1738–1743. [\[CrossRef\]](#)
- Li, D.; Li, X.; Li, T.; Dang, H.; Wang, B. Dioxopiperazine Alkaloids Produced by the Marine Mangrove Derived Endophytic Fungus *Eurotium Rubrum*. *Helv. Chim. Acta* **2008**, *91*, 1888–1893. [\[CrossRef\]](#)
- Lin, A.; Du, L.; Fang, Y.; Wang, F.; Zhu, T.; Gu, Q.; Zhu, W. iso- $\alpha$ -Cyclopiazonic acid, a new natural product isolated from the marine-derived fungus *Aspergillus flavus* C-F-3. *Chem. Nat. Compd.* **2009**, *45*, 677. [\[CrossRef\]](#)
- López-Cobeñas, A.; Cledera, P.; Sanchez, J.D.; López-Alvarado, P.; Ramos, M.; Avendaño López, C.; Menendez, J.C. Microwave-Assisted Synthesis of 2,5-Piperazinediones under Solvent-Free Conditions. *Synthesis* **2005**, *2005*, 3412–3422. [\[CrossRef\]](#)
- Wang, Y.; Yang, M.; Yuan, C.; Han, Y.; Jia, Z. Sesquiterpenes and Other Constituents from *Cacalia deltohylla*. *Pharmazie* **2003**, *58*, 596–598. [\[CrossRef\]](#)
- Sakai, N.; Moriya, T.; Konakahara, T. An Efficient One-Pot Synthesis of Unsymmetrical Ethers: A Directly Reductive Deoxygenation of Esters Using an InBr<sub>3</sub>/Et<sub>3</sub>SiH Catalytic System. *J. Org. Chem.* **2007**, *72*, 5920–5922. [\[CrossRef\]](#)
- Appendino, G.; Gibbons, S.; Giana, A.; Pagani, A.; Grassi, G.; Stavri, M.; Smith, E.; Rahman, M.M. Antibacterial Cannabinoids from *Cannabis sativa*: A Structure–Activity Study. *J. Nat. Prod.* **2008**, *71*, 1427–1430. [\[CrossRef\]](#)
- Skehan, P.; Storeng, R.; Scudiero, D.; Monks, A.; McMahon, J.; Vistica, D.; Warren, J.T.; Bokesch, H.; Kenney, S.; Boyd, M.R. New Colorimetric Cytotoxicity Assay for Anticancer-Drug Screening. *J. Natl. Cancer Inst.* **1990**, *82*, 1107–1112. [\[CrossRef\]](#)
- Sheldrick, G.M. SHELXT—integrated space-group and crystal-structure determination. *Acta Crystallogr. A Found. Adv* **2015**, *71 Pt 1*, 3–8. [\[CrossRef\]](#)
- Zhong, W.; Wang, J.; Shi, X.; Wei, X.; Chen, Y.; Zeng, Q.; Xiang, Y.; Chen, X.; Tian, X.; Xiao, Z.; et al. Eurotiumins A–E, Five New Alkaloids from the Marine-Derived Fungus *Eurotium* sp. SCSIO F452. *Mar. Drugs* **2018**, *16*, 136. [\[CrossRef\]](#)
- Prestinaci, F.; Pezzotti, P.; Pantosti, A. Antimicrobial resistance: A global multifaceted phenomenon. *Pathog. Glob. Health* **2015**, *109*, 309–318. [\[CrossRef\]](#)
- Yilmaz, S.; Sova, M.; Ergün, S. Antimicrobial activity of trans-cinnamic acid and commonly used antibiotics against important fish pathogens and nonpathogenic isolates. *J. Appl. Microbiol.* **2018**, *125*, 1714–1727. [\[CrossRef\]](#)

21. Qader, M.M.; Hamed, A.A.; Soldatou, S.; Abdelraof, M.; Elawady, M.E.; Hassane, A.S.I.; Belbahri, L.; Ebel, R.; Rateb, M.E. Antimicrobial and Antibiofilm Activities of the Fungal Metabolites Isolated from the Marine Endophytes *Epicoccum nigrum* M13 and *Alternaria alternata* 13A. *Mar. Drugs* **2021**, *19*, 232. [[CrossRef](#)] [[PubMed](#)]
22. Wu, H.H.; Tian, L.; Chen, G.; Xu, N.; Wang, Y.N.; Sun, S.; Pei, Y.-H. Six compounds from marine fungus Y26-02. *J. Asian Nat. Prod. Res.* **2009**, *11*, 748–751. [[CrossRef](#)]

## Article

# Isoquinoline Alkaloids as Protein Tyrosine Phosphatase Inhibitors from a Deep-Sea-Derived Fungus *Aspergillus puniceus*

Cheng-Mei Liu <sup>1,2</sup>, Fei-Hua Yao <sup>1,2</sup>, Xin-Hua Lu <sup>4</sup>, Xue-Xia Zhang <sup>4</sup>, Lian-Xiang Luo <sup>5</sup>, Xiao Liang <sup>1</sup> and Shu-Hua Qi <sup>1,3,\*</sup>

- <sup>1</sup> CAS Key Laboratory of Tropical Marine Bio-Resources and Ecology, Guangdong Key Laboratory of Marine Materia Medica, Innovation Academy of South China Sea Ecology and Environmental Engineering, South China Sea Institute of Oceanology, Chinese Academy of Sciences, Guangzhou 510301, China; liuchengmei19@mails.ucas.ac.cn (C.-M.L.); yaofeihua20@mails.ucas.ac.cn (F.-H.Y.); liangxiao@scsio.ac.cn (X.L.)
- <sup>2</sup> University of Chinese Academy of Sciences, Beijing 100049, China
- <sup>3</sup> Southern Marine Science and Engineering Guangdong Laboratory (Guangzhou), 1119 Haibin Road, Guangzhou 511458, China
- <sup>4</sup> New Drug Research & Development Co., Ltd., North China Pharmaceutical Group Corporation, Shijiazhuang 050015, China; luxinhua89@hotmail.com (X.-H.L.); zhangxuexiazxx@163.com (X.-X.Z.)
- <sup>5</sup> The Marine Biomedical Research Institute, Guangdong Medical University, Zhanjiang 524023, China; luolianxiang321@gdmu.edu.cn
- \* Correspondence: shuhuaqi@scsio.ac.cn; Tel.: +86-208-9022-112; Fax: +86-208-4458-964

**Citation:** Liu, C.-M.; Yao, F.-H.; Lu, X.-H.; Zhang, X.-X.; Luo, L.-X.; Liang, X.; Qi, S.-H. Isoquinoline Alkaloids as Protein Tyrosine Phosphatase Inhibitors from a Deep-Sea-Derived Fungus *Aspergillus puniceus*. *Mar. Drugs* **2022**, *20*, 78. <https://doi.org/10.3390/md20010078>

Academic Editors: Yonghong Liu and Xuefeng Zhou

Received: 25 December 2021

Accepted: 13 January 2022

Published: 17 January 2022

**Publisher's Note:** MDPI stays neutral with regard to jurisdictional claims in published maps and institutional affiliations.



**Copyright:** © 2022 by the authors. Licensee MDPI, Basel, Switzerland. This article is an open access article distributed under the terms and conditions of the Creative Commons Attribution (CC BY) license (<https://creativecommons.org/licenses/by/4.0/>).

**Abstract:** Punicusines A–N (1–14), 14 new isoquinoline alkaloids, were isolated from the extracts of a deep-sea-derived fungus, *Aspergillus puniceus* SCSIO z021. Their structures were elucidated by spectroscopic analyses. The absolute configuration of **9** was determined by ECD calculations, and the structures of **6** and **12** were further confirmed by a single-crystal X-ray diffraction analysis. Compounds **3–5** and **8–13** unprecedentedly contained an isoquinolinyl, a polysubstituted benzyl or a pyronyl at position C-7 of isoquinoline nucleus. Compounds **3** and **4** showed selective inhibitory activity against protein tyrosine phosphatase CD45 with IC<sub>50</sub> values of 8.4 and 5.6 μM, respectively, **4** also had a moderate cytotoxicity towards human lung adenocarcinoma cell line H1975 with an IC<sub>50</sub> value of 11.0 μM, and **14**, which contained an active center, -C=N<sup>+</sup>, exhibited antibacterial activity. An analysis of the relationship between the structures, enzyme inhibitory activity and cytotoxicity of 1–14 revealed that the substituents at C-7 of the isoquinoline nucleus could greatly affect their bioactivity.

**Keywords:** deep-sea-derived fungus; *Aspergillus puniceus*; isoquinoline alkaloid; protein tyrosine phosphatase inhibitor; cytotoxicity; antibacterial

## 1. Introduction

Isoquinoline alkaloids are a large group of alkaloids in the plant kingdom, showing diverse pharmacological and biological activities such as anticancer, anti-inflammatory, cholesterol-lowering, antihyperglycemic, antiplasmodial, antifungal, and antimicrobial activity, etc. [1]. According to their structural components, isoquinoline and tetrahydroisoquinoline alkaloids can be classified into over 20 sub-classes, mainly including simple isoquinoline, benzyloisoquinoline, bisbenzyloisoquinoline, proto-berberine alkaloid, and aporphine alkaloid, etc. [1]. The most famous representative of this group is antidiabetic berberine. However, only a few isoquinoline alkaloids have been isolated from fungi, such as TMC-120A, B and C from *Aspergillus ustus* [2] and *A. insuetus* [3]; chaetoinidicins A–C from *Chaetomium indicum* [4]; fusarimine from *Fusarium* sp. [5]; 8-methoxy-3,5-dimethylisoquinolin-6-ol from *Penicillium citrinum* [6]; azaphilone from *P. sclerotiorum* [7]; and spathullins A–B from *P. spathulatum* [8].



Malfunctions in protein tyrosine phosphatase (PTP) activity are linked to various diseases, ranging from cancer to neurological disorders and diabetes, such as CD45, SHP1, TCPTP, PTP1B and LAR linked to cancer, CD45, SHP1 and LAR also linked to neurological diseases, and PTP1B and LAR also linked to diabetes, etc. [9]. Some PTPs emerged as promising targets for therapeutic intervention in recent years [9,10]. However, achieving the selectivity of PTP inhibitors is a big challenge. In recent years, we obtained a series of natural compounds including anthraquinones [11], meroterpenoids [12], xanthone-type and anthraquinone-type mycotoxins [13], and oxaphenalenones [14] as PTP inhibitors from marine-derived fungi. In order to further explore diversified bioactive compounds from the deep-sea-derived fungus, *Aspergillus puniceus* SCSIO z021, we changed culture media and further conducted a chemical investigation of this strain cultured with a complex medium, which led to the characterization of 14 undescribed isoquinoline alkaloids, puniceusines A–N (1–14) (Figure 1). Compounds 1–14 were evaluated for their enzyme inhibitory activity against five kinds of PTPs, cytotoxicity towards human lung adenocarcinoma cell line H1975, and antibacterial activity. Herein, we report the isolation, structure elucidation and bioactivities of 1–14.

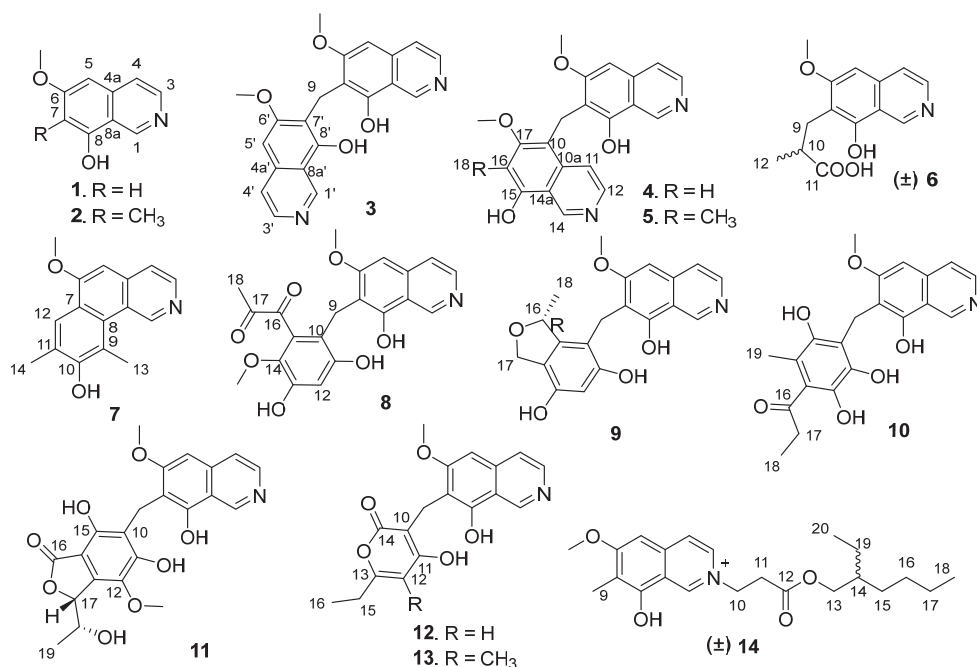


Figure 1. Structures of the isolated compounds 1–14.

## 2. Results and Discussion

Puniceusine A (1) has the molecular formula C<sub>10</sub>H<sub>9</sub>NO<sub>2</sub>, as determined by HRESIMS. The <sup>1</sup>H NMR spectrum (Table 1) showed the presence of one methoxy group at δ<sub>H</sub> 3.96 (3H, s) and five aromatic hydrogens at δ<sub>H</sub> 9.45 (1H, s), 8.40 (1H, d, *J* = 5.7 Hz), 8.06 (1H, d, *J* = 6.4 Hz), 7.13 (1H, s), 6.81 (1H, s). The <sup>13</sup>C NMR spectrum (Table 2) showed 10 carbon signals including one methoxy, five aromatic methines, and four aromatic non-protonated carbons. These NMR data were similar to those of 6,8-dimethoxyisoquinolin [15] and papraline [16], and the only clear difference between 1 and 6,8-dimethoxyisoquinolin was the disappearance of one oxygenated methyl, which indicated that 1 was also an isoquinoline alkaloid. This was supported by the HMBC spectrum showing correlations

from H-1 to C-3/C-4a/C-8a, H-3 to C-4/C-4a, H-4 to C-3/C-5/C-8a, H-5 to C-4/C-6/C-7/C-8a, and H-7 to C-5/C-6/C-8/C-8a. In addition, the HMBC correlation from  $\delta_{\text{H}}$  3.96 (3H, s) to C-6 suggested that a methoxy group was attached at C-6. Thus, the structure of **1** was determined to be 6-methoxy-8-hydroxy-isoquinolin.

**Table 1.**  $^1\text{H}$  NMR Data for Compounds **1–7** ( $\delta$  in ppm,  $J$  in Hz) in DMSO- $d_6$  or Methanol- $d_4$ .

| No.                 | <b>1</b> <sup>a,c</sup> | <b>2</b> <sup>a,d</sup> | <b>3</b> <sup>b,d</sup> | <b>4</b> <sup>a,d</sup> | <b>5</b> <sup>a,d</sup> | <b>6</b> <sup>a,d</sup>                                       | <b>7</b> <sup>b,d</sup> |
|---------------------|-------------------------|-------------------------|-------------------------|-------------------------|-------------------------|---|-------------------------|
| 1                   | 9.45, s                 | 9.41, s                 | 9.34, s                 | 9.59, s                 | 9.58, s                 | 9.49, s   | 9.87, s                 |
| 3                   | 8.40, d (5.7)           | 8.24 d (6.5)            | 8.08, d (6.3)           | 8.29, d (7.0)           | 8.30, d (6.6)           | 8.29, d (6.0)   | 8.47, d (6.3)           |
| 4                   | 8.06, d (6.4)           | 8.04 d (6.5)            | 7.90, d (6.3)           | 8.05, d (6.5)           | 8.09, d (6.6)           | 8.10, d (6.0)   | 8.22, d (6.3)           |
| 5                   | 7.13, s                 | 7.13 s                  | 6.95, s                 | 7.11, s                 | 7.18, s                 | 7.23, s   | 7.31, s                 |
| 7                   | 6.81, s                 |                         |                         |                         |                         |   |                         |
| 9                   |                         | 2.25, s                 | 4.32, s                 | 4.47, s                 | 4.61, s                 | 2.97,<br>dd (14.0, 5.5)<br>3.17,<br>dd (14.0, 8.5)<br>2.85, m |                         |
| 10                  |                         |                         |                         |                         |                         |   |                         |
| 11                  |                         |                         |                         | 8.58, d (7.0)           | 8.67, d (6.8)           |   |                         |
| 12                  |                         |                         |                         | 8.31, d (7.8)           | 8.39, d (6.8)           | 1.27, d (7.5)   | 8.24, s                 |
| 13                  |                         |                         |                         |                         |                         |   | 2.93, s                 |
| 14                  |                         |                         |                         | 9.52, s                 | 9.68, s                 |   | 2.51, s                 |
| 16                  |                         |                         |                         | 7.00, s                 |                         |   |                         |
| 18                  |                         |                         |                         |                         | 2.38, s                 |   |                         |
| 6-OCH <sub>3</sub>  | 3.96, s                 | 4.07, s                 | 4.09, s                 | 3.79, s                 | 3.84, s                 | 4.10, s   | 4.24, s                 |
| 6'-OCH <sub>3</sub> |                         |                         | 4.09, s                 |                         |                         |   |                         |
| 17-OCH <sub>3</sub> |                         |                         |                         | 3.98, s                 | 3.79, s                 |   |                         |

<sup>a</sup> 500 MHz for  $^1\text{H}$  NMR; <sup>b</sup> 700 MHz for  $^1\text{H}$  NMR; <sup>c</sup> DMSO- $d_6$ ; <sup>d</sup> Methanol- $d_4$ .

**Table 2.**  $^{13}\text{C}$  NMR data for Compounds **1–8** ( $\delta$  in ppm) in DMSO- $d_6$  or Methanol- $d_4$ .

| No.                 | <b>1</b> <sup>a,c</sup> | <b>2</b> <sup>a,d</sup> | <b>3</b> <sup>b,d</sup> | <b>4</b> <sup>a,d</sup> | <b>5</b> <sup>a,d</sup> | <b>6</b> <sup>a,d</sup> | <b>7</b> <sup>b,d</sup> | <b>8</b> <sup>a,c</sup> |
|---------------------|-------------------------|-------------------------|-------------------------|-------------------------|-------------------------|-------------------------|-------------------------|-------------------------|
| 1                   | 141.8, CH               | 141.5, CH               | 141.9, CH               | 142.4, CH               | 142.3, CH               | 142.3, CH               | 132.7, CH               | 141.2, CH               |
| 3                   | 133.2, CH               | 131.4, CH               | 130.8, CH               | 132.1, CH               | 132.0, CH               | 132.2, CH               | 123.5, CH               | 131.5, CH               |
| 4                   | 122.3, CH               | 123.7, CH               | 123.1, CH               | 123.7, CH               | 123.9, CH               | 123.8, CH               | 114.7, CH               | 122.0, CH               |
| 4a                  | 140.9, C                | 140.9, C                | 141.2, C                | 141.5, C                | 141.5, C                | 141.6, C                | 137.2, C                | 139.1, C                |
| 5                   | 97.8, CH                | 98.6, CH                | 96.1, C                 | 98.8, CH                | 99.4, CH                | 99.0, CH                | 90.3, CH                | 97.2, CH                |
| 6                   | 166.9, C                | 168.4, C                | 169.1, C                | 168.5, C                | 168.2, C                | 168.3, C                | 155.0, C                | 165.8, C                |
| 7                   | 103.5, CH               | 116.8, C                | 118.9, C                | 118.5, C                | 120.8, C                | 119.1, C                | 113.3, C                | 117.3, C                |
| 8                   | 158.6, C                | 155.7, C                | 163.9, C                | 156.3, C                | 156.2, C                | 156.4, C                | 121.2, C                | 155.8, C                |
| 8a                  | 115.5, C                | 117.5, C                | 118.7, C                | 117.8, C                | 117.9, C                | 117.9, C                | 114.0, C                | 115.8, C                |
| 9                   |                         | 9.2, CH <sub>3</sub>    | 19.4, CH <sub>2</sub>   | 20.7, CH <sub>2</sub>   | 21.3, CH <sub>2</sub>   | 28.0, CH <sub>2</sub>   | 112.0, C                | 19.3, CH <sub>2</sub>   |
| 10                  |                         |                         |                         | 113.6, C                | 120.0, C                | 40.4, CH                | 148.7, C                | 115.0, C                |
| 10a                 |                         |                         |                         | 139.7, C                | 138.9, C                |                         |                         |                         |
| 11                  |                         |                         |                         | 121.6, CH               | 122.7, CH               | 181.7, C                | 120.7, C                | 151.3, C                |
| 12                  |                         |                         |                         | 131.2, CH               | 131.0, CH               | 18.1, CH <sub>3</sub>   | 115.0, C                | 107.1, CH               |
| 13                  |                         |                         |                         |                         |                         |                         | 8.0, CH <sub>3</sub>    | 139.5, C                |
| 14                  |                         |                         |                         | 143.3, CH               | 143.4, CH               |                         | 8.4, CH <sub>3</sub>    | 148.1, C                |
| 14a                 |                         |                         |                         | 115.9, C                | 119.0, C                |                         |                         |                         |
| 15                  |                         |                         |                         | 161.0, C                | 156.7, C                |                         |                         | 130.2, C                |
| 16                  |                         |                         |                         | 100.1, CH               | 120.6, C                |                         |                         | 195.1, C                |
| 17                  |                         |                         |                         | 167.5, C                | 167.7, C                |                         |                         | 196.9, C                |
| 18                  |                         |                         |                         |                         | 10.8, CH <sub>3</sub>   |                         |                         | 23.7, CH <sub>3</sub>   |
| 6-OCH <sub>3</sub>  | 56.4, CH <sub>3</sub>   | 57.4, CH <sub>3</sub>   | 57.0, CH <sub>3</sub>   | 56.9, CH <sub>3</sub>   | 57.0, CH <sub>3</sub>   | 57.4, CH <sub>3</sub>   | 47.9, CH <sub>3</sub>   | 56.4, CH <sub>3</sub>   |
| 14-OCH <sub>3</sub> |                         |                         |                         |                         |                         |                         |                         | 59.7, CH <sub>3</sub>   |
| 17-OCH <sub>3</sub> |                         |                         |                         | 57.1, CH <sub>3</sub>   | 62.1, CH <sub>3</sub>   |                         |                         |                         |

<sup>a</sup> 125 MHz for  $^{13}\text{C}$  NMR; <sup>b</sup> 175 MHz for  $^{13}\text{C}$  NMR; <sup>c</sup> DMSO- $d_6$ ; <sup>d</sup> Methanol- $d_4$ .

Puniceusine B (**2**) was assigned the molecular formula  $C_{11}H_{11}NO_2$  by HRESIMS. The  $^1H$  NMR and  $^{13}C$  NMR data (Tables 1 and 2) showed great similarity to those of **1**, and the main difference between them was the additional presence of one methyl ( $\delta_H$  2.25, 3H, s;  $\delta_C$  9.2) and the disappearance of one aromatic hydrogen in **2**. The HMBC correlations from  $\delta_H$  2.25 to C-6/C-7/C-8 suggested the additional methyl attached at C-7. Hence, the structure of **2** was determined to be 6-methoxy-7-methyl-8-hydroxy-isoquinolin.

Puniceusine C (**3**) was found to have the molecular formula  $C_{21}H_{18}N_2O_4$  by HRESIMS that was nearly twice that of **2**. The  $^1H$  and  $^{13}C$  NMR data (Tables 1 and 2) showed great similarity to those of **2**, and the clearest difference between them was the disappearance of a methyl signal and the additional presence of a methylene signal ( $\delta_H$  4.32, 2H, s;  $\delta_C$  19.4) in **3**. The  $^1H$  NMR spectrum of **3** showed a double increase in the integral areas for H-1, H-3, H-4, H-5, and a methoxy group. The HMBC correlations (Figure 2) from  $\delta_H$  4.32 (H<sub>2</sub>-9) to C-6/C-7/C-8 suggested a methylene instead of a methyl attached at C-7. These data indicated that **3** was a symmetrical dimer of **1**, connected at positions C-7' and C-7 by a methylene C-9. Thus, the structure of **3** was determined as shown.

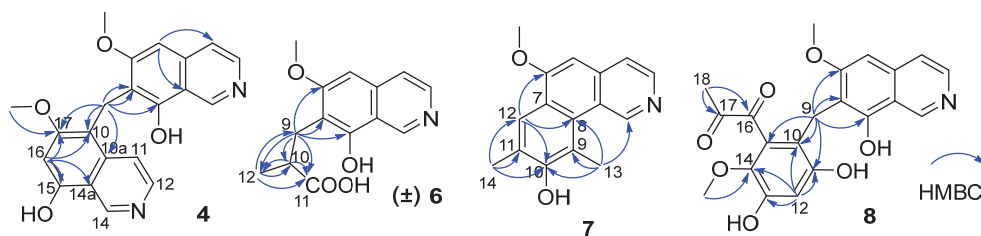


Figure 2. Key HMBC correlations of compounds **4**, **6**–**8**.

Puniceusine D (**4**) showed the same molecular formula of  $C_{21}H_{18}N_2O_4$  as that of **3** by analysis of its HRESIMS and NMR data (Tables 1 and 2). The  $^1H$  NMR spectrum showed the presence of two downfield hydrogens at  $\delta_H$  9.59 (1H, s) and 9.52 (1H, s); six aromatic hydrogens at  $\delta_H$  8.58 (1H, d,  $J = 7.0$  Hz), 8.31 (1H, d,  $J = 7.8$  Hz), 8.29 (1H, d,  $J = 7.0$  Hz), 8.05 (1H, d,  $J = 6.5$  Hz), 7.11 (1H, s), and 7.00 (1H, s); two methoxy groups at  $\delta_H$  3.79 (3H, s) and 3.98 (3H, s); and one methylene at  $\delta_H$  4.47 (2H, s). The  $^{13}C$  NMR spectrum showed 21 carbon signals including one methylene, two methoxyls, eight aromatic methines, and ten aromatic non-protonated carbons. These data showed similarity to those of **1**–**3**, which indicated that **4** was also a dimer of **1**. The HMBC correlations from H-5 to C-4/C-8a, from H-16 to C-10/C-14a/C-15/C-17, and from H<sub>2</sub>-9 to C-6/C-7/C-8/C-10/C-10a/C-17 (Figure 2) suggested that **4** was an asymmetric dimer of **1** connected at positions C-7 and C-10 by a methylene C-9. The two methoxy groups were attached at C-6 and C-17 based on the HMBC correlations of  $\delta_H$  3.98 (3H, s) with C-17 and  $\delta_H$  3.79 (3H, s) with C-6, respectively. Therefore, the structure of **4** was established as shown.

The molecular formula of puniceusine E (**5**) was determined as  $C_{22}H_{21}N_2O_4$  by HRESIMS. The  $^1H$  and  $^{13}C$  NMR data (Tables 1 and 2) of **5** were greatly similar to those of **4**, and the only obvious difference between them was the absence of one aromatic hydrogen and the additional presence of one methyl signal ( $\delta_H$  2.38, 3H, s;  $\delta_C$  10.8) in **5**. The HMBC correlations from H<sub>3</sub>-18 ( $\delta_H$  2.38) to C-15/C-16/C-17 suggested a methyl located at C-16 instead of a hydrogen. Thus, the structure of **5** was established as shown.

Puniceusine F (**6**) had the molecular formula  $C_{14}H_{15}NO_4$ , as determined by HRESIMS. The  $^1H$  and  $^{13}C$  NMR data (Tables 1 and 2) of **6** were similar to those of **1**, and the clearest difference between them was the disappearance of one aromatic hydrogen and the additional presence of one methyl ( $\delta_H$  1.27, d,  $J = 7.5$  Hz, 3H), one methylene, one methine, and one carboxyl group in **6**. The HMBC correlations (Figure 2) from H<sub>2</sub>-9 ( $\delta_H$  2.97 (dd,  $J = 14.0, 5.5$  Hz, 1H), 3.17 (dd,  $J = 14.0, 8.5$  Hz, 1H)) to C-6/C-7/C-8/C-10/C-11/C-12, from H-10 ( $\delta_H$  2.85, m, 1H) to C-11/C-12, and from H<sub>3</sub>-12 ( $\delta_H$  1.27, d,  $J = 7.5$  Hz, 3H) to C-9/C-10/C-11 suggested an isobutyric acid group attached at C-7 of the isoquinoline

nucleus. The optical rotation and measured CD data of **6** were zero, which indicated that **6** was a racemic mixture. This was supported by the HPLC analysis of **6** with a chiral column (CHIRALPAK IA 4.6 mm × 250 mm column) eluting with n-hexane/ethanol/TFA (68:32:0.2, *v/v*) (Figure S39). This structure was further confirmed by a single-crystal X-ray diffraction analysis (Figure 3).

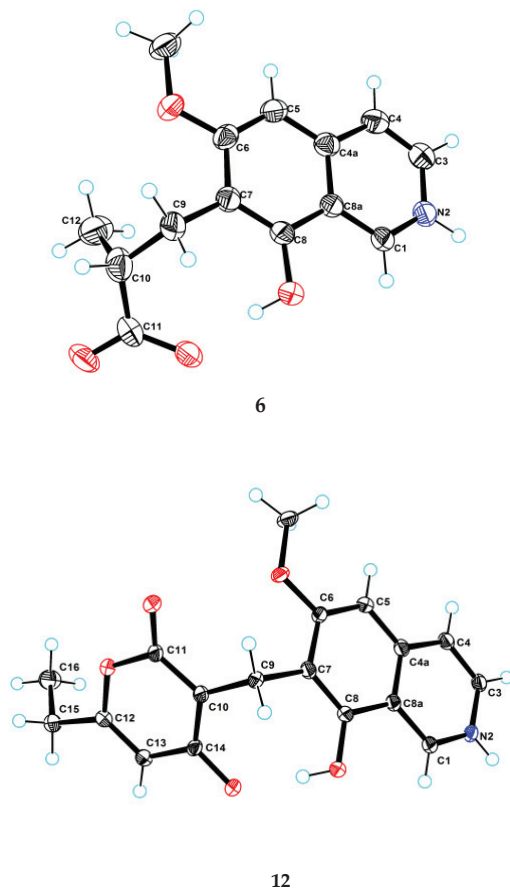


Figure 3. Ortep plot of the X-ray crystallographic data for **6** and **12**.

The molecular formula of puniceusine G (**7**) was determined to be  $C_{16}H_{15}NO_2$ , according to its HRESIMS. The  $^1H$  and  $^{13}C$  NMR data (Tables 1 and 2) of **7** were similar to those of **1**, and the clearest difference between them was the additional presence of two double bonds ( $\delta_C$  112.0 (C, C-9), 115.0 (CH, C-12), 120.7 (C, C-11), 148.7 (C, C-10)) and two methyls ( $\delta_H$  2.51 (3H, s, H-14), 2.93 (3H, s, H-13);  $\delta_C$  8.0, 8.4) in **7**. The HMBC correlations (Figure 2) from H-12 to C-6/C-8/C-10, from H<sub>3</sub>-13 to C-1/C-8/C-9/C-10, and from H<sub>3</sub>-14 to C-10/C-11/C-12, suggested a 3,5-dimethyl-4-hydroxyphenyl group attached at the isoquinoline nucleus by sharing C-7 and C-8 to form a benzo[*h*]isoquinoline unit. Therefore, the structure of **7** was established as shown.

Puniceusine H (**8**) had the molecular formula of  $C_{21}H_{19}NO_7$  as determined by its HRESIMS. The  $^1H$  and  $^{13}C$  NMR data (Tables 2 and 3) of **8** showed similarity to those of **4–6** with the presence of characteristic chemical shifts for a methylene C-9 ( $\delta_H$  4.01 (2H, s),  $\delta_C$  19.3 (CH<sub>2</sub>)). The HMBC correlations (Figure 2) from H<sub>2</sub>-9 to C-6/C-7/C-8/C-10/C-11/C-15, from H-12 ( $\delta_H$  6.58, 1H, s) to C-10/C-11/C-13/C-14, and from H<sub>3</sub>-19 ( $\delta_H$  3.52, 3H, s) to C-14 suggested a 2,4-dihydroxy-5-methoxyphenyl fragment connected with isoquinoline unit by a methylene at position C-7. In addition, the HMBC correlations from H<sub>3</sub>-18 ( $\delta_H$  2.30, 3H, s) to C-16 ( $\delta_C$  195.1, C)/C-17 ( $\delta_C$  196.9, C) suggested the presence of a 1,2-propanedione group that was exclusively assigned to attach at C-15 of the benzene ring based on the above data. Thus, the structure of **8** was established as shown.

**Table 3.**  $^1H$  NMR data for Compounds **8–14** ( $\delta$  in ppm,  $J$  in Hz) in DMSO-*d*<sub>6</sub> or Methanol-*d*<sub>4</sub>.

| No.                 | <b>8</b> <sup>a,c</sup> | <b>9</b> <sup>b,c</sup>   | <b>10</b> <sup>b,d</sup> | <b>11</b> <sup>a,d</sup> | <b>12</b> <sup>a,d</sup> | <b>13</b> <sup>a,d</sup> | <b>14</b> <sup>a,d</sup> |
|---------------------|-------------------------|---------------------------|--------------------------|--------------------------|--------------------------|--------------------------|--------------------------|
| 1                   | 9.49, s                 | 9.51, s                   | 9.47, s                  | 9.49, s                  | 9.48, s                  | 9.52, s                  | 9.64, s                  |
| 3                   | 8.36, d (6.6)           | 8.39, d (6.6)             | 8.23, d (6.6)            | 8.25, d (6.4)            | 8.26, d (5.5)            | 8.29, d (6.6)            | 8.37, d (6.9)            |
| 4                   | 8.08, d (6.6)           | 8.11, d (6.6)             | 8.05, d (6.6)            | 8.06, d (6.4)            | 8.06, d (5.5)            | 8.10, d (6.6)            | 8.08, d (6.9)            |
| 5                   | 7.11, s                 | 7.26, s<br>3.84, d        | 7.17, s                  | 7.16, s                  | 7.16, s                  | 7.23, s                  | 7.19, s                  |
| 9                   | 4.01, s                 | (14.9)4.03, d<br>(14.8)   | 3.96, s                  | 4.21, s                  | 3.92, s                  | 3.97, s                  | 2.29, s                  |
| 10                  |                         |                           |                          |                          |                          |                          | 4.88, t (6.3)            |
| 11                  |                         |                           |                          |                          |                          |                          | 3.18, t (6.3)            |
| 12                  | 6.58, s                 | 6.27, s                   |                          |                          | 6.12, s                  |                          |                          |
| 13                  |                         |                           |                          |                          |                          |                          | 4.00, d (5.7)            |
| 14                  |                         |                           |                          |                          |                          |                          | 1.46, m                  |
| 15                  |                         |                           |                          |                          | 2.52, q (7.5)            | 2.60, q (7.5)            | 1.16, m                  |
| 16                  |                         | 5.22, m<br>4.69, d (11.5) |                          |                          | 1.19, t (7.5)            | 1.17, t (7.5)            | 1.17, m                  |
| 17                  |                         | 4.84, dd (11.5,<br>2.5)   | 2.58, q (7.3)            | 5.56, d (2.5)            |                          | 2.01, s                  | 1.18, m                  |
| 18                  | 2.30, s                 | 1.35, d (6.2)             | 1.02, t (7.3)            | 4.36, qd (6.5,<br>2.5)   |                          |                          | 0.79, t (7.5)            |
| 19                  | 3.52, s                 |                           | 1.92, s                  | 0.94, d (6.5)            |                          |                          | 1.24, m                  |
| 20                  |                         |                           |                          |                          |                          |                          | 0.82, t (6.5)            |
| 6-OCH <sub>3</sub>  | 3.77, s                 | 4.00, s                   | 4.11, s                  | 4.03, s                  | 4.07, s                  | 4.13, s                  |                          |
| 12-OCH <sub>3</sub> |                         |                           |                          | 3.76, s                  |                          |                          |                          |

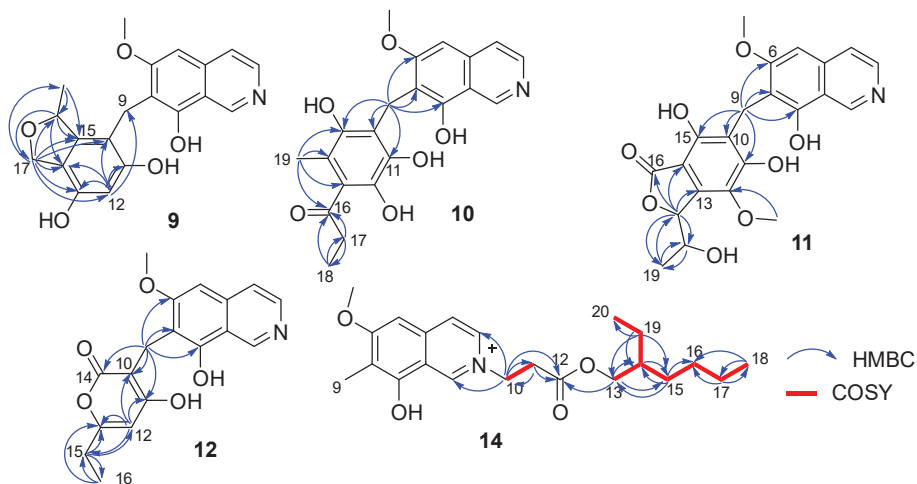
<sup>a</sup> 500 MHz for  $^1H$  NMR; <sup>b</sup> 700 MHz for  $^1H$  NMR; <sup>c</sup> DMSO-*d*<sub>6</sub>; <sup>d</sup> Methanol-*d*<sub>4</sub>.

Puniceusine I (**9**) had the molecular formula of  $C_{20}H_{19}NO_5$  according to its HRESIMS with 12 degrees of unsaturation. The  $^1H$  and  $^{13}C$  NMR data (Tables 3 and 4) of **9** were similar to those of **8**, and the clearest difference between them was the disappearance of two keto carbons and one methoxy and the additional presence of one oxygenated methylene ( $\delta_H$  4.84 (1H, dd,  $J$  = 11.5, 2.5 Hz), 4.69 (1H, dd,  $J$  = 11.5 Hz),  $\delta_C$  68.9, CH<sub>2</sub>) and one oxygenated methine ( $\delta_H$  5.22 (1H, m),  $\delta_C$  79.3, CH). A detailed analysis of HSQC and HMBC spectra proved that **9** also contained a 1,2,4,5,6-pentasubstituted-benzyl attached at C-7 of isoquinoline nucleus. In addition, the HMBC correlations from H-16 to C-14/C-15/C-17, from H<sub>2</sub>-17 to C-10/C-11/C-12/C-13/C-14/C-15/C-16/C-18, from H<sub>3</sub>-18 ( $\delta_H$  1.35, d,  $J$  = 6.2 Hz, 3H) to C-15/C-16 (Figure 4), suggested a 2-methyl-2,5-dihydrofuran ring connected with the benzene ring via C-14 and C-15. Therefore, the 2D structure of **9** was established as shown. The absolute configuration of **9** was further determined by electronic circular dichroism (ECD) calculations (Tables S1–S3).

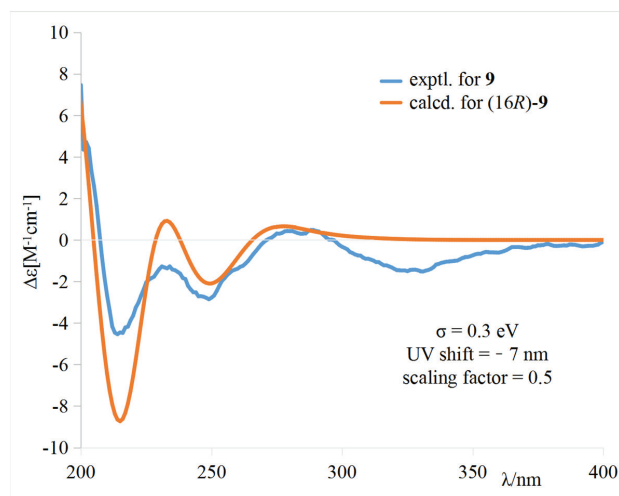
**Table 4.**  $^{13}\text{C}$  NMR data for Compounds 9–14 ( $\delta$  in ppm) in  $\text{DMSO-}d_6$  or  $\text{Methanol-}d_4$ .

| No.                | 9 <sup>b,c</sup>    | 10 <sup>b,d</sup>   | 11 <sup>a,d</sup>   | 12 <sup>a,d</sup>   | 13 <sup>a,d</sup>   | 14 <sup>a,d</sup>   |
|--------------------|---------------------|---------------------|---------------------|---------------------|---------------------|---------------------|
| 1                  | 141.2, CH           | 142.3, CH           | 142.0, C            | 142.2, CH           | 142.4, CH           | 145.4, CH           |
| 3                  | 131.5, CH           | 131.7, CH           | 131.6, CH           | 131.8, CH           | 132.0, CH           | 134.9, CH           |
| 4                  | 122.2, CH           | 123.6, CH           | 123.6, CH           | 123.6, CH           | 123.9, CH           | 124.4, CH           |
| 4a                 | 139.0, C            | 141.5, C            | 141.4, C            | 141.5, C            | 141.7, C            | 139.7, C            |
| 5                  | 97.7, CH            | 98.4, C             | 98.7, CH            | 98.8, C             | 98.9, CH            | 98.6, CH            |
| 6                  | 165.6, C            | 168.1, C            | 168.7, C            | 168.3, C            | 167.7, C            | 168.8, C            |
| 7                  | 117.7, C            | 119.2, C            | 118.7, C            | 119.1, C            | 118.8, C            | 117.1, C            |
| 8                  | 154.8, C            | 158.7, C            | 156.7, C            | 157.4, C            | 157.5, C            | 155.8, C            |
| 8a                 | 115.5, C            | 118.4, C            | 117.6, C            | 118.0, C            | 118.3, C            | 117.7, C            |
| 9                  | 19.8, $\text{CH}_2$ | 19.4, $\text{CH}_2$ | 18.9, $\text{CH}_2$ | 18.7, $\text{CH}_2$ | 19.3, $\text{CH}_2$ | 9.23, $\text{CH}_3$ |
| 10                 | 109.4, C            | 101.5, C            | 116.2, C            | 101.0, C            | 100.9, C            | 57.1, $\text{CH}_2$ |
| 11                 | 154.8, C            | 170.0, C            | 157.1, C            | 170.2, C            | 169.7, C            | 35.7, $\text{CH}_2$ |
| 12                 | 101.4, CH           | 163.1, C            | 136.8, C            | 101.2, CH           | 109.8, C            | 171.8, C            |
| 13                 | 150.1, C            | 113.8, C            | 137.4, C            | 167.4, C            | 162.7, C            | 68.4, $\text{CH}_2$ |
| 14                 | 115.9, C            | 154.4, C            | 104.2, C            | 171.2, C            | 170.7, C            | 40.0, CH            |
| 15                 | 145.3, C            | 171.6, C            | 153.0, C            | 27.4, $\text{CH}_2$ | 25.1, $\text{CH}_2$ | 31.3, $\text{CH}_2$ |
| 16                 | 79.3, CH            | 207.3, C            | 172.7, C            | 11.2, $\text{CH}_3$ | 11.8, $\text{CH}_3$ | 29.9, $\text{CH}_2$ |
| 17                 | 68.9, $\text{CH}_2$ | 36.6, $\text{CH}_2$ | 85.2, CH            |                     | 9.9, $\text{CH}_3$  | 23.9, $\text{CH}_2$ |
| 18                 | 21.3, $\text{CH}_3$ | 7.8, $\text{CH}_3$  | 68.6, CH            |                     |                     | 14.3, $\text{CH}_3$ |
| 19                 |                     | 10.4, $\text{CH}_3$ | 15.8, $\text{CH}_3$ |                     |                     | 24.6, $\text{CH}_2$ |
| 20                 |                     |                     |                     |                     |                     | 11.2, $\text{CH}_3$ |
| 6-O $\text{CH}_3$  | 56.7, $\text{CH}_3$ | 57.3, $\text{CH}_3$ | 57.2, $\text{CH}_3$ | 57.2, $\text{CH}_3$ | 57.5, $\text{CH}_3$ | 57.5, $\text{CH}_3$ |
| 12-O $\text{CH}_3$ |                     |                     | 61.1, $\text{CH}_3$ |                     |                     |                     |

<sup>a</sup> 125 MHz for  $^{13}\text{C}$  NMR; <sup>b</sup> 175 MHz for  $^{13}\text{C}$  NMR; <sup>c</sup>  $\text{DMSO-}d_6$ ; <sup>d</sup>  $\text{Methanol-}d_4$ .

**Figure 4.** Key COSY and HMBC correlations of compounds 9–12 and 14.

The calculated weighted ECD spectrum of (16*R*)-9 agreed well with the experimental ECD spectrum of 9 (Figure 5), leading to the assignment of the absolute configuration at C-16.



**Figure 5.** Comparison of the experimental and calculated ECD spectra of **9** in  $\text{CH}_3\text{OH}$ .

Puniceusine J (**10**) had the molecular formula of  $\text{C}_{21}\text{H}_{21}\text{NO}_6$ , as determined by its HRESIMS. The  $^1\text{H}$  and  $^{13}\text{C}$  NMR data of **10** (Tables 3 and 4) were very similar to those of **8** and **9**. A detailed analysis of HSQC and HMBC spectra proved that **10** also contained a benzyl attached at position C-7 of isoquinoline unit. The HMBC correlations of  $\text{H}_2$ -9 with C-6/C-7/C-8/C-10/C-11 ( $\delta_{\text{C}}$  170.0, C)/C-15 ( $\delta_{\text{C}}$  171.6, C) (Figure 4) suggested two hydroxyl groups attached at C-11 and C-15, respectively. In addition, the HMBC correlations from  $\text{H}_3$ -19 ( $\delta_{\text{H}}$  1.92, 3H, s) to C-13/C-14/C-15 suggested a methyl attached at C-14. Furthermore, the HMBC correlations (Figure 4) from  $\text{H}_2$ -17 ( $\delta_{\text{H}}$  2.58, 2H, q,  $J = 7.3$  Hz) to C-16/C-18, from  $\text{H}_3$ -18 ( $\delta_{\text{H}}$  1.02, 3H, t,  $J = 7.3$  Hz) to C-16/C-17, and from  $\text{H}_3$ -19 to C-16 suggested an 1-acetyl group attached at C-13. Lastly, the chemical shift of C-12 ( $\delta_{\text{C}}$  163.1, C) indicated a hydroxy group attached at C-12. Therefore, the structure of **10** was established as shown.

Puniceusine K (**11**) was found to have the molecular formula  $\text{C}_{22}\text{H}_{21}\text{NO}_8$  by HRESIMS. The  $^1\text{H}$  and  $^{13}\text{C}$  NMR data of **11** (Tables 3 and 4) were very similar to those of **10**. A detailed analysis of HSQC and HMBC spectra proved that **11** also contained a hexasubstituted benzyl attached at position C-7 of isoquinoline unit. The HMBC correlations of  $\text{H}_2$ -9 with C-6/C-7/C-8/C-10/C-11 ( $\delta_{\text{C}}$  157.1, C)/C-15 ( $\delta_{\text{C}}$  153.0, C) suggested two hydroxyl groups attached at C-11 and C-15, respectively. Additionally, the HMBC correlations (Figure 4) from H-17 ( $\delta_{\text{H}}$  5.56, d,  $J = 2.5$  Hz) to C-13/C-14/C-16/C-18/C-19, from H-18 ( $\delta_{\text{H}}$  4.36, qd,  $J = 6.5, 2.5$  Hz) to C-19, and from  $\text{H}_3$ -19 ( $\delta_{\text{H}}$  0.94, d,  $J = 6.5$  Hz, 3H) to C-17/C-18, suggested a 5-hydroxy-2-hexene-4-lactone group attached on the benzene ring via C-13 and C-14. In addition, the HMBC correlation of  $\delta_{\text{H}}$  3.76 (s, 3H) with C-12 ( $\delta_{\text{C}}$  136.8, C) suggested a methoxy group attached at C-12 of the benzene ring. The assignment of the substituent groups at positions C-12, C-13 and C-14 of the benzene ring was further supported by comparison of the  $^1\text{H}$  and  $^{13}\text{C}$  NMR data of the same isobenzofuran moiety in **11**, embeurekol C [17] and acetophthalidin [18]. In addition, the small  $^3J_{\text{HH}}$  value (2.5 Hz) between H-17 and H-18 in **11** was closely similar to that of embeurekol C [17]. Furthermore, the specific rotation value of **11** ( $[\alpha]_{\text{D}}^{25} -9.1$  (c 0.1,  $\text{CH}_3\text{OH}$ )) was close to that of embeurekol C ( $[\alpha]_{\text{D}}^{20} -17$  (c 0.05,  $\text{CH}_3\text{OH}$ )) [17], and the experimental ECD spectrum of **11** (Figure S76) was greatly similar to that of embeurekol C [17]. These data suggested that the absolute configuration of **11** was also 17R, 18S for that of embeurekol C.

Puniceusine L (**12**) had a molecular formula of  $C_{18}H_{17}NO_5$  on the basis of its HRESIMS and NMR data. Its  $^1H$  and  $^{13}C$  NMR data (Tables 3 and 4) showed a similarity to those of **8–11**. A detailed analysis of HSQC and HMBC spectra suggested that **12** contained the same isoquinoline unit as **8–11**. In addition, considering the molecular formula and unsaturation degrees of **12**, the HMBC correlations from  $H_2-9$  to  $C-6/C-7/C-8/C-10/C-11/C-14$ , from  $H_2-12$  to  $C-10/C-11/C-13/C-15$ , from  $H_2-15$  to  $C-12/C-13/C-16$ , and from  $H_3-16$  to  $C-13/C-15$  (Figure 4), suggested a 6-ethyl-4-hydroxy-2H-pyran-2-one unit attached at the methylene  $C-9$  of isoquinoline unit. The above assignment was further confirmed by a single crystal X-ray diffraction analysis (Figure 3).

Puniceusine M (**13**) had the molecular formula of  $C_{19}H_{19}NO_5$  on the basis of its HRESIMS. The  $^1H$  and  $^{13}C$  NMR data (Tables 3 and 4) were very similar to those of **12**. The only difference between them was the disappearance of one aromatic hydrogen and the additional presence of a methyl ( $\delta_H$  2.01 (3H, s),  $\delta_C$  9.9). The HMBC correlations from  $H_3-17$  ( $\delta_H$  2.01) to  $C-11/C-12/C-13$  suggested the additional methyl attached at  $C-12$ . Therefore, the structure of **13** was established as shown.

Puniceusine N (**14**) had the molecular formula  $C_{22}H_{32}NO_4^+$ , as determined by HRESIMS. The  $^1H$  and  $^{13}C$  NMR (Tables 3 and 4) data of **14** showed a similarity to those of **2**, and the clearest difference between them was the additional presence of two methyls, seven methylenes (one oxygenated), one methine, and one carboxyl in **14**. Detailed analysis of the HMBC and COSY spectra proved that **14** contained the same isoquinoline unit as that of **2**. In addition, combining with the COSY correlation of  $H_2-10$  ( $\delta_H$  4.88, t,  $J = 6.3$  Hz) with  $H_2-11$  ( $\delta_H$  3.18, t,  $J = 6.3$  Hz) (Figure 4), the HMBC correlations from  $H_2-10$  to  $C-1/C-3/C-11/C-12$  ( $\delta_C$  171.8, C), and from  $H_2-11$  to  $C-9/C-12$  (Figure 4), suggested a  $-CH_2-CH_2-COO-$  group attached at the nitrogen atom of isoquinoline unit. Furthermore, the sequential COSY correlations of  $H_2-13/H-14/H_2-15/H_2-16/H_2-17/H_2-18$ , and  $H-14/H_2-19/H_3-20$  (Figure 4), together with the HMBC correlations from  $H_2-13$  to  $C-12/C-14/C-15$ , from  $H_2-15$  to  $C-13/C-14/C-16$ , from  $H_2-17$  to  $C-16/C-18$ , from  $H_3-18$  to  $C-16/C-17$ , from  $H_2-19$  to  $C-13/C-14/C-15/C-20$ , and from  $H_3-20$  to  $C-14/C-19$  (Figure 4), suggested that the 2-ethylhexanol group connected with the carboxyl of the  $-CH_2-CH_2-COO-$  group to form an ester. The optical rotation and measured CD data of **14** were zero, which indicated **14** was a racemic mixture. However, an HPLC analysis of **14** with a chiral column (CHIRALPAK IA and IB, respectively, 4.6 mm  $\times$  250 mm column), eluting with n-hexane/ethanol/TFA (Figures S99 and S100), showed a big trailing peak. The reason for this could be that the two kinds of chiral columns were not suitable for the chiral separation of **14**. Thus, the structure of **14** was determined as shown.

All of the 14 compounds were evaluated for their enzyme inhibitory activity against five PTPs including CD45, SHP1, TCPTP, PTP1B and LAR, cytotoxicity towards human lung adenocarcinoma cell line H1975, and antibacterial activity. The results of protein phosphatase inhibition assays (Table 5) showed that only **3** and **4** selectively exhibited significant inhibitory activity against CD45 with  $IC_{50}$  values of 8.4 and 5.6  $\mu M$ , respectively, and **1**, **8**, **9**, **10**, **12** and **13** showed a mild inhibitory activity against several PTPs. A cytotoxicity assay (Table 5) showed that only **4** had a moderate cytotoxicity towards H1975 cell lines with an  $IC_{50}$  value of 11.0  $\mu M$ . The analysis of the relationship of their structures, enzyme inhibitory activity and cytotoxicity displayed that the substituents at  $C-7$  of the isoquinoline nucleus could greatly affect their bioactivity. In addition, antibacterial assays exhibited that **14** had medium antibacterial activity towards *Staphylococcus aureus*, methicillin-resistant *S. aureus* (MRSA), and *Escherichia coli*, with MIC values of 100  $\mu g/mL$ , and **4** could inhibit the growth of *E. coli* with a MIC value of 100  $\mu g/mL$ , while other compounds did not show clear antibacterial activity towards the three indicators. The results indicated that  $-C=N^+$  unit was an active center for the antibacterial activity of **14**.



**Table 5.** Inhibition activity against five phosphatases and cytotoxicity of 1–14.

| Comp.                           | Inhibitory Effect against Phosphatases (IC <sub>50</sub> in μM) |       |       |       |      | Cytotoxicity (IC <sub>50</sub> in μM) |
|---------------------------------|---|-------|-------|-------|------|---------------------------------------|
|                                 | CD45  | SHP1  | TCPTP | PTP1B | LAR  | H1975 Cell (after 24 h)               |
| 1                               | 29.7  | 38.3  | 196.9 | 182.2 | 100  | 76.2                                  |
| 2                               | >200  | >200  | >200  | >200  | >200 | >80                                   |
| 3                               | 8.4   | 20.7  | >200  | 64.5  | 21.9 | 71.3                                  |
| 4                               | 5.6   | 130.2 | >200  | 150   | 26.1 | 11.0                                  |
| 5                               | 102.6   | 145.1 | >200  | 200   | >200 | >80                                   |
| 6                               | >200  | 200   | >200  | >200  | >200 | >80                                   |
| 7                               | >200  | >200  | >200  | >200  | >200 | >80                                   |
| 8                               | 49.0  | 100   | >200  | 180   | >200 | >80                                   |
| 9                               | 27.2  | 41.8  | 57.7  | 68.8  | >200 | >80                                   |
| 10                              | 30.8  | >200  | >200  | >200  | 100  | >80                                   |
| 11                              | 100   | 145.4 | >200  | 190   | >200 | >80                                   |
| 12                              | 38.5  | 116.8 | >200  | 170   | 150  | >80                                   |
| 13                              | 11.1  | 40.26 | >200  | 37.9  | 32.6 | >80                                   |
| 14                              | 200   | >200  | >200  | >200  | >200 | >80                                   |
| Na <sub>3</sub> VO <sub>4</sub> | -   | 4.4   | 2.4   | 1.6   | -    | -                                     |
| AACQ                            | 0.29  | -     | -     | -     | -    | -                                     |

AACQ: 2-[(4-acetylphenyl)amino]-3-chloronaphthoquinone; “-”: Not tested.

### 3. Experimental Section

#### 3.1. General Experimental Procedure

The procedures were the same as previously reported [13,14].

#### 3.2. Fungal Material

The strain *Aspergillus puniceus* SCSIO z021 was isolated from a deep-sea sediment of Okinawa Trough (27°34.01' N and 126°55.59' E, ~1589 depth), which was located approximately 4.7 km from an active hydrothermal vent. The strain (GenBank accession number KX258801) was identified as *Aspergillus puniceus* through DNA extraction, ITS sequence amplification and sequence alignment, which has a 99% similarity to *A. puniceus* (GenBank accession number GU456970). The strain *A. puniceus* SCSIO z021 was deposited in the RNAM Center, South China Sea Institute of Oceanology, Chinese Academy of Science.

#### 3.3. Fermentation and Extraction

The fungus strain was cultivated on potato glucose agar (PDA) plate containing 3% sea salt at 28 °C for 7 days. The spores were selected and transferred to a complex culture medium (glucose 1%, D-mannitol 2%, maltose 2%, corn meal 0.05%, monosodium glutamate 1%, KH<sub>2</sub>PO<sub>4</sub> 0.05%, MgSO<sub>4</sub>·7H<sub>2</sub>O 0.03%, yeast extract 0.3%, sea salt 3%) to obtain a spore suspension that was cultured in a shaker at 28 °C for 3 days at a rotating speed of 180 rpm. The fungus was cultured in 1 L Erlenmeyer flasks each containing 300 mL of 3# medium (glucose 1%, D-mannitol 2%, maltose 2%, corn meal 0.05%, monosodium glutamate 1%, KH<sub>2</sub>PO<sub>4</sub> 0.05%, MgSO<sub>4</sub>·7H<sub>2</sub>O 0.03%, yeast extract 0.3%, sea salt 3%) at 28 °C for 33 days under static condition. After fermentation, the broth and mycelia were separated with gauze. The broth was extracted with XAD-16 resin and sequentially eluted with H<sub>2</sub>O and EtOH to obtain crude extract (61.7 g). The mycelia was extracted three times with acetone, and further extracted three times with EtOAc to yield a crude extract (48.2 g).

#### 3.4. Isolation and Purification

The combined extracts (109.9 g) were subjected to a normal-phase silica gel column eluting with a gradient of dichloromethane (DCM)/MeOH (100:0, 98:2, 95:5, 95:5, 90:10, 80:20, 70:30, 50:50, 0:100) to give nine subfractions (Fr.1–Fr.9) based on TLC analysis. Fr.4 (6.6 g) was separated by ODS column using MeOH–H<sub>2</sub>O–TFA (5:95:0.02 to 100:0:0.02) as eluent to afford 10 subfractions (Fr.4.1–Fr.4.10). Fr.4.1 was separated by Sephadex LH-20 eluting with MeOH followed by semipreparative HPLC (MeOH/H<sub>2</sub>O/TFA, 28:72:0.03,

3 mL/min) to yield **1** (11.6 mg,  $t_R = 15.8$  min). Fr.4.3 was subjected to Sephadex LH-20 using MeOH as mobile phase, which was further purified by semipreparative HPLC (CH<sub>3</sub>CN/H<sub>2</sub>O/TFA, 17:83:0.03, 3 mL/min) to yield **2** (30.7 mg,  $t_R = 16.3$  min). Fr.4.5 was isolated by Sephadex LH-20 eluting with MeOH, then purified by semipreparative HPLC (CH<sub>3</sub>CN/H<sub>2</sub>O/TFA, 25:75:0.03, 3 mL/min) to yield **7** (2.9 mg,  $t_R = 25.9$  min). Fr.4.6 was separated by Sephadex LH-20 with a mobile phase of MeOH, and then further purified by semipreparative HPLC (MeOH/H<sub>2</sub>O/TFA, 45:55:0.03, 3 mL/min) to yield **10** (2.8 mg,  $t_R = 16.1$  min) and **12** (15.2 mg,  $t_R = 14.5$  min). Fr.4.8 was isolated by silica gel column eluting with a gradient of CH<sub>2</sub>Cl<sub>2</sub>/MeOH (100:0, 80:1, 60:1, 40:1, 10:1, 5:1, 1:1, 0:100) to obtain three fractions, then Fr.4.8.1 was further purified by semipreparative HPLC (CH<sub>3</sub>CN/H<sub>2</sub>O/TFA, 49:51:0.03, 3 mL/min) to yield **14** (29.4 mg,  $t_R = 20.2$  min). Fr.6 (11.0 g) was separated by ODS column using MeOH-H<sub>2</sub>O-TFA (5:95:0.02 to 100:0:0.02) as mobile phase to yield eight subfractions (Fr.6.1–Fr.6.8). Fr.6.3 was purified by semipreparative HPLC (CH<sub>3</sub>CN/H<sub>2</sub>O/TFA, 21:79:0.03, 3 mL/min) to obtain **6** (4.0 mg,  $t_R = 19.5$  min), **3** (17.6 mg,  $t_R = 18.4$  min) and **4** (12.2 mg,  $t_R = 19.7$  min). Fr.6.6 was isolated by semipreparative HPLC (CH<sub>3</sub>CN/H<sub>2</sub>O/TFA, 24:76:0.03, 3 mL/min) to yield **11** (7.8 mg,  $t_R = 16.0$  min) and **5** (4.3 mg,  $t_R = 14.4$  min). Fr.6.7 was isolated by Sephadex LH-20 with MeOH as mobile phase, then further purified by semipreparative HPLC (CH<sub>3</sub>CN/H<sub>2</sub>O/TFA, 28:72:0.03, 3 mL/min) to yield **8** (4.1 mg,  $t_R = 39.2$  min) and **9** (2.8 mg,  $t_R = 18.4$  min). Fr.6.8 was separated by Sephadex LH-20, eluting with MeOH and further purified by semipreparative HPLC (CH<sub>3</sub>CN/H<sub>2</sub>O/TFA, 35:65:0.03, 3 mL/min) to get **13** (10.3 mg,  $t_R = 18.0$  min).

Puniceusine A (**1**): white acicular crystal; UV (CH<sub>3</sub>OH)  $\lambda_{max}$  (log  $\epsilon$ ) 204 (1.42), 208 (1.42), 241 (1.56), 258 (1.58), 357 (0.74) nm; <sup>1</sup>H and <sup>13</sup>C NMR, Tables 1 and 2; HRESIMS  $m/z$  176.0709 [M + H]<sup>+</sup> (calcd for C<sub>10</sub>H<sub>10</sub>NO<sub>2</sub>, 176.0706).

Puniceusine B (**2**): pale yellow powder; UV (CH<sub>3</sub>OH)  $\lambda_{max}$  (log  $\epsilon$ ) 206 (1.61), 245 (1.75), 260 (1.83), 305 (0.73), 360 (0.84) nm; <sup>1</sup>H and <sup>13</sup>C NMR, Tables 1 and 2; HRESIMS  $m/z$  190.0864 [M + H]<sup>+</sup> (calcd for C<sub>11</sub>H<sub>12</sub>NO<sub>2</sub>, 190.0863).

Puniceusine C (**3**): pale yellow powder; UV (CH<sub>3</sub>OH)  $\lambda_{max}$  (log  $\epsilon$ ) 205 (1.87), 244 (1.98), 262 (2.04), 332 (1.07) nm; IR (film)  $\nu_{max}$  3415, 1678, 1436, 1382, 1321, 1203, 1184, 1130, 1022, 954, 900, 840, 800, 723 cm<sup>-1</sup>; <sup>1</sup>H and <sup>13</sup>C NMR, Tables 1 and 2; HRESIMS  $m/z$  363.1339 [M + H]<sup>+</sup> (calcd for C<sub>21</sub>H<sub>19</sub>N<sub>2</sub>O<sub>4</sub>, 363.1349).

Puniceusine D (**4**): pale yellow powder; UV (CH<sub>3</sub>OH)  $\lambda_{max}$  (log  $\epsilon$ ) 207 (1.86), 243 (1.88), 260 (1.88) nm; IR (film)  $\nu_{max}$  3402, 1678, 1643, 1566, 1384, 1342, 1197, 1132, 1045, 989, 954, 842, 800, 723 cm<sup>-1</sup>; <sup>1</sup>H and <sup>13</sup>C NMR, Tables 1 and 2; HRESIMS  $m/z$  363.1339 [M + H]<sup>+</sup> (calcd for C<sub>21</sub>H<sub>19</sub>N<sub>2</sub>O<sub>4</sub>, 363.1338).

Puniceusine E (**5**): pale yellow powder; UV (CH<sub>3</sub>OH)  $\lambda_{max}$  (log  $\epsilon$ ) 206 (2.07), 248 (1.83), 265 (2.00), 337 (1.06) nm; IR (film)  $\nu_{max}$  1703, 1678, 1365, 1178, 0012, 835, 800, 721 cm<sup>-1</sup>; <sup>1</sup>H and <sup>13</sup>C NMR, Tables 1 and 2; HRESIMS  $m/z$  377.1496 [M + H]<sup>+</sup> (calcd for C<sub>22</sub>H<sub>21</sub>N<sub>2</sub>O<sub>4</sub>, 377.1486).

Puniceusine F (**6**): colorless crystals; [ $\alpha$ ]<sub>D</sub><sup>25</sup> 0 (c 0.10, CH<sub>3</sub>OH); UV (CH<sub>3</sub>OH)  $\lambda_{max}$  (log  $\epsilon$ ) 206 (1.63), 244 (1.76), 261 (1.71) nm; IR (film)  $\nu_{max}$  3419, 1703, 1681, 1363, 1201, 1180, 1134, 837, 800, 721 cm<sup>-1</sup>; <sup>1</sup>H and <sup>13</sup>C NMR, Tables 1 and 2; HRESIMS  $m/z$  262.1076 [M + H]<sup>+</sup> (calcd for C<sub>14</sub>H<sub>16</sub>NO<sub>4</sub>, 262.1074).

Puniceusine G (**7**): yellow powder; UV (CH<sub>3</sub>OH)  $\lambda_{max}$  (log  $\epsilon$ ) 200 (1.26), 246 (1.46) nm; IR (film)  $\nu_{max}$  3412, 1680, 1440, 1195, 1136, 1028, 844, 800, 725 cm<sup>-1</sup>; <sup>1</sup>H and <sup>13</sup>C NMR, Tables 1 and 2; HRESIMS  $m/z$  254.1182 [M + H]<sup>+</sup> (calcd for C<sub>16</sub>H<sub>16</sub>NO<sub>2</sub>, 254.1176).

Puniceusine H (**8**): pale yellow powder; UV (CH<sub>3</sub>OH)  $\lambda_{max}$  (log  $\epsilon$ ) 191 (1.61), 204 (2.08), 242 (1.06), 272 (1.12) nm; IR (film)  $\nu_{max}$  3367, 1680, 1456, 1417, 1394, 1201, 1139, 1020, 839, 802, 721 cm<sup>-1</sup>; <sup>1</sup>H and <sup>13</sup>C NMR, Tables 2 and 3; HRESIMS  $m/z$  398.1244 [M + H]<sup>+</sup> (calcd for C<sub>21</sub>H<sub>20</sub>NO<sub>7</sub>, 398.1234).

Puniceusine I (**9**): yellow powder; [ $\alpha$ ]<sub>D</sub><sup>25</sup> +60.7 (c 0.10, CH<sub>3</sub>OH); UV (CH<sub>3</sub>OH)  $\lambda_{max}$  (log  $\epsilon$ ) 205 (1.30), 237 (0.90), 244 (0.92), 276 (0.63) nm; ECD (CH<sub>3</sub>OH)  $\lambda_{max}$  ( $\Delta\epsilon$ ) 201 (+4.35), 202 (+4.71), 214 (−4.54), 232 (−1.32), 246 (−2.71), 279 (+0.44), 322 (−1.45) nm; IR (film)  $\nu_{max}$

3402, 1699, 1681, 1361, 1201, 1136, 837, 800, 721  $\text{cm}^{-1}$ ;  $^1\text{H}$  and  $^{13}\text{C}$  NMR, Tables 3 and 4; HRESIMS  $m/z$  354.1331  $[\text{M} + \text{H}]^+$  (calcd for  $\text{C}_{20}\text{H}_{20}\text{NO}_5$ , 354.1336).

Puniceusine J (10): pale yellow powder; UV ( $\text{CH}_3\text{OH}$ )  $\lambda_{\text{max}}$  ( $\log \epsilon$ ) 195 (2.08), 208 (1.06), 243 (1.12) nm; IR (film)  $\nu_{\text{max}}$  3406, 1678, 1392, 1321, 1203, 1132, 840, 800, 723  $\text{cm}^{-1}$ ;  $^1\text{H}$  and  $^{13}\text{C}$  NMR, Tables 3 and 4; HRESIMS  $m/z$  384.1455  $[\text{M} + \text{H}]^+$  (calcd for  $\text{C}_{21}\text{H}_{22}\text{NO}_6$ , 384.1442).

Puniceusine K (11): pale yellow powder;  $[\alpha]_{\text{D}}^{25}$   $-155.6$  ( $c$  0.10,  $\text{CH}_3\text{OH}$ ); UV ( $\text{CH}_3\text{OH}$ )  $\lambda_{\text{max}}$  ( $\log \epsilon$ ) 205 (1.30), 237 (0.90), 244 (0.92), 276 (0.63) nm; ECD ( $\text{CH}_3\text{OH}$ )  $\lambda_{\text{max}}$  ( $\Delta\epsilon$ ) 215 ( $-2.39$ ), 229 ( $+0.45$ ), 238 ( $+0.29$ ), 255 ( $+0.67$ ), 304 ( $-0.18$ ) nm; IR (film)  $\nu_{\text{max}}$  3390, 1674, 1435, 1371, 1319, 1199, 1134, 840, 800, 723  $\text{cm}^{-1}$ ;  $^1\text{H}$  and  $^{13}\text{C}$  NMR, Tables 3 and 4; HRESIMS  $m/z$  428.1348  $[\text{M} + \text{H}]^+$  (calcd for  $\text{C}_{22}\text{H}_{22}\text{NO}_8$ , 428.1340).

Puniceusine L (12): colorless crystals; UV ( $\text{CH}_3\text{OH}$ )  $\lambda_{\text{max}}$  ( $\log \epsilon$ ) 206 (2.14), 264 (2.04), 366 (1.12) nm; IR (film)  $\nu_{\text{max}}$  3080, 1678, 1643, 1396, 1319, 1197, 1130, 839, 798, 721  $\text{cm}^{-1}$ ;  $^1\text{H}$  and  $^{13}\text{C}$  NMR, Tables 3 and 4; HRESIMS  $m/z$  328.1195  $[\text{M} + \text{H}]^+$  (calcd for  $\text{C}_{18}\text{H}_{18}\text{NO}_5$ , 328.1179).

Puniceusine M (13): pale yellow powder; UV ( $\text{CH}_3\text{OH}$ )  $\lambda_{\text{max}}$  ( $\log \epsilon$ ) 207 (2.08), 244 (1.74), 267 (1.84) nm; IR (film)  $\nu_{\text{max}}$  3404, 1678, 1394, 1319, 1201, 1176, 1138, 1026, 837, 800, 721  $\text{cm}^{-1}$ ;  $^1\text{H}$  and  $^{13}\text{C}$  NMR, Tables 3 and 4; HRESIMS  $m/z$  342.1332  $[\text{M} + \text{H}]^+$  (calcd for  $\text{C}_{19}\text{H}_{20}\text{NO}_5$ , 342.1336).

Puniceusine N (14): pale yellow powder;  $[\alpha]_{\text{D}}^{25}$  0 ( $c$  0.10,  $\text{CH}_3\text{OH}$ ); UV ( $\text{CH}_3\text{OH}$ )  $\lambda_{\text{max}}$  ( $\log \epsilon$ ) 206 (1.89), 232 (1.61), 266 (2.08), 309 (1.06), 364 (1.12) nm; IR (film)  $\nu_{\text{max}}$  3423, 1680, 1363, 1195, 1182, 1128, 839, 800, 719  $\text{cm}^{-1}$ ;  $^1\text{H}$  and  $^{13}\text{C}$  NMR, Tables 3 and 4; HRESIMS  $m/z$  374.2329  $[\text{M}]^+$  (calcd for  $\text{C}_{22}\text{H}_{32}\text{NO}_4$ , 374.2326).

### 3.5. X-ray Crystallographic Analysis of 6 and 12

The crystal data were obtained on a Rigaku MicroMax 007 diffractometer (Rigaku Corporation, Tokyo, Japan) with  $\text{Cu K}\alpha$  radiation and a graphite monochromator. The crystal structures of 6 and 12 were solved by direct methods with the SHELXTL and refined by full-matrix, least-squares techniques. Crystallographic data for 6 and 12 were deposited with the Cambridge Crystallographic Data Centre as supplementary publication numbers, CCDC 2112471 and 2112479, respectively.

Crystal data for 6:  $\text{C}_{14}\text{H}_{14.0375}\text{NO}_4$ ,  $FW = 260.30$ ; colorless crystal from  $\text{MeOH}$ ; crystal size =  $0.15 \times 0.12 \times 0.1 \text{ mm}^3$ ;  $T = 100.00$  (10) K; monoclinic, space group  $\text{P}2_1/c$  (no. 14); unit cell parameters:  $a = 4.82780$  (10)  $\text{\AA}$ ,  $b = 13.4963$  (3)  $\text{\AA}$ ,  $c = 22.6665$  (7)  $\text{\AA}$ ,  $\alpha = 90^\circ$ ,  $\beta = 96.025$  (3)°,  $\gamma = 90^\circ$ ,  $V = 1468.73$  (6)  $\text{\AA}^3$ ,  $Z = 4$ ,  $D_{\text{calc}} = 1.177 \text{ g/cm}^3$ ,  $F(000) = 548.0$ ,  $\mu(\text{CuK}\alpha) = 0.724 \text{ mm}^{-1}$ ; 7185 reflections measured ( $7.634^\circ \leq 2\theta \leq 147.79^\circ$ ), 2852 unique ( $R_{\text{int}} = 0.0197$ ,  $R_{\text{sigma}} = 0.0255$ ), which were used in all calculations. The final  $R_1$  was 0.0487 ( $I > 2\sigma(I)$ ) and  $wR_2$  was 0.1406 (all data).

Crystal data for 12:  $\text{C}_{18}\text{H}_{17}\text{NO}_5$ ,  $FW = 327.32$ ; colorless crystal from  $\text{MeOH}$ ; crystal size =  $0.13 \times 0.12 \times 0.1 \text{ mm}^3$ ;  $T = 100.00$  (10) K; triclinic, space group  $\text{P}-1$  (no. 2); unit cell parameters:  $a = 7.6037$  (4)  $\text{\AA}$ ,  $b = 9.9253$  (5)  $\text{\AA}$ ,  $c = 10.5261$  (6)  $\text{\AA}$ ,  $\alpha = 70.543$  (5)°,  $\beta = 85.628$  (4)°,  $\gamma = 81.605$  (4)°,  $V = 740.68$  (7)  $\text{\AA}^3$ ,  $Z = 2$ ,  $D_{\text{calc}} = 1.468 \text{ g/cm}^3$ ,  $F(000) = 344.0$ ,  $\mu(\text{CuK}\alpha) = 0.897 \text{ mm}^{-1}$ ; 7019 reflections measured ( $8.914^\circ \leq 2\theta \leq 148.202^\circ$ ), 2880 unique ( $R_{\text{int}} = 0.0259$ ,  $R_{\text{sigma}} = 0.0317$ ) which were used in all calculations. The final  $R_1$  was 0.0419 ( $I > 2\sigma(I)$ ) and  $wR_2$  was 0.1150 (all data).

### 3.6. ECD Calculations

The ECD calculation for 9 was performed by Gaussian 16 program package. The procedures were the same as described in our previous study [13,14]. Briefly, the conformational search was performed by a MMFF model, then the conformers with lower relative energies ( $<10 \text{ kcal/mol}$ ) were subjected to geometry optimization with the DFT method at the B3LYP/6-311G(d) level. Vibrational frequency calculations were carried out at the same level to evaluate their relative thermal ( $\Delta E$ ) and free energies ( $\Delta G$ ) at 298.15 K. The geometry-optimized conformers were further calculated at the M06-2X/def2-TZVP level and the

solvent (methanol) effects were taken into consideration by using SMD. The optimized conformers with a Boltzmann distribution of more than 1% population were subjected to ECD calculation, which were performed by TDDFT methodology at the PBE1PBE/TZVP level. The ECD spectrum was generated by the software SpecDis using a Gaussian band shape with 0.3 eV exponential half-width from dipole-length dipolar and rotational strengths. The calculated spectrum of **9** was generated from the low-energy conformers according to the Boltzmann distribution of each conformer in MeOH solution. Details regarding optimized conformation geometries, thermodynamic parameters, and Boltzmann distributions (Tables S1–S3) of all conformations are provided in the Supporting Information.

### 3.7. Protein Phosphatase Inhibition Assays

The same methods as described in our previous study [13,14] were applied to test the inhibition activity of compounds **1–14** against five human protein tyrosine phosphatases (CD45, SHP1, TCPTP, PTP1B and LAR).

### 3.8. Cytotoxicity

Cytotoxic activity was evaluated using human lung adenocarcinoma cell line H1975 by CCK-8 method. Briefly, each of the test compounds was dissolved in DMSO and further diluted to give final concentrations of 80, 40, 20, 10, 5, 2.5, and 1.25 µg/mL, respectively. H1975 cells ( $5 \times 10^3$  cells/plate) were seeded in 96-well plates and treated with compounds at the indicated concentration for 24 h, and then 10 µL CCK-8 reagent was added to each well, and the plates were incubated at 37 °C for another 4 h. Next, the optical density was measured at a wavelength of 450 nm with the Bio-Rad (Hercules, CA, USA) microplate reader. Dose–response curves were generated, and the IC<sub>50</sub> values were calculated from the linear portion of log dose–response curves.

### 3.9. Antibacterial Assays

Antibacterial activities of **1–14** against *E. coli*, *S. aureus* and MRSA were evaluated using the 2-fold dilution assay in 96-microwell plates. Briefly, all the indicator bacteria were cultured on Luria–Bertani (LB) agar plates at 37 °C for 12 h, and then a single colony was picked into LB liquid medium and cultivated on a rotary shaker at 37 °C for 12 h. Then, the bacterial suspensions with LB medium were diluted until the difference of the OD<sub>600</sub> values between the bacterial suspensions and the medium was 0.01–0.02. Each of the tested compounds was dissolved in DMSO to give an initial concentration of 5 mg/mL, and further diluted with the bacterial suspensions by twofold serial dilution to give a final concentration of 100, 50, 25, 12.5, 6.25, and 3.125 µg/mL, respectively. The 96-well plates were incubated at 37 °C for 12 h. MIC value was determined as the lowest concentration with no visible bacterial growth. Ampicillin was used as the positive control and DMSO as the negative control. All experiments were performed three times.

## 4. Conclusions

Summarily, 14 new isoquinoline alkaloids (**1–14**) were obtained from the deep-sea-derived fungus, *A. puniceus* SCSIO z021. Compounds **3–5** and **8–13** unprecedentedly contained an isoquinolinyl, a polysubstituted benzyl or a pyronyl at position C-7 of the isoquinoline nucleus, which was different from 1-benzylisoquinoline analogues and other isoquinoline alkaloids from plants commonly containing substituents at positions C-1, N-2, C-3, C-4 or C-8 of isoquinoline skeleton. In addition, **3** and **4** showed selective inhibitory activity against CD45; **4** also had moderate cytotoxicity towards human lung adenocarcinoma cell line H1975, and **14** contained an active center  $-C=N^+$  which had evident antibacterial activity towards three indicator bacteria. An analysis of the relationship of the structures, enzyme inhibitory activity and cytotoxicity of **1–14** displayed that the substituents at C-7 of the isoquinoline nucleus could greatly affect their bioactivity. The results greatly enrich the structural diversity of isoquinoline alkaloids from fungi, and provide a potential lead compound for the development of a selective CD45 inhibitor and anticancer drug.

**Supplementary Materials:** The following supporting information can be downloaded at: <https://www.mdpi.com/article/10.3390/md20010078/s1>, Figures S1–S126: the 1D NMR, 2D NMR, HRES-IMS, IR, and UV spectra of compounds 1–14, Tables S1–S3: details of ECD calculation of compound 9, Tables S4 and S5: X-ray crystallographic data for compound 6 and X-ray crystallographic data for compound 12.

**Author Contributions:** Performing experiments, analyze data, and writing—original draft preparation, C.-M.L. and F.-H.Y.; test the activities, X.-H.L., X.-X.Z. and L.-X.L.; formal analysis, X.L.; resources, analyze data, writing—review and editing, supervision, and funding acquisition, S.-H.Q. All authors have read and agreed to the published version of the manuscript.

**Funding:** The authors are grateful for the financial support provided by the Key Special Project for Introduced Talents Team of Southern Marine Science and Engineering Guangdong Laboratory (Guangzhou) (GML2019ZD0406), National Natural Science Foundation of China (82173709), Key Science and Technology Project of Hainan Province (ZDKJ202018), Key-Area Research and Development Program of Guangdong Province (2020B1111030005), Institution of South China Sea Ecology and Environmental Engineering, Chinese Academy of Sciences (ISEE2021PY05), and Guangdong Provincial-level Special Funds for Promoting High-quality Economic Development (2020032).

**Acknowledgments:** The authors also appreciate the analytical facility center (Z.H.X., A.J.S., Y.Z., X.M., X.H.Z.) of the South China Sea Institute of Oceanology, Chinese Academy of Sciences, for acquiring NMR, HRESIMS, experimental ECD data, and X-ray crystallographic data.

**Conflicts of Interest:** The authors declare no competing financial interest.

## References

- Singh, S.; Pathak, N.; Fatima, E.; Negi, A.S. Plant isoquinoline alkaloids: Advances in the chemistry and biology of berberine. *Eur. J. Med. Chem.* **2021**, *226*, 113839. [[CrossRef](#)] [[PubMed](#)]
- Kohno, J.; Hiramatsu, H.; Nishio, M.; Sakurai, M.; Okuda, T.; Komatsubara, S. Structures of TMC-120A, B and C, novel isoquinoline alkaloids from *Aspergillus ustus* TC 1118. *Tetrahedron* **1999**, *55*, 11247–11252. [[CrossRef](#)]
- Copmans, D.; Kildgaard, S.; Rasmussen, S.A.; Slezak, M.; Dirks, N.; Partoens, M.; Esguerra, C.V.; Crawford, A.D.; Larsen, T.O.; de Witte, P.A.M. Zebrafish-based discovery of antiseizure compounds from the North Sea: Isoquinoline alkaloids TMC-120A and TMC-120B. *Mar. Drugs* **2019**, *17*, 607. [[CrossRef](#)] [[PubMed](#)]
- Li, G.Y.; Li, B.G.; Yang, T.; Liu, G.Y.; Zhang, G.L. Chaetoindicins A–C, three isoquinoline alkaloids from the fungus *Chaetomium indicum*. *Org. Lett.* **2006**, *8*, 3613–3615. [[CrossRef](#)] [[PubMed](#)]
- Yang, S.X.; Xiao, J.; Laatsch, H.; Holstich, J.J.; Dittrich, B.; Zhang, Q.; Gao, J.M. Fusarimine, a novel polyketide isoquinoline alkaloid, from the endophytic fungus *Fusarium* sp. In12, isolated from *Melia azedarach*. *Tetrahedron Lett.* **2012**, *53*, 6372–6375. [[CrossRef](#)]
- El-Neketi, M.; Ebrahim, W.; Lin, W.; Gedara, S.; Badria, F.; Saad, H.E.; Lai, D.; Proksch, P. Alkaloids and polyketides from *Penicillium citrinum*, an endophyte isolated from the Moroccan plant *Ceratonia siliqua*. *J. Nat. Prod.* **2013**, *76*, 1099–1104. [[CrossRef](#)] [[PubMed](#)]
- Yang, W.C.; Yuan, J.; Tan, Q.; Chen, Y.; Zhu, Y.J.; Jiang, H.M.; Zou, G.; Zang, Z.Z.; Wang, B.; She, Z.G. Peniazaphilones A–I, produced by co-culturing of mangrove endophytic fungi, *Penicillium sclerotiorum* THSH-4 and *Penicillium sclerotiorum* ZJHJ-18. *Chin. J. Chem.* **2021**, *39*, 3404–3412. [[CrossRef](#)]
- Nord, C.; Levenfors, J.J.; Bjerketorp, J.; Sahlberg, C.; Guss, B.; Öberg, B.; Broberg, A. Antibacterial isoquinoline alkaloids from the fungus *Penicillium spathulatum* Em19. *Molecules* **2019**, *24*, 4616. [[CrossRef](#)] [[PubMed](#)]
- Bialy, L.; Waldmann, H. Inhibitors of protein tyrosine phosphatases: Next-generation drugs? *Angew. Chem. Int. Ed. Engl.* **2005**, *44*, 3814–3839. [[CrossRef](#)] [[PubMed](#)]
- Barr, A.J. Protein tyrosine phosphatases as drug targets: Strategies and challenges of inhibitor development. *Future Med. Chem.* **2010**, *2*, 1563–1576. [[CrossRef](#)] [[PubMed](#)]
- Pan, D.Y.; Zhang, X.X.; Zheng, H.Z.; Zheng, Z.H.; Nong, X.H.; Liang, X.; Ma, X.; Qi, S.H. Novel anthraquinone derivatives as inhibitors of protein tyrosine phosphatases and indoleamine 2,3-dioxygenase 1 from the deep-sea derived fungus *Alternaria tenuissima* DFFSCS013. *Org. Chem. Front.* **2019**, *6*, 3252–3258. [[CrossRef](#)]
- Cheng, X.; Liang, X.; Zheng, Z.H.; Zhang, X.X.; Lu, X.H.; Yao, F.H.; Qi, S.H. Penicimeroterpenoids A–C, meroterpenoids with rearrangement skeletons from the marine-derived fungus *Penicillium* sp. SCSIO 41512. *Org. Lett.* **2020**, *16*, 6330–6333. [[CrossRef](#)] [[PubMed](#)]
- Liang, X.; Huang, Z.H.; Ma, X.; Zheng, Z.H.; Zhang, X.X.; Lu, X.H.; Qi, S.H. Mycotoxins as inhibitors of protein tyrosine phosphatases from the deep-sea-derived fungus *Aspergillus puniceus* SCSIO z021. *Bioorg. Chem.* **2021**, *107*, 104571. [[CrossRef](#)] [[PubMed](#)]

14. Liang, X.; Huang, Z.H.; Shen, W.B.; Lu, X.H.; Zhang, X.X.; Ma, X.; Qi, S.H. Talaromyxaones A and B: Unusual oxaphenalenone spirolactones as phosphatase inhibitors from the marine-derived fungus *Talaromyces purpureogenus* SCSIO 41517. *J. Org. Chem.* **2021**, *86*, 12831–12839. [[CrossRef](#)] [[PubMed](#)]
15. White, J.D.; Straus, D.S. Gattermann reaction of 3,5-dimethoxyphenylacetonitrile. Synthesis of 6,8-dioxyisoquinolines. *J. Org. Chem.* **2002**, *32*, 2689–2692. [[CrossRef](#)]
16. Atta-ur-Rahman; Ahmad, S.; Bhatti, M.K.; Choudhary, M.I. Alkaloidal constituents of *Fumaria indica*. *Phytochemistry* **1995**, *40*, 593–596. [[CrossRef](#)]
17. Ebrahim, W.; Aly, A.H.; Mándi, A.; Wray, V.; Essassi, E.; Ouchbani, T.; Bouhfid, R.; Lin, W.; Proksch, P.; Kurtán, T.; et al. O-heterocyclic embeurekols from *Embellisia eureka*, an endophyte of *Cladanthus arabicus*. *Chirality* **2013**, *25*, 250–256. [[CrossRef](#)] [[PubMed](#)]
18. Cui, C.B.; Ubukata, M.; Kakeya, H.; Onose, R.; Okada, G.; Takahashi, I.; Isono, K.; Osada, H. Acetophthalidin, a novel inhibitor of mammalian cell cycle, produced by a fungus isolated from a sea sediment. *J. Antibiot.* **1996**, *49*, 216–219. [[CrossRef](#)] [[PubMed](#)]



## Article

# Design, Semisynthesis, Insecticidal and Antibacterial Activities of a Series of Marine-Derived Geodin Derivatives and Their Preliminary Structure–Activity Relationships

Rong Chao <sup>1,†</sup>, Gulab Said <sup>1,2,†</sup>, Qun Zhang <sup>1</sup>, Yue-Xuan Qi <sup>3</sup>, Jie Hu <sup>1,3</sup>, Cai-Juan Zheng <sup>4</sup>, Ji-Yong Zheng <sup>3,\*</sup>, Chang-Lun Shao <sup>1,2</sup>, Guang-Ying Chen <sup>4</sup> and Mei-Yan Wei <sup>1,5,\*</sup>

- <sup>1</sup> Key Laboratory of Marine Drugs, The Ministry of Education of China, School of Medicine and Pharmacy, Ocean University of China, Qingdao 266003, China; chaorong1122@163.com (R.C.); gulabouc@gmail.com (G.S.); zhangqunnn@163.com (Q.Z.); hujiewrc@163.com (J.H.); shaochanglun@163.com (C.-L.S.)
- <sup>2</sup> Department of Chemistry, Women University Swabi, Swabi 23430, Pakistan
- <sup>3</sup> State Key Laboratory for Marine Corrosion and Protection, Luoyang Ship Material Research Institute (LSMRI), Qingdao 266061, China; qiyuexuan9475@163.com
- <sup>4</sup> Key Laboratory of Tropical Medicinal Resource Chemistry of Ministry of Education, Hainan Normal University, Haikou 570100, China; caijuan2002@163.com (C.-J.Z.); chgying123@163.com (G.-Y.C.)
- <sup>5</sup> College of Food Science and Engineering, Ocean University of China, Qingdao 266003, China
- \* Correspondence: zhengji@sunrui.net (J.-Y.Z.); mywei95@126.com (M.-Y.W.); Tel.: +86-532-68725022 (J.-Y.Z.); +86-532-8203-1381 (M.-Y.W.)
- † These authors contributed equally to this work.

**Citation:** Chao, R.; Said, G.; Zhang, Q.; Qi, Y.-X.; Hu, J.; Zheng, C.-J.; Zheng, J.-Y.; Shao, C.-L.; Chen, G.-Y.; Wei, M.-Y. Design, Semisynthesis, Insecticidal and Antibacterial Activities of a Series of Marine-Derived Geodin Derivatives and Their Preliminary Structure–Activity Relationships. *Mar. Drugs* **2022**, *20*, 82. <https://doi.org/10.3390/md20020082>

Academic Editors: Yonghong Liu and Xuefeng Zhou

Received: 28 December 2021

Accepted: 15 January 2022

Published: 18 January 2022

**Publisher's Note:** MDPI stays neutral with regard to jurisdictional claims in published maps and institutional affiliations.



**Copyright:** © 2022 by the authors. Licensee MDPI, Basel, Switzerland. This article is an open access article distributed under the terms and conditions of the Creative Commons Attribution (CC BY) license (<https://creativecommons.org/licenses/by/4.0/>).

**Abstract:** To enhance the biological activity of the natural product geodin (**1**), isolated from the marine-derived fungus *Aspergillus* sp., a series of new ether derivatives (**2–37**) was designed and semisynthesized using a high-yielding one-step reaction. In addition, the insecticidal and antibacterial activities of all geodin congeners were evaluated systematically. Most of these derivatives showed better insecticidal activities against *Helicoverpa armigera* Hübner than **1**. In particular, **15** showed potent insecticidal activity with an IC<sub>50</sub> value of 89 μM, comparable to the positive control azadirachtin (IC<sub>50</sub> = 70 μM). Additionally, **5**, **12**, **13**, **16**, **30** and **33** showed strong antibacterial activity against *Staphylococcus aureus* and *Aeromonas salmonicida* with MIC values in the range of 1.15–4.93 μM. The preliminary structure–activity relationships indicated that the introduction of halogenated benzyl especially fluorobenzyl, into **1** and substitution of 4-OH could be key factors in increasing the insecticidal and antibacterial activities of geodin.

**Keywords:** *Aspergillus* sp.; geodin; semisynthesize; insecticidal activity; antibacterial activity

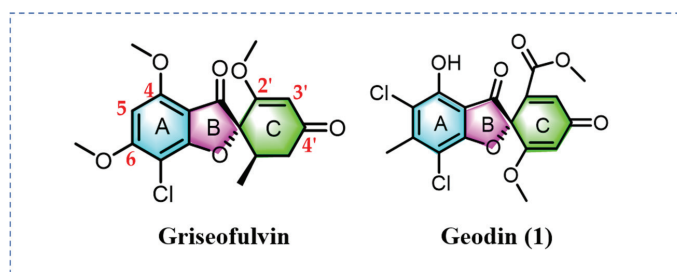
## 1. Introduction

Cotton bollworm (*Helicoverpa armigera* Hübner) is one of the most destructive agricultural pests known. This organism causes severe damage to a wide range of crops, such as cotton, sunflower, okra, tomato, chickpea, maize, potato and cabbage [1,2]. *H. armigera* is native to Africa, Asia, Europe, and Australasia and has become the most globally widespread species of *Helicoverpa* [3]. Consequently, *H. armigera* Hübner is responsible for about two billion dollars in direct economic losses each year [4]. Moreover, it has developed resistance against newer chemistries and conventional insecticides because of the extensive use of these chemical insecticides [5]. With the emergence of resistance in *H. armigera* Hübner to commercial insecticides, research on new insecticides has become particularly important. Marine natural products (MNP) continue to play highly significant roles in the pesticide development process and are potential sources of new drugs for treating plant diseases [6,7]. Introducing structural modifications to MNPs is one important strategy for



drug development initiatives to improve bioavailability, enhance biological activity and reduce toxicity [8].

During the course of our ongoing research into bioactive compounds from marine-derived fungi [9–15], a secondary metabolite belonging to the griseofulvin family, geodin (1), was isolated from the soft coral-derived fungus *Aspergillus* sp. (CHNSCLM-0151), collected from the South China Sea in 2015. Griseofulvin is a classic antifungal agent used clinically for the treatment of dermatomycoses and is an inhibitor of centrosomal clustering of cancer cell lines [16]. Griseofulvin and its analogues have been rigorously studied and some structure–activity relationships (SARs) clearly identified [16,17]. A library of 53 griseofulvin analogues with modifications on the 4, 5, 6, 2', 3' and 4' positions have been found to be less bioactive than the parent compound. Notably, a 2'-benzyloxy derivative with low activity against *Trichophyton rubrum* and *Trichophyton metagrophytes* was found to be among the most potent compounds identified against MDA-MB-231 cancer cells [16]. Geodin (1) shares the same grisan backbone as griseofulvin (Figure 1) and displays various interesting biological activities such as antimicrobial, glucose uptake for modulatory (rat adipocytes), fibrinolytic enhancement, antiviral and cytotoxic activities [18–20]. Most noteworthy from the current semisynthetic perspective, we have previously noted that geodin (1) exerts weak insecticidal activity [19]. Moreover, the previous study SAR study of 1 demonstrated that the phenolic hydroxyl group is not required for insecticidal activity [19]. In order to enhance the biological activity of 1, 36 new derivatives of geodin (1) were semisynthesized to evaluate insecticidal and antimicrobial activities; using this new panel of analogs, we also have extended SAR knowledge of 1.



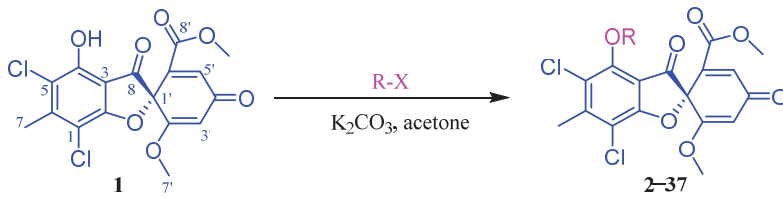
**Figure 1.** The structures of griseofulvin and geodin (1) which share the same grisan backbone (rings A, B and C).

## 2. Results and Discussion

### 2.1. Chemistry

The fungal strain *Aspergillus* sp. (CHNSCLM-0151) was cultivated in 50 L PDB medium at 28 °C with shaking for one week. Then the fermentation broth was extracted three times with an equal volume of EtOAc. The organic extracts were combined and concentrated under vacuum to afford a dry crude extract (35.7 g). The extract was subjected to vacuum liquid chromatography (VLC) on silica gel and eluted with a stepwise gradient of petroleum ether (PE)–EtOAc to afford six fractions (Fr. 1–Fr. 6). Fr. 5 was applied to reverse phase silica gel column and eluted with MeOH–H<sub>2</sub>O to obtain seven sub-fractions (Fr. 5-A and Fr. 5-G). Fr. 5-B was then purified with 65% MeOH–H<sub>2</sub>O to yield compound 1 (2.2 g).

The chemical structure of 1 was elucidated by analysis of NMR data and comparisons with literature [17]. Compound 1 contains an exchangeable proton, two singlet protons, two oxygenated methyl groups and a methyl. The substituents at the 4-OH were semisynthetically modified (Scheme 1) using benzyl bromide at a temperature of 40 °C for 6–12 h in the presence of K<sub>2</sub>CO<sub>3</sub> in dry acetone to produce compounds 2–37 (Figure 1 and Table 1). The structures of these derivatives (2–37) were fully characterized by extensive spectroscopic analyses (Figures S1–S111).

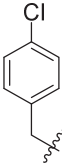
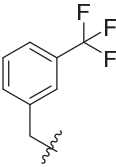
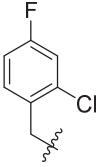
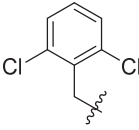
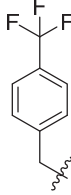
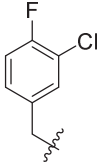
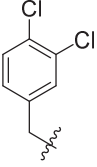
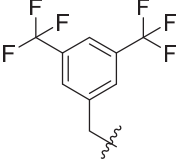
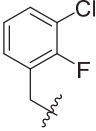
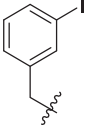
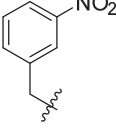
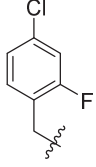
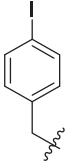
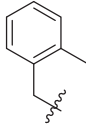
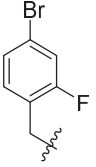
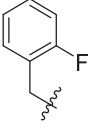
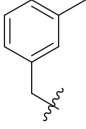
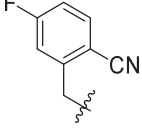
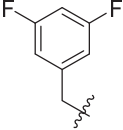
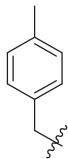
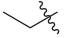


**Scheme 1.** General semisynthetic strategy employed to make ether derivatives of **1**.

**Table 1.** Structures of compounds **2–37**.

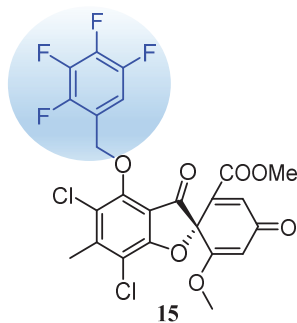
| No. | R | No. | R | No. | R |
|-----|---|-----|---|-----|---|
| 2   |   | 14  |   | 26  |   |
| 3   |   | 15  |   | 27  |   |
| 4   |   | 16  |   | 28  |   |
| 5   |   | 17  |   | 29  |   |
| 6   |   | 18  |   | 30  |   |

Table 1. Cont.

| No. | R   | No. | R   | No. | R   |
|-----|---|-----|---|-----|---|
| 7   |    | 19  |    | 31  |    |
| 8   |    | 20  |    | 32  |    |
| 9   |    | 21  |    | 33  |    |
| 10  |   | 22  |   | 34  |   |
| 11  |  | 23  |  | 35  |  |
| 12  |  | 24  |  | 36  |  |
| 13  |  | 25  |  | 37  |  |

## 2.2. Insecticidal Activity against *Helicoverpa armigera* Hübner

In this study, the insecticidal activities against *Helicoverpa armigera* Hübner of geodin (**1**) and 36 new derivatives modified at the 4-OH position were assessed. Most derivatives showed better insecticidal activity than marine natural product **1** (Table 2). Most of the derivatives were functionalized with benzyl analogues except for **37** which was modified with only an ethyl group and had no insecticidal activity. Compounds **2–4** and **35** were modified with bromobenzyl moieties and exhibited moderate insecticidal activity with  $IC_{50}$  values of 176  $\mu$ M (although **4** was inactive). In addition, the introduction of chlorobenzyl groups at the 4-OH position of **1** afforded the analogues **5–9** and **31–34** most of which showed higher insecticidal activity. However, the 2-chlorobenzyl derivative **5**, 2-chloro-4-fluorobenzyl derivative **31** and 4-chloro-2-fluorobenzyl derivative **33** displayed lower activity against *H. armigera* Hübner compared to parent **1**. Besides, the iodobenzyl analogues **10** and **11** had no insecticidal activity. Multiple studies have demonstrated that the introduction of a fluorine atom was useful for increasing insecticidal activity because of its unique properties such as electronegativity, size, and electrostatic interactions [21–25]. Herein, **12–21** were modified by fluorinated benzyl and most exhibited stronger activity (**16** and **19** were inactive). Especially, 2,3,4,5-tetrafluorobenzyl derivative **15** exhibited potent insecticidal activity comparable with the positive control azadirachtin with an  $IC_{50}$  value of 89  $\mu$ M (Figure 2). Moreover, the result of the antifouling activity of **15** against *Navicula exigua* and the settlement of the *Mytilus edulis* showed inactive and indicated **15** was non-toxic. In addition, non-halogenated benzyl derivatives **22–30** which were modified with nitro, methyl, phenyl and nitrile groups had good insecticidal activity except for 3-methylbenzyl compound **24** and 2-cyanobenzyl compound **30**. The above results indicated that the introduction of benzyl especially halogenated benzyl could enhance the insecticidal activity of **1**. Strikingly, further research on **15** was worth developing the low-toxicity and high-efficiency insecticide drug.



*H. armigera* Hubner  $IC_{50}$  = 89  $\mu$ M

**Figure 2.** The derivative **15** with significant insecticidal activity.

**Table 2.** Insecticidal and antibacterial activities of compounds 1–37 <sup>a</sup>.

| No.           | IC <sub>50</sub> (μM) (μg/mL) |                  | MIC (μM)               |                      |      |
|---------------|-------------------------------|------------------|------------------------|----------------------|------|
|               | Insecticidal Activity         |                  | Antimicrobial Activity |                      |      |
|               | <i>H. armigera</i> Hübner     | <i>S. aureus</i> | <i>A. salmonicida</i>  | <i>P. aeruginosa</i> |      |
| 1             | 500 (200)                     | >50              | >50                    | >50                  | >50  |
| 2             | 176 (100)                     | >50              | 2.20                   | >50                  | >50  |
| 3             | 176 (100)                     | >50              | >50                    | >50                  | >50  |
| 4             | >350 (>200)                   | 17.60            | 8.80                   | >50                  | >50  |
| 5             | >381 (>200)                   | 4.77             | 4.77                   | >50                  | >50  |
| 6             | 190 (100)                     | 9.55             | 4.77                   | >50                  | >50  |
| 7             | 190 (100)                     | >50              | >50                    | >50                  | >50  |
| 8             | 179 (100)                     | 8.96             | 4.48                   | >50                  | >50  |
| 9             | 179 (100)                     | >50              | 4.48                   | >50                  | >50  |
| 10            | >325 (>200)                   | 16.25            | 4.06                   | >50                  | >50  |
| 11            | >325 (>200)                   | >50              | 8.13                   | >50                  | >50  |
| 12            | 197 (100)                     | 4.93             | 2.46                   | >50                  | >50  |
| 13            | 190 (100)                     | 4.76             | 1.19                   | >50                  | >50  |
| 14            | 190 (100)                     | 9.52             | 2.38                   | >50                  | >50  |
| 15            | 89 (50)                       | 8.91             | 2.23                   | >50                  | >50  |
| 16            | >368 (>200)                   | 4.60             | 1.15                   | >50                  | >50  |
| 17            | 172 (100)                     | 17.27            | >50                    | >50                  | >50  |
| 18            | 179 (100)                     | 8.97             | >50                    | >50                  | >50  |
| 19            | >358 (>200)                   | 17.94            | 8.97                   | >50                  | >50  |
| 20            | 179 (100)                     | 17.94            | 4.49                   | >50                  | >50  |
| 21            | >319 (>200)                   | >50              | 4.00                   | >50                  | >50  |
| 22            | 187 (100)                     | >50              | >50                    | >50                  | >50  |
| 23            | 198 (100)                     | >50              | >50                    | >50                  | >50  |
| 24            | >397 (>200)                   | >50              | >50                    | >50                  | >50  |
| 25            | nt                            | >50              | >50                    | >50                  | >50  |
| 26            | 366 (200)                     | >50              | 2.29                   | >50                  | >50  |
| 27            | 176 (100)                     | >50              | >50                    | >50                  | >50  |
| 28            | 169 (100)                     | >50              | >50                    | >50                  | >50  |
| 29            | >388 (>200)                   | 9.72             | >50                    | >50                  | >50  |
| 30            | 194 (100)                     | 4.86             | 4.86                   | >50                  | >50  |
| 31            | >369 (>200)                   | 9.23             | 4.62                   | >50                  | >50  |
| 32            | 184 (100)                     | 9.23             | 9.23                   | >50                  | >50  |
| 33            | >369 (>200)                   | 4.62             | 2.31                   | >50                  | >50  |
| 34            | 369 (200)                     | 9.23             | >50                    | >50                  | >50  |
| 35            | 170 (100)                     | >50              | 4.27                   | >50                  | >50  |
| 36            | >375 (>200)                   | 18.97            | >50                    | >50                  | >50  |
| 37            | >468 (>200)                   | >50              | >50                    | 5.85                 | >50  |
| Azadirachtin  | 70 (50)                       | nt               | nt                     | nt                   | nt   |
| Sea-Nine 211  | nt                            | nt               | 0.27                   | 0.27                 | 0.27 |
| Ciprofloxacin | nt                            | 0.16             | nt                     | nt                   | nt   |

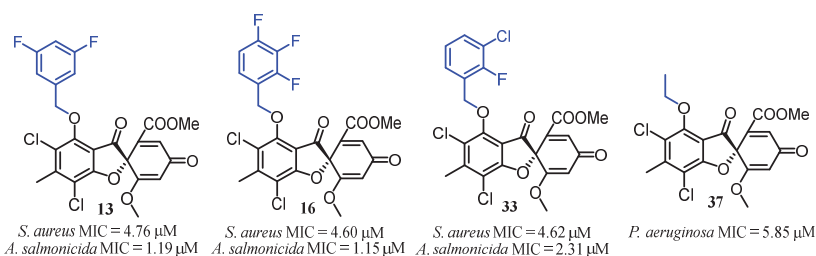
nt = not tested. <sup>a</sup> Results are the average of three independent experiments, each performed in duplicate. Standard deviations were less than ±10%.

### 2.3. Antibacterial Activity

Compounds 1–37 were also tested for their pharmacological activities against three bacteria, *Staphylococcus aureus*, *Aeromonas salmonicida* and *Pseudomonas aeruginosa* (Table 2). For *S. aureus*, 4-bromobenzyl derivative 4 and 3-iodobenzyl derivative 10 showed weak activity with MIC values of 17.60 and 16.25 μM, respectively (positive control ciprofloxacin, MIC = 0.16 μM). The chlorobenzyl analogues 5, 6 and 8 exhibited strong inhibitory activities with MIC values of 4.77, 9.55 and 8.96 μM, respectively. In addition, the introduction of fluorine atom improved the activity (12–20, MIC values: 4.76 to 17.94 μM). The cyanobenzyl derivatives 29 and 30 showed strong inhibitory activities (MIC values of 9.72 and 4.86 μM), while other non-halogenated benzyl derivatives 22–28 were inactive. Moreover, the simultaneous introduction of fluorine and chlorine atoms significantly enhanced antibacterial

activity (31–34, MIC values: 4.62 to 9.23  $\mu\text{M}$ ) while 4-bromo-2-fluorobenzyl derivative 35 was inactive. At the same time, 2-cyano-5-fluorobenzyl analogue 36 exhibited moderate inhibitory activity with an MIC value of 18.97  $\mu\text{M}$ .

For *A. salmonicida*, similarly, the introduction of halogenated benzyl strengthened the activity of geodin (1). Almost all of the compounds modified by benzyl groups substituted with fluorine, chlorine, bromine and iodine atoms showed better antibacterial activity than the parent 1. The derivatives 2, 5, 6, 8–10, 13–16, 20, 21, 31, 33 and 35 showed strong inhibitory activities with MIC values in the range of 1.15 to 4.77  $\mu\text{M}$  (Figure 3), while 4, 11, 19 and 32 showed moderate inhibitory activities against *A. salmonicida* with MIC values ranging from 8.13 to 9.23  $\mu\text{M}$  (positive control Sea-Nine 211, MIC = 0.27  $\mu\text{M}$ ). At the same time, the non-halogenated benzyl analogues 26 and 30 also exhibited strong activities with MIC values of 2.29 and 4.86  $\mu\text{M}$ .



**Figure 3.** The selective derivatives with strong antibacterial activities.

Interestingly, the ethyl derivative 37 showed selective inhibitory activity against *P. aeruginosa* with an MIC value of 5.85  $\mu\text{M}$  and the positive control Sea-Nine 211 had an MIC value of 0.27  $\mu\text{M}$  (Figure 3). The results revealed that the halogenated benzyl modification on 4-OH of geodin (1) improved the antibacterial activity against *S. aureus* and *A. salmonicida*. At the same time, the introduction of ethyl on the 4-OH position of geodin showed selective inhibitory activities against *P. aeruginosa*.

### 3. Materials and Methods

#### 3.1. General Experimental Procedures

$^1\text{H}$  and  $^{13}\text{C}$  NMR spectra were measured on an Agilent DD2 NMR spectrometer at 500 MHz and 125 MHz frequencies, respectively. For vacuum column chromatography silica gel (200–300 mesh, Qing Dao Hai Yang Chemical Group Co., Qingdao, China) and silica gel plates for thin layer chromatography (G60, F-254, and Yan Tai Zi Fu Chemical Group Co., Yan Tai, China) were used. HR-ESI-MS spectra were recorded on a Micro-mass Q-TOF spectrometer while UPLCMS spectra were measured on Waters UPLC<sup>®</sup> system using a C18 column [ACQUITY UPLC<sup>®</sup> BEH C18, 2.1  $\times$  50 mm, 1.7  $\mu\text{m}$ ; 0.5 mL/min] and ACQUITY QDA ESIMS scan from 150 to 1000 Da. For reverse phase Octadecylsilyl silica gel column was used. All the derivatives of compound 1 were semisynthesized by one step reaction. The products formation and reaction completion were checked by TLC at various intervals of time.

#### 3.2. Biological Material

*Aspergillus* sp. (CHNSCLM-0151) was isolated from the inner soft fresh tissue of a soft coral *Sinularia* sp., collected in 2015 from the coastal depth of the South China Sea. It was identified as *Aspergillus* sp., on the basis of its morphological and RNA base sequences. The fungus 512 base pair had 98% ITS sequence similarity with *Aspergillus* sp., NRRL58570 (GenBank No. HQ288052.1). The sequence data have been submitted to GenBank with accession number KY235298. The strain has been stored at the Key Laboratory of Marine Drugs, the Ministry of Education of China, School of Medicine and Pharmacy, Ocean University of China, Qingdao, China.

### 3.3. Extraction and Isolation

The pure spores of fungal strain were streaked onto PDA plates and incubated at 28 °C for one week. After the growth of fungus, small plugs of PDA containing the spores were aseptically put into 1000 mL Erlenmeyer flasks having about 60 g sterilized rice medium and 2% sodium chloride salt. The flasks were fermented at room temperature for 3 weeks, extracted three times with EtOAc, and evaporated under vacuum. The crude extract was subjected to normal phase silica gel column chromatography (CC) (200–300 mesh), eluting with a linear gradient of PE-EtOAc (*v/v*, gradient) to afford five fractions (Fr. 1–Fr. 5). Fraction 4 eluted with 40% EtOAc was further subjected to reverse phase silica gel CC, using MeOH and H<sub>2</sub>O as mobile phase. Compound 1 was eluted with 80% MeOH/H<sub>2</sub>O and further purified by recrystallization in MeOH/CH<sub>2</sub>Cl<sub>2</sub>.

#### Geodin (1)

White, solid; <sup>1</sup>H NMR (500 MHz, CDCl<sub>3</sub>) δ 7.47 (1H, s, OH-4), 7.14 (1H, d, *J* = 1.0 Hz, H-3'), 5.82 (1H, d, *J* = 1.0 Hz, H-5'), 3.73 (3H, s, H-7'), 3.70 (3H, s, H-9'), 2.57 (3H, s, H-7); <sup>13</sup>C NMR (125 MHz, CDCl<sub>3</sub>) δ 193.4 (C-8), 185.1 (C-4'), 168.0 (C-6'), 165.6 (C-2), 163.5 (C-8'), 149.5 (C-4), 146.7 (C-6), 137.6 (C-3'), 137.0 (C-2'), 114.9 (C-5), 109.6 (C-3), 109.0 (C-1), 104.5 (C-5'), 84.6 (C-1'), 57.1 (C-7'), 53.2 (C-9'), 18.9 (C-7), ESIMS *m/z* 398.9 [M + H]<sup>+</sup>.

### 3.4. General Synthetic Methods for Compounds 2–37

A corresponding benzyl bromide reagent (3–5 eq.) and anhydrous K<sub>2</sub>CO<sub>3</sub> (15 mg) were added to a stirred solution of 1 (40 mg, 0.10 mmol) in dry acetone (20 mL). The reaction mixture was stirred at 40 °C for 6–12 h. After the completion of the reaction, water was added to the reaction mixture, then the solution was extracted two times with EtOAc (40 mL). The organic layer was combined and dried under vacuum to give a crude residue which was purified through normal phase silica gel CC (200–300 mesh) eluting with a linear gradient of PE-EtOAc.

#### 3.4.1. Characterization Data of Compounds 2–37

Methyl(R)-4-((2-bromobenzyl)oxy)-5,7-dichloro-6'-methoxy-6-methyl-3,4'-dioxo-3H-spiro [benzofuran-2,1'-cyclohexane]-2',5'-diene-2'-carboxylate (2)

White, solid; yield 88.8%; <sup>1</sup>H NMR (500 MHz, CDCl<sub>3</sub>) δ 7.76 (1H, d, *J* = 7.5 Hz), 7.56 (1H, d, *J* = 8.0 Hz), 7.35 (1H, t, *J* = 7.5 Hz), 7.20 (1H, t, *J* = 8.0 Hz), 7.14 (1H, d, *J* = 1.0 Hz, H-3'), 5.82 (1H, s, H-5'), 5.45 (1H, d, *J* = 12.0 Hz), 5.40 (1H, d, *J* = 12.0 Hz), 3.75 (3H, s, H-7'), 3.70 (3H, s, H-9'), 2.59 (3H, s, H-7); <sup>13</sup>C NMR (125 MHz, CDCl<sub>3</sub>) δ 190.5 (C-8), 185.3 (C-4'), 168.4 (C-6'), 167.0 (C-2), 163.6 (C-8'), 151.1 (C-4), 146.1 (C-6), 137.7 (CH), 137.6 (C-3'), 135.9 (C-2'), 132.7 (CH), 130.3 (CH), 129.9 (CH), 127.7 (CH), 123.2 (C), 122.2 (C-5), 113.6 (C-3), 113.3 (C-1), 104.5 (C-5'), 84.3 (C-1'), 76.4 (CH<sub>2</sub>), 57.1 (C-7'), 53.2 (C-9'), 19.1 (C-7); HRESIMS *m/z* 566.9614 [M + H]<sup>+</sup> (calcd for C<sub>24</sub>H<sub>18</sub>BrCl<sub>2</sub>O<sub>7</sub><sup>+</sup>, 566.9607).

Methyl(R)-4-((3-bromobenzyl)oxy)-5,7-dichloro-6'-methoxy-6-methyl-3,4'-dioxo-3H-spiro [benzofuran-2, 1'-cyclohexane]-2',5'-diene-2'-carboxylate (3)

White, solid; yield 50.0%; <sup>1</sup>H NMR (500 MHz, CDCl<sub>3</sub>) δ 7.68 (1H, s), 7.47 (2H, t, *J* = 8.4 Hz), 7.23 (1H, d, *J* = 7.8 Hz), 7.15 (1H, d, *J* = 1.5 Hz, H-3'), 5.82 (1H, d, *J* = 1.5 Hz, H-5'), 5.34 (1H, d, *J* = 11.2 Hz), 5.25 (1H, d, *J* = 11.2 Hz), 3.75 (3H, s, H-7'), 3.69 (3H, s, H-9'), 2.59 (3H, s, H-7); <sup>13</sup>C NMR (125 MHz, CDCl<sub>3</sub>) δ 190.7 (C-8), 185.3 (C-4'), 168.4 (C-6'), 167.1 (C-2), 163.7 (C-8'), 150.6 (C-4), 146.2 (C-6), 138.5 (C), 137.8 (C-3'), 137.5 (C-2'), 131.7 (CH), 131.6 (CH), 130.2 (CH), 127.2 (CH), 122.6 (C), 113.8 (C-5), 113.5 (C-3), 109.0 (C-1), 104.5 (C-5'), 84.3 (C-1'), 75.8 (CH<sub>2</sub>), 57.1 (C-7'), 53.3 (C-9'), 19.1 (C-7); HRESIMS *m/z* 566.9612 [M + H]<sup>+</sup> (calcd for C<sub>24</sub>H<sub>18</sub>BrCl<sub>2</sub>O<sub>7</sub><sup>+</sup>, 566.9607).

Methyl(R)-4-((4-bromobenzyl)oxy)-5,7-dichloro-6'-methoxy-6-methyl-3,4'-dioxo-3H-spiro [benzofuran-2,1'-cyclohexane]-2',5'-diene-2'-carboxylate (4)

White, solid; yield 72.7%; <sup>1</sup>H NMR (500 MHz, CDCl<sub>3</sub>) δ 7.48 (2H, d, *J* = 8.5 Hz), 7.39 (2H, d, *J* = 8.0 Hz), 7.14 (1H, d, *J* = 1.0 Hz, H-3'), 5.81 (1H, d, *J* = 1.0 Hz, H-5'), 5.34 (1H, d, *J* = 11.5 Hz), 5.25 (1H, d, *J* = 11.5 Hz), 3.74 (3H, s, H-7'), 3.67 (3H, s, H-9'), 2.58 (3H, s, H-7); <sup>13</sup>C NMR (125 MHz, CDCl<sub>3</sub>) δ 190.7 (C-8), 185.2 (C-4'), 168.4 (C-6'), 167.1 (C-2), 163.6 (C-8'), 150.6 (C-4), 146.1 (C-6), 137.7 (C-3'), 137.5 (C-2'), 135.2 (C), 131.7 (CH×2), 130.5 (CH×2), 122.7 (C), 122.3 (C-5), 113.8 (C-3), 113.4 (C-1), 104.4 (C-5'), 84.3 (C-1'), 75.9 (CH<sub>2</sub>), 57.1 (C-7'), 53.2 (C-9'), 19.1 (C-7); HRESIMS *m/z* 566.9570 [M + H]<sup>+</sup> (calcd for C<sub>24</sub>H<sub>18</sub>BrCl<sub>2</sub>O<sub>7</sub><sup>+</sup>, 566.9607).

Methyl(R)-5, 7-dichloro-4-((2-chlorobenzyl) oxy)-6'-methoxy-6-methyl-3, 4'-dioxo-3H-spiro [benzofuran-2, 1'-cyclohexane]-2', 5'-diene-2'-carboxylate (5)

White, solid; yield 30.0%; <sup>1</sup>H NMR (500 MHz, CDCl<sub>3</sub>) δ 7.75 (1H, dd, *J* = 7.5, 2.0 Hz), 7.38 (1H, dd, *J* = 7.5, 2.0 Hz), 7.29 (2H, ddd, *J* = 7.5, 2.0 Hz), 7.14 (1H, d, *J* = 1.0 Hz, H-3'), 5.82 (1H, d, *J* = 1.0 Hz, H-5'), 5.48 (1H, d, *J* = 12.0 Hz), 5.41 (1H, d, *J* = 12.0 Hz), 3.75 (3H, s, H-7'), 3.70 (3H, s, H-9'), 2.59 (3H, s, H-7); <sup>13</sup>C NMR (CDCl<sub>3</sub>, 125 MHz) δ 190.5 (C-8), 185.3 (C-4'), 168.4 (C-6'), 167.0 (C-2), 163.6 (C-8'), 151.1 (C-4), 146.1 (C-6), 137.8 (C-3'), 137.6 (C-2'), 134.2 (C), 133.5 (CH), 130.4 (CH), 129.7 (CH), 129.5 (CH), 127.1 (C), 122.2 (C-5), 113.6 (C-3), 113.3 (C-1), 104.5 (C-5'), 84.2 (C-1'), 74.1 (CH<sub>2</sub>), 57.1 (C-7'), 53.2 (C-9'), 19.1 (C-7); HRESIMS *m/z* 523.0117 [M + H]<sup>+</sup> (calcd for C<sub>24</sub>H<sub>18</sub>Cl<sub>3</sub>O<sub>7</sub><sup>+</sup>, 523.0113).

Methyl(R)-5, 7-dichloro-4-((3-chlorobenzyl) oxy)-6'-methoxy-6-methyl-3, 4'-dioxo-3H-spiro [benzofuran-2, 1'-cyclohexane]-2', 5'-diene-2'-carboxylate (6)

White, solid; yield 92.3%; <sup>1</sup>H NMR (500 MHz, CDCl<sub>3</sub>) δ 7.52 (1H, s), 7.43 (1H, m), 7.30 (2H, overlapped), 7.14 (1H, d, *J* = 1.3 Hz, H-3'), 5.82 (1H, d, *J* = 1.3 Hz, H-5'), 5.35 (1H, d, *J* = 11.3 Hz), 5.26 (1H, d, *J* = 11.3 Hz), 3.75 (3H, s, H-7'), 3.69 (3H, s, H-9'), 2.58 (3H, s, H-7); <sup>13</sup>C NMR (125 MHz, CDCl<sub>3</sub>) δ 190.7 (C-8), 185.2 (C-4'), 168.4 (C-6'), 167.1 (C-2), 163.6 (C-8'), 150.6 (C-4), 146.1 (C-6), 138.2 (C-3'), 137.7 (C-2'), 137.5 (C), 134.4 (C), 129.9 (CH), 128.7 (CH×2), 126.7 (CH), 122.2 (C-5), 113.8 (C-3), 113.5 (C-1), 104.5 (C-5'), 84.3 (C-1'), 75.8 (CH<sub>2</sub>), 57.1 (C-7'), 53.2 (C-9'), 19.1 (C-7); HRESIMS *m/z* 523.0120 [M + H]<sup>+</sup> (calcd for C<sub>24</sub>H<sub>18</sub>Cl<sub>3</sub>O<sub>7</sub><sup>+</sup>, 523.0113).

Methyl(R)-5,7-dichloro-4-((4-chlorobenzyl)oxy)-6'-methoxy-6-methyl-3,4'-dioxo-3H-spiro [benzofuran-2,1'-cyclohexane]-2',5'-diene-2'-carboxylate (7)

White, solid; yield 50.0%; <sup>1</sup>H NMR (500 MHz, CDCl<sub>3</sub>) δ 7.46 (2H, d, *J* = 8.15 Hz), 7.33 (2H, d, *J* = 8.1 Hz), 7.14 (1H, s, H-3'), 5.81 (1H, s, H-5'), 5.34 (1H, d, *J* = 11.1 Hz), 5.26 (1H, d, *J* = 11.1 Hz), 3.74 (3H, s, H-7'), 3.68 (3H, s, H-9'), 2.58 (3H, s, H-7); <sup>13</sup>C NMR (125 MHz, CDCl<sub>3</sub>) δ 190.7 (C-8), 185.2 (C-4'), 168.4 (C-6'), 167.1 (C-2), 163.7 (C-8'), 150.7 (C-4), 146.1 (C-6), 137.8 (C-3'), 137.5 (C-2'), 134.7 (C), 134.5 (CH×2), 130.2 (CH×2), 128.8 (C), 122.3 (C-5), 113.8 (C-3), 113.5 (C-1), 104.5 (C-5'), 84.3 (C-1'), 75.9 (CH<sub>2</sub>), 57.1 (C-7'), 53.2 (C-9'), 19.1 (C-7); HRESIMS *m/z* 523.0120 [M + H]<sup>+</sup> (calcd for C<sub>24</sub>H<sub>18</sub>Cl<sub>3</sub>O<sub>7</sub><sup>+</sup>, 523.0113).

Methyl(R)-5, 7-dichloro-4-((2, 6-dichlorobenzyl) oxy)-6'-methoxy-6-methyl-3, 4'-dioxo-3H-spiro [benzofuran-2, 1'-cyclohexane]-2', 5'-diene-2'-carboxylate (8)

White, solid; yield 71.5%; <sup>1</sup>H NMR (500 MHz, CDCl<sub>3</sub>) δ 7.34 (1H, d, *J* = 0.5 Hz), 7.32 (1H, s), 7.23 (1H, ddd, *J* = 7.4, 1.4 Hz), 7.14 (1H, d, *J* = 1.4 Hz, H-3'), 5.81 (1H, d, *J* = 1.4 Hz, H-5'), 5.73 (1H, d, *J* = 11.5 Hz), 5.66 (1H, d, *J* = 11.5 Hz), 3.73 (3H, s, H-7'), 3.69 (3H, s, H-9'), 2.55 (3H, s, H-7); <sup>13</sup>C NMR (125 MHz, CDCl<sub>3</sub>) δ 190.3 (C-8), 185.3 (C-4'), 168.5 (C-6'), 166.9 (C-2), 163.5 (C-8'), 151.6 (C-4), 145.9 (C-6), 137.8 (C-3'), 137.5 (C-2'), 137.3 (C), 132.2 (CH), 130.8 (C×2), 128.5 (CH×2), 121.8 (C-5), 113.2 (C-3), 112.9 (C-1), 104.4 (C-5'), 84.3 (C-1'), 72.0 (CH<sub>2</sub>), 57.0 (C-7'), 53.1 (C-9'), 19.1 (C-7); HRESIMS *m/z* 556.9730 [M + H]<sup>+</sup> (calcd for C<sub>24</sub>H<sub>17</sub>Cl<sub>4</sub>O<sub>7</sub><sup>+</sup>, 556.9723).



Methyl(R)-5, 7-dichloro-4-((3, 4-dichlorobenzyl) oxy)-6'-methoxy-6-methyl-3, 4'-dioxo-3H-spiro [benzofuran-2, 1'-cyclohexane]-2', 5'-diene-2'-carboxylate (**9**)

White, solid; yield 94.3%; <sup>1</sup>H NMR (500 MHz, CDCl<sub>3</sub>) δ 7.61 (1H, d, *J* = 1.0 Hz), 7.44 (1H, d, *J* = 8.0 Hz), 7.38 (1H, d, *J* = 8.0 Hz), 7.14 (1H, d, *J* = 1.0 Hz, H-3'), 5.82 (1H, d, *J* = 1.0 Hz, H-5'), 5.33 (1H, d, *J* = 11.5 Hz), 5.25 (1H, d, *J* = 11.5 Hz), 3.75 (3H, s, H-7'), 3.69 (3H, s, H-9'), 2.58 (3H, s, H-7); <sup>13</sup>C NMR (125 MHz, CDCl<sub>3</sub>) δ 190.8 (C-8), 185.2 (C-4'), 168.3 (C-6'), 167.1 (C-2), 163.7 (C-8'), 150.3 (C-4), 146.2 (C-6), 137.7 (C-3'), 137.5 (C-2'), 136.4 (C), 132.7 (C), 132.6 (CH), 130.6 (CH×2), 128.0 (C), 122.2 (C-5), 113.8 (C-3), 113.7 (C-1), 104.5 (C-5'), 84.3 (C-1'), 75.1 (CH<sub>2</sub>), 57.1 (C-7'), 53.2 (C-9'), 19.1 (C-7); HRESIMS *m/z* 556.9730 [M + H]<sup>+</sup> (calcd for C<sub>24</sub>H<sub>17</sub>Cl<sub>4</sub>O<sub>7</sub><sup>+</sup>, 556.9723).

Methyl(R)-5, 7-dichloro-4-((3-iodobenzyl) oxy)-6'-methoxy-6-methyl-3, 4'-dioxo-3H-spiro [benzofuran-2, 1'-cyclohexane]-2', 5'-diene-2'-carboxylate (**10**)

White, solid; yield 94.1%; <sup>1</sup>H NMR (500 MHz, CDCl<sub>3</sub>) δ 7.88 (1H, s), 7.66 (1H, d, *J* = 7.8 Hz), 7.52 (1H, d, *J* = 7.8 Hz), 7.14 (1H, d, *J* = 7.8 Hz), 7.10 (1H, t, 7.8 Hz, H-3'), 5.82 (1H, d, *J* = 1.5 Hz, H-5'), 5.30 (1H, d, *J* = 11.2 Hz), 5.21 (1H, d, *J* = 11.2 Hz), 3.75 (3H, s, H-7'), 3.69 (3H, s, H-9'), 2.58 (3H, s, H-7); <sup>13</sup>C NMR (125 MHz, CDCl<sub>3</sub>) δ 190.7 (C-8), 185.2 (C-4'), 168.4 (C-6'), 167.0 (C-2), 163.6 (C-8'), 150.6 (C-4), 146.1 (C-6), 138.5 (C-3'), 137.7 (C-2'), 137.6 (C), 137.5 (CH×2), 130.3 (CH), 127.8 (CH), 122.2 (C-5), 113.8 (C-3), 113.5 (C-1), 104.5 (C-5'), 94.3 (C), 84.3 (C-1'), 75.7 (CH<sub>2</sub>), 57.1 (C-7'), 53.2 (C-9'), 19.1 (C-7); HRESIMS *m/z* 614.9468 [M + H]<sup>+</sup> (calcd for C<sub>24</sub>H<sub>18</sub>Cl<sub>2</sub>IO<sub>7</sub><sup>+</sup>, 614.9469).

Methyl(R)-5, 7-dichloro-4-((4-iodobenzyl) oxy)-6'-methoxy-6-methyl-3, 4'-dioxo-3H-spiro [benzofuran-2, 1'-cyclohexane]-2', 5'-diene-2'-carboxylate (**11**)

White, solid; yield 93.7%; <sup>1</sup>H NMR (500 MHz, CDCl<sub>3</sub>) δ 7.67 (2H, d, *J* = 8.3 Hz), 7.26 (2H, d, *J* = 8.3 Hz), 7.13 (1H, d, *J* = 1.4 Hz, H-3'), 5.81 (1H, d, *J* = 1.4 Hz, H-5'), 5.33 (1H, d, *J* = 11.3 Hz), 5.24 (1H, d, *J* = 11.3 Hz), 3.74 (3H, s, H-7'), 3.67 (3H, s, H-9'), 2.58 (3H, s, H-7); <sup>13</sup>C NMR (125 MHz, CDCl<sub>3</sub>) δ 190.7 (C-8), 185.2 (C-4'), 168.3 (C-6'), 167.0 (C-2), 163.6 (C-8'), 150.6 (C-4), 146.1 (C-6), 137.7 (C-3'), 137.6 (CH×2), 137.5 (C-2'), 135.8 (C), 130.6 (CH×2), 122.2 (C-5), 113.7 (C-3), 113.4 (C-1), 104.4 (C-5'), 94.5 (C), 84.2 (C-1'), 76.0 (CH<sub>2</sub>), 57.1 (C-7'), 53.2 (C-9'), 19.1 (C-7); HRESIMS *m/z* 614.9477 [M + H]<sup>+</sup> (calcd for C<sub>24</sub>H<sub>18</sub>Cl<sub>2</sub>IO<sub>7</sub><sup>+</sup>, 614.9469).

Methyl(R)-5, 7-dichloro-4-((2-fluorobenzyl) oxy)-6'-methoxy-6-methyl-3, 4'-dioxo-3H-spiro [benzofuran-2, 1'-cyclohexane]-2', 5'-diene-2'-carboxylate (**12**)

White, solid; yield 58.4%; <sup>1</sup>H NMR (500 MHz, CDCl<sub>3</sub>) δ 7.64 (1H, t, *J* = 7.5 Hz), 7.32 (1H, m, *J* = 7.5 Hz), 7.15 (2H, overlapped), 7.06 (1H, t, *J* = 9.5 Hz, H-3'), 5.82 (1H, d, *J* = 0.5 Hz, H-5'), 5.44 (1H, d, *J* = 11 Hz), 5.35 (1H, d, *J* = 11 Hz), 3.74 (3H, s, H-7'), 3.70 (3H, s, H-9'), 2.57 (3H, s, H-7); <sup>13</sup>C NMR (125 MHz, CDCl<sub>3</sub>) δ 190.6 (C-8), 185.3 (C-4'), 168.5 (C-6'), 167.1 (C-2), 163.6 (C-8'), 162.0 (C), 150.9 (C-4), 146.1 (C-6), 137.8 (C-3'), 137.6 (C-2'), 131.3 (C), 130.5 (CH), 124.3 (CH×2), 122.4 (CH), 115.5 (C-5), 113.8 (C-3), 113.4 (C-1), 104.4 (C-5'), 84.3 (C-1'), 70.5 (CH<sub>2</sub>), 57.1 (C-7'), 53.2 (C-9'), 19.1 (C-7); HRESIMS *m/z* 507.0413 [M + H]<sup>+</sup> (calcd for C<sub>24</sub>H<sub>18</sub>Cl<sub>2</sub>FO<sub>7</sub><sup>+</sup>, 507.0408).

Methyl(R)-5, 7-dichloro-4-((3, 5-difluorobenzyl) oxy)-6'-methoxy-6-methyl-3, 4'-dioxo-3H-spiro [benzofuran-2, 1'-cyclohexane]-2', 5'-diene-2'-carboxylate (**13**)

White, solid; yield 81.1%; <sup>1</sup>H NMR (500 MHz, CDCl<sub>3</sub>) δ 7.14 (1H, d, *J* = 1.4 Hz, H-3'), 7.05 (2H, overlapped), 6.76 (1H, dt, *J* = 2.2 Hz), 5.82 (1H, d, *J* = 1.4 Hz, H-5'), 5.37 (1H, d, *J* = 11.7 Hz), 5.28 (1H, d, *J* = 11.7 Hz), 3.75 (3H, s, H-7'), 3.69 (3H, s, H-9'), 2.58 (3H, s, H-7); <sup>13</sup>C NMR (125 MHz, CDCl<sub>3</sub>) δ 190.8 (C-8), 185.2 (C-4'), 168.3 (C-6'), 167.1 (C-2), 163.7 (C-8'), 162.1 (C), 150.2 (C-4), 146.3 (C-6), 140.0 (C-3'), 137.7 (C), 137.5 (C-2'), 122.1 (C), 111.3 (C-5), 111.1 (C-3), 110.1 (C-1), 104.5 (CH), 104.1 (CH), 103.9 (CH), 103.7 (C-5'), 84.2 (C-1'), 75.1 (CH<sub>2</sub>), 57.1 (C-7'), 53.2 (C-9'), 19.1 (C-7); HRESIMS *m/z* 525.0316 [M + H]<sup>+</sup> (calcd for C<sub>24</sub>H<sub>17</sub>Cl<sub>2</sub>F<sub>2</sub>O<sub>7</sub><sup>+</sup>, 525.0314).

Methyl(R)-5, 7-dichloro-4-((3, 4-difluorobenzyl) oxy)-6'-methoxy-6-methyl-3, 4'-dioxo-3H-spiro [benzofuran-2, 1'-cyclohexane]-2', 5'-diene-2'-carboxylate (**14**)

White, solid; yield 91.2%; <sup>1</sup>H NMR (500 MHz, CDCl<sub>3</sub>) δ 7.37 (1H, dt, *J* = 2.0 Hz), 7.25 (1H, m, H-3'), 7.14 (2H, overlapped), 5.82 (1H, d, *J* = 1.5 Hz, H-5'), 5.32 (1H, d, *J* = 11.0 Hz), 5.23 (1H, d, *J* = 11.0 Hz), 3.75 (3H, s, H-7'), 3.69 (3H, s, H-9'), 2.58 (3H, s, H-7); <sup>13</sup>C NMR (125 MHz, CDCl<sub>3</sub>) δ 190.8 (C-8), 185.2 (C-4'), 168.3 (C-6'), 167.1 (C-2), 163.7 (C-8'), 150.4 (C-4), 146.2 (C-6), 137.7 (C-3'), 137.5 (C-2'), 133.2 (C), 132.7 (C), 125.0 (C), 122.3 (CH), 118.1 (CH), 117.9 (CH), 117.4 (C), 117.3 (C-5), 113.9 (C-3), 113.7 (C-1), 104.5 (C-5'), 84.3 (C-1'), 75.3 (CH<sub>2</sub>), 57.1 (C-7'), 53.2 (C-9'), 19.1 (C-7); HRESIMS *m/z* 525.0325 [M + H]<sup>+</sup> (calcd for C<sub>24</sub>H<sub>17</sub>Cl<sub>2</sub>F<sub>2</sub>O<sub>7</sub><sup>+</sup>, 525.0314).

Methyl(R)-5, 7-dichloro-6'-methoxy-6-methyl-3, 4'-dioxo-4-((2, 3, 4, 5-tetrafluorobenzyl) oxy)-3H-spiro[benzofuran-2, 1'-cyclohexane]-2', 5'-diene-2'-carboxylate (**15**)

White, solid; yield 25.0%; <sup>1</sup>H NMR (500 MHz, CDCl<sub>3</sub>) δ 7.33 (1H, m), 7.14 (1H, d, *J* = 1.4 Hz, H-3'), 5.83 (1H, d, *J* = 1.4 Hz, H-5'), 5.39 (1H, d, *J* = 11.9 Hz), 5.31 (1H, d, *J* = 11.9 Hz), 3.76 (3H, s, H-7'), 3.71 (3H, s, H-9'), 2.58 (3H, s, H-7); <sup>13</sup>C NMR (125 MHz, CDCl<sub>3</sub>) δ 190.8 (C-8), 185.2 (C-4'), 168.2 (C-6'), 167.1 (C-2), 163.7 (C-8'), 149.9 (C-4), 146.3 (C-6), 137.6 (C-3'), 137.6 (C-2'), 137.6 (C), 122.3 (C), 119.9 (C), 116.2 (CH), 114.2 (C), 113.8 (C-5), 112.2 (C-3), 112.0 (C-1), 108.3 (C), 104.5 (C-5'), 84.3 (C-1'), 68.6 (CH<sub>2</sub>), 57.1 (C-7'), 53.2 (C-9'), 19.1 (C-7); HRESIMS *m/z* 561.0137 [M + H]<sup>+</sup> (calcd for C<sub>24</sub>H<sub>15</sub>Cl<sub>2</sub>F<sub>4</sub>O<sub>7</sub><sup>+</sup>, 561.0125).

Methyl(R)-5,7-dichloro-6'-methoxy-6-methyl-3, 4'-dioxo-4-((2, 3, 4-trifluorobenzyl)oxy)-3H-spiro [benzofuran-2, 1'-cyclohexane]-2', 5'-diene-2'-carboxylate (**16**)

White, solid; yield 31.0%; <sup>1</sup>H NMR (500 MHz, CDCl<sub>3</sub>) δ 7.37 (1H, m), 7.14 (1H, d, *J* = 1.4 Hz, H-3'), 6.97 (1H, m), 5.82 (1H, d, *J* = 1.4 Hz, H-5'), 5.40 (1H, d, *J* = 11.6 Hz), 5.30 (1H, d, *J* = 11.6 Hz), 3.75 (3H, s, H-7'), 3.70 (3H, s, H-9'), 2.57 (3H, s, H-7); <sup>13</sup>C NMR (125 MHz, CDCl<sub>3</sub>) δ 190.8 (C-8), 185.2 (C-4'), 168.3 (C-6'), 167.1 (C-2), 163.7 (C-8'), 150.3 (C-4), 146.2 (C-6), 137.7 (C-3'), 137.5 (C-2'), 125.1 (C), 122.4 (C), 121.0 (C-5), 113.9 (C-3), 113.9 (C-1), 112.4 (CH), 112.3 (C), 112.2 (C), 112.2 (CH), 104.5 (C-5'), 84.3 (C-1'), 69.3 (CH<sub>2</sub>), 57.1 (C-7'), 53.2 (C-9'), 19.1 (C-7); HRESIMS *m/z* 543.0213 [M + H]<sup>+</sup> (calcd for C<sub>24</sub>H<sub>16</sub>Cl<sub>2</sub>F<sub>3</sub>O<sub>7</sub><sup>+</sup>, 543.0220).

Methyl(R)-5,7-dichloro-6'-methoxy-6-methyl-3, 4'-dioxo-4-((perfluorophenyl) methoxy)-3H-spiro[benzofuran-2,1'-cyclohexane]-2', 5'-diene-2'-carboxylate (**17**)

White, solid; yield 20.0%; <sup>1</sup>H NMR (500 MHz, CDCl<sub>3</sub>) δ 7.13 (1H, d, *J* = 1.2 Hz, H-3'), 5.81 (1H, d, *J* = 1.2 Hz, H-5'), 5.55 (1H, d, *J* = 11.8 Hz), 5.38 (1H, d, *J* = 11.8 Hz), 3.75 (3H, s, H-7'), 3.70 (3H, s, H-9'), 2.57 (3H, s, H-7); <sup>13</sup>C NMR (125 MHz, CDCl<sub>3</sub>) δ 190.7 (C-8), 185.2 (C-4'), 168.3 (C-6'), 167.1 (C-2), 163.6 (C-8'), 149.8 (C-4), 146.2 (C-6), 137.6 (C-3'), 137.6 (C-2'), 135.0 (C), 127.4 (C), 122.4 (C), 117.0 (C), 114.4 (C-5), 114.1 (C-3), 113.9 (C-1), 109.7 (C), 104.5 (C-5'), 84.3 (C-1'), 63.1 (CH<sub>2</sub>), 57.1 (C-7'), 53.2 (C-9'), 19.1 (C-7); HRESIMS *m/z* 579.0034 [M + H]<sup>+</sup> (calcd for C<sub>24</sub>H<sub>14</sub>Cl<sub>2</sub>F<sub>5</sub>O<sub>7</sub><sup>+</sup>, 579.0031).

Methyl(R)-5, 7-dichloro-6'-methoxy-6-methyl-3, 4'-dioxo-4-((2-(trifluoromethyl) benzyl) oxy)-3H-spiro[benzofuran-2,1'-cyclohexane]-2', 5'-diene-2'-carboxylate (**18**)

White, solid; yield 50.0%; <sup>1</sup>H NMR (500 MHz, CDCl<sub>3</sub>) δ 8.06 (1H, d, *J* = 7.8 Hz), 7.66 (1H, d, *J* = 7.8 Hz), 7.62 (1H, t, *J* = 7.6 Hz), 7.44 (1H, t, *J* = 7.6 Hz), 7.14 (1H, d, *J* = 1.5 Hz, H-3'), 5.82 (1H, d, *J* = 1.4 Hz, H-5'), 5.48 (2H, q, *J* = 12.5 Hz), 3.74 (3H, s, H-7'), 3.70 (3H, s, H-9'), 2.60 (3H, s, H-7); <sup>13</sup>C NMR (125 MHz, CDCl<sub>3</sub>) δ 190.6 (C-8), 185.3 (C-4'), 168.4 (C-6'), 167.0 (C-2), 163.6 (C-8'), 151.0 (C-4), 146.1 (C-6), 137.7 (C-3'), 137.6 (C-2'), 135.0 (C), 132.3 (CH), 130.1 (CH), 128.2 (CH), 125.8 (CH), 125.7 (C), 125.4 (C), 122.1 (C-5), 113.7 (C-3), 113.6 (C-1), 104.5 (C-5'), 84.2 (C-1'), 72.9 (CH<sub>2</sub>), 57.1 (C-7'), 53.2 (C-9'), 19.1 (C-7); HRESIMS *m/z* 557.0386 [M + H]<sup>+</sup> (calcd for C<sub>25</sub>H<sub>18</sub>Cl<sub>2</sub>F<sub>3</sub>O<sub>7</sub><sup>+</sup>, 557.0376).

Methyl(R)-5,7-dichloro-6'-methoxy-6-methyl-3,4'-dioxo-4-((3-(trifluoromethyl)benzyl)oxy)-3H-spiro[benzofuran-2, 1'-cyclohexane]-2', 5'-diene-2'-carboxylate (**19**)

White, solid; yield 30.0%;  $^1\text{H NMR}$  (500 MHz,  $\text{CDCl}_3$ )  $\delta$  7.80 (1H, s), 7.76 (1H, d,  $J = 7.7$  Hz), 7.60 (1H, d,  $J = 7.7$  Hz), 7.50 (1H, t,  $J = 7.7$  Hz), 7.14 (1H, d,  $J = 1.3$  Hz, H-3'), 5.82 (1H, d,  $J = 1.3$  Hz, H-5'), 5.40 (1H, d,  $J = 11.4$  Hz), 5.33 (1H, d,  $J = 11.4$  Hz), 3.75 (3H, s, H-7'), 3.69 (3H, s, H-9'), 2.59 (3H, s, H-7);  $^{13}\text{C NMR}$  (125 MHz,  $\text{CDCl}_3$ )  $\delta$  190.8 (C-8), 185.2 (C-4'), 168.4 (C-6'), 167.1 (C-2), 163.7 (C-8'), 150.6 (C-4), 146.2 (C-6), 137.8 (C-3'), 137.5 (C-2'), 137.2 (C), 131.9 (C), 129.1 (CH), 125.4 (CH $\times$ 3), 122.3 (C-5), 113.8 (C-3), 113.7 (C-1), 104.5 (C-5'), 84.3 (C-1'), 75.9 (CH $_2$ ), 57.1 (C-7'), 53.2 (C-9'), 19.1 (C-7); HRESIMS  $m/z$  557.0380 [M + H] $^+$  (calcd for  $\text{C}_{25}\text{H}_{18}\text{Cl}_2\text{F}_3\text{O}_7^+$ , 557.0376).

Methyl(R)-5,7-dichloro-6'-methoxy-6-methyl-3, 4'-dioxo-4-((4-(trifluoromethyl) benzyl)oxy)-3H-spiro[benzofuran-2, 1'-cyclohexane]-2', 5'-diene-2'-carboxylate (**20**)

White, solid; yield 72.7%;  $^1\text{H NMR}$  (500 MHz,  $\text{CDCl}_3$ )  $\delta$  7.66 (2H, d,  $J = 8.3$  Hz), 7.62 (2H, d,  $J = 8.3$  Hz), 7.14 (1H, d,  $J = 1.3$  Hz, H-3'), 5.82 (1H, d,  $J = 1.3$  Hz, H-5'), 5.44 (1H, d,  $J = 11.5$  Hz), 5.35 (1H, d,  $J = 11.5$  Hz), 3.75 (3H, s, H-7'), 3.68 (3H, s, H-9'), 2.59 (3H, s, H-7);  $^{13}\text{C NMR}$  (125 MHz,  $\text{CDCl}_3$ )  $\delta$  190.8 (C-8), 185.2 (C-4'), 168.3 (C-6'), 167.1 (C-2), 163.7 (C-8'), 150.6 (C-4), 146.2 (C-6), 140.2 (C), 137.7 (C-3'), 137.5 (C-2'), 130.7 (CH), 130.5 (CH), 128.6 (CH $\times$ 2), 125.5 (C), 122.1 (C-5), 113.7 (C-3), 113.6 (C-1), 104.5 (C-5'), 84.3 (C-1'), 75.7 (CH $_2$ ), 57.1 (C-7'), 53.2 (C-9'), 19.1 (C-7); HRESIMS  $m/z$  557.0380 [M + H] $^+$  (calcd for  $\text{C}_{25}\text{H}_{18}\text{Cl}_2\text{F}_3\text{O}_7^+$ , 557.0376).

Methyl(R)-4-((3, 5-bis(trifluoromethyl)benzyl)oxy)-5, 7-dichloro-6'-methoxy-6-methyl-3, 4'-dioxo-3H-spiro[benzofuran-2, 1'-cyclohexane]-2', 5'-diene-2'-carboxylate (**21**)

White, solid; yield 66.3%;  $^1\text{H NMR}$  (500 MHz,  $\text{CDCl}_3$ )  $\delta$  8.03 (2H, s), 7.14 (1H, d,  $J = 1.3$  Hz, H-3'), 5.83 (1H, d,  $J = 1.3$  Hz, H-5'), 5.45 (1H, d,  $J = 12.0$  Hz), 5.40 (1H, d,  $J = 12.0$  Hz), 3.76 (3H, s, H-7'), 3.70 (3H, s, H-9'), 2.59 (3H, s, H-7);  $^{13}\text{C NMR}$  (125 MHz,  $\text{CDCl}_3$ )  $\delta$  190.9 (C-8), 185.2 (C-4'), 168.2 (C-6'), 167.1 (C-2), 163.8 (C-8'), 150.1 (C-4), 146.3 (C-6), 138.9 (C), 137.7 (C-3'), 137.5 (C-2'), 132.0 (C), 131.7 (CH), 128.5 (CH), 124.4 (CH), 122.45 (C), 122.43 (C), 122.3 (C), 122.1 (C-5), 114.1 (C-3), 113.8 (C-1), 104.6 (C-5'), 84.3 (C-1'), 74.9 (CH $_2$ ), 57.1 (C-7'), 53.3 (C-9'), 19.1 (C-7); HRESIMS  $m/z$  625.0253 [M + H] $^+$  (calcd for  $\text{C}_{26}\text{H}_{17}\text{Cl}_2\text{F}_6\text{O}_7^+$ , 625.0250).

Methyl(R)-5,7-dichloro-6'-methoxy-6-methyl-4-((3-nitrobenzyl)oxy)-3,4'-dioxo-3H-spiro[benzofuran-2,1'-cyclohexane]-2',5'-diene-2'-carboxylate (**22**)

White, solid; yield 50.0%;  $^1\text{H NMR}$  (500 MHz,  $\text{CDCl}_3$ )  $\delta$  8.38 (1H, s), 8.19 (1H, d,  $J = 8.0$  Hz), 7.92 (1H, d,  $J = 7.5$  Hz), 7.56 (1H, t,  $J = 7.9$  Hz), 7.13 (1H, d,  $J = 1.5$  Hz, H-3'), 5.82 (1H, d,  $J = 1.5$  Hz, H-5'), 5.40 (2H, q,  $J = 11.6$  Hz), 3.76 (s, 3H, H-7'), 3.69 (s, 3H, H-9'), 2.58 (s, 3H, H-7);  $^{13}\text{C NMR}$  (125 MHz,  $\text{CDCl}_3$ )  $\delta$  190.9 (C-8), 185.2 (C-4'), 168.3 (C-6'), 167.1 (C-2), 163.7 (C-8'), 150.2 (C-4), 148.4 (C-6), 146.3 (C), 138.3 (C), 137.7 (C-3'), 137.5 (C-2'), 134.6 (CH), 129.6 (CH), 123.5 (CH), 123.4 (CH), 122.2 (C-5), 113.9 (C-3), 113.8 (C-1), 110.1 (C), 104.5 (C-5'), 84.3 (C-1'), 75.3 (CH $_2$ ), 57.1 (C-7'), 53.3 (C-9'), 19.1 (C-7); HRESIMS  $m/z$  534.0367 [M + H] $^+$  (calcd for  $\text{C}_{24}\text{H}_{18}\text{Cl}_2\text{NO}_9^+$ , 534.0353).

Methyl(R)-5,7-dichloro-6'-methoxy-6-methyl-4-((2-methylbenzyl)oxy)-3,4'-dioxo-3H-spiro[benzofuran-2,1'-cyclohexane]-2',5'-diene-2'-carboxylate (**23**)

White, solid; yield 50.0%;  $^1\text{H NMR}$  (500 MHz,  $\text{CDCl}_3$ )  $\delta$  7.51 (1H, d,  $J = 7.50$  Hz), 7.26 (1H, t,  $J = 6.2$  Hz), 7.20 (2H, d,  $J = 8.5$  Hz), 7.15 (1H, d,  $J = 1.5$  Hz, H-3'), 5.82 (1H, d,  $J = 1.5$  Hz, H-5'), 5.38 (1H, d,  $J = 10.8$  Hz), 5.30 (1H, d,  $J = 10.8$  Hz), 3.75 (3H, s, H-7'), 3.69 (3H, s, H-9'), 2.58 (3H, s, H-7), 2.49 (3H, s);  $^{13}\text{C NMR}$  (125 MHz,  $\text{CDCl}_3$ )  $\delta$  190.6 (C-8), 185.3 (C-4'), 168.5 (C-6'), 167.0 (C-2), 163.6 (C-8'), 151.3 (C-4), 146.0 (C-6), 137.8 (C-2'), 137.7 (C-3'), 137.5 (C $\times$ 2), 134.3 (C), 130.4 (C), 130.1 (C), 128.9 (C), 126.1 (C), 122.3 (C-5), 113.8 (C-3), 113.1 (C-1), 104.4 (C-5'), 84.2 (C-1'), 75.3 (CH $_2$ ), 57.1 (C-7'), 53.2 (C-9'), 29.8 (CH $_3$ ), 19.1 (C-7); HRESIMS  $m/z$  503.0660 [M + H] $^+$  (calcd for  $\text{C}_{25}\text{H}_{21}\text{Cl}_2\text{O}_7^+$ , 503.0659).

Methyl(R)-5,7-dichloro-6'-methoxy-6-methyl-4-((3-methylbenzyl)oxy)-3,4'-dioxo-3H-spiro [benzofuran-2,1'-cyclohexane]-2',5'-diene-2'-carboxylate (**24**)

White, solid; yield 50.0%;  $^1\text{H NMR}$  (500 MHz,  $\text{CDCl}_3$ )  $\delta$  7.37 (1H, s), 7.33 (1H, d,  $J = 7.6$  Hz), 7.26 (1H, q,  $J = 7.6$  Hz), 7.15 (2H, Overlapped, H-3'), 5.82 (1H, d,  $J = 1.1$  Hz, H-5'), 5.32 (1H, d,  $J = 10.7$  Hz), 5.24 (1H, d,  $J = 10.7$  Hz), 3.74 (3H, s, H-7'), 3.68 (3H, s, H-9'), 2.59 (3H, s, H-7), 2.36 (3H, s);  $^{13}\text{C NMR}$  (125 MHz,  $\text{CDCl}_3$ )  $\delta$  190.6 (C-8), 185.3 (C-4'), 168.5 (C-6'), 167.0 (C-2), 163.6 (C-8'), 151.1 (C-4), 146.0 (C-6), 138.2 (C-2'), 137.8 (C-3'), 137.5 (C), 136.1 (C), 129.5 (CH), 129.4 (CH), 128.5 (CH), 125.8 (CH), 122.4 (C-5), 113.8 (C-3), 113.2 (C-1), 104.4 (C-5'), 84.2 (C-1'), 77.0 ( $\text{CH}_2$ ), 57.1 (C-7'), 53.2 (C-9'), 21.5 ( $\text{CH}_3$ ), 19.1 (C-7); HRESIMS  $m/z$  503.0664 [ $\text{M} + \text{H}$ ] $^+$  (calcd for  $\text{C}_{25}\text{H}_{21}\text{Cl}_2\text{O}_7^+$ , 503.0659).

Methyl(R)-5,7-dichloro-6'-methoxy-6-methyl-4-((4-methylbenzyl)oxy)-3,4'-dioxo-3H-spiro [benzofuran-2,1'-cyclohexane]-2',5'-diene-2'-carboxylate (**25**)

White, solid; yield 50.0%;  $^1\text{H NMR}$  (500 MHz,  $\text{CDCl}_3$ )  $\delta$  7.40 (2H, d,  $J = 7.9$  Hz), 7.16 (2H, d,  $J = 7.8$  Hz), 7.14 (1H, d,  $J = 1.2$  Hz, H-3'), 5.81 (1H, d,  $J = 1.2$  Hz, H-5'), 5.29 (2H, q,  $J = 10.7$  Hz), 3.73 (3H, s, H-7'), 3.67 (3H, s, H-9'), 2.57 (3H, s, H-7), 2.34 (3H, s);  $^{13}\text{C NMR}$  (125 MHz,  $\text{CDCl}_3$ )  $\delta$  190.6 (C-8), 185.3 (C-4'), 168.5 (C-6'), 167.0 (C-2), 163.6 (C-8'), 151.1 (C-4), 146.0 (C-6), 138.4 (C-2'), 137.8 (C-3'), 137.5 (C), 133.2 (C), 131.7 (CH), 130.5 (CH), 129.2 (CH), 128.9 (CH), 122.4 (C-5), 113.8 (C-3), 113.1 (C-1), 104.4 (C-5'), 84.3 (C-1'), 75.9 ( $\text{CH}_2$ ), 57.1 (C-7'), 53.2 (C-9'), 21.4 ( $\text{CH}_3$ ), 19.1 (C-7); HRESIMS  $m/z$  503.0663 [ $\text{M} + \text{H}$ ] $^+$  (calcd for  $\text{C}_{25}\text{H}_{21}\text{Cl}_2\text{O}_7^+$ , 503.0659).

Methyl(R)-4-((4-(tert-butyl)benzyl)oxy)-5,7-dichloro-6'-methoxy-6-methyl-3,4'-dioxo-3H-spiro [benzofuran-2,1'-cyclohexane]-2',5'-diene-2'-carboxylate (**26**)

White, solid; yield 42.0%;  $^1\text{H NMR}$  (500 MHz,  $\text{CDCl}_3$ )  $\delta$  7.48 (2H, d,  $J = 8.3$  Hz), 7.39 (2H, d,  $J = 8.3$  Hz), 7.15 (1H, d,  $J = 1.5$  Hz, H-3'), 5.82 (1H, d,  $J = 1.5$  Hz, H-5'), 5.33 (1H, d,  $J = 10.7$  Hz), 5.25 (1H, d,  $J = 10.7$  Hz), 3.73 (3H, s, H-7'), 3.67 (3H, s, H-9'), 2.59 (3H, s, H-7), 1.32 (9H, overlapped);  $^{13}\text{C NMR}$  (125 MHz,  $\text{CDCl}_3$ )  $\delta$  190.6 (C-8), 185.3 (C-4'), 168.5 (C-6'), 167.0 (C-2), 163.6 (C-8'), 151.6 (C-4), 151.2 (C), 146.0 (C-6), 137.8 (C-3'), 137.5 (C-2'), 133.3 (C), 128.5 (CH $\times$ 2), 125.5 (CH $\times$ 2), 122.4 (C-5), 113.8 (C-3), 113.1 (C-1), 104.4 (C-5'), 84.3 (C-1'), 76.8 ( $\text{CH}_2$ ), 57.1 (C-7'), 53.2 (C-9'), 34.7 (C), 31.4 ( $\text{CH}_3 \times 3$ ), 19.1 (C-7); HRESIMS  $m/z$  545.1131 [ $\text{M} + \text{H}$ ] $^+$  (calcd for  $\text{C}_{28}\text{H}_{27}\text{Cl}_2\text{O}_7^+$ , 545.1128).

Methyl(R)-4-([1,1'-biphenyl]-4-ylmethoxy)-5,7-dichloro-6'-methoxy-6-methyl-3,4'-dioxo-3H-spiro [benzofuran-2,1'-cyclohexane]-2',5'-diene-2'-carboxylate (**27**)

White, solid; yield 81.0%;  $^1\text{H NMR}$  (500 MHz,  $\text{CDCl}_3$ )  $\delta$  7.61 (6H, overlapped), 7.44 (2H, t,  $J = 7.8$  Hz), 7.35 (1H, dt,  $J = 7.3, 1.2$  Hz), 7.16 (1H, d,  $J = 1.4$  Hz, H-3'), 5.82 (1H, d,  $J = 1.4$  Hz, H-5'), 5.43 (1H, d,  $J = 10.9$  Hz), 5.34 (1H, d,  $J = 10.9$  Hz), 3.74 (3H, s, H-7'), 3.67 (3H, s, H-9'), 2.60 (3H, s, H-7);  $^{13}\text{C NMR}$  (125 MHz,  $\text{CDCl}_3$ )  $\delta$  190.6 (C-8), 185.2 (C-4'), 168.4 (C-6'), 167.1 (C-2), 163.6 (C-8'), 151.0 (C-4), 146.0 (C-6), 141.5 (C), 140.8 (C), 137.8 (C-3'), 137.5 (C-2'), 135.2 (C), 129.2 (CH $\times$ 2), 128.9 (CH $\times$ 2), 127.5 (CH), 127.3 (CH $\times$ 2), 127.2 (CH $\times$ 2), 122.4 (C-5), 113.8 (C-3), 113.3 (C-1), 104.4 (C-5'), 84.3 (C-1'), 76.6 ( $\text{CH}_2$ ), 57.1 (C-7'), 53.2 (C-9'), 19.1 (C-7); HRESIMS  $m/z$  565.0816 [ $\text{M} + \text{H}$ ] $^+$  (calcd for  $\text{C}_{30}\text{H}_{23}\text{Cl}_2\text{O}_7^+$ , 565.0815).

Methyl(R)-5,7-dichloro-4-((2'-cyano-[1,1'-biphenyl]-4-yl)methoxy)-6'-methoxy-6-methyl-3,4'-dioxo-3H-spiro [benzofuran-2,1'-cyclohexane]-2',5'-diene-2'-carboxylate (**28**)

White, solid; yield 32.0%;  $^1\text{H NMR}$  (500 MHz,  $\text{CDCl}_3$ )  $\delta$  7.76 (1H, dd,  $J = 7.7, 1.0$  Hz), 7.69 (2H, d,  $J = 8.1$  Hz), 7.65 (1H, ddd,  $J = 7.7, 1.0$  Hz), 7.58 (2H, d,  $J = 8.2$  Hz), 7.51 (1H, d,  $J = 7.3$  Hz), 7.45 (1H, ddd,  $J = 7.6, 1.0$  Hz), 7.15 (1H, d,  $J = 1.2$  Hz, H-3'), 5.83 (1H, d,  $J = 1.2$  Hz, H-5'), 5.43 (2H, q,  $J = 11.1$  Hz), 5.34 (2H, q,  $J = 11.1$  Hz), 3.75 (s, 3H, H-7'), 3.70 (s, 3H, H-9'), 2.60 (s, 3H, H-7);  $^{13}\text{C NMR}$  (125 MHz,  $\text{CDCl}_3$ )  $\delta$  190.7 (C-8), 185.3 (C-4'), 168.5 (C-6'), 167.1 (C-2), 163.7 (C-8'), 151.0 (C-4), 146.2 (C-6), 145.2 (C), 138.4 (C), 137.8 (C-3'), 137.6 (C-2'), 136.9 (C), 133.9 (C), 133.0 (CH), 130.2 (CH), 129.0 (CH $\times$ 2), 129.0 (CH $\times$ 2), 127.8 (CH), 122.4 (CH), 118.8 (C-5), 113.8 (C-3), 113.4 (C-1), 111.4 (C), 104.5 (C-5'), 84.3 (C-1'), 76.4 ( $\text{CH}_2$ ), 57.1

(C-7'), 53.2 (C-9'), 19.1 (C-7); HRESIMS  $m/z$  590.0770 [M + H]<sup>+</sup> (calcd for C<sub>31</sub>H<sub>22</sub>Cl<sub>2</sub>NO<sub>7</sub><sup>+</sup>, 590.0768).

Methyl(R)-5, 7-dichloro-4-((2-cyanobenzyl) oxy)-6'-methoxy-6-methyl-3, 4'-dioxo-3H-spiro [benzofuran-2, 1'-cyclohexane]-2', 5'-diene-2'-carboxylate (**29**)

White, solid; yield 87.7%; <sup>1</sup>H NMR (500 MHz, CDCl<sub>3</sub>) δ 7.90 (1H, d, *J* = 7.5 Hz), 7.68 (1H, dd, *J* = 7.5, 1.0 Hz), 7.64 (1H, ddd, *J* = 7.5, 1.0 Hz), 7.44 (1H, ddd, *J* = 7.5, 1.0 Hz), 7.14 (1H, d, *J* = 1.0 Hz, H-3'), 5.82 (1H, d, *J* = 1.5 Hz, H-5'), 5.47 (2H, q, *J* = 12.0 Hz), 3.75 (3H, s, H-7'), 3.70 (3H, s, H-9'), 2.59 (3H, s, H-7); <sup>13</sup>C NMR (125 MHz, CDCl<sub>3</sub>) δ 190.7 (C-8), 185.2 (C-4'), 168.3 (C-6'), 167.1 (C-2), 163.6 (C-8'), 150.5 (C-4), 146.2 (C-6), 139.6 (C), 137.6 (C-3'), 137.5 (C-2'), 133.1 (C), 132.8 (CH), 129.9 (CH), 129.0 (CH), 122.4 (CH), 117.1 (C-5), 113.9 (C-3), 113.7 (C-9), 111.9 (C), 104.5 (C-5'), 84.3 (C-1'), 74.0 (CH<sub>2</sub>), 57.1 (C-7'), 53.2 (C-9'), 19.1 (C-7); HRESIMS  $m/z$  514.0456 [M + H]<sup>+</sup> (calcd for C<sub>25</sub>H<sub>18</sub>Cl<sub>2</sub>NO<sub>7</sub><sup>+</sup>, 514.0455).

Methyl(R)-5, 7-dichloro-4-((4-cyanobenzyl) oxy)-6'-methoxy-6-methyl-3, 4'-dioxo-3H-spiro [benzofuran-2, 1'-cyclohexane]-2', 5'-diene-2'-carboxylate (**30**)

White, solid; yield 85.3%; <sup>1</sup>H NMR (500 MHz, CDCl<sub>3</sub>) δ 7.66 (4H, overlapped), 7.13 (1H, d, *J* = 1.3 Hz, H-3'), 5.82 (1H, d, *J* = 1.3 Hz, H-5'), 5.41 (1H, d, *J* = 11.9 Hz), 5.33 (1H, d, *J* = 11.9 Hz), 3.75 (3H, s, H-7'), 3.69 (3H, s, H-9'), 2.59 (3H, s, H-7); <sup>13</sup>C NMR (125 MHz, CDCl<sub>3</sub>) δ 190.8 (C-8), 185.1 (C-4'), 168.2 (C-6'), 167.1 (C-2), 163.7 (C-8'), 150.3 (C-4), 146.3 (C-6), 141.5 (C), 137.7 (C-3'), 137.5 (C-2'), 132.4 (CH×2), 128.8 (CH×2), 122.1 (C), 118.8 (C-5), 113.8 (C-3), 113.7 (C-1), 112.3 (C), 104.5 (C-5'), 84.3 (C-1'), 75.5 (CH<sub>2</sub>), 57.1 (C-7'), 53.2 (C-9'), 19.1 (C-7); HRESIMS  $m/z$  514.0460 [M + H]<sup>+</sup> (calcd for C<sub>25</sub>H<sub>18</sub>Cl<sub>2</sub>NO<sub>7</sub><sup>+</sup>, 514.0455).

Methyl(R)-5,7-dichloro-4-((2-chloro-4-fluorobenzyl)oxy)-6'-methoxy-6-methyl-3, 4'-dioxo-3H-spiro [benzofuran-2, 1'-cyclohexane]-2', 5'-diene-2'-carboxylate (**31**)

White, solid; yield 77.6%; <sup>1</sup>H NMR (500 MHz, CDCl<sub>3</sub>) δ 7.72 (1H, dd, *J* = 6.2, 2.3 Hz), 7.14 (2H, overlapped), 7.01 (1H, ddd, *J* = 8.5, 2.4 Hz, H-3'), 5.82 (1H, d, *J* = 1.0 Hz, H-5'), 5.42 (1H, d, *J* = 12.0 Hz), 5.35 (1H, d, *J* = 12.0 Hz), 3.75 (3H, s, H-7'), 3.70 (3H, s, H-9'), 2.58 (3H, s, H-7); <sup>13</sup>C NMR (125 MHz, CDCl<sub>3</sub>) δ 190.7 (C-8) 185.2 (C-4'), 168.4 (C-6'), 167.0 (C-2), 163.7 (C-8'), 161.6 (C), 150.8 (C-4), 146.1 (C-6), 137.7 (C-3'), 137.6 (C-2'), 132.0 (CH), 122.3 (C), 117.0 (CH), 116.8 (C), 114.4 (C), 114.2 (C-5), 113.7 (C-3), 113.6 (C-1), 104.5 (C-5'), 73.4 (CH<sub>2</sub>), 57.1 (C-7'), 53.2 (C-9'), 19.1 (C-7); HRESIMS  $m/z$  541.0029 [M + H]<sup>+</sup> (calcd for C<sub>24</sub>H<sub>17</sub>Cl<sub>3</sub>FO<sub>7</sub><sup>+</sup>, 541.0018).

Methyl(R)-5, 7-dichloro-4-((3-chloro-4-fluorobenzyl) oxy)-6'-methoxy-6-methyl-3, 4'-dioxo-3H-spiro [benzofuran-2, 1'-cyclohexane]-2', 5'-diene-2'-carboxylate (**32**)

White, solid; yield 78.5%; <sup>1</sup>H NMR (500 MHz, CDCl<sub>3</sub>) δ 7.58 (1H, dd, *J* = 7.0, 1.5 Hz), 7.42 (1H, m), 7.13 (2H, overlapped, H-3'), 5.82 (1H, d, *J* = 0.5 Hz, H-5'), 5.29 (1H, d, *J* = 11.0 Hz), 5.23 (1H, d, *J* = 11.0 Hz), 3.75 (3H, s, H-7'), 3.69 (3H, s, H-9'), 2.58 (3H, s, H-7); <sup>13</sup>C NMR (125 MHz, CDCl<sub>3</sub>) δ 190.7 (C-8), 185.1 (C-4'), 168.2 (C-6'), 167.0 (C-2), 163.6 (C-8'), 157.1 (C), 150.2 (C-4), 146.1 (C-6), 137.6 (C-3'), 137.4 (C-2'), 133.1 (C), 128.6 (CH×2), 122.2 (CH), 116.7 (C), 116.5 (C-5), 113.7 (C-3), 113.6 (C-1), 104.4 (C-5'), 84.2 (C-1'), 75.1 (CH<sub>2</sub>), 57.0 (C-7'), 53.1 (C-9'), 19.0 (C-7); HRESIMS  $m/z$  541.0031 [M + H]<sup>+</sup> (calcd for C<sub>24</sub>H<sub>17</sub>Cl<sub>3</sub>FO<sub>7</sub><sup>+</sup>, 541.0018).

Methyl(R)-5, 7-dichloro-4-((3-chloro-2-fluorobenzyl) oxy)-6'-methoxy-6-methyl-3, 4'-dioxo-3H-spiro [benzofuran-2, 1'-cyclohexane]-2', 5'-diene-2'-carboxylate (**33**)

White, solid; yield 94.5%; <sup>1</sup>H NMR (500 MHz, CDCl<sub>3</sub>) δ 7.57 (1H, t, *J* = 6.5 Hz), 7.38 (1H, t, *J* = 7.5 Hz), 7.14 (1H, s, H-3'), 7.10 (1H, t, *J* = 8.0 Hz), 5.82 (1H, s, H-5'), 5.45 (1H, d, *J* = 11.5 Hz), 5.34 (1H, d, *J* = 11.5 Hz), 3.75 (3H, s, H-7'), 3.70 (3H, s, H-9'), 2.58 (3H, s, H-7); <sup>13</sup>C NMR (CDCl<sub>3</sub>, 125 MHz) δ 190.7 (C-8), 185.2 (C-4'), 168.4 (C-6'), 167.1 (C-2), 163.6 (C-8'), 157.4 (C), 155.4 (C), 150.6 (C-4), 146.2 (C-6), 137.7 (C-3'), 137.5 (C-2'), 131.0 (C), 129.4 (CH×2), 124.8 (CH), 124.7 (CH), 122.4 (C-5), 113.8 (C-3), 113.7 (C-1), 104.5 (C-5'), 84.3 (C-1'),

70.1 (CH<sub>2</sub>), 57.1 (C-7'), 53.2 (C-9'), 19.1 (C-7); HRESIMS *m/z* 541.0021[M + H]<sup>+</sup> (calcd for C<sub>24</sub>H<sub>17</sub>Cl<sub>3</sub>FO<sub>7</sub><sup>+</sup>, 541.0018).

Methyl(R)-5, 7-dichloro-4-((4-chloro-2-fluorobenzyl) oxy)-6'-methoxy-6-methyl-3, 4'-dioxo-3H-spiro [benzofuran-2, 1'-cyclohexane]-2', 5'-diene-2'-carboxylate (34)

White, solid; yield 72.4%; <sup>1</sup>H NMR (500 MHz, CDCl<sub>3</sub>) δ 7.58 (1H, t, *J* = 8.0 Hz), 7.15 (2H, dd, *J* = 9.5, 1.5 Hz), 7.10 (1H, dd, *J* = 9.5, 1.5 Hz, H-3'), 5.82 (1H, d, *J* = 1.2 Hz, H-5'), 5.39 (1H, d, *J* = 11.6 Hz), 5.30 (1H, d, *J* = 11.6 Hz), 3.75 (3H, s, H-7'), 3.69 (3H, s, H-9'), 2.57 (3H, s, H-7); <sup>13</sup>C NMR (CDCl<sub>3</sub>, 125 MHz) δ 190.7 (C-8), 185.2 (C-4'), 168.4 (C-6'), 167.1 (C-2), 163.7 (C-8'), 150.5 (C-4), 146.1 (C-6), 137.7 (C-3'), 137.5 (C-2'), 132.1 (CH), 132.1 (C), 124.8 (CH), 124.7 (C), 122.4 (C), 116.4 (CH), 116.2 (C-5), 113.8 (C-3), 113.7 (C-1), 104.5 (C-5'), 84.3 (C-1'), 69.7 (CH<sub>2</sub>), 57.1 (C-7'), 53.2 (C-9'), 19.1 (C-7); HRESIMS *m/z* 541.0023 [M + H]<sup>+</sup> (calcd for C<sub>24</sub>H<sub>17</sub>Cl<sub>3</sub>FO<sub>7</sub><sup>+</sup>, 541.0018).

Methyl(R)-4-((4-bromo-2-fluorobenzyl) oxy)-5,7-dichloro-6'-methoxy-6-methyl-3, 4'-dioxo-3H-spiro [benzofuran-2, 1'-cyclohexane]-2', 5'-diene-2'-carboxylate (35)

White, solid; yield 52.0%; <sup>1</sup>H NMR (500 MHz, CDCl<sub>3</sub>) δ 7.52 (1H, t, *J* = 8.0 Hz), 7.30 (1H, dd, *J* = 8.0, 1.5 Hz), 7.25 (1H, dd, *J* = 8.0, 2.0 Hz), 7.14 (1H, d, *J* = 1.5 Hz, H-3'), 5.82 (1H, d, *J* = 1.5 Hz, H-5'), 5.38 (1H, d, *J* = 12.0 Hz), 5.29 (1H, d, *J* = 12.0 Hz), 3.75 (3H, s, H-7'), 3.69 (3H, s, H-9'), 2.57 (3H, s, H-7); <sup>13</sup>C NMR (125 MHz, CDCl<sub>3</sub>) δ 190.7 (C-8), 185.2 (C-4'), 168.3 (C-6'), 167.1 (C-2), 163.6 (C-8'), 161.7 (C), 159.7 (C), 150.5 (C-4), 146.1 (C-6), 137.7 (C-3'), 137.5 (C-2'), 132.3 (C), 127.7 (CH), 122.4 (CH), 119.3 (CH), 119.1 (C-5), 113.8 (C-3), 113.7 (C-1), 104.5 (C-5') 84.3 (C-1'), 69.7 (CH<sub>2</sub>), 57.1 (C-7'), 53.2 (C-9'), 19.1 (C-7); HRESIMS *m/z* 584.9522 [M + H]<sup>+</sup> (calcd for C<sub>24</sub>H<sub>17</sub>BrCl<sub>2</sub>FO<sub>7</sub><sup>+</sup>, 584.9513).

Methyl(R)-5, 7-dichloro-4-((2-cyano-5-fluorobenzyl) oxy)-6'-methoxy-6-methyl-3, 4'-dioxo-3H-spiro [benzofuran-2, 1'-cyclohexane]-2', 5'-diene-2'-carboxylate (36)

White solid; yield 60.0%; <sup>1</sup>H NMR (500 MHz, CDCl<sub>3</sub>) δ 7.67 (2H, m), 7.14 (2H, ddd, *J* = 9.2, 1.3 Hz, H-3'), 5.83 (1H, d, *J* = 1.3 Hz, H-5'), 5.47 (2H, q, *J* = 12.8 Hz), 3.76 (3H, s, H-7'), 3.71 (3H, s, H-9'), 2.60 (3H, s, H-7); <sup>13</sup>C NMR (125 MHz, CDCl<sub>3</sub>) δ 190.8 (C-8), 185.2 (C-4'), 168.2 (C-6'), 167.1 (C-2), 166.3 (C-8'), 163.7 (C), 150.1 (C-4), 146.3 (C-6), 137.6 (C-3'), 137.6 (C-2'), 135.1 (C), 135.1 (CH), 122.3 (CH), 117.2 (CH), 117.0 (C), 116.6 (C), 116.3 (C-5), 114.3 (C-3), 113.8 (C-1), 104.6 (C-5'), 84.3 (C-1'), 73.2 (CH<sub>2</sub>), 57.2 (C-7'), 53.3 (C-9'), 19.1 (C-7); HRESIMS *m/z* 532.0361 [M + H]<sup>+</sup> (calcd for C<sub>25</sub>H<sub>17</sub>Cl<sub>2</sub>FNO<sub>7</sub><sup>+</sup>, 532.0361).

Methyl(R)-5,7-dichloro-4-ethoxy-6'-methoxy-6-methyl-3,4'-dioxo3Hspiro[benzofuran-2, 1'-cyclohexane]-2',5'-diene-2'-carboxylate (37)

White, solid; yield 85.0%; <sup>1</sup>H NMR (500 MHz, CDCl<sub>3</sub>) δ 7.12 (1H, d, *J* = 1.5 Hz, H-3'), 5.80 (1H, s, H-5'), 4.34 (2H, dq, *J* = 7.0 Hz), 3.73 (3H, s, H-7'), 3.68 (3H, s, H-9'), 2.58 (3H, s, H-7), 1.43 (3H, t, *J* = 7.0 Hz), <sup>13</sup>C NMR (125 MHz, CDCl<sub>3</sub>) δ 190.4 (C-8), 185.3 (C-4'), 168.6 (C-6'), 167.0 (C-2), 163.6 (C-8'), 151.6 (C-4), 145.8 (C-6), 137.9 (C-3'), 137.5 (C-2'), 122.3 (C-5), 113.8 (C-3), 112.9 (C-1), 104.4 (C-5'), 84.3 (C-1'), 71.9 (CH<sub>2</sub>), 57.1 (C-7'), 53.2 (C-9'), 19.1 (C-7), 15.6 (CH<sub>3</sub>); HRESIMS *m/z* 427.0349 [M + H]<sup>+</sup> (calcd for C<sub>19</sub>H<sub>17</sub>Cl<sub>2</sub>O<sub>7</sub><sup>+</sup>, 427.0346).

### 3.5. Insecticidal Activity

The neonate larvae of *Helicoverpa armigera* Hübner were used to assess the insecticidal activity. The positive control was azadirachtin and DMSO was the negative control. Serial dilutions of the tested compounds were added alongside the positive control at 200, 100, 50, 25 and 12.5 μL/well with three replicates per treatment to the artificial diet for the newly hatched larvae while bioassay diet was placed into the six-well plates. New larvae were hatched at 25 °C and relative humidity of 80%. The number of dead larvae was recorded after treatments for 2, 4, 6 and 8 days [26].

### 3.6. Antibacterial Activity

The methods described by Fromtling et al. were used for the evaluation of antibacterial activities [27]. Ciprofloxacin and sea-nine 211 were used as positive controls. Bacterial species were cultured at 37 °C for 8 h in LB medium and diluted to 10<sup>6</sup> cfu/mL, using 96-well microplates, having 2 µL test sample and 198 µL of bacterial solutions. The plates were incubated at 37 °C for 24 h while DMSO was used as the negative control.

## 4. Conclusions

In summary, 36 new derivatives of marine-derived geodin (**1**) were semisynthesized successfully via one mild step reaction with high yields. Among them, **15** showed significant insecticidal activity equivalent to the positive drug, azadirachtin. Meanwhile, **37** showed selective antibacterial activity against *P. aeruginosa*. The results revealed that modification of the 4-OH and introduction of halogen atoms, especially fluorine and chlorine atoms, could enhance the insecticidal and antibacterial activities of **1**. These findings bring further evidence that geodin derivatives are active and provide new information supporting the importance of continued studies into the structure–activity relationships of griseofulvin analogs.

**Supplementary Materials:** The following supporting information can be downloaded at: <https://www.mdpi.com/article/10.3390/md20020082/s1>, Figures S1–S112: <sup>1</sup>H, <sup>13</sup>C-NMR and HRESIMS data and charts of all compounds.

**Author Contributions:** R.C., G.S. and Q.Z. contributed to extraction, isolation, identification, semisynthesis and manuscript preparation; Y.-X.Q. and J.H. contributed to investigation; C.-L.S. contributed to NMR analysis and structure elucidation; G.-Y.C. and C.-J.Z. contributed to biological evaluation; J.-Y.Z. and M.-Y.W. were the project leaders organizing and guiding the experiments and manuscript writing. All authors have read and agreed to the published version of the manuscript.

**Funding:** This work was supported by the Program of National Natural Science Foundation of China (Nos. U1706210, 41776141 and 41322037), the 2021 Provincial Postdoctoral Innovation Project (Shandong) (No. 862105033029), the Qingdao Postdoctoral Applied Research Project (No. 862105040001), the Research Fund of State Key Laboratory for Marine Corrosion and Protection of Luoyang Ship Material Research Institute (LSMRI) [No. KF190402], Key Laboratory of Tropical Medicinal Resource Chemistry of Ministry of Education, Hainan Normal University (RDZH2021003) and the Taishan Scholars Program, China (No. tsqn20161010).

**Institutional Review Board Statement:** Not applicable.

**Data Availability Statement:** Data are contained within the article or Supplementary Materials.

**Conflicts of Interest:** The authors declare no conflict of interest.

## References

1. Yao, S.Y.; Yang, Y.; Xue, Y.Y.; Zhao, W.L.; Liu, X.G.; Du, M.F.; Yin, X.M.; Guan, R.B.; Wei, J.Z.; An, S.H. New insights on the effects of spinosad on the development of *Helicoverpa armigera*. *Ecotox. Environ. Saf.* **2021**, *221*, 112452. [[CrossRef](#)] [[PubMed](#)]
2. Rahimi, V.; Hajizadeh, J.; Zibae, A.; Sendi, J.J. Effect of *polygonum persicaria* (polygonales: Polygonaceae) extracted agglutinin on life table and antioxidant responses in *Helicoverpa armigera* (Lepidoptera: Noctuidae) larvae. *J. Econ. Entomol.* **2018**, *111*, 662–671. [[CrossRef](#)] [[PubMed](#)]
3. Jones, M.C.; Parry, H.; Tay, T.W.; Reynolds, R.D.; Chapman, W.J. Movement ecology of pest *Helicoverpa*: Implications for ongoing spread. *Annu. Rev. Entomol.* **2019**, *64*, 277–295. [[CrossRef](#)] [[PubMed](#)]
4. Yuan, X.L.; Wang, X.F.; Xu, K.; Li, W.; Chen, D.; Zhang, P. Characterization of a new insecticidal anthraquinone derivative from an endophyte of *Acremonium vitellinum* against *Helicoverpa armigera*. *J. Agric. Food Chem.* **2020**, *68*, 11480–11487. [[CrossRef](#)]
5. Bilal, M.; Freed, S.; Ashraf, Z.M.; Syed Muhammad Zaka, M.S.; Khan, B.M. Activity of acetylcholinesterase and acid and alkaline phosphatases in different insecticide-treated *Helicoverpa armigera* (Hübner). *Environ. Sci. Pollut. Res.* **2018**, *25*, 22903–22910. [[CrossRef](#)]
6. Newman, J.D.; Cragg, M.G. Natural products as sources of new drugs over the nearly four decades from 01/1981 to 09/2019. *J. Nat. Prod.* **2020**, *83*, 770–803. [[CrossRef](#)]

7. Wang, T.N.; Li, L.; Zhou, Y.N.; Lu, A.D.; Li, H.Y.; Chen, J.X.; Duan, Z.Y.; Wang, Q.M. Structural simplification of marine natural products: Discovery of hamacanthin derivatives containing indole and piperazinone as novel antiviral and anti-phytopathogenic-fungus agents. *J. Agric. Food Chem.* **2021**, *69*, 10093–10103. [[CrossRef](#)]
8. Li, L.; Zou, J.Y.; Xu, C.J.; You, S.Y.; Li, Y.Q.; Wang, Q.M. Synthesis and anti-tobacco mosaic virus/fungicidal/insecticidal/antitumor bioactivities of natural product hemigossypol and its derivatives. *J. Agric. Food Chem.* **2021**, *69*, 1224–1233. [[CrossRef](#)]
9. Shao, C.L.; Wu, H.X.; Wang, C.Y.; Liu, Q.A.; Xu, Y.; Wei, M.Y.; Qian, P.Y.; Gu, Y.C.; Zheng, C.J.; She, Z.G.; et al. Potent antifouling resorcylic acid lactones from the gorgonian-derived fungus *Cochliobolus lunatus*. *J. Nat. Prod.* **2011**, *74*, 629–633. [[CrossRef](#)]
10. Jia, Y.L.; Wei, M.Y.; Chen, H.Y.; Guan, F.F.; Wang, C.Y.; Shao, C.L. (+)- and (–)-Pestaloxazine A, a pair of antiviral enantiomeric alkaloid dimers with a symmetric spiro[oxazinane-piperazinedione] skeleton from *Pestalotiopsis* sp. *Org. Lett.* **2015**, *17*, 4216–4219. [[CrossRef](#)]
11. Hou, X.M.; Li, Y.Y.; Shi, Y.W.; Fang, Y.W.; Chao, R.; Gu, Y.C.; Wang, C.Y.; Shao, C.L. Integrating molecular networking and <sup>1</sup>h nmr to target the isolation of chrysoseamides from a library of marine-derived *Penicillium* fungi. *J. Org. Chem.* **2019**, *84*, 1228–1237. [[CrossRef](#)]
12. Hou, X.M.; Liang, T.M.; Guo, Z.Y.; Wang, C.Y.; Shao, C.L. Discovery, absolute assignments, and total synthesis of aspersiamides A–C and their potent activity against *Mycobacterium marinum*. *Chem. Commun.* **2019**, *55*, 1104–1107. [[CrossRef](#)]
13. Chao, R.; Hou, X.M.; Xu, W.F.; Hai, Y.; Wei, M.Y.; Wang, C.Y.; Gu, Y.C.; Shao, C.L. Targeted isolation of asperheptatides from a coral-derived fungus using LC-MS/MS-based molecular networking and antitubercular activities of modified cinnamate derivatives. *J. Nat. Prod.* **2021**, *84*, 11–19. [[CrossRef](#)]
14. Hai, Y.; Wei, M.Y.; Wang, C.Y.; Gu, Y.C.; Shao, C.L. The intriguing chemistry and biology of sulfur-containing natural products from marine microorganisms (1987–2020). *Mar. Life Sci. Technol.* **2021**, *3*, 488–518. [[CrossRef](#)]
15. Xu, W.F.; Wu, N.N.; Wu, Y.W.; Qi, Y.X.; Wei, M.Y.; Pineda, M.L.; Ng, G.M.; Spadafora, C.; Zheng, J.Y.; Lu, L.; et al. Structure modification, antialgal, antiplasmodial, and toxic evaluations of a series of new marine-derived 14-membered resorcylic acid lactone derivatives. *Mar. Life Sci. Technol.* **2021**. [[CrossRef](#)]
16. Rønneest, H.M.; Rebacz, B.; Markworth, L.; Terp, H.A.; Larsen, O.T.; Krämer, A.; Clausen, H.M. Synthesis and Structure-activity relationship of griseofulvin analogues as inhibitors of centrosomal clustering in cancer cells. *J. Med. Chem.* **2009**, *52*, 3342–3347. [[CrossRef](#)]
17. Gulab, S.; Mou, X.F.; Fang, Y.W.; Liang, T.M.; Wei, M.Y.; Chen, G.Y.; Shao, C.L. Secondary metabolites isolated from the soft coral-derived fungus *Aspergillus* sp. from the South China Sea. *Chem. Nat. Compd.* **2018**, *54*, 547–549.
18. Rinderknecht, H.; Ward, J.L.; Bergel, F.; Morrison, A.L. Studies on antibiotic II Bacteriological activity and possible mode of action of certain nonnitrogenous natural and synthetic antibiotics. *J. Biochem.* **1947**, *41*, 463–469. [[CrossRef](#)]
19. Sato, S.; Okusa, N.; Ogawa, A.; Ikenoue, T.; Seki, T.; Tsuji, T. Identification and preliminary SAR studies of (+) geodin as a glucose uptake stimulator for rat adipocytes. *J. Antibiot.* **2005**, *58*, 583–589. [[CrossRef](#)]
20. Shinohara, C.; Chikanishi, T.; Nakashima, S.; Hashimoto, A.; Hamanaka, A.; Endo, A.; Hasumi, K. Enhancement of Fibrinolytic Activity of Vascular Endothelial Cells by Chaetoglobosin A, Crinipellin B, Geodin and Triticone B. *J. Antibiot.* **2000**, *53*, 262–268. [[CrossRef](#)]
21. Zou, X.Z.; Qiu, Z.X. Syntheses of 4-methoxymethylbenzyl permethrinates containing fluorine and their insecticidal activity. *J. Fluor. Chem.* **2002**, *116*, 173–179. [[CrossRef](#)]
22. Chen, Y.W.; Li, Y.X.; Pan, L.; Liu, J.B.; Wan, Y.Y.; Chen, W.; Xiong, L.X.; Yang, N.; Song, H.B. Synthesis, insecticidal activities and SAR of novel phthalamides targeting calcium channel. *Bioorgan. Med. Chem.* **2014**, *22*, 6366–6379. [[CrossRef](#)]
23. Zhao, Y.Y.; Gao, L.; Li, H.G.; Sun, P.W.; Meng, F.F.; Zhang, Y.; Xie, Y.T.; Sun, B.Q.; Zhou, S.; Ma, Y.; et al. Synthesis, insecticidal activities, and structure–activity relationship of phenylpyrazole derivatives containing a fluoro-substituted benzene moiety. *J. Agric. Food Chem.* **2020**, *68*, 11282–11289. [[CrossRef](#)]
24. Guo, Y.; Yan, Y.Y.; Yu, X.; Wang, Y.; Zhi, X.Y.; Hu, Y.; Xu, H. Synthesis and insecticidal activity of some novel fraxinellone-based esters. *J. Agric. Food Chem.* **2012**, *60*, 7016–7021. [[CrossRef](#)]
25. Wu, Q.L.; Cai, J.L.; Zhao, F.H.; Zhou, Z.Y.; Yang, D.Y.; Qin, Z.H. Synthesis and insecticidal activity of the fluorinated galegine analogues. *Nat. Prod. Res.* **2021**, *35*, 5773–5777. [[CrossRef](#)]
26. Bai, M.; Zheng, C.J.; Huang, G.L.; Mei, R.Q.; Wang, B.; Luo, Y.P.; Zheng, C.; Niu, Z.G.; Chen, G.Y. Bioactive meroterpenoids and isocoumarins from the mangrove-derived fungus *Penicillium* sp. TGM112. *J. Nat. Prod.* **2019**, *82*, 1155–1164. [[CrossRef](#)] [[PubMed](#)]
27. Fromtling, R.A.; Galgiani, J.N.; Pfaller, M.A.; Espinel-Ingroff, A.; Bartizal, K.F.; Bartlett, M.S.; Body, B.A.; Frey, C.; Hall, G.; Roberts, G.D.; et al. Multicenter evaluation of a broth microdilution antifungal susceptibility test for yeasts. *Antimicrob. Agents Chemother.* **1993**, *37*, 39–45. [[CrossRef](#)] [[PubMed](#)]





## Article

# A Novel Peptide Derived from *Arca inflata* Induces Apoptosis in Colorectal Cancer Cells through Mitochondria and the p38 MAPK Pathway

Chunlei Li <sup>1,2,†</sup>, Sirui Zhang <sup>3,†</sup>, Jianhua Zhu <sup>1,4</sup>, Weijuan Huang <sup>3</sup>, Yuanyuan Luo <sup>1</sup>, Hui Shi <sup>1</sup>, Dongbo Yu <sup>5</sup>, Ligo Chen <sup>2,6,\*</sup>, Liyan Song <sup>1,3,\*</sup> and Rongmin Yu <sup>1,2,4,\*</sup>

- <sup>1</sup> Biotechnological Institute of Chinese Materia Medica, Jinan University, 601 Huangpu Avenue West, Guangzhou 510632, China; lichunlei@jnu.edu.cn (C.L.); tzjh@jnu.edu.cn (J.Z.); yyluo000@163.com (Y.L.); sh613050@163.com (H.S.)
  - <sup>2</sup> Integrated Chinese and Western Medicine Postdoctoral Research Station, Jinan University, Guangzhou 510632, China
  - <sup>3</sup> Department of Pharmacology, Jinan University, 601 Huangpu Avenue West, Guangzhou 510632, China; zhangsiruijnu@126.com (S.Z.); wjhuang@jnu.edu.cn (W.H.)
  - <sup>4</sup> Department of Natural Product Chemistry, Jinan University, 601 Huangpu Avenue West, Guangzhou 510632, China
  - <sup>5</sup> Department of Cardiovascular Care, ThedaCare Regional Medical Center, Appleton, WI 54911, USA; dongbo.yu@thedacare.org
  - <sup>6</sup> Institute of Integrated Chinese & Western Medicine, Jinan University, 601 Huangpu Avenue West, Guangzhou 510632, China
- \* Correspondence: tchenly@jnu.edu.cn (L.C.); tsly@jnu.edu.cn (L.S.); tyrm@jnu.edu.cn (R.Y.); Tel.: +86-20-85226476 (L.C.); +86-20-85228205 (L.S.); +86-20-85220386 (R.Y.); Fax: +86-20-85226476 (L.C.); +86-20-85224766 (R.Y.)
- † These authors contributed equally to this work.

**Citation:** Li, C.; Zhang, S.; Zhu, J.; Huang, W.; Luo, Y.; Shi, H.; Yu, D.; Chen, L.; Song, L.; Yu, R. A Novel Peptide Derived from *Arca inflata* Induces Apoptosis in Colorectal Cancer Cells through Mitochondria and the p38 MAPK Pathway. *Mar. Drugs* **2022**, *20*, 110. <https://doi.org/10.3390/md20020110>

Academic Editors: Yonghong Liu and Xuefeng Zhou

Received: 27 December 2021

Accepted: 27 January 2022

Published: 29 January 2022

**Publisher's Note:** MDPI stays neutral with regard to jurisdictional claims in published maps and institutional affiliations.



**Copyright:** © 2022 by the authors. Licensee MDPI, Basel, Switzerland. This article is an open access article distributed under the terms and conditions of the Creative Commons Attribution (CC BY) license (<https://creativecommons.org/licenses/by/4.0/>).

**Abstract:** Colorectal carcinoma (CRC) is one of the major causes of cancer-related incidence and deaths. Here, we identified a novel antitumor peptide, P6, with a molecular weight of 2794.8 Da from a marine Chinese medicine, *Arca inflata* Reeve. The full amino acid sequence and secondary structure of P6 were determined by tandem mass de novo sequencing and circular dichroism spectroscopy, respectively. P6 markedly inhibited cell proliferation and colony formation, and induced apoptosis in CRC cells. Mechanistically, transcriptomics analysis and a serial functional evaluation showed that P6 induced colon cancer cell apoptosis through the activation of the p38-MAPK signaling pathway. Moreover, it was demonstrated that P6 exhibited antitumor effects in a tumor xenograft model, and induced cell cycle arrest in CRC cells in a concentration-dependent mode. These findings provide the first line of indication that P6 could be a potential therapeutic agent for CRC treatment.

**Keywords:** *Arca inflata*; antitumor peptide; apoptosis; MAPK signaling; calmodulin; colorectal cancer

## 1. Introduction

Colorectal cancer (CRC) is by far the third most common malignant tumor, and it ranks as the second leading cause of death from cancer in the world [1]. CRC deaths have ameliorated over the past few decades on account of headways in both early diagnosis and intervention; however, long-term declines in mortality have slowed during last five years [2,3]. At an early stage, the five-year survival rate of CRC is higher than 80%; nevertheless, it decreases to approximately 10% at the advanced stages [1]. Therefore, it is urgent to develop effective anti-CRC agents with low toxicity to effectively treat and prevent the recurrence and metastasis of CRC.

The ocean is home to most of the world's life. Diverse marine organisms live and thrive in an aquatic buffer system despite the many extreme physiologic stresses, such

as high salinity, high pressure, and extreme hypoxia. Living in such a special environment, many marine organisms have evolved with special adaptations and have become an affluent source of bioactive substances with broad health benefits [4]. Due to the specific environment in which marine organisms live, the structure of marine antitumor peptides is very different from that of terrestrial animal and plant peptides. Most of them are small molecular cyclic or linear peptides that are rich in polar amino acids, D-type amino acids, hydroxyl acids, thiophenol, and oxazole rings. Some also contain alkene and alkyne bonds, which greatly improve the biological stability and bioavailability of the peptides. Didemnin B is a phenolic peptide compound isolated from the tunicate *Trididem numsolidum* from the Caribbean [5]. It has been reported that the real source of didemnin B may be cyanobacteria symbiotic with the tunicates. Didemnin B can directly bind to palmitoyl protein thioesterase, and exhibits strong activity in multiple tumor models [6]. Pettit et al. isolated a pentapeptide, dolastatin 10, from *Dolabella auricularia*. Dolastatin 10 is a secondary metabolite of the cyanobacteria *Sym plocca*, symbiotic with the sea hare [7]. Dolastatin 10 has excellent antitumor activity and can strongly inhibit the binding of vinblastine to tubulin noncompetitively ( $K_d = 1.41 \mu\text{M}$ ) and can greatly affect microtubule assembly and microtubule-dependent guanosine triphosphate hydrolysis [8]. In addition, Dolastatin 15 is a cyanobacterial polypeptide isolated from the sea hare *D. Auricularia* from the Indian Ocean. It is a linear peptide containing seven amino acids or hydroxyl acid residues. Unlike dolastatin 10, dolastatin 15 binds directly to the vinblastine binding site of tubulin to exhibit prominent antitumor efficacy [9]. Moreover, natural peptides derived from marine organisms, some of which have been shown to act as signaling/regulatory molecules in various physiological processes, also exhibit potential antitumor effects [10]. Among them, lysine-rich peptides have shown selective cytotoxicity against both microbes and cancer cells [11]. Several studies have demonstrated that lysine-rich peptides have modes of action involving cellular uptake, mitochondrial apoptosis, and other intracellular events [12–14]. However, the mechanisms behind the cytotoxic and antitumor effects of lysine-rich peptides remain unclear.

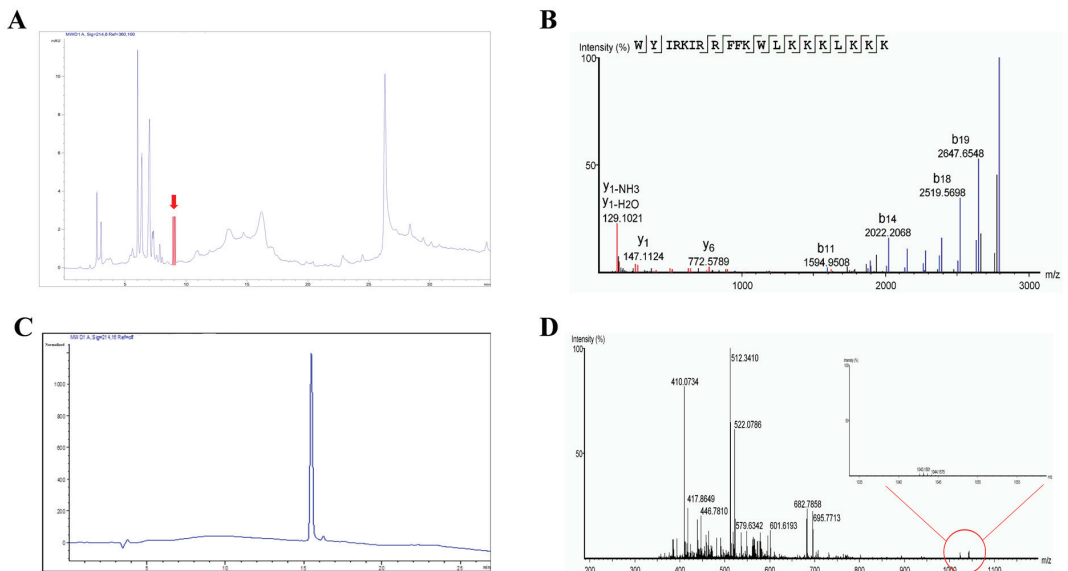
*Arca inflata* Reeve is a bivalve mollusk of the Arcidae family that prevails along the coastlines of Asia. The farming production of *A. inflata* reaches up to 350,000 tons per year in China. Furthermore, *A. inflata* is a traditional marine Chinese medicine that has several therapeutic functions, including in cancer treatment. Previously, we identified two antitumor polypeptides and a glucanase from *A. inflata* [15–17]. However, the antitumor mechanism in *A. inflata*-derived peptides remains insufficiently understood. In this study, we found that a new lysine-rich peptide, P6, displayed potent anticancer activity towards HT-29 and DLD-1 colorectal cancer cells. P6 induced  $\text{Ca}^{2+}$  overload, ROS production, and mitochondrial dysfunction, thereby triggering apoptosis through the activation of the p38-MAPK signaling pathway. Moreover, P6 exerted antitumor effects in a tumor xenograft model.

## 2. Results

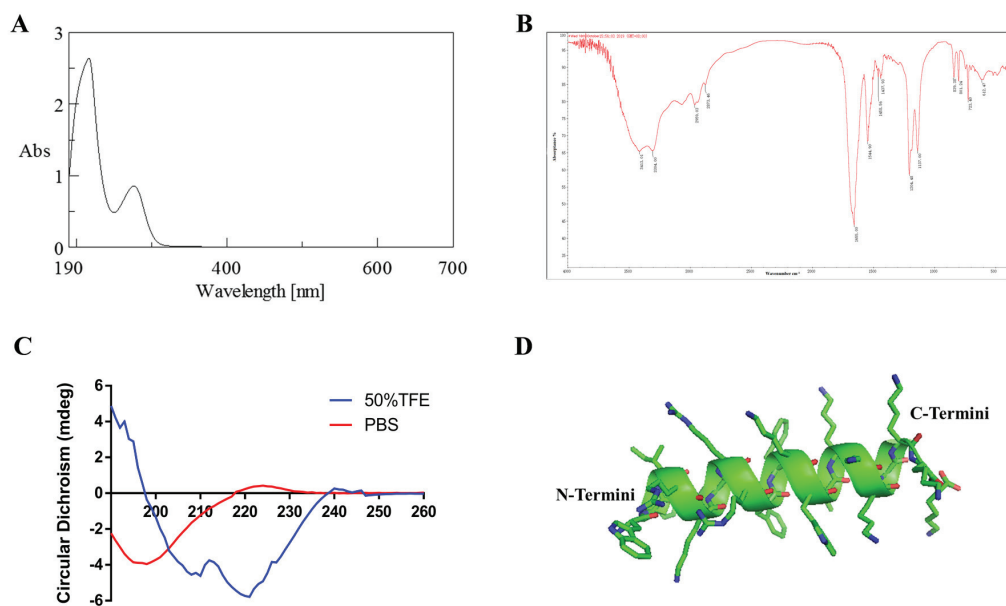
### 2.1. Identification and Physicochemical Properties of P6

*A. inflata* is a traditional marine Chinese medicine that has shown good efficacy in CRC treatment according to historical records in China. In our previous research, we were able to purify two polypeptides with moderate anti-neoplastic activity [15,16]. To further understand the antitumor constituents in *A. inflata* and their underlying anti-CRC mechanisms, we tracked the molecules that cause antitumor activity using peptide purification coupled with cytotoxicity experiments (Figure 1A). A peptide named P6 with a molecular weight of 2794.8 Da (Figure 1D) was subsequently identified from the hemolymph of *Arca inflata* (Figure 1C). The primary sequence of P6 was obtained as WYIRKIRRRFFKWLKLLKLLK by de novo sequencing (Figure 1B). The sequence of P6 is rich in lysine residues and shows no resemblance to any known animal-derived anticancer peptides when searched in non-redundant protein databases via the NCBI BLASTP server. The physicochemical properties of P6 were also tested (Figure 2). The UV-vis absorption

spectrum of P6 clearly showed a powerful absorption peak at approximately 210 nm and a shoulder peak at 280 nm, which are characteristic absorption peaks of the amide linkage of in the peptide primary structure and the aromatic amino acid residues of P6, respectively (Figure 2A). FT-IR spectroscopy was further applied to provide information about the conformational characterization of the peptides. As depicted in Figure 2B, two relatively strong bands that symbolizing amide I and amide II were observed at absorption frequencies of 1655.00 and 1544.90  $\text{cm}^{-1}$ , respectively, in the FT-IR spectrum. The amide I and amide II absorption distribution in P6 fits the standard bands for peptides of the amide I band, found between 1600 to 1700  $\text{cm}^{-1}$  (C=O stretch), and the amide II band, found at approximately 1550  $\text{cm}^{-1}$  (C=N stretch coupled with the N–H bending form) [18]. Additionally, absorption band frequencies at about 1650 and 1540  $\text{cm}^{-1}$  are regularly recognized as the helical structure of peptides [15,19]. The characteristic absorption at 1655.00 and 1544.90  $\text{cm}^{-1}$  implies that P6 consists of a high ratio of helical secondary conformation [15,20]. The CD spectrum of P6 was also detected. As shown in Figure 2C, P6 exhibited two positive peaks at 193 and 196 nm, as well as two negative ellipticity signals at 210 and 220 nm, which are a canonical peculiarity of peptide helical conformation. The three-dimensional structure of P6 was predicted as well (Figure 2D). The structure was compact with good amphipathicity, which results in a positively-charged hydrophilic surface and a hydrophobic surface (Figure 2D).



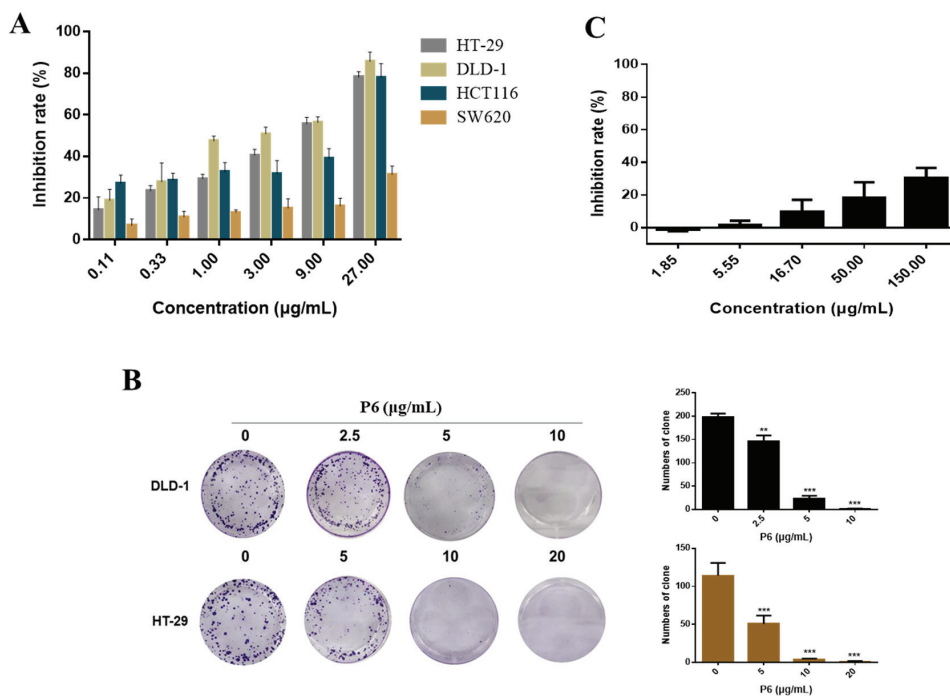
**Figure 1.** Purification and identification of peptide P6 from the hemolymph of *A. inflata*. (A) Isolation of native P6 (red arrow) from the pooled protein fraction by a C18 RP-HPLC column. (B) nanoESI-MS/MS analysis and sequencing of P6. (C) The purity of P6. (D) The precise molecular weight of P6 determined by ESI-MS.



**Figure 2.** Physicochemical properties of P6. (A) The ultraviolet spectrum of P6. (B) The infrared spectrum of P6. (C) The circular dichroism spectrum of P6. (D) The three-dimensional structure of P6. The structure of P6 is shown as a merged cartoon and stick pattern. Green represents carbon atoms, blue represents nitrogen atoms, and red represents oxygen atoms.

## 2.2. P6 Inhibits Human CRC Cell Growth

To assess the inhibitory effect of P6 on the proliferation of human CRC cells, an MTT assay was performed. Several CRC cell lines—HT-29, HCT116, SW620, and DLD-1—were treated with serial concentrations of P6 for 48 h. P6 markedly decreased cell viability in a concentration-dependent manner in the tested CRC cells (Figure 3A). Among these cell lines, we chose the most sensitive cell lines, DLD-1 and HT-29, with  $IC_{50}$  values of  $2.14 \pm 0.28 \mu\text{g}/\text{mL}$  and  $4.43 \pm 0.15 \mu\text{g}/\text{mL}$ , respectively, for further analysis (Table 1). For better comparison and investigation of the underlying anti-CRC mechanism of action of P6, we used 0, 5, 10, and 20  $\mu\text{g}/\text{mL}$  of P6 for HT-29 cells and 0, 2.5, 5, and 10  $\mu\text{g}/\text{mL}$  of P6 for DLD-1 cells in further studies, according to the  $IC_{50}$  values. Both the serial concentrations used in HT-29 and DLD-1 cell lines included two of the same concentrations (5 and 10  $\mu\text{g}/\text{mL}$ ). Hence, it is still feasible to make a comparison between these two tested cell lines. Meanwhile, P6 exhibited a weak effect on human normal liver cells (L02; Figure 3C), suggesting that P6 is selective towards cancer cells. Moreover, the long-term inhibitory effects of P6 on HT-29 and DLD-1 cell proliferation were investigated through a colony formation assay. As shown in Figure 3B, P6 inhibited the proliferation of HT-29 and DLD-1 cells in a concentration-dependent manner, which confirmed the results of the MTT assay.



**Figure 3.** In vitro cytotoxicity of P6. (A) The inhibition rates of HT-29, DLD-1, SW620, and HCT116 cells treated with P6 for 48 h were determined by MTT assay. (B) Statistical histogram of the results from the colony formation assay used to investigate the inhibitory effect of P6 on the colony formation of HT-29 and DLD-1 cells. Each value is the average ( $\pm$ SEM) of triplicate samples. \*\*  $p < 0.01$  and \*\*\*  $p < 0.001$ , compared with control. (C) The effect of P6 on the viability of human normal liver cells (L02).

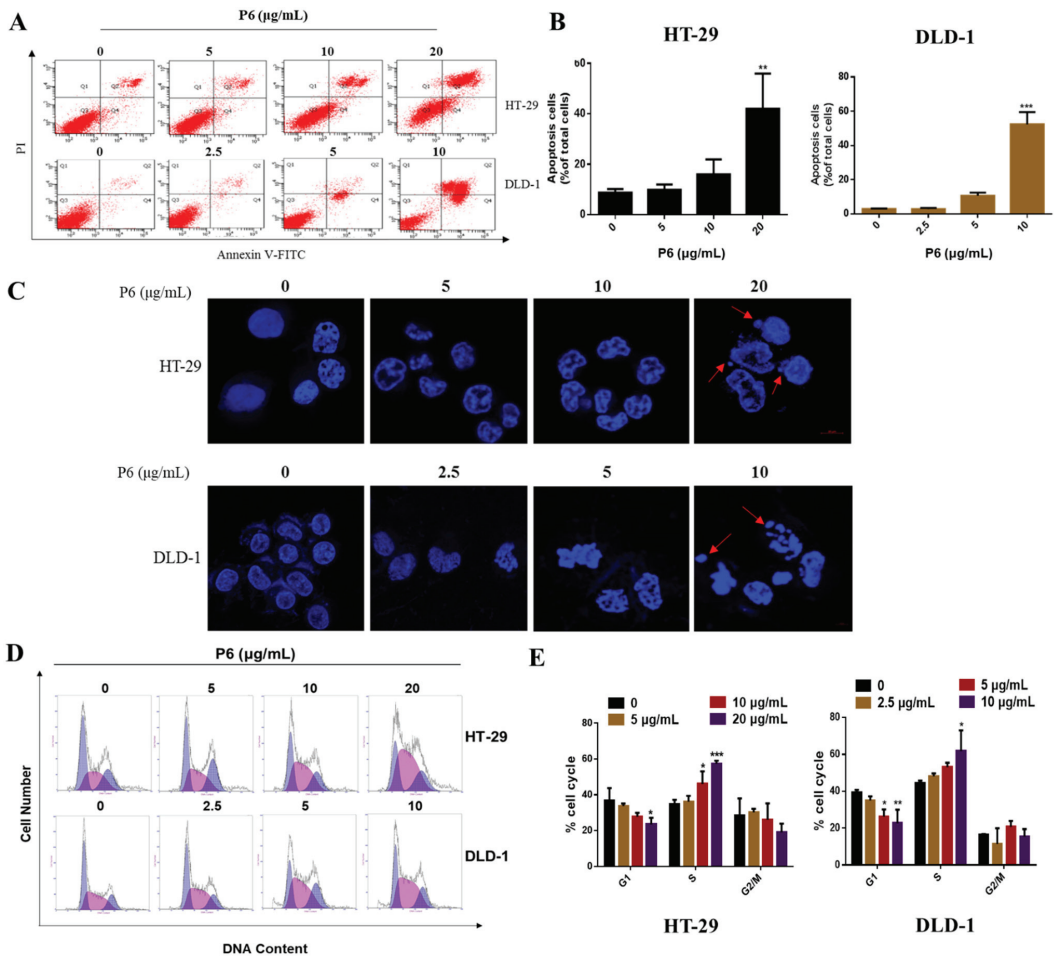
**Table 1.** The IC<sub>50</sub> values of P6 against colorectal cancer and normal cell lines.

| Cell Lines | IC <sub>50</sub> (µg/mL) |                 |
|------------|--------------------------|-----------------|
|            | P6                       | DDP             |
| HT-29      | 4.43 $\pm$ 0.15          | 1.90 $\pm$ 0.61 |
| DLD-1      | 2.14 $\pm$ 0.28          | 1.06 $\pm$ 0.41 |
| HCT116     | 10.88 $\pm$ 0.72         | 1.38 $\pm$ 0.20 |
| SW620      | >27                      | 1.08 $\pm$ 0.12 |
| L02        | >150                     | /               |

DDP—cis-diamminedichloro-platinum II.

### 2.3. P6 Induces Apoptosis and Cell Cycle Arrest in HT-29 and DLD-1 Cells

In order to detect whether P6 induced apoptosis, an important type of programmed cell death, CRC cells were treated with P6 for 48 h and then stained with Annexin V/PI and measured by flow cytometry. P6 produced a concentration-dependent induction of apoptosis in HT-29 and DLD-1 cells (Figure 4A,B). Subsequently, Hoechst 33342 staining was performed to detect nuclear fragmentation and apoptotic body production in the HT-29 and DLD-1 cells. As shown in Figure 4C, the apoptotic HT-29 and DLD-1 cells increased with P6 treatment at serial concentrations and were accompanied by the production of apoptotic bodies.



**Figure 4.** P6 induced cell apoptosis and cell cycle arrest in HT-29 and DLD-1 human CRC cells. (A) The pro-apoptotic effect of P6 on HT-29 and DLD-1 cells was analyzed by Annexin V-FITC/PI staining. (B) The Annexin V/PI staining of HT-29 and DLD-1 cells was quantified and displayed as a histogram. (C) Changes in HT-29 and DLD-1 cells treated with P6 were detected by Hoechst 33342 staining ( $\times 40$  magnification). The red arrows indicate apoptotic cells. (D) P6 altered the cell cycle distribution in the CRC cells HT-29 and DLD-1. The cell cycle distribution after treatment with serial concentrations of P6 for 48 h in the HT-29 and DLD-1 cells was analyzed by FACS. (E) Quantitative histogram of HT-29 and DLD-1 cell cycle phases. Each value is the average ( $\pm$  SD) of triplicate samples. \*  $p < 0.05$ , \*\*  $p < 0.01$ , and \*\*\*  $p < 0.001$ , compared with the control.

Cell cycle progression is closely related to cancer cell proliferation. To investigate the mechanism by which P6 was prompting CRC cell apoptosis, we used flow cytometry to determine the effect of P6 on the CRC cell cycle distribution. As shown in Figure 4D, P6 treatment induced a marked cell cycle arrest at the S/G2 transition in a concentration-dependent manner in both HT-29 and DLD-1 CRC cells. Subsequently, 10  $\mu\text{g}/\text{mL}$  of P6 caused nearly 50% of the CRC cells to arrest in S phase (Figure 4E). These results indicated that P6 could inhibit the proliferation of CRC cells through inducing cell cycle arrest at the S phase.

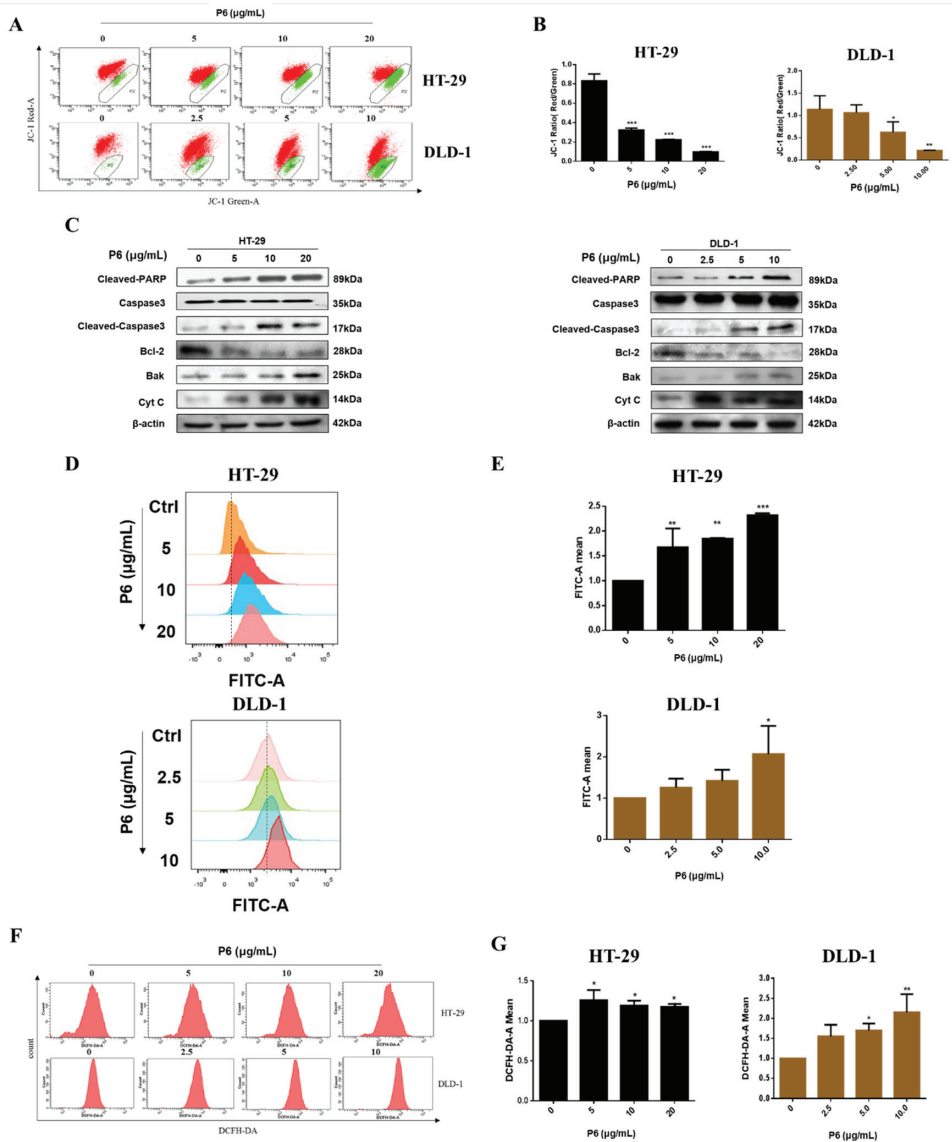
#### 2.4. P6 Induces Mitochondrial Apoptosis and Boosts $Ca^{2+}$ Influx in HT-29 and DLD-1 Cells

In order to further investigate the underlying mechanism of P6-induced apoptosis in HT-29 and DLD-1 cells, we further examined whether P6 induced apoptosis through arousing the mitochondrial pathway. JC-1 staining was applied to determine the mitochondrial membrane potential (MMP) changes in CRC cells. As demonstrated in Figure 5A,B, with the increase in apoptotic cells induced by P6, the green fluorescence of FITC-A also gradually increased. P6 induced marked MMP changes in a concentration-dependent manner in both CRC cell lines. By contrast, P6 showed an improved effect on HT-29 cells compared to DLD-1 cells. Western blotting detection verified the results of the mitochondrial membrane potential measurements. As depicted in Figure 5C, we found that P6 increased the expression levels of apoptosis-related proteins, including cleaved PARP and cleaved caspase-3, as well as the pro-apoptotic proteins Bak and Cyt C in a concentration-dependent manner. It is known that apoptosis is induced by the overexpression of Bak, which is recognized as a Bcl-2 antagonist. Moreover, P6 dampened the protein expression of the anti-apoptotic protein Bcl-2 in a concentration-dependent manner in HT-29 and DLD-1 cells (Figure 5A,B). Increased intracellular  $Ca^{2+}$  concentration is one of the hallmark events of cell apoptosis. Fluo-4 AM staining results showed that P6 produced a concentration-dependent increase in the intracellular  $Ca^{2+}$  concentration (Figure 5D,E). Additionally, mitochondrial  $Ca^{2+}$  overload induces an increase in intracellular ROS levels. Our results showed that P6 markedly increased intracellular ROS in both HT-29 and DLD-1 cells (Figure 5F,G). Together, these results revealed that P6 induced CRC cell apoptosis through  $Ca^{2+}$ -mediated mitochondrial pathways.

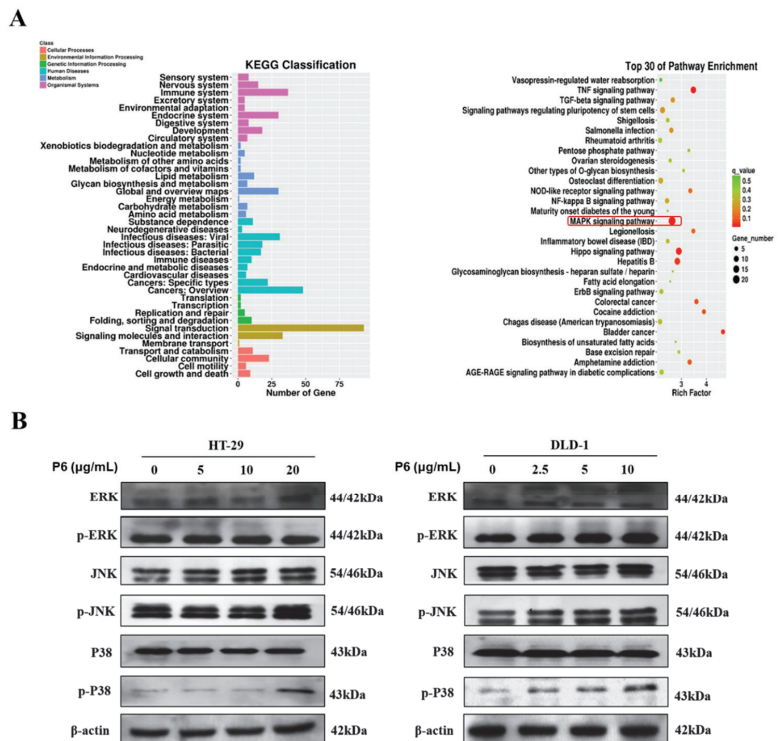
#### 2.5. The p38-MAPK Signaling Pathway Mediates the Effect of P6 on Apoptosis in CRC Cells

To further explore the underlying mechanism by which P6 exerted pro-apoptotic effects, total RNA was extracted from the HT-29 cells treated with or without P6 for RNA-seq analysis. As illustrated in Figure 6A, the analysis of RNA-seq data revealed the KEGG classification and the top 30 pathways modulated by P6. Signal transduction, including the MAPK signaling pathway, TNF signaling pathway, and Hippo signaling pathway, is strongly influenced by P6 treatment in HT-29 cells. These signaling cascades have been identified to be involved in the cell apoptosis procedure [21–23]. Next, a Western blotting assay was performed to verify the effect of P6 on the MAPK signaling pathway in HT-29 and DLD-1 cells. The results demonstrated that P6 markedly augmented the phosphorylation of p38 in both CRC cell lines, indicating that P6 activated the MAPK signaling pathway (Figure 6B). However, P6 treatment had no obvious effect on the phosphorylation of ERK and JNK in both HT-29 and DLD-1 cells. Therefore, one might propose that the P6-induced mitochondrial apoptosis was partially via the activation of p38-mediated MAPK signaling pathways in CRC cells.





**Figure 5.** P6 induced cell apoptosis by the mitochondrial pathway and boosted  $Ca^{2+}$  influx in CRC cells. (A) Mitochondrial membrane potential of HT-29 and DLD-1 cells induced by different concentrations of P6. Red fluorescence and green fluorescence imply that the mitochondrial membrane potential is normal and decreased, respectively. (B) The mitochondrial membrane potential of HT-29 and DLD-1 cells was quantified and displayed as a histogram. (C) Changes in the expression levels of apoptosis-related proteins in HT-29 and DLD-1 cells after P6 treatment for 24 h were determined by Western blotting. (D) Effects of P6 on  $Ca^{2+}$  influx in HT-29 and DLD-1 cells. (E) The  $Ca^{2+}$  influx in HT-29 and DLD-1 cells was quantified and displayed as a histogram. (F) Effects of P6 on ROS of HT-29 and DLD-1 cells. (G) ROS of HT-29 and DLD-1 cells were quantified and displayed as a histogram. Each value is the average ( $\pm$ SD) of triplicate samples. \*  $p < 0.05$ , \*\*  $p < 0.01$  and \*\*\*  $p < 0.001$ , compared to the control group.

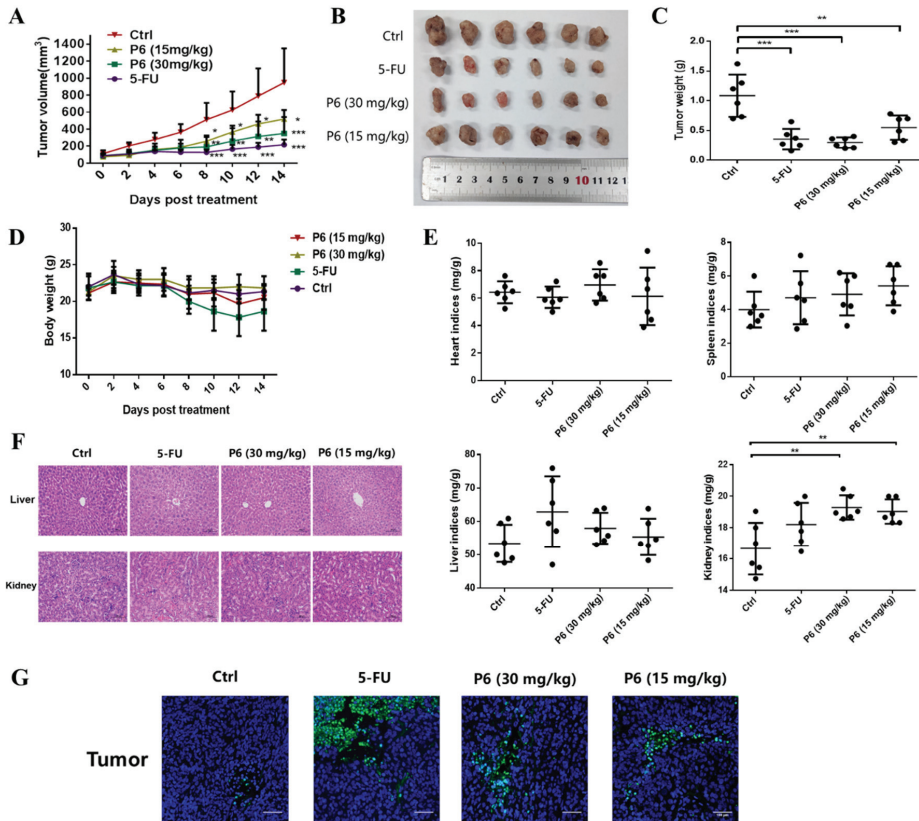


**Figure 6.** The p38-MAPK signaling pathway mediated the effect of P6 on apoptosis in CRC cells. (A) Total RNA was extracted from HT-29 cells treated with or without P6 and subjected to RNA sequencing. The histogram of differential genes in the KEGG classification and the scatter plot of differential genes from the KEGG enrichment analysis are shown, including the top 30 enriched KEGG pathways. (B) The effect of P6 on the MAPK pathway in HT-29 and DLD-1 cells with P6 treatment for 24 h.

2.6. P6 Suppresses the Growth of CRC Tumor Xenografts In Vivo

We further constructed a CRC HT-29 cell subcutaneous xenograft tumor model in BALB/c-nude mice to investigate the antitumor effect of P6 in vivo. The tumor volume (Figure 7A,B) and tumor weight (Figure 7C) of the P6-treated groups were significantly decreased compared to the model group after 14-day administration. According to record of tumor weight or tumor volume, P6 markedly inhibited the growth of subcutaneous tumors of HT-29 cells. As shown in Table 2, the tumor inhibition rates of the P6-treated groups (15 mg/kg and 30 mg/kg) reached 49.46% and 72.66%, respectively. Notably, the high dose P6-treated groups (30 mg/kg) showed an improved tumor inhibition rate compared to that of the 5-fluorouracil (5-FU)-treated group (67.28%). Moreover, the tumor growth curve showed that the tumor weight gradually decreased when the dose of P6 increased (Figure 7C). Meanwhile, body weight in each P6 treatment group showed a similar trend compared with the model group (Figure 7D). In addition, the organ indexes of the heart, spleen, liver, and kidney in the P6 treatment group showed no obvious difference when compared with the control group (Figure 7E). Hematoxylin and eosin (H&E) staining showed that, compared with the control group, there was no significant histological changes in the liver and kidneys in the P6 treatment group (15 and 30 mg/Kg). These results verified that P6 showed no obvious toxic side effects against mouse metabolic organs (Figure 7F).

Furthermore, TdT-mediated dUTP nick-end labeling (TUNEL) staining demonstrated that the P6-treated groups could induce cell apoptosis in tumor tissues (Figure 7G).



**Figure 7.** P6 suppressed the growth of HT-29 subcutaneous tumors in vivo. The antitumor activity of P6 was measured in xenograft nude mice. (A) Tumor volume curve. Results are expressed as mean ± SD; \*  $p < 0.05$ , \*\*  $p < 0.01$  and \*\*\*  $p < 0.001$  compared to the control group;  $n = 6$  per group. (B) Photo collection of xenograft subcutaneous tumors in nude mice. (C) Tumor weight after 14-day administration of P6. Results are expressed as mean ± SD; \*\*  $p < 0.01$  and \*\*\*  $p < 0.001$ , compared to the control group by one-way ANOVA and post hoc tests;  $n = 6$  per group. (D) Body weight of the nude mice during drug treatment. (E) Organ index of nude mice. \*\*  $p < 0.05$ , compared with the control group. (F) The liver and kidneys of xenograft mice were histologically analyzed by H&E staining (scale bar = 50 μm). (G) TUNEL staining of tumor tissue (scale bar = 100 μm).

**Table 2.** Effect of P6 on tumor inhibition rate (%) of HT-29 xenograft mice.

| Group          | Dose        | Tumor Weight (g) | Tumor Inhibition Rate (%) |
|----------------|-------------|------------------|---------------------------|
| Saline (Ctrl)  | 0.1 mL/10 g | 1.09 ± 0.36      | /                         |
| 5-FU           | 25 mg/kg    | 0.36 ± 0.17 ***  | 67.28                     |
| P6 (high dose) | 30 mg/kg    | 0.30 ± 0.09 ***  | 72.66                     |
| P6 (low dose)  | 15 mg/kg    | 0.55 ± 0.20 **   | 49.46                     |

Values represent the mean ± SD. \*\*  $p < 0.01$  and \*\*\*  $p < 0.001$ , compared with the model group;  $n = 6$ .

### 3. Discussion

Colorectal cancer (CRC) kills nearly one million people each year and is becoming the world's second most deadly cancer. As a consequence, CRC has produced a considerable disease burden and has become a major global public health problem [24]. At the present, 5-fluorouracil and oxaliplatin are still the first choice in the clinical chemotherapy treatment of CRC, including in the National Comprehensive Cancer Network (NCCN) Guidelines of CRC (version 2020.V1) [25]. However, the most serious treatment obstacle is the toxic side effects of 5-fluorouracil and oxaliplatin. For advanced CRC, there are only VEGFR receptor-targeted drugs (such as bevacizumab) and EGFR receptor-targeted drugs (such as cetuximab) on the market to date, which only have the effect of prolonging the approximately 3–5-months of survival for patients [26–28]. Additionally, due to their high treatment cost and significant side effects, these targeted drugs have greatly limited clinical applications [26–28]. Therefore, it is urgent to develop effective anti-CRC agents with low toxicity to effectively treat and prevent the recurrence and metastasis of CRC. Here, we report that P6, a novel peptide identified from the marine mollusk *Arca inflata*, was effective at suppressing CRC proliferation by inducing mitochondrial apoptosis (Figure 5). Moreover, P6 exhibited a prominent antitumor effect in the tumor xenograft model (Figure 7). Our study provides preliminary proof that P6 could be developed as a drug candidate for treating CRC.

Apoptosis, also known as programmed cell death, is the main mechanism for tumor cell death under the action of chemotherapeutic drugs [29]. An abnormal apoptosis signaling pathway, the loss of apoptosis signals, or the enhancement of anti-apoptosis signals can trigger a variety of pathological changes, leading to cancer or chemotherapy failure [30]. Under normal circumstances, apoptosis cannot trigger inflammation and the immune response; thus, promoting apoptosis has become an important strategy for tumor treatment [31]. There are two main apoptotic pathways in mammals, the death receptor pathway [32–35] and the mitochondrial pathway [36,37]. There is a cross between the two pathways, and certain signaling molecules can participate in different apoptotic pathways. In recent years, nearly a hundred peptides with antitumor activity have been discovered in marine organisms, of which more than 90% trigger apoptosis through targeted apoptotic mechanisms involving the mitochondria and death receptor pathways. Both apoptotic pathways require the mitochondrial-mediated activation of caspases. The mitochondrial pathway is the main mechanism of apoptosis induced by many antitumor drugs. The activation of mitochondrial apoptosis pathways is primarily due to several factors, including ROS production and  $\text{Ca}^{2+}$  overload in the cells [38]. When the  $\text{Ca}^{2+}$  homeostasis in tumor cells is disrupted, high levels of reactive oxygen species (ROS) are produced, resulting in the activation of cell apoptosis [38,39]. Interestingly, P6 showed a profound antitumor effect and induced tumor cell apoptosis by promoting ROS production and intracellular  $\text{Ca}^{2+}$  overload in CRC cells (Figure 5). It has been reported that  $\text{Ca}^{2+}$  overload could lead to mitochondrial dysfunction and mitochondrial ROS generation [39]. The underlying mode of action may include  $\text{Ca}^{2+}$ -stimulated nitric oxide production,  $\text{Ca}^{2+}$ -stimulated increase in metabolic rate,  $\text{Ca}^{2+}$ -induced cytochrome C (Cyt C) dissociation,  $\text{Ca}^{2+}$ -induced opening of the permeability transition pore with the subsequent release of Cyt C,  $\text{Ca}^{2+}$ -induced cardiolipin peroxidation, and  $\text{Ca}^{2+}$ /calmodulin dependent protein kinase activation. Several marine peptides can change the Bcl-2/Bax ratio, activate caspases, and release Cyt C to induce cell apoptosis by stimulating  $\text{Ca}^{2+}$  overload and ROS production in tumor cells [40]. In this study, we found that P6 suppressed CRC cell proliferation (Figure 3) and induced cell apoptosis (Figure 4) by producing a concentration-dependent increase in intracellular  $\text{Ca}^{2+}$  concentration (Figure 5D,E). Additionally, mitochondrial  $\text{Ca}^{2+}$  overload induces an increase in intracellular ROS levels. Our results showed that P6 markedly reduced the mitochondrial membrane potential and increased intracellular ROS levels in both HT-29 and DLD-1 cells (Figure 5B,E,G). The decrease in mitochondrial membrane potential indicated that the permeability of the mitochondrial membrane was increased and the internal cytochrome C was released at the same time, which induced apoptosis.

Furthermore, caspases are closely related to cell apoptosis. Many marine peptides induce tumor cell apoptosis by activating caspases. Pardaxin, a peptide consisting of 33 amino acid residues, is isolated from the secretions of a fish (*Pardachirus marmoratus*) found at the bottom of the Red Sea. Studies have shown that pardaxin can induce apoptosis in human fibrosarcoma HT-1080 cells, which is manifested by the increased activity of caspase-3, mitochondrial membrane potential changes, and the accumulation of reactive oxygen species (ROS) products [40]. P6 showed a similar effect, producing an increased activity of caspase-3 and mitochondrial membrane potential changes in CRC cells (Figure 5B,C). The subsequent Western blot results showed that P6 upregulated the expression of cytochrome C and the pro-apoptotic protein Bak (Figure 5C). It was further confirmed that P6 exerted an apoptosis-inducing effect through the mitochondrial pathway at the molecular level.

Mitogen-activated protein kinases (MAPK) form a crucial signaling pathway that regulates cell fate decisions in response to external stimuli. Among them, p38 MAPK family members play an important role in regulating cell proliferation, senescence, and tumorigenesis [41]. Previous studies have shown that the altered expression of p38 proteins is often observed in CRC; thus, the drug-induced activation of the p38 MAPK cascade could be a scenario worth exploring for sensitizing CRC cells to apoptotic death [41]. Herein, we hypothesized that P6 might be a promising antitumor molecule via the activation of the p38 pathway. Considering the cell proliferation-suppressing and apoptotic effects of P6 (Figure 6A), we further investigated whether P6 influenced p38 MAPK pathways. As expected, P6 markedly increased the protein levels of the p38 proteins but showed no influence on the ERK and JNK pathways (Figure 6B), indicating the activation of the p38 MAPK cascades. Additionally, p38 activation-mediated apoptosis is sometimes induced by secondary routes, such as through the production of ROS [42]. In the present study, P6 suppressed proliferation and induced apoptosis in both HT-29 and DLD-1 cells. Hence, the effects of P6 on inducing mitochondrial apoptosis were partially dependent on ROS production.

## 4. Materials and Methods

### 4.1. Isolation and Identification of P6

*Arca inflata* Reeve materials were purchased from Qingdao of Shandong province, China; the production lot number was 20190410. The collected hemolymph of *A. inflata* was mixed with PBS in a ratio of 1:3 (*w/v*) and underwent ultrasound for 40 min at 4 °C. The supernatant was collected by 10,000 rpm centrifugation for 30 min at 4 °C. The supernatant was salted out with 100% ammonium sulfate, and the precipitate was collected by centrifugation (10,000 rpm for 30 min at 4 °C). The precipitate was dissolved in 20 mM Tris-HCl (pH 8.0) and dialyzed (molecular weight cut-off: 1 kDa) for 48 h. The samples were further separated by HPLC (Welch LP-C8, 5 µm, 4.6 × 250 mm). The sixth peak containing peptides was highlighted in red. Due to their similar hydrophobicity, the peptides in this marked peak were difficult to separate using a conventional approach. Hence, LC-MS/MS was applied to identify the peptides. The most abundant peptide fragment was named P6. According to the identified peptide sequences, the top 5 most abundant peptide fragments in this peak were synthesized by GenScript Co. (Shanghai, China) using a solid-phase peptide synthesis procedure. Their antitumor activities were tested using an MTT assay; only P6 possessed antitumor activity.

### 4.2. Purity of P6

High-performance liquid chromatography (HPLC) was applied to detect the purity of P6 using an Agilent series 1100 HPLC system connected to a ZORBAX®300SB-C8 column (4.6 × 150 mm, 5 µm; Agilent, Foster City, CA, USA). Water-trifluoroacetic acid (solvent A; 100:0.1, *v/v*) and acetonitrile-trifluoroacetic acid (solvent B; 100:0.1, *v/v*) were used as elution solvents. The elution procedure was set as follows: 55% solvent A and 45% solvent B with the flow rate at 1 mL/min. The wavelength of the UV detector was at 280 nm, and column temperature was 30 °C.

#### 4.3. Molecular Weight Determination of P6

The precise molecular weight of P6 was determined using an ESI-MS spectrometer. The P6 sample was dissolved in distilled water and subsequently loaded into an API type 4000 QTRAP mass spectrometer (Applied Biosystems, Foster City, CA, USA). The mass spectrometer was used in the positive electrospray ionization (ESI + ve) mode. High-purity nitrogen gas was used for both drying (35 psi) and ESI nebulization (45 psi). The spectra were recorded over the mass/charge ( $m/z$ ) range of 500–3000.

#### 4.4. De Novo Sequencing of P6 by Tandem Mass Spectrometry (MS)

LC-MS/MS was used to determine the amino acid sequence of P6. After P6 was separated by HPLC, it was analyzed by a TripleTOF 5600 LCMS (AB SCIEX, Concord, ON, USA) connected to a nanoscale liquid-chromatography (LC) system (NanoLC-Ultra 2D; Eksigent, Dublin, CA, USA). Briefly, a reversed-phase C18 column (75  $\mu\text{m} \times 15 \text{ cm}$ , 3  $\mu\text{m}$ , 120 Å; ChromXP, Eksigent, USA) was applied for the separation of the desalted hydrolyzed peptides. Mixtures of 0.1% ( $v/v$ ) formic acid in 5% acetonitrile and 0.1% ( $v/v$ ) formic acid in 95% acetonitrile were used as the mobile phases A and B, respectively. The elution procedure was as follows: 5–40% B for 65 min, 40–100% B for 10 min, and maintained for 5 min. The ionization voltage and capillary temperature were set as 2.3 kV and 150 °C, respectively. The molecular masses of the purified peptides were detected in MS/MS mode. The acquired data were further analyzed by PEAKS software version 8.5 (Waterloo, ON, Canada). The peptides with de novo scores greater than 85% were selected for use in the study.

#### 4.5. Physicochemical Characterization of P6

Ultraviolet (UV) spectroscopy was used to detect whether P6 contained aromatic amino acids. UV-vis absorption spectroscopy was conducted with a UV-2450 UV-vis absorption spectrophotometer (Shimadzu, Osaka, Japan) equipped with a 1.0 cm quartz cell. P6 was dissolved in distilled water to prepare a 0.05 mg/mL solution, which was scanned in the wavelength range of 190–400 nm.

Infrared spectroscopy was used to analyze the functional groups of P6. P6 and potassium bromide were fully grinded and mixed, and the mixture was put into a mold for scanning by an EQUINOX55 FT-IR spectrometer (Bruker, Bremen, Germany). The scanning range was 400–4000  $\text{cm}^{-1}$ .

Circular dichroism was used to analyze the secondary structure conformation of P6. P6 was dissolved in distilled water to prepare a 0.05 mg/mL solution, and CD measurements were obtained using a Jasco J-810 spectropolarimeter (Japan Spectroscopic Co., Ltd., Hachioji, Tokyo, Japan) equipped with a 0.1 cm quartz cell. The average of eight scans was used to produce the final spectrum. The spectra were all corrected for solvent contributions. The scan speed was 50 nm/min, and the scan range was 260–190 nm. The other parameters were set as follows: response time of 0.5 s, bandwidth of 2 nm, data interval of 0.2 nm, and sensitivity of 20 mdeg.

The three-dimensional structure of P6 was predicted using the PEP-FOLD3 server, <https://bioserv.rpbs.univ-paris-diderot.fr/services/PEP-FOLD3/> (accessed on 24 December 2021).

#### 4.6. Reagents and Antibodies

N-acetyl-L-cysteine (A105420) was purchased from Aladdin (Shanghai, China).  $\beta$ -actin (1:1000, 3700), caspase-3 (1:1000, 9662), cleaved caspase-3 (1:1000, 9664), cleaved PARP (1:1000, 5625), Bcl-2 (1:1000, 5625), SAPK/JNK (1:1000, 9252), phospho-SAPK/JNK (1:1000, 4668), anti-rabbit IgG (1:4000, 7074S), anti-mouse IgG (1:4000, 7076S), Bak (1:1000, 12105), and cytochrome C (1:1000, 4280) were obtained from Cell Signaling Technology (Boston, Massachusetts, USA). The p38 MAPK (1:1000, AF6456), phospho-p38 MAPK (1:1000, AF3455), ERK1/2 (1:1000, AF0155), and phospho-ERK1/2 (1:1000, AF1014) were obtained from Affinity Biosciences (Pottstown, PA, USA).

#### 4.7. Cell Culture

The human colorectal cancer cell lines (HT-29, DLD-1, HCT116, and SW620) and human normal liver cells (L02) were obtained from the Chinese Academy of Sciences Cell Bank of Type Culture Collection (Shanghai, China). The HT-29 and HCT116 cells were cultured in DMEM medium (Gibco, Gaithersburg, MD, USA) supplemented with 10% fetal bovine serum (FBS; Biological Industries, Beit Haemek, Israel), 100 units/mL penicillin, and 100 µg/mL streptomycin. The DLD-1 cells and SW620 cells were cultured in RPMI 1640 medium (Gibco, Gaithersburg, MD, USA) supplemented with 10% fetal bovine serum (FBS; Biological Industries, Beit Haemek, Israel), 100 units/mL penicillin, and 100 units/mL streptomycin. The cells were maintained in a humidified incubator with 5% CO<sub>2</sub> at 37 °C.

#### 4.8. Cell Viability Assay

The cytotoxicity of P6 was investigated using the 3-(4,5-dimethylthiazol-2-yl)-2,5-diphenyltetrazolium bromide (MTT) assay. L02 cells ( $2.5 \times 10^3$  per well/100 µL), HT-29 cells, HCT116 cells, DLD-1 cells, and SW620 cells ( $1.5 \times 10^3$  per well/100 µL) were seeded into 96-well plates containing DMEM or RPIM 1640 medium, respectively. After 24 h incubation at 37 °C and 5% CO<sub>2</sub>, the medium was replaced with various concentrations (0–27 µg/mL) of P6 for 48 h. Finally, 10 µL MTT solution (5 mg/mL) was added to each well, and the cells were incubated for 4 h. The MTT formazan product was dissolved in 200 µL DMSO and shaken for 10 min on the micro-oscillator. The optical density (OD) at 570 nm was recorded using a Synergy HT microplate reader (BioTek, Winooski, VT, USA). Each concentration was repeated at least three times. The inhibition rate was calculated as:

$$(\%) = [1 - (D - D_0)/(D_1 - D_0)] \times 100\%.$$

where D was the OD value of the experimental group, D<sub>0</sub> was the OD value of the parallel solvent control group, and D<sub>1</sub> was the OD value of the blank control group.

#### 4.9. Colony Formation Assay

For the colony formation assays in monolayer cultures, the cells ( $1 \times 10^3$  per well) were incubated in 6-well plates for 24 h. Two milliliters of the prepared P6 solutions at different concentrations were added, and 2 mL of complete medium was added to the control group. After continuous treatment for 14 days, the medium was discarded and the cells were gently rinsed 2–3 times with PBS buffer (1 mL/well). Then, 300 µL of 4% paraformaldehyde was added to each well, incubated for 25 min, and the 4% paraformaldehyde was aspirated. Five hundred microliters of 0.1% crystal violet solution were added to each well, incubated for 25 min, and then gently rinsed with PBS buffer 2–3 times. After fixation and staining, the colonies were imaged.

#### 4.10. Cell Morphology Analysis

Hoechst 33342 staining measurements were performed with a Hoechst 33342 staining kit (C1022, Beyotime, Shanghai, China). The cells were seeded in confocal dishes at a cell density of  $3 \times 10^4$  cells/mL (200 µL/dish) and incubated at 37 °C and 5% CO<sub>2</sub>. After 24 h, the previous medium was discarded, and 200 µL of the prepared P6 solutions at different concentrations were added to the treatment group; 200 µL of complete medium was added to the control group. After 24 h of P6 treatment, the previous medium was aspirated and the cells were carefully rinsed 2–3 times. Two hundred microliters of Hoechst 33342 dye was added to each well, and after incubation in the dark for 15 min, the dye was discarded and the cells were carefully rinsed with PBS buffer 2–3 times. The photographs of the samples were recorded using a fluorescence microscope (Olympus, Tokyo, Japan).

#### 4.11. Cell Apoptosis Assay

Cell apoptosis was detected using an Annexin V-FITC/PI staining kit (FXP018-100, 4A Biotech, Beijing, China). Cells ( $1 \times 10^5$  per well) were seeded into 6-well plates and

incubated for 24 h with various concentrations of P6 (0, 5, 10, and 20 µg/mL for HT-29 cells or 0, 2.5, 5, and 10 µg/mL for DLD-1 cells) for 24 h. Then, the cells were washed, trypsinized, harvested, suspended in binding buffer, and stained with Annexin V-FITC and PI following the manufacturer's instructions. The suspended cells were incubated with FITC and PI in the dark at room temperature for 15 minutes. The samples were immediately analyzed by flow cytometry (BD FACSCanto, Canto, NJ, USA).

#### 4.12. Cell Cycle Assay

Cells ( $1 \times 10^5$  per well) were seeded into 6-well plates and incubated for 24 h with various concentrations of P6 (0, 5, 10, and 20 µg/mL for HT-29 cells or 0, 2.5, 5, and 10 µg/mL for DLD-1 cells) for 24 h. The cells were harvested and suspended in 70% ethanol. Then, the samples were stored at  $-20^\circ\text{C}$  for 2 h and stained with PI for 15 min in the dark at room temperature. The samples were immediately analyzed by flow cytometry (BD FACSCanto, Canto, NJ, USA).

#### 4.13. Mitochondrial Membrane Potential (MMP) Assay

The mitochondrial membrane potential of colorectal cancer cells was determined using a JC-1 staining kit (C2006, Beyotime, Shanghai, China) with flow cytometry. Colorectal cancer cells were seeded into a 6-well plate at a density of  $1 \times 10^5$  cells per well. After incubation overnight, the cells were treated with different concentrations of P6 (0, 5, 10, and 20 µg/mL for HT-29 or 0, 2.5, 5, and 10 µg/mL for DLD-1) for 24 h. Next, the cells were washed, trypsinized, harvested, and stained with JC-1 working buffer at  $37^\circ\text{C}$  for 20 min in the dark. The samples were washed three times with PBS and immediately analyzed by flow cytometry (BD FACSCanto, Canto, NJ, USA).

#### 4.14. Intracellular ROS Detection

A DCFH-DA staining kit (S0033, Beyotime, Shanghai, China) was used to detect intracellular ROS in CRC cells. Briefly, cells ( $1.5 \times 10^5$  per well) were seeded into a 6-well plate and incubated at  $37^\circ\text{C}$  and 5%  $\text{CO}_2$  for 24 h. Then, each well was covered with various concentrations of P6 (0, 5, 10, and 20 µg/mL for HT-29 or 0, 2.5, 5, and 10 µg/mL for DLD-1) for 24 h. Next, the cells were washed with pre-cooled PBS, trypsinized, and harvested. Finally, the cells were stained with DCFH-DA at  $37^\circ\text{C}$  for 30 min. The samples were washed three times with medium without serum and immediately analyzed by flow cytometry (BD FACSCanto, Canto, NJ, USA).

#### 4.15. Intracellular $\text{Ca}^{2+}$ Detection

Intracellular  $\text{Ca}^{2+}$  was detected using a Fluo-4 AM staining kit (S1060, Beyotime, Shanghai, China) and analyzed by flow cytometry. Colorectal cancer cells were seeded into a 6-well plate at a density of  $1 \times 10^5$  cells per well. After incubation overnight, the cells were treated with different concentrations of P6 (0, 5, 10, and 20 µg/mL for HT-29 cells or 0, 2.5, 5, and 10 µg/mL for DLD-1 cells) for 24 h. Next, the cells were washed, trypsinized, harvested, and stained with Fluo-4 AM at  $37^\circ\text{C}$  for 30 min in the dark. The samples were washed three times with PBS and immediately analyzed by flow cytometry (BD FACSCanto, Canto, NJ, USA).

#### 4.16. Western Blotting Analysis

HT-29 and DLD-1 cells were seeded into 6-well plates ( $5 \times 10^5$  per well) and incubated in medium for 24 h, after which the medium was replaced with various concentrations of P6 (0, 5, 10, and 20 µg/mL for HT-29 cells or 0, 2.5, 5, and 10 µg/mL for DLD-1 cells) for 24 h. Then, the cells were washed three times with pre-cooled PBS and lysed with RIPA buffer (P0013K, Beyotime, Shanghai, China) on ice. Protein samples were collected and boiled for 15 min. The concentrations of the protein samples were quantified using a BCA protein assay kit (P0012S, Beyotime, Shanghai, China). Equal amounts of denatured protein samples were separated on 10% to 12% (*w/v*) sodium dodecyl sulfate (SDS)-polyacrylamide



gels and transferred to polyvinylidene fluoride (PVDF) membranes (Bio-Rad, Hercules, CA, USA). The membranes were blocked in 5% BSA at room temperature for 2 h and incubated with primary antibodies overnight at 4 °C. Then, the membranes were incubated with horse radish peroxidase-linked secondary antibodies at room temperature for 2 h. After they were washed three times with TBST, the membranes were exposed to X-ray film to detect the expressions of the target proteins, which were enhanced using the ECL Kit (Tanon, Shanghai, China).

#### 4.17. RNA-Seq Analysis

HT-29 cells in the logarithmic growth phase were collected and passaged in 100 mm Petri dishes. When the cell growth covered approximately 70% of the Petri dishes, the P6 solution or medium solution was added. After 24-hour incubation, the previous medium was discarded. The cells were carefully rinsed twice with pre-cooled PBS buffer and 3 mL of TRIZOL lysis reagent was added to each group, lysed on ice for 5 min, and the cell lysates were collected. The purified total RNA from HT-29 cells treated with P6 or without P6 was extracted and sent to Shanghai Bohao Biotech. Co., Ltd. (SHBIO, Shanghai, China) for RNA-seq analysis using an Illumina HiSeq system after transcription. The quantity of gene expression was calculated by FPKM (fragments per kilobase of transcript per million fragments mapped). Genes with  $\log_2$  (fold change) > 1 and  $Q < 0.001$  were considered as differentially expressed genes (DEGs). Gene cluster analyses and enriched KEGG (Kyoto Encyclopedia of Genes and Genomes) pathway analyses were performed based on the DEGs.

#### 4.18. In Vivo Studies

All animal experiments were approved by the Medical Laboratory Animal Center of Jinan University and followed the ethical requirements for laboratory animals. Male BALB/c-nude mice were obtained from Beijing Huaifukang Biotechnology Co. Ltd. These mice were fed breeding feed and water in an SPF laboratory at room temperature. HT-29 cells ( $1.5 \times 10^6$  cells in 0.1 mL phosphate-buffered saline) were subcutaneously injected into the left armpit of 6-week-old male BALB/c nude mice. Tumor volume and body weight were measured every 2 days, and tumor volume was calculated using the following formula:  $(\text{short diameter})^2 \times (\text{long diameter})/2$ . When the tumor volume reached about  $100 \text{ mm}^3$ , these mice were randomly divided into four groups ( $n = 6$  in each group): the model group, 5-FU treatment group, P6 (30 mg/kg) treatment group, and P6 (15 mg/kg) treatment group. The reference drug (5-FU) and P6 were dissolved in normal saline and administered by subcutaneous injection at a volume of 0.1 mL/10g. After 14 days of administration, all mice were anesthetized by intraperitoneal injection of sodium pentobarbital (1 mg/20 g mouse) and euthanized. The organs were obtained for immunohistochemical experiments.

#### 4.19. Histopathologic Examination and TUNEL Staining

The organs were fixed in 10% buffered paraformaldehyde solution and sectioned at 4  $\mu\text{m}$  thicknesses. Hematoxylin and eosin (H&E) was used to stain the specimens. An optical microscope (Nikon, Tokyo, Japan) was used to observe the histopathological changes in the specimens.

A TUNEL assay was performed according to the manufacturer's instructions using a one-step TUNEL apoptosis assay kit (C1086, Beyotime, Shanghai, China). TUNEL-positive tissues or cells were imaged under a fluorescence microscope (Olympus, Tokyo, Japan).

#### 4.20. Statistical Analysis

The differences between two groups were analyzed by the two-tailed Student *t*-test, and comparisons of multiple groups were carried out using one-way analysis of variance (ANOVA). The data represent the mean  $\pm$  standard deviation (SD) in all figures.  $p < 0.05$  was chosen as the level of significant differences.

## 5. Conclusions

In summary, we identified a novel peptide termed P6 from the marine mollusc *Arca inflata* and demonstrated its anti-CRC effect in vivo and in vitro. Our results further indicated that P6 promoted Ca<sup>2+</sup> influx, a reduction in mitochondrial membrane potential, and the generation of ROS, and thereby induced apoptosis in colon cancer cells. Additionally, the MAPK pathway may contribute to the induction of apoptosis. These findings suggest that P6, which functions as a positive regulator of apoptosis, may be a potential molecule for acquiring therapeutic effects in CRC cells, and warrants further study in the future.

**Author Contributions:** Conceptualization, C.L., S.Z., L.S. and R.Y.; methodology, C.L., S.Z., J.Z. and W.H.; software, S.Z.; validation, J.Z., Y.L. and W.H.; formal analysis, C.L. and S.Z.; investigation, C.L., S.Z. and H.S.; resources, L.S.; data curation, J.Z.; writing—original draft preparation, C.L. and S.Z.; writing—review and editing, D.Y. and L.C.; visualization, S.Z. and L.S.; supervision, R.Y. and L.S.; project administration, L.S. and R.Y.; funding acquisition, C.L. and R.Y. All authors have read and agreed to the published version of the manuscript.

**Funding:** This study was financially supported by the National Natural Science Foundation of China (No. 82003910, 81673646 and 82174019), China Postdoctoral Science Foundation funded project (2020M673092), Guangdong Basic and Applied Basic Research Foundation (2020A1515110550), Ocean and Fisheries Science and Technology Development Projects of Guangdong Province (No. A201501C04), and Major Science and Technology Projects/Significant New Drugs Creation of Guangdong Province (No. 2013A022100032).

**Institutional Review Board Statement:** This study was conducted according to the guidelines of the Declaration of Helsinki and approved by the ethics committee of the Experimental Animal Center, Jinan University (Protocol no. IACUC 20201028-08, Date: 28 October 2020).

**Informed Consent Statement:** Not applicable.

**Data Availability Statement:** All data generated or analyzed during this study are included in this published article.

**Conflicts of Interest:** The authors declare no conflict of interest.

## References

- Jemal, A.; Siegel, R.; Ward, E.; Murray, T.; Xu, J.; Thun, M.J. Cancer statistics. *CA Cancer J. Clin.* **2007**, *57*, 43–66. [[CrossRef](#)] [[PubMed](#)]
- Bray, F.; Ferlay, J.; Soerjomataram, I.; Siegel, R.L.; Torre, L.A.; Jemal, A. Global cancer statistics 2018: GLOBOCAN estimates of incidence and mortality worldwide for 36 cancers in 185 countries. *CA Cancer J. Clin.* **2018**, *68*, 394–424. [[CrossRef](#)] [[PubMed](#)]
- Siegel, R.L.; Miller, K.D.; Goding Sauer, A.; Fedewa, S.A.; Butterly, L.F.; Anderson, J.C. Colorectal cancer statistics, 2020. *CA Cancer J. Clin.* **2020**, *70*, 145–164. [[CrossRef](#)] [[PubMed](#)]
- Ulrike, L. Marine-derived pharmaceuticals—Challenges and opportunities. *Biomol. Ther.* **2016**, *24*, 561–571.
- Urdiales, J.; Morata, P.; Castro, I.; Sánchez-Jiménez, F. Antiproliferative effect of dehydrodidemnin B (DDB), a depsipeptide isolated from *Mediterranean tunicates*. *Cancer Lett.* **1996**, *102*, 31–37. [[CrossRef](#)]
- Sondak, V.K.; Kopecky, K.J.; Liu, P.Y.; Fletcher, W.S.; Harvey, W.H.; Laufman, L.R. Didemnin B in metastatic malignant melanoma: A phase II trial of the southwest oncology group. *Anti-Cancer Drugs* **1994**, *5*, 147–150. [[CrossRef](#)]
- Pettit, G.R.; Kamano, Y.; Herald, C.L.; Tuinman, A.A.; Boettner, F.E.; Kizu, H. The isolation and structure of a remarkable marine animal antineoplastic constituent: Dolastatin 10. *J. Am. Chem. Soc.* **1987**, *109*, 6883–6885. [[CrossRef](#)]
- Bai, R.L.; Pettit, G.R.; Hamel, E. Binding of dolastatin 10 to tubulin at a distinct site for peptide antimetabolic agents near the exchangeable nucleotide and vinca alkaloid sites. *J. Biol. Chem.* **1990**, *265*, 17141–17149. [[CrossRef](#)]
- Bai, R.; Friedman, S.J.; Pettit, G.R.; Hamel, E. Dolastatin 15, a potent antimetabolic depsipeptide derived from *Dolabella auricularia*. *Biochem. Pharm.* **1992**, *43*, 2637–2645. [[CrossRef](#)]
- Cheung, R.C.F.; Ng, T.B.; Wong, J.H. Marine peptides: Bioactivities and applications. *Mar. Drugs* **2015**, *13*, 4006–4043. [[CrossRef](#)]
- Felicio, M.R.; Silva, O.N.; Goncalves, S.; Santos, N.C.; Franco, O.L. Peptides with Dual antimicrobial and anticancer activities. *Front. Chem.* **2017**, *5*, 5. [[CrossRef](#)] [[PubMed](#)]
- MacDougall, G.; Anderton, R.S.; Mastaglia, F.L.; Knuckey, N.W.; Meloni, B.P. Mitochondria and neuroprotection in stroke: Cationic arginine-rich peptides (CARPs) as a novel class of mitochondria-targeted neuroprotective therapeutics. *Neurobiol. Dis.* **2019**, *121*, 17–33. [[CrossRef](#)] [[PubMed](#)]

13. Wang, C.; Dong, S.; Zhang, L.; Zhao, Y.; Huang, L.; Gong, X.; Wang, H.; Shang, D. Cell surface binding, uptake and anticancer activity of L-K6, a lysine/leucine-rich peptide, on human breast cancer MCF-7 cells. *Sci. Rep.* **2017**, *7*, 8293. [[CrossRef](#)] [[PubMed](#)]
14. Morris, M.C.; Depollier, J.; Mery, J.; Heitz, F.; Divita, G. A peptide carrier for the delivery of biologically active proteins into mammalian cells. *Nat. Biotechnol.* **2001**, *19*, 1173–1176. [[CrossRef](#)] [[PubMed](#)]
15. Xu, J.; Chen, Z.; Song, L.; Chen, L.; Zhu, J.; Lv, S.; Yu, R. A new in vitro anti-tumor polypeptide isolated from *Arca inflata*. *Mar. Drugs* **2013**, *11*, 4773–4787. [[CrossRef](#)] [[PubMed](#)]
16. Zhu, J.; Xu, J.; Wang, Y.; Li, C.; Chen, Z.; Song, L.; Gao, J.; Yu, R. Purification and structural characterization of a novel anti-tumor protein from *Arca inflata*. *Int. J. Biol. Macromol.* **2017**, *105*, 103–110. [[CrossRef](#)] [[PubMed](#)]
17. Li, C.; Wen, Y.; He, Y.; Zhu, J.; Yin, X.; Yang, J.; Zhang, L.; Song, L.; Xia, X.; Yu, R. Purification and characterization of a novel  $\beta$ -1,3-glucanase from *Arca inflata* and its immune-enhancing effects. *Food Chem.* **2019**, *290*, 1–9. [[CrossRef](#)]
18. Katrahalli, U.; Kalalbandi, V.K.A.; Jaldappagari, S. The effect of anti-tubercular drug, ethionamide on the secondary structure of serum albumins: A biophysical study. *J. Pharm. Biomed. Anal.* **2012**, *59*, 102–108. [[CrossRef](#)]
19. Susi, H.; Timasheff, S.N.; Stevens, L. Infrared spectra and protein conformations in aqueous solutions I. The amide I band in H<sub>2</sub>O and D<sub>2</sub>O solutions. *J. Biol. Chem.* **1967**, *242*, 5460–5466. [[CrossRef](#)]
20. Cyril, R.; Naima, N.A.; Stephanie, M.; Jean-Pierre, H.; Pierre, L. Hydrolysis of haemoglobin surveyed by infrared spectroscopy: I. solvent effect on the secondary structure of haemoglobin. *J. Mol. Struct.* **1999**, *478*, 185–191.
21. Yue, J.; López, J.M. Understanding MAPK signaling pathways in apoptosis. *Int. J. Mol. Sci.* **2020**, *21*, 2346. [[CrossRef](#)] [[PubMed](#)]
22. Rath, P.C.; Aggarwal, B.B. TNF-induced signaling in apoptosis. *J. Clin. Immunol.* **1999**, *19*, 350–364. [[CrossRef](#)] [[PubMed](#)]
23. Saucedo, L.J.; Edgar, B.A. Filling out the Hippo pathway. *Nat. Rev. Mol. Cell Biol.* **2007**, *8*, 613–621. [[CrossRef](#)] [[PubMed](#)]
24. Favoriti, P.; Carbone, G.; Greco, M.; Pirozzi, F.; Pirozzi, R.E.; Corcione, F. Worldwide burden of colorectal cancer: A review. *Updates Surg.* **2016**, *68*, 7–11. [[CrossRef](#)] [[PubMed](#)]
25. Wolf, A.; Fontham, E.; Church, T.R.; Flowers, C.R.; Guerra, C.E.; LaMonte, S.J.; Etzioni, R.; McKenna, M.T.; Oeffinger, K.C.; Shih, Y.T.; et al. Colorectal cancer screening for average-risk adults: 2018 guideline update from the American Cancer Society. *CA Cancer J. Clin.* **2018**, *68*, 250–281. [[CrossRef](#)] [[PubMed](#)]
26. Franchi, M.; Barni, S.; Tagliabue, G.; Ricci, P.; Mazzucco, W.; Tumino, R.; Caputo, A.; Corrao, G. GRETA working group, Effectiveness of first-line Bevacizumab in metastatic colorectal cancer: The observational cohort study GRETA. *Oncologist* **2019**, *24*, 358–365. [[CrossRef](#)]
27. Cremolini, C.; Rossini, D.; Dell’Aquila, E.; Lonardi, S.; Conca, E.; Del Re, M.; Busico, A.; Pietrantonio, F.; Danesi, R.; Aprile, G.; et al. Rechallenge for patients with RAS and BRAF wild-type metastatic colorectal cancer with acquired resistance to first-line Cetuximab and Irinotecan: A phase 2 single-arm clinical trial. *JAMA Oncol.* **2019**, *5*, 343–350. [[CrossRef](#)]
28. Van Cutsem, E.; Köhne, C.H.; Hitre, E.; Zaluski, J.; Chang, C.R.; Chien, A.; Makhson, G.; D’Haens, T.; Pintér, R.; Lim, G.; et al. Cetuximab and chemotherapy as initial treatment for metastatic colorectal cancer. *N. Engl. J. Med.* **2009**, *360*, 1408–1417. [[CrossRef](#)]
29. Reed, J.C. Mechanisms of apoptosis. *Am. J. Pathol.* **2000**, *157*, 1415–1430. [[CrossRef](#)]
30. Burz, C.; Berindan-Neagoe, I.; Balacescu, O.; Irimie, A. Apoptosis in cancer: Key molecular signaling pathways and therapy targets. *Acta Oncol.* **2009**, *48*, 811–821. [[CrossRef](#)]
31. Liu, J.J.; Lin, M.; Yu, J.Y.; Bo, L.; Bao, J.K. Targeting apoptotic and autophagic pathways for cancer therapeutics. *Cancer Lett.* **2010**, *300*, 105–114. [[CrossRef](#)] [[PubMed](#)]
32. Abe, K.; Kurakin, A.; Mohseni-Maybodi, M.; Kay, B.; Khosravi-Far, R. The complexity of tnf-related apoptosis-inducing ligand. *Ann. N. Y. Acad. Sci.* **2010**, *926*, 52–63. [[CrossRef](#)] [[PubMed](#)]
33. Ozören, N.; El-Deiry, W.S. Cell surface death receptor signaling in normal and cancer cells. *Semin. Cancer Biol.* **2003**, *13*, 135–147. [[CrossRef](#)]
34. Peter, M.E.; Kramer, P.H. The CD95 (APO-1/Fas) DISC and beyond. *Cell Death Differ.* **2003**, *10*, 26–35. [[CrossRef](#)] [[PubMed](#)]
35. Thorburn, A. Death receptor-induced cell killing. *Cell Signal* **2004**, *16*, 139–144. [[CrossRef](#)]
36. Kroemer, G. Mitochondrial control of apoptosis: An introduction. *Biochem. Biophys. Res. Commun.* **2003**, *304*, 433–435. [[CrossRef](#)]
37. Gupta, S.; Kass, G.E.; Szegezdi, E.; Joseph, B. The mitochondrial death pathway: A promising therapeutic target in diseases. *J. Cell. Mol. Med.* **2009**, *13*, 1004–1033. [[CrossRef](#)]
38. Marchi, S.; Patergnani, S.; Missiroli, S.; Morciano, G.; Rimessi, A.; Wieckowski, M.R.; Giorgi, C.; Pinton, P. Mitochondrial and endoplasmic reticulum calcium homeostasis and cell death. *Cell Calcium* **2018**, *69*, 62–72. [[CrossRef](#)]
39. Peng, T.I.; Jou, M.J. Oxidative stress caused by mitochondrial calcium overload. *Ann. N. Y. Acad. Sci.* **2010**, *1201*, 183–188. [[CrossRef](#)]
40. Huang, T.C.; Lee, J.F.; Chen, J.Y. Pardaxin, an antimicrobial peptide, triggers caspase-dependent and ros-mediated apoptosis in ht-1080 cells. *Mar. Drugs* **2011**, *9*, 1995–2009. [[CrossRef](#)]
41. Wagner, E.F.; Nebreda, A.R. Signal integration by JNK and p38 MAPK pathways in cancer development. *Nat. Rev. Cancer* **2009**, *9*, 537–549. [[CrossRef](#)] [[PubMed](#)]
42. Dolado, I.; Swat, A.; Ajenjo, N.; De Vita, G.; Cuadrado, A.; Nebreda, A.R. p38 $\alpha$  MAP kinase as a sensor of reactive oxygen species in tumorigenesis. *Cancer Cell* **2007**, *11*, 191–205. [[CrossRef](#)] [[PubMed](#)]

## Article

# Molecular Details of Actinomycin D-Treated MRSA Revealed via High-Dimensional Data

Xuewei Xia <sup>1,†</sup>, Jun Liu <sup>2,†</sup>, Li Huang <sup>1</sup>, Xiaoyong Zhang <sup>3</sup>, Yunqin Deng <sup>1</sup>, Fengming Li <sup>1</sup>, Zhiyuan Liu <sup>1</sup> and Riming Huang <sup>1,\*</sup>

<sup>1</sup> Guangdong Provincial Key Laboratory of Food Quality and Safety, College of Food Science, South China Agricultural University, Guangzhou 510642, China; xiawxuewei@stu.scau.edu.cn (X.X.); huangli@stu.scau.edu.cn (L.H.); dengyq0811@163.com (Y.D.); lifengming@hzu.edu.cn (F.L.); aiden@stu.scau.edu.cn (Z.L.)

<sup>2</sup> Laboratory of Pathogenic Biology, Guangdong Medical University, Zhanjiang 524023, China; lj2388240@gdmu.edu.cn

<sup>3</sup> Joint Laboratory of Guangdong Province and Hong Kong Region on Marine Bioresource Conservation and Exploitation, College of Marine Sciences, South China Agricultural University, Guangzhou 510642, China; zhangxiaoyong@scau.edu.cn

\* Correspondence: huangriming@scau.edu.cn

† These authors contributed equally to this work.

**Abstract:** Methicillin-resistant *Staphylococcus aureus* (MRSA) is highly concerning as a principal infection pathogen. The investigation of higher effective natural anti-MRSA agents from marine *Streptomyces parvulus* has led to the isolation of actinomycin D, that showed potential anti-MRSA activity with MIC and MBC values of 1 and 8 µg/mL, respectively. Proteomics-metabolomics analysis further demonstrated a total of 261 differential proteins and 144 differential metabolites induced by actinomycin D in MRSA, and the co-mapped correlation network of omics, indicated that actinomycin D induced the metabolism pathway of producing the antibiotic sensitivity in MRSA. Furthermore, the mRNA expression levels of the genes *acnA*, *ebpS*, *clfA*, *icd*, and *gpmA* related to the key differential proteins were down-regulated measured by qRT-PCR. Molecular docking predicted that actinomycin D was bound to the targets of the two key differential proteins AcnA and Icd by hydrogen bonds and interacted with multiple amino acid residues of the proteins. Thus, these findings will provide a basic understanding to further investigation of actinomycin D as a potential anti-MRSA agent.

**Keywords:** methicillin-resistant *Staphylococcus aureus*; actinomycin D; *Streptomyces parvulus*; mechanism

**Citation:** Xia, X.; Liu, J.; Huang, L.; Zhang, X.; Deng, Y.; Li, F.; Liu, Z.; Huang, R. Molecular Details of Actinomycin D-Treated MRSA Revealed via High-Dimensional Data. *Mar. Drugs* **2022**, *20*, 114. <https://doi.org/10.3390/md20020114>

Academic Editors: Yonghong Liu and Xuefeng Zhou

Received: 24 December 2021

Accepted: 27 January 2022

Published: 31 January 2022

**Publisher's Note:** MDPI stays neutral with regard to jurisdictional claims in published maps and institutional affiliations.



**Copyright:** © 2022 by the authors. Licensee MDPI, Basel, Switzerland. This article is an open access article distributed under the terms and conditions of the Creative Commons Attribution (CC BY) license (<https://creativecommons.org/licenses/by/4.0/>).

## 1. Introduction

Antimicrobial resistance in microbial pathogens is an important health problem, as infections caused by drug-resistant bacteria increase the death rate every year all over the world [1,2]. Methicillin-resistant *Staphylococcus aureus* (MRSA) could cause many kinds of infections, such as skin abscess, endocarditis, joint infections, and necrotizing pneumonia. MRSA used to be mainly found in the hospital environment but has now also emerged in the community environment [3]. In the hospital environment, there are 60–70% *S. aureus* infections caused by MRSA, which causes the most significant number of spreading infections in all drug-resistant bacteria [4]. While highly effective therapeutic drugs, such as linezolid, daptomycin (lipopeptide), and Synercid<sup>®</sup>, are being applied to inhibit the pathogens, some reports indicated that these bacteria also show emerging resistance to these drugs [5]. Although the resistance of each new antibiotic eventually comes out within a short year time after its promotion, it is necessary to search for novel natural antibacterial agents to inhibit antibiotic-resistant bacteria of pathogenic microorganisms [6].

Recent research studies in medical science have triggered discovery of the novel natural antimicrobial agents from numerous microorganisms [7]. Among these microbes,

especially, the genus *Streptomyces* is one of the most important resources of searching for new antimicrobial agents because of its vital producers of new natural pharmaceutical precursors with diverse structural properties [8,9]. Approximately 67% of the natural therapeutic antibiotics originated from the genus *Streptomyces*, and there still are many potent natural isolates that need to be further explored [10]. Actinomycins are a major class of antibiotics in *Streptomyces*, among which actinomycin D is one of the most widely studied [11]. Actinomycin D has good antitumor activity and has been used as a clinical antitumor anticancer drug [12]. As an antibiotic, Actinomycin D and its analogs also have antibacterial activity against a variety of bacteria, most of which are Gram-positive, such as *S. aureus*, *S. epidermidis*, *Enterococcus faecalis*, with an exception for *Xanthomonas oryzae* being Gram-negative [13–15]. Moreover, it is reported that drug-resistant strains of the aforementioned Gram-positive bacteria also show similar actinomycin D susceptibility to their susceptible bacteria. Wang et al. [12] isolated actinomycin D from the marine-derived actinomycete *Streptomyces* sp. IMB094, which had a better antibacterial effect with MIC of 0.125–0.5 µg/mL on MRSA, methicillin-resistant *S. epidermidis*, and vancomycin-resistant *Enterococcus*.

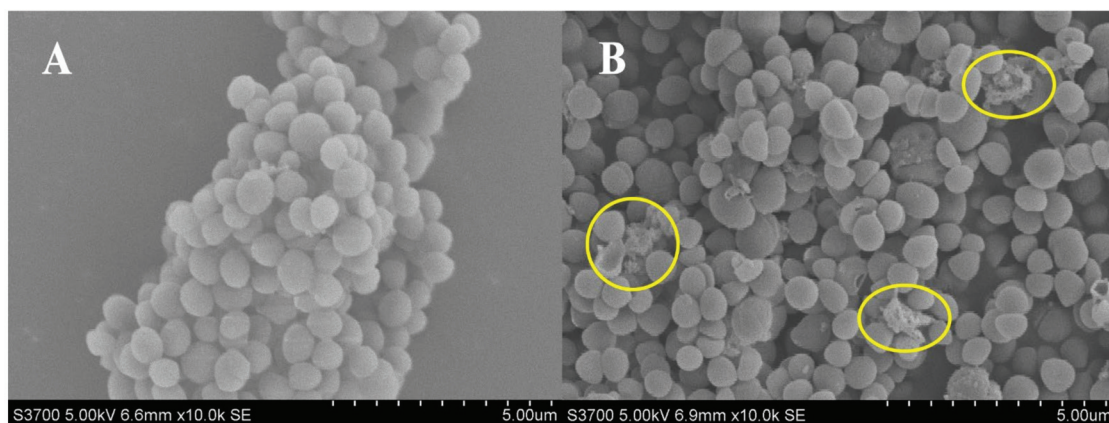
In the process of our searching for new natural anti-MRSA precursors, a marine antibacterial *Streptomyces parvulus* extract showed a stronger anti-MRSA effect. Our previous investigation on the secondary metabolites of *S. parvulus* revealed that actinomycin D was the main secondary metabolites of this strain [16]. Although there have been some studies on the screening of actinomycin D against MRSA, the mechanism remains unclear [12,13]. Thus, it is still necessary to obtain more information on the anti-MRSA mechanism of actinomycin D.

In this work, MRSA as the drug-resistant strains of *S. aureus* were different from the previous research object [16]. On the one hand, the same research route was adopted as before, through proteomics integrated with metabolomics analysis for actinomycin D-treated MRSA to confirm proteins and metabolites with observably changed expression and identify the functions, so as to clarify the inhibition and molecular effect details of actinomycin D to MRSA. On the other hand, different from previous methods, qRT-PCR was used to verify the mRNA expression levels of key differential proteins, and molecular docking was used to predict the docking mode of actinomycin D to key proteins. The effects of antibiotics on bacteria, and even drug-resistant bacteria, involve numerous and complex biomolecular networks, which meet great challenges to research key targets [17]. Omics analysis can provide us with a large information, and molecular docking as predictive biology may allow us to better obtain some key information from a lot of data [18]. These research studies will help to better understand the potential molecular role of actinomycin D on MRSA.

## 2. Results

### 2.1. Effect of Actinomycin D on Bacterial Morphology

Actinomycin D showed an obvious anti-MRSA activity, with MIC value of 1 µg/mL and MBC value of 8 µg/mL. Using SEM analysis, changes in the bacterial morphology exposed to actinomycin D were researched. The bacteria cultured without actinomycin D were performed as a control. As revealed in Figure 1, the control group bacteria showed an intact and smooth membrane with normal morphology. After being treated by actinomycin D, bacteria displayed the leaking of bacterial content, causing differences in morphology. Lysed cells and debris were observed in the treatment group.



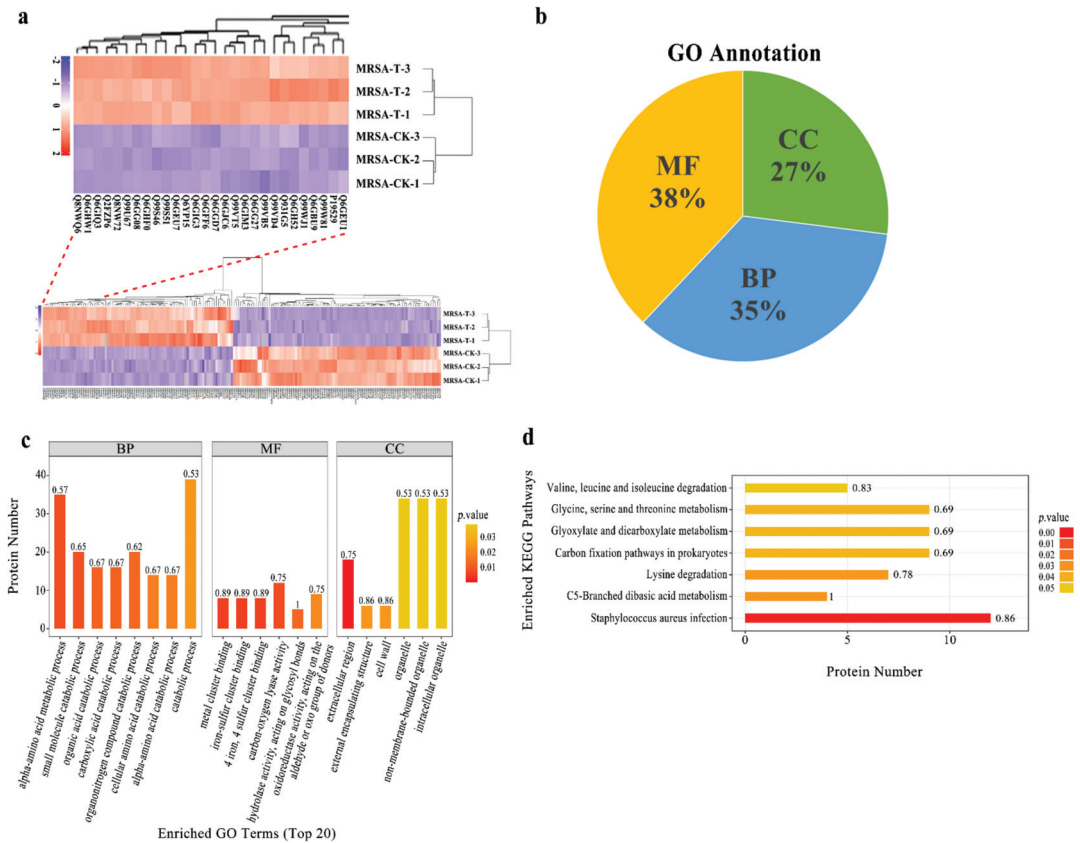
**Figure 1.** (A,B) SEM analysis of MRSA treated with and without actinomycin D. (A) Control group; (B) treatment group.

## 2.2. Effect of Actinomycin D on Protein Profiles

The label-free proteomic analysis method was used to analyze the MRSA affected by actinomycin D. Compared with the control group, 261 differentially expressed proteins (DEPs) were significantly changed in the group treated by actinomycin D screened with  $\log_2(\text{fold changes}) > \pm 2$  and  $p\text{-value} < 0.05$ , including 95 up-regulation and 166 down-regulation DEPs (Table S1). Among them, 9 proteins were regarded as up-regulated DEPs because they were not detected in the control group and 72 proteins were regarded as down-regulated DEPs because they were not detected in the treatment group. Hierarchical cluster study was conducted for all the identified DEPs of the two groups (Figure 2a). The DEPs in the group treated by actinomycin D did not cluster together as in the control group.

Gene ontology annotation gave an available way to profile the protein properties of the identified proteins. It was used to analyze the functions of the DEPs [19]. Furthermore, GO was categorized into three classifications, including biological process (BP), molecular function (MF), and cellular component (CC). The GO studies showed that the DEPs were sub-classified into 34 hierarchically-structured GO categories (Table S2). Thirty-eight percent DEPs were related to molecular function, 35% DEPs were related to biological process, and 27% DEPs were related to cellular component (Figure 2b). Concerning biological processes, 182 DEPs and 187 DEPs were related to the GO term of metabolic processes and cellular processes, respectively. In addition, the GO terms of biological regulation, response to the stimulus, regulation of the biological process, multi-organism process, cellular component organization or biogenesis, localization, signaling, and developmental processes were also involved. At the molecular function level, 167 DEPs were involved in catalytic activity, and 142 were related to binding. In the cellular component, most of the DEPs were ontologically involved in the function of the cell, cell wall, protein-containing complex, organelle, membrane, extracellular region, membrane part, and organelle part (Figure 2c).

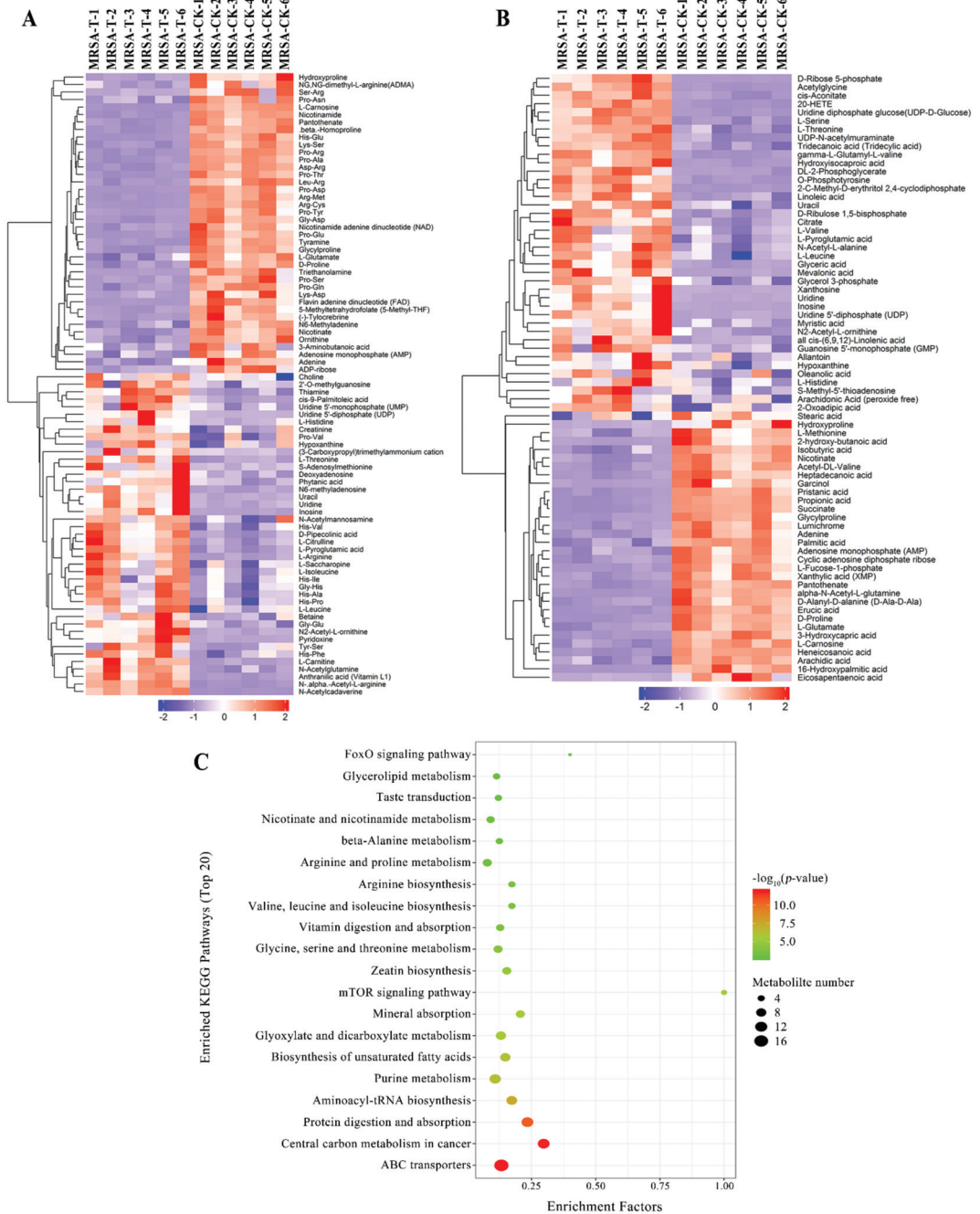
Many proteins are known as vital enzymes in metabolic pathways. The KEGG results showed that the 261 DEPs were involved in 110 signaling pathways in total (Table S3). From these, the top metabolic pathways with  $p\text{-value} < 0.05$  were *Staphylococcus aureus* infection, C5-branched dibasic acid metabolism, lysine degradation, carbon fixation pathways in prokaryotes, glyoxylate and dicarboxylate metabolism, glycine, serine, and threonine metabolism, and valine, leucine, and isoleucine degradation (Figure 2d). These results indicated that, under actinomycin D-treated MRSA, many DEPs might be the vital enzymes participated in metabolic pathways and performed different functions.



**Figure 2.** (a) Hierarchical cluster analysis for all the DEPs. MRSA-T: treatment group; MRSA-CK: control group. Down-regulated proteins are displayed as purple, and up-regulated proteins are displayed as red. Proteins that newly arising and undetected in the D-T were not embraced. (b) GO annotation for the DEPs. BP: biological process, MF: molecular function, CC: cellular component. (c) Enriched GO term (top 20). The numbers beside the bar indicated the enrichment factor, and the color of the bar indicates the *p*-value. (d) KEGG pathway enrichment of the identified DEPs.

### 2.3. Effect of Actinomycin D on Metabolite Profiles

Given the conditions of an orthogonal partial least-squares discrimination analysis (OPLS-DA) model (*p*-value < 0.05, variable importance in the projection (VIP) > 1), distinctly different metabolites were detected. The hierarchical cluster analysis was used to research changes in candidate metabolic processes and the accurate selection of marker metabolites (Figure 3a,b). At the same time, the relationship between samples and the differences in expression of metabolites in different samples can be more comprehensively and intuitively displayed. As a result, 144 obvious changed metabolites were identified (Table S4). In total, 72 metabolites were down-regulated, while 72 metabolites were up-regulated in the treatment group.



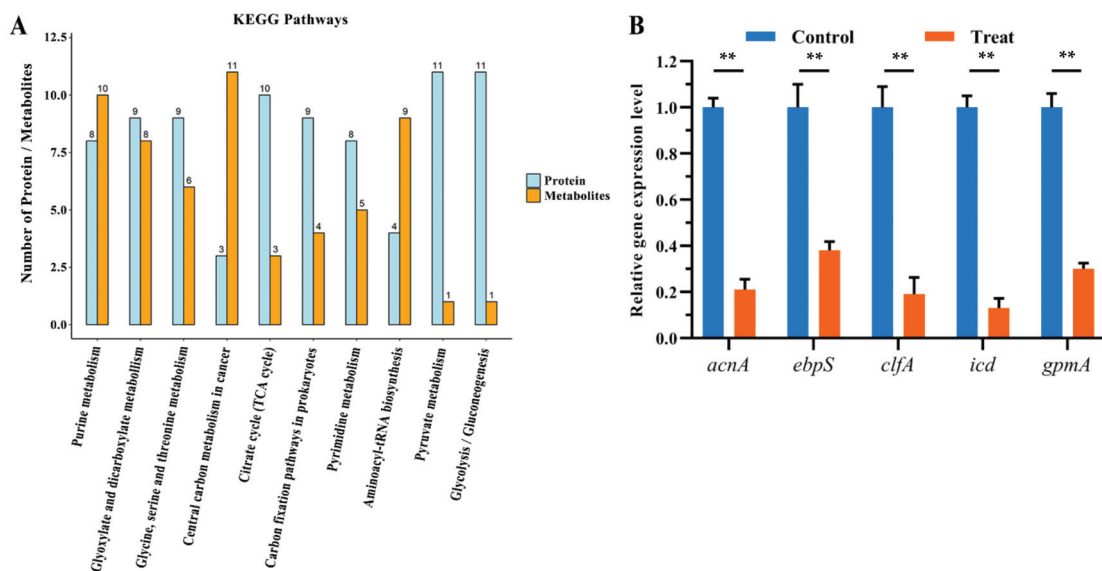
**Figure 3.** (A,B) Hierarchical cluster heat map of differential metabolites in positive mode (A) and negative mode (B). MRSA-T: treatment group; MRSA-CK: control group. Down-regulated proteins are displayed as purple, and up-regulated proteins are displayed as red. (C) Pathways encompassed by the differential metabolites (TOP 20).



For the analysis of related pathways, the distinctly changed metabolites were uploaded to the KEGG database, and the differentially expressed metabolites were mostly related to the ABC transporters, protein digestion and absorption, aminoacyl-tRNA biosynthesis, central carbon metabolism in cancer, and purine metabolism (Figure 3c). The changes of the metabolites contribute significant information for further research of the changes in the group treated by actinomycin D.

#### 2.4. Proteomics-Metabolomics Data Integrated Analysis

Based on the changes of proteins and metabolites, metabolic pathways were chosen as the carrier and performed a mapping analysis to combine the data of proteome and metabolome. A total of 66 metabolic pathways showed differences (Table S5). Research studies of these identified metabolic pathways revealed that they were mostly related to amino acid metabolism. Furthermore, we screened the metabolic pathways related to lysine degradation, glycine, serine, and threonine metabolism, and valine, leucine, and isoleucine degradation, among others (Figure 4a).



**Figure 4.** (A) Common pathways of vital proteins and metabolites. (B) Relative gene expression levels of gene *acnA*, *ebpS*, *clfA*, *icd*, and *gpmA* between the two groups (\*\*,  $p < 0.01$ ).

According to annotation, the significantly changed proteins and metabolites were mainly related to the glycine, serine, and threonine metabolism pathway. The proteins and metabolites that participated in glycine, serine, and threonine metabolism were quite active when treated by actinomycin D, in which 6 metabolites were up-regulated, and 8 proteins were down-regulated.

#### 2.5. Validation of Select DEPs by qRT-PCR

To verify the authenticity and accuracy of the proteomics data, the change of proteins was researched at the mRNA level using qRT-PCR. Considering that the DEPs in two groups are referred to many functional categories, we chose 5 genes that participated in TCA cycle, amino acid metabolism, as target genes for qRT-PCR analysis. Compared with the proteomics results, the mRNA expression levels of 5 genes among the target proteins experimented by qRT-PCR suggested coincident changes with the corresponding protein

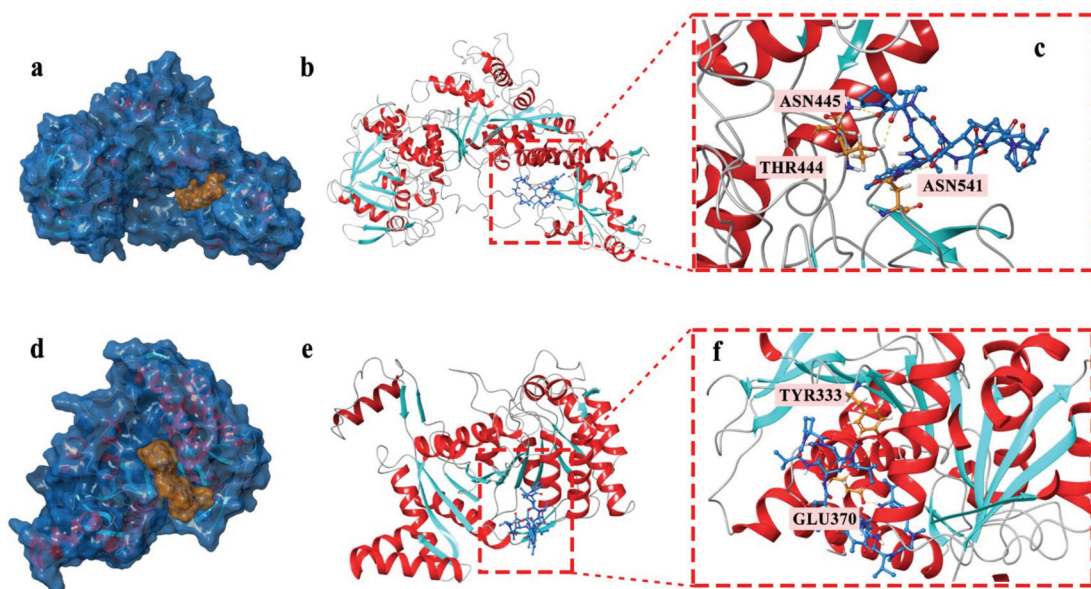
expression levels (Figure 4b). Therefore, the results showed that the proteomics results could be identified in the mRNA level.

## 2.6. Molecular Docking Studies

Based on the docking studies, the location of the hydrogen bond, docking score, and binding energy and ligand-protein pair was predicted and is listed in Table 1. According to the three-dimensional docking mode, we found that actinomycin D might bind to the targets of all three proteins by hydrogen bonds and interact with multiple amino acid residues of the proteins. Three hydrogen bonds were found between actinomycin D and ASN445, THR444, and ASN541 in AcnA as a possible binding way (Figure 5a–c). The predictive binding energy and docking score was calculated as  $-48.15$  kcal/mol and  $-5.729$ , respectively. Moreover, actinomycin D might bind to the amino acid residues of Icd located in TRY333 and GLU370 by hydrogen bond, and the predictive binding energy and the docking score were measured as  $-26.27$  kcal/mol and  $-5.65$ , individually (Figure 5d–f). In conclusion, hydrogen bonds might be the driving force for the interaction between actinomycin D and the proteins. The results indicated that actinomycin D could be bound to these proteins to inhibit the growth of MRSA.

**Table 1.** Molecular docking predictive data within the ligand-target molecule couples.

| Target | $\Delta G$ (kcal/mol) | Docking Score | Hydrogen Bond Location |
|--------|-----------------------|---------------|------------------------|
| AcnA   | $-48.15$              | $-5.729$      | ASN445, THR444, ASN541 |
| Icd    | $-26.27$              | $-5.65$       | TYR333, GLU370         |



**Figure 5.** (a–c) Actinomycin D accommodated in AcnA (a); overview of the docked pose (docking score:  $-5.729$ ) (b); hydrogen bond interactions of the actinomycin D with AcnA (c). (d–f) Actinomycin D accommodated in Icd (d); overview of the docked pose (docking score:  $-5.65$ ) (e); hydrogen bond interactions of the actinomycin D with Icd (f). The proteins models of AcnA and Icd used in molecular docking were homology models.

### 3. Discussion

Proteomics and metabolomics are subsequent additions performing the comprehension of the function and relating to sequential events in omics studies. Proteomics primarily exposes genetic modifications and exhibits the expression spectrum of the proteins containing the research of protein structure. On the contrary, metabolomics shows an intact analysis of the compounds with low molecular weight. It has been reported by Gahlaut et al. [20] that the comprehensive explication of biological responses in different conditions can be written at the level of transcriptomics, proteomics, and metabolomics, and modulations in the metabolome are reflected by proteome. The results show the significance of addressing the consolidation of proteome and metabolome in the current research. Akpunarlieva et al. [21] integrated proteome and metabolome to show us an approach of relating biochemistry to phenotype, further anchorage was furnished to the present study.

#### 3.1. Antibiotic Sensitivity of MRSA Affected by Actinomycin D

Glycine, serine, and threonine have an impact on the growth of microbes [22]. It has been reported that glycine, serine, and threonine metabolism is a significant pathway that refers to antibiotic sensitivity. Moreover, according to the research, the synergy of the promoted glycine, serine, and threonine metabolism and glucose can enhance the kanamycin-mediated killing [23]. According to the proteomics and metabolomics results, 9 DEPs (all down-regulated) and 6 differently metabolites (all up-regulated) participated in the glycine, serine, and threonine metabolism pathway. Via the oxidative cleavage of glycine, glycine cleavage system H protein (GcvH) is one of the four proteins that compose the glycine cleavage complex, vital for the synthesis of C<sub>1</sub> (one-carbon units) for cell metabolism. The abundance of this protein is promoted by exogenous glycine, and is suppressed by the presence of purines [24]. Glycine betaine is significant for the existence of bacteria in various environments [25]. Oxygen-dependent choline dehydrogenase (BetA) and GcvH oxidize choline to betaine aldehyde and subsequently convert to glycine betaine [26]. Interestingly, we found that choline and betaine were up-regulated. Furthermore, the results showed that GcvH and BetA were down-regulated. The down-regulation of GcvH and BetA inhibited the oxidization of choline to betaine aldehyde, and we presumed the protein hydrolysis might result in the up-regulation of betaine. 2,3-Bisphosphoglycerate-dependent phosphoglycerate mutase (GpmA) was down-regulated in the proteomics study; it may motivate the interchange between 2-phosphoglycerate and 3-phosphoglycerate. GpmA functions as a potential target for new antibiotics as a crucial enzyme in energy metabolism and glycolysis [27]. Dihydrolipoyl dehydrogenase (PdhD) involved in glycine, serine, and threonine metabolism is also regarded as vital enzymes for the anaplerosis of the TCA cycle [28]. Therefore, the down-regulation of the PdhD might disturb the TCA cycle. It has been reported that the TCA cycle plays an important role in mediating the biofilm formation of MRSA, specifically by influencing the matrix composition [29]. Moreover, a recent report has demonstrated that the fluctuation of TCA cycle is an antibiotic-resistant mechanism. Our omics studies showed the expression of isocitrate dehydrogenase (NADP) and aconitate hydratase A (AcnA) in the TCA cycle were decreased. AcnA could transform the citrate to cis-aconitate. The decrease of the AcnA would inhibit the conversion to disturb the TCA cycle. The results above indicated that actinomycin D might affect the antibiotic sensitivity of MRSA by disturbing the glycine, serine, and threonine metabolism and TCA cycle.

Furthermore, the bacterial cell wall is an important target of many antibiotics [30]. By scanning electron microscopy analysis, changes in the MRSA morphology were observed. According to the results, MRSA treated by actinomycin D could break the cell and showed a deep degree of abnormal cell shape. These results can be expounded by speculating that the cell wall may be damaged by actinomycin D. Moreover, the purine biosynthetic pathway plays a vital part in cell wall synthesis, and the whole purine biosynthetic pathway was indicated to be in invertible and robust restriction under the cases that the cell wall synthesis was disturbed [31]. The proteomics results in our research showed that the 4 proteins that

participated in purine metabolism were up-regulated, and 4 proteins were down-regulated. The metabolomics results showed that 4 metabolites related to purine metabolism were inhibited, and 5 metabolites were stimulated significantly. The disturbance of purine metabolism was influential for the purine content in the cell to cope with the growing need for ATP due to the superfluous cell wall material produced [32]. The results indicated that the purine metabolism pathway was disturbed in MRSA treated by actinomycin D. According to the omics analysis, some proteins involved in cell wall synthesis are down-regulated, including lactonase Drp35 (a 35-kDa drug-responsive protein), clumping factor A (ClfA), and elastin-binding protein of *S. aureus* (EbpS). Drp35 relates to the cell wall synthesis of MRSA, preserving the cell to exist in a serious environment [33]. ClfA, a staphylococcal surface protein, could bind with fibrinogen [34]. The EbpS is an adhesin functional for adhering to host cells by binding with elastin. It has been confirmed that the EbpS in MRSA could regulate zinc-dependent biofilm formation [35]. The down-regulation of these proteins might inhibit the growth of the cell wall to influence the antibiotic sensitivity of MRSA.

Given that oxidative stress is associated with antibiotic treatment, low levels of ROS could be used as an adjuvant to potentiate the antibacterial activity of commercial antibiotics [36]. During aerobic respiration, some reactive oxygen species (ROS) that impair the DNA, protein, and lipids within cells are produced. L-lactate dehydrogenase 1 (Ldh1), which was down-regulated in our study, responsible for catalyzing the conversion of pyruvate to lactate. Since Ldh1 converts NAD<sup>+</sup> to NADH in the actions, it plays a vital role in keeping the homeostasis of redox in bacteria [37]. NADPH can reduce glutathione through glutathione reductase, which transforms reactive H<sub>2</sub>O<sub>2</sub> to H<sub>2</sub>O by glutathione peroxidase. If NADPH is insufficient, the H<sub>2</sub>O<sub>2</sub> would attack the cell when transformed into hydroxyl free radicals [38]. The down-regulation of glutathione peroxidase showed that H<sub>2</sub>O<sub>2</sub> transformation was suppressed, which would cause the gathering of H<sub>2</sub>O<sub>2</sub>. Therefore, the increasing H<sub>2</sub>O<sub>2</sub> during the treatment of MRSA likely produced extra ROS, which might damage the cellular compounds. Glutathione is a vital antioxidant in bacteria and is used to prevent oxidative injury influenced by ROS [39]. Pathway study revealed that the enzymes related to glutathione metabolism were down-regulated, showing that the antioxidant shield system was broken. Moreover, two enzymes involved against ROS, including peroxidase and superoxide dismutase, were down-regulated, but catalase was up-regulated [40]. Based on the carbohydrate metabolism and glutathione metabolism that were restrained, as well as those proteomic data, we speculated that ROS might gather via increasing oxidative stress treated by actinomycin D. The accumulation of ROS results in apoptosis [41]. Thus, the increased oxidative stress during the treatment of MRSA likely produces more ROS that could damage cellular components, containing the cell membrane component, such as unsaturated fatty acids.

### 3.2. Virulence Factor of MRSA Affected by Actinomycin D

The Serine-aspartate repeat-containing protein D (SdrD) protein is vital for MRSA to bind to host cells, enhance the virulence, and exist in the blood [42]. ClfA is regarded as a critical MRSA virulence factor as a result of it having been suggested to increase cell virulence in experimental models of sepsis [43], skin infection [44], septic arthritis [45], and endocarditis [46]. ClfA combines with the dimeric host fibrinogen through the carboxyterminal domain of the fibrinogen gamma chain, causing bacterial aggregation in plasma or purified fibrinogen [47]. The down-regulation of the SdrD and ClfA proteins in the current research indicates that the cells have been suppressed by actinomycin D. Interestingly, the accessory gene regulator A (AgrA) and S-ribosylhomocysteine lyase (LuxS) proteins, respectively, exhibited down-regulation and up-regulation. Both of the proteins related to quorum-sensing have been suggested to play vital parts in many biological processes, containing host infection and biofilm formation [48]. Previous research showed that LuxS regulates virulence factors and plays a role in metabolism [49]. Thus, the different changed types of AgrA and LuxS might be due to their respective involvement in different functional

regulations. The result showed that actinomycin D might regulate virulence factors, such as SdrD, ClfA, AgrA, and LuxS, to reduce virulence.

#### 4. Materials and Methods

##### 4.1. Preparation of Actinomycin D

The preparation of actinomycin D from marine *Streptomyces parvulus* was performed according to the same method used in our previous study [16]. Briefly, strain SCAU-062 was identified as *Streptomyces parvulus* and deposited in the Joint Laboratory of Guangdong Province and Hong Kong Region on Marine Bioresource Conservation and Exploitation, College of Marine Sciences, South China Agricultural University.

The strain SCAU-062 was inoculated and cultivated in 150 replicate 1000 mL Erlenmeyer flasks, each containing 250 mL Luria Bertani (LB) broth (dextrose 1 g/L, yeast extract 5 g/L, peptone 10 g/L, sodium chloride 5 g/L), in a rotary shaker (150 rpm) at 28 °C. Cultivated for 7 days, a total of 30 L of fermentation broths was exhaustively extracted with ethyl acetate (3 times × 30 L) at 25 °C for 3 × 7 days. The solution was evaporated (P = 0.01 MP, T = 45 °C) to get a residue (5 g). The ethyl acetate soluble portion was applied to column chromatography on silica gel by using petroleum ether/acetone (from 7:3 to 0:1) as the eluent, giving eight fractions (A–H). Semi-preparative reversed-phase HPLC further purified fraction C (Waters Prep C18 column, 150 × 19 mm, 5 µm, 2 mL/min) to afford purified actinomycin D (45% MeOH/H<sub>2</sub>O, t<sub>R</sub> = 24.1 min) that was identified in our previous report [16].

##### 4.2. Microorganism and Medium

The strain MRSA ATCC 43300 was acquired from the American Type Culture Collection (ATCC, Manassas, VA, USA). After being incubated on LBA (peptone 10 g/L, sodium chloride 5 g/L, dextrose 1 g/L, yeast extract 5 g/L and agar 15 g/L) for 24 h at 37 °C, the strain MRSR ATCC 43300 was inoculated in 200 mL LB medium and cultivated on a shaker at 150 rpm for 24 h at 37 °C to gain the bacterial suspension.

##### 4.3. Minimum Inhibitory Concentration and Minimum Bactericidal Concentration Measurement of MRSA Effected by Actinomycin D

The minimum inhibitory concentration (MIC) of actinomycin D on MRSA was measured by a broth micro-dilution method described by Dellavelle et al. [50]. Briefly, the bacterial suspension (100 µL) of strain MRSA was incubated in Mueller-Hinton (MH) broth and cultivated at 150 rpm at 37 °C. Fifty microliters of different concentrations of actinomycin D (0.25, 0.5, 1, 2, 4, 8, 16, and 32 µg/mL) were added to the bacterial culture when the MRSA grew to logarithmic phase (OD<sub>600</sub> reached 0.3 to 0.5). For control, a positive control group consisted of 150 µL of MH broth and 50 µL of bacterial culture, and the negative control group contained 200 µL of MH broth only. All groups were cultured at 37 °C for 24 h, and OD was determined at 600 nm. Each treatment was performed in three replicates. The MIC value was calculated as described by Dellavelle et al. [50]. After measuring the MIC, fermented liquid of 100 µL from each well that shows no bacterial growth was streaked onto MH agar plates at 37 °C for 20 h. The value of minimum bactericidal concentration (MBC) was the lowest concentration that kills all of the initial bacterial population, showing no colonies on the MH agar [51].

##### 4.4. Scanning Electron Microscopy (SEM) Analysis

To research morphology under treatment of actinomycin D by SEM analysis, MRSA was incubated in 100 mL of LB broth for 24 h with or without actinomycin D treatment. The cells of MRSA were gathered by centrifugation and rinsed thrice with 0.1 M phosphate-buffered saline (PBS) buffer. Then, 2.5% Glutaraldehyde was used to fix the cells for 2 h. The rest of the process was conducted according to the method of Suo et al. [52]. The morphology of the bacteria was photographed by a Hitachi s-3700n tungsten filament SEM (Hitachi, Tokyo, Japan).

#### 4.5. Label-Free Quantitative Proteomics

The label-free quantitative proteomics analysis was performed by the previously described methods [28]. The measurements were carried out in sextuplicate.

##### 4.5.1. Sample Preparation

The MRSA was harvested by centrifugation (14,000 rpm, 3 min) and rinsed thrice with PBS buffer. The cells were processed for total protein extraction. The protein concentration was measured by BCA Protein Assay Kit (Bio-Rad, Hercules, CA, USA). Then, 250 µg protein of each sample was conducted by the reported Filter-aided sample preparation (FASP Digestion). A UV light spectral was used to estimate the peptide concentration density at 280 nm.

##### 4.5.2. Liquid Chromatography (LC)-Electrospray Ionization (ESI) Tandem MS (MS/MS) Analysis

C<sub>18</sub> Cartridges (Sigma-Aldrich, Saint Louis, MO, USA) were used to desalt peptides in every sample, and, finally, 0.1% (*v/v*) trifluoroacetic acid (40 µL) was added to reconstitute. MS experiments were conducted on a QExactive mass spectrometer (Thermo Fisher Scientific, Waltham, MA, USA). Those containing peptide (5 µg) of buffer A included 0.1% formic acid and 2% acetonitrile, separated with a gradient of buffer B including 0.1% formic acid and 80% acetonitrile, conducted by a C<sub>18</sub> reversed-phase column (Thermo Scientific Easy Column, Waltham, MA, USA) at a speed of 250 nL/min regulated using IntelliFlow technology for 120 min. The measure of the target value was based on predictive Automatic Gain Control (pAGC). Every sample was performed in MS experiments thrice.

##### 4.5.3. Sequence Database Search and Data Analysis

MaxQuant software version 1.3.0.5 (Max Planck Institute of Biochemistry, Munich, Germany) was used to conduct the MS data, and the data was retrieved in the UniProtKB *Staphylococcus aureus* database. Label-free quantification was conducted on MaxQuant as previous studies reported [53]. Software Origin version 6.1 (OriginLab, Northampton, MA, USA) was used to perform statistical analysis. The DEPs were selected by the following conditions:  $\log_2(\text{fold changes}) > \pm 2$ , and *p*-value < 0.05.

#### 4.6. Untargeted Metabolomics Methods

##### 4.6.1. Sample Collection and Preparation

The measurements were performed in triplicate. Four hundred microliters of acetonitrile/methanol (1:1, *v/v*, 4 °C) were mixed with 100 µL aliquots to eliminate the protein of the samples at 4 °C. The mixture was centrifuged (14,000 *g*, 4 °C) for 15 min, and then the supernatant was desiccated in a centrifuge. The cells were re-dissolved in 100 µL water/acetonitrile (1:1, *v/v*) solvent for LC-MS analysis. The samples of quality control (QC) were performed by mixing 10 µL of every single sample to control the reproducibility of instrumental research.

##### 4.6.2. LC-MS/MS Analysis

A UHPLC (1290 Infinity LC, Agilent Technologies, Santa Clara, CA, USA) and a quadrupole time-of-flight (TripleTOF 6600, AB Sciex, Boston, MA, USA) were conducted for the analysis. An ACQUITY UPLC BEH column (2.1 mm × 100 mm, 1.7 µm, Waters, Milford, MA, USA) was used to analyze the samples for separation. Then, 25 mM ammonium hydroxide and 25 mM ammonium acetate in water (A) and acetonitrile (B) were performed as the mobile phase in both ESI positive and negative patterns. The gradient conditions were 15% A kept for 1 min, increased to 35% in 11 min, then gradually increased to 60% in 0.1 min, retained for 4 min, then reduced to 15% in 0.1 min, and, finally, a 5 min equilibration was performed.

#### 4.6.3. Statistical Data Analysis

By ProteoWizard MSConvert, the MS data was transformed from wiff.scan files to mzXML files and exported to XCMS Online (<https://xcmsonline.scripps.edu>, accessed on 16 May 2019). For annotation of adducts and isotopes, the Collection of Algorithms of MEtabolite pRofile Annotation (CAMERA) was used. By comparing MS/MS spectra and accuracy  $m/z$  value ( $<25$  ppm) with an internal database built with available authentic standards, compound evaluation of metabolites was conducted. To show its contribution to the classification, we computed the VIP value of each variable in the OPLS-DA model. To measure the significance of each metabolite, metabolites in which the VIP exceeded 1.0 were further performed to Student's  $t$ -test at a univariate level ( $p$ -values  $< 0.05$ ) were regarded as statistically meaningful.

#### 4.7. Bioinformatics Analysis

Gene Ontology (GO) terms were used to map the identified protein sequences to determine the biological properties and functional classification of the screened differentially abundant proteins. An NCBI BLAST search was conducted for all detected sequences with the NCBI nr Medicago truncatula database for this analysis. GO analysis was performed by BLAST2GO [54]. Moreover, all differentially distinct proteins and metabolites were identified by the Kyoto Encyclopedia of Genes and Genomes (KEGG) [55]. The functional classifications and pathways ( $p$ -values  $< 0.05$ ) were regarded as having obvious enrichment. To inquire about the enriched KEGG proteins and metabolites by an R-based software for omics results integration, the significantly changed proteins and metabolites identified between the control group and treatment group were employed, respectively.

#### 4.8. qRT-PCR Analysis

The expression of genes *acnA*, *ebpS*, *clfA*, *icd*, and *gpmA* was verified by qRT-PCR. MRSA was harvested in the same requirement as the proteomics research. The measurements were carried out in triplicate. RNAprotect bacteria reagent (QIAGEN, Dusseldorf, Germany) was appended to the cells directly, to stabilize RNA. Total RNA Kit (GBCBIO Technologies, Guangzhou, China) was used to extract total RNA, and the concentration of RNA was detected by a Nanodrop 2000c spectrophotometer (Thermo Scientific, Waltham, MA, USA). qRT-PCR was conducted using a two-step method. RNA was firstly reverse-transcribed to cDNA (Vazyme, Nanjing, China); and RT-PCR was performed on QuantStudio 3 Real-Time PCR System (Applied Biosystems, Carlsbad, CA, USA) using Realtime PCR Super mix SYBRgreen with 40 cycles of denaturation for 15 s at 95 °C, annealing for 15 s at 55 °C, and extension for 42 s at 72 °C. The melting curve stage was conducted after amplification to confirm the specificity of the PCR amplification outcome. The relative quantitation was calculated by the  $2^{-\Delta\Delta CT}$  method [56]. The primer sequences are given in Table S6. 16S rRNA was selected as an internal reference.

#### 4.9. Molecular Docking Studies

For the docking study, the program Maestro 11.8 was used to predict the possible binding behavior between Aconitate hydratase A (AcnA, UniProtKB—Q6G9K9), Isocitrate dehydrogenase (Icd, UniProtKB—Q8NW61), and actinomycin D. Because the crystal structure of AcnA and Icd had not been resolved, we first needed to find the sequence from UniProt website (<https://www.uniprot.org/>, accessed on 10 September 2020) and construct a tertiary structure model of them. In this study, homology modeling was conducted by SWISS-MODEL (<https://swissmodel.expasy.org/>, accessed on 10 September 2020), and the PDB files of the template were available from the website. The details of the template were shown in Table S7. The structure of actinomycin D was obtained from PubChem (<https://pubchem.ncbi.nlm.nih.gov/>, ID: 2019, accessed on 10 September 2020). All water molecules were removed, and polar hydrogen was added for the molecular docking study. Finally, the model with the best docking score was used for further analysis.

## 5. Conclusions

A marine *S. parvulus* originated actinomycin D possessed a significant inhibitory effect on MRSA. The MIC and MBC values of actinomycin to MRSA were 1 and 8 µg/mL, respectively. Proteomics integrated with metabolomics analysis revealed 261 differential proteins (up-regulated 86, down-regulated 94, new 9 and undetectable 72) and 144 differential metabolites (up-regulated 68 and down-regulated 76), and the co-mapped correlation network of omics indicated that actinomycin D induced the metabolism pathway about antibiotic sensitive in MRSA. Furthermore, qRT-PCR verified the expression of mRNA for genes *acnA* and *icd*, and the encoding proteins related to antibiotic sensitivity were predicted by molecular docking. In summary, actinomycin D might affect the antibiotic sensitivity of MRSA by disturbing the glycine, serine, and threonine metabolism and TCA cycle, also inhibiting the growth of cell wall and damaging cell membrane component. In addition, it might regulate the virulence factor SdrD, ClfA, AgrA, and LuxS to reduce virulence. These findings will contribute to a better understanding of the possible molecular mechanism of anti-MRSA actinomycin D.

**Supplementary Materials:** The following supporting information can be downloaded at: <https://www.mdpi.com/article/10.3390/md20020114/s1>, Table S1: Protein quantification and analysis of significant differences, Table S2: GO annotation statistics table, Table S3: KEGG pathways in which differentially expressed proteins are involved, Table S4: Differential metabolites of leaves between the budding stage and mid-flowering stage, Table S5: Proteome-metabolome data co-analysis, Table S6: Sequences of the used primers, Table S7: The information of the template for molecular docking.

**Author Contributions:** Conceptualization, X.X., J.L. and L.H.; methodology, X.X., L.H., Y.D. and Z.L.; investigation, L.H.; writing—original draft preparation, X.X. and L.H.; writing—review and editing, J.L., X.Z. and R.H.; visualization, F.L.; supervision, R.H.; funding acquisition, R.H. All authors have read and agreed to the published version of the manuscript.

**Funding:** This research was funded by the Natural Science Foundation of Guangxi Province, grant number 2021GXNSFDA075010; the Program of Department of Natural Resources of Guangdong Province, grant numbers GDNRC(2020)038 and GDNRC(2021)53; the Guangdong Provincial Special Fund for Modern Agriculture Industry Technology Innovation Teams, grant numbers 2021KJ122; the Key-Area Research and Development Program of Guangdong Province, grant numbers 2020B1111030004; the General project of Guangdong Medical Science and Technology Research Foundation, grant number A2021207; the Characteristic innovation project of colleges and universities in Guangdong Province, grant number 2020KTSCX041; the Finance Special Project of Zhanjiang City, grant number 2021A05095; the Discipline construction project of Guangdong Medical University, grant number 4SG21279P.

**Institutional Review Board Statement:** Not applicable.

**Informed Consent Statement:** Not applicable.

**Data Availability Statement:** The data presented in this study are available in Supplementary Material here.

**Conflicts of Interest:** The authors declare no conflict of interest.

## References

1. Laxminarayan, R.; Matsoso, P.; Pant, S.; Brower, C.; Rottingen, J.A.; Klugman, K.; Davies, S. Access to effective antimicrobials: A worldwide challenge. *Lancet* **2016**, *387*, 168–175. [[CrossRef](#)]
2. Riahifard, N.; Mozaffari, S.; Aldakhil, T.; Nunez, F.; Alshammari, Q.; Alshammari, S.; Yamaki, J.; Parang, K.; Tiwari, R.K. Design, synthesis, and evaluation of amphiphilic cyclic and linear peptides composed of hydrophobic and positively-charged amino acids as antibacterial agents. *Molecules* **2018**, *23*, 2722. [[CrossRef](#)] [[PubMed](#)]
3. Taubes, G. The bacteria fight back. *Science* **2008**, *321*, 356–361. [[CrossRef](#)] [[PubMed](#)]
4. Snitser, O.; Russ, D.; Stone, L.K.; Wang, K.K.; Sharir, H.; Kozner, N.; Cohen, G.; Barr, H.M.; Kishony, R. Ubiquitous selection for *mecA* in community-associated MRSA across diverse chemical environments. *Nat. Commun.* **2020**, *11*, 6038. [[CrossRef](#)]
5. Umerska, A.; Strandh, M.; Cassisa, V.; Matougui, N.; Eveillard, M.; Saulnier, P. Synergistic Effect of Combinations Containing EDTA and the Antimicrobial Peptide AA230, an Arenicin-3 Derivative, on Gram-Negative Bacteria. *Biomolecules* **2018**, *8*, 122. [[CrossRef](#)]



6. Hirschwerk, D.; Ginocchio, C.C.; Bythrow, M.; Condon, S. Diminished susceptibility to daptomycin accompanied by clinical failure in a patient with methicillin-resistant *Staphylococcus aureus* Bacteremia. *Infect. Control Hosp. Epidemiol.* **2006**, *27*, 315–317. [[CrossRef](#)]
7. Lee, J.H.; Kim, E.; Choi, H.; Lee, J. Collismycin C from the Micronesian Marine Bacterium *Streptomyces* sp. MC025 Inhibits *Staphylococcus aureus* Biofilm Formation. *Mar. Drugs* **2017**, *15*, 387. [[CrossRef](#)]
8. Jiao, W.; Yuan, W.; Li, Z.; Li, J.; Li, L.; Sun, J.; Gui, Y.; Wang, J.; Ye, B.; Lin, H. Anti-MRSA actinomycins D-1-D-4 from the marine sponge-associated *Streptomyces* sp LHW52447. *Tetrahedron* **2018**, *74*, 5914–5919. [[CrossRef](#)]
9. Riahifard, N.; Tavakoli, K.; Yamaki, J.; Parang, K.; Tiwari, R. Synthesis and evaluation of antimicrobial activity of [R(4)W(4)K]-levofloxacin and [R(4)W(4)K]-levofloxacin-Q conjugates. *Molecules* **2017**, *22*, 957. [[CrossRef](#)]
10. Newman, D.J.; Cragg, G.M.; Snader, K.M. Natural products as sources of new drugs over the period 1981-2002. *J. Nat. Prod.* **2003**, *66*, 1022–1037. [[CrossRef](#)]
11. Bao, J.; He, F.; Li, Y.; Fang, L.; Wang, K.; Song, J.; Zhou, J.; Li, Q.; Zhang, H. Cytotoxic antibiotic angucyclines and actinomycins from the *Streptomyces* sp. XZHG99T. *J. Antibiot.* **2018**, *71*, 1018–1024. [[CrossRef](#)]
12. Wang, Q.; Zhang, Y.; Wang, M.; Tan, Y.; Hu, X.; He, H.; Xiao, C.; You, X.; Wang, Y.; Gan, M. Neo-actinomycins A and B, natural actinomycins bearing the 5H-oxazolol[4,5-b] phenoxazine chromophore, from the marine-derived *Streptomyces* sp IMB094. *Sci. Rep.* **2017**, *7*, 3591. [[CrossRef](#)]
13. Qureshi, K.A.; Bholay, A.D.; Rai, P.K.; Mohammed, H.A.; Khan, R.A.; Azam, F.; Jaremko, M.; Emwas, A.; Stefanowicz, P.; Waliczek, M.; et al. Isolation, characterization, anti-MRSA evaluation, and in-silico multi-target anti-microbial validations of actinomycin X-2 and actinomycin D produced by novel *Streptomyces smyrnaeus* UKAQ\_23. *Sci. Rep.* **2021**, *11*, 14539. [[CrossRef](#)]
14. Yao, Z.; Sun, C.; Xia, Y.; Wang, F.; Fu, L.; Ma, J.; Li, Q.; Ju, J. Mutasynthesis of Antibacterial Halogenated Actinomycin Analogues. *J. Nat. Prod.* **2021**, *84*, 2217–2225. [[CrossRef](#)]
15. Ogasawara, Y.; Shimizu, Y.; Sato, Y.; Yoneda, T.; Inokuma, Y.; Dairi, T. Identification of actinomycin D as a specific inhibitor of the alternative pathway of peptidoglycan biosynthesis. *J. Antibiot.* **2020**, *73*, 125–127. [[CrossRef](#)]
16. Lin, Y.; Huang, L.; Zhang, X.; Yang, J.; Chen, X.; Li, F.; Liu, J.; Huang, R. Multi-Omics Analysis Reveals Anti-*Staphylococcus aureus* Activity of Actinomycin D Originating from *Streptomyces parvulus*. *Int. J. Mol. Sci.* **2021**, *22*, 12231. [[CrossRef](#)]
17. Lopatkin, A.J.; Bening, S.C.; Manson, A.L.; Stokes, J.M.; Kohanski, M.A.; Badran, A.H.; Earl, A.M.; Cheney, N.J.; Yang, J.H.; Collins, J.J. Clinically relevant mutations in core metabolic genes confer antibiotic resistance. *Science* **2021**, *371*, eaba0862. [[CrossRef](#)]
18. Lopatkin, A.J.; Collins, J.J. Predictive biology: Modelling, understanding and harnessing microbial complexity. *Nat. Rev. Microbiol.* **2020**, *18*, 507–520. [[CrossRef](#)]
19. Ashburner, M.; Ball, C.A.; Blake, J.A.; Botstein, D.; Butler, H.; Cherry, J.M.; Davis, A.P.; Dolinski, K.; Dwight, S.S.; Eppig, J.T.; et al. Gene ontology: Tool for the unification of biology. The Gene Ontology Consortium. *Nat. Genet.* **2000**, *25*, 25–29. [[CrossRef](#)]
20. Gahlaut, A.; Vikas; Dahiya, M.; Gothwal, A.; Kulharia, M.; Chhillar, A.K.; Hooda, V.; Dabur, R. Proteomics & metabolomics: Mapping biochemical regulations. *Drug Invent. Today* **2013**, *5*, 321–326. [[CrossRef](#)]
21. Akpunarlieva, S.; Weidt, S.; Lamasudin, D.; Naula, C.; Henderson, D.; Barrett, M.; Burgess, K.; Burchmore, R. Integration of proteomics and metabolomics to elucidate metabolic adaptation in *Leishmania*. *J. Proteom.* **2017**, *155*, 85–98. [[CrossRef](#)]
22. Lai, S.; Zhang, Y.; Liu, S.; Liang, Y.; Shang, X.; Chai, X.; Wen, T. Metabolic engineering and flux analysis of *Corynebacterium glutamicum* for L-serine production. *Sci. China Life Sci.* **2012**, *55*, 283–290. [[CrossRef](#)]
23. Ye, J.Z.; Lin, X.M.; Cheng, Z.X.; Su, Y.B.; Li, W.X.; Ali, F.M.; Zheng, J.; Peng, B. Identification and efficacy of glycine, serine and threonine metabolism in potentiating kanamycin-mediated killing of *Edwardsiella piscicida*. *J. Proteom.* **2018**, *183*, 34–44. [[CrossRef](#)]
24. Yadav, U.; Sundd, M. Backbone chemical shift assignments of the glycine cleavage complex H protein of *Escherichia coli*. *Biomol. NMR Assign* **2018**, *12*, 163–165. [[CrossRef](#)] [[PubMed](#)]
25. Yilmaz, J.L.; Bulow, L. Enhanced stress tolerance in *Escherichia coli* and *Nicotiana tabacum* expressing a betaine aldehyde dehydrogenase/choline dehydrogenase fusion protein. *Biotechnol. Prog.* **2002**, *18*, 1176–1182. [[CrossRef](#)]
26. Xu, Z.; Sun, M.; Jiang, X.; Sun, H.; Dang, X.; Cong, H.; Qiao, F. Glycinebetaine biosynthesis in response to osmotic stress depends on jasmonate signaling in watermelon suspension cells. *Front. Plant Sci.* **2018**, *9*, 1469. [[CrossRef](#)]
27. Davies, D.R.; Staker, B.L.; Abendroth, J.A.; Edwards, T.E.; Hartley, R.; Leonard, J.; Kim, H.; Rychel, A.L.; Hewitt, S.N.; Myler, P.J.; et al. An ensemble of structures of Burkholderia pseudomallei 2,3-bisphosphoglycerate-dependent phosphoglycerate mutase. *Acta Crystallogr. Sect. F Struct. Biol. Commun.* **2011**, *67*, 1044–1050. [[CrossRef](#)]
28. Yu, Y.; Li, T.; Wu, N.; Ren, L.; Jiang, L.; Ji, X.; Huang, H. Mechanism of arachidonic acid accumulation during aging in *Mortierella alpina*: A large-scale label-free comparative proteomics study. *J. Agric. Food Chem.* **2016**, *64*, 9124–9134. [[CrossRef](#)]
29. De Backer, S.; Sabirova, J.; De Pauw, I.; De Greve, H.; Hernalsteens, J.P.; Goossens, H.; Malhotra-Kumar, S. Enzymes catalyzing the TCA- and urea cycle influence the matrix composition of biofilms formed by methicillin-resistant *Staphylococcus aureus* USA300. *Microorganisms* **2018**, *6*, 113. [[CrossRef](#)]
30. Goddard, T.N.; Patel, J.; Park, H.B.; Crawford, J.M. Dimeric stilbene antibiotics target the bacterial cell wall in drug-resistant gram-positive pathogens. *Biochemistry* **2020**, *59*, 1966–1971. [[CrossRef](#)]
31. Sobral, R.G.; Jones, A.E.; Des Etages, S.G.; Dougherty, T.J.; Peitzsch, R.M.; Gaasterland, T.; Ludovice, A.M.; de Lencastre, H.; Tomasz, A. Extensive and genome-wide changes in the transcription profile of *Staphylococcus aureus* induced by modulating the transcription of the cell wall synthesis gene murF. *J. Bacteriol.* **2007**, *189*, 2376–2391. [[CrossRef](#)] [[PubMed](#)]

32. Mongodin, E.; Finan, J.; Climo, M.W.; Rosato, A.; Gill, S.; Archer, G.L. Microarray transcription analysis of clinical *Staphylococcus aureus* isolates resistant to vancomycin. *J. Bacteriol.* **2003**, *185*, 4638–4643. [[CrossRef](#)] [[PubMed](#)]
33. Tanaka, Y.; Morikawa, K.; Ohki, Y.; Yao, M.; Tsumoto, K.; Watanabe, N.; Ohta, T.; Tanaka, I. Structural and mutational analyses of Drp35 from *Staphylococcus aureus*: A possible mechanism for its lactonase activity. *J. Biol. Chem.* **2007**, *282*, 5770–5780. [[CrossRef](#)] [[PubMed](#)]
34. Claes, J.; Ditkowski, B.; Liesenborghs, L.; Veloso, T.; Entenza, J.; Moreillon, P.; Vanassche, T.; Verhamme, P.; Hoylaerts, M.; Heying, R. Assessment of the dual role of clumping factor A in *S. Aureus* adhesion to endothelium in absence and presence of plasma. *Thromb Haemost.* **2018**, *118*, 1230–1241. [[CrossRef](#)]
35. Nakakido, M.; Aikawa, C.; Nakagawa, I.; Tsumoto, K. The staphylococcal elastin-binding protein regulates zinc-dependent growth/biofilm formation. *J. Biochem.* **2014**, *156*, 155–162. [[CrossRef](#)]
36. Shen, F.; Tang, X.; Cheng, W.; Wang, Y.; Wang, C.; Shi, X.; An, Y.; Zhang, Q.; Liu, M.; Liu, B.; et al. Fosfomycin enhances phagocyte-mediated killing of *Staphylococcus aureus* by extracellular traps and reactive oxygen species. *Sci. Rep.* **2016**, *6*, 19262. [[CrossRef](#)]
37. Richardson, A.R.; Libby, S.J.; Fang, F.C. A nitric oxide-inducible lactate dehydrogenase enables *Staphylococcus aureus* to resist innate immunity. *Science* **2008**, *319*, 1672–1676. [[CrossRef](#)]
38. Ye, C.; Wan, F.; Sun, Z.; Cheng, C.; Ling, R.; Fan, L.; Wang, A. Effect of phosphorus supplementation on cell viability, anti-oxidative capacity and comparative proteomic profiles of puffer fish (*Takifugu obscurus*) under low temperature stress. *Aquaculture* **2016**, *452*, 200–208. [[CrossRef](#)]
39. Pompella, A.; Visvikis, A.; Paolicchi, A.; De Tata, V.; Casini, A.F. The changing faces of glutathione, a cellular protagonist. *Biochem. Pharmacol.* **2003**, *66*, 1499–1503. [[CrossRef](#)]
40. Ullah, I.; Al-Johny, B.O.; Al-Ghamdi, K.; Al-Zahrani, H.; Anwar, Y.; Firoz, A.; Al-Kenani, N.; Almatry, M. Endophytic bacteria isolated from *Solanum nigrum* L., alleviate cadmium (Cd) stress response by their antioxidant potentials, including SOD synthesis by sodA gene. *Ecotoxicol. Environ. Saf.* **2019**, *174*, 197–207. [[CrossRef](#)]
41. Delgado, J.; Owens, R.A.; Doyle, S.; Asensio, M.A.; Nunez, F. Impact of the antifungal protein PgAFP from *Penicillium chrysogenum* on the protein profile in *Aspergillus flavus*. *Appl. Microbiol. Biotechnol.* **2015**, *99*, 8701–8715. [[CrossRef](#)]
42. Askarian, F.; Uchiyama, S.; Valderrama, J.A.; Ajayi, C.; Sollid, J.; van Sorge, N.M.; Nizet, V.; van Strijp, J.; Johannessen, M. Serine-Aspartate Repeat Protein D Increases *Staphylococcus aureus* Virulence and Survival in Blood. *Infect Immun.* **2017**, *85*, e00559-16. [[CrossRef](#)]
43. McAdow, M.; Kim, H.K.; Dedent, A.C.; Hendrickx, A.P.; Schneewind, O.; Missiakas, D.M. Preventing *Staphylococcus aureus* sepsis through the inhibition of its agglutination in blood. *PLoS Pathog.* **2011**, *7*, e1002307. [[CrossRef](#)]
44. Kwiecinski, J.; Jin, T.; Josefsson, E. Surface proteins of *Staphylococcus aureus* play an important role in experimental skin infection. *APMIS* **2014**, *122*, 1240–1250. [[CrossRef](#)]
45. Josefsson, E.; Hartford, O.; O'Brien, L.; Patti, J.M.; Foster, T. Protection against experimental *Staphylococcus aureus* arthritis by vaccination with clumping factor A, a novel virulence determinant. *J. Infect. Dis.* **2001**, *184*, 1572–1580. [[CrossRef](#)]
46. Moreillon, P.; Entenza, J.M.; Francioli, P.; McDevitt, D.; Foster, T.J.; Francois, P.; Vaudaux, P. Role of *Staphylococcus aureus* coagulase and clumping factor in pathogenesis of experimental endocarditis. *Infect. Immun.* **1995**, *63*, 4738–4743. [[CrossRef](#)]
47. McDevitt, D.; Francois, P.; Vaudaux, P.; Foster, T.J. Molecular characterization of the clumping factor (fibrinogen receptor) of *Staphylococcus aureus*. *Mol. Microbiol.* **1994**, *11*, 237–248. [[CrossRef](#)]
48. Le, K.Y.; Otto, M. Quorum-sensing regulation in staphylococci—an overview. *Front. Microbiol.* **2015**, *6*, 1174. [[CrossRef](#)]
49. Doherty, N.; Holden, M.T.; Qazi, S.N.; Williams, P.; Winzer, K. Functional analysis of luxS in *Staphylococcus aureus* reveals a role in metabolism but not quorum sensing. *J. Bacteriol.* **2006**, *188*, 2885–2897. [[CrossRef](#)]
50. Diaz Dellavalle, P.; Cabrera, A.; Alem, D.; Larranaga, P.; Ferreira, F.; Dalla Rizza, M. Antifungal Activity of Medicinal Plant Extracts against Phytopathogenic Fungus *Alternaria* spp. *Chil. J. Agric. Res.* **2011**, *71*, 231–239. [[CrossRef](#)]
51. Omara, S.T. MIC and MBC of honey and gold nanoparticles against methicillin-resistant (MRSA) and vancomycin-resistant (VISA) coagulase-positive *S. aureus* isolated from contagious bovine mastitis. *J. Genet. Eng. Biotechnol.* **2017**, *15*, 219–230. [[CrossRef](#)]
52. Suo, B.; Yang, H.; Wang, Y.; Lv, H.; Li, Z.; Xu, C.; Ai, Z. Comparative Proteomic and Morphological Change Analyses of *Staphylococcus aureus* During Resuscitation From Prolonged Freezing. *Front. Microbiol.* **2018**, *9*, 866. [[CrossRef](#)]
53. Luber, C.A.; Cox, J.; Lauterbach, H.; Fancke, B.; Selbach, M.; Tschopp, J.; Akira, S.; Wiegand, M.; Hochrein, H.; O'Keefe, M.; et al. Quantitative proteomics reveals subset-specific viral recognition in dendritic cells. *Immunity* **2010**, *32*, 279–289. [[CrossRef](#)]
54. Conesa, A.; Gotz, S. Blast2GO: A comprehensive suite for functional analysis in plant genomics. *Int. J. Plant Genom.* **2008**, *2008*, 619832. [[CrossRef](#)]
55. Kanehisa, M.; Goto, S.; Sato, Y.; Furumichi, M.; Tanabe, M. KEGG for integration and interpretation of large-scale molecular data sets. *Nucleic Acids Res.* **2012**, *40*, D109–D114. [[CrossRef](#)]
56. Schmittgen, T.D.; Livak, K.J. Analyzing real-time PCR data by the comparative C(T) method. *Nat. Protoc.* **2008**, *3*, 1101–1108. [[CrossRef](#)]



## Article

# Sdy-1 Executes Antitumor Activity in HepG2 and HeLa Cancer Cells by Inhibiting the Wnt/ $\beta$ -Catenin Signaling Pathway

Mengyu Sun <sup>1,†</sup>, Dongdong Zhou <sup>1,†</sup>, Jingwan Wu <sup>1</sup>, Jing Zhou <sup>2</sup> and Jing Xu <sup>1,\*</sup>

<sup>1</sup> One Health Institute, School of Chemical Engineering and Technology, Hainan University, Haikou 570228, China; summer@hainanu.edu.cn (M.S.); dongdongchoy@hainanu.edu.cn (D.Z.); 2021110817000019@hainanu.edu.cn (J.W.)

<sup>2</sup> Hainan Provincial Fine Chemical Engineering Research Center, School of Life Sciences, Hainan University, Haikou 570228, China; 993725@hainanu.edu.cn

\* Correspondence: happyjing3@hainanu.edu.cn

† These authors contributed equally to this work.

**Abstract:** Demethylcisterol A<sub>3</sub> (Sdy-1), a highly degraded sterol that we previously isolated from Chinese mangrove *Rhizophora mucronata* endophytic *Pestalotiopsis* sp. HQD-6, exhibits potent antitumor activity towards a variety of cancer cells. In this study, we further verified that Sdy-1 effectively inhibited the proliferation and migration of human liver (HepG2) and cervical cancer (HeLa) cells in vitro and it can induce cell apoptosis and arrest the cell cycle in the G1-phase. Mechanistically, we demonstrated that Sdy-1 executes its function via inhibition of the Wnt/ $\beta$ -catenin signaling pathway. Sdy-1 may not inhibit the Wnt signaling pathway through the cascade reaction from upstream to downstream, but directly acts on  $\beta$ -catenin to reduce its transcription level, thereby reducing the level of  $\beta$ -catenin protein and further reducing the expression of downstream related proteins. The possible interaction between Sdy-1 and  $\beta$ -catenin protein was further confirmed by molecular docking studies. In the nude mouse xenograft model, Sdy-1 can also significantly inhibit tumor growth. These results indicated that Sdy-1 is an efficient inhibitor of the Wnt signaling pathway and is a promising antitumor candidate for therapeutic applications.

**Keywords:** mangrove endophytic *Pestalotiopsis*; Sdy-1; antitumor activity; Wnt signaling;  $\beta$ -catenin

**Citation:** Sun, M.; Zhou, D.; Wu, J.; Zhou, J.; Xu, J. Sdy-1 Executes Antitumor Activity in HepG2 and HeLa Cancer Cells by Inhibiting the Wnt/ $\beta$ -Catenin Signaling Pathway. *Mar. Drugs* **2022**, *20*, 125. <https://doi.org/10.3390/md20020125>

Academic Editor:  
Orazio Tagliatalata-Scafati

Received: 25 November 2021

Accepted: 1 February 2022

Published: 5 February 2022

**Publisher's Note:** MDPI stays neutral with regard to jurisdictional claims in published maps and institutional affiliations.



**Copyright:** © 2022 by the authors. Licensee MDPI, Basel, Switzerland. This article is an open access article distributed under the terms and conditions of the Creative Commons Attribution (CC BY) license (<https://creativecommons.org/licenses/by/4.0/>).

## 1. Introduction

The Wnt signaling pathway plays an essential role in various cellular responses and oncogenesis, including cell morphology, proliferation, motility, and differentiation [1,2].  $\beta$ -catenin is a key component of the Wnt signaling pathway and acts as a coactivator for transcription factors of the T-cell factor / lymphoid-enhancing (TCF/LEF) family [3], and the bulk of  $\beta$ -catenin content in the cell is modulated by  $\beta$ -catenin protein stabilization. A complex of scaffolding protein Axin, glycogen synthase kinase-3 $\beta$  (GSK3 $\beta$ ), and adenomatous polyposis coli (APC) protein in the cytoplasm (Axin/GSK3 $\beta$ /APC) catalyzes  $\beta$ -catenin phosphorylation and sequentially leads to its recognition of ubiquitin-dependent proteasomal degradation in normal cells. The Wnt/ $\beta$ -catenin signaling is activated when the Wnt protein combines with the frizzled (fzd) receptor and the low-density lipoprotein receptor-related protein 5/6 (LRP5/6), which together recruit the scaffolding protein Dishevelled (Dvl). This results in a consecutive inhibition of GSK3 $\beta$  [4,5]. The recruited Axin complex induces unphosphorylated  $\beta$ -catenin, which is stabilized in the cytoplasm to translocate into the nucleus where it forms complexes with T-cell transcription factor (TCF)/lymphoid enhancer-binding factor (LEF). These complexes activate transcription of Wnt downstream regulatory genes, including Cyclin D1, CDK4, c-myc, and related genes [6].

Liver cancer is one of the six most common cancers in the world, with the seventh-highest incidence of cancer and the third-highest mortality rate, it is the leading cause

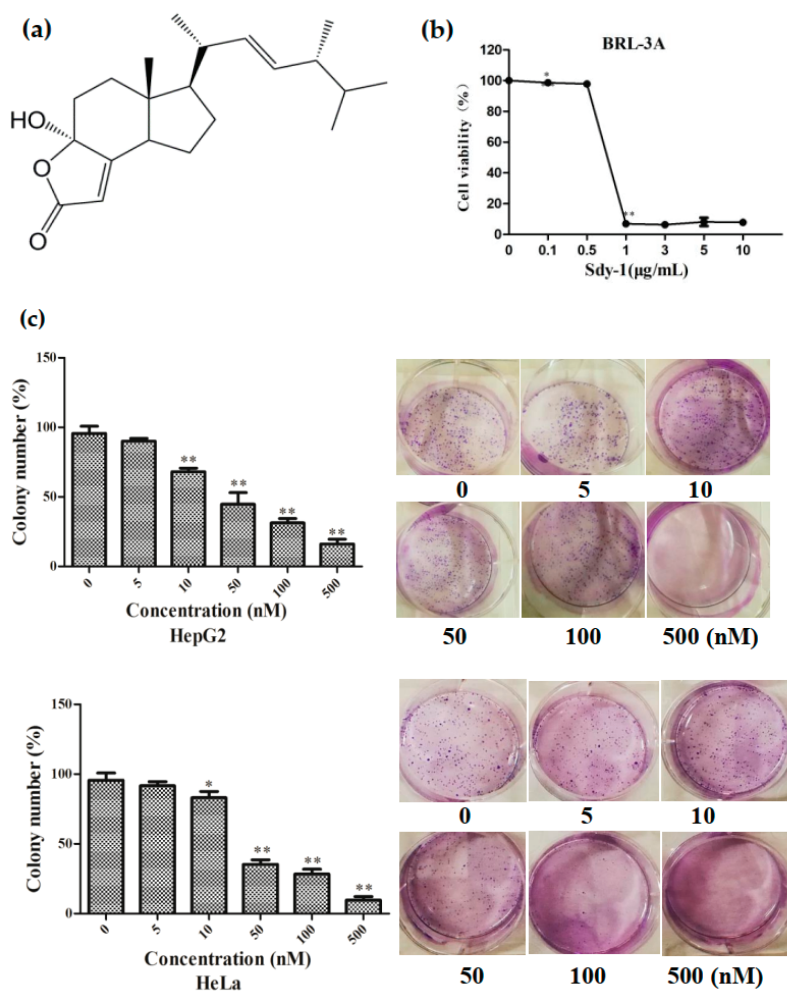
of cancer death among men under 60 in China [7–9]. Primary liver cancer comprises hepatocellular carcinoma (HCC), intrahepatic cholangiocarcinoma (iCCA), and other rare tumors, notably fibrolamellar carcinoma and hepatoblastoma [10]. Although hepatoblastoma accounts for a small proportion of liver malignancies, it is the most common liver malignancy in children, and in recent years its incidence has increased slowly and steadily at a rate of 1.2 to 1.5 new cases per million people per year [11,12]. At present, the treatment of hepatoblastoma is mainly chemotherapy and surgical resection, but the prognosis is still not optimistic [13]. Therefore, there is an urgent need to find personalized targeted therapies [14]. CTNNB1 (encoding  $\beta$ -catenin), APC and Axin mutations can be detected in up to 80% of cases of hepatoblastoma, indicating that the Wnt/ $\beta$ -catenin signaling pathway plays a vital role in the formation of hepatoblastoma [15–17]. Although cervical cancer is preventable, it remains the fourth most common cancer in females. Approximately 528,000 females are diagnosed with cervical cancer each year worldwide. Cervical cancer results in 266,000 deaths per year, of which 85% occur in developing countries [18]. Cervical cancer has no obvious symptoms at an early stage; therefore, most cases have reached an advanced stage when detected [19,20]. Shinohara et al. reported that  $\beta$ -catenin expression was increased in 73% of cervical cancer samples, with positive nuclear and cytoplasmic staining, and gene mutations were present in 20% of cases [21]. Thus, the use of Wnt pathway antagonists may be a potential therapeutic strategy for the treatment of cervical carcinogenesis.

Mangrove endophytic fungi are considered to be a promising source of structurally unique and biologically active natural products, so they are receiving increasing attention in academia and industries [22,23]. One fungal genus, *Pestalotiopsis*, is especially known for producing a wide variety of biologically active compounds [24–27]. Our preliminary screening for in vitro cytotoxicity showed that an endogenous strain of *Pestalotiopsis* sp. HQD-6 has a strong inhibitory effect on the growth of some human cancer cell lines (e.g., HeLa and HepG2 cells) with  $IC_{50}$  values of  $13.01 \pm 1.91 \mu\text{g/mL}$  and  $9.58 \pm 0.01 \mu\text{g/mL}$ , respectively. Chemical investigation of HQD-6 led to the isolation of a highly degraded sterol, demethylincisterol A<sub>3</sub> (Sdy-1), its structure was unequivocally determined by extensive NMR spectroscopic experiments as well as mass spectrometry (Figures S1–S8) and comparison with data reported in the literature [28,29]. It was first reported as a synthetic intermediate in the synthesis of 17-methylincisterol and was isolated from different kinds of edible and medicinal mushrooms and marine sponges [29–31]. This compound has cytotoxic effects on certain tumor cell lines [32]. In earlier studies in our laboratory, Sdy-1 was found to be highly cytotoxic to HepG2 and HeLa cells with  $IC_{50}$  values reached nM degree [28], but its specific mechanism is still unclear. Therefore, we studied the specific mechanism of action of Sdy-1 and found evidence that Sdy-1 reduces the viability of HepG2 and HeLa cells by inhibiting the Wnt signaling pathway.

## 2. Results

### 2.1. Sdy-1 Inhibits HepG2 and HeLa Cell Proliferation In Vitro

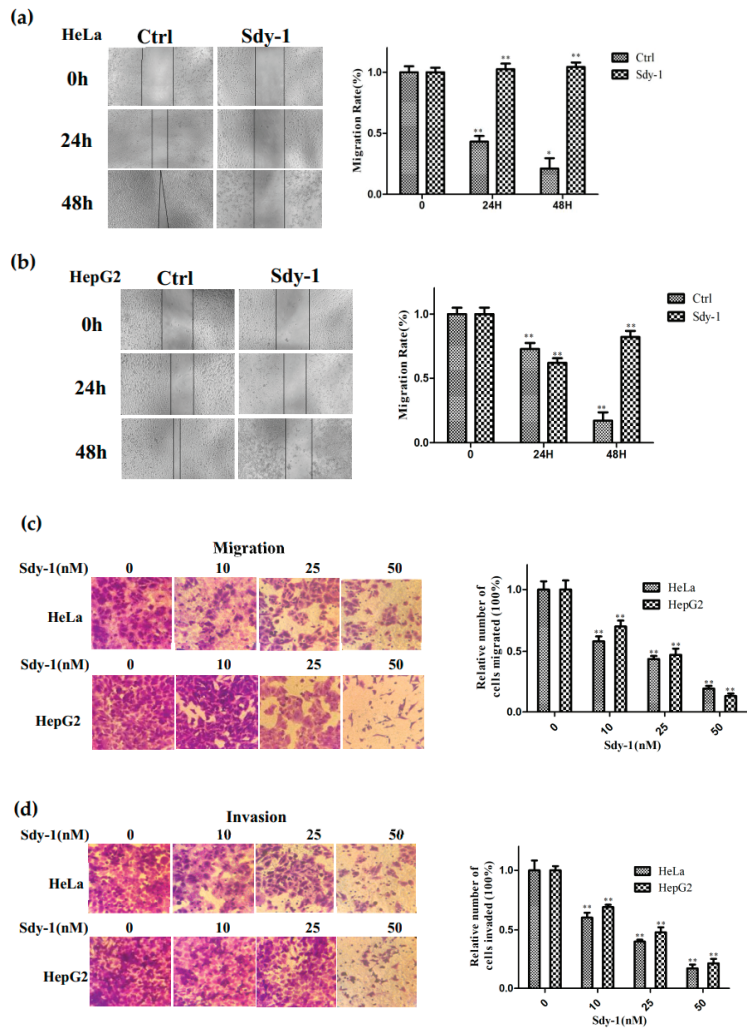
The chemical structure of Sdy-1 is shown in Figure 1a. We have proven in our previous research that Sdy-1 significantly hinders the proliferation of HepG2 and HeLa cells in vitro. The  $IC_{50}$  values of Sdy-1 for HepG2 and HeLa cells were  $14.16 \pm 0.56$  and  $0.17 \pm 0.00$  nM, respectively [28], while the  $IC_{50}$  of Sdy-1 to normal rat liver cell was  $1.58 \pm 0.05 \mu\text{M}$  (Figure 1b), which indicates that Sdy-1 has a selective killing effect. We further evaluated the long-term inhibitory effect of Sdy-1 on these two kinds of cells by colony formation assays. These assays showed that Sdy-1 had a noteworthy inhibitory impact on the colony-forming ability of HepG2 and HeLa tumor cells. The higher the Sdy-1 concentration, the lower the colony formation rate, which indicates that Sdy-1 has a strong long-term inhibitory effect on HepG2 and HeLa cell growth (Figure 1c).



**Figure 1.** Effects of Sdy-1 on the growth of cells. (a) Chemical structure of Sdy-1. (b) Cytotoxic effects of Sdy-1 on normal rat liver cell. (c) Effect of Sdy-1 on clone formation. Data are expressed as a mean  $\pm$  SD of three independent tests. \*  $p < 0.05$ , \*\*  $p < 0.01$  compared to the control group.

## 2.2. Sdy-1 Inhibits Migration and Invasion Progress of HepG2 and HeLa Cells

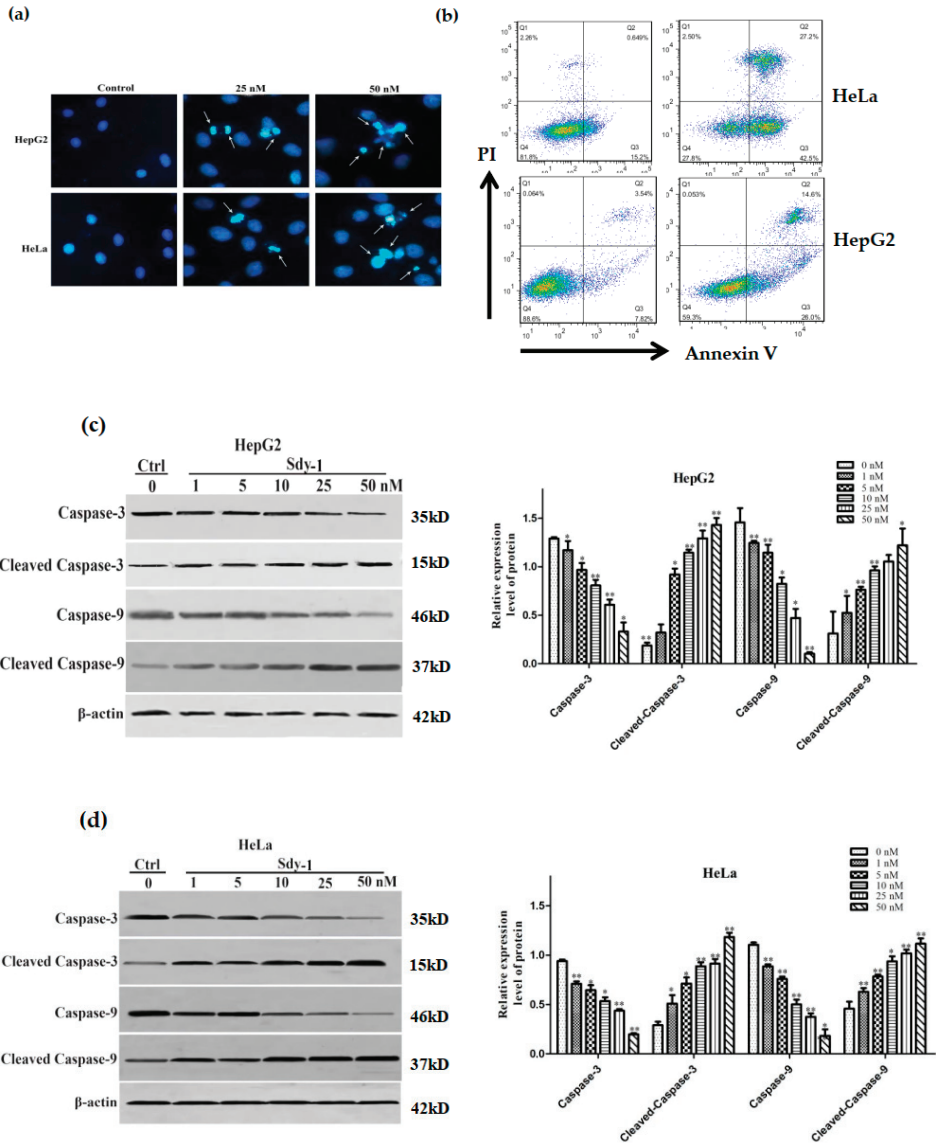
We tested the effect of Sdy-1 on the migration of the two cell types by the cell scratch test and transwell assays. As shown in Figure 2a,b, the size of the wound area after treatment is significantly larger than that of the untreated group, and the healing rate is slower as the drug concentration increases. Sdy-1 inhibited the migration of HepG2 and HeLa cells in a dose-dependent manner (Figure 2c). To further examine the effect of Sdy-1 on HepG2 and HeLa cells invasion, we performed transwell assays using Matrigel coated chambers. Compared with the blank group, the number of penetrated HepG2 and HeLa cells in the treatment groups with different concentrations of Sdy-1 decreased in a gradient compared with the blank control group (Figure 2d). These results indicated that Sdy-1 inhibited the migration and invasion abilities of HepG2 and HeLa cells in vitro.



**Figure 2.** Sdy-1 suppresses migration and invasion of HeLa and HepG2 cells. Sdy-1 inhibits migration of HeLa (a) and HepG2 (b) cells. The cell monolayer was scraped off and incubated with 10 nM Sdy-1 for 24 h and 48 h before photomicrographs. After treatment for 24 h, the cells were subjected to transwell assays (200×). Migration rate (c) and invasion rate (d) were measured (n = 3). \*  $p < 0.05$ , \*\*  $p < 0.01$  vs. the control group.

### 2.3. Sdy-1 Induces Cellular Apoptosis

The apoptosis-inducing effect of Sdy-1 was investigated by nuclear staining with Hoechst 33258. As shown in Figure 3a, chromatin condensation, nuclear fragmentation, and apoptotic bodies were clearly observed in the cells after treatment. In Figure 3b after flow cytometry assay, it was found that HeLa and HepG2 cells were treated with Sdy-1 for 48 h, the number of Annexin V-positive cells increased from 15.20%, 7.82% to 42.50% and 26.00%, and Annexin V-positive cells increased significantly, suggesting that Sdy-1 promoted tumor cell apoptosis. We also performed detection of the Caspase pathway in HepG2 and HeLa cells by Western blot. As shown in Figure 3c,d, Sdy-1 downregulated Caspase-3 and -9 proteins and upregulated cleaved Caspase-3 and cleaved Caspase-9 proteins.



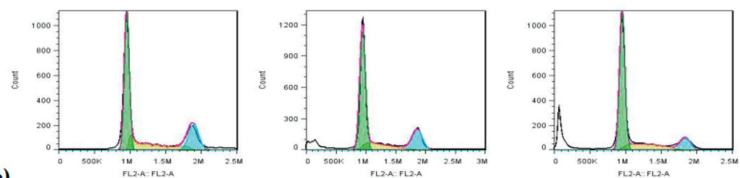
**Figure 3.** Sdy-1 induces cellular apoptosis. (a) HepG2 and HeLa were treated with two concentrations of Sdy-1 (25 or 50 nM) or 0.1% DMSO for 24 h, and apoptosis was observed by Hoechst 33258 staining. (b) Cell apoptotic death analyzed by Annexin V/PI staining. Cells were treated with 10 nM of Sdy-1 for 48 h, stained with Annexin V-FITC and PI for 30 min and analyzed by flow cytometry. Annexin V positive populations are considered as cells undergoing apoptosis. HepG2 (c) and HeLa (d) cells were treated with different concentrations of Sdy-1 (1, 5, 10, 25, or 50 nM) or 0.1% DMSO for 24 h. The expression of Caspase-3, Caspase-9, cleaved Caspase-3 and cleaved Caspase-9 were observed using Western blotting. Data are expressed as a mean  $\pm$  SD of three independent experiments. \*  $p < 0.05$ , \*\*  $p < 0.01$  vs. the control group.



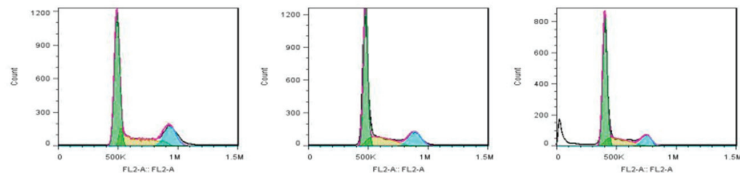
#### 2.4. Sdy-1 Induces G1 Arrest in HepG2 Cells

Our previous study showed that Sdy-1 induced cell-cycle arrest at G<sub>0</sub>/G<sub>1</sub> phase in a time-dependent increment in tumor cells [28]. Herein, we used flow cytometry to detect cell cycle distribution of HeLa and HepG cell lines with the treatment of different concentrations of Sdy-1 (0–50 nM without FBS) after 48 h. We found that Sdy-1 induced accumulation of the G<sub>0</sub>/G<sub>1</sub> phase in tested tumor cells accompanied by a decrease in S and G<sub>2</sub>/M phases was in line with a dose-dependent manner of Sdy-1. The percentage of tested tumor cells arrested in G<sub>0</sub>/G<sub>1</sub> phase with treatment of Sdy-1 were  $44.14 \pm 0.23\%$ ,  $54.55 \pm 0.42\%$  and  $55.81 \pm 1.04\%$  (in HeLa cells, Figure 4a) and  $53.34 \pm 1.31\%$ ,  $57.73 \pm 1.24\%$  and  $57.17 \pm 0.88\%$  (in HeLa cells, Figure 4b) at 0, 25, and 50 nM concentration of Sdy-1, respectively.

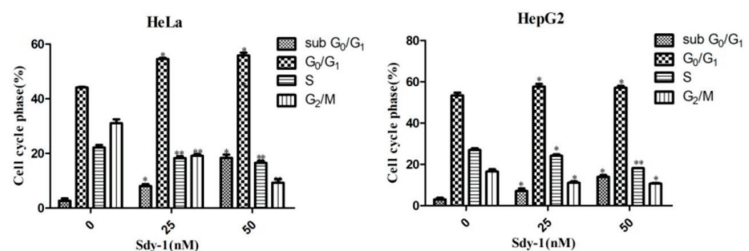
(a)



(b)



(c)



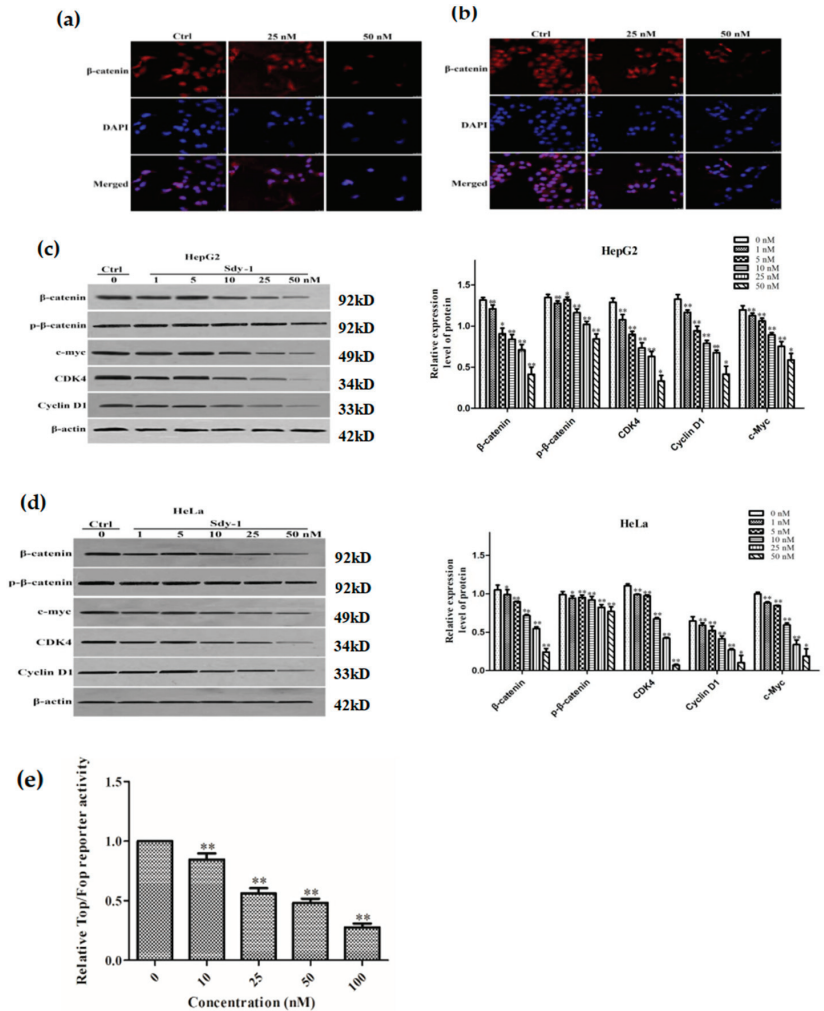
**Figure 4.** Flow cytometry detection of the effects of Sdy-1 on tumor cell cycle arrest. HeLa (a) and HepG2 (b) cells were stimulated with 25 and 50 nM Sdy-1 for 48 h, and then stained with PI for 30 min at room temperature. Phases of the cell cycle were measured by flow cytometry. (c) A statistical investigation was performed for changes of HeLa and HepG2 cell cycle at 48 h after Sdy-1 treatment. Data are expressed as a mean  $\pm$  SD of three independent tests. \*  $p < 0.05$ , \*\*  $p < 0.01$  vs. the control group.

The sub-G<sub>0</sub>/G<sub>1</sub> peak eventually shifted to a hypodiploid sub-G<sub>0</sub>/G<sub>1</sub> peak to  $18.35 \pm 1.21\%$  of HeLa cells and  $13.98 \pm 0.86\%$  of HepG cells after 48 h Sdy-1 treatment at 50 nM concentration, respectively, compared to untreated cells at the same phase ( $2.65 \pm 0.88\%$  of HeLa cells and  $3.05 \pm 0.78\%$  of HepG2 cells) (Figure 4c).

#### 2.5. Sdy-1 Changes the Level of $\beta$ -Catenin in the Cells

We investigated the localization of  $\beta$ -catenin, a key protein in Wnt signaling in cells, by immunofluorescence. The results are shown in Figure 5a,b. The content of  $\beta$ -catenin in

HepG2 and HeLa cells diminished significantly with increasing Sdy-1 concentration in cells. The results indicate that Sdy-1 has a tendency to reduce the distribution of  $\beta$ -catenin. This was a preliminary hint that Sdy-1 inhibition of tumor cell proliferation may be related to its hindrance of the Wnt signaling pathway.



**Figure 5.** Sdy-1 alters the level of  $\beta$ -catenin in cells on Wnt signaling pathway. After treatment of HepG2 (a) and HeLa (b) cells with 25 nM and 50 nM Sdy-1 for 24h, the levels of  $\beta$ -catenin were changed in the cells.  $\beta$ -catenin was determined by immunocytochemical staining using Cy3 goat anti-rabbit IgG. Whole HepG2 (c) or HeLa (d) cell lysates were prepared and the levels of  $\beta$ -catenin, p- $\beta$ -catenin, CDK4, c-myc, and Cyclin D1 were determined by Western blot analysis and normalized to  $\beta$ -actin. (e) HEK-293T cells were seeded into 24-well plate at a density of  $5 \times 10^4$  cells/well, and Top Flash or Fop Flash and pRL-TK were transfected into the cells using ExFect2000 transfection reagent. After transfection for 24 h, different concentrations of Sdy-1 or 0.1% DMSO were treated for 24 h and then tested using the Dual Luciferase Reporter Assay Kit. Representative data from three independent experiments are shown. \*  $p < 0.05$ , \*\*  $p < 0.01$  vs. the control group.

2.6. Sdy-1 Inhibits the Wnt Signaling Pathway

To further demonstrate the inhibitory impact of Sdy-1 on the Wnt pathway, we used TOPFlash or FOPFlash to transfect in HEK-293T cells and Western blotting to detect the levels of  $\beta$ -catenin, p- $\beta$ -catenin and its downstream proteins CDK4, cyclin D1, and c-myc in HepG2 and HeLa cells. The expression of downstream related proteins also decreased accordingly, indicating that Sdy-1 acts on the Wnt signaling pathway, it does affect the downstream of the Wnt signaling pathway (Figure 5c,d). Meanwhile, as the drug concentration increased, the fluorescence value of the cells decreased significantly, indicating that Sdy-1 has a significant inhibitory effect on the Wnt signaling pathway and the Western blot result displayed that the expression of total  $\beta$ -catenin protein was significantly reduced, and the level of p- $\beta$ -catenin did not increase. The results suggest that, but it may not affect the upstream of the Wnt signaling pathway and may not affect the Wnt signaling pathway through the cascade reaction that affects the Wnt signaling pathway from top to bottom (Figure 5c-e).

2.7. Sdy-1 Inhibits Transcription of the  $\beta$ -Catenin Gene in Cells

We investigated  $\beta$ -catenin levels in lysates of both tumor cell cytosol and nucleus after 24 h of Sdy-1 treatment (Figure 6a,b). The results showed that Sdy-1 inhibited the level of  $\beta$ -catenin in the cytoplasm and nuclear lysate of two kinds of tumor cells. Meanwhile, the treatment of HepG2 and HeLa cells with Sdy-1 clearly decreased the accumulation of  $\beta$ -catenin in the nucleus, which further confirmed the inhibition of Sdy-1 on nuclear translocation of  $\beta$ -catenin. As shown in Figure 6c, q-PCR showed that the expression level of the  $\beta$ -catenin gene decreased with increasing concentration. The effect was obvious at 50 nM. The decrease of mRNA means that the transcription of the  $\beta$ -catenin gene is reduced. This suggested that Sdy-1 may inhibit Wnt signaling by directly interfering with  $\beta$ -catenin mRNA transcription in the nucleus.

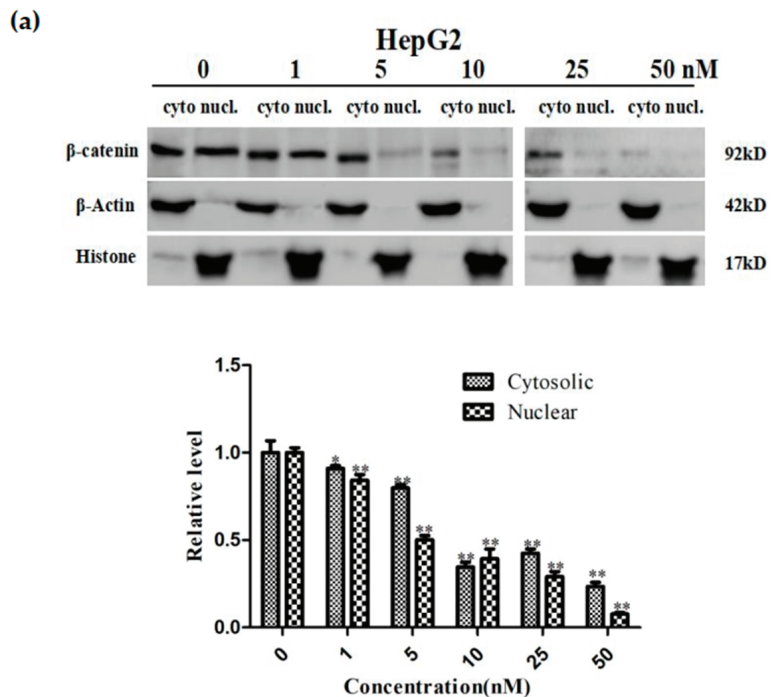
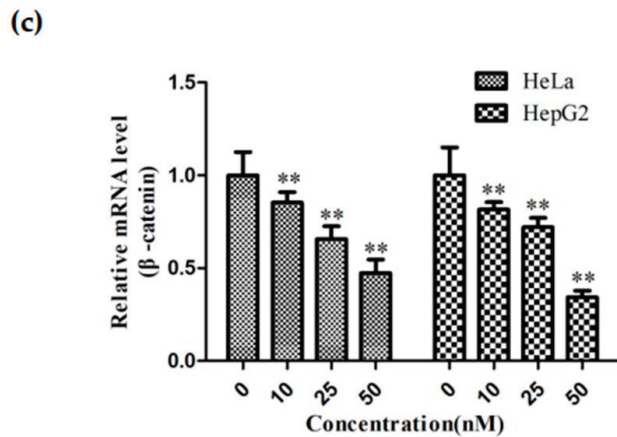
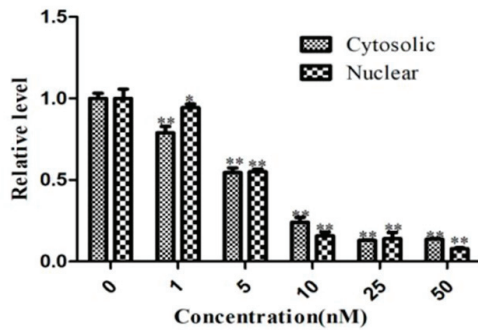
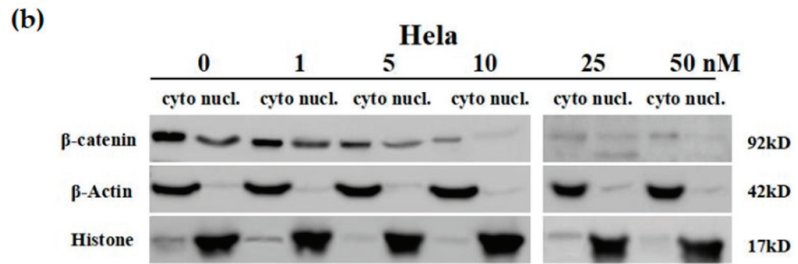


Figure 6. Cont.

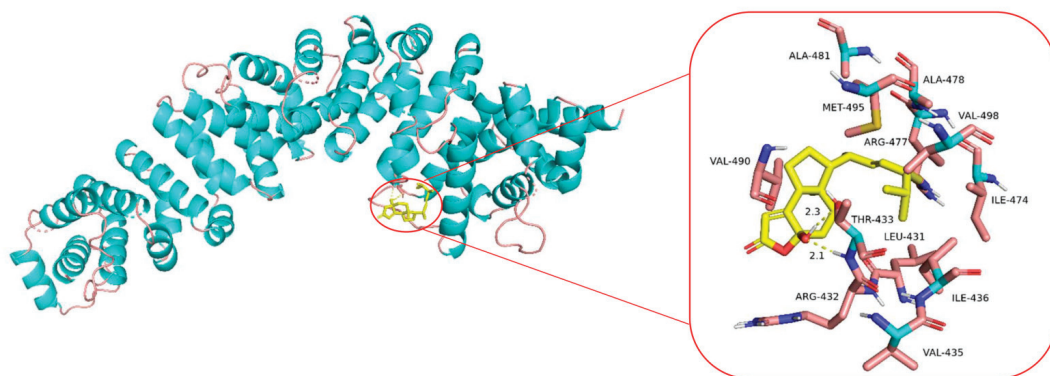


**Figure 6.** Effect of Sdy-1 on  $\beta$ -catenin gene synthesis in HepG2 and HeLa cells. (a) HepG2 and (b) HeLa cells were treated with 10, 25, or 50 nM Sdy-1 for 24 h. Cytoplasmic and nuclear lysates from HepG2 and HeLa cells,  $\beta$ -catenin levels were determined by Western blot analysis. (c) The mRNA expression of  $\beta$ -catenin after Sdy-1 treatment was detected by real-time quantitative PCR. Sdy-1 markedly reduced transcription of  $\beta$ -catenin in a dose-dependent manner. Data are expressed as mean  $\pm$  SD of three independent tests. \*  $p < 0.05$ , \*\*  $p < 0.01$  vs. the control group.

### 2.8. Molecular Docking Analysis of the Binding Interaction of Sdy-1 with $\beta$ -Catenin

Molecular docking was then performed to further understand the possible binding modes and binding affinities of the highly active Sdy-1 with the active sites of the  $\beta$ -catenin using Autodock 4.2. As shown in Figure 7, Sdy-1 formed two key hydrogen bonds with

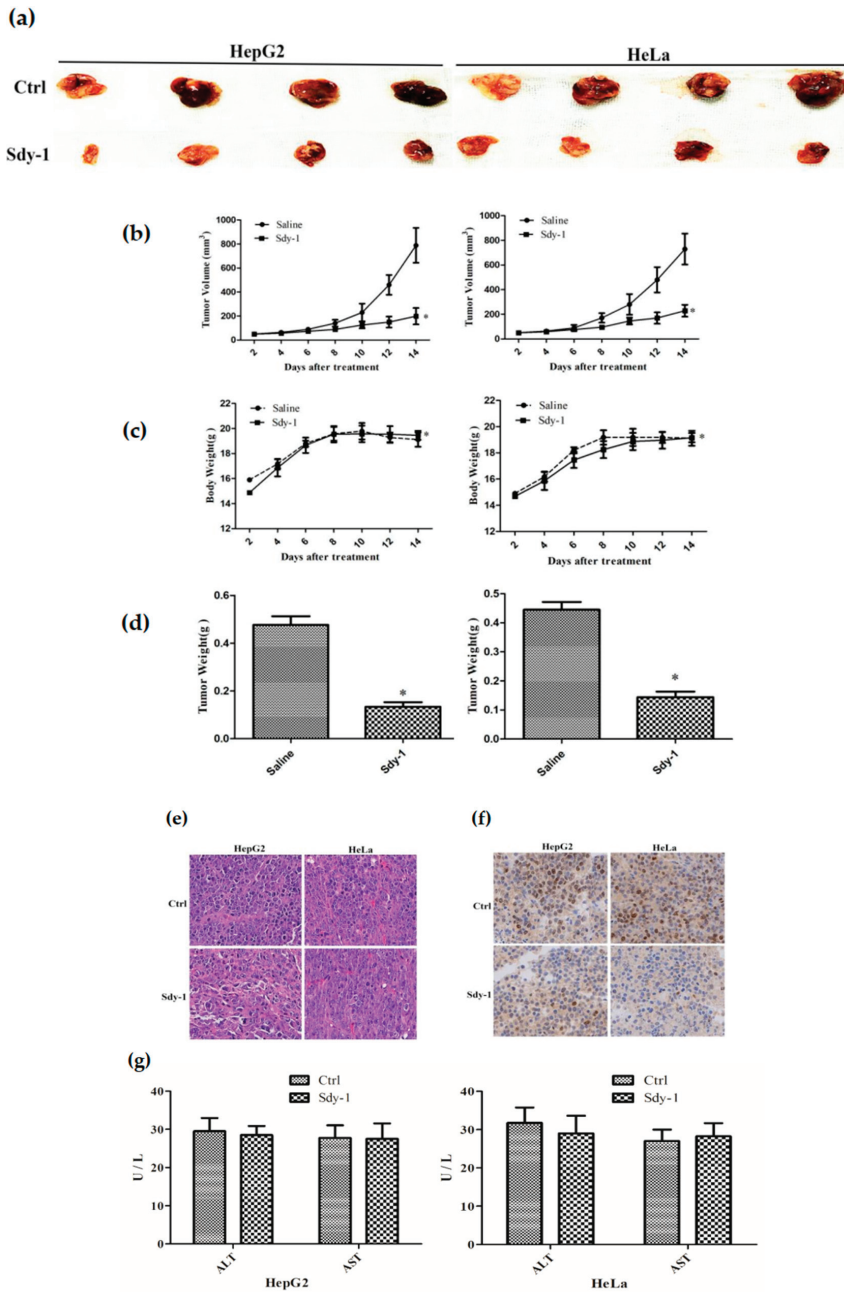
residue THR-433 with the binding energy of  $-5.92 \text{ kcal}\cdot\text{mol}^{-1}$ . Meanwhile, Sdy-1 formed hydrophobic interaction with residue ILE-436, ILE-474, ARG-477, VAL-490, VAL-498 and intermolecular interaction with residue LEU-431, ARG-432, PRO-434, ALA478, ALA-481, MET-495.



**Figure 7.** Molecular docking analysis of Sdy-1 binding to  $\beta$ -catenin. Molecular docking between Sdy-1 and  $\beta$ -catenin receptor was simulated using the AutoDock 4.2 program. The hydrogen bonds are indicated by yellow dashed lines.

### 2.9. Sdy-1 Inhibits Xenograft Tumor Model

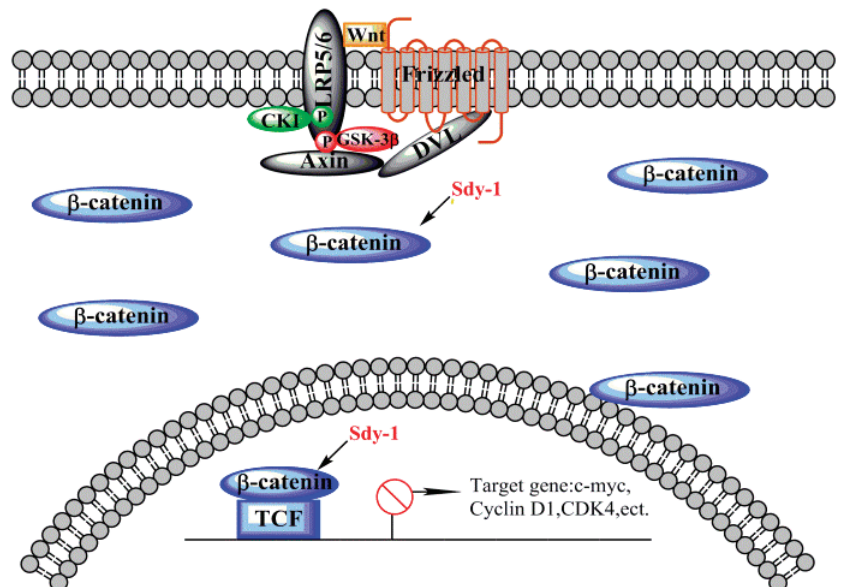
To validate the role of Sdy-1 *in vivo*, we constructed a nude mouse xenograft model. As shown in Figure 8a–d, after two weeks of treatment, the tumor volume of the treatment group is significantly smaller than that of the control group. HE staining showed that Sdy-1 significantly reduced the density of tumor cells (Figure 8e). In addition, Sdy-1 was found to significantly reduce the level of the cell proliferation marker Ki67 by immunohistochemical analysis (Figure 8f). These results indicate that Sdy-1 has an inhibitory effect on tumor cell growth. Moreover, there was no change in the morphology of hepatocytes in the Sdy-1 group, and the corresponding ALT/AST expression did not change (Figure 8g).



**Figure 8.** Effect of Sdy-1 on the xenograft model in nude mice. HepG2 and HeLa were injected into nude mice and then treated with drugs. On the next day, Sdy-1 (n = 4) or saline (n = 4) was intravenously injected at a dose of 0.1 mg/kg every other day for consecutive 14 days. The nude mice were sacrificed by cervical dissection to observe the tumor morphology (a). Mean tumor volume (b). Mean body weight (c). Mean tumor weight (d). And performed HE staining (e), immunohistochemical experiments to detect changes in Ki67 (f) and ALT/AST analysis (g). Representative data from six independent experiments are shown. \*  $p < 0.05$  vs. the control group.

### 3. Discussion

The mechanism by which the Wnt signaling pathway is involved in tumorigenesis involves cell proliferation and migration, cell cycle, and apoptosis [33]. Therefore, the development of anti-tumor drugs based on the Wnt signaling pathway is of great significance. Studies have shown that Sdy-1 can effectively inhibit the Wnt signaling pathway at nanomolar concentrations. As shown in Figure 9, Sdy-1 may inhibit the Wnt pathway by directly inhibiting  $\beta$ -catenin gene transcription instead of the cascade reaction from top to bottom in HepG2 and HeLa. At the same concentration level, Sdy-1 can inhibit the growth, migration and invasion of HepG2 and HeLa, it promotes apoptosis and causes G1 phase arrest in the HeLa cells cycle. In addition, in nude mouse xenograft models, Sdy-1 also shows good antitumor activity *in vivo*.



**Figure 9.** Sdy-1 acts on the Wnt signaling pathway. When the Wnt pathway is activated,  $\beta$ -catenin is in a free state and enters the nucleus to bind to TCF and activate downstream target genes. Sdy-1 can reduce free  $\beta$ -catenin and prevent transcription of downstream target genes.

In previous reports, Sdy-1 acts as a selective protein inhibitor that inhibits human protein tyrosine phosphatase SHP2-dependent cellular signaling [34,35]. It also affects the migration of tumor cells by activating the tyrosine-protein kinase SRC family and downstream targets [36]. Sdy-1 has been used as a potential immunosuppressive agent to inhibit tumor necrosis factor- $\alpha$ , interleukin-2 (IL-2), and IL-4 mRNA expression in human peripheral blood mononuclear cells (PBMCs) activated by phytohemagglutinin (PHA) while reducing the expression of cell proliferation factors NF-AT and NF- $\kappa$ B, as well as upstream cell calcium ion concentration and protein kinase C activity [30]. Flow cytometry assay suggests that sdy-1 promoted tumor cell apoptosis, and speculate that it may promote apoptosis by downregulating Caspases-3 and -9. We have also proven that it can inhibit the cell cycle [28]. Here, we show that Sdy-1 exerts antitumor activity by inhibiting the Wnt signaling pathway.

When the Wnt pathway is not activated,  $\beta$ -catenin forms a protein complex with APC, Axin, GSK-3 $\beta$ , etc. [37], GSK-3 $\beta$  phosphorylates  $\beta$ -catenin, thereby promoting the protease ubiquitination to degrade phosphorylated  $\beta$ -catenin [38,39]. Moreover, another part of  $\beta$ -catenin is adhered to by E-cadherin so that  $\beta$ -catenin has always been at a lower level in the cytoplasm [40]. Therefore, in cells where the Wnt pathway is not activated, p- $\beta$ -catenin

often has high levels in the cytoplasm and if the Wnt signaling pathway is inhibited by the upstream Axin/GSK-3 $\beta$ /APC or Frizzled associated proteins, p- $\beta$ -catenin will also be at a higher level in the cytoplasm [41]. We found that Sdy-1 can reduce the expression of the total  $\beta$ -catenin protein in the cell and did not increase the expression of p- $\beta$ -catenin, but decreased slightly, that is, Sdy-1 may have no effect on the cascade reaction prior to the phosphorylation of  $\beta$ -catenin, so we speculate that Sdy-1 has little effect on the upstream of the Wnt signaling pathway.

Then we consider the effect of Sdy-1 on the downstream of the Wnt signaling pathway. The free  $\beta$ -catenin protein in the cytoplasm accumulates in the cytoplasm, finally enters the nucleus, and combines with the transcription factor TCF/LEF to activate the transcriptional activities of target genes such as c-myc, Cyclin D1, CDK4, etc., thereby affecting the cell's proliferation and differentiation lead to canceration [42,43]. Therefore, we used real-time quantitative PCR technology to detect  $\beta$ -catenin genes in HepG2 and HeLa cells after Sdy-1 administration. It was found that compared with the control group, Sdy-1 reduced  $\beta$ -catenin gene transcription in both tumor cells, which indicates that Sdy-1 can inhibit the  $\beta$ -catenin gene transcription level, this results in a decrease in the synthesis of the  $\beta$ -catenin protein during the translation of  $\beta$ -catenin. This also echoes the previous experimental results that Sdy-1 reduced the total intracellular  $\beta$ -catenin protein expression and explained why the p- $\beta$ -catenin protein expression did not increase but decreased. Therefore, we believe that Sdy-1's inhibition of the Wnt signaling pathway is related to Sdy-1's inhibition of  $\beta$ -catenin gene synthesis. Our team also plans to detect the upstream proteins of the Wnt signaling pathway in future studies to further prove this conclusion.

Molecular docking has also been used to explore the behavior of small molecules in the binding site of a target protein on the basis of the shape, binding affinity and drug score [44]. There are some experimental known inhibitors that were docked against Wnt signaling-related targets which were consistent with the experimental data, but very few of them were targeted  $\beta$ -catenin directly [45,46]. In this study, AutoDock 4.2 was adopted to perform molecular docking to propose the hypothetical mechanism underlying the inhibitory activity of Sdy-1 against  $\beta$ -catenin. The docking results suggested that Sdy-1 could exhibit inhibitory effects towards  $\beta$ -catenin through binding to an active site on THR-433, which deserved further investigation.

## 4. Materials and Methods

### 4.1. Reagents

Sdy-1 was isolated from the *R. mucronata* endophytic *Pestalotiopsis* sp. HQD-6, which is a typical mangrove plant as described previously [28]. 3-(4,5-dimethylthiazol-2-yl)-2,5-diphenyltetrazolium bromide (MTT) was purchased from Sigma-Aldrich, St. Louis, Missouri, USA. Giemsa dye solution was obtained from Biosharp (Wuhan, China). Minimum Eagle's Medium (MEM) was obtained from Real Times Biotechnology Co. Ltd. (Beijing, China). Total RNA Extraction Reagent, HiScript 1st Strand cDNA Synthesis Kit, 2  $\times$  tap Master Mix and Annexin V-FITC/PI Apoptosis Detection Kit were purchased from Vazyme (Nanjing, China). Antibodies against Caspase-3, cleaved Caspase-3, Caspase-9, cleaved Caspase-9,  $\beta$ -catenin, p- $\beta$ -catenin, c-myc, CDK4, Cyclin D1,  $\beta$ -actin, HRP goat anti-mouse IgG and Cy3 goat anti-rabbit IgG were purchased from Boster Biological Technology Co. Ltd. (Wuhan, China). Hoechst33258 staining kit was purchased from Biyuntian Biotechnology Co., Ltd. (Shanghai, China). Propidium Iodide (PI) was from Biofroxx (Duisburg, Germany). The reporter plasmids Top Flash, Fop Flash, pRL-TK were from Miaoling Biological Technology Co., Ltd. (Wuhan, China). Other chemical reagents were purchased from Guangzhou chemical reagent factory (Guangzhou, China).

### 4.2. Cell Culture

HepG2 (liver cancer cell line), HeLa (cervical cancer cell line) and HEK-293T (human kidney cell line) were purchased from the Type Culture Collection of the Chinese Academy of Sciences, Shanghai, China. The rat liver BRL-3A cells were purchased from ATCC.



HepG2, HeLa and HEK-293T were cultured in MEM, and BRL-3A was cultured in DMEM containing 10% FBS, 1% penicillin-streptomycin, then these cells were cultured in the presence of 5% CO<sub>2</sub> at 37 °C. All cells were used for fewer than 6 months after resuscitation.

#### 4.3. MTT Assay

Cell viability was detected by the MTT method. BRL-3A cells in the logarithmic growth phase were digested with trypsin and plated in 96-well plates at a cell density of 5000 per well and underwent 24 h Sdy-1 treatments, then incubated in 0.5 mg/mL MTT for 4 h at 37 °C. Upon removal of the medium, 200 µL DMSO was added to dissolve the MTT formazan crystals. After shaking gently on the shaker, the absorbance of the plate was then read at 570 nM using a Microplate reader.

#### 4.4. Colony Formation Assay

For colony formation assay, cells ( $2 \times 10^2$  cells/well) were trypsinized and plated in 6-well plates in MEM medium with 10% fetal bovine serum incubated at 37 °C in 5% CO<sub>2</sub> for 24 h. Then adherent cells were dealt with different concentrations of Sdy-1 (5, 10, 50, 100, and 500 nM) or 0.1% DMSO. After the plates were incubated at 37 °C in 5% CO<sub>2</sub> for 14 days, the colonies were fixed and stained with Giemsa dye solution stain for 30 min. Finally, cells were washed with sterile water and dried under air. The number of colonies of more than 50 cells was counted and photographed.

#### 4.5. Scratch-Wound Assay

HepG2 and HeLa cells ( $2 \times 10^5$  cells/well) were seeded in a six-well plate and grown overnight. Scrape the cell monolayer in a straight line to create a “scratch” with a pipet tip and the scratched cells were removed by washing with PBS. Sdy-1 (10 nM) or 0.1% DMSO was added and migration of the cell monolayer from the edge of the scratch was recorded by measuring the distance at 0, 24 and 48 h under a microscope.

#### 4.6. Transwell Assays

Cells ( $2 \times 10^5$  cells/well) were seeded in 24 transwell chambers with 8-µm pore membrane in a serum-free medium in the absence and presence of Sdy-1 (10, 25, 50 nM). Medium with 20% FBS was added to the bottom chamber. Cells were incubated in a 5% CO<sub>2</sub> and 37 °C incubator for 6 h and then fixed with 4% PFA. The upper luminal cells were removed with cotton swabs, stained with 0.1% crystal violet, and then photographed microscopically. Bound crystal violet was dissolved with 33% acetic acid and absorbance was measured at 570 nm for quantitative analysis. For invasion assays, the chambers with 8-µm pore membranes were coated with 20 µL Matrigel. Other procedures were the same with the migration assay.

#### 4.7. Analysis of Cell Apoptosis

Hoechst 33258 staining was used to quantitatively determine the number of cells undergoing apoptosis. Cells ( $2 \times 10^5$  cells/well) were seeded in 6-well plates and incubated overnight to allow attachment. The cells were treated with Sdy-1 at different concentrations (25, 50 nM) or 0.1% DMSO for HepG2 and HeLa cells for 24 h and then fixed with 4% PFA for 10 min. Cells were then stained with Hoechst 33258 (0.5 mL) for 5 min and washed twice with PBS. A drop of fluorescence quencher was added before being subjected to a fluorescence microscope.

Annexin V-FITC/PI dual staining analysis is used for the detection of the apoptosis rate. Cells were plated in 6-well culture plates ( $5 \times 10^4$  cells/well) and underwent 48 h Sdy-1 treatments, after which the cells were washed with PBS and trypsinized. Then, the staining dye of Annexin V (5 µL) and PI (5 µL) was added to cells and incubated in the dark at 4 °C for 30 min. At last, the stained cells were analyzed using a flow cytometer.

#### 4.8. Cell Cycle Analysis

The cell cycle was assessed by flow cytometry using the propidium iodide (PI) staining. Cells were seeded at a density of  $2 \times 10^5$  cells/well in 6-well culture plates in the presence of 25, 50 nM Sdy-1 or 0.1% DMSO. After incubation at 37 °C for 48 h, the adherent cells were washed once with PBS, harvested with trypsin, collected by centrifugation (1,000 rpm for 5 min), and washed twice with cold PBS. Then, the cells were stained with 400  $\mu$ L PI (50  $\mu$ g/ mL) for 30 min at room temperature in the dark. After incubation, the cell-cycle kinetics were analyzed by flow cytometry at 488 nm excitation using FlowJo software.

#### 4.9. Luciferase Reporter Gene Assay

Luciferase assays were performed with the Luciferase assay systems kit Dual Luciferase Reporter Assay Kit (vazyme) according to the manufacturer's instructions. In brief, HEK-293T cells were seeded in 24-well plates at a density of  $5 \times 10^4$  cells/well and transfected with TopFlash or FopFlash (0.5  $\mu$ g) and internal control plasmid pRL-TK (0.5  $\mu$ g) using ExFect2000 (vazyme). After transfection for 24 h, Sdy-1 (10, 25, 50, 100 nM) or 0.1% DMSO were added and the cells incubated for 24 h, lysed in 1 $\times$  passive lysis buffer (vazyme), and collected for luciferase activity assay. Firefly luciferase activity was normalized for transfection efficiency by Renilla luciferase activity.

#### 4.10. Immunocytochemical Staining

Cells at a density of  $2 \times 10^4$  cells/well were seeded in 6-well plates and dealt with different concentrations of Sdy-1 (25, 50 nM) or 0.1% DMSO for 24 h. After treatment, cells were fixed with 4% paraformaldehyde for 30 min, followed by permeabilization in 0.5% Triton X-100 for 15 min and blocked for 1 h with 5% BSA, and then incubated with anti- $\beta$ -catenin primary antibodies overnight. The corresponding fluorescent secondary antibody was hatched for 1 h at room temperature within the dim. Nuclear staining was performed with the addition of a drop of DAPI overnight. Stained cells were washed with PBS and visualized using confocal microscopy.

#### 4.11. Western Blot Analysis

After dealing with Sdy-1 (1, 5, 10, 25, 50 nM) or 0.1% DMSO for 24 h, cells were collected and lysed in a RIPA buffer containing PMSF. The protein concentration was subjected to BSA Protein Assay Kit. The nuclear and cytoplasmic proteins were extracted using the cell structure nuclear and cytoplasmic protein extraction kit according to the manufacturer's protocol. The extracted proteins were quantitated and denatured with 5 $\times$  SDS-PAGE sample loading buffer by boiling for 10 min, subsequently separated on 10% sodium dodecyl sulfate polyacrylamide gel electrophoresis (SDS-PAGE) gels, and then transferred onto polyvinylidene fluoride (PVDF) membranes and blocked with 5% skimmed milk powder for 1 h. The primary antibodies against Caspase 3, cleaved Caspase 3, Caspase 9, cleaved Caspase 9, Cyclin D1, CDK4,  $\beta$ -catenin, p- $\beta$ -catenin, c-myc or  $\beta$ -actin was diluted with TBST containing 5% skim milk powder and the PVDF membrane was overlaid on the diluted antibody for 2 h at normal temperature. After the membranes were then washed with TBST three times and incubated with the diluted secondary antibody for 1 h at normal temperature. The luminescent liquid was added and incubated for 3 min, the membranes were placed in plastic sleeves and exposed to film in the dark.

#### 4.12. q-PCR Analysis

HepG2 and HeLa cells ( $4 \times 10^5$  cells/dish in 60-mm dishes) for 24 h, and then cells were treated with different concentrations of Sdy-1 (10, 25, 50 nM) or 0.1% DMSO for 12 h. Total RNA was extracted with TRIzol reagent and reverse transcribed using the HiScript First Strand cDNA Synthesis Kit with random primers according to the manufacturer's instructions. Q-PCR was performed with SYBR Green qPCR Master Mix (High ROX) using ABI StepOne Plus Real-time Detection System and Glyceraldehyde-3-phosphate dehydrogenase (GAPDH) was used as the internal control. Primers were:

Human  $\beta$ -catenin forward primer: 5'-TGCCAAGTGGGTGGTATAGAGG-3' and the reverse primer: 5'-CGCTGGGTATCCTGATGTGC-3'.

Human GAPDH forward primer: 5'-CCAGAACATCATCCCTGCCTCTACT-3' and the reverse primer: 5'-GGTTTTTCTAGACGGCAGGTCAGGT-3'.

#### 4.13. Molecular Docking Analyses

Molecular docking studies were performed to investigate the binding mode of Sdy-1 with  $\beta$ -catenin using AutoDock 4.2 software. The crystallographic structure of  $\beta$ -catenin (PDB-ID: 4r0z) was obtained from Research Collaboratory for Structural Bioinformatics Protein Data Bank (RCSB PDB, <http://www.rcsb.org>, 21 June 2021). The  $\beta$ -catenin protein was protonated and deleted water at pH 7 using the Clean Protein tool. The 3D structure of the small molecule was built and optimized by using Chem3D Ultra 14.0 software. The steepest gradient algorithm using the MM2 force field was applied for energy minimization to generate the best conformation. A docking site was defined as all residues within RMS tolerance of 1.0 Å. All other parameters were set as default. The binding energies between  $\beta$ -catenin and Sdy-1 were calculated by AutoDock 4.2 software with the Lamarckian genetic algorithm method [47]. The visual analysis of the best-scoring pose was shown using PyMOL software (Schrödinger, LLC: New York, NY, USA) [48].

#### 4.14. Nude Mouse Xenograft Model

All animal experiments were performed according to the protocols approved by the ethical review board of the Administrative Committee on Animal Research of Hainan University (Haikou, China), and the project identification code is HNUAUCC-2021-00082. BALB/c nude mice (4–5 weeks old) were purchased from Changsha Tianqin Biotechnology Co., Ltd. (Changsha, China) HepG2 or HeLa cells were injected into the right forelimb of nude mice at a density of  $5 \times 10^7$  cells/mL (150  $\mu$ L). Once the tumor volume reached about 50 mm<sup>3</sup>, the mice were randomly divided into two groups with the treated group (n=4) injected with Sdy-1 (0.1 mg/kg/2day) and a control group (n = 4) injected with an equal volume of saline. Subsequently, tumor volumes are measured with a caliper and calculated according to the formula: length  $\times$  width<sup>2</sup>/2. After treatment for two weeks, the mice were sacrificed by cervical dislocation and tumor samples were retrieved for histological evaluation. Then, the tumor tissue was stripped and formalin-fixed, paraffin-embedded, cut into 4- $\mu$ m sections, and immunohistochemically stained with hematoxylin and eosin (H&E). Anti-Ki-67 (Cell Signaling Technology Co., Ltd.: Danvers, MA, USA) immunohistochemical analysis and ALT, AST detection were performed.

#### 4.15. Statistical Analysis

Statistical analysis of the data was performed by one-way ANOVA followed by Dunnett's t test (SPSS 13.0 software, SPSS, New York, NY, USA), the difference was considered significant at the  $p < 0.05$  level, and the data were expressed as mean  $\pm$  standard deviation.

## 5. Conclusions

In summary, this study found that mangrove endophytic fungi originated Sdy-1 is a novel inhibitor of the Wnt signaling pathway. Sdy-1 effectively inhibits the abnormal activation of the Wnt signaling pathway by inhibiting the gene transcription of  $\beta$ -catenin. This study revealed the new mechanism of the anti-tumor effect of Sdy-1, providing a theoretical basis for the treatment of liver cancer and cervical cancer.

**Supplementary Materials:** The following supporting information can be downloaded at: <https://www.mdpi.com/article/10.3390/md20020125/s1>, Figures S1–S8: NMR spectroscopic experiments results and mass spectrometry data. Figure S1: <sup>1</sup>H-NMR of Sdy-1, Figure S2: <sup>13</sup>C-NMR of Sdy-1, Figure S3: DEPT of Sdy-1, Figure S4: <sup>1</sup>H-<sup>1</sup>H COSY of Sdy-1, Figure S5: HMQC of Sdy-1, Figure S6: HMBC of Sdy-1, Figure S7: NOESY of Sdy-1, Figure S8: ESI-MS of Sdy-1.

**Author Contributions:** J.X. designed and supervised this research, structure elucidation and final revision of the manuscript. M.S. and D.Z. performed the experiments and wrote the draft of the manuscript. J.W. carried out the molecular docking of Sdy-1 and  $\beta$ -catenin. J.Z. isolated Sdy-1. All authors have read and agreed to the published version of the manuscript.

**Funding:** This research was funded by the National Natural Science Foundation of China (No. 81973229/82160675), Key Research Program of Hainan Province (ZDYF2021SHFZ108), Key Science and Technology Project of Hainan Province (ZDKJ202008/ZDKJ202018) and High-level Talents Programs of Hainan Province (2019RC006) are gratefully acknowledged.

**Conflicts of Interest:** The authors declare no conflict of interest.

## References

- Nusse, R.; Clevers, H. Wnt/ $\beta$ -catenin signaling, disease, and emerging therapeutic modalities. *Cell* **2017**, *169*, 985–999. [[CrossRef](#)]
- Martinez-Ferre, A.; Navarro-Garberi, M.; Bueno, C.; Martinez, S. Wnt signal specifies the intralaminar limit and its organizer properties by regulating shh induction in the alar plate. *J. Neurosci.* **2013**, *33*, 3967–3980. [[CrossRef](#)]
- Wang, Z.; Li, B.; Zhou, L.; Yu, S.; Su, Z.; Song, J.; Sun, Q.; Sha, O.; Wang, X.; Jiang, W. Prodigiosin inhibits Wnt/ $\beta$ -catenin signaling and exerts anticancer activity in breast cancer cells. *Proc. Natl. Acad. Sci. USA* **2016**, *113*, 13150–13155. [[CrossRef](#)] [[PubMed](#)]
- Bisson, J.A.; Mills, B.; Paul, H.J.; Zwake, T.P.; David, C.E. Wnt5a and Wnt11 inhibit the canonical Wnt pathway and promote cardiac progenitor development via the Caspase-dependent degradation of AKT. *Dev. Biol.* **2015**, *398*, 80–96. [[CrossRef](#)] [[PubMed](#)]
- Greer, E.R.; Chao, A.T.; Bejsovec, A. Pebble/ECT2 RhoGEF negatively regulates the Wingless/Wnt signaling pathway. *Development* **2013**, *140*, 4937–4946. [[CrossRef](#)] [[PubMed](#)]
- Chiurillo, M.A. Role of the Wnt/ $\beta$ -catenin pathway in gastric cancer: An in-depth literature review. *World J. Exp. Med.* **2015**, *5*, 84–102. [[CrossRef](#)] [[PubMed](#)]
- Ma, X.; Tan, Y.T.; Yang, Y.; Gao, J.; Li, H.L.; Zhen, W.; Lan, Q.; Rothman, N.; Shu, X.O.; Xiang, Y.B. Pre-diagnostic urinary 15-F2t-isoprostane level and liver cancer risk: Results from the Shanghai Women’s and Men’s Health Studies. *Int. J. Cancer.* **2018**, *143*, 1896–1903. [[CrossRef](#)]
- Bray, F.; Ferlay, J.; Soerjomataram, I.; Siegel, R.L.; Torre, L.A.; Jemal, A. Global cancer statistics 2018: GLOBOCAN estimates of incidence and mortality worldwide for 36 cancers in 185 countries. *CA Cancer J. Clin.* **2018**, *68*, 394–424. [[CrossRef](#)]
- Chen, W.; Zheng, R.; Baade, P.D.; Zhang, S.; Zeng, H.; Bary, F.; Jemal, A.; Yu, X.Q.; He, J. Cancer statistics in China, 2015. *CA Cancer J. Clin.* **2016**, *66*, 115–132. [[CrossRef](#)]
- Sia, D.; Villanueva, A.; Friedman, S.L.; Llovet, J.M. Liver Cancer Cell of Origin, Molecular Class, and Effects on Patient Prognosis. *Gastroenterology* **2016**, *152*, 745–761. [[CrossRef](#)]
- Spector, L.G.; Birch, J. The epidemiology of hepatoblastoma. *Pediatr. Blood Cancer* **2012**, *59*, 776–779. [[CrossRef](#)]
- Ikeda, H.; Nakamura, Y. Trends in incidence of childhood malignant solid tumors in Japan: Estimation based on hospital-based registration. *J. Pediatr. Surg.* **2015**, *50*, 1506–1512. [[CrossRef](#)] [[PubMed](#)]
- Zsiros, J.; Brugieres, L.; Brock, P.; Roebuck, D.; Maibach, R.; Zimmermann, A.; Childs, M.; Pariente, D.; Lathier, V.; Otte, J.B.; et al. Dose-dense cisplatin-based chemotherapy and surgery for children with high-risk hepatoblastoma (SIOPEL-4): A prospective, single-arm, feasibility study. *Lancet Oncol.* **2013**, *14*, 834–842. [[CrossRef](#)]
- Kremer, N.; Walther, A.E.; Tiao, G.M. Management of hepatoblastoma: An update. *Curr. Opin. Pediatr.* **2014**, *26*, 362–369. [[CrossRef](#)] [[PubMed](#)]
- Tan, X.; Apte, U.; Micsenyi, A.; Kotsagrelis, E.; Luo, J.H.; Ranganathan, S.; Monga, D.K.; Bell, A.; Michalopoulos, G.K.; Monga, S.P.S. Epidermal growth factor receptor: A novel target of the Wnt/ $\beta$ -catenin pathway in liver. *Gastroenterology* **2005**, *129*, 285–302. [[CrossRef](#)] [[PubMed](#)]
- Cairo, S.; Armengol, C.; De Reynies, A.; Wei, Y.; Thomas, E.; Renard, C.; Goga, A.; Balakrishnan, A.; Semeraro, M.; Gresh, L.; et al. Hepatic stem-like phenotype and interplay of Wnt/ $\beta$ -catenin and Myc signaling in aggressive childhood liver cancer. *Cancer Cell* **2008**, *14*, 471–484. [[CrossRef](#)]
- Armengol, C.; Cairo, S.; Fabre, M. Wnt signaling and hepatocarcinogenesis: The hepatoblastoma model. *Int. J. Biochem. Cell Biol.* **2011**, *43*, 265–270. [[CrossRef](#)]
- de Sanjosé, S.; Serrano, B.; Castellsagué, X.; Brotons, M.; Muñoz, J.; Bruni, L.; Bosch, F.X. Human papillomavirus (HPV) and related cancers in the Global Alliance for Vaccines and Immunization (GAVI) countries. A WHO/ICO HPV Information Centre Report. *Vaccine* **2012**, *30*, D1–D83.
- Dutta, S.; Biswas, N.; Mukherjee, G. Evaluation of socio-demographic factors for non-compliance to treatment in locally advanced cases of cancer cervix in a Rural Medical College Hospital in India. *Indian J. Palliat. Care* **2013**, *19*, 158–165. [[CrossRef](#)]
- Uren, A.; Fallen, S.; Yuan, H.; Usubutun, A.; Kucukali, T.; Schlegel, R.; Toretzky, J.A. Activation of the canonical Wnt pathway during genital keratinocyte transformation: A model for cervical cancer progression. *Cancer Res.* **2005**, *65*, 6199–6206. [[CrossRef](#)]
- Shinohara, A.; Yokoyama, Y.; Wan, X.; Takahashi, Y.; Mori, Y.; Takami, T.; Shimokawa, K.; Tamaya, T. Cytoplasmic/nuclear expression without mutation of exon 3 of the  $\beta$ -catenin gene is frequent in the development of the neoplasm of the uterine cervix. *Gynecol. Oncol.* **2001**, *82*, 450–455. [[CrossRef](#)]
- Xu, J. Bioactive natural products derived from mangrove-associated microbes. *RSC Adv.* **2014**, *5*, 841–892. [[CrossRef](#)]

23. Xu, J. Biomolecules Produced by Mangrove-Associated Microbes. *Curr. Med. Chem.* **2011**, *18*, 5224–5266. [[CrossRef](#)] [[PubMed](#)]
24. Subban, K.; Subramani, R.; Johnpaul, M. A novel antibacterial and antifungal phenolic compound from the endophytic fungus *Pestalotiopsis mangiferae*. *Nat. Prod. Res.* **2013**, *27*, 1445–1449. [[CrossRef](#)] [[PubMed](#)]
25. Xu, M.F.; Jia, O.Y.; Wang, S.J.; Zhu, Q. A new bioactive diterpenoid from *Pestalotiopsis adusta*, an endophytic fungus from *Clodendrum canescens*. *Nat. Prod. Res.* **2016**, *30*, 2642–2647. [[CrossRef](#)] [[PubMed](#)]
26. Xu, J.; Ebada, S.S.; Proksch, P. *Pestalotiopsis* is a highly creative genus: Chemistry and bioactivity of secondary metabolites. *Fungal Divers.* **2010**, *44*, 15–31. [[CrossRef](#)]
27. Xu, J.; Yang, X.; Lin, Q. Chemistry and biology of *Pestalotiopsis*-derived natural products. *Fungal Divers.* **2014**, *66*, 37–68. [[CrossRef](#)]
28. Zhou, J.; Li, G.; Deng, Q.; Yang, X.; Xu, J. Cytotoxic constituents from the mangrove endophytic *Pestalotiopsis* sp. induce G<sub>0</sub>/G<sub>1</sub> cell cycle arrest and apoptosis in human cancer cells. *Nat. Prod. Res.* **2018**, *32*, 2968–2972. [[CrossRef](#)]
29. De Riccardis, F.; Spinella, A.; Izzo, L.; Giordano, A.; Sodano, G. Synthesis of (17R)-17-methylincisterol, a highly degraded marine steroid. *Tetrahedron Lett.* **1995**, *36*, 4303–4306. [[CrossRef](#)]
30. Tsai, W.J.; Yang, S.C.; Huang, Y.L.; Chen, C.C.; Chuang, K.A.; Kuo, Y.C. 4-Hydroxy-17-methylincisterol from *Agaricus blazei* decreased cytokine production and cell proliferation in human peripheral blood mononuclear cells via inhibition of NF-AT and NF- $\kappa$ B activation. *Evid. Based Compl. Alt.* **2013**, *2013*, 435916. [[CrossRef](#)]
31. Ueguchi, Y.; Matsunami, K.; Otsuka, H.; Kondo, K. Constituents of cultivated *Agaricus blazei*. *J. Nat. Med.* **2011**, *65*, 307–312. [[CrossRef](#)] [[PubMed](#)]
32. Mansoor, T.A.; Hong, J.; Lee, C.O.; Bae, S.J.; Im, K.S.; Jung, J.H. Cytotoxic sterol derivatives from a marine sponge *homaxinella* sp. *J. Nat. Prod.* **2005**, *68*, 331–336. [[CrossRef](#)] [[PubMed](#)]
33. Macdonald, B.T.; Tamai, K.; He, X. Wnt/ $\beta$ -Catenin Signaling: Components, Mechanisms, and Diseases. *Dev. Cell* **2009**, *17*, 9–26. [[CrossRef](#)] [[PubMed](#)]
34. Chen, C.; Liang, F.; Chen, B.; Sun, Z.; Xue, T.; Yang, R.; Luo, D. Identification of demethylincisterol A<sub>3</sub> as a selective inhibitor of protein tyrosine phosphatase Shp2. *Eur. J. Pharmacol.* **2017**, *795*, 124–133. [[CrossRef](#)] [[PubMed](#)]
35. Zhou, X.; Coad, J.; Ducatman, B.; Agazie, Y.M. SHP2 is up-regulated in breast cancer cells and in infiltrating ductal carcinoma of the breast, implying its involvement in breast oncogenesis. *Histopathology* **2008**, *53*, 389–402. [[CrossRef](#)] [[PubMed](#)]
36. Sausgruber, N.; Coissieux, M.M.; Britschgi, A.; Wyckoff, J.; Aceto, N.; Leroy, C.; Stadler, M.B.; Voshol, H.; Bonenfant, D.; Bentires-Alj, M. Tyrosine phosphatase SHP2 increases cell motility in triple-negative breast cancer through the activation of SRC-family kinases. *Oncogene* **2015**, *34*, 2272–2278. [[CrossRef](#)]
37. Korkut, C.; Ataman, B.; Ramachandran, P.; Ashley, J.; Barria, R.; Gherbesi, N.; Budnik, V. Trans-synaptic transmission of vesicular Wnt signals through Evi/Wntless. *Cell* **2009**, *139*, 393–404. [[CrossRef](#)]
38. Sato, T.; Van Es, J.H.; Snippert, H.J.; Stange, D.E.; Vries, R.G.; Van Den Born, M.; Barker, N.; Shroyer, N.F.; Van Den Wetering, M.; Clevers, H. Paneth cells constitute the niche for Lgr5 stem cells in intestinal crypts. *Nature* **2010**, *469*, 415–418. [[CrossRef](#)]
39. Strand, M.; Micchelli, C.A. Quiescent gastric stem cells maintain the adult *Drosophila* stomach. *Proc. Natl. Acad. Sci. USA* **2011**, *108*, 17696–17701. [[CrossRef](#)]
40. Zoni, E.; Van Der Pluijm, G.; Gray, P.C.; Kruithof-de Julio, M. Epithelial plasticity in cancer: Unmasking a micro RNA network for TGF- $\beta$ -, Notch-, and Wnt-mediated EMT. *J. Oncol.* **2015**, *15*, 753–760. [[CrossRef](#)]
41. Komiya, Y.; Habas, R. Wnt signal transduction pathways. *Organogenesis* **2008**, *4*, 68–75. [[CrossRef](#)] [[PubMed](#)]
42. Kim, W.; Kim, M.; Jho, E.H. Wnt/ $\beta$ -catenin signalling: From plasma membrane to nucleus. *Biochem. J.* **2013**, *450*, 9–21. [[CrossRef](#)] [[PubMed](#)]
43. Duchartre, Y.; Kim, Y.M.; Kahn, M. The Wnt signaling pathway in cancer. *Crit. Rev. Oncol. Hemat.* **2016**, *99*, 141–149. [[CrossRef](#)] [[PubMed](#)]
44. Gill, B.S.; Kumar, S. Ganoderic Acid A Targeting  $\beta$ -Catenin in Wnt Signaling Pathway: In Silico and In Vitro Study. *Interdiscip. Sci.* **2018**, *10*, 233–243. [[CrossRef](#)] [[PubMed](#)]
45. Roy, S.; Kar, M.; Roy, S.; Padhi, S.; Kumar, A.; Thakur, S.; Akhter, Y.; Gatto, G.; Banerjee, B. Inhibition of CD44 sensitizes cisplatin-resistance and affects Wnt/ $\beta$ -catenin signaling in HNSCC cells. *Int. J. Bio. Macromol.* **2020**, *149*, 501–512. [[CrossRef](#)]
46. Cui, C.; Zhou, X.; Zhang, W.; Qu, Y.; Ke, X. Is  $\beta$ -Catenin a Druggable Target for Cancer Therapy? *Trends Biochem. Sci.* **2018**, *43*, 623–634. [[CrossRef](#)]
47. Morris, G.M.; Huey, R.; Lindstrom, W.; Sanner, M.F.; Belew, R.K.; Goodsell, D.S.; Olson, A.J. AutoDock and AutoDockTools: Automated docking with selective receptor flexibility. *J. Comput. Chem.* **2009**, *30*, 2785–2791. [[CrossRef](#)]
48. Zeng, Y.; Cao, R.; Zhang, T.; Li, S.; Zhong, W. Design and synthesis of piperidine derivatives as novel human heat shock protein 70 inhibitors for the treatment of drug-resistant tumors. *Eur. J. Med. Chem.* **2015**, *97*, 19–31. [[CrossRef](#)]

## Article

# Citreobenzofuran D–F and Phomenone A–B: Five Novel Sesquiterpenoids from the Mangrove-Derived Fungus *Penicillium* sp. HDN13-494

Qian Wu <sup>1</sup>, Yimin Chang <sup>2</sup>, Qian Che <sup>1</sup>, Dehai Li <sup>1,2</sup>, Guojian Zhang <sup>1,2</sup> and Tianjiao Zhu <sup>1,2,\*</sup>

- <sup>1</sup> Key Laboratory of Marine Drugs, Chinese Ministry of Education, School of Medicine and Pharmacy, Ocean University of China, Qingdao 266003, China; wqian577@163.com (Q.W.); cheqian064@ouc.edu.cn (Q.C.); dehaili@ouc.edu.cn (D.L.); zhangguojian@ouc.edu.cn (G.Z.)
- <sup>2</sup> Laboratory for Marine Drugs and Bioproducts, Pilot National Laboratory for Marine Science and Technology (Qingdao), Qingdao 266237, China; yiminchang@163.com
- \* Correspondence: zhutj@ouc.edu.cn; Tel.: +86-532-8203-1619; Fax: +86-532-8203-3054

**Abstract:** Five new sesquiterpenoids, citreobenzofuran D–F (1–3) and phomenone A–B (4–5), along with one known compound, xylarenone A (6), were isolated from the culture of the mangrove-derived fungus *Penicillium* sp. HDN13-494. Their structures were deduced from extensive spectroscopic data, high-resolution electrospray ionization mass spectrometry (HRESIMS), and electronic circular dichroism (ECD) calculations. Furthermore, the absolute structures of **1** were determined by single-crystal X-ray diffraction analysis. Citreobenzofuran E–F (2–3) are eremophilane-type sesquiterpenoids with rare benzofuran frameworks, while phomenone A (4) contains a rare thiomethyl group, which is the first report of this kind of sesquiterpene with sulfur elements in the skeleton. All the compounds were tested for their antimicrobial and antitumor activity, and phomenone B (5) showed moderate activity against *Bacillus subtilis*, with an MIC value of 6.25  $\mu$ M.

**Keywords:** eremophilane sesquiterpenoids; mangrove-derived fungus; *Penicillium* sp.

**Citation:** Wu, Q.; Chang, Y.; Che, Q.; Li, D.; Zhang, G.; Zhu, T. Citreobenzofuran D–F and Phomenone A–B: Five Novel Sesquiterpenoids from the Mangrove-Derived Fungus *Penicillium* sp. HDN13-494. *Mar. Drugs* **2022**, *20*, 137. <https://doi.org/10.3390/md20020137>

Academic Editors: Yonghong Liu and Xuefeng Zhou

Received: 28 January 2022

Accepted: 9 February 2022

Published: 13 February 2022

**Publisher's Note:** MDPI stays neutral with regard to jurisdictional claims in published maps and institutional affiliations.



**Copyright:** © 2022 by the authors. Licensee MDPI, Basel, Switzerland. This article is an open access article distributed under the terms and conditions of the Creative Commons Attribution (CC BY) license (<https://creativecommons.org/licenses/by/4.0/>).

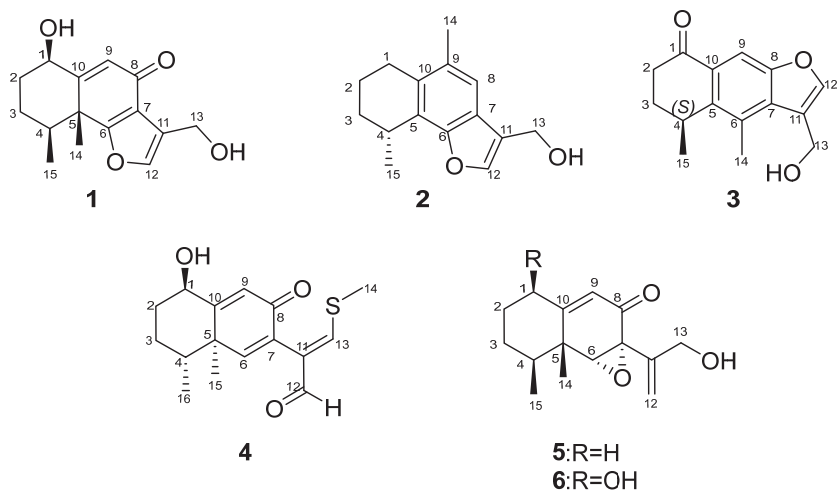
## 1. Introduction

Natural products play an increasingly crucial role in drug discovery, owing to their great chemical and bioactive diversity [1]. As is well known, fungi are a rich source of novel natural products [2], and, in the last two decades, the fungal sources of new metabolites have been broadened from terrestrial strains to marine habitats [3]. The ocean turned out to be an attractive environment, since the search for new biomedical products from marine microorganisms resulted in the isolation of approximately 10,000 metabolites, many of which were endowed with pharmacodynamic properties [4].

Mangrove is a special marine ecosystem that occurs in tropical and subtropical intertidal estuarine zones, and is characterized by high salinity and rich organic matter [5], which makes it an extremely diverse microbial resource. Mangrove-associated fungi, as the second-largest ecological group of marine fungi [6], have proven to be a rich source of natural products, with unique chemical structures and diverse pharmacological activities. Up to now, a large number of metabolites produced by mangrove fungi have been reported, including alkaloids, macrolides, polyketides, quinones, terpenes, and so on [6], which displayed diverse bioactivity, such as antibacterial, insecticidal, antioxidant, and cytotoxic, etc. These findings indicate that mangrove-derived fungi may possess great potential to produce novel and active secondary metabolites. As part of our ongoing work searching for natural products from mangrove-derived fungi, one fungus, *Penicillium* sp. HDN13-494, from the root soil sample of a mangrove plant in Wenchang, Hainan, was selected for further chemical studies. Herein, the details of isolation, structural elucidation, and bioactivities of its metabolites are reported.

## 2. Results and Discussion

Chemical studies of *Penicillium* sp. HDN13-494 led to the isolation of five new sesquiterpenoids (1–5) and one known compound (6) (Figure 1). Compound 4 represents the first example of eremophilane sesquiterpenoids containing sulfur elements. Citreobenzofuran D (1) and E (2) possess a rare cyclic system with 6,12-epoxy-eremophilane-type, which has only been reported twice in natural products [7,8].



**Figure 1.** Structures of compounds 1–6 isolated from the strain *Penicillium* sp. HDN13-494.

Citreobenzofuran D (1) was obtained as a brown triclinic crystal with the molecular formula  $C_{15}H_{18}O_4$ , determined by HRESIMS data ( $m/z$  261.1130  $[M - H]^-$ ) (Figure S8). The 1D NMR data (Tables 1 and 2) indicated that 1 shared the same skeleton with isoligularonic acid [7], except for the appearance of two hydroxyl groups at C-1 ( $\delta_C$  72.2) and C-13 ( $\delta_C$  55.2) (Table 1), which was supported by HMBC correlation from OH-1 to C-1, C-2, C-10, and from OH-13 to C-11 and C-13 (Figure 2). In addition, the deshielded singlet at C-9 ( $\delta_C$  125.5) and C-10 ( $\delta_C$  163.5) indicated the occurrence of alkenylation between them (Table 1). The relative configuration of 1 was elucidated as  $1R^*$ ,  $4S^*$ ,  $5R^*$  on the basis of NOESY correlations of H-1 with H-4, and H-14 with H-15 (Figure 3). To determine the absolute configuration of 1, the ECD calculations of the optimized conformations of (1*R*, 4*S*, 5*R*)-1a and (1*S*, 4*R*, 5*S*)-1b were obtained at the B3LYP/6-31+G(d) level. The overall pattern of the experimental ECD spectrum was in reasonable agreement with the calculated ECD spectrum of 1a (Figure 4), which indicated the 1*R*, 4*S*, and 5*R* absolute configuration of 1. Single-crystal X-ray diffraction analysis by Cu  $K\alpha$  radiation further confirmed the absolute configuration of 1 (Figure 5).

Citreobenzofuran E (2) was obtained as a green amorphous powder, with the molecular formula  $C_{15}H_{18}O_2$ , based on the HRESIMS spectrum ( $m/z$  229.1227  $[M - H]^-$ ) (Figure S15), indicating seven degrees of unsaturation. Detailed analysis of the 1D NMR data of 2 (Tables 1 and 2) revealed highly structural similarities to the known compound citreobenzofuran B [8]. The difference was the disappearance of the hydroxyl group at C-3 ( $\delta_C$  29.6), supported by the shielded singlet at  $\delta_C$  29.6 (Table 1), and the HSQC correlation between H<sub>2</sub>-3 and C-3 (Figure S12). The absolute configuration of 2 was assigned as 4*R* by comparing the experimental ECD with the calculated ECD (Figure 4).

Citreobenzofuran F (3) was obtained as a colorless oil, with the molecular formula  $C_{15}H_{16}O_3$ , determined by the HRESIMS data ( $m/z$  243.1032  $[M - H]^-$ ) (Figure S22). The 1D NMR data (Tables 1 and 2) revealed partial structural similarity to the known compound 3-formyl-4,5-dimethyl-8-oxo-5H-6,7-dihydronaphtho[2,3-*b*] furan [9]. The difference was

the replacement of carbonyl at C-13 with a hydroxyl group, which was supported by the chemical shift of C-13 ( $\delta_C$  54.9) (Table 1), and the HSQC correlation between H<sub>2</sub>-13 and C-13 (Figure S19). The absolute configuration of **3** was assigned as 4S by comparing the experimental ECD with the calculated ECD (Figure 4).

**Table 1.** <sup>13</sup>C NMR data for compounds **1**–**5** in DMSO-*d*<sub>6</sub>.

| No. | <b>1</b> <sup>a</sup> | <b>2</b> <sup>b</sup> | <b>3</b> <sup>a</sup> | <b>4</b> <sup>a</sup> | <b>5</b> <sup>b</sup> |
|-----|-----------------------|-----------------------|-----------------------|-----------------------|-----------------------|
| 1   | 72.2                  | 27.0                  | 197.9                 | 72.3                  | 32.6                  |
| 2   | 34.9                  | 18.7                  | 33.1                  | 34.9                  | 26.8                  |
| 3   | 25.8                  | 29.6                  | 29.1                  | 25.4                  | 30.0                  |
| 4   | 42.8                  | 27.5                  | 28.6                  | 42.1                  | 38.1                  |
| 5   | 44.6                  | 125.7                 | 141.9                 | 44.1                  | 41.1                  |
| 6   | 172.8                 | 152.8                 | 129.7                 | 158.0                 | 69.2                  |
| 7   | 117.2                 | 124.2                 | 131.7                 | 130.8                 | 62.0                  |
| 8   | 183.8                 | 118.4                 | 153.9                 | 183.3                 | 120.3                 |
| 9   | 125.5                 | 131.4                 | 107.6                 | 125.5                 | 131.4                 |
| 10  | 163.5                 | 130.8                 | 129.0                 | 167.2                 | 166.7                 |
| 11  | 124.5                 | 121.7                 | 122.7                 | 134.9                 | 145.6                 |
| 12  | 140.4                 | 141.5                 | 147.5                 | 188.4                 | 111.6                 |
| 13  | 55.2                  | 54.5                  | 54.9                  | 158.0                 | 62.2                  |
| 14  | 18.4                  | 20.2                  | 14.8                  | 17.5                  | 17.3                  |
| 15  | 17.8                  | 21.52                 | 19.4                  | 19.0                  | 16.0                  |
| 16  | –                     | –                     | –                     | 16.4                  | –                     |

<sup>a</sup> Spectra were recorded at 125 MHz for <sup>13</sup>C NMR using DMSO-*d*<sub>6</sub> as solvent. <sup>b</sup> Spectra were recorded at 100 MHz for <sup>13</sup>C NMR using DMSO-*d*<sub>6</sub> as solvent.

**Table 2.** <sup>1</sup>H NMR data for compounds **1**–**5** in DMSO-*d*<sub>6</sub>.

| No.   | <b>1</b> <sup>c</sup>            | <b>2</b> <sup>c</sup>                  | <b>3</b> <sup>d</sup>      | <b>4</b> <sup>c</sup>            | <b>5</b> <sup>c</sup>                              |
|-------|----------------------------------|--|----------------------------|----------------------------------|--|
| 1     | 4.52 (q, 2.9)                    | 2.52 (m), ovp.<br>2.67 (dd, 17.2, 4.4) | –                          | 5.22 (m)                         | 2.40 (tdd, 13.7, 5.3, 2.0)<br>2.67 (dd, 17.2, 4.4) |
| 2     | 1.88 (m), ovp.<br>1.51 (m), ovp. | 1.81 (m), ovp.                         | 2.86 (m)                   | 1.88 (m), ovp.                   | 1.30 (m)   |
| 3     | 1.84 (m), ovp.<br>1.44 (m), ovp. | 1.67 (s)                               | 2.46 (m), ovp.<br>2.19 (m) | 1.53 (m), ovp.<br>1.81 (m), ovp. | 1.77 (m), ovp.                                     |
| 4     | 1.54 (m), ovp.                   | 1.80 (m), ovp.<br>3.31 (m), ovp.       | 2.02 (d, 11.2)             | 1.38 (m), ovp.                   | 1.48 (m)   |
| 5     | –                                | –                                      | 3.46 (s)                   | 1.47 (m), ovp.                   | 1.73 (m), ovp.                                     |
| 6     | –                                | –                                      | –                          | –                                | –  |
| 7     | –                                | –                                      | –                          | 6.93 (s)                         | 3.36 (s)   |
| 8     | –                                | 7.26 (s)                               | –                          | –                                | –  |
| 9     | 6.13 (s)                         | –                                      | 7.85 (s)                   | 6.13 (s)                         | 5.67 (d, 1.9)                                      |
| 10    | –                                | –                                      | –                          | –                                | –  |
| 11    | –                                | –                                      | –                          | –                                | –  |
| 12    | 7.63 (s)                         | 7.71 (s)                               | 8.02 (s)                   | 9.28 (s)                         | 5.18 (q, 1.8)<br>5.06 (q, 1.5)                     |
| 13    | 4.57 (dd, 5.5, 1.4)              | 4.56 (d, 4.6)                          | 4.70 (s)                   | 8.01 (s)                         | 4.05 (m)   |
| 14    | 1.51 (s)                         | 2.23 (s)                               | 2.64 (s)                   | 2.50 (m), ovp.                   | 1.16 (s)   |
| 15    | 1.22 (d, 6.7)                    | 1.31 (d, 7.0)                          | 1.27 (d, 7.0)              | 1.30 (s)                         | 1.03 (d, 6.8)                                      |
| 16    | –                                | –                                      | –                          | 1.03 (d, 6.7)                    | –  |
| 1-OH  | 5.33 (d, 2.7)                    | –                                      | –                          | 4.37 (d, 2.9)                    | –  |
| 13-OH | 4.99 (t, 5.6)                    | 5.06 (br t, 5.4)                       | –                          | –                                | 4.84 (dd, 6.6, 4.5)                                |

<sup>c</sup> Spectra were recorded at 500 MHz for <sup>1</sup>H NMR using DMSO-*d*<sub>6</sub> as solvent. <sup>d</sup> Spectra were recorded at 400 MHz for <sup>1</sup>H NMR using DMSO-*d*<sub>6</sub> as solvent.



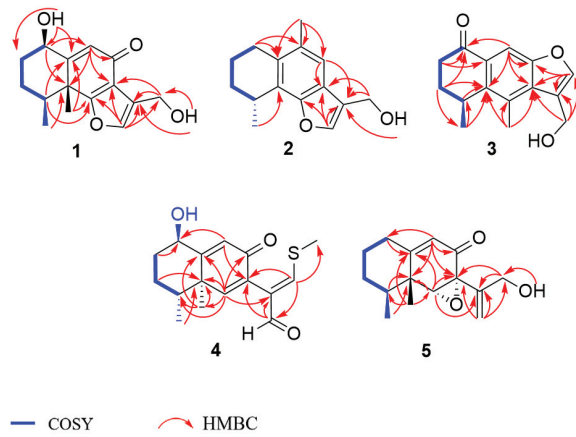


Figure 2. The key HMBC and COSY correlations of 1–5.

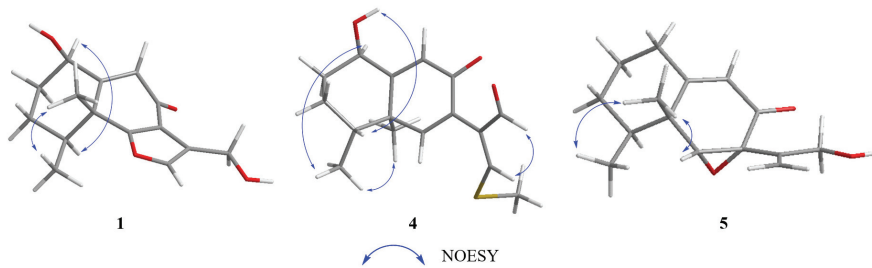


Figure 3. Selected NOESY correlations of compounds 1, 4 and 5.

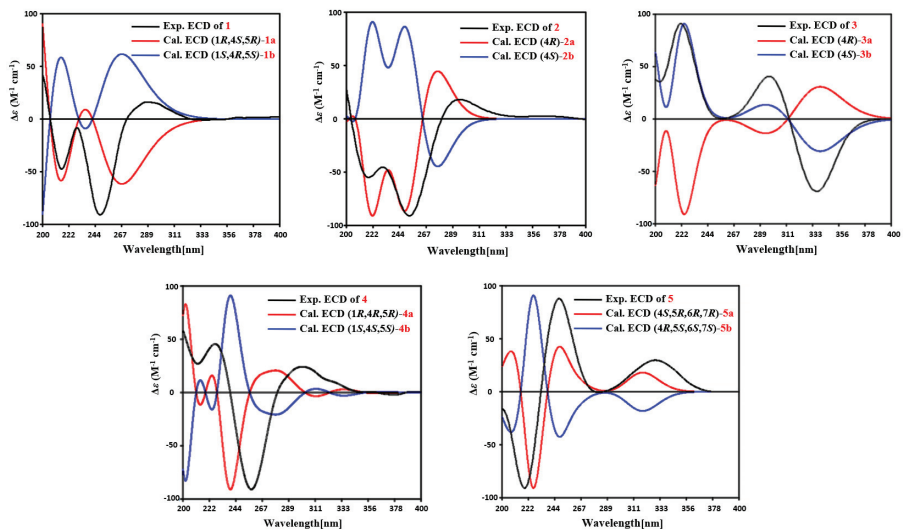


Figure 4. Comparison of calculated ECD spectra and experimental spectra of compounds 1–5.

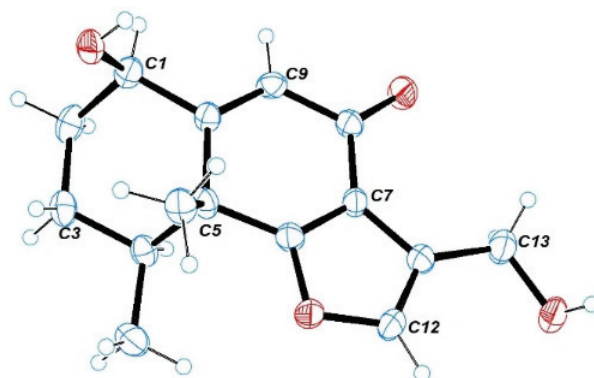


Figure 5. ORTEP drawing for the crystal structure of **1** (35% probability ellipsoids).

Phomenone A (**4**) was obtained as a colorless powder. The HRESIMS spectrum suggested that the molecular formula is  $C_{16}H_{20}O_3S$  ( $m/z$  293.1205  $[M + H]^+$ ) (Figure S30). The  $^1H$  and  $^{13}C$  NMR spectra of **4** were similar to those of paraconiothin G [10], except for the oxidation of the hydroxyl group at C-12 ( $\delta_C$  188.4) to an aldehyde group, and the appearance of the methylthio group at C-13 ( $\delta_C$  158.0) (Table 1). These changes were confirmed by the HMBC correlations from H-13 ( $\delta_H$  8.01) to C-14 ( $\delta_C$  17.5) and C-12 ( $\delta_C$  188.4), and from H-12 ( $\delta_H$  9.28) to C-7 ( $\delta_C$  130.8) and C-11 ( $\delta_C$  134.9) (Figure 2). The relative configuration of **4** was assigned, by NOESY correlations to between 1-OH and H-4, H-1 and H-15, H-15 and H-16, and H-12 and H-13 (Figure 3). The agreement between the calculated ECD spectrum of (1*R*, 4*R*, 5*R*)-**4a** and the experimental ECD spectrum suggested that the absolute configuration of **4** is 1*R*, 4*R*, 5*R* (Figure 4).

Phomenone B (**5**) was obtained as a colorless oil, with the molecular formula  $C_{15}H_{20}O_3$ , determined by HRESIMS analysis ( $m/z$  247.1343  $[M - H]^-$ ) (Figure S38). According to the 1D NMR data, compound **5** (Tables 1 and 2) was similar to a known mycotoxigenic sesquiterpenoid, xylarenones A [11], except for the disappearance of the hydroxyl group at C-1, which was supported by the shielded singlets at  $\delta_C$  32.6 (Table 1). The H-6, 14- $CH_3$ , and 15- $CH_3$  were suggested to be located on the same face of the octahydronaphthalene ring, based on the NOESY correlation of H-6 ( $\delta_H$  3.36) with H-15 ( $\delta_H$  1.03), and H-14 ( $\delta_H$  1.16) with H-15 (Figure 3). Thus, the relative configuration was determined as 4*S*\*, 5*R*\*, 6*R*\*, 7*R*\*. The overall pattern of the experimental ECD spectrum was in reasonable agreement with the calculated ECD spectrum of (4*S*, 5*R*, 6*R*, 7*R*)-**5a** (Figure 4), which indicated the 4*S*, 5*R*, 6*R* and 7*R* absolute configuration of **5**.

The known compound was identified as xylarenones A (**6**) [11] by comparison of the spectroscopic data with the literature values.

Compounds **1–6** were tested for their antimicrobial (Table 3) and antitumor activity against K562, MDA-MB-231, L-02, H69AR, and ASPC-1. Compound **5** showed promising antimicrobial activity against *B. subtilis*, with an MIC value of 6.25  $\mu$ M, while the other compounds exerted no activity for all the tested strains. Moreover, none of the compounds displayed obvious anticancer activity.

Table 3. MIC values ( $\mu\text{M}$ ) of compounds 1–6.

| Compounds              | MIC( $\mu\text{M}$ )     |                         |                                |                         |                         |      |
|------------------------|--------------------------|-------------------------|--------------------------------|-------------------------|-------------------------|------|
|                        | <i>Bacillus subtilis</i> | <i>Proteus vulgaris</i> | <i>Acinetobacter baumannii</i> | <i>Candida albicans</i> | <i>Escherichia coli</i> | MRSA |
| Citreobenzofuran D (1) | >50                      | >50                     | >50                            | >50                     | >50                     | >50  |
| Citreobenzofuran E (2) | >50                      | >50                     | >50                            | >50                     | >50                     | >50  |
| Citreobenzofuran F (3) | >50                      | >50                     | >50                            | >50                     | >50                     | >50  |
| Phomenone A (4)        | >50                      | >50                     | >50                            | >50                     | 50                      | >50  |
| Phomenone B (5)        | 6.25                     | >50                     | >50                            | >50                     | >50                     | >50  |
| xylarenones A (6)      | >50                      | >50                     | >50                            | >50                     | >50                     | >50  |

### 3. Materials and Methods

#### 3.1. General Experimental Procedures

Specific rotations were obtained on a JASCO P-1020 digital polarimeter. UV spectra were recorded on a HITACHI 5430. IR spectra were measured on a Bruker Tensor-27 spectrophotometer in KBr discs. NMR spectra were recorded on a JEOLJN M-ECP 600 spectrometer (JEOL, Tokyo, Japan) or an Agilent 500 MHz DD2 spectrometer using tetramethylsilane as an internal standard. HRMS were obtained on a Thermo Scientific LTQ Orbitrap XL mass spectrometer (Thermo Fisher Scientific, Waltham, MA, USA) or Micromass Q-TOF ULTIMA GLOBAL GAA076 LC mass spectrometer (Waters Corporation, Milford, MA, USA). Semipreparative HPLC was performed on an ODS column (YMC-Pack ODS-A, 10  $\times$  250 mm, 5  $\mu\text{m}$ , 3 mL/min).

#### 3.2. Materials and Culture Conditions

The fungal strain, *Penicillium* sp. HDN13-494, was isolated from the root soil sample of a mangrove plant in Wenchang. The strain was identified by internal transcribed spacer (ITS) sequence (GenBank No. OM283301). The strain was incubated in media potato dextrose agar (PDA, 20% potato, 2% dextrose, and 2% agar) at 28  $^{\circ}\text{C}$  for 5 days for sporulation. For compound production, the strains were cultured in PDB (potato dextrose broth) at 28  $^{\circ}\text{C}$ , 180 rpm, for 9 days. The strain was deposited at the Marine Medicinal Bioresources Center, Ocean University of China, Qingdao, China.

#### 3.3. Fermentation

The strain was grown on PDA plates for 5 days at 28  $^{\circ}\text{C}$ . The spores of *Penicillium* sp. HDN13-494 were inoculated into 500 mL Erlenmeyer flasks containing 150 mL of PDB medium, pH = 7.0 (in seawater collected from Huiquan Bay, Yellow Sea), and cultured at 28  $^{\circ}\text{C}$  for 9 days on a rotary shaker at 180 rpm. A total of 10 L of broth was extracted with EtOAc (4  $\times$  10 L) to generate the extract (30 g).

#### 3.4. Extraction and Purification

All the fermentation broth (10 L) was filtered through cheese cloth to separate the supernatant from the mycelia. The supernatant was extracted with EtOAc (4  $\times$  10 L), and the mycelia was macerated and extracted with methanol (3  $\times$  5 L). All extracts were evaporated under reduced pressure to give a crude gum. The extract was chromatographed over ODS, eluting with a gradient of increasing MeOH/H<sub>2</sub>O (30–100%) to afford twelve fractions (Fr.1 to Fr.12). Fr.4 was further separated by RP-HPLC, first using 72% MeOH/H<sub>2</sub>O to yield 4 (3 mg). By using 60% MeCN/H<sub>2</sub>O separated on an RP-HPLC column, compounds 2 (1.4 mg) and 5 (1.4 mg) were obtained from Fr.5, compound 3 (26.4 mg) was obtained from Fr.6 using 55% MeOH/H<sub>2</sub>O, while 1 (1.4 mg) and 6 (2.3 mg) were yielded using 58% MeOH/H<sub>2</sub>O from Fr.7.

Citreobenzofuran D (1): brown triclinic crystal (MeOH); m.p. 204–205  $^{\circ}\text{C}$ ;  $[\alpha]_{\text{D}}^{25}$  –42.2 (c 0.1, MeOH); UV (MeOH)  $\lambda_{\text{max}}$  (log  $\epsilon$ ): 231(1.7), 295(0.6) nm; ECD (c 0.1 mM, MeOH)  $\lambda_{\text{max}}$  ( $\Delta \epsilon$ ) 216 (–1.00), 249 (–1.90), 288 (0.34) nm; IR (KBr)  $\nu_{\text{max}}$  3259, 2935, 1655, 1208,

1030  $\text{cm}^{-1}$ ;  $^1\text{H}$  and  $^{13}\text{C}$  NMR data see Tables 1 and 2; HRESIMS  $m/z$  261.1130  $[\text{M} - \text{H}]^-$  (calcd. for  $\text{C}_{15}\text{H}_{17}\text{O}_4$ , 261.1132).

Citreobenzofuran E (2): green amorphous powder;  $[\alpha]_{\text{D}}^{25}$   $-14.1$  (c 0.1, MeOH); UV (MeOH)  $\lambda_{\text{max}}$  (log  $\epsilon$ ): 214 (1.6), 279 (0.2) nm; ECD (c 0.1 mM, MeOH)  $\lambda_{\text{max}}$  ( $\Delta \epsilon$ ) 216 ( $-0.53$ ), 252 ( $-0.78$ ), 292 (0.15) nm; IR (KBr)  $\nu_{\text{max}}$  3421, 2928, 1684, 1210  $\text{cm}^{-1}$ ;  $^1\text{H}$  and  $^{13}\text{C}$  NMR data see Tables 1 and 2; HRESIMS  $m/z$  229.1227  $[\text{M} - \text{H}]^-$  (calcd. for  $\text{C}_{15}\text{H}_{17}\text{O}_2$ , 229.1234).

Citreobenzofuran F (3): colorless oil;  $[\alpha]_{\text{D}}^{25}$   $-24.0$  (c 0.1, MeOH); UV (MeOH)  $\lambda_{\text{max}}$  (log  $\epsilon$ ): 223(1.5), 295(1.0) nm; ECD (c 0.1 mM, MeOH)  $\lambda_{\text{max}}$  ( $\Delta \epsilon$ ) 211 (0.47), 298 (0.13), 338 (6.91) nm; IR (KBr)  $\nu_{\text{max}}$  3409, 2927, 1668, 1675, 1176  $\text{cm}^{-1}$ ;  $^1\text{H}$  and  $^{13}\text{C}$  NMR data see Tables 1 and 2; HRESIMS  $m/z$  243.1032  $[\text{M} - \text{H}]^-$  (calcd. for  $\text{C}_{15}\text{H}_{15}\text{O}_3$ , 243.1027).

Phenomenone A (4): colorless powder;  $[\alpha]_{\text{D}}^{25}$   $-4.3$  (c 0.1, MeOH); UV (MeOH)  $\lambda_{\text{max}}$  (log  $\epsilon$ ): 201(1.6), 221(1.5), 298 (1.3) nm; ECD (c 0.1 mM, MeOH)  $\lambda_{\text{max}}$  ( $\Delta \epsilon$ ) 211 (0.47), 298 (0.13), 338 (6.91) nm; IR (KBr)  $\nu_{\text{max}}$  3420, 2930, 1675, 1208  $\text{cm}^{-1}$ ;  $^1\text{H}$  and  $^{13}\text{C}$  NMR data see Tables 1 and 2; HRESIMS  $m/z$  293.1205  $[\text{M} + \text{H}]^+$  (calcd. for  $\text{C}_{16}\text{H}_{21}\text{O}_3\text{S}$ , 293.1206).

Phenomenone B (5): colorless oil;  $[\alpha]_{\text{D}}^{25}$   $+336.24$  (c 0.1, MeOH); UV (MeOH)  $\lambda_{\text{max}}$  (log  $\epsilon$ ): 202(0.5), 248(1.8) nm; ECD (c 0.1 mM, MeOH)  $\lambda_{\text{max}}$  ( $\Delta \epsilon$ ) 216 ( $-6.80$ ), 248 (7.00), 329 (2.37) nm; IR (KBr)  $\nu_{\text{max}}$  3749, 2935, 1671  $\text{cm}^{-1}$ ;  $^1\text{H}$  and  $^{13}\text{C}$  NMR data see Tables 1 and 2; HRESIMS  $m/z$  247.1343  $[\text{M} - \text{H}]^-$  (calcd. for  $\text{C}_{15}\text{H}_{19}\text{O}_3$ , 247.1340).

### 3.5. X-ray Crystal Structure Analysis

Compound 1 was obtained as brown triclinic crystals from MeOH with the molecular formula  $\text{C}_{31}\text{H}_{40}\text{O}_9$ . The suitable crystal was selected and analyzed on a CCD area detector diffractometer (Bruker Smart Apex II) using Cu  $K\alpha$  radiation. The crystallographic data for 1 (CCDC 2128584) was deposited in the Cambridge Crystallographic Data Centre.

Crystal data for citreobenzofuran D (1):  $\text{C}_{31}\text{H}_{40}\text{O}_9$  ( $M = 556.63$ ), triclinic, space group P1,  $a = 7.6499(4)$  Å,  $b = 9.7072(7)$  Å,  $c = 11.2321(7)$  Å,  $\alpha = 103.630(6)^\circ$ ,  $\beta = 90.229(5)^\circ$ ,  $\gamma = 104.053(5)^\circ$ ,  $V = 721.01(8)$  Å<sup>3</sup>,  $Z = 1$ ,  $T = 293(2)$  K,  $\mu$  (Cu  $K\alpha$ ) =  $0.770$  mm<sup>-1</sup>,  $D_{\text{calc}}$  =  $1.282$  g/cm<sup>3</sup>, 4156 reflections measured ( $4.417^\circ \leq \theta \leq 67.244^\circ$ ), 2898 unique ( $R_{\text{int}} = 0.0232$ ), which were used in all calculations. The final  $R_1$  was 0.0351 ( $I > 2\sigma(I)$ ) and  $\omega R_2$  was 0.0945, flack =  $-0.1(2)$ .

### 3.6. Computational Section

Conformational searches were performed by employing the systematic procedure implemented in *Spartan*'14, using the MMFF (Merck molecular force field). All MMFF minima were reoptimized with DFT calculations at the B3LYP/6-31+G(d) level using the Gaussian09 program. The geometry was optimized starting from various initial conformations, with vibrational frequency calculations confirming the presence of minima. Time-dependent DFT calculations were performed on lowest-energy conformations (>5% population) for each configuration using 20 excited states and using a polarizable continuum model for MeOH. ECD spectra were generated using the program SpecDis by applying a Gaussian band shape with a 0.30 eV width and 25 blue shifts to facilitate comparison to the experimental data.

### 3.7. Cytotoxicity Assay

Cytotoxic activities of compounds 1–6 were evaluated against the K562 (using the MTT method), MDA-MB-231, L-02, H69AR and ASPC-1 (using the SRB method) cell lines. Adriamycin (ADM) was used as a positive control. The detailed methodologies for biological testing have been described in previous reports [12,13].

### 3.8. Antimicrobial Activity

Antibacterial activities of compounds 1–6 were evaluated against *B. subtilis*, *Proteus vulgaris*, *Acinetobacter baumannii*, *Candida. albicans*, *Escherichia. coli*, and MRSA (Methicillin-resistant *Staphylococcus aureus*) by using the agar dilution method as previously reported [14]. Ciprofloxacin was used as a positive control.

#### 4. Conclusions

In summary, five new sesquiterpenoids, citreobenzofuran D–F (1–3) and phomenone A–B (4–5), along with one known compound, xylarenones A (6), were isolated from a mangrove-derived fungus, *Penicillium* sp. HDN13-494. Compounds 1, 4 and 5 are canonical eremophilane structures, while compounds 2 and 3 possess rare benzofuran structures in the skeletons. The biological activity assay showed that compound 5 possessed mild antimicrobial activity against *Bacillus subtilis*. Our research results expanded the diversity of the secondary metabolite in mangrove-derived fungi, and also enriched the diversity of terpenoids in natural products.

**Supplementary Materials:** The following are available online at <https://www.mdpi.com/article/10.3390/md20020137/s1>: Figure S1: HPLC analysis of the crude extract of *Penicillium* sp. HDN13-494; Figures S2–S9: 1D, 2D NMR, HRESIMS and IR spectra of compound 1; Figures S10–S16: 1D, 2D NMR, HRESIMS and IR spectra of compound 2; Figures S17–S23: 1D, 2D NMR, HRESIMS and IR spectra of compound 3; Figures S24–S31: 1D, 2D NMR, HRESIMS and IR spectra of compound 4; Figures S32–S39: 1D, 2D NMR, HRESIMS and IR spectra of compound 5; Figures S40–S44: DFT-optimized structures for low-energy conformers of 1–5 at B3LYP/TZVP level in DMSO (CPCM) (conformer populations were calculated using the Gibbs free energy and Boltzmann population at 298 K estimated thereof); Tables S1–S5: harmonic frequencies of 1–5; Tables S6–S10: important thermodynamic parameters (a.u.) and Boltzmann distributions of the optimized compounds 1–5 at B3LYP/TZVP level of theory with PCM solvent model for DMSO.

**Author Contributions:** The contributions of the respective authors are as follows: Q.W. drafted the work and performed the fermentation, extraction, as well as the isolation. Q.W. and Y.C. elucidated the constituents and performed the biological evaluations. Q.C., G.Z. and D.L. contributed to checking and confirming all procedures for isolation and identification. T.Z. designed the study, supervised the laboratory work, and contributed to the critical reading of the manuscript, and was also involved in the structural determination and bioactivity elucidation. All authors have read and agreed to the published version of the manuscript.

**Funding:** This research was funded by the National Natural Science Foundation of China Major Project for Discovery of New Leading Compounds (81991522), the National Science and Technology Major Project for Significant New Drugs Development (2018ZX09735004), the Marine S&T Fund of Shandong Province for Qingdao Pilot National Laboratory for Marine Science and Technology (2018SDKJ0401-2), Major Basic Research Programs of Natural Science Foundation of Shandong Province (ZR2019ZD18), the Fundamental Research Funds for the Central Universities (201941001), the Taishan Scholar Youth Expert Program in Shandong Province (tsqn201812021, 202103153), the Youth Innovation Plan of Shandong province (2019KJM004) and the National Natural Science Foundation of China (U1906212).

**Institutional Review Board Statement:** Not applicable.

**Data Availability Statement:** Data are contained within the article.

**Conflicts of Interest:** The authors declare no conflict of interest.

#### References

1. Casertano, M.; Menna, M.; Imperatore, C. The Ascidian-Derived Metabolites with Antimicrobial Properties. *Antibiotics* **2020**, *9*, 510. [[CrossRef](#)] [[PubMed](#)]
2. Carroll, A.R.; Copp, B.R.; Davis, R.A.; Keyzers, R.A.; Prinsep, M.R. Marine Natural Products. *Nat. Prod. Rep.* **2020**, *37*, 175–223. [[CrossRef](#)] [[PubMed](#)]
3. Schueffler, A.; Anke, T. Fungal Natural Products in Research and Development. *Nat. Prod. Rep.* **2014**, *31*, 1425–1448. [[CrossRef](#)] [[PubMed](#)]
4. Kavisri, M.; Abraham, M.; Prabakaran, G.; Elangovan, M. Meivelu Moovendhan Phytochemistry, Bioactive Potential and Chemical Characterization of Metabolites from Marine Microalgae (*Spirulina platensis*) Biomass. *Biomass Convers. Biorefin.* **2021**. [[CrossRef](#)]
5. Cadamuro, R.D.; da Silveira Bastos, I.M.A.; da Silva, I.T.; da Cruz, A.C.C.; Robl, D.; Sandjo, L.P.; Alves, S.; Lorenzo, J.M.; Rodríguez-Lázaro, D.; Treichel, H.; et al. Bioactive Compounds from Mangrove Endophytic Fungus and Their Uses for Microorganism Control. *J. Fungi* **2021**, *7*, 455. [[CrossRef](#)] [[PubMed](#)]

6. Chen, S.; Cai, R.; Liu, Z.; Cui, H.; She, Z. Secondary Metabolites from Mangrove-Associated Fungi: Source, Chemistry and Bioactivities. *Nat. Prod. Rep.* **2022**. [[CrossRef](#)] [[PubMed](#)]
7. Yuan, Y.L.; Fang, L.Z.; Bai, S.P.; Liang, H.J.; Ye, D.D. A Novel Eremophilane Sesquiterpenoid from *Ligularia intermedia* Roots and Rhizomes. *Chem. Nat. Compd.* **2013**, *49*, 258–260. [[CrossRef](#)]
8. Kosemura, S. Meroterpenoids from *Penicillium citreo-viride* B. IFO 4692 and 6200 Hybrid. *Tetrahedron* **2003**, *59*, 5055–5072. [[CrossRef](#)]
9. Vishnoi, S.P.; Shoeb, A.; Kapil, R.S.; Popli, S.P. A Furanoeremophilane from *Vitex negundo*. *Phytochemistry* **1983**, *22*, 597–598. [[CrossRef](#)]
10. Nakashima, K.I.; Tomida, J.; Hirai, T.; Kawamura, Y.; Inoue, M. Paraconiothins A–J: Sesquiterpenoids from the Endophytic Fungus *Paraconiothyrium brasiliense* ECN258. *J. Nat. Prod.* **2019**, *82*, 3347–3356. [[CrossRef](#)] [[PubMed](#)]
11. Hu, Z.Y.; Li, Y.Y.; Huang, Y.J.; Su, W.J.; Shen, Y.M. Three New Sesquiterpenoids from *Xylaria* Sp. NCY2. *Helv. Chim. Acta* **2008**, *91*, 46–52. [[CrossRef](#)]
12. Mosmann, T. Rapid Colorimetric Assay for Cellular Growth and Survival: Application to Proliferation and Cytotoxicity Assays. *J. Immunol. Methods* **1983**, *65*, 55–63. [[CrossRef](#)]
13. Bringmann, G.; Lang, G.; Maksimenka, K.; Hamm, A.; Gulder, T.A.M.; Dieter, A.; Bull, A.T.; Stach, J.E.M.; Kocher, N.; Müller, W.E.G.; et al. Gephyromycin, the First Bridged Angucyclinone, from *Streptomyces Griseus* Strain NTK 14. *Phytochemistry* **2005**, *66*, 1366–1373. [[CrossRef](#)] [[PubMed](#)]
14. Yu, G.; Wu, G.; Sun, Z.; Zhang, X.; Che, Q.; Gu, Q.; Zhu, T.; Li, D.; Zhang, G. Cytotoxic Tetrahydroxanthone Dimers from the Mangrove-Associated Fungus *Aspergillus versicolor* HDN1009. *Mar. Drugs* **2018**, *16*, 335. [[CrossRef](#)] [[PubMed](#)]



Review

# Secondary Metabolites from Marine Sponges of the Genus *Oceanapia*: Chemistry and Biological Activities

Meng-Juan Xu, Lin-Jing Zhong, Jun-Kun Chen, Qing Bu and Lin-Fu Liang \*

College of Materials Science and Engineering, Central South University of Forestry and Technology, Changsha 410004, China; shine0805@163.com (M.-J.X.); zljswan120101@163.com (L.-J.Z.); cjk\_kg@outlook.com (J.-K.C.); 17355249596@163.com (Q.B.)

\* Correspondence: lianglinfu@csuft.edu.cn

**Abstract:** In this review, we summarized the distribution of the chemically investigated *Oceanapia* sponges, including the isolation and biological activities of their secondary metabolites, covering the literature from the first report in 1989 to July 2019. There have been 110 compounds reported during this period, including 59 alkaloids, 33 lipids, 14 sterols and 4 miscellaneous compounds. Besides their unique structures, they exhibited promising bioactivities ranging from insecticidal to antibacterial. Their complex structural characteristics and diverse biological properties have attracted a great deal of attention from chemists and pharmaceuticals seeking to perform their applications in the treatment of disease.

**Keywords:** *Oceanapia*; sponge; secondary metabolites; biological activities

**Citation:** Xu, M.-J.; Zhong, L.-J.; Chen, J.-K.; Bu, Q.; Liang, L.-F. Secondary Metabolites from Marine Sponges of the Genus *Oceanapia*: Chemistry and Biological Activities. *Mar. Drugs* **2022**, *20*, 144. <https://doi.org/10.3390/md20020144>

Academic Editors: Yonghong Liu and Xuefeng Zhou

Received: 10 December 2021

Accepted: 11 February 2022

Published: 16 February 2022

**Publisher's Note:** MDPI stays neutral with regard to jurisdictional claims in published maps and institutional affiliations.



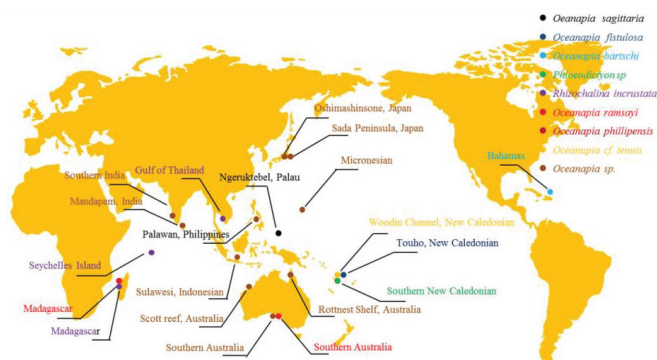
**Copyright:** © 2022 by the authors. Licensee MDPI, Basel, Switzerland. This article is an open access article distributed under the terms and conditions of the Creative Commons Attribution (CC BY) license (<https://creativecommons.org/licenses/by/4.0/>).

## 1. Introduction

Marine sponges, living in harsh marine conditions from tropic to polar regions, offer an enormous source of natural products bearing unique structures and significant bioactivities, making them ideal candidates for drug discovery projects [1]. Of them, the animals belonging to the genus *Oceanapia* (phylum, Porifera; class, Demospongiae; subclass, Heteroscleromorpha; order, Haplosclerida; family, Phloeodictyidae) have proven to be a biochemical warehouse for secondary metabolites, such as alkaloids, lipids, sterols, etc. It is particularly interesting that these compounds exhibited a wide range of biological features ranging from antibacterial and cytotoxic to ichthyotoxic activities [2]. In order to better understand the natural products from this genus, there would be a demand for a review.

Notably, several other generic names (*Phloeodictyon* Carter, 1882; *Rhizochalina* Schmidt, 1870; *Biminia* Wiedenmayer, 1977; *Foliolina* Schmidt, 1870) are now considered as synonyms for *Oceanapia* [3]. However, there is no associated reference on secondary metabolites of two genera *Biminia* and *Foliolina* listed in *SciFinder Scholar*. Therefore, this review covers topics on three nominal genera, *Oceanapia*, *Phloeodictyon* and *Rhizochalina*, covering different types of compounds, with a literature survey from 1989 to July 2019. During this period, 110 compounds have been reported, including 59 alkaloids, 33 lipids, 14 sterols and 4 other miscellaneous compounds. More than eight species of *Oceanapia* sponges have been chemically investigated including *Oceanapia sagittaria*, *Oceanapia fistulosa*, *Oceanapia bartschi*, *Phloeodictyon* sp., *Rhizochalina incrustata*, *Oceanapia ramsayi*, *Oceanapia phillipensis*, *Oceanapia* cf. *tenuis* and *Oceanapia* sp. The global distribution of the chemically investigated marine *Oceanapia* sponges according to their species is shown in Figure 1.





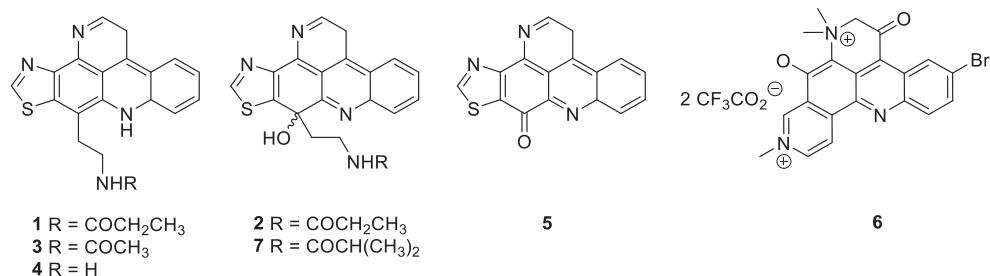
**Figure 1.** Global distribution of the chemically investigated marine *Oceanapia* sponges according to their species.

## 2. Alkaloids

Alkaloids were encountered most frequently. They can be classified as pyridoacridine alkaloids, quinolizidine alkaloids, sesquiterpene alkaloid, phloeodictine alkaloidalkaloids, bromotyrosine alkaloids, indole alkaloids and nucleotide alkaloids, according to their skeletons.

### 2.1. Pyridoacridine Alkaloids

Faulkner's group found the sponge *Oceanapia sagittaria* from Palau contained two pyridoacridine alkaloids dercitamide (**1**) and sagitol (**2**) (Figure 2). Of them, **2** was the first pyridoacridine alkaloid from a marine sponge in which the aromatic system had been disrupted. Interestingly, **2** could be obtained by autoxidation of **1**. Faulkner et al. suggested that **2** was not an artifact that was supported by CD measurements. [4]. Two years later, Proksch et al. reported three pyridoacridine alkaloids kuanoniamine C (**1**), kuanoniamine D (**3**) and *N*-deacetylkuanoniamine C (**4**) were afforded by the Micronesia sponge *Oceanapia* sp. [5]. It may be worthy to point out that the structures of dercitamide and kuanoniamide C were established to be identical by Faulkner and his co-workers [6]. Herein, the same numbering was assigned for these two different nomenclative compounds. Proksch et al. performed many bioassays for these three alkaloids. When incorporated into an artificial diet, compounds **1** and **3** exhibited insecticidal activity toward neonate larvae of the polyphagous pest insect *Spodoptera littoralis* (LC<sub>50</sub> of 156 and 59 ppm, respectively). Both compounds also showed toxicity in the brine shrimp lethality test with LC<sub>50</sub> values of 37 and 19 µg/mL, respectively. Although the *N*-deacyl derivative **4** did not show any remarkable effect in either of the abovementioned bioassays, it appeared to be active in the cytotoxic biotests against two human cell lines. The IC<sub>50</sub> of **4** was 1.2 µg/mL toward HeLa cells and 2.0 µg/mL toward MONO-MAC 6 cells. In receptor binding assays, compound **3** showed affinity to A<sub>1</sub>- and A<sub>2A</sub>-adenosine receptors with K<sub>i</sub> values of 2.94 and 13.7 µM, respectively. Compound **1** was less active than its homologue **3**, whereas the *N*-deacyl derivative **4** showed no affinity toward adenosine receptors. In addition, compounds **1**, **3** and **4** exhibited moderate affinity to benzodiazepine binding sites of GABA<sub>A</sub> receptors [5]. Meanwhile, Proksch et al. explored the distribution of compounds **1** and **3** in the sponge *Oceanapia* sp., as well as its ecological implications. It was found that the secondary metabolites **1** and **3** showed a sharp increase from the basal root to the capitum. The feeding assays against the spongivorous angelfish *Pomacanthus imperator* showed that **1** and **3** significantly deterred feeding by natural assemblages of reef fishes at fistule concentrations, confirming their role as defensive agents [7].



**Figure 2.** The chemical structures of pyridoacridine alkaloids 1–7.

Kijjoo and his co-workers reported another specimen, *O. sagittaria* from the Gulf of Thailand, afforded kuanoniamine C (**1**) and its relative compound kuanoniamine A (**5**). In this study, compounds **1** and **5** were evaluated for cytotoxic effects against five human tumor cell lines MCF-7 (ER+), MDA-MB-231 (ER-), SF-268, NCI-H460 and UACC-62, and one human non-tumor cell line, MRC-5, by the SRB method. Compound **5** was found to be a potent growth inhibitor of all tumor and the non-tumor cell lines while **1** was less potent but showed high selectivity toward the estrogen-dependent (ER+) breast cancer cell line MCF-7. Furthermore, **5** was shown to be a more potent inhibitor of DNA synthesis than **1**. It was also found that **5** caused an extensive reduction in the MCF-7 cells in the G2/M phase as well as an increase in the apoptotic cells [8].

Bioassay-guided fractionation of the MeOH extract of an Australian sponge *Oceanapia* sp. performed by Carroll's group, using the aspartyl semialdehyde dehydrogenase (ASD) to detect antibacterial activity, led to the discovery of a bright blue compound, petrosamine B (**6**). It was found **6** was a weak inhibitor of ASD with an IC<sub>50</sub> of 306 μM [9]. In Ibrahim's investigation of the Indonesian sponge *Oceanapia* sp., sagitol C (**7**) together with the two abovementioned compounds **1** and **2** were disclosed. The cytotoxic effect of **7** was tested against mouse lymphoma (L5178Y), rat brain (PC12) and human cervix (Hela) cell lines. It exhibited 93%, 88% and 76% growth suppression against the tested cell lines at a concentration of 24.6 μM and 81%, 74% and 37% at a concentration of 12.3 μM with ED<sub>50</sub> values of 0.7, 0.9 and 2.3 μM, respectively [10].

## 2.2. Quinolizidine Alkaloids

A bisquinolizidine alkaloid, petrosin (**8**), and a series of bis-1-oxaquinolizidine alkaloids, xestospongins C–J (**9–16**) (Figure 3), were all obtained by Singh and his partners from the ethyl acetate extract of the sponge *Oceanapia* sp., which was collected from the southern coast of India. The relative stereochemistry of **8** was established by single-crystal X-ray analysis as 1S\*,2R\*,4R\*,9S\*,15R\*,17R\*,22S\*,23S\*. Compounds **9** and **10** were found to be active against several pathogens such as *Cryptococcus neoformans*, *Aspergillus funigatus*, *Candida albicans* and *Aspergillus niger* [11].

## 2.3. Sesquiterpene Alkaloid

Faulkner's group disclosed the major metabolite of the *Philippine* sponge *Oceanapia* sp. was the antimicrobial alkaloid oceanapamine (**17**) (Figure 4), isolated as trifluoroacetate (TFA) salt. The structure of **17** consisted of a monocyclic sesquiterpene attached to a histamine residue, representing the sole sesquiterpene–alkaloid hybrid from the genus *Oceanapia*. Compared with related model compounds, the absolute configuration of **17** was assigned as 6R. The TFA salt of **17** was screened rather broadly but only exhibited antimicrobial activity. In the standard disk (6-mm) assay, **17** inhibited *Bacillus subtilis* and *Escherichia coli* at 25 μg/disk, *Staphylococcus aureus* and *C. albicans* at 50 μg/disk and *Pseudomonas aeruginosa* at 100 μg/disk [12].

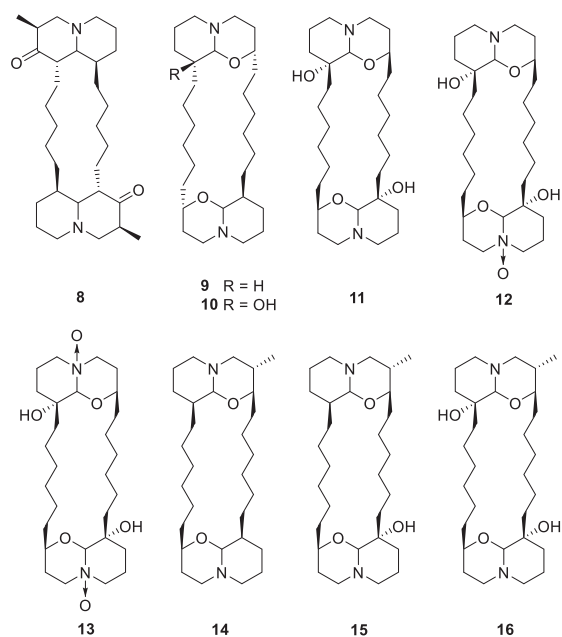


Figure 3. The chemical structures of quinolizidine alkaloids 8–16.

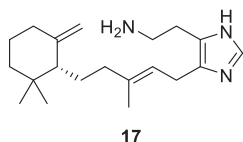
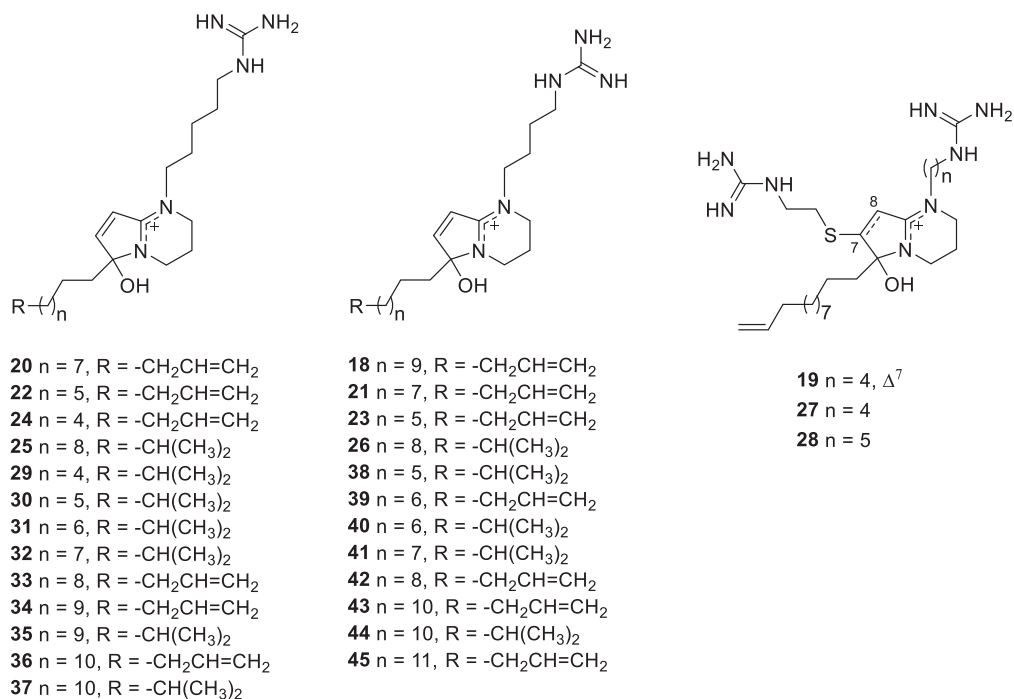


Figure 4. The chemical structure of sesquiterpene alkaloid 17.

#### 2.4. Phloeodictyne Alkaloids

The phloeodictyne framework was characterized by a fused alkaloidal skeleton, 1,2,3,4-tetrahydropyrrolo[1,2-*a*]pyrimidinium, bearing a variable-length alkyl (or alkenyl) side chain at C-6 and a four/five methylene chain ending in a guanidine group at N-1, while a thioethylguanidine chain may have been present at C-7 or not. Kourany-Lefoll et al. first reported this group of alkaloids in the haploslerid sponge *Phloeodictyon* sp. living in deep New Caledonian waters. Included were the pure compounds phloeodictines A (18) and B (19) and the inseparable mixtures of phloeodictines A1 (20) and A2 (21), A3 (22), A4 (23) and A5 (24), A6 (25) and A7 (26) and C1 (27) and C2 (28) (Figure 5). Compounds 18 and 19 had been tested against several bacteria using the standard microdilution plate assay and revealed to have potent activity with the following respective MICs ( $\mu\text{g/mL}$ ): *S. aureus* (1, 3), *E. coli* (1, 30), *P. aeruginosa* (10, >30) and *Streptococcus fecalis* (5, >15). On the other hand, the mixtures A (20+21), B (22+23+24), C (25+26) and D (27+28) were found to possess a wider spectrum of antibacterial activity (respective MICs,  $\mu\text{g/mL}$ ): *S. aureus* (3, 30, 1, 3), *E. coli* (3, 30, 3, >30), *P. aeruginosa* (30, >30, 30, >30), *Clostridium perfringens* (30, >30, 1, >100), *Bacteroides fragilis* (10, ~30, 3, >100) and *Peptococcus assackarolyticus* (10, >30, 3, >100). Furthermore, compounds 18, 19 and mixtures A–D also exhibited in vitro cytotoxicity toward KB human nasopharyngeal carcinoma cells with  $\text{IC}_{50}$  values of 1.5, 11.2, 2.2, 3.5, 0.6 and 1.8  $\mu\text{g/mL}$ , respectively [13,14]. Ten years later, Snider and his co-worker completed the first synthesis of ( $\pm$ )-21 [15].



**Figure 5.** The chemical structures of phloeodictine alkaloids 18–45.

Phloeodictines were also found to be components of the sponge *Oceanapia* [= *Phloeodictyon*] *fistulosa* in New Caledonian shallow waters by Mancini et al. They were clarified as a wide structural variety including the known 18–28 and new analogues 29–45 as corresponding mixtures. The complexity of the mixtures, and the very similar behavior of their components, prevented their isolation in pure form. However, crude mixtures and HPLC-enriched fractions were suitable for bioassays and proved to be active against chloroquine-resistant *Plasmodium falciparum*, with  $IC_{50}$  values ranging from 0.6 to 6  $\mu M$ , while cytotoxicity against the human A-549 cell line was low. These biological data might serve to illustrate preliminary structure–activity relationships: 1. The length of the C-6 chain had a greater influence on the bioactivity level than the nature of its terminal portion; 2. methylation of the guanidine moiety lowered the activity. This study showed good prospects for these alkaloids as leads for novel antimalarial agents [16].

### 2.5. Bromotyrosine Alkaloids

Four bromotyrosine alkaloids 46–49 (Figure 6) were all isolated from an Australian non-verongid sponge *Oceanapia* sp. by Bewley's group. Among them, 46 contained an unprecedented imidazolyl-quinolinone substructure attached to a bromotyrosine-derived spiro-isoxazoline. In the bioassay, compounds 46–49 inhibited mycothiol S-conjugate amidase by 50% at 2, 100, 3 and 37 mM, respectively. These four alkaloids represented the first examples of natural products that inhibited an enzyme central to a mycothiol-dependent detoxification pathway found in mycobacteria [17].

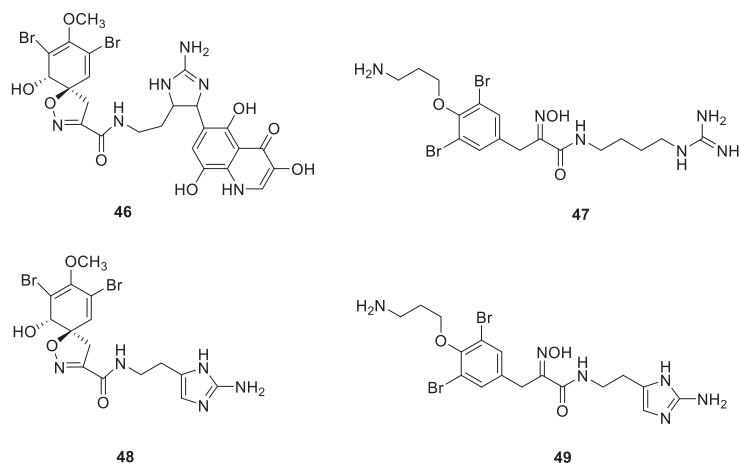


Figure 6. The chemical structures of bromotyrosine alkaloids 46–49.

### 2.6. Indole Alkaloids

6-Bromo-5-hydroxy-3-indolecarboxyaldehyde (**50**) along with two other brominated indoles 6-bromo-3-indolecarboxyaldehyde (**51**) and 3-bromoindole (**52**) (Figure 7) were discovered in the Caribbean sponge *Oceanapia bartschi* by Fattorusso's group [18]. Their structurally related non-brominated indole 3-formylindole (**53**) was disclosed in the Thai sponge *O. sagittaria* [8]. Crews' group investigated the Indonesian sponge *Oceanapia* sp., leading to another two brominated indoles, 6-Br-conicamin (**54**) and 6-Br-8-keto-conicamin A (**55**). Meanwhile, they synthesized **55** in this study. In the bioassay, the low micromolar in vitro activity of **55** against the PANC-1 cell line ( $IC_{50}$  1.5 mM for the natural product vs. 4.1 mM for the synthetic material) was exciting, which was similar to that of the clinical therapeutics (5FU:  $IC_{50}$  = 7.0 mM; gemcitabine:  $IC_{50}$  = 0.02 mM). Furthermore, ten additional analogs were prepared for further study on the structure–activity relationship. The continued study indicated that the quaternary amine functionality and bromination of the indole ring of **55** were critical for activity against PANC-1 [19]. The Indian sponge *Oceanapia* sp. afforded coixol (**56**), an active compound in the brine shrimp assay ( $LC_{50}$  =  $52.93 \pm 6.48$  ppm). This was the first report of coixol from a marine source [20].

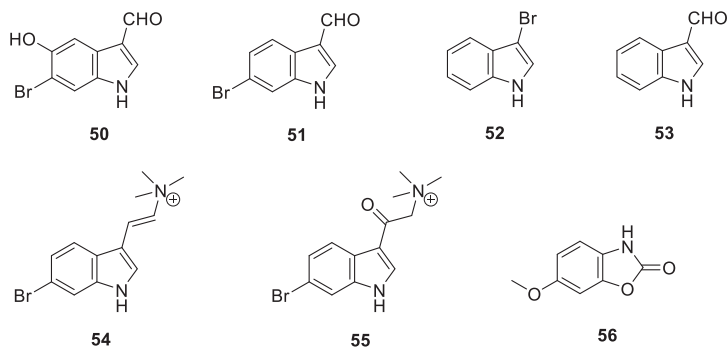
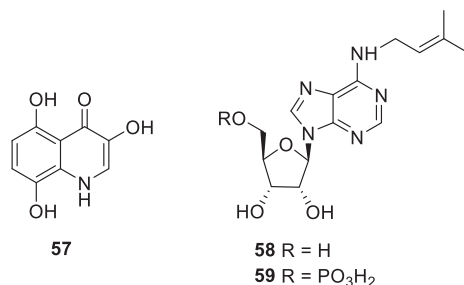


Figure 7. The chemical structures of indole alkaloids 50–56.

### 2.7. Nucleotide Alkaloids

In the study of an Australian sponge *Oceanapia* sp., uranidine (57) (Figure 8) was discovered as one component of the major alkaloids [17]. Very recently, *N*<sup>6</sup>-isopentenyladenosine (i<sup>6</sup>A, 58), along with *N*<sup>6</sup>-isopentenyladenosine 5'-monophosphate (i<sup>6</sup>AP, 59), was isolated from a Japanese sponge *Oceanapia* sp. This was the first report of i<sup>6</sup>A (58) and i<sup>6</sup>AP (59) from a marine sponge. In the cytotoxic biotest, 58 exhibited cytotoxic activity against HeLa cells with an IC<sub>50</sub> value of 2.1 μM. On the other hand, 59 was inactive at a concentration of 50 μM. Further observations demonstrated that the cell cycle was arrested at the G1 phase by 58, which indicated targeting of the Akt/NF-κB pathway [21].



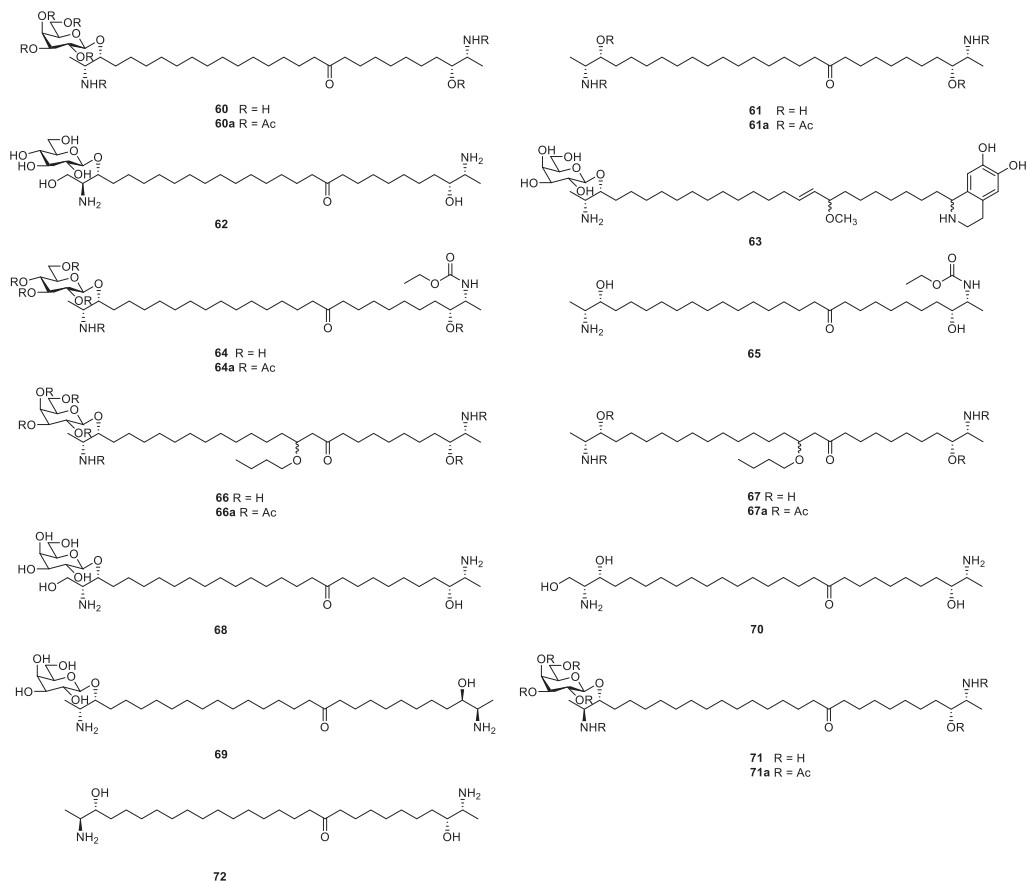
**Figure 8.** The chemical structures of nucleotide alkaloids 57–59.

## 3. Lipids

Lipids were the second-largest group of the *Oceanapia* secondary metabolites. They could be divided into sphingolipids, ceramides and cerebrosides, dithiocyanates and polyacetylenes, according to their structure features.

### 3.1. Sphingolipids

An antimicrobial galactopyranosyl pseudodimeric  $\alpha,\omega$ -bipolar sphingolipid, rhizochalin (60) (Figure 9), was isolated by Makarieva et al. from the sponge *Rhizochalina incrustata* near the north-west shore of Madagascar Island [22]. This was the first report of sphingolipids in the sponge of the genus *Oceanapia*. The effects of 60 on cell membranes were studied in Ehrlich ascites cells, spleen lymphocytes and erythrocytes, and phospholipid liposomes, respectively. At 10–100 mg/mL, this compound altered membrane permeability. These effects might be related to the cytostatic activity of 60 [23]. Ten years later, Molinski and his co-workers determined the absolute stereochemistry of (-)-rhizochalin (60) as 2*R*,3*R*,26*R*,27*R* by application of a general CD method based on the superposition of additive excitation couplings in tetrabenzoyl derivatives of bis-amino alkanols [24]. In Gaydou et al.'s study of a specimen of *Oceanapia ramsayi* collected at Itampolo on the west coast of Madagascar, rhizochalin (60) was found together with its corresponding aglycone rhizochalinin (61), which were both identified by their corresponding peracetates 60a and 61a [25]. A series of cytotoxic bioassays for 60 and 61 against different cell lines including the mechanisms had been carried out. Fedorov et al. reported 60 and 61 were cytotoxic against JB6 P+ Cl41, HeLa and THP-1 cell lines with IC<sub>50</sub> values ranging from 2.8 to 22.1 μM. A more in-depth study revealed 60 inhibited the EGF-induced transformation of JB6 P+ Cl41 cells in a dose-dependent manner [26]. Stonik and Kwak observed 60 and 61 induced apoptosis of HL-60 cells, of which the latter showed a stronger ability. Further detailed study showed the usual mitochondrial membrane permeability changes and the decrease in protein levels of procaspases-8, -9 and -3 correlated with their apoptotic activity [27]. Choi et al. disclosed 61 induced apoptosis via activation of AMP-activated protein kinase in HT-29 colon cancer cells [28].



**Figure 9.** The chemical structures of sphingolipids 60–72.

Oceanapiside (**62**), a new *bis- $\alpha,\omega$* -amino alcohol glycoside from the marine sponge *Oceanapia phillipensis* collected in southern Australia, was reported by Molinski's group [29]. Soon after, the absolute stereochemistry of **62** was assigned 2*S*,3*R*,26*R*,27*R* by analysis of CD spectra of its perbenzoate [30]. Compound **62** exhibited significant antifungal activity against the fluconazole-resistant yeast *Candida glabrata* with an MIC of 10  $\mu\text{g}/\text{mL}$  in broth dilution experiments [29]. In addition, *in vitro* antifungal activity of a series of  $\alpha,\omega$ -bifunctionalized amino alcohols derived from **62** against *C. glabrata* was measured. The dimeric bifunctionalized lipids exhibited activity about 10-fold higher than D-sphingosine, which was a larger factor than expected from the simple additive effects of vicinal amino alcohol groups [31]. It may be worth pointing out that the application of a combined method including micromolarscale Baeyer–Villiger oxidation and LC–MS interpretation by Makarieva et al. led to a revision of the structure of **62**, in which the placement of the keto group should be at C-18 rather than C-11 [32]. Oceanalin A (**63**), a unique hybrid  $\alpha,\omega$ -bifunctionalized sphingoid tetrahydroisoquinoline  $\beta$ -glycoside, was discovered in the sponge *Oceanapia* sp. collected off the northwest coast of Australia. Its absolute structure 2*R*,3*R* was elucidated by chemical correlation with the known rhizochalin **60**. Compound **63** exhibited *in vitro* antifungal activity against *C. glabrata* with an MIC of 30  $\mu\text{g}/\text{mL}$  [33].

Rhizochalin A (**64**), the fourth representative of two-headed glycosphingolipids, was isolated as its peracetate (**64a**) from the sponge *R. incrustata* collected in the Seychelles

Islands. Based on the chemical correlation, the absolute configuration 2*R*,3*R*,26*R*,27*R* of **64** was determined to be the same as that of **60**. It might be worth pointing out that **64a** was the first example of a natural product among known sphingolipids, including the family of two-headed sphingolipids, that contained the rare *N*-alkyl carbamoyl group [34]. Soon after, rhizochalinin A (**65**), the aglycone of rhizochalin A (**64**), was discovered in the former specimen. Compound **65** exhibited antileukemic activity against human leukemia THP-1 cells (IC<sub>50</sub> = 7.5 μM) [35]. Two new, two-headed sphingolipid-like compounds, rhizochalin B (**66**) and its aglycone rhizochalinin B (**67**), were obtained as their corresponding peracetates (**66a**, **67a**) from the marine sponge *Oceanapia* sp. collected near the Scott reef (northwest of Australia). They differed from classical sphingolipids in the α,ω-position of the basic groups, resembling the polar ends of sphingoid bases, and often contained a terminal methyl group instead of the hydroxymethyl group. Notably, the stereochemistry of C-16 in compounds **66** and **67** remained unknown [36].

From the sponge *R. incrustata* collected in Madagascar, two new representatives of two-headed glycosphingolipids, rhizochalins C (**68**) and D (**69**), were discovered. Based on the analysis of <sup>1</sup>H NMR data and CD spectra of their corresponding perbenzoates, the absolute configurations of **68** and **69** were assigned 2*R*,3*R*,26*R*,27*R* and 2*R*,3*R*,27*R*,28*R*, respectively. In contrast to the regular 2*S*,3*R*-configuration found in normal sphingoid bases, **68** contained the rare 2*R*,3*R* *threo* stereochemistry, while **69** possessed an odd-numbered C-29 hydrocarbon chain instead of C-28 found in canonical members of this series. It was a pity to find that rhizochalins C (**68**) and D (**69**) were not active (ED<sub>50</sub> > 150 μM) against the fluconazole-resistant yeast *C. glabrata* [32]. In 2009, further study on this specimen led to a new antileukemic two-headed sphingolipid rhizochalinin C (**70**), which was the aglycone of rhizochalin C (**68**). In the bioassay, **70** exhibited a cytotoxic effect against THP-1 (IC<sub>50</sub> = 6.7 μM) but was inactive against JB6 P+ Cl41 and HeLa cell lines [26]. Four years later, Molinski and his co-worker reported the first total synthesis of rhizochalinin C (**70**) [37].

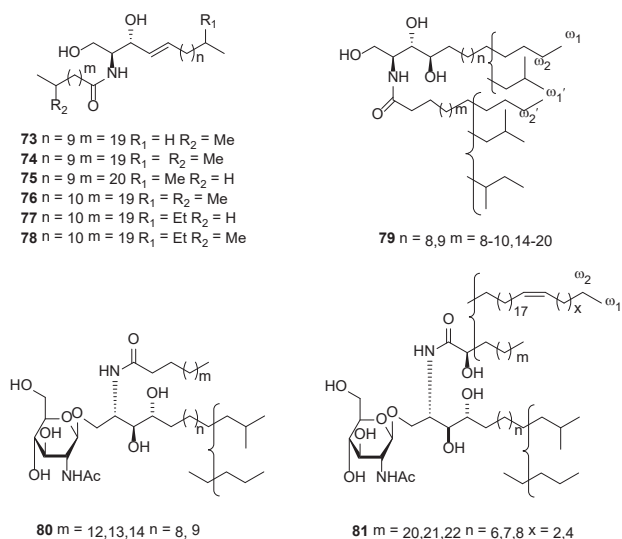
Isorhizochalin (**71**), isolated as its peracetate (**71a**), was a minor bipolar sphingolipid of stereodivergent biogenesis from the *R. incrustata*. Similar to **60**, its absolute stereochemistry was elucidated as 2*S*,3*R*,26*R*,27*R* by analysis of the CD spectrum of its perbenzoate. **71** was a C-2 epimer of **60** with an *erythro* configuration at the glycosylated 2-amino-3-alkanol-α-terminus, in contrast to the canonical *threo* configuration for other representatives of this structural group. In the bioassay, its aglycone, isorhizochalinin (**72**), showed cytotoxicity against human leukemia HL-60 and THP-1 cells with IC<sub>50</sub> values of 2.90 and 2.20 μM, respectively [38].

### 3.2. Ceramides and Cerebrosides

Chemical investigation on the sponge *Oceanapia* cf. *tenuis* collected in Woodin Channel, New Caledonia, led to a series of ceramides, named oceanapins A–F (**73**–**78**) (Figure 10), which were unique for branching at both the sphingosine and fatty-acid chains. A pair of Mosher's esters of the silyl ether derived from oceanapin D (**76**) was prepared, and the subsequent study on their NMR spectra revealed the 2'*S*,3'*R* absolute configuration for the source compound **76** [39].

An inseparable mixture of ceramides **79** (Figure 10) containing nonbranched and *iso*-branched C<sub>18</sub> and C<sub>19</sub>-phytosphingosines acylated with nonhydroxylated fatty acids were disclosed in the ethanolic extract of the Australian sponge *Oceanapia* sp. This was the first report of natural *iso*-C<sub>19</sub>-phytosphingosine-containing ceramides. Although no bioactivity was reported for these ceramides, the crude ethanolic extract exhibited antimicrobial activities against *S. aureus*, *B. subtilis*, *E. coli* and *C. albicans* as well as cytotoxic properties against the Erlich murine carcinoma [40]. In another study on the Australian sponge *Oceanapia* sp., two cerebrosides **80** and **81** containing *N*-acetylglucosamine were obtained [41].

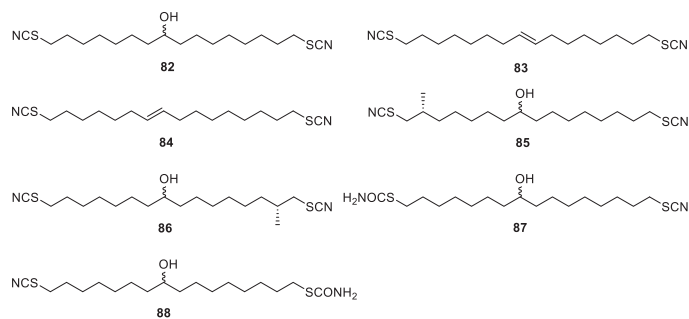




**Figure 10.** The chemical structures of ceramides and cerebrosides 73–81.

### 3.3. Dithiocyanates

The aqueous ethanol extract of an *Oceanapia* sp. collected off the northern Rottneest Shelf, Australia, displayed potent nematocidal activity against the commercial livestock parasite *Haemonchus contortus* ( $LD_{99} = 135 \mu\text{g/mL}$ ). Bioassay-directed fractionation yielded the bioactive principle component thiocyanatin A (**82**) ( $LD_{99} = 1.3 \mu\text{g/mL}$ ), together with the inseparable pairs of inactive analogues thiocyanatins B (**83**) and C (**84**),  $\beta$ -methyl branched bithiocyanates thiocyanatins D1 (**85**) and D2 (**86**) ( $LD_{99} = 3.1 \mu\text{g/mL}$ ) and thiocarbamate thiocyanates thiocyanatins E1 (**87**) and E2 (**88**) (Figure 11). Their structure assignments were confirmed by chemical synthesis and comparisons with synthetic model compounds. However, the stereochemical character of C-8 in **82** and **85–88** remained unknown. In addition to featuring an unprecedented dithiocyanate functionality, thiocyanatins **82–88** possessed an unusual 1,16-difunctionalized *n*-hexadecane carbon skeleton and were revealed as a hitherto unknown class of nematocidal agent. Preliminary structure–activity relationship investigations highlighted the importance of both the secondary -OH and -SCN functionalities and the influence of chain length on nematocidal activity [42,43].



**Figure 11.** The chemical structures of dithiocyanates 82–88.

### 3.4. Polyacetylenes

The study on the Indonesian sponge *Oceanapia* sp. led to three bromo-substituted polyunsaturated  $C_{16}$  fatty acids (7*E*,13*E*,15*Z*)-14,16-dibromohexadeca-7,13,15-trien-5-ynoic

acid (**89**), (5*Z*,7*E*,9*E*,13*E*,15*Z*)-6,14,16-tribromohexadeca-5,7,9,13,15-pentaenoic acid (**90**) and (7*E*,9*E*,13*E*,15*Z*)-14,16-dibromohexadeca-7,9,13,15-tetraen-5-ynoic acid (**91**) (Figure 12). Their common structural feature was a (13*E*,15*Z*)-14,16-dibromo-diene terminus. They differed in their C-5 to C-10 segments in unsaturation and halogenation. The cytotoxicity bioassay was tested on the mixture, since compounds **89–91** were unstable when pure, which showed only weak cytotoxicity (2+ at 10 µg/mL) against KB cells. Compound **91** showed mild antimicrobial activity against Gram-positive bacteria [44]. A C<sub>14</sub> acetylenic acid 7*E*,11*E*-tetradecadiene-5,9-diynoic acid (**92**) was isolated as an antimicrobial principle from the sponge of *Oceanapia* sp. collected in Kamagi Bay on the Sada Peninsula. This compound was the first example of a midchain acetylenic acid without a bromine atom, as well as the first reported member of a marine acetylene containing a CH=CH–C≡C–CH=CH–C≡C unit. In the bioassay, **92** exhibited some selectivity in antimicrobial activity. It was moderately active against four mutants of *Saccharomyces cerevisiae* and *C. albicans* but was inactive against *Penicillium chrysogenum* and *Mortierella ramanniana*. It also exhibited inhibitory effects against both Gram-positive and Gram-negative bacteria [45].

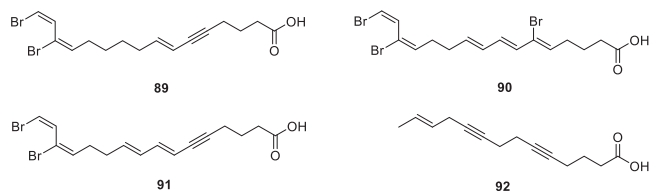


Figure 12. The chemical structures of polyacetylenes **89–92**.

#### 4. Sterols

The sterol profile of a north-western Australian marine sponge *Oceanapia* sp. was reported for the first time by Stonik et al. It contained stanols (**93–102**) and  $\Delta^5$ -sterols (**103–105**) with 24*R*-24,25-methylene-5 $\alpha$ -cholestan-3 $\beta$ -ol (**99**) (Figure 13) as the main constituent [46]. Notably, the structure of the major cyclopropane-containing stanol **99** was firstly obtained from *Rhizochalina* (= *Oceanapia*) *incrustedata* off the coast of the Seychelles Islands [47]. In the investigation on the marine sponge *O. sagittaria* from the Gulf of Thailand, 24 $\alpha$ -methylcholestanol (**106**) was isolated [8].

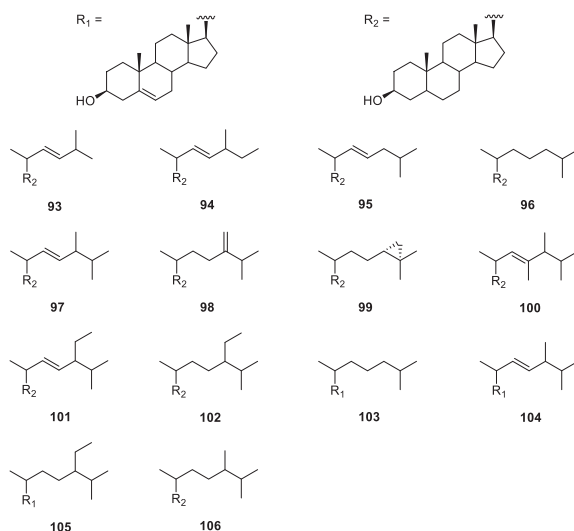


Figure 13. The chemical structures of sterols **93–106**.

## 5. Other Miscellaneous

The organic extract from the Caribbean *O. bartschi* was shown to contain the antibiotic diterpene ambliol A (**107**) (Figure 14) [18]. Three aromatic compounds, *p*-hydroxybenzaldehyde (**108**), *p*-hydroxybenzoic acid (**109**) and phenylacetic acid (**110**), were found in the sponge *O. sagittaria* collected from the Gulf of Thailand [8].

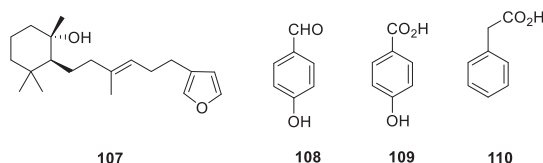
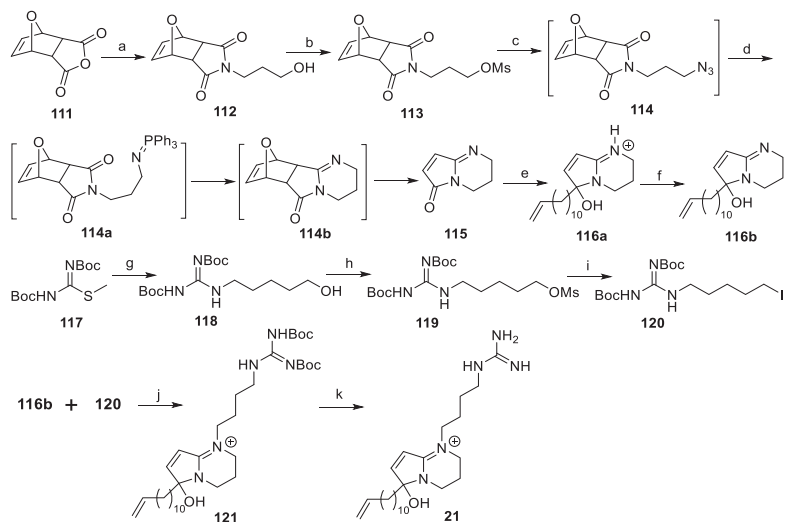


Figure 14. The chemical structures of miscellaneous 107–110.

## 6. Chemical Synthesis of Four Secondary Metabolites

### 6.1. Synthesis of (±)-Phloeodictine A1 ((±)-**21**)

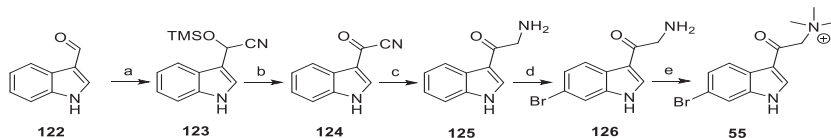
The (±)-phloeodictine A1 ((±)-**21**) was synthesized by a convergent route by Snider et al. as shown in Scheme 1 [15]. Furan-maleic anhydride Diels-Alder adduct **111** was used as the starting material for the 6-hydroxy-1,2,3,4-tetrahydropyrrolo[1,2-*a*]pyrimidinium skeleton. Imide **112** was obtained from **111** via a reaction with 3-aminopropanol, which was quantitatively converted to mesylate **113**. The reaction of **113** with NaN<sub>3</sub> provided azide **114**. The Eguchi aza-Wittig reaction of **114** afforded **114b**, which was followed by a thermal retro Diels-Alder reaction to liberate **115**. The addition of Grignard reagents to **115** produced **116a**. Washing a CH<sub>2</sub>Cl<sub>2</sub> solution of **116a** with 1 M NaOH solution afforded **116b**. In addition, Snider et al. selected a convergent route for iodide **120** containing a protected guanidine on the other end of the chain. The approach was that the reaction of **117** with the appropriate ω-amino-1-alkanol in THF gave **118**, then mesylation and successive displacement with iodide afforded **120**. Finally, alkylation of **116b** with **120** afforded **121**, and subsequent deprotection of **121** completed the synthesis of **21**.



Scheme 1. Synthetic route of phloeodictine A1 (**21**). Reagents: (a) 3-aminopropanol, MeOH, 56 °C, 3 d; (b) Et<sub>3</sub>N, MsCl, CH<sub>2</sub>Cl<sub>2</sub>, 0 °C; (c) NaN<sub>3</sub>, DMF, 25 °C, 14 h; (d) Ph<sub>3</sub>P, toluene, reflux 4 h; (e) 11-dodecenylyl magnesium bromide, CeCl<sub>3</sub>, THF, 0 °C; (f) 1M NaOH; (g) ω-amino-1-pentanol, THF, 50 °C, 2 h; (h) MsCl, Et<sub>3</sub>N, CH<sub>2</sub>Cl<sub>2</sub>, 0 °C (i) NaI, NaHCO<sub>3</sub>, acetone, reflux, 4 h; (j) DMSO-d<sub>6</sub>, 25 °C, 24 h; (k) TFA/CH<sub>2</sub>Cl<sub>2</sub> (1:1), 2 h.

### 6.2. Synthesis of 6-Br-8-keto-conicamin A (55)

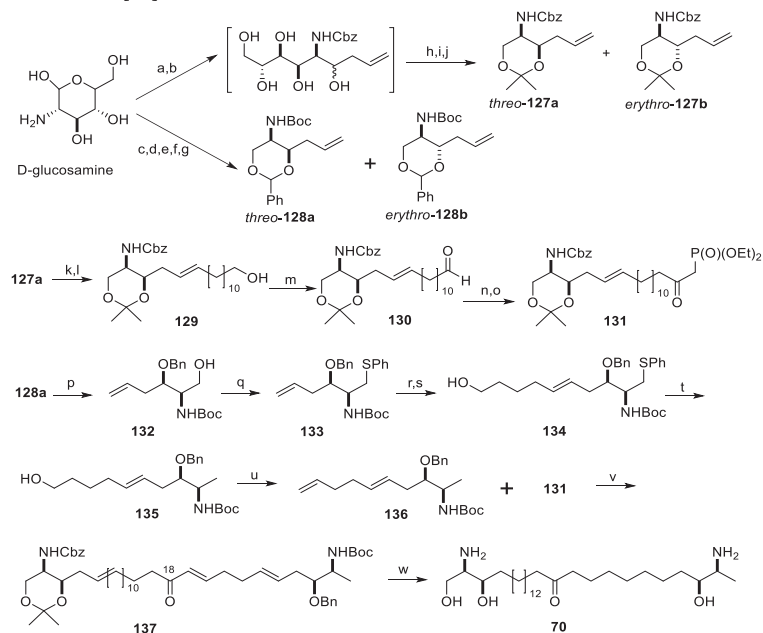
In Crews et al.'s work, indole-3-carboxaldehyde **122** was used as the starting material as outlined in Scheme 2 [19]. First, **122** was esterified to yield its cyanohydrin silylether **123**, then the oxidation of **123** via DDQ followed by hydrogenation led to keto-tryptamine synthon **125**. Bromination of **125** proceeded in a straightforward fashion, producing the bromo-keto-tryptamine **126**. The final step involved the methylation of **126** to afford 6-Br-8-keto-conicamin A (**55**).



**Scheme 2.** Synthetic route of 6-Br-8-keto-conicamin A (**55**). Reagents: (a): TMSCN, DME, reflux 1.5 h, cool; (b): DDQ (dropwise), Dioxane, rt; (c): H<sub>2</sub>, Pd/C, AcOH; (d): Br<sub>2</sub>, rt 24 h, HCOOH:CH<sub>3</sub>COOH (1:1); (e): MeI, rt 16 h, MeOH, KHCO<sub>3</sub>.

### 6.3. Synthesis of Rhizochalinin C (70)

Molinski et al. disclosed an optimized procedure for rapid diastereoselective access to *L*-threo-sphingoid base synthons, using a remarkable one-pot conversion of unprotected D-glucosamine into useful D-serine synthons based on In<sup>0</sup>-mediated allylation. This method was successfully applied to rhizochalinin C (**70**), which was elaborated as shown in Scheme 3 [37].

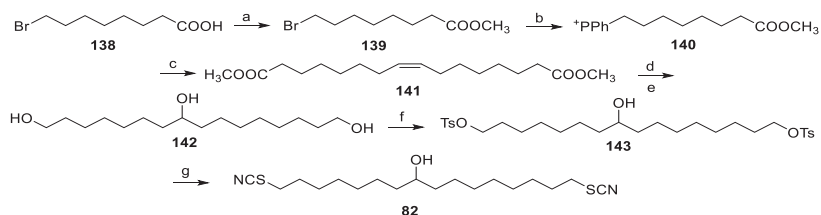


**Scheme 3.** Synthetic route of rhizochalinin C (**70**). Reagents: (a) In<sup>0</sup>, allyl bromide, 1,4-dioxane:H<sub>2</sub>O (3:1), 100 °C; (b) CBZ-Cl, NaHCO<sub>3</sub> (aq.); (c) In<sup>0</sup>, allyl bromide, 1,4-dioxane:H<sub>2</sub>O (3:1), 100 °C; (d) (Boc)<sub>2</sub>O, NaHCO<sub>3</sub> (aq.); (e) NaIO<sub>4</sub>, H<sub>2</sub>O; (f) NaBH<sub>4</sub>, MeOH; (g) CSA, (MeO)<sub>2</sub>C(CH<sub>3</sub>)<sub>2</sub>; (h) NaIO<sub>4</sub>, H<sub>2</sub>O; (i) NaBH<sub>4</sub>, MeOH; (j) CSA, (MeO)<sub>2</sub>C(CH<sub>3</sub>)<sub>2</sub>; (k) tetradec-13-enyl acetate, Grubbs II catalyst, CH<sub>2</sub>Cl<sub>2</sub>, reflux; (l) NaOMe, MeOH; (m) DMP, CH<sub>2</sub>Cl<sub>2</sub>; (n) (EtO)<sub>2</sub>P(O)CH<sub>3</sub>, n-BuLi, THF, −78 °C; (o) DMP, CH<sub>2</sub>Cl<sub>2</sub>; (p) AlH<sub>3</sub>, Et<sub>2</sub>O, 0 °C; (q) PhSPh, n-Bu<sub>3</sub>P, THF; (r) 4-penten-1-ylacetate, Grubbs II cat., CH<sub>2</sub>Cl<sub>2</sub>, reflux; (s) NaOMe, MeOH; (t) Ra-Ni; (u) DMP, CH<sub>2</sub>Cl<sub>2</sub>; (v) Ba(OH)<sub>2</sub>, wet THF; (w) 10 M HCl, MeOH, H<sub>2</sub>, 2 atm, Pd–C.

The allyl-substituted compounds **127a** and **128a** that were procured from the Barbier allylation of D-glucosamine were followed by differential protections of NH<sub>2</sub> and OH groups. **127a** was subjected to olefin cross-metathesis with tetradec-13-enyl acetate, after methanolysis, to provide the primary alcohol **129**. Then, Dess–Martin oxidation of **129** led to the corresponding aldehyde **130**, which was followed by the addition of the anion derived from diethyl methylphosphonate, and oxidation delivered the β-ketophosphonate **131**. The alcohol **132**, the reduction product of **128a**, was transformed into the phenylthio ether to give **133**. Olefin cross-metathesis of **133** with 4-penten-1-yl acetate followed by methanolysis yielded the primary alcohol **134**. Reduction of **134** delivered protected *threo*-2-amino-3-alkanol **135**, and the subsequent oxidation of **135** led to the aldehyde **136**. The Horner–Emmons–Wadsworth reaction of aldehyde **131** and **136** under Paterson conditions gave the α,β-unsaturated ketone **137**, which was deprotected to yield **70**.

#### 6.4. Synthesis of Thiocyanatin A (**82**)

Capon et al. reported the seven-step total synthesis of thiocyanatin A (**82**) starting from 8-bromooctanoic acid (**138**) [43]. The esterification of 8-bromooctanoic acid (**138**) yielded its methyl ester **139**, which was converted to the Wittig salt **140**. The following one-pot oxidation–Wittig coupling afforded the olefin–diester **141**. The triol **142** was obtained by the epoxidation of **141** with *m*-CPBA and the successive reduction of the corresponding epoxide with LiAlH<sub>4</sub>. Treatment of **142** with TsCl gave the ditosylate **143**. Finally, the displacement of the tosylate groups by thiocyanate afforded racemic thiocyanatin A (**82**) as outlined in Scheme 4.



**Scheme 4.** Synthetic route of thiocyanatin A (**82**). Reagents: (a) H<sub>2</sub>SO<sub>4</sub>, MeOH, reflux 16 h; (b) PPh<sub>3</sub>, MeCN, reflux 16 h; (c) NaHMDS, THF/DMPU, O<sub>2</sub>, 60 °C, 16 h; (d) *m*-CPBA, CH<sub>2</sub>Cl<sub>2</sub>, rt, 16 h; (e) LiAlH<sub>4</sub>, reflux 20 h; (f) *p*-TsCl, CH<sub>2</sub>Cl<sub>2</sub>, DMAP/NEt<sub>3</sub>, rt, 32 h; (g) KSCN, THF, reflux 16 h.

## 7. Conclusions and Perspectives

A huge library of secondary metabolites was reported from the sponges of the genus *Oceanapia*, with up to 110 compounds with unique structures, from 1989 to July 2019. More than eight species of *Oceanapia* sponges have been chemically investigated, including *Oceanapia sagittaria*, *Oceanapia fistulosa*, *Oceanapia bartschi*, *Phloeodictyon* sp., *Rhizochalina incrustata*, *Oceanapia ramsayi*, *Oceanapia phillipensis*, *Oceanapia* cf. *tenuis* and *Oceanapia* sp. The chemical structures were classified as alkaloids, lipids, sterols and other miscellaneous. Among them, alkaloids were encountered most frequently. These compounds exhibited diverse biological properties ranging from insecticidal, cytotoxic and antifeedant to antibacterial. Their unique structures and promising bioactivities have attracted a great deal of attention from synthetic chemists for their total synthesis.

**Author Contributions:** Conceptualization, L.-F.L.; investigation, M.-J.X., L.-J.Z., J.-K.C. and Q.B.; writing—original draft preparation, M.-J.X. and L.-F.L.; writing—review and editing, L.-F.L.; funding acquisition, L.-F.L. All authors have read and agreed to the published version of the manuscript.

**Funding:** This research was funded by the National Natural Science Foundation of China (No. 41876194).

**Conflicts of Interest:** The author declares no conflict of interest.

## References

1. Jiménez, C. Marine natural products in medicinal chemistry. *ACS Med. Chem. Lett.* **2018**, *9*, 959–961. [[CrossRef](#)] [[PubMed](#)]
2. Carroll, A.R.; Copp, B.R.; Davis, R.A.; Keyzers, R.A.; Prinsep, M.R. Marine natural products. *Nat. Prod. Rep.* **2019**, *36*, 122–173. [[CrossRef](#)] [[PubMed](#)]
3. Desqueyroux-Faúndez, R.; Valentine, C. Family Phloeodictyidae Carter, 1882. In *Systema Porifera: A Guide to the Classification of Sponges*; Hooper, J.N.A., Van Soest, R.W.M., Willenz, P., Eds.; Springer: Boston, MA, USA, 2002; pp. 893–905.
4. Salomon, C.E.; Faulkner, D.J. Sagitol, a pyridoacridine alkaloid from the sponge *Oceanapia sagittaria*. *Tetrahedron Lett.* **1996**, *37*, 9147–9148. [[CrossRef](#)]
5. Eder, C.; Schupp, P.; Proksch, P.; Wray, V.; Steube, K.; Müller, C.E.; Frobenius, W.; Herderich, A.M.; van Soest, R.W.M. Bioactive pyridoacridine alkaloids from the Micronesian sponge *Oceanapia* sp. *J. Nat. Prod.* **1998**, *61*, 301–305. [[CrossRef](#)] [[PubMed](#)]
6. Gunawardana, G.P.; Koehn, F.E.; Lee, A.Y.; Clardy, J.; He, H.Y.; Faulkner, D.J. Pyridoacridine alkaloids from deep-water marine sponges of the family Pachastrellidae: Structure revision of dercitin and related compounds and correlation with the kuanoniamines. *J. Org. Chem.* **1992**, *57*, 1523–1526. [[CrossRef](#)]
7. Schupp, P.; Eder, C.; Paul, V.; Proksch, P. Distribution of secondary metabolites in the sponge *Oceanapia* sp. and its ecological implications. *Mar. Biol.* **1999**, *135*, 573–580. [[CrossRef](#)]
8. Kijjoo, A.; Wattanadilok, R.; Campos, N.; Herz, W.; Nascimento, M.S.J.; Pinto, M. Anticancer activity evaluation of kuanoniamines A and C isolated from the marine sponge *Oceanapia sagittaria*, collected from the Gulf of Thailand. *Mar. Drugs* **2007**, *5*, 6–22. [[CrossRef](#)]
9. Carroll, A.R.; Ngo, A.; Quinn, R.J.; Redburn, J.; Hooper, J.N.A. Petrosamine B, an inhibitor of the *Helicobacter pylori* enzyme aspartyl semialdehyde dehydrogenase from the Australian sponge *Oceanapia* sp. *J. Nat. Prod.* **2005**, *68*, 804–806. [[CrossRef](#)]
10. Ibrahim, S.R.M.; Mohamed, G.A.; Elkhayat, E.S.; Fouad, M.A.; Proksch, P. Sagitol C, a new cytotoxic pyridoacridine alkaloid from the sponge *Oceanapia* sp. *Bull. Fac. Pharm. Cairo Univ.* **2013**, *51*, 229–232. [[CrossRef](#)]
11. Singh, K.S.; Das, B.; Naik, C.G. Quinolizidines alkaloids: Petrosin and xestospongins from the sponge *Oceanapia* sp. *J. Chem. Sci.* **2011**, *123*, 601–607. [[CrossRef](#)]
12. Boyd, K.G.; Harper, M.K.; Faulkner, D.J. Oceanapamine, a sesquiterpene alkaloid from the Philippine sponge *Oceanapia* sp. *J. Nat. Prod.* **1995**, *58*, 302–305. [[CrossRef](#)] [[PubMed](#)]
13. Kourany-Lefoll, E.; Pais, M.; Sévenet, T.; Guittet, E.; Montagnac, A.; Fontaine, C.; Guenard, D.; Adeline, M.T.; Debitus, C. Phloeodictines A and B: New antibacterial and cytotoxic bicyclic amidinium salts from the New Caledonian sponge, *Phloeodictyon* sp. *J. Org. Chem.* **1992**, *57*, 3832–3835. [[CrossRef](#)]
14. Kourany-Lefoll, E.; Laprévotte, O.; Sévenet, T.; Montagnac, A.; Pais, M.; Debitus, C. Phloeodictines A1–A7 and C1–C2, antibiotic and cytotoxic guanidine alkaloids from the New Caledonian sponge, *Phloeodictyon* sp. *Tetrahedron* **1994**, *50*, 3415–3426. [[CrossRef](#)]
15. Neubert, B.J.; Snider, B.B. Synthesis of (±)-phloeodictine A1. *Org. Lett.* **2003**, *5*, 765–768. [[CrossRef](#)]
16. Mancini, I.; Guella, G.; Sauvain, M.; Debitus, C.; Duigou, A.-G.; Ausseil, F.; Menou, J.-L.; Pietra, F. New 1,2,3,4-tetrahydropyrrolo[1,2-a]pyrimidinium alkaloids (phloeodictynes) from the New Caledonian shallow-water haplosclerid sponge *Oceanapia fistulosa*. Structural elucidation from mainly LC-tandem-MS-soft-ionization techniques and discovery of antiplasmodial activity. *Org. Biomol. Chem.* **2004**, *2*, 783–787. [[CrossRef](#)]
17. Nicholas, G.M.; Newton, G.L.; Fahey, R.C.; Bewley, C.A. Novel bromotyrosine alkaloids: Inhibitors of mycothiol S-conjugate amidase. *Org. Lett.* **2001**, *3*, 1543–1545. [[CrossRef](#)]
18. Cafieri, F.; Fattorusso, E.; Mahajnah, Y.; Mangoni, A. 6-Bromo-5-hydroxy-3-indolecarboxaldehyde from the Caribbean sponge *Oceanapia bartschi*. *Z. Naturforsch. B-J. Chem. Sci.* **1993**, *48*, 1408–1410. [[CrossRef](#)]
19. Lorig-Roach, N.; Hamkins-Indik, F.; Johnson, T.A.; Tenney, K.; Valeriote, F.A.; Crews, P. The potential of achiral sponge-derived and synthetic bromoindoles as selective cytotoxins against PANC-1 tumor cells. *Tetrahedron* **2018**, *74*, 217–223. [[CrossRef](#)]
20. Venkateswarlu, Y.; Reddy, N.S.; Ramesh, P.; Rao, J.V. Coixol: A bioactive principle from a marine sponge *Oceanapia* sp. *Biochem. Syst. Ecol.* **1999**, *27*, 519–520. [[CrossRef](#)]
21. Nakamukai, S.; Ise, Y.; Ohtsuka, S.; Okada, S.; Matsunaga, S. Isolation and identification of N6-isopentenyladenosine as the cytotoxic constituent of a marine sponge *Oceanapia* sp. *Biosci. Biotechnol. Biochem.* **2019**, *83*, 1985–1988. [[CrossRef](#)]
22. Makarieva, T.N.; Denisenko, V.A.; Stonik, V.A.; Milgrom, Y.M.; Rashkes, Y.V. Rhizochalin, a novel secondary metabolite of mixed biosynthesis from the sponge *Rhizochalina incrustata*. *Tetrahedron Lett.* **1989**, *30*, 6581–6584. [[CrossRef](#)]
23. Popov, A.M.; Makarieva, T.N.; Stonik, V.A. Membrane activity of rhizochalin isolated from *Rhizochalina incrustata*. *Biofizika* **1990**, *35*, 883–884. [[PubMed](#)]
24. Molinski, T.F.; Makarieva, T.N.; Stonik, V.A. (–)-Rhizochalin is a dimeric enantiomeric (2R)-sphingolipid: Absolute configuration of pseudo-C<sub>2v</sub>-symmetric bis-2-amino-3-alkanols by CD. *Angew. Chem. Int. Ed.* **2000**, *39*, 4076–4079. [[CrossRef](#)]
25. Bensemhoun, J.; Bombarda, I.; Akin, M.; Faure, R.; Vacelet, J.; Gaydou, E.M. Marine bifunctional sphingolipids from the sponge *Oceanapia ramsayi*. *Molecules* **2008**, *13*, 772–778. [[CrossRef](#)] [[PubMed](#)]
26. Fedorov, S.N.; Makarieva, T.N.; Guzii, A.G.; Shubina, L.K.; Kwak, J.Y.; Stonik, V.A. Marine two-headed sphingolipid-like compound rhizochalin inhibits EGF-induced transformation of JB6 P+ Cl41 cells. *Lipids* **2009**, *44*, 777–785. [[CrossRef](#)] [[PubMed](#)]
27. Jin, J.-O.; Shastina, V.; Park, J.-I.; Han, J.-Y.; Makarieva, T.; Fedorov, S.; Rasskazov, V.; Stonik, V.; Kwak, J.-Y. Differential induction of apoptosis of leukemic cells by rhizochalin, two headed sphingolipids from sponge and its derivatives. *Biol. Pharm. Bull.* **2009**, *32*, 955–962. [[CrossRef](#)]

28. Khanal, P.; Kang, B.S.; Yun, H.J.; Cho, H.-G.; Makarieva, T.N.; Choi, H.S. Aglycon of rhizochalin from the *Rhizochalina incrustata* induces apoptosis via activation of AMP-activated protein kinase in HT-29 colon cancer cells. *Biol. Pharm. Bull.* **2011**, *34*, 1553–1558. [[CrossRef](#)]
29. Nicholas, G.M.; Hong, T.W.; Molinski, T.F.; Lerch, M.L.; Cancilla, M.T.; Lebrilla, C.B. Oceanapiside, an antifungal bis- $\alpha,\omega$ -amino alcohol glycoside from the marine sponge *Oceanapia phillipensis*. *J. Nat. Prod.* **1999**, *62*, 1678–1681. [[CrossRef](#)]
30. Nicholas, G.M.; Molinski, T.F. Enantiodivergent biosynthesis of the dimeric sphingolipid oceanapiside from the marine sponge *Oceanapia phillipensis*. Determination of remote stereochemistry. *J. Am. Chem. Soc.* **2000**, *122*, 4011–4019. [[CrossRef](#)]
31. Nicholas, G.M.; Li, R.; MacMillan, J.B.; Molinski, T.F. Antifungal activity of bifunctional sphingolipids. intramolecular synergism within long-chain  $\alpha,\omega$ -bis-aminoalcohols. *Bioorganic Med. Chem. Lett.* **2002**, *12*, 2159–2162. [[CrossRef](#)]
32. Makarieva, T.N.; Dmitrenok, P.S.; Zakharenko, A.M.; Denisenko, V.A.; Guzii, A.G.; Li, R.; Skepper, C.K.; Molinski, T.F.; Stonik, V.A. Rhizochalins C and D from the sponge *Rhizochalina incrustata*. A rare three-sphingolipid and a facile method for determination of the carbonyl position in  $\alpha,\omega$ -bifunctionalized ketosphingolipids. *J. Nat. Prod.* **2007**, *70*, 1991–1998. [[CrossRef](#)] [[PubMed](#)]
33. Makarieva, T.N.; Denisenko, V.A.; Dmitrenok, P.S.; Guzii, A.G.; Santalova, E.A.; Stonik, V.A.; MacMillan, J.B.; Molinski, T.F. Oceanalin A, a hybrid  $\alpha,\omega$ -bifunctionalized sphingoid tetrahydroisoquinoline  $\beta$ -glycoside from the marine sponge *Oceanapia* sp. *Org. Lett.* **2005**, *7*, 2897–2900. [[CrossRef](#)]
34. Makarieva, T.N.; Guzii, A.G.; Denisenko, V.A.; Dmitrenok, P.S.; Santalova, E.A.; Pokanevich, E.V.; Molinski, T.F.; Stonik, V.A. Rhizochalin A, a novel two-headed sphingolipid from the sponge *Rhizochalina incrustata*. *J. Nat. Prod.* **2005**, *68*, 255–257. [[CrossRef](#)] [[PubMed](#)]
35. Makarieva, T.N.; Zakharenko, A.M.; Denisenko, V.A.; Dmitrenok, P.S.; Guzii, A.G.; Shubina, L.K.; Kapustina, I.I.; Fedorov, S.N. Rhizochalinin A, a new antileukemic two-headed sphingolipid from the sponge *Rhizochalina incrustata*. *Chem. Nat. Compd.* **2007**, *43*, 468–469. [[CrossRef](#)]
36. Makarieva, T.N.; Guzii, A.G.; Denisenko, V.A.; Dmitrenok, P.S.; Stonik, V.A. New two-headed sphingolipid-like compounds from the marine sponge *Oceanapia* sp. *Russ. Chem. Bull.* **2008**, *57*, 669–673. [[CrossRef](#)]
37. Ko, J.; Molinski, T.F. D-Glucosamine-derived synthons for assembly of L-threo-sphingoid bases. Total synthesis of rhizochalinin C. *J. Org. Chem.* **2012**, *78*, 498–505. [[CrossRef](#)]
38. Makarieva, T.N.; Zakharenko, A.M.; Dmitrenok, P.S.; Guzii, A.G.; Denisenko, V.A.; Savina, A.S.; Dalisay, D.S.; Molinski, T.F.; Stonik, V.A. Isorhizochalin: A minor unprecedented bipolar sphingolipid of stereodivergent biogenesis from the *Rhizochalina incrustata*. *Lipids* **2009**, *44*, 1155–1162. [[CrossRef](#)]
39. Mancini, I.; Guella, G.; Pietra, F.; Debitus, C. Oceanapins A–F, unique branched ceramides isolated from the haplosclerid sponge *Oceanapia* cf. *tenuis* of the Coral Sea. *Helv. Chim. Acta* **1994**, *77*, 51–58. [[CrossRef](#)]
40. Guzii, A.G.; Makarieva, T.N.; Svetashev, V.I.; Denisenko, V.A.; Dmitrenok, P.S.; Pokanevich, E.V.; Santalova, E.A.; Krasokhin, V.B.; Stonik, V.A. New ceramides from sea sponge *Oceanapia* sp. *Russ. J. Bioorg. Chem.* **2006**, *32*, 288–294. [[CrossRef](#)]
41. Guzii, A.G.; Makarieva, T.N.; Denisenko, V.A.; Svetashev, V.I.; Rodkina, S.A.; Dmitrenok, P.S.; Anastuyuk, S.D.; Stonik, V.A. New cerebrosides from the marine sponge *Oceanapia* sp. *Russ. Chem. Bull.* **2006**, *55*, 928–933. [[CrossRef](#)]
42. Capon, R.J.; Skene, C.; Liu, E.H.-T.; Lacey, E.; Gill, J.H.; Heiland, K.; Friedel, T. The isolation and synthesis of novel nematocidal dithiocyanates from an Australian marine sponge, *Oceanapia* sp. *J. Org. Chem.* **2001**, *66*, 7765–7769. [[CrossRef](#)] [[PubMed](#)]
43. Capon, R.J.; Skene, C.; Liu, E.H.-T.; Lacey, E.; Gill, J.H.; Heiland, K.; Friedel, T. Nematocidal thiocyanatins from a southern Australian marine sponge *Oceanapia* sp. *J. Nat. Prod.* **2004**, *67*, 1277–1282. [[CrossRef](#)] [[PubMed](#)]
44. Ichiba, T.; Scheuer, P.J.; Kelly-Borges, M. Sponge-derived polyunsaturated C<sub>16</sub> di- and tribromocarboxylic acids. *Helv. Chim. Acta* **1993**, *76*, 2814–2816. [[CrossRef](#)]
45. Matsunaga, S.; Okada, Y.; Fusetani, N.; van Soest, R.W.M. An antimicrobial C<sub>14</sub> acetylenic acid from a marine sponge *Oceanapia* species. *J. Nat. Prod.* **2000**, *63*, 690–691. [[CrossRef](#)] [[PubMed](#)]
46. Santalova, E.A.; Makarieva, T.N.; Ponomarenko, L.P.; Denisenko, V.A.; Krasokhin, V.B.; Mollo, E.; Cimino, G.; Stonik, V.A. Sterols and related metabolites from five species of sponges. *Biochem. Syst. Ecol.* **2007**, *35*, 439–446. [[CrossRef](#)]
47. Makarieva, T.N.; Stonik, V.A.; Ponomarenko, L.P.; Kalinovskiy, A.I. Isolation of (24R)-24,25-methylene-5 $\alpha$ -cholestan-3 $\beta$ -ol, a new cyclopropane-containing sponge sterol. *J. Chem. Res.* **1996**, *10*, 468–469. [[CrossRef](#)]

## Article

# Synthesis of Marine Cyclopeptide Galaxamide Analogues as Potential Anticancer Agents

Daichun Li <sup>†</sup>, Xiaojian Liao <sup>†</sup>, Shenghui Zhong, Bingxin Zhao <sup>\*</sup> and Shihai Xu <sup>\*</sup>

Department of Chemistry, College of Chemistry and Materials Science, Jinan University, Guangzhou 510632, China; ldcman1733061011@stu2017.jnu.edu.cn (D.L.); tliaoqxj@jnu.edu.cn (X.L.); zhongsh@stu2014.jnu.edu.cn (S.Z.)

<sup>\*</sup> Correspondence: bxzhao@jnu.edu.cn (B.Z.); txush@jnu.edu.cn (S.X.)

<sup>†</sup> These authors contributed equally to this work.

**Abstract:** In this paper, eight new galaxamide analogues (**Z-1~Z-8**) were synthesized and evaluated for their cytotoxic activities against five cancer cell lines, MCF-7, MD-MBA-231, HepG2, Hela, and A549, using MTT assays. The modified analogue **Z-6** displayed broad spectrum cytotoxic activity toward each tested cell line with IC<sub>50</sub> values of 1.65 ± 0.30 (MCF-7), 2.91 ± 0.17 (HepG2), 4.59 ± 0.27 (MD-MBA-231), 5.69 ± 0.37 (Hela), and 5.96 ± 0.41 (A549) µg/mL, respectively. The galaxamides **Z-3** and **Z-6** induced concentration-dependent apoptosis of the MCF-7 cells after 72 h as evaluated by the flow cytometry experiment. The results showed that these compounds could induce MCF-7 cell apoptosis by arresting the G0/G1 phase of the cell cycle and finally achieving the effect of inhibiting the proliferation of MCF-7 cells.

**Keywords:** drug design; anticancer; apoptosis; cyclic pentapeptide; galaxamide analogues

**Citation:** Li, D.; Liao, X.; Zhong, S.; Zhao, B.; Xu, S. Synthesis of Marine Cyclopeptide Galaxamide Analogues as Potential Anticancer Agents. *Mar. Drugs* **2022**, *20*, 158. <https://doi.org/10.3390/md20030158>

Academic Editors: Yonghong Liu and Xuefeng Zhou

Received: 20 January 2022

Accepted: 18 February 2022

Published: 22 February 2022

**Publisher's Note:** MDPI stays neutral with regard to jurisdictional claims in published maps and institutional affiliations.



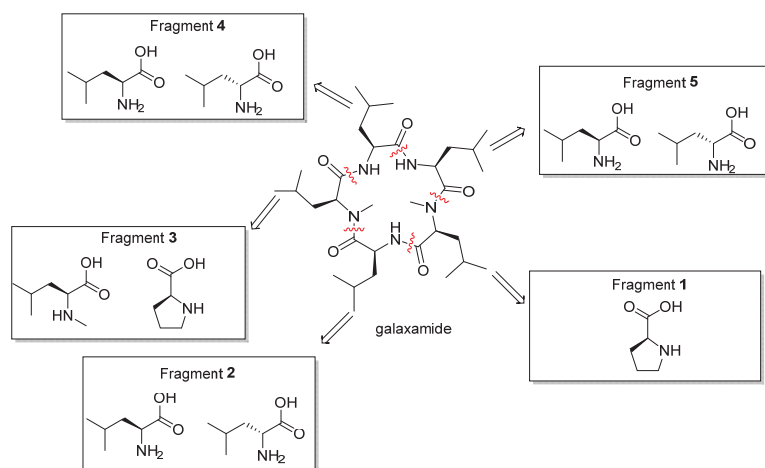
**Copyright:** © 2022 by the authors. Licensee MDPI, Basel, Switzerland. This article is an open access article distributed under the terms and conditions of the Creative Commons Attribution (CC BY) license (<https://creativecommons.org/licenses/by/4.0/>).

## 1. Introduction

Cyclopeptides mainly isolated from various marine species, which exhibited antitumor, [1–3] antiviral, [4] anti-inflammatory [5,6] and antibacterial [7–9] activities. Cyclopeptides usually exhibited superior biological activities due to their conformational rigidity and resistance to proteolytic degradation. [10] Therefore, cyclopeptides had attracted great attention and become one of the important components in the development of antitumor drugs. [11] To enhance the antitumor activity of cyclopeptides, they were always modified by changing the configurations of amino acid residues. In addition, the fragment of proline was widely existing in natural cyclopeptides, [12] which might be the active group for antitumor and antibacterial activities.

In our group, previous phytochemical investigation on the alga *Galaxaura filamentosa* had led to the isolation of a novel cyclic pentapeptide, galaxamide (Figure 1). It was composed of five *L*-leucines including two *N*-methylated ones, which showed significant antitumor activities against GRC-1 and HepG2 cell lines. [13] In the preliminary work, the galaxamide analogues had been synthesized by replacing one of the leucines with phenylalanine and changing the configuration of amino acids, which also showed potential antitumor activities. [14–16]





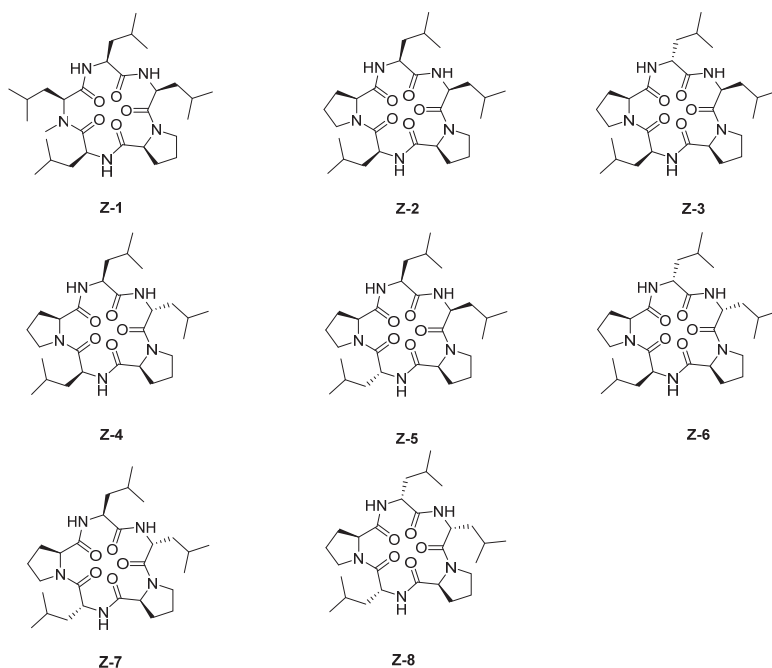
**Figure 1.** Design in the series of galaxamide analogues.

In this paper, eight new galaxamide analogues (**Z-1**~**Z-8**) were synthesized by replacing one or two *N*-Me-*L*-leucines in the galaxamide with *L*-proline or changing the stereo configuration of leucine. In vitro antitumor activities of these new compounds against MCF-7, HepG2, Hela, MD-MBA-231, A549, and HUVEC cell lines were also evaluated by MTT assay. On the one hand, a great majority of the synthesized compounds showed strong antitumor activities. On the other hand, they showed weak inhibitory effects on the non-neoplastic cells. Particularly, the  $IC_{50}$  values of **Z-3** and **Z-6** on all of the tested cancer cell lines were smaller than those of galaxamide. Furthermore, we described the effects as well as the antitumor mechanisms of **Z-3**, **Z-6**, and galaxamide as they induced apoptosis of MCF-7 cells.

## 2. Results and Discussion

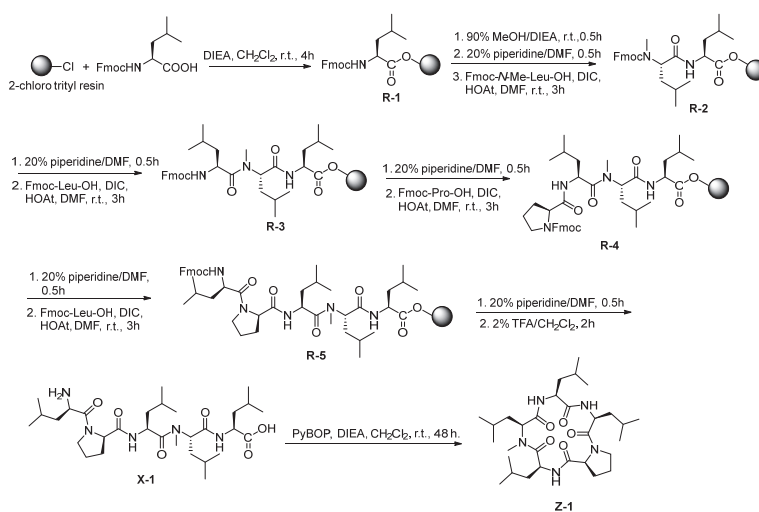
### 2.1. Chemistry

On the basis of galaxamide, eight new galaxamide derivatives were designed and synthesized by replacing one or two *N*-Me-*L*-leucine with *L*-proline or changing the stereo configuration of leucine from *L* to *D* (Figures 1 and 2).

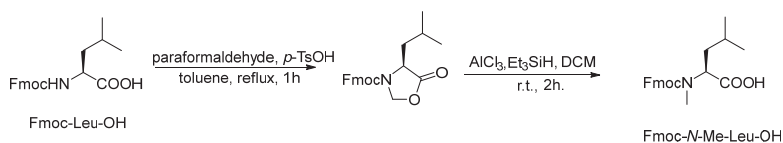


**Figure 2.** The structures of Z-1~Z-8.

First, the linear pentapeptide was synthesized by using Fmoc peptide synthetic strategy with 2-chloro trityl resin. [17] Furthermore, the cyclic peptide was compounded by liquid-phase cyclization. The cyclization site of the linear pentapeptide was selected between two consecutive leucines. The detailed schematic illustration of the synthetic route was shown in Scheme 1 (taking Z-1 as an example). Among them, Fmoc-N-Me-Leu-OH was synthesized by the oxazolidinone intermediate method (Scheme 2). [18]



**Scheme 1.** Synthesis scheme of Z-1.



**Scheme 2.** Synthesis scheme of Fmoc-N-Me-Leu-OH.

## 2.2. Biological Activity

### 2.2.1. Inhibitory Activities of Galaxamide and Its Analogues

The cytotoxicity of the synthesized compounds against five different human cancer cell lines (MCF-7, MD-MBA-231, HepG2, HeLa and A549) and one type of normal human cell line (HUVEC) was investigated by MTT assay, the  $IC_{50}$  values of which are shown in Table 1. The results indicated that **Z-3** and **Z-6** exhibited stronger cytotoxic activities against each cell line than galaxamide, but that they showed weaker inhibitory effects on HUVEC. Particularly, **Z-6** had the strongest inhibition rate.

**Table 1.** The inhibitory effects of galaxamide and its analogues against several cell lines.

| Compd.     | $IC_{50}$ ( $\mu\text{g/mL}$ ) |                  |                  |                  |                  |                  |
|------------|--------------------------------|------------------|------------------|------------------|------------------|------------------|
|            | MCF-7                          | HepG2            | MD-MBA-231       | HeLa             | A549             | HUVEC            |
| galaxamide | 11.33 $\pm$ 2.95               | 5.20 $\pm$ 0.52  | 8.73 $\pm$ 0.29  | 8.53 $\pm$ 0.73  | 6.99 $\pm$ 0.63  | >40              |
| <b>Z-1</b> | 5.85 $\pm$ 1.28                | 7.57 $\pm$ 0.17  | 17.81 $\pm$ 0.60 | 11.56 $\pm$ 0.65 | 4.92 $\pm$ 0.84  | >40              |
| <b>Z-2</b> | 4.68 $\pm$ 1.22                | 11.95 $\pm$ 0.64 | 14.45 $\pm$ 1.10 | 14.50 $\pm$ 0.36 | 7.97 $\pm$ 2.06  | >40              |
| <b>Z-3</b> | 2.25 $\pm$ 0.42                | 5.05 $\pm$ 0.45  | 6.34 $\pm$ 0.60  | 5.57 $\pm$ 0.45  | 6.43 $\pm$ 0.43  | >40              |
| <b>Z-4</b> | 4.88 $\pm$ 0.58                | 15.23 $\pm$ 1.14 | 22.09 $\pm$ 1.12 | 7.38 $\pm$ 0.83  | 9.85 $\pm$ 0.95  | >40              |
| <b>Z-5</b> | 13.43 $\pm$ 1.96               | 14.98 $\pm$ 0.93 | 8.48 $\pm$ 1.12  | 12.12 $\pm$ 0.95 | 9.50 $\pm$ 1.13  | >40              |
| <b>Z-6</b> | 1.65 $\pm$ 0.30                | 2.91 $\pm$ 0.17  | 4.59 $\pm$ 0.27  | 5.69 $\pm$ 0.37  | 5.96 $\pm$ 0.41  | 38.72 $\pm$ 0.67 |
| <b>Z-7</b> | 13.28 $\pm$ 3.28               | 13.85 $\pm$ 1.99 | 16.52 $\pm$ 1.70 | 18.21 $\pm$ 1.35 | 9.97 $\pm$ 1.00  | >40              |
| <b>Z-8</b> | 7.82 $\pm$ 1.18                | 9.00 $\pm$ 0.83  | 20.16 $\pm$ 2.24 | 7.97 $\pm$ 0.61  | 15.88 $\pm$ 1.42 | >40              |

### 2.2.2. Effects of Analogues on the Cell Cycle of MCF-7

Compounds **Z-3** and **Z-6** exhibited better inhibition effects on the growth of all cancer cell lines than the others, especially on that of MCF-7. Therefore, propidium iodide (PI) staining method was used to further investigate the changes in the cell cycle distribution of MCF-7. In particular, MCF-7 cells were exposed to galaxamide, **Z-3**, and **Z-6** with concentrations of 0, 2.5, 5, and 10  $\mu\text{g/mL}$  for 72 h. Generally, the main effects of galaxamide, **Z-3**, and **Z-6** on MCF-7 cells were in the G<sub>0</sub>/G<sub>1</sub> phase. There was no obvious sub diploid peak in flow cytometry. However, as the concentration increased, the number of cells in the G<sub>0</sub>/G<sub>1</sub> phase also gradually increased. Hence, the effects of galaxamide, **Z-3**, and **Z-6** on MCF-7 cells mainly blocked the growth of cells in the G<sub>0</sub>/G<sub>1</sub> phase (Figure 3).

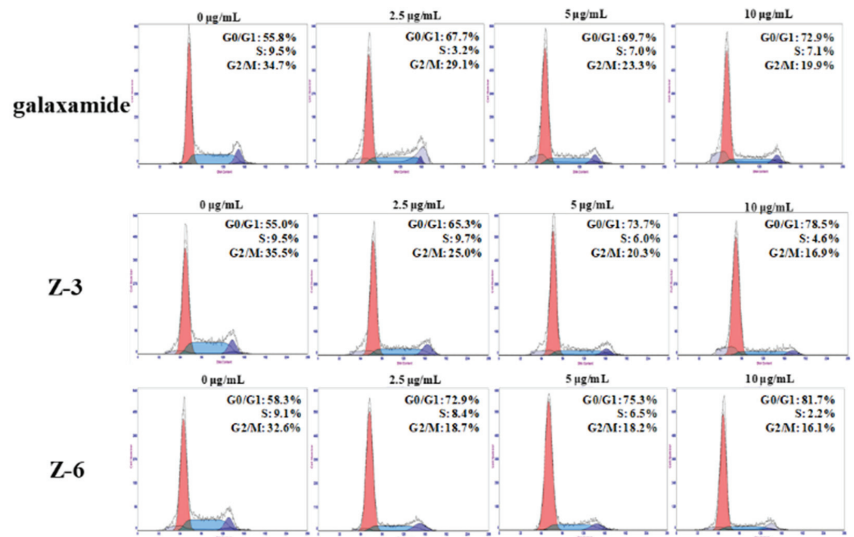


Figure 3. Cell cycle phase in MCF-7 induced by galaxamide, Z-3, and Z-6 when exposed for 72 h.

### 2.2.3. Apoptotic Mechanism Study of Galaxamide and Its Analogues

The Annexin V-FITC/PI double staining method was used to analyze the changes in the apoptosis of MCF-7 cells after 72 h of galaxamide, Z-3, and Z-6 exposure. The results showed that the apoptosis rate of MCF-7 increased with the increasing of the concentration after 72 h of incubation. At low concentrations, the effects of all the tested compounds were not obvious. When the concentration reached 10 µg/mL, the apoptotic effects of galaxamide, Z-3, and Z-6 on MCF-7 cells were more obvious in the late apoptotic state. Particularly, the apoptotic effects of Z-3 and Z-6 on MCF-7 cells were significantly higher than those of galaxamide (Figure 4).

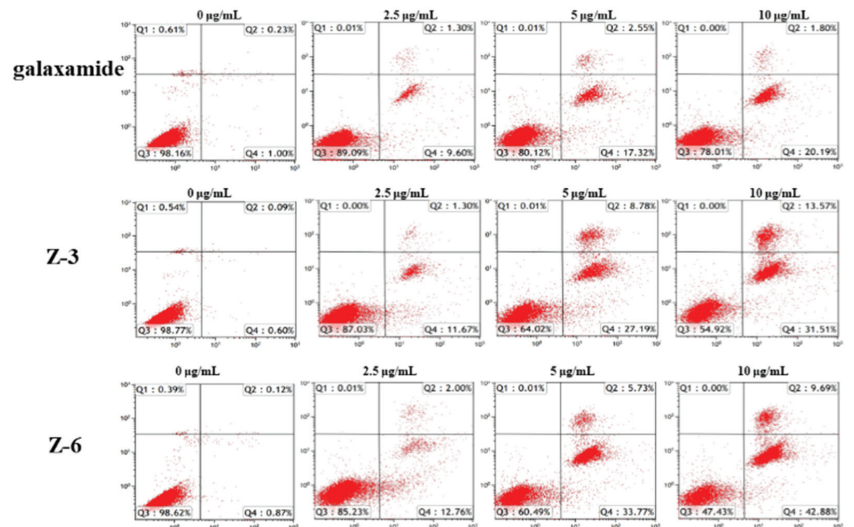
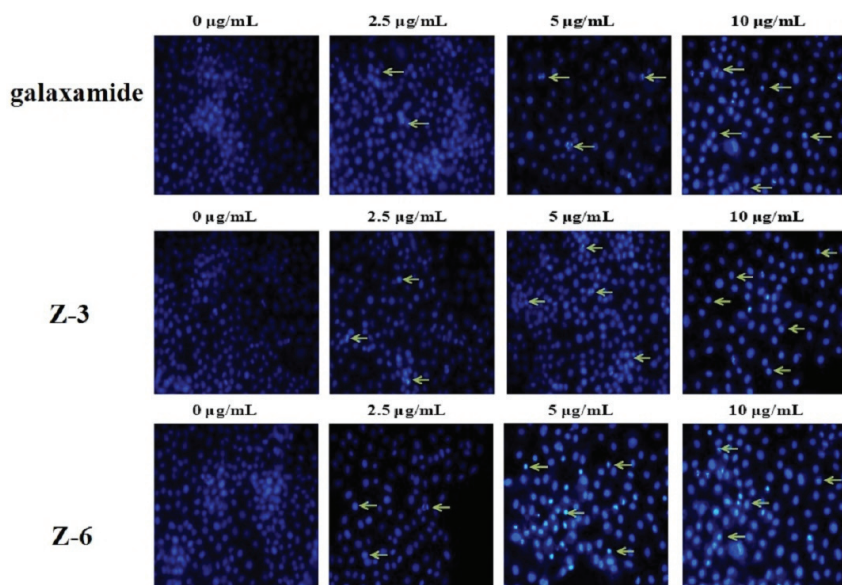


Figure 4. Monomers used in the synthesis of galaxamide analogues.

#### 2.2.4. Effects of Galaxamide and Its Analogues on Cell Nuclear Integrity

The morphological alteration of MCF-7 cells was analyzed by the method of Hoechst 33,342 staining (Figure 5). After the MCF-7 cell line was treated with galaxamide, Z-3, and Z-6 for 72 h, the morphology of the nuclei was significantly changed. The pyknotic nuclei increased with the increasing concentration of these compounds. At the same time, karyorrhexis and karyolysis were observed, indicating that these compounds could cause obvious cell apoptosis.



**Figure 5.** Morphological observation of galaxamide and its analogues inducing apoptosis in MCF-7 cells as indicated by Hoechst 33,342 staining.

### 3. Materials and Methods

#### 3.1. General

NMR spectra were measured on a Bruker Avance 300 spectrometer (Bruker, Billerica, MA, USA) in  $\text{CDCl}_3$ . Chemical shifts are reported as  $\delta$  values in parts per million (ppm) relative to tetramethyl silane (TMS) and  $J$  values are expressed in Hertz. The ESI mass spectra were obtained on a LCQ DECA XP LC-MS mass spectrometer. Silica gel (200–300 mesh) for column chromatography and silica GF254 for TLC were produced by the Qingdao Marine Chemical Company (Qingdao, China). All reactions avoiding water and air were carried out under nitrogen atmosphere conditions. The starting materials and reagents used in reactions were obtained commercially from Acros, Aldrich, and GL Biochem, and used without purification, unless otherwise indicated.

#### 3.2. Compounds

##### 3.2.1. Synthesis of Fmoc-N-Me-Leu-OH

A solution of Fmoc-Leu-OH (7.07 g, 2 mmol), paraformaldehyde (4.00 g), and *p*-toluenesulphonic acid (0.20 g, catalytic amount) in toluene (100 mL) were suspended in a 250 mL three neck RBF. The mixture was stirred and refluxed for 30 min in a Dean-Stark setup and monitored by TLC. Following this, the solution was allowed to be cooled and poured into saturated aqueous  $\text{NaHCO}_3$ . The organic layer was dried over anhydrous sodium sulfate and concentrated, the residue was purified by column chromatography on

silica gel (eluant ratio of  $V_{\text{petroleum ether}}/V_{\text{ethylacetate}} = 8:1$ ) to obtain 7.15 g of white powder with a yield of 97.9%.

Then, the white powder (7.00 g, 2 mmol),  $\text{AlCl}_3$  (4.00 g, 3 mmol), triethylsilane (5 mL), and dry DCM (150 mL) solution were added to a 250 mL round-bottom flask. The reaction was stirred at ambient temperature until the TLC showed an absence of the starting material. The organic phase was washed with 1M HCl. Subsequently, the organic layer was dried and filtered concentrated with anhydrous sodium sulfate. It was then dried once more under a vacuum and purified using silica-gel column chromatography (eluant ratio of  $V_{\text{petroleum ether}}/V_{\text{ethyl acetate}} = 8:1$ ). Finally, 6.54 g of white powder was obtained with a yield of 92.7%.  $^1\text{H NMR}$  (300 MHz,  $\text{DMSO-}d_6$ ),  $\delta_{\text{H}}$ : 12.77 (s, 1H), 7.90 (t,  $J = 7.5$  Hz, 2H), 7.65 (td,  $J = 7.8, 3.8$  Hz, 2H), 7.49–7.38 (m, 2H), 7.38–7.28 (m, 2H), 4.69–4.45 (m, 1H), 4.46–4.13 (m, 3H), 2.72 (s, 3H), 1.80–1.43 (m, 2H), 1.37 (d,  $J = 12.2$  Hz, 1H), 1.00–0.60 (m, 6H); ESI-MS  $m/z$ : 368.2  $[\text{M} + \text{H}]^+$ , 385.1  $[\text{M} + \text{NH}_4]^+$ , 390.1  $[\text{M} + \text{Na}]^+$ .

### 3.2.2. Synthesis of Linear Pentapeptide HO-Leu-N-Me-Leu-Leu-Pro-Leu-H (X-1)

Synthesis of Fmoc-Leu-Resin (**R-1**). The linear peptide was synthesized by using 2-chlorotriptyl chloride (CTC) resin following the standard Fmoc strategy. Firstly, using 15 mL of dichloromethane dissolved Fmoc-Leu-OH (1.06 g, 3 mmol), and then adding 0.5 mL of DIEA. Then, the liquid was added to the peptide synthesis tube containing the CTC resin (1.00 g, load: 0.985 mmol/g). The reaction tube was placed on a shaker at room temperature for reaction 4 h. After the reaction, the resin was washed with DCM ( $3 \times 5$  mL), DMF ( $3 \times 5$  mL), and MeOH ( $3 \times 5$  mL). After filtration, the remaining unreacted sites of the resin were capped with a solution of DCM/MeOH/DIEA (4:5:1, 10 mL) for 30 min. Deprotection of Fmoc group was carried out using 20% piperidine in DMF for ( $2 \times 10$  min) at room temperature.

Synthesis of Fmoc-N-Me-Leu-Leu-Resin (**R-2**). Fmoc-N-Me-Leu-OH (1.10 g, 3 mmol), HOAt (0.41 g, 3 mmol), and DIC (0.47 mL, 3 mmol) were dissolved in 15 mL of DMF and reacted at room temperature for 5 min. Following this, the reaction solution was added to the peptide synthesis tube which contained the previously synthesized **R-1**, and was placed on a shaker to react for 3 h at room temperature. After filtration, the resin was washed with DCM ( $3 \times 5$  mL), DMF ( $3 \times 5$  mL), and MeOH ( $3 \times 5$  mL). The reaction was monitored using the Kaiser test for the primary amine and the chloranil test for the secondary amine.

Synthesis of Fmoc-Leu-N-Me-Leu-Leu-Resin (**R-3**). After deprotection of the Fmoc group, the method of synthesizing **R-3** was the same as that of **R-2**. Finally, the Fmoc-Leu-OH was connected to **R-2** to synthesize **R-3**.

Synthesis of Fmoc-Pro-Leu-N-Me-Leu-Leu-Resin (**R-4**). After deprotection of the Fmoc group, the method of synthesizing **R-4** was the same as that of **R-2**. Finally, the Fmoc-Pro-OH was connected to **R-3** to synthesize **R-4**.

Synthesis of Fmoc-Leu-Pro-Leu-N-Me-Leu-Leu-Resin (**R-5**). After deprotection of the Fmoc group, the method of synthesizing **R-5** was the same as that of **R-2**. Finally, the Fmoc-Leu-OH was connected to **R-4** to synthesize **R-5**.

Cleavage of resin peptides. Cleavage was performed using 1% TFA in DCM for ( $2 \times 30$  min) at rt. After cleavage, the filtrate was immediately neutralized with 1% pyridine in MeOH and concentrated under reduced pressure. The crude peptide was isolated via precipitation from diethyl ether (20 mL) and collected through centrifuge as a white solid, which can be directly used for a macrocyclization reaction without further purification.

### 3.2.3. Synthesis of Linear Pentapeptide HO-Leu-Pro-Leu-Pro-Leu-H (X-2)

The method of synthesizing **X-2** was the same as that of **X-1**.

### 3.2.4. Synthesis of Linear Pentapeptide HO-D-Leu-Pro-Leu-Pro-Leu-H (X-3)

The method of synthesizing **X-3** was the same as that of **X-1**.

### 3.2.5. Synthesis of Linear Pentapeptide HO-Leu-Pro-Leu-Pro-D-Leu-H (**X-4**)

The method of synthesizing **X-4** was the same as that of **X-1**.

### 3.2.6. Synthesis of Linear Pentapeptide HO-Leu-Pro-D-Leu-Pro-Leu-H (**X-5**)

The method of synthesizing **X-5** was the same as that of **X-1**.

### 3.2.7. Synthesis of Linear Pentapeptide HO-D-Leu-Pro-Leu-Pro-D-Leu-H (**X-6**)

The method of synthesizing **X-6** was the same as that of **X-1**.

### 3.2.8. Synthesis of Linear Pentapeptide HO-Leu-Pro-D-Leu-Pro-D-Leu-H (**X-7**)

The method of synthesizing **X-7** was the same as that of **X-1**.

### 3.2.9. Synthesis of Linear Pentapeptide HO-D-Leu-Pro-D-Leu-Pro-D-Leu-H (**X-8**)

The method of synthesizing **X-8** was the same as that of **X-1**.

### 3.2.10. Synthesis of Cyclo (Leu-N-Me-Leu-Leu-Pro-Leu) (**Z-1**)

Firstly, **X-1** (0.10 g, 0.15 mmol) and PyBOP (0.27 g, 0.52 mmol) were dissolved in dichloromethane (400 mL) using a 500-mL round-bottom flask. Subsequently, this mixture reacted at room temperature for 48 h with the addition of DIEA to adjust the pH around 7–8. After that, saturated NaHCO<sub>3</sub> and H<sub>2</sub>O were used to wash this reaction solution separately. The resultant organic phase was dried with anhydrous Na<sub>2</sub>SO<sub>4</sub> and concentrated. Then, the obtained solid was purified by RP-HPLC (Agilent Eclipse ZORBAX SB-C18, 5 μm, 9.4 × 250 nm) to obtain 39.4 mg of white powder with a yield of 40.7%. <sup>1</sup>H NMR (300 MHz, Chloroform-*d*), δ<sub>H</sub> 7.16 (d, *J* = 8.8 Hz, 1H), 6.81 (d, *J* = 8.2 Hz, 1H), 6.67 (d, *J* = 7.6 Hz, 1H), 4.85 (td, *J* = 8.5, 5.1 Hz, 1H), 4.55–4.45 (m, 1H), 4.34 (dd, *J* = 7.2, 3.5 Hz, 1H), 4.25 (td, *J* = 10.0, 4.0 Hz, 1H), 3.76 (dd, *J* = 11.7, 8.9 Hz, 1H), 3.61–3.45 (m, 4H), 3.27 (s, 3H), 2.06–1.37 (m, 14H), 0.85–1.05 (m, 24H); <sup>13</sup>C NMR (75 MHz, Chloroform-*d*), δ<sub>C</sub> 174.2, 172.6, 172.5, 171.7, 171.0, 77.2, 69.0, 61.2, 54.1, 50.8, 48.8, 47.9, 42.0, 41.5, 39.5, 38.2, 37.7, 32.3, 25.8, 25.1, 25.0, 24.7, 24.4, 23.5, 23.3, 23.2, 23.0, 22.0 (2C), 21.5; HR-ESI-MS *m/z*: 564.4 [M + H]<sup>+</sup>, 580.7 [M + NH<sub>4</sub>]<sup>+</sup>, 586.6 [M + Na]<sup>+</sup>.

### 3.2.11. Synthesis of Cyclo (Leu-Pro-Leu-Pro-Leu) (**Z-2**)

The method of synthesizing **Z-2** was followed as per that described for **Z-1**. Finally, 34.3 mg of white powder with a yield of 35.5% were obtained. <sup>1</sup>H NMR (300 MHz, Chloroform-*d*), δ<sub>H</sub> 7.44–7.33 (m, 2H), 7.17 (d, *J* = 8.1 Hz, 1H), 4.80 (ddd, *J* = 22.2, 11.0, 6.4 Hz, 1H), 4.63 (dd, *J* = 11.7, 7.3 Hz, 2H), 4.29 (t, *J* = 9.3 Hz, 1H), 3.72 (dd, *J* = 14.8, 7.8 Hz, 1H), 3.56 (dd, *J* = 10.5, 5.7 Hz, 2H), 2.48–1.37 (m, 19H), 1.13–0.79 (m, 18H); <sup>13</sup>C NMR (75 MHz, Chloroform-*d*), δ<sub>C</sub> 173.4, 172.6, 171.9, 171.0, 170.8, 61.0, 60.4, 53.2, 49.2, 48.8, 47.7, 47.2, 42.4, 42.3, 40.7, 27.4, 25.2, 25.1, 25.0 (2C), 24.9, 23.5, 23.3 (2C), 22.1, 21.9, 21.3, 21.1; HR-ESI-MS *m/z*: 534.4 [M + H]<sup>+</sup>, 550.7 [M + NH<sub>4</sub>]<sup>+</sup>, 556.8 [M + Na]<sup>+</sup>.

### 3.2.12. Synthesis of Cyclo (Leu-Pro-Leu-Pro-Leu) (**Z-3**)

The method of synthesizing **Z-3** was followed as per described for **Z-1**. Finally, 52.1 mg of white powder with a yield of 53.9% were obtained. <sup>1</sup>H NMR (300 MHz, Chloroform-*d*), δ<sub>H</sub> 7.62 (d, *J* = 8.7 Hz, 1H), 7.47 (d, *J* = 8.4 Hz, 1H), 6.87 (d, *J* = 9.0 Hz, 1H), 4.80 (t, *J* = 7.7 Hz, 2H), 4.69 (d, *J* = 7.8 Hz, 1H), 4.51 (td, *J* = 10.0, 4.1 Hz, 1H), 4.25 (t, *J* = 6.6 Hz, 1H), 3.89–3.51 (m, 4H), 2.39 (t, *J* = 8.8 Hz, 1H), 2.29–1.82 (m, 8H), 1.78–1.36 (m, 8H), 0.93 (d, *J* = 6.6 Hz, 18H); <sup>13</sup>C NMR (75 MHz, Chloroform-*d*), δ<sub>C</sub> 172.6, 172.0, 171.9, 171.9, 171.0, 61.0, 59.9, 51.5, 49.3, 49.1, 47.6, 47.4, 41.0, 40.9, 40.4, 29.2, 27.0, 25.3, 25.1, 25.0, 24.7, 24.6, 23.5, 23.1, 23.0, 22.4, 21.7, 21.4; HR-ESI-MS *m/z*: 534.7 [M + H]<sup>+</sup>, 550.7 [M + NH<sub>4</sub>]<sup>+</sup>, 556.8 [M + Na]<sup>+</sup>.

### 3.2.13. Synthesis of Cyclo (Leu-Pro-D-Leu-Pro-Leu) (**Z-4**)

The method of synthesizing **Z-4** was followed as per that described for **Z-1**. Finally, 35.2 mg of white powder with a yield of 36.4% were obtained. <sup>1</sup>H NMR (300 MHz,

Chloroform-*d*),  $\delta_{\text{H}}$  8.07 (d,  $J = 8.0$  Hz, 1H), 7.16 (d,  $J = 9.1$  Hz, 1H), 6.57 (d,  $J = 8.8$  Hz, 1H), 4.86 (d,  $J = 7.6$  Hz, 1H), 4.79 (t,  $J = 7.9$  Hz, 1H), 4.72–4.60 (m, 1H), 4.51 (td,  $J = 9.1$ , 5.0 Hz, 1H), 4.37 (dd,  $J = 8.5$ , 3.9 Hz, 1H), 3.98 (dt,  $J = 11.1$ , 6.0 Hz, 1H), 3.61 (td,  $J = 9.3$ , 4.1 Hz, 1H), 3.56–3.42 (m, 2H), 2.29 (qt,  $J = 9.2$ , 4.6 Hz, 2H), 2.16 (dt,  $J = 15.5$ , 8.0 Hz, 1H), 2.10–1.84 (m, 6H), 1.81–1.43 (m, 7H), 1.32 (dt,  $J = 12.0$ , 6.7 Hz, 1H), 1.05–0.83 (m, 18H);  $^{13}\text{C}$  NMR (75 MHz, Chloroform-*d*),  $\delta_{\text{C}}$  172.9, 172.2, 171.4, 171.3, 171.0, 77.3, 62.0, 58.7, 51.5, 50.3, 49.5, 47.3, 40.2, 40.0, 39.7, 29.7, 25.8, 25.2, 24.9 (2C), 24.7 (2C), 23.3, 23.2, 22.8, 22.5, 21.6, 21.5; HR-ESI-MS  $m/z$ : 534.4 [M + H]<sup>+</sup>, 550.7 [M + NH<sub>4</sub>]<sup>+</sup>, 556.8 [M + Na]<sup>+</sup>.

### 3.2.14. Synthesis of Cyclo (Leu-Pro-Leu-Pro-D-Leu) (Z-5)

The method of synthesizing **Z-5** was followed as per that described for **Z-1**. Finally, 57.0 mg of white powder with a yield of 58.9% were obtained.  $^1\text{H}$  NMR (300 MHz, Chloroform-*d*),  $\delta_{\text{H}}$  8.62 (d,  $J = 9.0$  Hz, 1H), 7.12 (d,  $J = 8.7$  Hz, 1H), 6.93 (d,  $J = 6.7$  Hz, 1H), 4.77 (q,  $J = 7.9$  Hz, 1H), 4.66–4.50 (m, 3H), 4.40 (dt,  $J = 8.6$ , 6.1 Hz, 1H), 4.28–4.02 (m, 2H), 3.68 (td,  $J = 9.2$ , 3.9 Hz, 1H), 3.47 (td,  $J = 9.5$ , 6.7 Hz, 1H), 2.41–2.17 (m, 1H), 2.17–1.81 (m, 8H), 1.81–1.50 (m, 6H), 1.51–1.35 (m, 2H), 1.02–0.84 (m, 18H);  $^{13}\text{C}$  NMR (75 MHz, Chloroform-*d*),  $\delta_{\text{C}}$  174.0, 172.7, 171.7, 171.0, 170.9, 60.6, 59.2, 50.8, 49.9, 48.9, 47.5, 46.8, 41.3, 39.5, 37.8, 29.9, 28.1, 25.1, 24.8 (3C), 24.0, 23.3, 23.0 (2C), 22.5, 22.4, 22.0; HR-ESI-MS  $m/z$ : 534.4 [M + H]<sup>+</sup>, 550.7 [M + NH<sub>4</sub>]<sup>+</sup>, 556.8 [M + Na]<sup>+</sup>.

### 3.2.15. Synthesis of Cyclo (D-Leu-Pro-Leu-Pro-D-Leu) (Z-6)

The method of synthesizing **Z-6** was followed as per that described for **Z-1**. Finally, 33.4 mg of white powder with a yield of 34.5% were obtained.  $^1\text{H}$  NMR (300 MHz, Chloroform-*d*),  $\delta_{\text{H}}$  8.00 (d,  $J = 7.3$  Hz, 1H), 7.59 (d,  $J = 6.8$  Hz, 1H), 7.27 (d,  $J = 9.2$  Hz, 1H), 4.77 (td,  $J = 9.5$ , 4.2 Hz, 1H), 4.64 (d,  $J = 7.6$  Hz, 1H), 4.55 (d,  $J = 7.5$  Hz, 2H), 4.24–4.12 (m, 1H), 4.07 (dt,  $J = 11.5$ , 6.3 Hz, 1H), 3.91 (q,  $J = 8.5$  Hz, 1H), 3.63–3.41 (m, 2H), 2.48–1.29 (m, 18H), 1.11–0.76 (m, 18H);  $^{13}\text{C}$  NMR (75 MHz, Chloroform-*d*),  $\delta_{\text{C}}$  174.4, 172.4, 172.1, 171.8, 171.3, 60.8, 59.8, 55.8, 50.2, 49.1, 47.4, 47.0, 41.0, 39.8, 39.1, 29.7, 26.7, 25.2, 25.1, 24.9, 24.8, 24.3, 23.3, 23.2, 23.0, 22.0, 21.7 (2C); HR-ESI-MS  $m/z$ : 534.4 [M + H]<sup>+</sup>, 550.7 [M + NH<sub>4</sub>]<sup>+</sup>, 556.8 [M + Na]<sup>+</sup>.

### 3.2.16. Synthesis of Cyclo (Leu-Pro-D-Leu-Pro-D-Leu) (Z-7)

The method of synthesizing **Z-7** was followed as per that described for **Z-1**. Finally, 52.8 mg of white powder with a yield of 54.6% were obtained.  $^1\text{H}$  NMR (300 MHz, Chloroform-*d*),  $\delta_{\text{H}}$  8.03 (d,  $J = 8.3$  Hz, 1H), 7.17 (d,  $J = 9.0$  Hz, 1H), 6.60 (d,  $J = 8.8$  Hz, 1H), 4.79–4.86 (m, 1H), 4.74 (d,  $J = 7.9$  Hz, 1H), 4.69–4.60 (m, 1H), 4.46 (td,  $J = 9.3$ , 4.7 Hz, 1H), 4.31 (dd,  $J = 9.0$ , 3.9 Hz, 1H), 3.97 (dd,  $J = 10.1$ , 5.4 Hz, 1H), 3.40–3.62 (m, 3H), 2.39–2.18 (m, 2H), 2.18–2.08 (m, 1H), 2.08–1.79 (m, 6H), 1.75–1.42 (m, 7H), 1.29 (ddd,  $J = 13.6$ , 9.7, 3.8 Hz, 1H), 1.03–0.81 (m, 18H);  $^{13}\text{C}$  NMR (75 MHz, Chloroform-*d*),  $\delta_{\text{C}}$  172.6, 172.3, 171.4, 171.3, 171.2, 62.0, 58.6, 51.5, 50.1, 49.5, 47.2, 46.4, 40.3, 40.0, 39.7, 29.6, 25.6, 25.2, 25.0, 24.9, 24.7, 24.7, 23.3, 23.2, 22.8, 22.5, 21.6, 21.5; HR-ESI-MS  $m/z$ : 534.4 [M + H]<sup>+</sup>, 550.7 [M + NH<sub>4</sub>]<sup>+</sup>, 556.8 [M + Na]<sup>+</sup>.

### 3.2.17. Synthesis of Cyclo (D-Leu-Pro-D-Leu-Pro-D-Leu) (Z-8)

The method of synthesizing **Z-8** was followed as per that described for **Z-1**. Finally, 44.7 mg of white powder with a yield of 46.2% were obtained.  $^1\text{H}$  NMR (300 MHz, Chloroform-*d*),  $\delta_{\text{H}}$  7.94 (d,  $J = 8.4$  Hz, 1H), 7.17 (d,  $J = 9.1$  Hz, 1H), 6.53 (d,  $J = 8.8$  Hz, 1H), 4.85 (d,  $J = 7.5$  Hz, 1H), 4.78 (d,  $J = 8.1$  Hz, 1H), 4.68 (d,  $J = 8.3$  Hz, 1H), 4.50 (td,  $J = 9.4$ , 4.6 Hz, 1H), 4.34 (dd,  $J = 8.8$ , 4.0 Hz, 1H), 3.97 (dt,  $J = 11.9$ , 6.2 Hz, 1H), 3.60–3.43 (m, 3H), 2.31 (td,  $J = 12.9$ , 5.2 Hz, 2H), 2.16 (dt,  $J = 11.8$ , 8.1 Hz, 1H), 2.11–1.82 (m, 6H), 1.80–1.42 (m, 7H), 1.32 (ddd,  $J = 13.6$ , 9.8, 3.8 Hz, 1H), 1.25–0.85 (m, 18H);  $^{13}\text{C}$  NMR (75 MHz, Chloroform-*d*),  $\delta_{\text{C}}$  172.7, 172.1, 171.4, 171.3, 171.1, 62.0, 58.5, 51.4, 50.1, 49.5, 47.3, 46.5, 40.4, 40.0, 39.8, 29.7, 25.4, 25.2, 25.0, 24.9, 24.7, 24.7, 23.3, 23.2, 22.8, 22.5, 21.5 (2C); HR-ESI-MS  $m/z$ : 534.4 [M + H]<sup>+</sup>, 550.7 [M + NH<sub>4</sub>]<sup>+</sup>, 556.8 [M + Na]<sup>+</sup>.



### 3.3. *In Vitro* Cytotoxic Assays

Cell culture: MCF-7/MD-MAB-231 (human breast cancer cell line ATCC HTB-22/HTB-26), Hep G2 (human liver cancer cell line ATCC HB-8065), Hela (human cervical carcinoma cell line ATCC CCL-2), A459 (human lung cancer cell line ATCC CCL-185), and HUVEC (primary umbilical vein endothelial cell line ATCC PCS-100-010) were obtained from the Jinan Department of Pathology, University School of Medicine (Jinan University, Guangzhou, China). The cells were cultured in a Modified Eagle's Medium (DMEM) including 10% fetal bovine serum, 1% penicillin-streptomycin, and antifungal agent, and cultured under standard conditions (5% CO<sub>2</sub> atmosphere and temperature at 37 °C).

### 3.4. MTT Assay

The MTT method was used to evaluate the cytotoxicities of galaxamide and its analogues on the five cancerous cells. In this experiment, the number of regulated cells was  $2 \times 10^3$  cells/well. Then, the cells, as well as galaxamide and its analogues of different concentrations (0, 2.5, 5, and 10 µg/mL), were seeded on a 96-well cell culture plate and cultured in a 37 °C, 5% CO<sub>2</sub> incubator for 72 h. After that, 20 µL/well of MTT solution (5 mg/mL phosphate-buffered saline) was added and incubated for 5 h. The medium was discarded and replaced with 100 µL/well of DMSO to dissolve the formazan salt. The color intensity of the cell culture at 570 nm was measured using a microplate spectrophotometer (SpectroAma™ 250, Winooski, VT, USA).

### 3.5. Flow Cytometry Experiments

The concentration of  $1 \times 10^4$  cells per well of MCF-7 cells were seeded in 96-well plates. The cell cultures were added to the compounds with a concentration of 0, 2.5, 5, and 10 µg/mL, and incubated for 72 h. After that, 5 µL of Annexin V-fluorescein isothiocyanate (FITC) and 5 µL of PI were added for dual staining of the cells for analysis by FACS flow cytometry. Cell cycles and apoptotic cells were determined by counting the FITC-positive and PI-negative fractions.

### 3.6. Cell Apoptotic Analysis

The apoptotic cells were quantified according to the instructions provided in an Annexin V-FITC (Sigma-Aldrich, St. Louis, MO, USA) cell apoptosis assay kit. Briefly, about  $1.5 \times 10^5$  cells were plated in 96-well plates and treated with galaxamide and its representative analogues (0, 2.5, 5, and 10 µg/mL) for 48 h. The cells were then resuspended in a 200-mL binding buffer. Afterward, 5 mL of annexin V-fluorescein isothiocyanate (FITC) was added, followed by incubation in darkness at room temperature for 10 min. The cells were again resuspended in 200 mL binding buffer and stained with 5 mL PI. The prepared cells were then analyzed using a flow cytometry (Coulter Epics Elite, Miami, FL, USA). The cells in the FITC-positive and PI-negative fractions were regarded as apoptotic cells.

### 3.7. Hoechst 33,342 Staining

Test compounds at 0, 2.5, 5, and 10 µg/mL were added to the cell cultures which included the exponentially growing MCF-7 cells ( $1 \times 10^5$ ), and incubated for 48 h. After that, the cell culture was washed with 1 mL of PBS and then added with 3 mL of 4% paraformaldehyde solution for 15 min. Then, 1 mL of the prepared Hoechst 33,342 staining solution was added. The resulting mixture was incubated at room temperature for 15 min in the dark. Ultimately, cell staining was observed with a fluorescence microscope.

## 4. Conclusions

In this paper, eight new cyclic pentapeptides (**Z-1~Z-8**) were synthesized, and were designed by replacing one or two *N*-Me-*L*-leucine with *L*-proline or changing the stereo configuration of leucine. The anticancer activities of these new compounds were also tested against five human cancer cell lines. The results showed that the inhibitory effects of most analogues were much better than that of galaxamide. Moreover, all tested compounds

exhibited low cytotoxic activity against the normal liver cell line HUVEC. Compound **Z-6** displayed the strongest inhibitory effects against HepG2, MCF-7, and MD-MAB-231 cells with IC<sub>50</sub> values of  $2.91 \pm 0.17$ ,  $1.65 \pm 0.30$ ,  $4.59 \pm 0.27$  µg/mL, respectively. These galaxamide analogues arrested the cell cycle in the G0/G1 phase and induced apoptosis, which was later confirmed by the representative compounds **Z-3** and **Z-6**. In our preliminary work, a series of galaxamide analogues had been synthesized by replacing one of the amino acids to phenylalanine, the cytotoxic activities of which were also tested against several cancerous cell lines. [14,16] The results showed that most of these newly synthesized compounds exhibited stronger inhibitory activities against MCF-7 cells than the previous ones, which suggests that proline might be the active group of these analogues against MCF-7 cells. The structure-activity relationship needs further investigation.

**Supplementary Materials:** The following supporting information can be downloaded at: <https://www.mdpi.com/article/10.3390/md20030158/s1>, Figures S1–S24: The analyzed data of HR-ESI-MS and NMR spectra of compounds **Z-1**–**Z-8**.

**Author Contributions:** D.L. and X.L. synthesized compounds; D.L. wrote this paper; S.Z. performed biological experiments; and B.Z. and S.X. conceived and designed the experiments. All authors have read and agreed to the published version of the manuscript.

**Funding:** This research was funded by the Department of Natural Resources of the Guangdong Province (Nos. GDNRC [2020] 037 and GDNRC [2021] 48); the National Key Research and Development Plan of China (Nos. 2018YFC0310900 and 2019YFD0901905); the National Natural Science Foundation of China (Nos. 41876145, 81874292 and 21672084); and the Science and Technology Planning Project of Guangzhou (Nos. 202102010066 and 201704030042).

**Institutional Review Board Statement:** Not applicable.

**Informed Consent Statement:** Not applicable.

**Data Availability Statement:** Data are contained within the article or Supplementary Material.

**Conflicts of Interest:** The authors declare no conflict of interest.

## References

- Hamann, M.T.; Otto, C.S.; Scheuer, P.J. Bioactive peptides from a marine mollusk *elysiarufescens* and its algal diet *Bryopsis* sp. *J. Org. Chem.* **1996**, *61*, 6594–6600. [[CrossRef](#)] [[PubMed](#)]
- Pettit, G.F.; Cichacz, Z.; Barkoczy, J.; Dorsaz, A.; Herald, D.L.; Williams, M.D.; Doubek, D.L.; Schmidt, J.M.; Tackett, L.P.; Brune, D.C. Isolation and structure of the marine sponge cell growth inhibitory cyclic peptide phakellistin. *J. Nat. Prod.* **1993**, *56*, 260–267. [[CrossRef](#)] [[PubMed](#)]
- Ratnayake, A.S.; Bugni, T.S.; Feng, X.D.; Harper, M.K.; Skalicky, J.J.; Mohammed, K.A.; Andjelic, C.D.; Barrows, L.R.; Ireland, C.M. Theopapuamide, a cyclic depsipeptide from a papua new guinea lithistid sponge *Theonella swinhoei*. *J. Nat. Prod.* **2006**, *69*, 1582–1586. [[CrossRef](#)] [[PubMed](#)]
- Zampella, A.; D'Auria, M.V.; Paloma, L.G.; Casapullo, A.; Minala, L.; Debitus, C.; Henin, Y.; Callipeltin, A. An anti-HIV cyclic depsipeptide from the new caledonian lithistida sponge *Callipelta* sp. *J. Am. Chem. Soc.* **1996**, *118*, 6202–6209. [[CrossRef](#)]
- Kashinath, K.; Vasudevan, N.; Reddy, D.S. Studies toward the synthesis of potent anti-inflammatory peptides solomonamides A and B: Synthesis of a macrocyclic skeleton and key fragment 4-amino-6-(2'-amino-4'-hydroxyphenyl)-3-hydroxy-2-methyl-6-oxohexanoic acid (AHMOA). *Org. Lett.* **2012**, *14*, 6222–6225. [[CrossRef](#)] [[PubMed](#)]
- Festa, C.; De Marino, S.; Sepe, V.; Monti, M.C.; Luciano, P.; Valeria D'Auria, M.; Debitus, C.; Bucci, M.; Vellecco, V.; Zampella, A. Perthamides C and D, two new potent anti-inflammatory cyclopeptides from a solomon lithistid sponge *Theonella swinhoei*. *Tetrahedron* **2009**, *65*, 10424–10429. [[CrossRef](#)]
- Bewley, C.A.; Detritus, C.; Faulkner, D.J. Microsclerodermins A and B. antifungal cyclic peptides from the lithistid sponge *Microscleroderma* sp. *J. Am. Chem. Soc.* **1994**, *116*, 7631–7636. [[CrossRef](#)]
- Schmidt, E.W.; Faulkner, D.J. Microsclerodermins C-E, antifungal cyclic peptides from the lithistid marine sponges *Theonella* sp. and *Microscleroderma* sp. *Tetrahedron* **1998**, *54*, 3043–3056. [[CrossRef](#)]
- Qureshi, A.; Colin, P.L.; Faulkner, D.J. Microsclerodermins F-I, antitumor and antifungal cyclic peptides from the lithistid sponge *Microscleroderma* sp. *Tetrahedron* **2000**, *56*, 3679–3685. [[CrossRef](#)]
- Ahmed, M.I.; Harper, J.B.; Hunter, L. Incrementally increasing the length of a peptide backbone: Effect on macrocyclization efficiency. *Org. Biomol. Chem.* **2014**, *12*, 4598–4601. [[CrossRef](#)] [[PubMed](#)]

11. Suarez-Jimenez, G.M.; Burgos-Hernandez, A.; Ezquerro-Brauer, J.M. Bioactive peptides and depsipeptides with anticancer potential: Sources from marine animals. *Mar. Drugs* **2012**, *10*, 963–986. [[CrossRef](#)] [[PubMed](#)]
12. Fang, W.Y.; Dahiya, R.; Qin, H.L.; Mourya, R.; Maharaj, S. Natural proline-rich cyclopolypeptides from marine organisms: Chemistry, synthetic methodologies and biological status. *Mar. Drugs* **2016**, *14*, 194–216. [[CrossRef](#)] [[PubMed](#)]
13. Xu, W.J.; Liao, X.J.; Xu, S.H.; Diao, J.Z.; Du, B.; Zhou, X.L.; Pan, S.S. Isolation, structure determination, and synthesis of galaxamide, a rare cytotoxic cyclic pentapeptide from a marine algae *Galaxaura filamentosa*. *Org. Lett.* **2008**, *10*, 4569–4572. [[CrossRef](#)] [[PubMed](#)]
14. Xiao, X.; Liao, X.J.; Qiu, S.L.; Liu, Z.H.; Du, B.; Xu, S.H. Paper synthesis, cytotoxicity and apoptosis induction in human tumor cells by galaxamide and its analogues. *Mar. Drugs* **2014**, *12*, 4521–4538. [[CrossRef](#)] [[PubMed](#)]
15. Lunagariya, J.; Zhong, S.H.; Chen, J.; Bai, D.; Bhadja, P.; Long, W.; Liao, X.; Tang, X.; Xu, S. Design and synthesis of analogues of marine natural product galaxamide, an *N*-methylated cyclic pentapeptide, as potential anti-tumor agent in vitro. *Mar. Drugs* **2016**, *14*, 161–184. [[CrossRef](#)] [[PubMed](#)]
16. Bai, D.F.; Yu, S.M.; Zhong, S.H.; Zhao, B.X.; Qiu, S.L.; Chen, J.W.; Lunagariya, J.; Liao, X.J.; Xu, S.H. *D*-amino acid position influences the antiCancer activity of galaxamide analogs: An apoptotic mechanism study. *Int. J. Mol. Sci.* **2017**, *18*, 544. [[CrossRef](#)] [[PubMed](#)]
17. Redman, J.E.; Ghadiri, M.R. Synthesis of photoactive *p*-azidotetrafluorophenylalanine containing peptide by solid-phase fmoc methodology. *Org. Lett.* **2002**, *4*, 4467–4469. [[CrossRef](#)] [[PubMed](#)]
18. Zhang, S.; Govender, T.; Norstrom, T.; Arvidsson, P.I. An improved synthesis of fmoc-*N*-methyl- $\alpha$ -amino acids. *J. Org. Chem.* **2005**, *70*, 6918–6920. [[CrossRef](#)] [[PubMed](#)]

## Article

# Preparation, Identification, Molecular Docking Study and Protective Function on HUVECs of Novel ACE Inhibitory Peptides from Protein Hydrolysate of Skipjack Tuna Muscle

Shuo-Lei Zheng<sup>1</sup>, Qian-Bin Luo<sup>2</sup>, Shi-Kun Suo<sup>1</sup>, Yu-Qin Zhao<sup>1</sup>, Chang-Feng Chi<sup>2,\*</sup> and Bin Wang<sup>1,\*</sup>

<sup>1</sup> Zhejiang Provincial Engineering Technology Research Center of Marine Biomedical Products, School of Food and Pharmacy, Zhejiang Ocean University, Zhoushan 316022, China; 15757488926@139.com (S.-L.Z.); 13275896859@163.com (S.-K.S.); zhaoy@hotmail.com (Y.-Q.Z.)

<sup>2</sup> National and Provincial Joint Laboratory of Exploration and Utilization of Marine Aquatic Genetic Resources, National Engineering Research Center of Marine Facilities Aquaculture, School of Marine Science and Technology, Zhejiang Ocean University, Zhoushan 316022, China; iloveiceice@sina.com

\* Correspondence: chchangfeng@hotmail.com (C.-F.C.); wangbin@zjou.edu.cn (B.W.); Tel./Fax: +86-580-255-4818 (C.-F.C.); +86-580-255-4781 (B.W.)

**Citation:** Zheng, S.-L.; Luo, Q.-B.; Suo, S.-K.; Zhao, Y.-Q.; Chi, C.-F.; Wang, B. Preparation, Identification, Molecular Docking Study and Protective Function on HUVECs of Novel ACE Inhibitory Peptides from Protein Hydrolysate of Skipjack Tuna Muscle. *Mar. Drugs* **2022**, *20*, 176. <https://doi.org/10.3390/md20030176>

Academic Editors: Yonghong Liu and Xuefeng Zhou

Received: 2 February 2022

Accepted: 25 February 2022

Published: 27 February 2022

**Publisher's Note:** MDPI stays neutral with regard to jurisdictional claims in published maps and institutional affiliations.



**Copyright:** © 2022 by the authors. Licensee MDPI, Basel, Switzerland. This article is an open access article distributed under the terms and conditions of the Creative Commons Attribution (CC BY) license (<https://creativecommons.org/licenses/by/4.0/>).

**Abstract:** To prepare bioactive peptides with high angiotensin-I-converting enzyme (ACE)-inhibitory (ACEi) activity, Alcalase was selected from five kinds of protease for hydrolyzing Skipjack tuna (*Katsuwonus pelamis*) muscle, and its best hydrolysis conditions were optimized using single factor and response surface experiments. Then, the high ACEi protein hydrolysate (TMPH) of skipjack tuna muscle was prepared using Alcalase under the optimum conditions of enzyme dose 2.3%, enzymolysis temperature 56.2 °C, and pH 9.4, and its ACEi activity reached 72.71% at 1.0 mg/mL. Subsequently, six novel ACEi peptides were prepared from TMPH using ultrafiltration and chromatography methods and were identified as Ser-Pro (SP), Val-Asp-Arg-Tyr-Phe (VDRYF), Val-His-Gly-Val-Val (VHGVV), Tyr-Glu (YE), Phe-Glu-Met (FEM), and Phe-Trp-Arg-Val (FWRV), with molecular weights of 202.3, 698.9, 509.7, 310.4, 425.6, and 606.8 Da, respectively. SP and VDRYF displayed noticeable ACEi activity, with IC<sub>50</sub> values of 0.06 ± 0.01 and 0.28 ± 0.03 mg/mL, respectively. Molecular docking analysis illustrated that the high ACEi activity of SP and VDRYF was attributed to effective interaction with the active sites/pockets of ACE by hydrogen bonding, electrostatic force, and hydrophobic interaction. Furthermore, SP and VDRYF could significantly up-regulate nitric oxide (NO) production and down-regulate endothelin-1 (ET-1) secretion in HUVECs after 24 h treatment, but also abolish the negative effect of 0.5 μM norepinephrine (NE) on the generation of NO and ET-1. Therefore, ACEi peptides derived from skipjack tuna (*K. pelamis*) muscle, especially SP and VDRYF, are beneficial components for functional food against hypertension and cardiovascular diseases.

**Keywords:** skipjack tuna (*Katsuwonus pelamis*) muscle; angiotensin-I-converting enzyme (ACE) peptide; molecular docking; nitric oxide (NO); endothelin-1 (ET-1)

## 1. Introduction

The incidence rates of cardiovascular diseases (CVDs), including coronary artery disease, rheumatic heart disease, hypertension and stroke, have increased noticeably over the past few years and have triggered the deaths of nearly 17.9 million people [1]. These chronic diseases are interrelated and associated with atherosclerosis, which is the primary cause of CVDs [2]. Endothelial dysfunction is recognized as a vital early event for the atherosclerosis developing process, preceding gross morphological-related signs and clinical-related symptoms [3]. Physiologically, endothelial cells are located inside intima, i.e., the vasculature's inner lining and critically regulate vascular tone through the release of mediators (e.g., endothelin (ET-1) and nitric oxide (NO)) [4]. Angiotensin-I-converting enzyme (ACE) can convert angiotensin I (Ang I) to Ang II for inactivating the vasodilator

bradykinin, and ACE inhibitory (ACEi) activity is a vital method for mediating systemic hypertension [5,6]. After captopril (Cap), as the first ACE inhibitor, was recommended by the FDA in 1981, several synthesized ACE inhibitors (e.g., enalapril and lisinopril), developed based on a snake venom peptide scaffold, have been used as anti-hypertensive agents in various clinical conditions and have shown some serious side effects [7]. Therefore, searching for functional peptide molecules for controlling endothelial dysfunction and inhibiting ACE is promising for atherosclerosis therapy and decreasing CVDs' risk.

Currently, bioactive peptides have been prepared from a variety of protein resources and exhibit a variety of biological activities [8–10]. Among these peptides, ACEi peptides represent a promising alternative to synthetic drugs to control hypertension [11,12]. For instance, canary seed peptides (CSP) have great potential as anti-hypertensive and anti-obesity agents due to their inhibition activity on ACE and pancreatic lipase, and their non-competitive inhibitory activity was due to their destabilization of the transition state and Zn(II) coordination in ACE [13]. Noncompetitive ACEi peptides of TYLPVH (IC<sub>50</sub> 1.37 μM) and GRVSNCAA (IC<sub>50</sub> 57.93 μM) from *Ruditapes philippinarum* can lower systolic blood pressure in the single blood pressure test and promote NO secretion and reduced ET-1 production [14]. The ACEi peptide of KYIPIQ found in yak milk casein can promote NO synthesis and the expression of phosphorylated endothelial NO synthase (eNOS) in HUVECs by activating the protein kinase B (Akt) pathway [15]. Therefore, these results suggest that ACEi peptides derived from food protein resources have the potential to be good for human health on anti-hypertension.

Recently, many commercialization efforts have been made to produce functional food enriched with ACEi peptides. For instance, the fermentation technology of milk and soybean has been optimized to enhance the release of ACE inhibitory peptides, and the fermented products were applied to generate a type of antihypertensive function food [16]. Moreover, fermented antihypertensive milk products are available in the market, such as the Japanese brand Ameal S and Calpis (Calpis Co., Tokyo, Japan) containing IPP and VPP [17]. In addition, some lactic acid bacteria for producing ACEi peptides have been patented. For instance, *Lactobacillus helveticus* Cardi-04 (Chr. Hansen, Horsholm, Denmark) has been patented to prepare antihypertensive peptides and functional foods (WO 2003/082019 A3 and WO 2004/015125 A1). Additionally, a US patent (US 8,865,155) reported the production method of fermented milk with antihypertensive peptides using *L. lactis* (NRRL-B50571) [18]. However, limited efforts have been made to investigate the activity changes of ACEi peptides during different food processing, and further studies are required to optimize the manufacturing procedure of ACEi peptides in functional foods.

Skipjack tuna (*Katsuwonus pelamis*) is a commercially important marine product worldwide and is considered a high-protein, low-fat, and low-calorie food [19,20]. Functional molecules such as collagens/gelatin, unsaturated fatty acid, protease, and polysaccharides have been generated from skipjack tuna and its by-products and exhibit potential application prospects and various biological activities, e.g., preventing arteriosclerosis, anti-inflammatory, and anticancer, as well as lowering blood cholesterol levels [21,22]. Presently, various bioactive peptides have been found in tuna by-products, such as bone/frame [23,24], scale [25], roe [20,26], and head and viscera [27,28]. In addition, Maeda et al., reported that the dietary dark muscle protein of tuna could reduce hepatic steatosis and promote serum high-density lipoprotein cholesterol in obese Type-2 diabetic/obese KK-A (y) mice [29]. Chi et al., found that protein hydrolysate of tuna muscle showed significant antioxidant activity [30]. These results indicate that tuna muscles are high-quality protein resources for the preparation of active peptides [30]. Therefore, the objectives of the research were to optimize the preparation process of ACEi protein hydrolysate of skipjack tuna muscle, identify the prepared ACEi peptides, and evaluate the bioactivity of the prepared ACEi peptides.

## 2. Results and Discussion

### 2.1. Amino Acid Composition of Skipjack Tuna Muscle

As presented in Table 1, skipjack tuna muscles were rich in Asp, Glu, Leu, and Lys and exhibited a 41.62% weight of essential amino acids/weight of amino acids (WEAA/WTAA) and 85.99% essential amino acids/weight of non-essential amino acids (WEAA/WNEAA). After defatting, the ratios of WEAA/WTAA and WEAA/WNEAA changed to 40.94% and 83.59%, respectively. FAO/WHO suggested that amino acids composed of high-quality protein exhibited nearly 40% WEAA/WTAA, as well as over 60% WEAA/WNEAA. The presented data indicate that the ratio of WEAA/WTAA of skipjack tuna muscle was slightly higher than 40%, and the ratio of WEAA/WNEAA was significantly greater than 60%. Therefore, skipjack tuna muscle can serve as a high-quality protein resource.

**Table 1.** Amino acid composition of skipjack tuna (*Katsuwonus pelamis*) muscle (g/100g).

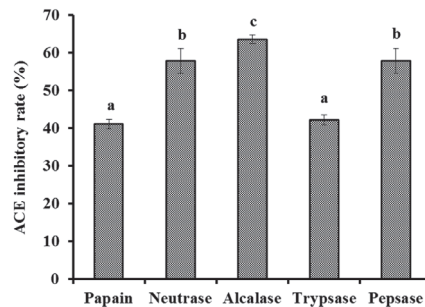
| Amino Acid        | Content (g/100g)   |                 |
|-------------------|--------------------|-----------------|
|                   | Undeffatted Muscle | Defatted Muscle |
| Asp               | 8.369              | 8.936           |
| Thr               | 4.034              | 4.316           |
| Ser               | 3.394              | 3.655           |
| Glu               | 12.843             | 13.785          |
| Pro               | 2.845              | 3.070           |
| Gly               | 3.683              | 4.128           |
| Ala               | 4.988              | 5.417           |
| Cys               | 0.443              | 0.507           |
| Val               | 4.540              | 4.835           |
| Met               | 2.390              | 2.528           |
| Ile               | 4.026              | 4.285           |
| Leu               | 7.205              | 7.620           |
| Tyr               | 2.970              | 3.234           |
| Phe               | 3.952              | 3.944           |
| Lys               | 7.851              | 8.189           |
| His               | 3.128              | 3.427           |
| Arg               | 5.023              | 5.369           |
| WTAA              | 81.686             | 87.245          |
| WEAA              | 33.998             | 35.717          |
| WEAA/WTAA (100%)  | 41.62              | 40.94           |
| WHEAA             | 8.15               | 8.80            |
| WNEAA             | 39.54              | 42.73           |
| WEAA/WNEAA (100%) | 85.99              | 83.59           |

AA, amino acid; WTAA, weight of total amino acid; WEAA, weight of essential amino acid; WHEAA, weight of half essential amino acid; WNEAA, weight of non-essential amino acid.

### 2.2. Preparation of Protein Hydrolysate of Skipjack Tuna Muscle

#### 2.2.1. Screening of Protease Species

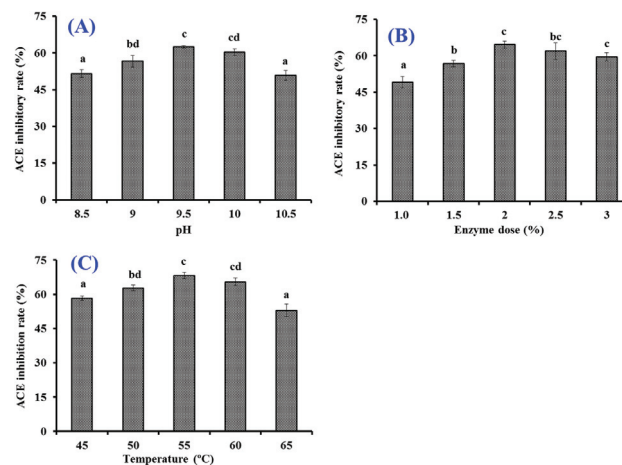
Protein hydrolysates of skipjack tuna muscle were produced by five kinds of proteases (Figure 1). At 1.0 mg/mL, the ACEi rate of protein hydrolysate produced using Alcalase was  $63.57 \pm 1.13\%$ , which was significantly higher than the rates of protein hydrolysates produced using papain ( $41.08 \pm 1.25\%$ ), Neutrase ( $57.83 \pm 3.23\%$ ), trypsin ( $42.19 \pm 1.35\%$ ), and pepsin ( $57.83 \pm 3.23\%$ ), respectively ( $p < 0.05$ ). These biological functions of protein hydrolysates are in close contact with the structure of bio-peptides [12,31]. Thus, Alcalase, Neutrase, pepsin, papain, trypsin, and their combinations are frequently applied to yield protein hydrolysates from various protein sources [32–34]. The present results further supported the conclusion that the specificity of proteases could markedly influence the peptide composition and biological functions of protein hydrolysates [33,35]. Therefore, Alcalase was selected to prepare a protein hydrolysate of tuna muscle.



**Figure 1.** Effects of papain (55 °C, pH 7.0), pepsase (37.5 °C, pH 2.0), Alcalase (55 °C, pH 9.5), Neutrase (55 °C, pH 7.0), and trypsin (37.5 °C, pH 7.8) with enzyme dose of 2% (*w/w*) for 3h on the ACE inhibitory (ACEi) activity of protein hydrolysates from skipjack tuna muscle. <sup>a-c</sup> Values with same letters indicate no significant difference ( $p > 0.05$ ).

### 2.2.2. Optimization of the Hydrolysis Conditions of Alcalase Using Single Factor Experiment

As shown in Figure 2, the effects of hydrolysis conditions of Alcalase including pH, temperature, and enzyme dose on the ACEi activity of protein hydrolysates were optimized by a single factor experiment. Figure 2A indicates that pH values significantly influenced the ACEi activity of protein hydrolysates, and the ACEi activity ( $56.57 \pm 2.42\%$  to  $60.29 \pm 1.44\%$ ) of protein hydrolysates prepared at pH 9 and 10 was significantly higher than those of protein hydrolysates prepared at pH 8.5 and 10.5 ( $p < 0.05$ ). Figure 2B shows that the ACEi activity of protein hydrolysates was dramatically affected by the enzyme dose, and the ACEi activity ( $64.64 \pm 1.37\%$ ) of protein hydrolysate prepared at the dose of 2.0% was significantly higher than those of hydrolysates prepared at other tested enzyme doses ( $p < 0.05$ ). Additionally, the ACEi activity of protein hydrolysate slowly descended when the dose was higher than 2.0%. Figure 2C illustrates that the ACEi activity of hydrolysates increased remarkably when the temperature increased from 45 to 55 °C and achieved the highest value ( $68.33 \pm 1.36\%$ ) at 55 °C, and there was a very significant decline in ACEi activity when the temperature was higher than 60 °C. Therefore, the range of hydrolysis conditions for Alcalase was narrowed to 9–10, 50–60 °C, and 1.5–2.5% for pH, temperature, and enzyme dose, respectively.



**Figure 2.** Effects of different hydrolysis conditions on ACEi activity of protein hydrolysates from skipjack tuna muscle. (A) pH; (B) enzyme dose (%); (C) temperature (°C). <sup>a-d</sup> Values with same letters indicate no significant difference ( $p > 0.05$ ).

### 2.2.3. Optimization of the Hydrolysis Conditions of Alcalase by Response Surface Experiment

According to the single-factor experiment data (Figure 2), the range of hydrolysis conditions for Alcalase was narrowed to 9–10, 50–60 °C, and 1.5–2.5% for pH, temperature, and enzyme dose, respectively. Moreover, ACEi activity under a response surface experiment design of three-level, three-factor factorial is presented in Table 2. After regression fitting of response values and variables in Table 2 by design-Expert 8.0.6, the quadratic multinomial regression equation disclosing the relationship between the ACEi rate (Y) and the variables (pH ( $X_1$ ), temperature ( $X_2$ ) and enzyme dose ( $X_3$ )) was as given below:

$$Y (\%) = 69.05 - 3.16X_1 + 2.6X_2 + 3.12X_3 + 0.34X_1X_2 + 3.63X_1X_3 - 2.5X_2X_3 - 4X_1^2 - 2.95X_2^2 - 1.89X_3^2 \quad (1)$$

**Table 2.** Box–Behnken design and experimental results of response surface methodology.

| Run | Independent Variables <sup>a</sup> |                        |                       | Dependent Variables <sup>b</sup> |
|-----|------------------------------------|------------------------|-----------------------|----------------------------------|
|     | $X_1$ (pH)                         | $X_2$ (temperature/°C) | $X_3$ (enzyme dose/%) | Y (ACEi rate %)                  |
| 1   | 9                                  | 55                     | 1.5                   | 66.01                            |
| 2   | 9                                  | 60                     | 2                     | 67.19                            |
| 3   | 9.5                                | 60                     | 2.5                   | 67.56                            |
| 4   | 10                                 | 55                     | 2.5                   | 67.56                            |
| 5   | 10                                 | 55                     | 1.5                   | 53.06                            |
| 6   | 9                                  | 55                     | 2.5                   | 66.00                            |
| 7   | 10                                 | 60                     | 2                     | 61.95                            |
| 8   | 9.5                                | 55                     | 2                     | 68.00                            |
| 9   | 10                                 | 50                     | 0                     | 56.32                            |
| 10  | 9.5                                | 50                     | 1.5                   | 55.86                            |
| 11  | 9.5                                | 55                     | 2                     | 70.58                            |
| 12  | 9                                  | 50                     | 2                     | 63.93                            |
| 13  | 9.5                                | 55                     | 2                     | 66.82                            |
| 14  | 9.5                                | 50                     | 2.5                   | 66.11                            |
| 15  | 9.5                                | 55                     | 2                     | 68.39                            |
| 16  | 9.5                                | 55                     | 2                     | 67.90                            |
| 17  | 9.5                                | 60                     | 1.5                   | 67.31                            |

<sup>a</sup> Independent variables:  $X_1$ , pH;  $X_2$ , temperature;  $X_3$ , enzyme dose; <sup>b</sup> dependent variables: Y, ACEi rate.

The results of the significance test of the coefficients of the regression model and variance analysis results of the equation are shown in Table 3, where  $X_1$ ,  $X_2$ ,  $X_3$ ,  $X_1X_3$ ,  $X_2X_3$ ,  $X_1^2$ , and  $X_2^2$  had significant negative effects on ACEi rate with  $p < 0.05$ . The results showed that the effects of various variances on enzymatic hydrolysis process parameters had an interaction effect, rather than a simple linear relationship. The determination coefficient ( $R^2$ ) of ACEi rate was 0.9689, meaning that 96.89% of the observed results could be fitted well by this regression equation. The relationship between independent variables and the response value could be well described by the regression equation. Therefore, the equation can reliably be applied to predict the optimal process conditions for preparing ACEi hydrolysate of skipjack tuna muscle by Alcalase. In addition, the analysis results in Table 3 indicated that the order of influence of each variance on ACEi rate was: enzyme dose ( $X_3$ ) > pH ( $X_1$ ) > temperature ( $X_2$ ).

According to the regression equation, the 3D response surface results of multiple non-linear regression models (Figure 3) were applied to illustrate the interactive influence of the variables and their mutual interaction on the ACEi rate. As shown in Figure 3A, ACEi rate increases to a certain extent when pH value increases within a certain range, but ACEi rate decreased instead of increasing when the pH value exceeded this range. The effect of temperature (Figure 3B) and enzyme dosage (Figure 3C) showed the similar trends. The shape (elliptic or round) of contour map can reflect the strength and significance of the interaction between two independent variables. Elliptic indicates that the interaction



between the two independent variables is evident; round indicates that the interaction between the two factors is not evident. The contour maps of Figure 3B,C were elliptic, indicating that the influence between the two factors ( $X_1 X_3$  and  $X_2 X_3$ ) was evident. The contour map of Figure 3A tended to be round, indicating that the interaction between pH and temperature was not significant when other factors were fixed. These results agreed well with the data summarized in Table 2. According to the analysis of Design-Expert 8.0.6 software, the optimal processing conditions of Alcalase for preparing protein hydrolysate of tuna muscle were as follows: pH 9.4, enzyme dosage 2.3%, and temperature 56.2 °C. Using optimum hydrolysis conditions, the ACEi rate of prepared hydrolysate (referred to as TMPH) of tuna muscle was 72.71%, which was very close to the predicted 73.20% and confirmed the validity and adequacy of the predicted equation.

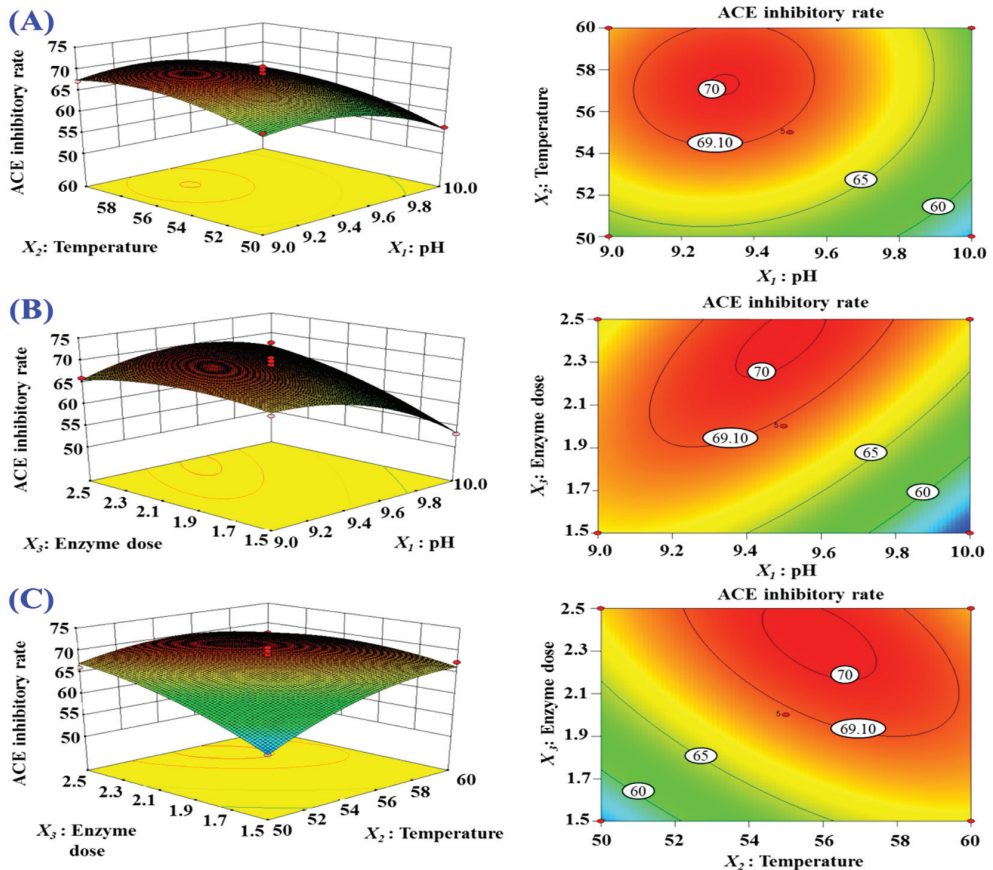


Figure 3. Response surface graph for ACEi rate as a function of (A) temperature and pH, (B) enzyme dose and pH, and (C) enzyme dose and temperature during the hydrolysis of skipjack tuna muscle with Alcalase.

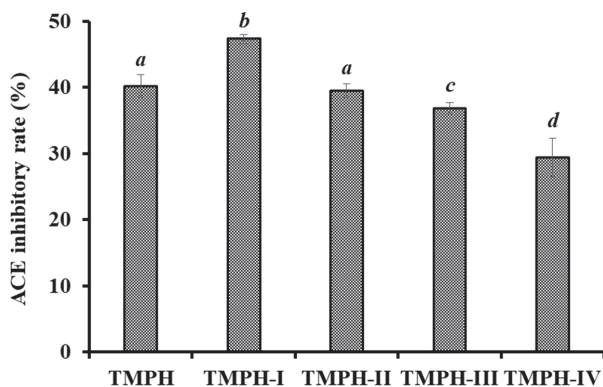
**Table 3.** ANOVA for response surface quadratic model: estimated regression model of relationship between dependent variables and independent variables.

| Source                        | Sum of Squares | df | Mean Square | F-Value | p-Value | Significant     |
|-------------------------------|----------------|----|-------------|---------|---------|-----------------|
| Model                         | 407.86         | 9  | 45.32       | 24.24   | 0.0002  | significant     |
| X <sub>1</sub> -pH            | 73.45          | 1  | 73.45       | 39.29   | 0.0004  |                 |
| X <sub>2</sub> -Temperature   | 59.35          | 1  | 59.35       | 31.75   | 0.0008  |                 |
| X <sub>3</sub> -Enzyme dose   | 78.06          | 1  | 78.06       | 41.76   | 0.0003  |                 |
| X <sub>1</sub> X <sub>2</sub> | 1.4            | 1  | 1.4         | 0.75    | 0.4148  |                 |
| X <sub>1</sub> X <sub>3</sub> | 52.64          | 1  | 52.64       | 28.16   | 0.0011  |                 |
| X <sub>2</sub> X <sub>3</sub> | 25             | 1  | 25          | 13.37   | 0.0081  |                 |
| X <sub>1</sub> <sup>2</sup>   | 60.02          | 1  | 60.02       | 32.11   | 0.0008  |                 |
| X <sub>2</sub> <sup>2</sup>   | 31.22          | 1  | 31.22       | 16.7    | 0.0047  |                 |
| X <sub>3</sub> <sup>2</sup>   | 15.41          | 1  | 15.41       | 8.24    | 0.024   |                 |
| Residual                      | 13.09          | 7  | 1.87        |         |         |                 |
| Lack of Fit                   | 4.27           | 3  | 1.42        | 0.65    | 0.6256  | not significant |
| Pure Error                    | 8.82           | 4  | 2.2         |         |         |                 |
| Cor Total                     | 420.95         | 16 |             |         |         |                 |

### 2.3. ACEi Peptides Prepared from TMPH

#### 2.3.1. Ultrafiltration of TMPH

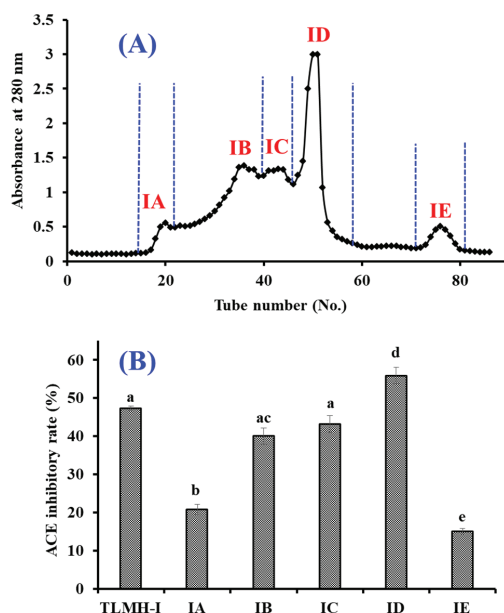
Through 3.5, 5, and 10 kDa ultrafiltration membranes, the TMPH underwent the fractionation into four different MW fractions (TMPH-I, TMPH-II, TMPH-III, and TMPH-IV). According to Figure 4, the ACEi activity of TMPH-I was  $47.26 \pm 0.64\%$  at 0.5 mg/mL ( $p < 0.05$ ), which was remarkably higher than those of TMPH ( $40.17 \pm 1.74\%$ ), TMPH-II ( $39.48 \pm 1.05\%$ ), TMPH-III ( $36.84 \pm 0.86\%$ ), and TMPH-IV ( $29.38 \pm 2.88\%$ ), respectively. Polypeptides with large size are difficult to enter and bind to the active site of ACE, resulting in a decrease in their inhibitory activity [12]. Therefore, ultrafiltration technology is often applied to pool bioactive peptides with small MWs from protein hydrolysates [36–38]. The present data were in agreement with the reported literatures that low MW peptide fractions of protein hydrolysates from *Saurida elongate* [39], tuna frame [24], Antarctic krill [6], *Katsuwana pelamis* [40], *Okamejei kenoeji* [41], and squid (*Dosidicus gigas*) skin [42] had the highest ACEi activity. Then, TMPH-I with the smallest MW revealed strong ACEi activity and was selected for further separation.



**Figure 4.** ACEi rates of ultrafiltration fractions (TMPH-I, TMPH-II, TMPH-III and TMPH-IV) of TMPH at 0.5 mg/mL. <sup>a–d</sup> Values with same letters indicate no significant difference ( $p > 0.05$ ).

### 2.3.2. Gel Permeation Chromatography (GPC) of TMPH-I

TMPH-I was divided into five peptide fractions (IA-ID) by Sephadex G-25 chromatography and their ACEi rates were shown in Figure 5. At 0.5 mg/mL, the ACEi rate of ID was  $55.87 \pm 2.15\%$ , which was remarkably ( $p < 0.05$ ) higher than those of TMPH-I ( $47.26 \pm 0.64\%$ ), IA ( $20.77 \pm 1.36\%$ ), IB ( $39.99 \pm 2.13\%$ ), IC ( $43.19 \pm 2.19\%$ ), and IE ( $15.07 \pm 0.72\%$ ), respectively (Figure 5). Then, the peptide fraction of ID was chosen for RP-HPLC isolation.



**Figure 5.** Chromatogram profile of TMPH-I isolated by Sephadex G-25 (A) and the ACEi rates of prepared subfractions (IA-IE) from TMPH-I at 0.5 mg/mL (B). <sup>a-e</sup> Values with same letters indicate no significant difference ( $p > 0.05$ ).

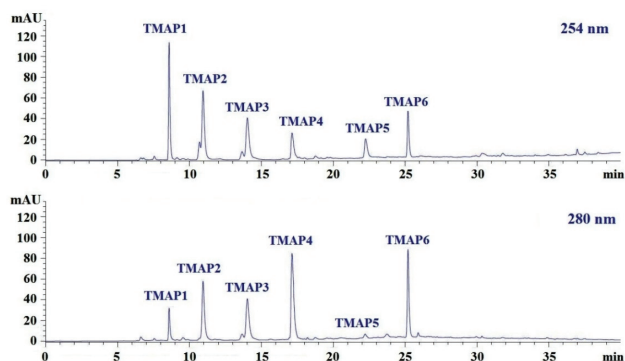
### 2.3.3. RP-HPLC Purification of TMPH-ID

ID was finally purified by RP-HPLC with a Zorbax 300SB-C18 column ( $9.4 \times 250$  mm,  $5 \mu\text{m}$ ) (Figure 6). According to the elution profiles of ID fraction at 254 and 280 nm, six peptides with retention times of 8.590 min (TMAP1), 10.950 min (TMAP2), 14.032 min (TMAP3), 17.139 min (TMAP4), 22.258 min (TMAP5), and 25.209 min (TMAP6) were collected and lyophilized (Table 4).

**Table 4.** Amino acid sequences, molecular weights (MWs), and ACEi activity ( $\text{IC}_{50}$  value) of six isolated peptides (TMAP1-TMAP6) from protein hydrolysates of skipjack tuna muscle (TMPH).

| Retention Time (min) | Amino Acid Sequence         | Observed MW/Theoretical MW (Da) | $\text{IC}_{50}$ (mg/mL) |
|----------------------|-----------------------------|---------------------------------|--------------------------|
| TMAP1                | Ser-Pro (SP)                | 202.3/202.2                     | $0.06 \pm 0.01^a$        |
| TMAP2                | Val-Asp-Arg-Tyr-Phe (VDRYF) | 698.9/698.8                     | $0.28 \pm 0.03^a$        |
| TMAP3                | Val-His-Gly-Val-Val (VHGVV) | 509.7/509.6                     | $0.90 \pm 0.16^b$        |
| TMAP4                | Tyr-Glu (YE)                | 310.4/310.3                     | $0.80 \pm 0.03^b$        |
| TMAP5                | Phe-Glu-Met (FEM)           | 425.6/425.5                     | $2.18 \pm 0.20^c$        |
| TMAP6                | Phe-Trp-Arg-Val (FWRV)      | 606.8/606.7                     | $0.76 \pm 0.10^b$        |

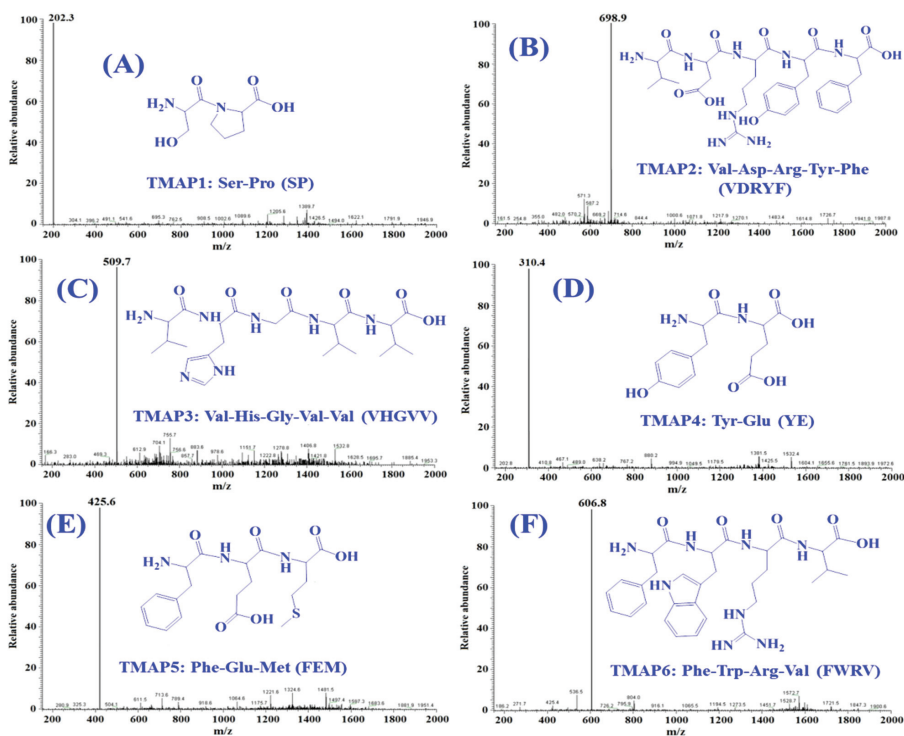
<sup>a-c</sup> Values with same letters indicate no significant difference ( $p > 0.05$ ).  $\text{IC}_{50}$  (half maximal inhibitory concentration) is the concentration of inhibitor required for 50% inhibition of ACE.



**Figure 6.** Elution profiles of subfraction ID by RP-HPLC using a gradient of acetonitrile containing 0.06% trifluoroacetic acid at 254 nm and 280 nm.

#### 2.4. Peptide Sequences and MWs Determination

By employing Protein/Peptide Sequencer, six peptides (TMAP1-TMAP6) sequences were identified as Ser-Pro (SP, TMAP1), Val-Asp-Arg-Tyr-Phe (VDRYF, TMAP2), Val-His-Gly-Val-Val (VHGVV, TMAP3), Tyr-Glu (YE, TMAP4), Phe-Glu-Met (FEM, TMAP5), and Phe-Trp-Arg-Val (FWRV, TMAP6), respectively, and their MWs were determined as 202.3, 698.9, 509.7, 310.4, 425.6, and 606.8 Da, respectively (Figure 7), which were in good agreement with their theoretical MWs (Table 4).



**Figure 7.** Mass spectrogram of six ACEi peptides (TMAP1-TMAP6) from protein hydrolysate of skipjack tuna muscle (STPM). (A) TMAP1; (B) TMAP2; (C) TMAP3; (D) TMAP4; (E) TMAP5; (F) TMAP6.

## 2.5. Bioactive Properties of Six ACEi Peptides (TMAP1-TMAP6)

### 2.5.1. ACEi Activity and Molecular Docking Analysis

Table 4 showed that the  $IC_{50}$  values of TMAP1 and TMAP2 on ACE were  $0.06 \pm 0.01$  and  $0.28 \pm 0.03$  mg/mL, which were significantly lower than those of TMAP3 ( $0.90 \pm 0.16$  mg/mL), TMAP4 ( $0.80 \pm 0.03$  mg/mL), TMAP5 ( $2.18 \pm 0.20$  mg/mL), and TMAP6 ( $0.76 \pm 0.10$  mg/mL), respectively ( $p < 0.05$ ). Additionally, the  $IC_{50}$  values of TMAP1 and TMAP2 were lower than those of ACEi peptides from protein hydrolysates of seaweed pipefish (HWTTQR: 1.44 mg/mL [43], Antarctic krill (WF: 0.32 mg/mL; YAK: 1.26 mg/mL; FQK: 1.76 mg/mL [6]), skate (MVGSA PGVL: 3.09 mg/mL; LGPLGHQ: 4.22 mg/mL [44], stone fish (LAPPTM: 1.31 mg/mL; EVLIQ: 1.44 mg/mL; EHPVL: 1.68 mg/mL [45], and lizardfish (AGPPGS-DGQPGA: 544.10 mg/mL [46], respectively. The present results demonstrate that TMAP1-TMAP6, especially TMAP1 and TMAP2, had significantly ACEi activity and could serve as functional molecules applied in antihypertensive products.

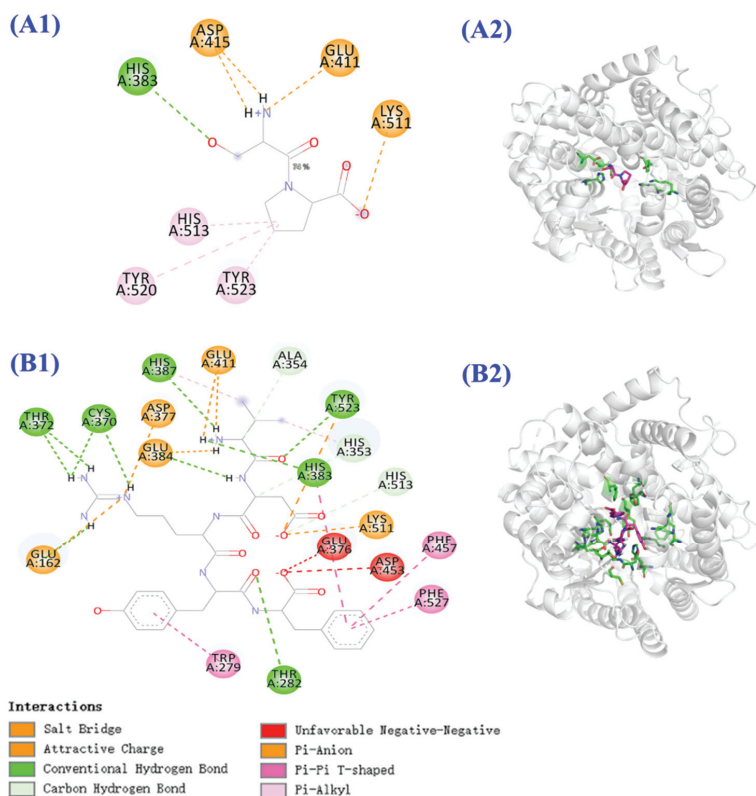
A molecular docking experiment was performed to analyze the mechanism of ACEi peptides (TMAP1 and TMAP2) and ACE (Figure 8). ACE has three major active site pockets (S1, S2, and S1'). The S1 pocket includes Ala354, Glu384, and Tyr523 residues; the S2 pocket includes Gln281, His353, Lys511, His513, and Tyr520 residues; and S1' contains Glu162 residues [12]. Cap is a widely recognized ACE inhibitor and interacts at the sites of Gln281, His353, Ala354, Glu384, Lys511, His513, Tyr520, and Tyr523 residues of ACE, which indicates that these amino acid residues play key roles in ACE binding [12]. Figure 8A indicated that TMAP1 formed a hydrogen bond with His383 residue and a hydrophobic interaction with His513, Tyr523, and Tyr520 residues of ACE, and interacted with Asp415, Glu411, and Lys511 residues of ACE by electrostatic force. Figure 8B proved that TMAP2 (VDRYF) formed hydrogen bonds with Ala354, His353, His513, Tyr523, His383, Thr282, His387, Cys370, and Tyr372 residues of ACE, among which it formed hydrogen bonds with active pockets of S1 (Ala354 residue) and S2 (His353 and His513 residues). In addition, TMAP2 (VDRYF) interacted with Phe457, Phe527, and Trp279 residues of ACE through hydrophobic effect and interacted with Glu411, Asp377, Glu384, Glu162, and Lys511 residues of ACE through electrostatic force. The molecular docking analysis demonstrated that TMAP1 and TMAP2 exhibit better ACEi activity, attributed to the effective interaction with the active sites of ACE by hydrogen bonding, electrostatic force, and hydrophobic interaction. Meanwhile, the ACEi activity of TMAP2 should be related to the interaction with active pockets.

The molecular docking analysis indicated that the affinity of TMAP1 and TMAP2 with ACE was  $-5.7$  and  $-9.7$  kcal/mol, which was similar to those of YSK ( $-7.9$  kcal/mol [47], YVVF ( $-9.8$  and  $-8.8$  kcal/mol for C-domain and N-domain affinity), WMY ( $-9.3$  and  $-8.5$  kcal/mol for C-domain and N-domain affinity), and LVLL ( $-8.6$  and  $-7.5$  kcal/mol for C-domain and N-domain affinity) [48].

Molecular size and amino acid sequence are two critical factors influencing the ACEi ability of antihypertensive peptides [49,50]. Molecular size determines the affinity of a peptide with the ACE active site because large peptides cannot accommodate to the narrow binding channel of ACE [12]. Abdelhedi et al. reported that ACEi tripeptides VPP and IPP could easily enter the ACE channel and coordinate with  $Zn^{2+}$ , but larger peptides composed of 7–11 amino acid residues, such as ALPMHIR, VKPLPQSG, AVVPPSDKM, GPAGPRGPAG, and TTMYPGIA, showed low interaction scores combining with the ACE active site [51]. In the study, TMAP1 and TMAP2 were dipeptides or pentapeptides, and the small size increased their access to the binding channel of the ACE active site.

The amino acid sequence is another factor affecting the ACEi ability of antihypertensive peptides. ACE consists of C- and N-domains, and each contains a binding active site of zinc cofactor [52]. Therefore, the C- and N-terminal amino acids are important to the activity of antihypertensive peptides. Presently, the kind of C-terminal amino acids on the ACEi activity and mechanism has been widely discussed. Zheng et al. indicated that branched-chain (Leu and Ile) and aromatic (Tyr and Phe) amino acids or Pro were the main residues in their C-terminal tripeptides [53]. Hayes et al. found that hydrophobic amino

acids, such as Phe, Trp, Tyr, Val, Leu, and Ile, favored combination with the C-terminal active site of ACE [54]. Pro has aroused great attention amongst researchers because Pro occurs frequently at the C-terminus of antihypertensive peptides, such as LYPPP, YSMYPP, VGLYP, EVSQGRP, YP, and KDEDTEEVP, and could enhance the resistant ability of peptides against gastro-intestinal digestion and kept good bioavailability [4]. Therefore, Pro and Phe residues at the C-terminus of TMAP1 and TMAP2 are particularly critical for their ACEi activity.



**Figure 8.** Molecular docking results of TMAP1 and TMAP2 with ACE. **(A1)** 2D details of ACE and TMAP1 interaction. **(A2)** 3D interaction details for TMAP1. **(B1)** 2D details of ACE and TMAP2 interaction. **(B2)** 3D interaction details for TMAP2.

The function of N-terminal amino acids is less discussed compared with C-terminal amino acids. Auwal et al. illustrated that branched aliphatic or dicarboxylic amino acids (Val, Ala, Ile, and Leu) at the N-terminus could strengthen ACEi ability of peptides [45]. Then, Val residue at the N-terminus of TMAP2 could improve its ACEi ability. In addition, Ser residue was found in some ACEi peptides, such as VSQLTR ( $IC_{50}$  105  $\mu$ M) [55], YSK ( $IC_{50}$  76 mM) [47], and SPRCR ( $IC_{50}$  41  $\mu$ M) [56]. Therefore, Ser residue, especially its hydroxyl group, should play a vital effect in the ACEi capability of TMAP1, and the result was confirmed by Figure 8B that the hydroxyl group of Ser residue formed hydrogen bonds with the His383 residue of ACE.

## 2.5.2. Effects of TMAP1 and TMAP2 on HUVECs

### Effects of TMAP1 and TMAP2 on Cell Viability

The effects of TMAP1 and TMAP6 on the viability of HUVECs at concentrations of 100–400  $\mu\text{M}$  were shown in Figure 9. After being incubated for 24 h at the determined concentrations, the cell viability of the TMAP1 group ranged from  $102.63 \pm 6.79\%$  to  $106.64 \pm 0.82\%$ , and the cell viability of the TMAP2 group ranged from  $97.18 \pm 0.86\%$  to  $106.05 \pm 1.91\%$ . The cell viability of the TMAP1 and TMAP2 groups was higher than 90% of the blank control, which indicated that TMAP1 and TMAP2 did not induce significant cell toxicity in HUVECs.

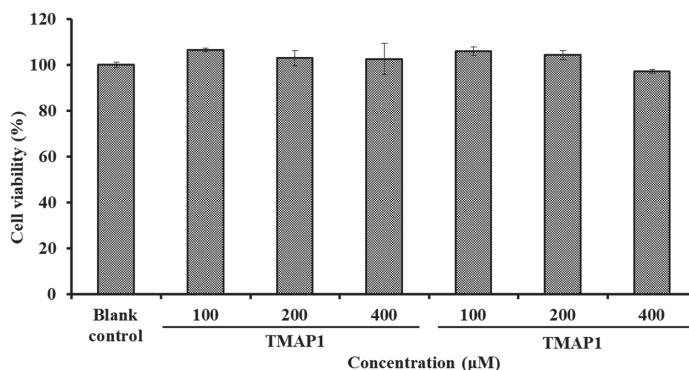


Figure 9. The cell viability of HUVECs treated with TMAP1 and TMAP2 for 24 h.

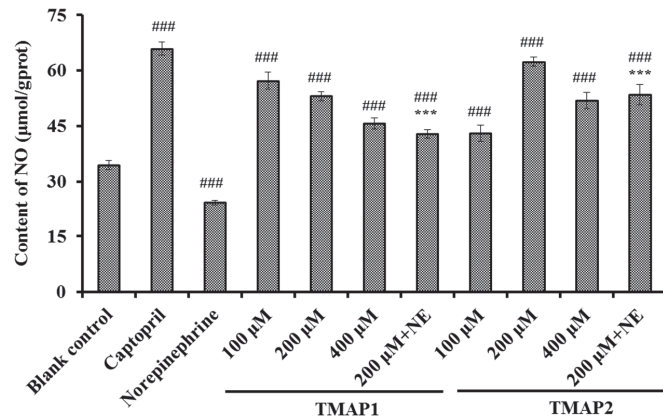
Vascular endothelial cells enshroud the inner surface of blood vessels and are crucial regulatory factors of vascular tone through generating vasodilatory and vasoconstrictory agents. Thus, HUVECs are usually used as model cells for illustrating the mechanism of blood pressure regulation [4,12]. Cells maintain an appropriate balance between proliferation and death in normal tissues, and bioactive compounds with strong cell proliferation inhibition indicate their potential toxicity to normal organs and tissues, and are thought to be ill-suited to the development of non-antitumor health products [12,57]. The present results indicate that TMAP1 and TMAP2 were not significantly toxic to HUVECs and should be suitable for producing antihypertensive products.

### Effects of TMAP1 and TMAP2 on NO Production

According to Figure 10, Cap could significantly increase the level ( $65.96 \pm 1.83 \mu\text{mol/gprot}$ ) of NO in HUVECs in comparison with the control group ( $34.41 \pm 1.27 \mu\text{mol/gprot}$ ) ( $p < 0.001$ ). Similarly, the NO levels in HUVECs treated with TMAP1 and TMAP2 at 100, 200, and 400  $\mu\text{M}$  were significantly increased compared with the control group ( $p < 0.001$ ), and the NO levels of TMAP1 and TMAP2 groups increased to  $57.25 \pm 2.31$  and  $51.88 \pm 2.16 \mu\text{mol/gprot}$  at 400  $\mu\text{M}$ . Additionally, NE could significantly decrease the level of NO ( $24.25 \pm 0.63 \mu\text{mol/gprot}$ ) compared with the control group ( $p < 0.001$ ), but the negatively influence of NE on reducing NO content was partially offset by TMAP1 and TMAP2 treatment at a 200  $\mu\text{M}$  concentration ( $p < 0.001$ ).

NO can antagonize the vascular tone function of angiotensin II by down-regulating the synthesis of ang II type 1 receptor and ACE, which is further involved in regulating the peripheral and central function of the cardiovascular system and exerts vasoprotective effects [4]. In addition, NO refers to the most potent vascular endothelium-derived vasodilator, but its formation is decreased in atherosclerosis [58]. Therefore, the deficiency of NO will increase the risks of cardiovascular in pathologic situations, and improving endothelial NO production represents reasonable therapeutic strategy for atherosclerosis [6]. Previous studies have shown that some ACEi peptides, such as WF, YRK, FQK,

FAS, GRVSNCAA, and TYLPVH, exerted their antihypertensive activity by increasing the NO production of HUVEC [38]. The present data indicate that TMAP1 and TMAP2 could significantly increase the production of NO in HUVECs and even reverse the downtrend of NO production caused by NE.



**Figure 10.** The production of nitric oxide (NO) of HUVECs treated with TMAP1 and TMAP2 for 24 h. Cell group treated with captopril (Cap) was designed as a positive control. ###  $p < 0.001$  vs. control group; \*\*\*  $p < 0.001$  vs. norepinephrine (NE) group.

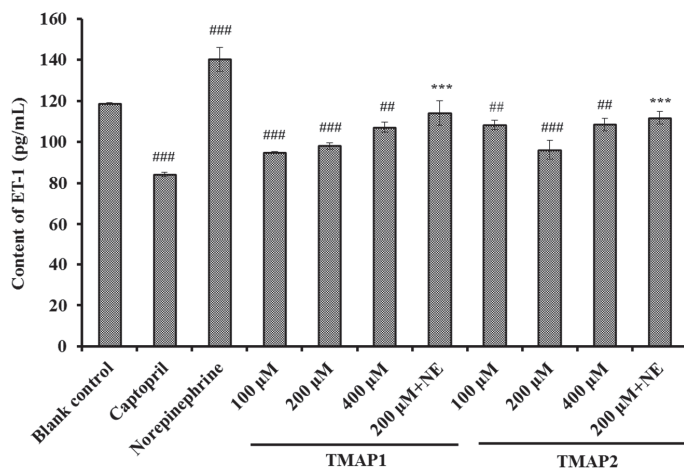
#### Effects of TMAP1 and TMAP2 on ET-1 Secretion

According to Figure 11, the ET-1 secretion of HUVECs was significantly decreased to  $84.16 \pm 1.18$  pg/mL by 0.5 μM Cap treatment compared with the control group ( $118.68 \pm 0.53$  pg/mL) ( $p < 0.001$ ). In addition, the ET-1 secretion of HUVECs significantly ( $p < 0.001$  or  $p < 0.01$ ) decreased by TMAP1 and TMAP2 under the tested concentrations, and the ET-1 levels of TMAP1 and TMAP2 groups reduced to  $94.86 \pm 0.39$ , and  $92.09 \pm 4.58$  pg/mL at 400 μM. Conversely, NE could significantly increase ET-1 secretion ( $140.23 \pm 5.81$  pg/mL) compared with the control group ( $p < 0.01$ ), but the ET-1 secretion negatively affected by NE was partially abrogated by TMAP1 and TMAP2 treatment, and ET-1 secretion decreased to  $114.08 \pm 5.82$  pg/mL and  $111.78 \pm 3.06$  pg/mL at 200 μM ( $p < 0.01$ ).

ET-1 is a known vasoconstriction factor similar to Ang II and is capable of inducing endothelial dysfunction related to atherosclerosis and hypertension [6,59]. Zhang et al. reported that GRVSNCAA and TYLPVH from *R. philippinarum* played their antihypertension function through significantly lessening ET-1 generation [38], and ACEi peptides of WF, YRK, FQK, and FAS from Antarctic krill showed a similar activity of reducing ET-1 content [6]. The available results illustrated that TMAP1 and TMAP2 displayed similar capabilities to significantly decrease the secretion of ET-1 and reverse the uptrend of ET-1 secretion caused by NE in HUVECs.

As suggested from the mentioned outcomes, ACEi peptides from skipjack tuna muscle noticeably facilitate NO production while controlling ET-1 secretion in HUVECs. In addition, the peptides reversed the impact of NE upon NO- and ET-1-secreting processes in HUVECs. According to the mentioned findings, the ACEi peptides isolated from skipjack tuna muscle exert protection-related effects upon vascular endothelial functions and display an antihypertensive mechanism analogous to that of Cap.





**Figure 11.** The endothelin-1 (ET-1) secretion of HUVECs treated with TMAP1 and TMAP2 for 24 h. Cell group treated with captopril (Cap) was designed as a positive control. ###  $p < 0.001$  and ##  $p < 0.01$  vs. control group; \*\*\*  $p < 0.001$  vs. norepinephrine (NE) group.

### 3. Materials and Methods

#### 3.1. Materials

Skipjack tuna (*K. pelamis*) muscle was provided by Ningbo Today Food Co., Ltd (China). Sephadex G-25 resins and NO assay kit (Nitrate reductase approach, A012-1) were purchased from Nanjing Jiancheng Bioengineering Institute (China). ET-1 ELISA Kit (HM10108) was purchased from Shanghai Qiaodu Biotechnology Co. Ltd. (China). Trypsase ( $\geq 20,000$  U/g), pepsase ( $\geq 500,000$  U/g), papain ( $\geq 400,000$  U/g), ACE (A6778) and N-[3-(2-Furyl) acryloyl]-Phe-Gly-Gly (FAPGG, F713) were purchased from Sigma-Aldrich (Shanghai) Trading Co., Ltd. (China). Alcalase (B8360,  $2.0 \times 10^5$  U/g), 3-(4,5-Dimethylthiazol-2-yl)-2,5-diphenyltetrazolium bromide (MTT; M8180), Penicillin-Streptomycin Liquid (P1400), dimethylsulfoxide (DMSO), fetal bovine serum (FBS; 11011-8611), HEPES buffer (H8090), norepinephrine (NE; IN0530), and Cap (C7510) were purchased from Beijing Solarbio Science & Technology Co., Ltd. (China). ACEi Peptides of (TMAP1-TMAP6) with purity higher than 98% were synthesized in Shanghai Apeptide Co. Ltd. (China).

#### 3.2. Determination of Amino Acid Composition and ACEi Activity

Amino acid composition of skipjack tuna muscle was determined according to the previous method [60].

The ACEi activity was determined by employing FAPGG as the substrate with the previous protocol [6]. The assay was conducted in a Tris-HCl buffer (50 mM, pH 8.3) containing 300 mM NaCl. The same buffer was used to dilute the protein hydrolysates, enzyme, and substrate. The initial assay volume consisted of 50  $\mu$ L of the substrate (3 mM), 50  $\mu$ L of the ACE enzyme solution containing 1.25 mU of declared enzyme activity, and 50  $\mu$ L of assay sample. All these solutions were incubated for 30 min at 37 °C in a water bath first without mixing and then for an additional 30 min after mixing. Glacial acetic acid (150  $\mu$ L) was added to stop ACE activity. The reaction mixture was separated by HPLC to determine the hippuric acid (HA) content produced due to ACE activity on the substrate. The content of free HA was determined using a HPLC system (Agilent 1200, Agilent Ltd., Santa Clara, CA, USA) on a Zorbax, SB C-18 column (4.6  $\times$  250 mm, 5  $\mu$ m) using an isocratic system (pH 3.0) consisting of 12.5% (*v/v*) acetonitrile in deionised water. The sample (10  $\mu$ L) was eluted at a flow rate of 1.0 mL/min and measured by monitoring the absorbance at 228 nm. In the HPLC method, the fitted linear equation between the peak area (*y*) and HA content (*x*) was calculated by the method of least squares,

as  $y = 6052x - 4.9429$  ( $R^2 = 0.9998$ ). The HA content was calculated by the peak area. The control reaction mixture contained 50  $\mu\text{L}$  of buffer instead of the assay sample, and the control was expected to liberate the maximum amount of HA from the substrate due to uninhibited ACE activity. The percent inhibition of ACE activity was calculated as follows:

$$\text{Inhibition activity (\%)} = [(\text{HA control} - \text{HA sample}) / \text{HA control}] \times 100\%.$$

### 3.3. Preparation of Protein Hydrolysate of Skipjack Tuna Muscle

#### 3.3.1. Screening of Protease Species

The skipjack tuna muscle was pounded into a homogenate and defatted, as previously described [61]. The homogenate and isopropanol were mixed in a ratio of 1:4 ( $w/v$ ) and stirred continuously for 4 h at 35 °C. Isopropanol was replaced every 2 h. The precipitate was collected by centrifugation at 9000 rpm for 15 min at 4 °C, freeze-dried, and stored at  $-20$  °C.

Defatted tuna muscle powders were dispersed in distilled water (1%,  $w/v$ ) and hydrolyzed for 3 h with an enzyme dose of 2% ( $w/w$ ) using papain (55 °C, pH 7.0), pepsase (37.5 °C, pH 2.0), Alcalase (55 °C, pH 9.5), Neutrase (55 °C, pH 7.0), and trypsin (37.5 °C, pH 7.8), respectively. After that, the enzymolysis reaction was stopped at 95 °C for 20 min and centrifuged at  $8000 \times g$  for a quarter of an hour at  $-4$  °C. The resulting supernatant was lyophilized and stored at  $-20$  °C. The protein hydrolysate produced by Alcalase showed the highest ACEi activity.

#### 3.3.2. Optimization of the Hydrolysis Conditions of Alcalase

A single-factor experiment was applied to optimize the hydrolysis conditions of Alcalase. pH (8.5, 9.0, 9.5, 10.0, and 10.5), hydrolysis temperature (45 °C, 50 °C, 55 °C, 60 °C, and 65 °C), and enzyme dose (1.0%, 1.5%, 2.0%, 2.5%, and 3.0%) were chosen for the present investigation.

According to the single-factor experiment results, a response surface methodology was employed to estimate the influence of independent variables ( $X_1$ , pH;  $X_2$ , temperature;  $X_3$ , enzyme dose) in glycine-sodium hydroxide buffer (0.05 M) on ACEi activity [62,63]. The Box–Behnken design of three levels ( $X_1$ : 9, 9.5, and 10;  $X_2$ : 50, 55, and 60 °C;  $X_3$ : 1.5, 2.0, and 2.5%) was used to analyze the effects of three variables on ACEi activity. The experimental operation after hydrolysis is the same as in Section 3.3.1. The protein hydrolysate prepared under the optimal enzymolysis conditions was referred to as TMPH.

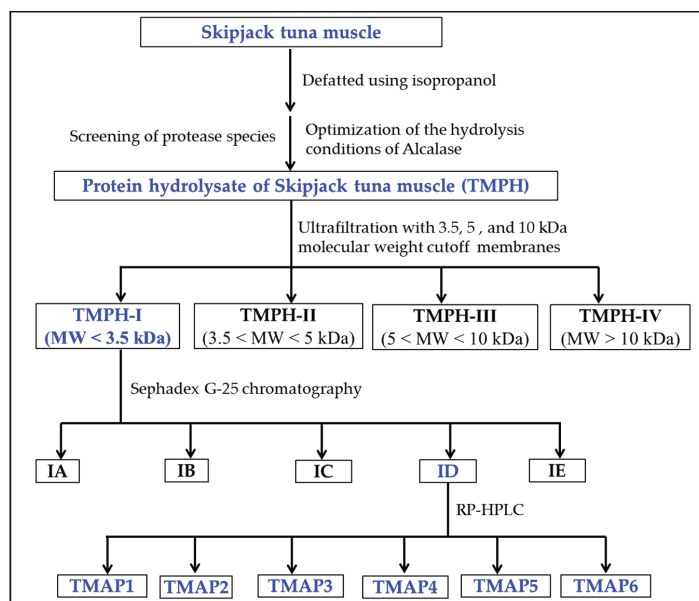
#### 3.4. Separation Process of ACEi Peptides from TMPH

ACEi peptides were purified from TMPH using the following designed process (Figure 12).

TMPH (100.0 mg/mL) was fractionated with three MW cutoff membranes (10, 5, and 3.5 kDa) at 0.50 MPa, 4 °C, and four fractions including TMPH-I (<3.5 kDa), TMPH-II (3.5–5 kDa), TMPH-III (5–10 kDa), and TMPH-IV (>10 kDa) were collected and lyophilized. TMPH-I exhibited the maximum ACEi activity among four fractions.

TMPH-I solution (5 mL, 50.0 mg/mL) was fractionated with Sephadex G-25 column (3.6  $\times$  150 cm) eluted with ultrapure water under 0.6 mL/min flow rate. Each eluate (1.8 mL) was collected by monitoring absorbance at 280 nm. Five subfractions (IA, IB, IC, ID, and IE) were isolated from TMPH-I solution and lyophilized. The ACEi activity of ID was higher than those of the other four fractions.

The ID solution (20  $\mu\text{L}$ , 100.0  $\mu\text{g/mL}$ ) received final separation by RP-HPLC on a Zorbax 300SB-C18 column (9.4  $\times$  250 mm, 5  $\mu\text{m}$ ) with a linear gradient of acetonitrile (1% acetonitrile in 7 min; 1–10% acetonitrile in 7 min; 10–30% acetonitrile in 7 min; 30–60% acetonitrile in 7 min; 60–100% acetonitrile in 7 min; and 100 B in 5 min) inside 0.06% trifluoroacetic acid (TFA) at 2.0 mL/min flow rate. The eluate absorbance was monitored at 254 and 280 nm. Six peptides (TMAP1 to TMAP6) were collected according to the elution chromatogram, dialyzed with MW cut-off dialysis tube of 100 Da, lyophilized, and followed by in-depth analysis for their amino acid sequences.



**Figure 12.** Flow diagram of purifying ACEi peptides from protein hydrolysate (TMPH) of skipjack tuna muscle prepared using Alcalase.

### 3.5. Identification of Sequence and MWs of ACEi Peptide

The sequences of TMAP1 to TMAP6 were analyzed using an Applied Biosystems 494 protein sequencer (Perkin Elmer, USA) [58]. Edman degradation was performed according to the standard program supplied by Applied Biosystems.

The precise MWs of TMAP1 to TMAP6 were determined by employing a Q-TOF mass spectrometric device (Micromass, Waters, Milford, MA, USA) in the combination of an electrospray ionization (ESI) source [64]. Nitrogen was maintained at 40 psi for nebulization and 9 L/min at 350 °C for evaporation temperature. The data were collected in centroid mode from  $m/z$  200 to 2000.

### 3.6. Molecular Docking Experiment of TMAP1 and TMAP2

The molecular docking experiment was commissioned to Shanghai NovoPro Biotechnology Co., Ltd (Shanghai, China). The crystal structure of human ACE-lisinopril complex (1O8A.pdb) and Cap were acquired from the RCSB PDB Protein Data Bank (PDB code: 1UZF). The interaction between ACE and MCO was analyzed to determine the position and size of the binding pocket using Chimera software. All non-standard residues in the 1UZF model were deleted, and AutodockTools were used to convert PDB files into PDBQT files (adding Gasteiger charge and setting key distortion). Peptide molecules were converted into SMILES format by PepSMI tool, 3D models were drawn by Discovery Studio program, and energy minimization was performed using steepest-descent and conjugate-gradient techniques. Molecular docking and free energy calculation were carried out using flexible docking tool of Autodock Vina. Finally, the interaction between ACE and peptide molecules was analyzed by Chimera software. The best ranked docking poses of TMAP1 and TMAP2 in the active site of ACE were acquired on the binding-energy value and scores.

### 3.7. Effects of TMAP1 and TMAP2 on HUVECs

#### 3.7.1. HUVECs Culture and Cell Viability Assessment using MTT Assay

After thawing, HUVECs were maintained in cultured flasks and cultured to confluence in DMEM containing 1% Penicillin-Streptomycin liquid, supplemented with 10% FBS. HUVECs received the culturing process at 37°C in a humidified 5% CO<sub>2</sub> atmosphere [6].

The cell viability of TMAP1 and TMAP2 on HUVECs were assessed using the MTT assay on manufacturer's instructions [65,66]. In brief, cells were incubated in 96-well plates at density of  $0.8 \times 10^4$  cells per well with 180 µL completed DMEM. Following a confluency of 50–60% in the 96-well plates, the cells were treated with 20 µL peptides under designed concentrations (100, 200, and 400 µM) and further cultured for 24 h at 37 °C. Subsequently, the cells were added to 20 µL MTT solution (5 mg/mL) and incubated for 4 h. Finally, DMSO was added into each well, and the absorbance (A) at 490 nm was determined. The cell viability was calculated as:

$$\text{Cell viability (\%)} = (A_{\text{experiment group}} / A_{\text{control group}}) \times 100 \quad (2)$$

#### 3.7.2. Evaluation of NO and ET-1 Production

The NO and ET-1 contents of HUVECs were determined after a 24 h treatment of ACEi peptides [6]. HUVECs were processed in 6 well plates and the treating process with Cap (1 µM), NE (0.5 µM) or designed concentrations of ACEi peptides (100–400 µM) for 24 h, or treated with both NE (0.5 µM) and 200 µM ACEi peptides for 24 h. NO and ET-1 production in treated cells were measured by employing human NO and ET-1 assay kit as manufactures' protocol, separately.

#### 3.8. Statistical Analysis

All data are expressed as the mean ± standard deviation (SD) with triplicate and analyzed by SPSS 20.0 (SPSS Corporation, Chicago, IL, USA). Significant differences were obtained by employing ANOVA test with Dunnett or Tukey Test ( $p < 0.05$ ,  $p < 0.01$ , or  $p < 0.001$ ).

## 4. Conclusions

In conclusion, the conditions of Alcalase for hydrolyzing the skipjack tuna muscle protein were optimized using single-factor and response-surface experiments, and six ACEi peptides were purified from the protein hydrolysate prepared under optimum conditions of Alcalase and were identified as SP, VDRYF, VHGVV, YE, FEM, and FWRV, respectively. SP and VDRYF displayed noticeable ACEi activity, attributed to the effective interaction with the active sites/pockets of ACE by hydrogen bonding, electrostatic force, and hydrophobic interaction. Moreover, SP and VDRYF could alleviate the negative effects of NE-constrained NO production and NE-induced ET-1 secretion. The mentioned results suggest the huge potential of ACEi peptides of skipjack tuna muscle for nutraceutical or therapeutic-related use to regulate cardiovascular disease. The findings also demonstrate one conductive influence exerted by marine natural proteins as potential ACEi peptide sources for antihypertensive treatment. Our further studies will explore the in vivo experiment of the prepared ACEi peptides for clarifying their mechanisms to control high blood pressure.

**Author Contributions:** S.-L.Z.: Data curation, Methodology, Formal analysis. Q.-B.L.: Data curation, Writing—original draft. S.-K.S.: Data curation, Formal analysis. Y.-Q.Z.: Data curation, Methodology, Formal analysis. C.-F.C.: Conceptualization, Methodology, Supervision. B.W.: Supervision, Funding acquisition, Writing—review and editing. All authors have read and agreed to the published version of the manuscript.

**Funding:** This work was funded by the National Natural Science Foundation of China (No. 82073764), the Ten-thousand Talents Plan of Zhejiang Province (No. 2019R52026), and Science and Technology Planning Project of Zhoushan of China (No. 2019C21015).

**Institutional Review Board Statement:** Not applicable.

**Informed Consent Statement:** Not applicable.

**Data Availability Statement:** Data are contained within the article.

**Conflicts of Interest:** The authors declare no competing financial interest.

## Abbreviations

ACE: angiotensin-I-converting enzyme; ACEi, angiotensin-I-converting enzyme inhibitory; ET-1, endothelin-1; NO, nitric oxide; CVD, cardiovascular diseases; MW, molecular weight; Ang, angiotensin; Cap, captopril; NE, norepinephrine; eNOS, endothelial NO synthase; FAPGG, N-[3-(2-Furyl)acryloyl]-Phe-Gly-Gly; TMAP1, Ser-Pro (SP); TMAP2, Val-Asp-Arg-Tyr-Phe (VDRYF); TMAP3, Val-His-Gly-Val-Val (VHGVV); TMAP4, Tyr-Glu (YE); TMAP5, Phe-Glu-Met (FEM); TMAP6, Phe-Trp-Arg-Val (FWRV); AA, amino acid; WTAA, weight of total amino acid; WEAA, weight of essential amino acid; WHEAA, weight of half essential amino acid; WNEAA, weight of non-essential amino acid; TMPH, protein hydrolysate of tuna muscle prepared using Alcalase under the optimum hydrolysis conditions; GPC, gel permeation chromatography; RP-HPLC, Reversed-phase high performance liquid chromatography; HUVECs, Human umbilical vein endothelial cells; MTT, 3-(4,5-Dimethylthiazol-2-yl)-2,5-diphenyltetrazolium bromide.

## References

- Liu, X.; Li, F.; Zheng, Z.; Li, G.; Zhou, H.; Zhang, T.; Tang, Y.; Qin, W. Association of morning hypertension with chronic kidney disease progression and cardiovascular events in patients with chronic kidney disease and hypertension. *Nutr. Metab. Cardiovas.* **2022**, *12*, 021. [\[CrossRef\]](#)
- Thomas, H.; Diamond, J.; Vieco, A.; Chaudhuri, S.; Shinnar, E.; Cromer, S.; Perel, P.; Mensah, G.A.; Narula, J.; Johnson, C.O.; et al. Global atlas of cardiovascular disease 2000–2016: The path to prevention and control. *Glob. Heart* **2018**, *13*, 143–163. [\[CrossRef\]](#)
- Ning, D.S.; Ma, J.; Peng, Y.M.; Li, Y.; Chen, Y.T.; Li, S.X.; Liu, Z.; Li, Y.Q.; Zhang, Y.X.; Jian, Y.P.; et al. Apolipoprotein A-I mimetic peptide inhibits atherosclerosis by increasing tetrahydrobiopterin via regulation of GTP-cyclohydrolase 1 and reducing uncoupled endothelial nitric oxide synthase activity. *Atherosclerosis* **2021**, *328*, 83–91. [\[CrossRef\]](#)
- Abdelhedi, O.; Nasri, M. Basic and recent advances in marine antihypertensive peptides: Production, structure-activity relationship and bioavailability. *Trends Food Sci. Technol.* **2019**, *88*, 43–557. [\[CrossRef\]](#)
- Ju, D.T.; Kuo, W.W.; Ho, T.J.; Chang, R.L.; Lin, W.T.; Day, C.H.; Viswanadha, V.V.P.; Liao, P.H.; Huang, C.Y. Bioactive peptide VHVV upregulates the long-term memory-related biomarkers in adult spontaneously hypertensive rats. *Int. J. Mol. Sci.* **2019**, *20*, 3069. [\[CrossRef\]](#)
- Zhao, Y.Q.; Zhang, L.; Tao, J.; Chi, C.F.; Wang, B. Eight antihypertensive peptides from the protein hydrolysate of Antarctic krill (*Euphausia superba*): Isolation, identification, and activity evaluation on human umbilical vein endothelial cells (HUVECs). *Food Res. Int.* **2019**, *121*, 197–204. [\[CrossRef\]](#)
- Jimsheena, V.K.; Gowda, L.R. Angiotensin I-converting enzyme (ACE) inhibitory peptides derived from Arachin by simulated gastric digestion. *Food Chem.* **2011**, *125*, 561–569. [\[CrossRef\]](#)
- Hu, X.M.; Wang, Y.M.; Zhao, Y.Q.; Chi, C.F.; Wang, B. Antioxidant peptides from the protein hydrolysate of monkfish (*Lophius litulon*) muscle: Purification, identification, and cytoprotective function on HepG2 cells damage by H<sub>2</sub>O<sub>2</sub>. *Mar. Drugs* **2020**, *18*, 153. [\[CrossRef\]](#)
- Chakrabarti, S.; Guha, S.; Majumder, K. Food-derived bioactive peptides in human health: Challenges and opportunities. *Nutrients* **2018**, *10*, 1738. [\[CrossRef\]](#)
- Pan, X.Y.; Wang, Y.M.; Li, L.; Chi, C.F.; Wang, B. Four antioxidant peptides from protein hydrolysate of red stingray (*Dasyatis akajebi*) cartilages: Isolation, identification, and in vitro activity evaluation. *Mar. Drugs* **2019**, *17*, 263. [\[CrossRef\]](#)
- Abachi, S.; Bazinet, L.; Beaulieu, L. Antihypertensive and angiotensin-I-converting enzyme (ACE)-inhibitory peptides from fish as potential cardioprotective compounds. *Mar. Drugs* **2019**, *17*, 613. [\[CrossRef\]](#)
- Fan, H.; Liao, W.; Wu, J. Molecular interactions, bioavailability, and cellular mechanisms of angiotensin-converting enzyme inhibitory peptides. *J. Food Biochem.* **2019**, *43*, e12572. [\[CrossRef\]](#)
- Urbizo-Reyes, U.; Liceaga, A.M.; Reddivari, L.; Kim, K.H.; Anderson, J.M. Enzyme kinetics, molecular docking, and in silico characterization of canary seed (*Phalaris canariensis* L.) peptides with ACE and pancreatic lipase inhibitory activity. *J. Funct. Foods* **2022**, *88*, 104892. [\[CrossRef\]](#)
- Zhang, Y.; Pan, D.; Yang, Z.; Gao, X.; Dang, Y. Angiotensin I-Converting enzyme (ACE) inhibitory and dipeptidyl peptidase-4 (DPP-IV) inhibitory activity of umami peptides from *Ruditapes philippinarum*. *LWT-Food Sci. Technol.* **2021**, *144*, 111265. [\[CrossRef\]](#)
- Lin, K.; Ma, Z.; Ramachandran, M.; Souza, C.D.; Han, X.; Zhang, L.W. ACE inhibitory peptide KYIPIQ derived from yak milk casein induces nitric oxide production in HUVECs and diffuses via a transcellular mechanism in Caco-2 monolayers. *Process Biochem.* **2020**, *99*, 103–111. [\[CrossRef\]](#)

16. Chen, H.; Ma, L.; Qi, J.; Cao, J.; Tan, Y. Optimization of fermentation conditions for the production of angiotensin-converting enzyme (ACE) inhibitory peptides from cow milk by *Lactobacillus bulgaricus* LB6. *Acta Univ. Cibiniensis Food Technol.* **2019**, *23*, 19–26. [[CrossRef](#)]
17. Song, T.; Lv, M.; Zhang, L.; Zhang, X.; Song, G.; Huang, M.; Zheng, L.; Zhao, M. The protective effects of tripeptides VPP and IPP against small extracellular vesicles from angiotensin II-induced vascular smooth muscle cells mediating endothelial dysfunction in human umbilical vein endothelial cells. *J. Agric. Food Chem.* **2020**, *68*, 13730–13741. [[CrossRef](#)]
18. Beltran-Barrientos, L.M.; Hernandez-Mendoza, A.; Torres-Llanaez, M.J.; Gonzalez-Cordova, A.F.; Vallejo-Cordoba, B. Fermented-milk as antihypertensive functional food. *J. Dairy Sci.* **2016**, *99*, 4099–4110. [[CrossRef](#)]
19. Yu, D.; Chi, C.F.; Wang, B.; Ding, G.F.; Li, Z.R. Characterization of acid and pepsin soluble collagens from spine and skull of skipjack tuna (*Katsuwonus pelamis*). *Chin. J. Nat. Med.* **2014**, *12*, 712–720. [[CrossRef](#)]
20. Wang, J.; Wang, Y.M.; Li, L.Y.; Chi, C.F.; Wang, B. Twelve antioxidant peptides from protein hydrolysate of skipjack tuna (*Katsuwonus pelamis*) roe prepared by Flavourzyme: Purification, sequence identification, and activity evaluation. *Front. Nutr.* **2022**, *8*, 813780. [[CrossRef](#)]
21. Kim, Y.M.; Kim, E.Y.; Kim, I.H.; Nam, T.J. Peptide derived from desalinated boiled tuna extract inhibits adipogenesis through the down regulation of C/EBP- $\alpha$  and PPAR- $\gamma$  in 3T3-L1 adipocytes. *Int. J. Mol. Sci.* **2015**, *35*, 1362–1368.
22. Wang, Y.M.; Li, X.Y.; Wang, J.; He, Y.; Chi, C.F.; Wang, B. Antioxidant peptides from protein hydrolysate of skipjack tuna milt: Purification, identification, and cytoprotection on H<sub>2</sub>O<sub>2</sub> damaged human umbilical vein endothelial cells. *Process Biochem.* **2022**, *113*, 258–269. [[CrossRef](#)]
23. Yang, X.R.; Zhao, Y.Q.; Qiu, Y.T.; Chi, C.F.; Wang, B. Preparation and characterization of gelatin and antioxidant peptides from gelatin hydrolysate of skipjack tuna (*Katsuwonus pelamis*) bone stimulated by in vitro gastrointestinal digestion. *Mar. Drugs* **2019**, *17*, 78. [[CrossRef](#)]
24. Lee, S.H.; Qian, Z.J.; Kim, S.K. A novel angiotensin I converting enzyme inhibitory peptide from tuna frame protein hydrolysate and its antihypertensive effect in spontaneously hypertensive rats. *Food Chem.* **2010**, *118*, 96–102. [[CrossRef](#)]
25. Qiu, Y.T.; Wang, Y.M.; Yang, X.R.; Zhao, Y.Q.; Chi, C.F.; Wang, B. Gelatin and antioxidant peptides from gelatin hydrolysate of skipjack tuna (*Katsuwonus pelamis*) scales: Preparation, identification and activity evaluation. *Mar. Drugs* **2019**, *17*, 565. [[CrossRef](#)]
26. Han, J.; Huang, Z.; Tang, S.; Lu, C.; Wan, H.; Zhou, J.; Li, Y.; Ming, T.; Jim Wang, Z.; Su, X. The novel peptides ICRD and LCGEC screened from tuna roe show antioxidative activity via Keap1/Nrf2-ARE pathway regulation and gut microbiota modulation. *Food Chem.* **2020**, *327*, 127094. [[CrossRef](#)]
27. Martínez-Alvarez, O.; Batista, I.; Ramos, C.; Montero, P. Enhancement of ACE and prolyl oligopeptidase inhibitory potency of protein hydrolysates from sardine and tuna by-products by simulated gastrointestinal digestion. *Food Funct.* **2016**, *7*, 2066–2073. [[CrossRef](#)]
28. Zhang, L.; Zhao, G.X.; Zhao, Y.Q.; Qiu, Y.T.; Chi, C.F.; Wang, B. Identification and active evaluation of antioxidant peptides from protein hydrolysates of skipjack tuna (*Katsuwonus pelamis*) head. *Antioxidants* **2019**, *8*, 318. [[CrossRef](#)]
29. Maeda, H.; Hosomi, R.; Fukuda, M.; Ikeda, Y.; Yoshida, M.; Fukunaga, K. Dietary tuna dark muscle protein attenuates hepatic steatosis and increases serum high-density lipoprotein cholesterol in obese type-2 diabetic/obese KK-A(y) mice. *J. Food Sci.* **2017**, *82*, 1231–1238. [[CrossRef](#)]
30. Chi, C.F.; Hu, F.Y.; Wang, B.; Li, Z.R.; Luo, H.Y. Influence of amino acid compositions and peptide profiles on antioxidant capacities of two protein hydrolysates from skipjack tuna (*Katsuwonus pelamis*) dark muscle. *Mar. Drugs* **2015**, *13*, 2580–2601. [[CrossRef](#)]
31. Abdelhedi, O.; Nasri, R.; Jridi, M.; Mora, L.; Oseguera-Toledo, M.E.; Aristoy, M.C.; Amara, I.B.; Toldrá, F.; Nasri, M. In silico analysis and antihypertensive effect of ACE-inhibitory peptides from smooth-hound viscera protein hydrolysate: Enzyme-peptide interaction study using molecular docking simulation. *Process Biochem.* **2017**, *58*, 145–159. [[CrossRef](#)]
32. Wang, B.; Li, L.; Chi, C.F.; Ma, J.H.; Luo, H.Y.; Xu, Y.F. Purification and characterisation of a novel antioxidant peptide derived from blue mussel (*Mytilus edulis*) protein hydrolysate. *Food Chem.* **2013**, *138*, 1713–1717. [[CrossRef](#)] [[PubMed](#)]
33. Sila, A.; Bougatef, A. Antioxidant peptides from marine by-products: Isolation, identification and application in food systems. A review. *J. Funct. Foods* **2016**, *21*, 10–26. [[CrossRef](#)]
34. Pan, X.; Zhao, Y.Q.; Hu, F.Y.; Wang, B. Preparation and identification of antioxidant peptides from protein hydrolysate of skate (*Raja porosa*) cartilage. *J. Funct. Foods* **2016**, *25*, 220–230. [[CrossRef](#)]
35. Wang, W.Y.; Zhao, Y.Q.; Zhao, G.X.; Chi, C.F.; Wang, B. Antioxidant peptides from collagen hydrolysate of redlip croaker (*Pseudosciaena polyactis*) scales: Preparation, characterization, and cytoprotective effects on H<sub>2</sub>O<sub>2</sub>-damaged HepG2 cells. *Mar. Drugs* **2020**, *18*, 156. [[CrossRef](#)]
36. Chi, C.F.; Hu, F.Y.; Wang, B.; Li, T.; Ding, G.F. Antioxidant and anticancer peptides from protein hydrolysate of blood clam (*Tegillarca granosa*) muscle. *J. Funct. Foods* **2015**, *15*, 301–313. [[CrossRef](#)]
37. Tao, J.; Zhao, Y.Q.; Chi, C.F.; Wang, B. Bioactive peptides from cartilage protein hydrolysate of spotless smoothhound and their antioxidant activity in vitro. *Mar. Drugs* **2018**, *16*, 100. [[CrossRef](#)]
38. Zhang, S.X.; Zhao, G.X.; Suo, S.K.; Wang, Y.M.; Chi, C.F.; Wang, B. Purification, identification, activity evaluation, and stability of antioxidant peptides from Alcalase hydrolysate of Antarctic krill (*Euphausia superba*) proteins. *Mar. Drugs* **2021**, *19*, 347. [[CrossRef](#)]

39. Sun, L.; Wu, S.; Zhou, L.; Wang, F.; Lan, X.; Sun, J.; Tong, Z.; Liao, D. Separation and characterization of angiotensin I converting enzyme (ACE) inhibitory peptides from *Saurida elongata* proteins hydrolysate by IMAC-Ni<sup>2+</sup>. *Mar. Drugs* **2017**, *15*, 29–39. [[CrossRef](#)]
40. Intarasirisawat, R.; Benjakula, S.; Wub, J.; Visessanguan, W. Isolation of antioxidative and ACE inhibitory peptides from protein hydrolysate of skipjack (*Katsurwana pelamis*) roe. *J. Funct. Foods* **2013**, *5*, 1854–1862. [[CrossRef](#)]
41. Ngo, D.H.; Kang, K.H.; Ryu, B.; Vo, T.S.; Jung, W.K.; Byun, H.G.; Kim, S.K. Angiotensin-I converting enzyme inhibitory peptides from antihypertensive skate (*Okamejei kenoei*) skin gelatin hydrolysate in spontaneously hypertensive rats. *Food Chem.* **2015**, *174*, 37–43. [[CrossRef](#)] [[PubMed](#)]
42. Alemán, A.; Gómez-Guillén, M.C.; Montero, P. Identification of ace-inhibitory peptides from squid skin collagen after in vitro gastrointestinal digestion. *Food Res. Int.* **2013**, *54*, 790–795. [[CrossRef](#)]
43. Wijesekara, I.; Qian, Z.J.; Ryu, B.; Ngo, D.H.; Kim, S.K. Purification and identification of antihypertensive peptides from seaweed pipefish (*Syngnathus schlegelii*) muscle protein hydrolysate. *Food Res. Int.* **2011**, *44*, 703–707. [[CrossRef](#)]
44. Ngo, D.H.; Ryu, B.; Kim, S.K. Active peptides from skate (*Okamejei kenoei*) skin gelatin diminish angiotensin-I converting enzyme activity and intracellular free radical-mediated oxidation. *Food Chem.* **2014**, *143*, 246–255. [[CrossRef](#)]
45. Auwal, S.M.; Abidin, N.Z.; Zarei, M.; Tan, C.P.; Saari, N. Identification, structure-activity relationship and in silico molecular docking analyses of five novel angiotensin I-converting enzyme (ACE)-inhibitory peptides from stone fish (*Actinopyga lecanora*) hydrolysates. *PLoS ONE* **2019**, *14*, e0197644.
46. Chen, J.; Liu, Y.; Wang, G.; Sun, S.; Liu, R.; Hong, B.; Gao, R.; Bai, K. Processing optimization and characterization of angiotensin-I-converting enzyme inhibitory peptides from lizardfish (*Synodus macrops*) scale gelatin. *Mar. Drugs* **2018**, *16*, 228. [[CrossRef](#)]
47. Wang, X.; Chen, H.; Fu, X.; Li, S.; Wei, J. A novel antioxidant and ACE inhibitory peptide from rice bran protein: Biochemical characterization and molecular docking study. *LWT-Food Sci. Technol.* **2017**, *75*, 93–99. [[CrossRef](#)]
48. Xu, Z.; Wu, C.; Sun-Waterhouse, D.; Zhao, T.; Waterhouse, G.I.N.; Zhao, M.; Su, G. Identification of post-digestion angiotensin-I converting enzyme (ACE) inhibitory peptides from soybean protein isolate: Their production conditions and in silico molecular docking with ACE. *Food Chem.* **2021**, *345*, 128855. [[CrossRef](#)] [[PubMed](#)]
49. Kleekayai, T.; Harnedy, P.A.; O’Keeffe, M.B.; Poyarkov, A.A.; CunhaNeves, A.; Suntornasuk, W.; FitzGerald, R.J. Extraction of antioxidant and ACE inhibitory peptides from Thai traditional fermented shrimp pastes. *Food Chem.* **2015**, *176*, 441–447. [[CrossRef](#)] [[PubMed](#)]
50. Sun, S.; Xu, X.; Sun, X.; Zhang, X.; Chen, X.; Xu, N. Preparation and identification of ACE inhibitory peptides from the marine macroalga *Ulva intestinalis*. *Mar. Drugs* **2019**, *17*, 179. [[CrossRef](#)]
51. Abdelhedi, O.; Nasri, R.; Mora, L.; Jridi, M.; Toldra, F.; Nasri, M. In silico analysis and molecular docking study of angiotensin I-converting enzyme inhibitory peptides from smooth-hound viscera protein hydrolysates fractionated by ultrafiltration. *Food Chem.* **2018**, *239*, 453–463. [[CrossRef](#)]
52. Deddish, P.A.; Wang, J.; Michel, B.; Morris, P.W.; Davidson, N.O.; Skidgel, R.A.; Erdős, E.G. Naturally occurring active N-domain of human angiotensin I-converting enzyme. *Proc. Natl. Acad. Sci. USA* **1994**, *91*, 7807–7811. [[CrossRef](#)]
53. Zheng, Y.; Li, Y.; Zhang, Y.; Ruan, X.; Zhang, R. Purification, characterization, synthesis, in vitro ACE inhibition and in vivo antihypertensive activity of bioactive peptides derived from oil palm kernel glutelin-2 hydrolysates. *J. Funct. Foods* **2017**, *28*, 48–58. [[CrossRef](#)]
54. Hayes, M.; Mora, L.; Hussey, K.; Aluko, R.E. Boarfish protein recovery using the pH-shift process and generation of protein hydrolysates with ACE-inhibitory and antihypertensive bioactivities in spontaneously hypertensive rats. *Innov. Food Sci. Emerg.* **2016**, *37*, 253–260. [[CrossRef](#)]
55. Ko, J.Y.; Kang, N.; Lee, J.H.; Kim, J.S.; Kim, W.S.; Park, S.J.; Kim, Y.T.; Jeon, Y.J. Angiotensin I-converting enzyme inhibitory peptides from an enzymatic hydrolysate of flounder fish (*Paralichthys olivaceus*) muscle as a potent anti-hypertensive agent. *Process Biochem.* **2016**, *51*, 535–541. [[CrossRef](#)]
56. Wu, S.; Sun, J.; Tong, Z.; Lan, X.; Zhao, Z.; Liao, D. Optimization of hydrolysis conditions for the production of angiotensin-I converting enzyme-inhibitory peptides and isolation of a novel peptide from lizard fish (*Saurida elongata*) muscle protein hydrolysate. *Mar. Drugs* **2012**, *10*, 1066–1080. [[CrossRef](#)] [[PubMed](#)]
57. Cai, S.Y.; Wang, Y.M.; Zhao, Y.Q.; Chi, C.F.; Wang, B. Cytoprotective effect of antioxidant pentapeptides from the protein hydrolysate of swim bladders of miuiy croaker (*Miichthys miuiy*) against H<sub>2</sub>O<sub>2</sub>-mediated human umbilical vein endothelial cell (HUVEC) injury. *Int. J. Mol. Sci.* **2019**, *20*, 5425. [[CrossRef](#)]
58. Zhao, W.H.; Luo, Q.B.; Pan, X.; Chi, C.F.; Sun, K.L.; Wang, B. Preparation, identification, and activity evaluation of ten antioxidant peptides from protein hydrolysate of swim bladders of miuiy croaker (*Miichthys miuiy*). *J. Funct. Foods* **2018**, *47*, 503–511. [[CrossRef](#)]
59. Ito, H.; Hirata, Y.; Adachi, S.; Tanaka, M.; Tsujino, M.; Koike, A.; Nogami, A.; Murumo, F.; Hiroe, M. Endothelin-1 is an autocrine/paracrine factor in the mechanism of angiotensin II-induced hypertrophy in cultured rat cardiomyocytes. *J. Clin. Invest.* **1993**, *92*, 398–403. [[CrossRef](#)]
60. Li, Z.R.; Wang, B.; Chi, C.F.; Zhang, Q.H.; Gong, Y.D.; Tang, J.J.; Luo, H.Y.; Ding, G.F. Isolation and characterization of acid soluble collagens and pepsin soluble collagens from the skin and bone of spanish mackerel (*Scomberomorus niphonius*). *Food Hydrocolloid.* **2013**, *31*, 103–113. [[CrossRef](#)]

61. He, Y.; Pan, X.; Chi, C.F.; Sun, K.L.; Wang, B. Ten new pentapeptides from protein hydrolysate of miiuy croaker (*Miichthys miiuy*) muscle: Preparation, identification, and antioxidant activity evaluation. *LWT-Food Sci.Technol.* **2019**, *105*, 1–8. [[CrossRef](#)]
62. Korkmaz, K.; Tokur, B. Optimization of hydrolysis conditions for the production of protein hydrolysates from fishss wastes using response surface methodology. *Food Biosci.* **2022**, *45*, 101312. [[CrossRef](#)]
63. Wang, D.; Shahidi, F. Protein hydrolysate from turkey meat and optimization of its antioxidant potential by response surface methodology. *Poultry Sci.* **2018**, *97*, 1824–1831. [[CrossRef](#)] [[PubMed](#)]
64. Chi, C.F.; Hu, F.Y.; Wang, B.; Ren, X.J.; Deng, S.G.; Wu, C.W. Purification and characterization of three antioxidant peptides from protein hydrolyzate of croceine croaker (*Pseudosciaena crocea*) muscle. *Food Chem.* **2015**, *168*, 662–667. [[CrossRef](#)]
65. Pan, X.; Zhao, Y.Q.; Hu, F.Y.; Chi, C.F.; Wang, B. Anticancer activity of a hexapeptide from skate (*Raja porosa*)cartilage protein hydrolysate in HeLa cells. *Mar. Drugs* **2016**, *14*, 153. [[CrossRef](#)]
66. Wang, Y.M.; Pan, X.; He, Y.; Chi, C.F.; Wang, B. Hypolipidemic activities of two pentapeptides (VIAPW and IRWWW) from miiuy croaker (*Miichthys miiuy*) muscle on lipid accumulation in HepG2 cells through regulation of AMPK pathway. *Appl. Sci.* **2020**, *10*, 817. [[CrossRef](#)]





## Article

# Sesquiterpene and Sorbicillinoid Glycosides from the Endophytic Fungus *Trichoderma longibrachiatum* EN-586 Derived from the Marine Red Alga *Laurencia obtusa*

Ying Wang<sup>1,2,3</sup>, Xiao-Ming Li<sup>1,2,4</sup>, Sui-Qun Yang<sup>1,2,4</sup>, Fan-Zhong Zhang<sup>1,2,3</sup>, Bin-Gui Wang<sup>1,2,3,4</sup>, Hong-Lei Li<sup>1,2,4,\*</sup> and Ling-Hong Meng<sup>1,2,3,4,\*</sup>

- <sup>1</sup> CAS and Shandong Province Key Laboratory of Experimental Marine Biology, Institute of Oceanology, Chinese Academy of Sciences, Nanhai Road 7, Qingdao 266071, China; wangying194@mails.ucas.ac.cn (Y.W.); lixmqd@qdio.ac.cn (X.-M.L.); suiqunyang@163.com (S.-Q.Y.); fanyzsfz@163.com (F.-Z.Z.); wangbg@ms.qdio.ac.cn (B.-G.W.)
  - <sup>2</sup> Laboratory of Marine Biology and Biotechnology, Qingdao National Laboratory for Marine Science and Technology, Wenhai Road 1, Qingdao 266237, China
  - <sup>3</sup> University of Chinese Academy of Sciences, Yuquan Road 19A, Beijing 100049, China
  - <sup>4</sup> Center for Ocean Mega-Science, Chinese Academy of Sciences, Nanhai Road 7, Qingdao 266071, China
- \* Correspondence: lihonglei@qdio.ac.cn (H.-L.L.); m8545303@163.com (L.-H.M.);  
Tel.: +86-532-8289-8890 (H.-L.L. & L.-H.M.)

**Abstract:** An unusual sesquiterpene glycoside trichoacorside A (**1**) and two novel sorbicillinoid glycosides sorbicillisides A (**2**) and B (**3**), together with a known compound sorbicillin (**4**), were isolated and identified from the culture extract of an endophytic fungus *Trichoderma longibrachiatum* EN-586, obtained from the marine red alga *Laurencia obtusa*. Trichoacorside A (**1**) is the first representative of a glucosamine-coupled acorane-type sesquiterpenoid. Their structures were elucidated based on detailed interpretation of NMR and mass spectroscopic data. The absolute configurations were determined by X-ray crystallographic analysis, chemical derivatization, and DP+ probability analysis. The antimicrobial activities of compounds **1–4** against several human, aquatic, and plant pathogens were evaluated.

**Keywords:** *Trichoderma longibrachiatum*; sesquiterpene glycoside; secondary metabolites; antimicrobial activity

**Citation:** Wang, Y.; Li, X.-M.; Yang, S.-Q.; Zhang, F.-Z.; Wang, B.-G.; Li, H.-L.; Meng, L.-H. Sesquiterpene and Sorbicillinoid Glycosides from the Endophytic Fungus *Trichoderma longibrachiatum* EN-586 Derived from the Marine Red Alga *Laurencia obtusa*. *Mar. Drugs* **2022**, *20*, 177. <https://doi.org/10.3390/md20030177>

Academic Editors: Yonghong Liu and Xuefeng Zhou

Received: 16 February 2022

Accepted: 25 February 2022

Published: 28 February 2022

**Publisher's Note:** MDPI stays neutral with regard to jurisdictional claims in published maps and institutional affiliations.



**Copyright:** © 2022 by the authors. Licensee MDPI, Basel, Switzerland. This article is an open access article distributed under the terms and conditions of the Creative Commons Attribution (CC BY) license (<https://creativecommons.org/licenses/by/4.0/>).

## 1. Introduction

The prevalence of microbial resistance has become a serious public health threat, highlighting the urgency of screening for new active molecules [1]. Acorane-type sesquiterpenes and sorbicillinoids are common secondary metabolites discovered in several genera of fungi, which displayed various biological activities, including antimicrobial, cytotoxic, anti-inflammatory, and radical-scavenging activities [2–5]. Though related analogues with unique and diverse structural features have been reported, their glycosides are unusual in natural products research. Marine-derived fungi have shown great potential for structurally unique secondary metabolites with interesting biological and pharmacological properties [6,7], among which algicolous fungi represent an important source of active metabolites [7,8].

The marine red alga *Laurencia obtusa* distributed widely on the coastlines and was used as a traditional medicinal and edible species in China [9,10]. In our ongoing research for bioactive secondary metabolites from marine-derived fungi [11–14], the endophytic fungus *Trichoderma longibrachiatum* EN-586, which was obtained from the inner tissue of the marine red alga *Laurencia obtusa*, attracted our attention due to its unique secondary metabolite profile. Chemical investigation on the culture extract of *T. longibrachiatum* EN-586 resulted in the isolation and identification of an unusual sesquiterpene glycoside, trichoacorside

A (1), and two novel sorbicillinoid glycosides, sorbicillisides A (2) and B (3), together with a known compound sorbicillin (4). Herein, we report the chemical investigation of a rice-based culture of *T. longibrachiatum* EN-586 including the isolation, structure elucidation, and biological evaluation of compounds 1–4.

## 2. Results and Discussion

### 2.1. Structure Elucidation

Isolation and purification of the EtOAc extract of *T. longibrachiatum* EN-586 on solid rice medium by a combination of column chromatography including Lobar LiChroprep RP-18, silica gel, Sephadex LH-20, and semipreparative HPLC, yielded compounds 1–4 (Figure 1).

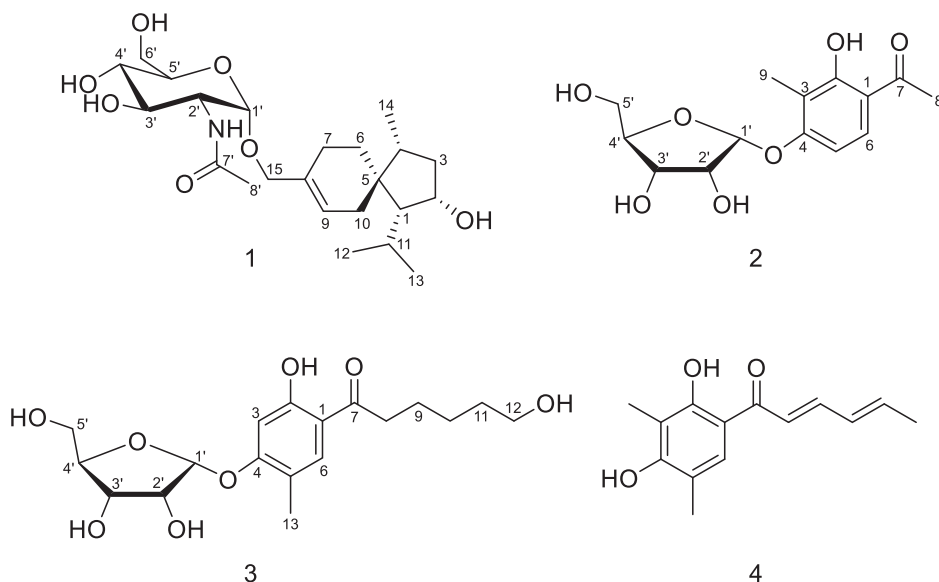


Figure 1. Chemical structures of compounds 1–4.

Trichoacorside A (1) was obtained as yellowish oil and its molecular formula was deduced to be  $C_{23}H_{39}NO_7$  by HRESIMS ion peak at  $m/z$  442.2799  $[M + H]^+$  (calcd for  $C_{23}H_{40}NO_7$ , 442.2799), with five degrees of unsaturation (Figure S7). The  $^{13}C$  NMR and DEPT data of 1 (Table 1 and Figure S2) showed 23 carbon signals, containing four methyls, six methylenes (including two oxygenated), 10 methines (including five oxygenated, one nitrogenated, and one olefinic), and three non-protonated carbons (including one olefinic and one carbonyl). Its  $^1H$  NMR and HSQC spectra (Table 1 and Figures S1 and S4), allowed the assignment of five additional exchangeable protons at  $\delta_H$  4.46, 4.54, 4.80, 5.03, and 7.60. Detailed analysis of the NMR data indicated that compound 1 was a sesquiterpene glycoside. The aglycon was found to be an acorane-type sesquiterpene, which was similar to 2 $\beta$ -hydroxytrichoacorenol [3]. However, signals for the hydroxylated methine at C-7 ( $\delta_{C/H}$  69.0/4.25) in 2 $\beta$ -hydroxytrichoacorenol disappeared in those of 1. Instead, signals for an additional methylene resonating at  $\delta_C$  26.2 and  $\delta_H$  1.38, 1.71 ( $CH_2$ -7) were observed in the NMR spectra of 1. These data suggested that the aglycon was a dehydroxylated analogue of 2 $\beta$ -hydroxytrichoacorenol at C-7, which was confirmed by the COSY correlation between H-6 and H-7 (Figure S3) as well as the HMBC correlations from H-6 to C-8 and C-10 and from H-7 to C-5, C-9, and C-15 (Figure S5a–c). Moreover, resonances of the methyl group at  $\delta_C$  19.4 and  $\delta_H$  1.76 ( $CH_3$ -15) in the NMR spectra of 2 $\beta$ -hydroxytrichoacorenol were replaced by an oxygenated methylene resonating at  $\delta_C$  66.6 and  $\delta_H$  4.01 and 4.08 ( $CH_2$ -15)

in **1**, accounting for the glycosidic site at C-15, which was further supported by the key HMBC correlation from H-1' to C-15. The *N*-acetylglucosamine was established by the relevant correlations from H-1' through H-2', H-3', and H-4' to H-5', and then to H-6' and from the proton of 2'-NH to H-2' in the COSY spectrum and by the key HMBC correlations from H-1' to C-5' and from the proton of 2'-NH to C-7' (Figure 2), and by the identical coupling patterns to the *N*-acetylglucosamine part of deinococcucins A–D [11], as well as by the related NOESY correlations (Figure 3). The chemical shift and coupling data of the anomeric proton at  $\delta_{\text{H}}$  4.65 (1H, d,  $J = 3.4$ , H-1') in the  $^1\text{H}$  NMR spectrum were indicative of an  $\alpha$ -configuration [15,16].

**Table 1.**  $^1\text{H}$  and  $^{13}\text{C}$  NMR data for compounds **1–3** in DMSO- $d_6$  <sup>a</sup>.

| No.   | 1  |                       | 2                             |                       | 3                             |                       |
|-------|--|-----------------------|-------------------------------|-----------------------|-------------------------------|-----------------------|
|       | $\delta_{\text{H}}$ (J in Hz)                          | $\delta_{\text{C}}$   | $\delta_{\text{H}}$ (J in Hz) | $\delta_{\text{C}}$   | $\delta_{\text{H}}$ (J in Hz) | $\delta_{\text{C}}$   |
| 1     | 1.24, overlap  | 59.3, CH              |                               | 113.9, C              |                               | 113.2, C              |
| 2     | 4.22, brs  | 64.6, CH              |                               | 161.2, C              |                               | 162.0, C              |
| 3     | $\alpha$ 1.12, dd (11.4, 3.7)<br>$\beta$ 1.67, m       | 28.5, CH <sub>2</sub> |                               | 113.9, C              | 6.59, s                       | 102.1, CH             |
| 4     | 1.55, m  | 46.2, CH              |                               | 161.0, C              |                               | 161.3, C              |
| 5     |  | 44.2, C               | 6.75, d (9.0)                 | 106.2, CH             |                               | 118.5, C              |
| 6     | $\alpha$ 1.19, m<br>$\beta$ 1.63, m                    | 31.8, CH <sub>2</sub> | 7.77, d (9.0)                 | 130.2, CH             | 7.71, s                       | 131.8, CH             |
| 7     | $\alpha$ 1.38, m<br>$\beta$ 1.71, overlap              | 26.2, CH <sub>2</sub> |                               | 203.9, C              |                               | 205.3, C              |
| 8     |  | 137.3, C              | 2.58, s                       | 26.4, CH <sub>3</sub> | 2.97, t (7.3)                 | 37.6, CH <sub>2</sub> |
| 9     | 5.69, brs  | 124.1, CH             | 2.05, s                       | 7.8, CH <sub>3</sub>  | 1.62, m                       | 24.1, CH <sub>2</sub> |
| 10    | $\alpha$ 1.79, overlap<br>$\beta$ 2.07, dt (18.9, 3.0) | 34.5, CH <sub>2</sub> |                               |                       | 1.35, m                       | 25.2, CH <sub>2</sub> |
| 11    | 1.61, m  | 29.8, CH              |                               |                       | 1.45, m                       | 32.3, CH <sub>2</sub> |
| 12    | 0.88, d (6.5)  | 23.3, CH <sub>3</sub> |                               |                       | 3.39, dt (6.3, 11.5)          | 60.6, CH <sub>2</sub> |
| 13    | 0.83, d (6.5)  | 22.8, CH <sub>3</sub> |                               |                       | 2.13, s                       | 15.3, CH <sub>3</sub> |
| 14    | 0.80, d (6.7)  | 14.2, CH <sub>3</sub> |                               |                       |                               |                       |
| 15    | $\alpha$ 4.08, d (13.0)<br>$\beta$ 4.01, d (13.0)      | 66.6, CH <sub>2</sub> |                               |                       |                               |                       |
| 2-OH  | 4.54, d (6.0)  |                       | 12.84, s                      |                       | 12.51, s                      |                       |
| 12-OH |  |                       |                               |                       | 4.33, t (5.1)                 |                       |
| 1'    | 4.65, d (3.4)  | 96.1, CH              | 5.75, d (4.4)                 | 99.9, CH              | 5.71, d (4.4)                 | 99.7, CH              |
| 2'    | 3.65, td (8.1, 3.4)                                    | 53.9, CH              | 4.11, m                       | 71.4, CH              | 4.11, m                       | 71.4, CH              |
| 3'    | 3.45, dd (10.9, 8.1)                                   | 70.8, CH              | 3.96, overlap                 | 69.1, CH              | 3.96, overlap                 | 69.1, CH              |
| 4'    | 3.15, d (9.0)  | 70.6, CH              | 3.98, overlap                 | 86.5, CH              | 3.96, overlap                 | 86.5, CH              |
| 5'    | 3.39, ddd (10.0, 5.4, 2.3)                             | 72.9, CH              | 3.47, d (3.6)                 | 61.4, CH <sub>2</sub> | 3.47, dd (3.6, 4.9)           | 61.4, CH <sub>2</sub> |
| 6'    | $\alpha$ 3.49, overlapped<br>$\beta$ 3.60, m           | 60.8, CH <sub>2</sub> |                               |                       |                               |                       |
| 7'    |  | 169.3, C              |                               |                       |                               |                       |
| 8'    | 1.82, s  | 22.6, CH <sub>3</sub> |                               |                       |                               |                       |
| 2'-OH |  |                       | 4.61, brs                     |                       | 4.56, d (8.7)                 |                       |
| 2'-NH | 7.60, d (8.1)  |                       |                               |                       | 4.92, d (4.6)                 |                       |
| 3'-OH | 4.80, brs  |                       | 4.95, brs                     |                       |                               |                       |
| 4'-OH | 5.03, brs  |                       |                               |                       |                               |                       |
| 5'-OH |  |                       | 4.80, brs                     |                       | 4.81, t (4.9)                 |                       |
| 6'-OH | 4.46, dd (11.8, 3.5)                                   |                       |                               |                       |                               |                       |

<sup>a</sup>  $^1\text{H}$  and  $^{13}\text{C}$  data were recorded at 500 and 125 MHz, respectively.

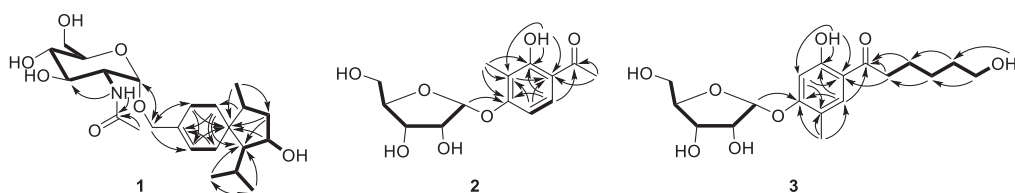


Figure 2. Key HMBC (arrows) and COSY (bold lines) correlations of compounds 1–3.

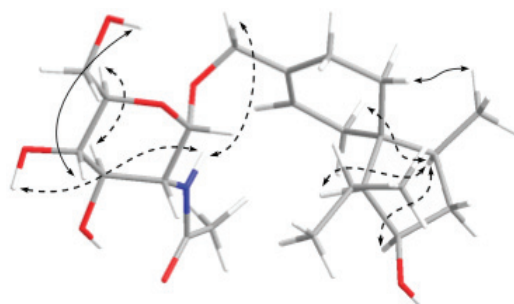


Figure 3. Key NOESY correlations for compound 1. (Solid line indicates  $\beta$ -orientation and dashed line represents  $\alpha$ -orientation).

The presence of glucosamine moiety and its absolute configuration of compound 1 was further determined by gas chromatography-mass spectroscopy (GC/MS) analysis of the acidic hydrolysate of 1 derivatized with hexamethyldisilazane (HMDS) and trimethylchlorosilane (TMS-Cl). The derivative of glucosamine from *N*-acetylglucosamine in 1 exhibited the same retention time as that of the authentic D-glucosamine derivative, indicating the D-form glucosamine in 1 (Figure S24) [15].

The relative configuration of sesquiterpene moiety was established by analysis of the NOESY spectrum (Figure 3 and Figure S6). The key NOE correlations from H-4 to H-1, H-2, and H-10 oriented these protons toward the same side, while the NOE enhancement from H<sub>3</sub>-14 to H-6 indicated that they were on the opposite side of the molecule. To establish the absolute configuration of the molecule, two possible isomers [(1*S*,2*R*,4*S*,5*R*)-*N*-acetyl- $\alpha$ -D-glucosamine and (1*R*,2*S*,4*R*,5*S*)-*N*-acetyl- $\alpha$ -D-glucosamine] (Figure 4) were subjected to DP4+ probability analysis. The proton and carbon data of the two possible isomers were calculated based on DP4+ protocol and the results were analyzed with the experimental values [17]. The statistical DP4+ probability analysis of both <sup>1</sup>H and <sup>13</sup>C data suggested that the isomer (1*R*,2*S*,4*R*,5*S*)-*N*-acetyl- $\alpha$ -D-glucosamine was the equivalent structure with the probability of 100.00% (above 95%) (Figure S25) [17].

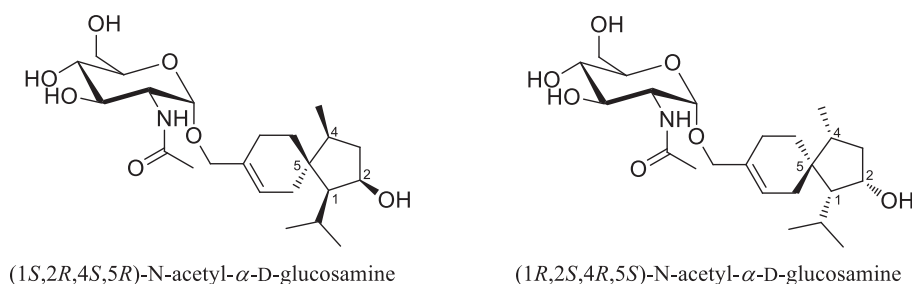


Figure 4. Structures of two possible isomers for DP4+ probability analysis of 1.

Sorbicilliside A (**2**) was originally isolated as a colorless solid. The molecular formula was determined as  $C_{14}H_{18}O_7$  according to the HRESIMS ion peak at  $m/z$  297.0974  $[M - H]^-$  (calcd for  $C_{14}H_{17}O_7$ , 297.0980), implying six unsaturation equivalents (Figure S14). The  $^1H$  and  $^{13}C$  NMR as well as HSQC spectra of **2** (Table 1, Figures S8, S9 and S11) indicated the presence of a ribose moiety, a 1,2,3,4-tetrasubstituted benzene ring, two methyls, and a ketone group as well as an exchangeable proton ( $\delta_H$  12.84). The NMR spectroscopic data displayed signals characteristic of a phenolic glycoside, which were similar to those reported for 4-hydroxy-2-*O*- $\alpha$ -ribofuranosyl-5-methylacetophenone [18]. The  $\alpha$ -ribose moiety was determined by the resonance for the anomeric proton at  $\delta_H$  5.75 (1H, d,  $J = 4.4$  Hz, H-1') and the glycosidic site was established unambiguously by the HMBC correlation from H-1' ( $\delta_H$  5.75) to C-4 ( $\delta_C$  161.0) [18,19]. The phenolic moiety was established by the COSY correlation of two aromatic methine protons (H-5 and H-6) (Figure S10) as well as the key HMBC correlations from H-5 to C-1 and C-3 and from H-6 to C-2, C-4, and C-7 (Figure 2 and Figure S12). The HMBC correlations from H<sub>3</sub>-8 to C-1 and C-7, from H<sub>3</sub>-9 to C-3 and C-4, and from the proton of 2-OH to C-2 and C-3 assigned the positions of the substituents on the benzene ring (Figure 2). The planar structure of **2** was thus established. Unfortunately, the relative configuration of **2** cannot be assigned as no useful signals observed in the NOESY spectrum (Figure S13).

To clarify the absolute configuration of the ribose moiety, suitable crystals were obtained by dissolving the sample in MeOH-H<sub>2</sub>O (50:1) followed by slow evaporation of the solvents under refrigeration (4 °C). X-ray single crystal diffraction experiment using Cu  $K\alpha$  radiation (Figure 5) confirmed the structure of **2**. The Flack parameter 0.12(13) allowed for the unambiguous assignment of the ribose moiety as  $\alpha$ -D-ribose.

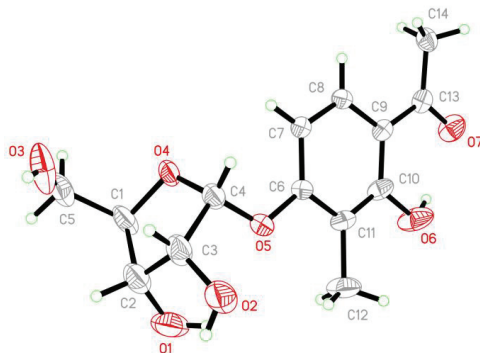


Figure 5. X-ray crystallographic structure of compound **2**.

Sorbicilliside B (**3**) was isolated as a colorless solid with the molecular formula of  $C_{18}H_{26}O_8$  according to the HRESIMS ion peaks at  $m/z$  371.1711  $[M + H]^+$  (calcd for  $C_{18}H_{27}O_8$ , 371.1700) and 393.1529  $[M + Na]^+$  (calcd for  $C_{18}H_{26}O_8Na$ , 393.1520), accounting for six degrees of unsaturation (Figure S22). The  $^1H$  and  $^{13}C$  NMR spectra of **3** (Table 1, Figures S16 and S17) also showed signals of a ribose moiety, a 1,2,4,5-tetrasubstituted benzene ring, a methyl, five methylenes (including an oxygenated), and a ketone group, as well as two exchangeable protons ( $\delta_H$  4.33 and 12.51). The NMR and ECD data (Figures S16–S21 and S23) of **3** showed resemblance to those of **2** (Figures S8–S13 and S15). However, one of the methyl signals resonating at  $\delta_C$  26.4 and  $\delta_H$  2.58 (CH<sub>3</sub>-8) in **2** were missing in the NMR spectra of **3**, while resonances for five methylenes (with one oxygenated) and an exchangeable proton ( $\delta_H$  4.33) were present in **3** (Table 1), implying the replacement of the methyl in **2** by a pentanol group in **3**. In addition, the methyl substituent on the benzene ring moved from C-3 in **2** to C-5 in **3** as supported by HMBC correlations (Figure 2), resulting in the 1,2,4,5-tetrasubstituted benzene ring of **3**. The planar structure of **3** was further identified by a series of mutually coupled resonances from H-8 through

the proton of 12-OH via H-9 through H-12 in the COSY spectrum as well as the key HMBC correlations from H-6 and H-8 to C-7 and from H-1' to C-4 (Figure 2), with the aglycone part identical to trichosorbicillin G [4]. The absolute configuration of the ribose moiety was further determined by HPLC analysis of the *O*-tolyl isothiocyanate derivative of its acidic hydrolysate [20,21]. The HPLC profiles showed that the product of acidic hydrolysis derivative of compound 3 shared the same retention time as that of  $\alpha$ -D-ribose derivative (Figure S26).

In addition to a novel acorane-type sesquiterpenoid (1) and two new sorbicillinoid glycosides (2–3), the known compound sorbicillin (4), was also isolated and identified by detailed spectroscopic analysis and comparison with the reported data [22].

## 2.2. Antimicrobial Activity

Compounds 1–4 were evaluated for their antimicrobial activities against human-, aquatic-, and plant-pathogenic microbes (Table 2). Compound 1 exhibited moderate activity against methicillin-resistant *Staphylococcus aureus*, the aquatic pathogenic bacterium *Vibrio harveyi* as well as most of the tested plant-pathogenic fungi with MIC values ranging from 4 to 64  $\mu$ g/mL. Compounds 2 and 3 displayed potent activity against *Aeromonas hydrophilia*, both with MIC value of 4  $\mu$ g/mL, which is comparable to the positive control chloramphenicol (MIC = 2  $\mu$ g/mL). In addition, compound 4 demonstrated a broad-spectrum of antimicrobial activity against the tested strains with MIC values ranging from 1 to 64  $\mu$ g/mL. These data indicated that the side chain of the sorbicillinoid glycosides showed a weaker effect on their antimicrobial activities (2 vs. 3), while the glycosylation in sorbicillinoid derivatives might increase their activity against the opportunistic pathogen *Aeromonas hydrophilia* (2 and 3 vs. 4).

**Table 2.** Antimicrobial activities of compounds 1–4 (MIC,  $\mu$ g/mL) <sup>a</sup>.

| Strains  | Compounds |    |    |    |                  |
|--|-----------|----|----|----|------------------|
|  | 1         | 2  | 3  | 4  | Positive Control |
| <i>A. brassicae</i> <sup>b</sup>                                   | 32        | -  | -  | 16 | 0.5              |
| <i>C. cornigerum</i> <sup>b</sup>                                  | 64        | -  | -  | 64 | 0.5              |
| <i>C. gloeosporioides</i> <sup>b</sup>                             | 16        | 64 | 32 | -  | 0.5              |
| <i>C. gloeosporioides</i> Penz <sup>b</sup>                        | 16        | 32 | 32 | 2  | 0.5              |
| <i>C. spicifera</i> <sup>b</sup>                                   | 8         | 16 | 8  | 2  | 0.25             |
| <i>F. graminearum</i> <sup>b</sup>                                 | -         | -  | -  | 32 | 0.5              |
| <i>F. oxysporum</i> <sup>b</sup>                                   | 32        | 32 | 32 | 1  | 0.5              |
| <i>F. oxysporum</i> f. sp. <i>radicis lycopersici</i> <sup>b</sup> | 32        | -  | 64 | 32 | 0.5              |
| <i>F. proliferatum</i> <sup>b</sup>                                | 32        | 64 | 64 | 2  | 0.5              |
| <i>P. digitatum</i> <sup>b</sup>                                   | 64        | 32 | 32 | 16 | 0.5              |
| <i>P. piricola</i> Nose <sup>b</sup>                               | 32        | -  | 64 | 2  | 0.5              |
| <i>A. hydrophilia</i> <sup>c</sup>                                 | 64        | 4  | 4  | 8  | 2                |
| <i>E. coli</i> <sup>c</sup>  | -         | 64 | 16 | 16 | 1                |
| methicillin-resistant <i>S. aureus</i> <sup>c</sup>                | 64        | -  | -  | 16 | 8                |
| <i>P. aeruginosa</i> <sup>c</sup>                                  | -         | -  | -  | 16 | 1                |
| <i>V. harveyi</i> <sup>c</sup>                                     | 4         | 16 | 16 | 16 | 0.5              |
| <i>V. parahaemolyticus</i> <sup>c</sup>                            | -         | -  | -  | 4  | 0.5              |

<sup>a</sup> (-) = MIC > 64  $\mu$ g/mL. <sup>b</sup> Amphotericin B as positive control. <sup>c</sup> Chloramphenicol as positive control.

## 3. Materials and Methods

### 3.1. General Experimental Procedures

Column chromatography was performed with commercially available silica gel (200–300 mesh, Qingdao Haiyang Chemical Co., Qingdao, China), Sephadex LH-20 (American Pharmacia) and Lobar LiChroprep RP-18 (40–63  $\mu$ m, Merck), notably all solvents were used in their anhydrous forms. Thin-layer chromatography (TLC) plates were carried out

using precoated silica gel plates GF254 (Qingdao Haiyang Chemical Factory) and analytical HPLC were performed using a Dionex system equipped with P680 pump, ASI-100 automated sample injector, and UVD340U multiple wavelength detector controlled by Chromeleon software (version 6.80). One-dimensional and two-dimensional NMR spectra were determined at 500 MHz for  $^1\text{H}$  and 125 MHz for  $^{13}\text{C}$  in  $\text{DMSO}-d_6$ , respectively, on a Bruker Avance 500 spectrometer. Low- or high-resolution ESI mass spectra were recorded on a Waters Micromass Q-TOF Premier and a Thermo Fisher Scientific LTQ Orbitrap XL mass spectrometer. The ECD spectra were measured with  $\text{CH}_3\text{OH}$  as solvent on a Jasco J-715 spectropolarimeter. Melting points were examined on a SGW X-4 micro-melting-point apparatus. Optical rotations were recorded with a Jasco P-1020 digital polarimeter. UV absorption were evaluated on a Gold S54 Ultraviolet-visible spectrophotometer.

### 3.2. Fungal Material

The fungus *Trichoderma longibrachiatum* EN-586 was obtained from the inner tissue of the marine red alga *Laurencia obtusa* collected from the coast of Qingdao, China in August 2016. The fungal strain was identified based on the morphology and ITS region of the rDNA as described previously [23]. The resulting sequence data *T. longibrachiatum* EN-586 is the same (100%) as that of *T. longibrachiatum* CGAJ1T-2 with accession no. KY495196.1, which has been deposited in GenBank with the accession no. OM060242. The fungus *T. longibrachiatum* EN-586 is preserved at the Key Laboratory of Experimental Marine Biology, Institute of Oceanology of the Chinese Academy of Sciences (IOCAS).

### 3.3. Fermentation, Extraction, and Isolation

The fresh mycelia of *T. longibrachiatum* EN-586 were cultured on PDA medium at  $28^\circ\text{C}$  for 6 days and then inoculated on the rice solid medium in  $60 \times 1$  L conical flasks (each flask contained 70 g rice, 0.1 g corn flour, 0.3 g peptone, and 100 mL natural seawater) for 30 days at room temperature. The whole fermented cultures were repeatedly soaked and extracted for three times with  $\text{EtOAc}$ , which was evaporated and concentrated under vacuum to obtain a crude extract (28.7 g).

The extract was fractionated by silica gel vacuum liquid chromatography (VLC) using different solvents of increasing polarity from Petroleum ether (PE)/ $\text{EtOAc}$  to  $\text{CH}_2\text{Cl}_2$ /MeOH to yield ten fractions (Fr. 1–10). Fr. 9 (3.9 g) was fractionated by CC over Lobar LiChroprep RP-18 with a MeOH- $\text{H}_2\text{O}$  gradient to yield 10 subfractions (Fr. 9.1–9.10). Fr. 9.4 (156.3 mg) was purified by CC on Sephadex LH-20 (MeOH) and preparative TLC ( $20 \times 20$  cm, developing solvents:  $\text{CH}_2\text{Cl}_2$ /MeOH 5:1) to obtain compound **1** (3.0 mg). Purification of Fr.4 (2.2 g) with column chromatography (CC) over Lobar LiChroprep RP-18 with a MeOH- $\text{H}_2\text{O}$  gradient (from 10:90 to 100) yielded 8 subfractions (Fr. 4.1–4.8). Fr. 4.6 (25.3 mg) was purified by CC on Sephadex LH-20 (MeOH), and then by semipreparative HPLC (Elite ODS-BP column,  $10 \mu\text{m}$ ;  $20 \times 250$  mm; 50% MeOH- $\text{H}_2\text{O}$ , 8 mL/min) to obtain compound **2** (4.8 mg,  $t_{\text{R}}$ 23.1 min). Fr.8 (3.8 g) was fractionated by CC over Lobar LiChroprep RP-18 with a MeOH- $\text{H}_2\text{O}$  gradient to yield 8 subfractions (Fr. 8.1–8.8). Fr. 8.3 (183.8 mg) was further purified by CC on Sephadex LH-20 (MeOH) and preparative TLC ( $20 \times 20$  cm, developing solvents:  $\text{CH}_2\text{Cl}_2$ /MeOH 20:1) and then by semipreparative HPLC (Elite ODS-BP column,  $10 \mu\text{m}$ ;  $20 \times 250$  mm; 60% MeOH- $\text{H}_2\text{O}$ , 8 mL/min) to yield compound **3** (4.9 mg,  $t_{\text{R}}$ 27.4 min). Fr.8.8 (348.9 mg) was subjected to CC silica gel eluting with PE/ $\text{EtOAc}$  (4:1) to obtain compound **4** (3.2 mg).

*Trichoacorside A* (**1**): yellowish oil;  $[\alpha]_{\text{D}}^{25} +88.9$  ( $c$  0.09, MeOH);  $^1\text{H}$  and  $^{13}\text{C}$  NMR data (Table 1); HRESI-MS  $m/z$  442.2799  $[\text{M} + \text{H}]^+$ , (calcd for  $\text{C}_{23}\text{H}_{40}\text{NO}_7$ , 442.2799).

*Sorbicilliside A* (**2**): colorless crystals; mp  $78\text{--}80^\circ\text{C}$ ;  $[\alpha]_{\text{D}}^{25} +100.0$  ( $c$  0.09, MeOH); ECD (0.67 mM, MeOH)  $\lambda_{\text{max}}$  ( $\Delta\epsilon$ ) 219 (−5.46), 232 (+2.71), 243 (−2.49), 270 (+15.31), 331 (−3.21), 368 (−2.01) nm; UV (MeOH)  $\lambda_{\text{max}}$  ( $\log \epsilon$ ) 216 (3.36), 278 (3.20), 320 (2.64) nm;  $^1\text{H}$  and  $^{13}\text{C}$  NMR data (Table 1); HRESIMS  $m/z$  297.0974  $[\text{M} - \text{H}]^-$  (calcd for  $\text{C}_{14}\text{H}_{17}\text{O}_7$ , 297.0980).

*Sorbicilliside B* (**3**): white solid;  $[\alpha]_{\text{D}}^{25} +100.0$  ( $c$  0.02, MeOH); ECD (0.54 mM, MeOH)  $\lambda_{\text{max}}$  ( $\Delta\epsilon$ ) 207 (−11.32), 231 (+27.50), 246 (−0.95), 272 (+16.66), 326 (+6.53), 376 (−2.64) nm;



UV (MeOH)  $\lambda_{\max}$  (log  $\epsilon$ ) 213 (3.22), 230 (3.03), 274 (3.08), 327 (2.78) nm;  $^1\text{H}$  and  $^{13}\text{C}$  NMR data (Table 1); HRESIMS  $m/z$  371.1700  $[\text{M} + \text{H}]^+$  (calcd for  $\text{C}_{18}\text{H}_{27}\text{O}_8$ , 371.1711),  $m/z$  393.1520  $[\text{M} + \text{Na}]^+$  (calcd for  $\text{C}_{18}\text{H}_{26}\text{O}_8\text{Na}$ , 393.1529).

### 3.4. X-ray Crystallographic Analysis of Compound 2

By dissolving compound 2 in the solvent of MeOH-H<sub>2</sub>O (50:1) and storing it in a refrigerator with slow evaporation, suitable crystals were obtained. The crystallographic data [24] were collected over a Bruker D8 Venture CCD diffractometer equipped with graphite-monochromatic Cu-K $\alpha$  radiation ( $\lambda = 1.54178 \text{ \AA}$ ) at 295(2) K. The absorption data were optimized by using the program SADABS [25]. The structures were elucidated strictly with the SHELXTL software package [26,27]. All non-hydrogen atoms were refined anisotropically. The H atoms connected to C atoms were calculated theoretically, and those to O atoms were assigned by difference Fourier maps. The absolute structures were determined by refinement of the Flack parameter [28]. The structures were optimized by full-matrix least-squares techniques.

*Crystal data for compound 2:*  $\text{C}_{14}\text{H}_{18}\text{O}_7$ , fw = 298.28, Orthorhombic space group C 2 2 21, unit cell dimensions  $a = 6.9716(8) \text{ \AA}$ ,  $b = 13.646(2) \text{ \AA}$ ,  $c = 32.020(4) \text{ \AA}$ ,  $V = 3046.2(7) \text{ \AA}^3$ ,  $\alpha = \beta = \gamma = 90^\circ$ ,  $Z = 8$ ,  $d_{\text{calcd}} = 1.301 \text{ mg/m}^3$ , crystal dimensions  $0.160 \times 0.150 \times 0.120 \text{ mm}$ ,  $\mu = 0.893 \text{ mm}^{-1}$ , and  $F(000) = 1264$ . The 2809 measurements yielded 2265 independent reflections after equivalent data were averaged, and Lorentz and polarization corrections were applied. The final refinement gave  $R_1 = 0.0719$  and  $wR_2 = 0.2121$  [ $I > 2\sigma(I)$ ]. The Flack parameter was 0.12(13) in the final refinement for all 2809 reflections with 2265 Friedel pairs.

### 3.5. Acid Hydrolysis and Derivatization of Compound 1

The absolute configuration of the glucosamine moiety in compound 1 was determined by the acid hydrolysis with 3 N HCl (0.5 mL) at 80 °C for 2 h to afford sugar moieties and aglycone and after being cooled to room temperature for over 5 hours, the solution mixture was evaporated with the laboratory bench circulating water vacuum pump and then redissolved in pyridine (0.5 mL) with the mixture of hexamethyldisilazane (HMDS) and trimethylchlorosilane (TMS-Cl) (60  $\mu\text{L}$ ,  $v/v$  2:1), furthermore, the solution was heated at 60 °C for 1 hour. The solution was dried with the multifunctional circulating water vacuum pump, the sugar residue was separated with water and  $\text{CH}_2\text{Cl}_2$  (1 mL,  $v/v$  1:1). The  $\text{CH}_2\text{Cl}_2$  layer was injected into a gas chromatograph based on the previously reported protocol [15,29]. The derivatives of the sugar residue in compound 1 and the authentic D-glucosamine (Solarbio science & technology Co., Ltd, Beijing, China) were analyzed by gas chromatograph-mass (GC, Agilent 7890A/5975C, American, 2012.8) using an HP5 Column (0.25 mm  $\times$  30 m  $\times$  0.25, Agilent Technologies, Inc., Santa Clara, CA, USA), which was employed with a 41 min temperature program as follows: the initial temperature was maintained at 60 °C for 3 min, ramped to 200 °C at a rate of 4 °C/min, then followed by a 3 min hold at 200 °C. The injector and detector temperatures were maintained at 200 °C, the sample size was controlled at 1  $\mu\text{L}$  and the flow rate of the carrier gas (helium) was 1.0 mL/min, moreover, the split ratio was 10:1. Consequently, the peak of the derivative was detected at 22.486 min (Figure S24), which was identical to the authentic D-glucosamine treated and analyzed using the same protocol, thereby determining the absolute configuration of the glucosamine in 1 as the D-form.

### 3.6. Acid Hydrolysis and Derivatization of Compound 3

The absolute configuration of the ribose moiety in compound 3 was established by acid hydrolysis and derivatization. The hydrolyzed sugar fraction (0.5 mg) was dissolved in pyridine (100  $\mu\text{L}$ ) containing L-cysteine methyl ester hydrochloride (0.5 mg), incubated at 60 °C for 1 h. A solution of *o*-tolyl isothiocyanate (10  $\mu\text{L}$ ) was then added to the mixture and incubated at 60 °C for another 1 h. The mixture was evaporated and dissolved in MeOH to perform reverse-phase HPLC for analysis based on the protocol in the literature [21]. The derivatives of the sugar residue in compound 3 and the authentic D/L-ribose (Aladdin

Bio-Chem Technology Co., Ltd., Shanghai, China) were analyzed by analytical HPLC (Elite C18 column, 10  $\mu$ m; 4.6  $\times$  250 mm; 10% acetonitrile-H<sub>2</sub>O for 5 min, then ramped to 100% acetonitrile at a rate of 3%/min, maintained this ratio for 10 min, afterwards, ramped to 10% acetonitrile-H<sub>2</sub>O at a rate of 18%/min, at last, maintained 10% acetonitrile-H<sub>2</sub>O for 10 min; column temperature of 35 °C; flow rate at 1.0 mL/min; detection wavelength at 250 nm), which was equipped with P680 pump, an ASI-100 automated sample injector, a UVD340U multiple wavelength detector controlled by Chromeleon software (version 6.80) and performed on a Dionex HPLC system. The absolute configuration of ribose moiety in compound **3** was determined by comparison of the retention times to those of the authentic derivatives ( $t_R$ : D-ribose derivative, 21.865 min, L-ribose derivative, 20.789 min) (Figure S26).

### 3.7. Computational NMR Chemical Shift Calculation and DP4+ Analysis of Compound **1**

All the theoretical calculations were performed in Gaussian 09 program package. Conformational searches for the possible isomers were carried out through molecular mechanics using the MMFF method with Macromodel software (Schrödinger, LLC., New York, NY, USA) and the corresponding stable conformer, from which distributions higher than 2% were collected. Subsequently, B3LYP/6-31G(d) PCM level in DMSO was used to optimize the conformers. The NMR shielding tensors of all optimized conformers were calculated using the DFT method at mPW1PW91\6-31+G (d) PCM level in DMSO, and then an average based on Boltzmann distribution theory was performed using an equation described previously [17,30]. GIAO (gauge-independent atomic orbital) NMR chemical calculations were conducted using an equation described previously. Finally, the NMR chemical shifts and shielding tensors (<sup>1</sup>H and <sup>13</sup>C) were analyzed and compared with the experimental chemical shifts using DP4+ probability (Figure S25) [30,31].

### 3.8. Antimicrobial Activity Assay

The antimicrobial activities of the compounds **1–4** against the human and aquatic pathogenic bacteria (*Aeromonas hydrophilia* QDIO-1, *Escherichia coli* EMBLC-1, methicillin-resistant *Staphylococcus aureus* (MRSA) EMBLC-4, *Pseudomonas aeruginosa* QDIO-4, *Vibrio harveyi* QDIO-7 and *V. parahaemolyticus* QDIO-8) as well as the plant pathogenic fungi (*Alternaria brassicae* QDIO-11, *Ceratobasidium cornigerum* QDAU-6, *Colletotrichum gloeosporioides* QDAU-31, *C. gloeosporioides* Penz. QDIO-22, *Curvularia spicifera* QDAU-29, *Fusarium graminearum* QDAU-4, *F. oxysporum* QDAU-25, *F. oxysporum* f. sp. *radicis lycopersici* QDAU-10, *F. proliferatum* QDAU-30, *Penicillium digitatum* QDAU-14, and *Physalospora piricola* Nose. QDAU-15) were determined by a serial dilution technique using 96-well microtiter plates as previously reported [32]. Amphotericin B was used as a positive control for fungi, while chloramphenicol as a positive control for bacteria. The human and aquatic pathogenic bacteria and plant pathogenic fungi were offered by the Institute of Oceanology, Chinese Academy of Sciences.

## 4. Conclusions

In summary, we isolated and identified three new glycoside compounds (**1–3**) from the marine red alga endophytic fungus *Trichoderma longibrachiatum* EN-586. It is noteworthy that compound **1** represents an unprecedented acorane-type sesquiterpenoid coupled to glucosamine. Compounds **2** and **3** may prove useful as antibiotic agents against the opportunistic pathogen *Aeromonas hydrophilia*.

**Supplementary Materials:** The following supporting information can be downloaded at: <https://www.mdpi.com/article/10.3390/md20030177/s1>, Figure S1: <sup>1</sup>H NMR (500 MHz, DMSO-*d*<sub>6</sub>) spectrum of compound **1**; Figure S2: <sup>13</sup>C NMR (125 MHz, DMSO-*d*<sub>6</sub>) and DEPT spectra of compound **1**; Figure S3: COSY spectrum of compound **1**; Figure S4: HSQC spectrum of compound **1**; Figure S5a: HMBC spectrum of compound **1**; Figure S5b: Enlarged HMBC spectrum of compound **1** (lower field); Figure S5c: Enlarged HMBC spectrum of compound **1** (higher field); Figure S6: NOESY spectrum of compound **1**; Figure S7: HRESIMS spectrum of compound **1**; Figure S8: <sup>1</sup>H NMR

(500 MHz, DMSO- $d_6$ ) spectrum of compound 2; Figure S9:  $^{13}\text{C}$  NMR (125 MHz, DMSO- $d_6$ ) and DEPT spectra of compound 2; Figure S10: COSY spectrum of compound 2; Figure S11: HSQC spectrum of compound 2; Figure S12: HMBC spectrum of compound 2; Figure S13: NOESY spectrum of compound 2; Figure S14: HRESIMS spectrum of compound 2; Figure S15: ECD spectrum of compound 2; Figure S16:  $^1\text{H}$  NMR (500 MHz, DMSO- $d_6$ ) spectrum of compound 3; Figure S17:  $^{13}\text{C}$  NMR (125 MHz, DMSO- $d_6$ ) and DEPT spectra of compound 3; Figure S18: COSY spectrum of compound 3; Figure S19: HSQC spectrum of compound 3; Figure S20: HMBC spectrum of compound 3; Figure S21: NOESY spectrum of compound 3; Figure S22: HRESIMS spectrum of compound 3; Figure S23: ECD spectrum of compound 3; Figure S24: Determination of absolute configuration of glucosamine in compound 1; Figure S25: DP4+ probability Excel sheets of compound 1; Figure S26: Determination of absolute configuration of ribose in compound 3.

**Author Contributions:** Y.W. performed the experiments and prepared the manuscript; X.-M.L. performed the 1D and 2D NMR experiments; S.-Q.Y. contributed to part of the structure determination; F.-Z.Z. contributed the optimization of fermentation; B.-G.W. supervised the research work; H.-L.L. and L.-H.M. contributed to part of the structure determination, supervised the research work and revised the manuscript. All authors have read and agreed to the published version of the manuscript.

**Funding:** This research was funded by the National Natural Science Foundation of China (42176115 and 42006079), the Qingdao National Laboratory for Marine Science and Technology (YQ2018NO08 and OF2019NO03), and the National Natural Science Foundation of Jiangsu province (No. BK20201211).

**Institutional Review Board Statement:** Not applicable.

**Informed Consent Statement:** Not applicable.

**Data Availability Statement:** Not applicable.

**Acknowledgments:** The authors appreciate the High Performance Computing Environment Qingdao Branch of Chinese Academy of Science (CAS)–High Performance Computing Center of Institute of Oceanology of CAS for CPU time.

**Conflicts of Interest:** The authors declare no conflict of interest.

## References

- Baquero, F. Threats of antibiotic resistance: An obliged reappraisal. *Int. Microbiol.* **2021**, *24*, 499–506. [[CrossRef](#)]
- André, A.; Wojtowicz, N.; Touré, K.; Stien, D.; Eparvier, V. New acorane sesquiterpenes isolated from the endophytic fungus *Colletotrichum gloeosporioides* SNB-GSS07. *Tetrahedron Lett.* **2017**, *58*, 1269–1272. [[CrossRef](#)]
- Li, G.H.; Yang, Z.S.; Zhao, P.J.; Zheng, X.; Luo, S.L.; Sun, R.; Niu, X.M.; Zhang, K.Q. Three new acorane sesquiterpenes from *Trichoderma* sp. YMF1.02647. *Phytochem. Lett.* **2011**, *4*, 86–88. [[CrossRef](#)]
- Wu, S.H.; Zhao, L.X.; Chen, Y.W.; Huang, R.; Miao, C.P.; Wang, J. Sesquiterpenoids from the endophytic fungus *Trichoderma* sp. PR-35 of *Paeonia delavayi*. *Chem. Biodivers.* **2011**, *8*, 1717–1723. [[CrossRef](#)] [[PubMed](#)]
- Zhang, P.P.; Deng, Y.L.; Lin, X.J.; Chen, B.; Li, J.; Liu, H.J.; Chen, S.H.; Liu, L. Anti-inflammatory mono- and dimeric sorbicillinoids from the marine-derived Fungus *Trichoderma reesei* 4670. *J. Nat. Prod.* **2019**, *82*, 947–957. [[CrossRef](#)]
- Rateb, M.E.; Ebel, R. Secondary metabolites of fungi from marine habitats. *Nat. Prod. Rep.* **2011**, *28*, 290–344. [[CrossRef](#)]
- Ji, N.Y.; Wang, B.G. Mycochemistry of marine algaliculous fungi. *Fungal Divers.* **2016**, *80*, 301–342. [[CrossRef](#)]
- Bugni, T.S.; Ireland, C.M. Marine-derived fungi: A chemically and biologically diverse group of microorganisms. *Nat. Prod. Rep.* **2004**, *21*, 143–163. [[CrossRef](#)]
- González, A.G.; Martín, J.D.; Norte, M.; Rivera, P.; Ruano, J.Z. Two new  $\text{C}_{15}$  acetylenes from the marine red alga *Laurencia obtusa*. *Tetrahedron* **1984**, *40*, 3443–3447. [[CrossRef](#)]
- Swamy, M.L.A. Marine algal sources for treating bacterial diseases. *Adv. Food Nutr. Res.* **2011**, *64*, 72–81.
- Li, H.L.; Yang, S.Q.; Li, X.M.; Li, X.; Wang, B.G. Structurally diverse alkaloids produced by *Aspergillus creber* EN-602, an endophytic fungus obtained from the marine red alga *Rhodomela confervoides*. *Bioorg. Chem.* **2021**, *110*, 104822. [[CrossRef](#)] [[PubMed](#)]
- Li, H.L.; Li, X.M.; Yang, S.Q.; Meng, L.H.; Li, X.; Wang, B.G. Prenylated phenol and benzofuran derivatives from *Aspergillus terreus* EN-539, an endophytic fungus derived from marine red alga *Laurencia okamurai*. *Mar. Drugs* **2019**, *17*, 605. [[CrossRef](#)] [[PubMed](#)]
- Meng, L.H.; Li, X.M.; Zhang, F.Z.; Wang, Y.N.; Wang, B.G. Talascortenes A–G, highly oxygenated diterpenoid acids from the sea-anemone-derived endozoic fungus *Talaromyces scorteus* AS-242. *J. Nat. Prod.* **2020**, *83*, 2528–2536. [[CrossRef](#)] [[PubMed](#)]
- Hu, X.Y.; Wang, C.Y.; Li, X.M.; Yang, S.Q.; Li, X.; Wang, B.G.; Si, S.Y.; Meng, L.H. Cytochalasin derivatives from the endozoic *Curvularia verruculosa* CS-129, a fungus isolated from the deep-sea squat lobster *Shinkaia crosnieri* living in the cold seep environment. *J. Nat. Prod.* **2021**, *84*, 3122–3130. [[CrossRef](#)] [[PubMed](#)]

15. Shin, B.; Park, S.H.; Kim, B.Y.; Jo, S.I.; Lee, S.K.; Shin, J.; Oh, D.C. Deinococcins A–D, aminoglycolipids from *Deinococcus* sp., a gut bacterium of the carpenter Ant *Camponotus japonicus*. *J. Nat. Prod.* **2017**, *80*, 2910–2916. [[CrossRef](#)] [[PubMed](#)]
16. Chang, J.; Xuan, L.J.; Xu, Y.M.; Zhang, J.S. Seven new sesquiterpene glycosides from the root bark of *Dictamnus dasycarpus*. *J. Nat. Prod.* **2001**, *64*, 935–938. [[CrossRef](#)]
17. Grimblat, N.; Zanardi, M.M.; Sarotti, A.M. Beyond DP4: An improved probability for the stereochemical assignment of isomeric compounds using quantum chemical calculations of NMR shifts. *J. Org. Chem.* **2015**, *80*, 12526–12534. [[CrossRef](#)]
18. Rebolgar-Ramos, D.; Macías-Ruvalcaba, M.L.; Figueroa, M.; Raja, H.A.; González-Andrade, M.; Mata, R. Additional  $\alpha$ -glucosidase inhibitors from *Malbranchea flavorosea* (Leotiomycetes, Ascomycota). *J. Antibiot.* **2018**, *71*, 862–871. [[CrossRef](#)]
19. May, D.S.; Kang, H.S.; Santarsiero, B.D.; Krunic, A.; Shen, Q.; Burdette, J.E.; Swanson, S.M.; Orjala, J. Ribocyclophanes A–E, glycosylated cyclophanes with antiproliferative activity from two cultured terrestrial cyanobacteria. *J. Nat. Prod.* **2018**, *81*, 572–578. [[CrossRef](#)]
20. Tanaka, T.; Nakashima, T.; Ueda, T.; Tomii, K.; Kouno, I. Facile discrimination of aldose enantiomers by reversed-phase HPLC. *Chem. Pharm. Bull.* **2007**, *55*, 899–901. [[CrossRef](#)]
21. Bang, S.; Chae, H.S.; Lee, C.; Choi, H.G.; Ryu, J.; Li, W.; Lee, H.; Jeong, G.S.; Chin, Y.W.; Shim, S.H. New aromatic compounds from the fruiting body of *Sparassis crispa* (wulf.) and their inhibitory activities on proprotein convertase subtilisin/kexin type 9 mRNA expression. *J. Agric. Food Chem.* **2017**, *65*, 6152–6157. [[CrossRef](#)] [[PubMed](#)]
22. Lan, W.J.; Zhao, Y.; Xie, Z.L.; Liang, L.Z.; Shao, W.Y.; Zhu, L.P.; Yang, D.P.; Zhu, X.F.; Li, H.J. Novel sorbicillin analogues from the marine fungus *Trichoderma* sp. associated with the Seastar *Acanthaster planci*. *Nat. Prod. Commun.* **2012**, *7*, 1337–1340. [[CrossRef](#)] [[PubMed](#)]
23. Wang, S.; Li, X.M.; Teuscher, F.; Li, D.L.; Diesel, A.; Ebel, R.; Proksch, P.; Wang, B.G. Chaetopyranin, a benzaldehyde derivative, and other related metabolites from *Chaetomium globosum*, an endophytic fungus derived from the marine red alga *Polysiphonia urceolata*. *J. Nat. Prod.* **2006**, *69*, 1622–1625. [[CrossRef](#)]
24. Crystallographic Data of Compound 2 Have Been Deposited in the Cambridge Crystallographic Data Centre as CCDC 2131452. Available online: <http://www.ccdc.cam.ac.uk/datarequest/cif> (accessed on 29 December 2021).
25. Sheldrick, G.M. *SADABS, Software for Empirical Absorption Correction*; University of Gottingen: Gottingen, Germany, 1996.
26. Sheldrick, G.M. *SHELXL, Structure Determination Software Programs*; Bruker Analytical X-ray system Inc.: Madison, WI, USA, 1997.
27. Sheldrick, G.M. *SHELXL, Program for the Refinement of Crystal Structures*; University of Gottingen: Gottingen, Germany, 2014.
28. Parsons, S.; Flack, H.D.; Wagner, T. Use of intensity quotients and differences in absolute structure refinement. *Acta Crystallogr. Sect. B Struct. Sci. Cryst. Eng. Mater.* **2013**, *B69*, 249–259. [[CrossRef](#)]
29. Shin, J.; Lee, H.S.; Woo, L.; Rho, J.R.; Seo, Y.; Cho, K.W.; Sim, C.J. New triterpenoid saponins from the sponge *Erylus nobilis*. *J. Nat. Prod.* **2001**, *64*, 767–771. [[CrossRef](#)]
30. Lee, S.R.; Lee, D.; Park, M.; Lee, J.C.; Park, H.; Kang, K.S.; Kim, C.; Beemelmans, C.; Kim, K.H. Absolute configuration and corrected NMR assignment of 17-hydroxycyclooctatin, a fused 5-8-5 tricyclic diterpene. *J. Nat. Prod.* **2020**, *83*, 354–361. [[CrossRef](#)]
31. Kawazoe, R.; Matsuo, Y.; Saito, Y.; Tanaka, T. Computationally assisted structural revision of flavoalkaloids with a seven-membered ring: Aquileidine, isoaquileidine, and cheliensisine. *J. Nat. Prod.* **2020**, *83*, 3347–3353. [[CrossRef](#)]
32. Chi, L.P.; Li, X.M.; Wan, Y.P.; Li, X.; Wang, B.G. Ophiobolin sesterterpenoids and farnesylated phthalide derivatives from the deep sea cold-seep-derived fungus *Aspergillus insuetus* SD-512. *J. Nat. Prod.* **2020**, *83*, 3652–3660. [[CrossRef](#)]



## Article

# Anti-Osteoclastogenic and Antibacterial Effects of Chlorinated Polyketides from the Beibu Gulf Coral-Derived Fungus *Aspergillus unguis* GXIMD 02505

Yanting Zhang <sup>1,†</sup>, Zhichao Li <sup>2,†</sup>, Bingyao Huang <sup>1</sup>, Kai Liu <sup>1</sup>, Shuai Peng <sup>1</sup>, Xinming Liu <sup>1</sup>, Chenghai Gao <sup>1</sup>, Yonghong Liu <sup>1,\*</sup>, Yanhui Tan <sup>2,\*</sup> and Xiaowei Luo <sup>1,\*</sup>

<sup>1</sup> Institute of Marine Drugs, Guangxi University of Chinese Medicine, Nanning 530200, China; ting9097@163.com (Y.Z.); hby03502@126.com (B.H.); kailiu@gxctmu.edu.cn (K.L.); pengshuai0208@163.com (S.P.); leosimon0917@gmail.com (X.L.); gaoch@gxctmu.edu.cn (C.G.)

<sup>2</sup> State Key Laboratory for Chemistry and Molecular Engineering of Medicinal Resources, School of Chemistry and Pharmaceutical Sciences, Guangxi Normal University, Guilin 541004, China; lizhichao3278@163.com

\* Correspondence: yonghongliu@scsio.ac.cn (Y.L.); tyh533@126.com (Y.T.); luoxiaowei1991@126.com (X.L.)

† These authors contributed equally to this work.

**Abstract:** One new depsidone derivative, aspergillusidone H (**3**), along with seven known biosynthetically related chlorinated polyketides, were obtained from the Beibu Gulf coral-derived fungus *Aspergillus unguis* GXIMD 02505. Their structures were determined by comprehensive physicochemical and spectroscopic data interpretation. Notably, the X-ray crystal structure of **2** and the previously unknown absolute configuration of **8**, assigned by ECD calculations, are described here for the first time. Compounds **1**–**5**, **7** and **8** exhibited inhibition of lipopolysaccharide (LPS)-induced NF- $\kappa$ B in RAW 264.7 macrophages at 20  $\mu$ M. In addition, the two potent inhibitors (**2** and **7**) dose-dependently suppressed RANKL-induced osteoclast differentiation without any evidence of cytotoxicity in bone marrow macrophages cells (BMMs). This is the first report of osteoclastogenesis inhibitory activity for the metabolites of these kinds. Besides, compounds **1**, **2**, **4**, and **6**–**8** showed inhibitory activity against marine biofilm-forming bacteria, methicillin-resistant *Staphylococcus aureus*, *Microbulbifer variabilis*, *Marinobacterium jannaschii*, and *Vibrio pelagius*, with their MIC values ranging from 2 to 64  $\mu$ g/mL. These findings provide a basis for further development of chlorinated polyketides as potential inhibitors of osteoclast differentiation and/or for use as anti-fouling agents.

**Keywords:** marine fungi; *Aspergillus unguis*; depsides; depsidones; osteoclast differentiation; antibacterial

**Citation:** Zhang, Y.; Li, Z.; Huang, B.; Liu, K.; Peng, S.; Liu, X.; Gao, C.; Liu, Y.; Tan, Y.; Luo, X. Anti-Osteoclastogenic and Antibacterial Effects of Chlorinated Polyketides from the Beibu Gulf Coral-Derived Fungus *Aspergillus unguis* GXIMD 02505. *Mar. Drugs* **2022**, *20*, 178. <https://doi.org/10.3390/md20030178>

Academic Editor: Orazio Tagliatalata-Scafati

Received: 14 January 2022

Accepted: 25 February 2022

Published: 28 February 2022

**Publisher's Note:** MDPI stays neutral with regard to jurisdictional claims in published maps and institutional affiliations.



**Copyright:** © 2022 by the authors. Licensee MDPI, Basel, Switzerland. This article is an open access article distributed under the terms and conditions of the Creative Commons Attribution (CC BY) license (<https://creativecommons.org/licenses/by/4.0/>).

## 1. Introduction

Bone is a rigid, yet dynamic, organ that provides maximal strength with minimal mass, supporting the human body and producing indispensable red and white blood cells [1]. Normal bone homeostasis is known to be regulated and maintained by two bone remodeling metabolic processes, bone resorption by osteoclasts and bone formation by osteoblasts [2]. With an ageing population, osteoporosis, particularly postmenopausal osteoporosis, will pose severe worldwide concern to public health and economic development [3]. Thus, the development of therapeutic agents to treat osteoporosis is urgently needed. The differentiation of the osteoclast is modulated by two critical factors, the macrophage colony stimulation factor (M-CSF) and the receptor activator of the nuclear factor kappa-B (NF- $\kappa$ B) ligand (RANKL). RANKL signaling pathways have been recently proposed as key targets for inhibiting osteoclast differentiation and bone resorption [4]. Hence, many efforts have been recently devoted to the discovery of lead compounds from natural sources that target RANKL-induced osteoclast differentiation for attenuating enhanced bone resorption and bone loss [5].

Depside, depsidone, and diphenyl ethers are biosynthetically-related aromatic polyketides originated normally from the condensation of orsellinic acid, orcinol, and/or

polyphenolic units by ether and/or ester bonds [6], which are widely encountered in lichens, as well as in some fungi (especially in *Aspergillus unguis*) and higher plants [7]. Their variable linked patterns and different substituents lead to rich structural diversity. Naturally occurring depsides and depsidones were recently found with a wide array of remarkable bioactivities, including antimicrobial [8,9],  $\alpha$ -glucosidase inhibitory [10,11], anti-inflammatory [12,13], cytotoxic [12], antioxidant [14], and anti-viral activities [15], arousing considerable interest from the communities of chemistry and pharmacology [6,16]. Curiously, a depsidone natural product, norstictic acid, was very recently reported as a key selective allosteric transcriptional regulator in a patient-derived model of triple-negative breast cancer [17].

In our continuing endeavor to discover biologically active compounds from marine fungi, a series of structurally novel secondary metabolites (SM) with promising pharmacological effects have been recently discovered, including anti-tumor ascochlorins [18,19], chloroazaphilones [20] and diketopiperazine alkaloids [21], as well as nitrobenzoyl sesquiterpenoids as novel inhibitors of osteoclast differentiation [4]. In this study, a coral-derived fungus *Aspergillus unguis* GXIMD 02505 has drawn our attention, due to the intriguing characteristics of abundant chlorinated SMs as observed by the HPLC-UV/MS profile of its extract. Subsequent chemical investigation led to the isolation of eight diverse chlorinated aromatic polyketides (Figure 1) guided by the HPLC-UV/MS method. Several of them have displayed inhibitory effects on osteoclastogenesis by suppressing RANKL-induced NF- $\kappa$ B activation and on marine biofilm-forming bacteria. Herein, the isolation and structural determination, as well as their inhibitory activities on RANKL-induced osteoclastogenesis and antibacterial effects, are described in detail.

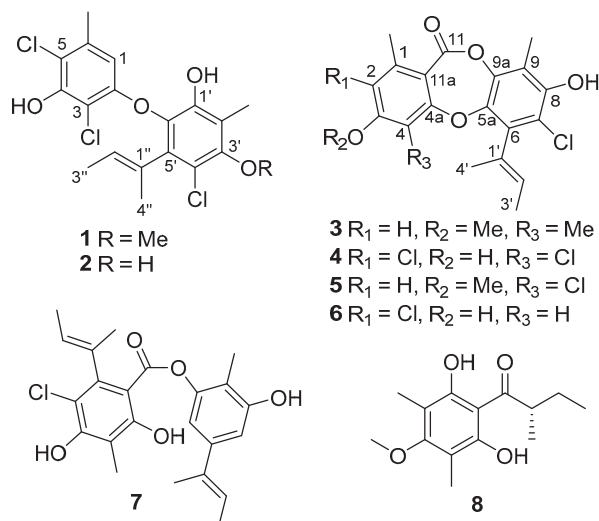


Figure 1. Structures of compounds 1–8.

## 2. Results and Discussion

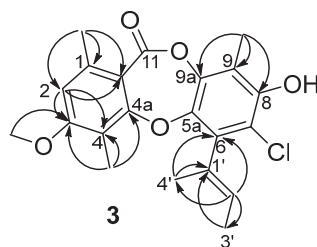
The cultures of *A. unguis* GXIMD 02505, based on rice fermentation, were extracted with EtOAc three times. The whole extract was then performed on the repeated column chromatography involving silica gel, reversed-phase silica gel C18, and semipreparative HPLC. The HPLC-DAD-guided purification resulted in the discovery of eight chlorinated aromatic polyketides, including two diphenyl ethers (1 and 2), four depsidones (3–6), one depside (7), and one related block (8). These obtained known compounds were identified as aspergillusethers J (1) [22] and F (2) [8], normidulin (4) [8,23], aspergillusidones B and C (5 and 6) [23], guisinol (7) [24], and 1-(2,6-dihydroxy-4-methoxy-3,5-dimethylphenyl)-

2-methylbutan-1-one (**8**) [25], respectively, by comparing their physicochemical and spectroscopic data with those reported. Notably, the X-ray crystal structure of **2** is described herein for the first time (Figure S19).

Compound **3** was obtained as white amorphous solid with the molecular formula  $C_{21}H_{21}ClO_5$ , as determined by a cluster of ion peaks at  $m/z$  389.1159/391.1134 ( $[M + H]^+$ ) with a ratio of 3:1 in the HR-ESI-MS spectrum, indicative of a monochlorinated compound. The IR spectrum showed hydroxy and double-bond absorption bands at 3446 and  $1653\text{ cm}^{-1}$ , respectively. The UV spectrum exhibited absorption bands at 207 and 270 nm, indicating the presence of a benzene chromophore [8]. The  $^1\text{H}$  NMR data (Table 1) along with the HSQC experiment of **3** displayed the signals of two aromatic or olefinic protons, assigned to H-2 ( $\delta_{\text{H}}$  6.73, s) and H-2' ( $\delta_{\text{H}}$  5.40, q,  $J = 6.8\text{ Hz}$ ), five methyls, 1-Me ( $\delta_{\text{H}}$  2.45), 4-Me ( $\delta_{\text{H}}$  2.15), 9-Me ( $\delta_{\text{H}}$  2.24), H<sub>3</sub>-3' ( $\delta_{\text{H}}$  1.82, d,  $J = 6.8\text{ Hz}$ ), and H<sub>3</sub>-4' ( $\delta_{\text{H}}$  1.91, s), and one methoxyl, 3-OMe ( $\delta_{\text{H}}$  3.87). Besides the above eight corresponding hydrogen-bearing carbons, twelve aromatic or olefinic (five oxygenated) ones and a carbonyl ( $\delta_{\text{C}}$  165.3) remained in the  $^{13}\text{C}$  NMR spectrum. The aforementioned NMR data of **3** highly resembled those of the co-isolation of a known compound, aspergillusidone B (**5**). A significant difference was the appearance of a methyl group ( $\delta_{\text{H/C}}$  2.15/10.2) at C-4 ( $\delta_{\text{C}}$  116.1) in **3** instead of a chlorine atom in **5**, which was also verified by the HMBC correlations (Figure 2) from 4-CH<sub>3</sub> to C-3 ( $\delta_{\text{C}}$  163.0), C-4, and C-4a ( $\delta_{\text{C}}$  162.3). Consequently, **3** was assigned as aspergillusidone H. Besides, the previously unknown absolute configuration of **8** was determined by ECD calculations for the first time (Figure 3).

**Table 1.**  $^1\text{H}$  (700 MHz) and  $^{13}\text{C}$  (175 MHz) NMR Data for **3** ( $\text{CD}_3\text{OD}$ ).

| Position | $\delta_{\text{C}}$ , Type | $\delta_{\text{H}}$ (J in Hz) | HMBC      |
|----------|----------------------------|-------------------------------|-----------|
| 1        | 144.0, C                   |                               |           |
| 1-Me     | 21.6, CH <sub>3</sub>      | 2.45, s                       | 1, 2, 11a |
| 2        | 111.2, CH                  | 6.73, s                       | 3, 4, 11a |
| 3        | 163.0, C                   |                               |           |
| 3-OMe    | 56.4, CH <sub>3</sub>      | 3.87, s                       | 3         |
| 4        | 116.1, C                   |                               |           |
| 4-Me     | 10.2, CH <sub>3</sub>      | 2.15, s                       | 3, 4, 4a  |
| 4a       | 162.3, C                   |                               |           |
| 5a       | 143.6, C                   |                               |           |
| 6        | 135.7, C                   |                               |           |
| 7        | 117.3, C                   |                               |           |
| 8        | 143.7, C                   |                               |           |
| 9        | 117.8, C                   |                               |           |
| 9-Me     | 9.2, CH <sub>3</sub>       | 2.24, s                       | 8, 9a, 9  |
| 9a       | 150.2, C                   |                               |           |
| 11       | 165.3, C                   |                               |           |
| 11a      | 114.2, C                   |                               |           |
| 1'       | 131.8, C                   |                               |           |
| 2'       | 128.5, CH                  | 5.40, q (6.8)                 | 6, 3', 4' |
| 3'       | 14.0, CH <sub>3</sub>      | 1.82, d (6.8)                 | 1'        |
| 4'       | 17.7, CH <sub>3</sub>      | 1.91, s                       | 6, 1'     |



**Figure 2.** Key HMBC correlations for compound **3**.



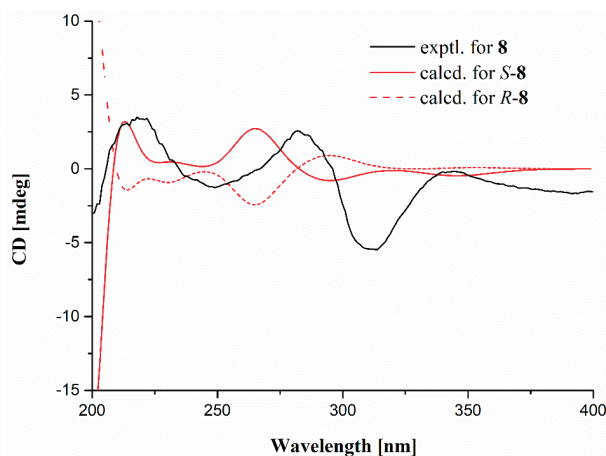


Figure 3. The experimental and calculated ECD spectra of 8.

Marine natural products have been recently found as a vital source of inhibitors of RANKL-induced osteoclastogenesis [4,26]. All of the compounds were then evaluated for their inhibitory effects against RANKL induced osteoclastogenesis in RAW 264.7 macrophages using the luciferase reporter gene, and in bone marrow macrophage cells (BMMs) by tartate-resisant acid phosphatase (TRAP) assays. Compounds 1–5, 7 and 8 exhibited inhibition of lipopolysaccharide (LPS)-induced NF- $\kappa$ B activation in RAW 264.7 macrophages at 20  $\mu$ M ( $p < 0.001$ ) (Figure 4). To further investigate the binding modes of the two potent inhibitors (2 and 7) with NF- $\kappa$ B p65, a molecular docking study was primarily carried out using the Schrödinger suits software. The theoretical binding modes of 2 and 7 with NF- $\kappa$ B p65 protein was shown in Figure 5 with the nearly identical glide scores of  $-3.391$  and  $-3.076$  kcal/mol, respectively, which were consistent with the above NF- $\kappa$ B luciferase activity. Detailed analysis showed that the three hydroxy groups in 2 interact tightly via hydrogen bonds with the surrounding amino acid residues, GLU193, THR52, ARG30, and GLN29, meanwhile, the chlorine atom at C-3 also interacts with GLN29 by a halogen bond. Likewise, there are mainly hydrogen bond interactions between the residues of ASP217, ARG33, ARG187, and the hydroxy and ester groups in 7. Moreover, compound 7 could block RANKL-induced NF- $\kappa$ B p65 nuclear translocation, as demonstrated by preliminary Western blotting analysis (Figure 6).

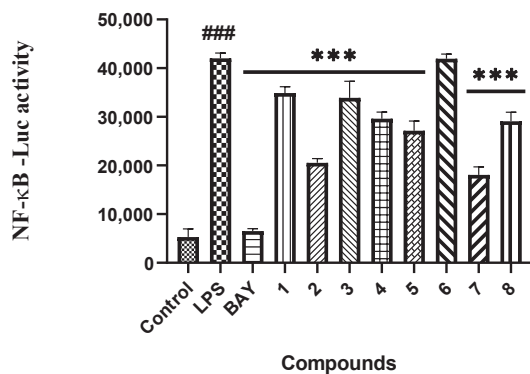
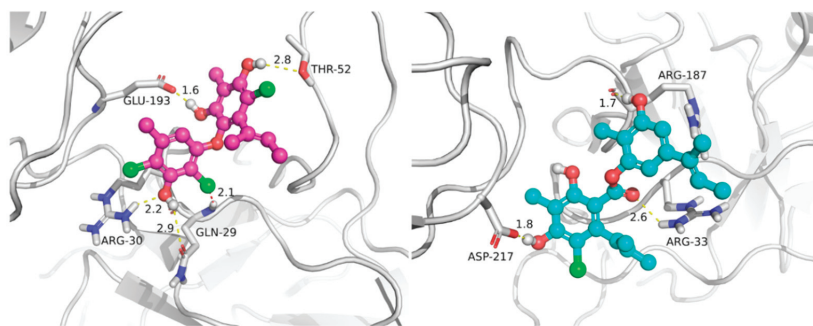
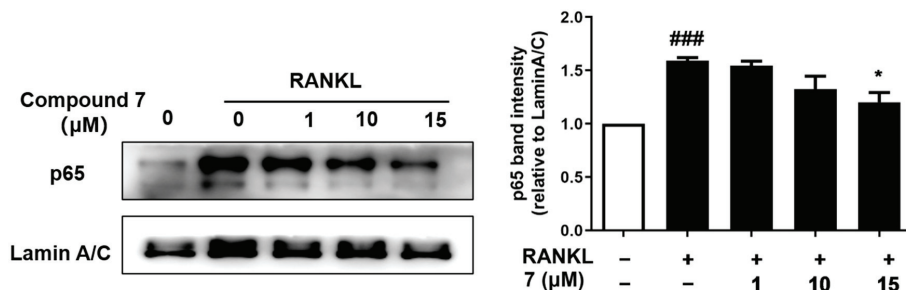


Figure 4. The inhibitory effects of compounds 1–8 on LPS-induced NF- $\kappa$ B activation in RAW264.7 cells at 20  $\mu$ M.  $n = 3$ . ###  $p < 0.001$  vs. control group (untreated); \*\*\*  $p < 0.001$  vs. LPS-induced group. BAY (BAY11-7082 treated, positive control).



**Figure 5.** The predicted binding modes of compounds **2** (left) and **7** (right) with NF- $\kappa$ B p65 (PDB code: 3GUT, chain A) by molecular docking. The protein receptor is shown by cartoon and the highlighted interacting residues are shown by thick sticks. The yellow dashed lines represent hydrogen bonds. The red dashed line represents a halogen bond.

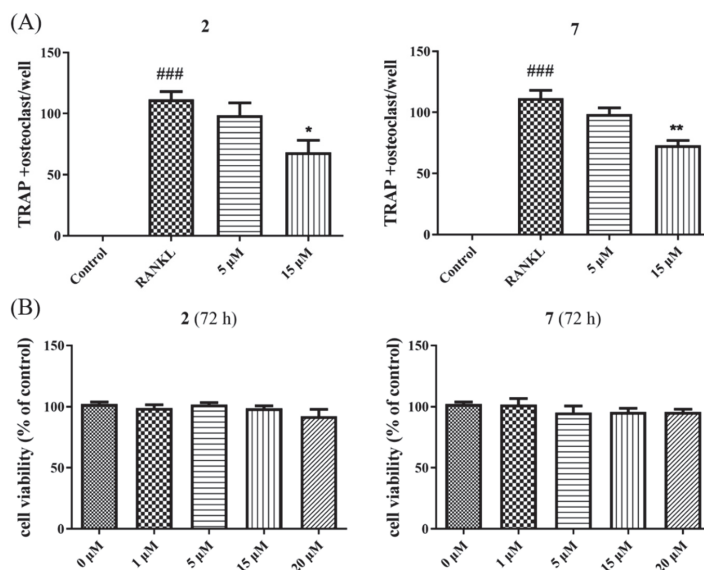


**Figure 6.** Compound **7** suppressed the RANKL-induced NF- $\kappa$ B p65 nuclear translocation in RAW264.7 cells. RAW264.7 cells were cultured with **7** (1, 10, or 15  $\mu$ M) for 4 h, stimulated with RANKL (100 ng/mL) for 30 min, and then analyzed by Western blotting with p65 and lamin A/C. The relative nuclear protein expression levels of p65 to lamin A/C were determined using ImageJ software.  $n = 3$ , ###  $p < 0.001$  vs. untreated control, \*  $p < 0.05$  vs. RANKL-treated control.

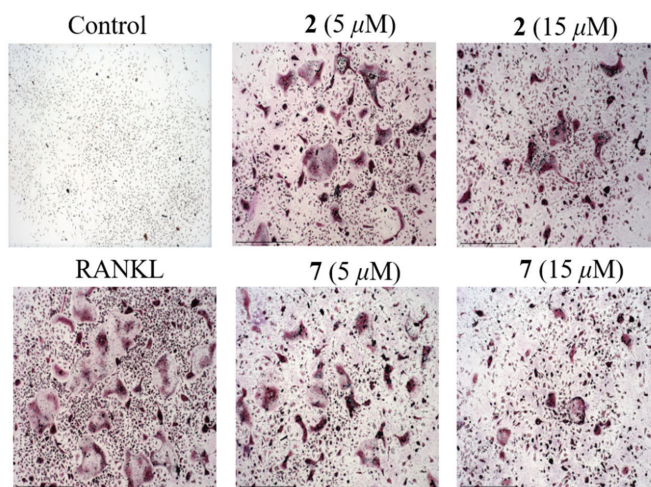
Given that NF- $\kappa$ B plays a vital role in RANKL-induced osteoclast differentiation [4], the two potent inhibitors (**2** and **7**) were then further evaluated for the effects on RANKL-induced osteoclastogenesis in BMMs. Both of them dose-dependently suppressed RANKL-induced osteoclast differentiation without any evidence of cytotoxicity (Figures 7 and 8). To our knowledge, the potent osteoclast differentiation inhibitory activity is revealed for these polyketides for the first time.

Marine biofouling, mainly accumulated by marine bacteria, algae, and invertebrates, adheres to the man-made surfaces of marine infrastructures, and is a thorny worldwide issue that causes huge losses in both marine technical and economic development [27]. Marine natural products (especially from marine microorganisms) have been recently evidenced as promising sources of antifouling lead compounds [28,29]. Thus, these isolated compounds were also evaluated for inhibitory activity against a series of marine biofilm-forming bacteria, including methicillin-resistant *Staphylococcus aureus* (MRSA), *Pseudomonas aeruginosa*, *Vibrio parahaemolyticus*, *V. alginolyticus*, *V. tubiashii*, *Microbulbifer variabilis*, *Marinobacterium jannaschii*, *V. pelagius*, *V. rotiferianus*, and *Alteromonas macleodii*. Among them, compounds **2** and **4** showed significant activity against MRSA with the same MIC value of 2  $\mu$ g/mL, as compared to that of the positive control ampicillin (1  $\mu$ g/mL) (Table 2). Besides, compounds **1**, **6**, and **7** displayed moderate anti-MRSA activity with the MIC values ranging from 16 to 32  $\mu$ g/mL. Compounds **1**, **2**, **4**, and **6–8** showed inhibition towards *M. variabilis*, *M. jannaschii*, and *V. pelagius*, with their MIC values ranging from 8

to 64  $\mu\text{g}/\text{mL}$ . By comparison of the structural characteristics between these compounds, a preliminary structure–activity relationship is discussed. The hydroxy group at C-3' in 2 would probably increase both anti-osteoclastogenic and antibacterial activity against MRSA, *M. variabilis*, and *M. jannaschii*. Moreover, the chlorine atom at C-4 in 4 would probably promote the activity against MRSA, *M. jannaschii*, and *V. pelagius*.



**Figure 7.** TRAP-positive multinucleated cells were regarded as quantified (A). Cell viability of 2 and 7 at different concentrations in BMMs for 72 h were measured by cell counting kit 8 assay (B).  $n = 3$ . ###  $p < 0.001$  vs. control group; \*  $p < 0.05$ , \*\*  $p < 0.01$  vs. RANKL group.



**Figure 8.** Representative images showing that RANKL induced osteoclast differentiation was inhibited by compounds 2 and 7 in a dose-dependent manner in BMMs. (magnification = 100 $\times$ ; scale bar = 500  $\mu\text{m}$ ).

**Table 2.** Antibacterial activities of compounds 1–8.

| Compound | Minimum Inhibitory Concentration (MIC, µg/mL) |                      |                     |                 |
|----------|---|----------------------|---------------------|-----------------|
|          | MRSA  | <i>M. variabilis</i> | <i>M. jamaschii</i> | <i>Pelagius</i> |
| 1        | 16  | 32                   | 64                  | -               |
| 2        | 2   | 16                   | 32                  | -               |
| 3        | -   | -                    | -                   | -               |
| 4        | 2   | 8                    | 16                  | 64              |
| 5        | >128  | 128                  | -                   | -               |
| 6        | 32  | 8                    | 32                  | -               |
| 7        | 16  | 64                   | >128                | -               |
| 8        | >128  | 8                    | 32                  | -               |
| control  | 1 <sup>d</sup>                                | 1 <sup>a</sup>       | 1 <sup>a</sup>      | 1 <sup>b</sup>  |
|          |   | 16 <sup>b</sup>      | 16 <sup>b</sup>     |                 |
|          |   | 32 <sup>c</sup>      | 8 <sup>c</sup>      |                 |

“-” = Inactive, <sup>a</sup> Chloramphenicol, <sup>b</sup> Nalidixic acid, <sup>c</sup> Streptomycin, <sup>d</sup> Ampicillin.

### 3. Materials and Methods

#### 3.1. General Experimental Procedures

UV and IR spectra were recorded on an UV Thermo Fisher scientific Evolution 350 spectrometer (Thermo Fisher Scientific Corporation, Waltham, MA, USA) and an IR Affinity-1 spectrometer, respectively (Shimadzu Corporation, Nakagyo-ku, Kyoto, Japan). ECD spectra were measured on a JASCO J-1500 polarimeter (JASCO Corporation, Tokyo, Japan). The NMR spectra were obtained on a Bruker Avance spectrometer (Bruker BioSpin, Fällanden, Switzerland) operating at 500 or 700 MHz for <sup>1</sup>H NMR, and 125 or 175 MHz for <sup>13</sup>C NMR, using TMS as an internal standard. HR-ESIMS spectra were collected on a Waters Xevo G2-S TOF mass spectrometer (Waters Corporation, USA). X-ray diffraction intensity data were performed on an XtalLAB PRO single-crystal diffractometer using Cu K $\alpha$  radiation (Rigaku, Japan). TLC and column chromatography (CC) were performed on plates precoated with silica gel GF254 (10–40 µm) and over silica gel (200–300 mesh) (Qingdao Marine Chemical Factory, China), respectively. All solvents employed were of analytical grade (Tianjin Damao Chemical and Industry Factory, Tianjin, China). Semi-preparative high-performance liquid chromatography (Semi-pre HPLC) was performed on a Shimadzu Prominence-I LC 2030 system (Shimadzu, Tokyo, Japan), equipping with an ODS column (YMC-pack ODS-A, YMC Co. Ltd., Kyoto, Japan, 10 × 250 mm, 5 µm, 2.5 mL/min). The artificial sea salt was a commercial product (Guangzhou Haili Aquarium Technology Company, Guangzhou, China).

#### 3.2. Fungal Strain and Fermentation

The strain GXIMD 02505 was isolated from a coral, *Pocillopora damicornis*, that was collected from the Weizhou Islands coral reef in Guangxi Zhuang autonomous region, China, in March 2019. It was taxonomically identified as *Aspergillus unguis* GXIMD 02505 by sequence analysis of the internal spacer (ITS) region of the rDNA (GenBank accession no. OL989238). A voucher specimen was deposited in our lab. The strain GXIMD 02505 was cultured on Müller Hinton broth (MB) agar plates (malt extract 15 g, artificial sea salt 15 g, and agar 20 g) at 25 °C for 7 days. Then, it was inoculated in the seed medium (malt extract 15 g and artificial sea salt 15 g in 1.0 L tap distilled H<sub>2</sub>O, pH 7.4–7.8) at 25 °C on a rotary platform shaker at 180 rpm for 48 h. Subsequently, a large-scale fermentation of *A. unguis* GXIMD 02505 was carried out in modified rice solid medium (150 g rice, 2.7 g malt extract, 2.7 g artificial sea salt, 1.8 g bacteriological peptone, and 180 mL H<sub>2</sub>O) employing 1 L × 72 Erlenmeyer flasks at room temperature for 60 days. The whole fermented cultures were extracted with EtOAc three times to provide a brown extract (94 g).

### 3.3. Extraction and Isolation

The rice fermentation products were extracted with ethyl acetate (EtOAc) and evaporated in vacuo to obtain the crude extract (94 g). The EtOAc crude extract was fractionated by medium pressure liquid chromatography (MPLC) using a step gradient elution with petroleum ether/CH<sub>2</sub>Cl<sub>2</sub>/MeOH (petroleum ether/CH<sub>2</sub>Cl<sub>2</sub>, 1:0–0:1; CH<sub>2</sub>Cl<sub>2</sub>/methanol, 1:0–1:1, *v/v*), which afforded 10 fractions (Frs.1–10) based on TLC (GF<sub>254</sub>) properties. Fr.2 was separated into 14 subfractions (Frs.2-1–2-14) via reversed-phase MPLC with MeOH/H<sub>2</sub>O (10–100%) and then Fr.2-7 was purified by semipreparative high performance liquid chromatography (HPLC) with MeOH/H<sub>2</sub>O (83:17, *v/v*, 5.0 mL/min) to yield compound **8** (*t*<sub>R</sub> = 42 min, 1.5 mg). Fr.2-9 was further purified by semipreparative HPLC on a YMC ODS column eluting with MeOH/H<sub>2</sub>O (83:17, *v/v*, adding 0.02% trifluoroacetic acid (TFA), 2.0 mL/min) to obtain compound **4** (*t*<sub>R</sub> = 37 min, 17 mg). Fr.2-13 was purified by semipreparative HPLC on naphthyl column with MeOH/H<sub>2</sub>O (81:19, *v/v*, adding 0.02%TFA, 2.0 mL/min) to yield compounds **3** (*t*<sub>R</sub> = 54 min, 1.6 mg) and **5** (*t*<sub>R</sub> = 58 min, 8.4 mg). Besides, Fr.3 was directly separated by semipreparative HPLC with MeOH/H<sub>2</sub>O (87:13, *v/v*, 5.0 mL/min) to obtained compounds **1** (*t*<sub>R</sub> = 36 min, 17 mg), **2** (*t*<sub>R</sub> = 20 min, 22 mg), **6** (*t*<sub>R</sub> = 31 min, 12 mg), and **7** (*t*<sub>R</sub> = 57 min, 11 mg).

Aspergillusidone H (**3**): white amorphous solid; UV (MeOH) λ<sub>max</sub> (logε) 270 (2.82), 207 (3.43) nm; IR (film) ν<sub>max</sub> 3446, 1683, 1653, 1269, 1205, 1139 cm<sup>-1</sup>; <sup>1</sup>H and <sup>13</sup>C NMR data, Table 1; HR-ESIMS *m/z* 389.1159 [M + H]<sup>+</sup> (calcd for C<sub>21</sub>H<sub>22</sub>ClO<sub>5</sub>, 389.1156), 411.0967 [M + Na]<sup>+</sup> (calcd for C<sub>21</sub>H<sub>21</sub>ClNaO<sub>5</sub>, 411.0975).

### 3.4. Computational Methods

The calculated ECD curve of **8** was performed by the Gaussian 16 software, referred to in our previously reported method [18]. In brief, Merck molecular force field (MMFF) calculations were carried out by means of the Spartan 14 software (Wavefunction Inc., Irvine, CA, USA). Low-energy conformers with a Boltzmann distribution over 1% were chosen for DFT/TD-DFT calculations at the B3LYP/6-311+G (d, p)//B3LYP/6-31+G (d) level in methanol by adopting 50 excited states. The ECD data were generated by the SpecDis 3.0 (University of Wurzburg, Wurzburg, Germany) using a half band width of 0.19 eV and shifted by −11 nm to facilitate comparison to the experimental data.

### 3.5. X-ray Crystallography

The crystallographic data of compound **2** obtained in MeOH was collected on a Rigaku XtaLAB PRO single-crystal diffractometer using Cu Kα radiation (λ = 1.54178 Å). Briefly, its X-ray crystal structure was solved by direct methods using SHELXS97, expanded by difference Fourier techniques, and refined by full-matrix least-squares calculation finally. The non-hydrogen atoms were refined anisotropically, and all hydrogen atoms were fixed at the geometrically ideal positions.

Crystal data for aspergillusether F (**2**): C<sub>18</sub>H<sub>17</sub>Cl<sub>3</sub>O<sub>4</sub>•4CH<sub>3</sub>OH, Mr = 499.79, crystal size 0.15 × 0.05 × 0.06 mm<sup>3</sup>, triclinic, *a* = 10.2737(4) Å, *b* = 10.5413(10) Å, *c* = 12.6374(8) Å, α = 109.081(7)°, β = 111.110(5)°, γ = 90.805(5)°, *V* = 1193.05(16) Å<sup>3</sup>, *T* = 100.00(10) K, space group *P*-1, *Z* = 2, μ(CuKα) = 1.391 mm<sup>-1</sup>, 10939 reflections collected, 4203 independent reflections (*R*<sub>int</sub> = 0.0643). The final *R*<sub>1</sub> values were 0.0751 (*I* > 2σ(*I*)). The final w*R*(*F*<sup>2</sup>) values were 0.2040 (*I* > 2σ(*I*)). The final *R*<sub>1</sub> values were 0.0880 (all data). The final w*R*(*F*<sup>2</sup>) values were 0.2175 (all data). The goodness of fit on *F*<sup>2</sup> was 0.999. The crystallographic data for the structure of aspergillusether F have been deposited in the Cambridge Crystallographic Data Centre (deposition number: CCDC 2130596).

### 3.6. Anti-Osteoclastogenic Assay

These isolates were evaluated for their inhibitory activities of LPS-induced NF-κB activation in RAW264.7 cells, as detected by a luciferase reporter gene assay as described previously [4]. In brief, the RAW264.7 cells, stably transfected with NF-κB luciferase reporter gene, were plated in triplicate for all treatments and controls in 96-well plates,

and then pretreated with these compounds (20  $\mu\text{M}$ ) and BAY11-7082 (NF- $\kappa\text{B}$  inhibitor as positive control, 5  $\mu\text{M}$ , Sigma-Aldrich) for 30 min, followed by 5  $\mu\text{g}/\text{mL}$  LPS stimulation for 8 h. Cells were harvested, and luciferase activities were measured by the luciferase assay system (Promega, Madison, WI, USA). The dose-dependent effects of compounds (1, 5, 10, 20, and 50  $\mu\text{M}$ ) on LPS induced NF- $\kappa\text{B}$  luciferase activity were also assayed by the same procedure.

For further exploration of the potential inhibition on osteoclastogenesis by compounds 2 and 7, concentrations of 5 and 15  $\mu\text{M}$  were added in BMMs with both murine macrophage-stimulating factor (M-CSF) (50 ng/mL) and RANKL (100 ng/mL) stimulation for 3 days. Then, the cells were fixed and stained for tartrate-resistant acidic phosphatase activity (TRAP) and images were taken by an inverted microscope (Nikon, Japan). A CCK-8 kit was used to evaluate the cytotoxic effects of 2 and 7 on BMMs. BMMs ( $1 \times 10^5$  cells/mL) with M-CSF (50 ng/mL) were seeded with 2 and 7 (0, 1, 5, 15, 20  $\mu\text{M}$ ) in 96-well plate for 72 h. Besides, NF- $\kappa\text{B}$  p65 nuclear translocation assay by compound 7 was performed by a confocal microscope as described previously [4]. Data are expressed as the mean  $\pm$  SD and analyzed using GraphPad Prism 7.0 software (San Diego, CA, USA). Statistical differences among groups were performed using one-way analysis of variance (ANOVA) with the Bonferroni *post-hoc* test. A *p*-value of  $<0.05$  was considered statistically significant.

### 3.7. Antibacterial Assay

Antibacterial effects against a panel of marine biofilm-forming bacterial strains, including methicillin-resistant *Staphylococcus aureus*, *Pseudomonas aeruginosa*, *Vibrio parahaemolyticus*, *V. alginolyticus*, *V. tubiashii*, *Microbulbifer variabilis*, *Marinobacterium jannaschii*, *V. pelagius*, *V. rotiferianus*, and *Alteromonas macleodii*, were tested using our previously reported method [30]. Chloramphenicol, nalidixic acid, streptomycin, and/or ampicillin were used as positive controls.

### 3.8. Molecular Docking

The Schrödinger 2019-4 suite (Schrödinger Inc., New York, NY, USA) was employed to perform the docking study [18]. The crystal structure of human NF- $\kappa\text{B}$  p65 was obtained from Protein Data Bank (<http://www.pdb.org>, accessed on 10 January 2022) (PDB code: 3GUT, chain A). The initial structure of protein was first automatically corrected by “Protein Preparation” module. Then, the binding site was putatively similar to the pocket of HIV-1 LTR, which was included in the crystal structure. The ligands were then flexibly docked to the pocket by the Glide module with standard precision mode. The docking pose with best glide score was chosen for presenting the bind mode of the molecule. The PyMOL software (DeLano Scientific, Palo Alto, CA, USA) was used to obtain the 3D structures of the binding models.

## 4. Conclusions

The chemical investigation of the Beibu Gulf coral-derived fungus *Aspergillus unguis* GXIMD 02505 led to the characterization of eight chlorinated aromatic polyketides, including a new depsidone derivative (3), together with seven known biosynthetically related analogs. The X-ray crystal structure of 2 and the absolute configuration of 8 assigned by ECD calculations are described herein for the first time. Compounds 1–5, 7 and 8 displayed inhibition of LPS-induced NF- $\kappa\text{B}$  in RAW 264.7 macrophages at 20  $\mu\text{M}$ . Moreover, the two potent inhibitors (2 and 7) further dose-dependently suppressed RANKL-induced osteoclast differentiation without any evidence of cytotoxicity in BMMs. Compound 7 could block RANKL-induced NF- $\kappa\text{B}$  p65 nuclear translocation. Besides, compounds 1, 2, 4, and 6–8 showed inhibitory activity against MRSA, *M. variabilis*, *M. jannaschii*, and *V. pelagius*, with their MIC values ranging from 2 to 64  $\mu\text{g}/\text{mL}$ . The structure–activity relationship is primarily discussed. This is the first report to report the inhibitory activity of these chlorinated aromatic polyketides on osteoclast differentiation. Our findings would not only expand the structural diversity of chlorinated depsidones, but also provide a basis for

discovering lead compounds to treat skeletal diseases characterized by excessive osteoclast differentiation, as well as for use as anti-fouling agents.

**Supplementary Materials:** The following supporting information can be downloaded at: <https://www.mdpi.com/article/10.3390/md20030178/s1>. The NMR, HR-ESIMS, UV, and IR spectra of compounds **1** and **3** (Figures S1–S18), the X ray crystal structure of compound **2** (Figure S19), the calculated ECD data of **8** (Figure S20 and Tables S1 and S2), physicochemical data of known compounds **2**, **4–8**, antibacterial activity by agar diffusion method (Figures S21–S28) and the ITS sequence of *A. unguis* GXIMD 02505.

**Author Contributions:** Conceptualization, Y.L. and X.L. (Xiaowei Luo); Data curation, Y.Z., Z.L., S.P., C.G., Y.T. and X.L. (Xiaowei Luo); Funding acquisition, Y.L. and X.L. (Xiaowei Luo); Investigation, Y.Z., Z.L., Y.T. and X.L. (Xiaowei Luo); Methodology, Y.Z. and B.H.; Resources, X.L. (Xinming Liu); Software, K.L.; Supervision, Y.L., Y.T. and X.L. (Xiaowei Luo); Writing—original draft, Y.Z. and X.L. (Xiaowei Luo); Writing—review & editing, X.L. (Xiaowei Luo). All authors have read and agreed to the published version of the manuscript.

**Funding:** This research was supported by the Special Fund for Bagui Scholars of Guangxi (Yonghong Liu), the National Natural Science Foundation of China (U20A20101, 82104496), the Natural Science Foundation of Guangxi (2021GXNSFDA075010, 2020GXNSFGA297002), the Specific Research Project of Guangxi for Research Bases and Talents (AD19110013), Guangxi Young and Middle-aged University Teachers' Scientific Research Ability Enhancement Project (2021KY0315), the Special Fund for Hundred Talents Program for Universities in Guangxi (Kai Liu), the Scientific Research Foundation of Guangxi University of Chinese Medicine (2018006, 2018ZD005, 2019BS021, 2020QN025).

**Institutional Review Board Statement:** Not applicable.

**Acknowledgments:** We acknowledge X.Z. of South China Agricultural University to provide several marine biofilm-forming bacterial strains.

**Conflicts of Interest:** The authors declare that they have no conflict of interest.

## References

- Boyle, W.J.; Simonet, W.S.; Lacey, D.L. Osteoclast differentiation and activation. *Nature* **2003**, *423*, 337–342. [[CrossRef](#)] [[PubMed](#)]
- Jacome Galarza, C.E.; Percin, G.I.; Muller, J.T.; Mass, E.; Lazarov, T.; Eitler, J.; Rauner, M.; Yadav, V.K.; Crozet, L.; Bohm, M.; et al. Developmental origin, functional maintenance and genetic rescue of osteoclasts. *Nature* **2019**, *568*, 541–545. [[CrossRef](#)] [[PubMed](#)]
- Rachner, T.D.; Khosla, S.; Hofbauer, L.C. Osteoporosis: Now and the future. *Lancet* **2011**, *377*, 1276–1287. [[CrossRef](#)]
- Tan, Y.H.; Deng, W.D.; Zhang, Y.Y.; Ke, M.H.; Zou, B.H.; Luo, X.W.; Su, J.B.; Wang, Y.Y.; Xu, J.L.; Nandakumar, K.S.; et al. A marine fungus-derived nitrobenzoyl sesquiterpenoid suppresses receptor activator of NF- $\kappa$ B ligand-induced osteoclastogenesis and inflammatory bone destruction. *Br. J. Pharmacol.* **2020**, *177*, 4242–4260. [[CrossRef](#)]
- Wang, X.Y.; Yamauchi, K.; Mitsunaga, T. A review on osteoclast diseases and osteoclastogenesis inhibitors recently developed from natural resources. *Fitoterapia* **2020**, *142*, 104482. [[CrossRef](#)] [[PubMed](#)]
- Morshed, M.T.; Vuong, D.; Crombie, A.; Lacey, A.E.; Karuso, P.; Lacey, E.; Piggott, A.M. Expanding antibiotic chemical space around the nidulin pharmacophore. *Org. Biomol. Chem.* **2018**, *16*, 3038–3051. [[CrossRef](#)]
- Ibrahim, S.R.M.; Mohamed, G.A.; Al Haidari, R.A.; El Kholi, A.A.; Zayed, M.F.; Khayat, M.T. Biologically active fungal depsidones: Chemistry, biosynthesis, structural characterization, and bioactivities. *Fitoterapia* **2018**, *129*, 317–365. [[CrossRef](#)]
- Saetang, P.; Rukachaisirikul, V.; Phongpaichit, S.; Preedanon, S.; Sakayaroj, J.; Hadsadee, S.; Jungsuttiwong, S. Antibacterial and antifungal polyketides from the fungus *Aspergillus unguis* PSU-MF16. *J. Nat. Prod.* **2021**, *84*, 1498–1506. [[CrossRef](#)]
- Niu, S.W.; Liu, D.; Shao, Z.Z.; Huang, J.; Fan, A.L.; Lin, W.H. Chlorinated metabolites with antibacterial activities from a deep-sea-derived *Spiromastix* fungus. *RSC Adv.* **2021**, *11*, 29661–29667. [[CrossRef](#)]
- Duong, T.H.; Hang, T.X.H.; Pogam, P.L.; Tran, T.N.; Mac, D.H.; Dinh, M.H.; Sichaem, J.  $\alpha$ -Glucosidase inhibitory depsidones from the lichen *Parmotrema tsavoense*. *Planta Med.* **2020**, *86*, 776–781. [[CrossRef](#)]
- Devi, A.P.; Duong, T.H.; Ferron, S.; Beniddir, M.A.; Dinh, M.H.; Nguyen, V.K.; Pham, N.K.T.; Mac, D.H.; Boustie, J.; Chavasiri, W.; et al. Salazinic acid-derived depsidones and diphenylethers with  $\alpha$ -glucosidase inhibitory activity from the lichen *Parmotrema dilatatum*. *Planta Med.* **2020**, *86*, 1216–1224. [[CrossRef](#)] [[PubMed](#)]
- Chen, Y.; Sun, L.T.; Yang, H.X.; Li, Z.H.; Liu, J.K.; Ai, H.L.; Wang, G.K.; Feng, T. Depsidones and diaryl ethers from potato endophytic fungus *Boeremia exigua*. *Fitoterapia* **2020**, *141*, 104483. [[CrossRef](#)] [[PubMed](#)]
- Ding, Y.; An, F.L.; Zhu, X.J.; Yu, H.Y.; Hao, L.L.; Lu, Y.H. Curdepsidones B–G, six depsidones with anti-inflammatory activities from the marine-derived fungus *Curvularia* sp. IFB-Z10. *Mar. Drugs* **2019**, *17*, 266. [[CrossRef](#)] [[PubMed](#)]
- Bay, M.V.; Nam, P.C.; Quang, D.T.; Mechler, A.; Hien, N.K.; Hoa, N.T.; Vo, Q.V. Theoretical study on the antioxidant activity of natural depsidones. *ACS Omega* **2020**, *5*, 7895–7902. [[CrossRef](#)]

15. Zeukang, R.D.; Siwe-Noundou, X.; Fotsing, M.T.; Kuate, T.T.; Mbafor, J.T.; Krause, R.W.M.; Choudhary, M.I.; de Theodore Atchade, A. Cordidepsine is a potential new anti-HIV depsidone from *Cordia millenii*, baker. *Molecules* **2019**, *24*, 3202. [[CrossRef](#)]
16. Morshed, M.T.; Nguyen, H.T.; Vuong, D.; Crombie, A.; Lacey, E.; Ogunniyi, A.D.; Page, S.W.; Trott, D.J.; Piggott, A.M. Semisynthesis and biological evaluation of a focused library of unguinol derivatives as next-generation antibiotics. *Org. Biomol. Chem.* **2021**, *19*, 1022–1036. [[CrossRef](#)]
17. Garlick, J.M.; Sturlis, S.M.; Bruno, P.A.; Yates, J.A.; Peiffer, A.L.; Liu, Y.; Goo, L.; Bao, L.; De Salle, S.N.; Tamayo-Castillo, G.; et al. Norstictic acid is a selective allosteric transcriptional regulator. *J. Am. Chem. Soc.* **2021**, *143*, 9297–9302. [[CrossRef](#)]
18. Luo, X.W.; Cai, G.D.; Guo, Y.F.; Gao, C.H.; Huang, W.F.; Zhang, Z.H.; Lu, H.M.; Liu, K.; Chen, J.H.; Xiong, X.F.; et al. Exploring marine-derived ascochlorins as novel human dihydroorotate dehydrogenase inhibitors for treatment of triple-negative breast cancer. *J. Med. Chem.* **2021**, *64*, 13918–13932. [[CrossRef](#)]
19. Guo, L.; Luo, X.W.; Yang, P.; Zhang, Y.T.; Huang, J.L.; Wang, H.; Guo, Y.F.; Huang, W.F.; Chen, Z.Q.; Wang, S.S.; et al. Ilicicolin a exerts antitumor effect in castration-resistant prostate cancer via suppressing EZH2 signaling pathway. *Front. Pharmacol.* **2021**, *12*, 723729. [[CrossRef](#)]
20. Luo, X.W.; Lin, X.P.; Tao, H.M.; Wang, J.F.; Li, J.Y.; Yang, B.; Zhou, X.F.; Liu, Y.H. Isochromophilones A–F, cytotoxic chloroazaphilones from the marine mangrove endophytic fungus *Diaporthe* sp. SCSIO 41011. *J. Nat. Prod.* **2018**, *81*, 934–941. [[CrossRef](#)]
21. Luo, X.W.; Chen, C.M.; Tao, H.M.; Lin, X.P.; Yang, B.; Zhou, X.F.; Liu, Y.H. Structurally diverse diketopiperazine alkaloids from the marine-derived fungus *Aspergillus versicolor* SCSIO 41016. *Org. Chem. Front.* **2019**, *6*, 736–740. [[CrossRef](#)]
22. Sadorn, K.; Saepua, S.; Bunbamrung, N.; Boonyuen, N.; Komwijit, S.; Rachtawee, P.; Pittayakhajonwut, P. Diphenyl ethers and depsidones from the endophytic fungus *Aspergillus unguis* BCC54176. *Tetrahedron* **2022**, *105*, 132612. [[CrossRef](#)]
23. Sureram, S.; Wiyakrutta, S.; Ngamrojanavanich, N.; Mahidol, C.; Ruchirawat, S.; Kittakoop, P. Depsidones, aromatase inhibitors and radical scavenging agents from the marine-derived fungus *Aspergillus unguis* CRI282-03. *Planta Med.* **2012**, *78*, 582–588. [[CrossRef](#)] [[PubMed](#)]
24. Nielsen, J.; Nielsen, P.H.; Frisvad, J.C. Fungal depside, guisinol, from a marine derived strain of *Emericella unguis*. *Phytochemistry* **1999**, *50*, 263–265. [[CrossRef](#)]
25. Cheng, Q.; Snyder, J.K. Notizen: Two new phloroglucinol derivatives with phosphodiesterase inhibitory activity from the leaves of *Eucalyptus robusta*. *Z. Fitt. Nat. B* **1991**, *46*, 1275–1277. [[CrossRef](#)]
26. Liu, D.H.; Sun, Y.Z.; Kurtan, T.; Mandi, A.; Tang, H.; Li, J.; Su, L.; Zhuang, C.L.; Liu, Z.Y.; Zhang, W. Osteoclastogenesis regulation metabolites from the coral-associated fungus *Pseudallescheria boydii* TW-1024-3. *J. Nat. Prod.* **2019**, *82*, 1274–1282. [[CrossRef](#)]
27. Ding, W.; Ma, C.F.; Zhang, W.P.; Chiang, H.; Tam, C.; Xu, Y.; Zhang, G.Z.; Qian, P.Y. Anti-biofilm effect of a butenolide/polymer coating and metatranscriptomic analyses. *Biofouling* **2018**, *34*, 111–122. [[CrossRef](#)]
28. Liu, L.L.; Wu, C.H.; Qian, P.Y. Marine natural products as antifouling molecules—A mini-review (2014–2020). *Biofouling* **2020**, *36*, 1210–1226. [[CrossRef](#)]
29. Wang, K.L.; Wu, Z.H.; Wang, Y.; Wang, C.Y.; Xu, Y. Mini-review: Antifouling natural products from marine microorganisms and their synthetic analogs. *Mar. Drugs* **2017**, *15*, 266. [[CrossRef](#)]
30. Chen, C.M.; Chen, W.H.; Tao, H.M.; Yang, B.; Zhou, X.F.; Luo, X.W.; Liu, Y.H. Diversified polyketides and nitrogenous compounds from the mangrove endophytic fungus *Penicillium steckii* SCSIO 41025. *Chin. J. Chem.* **2021**, *39*, 2132–2140. [[CrossRef](#)]





## Article

# Pyranodipyran Derivatives with Tyrosyl DNA Phosphodiesterase 1 Inhibitory Activities and Fluorescent Properties from *Aspergillus* sp. EGF 15-0-3

Xia Wei <sup>1,†</sup>, Fang-Ting Wang <sup>2,†</sup>, Mei-Xia Si-Tu <sup>1</sup>, Hao Fan <sup>1</sup>, Jin-Shan Hu <sup>1</sup>, Hao Yang <sup>2</sup>, Shan-Yue Guan <sup>3</sup>, Lin-Kun An <sup>2,\*</sup> and Cui-Xian Zhang <sup>1,\*</sup>

<sup>1</sup> School of Pharmaceutical Sciences, Guangzhou University of Chinese Medicine, Guangzhou 510006, China; weixia6994@163.com (X.W.); stmxlalala@163.com (M.-X.S.-T.); fh\_tcm@163.com (H.F.); hujinshan\_zoe@163.com (J.-S.H.)

<sup>2</sup> School of Pharmaceutical Sciences, Sun Yat-Sen University, Guangzhou 510006, China; wangft5@mail2.sysu.edu.cn (F.-T.W.); yangh328@mail2.sysu.edu.cn (H.Y.)

<sup>3</sup> Instrumental Analysis & Research Center, Sun Yat-Sen University, Guangzhou 510275, China; pugsghy@mail.sysu.edu.cn

\* Correspondence: lssalk@mail.sysu.edu.cn (L.-K.A.); zhangcuixian@gzucm.edu.cn (C.-X.Z.); Tel.: +86-020-39943413 (L.-K.A.); +86-20-39358920 (C.-X.Z.)

† These authors contributed equally to this work.

**Citation:** Wei, X.; Wang, F.-T.; Si-Tu, M.-X.; Fan, H.; Hu, J.-S.; Yang, H.; Guan, S.-Y.; An, L.-K.; Zhang, C.-X. Pyranodipyran Derivatives with Tyrosyl DNA Phosphodiesterase 1 Inhibitory Activities and Fluorescent Properties from *Aspergillus* sp. EGF 15-0-3. *Mar. Drugs* **2022**, *20*, 211. <https://doi.org/10.3390/md20030211>

Academic Editors: Yonghong Liu and Xuefeng Zhou

Received: 18 February 2022

Accepted: 13 March 2022

Published: 17 March 2022

**Publisher's Note:** MDPI stays neutral with regard to jurisdictional claims in published maps and institutional affiliations.



**Copyright:** © 2022 by the authors. Licensee MDPI, Basel, Switzerland. This article is an open access article distributed under the terms and conditions of the Creative Commons Attribution (CC BY) license (<https://creativecommons.org/licenses/by/4.0/>).

**Abstract:** Four new benzodipyran racemates, namely (±)-aspergiletals A–D (3–6), representing a rare pyrano[4,3-*h*]chromene scaffold were isolated together with eurotiumide G (1) and eurotiumide F (2) from the soft-coral-derived fungus *Aspergillus* sp. EGF 15-0-3. All the corresponding optically pure enantiomers were successfully separated by a chiral HPLC column. The structures and configurations of all the compounds were elucidated based on the combination of NMR and HRESIMS data, chiral separation, single-crystal X-ray diffraction, quantum chemical <sup>13</sup>C NMR, and electronic circular dichroism calculations. Meanwhile, the structure of eurotiumide G was also revised. The TDP1 inhibitor activities and photophysical properties of the obtained compounds were evaluated. In the TDP1 inhibition assay, as a result of synergy between (+)-6 and (–)-6, (±)-6 displayed strong inhibitory activity to TDP1 with IC<sub>50</sub> values of 6.50 ± 0.73 μM. All compounds had a large Stokes shift and could be utilized for elucidating the mode of bioactivities by fluorescence imaging.

**Keywords:** soft-coral-derived fungus; pyranodipyran derivatives; tyrosyl DNA phosphodiesterase 1 inhibitory activities; fluorescent properties

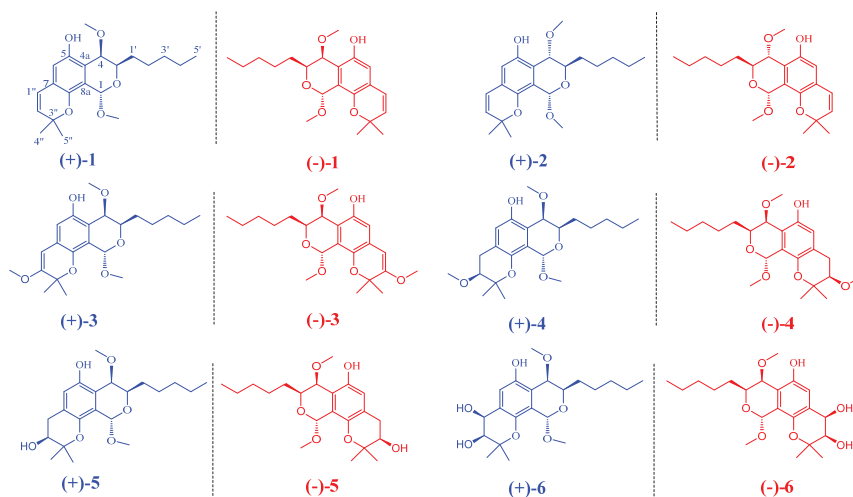
## 1. Introduction

Tyrosyl DNA phosphodiesterase 1 (TDP1) has recently been considered as a rational anticancer target [1,2] owing to its ability to break down various DNA adducts induced by chemotherapeutic drugs [3,4], such as topotecan, irinotecan, 10-hydroxycamptothecin, and belotecan [5,6]. TDP1 inhibitors can potentiate the combined anticancer activities of Top1-target anticancer drugs and overcome cancer cell resistance to therapeutic drugs in some cancers [7–9]. However, most TDP1 inhibitors today are synthetic compounds [10].

Benzodipyran is a small but unique class that mostly comes from chemical synthesis [11]. The biological activity of benzopyran scaffolds has gained considerable attention over the last few decades [12]. However, benzodipyran bearing a pyrano[4,3-*h*]chromene unit in its backbone is rare in nature, with only two examples reported to date [13].

During our continuing search for natural TDP1 inhibitors [14–18], four new benzodipyran racemates, namely (±)-aspergiletals A–D (3–6), representing a rare pyrano[4,3-*h*]chromene scaffold were isolated together with eurotiumide G (1) and eurotiumide F (2) from the soft-coral-derived fungus *Aspergillus* sp. EGF 15-0-3 (Figure 1). Biogenetically, these rare scaffolds were formed by a cascade sequence of epoxidation, nucleophilic

cyclization, and oxidation from benzene carbaldehydes. Structurally, 3–6 share the rare pyrano[4,3-*h*]chromene framework but differ in the oxygenation patterns on the 2H-pyran ring. Due to the high substitution of two pyran rings, the stereochemical complexity of these molecules makes it challenging to elucidate their absolute configurations. Based on the combination of NMR and HRESIMS data, chiral separation, quantum chemical  $^{13}\text{C}$  NMR, electronic circular dichroism calculations, and single-crystal X-ray diffraction, the absolute configurations of all the compounds were unambiguously determined. Meanwhile, the structure of eurotiomide G, was also revised. All compounds were screened for TDP1 inhibition, and the photophysical properties were evaluated. Herein, the isolation and structure elucidation, hypothetical biogenetic pathway, TDP1 inhibitor activities, and the photophysical properties of 1–6 are presented.



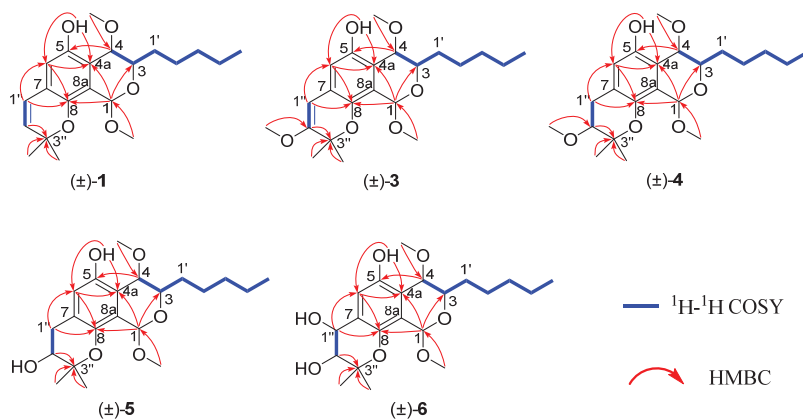
**Figure 1.** Chemical structures of compounds 1–6 from *Aspergillus* sp. EGF 15-0-3.

## 2. Results

Previously, the metabolite capability of the title strain was preliminarily accessed by integration of the OSMAC strategy and LC–MS/MS analyses [16]. As a result, the chemical profiles of benzodipyran were identified in four different media (Figure S1), indicating that benzodipyran was produced in 4 out of 18 tested media. The rice medium was selected for further scale fermentation, and the EtOAc crude extract was subjected to silica gel, Sephadex LH-20, and semipreparative HPLC to obtain six benzodipyran racemates.

Compound 1 was isolated as yellow oil with a molecular formula of  $\text{C}_{21}\text{H}_{30}\text{O}_5$  by its HR-ESI-MS  $m/z$  361.2003  $[\text{M}-\text{H}]^-$  (calculated for 361.2015), indicating the presence of seven degrees of unsaturation. The UV spectrum showed the absorption maxima at 235, 266, 276, and 341 nm. The IR spectrum showed absorption bands for hydroxyl ( $3423\text{ cm}^{-1}$ ), alkane ( $2937$  and  $2923\text{ cm}^{-1}$ ), and phenyl ( $1560$  and  $1461\text{ cm}^{-1}$ ) groups. Comprehensive analyses of the 1D NMR (Table 1) and HSQC spectra of 1 revealed the presence of a penta-substituted benzene ring ( $\delta_{\text{H}}$  6.58 (s, H-6);  $\delta_{\text{C}}$  117.8, 149.1, 113.3, 122.5, 143.4, and 124.1), one cis-disubstituted double bond ( $\delta_{\text{H}}$  6.28 (d,  $J = 10.0$ , H-1'') and 5.68 (d,  $J = 10.0$ , H-2'');  $\delta_{\text{C}}$  122.2 and 132.4), an acetal ( $\delta_{\text{H}}$  5.56 (1H, s);  $\delta_{\text{C}}$  95.4), an oxygenated quaternary carbon signal at  $\delta_{\text{C}}$  77.4, two oxygenated methines ( $\delta_{\text{H}}$  4.20 (td,  $J = 6.8, 3.2$ , H-3) and 4.44 (d,  $J = 3.2$ , H-4);  $\delta_{\text{C}}$  70.2 and 68.8), two methoxys ( $\delta_{\text{H}}$  3.54 (s,  $\text{OCH}_3$ -1) and 3.18 (s,  $\text{OCH}_3$ -4);  $\delta_{\text{C}}$  55.8 and 53.9), four methylenes ( $\delta_{\text{H}}$  1.79 (m,  $\text{H}_2$ -1'), 1.66 (m,  $\text{H}_2$ -2'), 1.61 (m,  $\text{H}_2$ -3'), and 1.51 (m,  $\text{H}_2$ -4');  $\delta_{\text{C}}$  30.4, 25.9, 32.0, and 22.8), and three methyls ( $\delta_{\text{H}}$  0.93 (t,  $J = 6.4$ ,  $\text{H}_3$ -5'), 1.41 (s,  $\text{H}_3$ -4''), and 1.41 (s,  $\text{H}_3$ -5'');  $\delta_{\text{C}}$  14.2, 27.4, and 28.0). The aforementioned spectroscopic data were highly similar to those of eurotiomide G, a natural racemate isolated from the

gorgonian-derived fungus *Eurotium* sp. XS-200900E6 [13], suggesting **1** might be the same compound as eurotiumide G. Further interpretation of the  $^1\text{H}$ - $^1\text{H}$  COSY and HMBC spectra of **1** (Figure 2) confirmed the assumption.



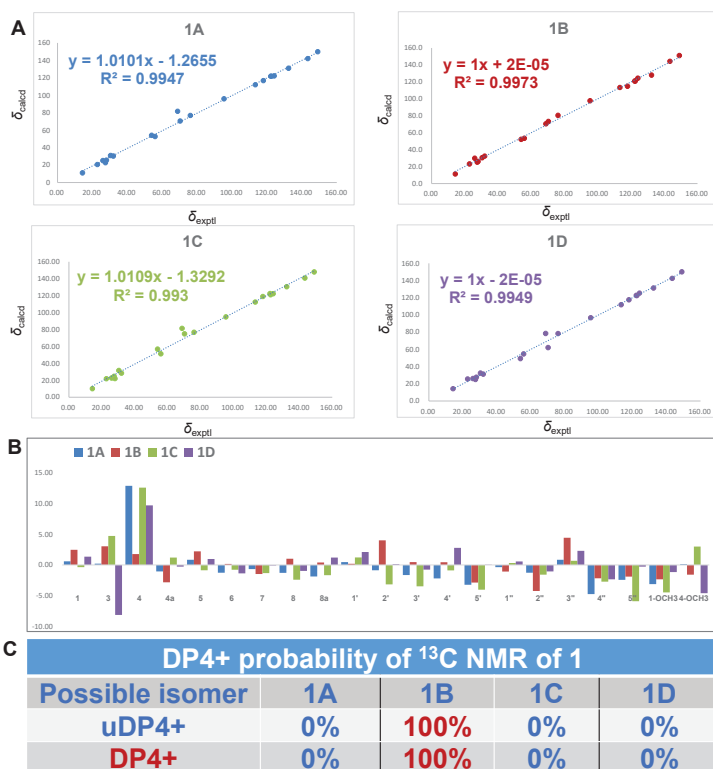
**Figure 2.**  $^1\text{H}$ - $^1\text{H}$  COSY and key HMBC correlations of **1** and **3**-**6**.

Interestingly, when we attempted to evaluate the relative configuration of **1**, we found that although the NMR data of **1** were consistent with eurotiumide G reported by Wang [13] et al. as a natural racemate from the gorgonian-derived fungus *Eurotium* sp. XS-200900E6, and by Namba [19] et al. as a synthesis through asymmetric total synthesis, their relative configurations were in conflict. Although the structure of original eurotiumide G were claimed to be revised by synthesis, small molecules with different stereo configurations may have highly similar spectra. Meanwhile, according to the key NOE correlations described in the originally reported literature, it seems that the structure of eurotiumide G they proposed is correct. This interesting phenomenon aroused our curiosity and we wondered whether these two molecules happened to have very similar NMR spectra as to be indistinguishable or the original proposed structure of eurotiumide G was incorrect. Therefore, GIAO-based quantum chemical  $^{13}\text{C}$  NMR calculations at mPW1PW91/6-31+G(d,p) level using chloroform as solution were performed to clarify the relative configuration of **1** (eurotiumide G) unambiguously. There were four possible relative configurations that needed to be taken into account:  $1R^*,3R^*,4R^*$ -**1** (**1A**);  $1R^*,3S^*,4S^*$ -**1** (**1B**);  $1S^*,3S^*,4R^*$ -**1** (**1C**); and  $1R^*,3S^*,4R^*$ -**1** (**1D**). As a result, the calculated carbon chemical shifts of **1B** were in excellent agreement with the experimental data, with coefficient value ( $R^2$ ) of 0.9973, while the predicted data for the rest of the configurations did not match the experimental ones as indicated by  $R^2$  of 0.9947, 0.9930, and 0.9949, respectively. Furthermore, DP4+ probability of 100% in favor of **1B** suggested the relative configuration of the synthesis by Namba et al. was indeed correct, and the relative configuration of **1** was unambiguously concluded as  $1R^*,3S^*,4S^*$  (Figure 3).

Table 1. <sup>1</sup>H NMR data (400 MHz) and <sup>13</sup>C NMR data (100 MHz) of 1–6 ( $\delta$  in ppm, J in Hz) <sup>a</sup>.

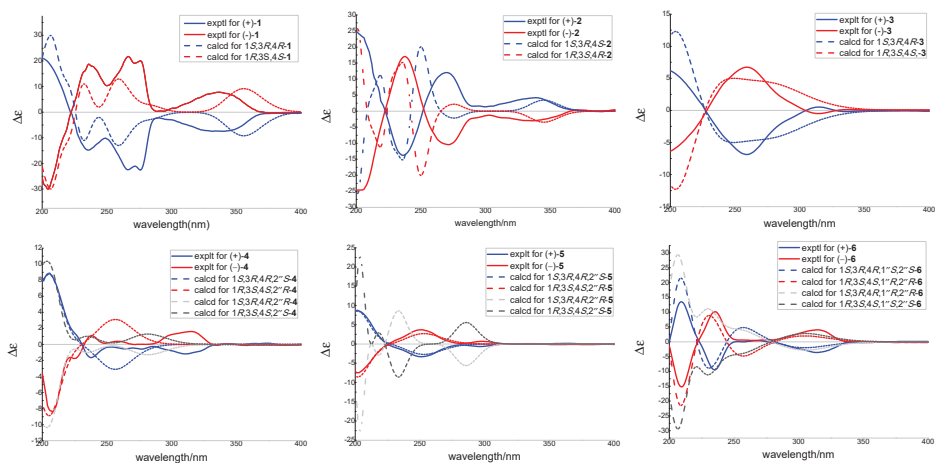
| No.                  | 1 <sup>b</sup>                |                            | 2 <sup>b</sup>                |                            | 3 <sup>b</sup>                |                            | 4 <sup>b</sup>                |                            | 5 <sup>b</sup>                       |                            | 6 <sup>c</sup>                |                            |
|----------------------|-------------------------------|----------------------------|-------------------------------|----------------------------|-------------------------------|----------------------------|-------------------------------|----------------------------|--------------------------------------|----------------------------|-------------------------------|----------------------------|
|                      | $\delta_{\text{H}}$ , mult, J | $\delta_{\text{C}}$ , mult | $\delta_{\text{H}}$ , mult, J | $\delta_{\text{C}}$ , mult | $\delta_{\text{H}}$ , mult, J | $\delta_{\text{C}}$ , mult | $\delta_{\text{H}}$ , mult, J | $\delta_{\text{C}}$ , mult | $\delta_{\text{H}}$ , mult, J        | $\delta_{\text{C}}$ , mult | $\delta_{\text{H}}$ , mult, J | $\delta_{\text{C}}$ , mult |
| 1                    | 5.56, s                       | 95.4, CH                   | 5.42, s                       | 95.2, CH                   | 5.91, s                       | 95.0, CH                   | 5.51, s                       | 95.3, CH                   | 5.52, s                              | 95.2, CH                   | 5.55, s                       | 96.6, CH                   |
| 2                    | 4.20, dt (6.8, 3.2)           | 70.2, CH                   | 4.20, dt (10.0, 3.0)          | 64.8, CH                   | 4.26, dt (6.8, 3.2)           | 70.8, CH                   | 4.18, dt (7.2, 3.2)           | 70.1, CH                   | 4.18, dt (7.0, 3.2)                  | 70.5, CH                   | 4.00, ddd (7.2, 4.4, 1.6)     | 72.6, CH                   |
| 3                    | 4.44, d (3.2)                 | 68.8, CH                   | 4.63, d (10.0)                | 76.0, CH                   | 4.56, d (3.2)                 | 68.9, CH                   | 4.44, d (3.2)                 | 68.7, CH                   | 4.43, d (3.2)                        | 68.9, CH                   | 4.34, d (1.6)                 | 70.9, CH                   |
| 4                    |                               | 117.8, C                   |                               | 117.8, C                   |                               | 114.9, C                   |                               | 117.3, C                   |                                      | 116.5, C                   |                               | 117.9, C                   |
| 4a                   |                               | 149.1, C                   |                               | 149.4, C                   |                               | 151.3, C                   |                               | 150.5, C                   |                                      | 150.2, C                   |                               | 151.4, C                   |
| 5                    | 6.58, s                       | 113.3, CH                  | 6.51, s                       | 113.4, CH                  | 7.05, s                       | 106.9, CH                  | 6.75, s                       | 112.8, CH                  | 6.76, s                              | 112.9, CH                  | 6.89, s                       | 112.9, CH                  |
| 6                    |                               | 122.5, C                   |                               | 122.5, C                   |                               | 129.4, C                   |                               | 116.2, C                   |                                      | 117.4, C                   |                               | 123.0, C                   |
| 7                    |                               | 143.4, C                   |                               | 143.0, C                   |                               | 146.3, C                   |                               | 149.3, C                   |                                      | 149.6, C                   |                               | 150.9, C                   |
| 8                    |                               | 124.1, C                   |                               | 124.2, C                   |                               | 119.9, C                   |                               | 128.8, C                   |                                      | 128.8, C                   |                               | 131.3, C                   |
| 8a                   | 1.79, m                       | 30.4, CH <sub>2</sub>      | 1.78, m                       | 31.9, CH <sub>2</sub>      | 1.86, m                       | 30.5, CH <sub>2</sub>      | 1.65, m                       | 30.8, CH <sub>2</sub>      | 1.80, m                              | 30.4, CH <sub>2</sub>      | 1.30, m                       | 31.9, CH <sub>2</sub>      |
| 1'                   | 1.66, m                       | 25.9, CH <sub>2</sub>      | 1.66, m                       | 25.2, CH <sub>2</sub>      | 1.41, m                       | 26.0, CH <sub>2</sub>      | 1.61, m                       | 26.0, CH <sub>2</sub>      | 1.25, m                              | 26.0, CH <sub>2</sub>      | 1.45, m                       | 26.8, CH <sub>2</sub>      |
| 2'                   | 1.61, m                       | 32.0, CH <sub>2</sub>      | 1.62, m                       | 32.0, CH <sub>2</sub>      | 1.40, m                       | 32.0, CH <sub>2</sub>      | 1.39, m                       | 32.0, CH <sub>2</sub>      | 1.39, m                              | 32.0, CH <sub>2</sub>      | 1.40, m                       | 33.0, CH <sub>2</sub>      |
| 3'                   | 1.51, m                       | 22.8, CH <sub>2</sub>      | 1.51, m                       | 22.8, CH <sub>2</sub>      | 1.40, m                       | 22.8, CH <sub>2</sub>      | 1.51, m                       | 30.4, CH <sub>2</sub>      | 1.33, m                              | 22.8, CH <sub>2</sub>      | 1.42, m                       | 23.7, CH <sub>2</sub>      |
| 4'                   | 0.93, t (6.4)                 | 14.2, CH <sub>3</sub>      | 0.92, t (7.2)                 | 14.2, CH <sub>3</sub>      | 0.94, t (6.8)                 | 14.3, CH <sub>3</sub>      | 0.93, t (6.6)                 | 14.2, CH <sub>3</sub>      | 0.93, t (6.4)                        | 14.2, CH <sub>3</sub>      | 0.95, t (6.8)                 | 14.4, CH <sub>3</sub>      |
| 5'                   | 6.28, d (10.0)                | 122.2, CH                  | 6.28, d (9.6)                 | 122.1, CH                  | 6.57, s                       | 103.8, CH                  | 1.81, m                       | 22.8, CH <sub>2</sub>      | 3.18, m <sup>a</sup> , 3.14, d (8.4) | 31.0, CH <sub>2</sub>      | 5.31, d (4.8)                 | 74.0, CH                   |
| 1''                  | 5.68, d (10.0)                | 132.4, CH                  | 5.68, d (9.6)                 | 132.2, CH                  |                               | 161.5, C                   | 4.74, dt (6.8, 3.2)           | 88.4, CH                   | 4.69, t (8.4)                        | 89.7, CH                   | 4.20, t (4.8)                 | 98.3, CH                   |
| 2''                  |                               | 77.4, C                    |                               | 77.4, C                    |                               | 73.6, C                    |                               | 76.1, C                    |                                      | 72.1, C                    |                               | 72.0, C                    |
| 3''                  | 1.41, s                       | 27.4, CH <sub>3</sub>      | 1.41, s                       | 27.6, CH <sub>3</sub>      | 1.62, s                       | 25.9, CH <sub>3</sub>      | 1.24, s                       | 22.2, CH <sub>3</sub>      | 1.33, s                              | 24.3, CH <sub>3</sub>      | 1.27, s                       | 25.4, CH <sub>3</sub>      |
| 4''                  | 1.41, s                       | 28.0, CH <sub>3</sub>      | 1.40, s                       | 28.0, CH <sub>3</sub>      | 1.61, s                       | 25.1, CH <sub>3</sub>      | 1.13, s                       | 19.6, CH <sub>3</sub>      | 1.19, s                              | 26.1, CH <sub>3</sub>      | 1.25, s                       | 25.8, CH <sub>3</sub>      |
| 5''                  | 3.54, s                       | 55.8, CH <sub>3</sub>      | 3.53, s                       | 56.1, CH <sub>3</sub>      | 3.63, s                       | 55.9, CH <sub>3</sub>      | 3.53, s                       | 55.8, CH <sub>3</sub>      | 3.53, s                              | 55.6, CH <sub>3</sub>      | 3.45, s                       | 58.4, CH <sub>3</sub>      |
| 1-OCH <sub>3</sub>   | 3.18, s                       | 53.9, CH <sub>3</sub>      | 3.18, s                       | 51.4, CH <sub>3</sub>      | 3.20, s                       | 53.9, CH <sub>3</sub>      | 3.26, s                       | 53.8, CH <sub>3</sub>      | 3.19, s                              | 53.9, CH <sub>3</sub>      | 3.35, s                       | 49.6, CH <sub>3</sub>      |
| 2''-OCH <sub>3</sub> |                               |                            |                               |                            | 3.15, s                       | 51.3, CH <sub>3</sub>      | 3.17, s                       | 50.2, CH <sub>3</sub>      |                                      |                            |                               |                            |

<sup>a</sup> Overlapped signals are reported without designating multiplicity, <sup>b</sup> in CDCl<sub>3</sub>, <sup>c</sup> in CD<sub>3</sub>OD.

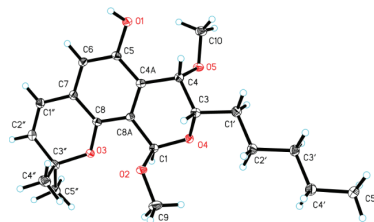


**Figure 3.**  $^{13}\text{C}$  NMR calculation results of four possible isomers of **1**. (A) Linear correlation plots of predicted versus experimental  $^{13}\text{C}$  NMR chemical shifts; (B) relative errors and standard deviations between the predicted  $^{13}\text{C}$  NMR chemical shifts of four potential structures and recorded  $^{13}\text{C}$  NMR data; (C) the DP4+ probability of  $^{13}\text{C}$  NMR chemical shifts.

However, as for the absolute configuration of eurotiumide G enantiomers, although the absolute configurations were previously established using enantioselective synthetic routes [19], the method they used to determine the structure was based on a Mo  $K\alpha$  radiation of X-ray crystallographic analysis with poor flack parameter of 0.3 (4), which may be unreliable. With the optical rotation value close to zero as well as almost no signal in its ECD spectrum, **1** was assumed to be a racemic mixture and subsequently separated into a pair of enantiomers, (+)-**1** and (−)-**1**, with a ratio of 1:1 via a chiral HPLC column. The absolute configurations of (+)-**1** and (−)-**1** were further determined by quantum chemical ECD calculation (Figure 4) and Cu  $K\alpha$  radiation of X-ray crystallographic analysis with quality flack parameter of 0.11(16) (Figure 5). Hence, based on the combination of the above evidence, the structure including absolute configurations of **1** was unambiguously established, and the (+) eurotiumide G and (−) eurotiumide G were revised correctly as 1*S*,3*R*,4*R* and 1*R*,3*S*,4*S*, respectively.



**Figure 4.** Experimental and calculated ECD spectra of (+)-1, (−)1, (+)-2, (−)2, (+)-3, (−)3, (+)-4, (−)4, (+)-5, (−)5, (+)-6, and (−)6.



**Figure 5.** X-ray ORTEP drawing of (−)1.

Interpretation of the 1D and 2D NMR of **2** indicated that it was eurotiumide F, which was also obtained as a racemate from the gorgonian-derived fungus *Eurotium* sp. XS-200900E6 [13]. Similar to eurotiumide G, the absolute configuration of eurotiumide F was not solved thoroughly. In our experiments, the chiral resolution of **2** was successfully carried out, and the absolute configuration of (+)-**2** and (−)-**2** were determined as 1*S*,3*R*,4*S* and 1*R*,3*S*,4*R* by quantum chemical ECD calculations (Figure 4). In addition, considering the experimental and calculated ECD spectra of compound **2** was complex and did not seem to be perfectly matched in the region between 200 and 220 nm, GIAO-based quantum chemical <sup>13</sup>C NMR calculations were performed to further confirm correctness of the relative configuration of **2**. As shown in Figure S2, the calculated carbon chemical shifts of 1*R*<sup>\*</sup>,3*S*<sup>\*</sup>,4*R*<sup>\*</sup>-**2** (**2D**) were in excellent agreement with the experimental data with coefficient value (*R*<sup>2</sup>) of 0.999 and DP4+ probability of 100% (Figure S2), indicating the correct stereochemical assignments of both enantiomers.

Aspergiletal A (**3**) was isolated as yellow oil with a molecular formula of C<sub>22</sub>H<sub>32</sub>O<sub>6</sub> by its HR-ESI-MS *m/z* 391.2120 [M−H]<sup>−</sup> (calculated for 391.2121), indicating the presence of seven degrees of unsaturation. Comprehensive analyses of the 1D NMR (Table 1) spectra of **3** with those of **1** suggested **3** was highly similar to **1**, and the major differences were the appearance of an additional methoxyl group ( $\delta_{\text{H}}$  3.15 (s, OCH<sub>3</sub>-2'');  $\delta_{\text{C}}$  51.3) and an olefinic proton ( $\delta_{\text{H}}$  5.68 (d, H-2'')) of **1** being absent in **3**. Interpretation of the HMBC spectrum from OCH<sub>3</sub>-2'' to C-2'' located the methoxyl group at C-2'' (Figure 2). The coupling constant of H-3 and H-4 and key NOE correlations of **3** were similar to **1**, so the relative structure of **3** was determined as 1*S*<sup>\*</sup>,3*R*<sup>\*</sup>,4*R*<sup>\*</sup>. Moreover, **3** was a racemic mixture and successfully separated into a pair of enantiomers (+)-**3** and (−)-**3** by a chiral HPLC column. The absolute

configuration of (+)-**3** and (−)-**3** were established as 1*S*,3*R*,4*R* and 1*R*,3*S*,4*S*, respectively, using the quantum chemical ECD calculation method (Figure 4).

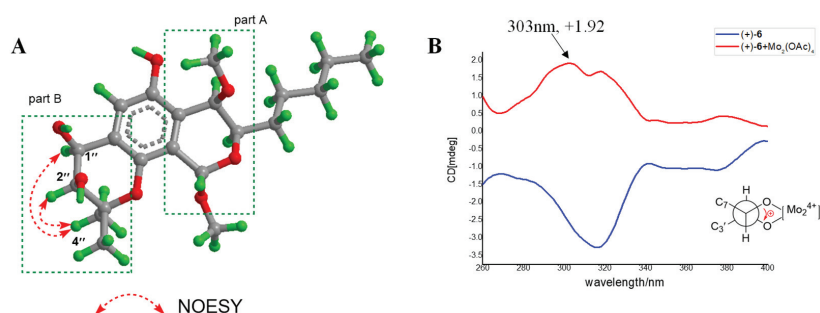
Aspergiletal B (**4**) was isolated as yellow oil with a molecular formula of C<sub>22</sub>H<sub>34</sub>O<sub>6</sub> by its HR-ESI-MS *m/z* 393.2298 [M−H]<sup>−</sup>, (calculated for 393.2277). Interpretation of the NMR spectroscopic data as well as the molecular formula of **4** indicated that it was a dihydro analogue of **3**. The main difference was the appearance of one methylene (δ<sub>H</sub> 1.81 (m, H-1''); δ<sub>C</sub> 22.8] and one oxygenated methine (δ<sub>H</sub> 4.74 (dt, *J* = 6.8, 3.2, H-2''); δ<sub>C</sub> 88.4) in **4** instead of two olefin carbons (δ<sub>H</sub> 6.57 (s, H-1''), δ<sub>C</sub> 103.8 and 161.5) in **3**. This conclusion was confirmed by further interpretation of the <sup>1</sup>H–<sup>1</sup>H COSY and HMBC spectra of **4** (Figure 2). As the structure of **4** contained two isolated stereocenters, C-1–C-4 in part A and C-1''–C-2'' in part B, separated by a pentasubstituted benzene ring, the relative configuration of isolated stereocenter was independently investigated. Based on the coupling constants of the observed protons and key NOESY correlations, the relative configuration of part A was concluded as 1*S*\*,3*R*\*,4*R*\*. Due to the lack of confident NOE correlations, it was insufficient to make conclusions on the relative configurations of two individual stereocenters using NMR methods alone. The optical values of **4** in MeOH solvent was close to zero, indicating **4** was a racemate. In order to establish the relative and absolute configurations of **4**, it was subsequently separated by a chiral HPLC column, and quantum chemical ECD calculation was carried out. In terms of the whole-compound stereochemistry, four possible absolute configurations needed to be considered: 1*S*,3*R*,4*R*,2''*S*-**4** (**4A**); 1*R*,3*S*,4*S*,2''*R*-**4** (**4B**); 1*S*,3*R*,4*R*,2''*R*-**4** (**4C**); and 1*R*,3*S*,4*S*,2''*S*-**4** (**4D**). As shown in Figure 4, the comparison of predicted ECD curves of 1*S*,3*R*,4*R*,2''*S*-**4** (**4A**) and 1*R*,3*S*,4*S*,2''*R*-**4** (**4B**) with the experimental ones of (+)-**4** and (−)-**4** showed quite good agreement (Figure 4), which allowed the absolute configurations of (+)-**4** and (−)-**4** to be established. Similar to **2**, as the experimental and calculated ECD spectra of compound **4** did not seem to be perfectly matched in the region between 230 and 280 nm, GIAO-based quantum chemical <sup>13</sup>C NMR calculations were also performed, and the result showed that the stereochemistry of compound **4** that we had derived was correct (Figure S3).

Aspergiletal C (**5**) was isolated as yellow oil with a molecular formula of C<sub>21</sub>H<sub>32</sub>O<sub>6</sub> by its HR-ESI-MS *m/z* 379.2123 [M−H]<sup>−</sup>, (calculated for 379.2121). The 1D NMR data of **5** was structurally similar to those of **4**, except for the difference of the resonance assigned to C-1'' and absence of the signal corresponding to C-2'' methoxyl (δ<sub>H</sub> 3.17 (s); δ<sub>C</sub> 50.2), suggesting the presence of C-2'' hydroxyl in **5**. Similar to **4**, **5** was also a racemate and contained two isolated stereocenters, and the absolute configurations of (+)-**5** and (−)-**5** were independently assigned as 1*S*,3*R*,4*R*,2''*S*-**5** and 1*R*,3*S*,4*S*,2''*R*-**5** (Figure 4). Certainly, the absolute stereochemical configuration at C-2'' of **5** could be determined by Mosher's method. However, unfortunately, **5** was only obtained with total amount of 1.0 mg. When **5** was chiral separated by HPLC, only 0.5 mg each of (+)-**5** and (−)-**5** were obtained, making it difficult to perform Mosher's method. Considering there were two isolated stereocenters in **5**, the stereochemistry of compound **5** was also confirmed using GIAO-based quantum chemical <sup>13</sup>C NMR calculations (Figure S4).

Aspergiletal D (**6**) was isolated as yellow oil with a molecular formula of C<sub>21</sub>H<sub>32</sub>O<sub>7</sub> by its HR-ESI-MS *m/z* 395.2076 [M−H]<sup>−</sup>, (calculated for 395.2070). The 1D NMR data highly resembled those of **5**, suggesting **6** had the same scaffold as **5**, except for the appearance of the oxygenated methine (δ<sub>H</sub> 5.31 (d, *J* = 4.8, H-1''); δ<sub>C</sub> 74.0) instead of methylene (δ<sub>H</sub> 3.18 (m, H-1''a) and 3.14 (d, *J* = 8.4, H-1''b); δ<sub>C</sub> 31.0). This suggested the presence of C-1'' hydroxyl in **6**. Similarly, **6** was a racemate and contained two isolated stereocenters, and the relative configuration of part A in **6** was established as 1*S*\*,3*R*\*,4*R*\*. Meanwhile, the key NOE correlations of H-1''/H-2'' and H<sub>3</sub>-4'' as well as small coupling constant (*J*<sub>1'',2''</sub> = 4.8 Hz) for part B in **6** indicated that H-1'' and H-2'' were in *cis*-diaxial (Figure 6A). The absolute configuration of the 1'',2''-diol unit in part B of **6** could be assigned by measuring the Mo<sub>2</sub>(OAc)<sub>4</sub> induced circular dichroism spectrum (ICD) of Mo complex of (+)-**6**. The ICD spectrum showed a positive sign of Cotton effect (CE) at 303 nm (Figure 6B), allowing the assignment of C-1'' and C-2'' as 1''*S*,2''*S* based on the empir-

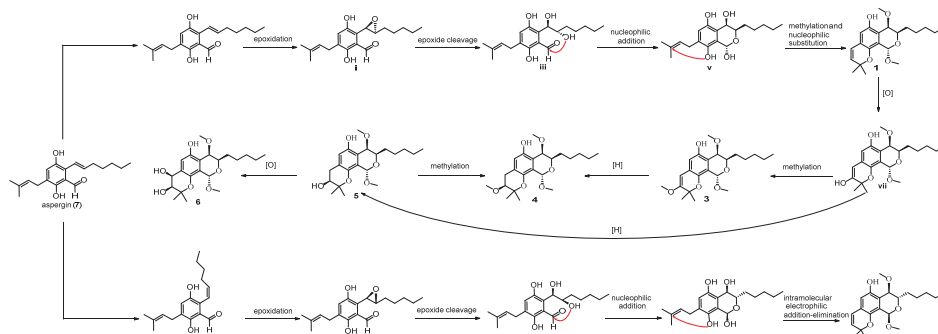


ical rule [20,21]. Finally, the absolute configurations of (+)-6 and (−)-6 were independently assigned as 1*S*,3*R*,4*R*,1''*S*,2''*S*-6 and 1*R*,3*S*,4*S*,1''*R*,2''*R*-6 by quantum chemical ECD calculation (Figure 4). Similar to 5, the stereochemistry of 6 was also confirmed using GIAO-based quantum chemical <sup>13</sup>C NMR calculations (Figure S5).



**Figure 6.** (A) Key NOE correlations of 6; (B) CD spectra of (+)-6 and Mo complex of (+)-6 recorded in DMSO (the Newman projection represents the preferred conformation of the vic-diol in the chiral Mo complex).

Based on the coisolation of the precursor aspergin (7), a plausible biosynthetic pathway for compounds 1–6 is proposed in Scheme 1. Epoxidation of the unsaturated C<sub>7</sub>-alkyl chain in 7 was followed by isomerization of the double bond and epoxidation to obtain **i** and **ii**. Subsequently, selective epoxide cleavage of **i** and **ii** were used to obtain the key intermediates **iii** and **iv**, respectively. Then, intermediates **iii** and **iv** were transformed to **v** and **vi**, respectively, under nucleophilic addition. Next, **v** and **vi** were subjected to methylation and intramolecular electrophilic addition–elimination to produce **1** and **2**, respectively. The subsequent sequence of oxidation, methylation, reduction, and oxidation of **1** led to the furnishment of 3–6, respectively.



**Scheme 1.** Hypothetical biogenetic pathways for 1–6.

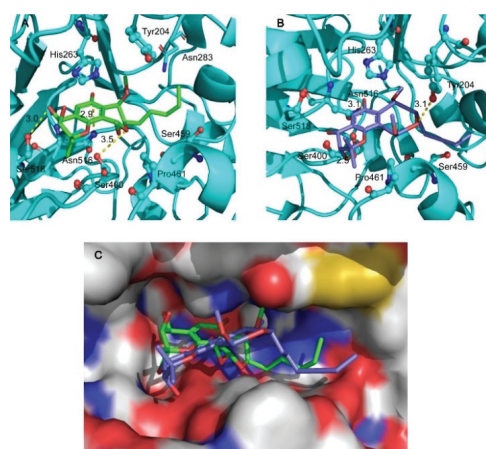
Considering the chiral properties of compounds will affect their activity, all of the obtained compounds, including racemates and enantiomers, were screened for TDP1 inhibition through a fluorescence assay using a quenched fluorescent single-stranded oligonucleotide (5'-FAM-AGGATCTAAAAGACTT-BHQ-3') as substrate. Indeed, (+)-6, (−)-6, and (±)-6 exhibited different inhibitory activity against the TDP1 enzyme with IC<sub>50</sub> values of 27.76 ± 1.73, 37.31 ± 3.63, and 6.50 ± 0.73 μM, respectively (Table 2). To further investigate the mechanism of the TDP1 inhibitory activity of (+)-6 and (−)-6, a hypothetical binding mode was built using in silico docking from the X-ray crystal structure of humanized TDP1-inhibitor (PDB: 6DJJ) [22] to evaluate the mode of interactions of (+)-6

and (−)-6 with TDP1. The inhibitor was docked into the binding site. The hypothetical structural position of the top-ranked (+)-6 is shown in Figure 7A. The tricyclic core of (+)-6 binds to the DNA binding groove in the proximity of the catalytically important residue His263, indicating a potential  $\pi$ - $\pi$  stacking interaction stabilizing the inhibitor TDP1 complex. Three hypothetical hydrogen bonds were observed between the phenol hydroxy group and the amide group of residue Asn516 (2.9 Å), the 1''-hydroxy group and Ser518 residue (3.0 Å), and the pyran O atom and Ser400 residue (3.5 Å), which might contribute to TDP1 inhibition. Similarly, the polycyclic core scaffold of (−)-6 also lied along the DNA binding groove (Figure 7B), and the H-bonds (3.1 Å) between the phenol hydroxy group and the amide group of residue Asn516 was also observed. In addition, two H-bonds formed between the 2''-hydroxyl group and Ser400 residue (2.5 Å) and the pyran oxygen atom and phenol hydroxy group of Tyr204 residue (3.1 Å). As shown in Figure 7C, the configuration of (+)-6 was more geometrically suitable for the narrow catalytic pocket than (−)-6, leading to closer proximity to the catalytic domain. The gold score values of (+)-6 and (−)-6 were 55.62 and 44.90, respectively. Interestingly, although the mode of interactions of (+)-6 and (−)-6 with TDP1 were similar, with the racemate ( $\pm$ )-6 exhibiting stronger inhibitory activity against the TDP1 enzyme with  $IC_{50}$  value of  $6.50 \pm 0.73 \mu M$ , which may be a result of synergy between (+)-6 and (−)-6. The mechanism of the TDP1 inhibitory activity of ( $\pm$ )-6 remains to be validated by biophysical assays in further research.

**Table 2.** TDP1 enzyme inhibition of the isolated compounds 1–6 ( $IC_{50} \pm SD$  in  $\mu M$ )<sup>a</sup>.

| Compound    | TDP1 Inhibition ( $\mu M$ ) | Compound    | TDP1 Inhibition ( $\mu M$ ) |
|-------------|-----------------------------|-------------|-----------------------------|
| ( $\pm$ )-1 | >100                        | ( $\pm$ )-4 | >100                        |
| (+)-1       | >100                        | (+)-4       | >100                        |
| (−)-1       | >100                        | (−)-4       | >100                        |
| ( $\pm$ )-2 | $57.81 \pm 2.20$            | ( $\pm$ )-5 | >100                        |
| (+)-2       | >100                        | (+)-5       | >100                        |
| (−)-2       | >100                        | (−)-5       | >100                        |
| ( $\pm$ )-3 | >100                        | ( $\pm$ )-6 | $6.50 \pm 0.73$             |
| (+)-3       | >100                        | (+)-6       | $27.76 \pm 1.73$            |
| (−)-3       | >100                        | (−)-6       | $37.31 \pm 3.63$            |

<sup>a</sup>  $IC_{50}$  value, defined as the concentration of the compound to inhibit 50% of TDP1 activity. Every experiment was independently repeated at least three times.



**Figure 7.** Hypothetical binding mode of (+)-6 (A) or (−)-6 (B) in the complex with TDP1 (PDB: 6DJD). (C) Overlay of the binding mode of (+)-6 or (−)-6 with TDP1. The TDP1 inhibitor (+)-6 is represented as a green stick model, (−)-6 is represented as a purple stick model, and the protein is represented as a cartoon model (A,B) and as a surface model (C).

In addition, the fluorescent properties of 1–6 were also evaluated. Interestingly, all the probes emitted detectable fluorescence (Figure 8). Fluorescence measurements revealed that all the compounds had a large Stokes shift (up to 266 nm, Table 3), suggesting they were capable of the resistance of fluorescence quenching. Surprisingly, the fluorescence of 1 increased substantially with time, indicating a structural change to a more fluorescent, undetermined species upon 365 nm irradiation. Compound 2 responded similarly to 1 but with a smaller magnitude improvement in fluorescence. In contrast, 4 appeared to be inert to photobleaching compared to 3, 5, and 6, all of which showed significant loss of fluorescence with time (Figure 9). Meanwhile, compounds 1–6 with the concentration of 100  $\mu\text{M}/\text{mL}$  were exposed to 485 nm UV light, and their fluorescence emission spectra were recorded (Figure 10) as a control experiment because the assay used to assess TDP1 inhibition was a fluorescence assay. As the figure shows, 1–6 did not exhibit fluorescence emission spectra at 510 nm when exposed to 485 nm UV light. In addition, during the TDP1 inhibition assay, the tested compound solutions were read by a Flash multimode reader at Ex485/Em510 nm to identify false-positive compounds that had autofluorescence. The above results indicate that the fluorescence of the compounds did not interfere with the inhibition results.

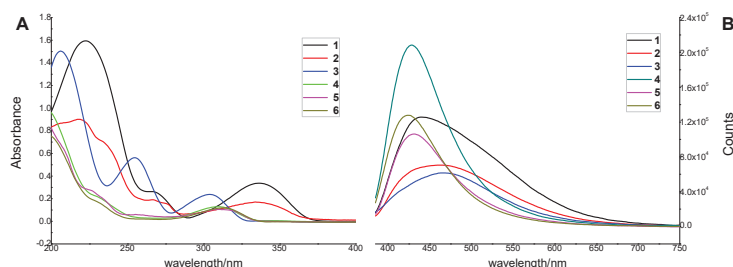


Figure 8. (A) Absorption spectra of 1–6 in MeOH; (B) fluorescence emission spectra of 1–6 in MeOH.

Table 3. Fluorescent properties of 1–6 <sup>a</sup>.

| Probes | $\lambda_{\text{abs}}$ | $\lambda_{\text{em}}^{\text{b}}$ | Stokes Shift | $\epsilon$ [ $\text{M}^{-1}\text{cm}^{-1}$ ] | $\phi_{\text{F}}$ |
|--------|------------------------|----------------------------------|--------------|--|-------------------|
| 1      | 221                    | 445                              | 224          | 125388.61                                    | 0.0392            |
| 2      | 223                    | 464                              | 241          | 70590.11                                     | 0.0225            |
| 3      | 206                    | 472                              | 266          | 61279.01                                     | 0.0048            |
| 4      | 225                    | 428                              | 203          | 208307.41                                    | 0.0649            |
| 5      | 203                    | 432                              | 229          | 106186.60                                    | 0.0482            |
| 6      | 225                    | 424                              | 199          | 127827.28                                    | 0.0416            |

<sup>a</sup> All test samples were prepared at the concentration of 300  $\mu\text{g}/\text{mL}$  in MeOH. <sup>b</sup> Determined at  $\lambda_{\text{exc}} = 365$  nm.

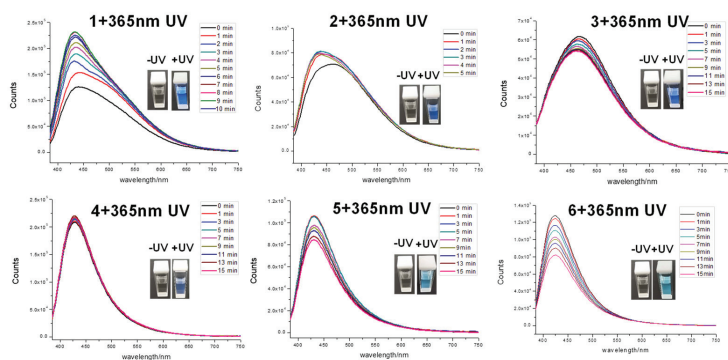
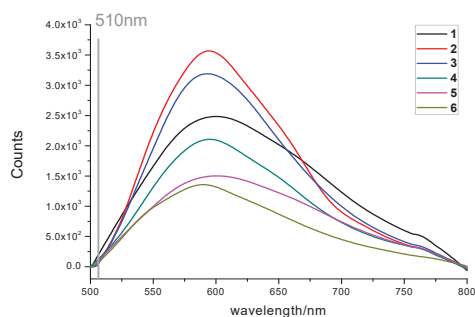


Figure 9. Change in fluorescence emission spectra of 1–6 in MeOH upon photoirradiation with 365 nm UV light.



**Figure 10.** Fluorescence emission spectra of 1–6 in MeOH upon photoirradiation with 485 nm UV light with concentration of 100  $\mu\text{M}/\text{mL}$ .

### 3. Materials and Methods

#### 3.1. General Experimental Procedures

Details of the instruments and materials used in this work are included in the Supporting Information.

#### 3.2. Fungal Strain and Fermentation

The fungal strain EGF 15-0-3 was isolated from a soft coral collected from the South China Sea and identified as *Aspergillus* sp. [23]. A voucher sample of EGF15-0-3 was preserved at the Lab of Marine Natural Medicine, Guangzhou University of Chinese Medicine, P. R. China.

The fungus was cultured on a plate containing PDB medium at 28 °C for 3 days. A single colony was transferred aseptically to an Erlenmeyer flask containing PDB medium and incubated on a rotatory shaker at 165 rpm at 28 °C for 3 days to obtain the seed culture. Subsequently, the seed culture was subcultured in polished glutinous rice medium (autoclaved sterilization with rice and artificial seawater) and incubating at 28 °C for 35 days under static conditions.

#### 3.3. Extraction and Isolation

After 35 days of cultivation, the rice medium (10 kg) of EGF 15-0-3 was extracted with ethyl acetate three times (8 h per time) on a rotatory shaker at 165 rpm and concentrated under reduced pressure at 40 °C to yield 50.0 g of the EtOAc residue. The residue was then subjected to silica gel column eluted with a gradient mixture of petroleum ether/ethyl acetate (100:0 to 0:100, *v/v*) to obtain 10 major fractions (Fr. A–Fr. J) by TLC analysis. Fr. J (4.0 g) was separated into 7 fractions (Fr. J1–Fr. J7) by Sephadex LH-20 column chromatography (GE Healthcare, China) with MeOH. Fraction J4 (1.2 g) was further separated using preparative HPLC with 80% aqueous MeOH (flow rate of 8.0 mL/min) to yield 13 subfractions (Fr. J41–Fr. J413). Subfraction J45 ( $t_R = 15.3$  min, 28.0 mg) was purified by repeated semipreparative HPLC with aqueous MeOH ( $V_{\text{MeOH}}:V_{\text{H}_2\text{O}}=60:40$ , flow rate of 3.0 mL/min) to yield 6 ( $t_R = 36.2$  min, 4.0 mg) and 5 ( $t_R = 41.6$  min, 1.0 mg); subfraction J49 ( $t_R = 20.1$  min, 21.0 mg) was purified by repeated semipreparative HPLC using aqueous MeOH as mobile phase ( $V_{\text{MeOH}}:V_{\text{H}_2\text{O}} = 70:30$ , flow rate of 3.0 mL/min) to yield 3 ( $t_R = 30.7$  min, 3.0 mg); and subfraction J412 ( $t_R = 50.1$  min, 107.0 mg) was purified by repeated semipreparative HPLC with aqueous MeOH or MeCN (flow rate of 3.0 mL/min) to yield 1 ( $t_R = 25.3$  min, 20.0 mg), 4 ( $t_R = 28.7$  min, 3.0 mg), and 2 ( $t_R = 40.2$  min, 4.0 mg).

#### 3.4. Structural Characterizations of 1–6

(±)-Eurotiomide G (1): yellow oil (MeOH),  $[\alpha]_D^{20}$  0 (c 0.02, MeOH), UV (MeOH)  $\lambda_{\text{max}}$  (log  $\epsilon$ ) 221 (1.62), 266 (0.28), 336 (0.34) nm; IR (KBr)  $\nu_{\text{max}}$  3423, 2937, 2923, 2900, 1619, 1460,

1260, 1099  $\text{cm}^{-1}$ ; HRESIMS  $m/z$ : 361.2003  $[\text{M}-\text{H}]^-$  (calculated for  $\text{C}_{21}\text{H}_{29}\text{O}_5$  361.2015);  $^1\text{H}$  MNR (400 MHz) and  $^{13}\text{C}$  NMR (100 MHz) data in  $\text{CDCl}_3$ , see Table 1.

(+)-1:  $[\alpha]_{\text{D}}^{20} +12.6$  (c 0.30, MeOH),  $[\alpha]_{\text{D}}^{20} +15.0$  (c 0.20,  $\text{CH}_2\text{Cl}_2$ ), CD (MeOH)  $\lambda_{\text{max}}$  ( $\Delta\epsilon$ ) 235 (−15.8), 267 (−24.0), 332 (−7.9) nm.

(−)-1:  $[\alpha]_{\text{D}}^{20} -10.9$  (c 0.30, MeOH),  $[\alpha]_{\text{D}}^{20} -15.3$  (c 0.20,  $\text{CH}_2\text{Cl}_2$ ), CD (MeOH)  $\lambda_{\text{max}}$  ( $\Delta\epsilon$ ) 236 (20.0), 266 (23.2), 332 (8.3) nm.

(±)-Eurotiumide F (2): yellow oil (MeOH),  $[\alpha]_{\text{D}}^{20} 0$  (c 0.02, MeOH), HRESIMS  $m/z$ : 361.2023  $[\text{M}-\text{H}]^-$  (calculated for  $\text{C}_{21}\text{H}_{29}\text{O}_5$  361.2015);  $^1\text{H}$  MNR (400 MHz) and  $^{13}\text{C}$  NMR (100 MHz) data in  $\text{CDCl}_3$ , see Table 1.

(+)-2:  $[\alpha]_{\text{D}}^{20} +17.2$  (c 0.30, MeOH), CD (MeOH)  $\lambda_{\text{max}}$  ( $\Delta\epsilon$ ) 236 (−13.7), 270 (12.0) nm, 339 (4.2) nm.

(−)-2:  $[\alpha]_{\text{D}}^{20} -15.7$  (c 0.30, MeOH), CD (MeOH)  $\lambda_{\text{max}}$  ( $\Delta\epsilon$ ) 237 (17.0), 271 (−10.4) nm, 337 (−3.0) nm.

(±)-Aspergiletal A (3): yellow oil (MeOH),  $[\alpha]_{\text{D}}^{20} 0$  (c 0.02, MeOH), UV (MeOH)  $\lambda_{\text{max}}$  ( $\log \epsilon$ ) 206 (1.49), 254 (0.58), 302 (0.24) nm; IR (KBr)  $\nu_{\text{max}}$  3347, 2937, 1699, 1562, 1411, 1347, 1112  $\text{cm}^{-1}$ ; HRESIMS  $m/z$ : 391.2120  $[\text{M}-\text{H}]^-$  (calculated for  $\text{C}_{22}\text{H}_{31}\text{O}_6$  391.2121);  $^1\text{H}$  MNR (400 MHz) and  $^{13}\text{C}$  NMR (100 MHz) data in  $\text{CDCl}_3$ , see Table 1.

(+)-3:  $[\alpha]_{\text{D}}^{20} +16.6$  (c 0.20, MeOH), CD (MeOH)  $\lambda_{\text{max}}$  ( $\Delta\epsilon$ ) 257 (−18.5), 309 (1.4) nm.

(−)-3:  $[\alpha]_{\text{D}}^{20} -14.0$  (c 0.20, MeOH), CD (MeOH)  $\lambda_{\text{max}}$  ( $\Delta\epsilon$ ) 254 (19.4), 309 (−1.3) nm.

(±)-Aspergiletal B (4): yellow oil (MeOH),  $[\alpha]_{\text{D}}^{20} 0$  (c 0.02, MeOH), UV (MeOH)  $\lambda_{\text{max}}$  ( $\log \epsilon$ ) 225 (0.26), 309 (0.13) nm; IR (KBr)  $\nu_{\text{max}}$  3382, 2927, 2856, 1693, 1461, 1380, 1230, 1105, 1041  $\text{cm}^{-1}$ ; HRESIMS  $m/z$ : 393.2298  $[\text{M}-\text{H}]^-$  (calculated for  $\text{C}_{22}\text{H}_{33}\text{O}_6$  393.2277);  $^1\text{H}$  MNR (400 MHz) and  $^{13}\text{C}$  NMR (100 MHz) data in  $\text{CDCl}_3$ , see Table 1.

(+)-4:  $[\alpha]_{\text{D}}^{20} +24.5$  (c 0.30, MeOH), CD (MeOH)  $\lambda_{\text{max}}$  ( $\Delta\epsilon$ ) 206 (8.8), 237 (−1.6), 310 (−1.2) nm.

(−)-4:  $[\alpha]_{\text{D}}^{20} -22.6$  (c 0.30, MeOH), CD (MeOH)  $\lambda_{\text{max}}$  ( $\Delta\epsilon$ ) 208 (−8.3), 238 (1.1), 315 (1.6) nm.

(±)-Aspergiletal C (5): yellow oil (MeOH),  $[\alpha]_{\text{D}}^{20} 0$  (c 0.02, MeOH), UV (MeOH)  $\lambda_{\text{max}}$  ( $\log \epsilon$ ) 203 (2.53), 249 (3.27), 270 (3.87) nm; IR (KBr)  $\nu_{\text{max}}$  3407, 2933, 2859, 1621, 1461, 1365, 1259, 1016  $\text{cm}^{-1}$ ; HRESIMS  $m/z$ : 379.2123  $[\text{M}-\text{H}]^-$  (calculated for  $\text{C}_{21}\text{H}_{31}\text{O}_6$  379.2121);  $^1\text{H}$  MNR (400 MHz) and  $^{13}\text{C}$  NMR (100 MHz) data in  $\text{CDCl}_3$ , see Table 1.

(+)-5:  $[\alpha]_{\text{D}}^{20} +20.4$  (c 0.30, MeOH), CD (MeOH)  $\lambda_{\text{max}}$  ( $\Delta\epsilon$ ) 202 (8.7), 251 (−3.3), 296 (−0.7) nm.

(−)-5:  $[\alpha]_{\text{D}}^{20} -18.2$  (c 0.30, MeOH), CD (MeOH)  $\lambda_{\text{max}}$  ( $\Delta\epsilon$ ) 204 (−7.5), 251 (3.7), 298 (0.7) nm.

(±)-Aspergiletal D (6): yellow oil (MeOH),  $[\alpha]_{\text{D}}^{20} 0$  (c 0.02, MeOH), UV (MeOH)  $\lambda_{\text{max}}$  ( $\log \epsilon$ ) 225 (0.22), 311 (0.12) nm; IR (KBr)  $\nu_{\text{max}}$  3384, 2923, 2788, 1685, 1618, 1461, 1382, 1105, 1047  $\text{cm}^{-1}$ ; HRESIMS  $m/z$ : 395.2076  $[\text{M}-\text{H}]^-$  (calculated for  $\text{C}_{21}\text{H}_{31}\text{O}_7$  395.2070);  $^1\text{H}$  MNR (400 MHz) and  $^{13}\text{C}$  NMR (100 MHz) data in  $\text{CD}_3\text{OD}$ , see Table 1.

(+)-6:  $[\alpha]_{\text{D}}^{20} +27.0$  (c 0.30, MeOH), CD (MeOH)  $\lambda_{\text{max}}$  ( $\Delta\epsilon$ ) 210 (13.5), 235 (−9.5), 313 (−3.6) nm.

(−)-6:  $[\alpha]_{\text{D}}^{20} -25.0$  (c 0.30, MeOH), CD (MeOH)  $\lambda_{\text{max}}$  ( $\Delta\epsilon$ ) 209 (−15.2), 235 (10.16), 314 (4.1) nm.

### 3.5. Chiral Separation of 1–6

Compounds 1–6 were subsequently performed on a semipreparative HPLC with a chiral chromatographic column (FLM Chiral ND (2)) (Guangzhou FLM Scientific Instrument Co., Ltd., Guangzhou, China) and successfully separated into the optical pure enantiomers. More detailed information are included in the Supporting Information.

### 3.6. Quantum Chemical Calculations

Firstly, random conformational searches were performed by SYBYL X 2.1.1 program (Tripos) using MMFF94s molecular force field, with an energy cutoff of 10  $\text{kcal mol}^{-1}$  to the global minima to obtain the conformers, and the obtained conformers were subsequently

subjected to structural optimization using Gaussian 09 software at the B3LYP/6-31+G(d) level. The optimized stable conformers were performed at mPW1PW91/6-311+G(d,p) level with chloroform or methanol as the solvent for quantum chemical NMR calculations, and ECD calculations were performed at the B3LYP/6-31+G\* level in the gas phase using Gaussian 09 software package [24] according to previous reports [25]. Boltzmann distributions of the overall NMR and ECD data were estimated and subsequently compared with the experimental ones. The DP4+ analysis was performed according to the published protocol [26]. The ECD spectra were produced by SpecDis 1.70.1 software (University of Wuerzburg, Wuerzburg, Germany) [27].

### 3.7. X-ray Crystallographic Analysis

Crystal (–)-**1** was obtained using the solvent vapor diffusion method. The intensity data of (–)-**1** was recorded on a Rigaku Oxford Diffraction Supernova diffractometer (Agilent SuperNova, America) with Cu K $\alpha$  radiation ( $\lambda = 1.54184 \text{ \AA}$ ). The crystal structure was solved and refined with a similar method reported previously [28]. For the structural refinements, nonhydrogen atoms were refined anisotropically and the hydrogen atom positions were geometrically idealized and allowed to ride on their parent atoms. Crystal data of (–)-**1** in the standard CIF format were deposited with the Cambridge Crystallographic Data Centre with CCDC number 1981300. The crystallographic data of (–)-**1** are shown in Table S1.

Crystal data for (–)-**1**: orthorhombic, C<sub>21</sub>H<sub>32</sub>O<sub>5</sub>, M = 362.45, a = 6.0081(2) Å, b = 15.4529(5) Å, c = 21.4935(8) Å,  $\alpha = 90$ ,  $\beta = 90$ ,  $\gamma = 90$ , V = 1995.51(12) Å<sup>3</sup>, space group P2<sub>1</sub>2<sub>1</sub>2<sub>1</sub>, Z = 4, Dx = 1.206 g/m<sup>3</sup>,  $\mu(\text{Cu K}\alpha) = 0.687 \text{ mm}^{-1}$ , and F(000) = 784.0. Independent reflections: 3927 ( $R_{\text{int}} = 0.0485$ ,  $R_{\text{sigma}} = 0.0547$ ), The final R1 values were 0.0448, wR2 = 0.0986 [ $I > 2 \sigma(I)$ ]. Flack parameter = 0.11(16).

### 3.8. TDP1 Inhibition Assay

The TDP1 inhibition was tested through a fluorescence assay according to a previously reported method [29]. Detailed procedures are included in the Supporting Information.

### 3.9. Molecular Modeling

Molecular Modeling was according to a previously reported method [8]. Details are included in the Supporting Information.

### 3.10. Measurement of Fluorescent Properties

Each probe was prepared at 300  $\mu\text{g/mL}$  in MeOH. The absorption spectra were recorded from 200 to 400 nm using a Chirascan circular dichroism spectrometer (Jasco, Tokyo, Japan). The fluorescence spectra were recorded from 385 to 750 nm with an excitation wavelength of 365 nm using Edinburgh Instruments FLS1000. For UV-irradiated probes, each probe was exposed to 365 nm UV light from a handheld UV lamp for a certain time, and the fluorescence spectra were then recorded using the same method mentioned above.

## 4. Conclusions

Four new benzodipyrans representing a rare pyrano[4,3-*h*]chromene scaffold, possibly originating from a cascade sequence of epoxidation, intramolecular electrophilic addition–elimination, and oxidation from the aspergin side chain, were isolated from the soft-coral-derived fungus *Aspergillus* sp. EGF 15-0-3. They were successfully separated by a chiral HPLC, and their absolute stereochemistry were determined according to XRD (Cu K $\alpha$ ), Snatzke's method, and ECD calculations. Meanwhile, the structure of eurotiamide G was also revised. The enzyme assay indicated **6** to be a novel TDP1 inhibitor, showing strong TDP1 inhibition ability with IC<sub>50</sub> value of  $6.50 \pm 0.73 \mu\text{M}$ . Preliminary results of molecular docking showed that different configurations of (+)-**6** and (–)-**6** would bring different hydrogen bond interactions and that (+)-**6** was more geometrically suitable for the narrow catalytic pocket than (–)-**6**, leading to closer proximity to the catalytic domain.

However, the strong inhibitory activity against the TDP1 enzyme by ( $\pm$ )-**6** indicated that the combination of the enantiomers provided inhibitory synergy. The mechanism of the significant TDP1 inhibitory activity of ( $\pm$ )-**6** remains to be validated by biophysical assays in further research. In addition, the superior fluorescent properties of benzodipyran derivatives could be utilized for elucidating the mode of bioactivities by fluorescence imaging.

**Supplementary Materials:** The following supporting information can be downloaded at <https://www.mdpi.com/article/10.3390/md20030211/s1>, Figure S1. UPLC-MS/MS analyses of the EtOAc extract of *Aspergillus* sp. EGF15-0-3 in different media; Figures S2–S5:  $^{13}\text{C}$  NMR calculation results of possible isomers of **2**, **4**, **5**, and **6**; Figures S6–S11: Chiral separations of **1–6**; Table S1: Crystal data and structure refinement for (–)-**1**; Tables S2–S6: Experimental chemical shifts and calculated unscaled shifts for PD4+ probability analysis for **1**, **2**, **4**, **5**, and **6**; Tables S7–S15: Details of ECD calculations of **1–6**; Figures S12–S17: Key molecular orbitals **1–6**; Figures S18–S67: the UV, IR, HRESIMS, 1D NMR, and 2D NMR spectra of compounds **1–6**.

**Author Contributions:** Conceptualization, C.-X.Z.; data curation, F.-T.W., H.F., J.-S.H., H.Y., S.-Y.G. and L.-K.A.; formal analysis, M.-X.S.-T.; funding acquisition, C.-X.Z.; investigation, X.W. and F.-T.W.; software, H.F., J.-S.H. and H.Y.; supervision, L.-K.A. and C.-X.Z.; writing—original draft, X.W.; writing—review and editing, L.-K.A. and C.-X.Z. All authors have read and agreed to the published version of the manuscript.

**Funding:** This work was financially supported the Special Project for Marine Economic Department of Natural Resources of Guangdong Province (GDNRC[2020]039 and GDNRC[2021]48), the National Natural Science Foundation of China (No. 81741160), Guangdong Basic and Applied Basic Research Foundation (2022A1515010802), and the Science and Technology Planning Project of Guangdong Province (Nos. 2017A020217008 and 2015A020216017). This paper is dedicated to professors Long-Mei Zeng and Jing-Yu Su on the occasion of their 92nd birthday.

**Institutional Review Board Statement:** Not applicable.

**Conflicts of Interest:** The authors declare no conflict of interest.

## References

- Dexheimer, T.S.; Antony, S.; Marchand, C.; Pommier, Y. Tyrosyl-DNA Phosphodiesterase as a target for anticancertherapy. *Anti-Cancer Agents Med. Chem.* **2008**, *8*, 381–389. [[CrossRef](#)] [[PubMed](#)]
- Comeaux, E.Q.; Waardenburg, R.C.A.M.V. Tyrosyl-DNA phosphodiesterase I resolves both naturally and chemically induced DNA adducts and its potential as a therapeutic target. *Drug Metab. Rev.* **2014**, *46*, 494–507. [[CrossRef](#)] [[PubMed](#)]
- Interthal, H.; Pouliott, J.J.; Champoux, J.J. The tyrosyl-DNA phosphodiesterase Tdp1 is a member of the phospholipase D superfamily. *Proc. Natl. Acad. Sci. USA* **2001**, *98*, 12009–12014. [[CrossRef](#)] [[PubMed](#)]
- Sun, Y.; Saha, S.; Wang, W.; Saha, L.K.; Huang, S.N.; Pommier, Y. Excision repair of topoisomerase DNA-protein crosslinks (TOPDPC). *DNA Repair*. **2020**, *89*, 102837. [[CrossRef](#)] [[PubMed](#)]
- Nivens, M.C.; Felder, T.; Galloway, A.H.; Pena, M.M.; Pouliot, J.J.; Spencer, H.T. Engineered resistance to camptothecin and antifolates by retroviral coexpression of tyrosyl DNA phosphodiesterase-I and thymidylate synthase. *Cancer Chemother. Pharmacol.* **2004**, *53*, 107–115.
- Barthelmes, H.U.; Habermeyer, M.; Christensen, M.O.; Mielke, C.; Interthal, H.; Pouliot, J.J.; Boege, F.; Marko, D. TDP1 overexpression in human cells counteracts DNA damage mediated by topoisomerases I and II. *J. Biol. Chem.* **2004**, *279*, 55618–55625. [[CrossRef](#)] [[PubMed](#)]
- Zakharenko, A.; Luzina, O.; Koval, O.; Nilov, D.I.; Gushchina, N.; Dyrkheeva, V.; Svedas, N.; Salakhutdinov, O.L. Tyrosyl-DNA phosphodiesterase 1 inhibitors: Usnic acid enamines enhance the cytotoxic effect of camptothecin. *J. Nat. Prod.* **2016**, *79*, 2961–2967. [[CrossRef](#)] [[PubMed](#)]
- Zhang, X.R.; Wang, H.W.; Tang, W.L.; Zhang, Y.; Yang, H.; Hu, D.X.; Ravji, A.; Marchand, C.; Kiselev, E.; Ofori-Atta, K.; et al. Discovery, Synthesis, and evaluation of oxynitidine derivatives as dual Inhibitors of DNA topoisomerase IB (TOP1) and tyrosyl-DNA phosphodiesterase 1 (TDP1), and potential antitumor agents. *J. Med. Chem.* **2018**, *61*, 9908–9930. [[CrossRef](#)] [[PubMed](#)]
- Kovaleva, K.; Oleshko, O.; Mamontova, E.; Yarovaya, O.; Zakharova, O.; Zakharenko, A.; Kononova, A.; Dyrkheeva, N.; Cheresiz, S.; Pokrovsky, A.; et al. Dehydroabietylamine ureas and thioureas as tyrosyl-DNA phosphodiesterase 1 inhibitors that enhance the antitumor effect of temozolomide on glioblastoma cells. *J. Nat. Prod.* **2019**, *82*, 2443–2450. [[CrossRef](#)] [[PubMed](#)]
- Laev, S.S.; Salakhutdinov, N.F.; Lavrik, O.I. Tyrosyl-DNA phosphodiesterase inhibitors: Progress and potential. *Bioorgan. Med. Chem.* **2016**, *24*, 5017–5027. [[CrossRef](#)] [[PubMed](#)]
- Bantick, J.R.; Cairns, H.; Chambers, A.; Hazard, R.; King, J.; Lee, T.B. Benzodipyran derivatives with anti-allergic activity. *J. Med. Chem.* **1976**, *19*, 817–821. [[CrossRef](#)] [[PubMed](#)]

12. Chen, C.Y.; Liu, N.Y.; Lin, H.C.; Lee, C.Y.; Hung, C.C.; Chang, C.S. Synthesis and bioevaluation of novel benzodipyrone derivatives as P-glycoprotein inhibitors for multidrug resistance reversal agents. *Eur. J. Med. Chem.* **2016**, *118*, 219–229. [[CrossRef](#)] [[PubMed](#)]
13. Chen, M.; Shao, C.L.; Wang, K.L.; Xu, Y.; She, Z.G.; Wang, C.Y. Dihydroisocoumarin derivatives with antifouling activities from a gorgonian-derived *Eurotium* sp. fungus. *Tetrahedron* **2014**, *70*, 9132–9138. [[CrossRef](#)]
14. Xiao, L.G.; Zhang, Y.; Zhang, H.L.; Li, D.; Gu, Q.; Tang, G.H.; Yu, Q.; An, L.K. Spiroconyone A, a new phytosterol with a spiro [5,6] ring system from *Conyza japonica*. *Org. Biomol. Chem.* **2020**, *18*, 5130–5136. [[CrossRef](#)] [[PubMed](#)]
15. Zhang, H.L.; Zhang, Y.; Yan, X.L.; Xiao, L.G.; Hu, D.X.; Yu, Q.; An, L.K. Secondary metabolites from *Isodon ternifolius* (D. Don) Kudo and their anticancer activity as DNA topoisomerase IB and Tyrosyl-DNA phosphodiesterase 1 inhibitors. *Bioorg. Med. Chem.* **2020**, *28*, 115527. [[CrossRef](#)] [[PubMed](#)]
16. Wei, X.; Su, J.C.; Hu, J.S.; He, X.X.; Lin, S.J.; Zhang, D.M.; Ye, W.C.; Chen, M.F.; Lin, H.W.; Zhang, C.X. Probing indole diketopiperazine-based hybrids as environmental-induced products from *Aspergillus* sp. EGF 15-0-3. *Org. Lett.* **2022**, *24*, 158–163. [[CrossRef](#)] [[PubMed](#)]
17. Cheng, Y.J.; Chen, N.N.; Li, J.; Su, J.C.; Yang, J.Y.; Zhang, C.X.; Lin, H.W.; Zhou, Y.J. Antimicrobial chlorinated carbazole alkaloids from the sponge-associated actinomycete *Streptomyces diacarni* LHW51701. *Chin. J. Chem.* **2021**, *39*, 1188–1192. [[CrossRef](#)]
18. Liu, B.X.; Wei, X.; Xiao, X.J.; Zhang, Q.; Zhang, C.X. Research on benzaldehydes from the soft coral-associated symbiotic fungus *Aspergillus* sp. EGF15-0-3. *J. Trop. Oceanogr.* **2021**, *40*, 63–69.
19. Nakayama, A.; Sato, H.; Nagano, S.J.; Karanjit, S.; Imagawa, H.; Namba, K. Asymmetric total syntheses and structure elucidations of (+)-eurotiumide F and (+)-eurotiumide G. *Chem. Pharm. Bull.* **2019**, *67*, 953–958. [[CrossRef](#)]
20. Snatzke, G.; Wagner, U.; Wolff, H.P. Circular dichroism—LXXVI: Cottonogenic derivatives of chiral bidentate ligands with the complex  $[\text{Mo}_2(\text{O}_2\text{CCH}_3)_4]$ . *Tetrahedron* **1981**, *37*, 349–361. [[CrossRef](#)]
21. Görecki, M.; Jabłońska, E.; Kruszewska, A.; Suszczyńska, A.; Urbańczyk-Lipkowska, Z.; Gerards, M.; Morzycki, J.W.; Szczepek, W.J.; Frelek, J. Practical method for the absolute configuration assignment of *tert/tert* 1,2-diols using their complexes with  $\text{Mo}_2(\text{OAc})_4$ . *J. Org. Chem.* **2007**, *72*, 2906–2916. [[CrossRef](#)] [[PubMed](#)]
22. Lountos, G.T.; Zhao, X.Z.; Evgeny, K.; Tropea, J.E.; Needle, D.; Pommier, Y.; Burke, T.R.; Waugh, D.S. Identification of a ligand binding hot spot and structural motifs replicating aspects of tyrosyl-DNA phosphodiesterase I (TDP1) phosphoryl recognition by crystallographic fragment cocktail screening. *Nucleic Acids Res.* **2019**, *19*, 10134–10150. [[CrossRef](#)] [[PubMed](#)]
23. Wei, X.; Feng, C.; Wang, S.Y.; Zhang, D.M.; Li, X.H.; Zhang, C.X. New indole diketopiperazine alkaloids from soft coral-associated epiphytic fungus *Aspergillus* sp. EGF 15-0-3. *Chem. Biodivers.* **2020**, *17*, e2000106. [[CrossRef](#)]
24. Frisch, M.J.; Trucks, G.W.; Schlegel, H.B.; Scuseria, G.E.; Robb, M.A.; Cheeseman, J.R.; Scalmani, G.; Barone, V.; Mennucci, B.; Petersson, G.A.; et al. (Eds.) *Gaussian 09, Revision A.02*; Gaussian, Inc.: Wallingford, CT, USA, 2009.
25. Song, J.G.; Su, J.C.; Song, Q.Y.; Huang, R.L.; Tang, W.; Hu, L.J.; Huang, X.J.; Jiang, R.W.; Li, Y.L.; Ye, W.C.; et al. Cleistocaltones A and B, Antiviral phloroglucinol–terpenoid adducts from *Cleistocalyx operculatus*. *Org. Lett.* **2019**, *21*, 9579–9583. [[CrossRef](#)] [[PubMed](#)]
26. Grimblat, N.; Zanardi, M.M.; Sarotti, A.M. Beyond DP4: An improved probability for the stereochemical assignment of isomeric compounds using quantum chemical calculations of NMR shifts. *J. Org. Chem.* **2015**, *80*, 12526–12534. [[CrossRef](#)]
27. Bruhn, T.; Schaumloffel, A.; Hemberger, Y.; Pescitelli, G. *SpecDis Version 1.70*; University of Wuerzburg: Wuerzburg, Germany, 2017.
28. Su, J.C.; Wang, S.; Cheng, W.; Huang, X.J.; Li, M.M.; Jiang, R.W.; Li, Y.L.; Wang, L.; Ye, W.C.; Wang, Y. Phloroglucinol derivatives with unusual skeletons from *Cleistocalyx operculatus* and their in vitro antiviral activity. *J. Org. Chem.* **2018**, *83*, 8522–8532. [[CrossRef](#)]
29. Hu, D.X.; Tang, W.L.; Zhang, Y.; Yang, H.; Wang, W.; Agama, K.; Pommier, Y.; An, L.K. Synthesis of methoxy-, methylenedioxy-, hydroxy-, and haloSubstituted benzophenanthridinone derivatives as DAN topoisomerase IB (TOP1) and tyrosyl-DNA phosphodiesterase 1 (TDP1) inhibitors and their biological activity for drug-resistant cancer. *J. Med. Chem.* **2021**, *64*, 7617–7629. [[CrossRef](#)]





## Article

# Butenolides from the Coral-Derived Fungus *Aspergillus terreus* SCSIO41404

Qingyun Peng<sup>1,2,†</sup>, Weihao Chen<sup>1,3,†</sup>, Xiuping Lin<sup>3</sup>, Jiao Xiao<sup>4</sup>, Yonghong Liu<sup>1,3,4</sup> and Xuefeng Zhou<sup>1,3,\*</sup>

<sup>1</sup> Southern Marine Science and Engineering Guangdong Laboratory (Guangzhou), Guangzhou 511458, China; pengqingyun18@mails.ucas.ac.cn (Q.P.); chenweihao17@mails.ucas.ac.cn (W.C.); yonghongliu@scsio.ac.cn (Y.L.)

<sup>2</sup> Research Center for Deepsea Bioresources, Sanya 572025, China

<sup>3</sup> CAS Key Laboratory of Tropical Marine Bio-Resources and Ecology/Guangdong Key Laboratory of Marine Materia Medica, South China Sea Institute of Oceanology, Chinese Academy of Sciences, Guangzhou 510301, China; xiupinglin@hotmail.com

<sup>4</sup> Wuya College of Innovation, Shenyang Pharmaceutical University, Shenyang 110016, China; xj110121@126.com

\* Correspondence: xzfzhou@scsio.ac.cn

† These authors contributed equally to this work.

**Abstract:** Five undescribed butenolides including two pairs of enantiomers, (+)-asperteretal G (**1a**), (−)-asperteretal G (**1b**), (+)-asperteretal H (**2a**), (−)-asperteretal H (**2b**), asperteretal I (**3**), and *para*-hydroxybenzaldehyde derivative, (*S*)-3-(2,3-dihydroxy-3-methylbutyl)-4-hydroxybenzaldehyde (**14**), were isolated together with ten previously reported butenolides **4–13**, from the coral-derived fungus *Aspergillus terreus* SCSIO41404. Enantiomers **1a/1b** and **2a/2b** were successfully purified by high performance liquid chromatography (HPLC) using a chiral column, and the enantiomers **1a** and **1b** were new natural products. Structures of the unreported compounds, including the absolute configurations, were elucidated by NMR and MS data, optical rotation, experimental and calculated electronic circular dichroism, induced circular dichroism, and X-ray crystal data. The isolated butenolides were evaluated for antibacterial, cytotoxic, and enzyme inhibitory activities. Compounds **7** and **12** displayed weak antibacterial activity, against *Enterococcus faecalis* (IC<sub>50</sub> = 25 µg/mL) and *Klebsiella pneumoniae* (IC<sub>50</sub> = 50 µg/mL), respectively, whereas **6** showed weak inhibitory effect on acetylcholinesterase. Nevertheless, most of the butenolides showed inhibition against pancreatic lipase (PL) with an inhibition rate of 21.2–73.0% at a concentration of 50 µg/mL.

**Keywords:** butenolides; enantiomers; *Aspergillus terreus*; pancreatic lipase

**Citation:** Peng, Q.; Chen, W.; Lin, X.; Xiao, J.; Liu, Y.; Zhou, X. Butenolides from the Coral-Derived Fungus *Aspergillus terreus* SCSIO41404. *Mar. Drugs* **2022**, *20*, 212. <https://doi.org/10.3390/md20030212>

Academic Editor: Anake Kijjoo

Received: 20 January 2022

Accepted: 15 March 2022

Published: 17 March 2022

**Publisher's Note:** MDPI stays neutral with regard to jurisdictional claims in published maps and institutional affiliations.



**Copyright:** © 2022 by the authors. Licensee MDPI, Basel, Switzerland. This article is an open access article distributed under the terms and conditions of the Creative Commons Attribution (CC BY) license (<https://creativecommons.org/licenses/by/4.0/>).

## 1. Introduction

Marine-derived fungi have been proven to be a valuable and rich source of novel and bioactive natural products [1]. Butenolides or butyrolactones, possessing the  $\alpha,\beta$ -unsaturated  $\gamma$ -butyrolactone skeleton, were frequently isolated from fungi, especially the *Aspergillus* species [2]. Butenolides have been reported to show diverse biological activities, including anti-inflammatory, cytotoxic, antiviral, antioxidant, antimicrobial, antidiabetic, protein kinase-inhibitory, and  $\alpha$ -glucosidase-inhibitory activities [2–4]. Furthermore, in vivo pharmacological, pharmacokinetics, and metabolism studies have been recently reported [3,5,6], indicating that they could be potential drug leads. Butenolides have also been reported as mycotoxins, possessing significant toxicity such as hepatic and renal oxidative damage [7]. For naturally occurring butenolides, racemic or scalemic mixtures are common [4]. Therefore, separation of racemic or scalemic mixtures to obtain enantiopure compounds is a very difficult task in natural products research. For a discovery of bioactive secondary metabolites, the coral-derived fungus *Aspergillus terreus* SCSIO41404 was investigated. Consequently, five undescribed butenolides (**1a**, **1b**, **2a**, **2b**, and **3**), ten previously reported compounds (**4–13**), and an undescribed *para*-hydroxybenzaldehyde derivative (**14**) were

isolated and identified from the ethyl acetate (EtOAc) extract of the fungal fermentation (Figure 1). Mixtures of **1a/1b** and **2a/2b** were successfully separated by HPLC using a chiral column to afford two pairs of enantiomers. The first pair of enantiomers (**1a** and **1b**) are considered to be new natural products, since the mixture **1a/1b** has previously been obtained synthetically [8]. Herein, we report the isolation, structure determination, and preliminary antibacterial, cytotoxic, and enzyme inhibitory activity assays of these compounds.

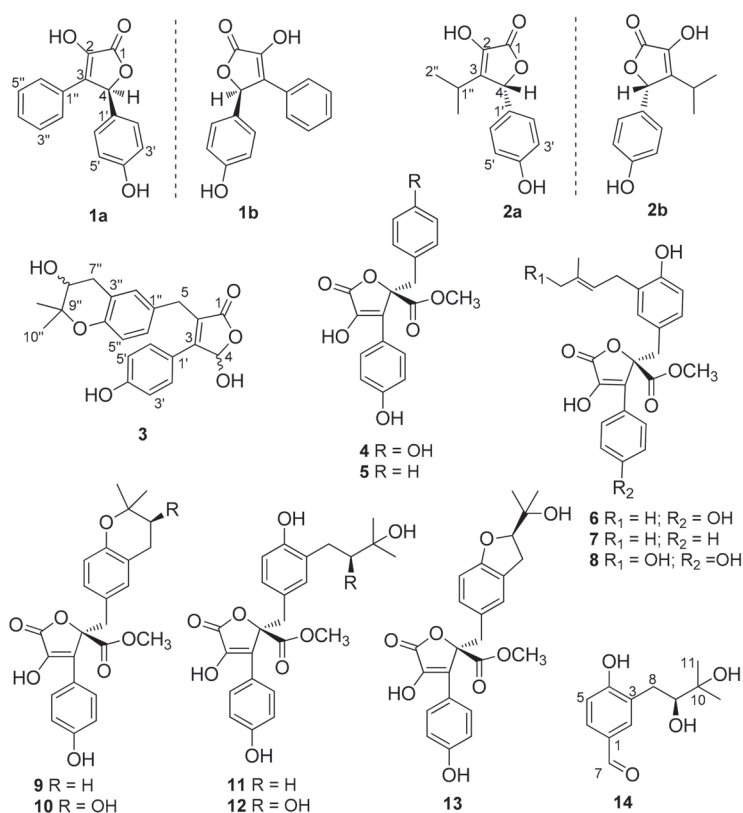


Figure 1. Structures of (1–14).

## 2. Results and Discussion

The wheat culture of *Aspergillus* sp. SCSIO41404 was extracted with EtOAc. Several chromatographic methods, including silica gel column and semi-preparative HPLC with octadecylsilyl (ODS) column, were used for isolation of the 16 compounds (Figure 1).

Compound **1** was isolated as a yellow powder and its molecular formula C<sub>16</sub>H<sub>12</sub>O<sub>4</sub> was based on HRESIMS  $m/z$  269.0811 [M + H]<sup>+</sup> (calcd for C<sub>16</sub>H<sub>13</sub>O<sub>4</sub>, 269.0808), accounting for eleven degrees of unsaturation. The <sup>1</sup>H NMR spectrum (Table 1) showed an A<sub>2</sub>B<sub>2</sub> spin system of the *para*-disubstituted benzene ring [ $\delta_{\text{H}}$  7.17 (2H, d,  $J$  = 8.6 Hz, H-2', H-6') and 6.74 (2H, d,  $J$  = 8.6 Hz, H-3', H-5')], a monosubstituted benzene ring [ $\delta_{\text{H}}$  7.63 (2H, d,  $J$  = 7.4 Hz, H-2'', H-6''), 7.28 (2H, t,  $J$  = 7.4 Hz, H-3'', H-5'') and 7.23 (1H, t,  $J$  = 7.4 Hz, H-4'')], and a singlet at  $\delta_{\text{H}}$  6.26 (1H, H-4). Besides the above six corresponding hydrogen-bearing carbon signals [ $\delta_{\text{C}}$  130.6 (C-2'/6'), 116.7 (C-3'/5'), 128.9 (C-2''/6''), 129.3 (C-3''/5''), 129.4 (C-4''), 82.4 (C-4)], six carbons remained in the <sup>13</sup>C NMR spectrum, including an ester carbonyl [ $\delta_{\text{C}}$  171.5 (C-1)] and five non-protonated sp<sup>2</sup> carbons [ $\delta_{\text{C}}$  140.2 (C-2), 132.2 (C-3),

128.4 (C-1'), 159.7 (C-4'), and 129.5 (C-1''). The carbon signals ( $\delta_C$  171.5, 140.2, 132.2, 82.4) and the HMBC correlations from H-4 to C-1, C-2 and C-3, indicated the presence of the butenolide skeleton (Figure 2) [9]. These data showed a close similarity to a synthetic racemic furanone derivative (3-hydroxy-5-(4-hydroxyphenyl)-4-phenyl-2(5H)-furanone, **5d** in the reference) [8]. Moreover, the other key HMBC correlations (Figure 2), from H-4 to C-1' and C-1'', from H-2'/H-6' to C-4 ( $\delta_C$  82.4) and C-4', confirmed a planar structure of **1**, which was assigned the trivial name asperteretal G (**1**).

**Table 1.**  $^1\text{H}$  NMR (700 MHz) and  $^{13}\text{C}$  NMR (175 MHz) Data for **1–3** in  $\text{CD}_3\text{OD}$ .

| No   | 1                 |                      | 2                     |                      | 3                     |                                    |
|------|-------------------|----------------------|-----------------------|----------------------|-----------------------|------------------------------------|
|      | $\delta_C$ , Type | $\delta_H$ (J in Hz) | $\delta_C$ , Type     | $\delta_H$ (J in Hz) | $\delta_C$ , Type     | $\delta_H$ (J in Hz)               |
| 1    | 171.5, C          |                      | 172.5, C              |                      | 175.1, C              |                                    |
| 2    | 140.2, C          |                      | 138.5, C              |                      | 125.7, C              |                                    |
| 3    | 132.2, C          |                      | 141.0, C              |                      | 158.5, C              |                                    |
| 4    | 82.4, CH          | 6.26, s              | 83.0, CH              | 5.72, s              | 99.2, CH              | 6.48, s                            |
| 5    |                   |                      |                       |                      | 30.0, CH <sub>2</sub> | 3.72, overlapped<br>3.80, d (15.7) |
| 1'   | 128.4, C          |                      | 127.6, C              |                      | 123.3, C              |                                    |
| 2'   | 130.6, CH         | 7.17, d (8.6)        | 130.1, CH             | 7.09, d (8.6)        | 131.7, CH             | 7.48, d (8.8)                      |
| 3'   | 116.7, CH         | 6.74, d (8.6)        | 116.5, CH             | 6.79, d (8.6)        | 116.6, CH             | 6.83, d (8.8)                      |
| 4'   | 159.7, C          |                      | 159.7, C              |                      | 160.9, C              |                                    |
| 5'   | 116.7, CH         | 6.74, d (8.6)        | 116.5, CH             | 6.79, d (8.6)        | 116.6, CH             | 6.83, d (8.8)                      |
| 6'   | 130.6, CH         | 7.17, d (8.6)        | 130.1, CH             | 7.09, d (8.6)        | 131.7, CH             | 7.48, d (8.8)                      |
| 1''  | 129.5, C          |                      | 27.4, CH              | 2.49, hept (7.0)     | 130.6, C              |                                    |
| 2''  | 128.9, CH         | 7.63, d (7.4)        | 21.0, CH <sub>3</sub> | 0.99, d (7.0)        | 130.3, CH             | 6.92, d (2.3)                      |
| 3''  | 129.3, CH         | 7.28, t (7.4)        | 20.1, CH <sub>3</sub> | 1.08, d (7.0)        | 121.4, C              |                                    |
| 4''  | 129.4, CH         | 7.23, t (7.4)        |                       |                      | 153.0, C              |                                    |
| 5''  | 129.3, CH         | 7.28, t (7.4)        |                       |                      | 118.1, CH             | 6.66, d (8.4)                      |
| 6''  | 128.9, CH         | 7.63, d (7.4)        |                       |                      | 128.2, CH             | 6.95, dd (8.4, 2.3)                |
| 7''  |                   |                      |                       |                      | 32.2, CH <sub>2</sub> | 2.66, dd (16.6, 7.3)               |
| 8''  |                   |                      |                       |                      | 70.5, CH              | 2.95, dd (16.6, 4.8)               |
| 9''  |                   |                      |                       |                      | 78.0, C               | 3.72, overlapped                   |
| 10'' |                   |                      |                       |                      | 25.8, CH <sub>3</sub> | 1.30, s                            |
| 11'' |                   |                      |                       |                      | 21.2, CH <sub>3</sub> | 1.23, s                            |

Although **1** has one stereogenic carbon (C-4), its optical rotation was close to zero and the inapparent Cotton effect in the electronic circular dichroism (ECD) spectrum suggested that **1** was not enantiomerically pure. Therefore, **1** was subject to a separation by HPLC using a chiral column CHIRALPAK IC, eluted with isopropanol (IPA)/n-hexane (Hex): 18/82, to obtain two pure enantiomers (**1a** and **1b**, two well-separated peaks in a ratio of approximately 1:1) (Figure 3). The enantiomers **1a** and **1b** possessed opposite Cotton effects in the ECD spectra, and their absolute configurations were determined by comparison of the experimental ECD spectra with those calculated for each enantiomer (Figure 4A,C). The ECD spectra of **1a** and **1b** showed positive and negative Cotton effects in the regions of  $\pi \rightarrow \pi^*$  transition (260–280 nm), respectively, indicating the 4S and 4R absolute configurations for **1a** and **1b**, respectively, since **1a** was obtained as a suitable crystal, and its X-ray analysis was performed. The structure of **1a** and the absolute configuration of C-4 were confirmed as shown in the ortep diagram (Figure 5). The crystal data collected on a XtalLAB PRO single-crystal diffractometer using Cu K $\alpha$  radiation are in Table S1. Therefore, this pair of enantiomers, as new natural products, were obtained for the first time, and named (+)-asperteretal G (**1a**) and (–)-asperteretal G (**1b**).

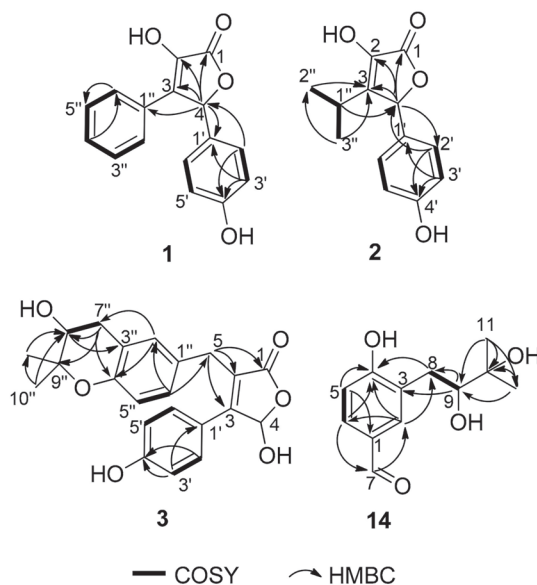


Figure 2. Key COSY and HMBC correlations in (1–3) and (14).

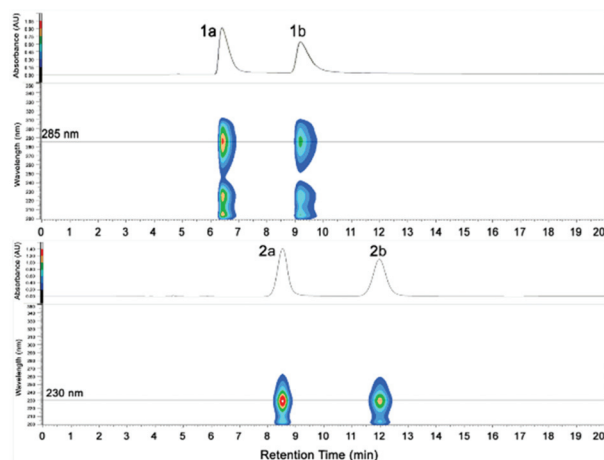


Figure 3. HPLC chromatograms of (±)-1 and (±)-2.

Compound **2** was obtained as a colorless oil. Its molecular formula was established as  $C_{13}H_{14}O_4$  by HRESIMS  $m/z$  235.0969  $[M + H]^+$  (calcd for  $C_{13}H_{15}O_4$ , 235.0965), accounting for seven degrees of unsaturation. In the  $^1H$  NMR spectrum (Table 1) of **2**, the proton signals of a *para*-disubstituted benzene ring [ $\delta_H$  7.09 (2H, d,  $J = 8.6$  Hz, H-2', H-6') and 6.79 (2H, d,  $J = 8.6$  Hz, H-3', H-5')] and an isopropyl group [2.49 (1H, hept,  $J = 7.0$  Hz, H-1''), 0.99 (3H, d,  $J = 7.0$  Hz, H-2''), and 1.08 (3H, d,  $J = 7.0$  Hz, H-3'')] were clearly observed. Analysis of the NMR data (Table 1) indicated that **2** had a similar skeleton to that of **1**, except for the phenyl group attached to C-3 in **1** was replaced by an isopropyl group, which was confirmed by HMBC correlations from H<sub>3</sub>-2'' and H<sub>3</sub>-3'' to C-3 (Figure 2). HMBC correlations from H-4 ( $\delta_H$  5.72, s) to C-1 ( $\delta_C$  172.5), C-3 ( $\delta_C$  141.0) and C-2 ( $\delta_C$  138.5), from H-2'/H-6' to C-4 ( $\delta_C$  83.0) and C-4' ( $\delta_C$  159.7), and COSY correlations from H-1'' to H<sub>3</sub>-2'',

H-1'' and H<sub>3</sub>-3'', confirmed the structure of **2**. Therefore, the planar structure of **2**, named asperteretal H (**2**), was elucidated as shown.

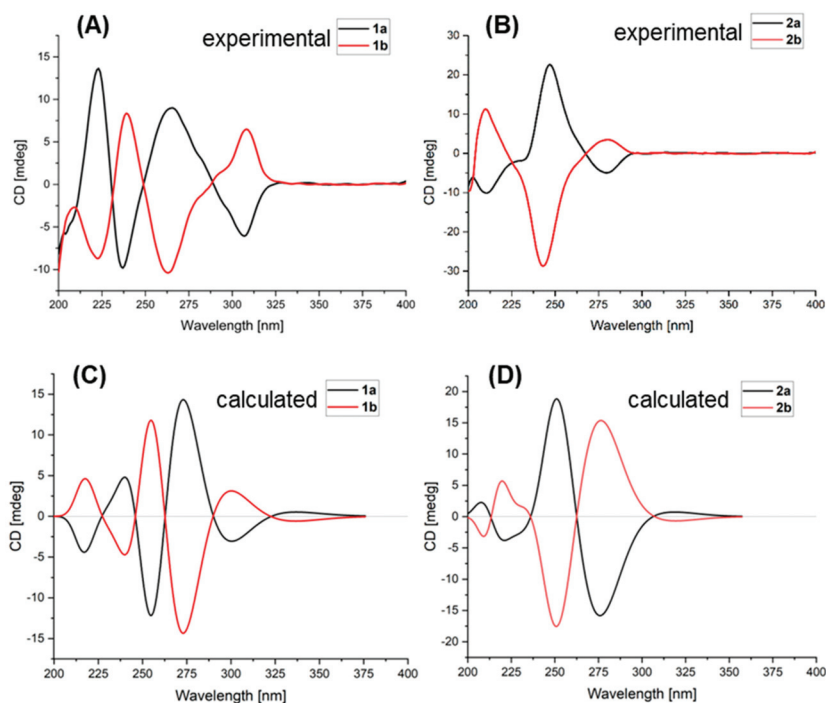


Figure 4. Experimental and calculated ECD spectra of **1a**, **1b** (A,C), **2a**, and **2b** (B,D).

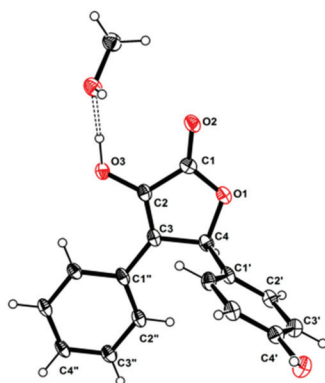


Figure 5. The ortep view of **1a**.

Similarly, the optical rotation and the inapparent ECD Cotton effect also suggested that **2** was not enantiomerically pure. The enantiomers **2a** and **2b** were also successfully separated by HPLC with a chiral column CHIRALPAK IC, eluted with IPA/Hex: 12/88 (two well-separated peaks in a ratio of approximately 1:1) (Figure 3). Enantiomers **2a** and **2b** showed opposite Cotton effects in the ECD spectra, and their absolute configurations were also determined by comparison of the experimental with the calculated ECD spectra for each enantiomer (Figure 4B,D). The positive and negative Cotton effects of **2a** and **2b**

in the region near 250 nm, respectively, supporting the 4*R* and 4*S* absolute configurations for **2a** and **2b**, respectively [10,11]. Thus, this pair of enantiomers were identified as (+)-asperteretal H (**2a**) and (−)-asperteretal H (**2b**).

Compound **3** was obtained as a yellow oil. Its molecular formula C<sub>22</sub>H<sub>22</sub>O<sub>6</sub> was determined based on HRESIMS *m/z* 381.1340 [M − H]<sup>−</sup> (calcd for C<sub>22</sub>H<sub>21</sub>O<sub>6</sub>, 381.1344), accounting for twelve degrees of unsaturation. The <sup>1</sup>H NMR spectrum (Table 1) revealed diagnostic signals of a *para*-disubstituted [ $\delta_{\text{H}}$  7.48 (2H, d, *J* = 8.8 Hz, H-2', H-6') and 6.83 (2H, d, *J* = 8.8 Hz, H-3', H-5')] and a 1,3,4-trisubstituted benzene rings [ $\delta_{\text{H}}$  6.92 (d, *J* = 2.3 Hz, H-2''), 6.66 (d, *J* = 8.4 Hz, H-5'') and 6.95 (dd, *J* = 8.4, 2.3 Hz, H-6'')], two oxygen-bearing methines [ $\delta_{\text{H}}$  6.48 (s, H-4), 3.72 (H-8'')], two methylenes [ $\delta_{\text{H}}$  3.80 (d, *J* = 15.7 Hz H-5a), 3.72 (H-5b), 2.95 (dd, *J* = 16.6, 4.8 Hz, H-7''a) and 2.66 (dd, *J* = 16.6, 7.3 Hz, H-7''b)], and two methyls [ $\delta_{\text{H}}$  1.30 (3H, s, H-10''), 1.23 (3H, s, H-11'')]. The <sup>13</sup>C NMR spectrum (Table 1), in combination with DEPT and HSQC spectra, revealed the presence of 20 carbon resonances including two methyls [ $\delta_{\text{C}}$  25.8 (C-10''), 21.2 (C-11'')], two sp<sup>3</sup> methylenes [ $\delta_{\text{C}}$  32.2 (C-7''), 30.0 (C-5)], eight protonated sp<sup>2</sup> ( $\delta_{\text{C}}$  131.7, 131.7, 130.3, 128.2, 118.1, 116.6, 116.6, 99.2), one sp<sup>3</sup> oxygenated methine ( $\delta_{\text{C}}$  70.5) and one ester carbonyl ( $\delta_{\text{C}}$  175.1), seven on-protonated sp<sup>2</sup> ( $\delta_{\text{C}}$  160.9, 153.0, 158.5, 130.6, 125.7, 123.3, 121.4), and one sp<sup>3</sup> oxygenated methine ( $\delta_{\text{C}}$  78.0). Its 1D-NMR data were similar to those of asperteretal E [4], except that H<sub>2</sub>-8'' of asperteretal E was replaced by a hydroxyl group (C-8'',  $\delta_{\text{H/C}}$  3.72/70.5). COSY correlation from H<sub>2</sub>-7'' to H-8'' and HMBC correlations from H-8'' to C-3'' and H<sub>2</sub>-7'', H<sub>3</sub>-10'', H<sub>3</sub>-11'' to C-8'' confirmed a planar structure of **3**. Compound **3** was named asperteretal I. Since there are two stereogenic carbons (C-4 and C-8''), there are four possible stereomers for **3**. The inapparent ECD Cotton effect (Figure S1) spectra suggested that **3** was not enantiomerically pure [4]. Our effort to separate the isomers of **3** with various chiral columns and mobile phase systems was not successful. Therefore, the absolute configurations of C-4 and C-8'' in **3** were still undetermined.

Compound **14** was isolated as a yellow oil and had a molecular formula C<sub>12</sub>H<sub>16</sub>O<sub>4</sub> as determined by HRESIMS *m/z* 223.0976 [M − H]<sup>−</sup> (calcd for C<sub>12</sub>H<sub>15</sub>O<sub>4</sub>, 223.0976), accounting for five degrees of unsaturation. Analysis of the NMR data indicated that **14** possessed an aldehyde group ( $\delta_{\text{H}}$  9.75, s,  $\delta_{\text{C}}$  193.1, CHO-7), a 1,2,4-trisubstituted benzene ring ( $\delta_{\text{H}}$  7.75, d, *J* = 2.0 Hz,  $\delta_{\text{C}}$  134.8, CH-2;  $\delta_{\text{H}}$  7.64, dd, *J* = 8.3, 2.0 Hz,  $\delta_{\text{C}}$  131.5, CH-6;  $\delta_{\text{H}}$  6.91, d, *J* = 8.3 Hz,  $\delta_{\text{C}}$  116.7, CH-5), an oxygen-bearing sp<sup>3</sup> methine ( $\delta_{\text{H}}$  3.63, dd, *J* = 10.4, 1.8 Hz,  $\delta_{\text{C}}$  79.4, CH-9), a sp<sup>3</sup> methylene ( $\delta_{\text{H}}$  3.07, dd, *J* = 14.1, 1.8 Hz, 2.60, dd, *J* = 14.1, 10.4 Hz,  $\delta_{\text{C}}$  33.8, CH<sub>2</sub>-8), and two methyls ( $\delta_{\text{H}}$  1.25, 6H, s,  $\delta_{\text{C}}$  25.7, 25.1, CH<sub>3</sub>-11 and CH<sub>3</sub>-12). These data were similar to those of 3-(2,3-dihydroxy-isopentyl)-4-hydroxy-acetophenone [12] except for the replacement of the acetyl group on C-1 of 3-(2,3-dihydroxy-isopentyl)-4-hydroxy-acetophenone with an aldehyde group (CHO-7) in **14** [12]. Moreover, the HMBC correlations from H-6 to C-7 and H-7 to C-2 further determined the structure (Figure 1). The absolute configuration of C-9 was determined to be *S* by using the Mo<sub>2</sub>(OAc)<sub>4</sub>-induced circular dichroism method (a positive cotton effect at 314 nm) (Figure 6) [13]. Thus, **14** was identified as (S)-3-(2,3-dihydroxy-3-methylbutyl)-4-hydroxybenzaldehyde.

The previously reported compounds were identified as butyrolactone II (**4**) [14], methyl I-2-benzyl-4-hydroxy-3-(4-hydroxyphenyl)-5-oxo-2,5-dihydrofuran-2-carboxylate (**5**) [8,15], butyrolactone I (**6**) [16], versicolactone B (**7**) [17], aspernolide D (**8**) [18], aspernolide A (**9**) [19], butyrolactone V (**10**) [16], terrelactone (**11**) [20], butyrolactone VI (**12**) [21], and butyrolactone IV (**13**) [16] by comparison of their spectroscopic data (Supporting Information, Figures S26–S35) with those reported in the literature.

Compounds **1–14** were evaluated for their cytotoxic activity against human lung carcinoma (A549) and human hepatocellular carcinoma (HepG2) cell lines, but none showed cytotoxicity at a concentration of 50  $\mu\text{M}$ . Most of the compounds were screened for their enzyme inhibitory effects against pancreatic lipase (PL) and acetylcholinesterase (AChE) *in vitro*, and also antibacterial activity against five pathogenic bacteria, *Staphylococcus aureus* ATCC 29213, *Enterococcus faecalis* ATCC 29212, *Klebsiella pneumoniae* ATCC 13883, methicillin-resistant *S. aureus* (MRSA, clinical strain), and methicillin-resistant *S. epidermidis*

(MRSE, clinical strain) (Table 2). Only 7 and 12 displayed weak antibacterial activity against *E. faecalis* (IC<sub>50</sub> value of 25 µg/mL) and *K. pneumoniae* (IC<sub>50</sub> value of 50 µg/mL), respectively. Compound 6 displayed weak inhibitory effect on AChE (35.2%, at 50 µg/mL concentration). Nevertheless, most of the butenolides (1a/1b, 2a/2b, 3, 6, 7, 10, 12, and 13) showed inhibition against PL with inhibition rate of 21.2–73.0% at a concentration of 50 µg/mL (Table 2).

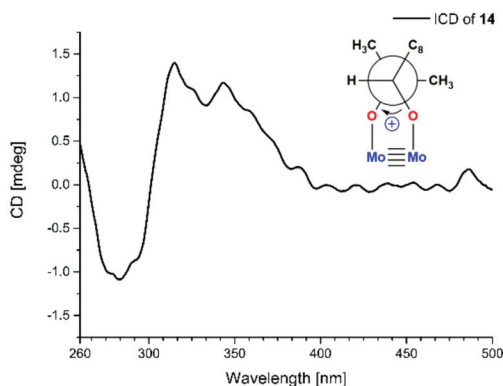


Figure 6. Mo<sub>2</sub>(Oac)<sub>4</sub>-induced CD spectrum of 14.

Table 2. The enzyme inhibitory and antibacterial activities of 1–7 and 10–13.

| Comp.   | Enzyme Inhibition Rate at 50 µg/mL (%) |                   | Antibacterial Activities (MIC, µg/mL) |                      |
|---------|--|-------------------|---------------------------------------|----------------------|
|         | PL                                     | AChE              | <i>E. faecalis</i>                    | <i>K. pneumoniae</i> |
| 1a/1b   | 58.8                                   | <10               | >100                                  | >100                 |
| 2a/2b   | 67.2                                   | <10               | >100                                  | >100                 |
| 3       | 35.5                                   | <10               | >100                                  | >100                 |
| 4       | <10                                    | <10               | >100                                  | >100                 |
| 5       | <10                                    | <10               | >100                                  | >100                 |
| 6       | 37.6                                   | 35.2              | >100                                  | 100                  |
| 7       | 73.0                                   | <10               | 25                                    | >100                 |
| 10      | 54.1                                   | <10               | >100                                  | >100                 |
| 11      | <10                                    | <10               | >100                                  | >100                 |
| 12      | 21.2                                   | <10               | >100                                  | 50                   |
| 13      | 66.8                                   | <10               | >100                                  | >100                 |
| Control | 86.5 <sup>a</sup>                      | 83.7 <sup>b</sup> | 4 <sup>c</sup>                        | 0.5 <sup>c</sup>     |

<sup>a</sup> Orlistat, <sup>b</sup> tacrine, and <sup>c</sup> ampicillin were used as positive controls.

### 3. Materials and Methods

#### 3.1. General Experimental Procedures

UV spectra were measured on a Shimadzu UV-2600 PC spectrophotometer (Shimadzu, Kyoto, Japan). Optical rotations were recorded on a PerkinElmer MPC 500 (Waltham, MA, USA) polarimeter. For ECD spectra, Chirascan circular dichroism spectrometer (Applied Photophysics, Leatherhead Surrey, UK) was used. NMR spectra were acquired by a Bruker Avance spectrometer (Bruker, Billerica, MA, USA) at 700 MHz for <sup>1</sup>H and 175 MHz for <sup>13</sup>C. HRESIMS spectra were recorded on a Bruker miXis TOF-QII mass spectrometer (Bruker, Billerica, MA, USA). X-ray diffraction intensity data were measured on an Agilent Xcalibur Nova single-crystal diffractometer (Santa Clara, CA, USA) using Cu K $\alpha$  radiation. TLC and column chromatography were performed on plates precoated with silica gel GF<sub>254</sub> (10–40 µm) and over silica gel (200–300 mesh) (Qingdao Marine Chemical Factory, Qingdao, China), respectively. Spots were detected on TLC (Qingdao Marine Chemical Factory, Qingdao, China) under 254 nm UV light. Semi-preparative HPLC was performed using an ODS column (YMC-pack ODS-A, YMC Co., Ltd., Kyoto, Japan, 10 mm × 250 mm, 5 µm).



### 3.2. Fungal Material

The fungal strain *Aspergillus* sp. SCSIO41404 was isolated from a soft coral *Simularia* sp., collected in the Luhuitou waters (109°29′37.3″ E, 18°11′33.4″ N) of Sanya Bay in the South China Sea, in June 2019. The strain was stored on Muller Hinton broth (MB) agar (malt extract 15 g, sea salt 10 g, agar 15 g, H<sub>2</sub>O 1 L, pH 7.4–7.8) at 4 °C and deposited in the CAS Key Laboratory of Tropical Marine Bio-resources and Ecology, South China Sea Institute of Oceanology, Chinese Academy of Sciences, Guangzhou, China. The strain was identified as *Aspergillus terreus* based on the ITS region of the rDNA (GenBank accession No. KU866665.1) (Table S2).

### 3.3. Fermentation and Extraction

The seed medium (malt extract 15 g, sea salt 10 g, H<sub>2</sub>O 1 L, pH 7.4–7.8) in 500 mL Erlenmeyer flasks (150 mL/flask) was incubated at 28 °C for 3 days on a rotating shaker (180 rpm). The seed medium was added to the wheat fermentation medium (wheat 200 g, sea salt 10g, H<sub>2</sub>O 200 mL) in a 1000 mL Erlenmeyer flask. In total, 40 Erlenmeyer flasks were incubated for 30 days at 25 °C without shaking. The whole wheat cultures were crushed and extracted with EtOAc three times to afford an organic extract.

### 3.4. Isolation and Purification

The EtOAc extract (638.1 g) was subjected to silica gel column chromatography eluted with PE-EtOAc-MeOH (50:1:0 to 0:0:1, *v/v*) in gradient to yield seven fractions (Fr.s.1–7). Fr.1 was subjected to HPLC with an ODS column, eluted with MeOH/H<sub>2</sub>O (5–100%) to afford six subfractions (Fr.s.1-1–1-6). Fr.1-4 was purified by semipreparative HPLC (47% MeOH/H<sub>2</sub>O, 2 mL/min) to yield **5** (4.8 mg). Fr.2 was subjected to MPLC with an ODS column, eluted with MeOH/H<sub>2</sub>O (10–100%) to afford eight subfractions (Fr.s.2-1–2-8). Fr.2-3 was purified by semipreparative HPLC (60% MeOH/H<sub>2</sub>O, 2 mL/min) to yield **1** (5.9 mg) and **2** (8.5 mg). Fr.3 was purified by semipreparative HPLC (65% MeCN/H<sub>2</sub>O, 2 mL/min) to yield **7** (10.2 mg). Fr.4 gave predominantly **6** (25 g). Fr.5 was purified by semipreparative HPLC (65% MeOH/H<sub>2</sub>O, 2 mL/min) to give **4** (8.9 mg), **9** (3.2 mg), **10** (17.3 mg), and **13** (5.3 mg). Fr.6 was subjected to MPLC with an ODS column, eluting with MeOH/H<sub>2</sub>O (5%–100%) to give eight subfractions (Fr.s.6-1–6-8). Fr.6-4 was purified by semipreparative HPLC (42% MeOH/H<sub>2</sub>O, 2 mL/min) to yield **14** (2.5 mg). Fr.6-6 was purified by semipreparative HPLC (29% MeCN/H<sub>2</sub>O, 2 mL/min) to yield **3** (1.6 mg), **8** (0.81 mg), **11** (5.4 mg), and **12** (10.2 mg).

*Asperteretal G* (**1**): yellow powder; UV (MeOH)  $\lambda_{\max}$  (log  $\epsilon$ ) = 203 (4.37), 221 (4.21), 226 (4.20), 286 (4.17), 327 (3.80) nm; <sup>1</sup>H and <sup>13</sup>C NMR data, Table 1; HRESIMS *m/z* 269.0811 [M + H]<sup>+</sup> (calcd for C<sub>16</sub>H<sub>13</sub>O<sub>4</sub>, 269.0808) (Figures S2–S9).

(+)-*asperteretal G* (**1a**):  $[\alpha]_D^{25} +36.9$  (c 0.1, MeOH); ECD (0.2 mg/mL, IPA)  $\lambda_{\max}$  ( $\Delta\epsilon$ ) 223 (+5.56), 237 (−4.04), 265 (+3.67), 307 (−2.51) nm.

(−)-*asperteretal G* (**1b**):  $[\alpha]_D^{25} -23.7$  (c 0.1, MeOH); ECD (0.2 mg/mL, IPA)  $\lambda_{\max}$  ( $\Delta\epsilon$ ) 223 (−3.57), 239 (+3.40), 263 (−4.23), 308 (+2.64) nm.

*Asperteretal H* (**2**): colorless oil; UV (MeOH)  $\lambda_{\max}$  (log  $\epsilon$ ) = 202 (4.28), 230 (4.33), 277 (3.53), 283 (3.51), 310 (3.42) nm; <sup>1</sup>H and <sup>13</sup>C NMR data, Table 1; HRESIMS *m/z* 235.0969 [M + H]<sup>+</sup> (calcd for C<sub>13</sub>H<sub>15</sub>O<sub>4</sub>, 235.0965) (Figures S10–S17).

(+)-*asperteretal H* (**2a**):  $[\alpha]_D^{25} +68.2$  (c 0.1, MeOH); ECD (0.2 mg/mL, IPA)  $\lambda_{\max}$  ( $\Delta\epsilon$ ) 210 (−3.59), 247 (+8.08), 280 (−1.76) nm.

(−)-*asperteretal H* (**2b**):  $[\alpha]_D^{25} -39.7$  (c 0.1, MeOH); ECD (0.2 mg/mL, IPA)  $\lambda_{\max}$  ( $\Delta\epsilon$ ) 210 (+4.10), 243 (−10.27), 281 (+1.24) nm.

*Asperteretal I* (**3**): yellow oil;  $[\alpha]_D^{25} +8.0$  (c 0.1, MeOH); UV (MeOH)  $\lambda_{\max}$  (log  $\epsilon$ ) = 203 (4.45), 305 (4.09) nm; <sup>1</sup>H and <sup>13</sup>C NMR data, Table 1; HRESIMS *m/z* 381.1340 [M − H]<sup>−</sup> (calcd for C<sub>22</sub>H<sub>21</sub>O<sub>6</sub>, 381.1344) (Figures S18–S25).

(S)-3-(2,3-Dihydroxy-3-methylbutyl)-4-hydroxybenzaldehyde (**14**): yellow oil;  $[\alpha]_D^{25} +7.7$  (c 0.10, MeOH); UV (MeOH)  $\lambda_{\max}$  (log  $\epsilon$ ) = 203 (3.88), 224 (3.49), 276 (3.13) nm; <sup>1</sup>H NMR (700 MHz, CD<sub>3</sub>OD)  $\delta_H$  9.75 (1H, s, H-7), 7.75 (1H, d, J = 2.0 Hz, H-2), 7.64 (1H, dd, J = 8.3,

2.0 Hz, H-6), 6.91 (1H, d,  $J = 8.3$  Hz, H-5), 3.63 (1H, dd,  $J = 10.4, 1.8$  Hz, H-9), 3.07 (1H, dd,  $J = 14.1, 1.8$  Hz, H<sub>3</sub>-8), 2.60 (1H, dd,  $J = 14.1, 10.4$  Hz, H<sub>5</sub>-8), 1.25 (6H, s, H-11, H-12); <sup>13</sup>C NMR (175 MHz, CD<sub>3</sub>OD)  $\delta_C$  193.1 (CH, C-7), 164.0 (qC, C-4), 134.8 (CH, C-2), 131.5 (CH, C-6), 130.1 (qC, C-1), 129.1 (qC, C-3), 116.7 (CH, C-5), 79.4 (CH, C-9), 73.9 (qC, C-10), 33.8 (CH<sub>2</sub>, C-8), 25.7 (CH<sub>3</sub>, C-12), 25.1 (CH<sub>3</sub>, C-11); HRESIMS  $m/z$  223.0976 [M – H]<sup>–</sup> (calcd for C<sub>12</sub>H<sub>15</sub>O<sub>4</sub>, 223.0976) (Figures S36–S43).

### 3.5. X-ray Crystallographic Analysis

Colorless crystals of **1a** were obtained in MeOH/CHCl<sub>3</sub> (1:2) followed by slow evaporation at 4 °C and the crystals' data were collected on a XtalLAB PRO single-crystal diffractometer using Cu K $\alpha$  radiation. The X-ray crystal structure of **1a** was solved using SHELXS97, expanded by difference Fourier techniques, and refined by full-matrix least-squares calculation finally. All non-hydrogen atoms were refined anisotropically, and hydrogen atoms were fixed at calculated positions. Crystallographic data of **1a** (Table S1) have been deposited in the Cambridge Crystallographic Data Centre (deposition number: CCDC 2077455). These data can be obtained, free of charge, on application to CCDC, 12 Union Road, Cambridge CB21EZ, UK [fax: +44(0)-1223-336033 or e-mail: deposit@ccdc.cam.ac.uk].

### 3.6. Mo<sub>2</sub>(AcO)<sub>4</sub>-Induced Circular Dichroism

Mo<sub>2</sub>(AcO)<sub>4</sub> (1.0 mg) and **14** (1.0 mg) were dissolved in dimethyl sulfoxide (DMSO) (1 mL) to use as stock solutions, which were mixed by 1:2 *v/v*. After mixing, the CD spectrum was recorded immediately and scanned every 5 min, until a stationary ICD spectrum (the CD of **14** in Mo<sub>2</sub>(AcO)<sub>4</sub> solution subtracted from inherent CD of **14** in DMSO) was observed. The sign of the diagnostic band at around 310 nm in the ICD spectrum was correlated to the absolute configuration of C-9 of **14** [22].

### 3.7. ECD Calculation

The structures of **1a**, **1b**, **2a**, and **2b** were subjected to random conformational searches using the Spartan'14 software with the MMFF method, as used previously [23]. The conformers with a Boltzmann population of over 5% were chosen for ECD calculations using the Gaussian 09 software [24], and the stable conformers were initially optimized at the B3LYP/6-31+G(d,p) level in MeOH using the CPCM model. The overall theoretical calculation of ECD was achieved in MeOH using time-dependent density functional theory at the B3LYP/6-31+G(d,p) level. The ECD spectra were generated using the SpecDis 1.6 (University of Würzburg, Würzburg, Germany) and Prism 5.0 (GraphPad Software Inc., San Diego, CA, USA) software with a half-bandwidth of 0.3–0.4 eV, according to the Boltzmann-calculated contribution of each conformer after UV correction.

### 3.8. Bioassay

The cytotoxic activity of the obtained compounds was evaluated by the MTT method as reported in our previous study [25]. The antibacterial activity against five bacterial strains, *Staphylococcus aureus* ATCC 29213, *Enterococcus faecalis* ATCC 29212, *Klebsiella pneumoniae* ATCC 13883, methicillin-resistant *S. aureus* (MRSA, clinical strain), and methicillin-resistant *S. epidermidis* (MRSE, clinical strain) was evaluated using a modified broth microdilution method [25,26]. The acetylcholinesterase and PL inhibitory activities were evaluated according to the methods used in our previous study [26,27].

## 4. Conclusions

We describe here the isolation and structure elucidation of five undescribed and ten previously reported butenolides from the coral-derived fungus *Aspergillus terreus* SCSIO41404, together with an undescribed *para*-hydroxybenzaldehyde derivative (*S*)-3-(2,3-dihydroxy-3-methylbutyl)-4-hydroxybenzaldehyde. Two pairs of enantiomers were separated by HPLC using a chiral column, and enantiomers (+)-asperterretal G (**1a**) and (–)-asperterretal G (**1b**)

were new natural products. After preliminary antibacterial, cytotoxic and enzyme inhibitory bioassays of these compounds, several natural butenolides showed inhibition against PL. This is the first report of the PL inhibitor activity of butenolides, and the effects of these butenolides on the regulation of lipid metabolism deserve further study [28].

**Supplementary Materials:** The following supporting information can be downloaded at: <https://www.mdpi.com/article/10.3390/md20030212/s1>, ITS sequence data of the strain; physicochemical data of 4–13; Table S1: X-ray crystallographic data of 1; Table S2: Primer sequences for the genes; Figure S1: Experimental ECD spectrum of 3; Figures S2–S25: NMR, HRESIMS and UV spectroscopic data of 1–3; Figures S26–S35: <sup>1</sup>H NMR spectra of 4–13; Figures S36–S43: NMR, HRESIMS and UV spectroscopic data of 14 (PDF); Crystallographic data of 1 (CIF).

**Author Contributions:** Conceptualization, X.Z.; methodology, Q.P. and W.C.; investigation, Q.P., W.C. and J.X.; resources, X.L.; writing—original draft preparation, Q.P.; writing—review and editing, W.C., X.L., J.X., Y.L. and X.Z.; supervision and project administration, X.Z.; funding acquisition, Y.L. and X.Z. All authors have read and agreed to the published version of the manuscript.

**Funding:** This research was funded by the Key Area Research and Development Program of Guangdong Province (2020B1111030005), Key Special Project for Introduced Talents Team of Southern Marine Science and Engineering Guangdong Laboratory (Guangzhou) (GML2019ZD0406), Guangdong Local Innovation Team Program (2019BT02Y262), National Natural Science Foundation of China (U20A20101, 81973235), and Liao Ning Revitalization Talents Program (XLYC1802037).

**Institutional Review Board Statement:** Not applicable.

**Data Availability Statement:** Not applicable.

**Acknowledgments:** The authors gratefully acknowledge the assistance of Xiao, Zheng, Sun, and Zhang in the analytical facility center of the SCSIO for recording spectroscopic data.

**Conflicts of Interest:** The authors declare no conflict of interest.

## References

- Shabana, S.; Lakshmi, K.R.; Satya, A.K. An updated review of secondary metabolites from marine fungi. *Mini-Rev. Med. Chem.* **2021**, *21*, 602–642. [[CrossRef](#)] [[PubMed](#)]
- Cheng, Z.; Li, Y.; Liu, W.; Liu, L.; Liu, J.; Yuan, W.; Luo, Z.; Xu, W.; Li, Q. Butenolide derivatives with  $\alpha$ -glucosidase inhibitions from the deep-sea-derived fungus *Aspergillus terreus* YPGA10. *Mar. Drugs* **2019**, *17*, 332. [[CrossRef](#)] [[PubMed](#)]
- Liu, B.; Chen, N.; Xu, Y.; Zhang, J.W.; Sun, Y.; Zhao, L.Z.; Ji, Y.B. A new benzophenone with biological activities from metabolites of butyrolactone I in rat faeces. *Nat. Prod. Res.* **2021**, *35*, 2489–2497. [[CrossRef](#)] [[PubMed](#)]
- Sun, Y.; Liu, J.; Li, L.; Gong, C.; Wang, S.; Yang, F.; Hua, H.; Lin, H. New butenolide derivatives from the marine sponge-derived fungus *Aspergillus terreus*. *Bioorg. Med. Chem. Lett.* **2018**, *28*, 315–318. [[CrossRef](#)]
- Chen, S.; Zhang, Y.; Niu, X.; Mohyuddin, S.G.; Wen, J.; Bao, M.; Yu, T.; Wu, L.; Hu, C.; Yong, Y.; et al. Coral-derived endophytic fungal product, butyrolactone-I, alleviates LPS induced intestinal epithelial cell inflammatory response through TLR4/NF- $\kappa$ B and MAPK signaling pathways: An in vitro and in vivo studies. *Front. Nutr.* **2021**, *8*, 748118. [[CrossRef](#)]
- Wu, L.; Xie, C.L.; Yang, X.W.; Chen, G. Pharmacokinetics and metabolism study of deep-sea-derived butyrolactone I in rats by UHPLC–MS/MS and UHPLC–Q-TOF-MS. *Mar. Drugs* **2022**, *20*, 11. [[CrossRef](#)]
- Wang, Y.M.; Wang, H.J.; Peng, S.Q. In ovo exposure of a Fusarium mycotoxin butenolide induces hepatic and renal oxidative damage in chick embryos, and antioxidants provide protections. *Toxicol. In Vitro* **2009**, *23*, 1354–1359. [[CrossRef](#)]
- Weber, V.; Coudert, P.; Rubat, C.; Duroux, E.; Vallee-Goyet, D.; Gardette, D.; Bria, M.; Albuissou, E.; Leal, F.; Gramain, J.C.; et al. Novel 4,5-diaryl-3-hydroxy-2(5H)-furanones as anti-oxidants and anti-inflammatory agents. *Bioorgan. Med. Chem.* **2002**, *10*, 1647–1658. [[CrossRef](#)]
- Ye, Y.Q.; Xia, C.F.; Yang, J.X.; Yang, Y.C.; Qin, Y.; Gao, X.M.; Du, G.; Li, X.M.; Hu, Q.F. Butyrolactones derivatives from the fermentation products of an endophytic fungus *Aspergillus versicolor*. *Bull. Korean Chem. Soc.* **2014**, *35*, 3059–3062. [[CrossRef](#)]
- Gawronski, J.K.; Oeveren, V.A.; Hanncke, V.D.D.; Leung, C.W.; Feringa, B.L. Simple circular dichroic method for the determination of absolute configuration of 5-substituted 2(5H)-furanones. *J. Org. Chem.* **1996**, *61*, 1513–1515. [[CrossRef](#)]
- Uchida, I.; Kuriyama, K. The  $\pi$ - $\pi$  circular dichroism of  $\delta\beta$ -unsaturated  $\gamma$ -lactones. *Tetrahedron Lett.* **1974**, *15*, 3761–3764. [[CrossRef](#)]
- Piacente, S.; Aquino, R.; Detommasi, N.; Deugaz, O.L.; Orellana, H.C. p-hydroxyacetophenone derivatives from *Werneria ciliolata*. *Phytochemistry* **1992**, *31*, 2182–2184. [[CrossRef](#)]
- Di Bari, L.; Pescitelli, G.; Pratelli, C.; Pini, D.; Salvadori, P. Determination of absolute configuration of acyclic 1,2-diols with Mo<sub>2</sub>(OAc)<sub>4</sub>. 1. Snatzke's method revisited. *J. Org. Chem.* **2001**, *66*, 4819–4825. [[CrossRef](#)]

14. Pang, X.; Zhao, J.Y.; Fang, X.M.; Zhang, T.; Zhang, D.W.; Liu, H.Y.; Su, J.; Cen, S.; Yu, L.Y. Metabolites from the plant endophytic fungus *Aspergillus* sp. CPMC 400735 and their anti-HIV activities. *J. Nat. Prod.* **2017**, *80*, 2595–2601. [[CrossRef](#)]
15. Morishima, H.; Fujita, K.; Nakano, M.; Atsumi, S.; Ookubo, M.; Kitagawa, M.; Matsumoto, H.; Okuyama, A.; Okabe, T. Preparation, antitumor activity, and formulations of dihydrofuran compounds. Japanese Patent JP 06100445, 1994.
16. Liao, W.Y.; Shen, C.N.; Lin, L.H.; Yang, Y.L.; Han, H.Y.; Chen, J.W.; Kuo, S.C.; Wu, S.H.; Liaw, C.C. Asperjinone, a nor-neolignan, and terrein, a suppressor of ABCG2-expressing breast cancer cells, from Thermophilic *Aspergillus terreus*. *J. Nat. Prod.* **2012**, *75*, 630–635. [[CrossRef](#)]
17. Zhou, M.; Du, G.; Yang, H.Y.; Xia, C.F.; Yang, J.X.; Ye, Y.Q.; Gao, X.M.; Li, X.N.; Hu, Q.F. Antiviral butyrolactones from the endophytic fungus *Aspergillus versicolor*. *Planta Med.* **2015**, *81*, 235–240. [[CrossRef](#)]
18. Zhou, M.; Lou, J.; Li, Y.K.; Wang, Y.D.; Zhou, K.; Ji, B.K.; Dong, W.; Gao, X.M.; Du, G.; Hu, Q.F. Butyrolactones from the endophytic fungus *Aspergillus versicolor* and their anti-tobacco mosaic virus activity. *J. Brazil. Chem. Soc.* **2015**, *26*, 545–549.
19. Parvatkar, R.R.; D'Souza, C.; Tripathi, A.; Naik, C.G. Aspernolides A and B, butenolides from a marine-derived fungus *Aspergillus terreus*. *Phytochemistry*. **2009**, *70*, 128–132. [[CrossRef](#)]
20. Wang, Y.; Zheng, J.K.; Liu, P.P.; Wang, W.; Zhu, W.M. Three new compounds from *Aspergillus terreus* PT06-2 grown in a high salt medium. *Mar. Drugs* **2011**, *9*, 1368. [[CrossRef](#)]
21. Haritakun, R.; Rachtawee, P.; Chanthaket, R.; Boonyuen, N.; Isaka, M. Butyrolactones from the fungus *Aspergillus terreus* BCC 4651. *Chem. Pharm. Bull.* **2010**, *58*, 1545–1548. [[CrossRef](#)]
22. Wang, J.J.; Liang, Z.; Li, K.L.; Yang, B.; Liu, Y.H.; Fang, W.; Tang, L.; Zhou, X.F. Ene-yne hydroquinones from a marine-derived strain of the fungus *Pestalotiopsis neglecta* with effects on liver X receptor alpha. *J. Nat. Prod.* **2020**, *83*, 1258–1264. [[CrossRef](#)]
23. Li, K.; Su, Z.; Gao, Y.; Lin, X.; Pang, X.; Yang, B.; Tao, H.; Luo, X.; Liu, Y.; Zhou, X. Cytotoxic minor piericidin derivatives from the Actinomycete Strain *Streptomyces psammoticus* SCSIO NS126. *Mar. Drugs* **2021**, *19*, 428. [[CrossRef](#)] [[PubMed](#)]
24. Frisch, M.J.; Trucks, G.W.; Schlegel, H.B.; Scuseria, G.E.; Robb, M.A.; Cheeseman, J.R.; Scalmani, G.; Barone, V.; Mennucci, B.; Petersson, G.A.; et al. *Gaussian 09, Revision x.x*; Gaussian, Inc.: Wallingford, CT, USA, 2009.
25. Cai, J.; Chen, C.; Tan, Y.; Chen, W.; Luo, X.; Luo, L.; Yang, B.; Liu, Y.; Zhou, X. Bioactive polyketide and diketopiperazine derivatives from the mangrove-sediment-derived fungus *Aspergillus* sp. SCSIO41407. *Molecules* **2021**, *26*, 4851. [[CrossRef](#)] [[PubMed](#)]
26. Pang, X.Y.; Lin, X.P.; Yang, J.; Zhou, X.F.; Yang, B.; Wang, J.J.; Liu, Y.H. Spiro-phthalides and isocoumarins isolated from the marine-sponge-derived fungus *Setosphaeria* sp. SCSIO41009. *J. Nat. Prod.* **2018**, *81*, 1860–1868. [[CrossRef](#)] [[PubMed](#)]
27. Peng, Q.Y.; Cai, J.; Long, J.Y.; Yang, B.; Lin, X.P.; Wang, J.F.; Xiao, J.; Liu, Y.H.; Zhou, X.F. New azaphthalide and phthalide derivatives from the marine coral-derived fungus *Aspergillus* sp. SCSIO41405. *Phytochem. Lett.* **2021**, *43*, 94–97. [[CrossRef](#)]
28. Liu, T.T.; Liu, X.T.; Chen, Q.X.; Shi, Y. Lipase inhibitors for obesity: A review. *Biomed. Pharmacother.* **2020**, *128*, 110314. [[CrossRef](#)] [[PubMed](#)]



## Article

# Fucoxanthin Attenuates Free Fatty Acid-Induced Nonalcoholic Fatty Liver Disease by Regulating Lipid Metabolism/Oxidative Stress/Inflammation via the AMPK/Nrf2/TLR4 Signaling Pathway

Jiena Ye <sup>†</sup>, Jiawen Zheng <sup>†</sup>, Xiaoxiao Tian, Baogui Xu, Falei Yuan, Bin Wang, Zuisu Yang <sup>\*</sup> and Fangfang Huang <sup>\*</sup>

Zhejiang Provincial Engineering Technology Research Center of Marine Biomedical Products, School of Food and Pharmacy, Zhejiang Ocean University, Zhoushan 316022, China; z20105500018@zjou.edu.cn (J.Y.); jwzheng1996@163.com (J.Z.); z18095135044@zjou.edu.cn (X.T.); Z19105500022@zjou.edu.cn (B.X.); yuanfalei@zjou.edu.cn (F.Y.); wangbin@zjou.edu.cn (B.W.)

<sup>\*</sup> Correspondence: yzs@zjou.edu.cn (Z.Y.); huangff@zjou.edu.cn (F.H.)

<sup>†</sup> These authors contributed equally to this work.

**Abstract:** Fucoxanthin, a xanthophyll carotenoid abundant in brown algae, is reported to have several biological functions, such as antioxidant, anti-inflammatory, and anti-tumor activities, in mice. We investigated the effects and mechanisms of fucoxanthin in the mixture oleate/palmitate = 2/1(FFA)-induced nonalcoholic fatty liver disease (NAFLD) cell model in this study. The results showed that the content of superoxide dismutase in the FFA group was  $9.8 \pm 1.0$  U/mgprot, while that in the fucoxanthin high-dose (H-Fx) group ( $2 \mu\text{g/mL}$ ) increased to  $22.9 \pm 0.6$  U/mgprot. The content of interleukin- $1\beta$  in the FFA group was  $89.3 \pm 3.6$  ng/mL, while that in the H-Fx group was reduced to  $53.8 \pm 2.8$  ng/mL. The above results indicate that fucoxanthin could alleviate the FFA-induced oxidative stress and inflammatory levels in the liver cells. Oil red-O staining revealed visible protrusions and a significant decrease in the number of lipid droplets in the cytoplasm of cells in the fucoxanthin group. These findings on the mechanisms of action suggest that fucoxanthin can repair FFA-induced NAFLD via the adenosine monophosphate-activated protein kinase (AMPK) signaling pathway and nuclear factor erythroid-2-related factor 2-mediated (Nrf2) signaling pathway, as well as by downregulating the expression of the Toll-like receptor 4-mediated (TLR4) signaling pathway. Fucoxanthin exhibited alleviating effects in the FFA-induced NAFLD model and could be explored as a potential anti-NAFLD substance.

**Keywords:** NAFLD; fucoxanthin; adenosine monophosphate-activated protein kinase (AMPK); nuclear factor erythroid-2-related factor 2-mediated (Nrf2); Toll-like receptor 4-mediated (TLR4)

**Citation:** Ye, J.; Zheng, J.; Tian, X.; Xu, B.; Yuan, F.; Wang, B.; Yang, Z.; Huang, F. Fucoxanthin Attenuates Free Fatty Acid-Induced Nonalcoholic Fatty Liver Disease by Regulating Lipid Metabolism/Oxidative Stress/Inflammation via the AMPK/Nrf2/TLR4 Signaling Pathway. *Mar. Drugs* **2022**, *20*, 225. <https://doi.org/10.3390/md20040225>

Academic Editors: Yonghong Liu and Xuefeng Zhou

Received: 8 March 2022

Accepted: 23 March 2022

Published: 25 March 2022

**Publisher's Note:** MDPI stays neutral with regard to jurisdictional claims in published maps and institutional affiliations.



**Copyright:** © 2022 by the authors. Licensee MDPI, Basel, Switzerland. This article is an open access article distributed under the terms and conditions of the Creative Commons Attribution (CC BY) license (<https://creativecommons.org/licenses/by/4.0/>).

## 1. Introduction

Nonalcoholic fatty liver disease (NAFLD), a heterogeneous disease with highly variable molecular mechanisms, has a high prevalence and is the most common chronic liver disease in the world [1]. The liver metabolizes lipids and stores triglycerides (TG) derived from the conversion of excess fatty acids [2]. Fatty liver disease, a condition in which the amount of TG accounts for more than 5% of the weight of the liver, impairs organ function. The accumulation of TG in the liver is thought to be an adaptive response to compensate for the increased cellular content of free fatty acids (FFAs), thereby preventing the onset of hepatocellular damage [3]. The increasing prevalence of factors such as obesity, diabetes, and inflammation, which are associated with NAFLD, has sparked growing interest in the disease [4].

NAFLD encompasses multiple damaging “hits” [5], such as insulin resistance, which lead to disorders of the lipid metabolism, and oxidative stress, which is an inflammatory response induced by reactive oxygen species. Lipid peroxidation reactions can induce and amplify cellular damage, mainly due to the formation of oxidation products generated by

the reaction. Recent evidence suggests that hepatic accumulation of excess FFAs promotes increased  $\beta$ -oxidation, which ultimately leads to oxidative stress [6,7]. FFAs activate Kupffer cells through indirect stimulation of the toll-like receptor 4-mediated (TLR4)-mediated signaling pathway, leading them to adopt a pro-inflammatory phenotype [8]. Recent evidence suggests that activation of the TLR4 signaling pathway helps reduce palmitate-induced hepatotoxicity. *Gynostemma pentaphyllum* can improve the level of inflammatory factors in the NAFLD model by regulating the TLR4 signaling pathway [9,10]. Adenosine monophosphate-activated protein kinase (AMPK) is mainly expressed in the liver and skeletal muscle, and regulates lipid metabolism. Kangtaizhi granules, a Chinese medicine compound, effectively ameliorate the mixture of oleate/palmitate = 2/1(FFA)-induced lipid accumulation in HepG2 cells via the AMPK signaling pathway, thereby preventing nonalcoholic steatosis [11]. M3G, one of the main anthocyanins in blueberries, acts on the FFA-induced NAFLD cell model by activating the Nrf2/ARE (antioxidant response element) signaling pathway [12].

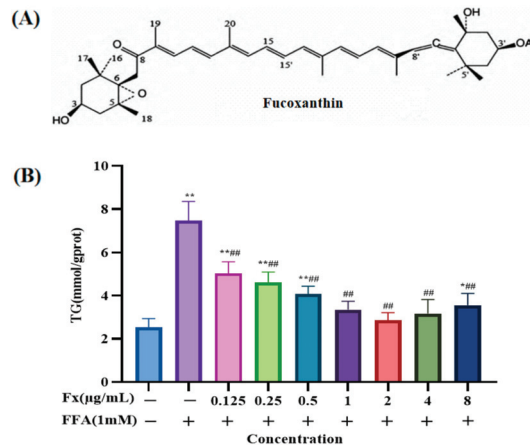
Fucoanthin, an orange-red carotenoid, can be isolated from brown algae [13]. Fucoanthin exhibits a strong antioxidant activity by inhibiting 2,2-Diphenyl-1-picrylhydrazyl (DPPH) and 2,2'-Azinobis-(3-ethylbenzthiazoline-6-sulphonate) (ABTS) radicals, and alleviates obesity by reducing lipogenesis [14,15]. Fucoanthin also has anti-inflammatory, anti-bacterial, and anti-cancer properties [16,17]. Fucoanthin not only improves lipid metabolism, but also attenuates mitochondrial dysfunction. Fucoanthin alleviates palmitate-induced inflammatory responses in RAW 264.7 cells [18]. In addition to inhibiting hepatic oxidative stress and inflammation, fucoanthin prevents the early phase of fibrosis in diet-induced nonalcoholic steatohepatitis in mice [19]. Potential protective functions of fucoanthin against the development of NAFLD have been recognized [20,21]. Low molecular weight fucoidan and high stability fucoanthin ameliorate hepatic steatosis, inflammation, fibrosis, and insulin resistance in NAFLD patients [22]. Fucoanthin significantly inhibits the expression of sterol regulatory element binding proteins-1c (SREBP-1c) and decreases the expression of fatty acid synthase (FAS), phosphorylated AMPK, and phosphorylated acetyl-CoA carboxylase (ACC) in oleic acid-induced FL83B cells [23]. *Nitzschia laevis* extract prevents NAFLD by significantly inhibiting lipid accumulation in HepG2 cells, and increasing the gene and protein expression of phosphorylated ACC [24]. Recent studies found that fucoanthin also enhances the expression of heme oxygenase-1 (HO-1) and nicotinamide quinone oxidoreductase 1 (NQO1), leading to antioxidant effects in murine hepatic BNL CL.2 cells [25]. Fucoanthin enhances the antioxidant response mediated by nuclear factor-erythroid factor 2-related factor 2 (Nrf2), and inhibition of TLR4-induced signaling pathways is associated with the prevention of liver inflammation [26]. Whether the reparative effects of fucoanthin on the FFA-induced NAFLD cell model are related to FAS, SREBP-1c protein, Nrf2, and TLR4 pathways, however, remains unclear. In this study, we used FFA-induced nonalcoholic fatty liver cells as a model and investigated whether fucoanthin regulated AMPK, Nrf2, and TLR4 pathways in FFA-induced NAFLD.

## 2. Results

### 2.1. Determination of the Dosing Concentration

The TG content in the cells of each group was measured under treatment with different concentrations of fucoanthin after FFA induction for 24 h. The TG content was significantly higher in the FFA group ( $7.5 \pm 0.7$  mmol/gprot) than that in the control group ( $2.5 \pm 0.3$  mmol/gprot) (Figure 1B) ( $p < 0.01$ ), demonstrating that the NAFLD cell model was successfully constructed. Establishing useful cellular models of lipid accumulation will significantly contribute to studies of the mechanisms of NAFLD, as well as its effective prevention and treatment [3]. Due to the short study period and reproducibility, in vitro cellular models of lipid accumulation have become a major approach for exploring this disease. Saturated or unsaturated fatty acid stimulation, causing intracellular lipid accumulation, is commonly used to construct NAFLD cell models [27,28]. FFA, consisting of oleic and palmitic acids [27], acts on the liver cells to cause intracellular lipid accumulation.

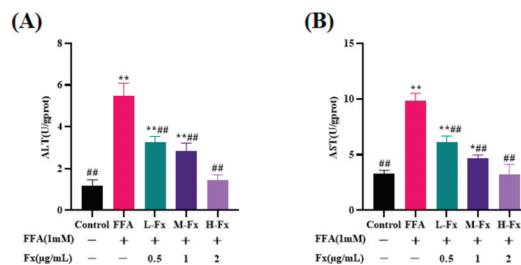
FFA modeling methods can simulate the pathogenic process of NAFLD caused by disorders of the lipid metabolism, thereby facilitating studies of the specific mechanism of NAFLD and contributing to the development of novel therapeutic approaches [29]. The results of this study show that fucoxanthin intervention alone significantly reduced the NAFLD cell model TG level. When the concentration of fucoxanthin was 2 µg/mL, the treatment was the most effective. Therefore, the doses of 0.5 µg/mL (L-Fx group), a medium dose of 1 µg/mL (M-Fx group), and a high dose of 2 µg/mL (H-Fx group) were chosen to conduct the subsequent experiments.



**Figure 1.** (A) Chemical structure of fucoxanthin. (B) Effect of different concentrations of fucoxanthin on the levels of triglycerides (TG) in FFA-treated liver cells. Data are expressed as mean ± standard deviation (n = 3), \* p < 0.05, \*\* p < 0.01 vs. control group, ### p < 0.01 vs. FFA group.

2.2. Effect of Fucoxanthin on Intracellular Alanine Transaminase (ALT) and Aspartate Transaminase (AST) Viability

ALT and AST levels are important indicators of hepatocyte injury. When severe necrosis occurs in hepatocytes, the permeability of cell membranes increases, causing ALT and AST to enter the bloodstream, and the hepatocyte injury will increase significantly. The ALT and AST in FFA-induced liver cells were 5.5 ± 0.5 U/gprot and 9.8 ± 0.6 U/gprot, respectively. After fucoxanthin treatment, both ALT and AST were significantly reduced, and the expression level dropped to 1.4 ± 0.2 U/gprot and 3.3 ± 0.7 U/gprot, respectively (Figure 2) (p < 0.01). ALT and AST levels, as sensitive indicators of hepatocyte injury, increased significantly after FFA treatment, but reduced to different degrees after treatment with fucoxanthin. These findings demonstrated that fucoxanthin has significant reparative effects against the cell damage caused by FFA.

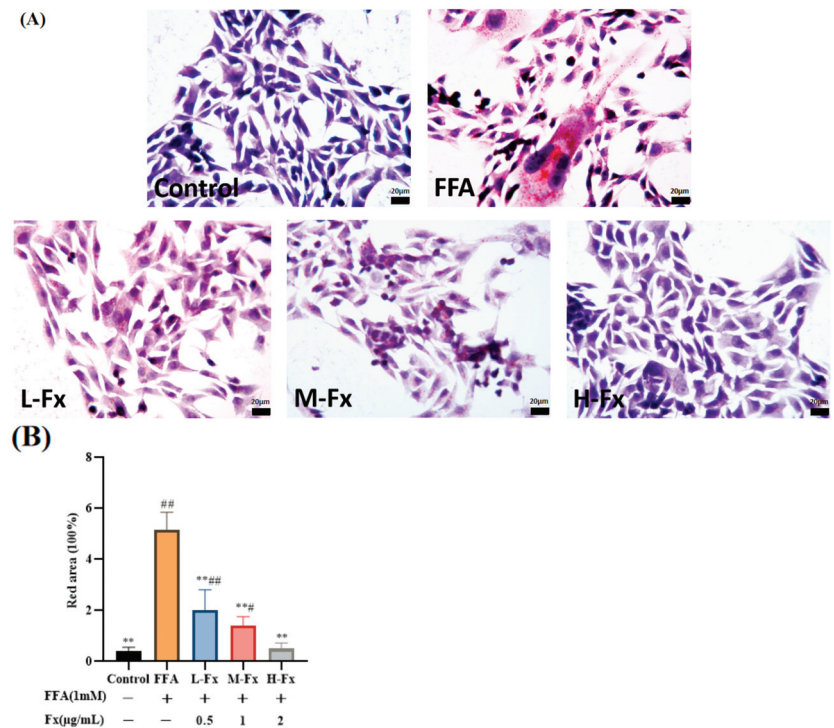


**Figure 2.** Effects of fucoxanthin on the levels of alanine transaminase (ALT) (A) and aspartate transaminase (AST) (B) activities in FFA-treated liver cells. Data are expressed as mean ± standard deviation (n = 3), \* p < 0.05, \*\* p < 0.01 vs. control group, ### p < 0.01 vs. FFA group.



### 2.3. Effect of Fucoxanthin on Intracellular Lipid Accumulation

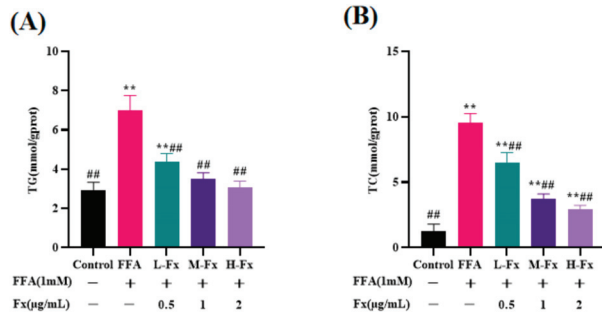
The distribution of cellular lipid droplets and the morphologic changes of cells in each experimental group were observed by Oil Red O staining, and the parts of the cytoplasm with red represented lipid droplets (Figure 3). The cells of the control group were tightly connected and had relatively clear edges. At the same time, there were protrusions and good extensions around the cells. It can also be observed that the lipid droplet content in the cytoplasm is relatively low, and the nuclei were clearly visible. On the contrary, FFA-treated cells showed obvious lipid accumulation, reduced cell protrusions, partially solidified nuclei, obvious changes in the morphology of some cells, and an obvious increase of lipid droplets in the cytoplasm, with a large amount of lipid deposition, indicating that hepatocytes were damaged (Figure 3B). Lipid droplets in the cytoplasm of the fucoxanthin group was significantly decreased with the concentration ranging from 0.5 to 2  $\mu\text{g}/\text{mL}$ , indicating that fucoxanthin could improve FFA-induced hepatic steatosis.



**Figure 3.** Oil Red O staining of FFA-treated liver cells ( $\times 400$ , scale bars of images are 20  $\mu\text{m}$ ) (A) and oil droplets analyzed by Image J (B). Data are expressed as mean  $\pm$  standard deviation ( $n = 5$ ), \*\*  $p < 0.01$  vs. control group, #  $p < 0.05$ , ##  $p < 0.01$  vs. FFA group.

### 2.4. Effect of Fucoxanthin on Intracellular TG and Total Cholesterol (TC) Content

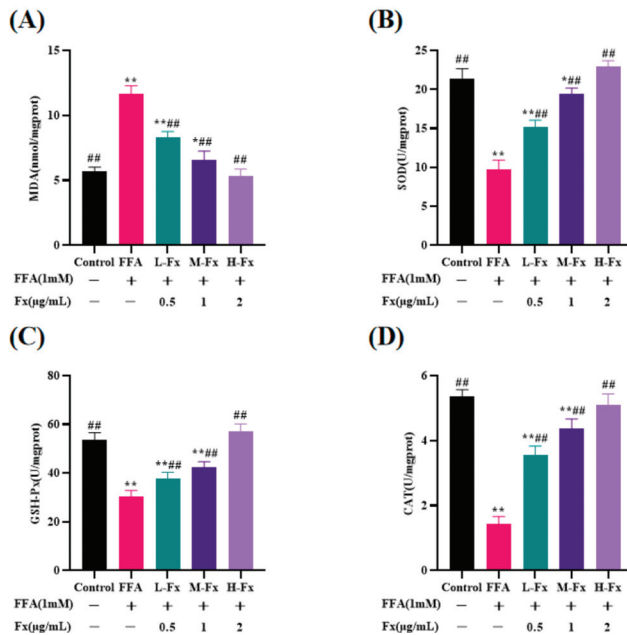
Compared with the control group, the TC and TG contents were increased in the FFA-induced hepatocyte steatosis group (Figure 4) ( $p < 0.01$ ), indicating that FFA induction leads to lipid accumulation. In contrast to the FFA-treated group, the fucoxanthin group had a significantly reduced TC and TG content, and this finding was consistent with the results of Oil Red O staining. These phenomena were significantly improved by treatment with fucoxanthin, indicating that fucoxanthin could effectively attenuate FFA-induced lipid deposition in the liver cells.



**Figure 4.** Effects of fucoxanthin on the levels of TG (A) and total cholesterol (TC) (B) in the FFA-treated liver cells. Data are expressed as mean ± standard deviation ( $n = 3$ ), \*\*  $p < 0.01$  vs. control group, ##  $p < 0.01$  vs. FFA group.

2.5. Effect of Fucoxanthin on Intracellular Antioxidant Enzyme Activity

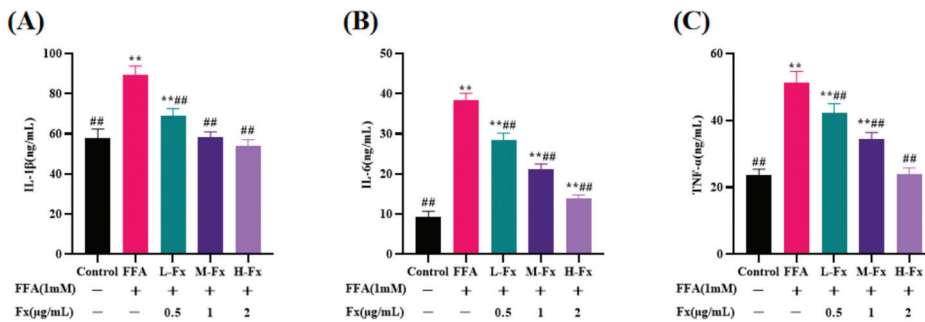
Lipid peroxidation in the cells was assessed by measuring the intracellular malondialdehyde (MDA) content and the activity of antioxidant enzymes, including superoxide dismutase (SOD), glutathione peroxidase (GSH-Px) and catalase (CAT). After incubating with FFA, the MDA content was dramatically higher in the cells than in the Control group, while the activity of the antioxidant enzymes (SOD, GSH-Px, and CAT) was remarkably reduced (Figure 5) ( $p < 0.01$ ). The cellular MDA level decreased from  $11.7 \pm 0.5$  nmol/mgprot in the FFA group to  $5.3 \pm 0.5$  nmol/mgprot in the H-Fx group, suggesting that fucoxanthin improves in-cell lipid peroxidation in the cells induced by FFA.



**Figure 5.** Effects of fucoxanthin on the levels of malondialdehyde (MDA) (A), superoxide dismutase (SOD) (B), glutathione peroxidase (GSH-Px) (C), and catalase (CAT) (D) in FFA-treated liver cells. Data are expressed as mean ± standard deviation ( $n = 3$ ), \*  $p < 0.05$ , \*\*  $p < 0.01$  vs. control group, ##  $p < 0.01$  vs. FFA group.

## 2.6. Effect of Fucoxanthin on Intracellular Pro-Inflammatory Cytokines Content

Previous studies have demonstrated that progressive NAFLD could lead to an inflammatory response, causing the release of pro-inflammatory factors [30]. Therefore, the secretion levels of interleukin (IL)-6, IL-1 $\beta$ , and tumor necrosis factor- $\alpha$  (TNF- $\alpha$ ) in the cell culture medium were measured with an enzyme-linked immunosorbent assay. The expressions of IL-6, IL-1 $\beta$ , and TNF- $\alpha$  were partly regulated in FFA-induced cells. The expressions of IL-6, IL-1 $\beta$ , and TNF- $\alpha$  proteins were significantly increased in FFA-induced the liver cells compared with the control group (Figure 6) ( $p < 0.01$ ). A marked decrease in the expression of IL-6, IL-1 $\beta$ , and TNF- $\alpha$  protein was observed following treatment with fucoxanthin.



**Figure 6.** Effects of fucoxanthin on the levels of interleukin (IL)-1 $\beta$  (A), IL-6 (B) and tumor necrosis factor- $\alpha$  (TNF- $\alpha$ ) (C) in FFA-treated liver cells. Data are expressed as mean  $\pm$  standard deviation ( $n = 3$ ), \*\*  $p < 0.01$  vs. control group, ##  $p < 0.01$  vs. FFA group.

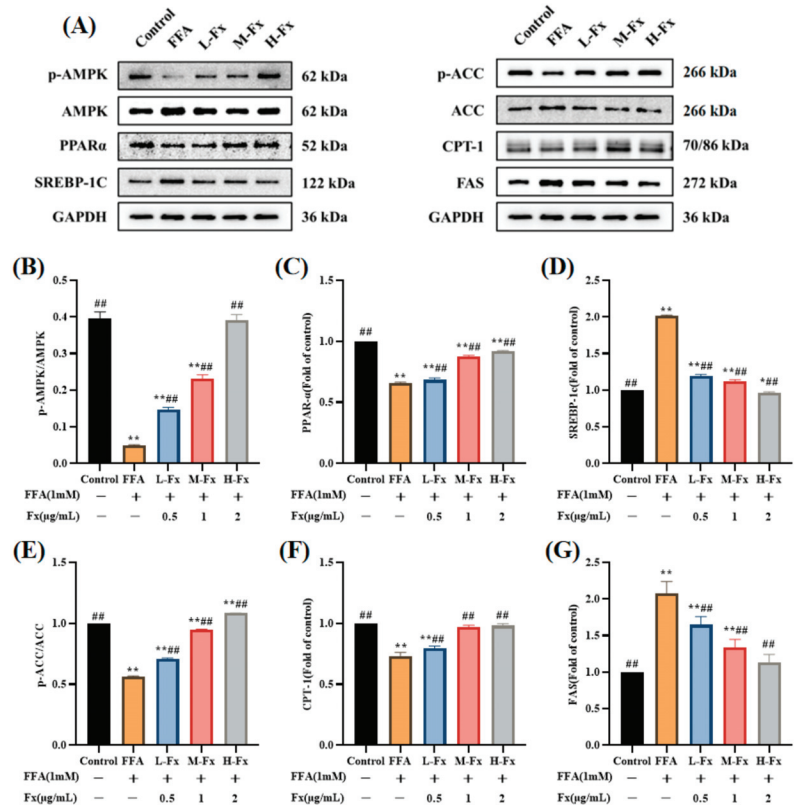
## 2.7. Effects of AMPK Activation and Expression of Genes Related to Lipid Metabolism

Lipid metabolism in the liver is influenced by the balanced relationship between the lipid synthesis pathway and the  $\beta$ -oxidation pathway. To elucidate the mechanism of fucoxanthin to inhibit FFA-induced lipid accumulation in hepatocytes, the expression levels of the AMPK pathway-related proteins were examined (Figure 7) ( $p < 0.01$ ). Activation of the AMPK protein both promotes fatty acid oxidation and inhibits lipid and cholesterol synthesis. Figure 7 shows that the significant reduction of phosphorylated AMPK levels in the FFA group was reversed by fucoxanthin. SREBP-1c and peroxisome proliferator-activated receptor  $\alpha$  (PPAR $\alpha$ ) are important transcription factors that regulate the lipid metabolism in hepatocytes, and fucoxanthin regulates lipid metabolism in the liver by activating AMPK, thereby upregulating PPAR $\alpha$  and downregulating the expression of SREBP-1c. FFA induction affects the expression of ACC and FAS, proteins related to lipid synthesis, and the results show that the phosphorylated ACC expression decreased and FAS levels increased in the FFA group, while the fucoxanthin group showed a recovery of the expression of both proteins. Carnitine palmitoyltransferase-1 (CPT-1) is a key enzyme involved in fatty acid oxidation, FFA induces a decrease in the level of CPT-1, and fucoxanthin treatment can reverse the above changes, indicating that fucoxanthin could improve hepatic steatosis by increasing fatty acid oxidation.

## 2.8. Effects of Fucoxanthin on the Nrf2-Mediated Antioxidant Response

A recent study showed that liraglutide has a protective effect against FFA-induced oxidative stress, possibly via modulation of the Nrf2 pathway in the liver cells [31]. To further clarify the mechanism underlying the effect of fucoxanthin on FFA-induced intracellular lipid peroxidation, the expression of Nrf2 and its client proteins was examined. The expression of the Kelch-like ECH-associated protein 1 (Keap-1) protein was increased in the FFA group, and the expression of the Nrf2 protein was remarkably reduced (Figure 8) ( $p < 0.01$ ). In contrast, the Keap-1 protein level was downregulated after treatment with fucoxanthin, while the expression of the Nrf2 protein was significantly restored. In ad-

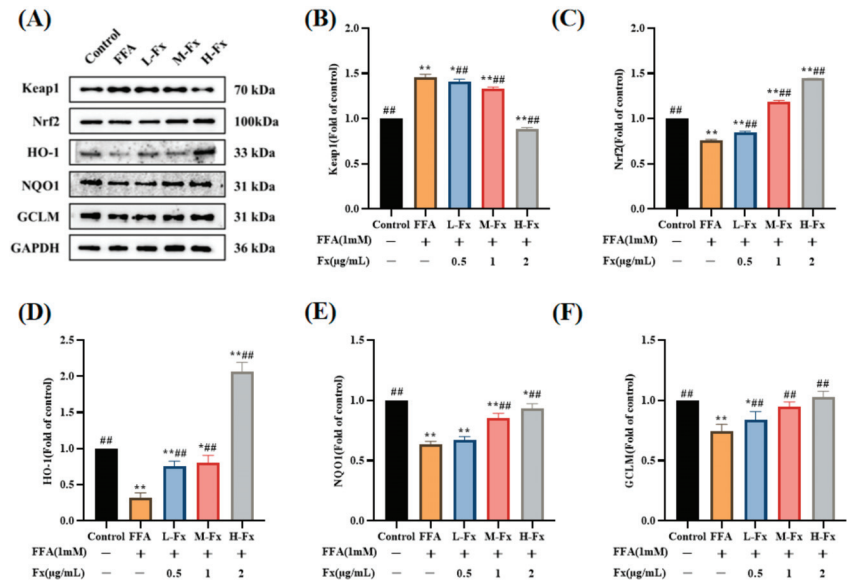
dition, the expression levels of the downstream antioxidant proteins HO-1, NQO1, and glutamate-cysteine ligase modifier subunit (GCLM), which are associated with Nrf2 protein expression, were also significantly reversed. These results indicate that fucoxanthin reduces oxidative stress in hepatocytes by activating the Nrf2-mediated antioxidant response.



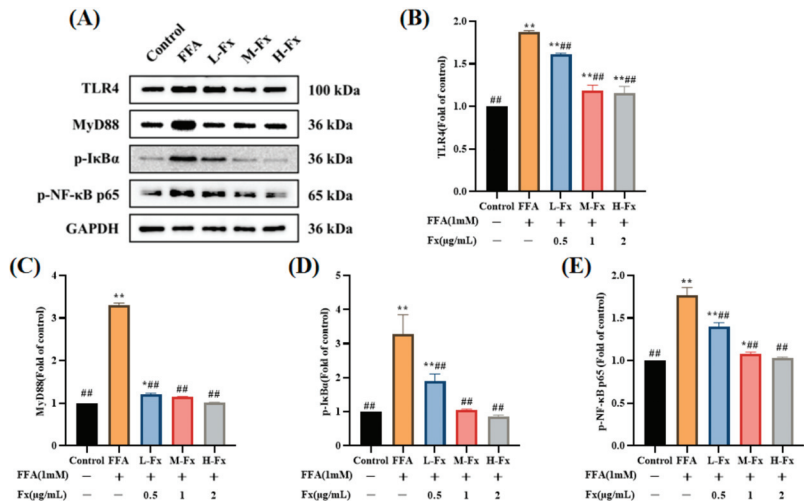
**Figure 7.** Effects of adenosine monophosphate-activated protein kinase (AMPK) activation and expression of genes related to lipid metabolism. (A) Western blot analysis of p-AMPK, AMPK, sterol regulatory element binding proteins-1c (SREBP-1c) and peroxisome proliferator-activated receptor α (PPARα), phosphorylated acetyl-CoA carboxylase (ACC) and ACC, carnitine palmitoyltransferase-1 (CPT-1), and fatty acid synthase (FAS) in the FFA-treated cells; (B) quantitative analysis for p-AMPK/AMPK; (C) quantitative analysis for PPARα; (D) quantitative analysis for SREBP-1c; (E) quantitative analysis for p-ACC/ACC; (F) quantitative analysis for CPT-1; (G) quantitative analysis for FAS. Data are expressed as mean ± standard deviation (n = 3), \* p < 0.05, \*\* p < 0.01 vs. control group, ## p < 0.01 vs. FFA group.

### 2.9. Effect of Fucoxanthin on the TLR4-Induced Inflammatory Response

The protein expression of the TLR4 signaling pathway in each group of the liver cells is shown in Figure 9. The expression of TLR4 and its downstream proteins myeloid differentiation factor 88 (MyD88), p-IκBα, and p-NF-κBp65 was significantly upregulated in the FFA group, and was significantly inhibited by treatment with fucoxanthin. Research has shown that feprazone prevented FFA-induced activation of the TLR4/MyD88/NF-κB signaling pathway [32]. These results suggest that the TLR4 signaling pathway could be a target in anti-inflammation and lipid metabolism disorders.



**Figure 8.** Effects of fucoxanthin on the nuclear factor erythroid-2-related factor 2-mediated (Nrf2) antioxidant response. (A) western blot analysis of kelch-like ECH-associated protein 1 (Keap-1), Nrf2, heme oxygenase-1 (HO-1), nicotinamide quinone oxidoreductase 1 (NQO1) and glutamate-cysteine ligase modifier subunit (GCLM) in the FFA-treated cells; (B) quantitative analysis for Keap-1; (C) quantitative analysis for Nrf2; (D) quantitative analysis for HO-1; (E) quantitative analysis for NQO1; (F) quantitative analysis for GCLM. Data are expressed as mean  $\pm$  standard deviation ( $n = 3$ ), \*  $p < 0.05$ , \*\*  $p < 0.01$  vs. control group, ##  $p < 0.01$  vs. FFA group.



**Figure 9.** Effects of fucoxanthin on the toll-like receptor 4-mediated (TLR4)-induced inflammatory response. (A) Western blot analysis of TLR4, myeloid differentiation factor 88 (MyD88), and p-IκBα and p-NF-κB p65 in the FFA-treated cells; (B) the protein levels of TLR4; (C) the protein levels of MyD88; (D) the protein levels of p-IκBα; (E) the protein levels of p-NF-κB p65. Data are expressed as mean  $\pm$  standard deviation ( $n = 3$ ), \*  $p < 0.05$ , \*\*  $p < 0.01$  vs. control group, ##  $p < 0.01$  vs. FFA group.

### 3. Discussion

In this study, the intracellular TG content was used for screening to determine the optimal treatment concentration of fucoxanthin. Our results demonstrated that the TG and TC contents in the liver cells were markedly increased after the induction with FFA, and the results of Oil Red O staining showed that the cells underwent steatosis. These phenomena were significantly improved by treatment with fucoxanthin, indicating that fucoxanthin improves FFA-induced lipid deposition in the liver cells. ALT and AST levels as sensitive indicators of hepatocyte injury were significantly increased after FFA induction in the liver cells, and were reduced to different degrees after treatment with fucoxanthin. These findings demonstrated that fucoxanthin has significant reparative effects against liver cell damage caused by FFA ( $p < 0.01$ ). In addition, inflammatory factor levels were significantly increased in the FFA-induced hepatocyte medium, and the release of inflammatory factors IL-1 $\beta$ , IL-6, and TNF- $\alpha$  was considerably reduced by treatment with fucoxanthin ( $p < 0.01$ ). Western blotting results demonstrated that the expressions of TLR4, MyD88, p-I $\kappa$ B $\alpha$ , and p-NF- $\kappa$ Bp65 in the FFA group were significantly increased ( $p < 0.01$ ), and the protein expressions of MyD88 and p-I $\kappa$ B $\alpha$  increased more than three-fold. There was no significant difference between the fucoxanthin treatment and the normal group. These results revealed that fucoxanthin has a repairing effect on FFA-induced liver cells by reducing inflammation.

AMPK acts as an energy receptor that systematically regulates energy homeostasis, and is therefore considered a potential target for the treatment of metabolic syndrome [33]. AMPK activity is reduced in the adipose tissue of obese animals and humans, and the restriction of the nutritional intake further increases AMPK activity, thus slowing the progression of obesity [34]. Previous studies have revealed that fucoxanthin regulates gluconeogenesis by activating AMPK in diabetic and obese mouse models [35,36]. We also reported that fucoxanthin increases the AMPK phosphorylation level, which is the main kinase regulator of the downstream lipogenic enzymes ACC, SREBP-1c, and FAS [37,38]. Among them, ACC is mainly found in the cytoplasm of tissues where lipids are synthesized [39]. In the liver, ACC catalyzes the formation of malonyl coenzyme A, which synthesizes long-chain fatty acid precursors [40]. SREBP-1c, an important transcription factor, is a key enzyme in the regulation of fatty acid synthesis [41], and FAS is a key enzyme of de novo fatty acid synthesis [42]. In the present research, we found that fucoxanthin could reduce lipid production by activating AMPK, thus inhibiting the expression of ACC, SREBP-1c, and FAS—key genes involved in lipid synthesis.

The PPAR $\alpha$  expression is reduced in patients with NAFLD, compared with a high expression in normal liver [43]. Activation of PPAR $\alpha$  induces the expression of fatty acid oxidation and export-related genes, and participates in the regulation of liver lipid metabolism by reducing liver lipid deposition [44,45]. CPT-1 is a key enzyme involved in fatty acid oxidation. Studies have found that PPAR $\alpha$  can also increase fatty acid oxidation by inducing CPT-1 expression [46]. We found that FFA induced an increase in the amount of MDA, a lipid peroxide marker, and a decrease in activities of the antioxidant enzymes SOD, GSH-Px, and CAT, as well as decrease in the PPAR $\alpha$  and CPT-1 expression levels. The imbalance of the liver oxidation-antioxidant system is caused by the accumulation of free radicals causing lipid peroxidation [47]. Fucoxanthin, however, increased the expression of PPAR $\alpha$  and CPT-1, and decreased the MDA content. Meanwhile, fucoxanthin increased SOD, GSH-Px, and CAT activities and restored the expression of Nrf2-mediated antioxidant pathway-related proteins, thus regulating the cellular antioxidant system (Figure 10). The results suggest that PPAR $\alpha$  is another effective target of fucoxanthin to improve lipid deposition in hepatocytes, and can improve the balance of cellular lipid metabolism through the PPAR $\alpha$  pathway, thus reducing hepatocyte lipid accumulation. The structure of fucoxanthin contains propadiene, containing allene bond, 5,6-epoxy group, conjugated polyene chain, and other structures (Figure 1A); therefore, it has strong antioxidant properties. However, our work also has shortcomings, for example the fucoxanthin we provided was of low purity, and we should improve the purity of fucoxanthin and explore what these substances are.

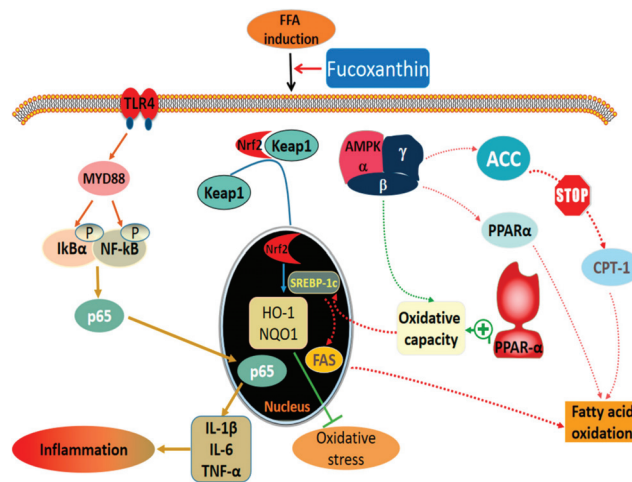


Figure 10. Mechanisms of fucoxanthin on alleviating NAFLD.

## 4. Materials and Methods

### 4.1. Chemicals and Reagents

Fucoxanthin with a purity of 70% was purchased by Shandong Jiejing Group Corporation (Rizhao, China). AST, ALT, TC, TG, SOD, CAT, GSH-Px, MDA, and Oil Red O staining solution kits were all obtained from the Jiancheng Bioengineering Institute (Nanjing, China). Enzyme-linked immunosorbent assay (ELISA) kits and a bicinchoninic acid protein assay kit were obtained from BOSTER (Wuhan, China). AMPK, phosphorylated AMPK, PPAR $\alpha$ , SREBP-1c, ACC, phosphorylated ACC, FAS, and CPT-1 antibodies were on sale at Affinity Biosciences, Inc. (Cincinnati, OH, USA). HO-1, Keap-1, GCLM, Nrf2, NQO1, GAPDH, MyD88, TLR4, phosphorylated IkB $\alpha$ , and phosphorylated NF- $\kappa$ Bp65 antibodies were obtained from Wuhan Sanying Biotechnology Co. (Wuhan, China).

### 4.2. Cell Culture

Normal human Chang liver cells, purchased from the Cell Center of Xiangya School of Medicine, Central South University, were cultured in our laboratory for passaging. The thawed cells were transferred to 10 mL centrifuge tubes under an aseptic environment and centrifuged with 4 mL Dulbecco's modified Eagle's medium high sugar medium, the supernatant was discarded and the cell precipitate was left, and then 5–6 mL of the culture medium was added and gently blown to make it evenly dispersed into a single cell suspension, which was placed at 37 °C in a 5% CO<sub>2</sub> incubator.

### 4.3. Establishment of NAFLD Cell Model

The NAFLD cell model was established by referring to the method of Qing Xiao et al. [48]. We dissolved oleic acid and palmitic acid with sodium hydroxide, and mixed them with the nutrient solution at the ratio of oleic acid/palmitic acid (2:1, v/v) to make a 10 mM total FFA mixture, and then the mixture was filtered. The 10 mM total FFA mixture was diluted in a culture medium (1:10) to acquire the 1 mM final concentration. The cells were treated with 1 mM FFA for 24 h to induce fatty degeneration as a NAFLD cell model.

### 4.4. Measurement of Lipid and Peroxidation Levels

The cells were seeded in a six-well plate at a density of  $1 \times 10^5$  cells/well and were then cultured for 24 h. The cells were induced with FFA for 24 h and the old medium was discarded. The cells were treated with different concentrations of fucoxanthin (0.125, 0.25, 0.5, 1, 2, 4, and 8  $\mu$ g/mL), which were dissolved in a culture medium without FFA for 24 h. Then, the cells were digested, centrifuged, and washed routinely with pre-chilled

phosphate-buffered saline (PBS). We added 200  $\mu$ L of Triton 100-X to each well and they were lysed on ice for 30 min. We then centrifuged at 3000 rpm for 10 min; collected the supernatant; and determined the levels of MDA, SOD, GSH-Px, CAT, TC, and TG in the cells using commercial kits, according to the manufacturer's instructions.

#### 4.5. ALT and AST Activity in Cells

The cells were seeded in a six-well plate at a density of  $1 \times 10^5$  cells/well, and after the treatment described above, each group of supernatant from the cell lysate in the six-well plates was taken as the sample to be measured [48]. The corresponding concentrations were measured using ALT and AST kits, respectively.

#### 4.6. Measurement of Pro-Inflammatory Cytokines in Cells

According to the manufacturer's instructions, an ELISA kit was used to quantify the levels of IL-1 $\beta$ , IL-6, and TNF- $\alpha$  in the cells. The expression values were calculated by bringing in a standard curve, and all data were repeated three times.

#### 4.7. Oil Red O Staining

The cells were seeded in a six-well plate at a density of  $1 \times 10^5$  cells/well, and lipid droplets were produced according to the previously described method [48]. The cells were fixed at room temperature for 10 min by adding an appropriate amount of 10% paraformaldehyde, and were incubated with Oil Red O reagent for 15 min, and then restained with hematoxylin for 5 min and sealed. The accumulation of lipid droplets inside the cells was observed under a microscope, and they were photographed and recorded. Finally, the quantification of lipid droplets was analyzed using ImageJ software.

#### 4.8. Western Blot Analysis

The cells were cultured in 1 mM FFA for 24 h as NAFLD model cells. After 24 h, the normal medium continued to incubate for 24 h. The normal group consisted of the cells cultured in a normal medium for 48 h. After the collected cells were lysed on ice with RIPA lysis buffer for 30 min, the supernatant was centrifuged and the protein concentration of each sample was determined using the BCA method. Then, we added an appropriate amount of 5 $\times$  protein loading buffer and denatured the protein in a metal bath at 95  $^{\circ}$ C for 10 min, and stored it at  $-20^{\circ}$  C after sealing. It was then added to each well, after the electrophoresis proteins of different molecular weights were separated by SDS-PAGE and were transferred to polyvinylidene difluoride membranes. The detection was performed on the Fluor Chem FC3 system (Protein Simple, Waltham, MA, USA) using the enhanced chemiluminescence reagent (ECL, Solarbio, Beijing, China) (Figure S1). Image Lab software was used to analyze the protein levels, and  $\beta$ -actin was used as the internal control.

#### 4.9. Statistical Analysis

Each treatment was carried out in triplicate, and data were expressed as mean  $\pm$  standard deviation. Statistical results between experimental groups were analyzed by one-way ANOVA using SPSS 23.0 software.  $p < 0.05$  indicates that the data are significantly different, and  $p < 0.01$  indicates that the data are extremely significantly different, all of which are statistically significant. The results were subjected to the Brown–Forsythe analysis using GraphPad Prism 8.3.0,  $p \geq 0.05$  indicated that SDs were not significantly different (default  $p \geq 0.05$  without special markers).

## 5. Conclusions

In summary, fucoxanthin can alleviate oxidative stress, lipid accumulation, and inflammation in the NAFLD model of liver cells. Fucoxanthin treatment could reduce the concentration of oxidation products and the content of inflammatory factors, increase the activity of antioxidant enzymes, and then reverse the damage of the liver cell induced by FFA and reduce oxidative stress. Fucoxanthin treatment could also down-regulate the



protein level of SREBP-1c and FAS, while activating the Nrf2 antioxidant signaling pathway and inhibiting the TLR4-mediated inflammation pathway, thereby protecting the cells.

**Supplementary Materials:** The following supporting information can be downloaded at: <https://www.mdpi.com/article/10.3390/md20040225/s1>, Figure S1: Original image of Western blot.

**Author Contributions:** Conceptualization: J.Y. and Z.Y.; data analysis: J.Z., Z.Y. and X.T.; performing experiments: J.Y., J.Z., B.X. and B.W.; writing and revising: J.Y., F.Y. and F.H.; funding acquisition: B.W. and Z.Y. All authors have read and agreed to the published version of the manuscript.

**Funding:** This research was funded by the National Natural Science Foundation of China (no. 82,073,764), The Ten-thousand Talents Plan of Zhejiang Province (no. 2019R52026), and the Zhejiang Provincial Public Welfare Technology Research Program (LGN21D060002).

**Institutional Review Board Statement:** Not applicable.

**Informed Consent Statement:** Not applicable.

**Data Availability Statement:** Not applicable.

**Conflicts of Interest:** The authors declare no conflict of interest.

## References

1. Chen, Y.; Varghese, Z.; Ruan, X.Z. The molecular pathogenic role of inflammatory stress in dysregulation of lipid homeostasis and hepatic steatosis. *Genes Dis.* **2014**, *1*, 106–112. [PubMed]
2. Lauschke, V.M.; Mkrтчian, S.; Ingelman-Sundberg, M. The role of microRNAs in liver injury at the crossroad between hepatic cell death and regeneration. *Biochem. Biophys. Res. Commun.* **2017**, *482*, 399–407. [PubMed]
3. Kawano, Y.; Cohen, D.E. Mechanisms of hepatic triglyceride accumulation in non-alcoholic fatty liver disease. *J. Gastroenterol.* **2013**, *48*, 434–441. [PubMed]
4. Bertuccio, P.; Turati, F.; Carioli, G.; Rodriguez, T.; La Vecchia, C.; Malvezzi, M.; Negri, E. Global trends and predictions in hepatocellular carcinoma mortality. *J. Hepatol.* **2017**, *67*, 302–309.
5. Reimer, K.C.; Wree, A.; Roderburg, C.; Tacke, F. New drugs for NAFLD: Lessons from basic models to the clinic. *Hepatol. Int.* **2020**, *14*, 8–23.
6. Brenner, C.; Galluzzi, L.; Kepp, O.; Kroemer, G. Decoding cell death signals in liver inflammation. *J. Hepatol.* **2013**, *59*, 583–594.
7. Peverill, W.; Powell, L.W.; Skoien, R. Evolving concepts in the pathogenesis of NASH: Beyond steatosis and inflammation. *Int. J. Mol. Sci.* **2014**, *15*, 8591–8638.
8. Marra, F.; Lotersztajn, S. Pathophysiology of NASH: Perspectives for a targeted treatment. *Curr. Pharm. Des.* **2013**, *19*, 5250–5269.
9. Shen, C.; Ma, W.; Ding, L.; Li, S.; Dou, X.; Song, Z. The TLR4-IRE1 $\alpha$  pathway activation contributes to palmitate-elicited lipotoxicity in hepatocytes. *J. Cell Mol. Med.* **2018**, *22*, 3572–3581.
10. Shen, S.; Wang, K.; Zhi, Y.; Shen, W.; Huang, L. Gypenosides improves nonalcoholic fatty liver disease induced by high-fat diet induced through regulating LPS/TLR4 signaling pathway. *Cell Cycle* **2020**, *19*, 3042–3053.
11. Wu, Z.; Zhang, Y.; Gong, X.; Cheng, G.; Pu, S.; Cai, S. The preventive effect of phenolic-rich extracts from Chinese sumac fruits against nonalcoholic fatty liver disease in rats induced by a high-fat diet. *Food Funct.* **2020**, *11*, 799–812. [PubMed]
12. Xu, Y.; Ke, H.; Li, Y.; Xie, L.; Su, H.; Xie, J.; Mo, J.; Chen, W. Malvidin-3-O-Glucoside from Blueberry Ameliorates Nonalcoholic Fatty Liver Disease by Regulating Transcription Factor EB-Mediated Lysosomal Function and Activating the Nrf2/ARE Signaling Pathway. *J. Agric. Food Chem.* **2021**, *69*, 4663–4673. [PubMed]
13. Lin, H.V.; Tsou, Y.C.; Chen, Y.T.; Lu, W.J.; Hwang, P.A. Effects of Low-Molecular-Weight Fucooidan and High Stability Fucoxanthin on Glucose Homeostasis, Lipid Metabolism, and Liver Function in a Mouse Model of Type II Diabetes. *Mar. Drugs* **2017**, *15*, 113–127.
14. Vasantharaja Raguraman, S.A.L.; MubarakAli, D.; Narendrakumar, G.; Thirugnanasambandam, R.; Kirubakaran, R.; Thajuddin, N. Unraveling rapid extraction of fucoxanthin from Padina tetrastratica: Purification, characterization and biomedical application. *Process Biochem.* **2018**, *73*, 211–219.
15. Nasab, S.B.; Homaei, A.; Pletschke, B.I.; Salinas-Salazar, C.; Castillo-Zacarias, C.; Parra-Saldívar, R. Marine resources effective in controlling and treating diabetes and its associated complications. *Process Biochem.* **2020**, *92*, 313–342.
16. Peng, J.; Yuan, J.P.; Wu, C.F.; Wang, J.H. Fucoxanthin, a marine carotenoid present in brown seaweeds and diatoms: Metabolism and bioactivities relevant to human health. *Mar. Drugs* **2011**, *9*, 1806–1828.
17. Gammone, M.A.; Riccioni, G.; D’Orazio, N. Marine Carotenoids against Oxidative Stress: Effects on Human Health. *Mar. Drugs* **2015**, *13*, 6226–6246.
18. Li, S.; Ren, X.; Wang, Y.; Hu, J.; Wu, H.; Song, S.; Yan, C. Fucoxanthin alleviates palmitate-induced inflammation in RAW 264.7 cells through improving lipid metabolism and attenuating mitochondrial dysfunction. *Food Funct.* **2020**, *11*, 3361–3370.

19. Takatani, N.; Kono, Y.; Beppu, F.; Okamatsu-Ogura, Y.; Yamano, Y.; Miyashita, K.; Hosokawa, M. Fucoxanthin inhibits hepatic oxidative stress, inflammation, and fibrosis in diet-induced nonalcoholic steatohepatitis model mice. *Biochem. Biophys. Res. Commun.* **2020**, *528*, 305–310.
20. Ferramosca, A.; Di Giacomo, M.; Zara, V. Antioxidant dietary approach in treatment of fatty liver: New insights and updates. *World J. Gastroenterol.* **2017**, *23*, 4146–4157.
21. Lee, Y.; Hu, S.; Park, Y.K.; Lee, J.Y. Health Benefits of Carotenoids: A Role of Carotenoids in the Prevention of Non-Alcoholic Fatty Liver Disease. *Prev. Nutr. Food Sci.* **2019**, *24*, 103–113. [[PubMed](#)]
22. Shih, P.H.; Shiue, S.J.; Chen, C.N.; Cheng, S.W.; Lin, H.Y.; Wu, L.W.; Wu, M.S. Fucoidan and Fucoxanthin Attenuate Hepatic Steatosis and Inflammation of NAFLD through Modulation of Leptin/Adiponectin Axis. *Mar. Drugs* **2021**, *19*, 148. [[PubMed](#)]
23. Chang, Y.-H.; Chen, Y.-L.; Huang, W.-C.; Liou, C.-J. Fucoxanthin attenuates fatty acid-induced lipid accumulation in FL83B hepatocytes through regulated Sirt1/AMPK signaling pathway. *Biochem. Biophys. Res. Commun.* **2018**, *495*, 197–203.
24. Guo, B.; Zhou, Y.; Liu, B.; He, Y.; Chen, F.; Cheng, K.W. Lipid-Lowering Bioactivity of Microalga *Nitzschia laevis* Extract Containing Fucoxanthin in Murine Model and Carcinomic Hepatocytes. *Pharmaceuticals* **2021**, *14*, 1004. [[PubMed](#)]
25. Muradian, K.; Vaiserman, A.; Min, K.J.; Fraifeld, V.E. Fucoxanthin and lipid metabolism: A minireview. *Nutr. Metab. Cardiovasc. Dis.* **2015**, *25*, 891–897. [[PubMed](#)]
26. Zheng, J.; Tian, X.; Zhang, W.; Zheng, P.; Huang, F.; Ding, G.; Yang, Z. Protective Effects of Fucoxanthin against Alcoholic Liver Injury by Activation of Nrf2-Mediated Antioxidant Defense and Inhibition of TLR4-Mediated Inflammation. *Mar. Drugs* **2019**, *17*, 552–567.
27. Chung, S.; Hwang, J.T.; Park, J.H.; Choi, H.K. Free fatty acid-induced histone acetyltransferase activity accelerates lipid accumulation in HepG2 cells. *Nutr. Res. Pract.* **2019**, *13*, 196–204.
28. Liu, Y.; Xu, W.; Zhai, T.; You, J.; Chen, Y. Silibinin ameliorates hepatic lipid accumulation and oxidative stress in mice with non-alcoholic steatohepatitis by regulating CFLAR-JNK pathway. *Acta Pharm. Sin. B* **2019**, *9*, 745–757.
29. Liu, Y.; Liao, L.; Chen, Y.; Han, F. Effects of daphnetin on lipid metabolism, insulin resistance and oxidative stress in OA-treated HepG2 cells. *Mol. Med. Rep.* **2019**, *19*, 4673–4684.
30. Ma, J.; Li, M.; Kalavagunta, P.K.; Li, J.; He, Q.; Zhang, Y.; Ahmad, O.; Yin, H.; Wang, T.; Shang, J. Protective effects of cichoric acid on H(2)O(2)-induced oxidative injury in hepatocytes and larval zebrafish models. *Biomed. Pharm.* **2018**, *104*, 679–685.
31. Zhu, C.G.; Luo, Y.; Wang, H.; Li, J.Y.; Yang, J.; Liu, Y.X.; Qu, H.Q.; Wang, B.L.; Zhu, M. Liraglutide Ameliorates Lipotoxicity-Induced Oxidative Stress by Activating the NRF2 Pathway in HepG2 Cells. *Horm. Metab. Res.* **2020**, *52*, 532–539. [[PubMed](#)]
32. Song, M.; Meng, L.; Liu, X.; Yang, Y. Feprazone Prevents Free Fatty Acid (FFA)-Induced Endothelial Inflammation by Mitigating the Activation of the TLR4/MyD88/NF- $\kappa$ B Pathway. *ACS Omega* **2021**, *6*, 4850–4856.
33. Ning, C.; Gao, X.; Wang, C.; Huo, X.; Liu, Z.; Sun, H.; Yang, X.; Sun, P.; Ma, X.; Meng, Q.; et al. Protective effects of ginsenoside Rg1 against lipopolysaccharide/d-galactosamine-induced acute liver injury in mice through inhibiting toll-like receptor 4 signaling pathway. *Int. Immunopharmacol.* **2018**, *61*, 266–276. [[PubMed](#)]
34. Ning, C.; Gao, X.; Wang, C.; Huo, X.; Liu, Z.; Sun, H.; Yang, X.; Sun, P.; Ma, X.; Meng, Q.; et al. Hepatoprotective effect of ginsenoside Rg1 from Panax ginseng on carbon tetrachloride-induced acute liver injury by activating Nrf2 signaling pathway in mice. *Environ. Toxicol.* **2018**, *33*, 1050–1060. [[PubMed](#)]
35. Li, M.; Cai, S.Y.; Boyer, J.L. Mechanisms of bile acid mediated inflammation in the liver. *Mol. Asp. Med.* **2017**, *56*, 45–53.
36. Masarone, M.; Rosato, V.; Dallio, M.; Gravina, A.G.; Aglitti, A.; Loguercio, C.; Federico, A.; Persico, M. Role of Oxidative Stress in Pathophysiology of Nonalcoholic Fatty Liver Disease. *Oxidative Med. Cell. Longev.* **2018**, *2018*, 9547613.
37. Zhao, J.; Shi, Z.; Liu, S.; Li, J.; Huang, W. Ginsenosides Rg1 from Panax ginseng: A Potential Therapy for Acute Liver Failure Patients? *Evid. Based Complement. Altern. Med.* **2014**, *2014*, 538059.
38. Huang, W.C.; Liao, P.C.; Huang, C.H.; Hu, S.; Huang, S.C.; Wu, S.J. Osthole attenuates lipid accumulation, regulates the expression of inflammatory mediators, and increases antioxidants in FL83B cells. *Biomed. Pharm.* **2017**, *91*, 78–87.
39. Geisler, S.; Holmström, K.M.; Skujat, D.; Fiesel, F.C.; Rothfuss, O.C.; Kahle, P.J.; Springer, W. PINK1/Parkin-mediated mitophagy is dependent on VDAC1 and p62/SQSTM1. *Nat. Cell Biol.* **2010**, *12*, 119–131.
40. Xiao, J.; Wang, F.; Wong, N.K.; He, J.; Zhang, R.; Sun, R.; Xu, Y.; Liu, Y.; Li, W.; Koike, K.; et al. Global liver disease burdens and research trends: Analysis from a Chinese perspective. *J. Hepatol.* **2019**, *71*, 212–221.
41. Zhao, H.; Wang, Z.; Tang, F.; Zhao, Y.; Feng, D.; Li, Y.; Hu, Y.; Wang, C.; Zhou, J.; Tian, X.; et al. Carnosol-mediated Sirtuin 1 activation inhibits Enhancer of Zeste Homolog 2 to attenuate liver fibrosis. *Pharm. Res.* **2018**, *128*, 327–337.
42. Giudetti, A.M.; Guerra, F.; Longo, S.; Beli, R.; Romano, R.; Manganelli, F.; Nolano, M.; Mangini, V.; Santoro, L.; Bucci, C. An altered lipid metabolism characterizes Charcot-Marie-Tooth type 2B peripheral neuropathy. *Biochim. Biophys. Acta Mol. Cell Biol. Lipids* **2020**, *1865*, 158805. [[PubMed](#)]
43. Wang, J.; Li, Y. CD36 tango in cancer: Signaling pathways and functions. *Theranostics* **2019**, *9*, 4893–4908. [[PubMed](#)]
44. Quintana-Castro, R.; Aguirre-Maldonado, I.; Soto-Rodríguez, I.; Deschamps-Lago, R.A.; Gruber-Pagola, P.; Urbina de Larrea, Y.K.; Juárez-Rivera, V.E.; Ramos-Manuel, L.E.; Alexander-Aguilera, A. Cd36 gene expression in adipose and hepatic tissue mediates the lipids accumulation in liver of obese rats with sucrose-induced hepatic steatosis. *Prostaglandins Other Lipid Mediat.* **2020**, *147*, 106404.
45. Wu, W.; Wang, S.; Liu, Q.; Shan, T.; Wang, X.; Feng, J.; Wang, Y. AMPK facilitates intestinal long-chain fatty acid uptake by manipulating CD36 expression and translocation. *FASEB J.* **2020**, *34*, 4852–4869.

46. Zhang, P.; Ge, Z.; Wang, H.; Feng, W.; Sun, X.; Chu, X.; Jiang, C.; Wang, Y.; Zhu, D.; Bi, Y. Prolactin improves hepatic steatosis via CD36 pathway. *J. Hepatol.* **2018**, *68*, 1247–1255.
47. Ginsberg, H.N. Selective Trafficking of Fatty Acids in the Liver: Add Them2 to the List of Influencers. *Hepatology* **2019**, *70*, 462–464.
48. Xiao, Q.; Zhang, S.; Yang, C.; Du, R.; Zhao, J.; Li, J.; Xu, Y.; Qin, Y.; Gao, Y.; Huang, W. Ginsenoside Rg1 Ameliorates Palmitic Acid-Induced Hepatic Steatosis and Inflammation in HepG2 Cells via the AMPK/NF- $\kappa$ B Pathway. *Int. J. Endocrinol.* **2019**, *2019*, 7514802.

## Article

# Adsorption Characteristics and Enrichment of Emodin from Marine-Derived *Aspergillus flavipes* HN4-13 Extract by Macroporous Resin XAD-16

Lizhi Gong <sup>1,2</sup>, Yuzhen Wu <sup>2</sup>, Xiaohan Qiu <sup>2</sup>, Xiujuan Xin <sup>2</sup>, Faliang An <sup>2,\*</sup> and Miaomiao Guo <sup>1,\*</sup>

<sup>1</sup> Key Laboratory of Cosmetic, China National Light Industry, Beijing Technology and Business University, No. 11/33, Fucheng Road, Beijing 100048, China; y30191249@mail.ecust.edu.cn

<sup>2</sup> State Key Laboratory of Bioreactor Engineering, East China University of Science and Technology, 130 Meilong Road, Shanghai 200237, China; y30200462@mail.ecust.edu.cn (Y.W.); y30180978@mail.ecust.edu.cn (X.Q.); xinxj@ecust.edu.cn (X.X.)

\* Correspondence: flan2016@ecust.edu.cn (F.A.); guomiaomiao7@163.com (M.G.); Tel.: +86-21-6425-3823 (F.A.); +86-010-68987110 (M.G.)

**Abstract:** Emodin, a hydroxyanthraquinone derivative, has been used as medicine for more than 2000 years due to its extensive pharmacological activities. Large-scale production of emodin has been achieved by optimizing the fermentation conditions of marine-derived *Aspergillus flavus* HN4-13 in a previous study. However, the fermentation broth contained complex unknown components, which adversely affected the study of emodin. Herein, the conditions for the enrichment of emodin from *A. flavipes* HN4-13 extract using XAD-16 resin were optimized, and a separation method with high efficiency, simple operation, a low cost, and a large preparative scale was established. The adsorption process of emodin on the XAD-16 resin conformed to pseudo-second-order kinetics and Langmuir models. The optimal conditions for the adsorption process were as follows: An emodin concentration, flow rate, and loading volume of 0.112 mg/mL, 2 BV/h, and 10 BV, respectively. For desorption, 50% ethanol was used to elute impurities and 80% ethanol was used to desorb emodin. After enrichment with XAD-16 resin, the emodin content increased from 1.16% to 11.48%, and the recovery rate was 75.53% after one-step treatment. These results demonstrate the efficiency of the simple adsorption–desorption strategy, using the XAD-16 resin for emodin enrichment.

**Keywords:** *Aspergillus flavipes* HN4-13; emodin; macroporous resin XAD-16; adsorption kinetics and isotherms; enrichment

**Citation:** Gong, L.; Wu, Y.; Qiu, X.; Xin, X.; An, F.; Guo, M. Adsorption Characteristics and Enrichment of Emodin from Marine-Derived *Aspergillus flavipes* HN4-13 Extract by Macroporous Resin XAD-16. *Mar. Drugs* **2022**, *20*, 231. <https://doi.org/10.3390/md20040231>

*Drugs* **2022**, *20*, 231. <https://doi.org/10.3390/md20040231>

Academic Editors: Yonghong Liu and Xuefeng Zhou

Received: 28 February 2022

Accepted: 25 March 2022

Published: 28 March 2022

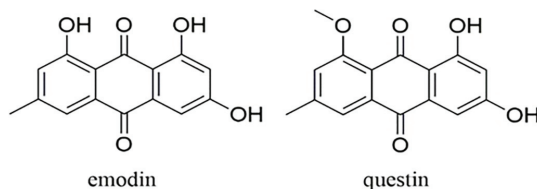
**Publisher's Note:** MDPI stays neutral with regard to jurisdictional claims in published maps and institutional affiliations.



**Copyright:** © 2022 by the authors. Licensee MDPI, Basel, Switzerland. This article is an open access article distributed under the terms and conditions of the Creative Commons Attribution (CC BY) license (<https://creativecommons.org/licenses/by/4.0/>).

## 1. Introduction

Emodin (1,3,8-trihydroxy-6-methylanthraquinone) is a hydroxyanthraquinone derivative with a variety of activities, including cathartic, anticancer [1], anti-inflammatory, antioxidant [2], antibacterial [3], and anti-diabetic properties [4]. Previous research has indicated that emodin can be used as a potential drug for the prevention and treatment of diseases, such as asthma [5], osteoarthritis [6], Alzheimer's disease (AD) [7], hepatic disease [8], and cancer [9–11]. Emodin is also used as an industrial additive in food and cosmetics [12]. As mentioned above, emodin has broad application prospects and, thus, a high market demand. Questin, a derivative of emodin, with antibacterial activity, can be converted into emodin via a demethylation reaction [13]. The chemical structures of emodin and questin are shown in Figure 1.



**Figure 1.** Chemical structures of emodin and questin.

At present, emodin is mainly separated from the traditional Chinese medicinal herb *Rheum palmatum* Linn [12]. Disadvantageously, however, the plant requires a long period, and a complex process is required to separate emodin from the plant extract, with a low recovery rate [14]. The chemical synthesis of emodin has the disadvantages of low yields and a complex route. Chalothorn et al. synthesized emodin in an eight-step complex chemical reaction with a total yield of only 37% [15]. Recently, microorganisms have been found to be a rich source of bioactive metabolites, and emodin is also reportedly contained in the secondary metabolites of fungi from *Aspergillus* and *Penicillium* genera [13,16]. In a previous experiment in our lab, by optimizing the fermentation conditions of marine-derived *A. flavipes* HN4-13 in  $\text{KH}_2\text{PO}_4$ -supplemented medium, the yield of emodin was increased ten-fold (to 185.56 mg/L) at the shake flask level [17], which is conducive to large-scale production of emodin. However, the fermentation broth contained complex unknown components that adversely affected the study of the biological activity of emodin. Therefore, it is highly desirable to establish a simple and efficient method to enrich emodin from *A. flavipes* HN4-13 extract.

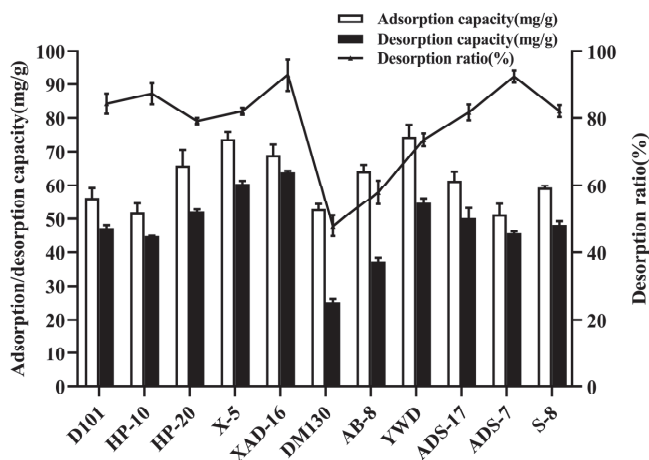
Macroporous resins have the advantages of a large specific surface area, strong adsorption, stable physical and chemical properties, a fast adsorption rate, excellent selectivity, high repeatability, and low cost [18]. These resins are widely used in the production of medicines and natural products [19,20], making up for the deficiencies of traditional membrane-separation technology and solvent-extraction methods. Amberlite XAD resins are styrene–divinylbenzene copolymers, which mainly adsorb organic matters through hydrophobic bonds [21]. Among them, XAD-16 resin has a good adsorption capacity for weakly polar compounds with its pore size of 200 Å and surface area of 800 m<sup>2</sup>/g [22]. Compared with some modified adsorbents, XAD-16 resin is more suitable for industrial large-scale production due to its lower cost and easier access [23,24]. Therefore, in this study, a systematic separation process using macroporous resin was designed and developed to obtain sufficient emodin. The separation process was optimized including the static and dynamic adsorption and desorption variables. Furthermore, to improve the emodin content, questin in the desorption solution was transferred into emodin by a one-step demethylation reaction [15]. Overall, a simply executed, low-cost method with high separation efficiency was developed for emodin enrichment. Herein, we report the systematic separation process for the large-scale production of emodin from fermented *A. flavipes* HN4-13 extract. This study laid the theoretical foundation for the industrial application of emodin and was of great significance to the further research and application of emodin activity.

## 2. Results

### 2.1. Resin Screening

The characteristics of 11 resins with different polarities and pore sizes for emodin adsorption are compared in Figure 2. Among them, XAD-16 resin had a relatively high adsorption capacity and maximum desorption capacity, with values of 73.73 mg/g and 63.91 mg/g, respectively. From the resin parameters in Table 1 and the experimental data in Figure 2, it was deduced that the polarity of the resin greatly affected the adsorption and desorption processes, consistent with a previous report [25]. Emodin is a weakly polar compound and considering the principle underlying the adsorption for compounds

on resins, the adsorption capacity of weakly polar and non-polar resins for emodin is higher than that of polar resins [26]. Therefore, the emodin adsorption capacities of HP-20, X-5, XAD-16, YWD, and AB-8 were generally superior to those of S-8 and ADS-7 as polar resins. In addition, resins with larger pore sizes and surface area tend to have higher mass exchange rates, and thus, higher desorption and recovery rates [25]. XAD-16 has a large specific surface area of 800 m<sup>2</sup>/g and a pore size of 15 nm, which can also improve the adsorption capacity of emodin. Therefore, XAD-16 was selected for the enrichment of emodin. The application of XAD-16 in natural product separation and enrichment has been widely reported [27,28].



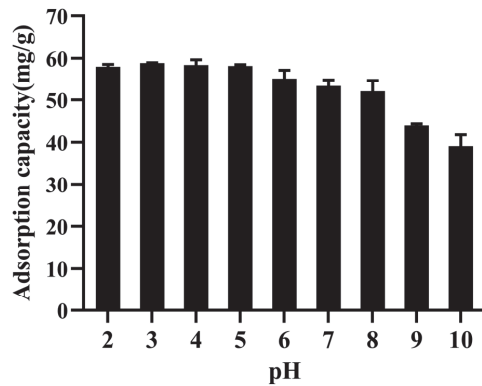
**Figure 2.** Resin screening for enrichment of emodin. Initial concentration of emodin in the solution: 0.390 mg/mL; desorption solution: 95% ethanol (*v/v*); operating temperature: 25 °C; shaking speed: 120 rpm. Results are the mean of three determinations.

**Table 1.** Physical and chemical properties of various resins.

| Resin  | Polarity     | Surface Area (m <sup>2</sup> /g) | Average Pore Diameter (nm) | Particle Diameter (mm) |
|--------|--------------|----------------------------------|----------------------------|------------------------|
| D101   | non-polar    | 400–600                          | 10–12                      | 0.2–0.6                |
| HP-10  | non-polar    | 500–650                          | 15–50                      | 0.6–0.7                |
| HP-20  | non-polar    | 850–1000                         | 25–50                      | 0.6–0.7                |
| X-5    | non-polar    | 500–600                          | 29–30                      | 0.3–1.25               |
| XAD-16 | non-polar    | 800                              | 15                         | 0.7                    |
| DM130  | weak polar   | 100                              | 25–30                      | 0.3–1.25               |
| AB-8   | weak polar   | 480–520                          | 13–14                      | 0.3–1.25               |
| YWD    | weak polar   | 500–550                          | 9–10                       | 0.3–1.2                |
| ADS-17 | middle polar | 90–150                           | 25–30                      | 0.3–1.25               |
| ADS-7  | polar        | 100                              | 25–30                      | 0.3–1.25               |
| S-8    | polar        | 100–120                          | 28–30                      | 0.3–1.25               |

## 2.2. Effect of the Solution pH on XAD-16 Resin Adsorption Capacity

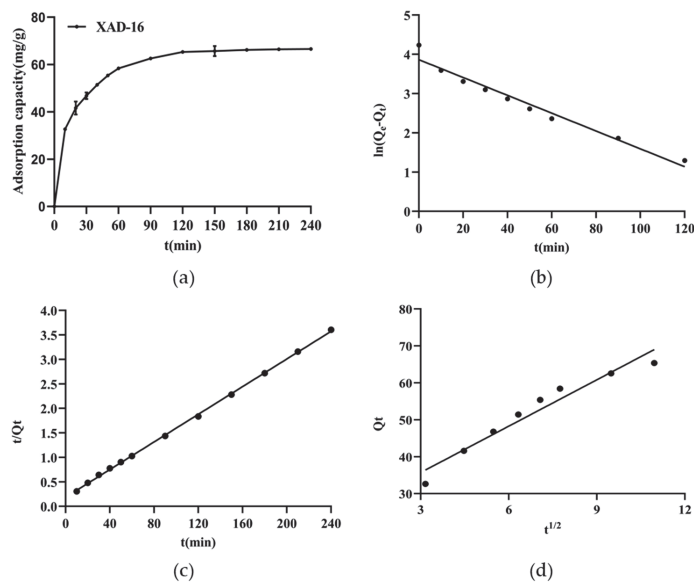
As shown in Figure 3, the adsorption capacity of the XAD-16 resin for emodin was the highest at pH 3.0, and the adsorption capacity under acidic conditions was higher than that under alkaline conditions. Emodin was mainly combined with XAD-16 resin through hydrophobic interactions. In the alkaline condition, as a phenolic acid compound, the phenolic hydroxyl of emodin was dissociated into the corresponding anionic form, resulting in the weakened hydrophobic interaction with the resin [29]. However, dissociation was inhibited under acidic conditions. Therefore, the optimum pH for the adsorption process was 3.0, indicating that there was no need to adjust the pH of the sample solution.



**Figure 3.** Effect of the solution pH on XAD-16 resin adsorption capacity. Initial concentration of emodin in the solution: 0.3900 mg/mL; operating temperature: 25 °C; shaking speed: 120 rpm. Results are the mean of three determinations.

### 2.3. Adsorption Kinetics Experiments

The adsorption kinetics curve can be used to characterize the adsorption efficiency and capacity of the resin when the adsorption process reaches equilibrium. The data reflect the adsorption of the solute on the resin during different time periods. The kinetics curve for the adsorption of emodin on the XAD-16 resin was shown in Figure 4a. In the first 60 min of the adsorption process, the adsorption capacity increased rapidly, and then the growth rate continued to slow down. After 120 min, the adsorption of emodin on the resin reached equilibrium. Consequently, 120 min was selected as the optimal static adsorption time.



**Figure 4.** (a) The static adsorption kinetic curve of emodin on XAD-16 resin; (b) the linear plots of pseudo-first-order kinetics; (c) the linear plots of pseudo-second-order kinetics; (d) the linear plots of Weber and Morris intra-particle diffusion models. Initial concentration of emodin in the solution: 0.390 mg/mL; desorption solution: 95% ethanol (*v/v*); operating temperature: 25 °C; shaking speed: 120 rpm. Results in (a) are the mean of three determinations.

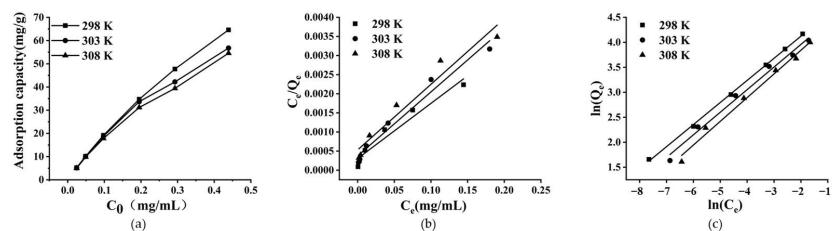
To clarify the process of emodin adsorption on XAD-16, the experimental data were fitted with pseudo-first-order kinetics, pseudo-second-order kinetics, and Weber and Morris intra-particle diffusion kinetics models. The results were shown in Figure 4b–d. The relevant parameters for the three models summarized in Table 2 indicated that the  $Q_e$  value of the pseudo-second-order kinetic model is much more in line with the experimental  $Q_e$  value (63.91 mg/g), indicating that the rate-determining step in the adsorption process is related to the concentrations of both emodin and resin [30]. Moreover, the  $R^2$  value of the pseudo-second-order kinetic model is higher than the  $R^2$  value of the pseudo-first-order kinetics model, which also demonstrates that the pseudo-second-order kinetics model is more appropriate for describing emodin adsorption on XAD-16. For the Weber and Morris intra-particle diffusion kinetics model, the straight line did not cross the origin of coordinates, indicating that the adsorption process of emodin on XAD-16 was affected by many factors, such as interparticle diffusion and boundary layer diffusion [31].

**Table 2.** Kinetic parameters for adsorption of emodin on XAD-16 resin.

| Kinetic Model                                   | Equation                             | $R^2$  | Parameters  |
|---|--------------------------------------|--------|---|
| Pseudo-first-order model                        | $\ln Q_e - Q_t = 3.864 - 0.0227t$    | 0.9652 | $k_1 = 0.052$<br>$Q_e^{cal} = 47.66 \text{ mg/g}$   |
| Pseudo-second-order model                       | $\frac{t}{Q_t} = 0.01411t + 0.1870$  | 0.9995 | $k_2 = 0.00107$<br>$Q_e^{cal} = 70.87 \text{ mg/g}$ |
| Weber and Morris intra-particle diffusion model | $Q_t = 4.184t^{\frac{1}{2}} + 23.17$ | 0.9459 | $k_t = 4.184$<br>$C = 23.17$                        |

#### 2.4. Adsorption Isotherms and Thermodynamic Experiments

To interpret the process of emodin adsorption on the XAD-16 resin more comprehensively, the adsorption isotherms and thermodynamic models were established. As shown in Figure 5a, with an increase in the initial concentration of emodin in the solution, the adsorption capacity of XAD-16 increased, but the increasing trend was continuously alleviated. It was speculated that the adsorption of emodin on XAD-16 tended to be saturated, so increasing the concentration of emodin could not improve the adsorption capacity of the resin. Therefore, the initial concentration of emodin used in subsequent experiments was 0.112 mg/mL. When the initial concentration of emodin was fixed, the adsorption capacity of resin increased with decreasing temperature. At 298 K, the adsorption capacity of XAD-16 for emodin was higher than that at 303 K and 308 K, indicating that the adsorption process was exothermic. In consideration of the experimental results and the actual operating conditions, 298 K was selected as the optimal operating temperature.



**Figure 5.** (a) Adsorption isotherms of emodin on XAD-16 at 298, 303 and 308 K; (b) the linear plots of Langmuir model; (c) the linear plots of Freundlich model. Initial concentrations of emodin in adsorption solution: 0.024, 0.049, 0.112, 0.195, 0.293, and 0.439 mg/mL; shaking speed: 120 rpm.

Adsorption isotherms are used to describe the distribution of solutes in solvents and adsorbents. They are related to the characteristics of the adsorbents and the interactions between the adsorbents and the solutes [32]. The Langmuir model assumes that the target adsorbed on the adsorbent is a single layer and that there is no interaction with the solute.



However, the Freundlich isotherm model describes multi-layer adsorption, assuming that the ratio of the solute adsorbed on the adsorbent to the concentration of the solute in the solution exists as a function of the solution concentration [33]. As shown in Figure 5b,c, the Langmuir and Freundlich models were used to explain the thermodynamics of emodin adsorption on XAD-16. The relevant parameters of the two models at 298, 303, and 308 K were summarized in Table 3. The  $R^2$  values of the Freundlich model were higher than that of the Langmuir model at the same temperatures, which implied that the adsorption process of emodin on XAD-16 was more in line with the Freundlich model and it belonged to multi-layer adsorption. The  $K_F$  value decreased with the increase in temperature, suggesting that the adsorption process was exothermic. The  $1/n$  value was within 0.1–0.5, indicating that the adsorption of emodin on XAD-16 was relatively facile.

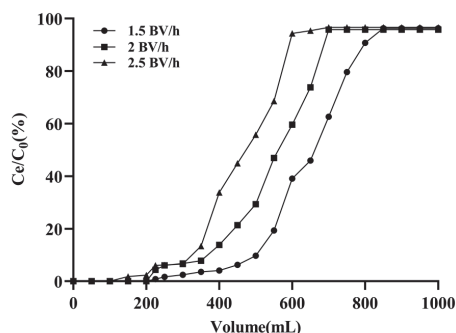
**Table 3.** Langmuir and Freundlich parameters of emodin on XAD-16.

| T (K) | Langmuir Model |       |        | Freundlich Model |        |        | $\Delta G$<br>(kJ/mol) | $\Delta H$<br>(kJ/mol) | $\Delta S$<br>(kJ/mol) |
|-------|----------------|-------|--------|------------------|--------|--------|------------------------|------------------------|------------------------|
|       | $Q_m$          | $K_L$ | $R^2$  | $K_F$            | $1/n$  | $R^2$  |                        |                        |                        |
| 298   | 69.44          | 48.00 | 0.9215 | 149.5            | 0.4421 | 0.9993 | −9.591                 | −22.97                 | −0.045                 |
| 303   | 59.88          | 41.75 | 0.9702 | 129.3            | 0.4522 | 0.9896 | −9.401                 |                        |                        |
| 308   | 58.14          | 34.40 | 0.9624 | 120.3            | 0.4742 | 0.9895 | −9.060                 |                        |                        |

The relevant adsorption thermodynamic parameters at 298, 303, and 308 K are shown in Table 3.  $\Delta G < 0$  implied that the adsorption process was spontaneous and feasible. In addition, the absolute value of  $\Delta G$  decreased with increasing temperature, indicating that low temperature was more conducive to the adsorption process [34,35].  $\Delta H < 0$  indicated that the adsorption process was exothermic, and  $\Delta H < 43$  kJ/mol showed that the process was a physical adsorption process [36,37].  $\Delta S < 0$  suggested that the process is a process with a reduced degree of system confusion.

### 2.5. Dynamic Breakthrough Curves of Emodin on XAD-16

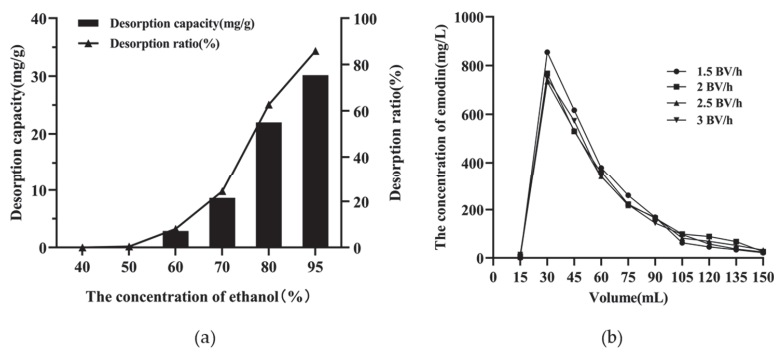
By studying the dynamic adsorption process, the dynamic breakthrough curve was constructed, and the sample volume and loading flow rate were optimized. As shown in Figure 6, a faster loading flow rate (2.5 BV/h) was conducive to reducing the time required for the resin to reach the breakthrough point (the emodin concentration in the effluent was 5% of the initial concentration), but the adsorption capacity of the XAD-16 for emodin was decreased. Therefore, a low flow rate was superior to a high flow rate, but the too-low flow rate (1.5 BV/h) would prolong the experimental operation time and greatly increase the loading volume, which was inconsistent with the concept of green production for environmental protection. Hence, 2 BV/h was selected as the optimal loading flow rate, and the loading volume was 200 mL (10 BV).



**Figure 6.** Dynamic breakthrough curve of emodin on XAD-16. Initial concentration of emodin in adsorption solution was 0.112 mg/mL.

## 2.6. Optimal Eluent Concentration and Flow Rate for Dynamic Desorption

The elution efficiency of emodin adsorbed on resin varied with the concentration of ethanol solution. As shown in Figure 7a, the emodin content in the desorption solution was low when 40% or 50% ethanol was used as the eluent. With an increase in the ethanol concentration from 70% to 80%, the desorption amount and desorption rate of emodin increased significantly, and the impurity content in the eluate was relatively low. Therefore, in this experiment, a 50% ethanol solution was used as the eluent to elute impurities, and an 80% ethanol solution was used as the desorption solution.



**Figure 7.** (a) The selection of eluent concentration of emodin on XAD-16; (b) dynamic desorption curve of emodin on XAD-16.

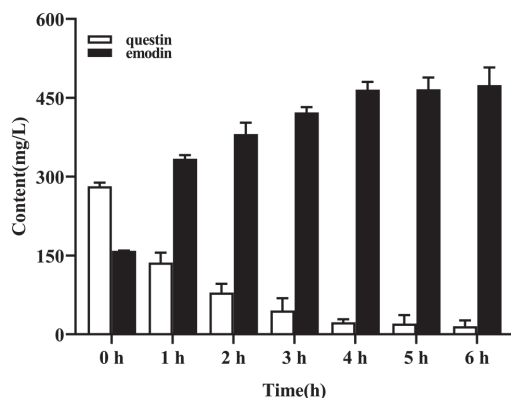
When the adsorption of emodin on XAD-16 reached equilibrium, the resin column was first rinsed with 6 BV deionized water, followed by 6 BV 50% ethanol solution to remove the impurities. Subsequently, elution was performed using 80% ethanol at flow rates of 1.5, 2.0, 2.5, and 3.0 BV/h, respectively. As shown in Figure 7b, the emodin content in the eluent was the highest at a flow rate of 1.5 BV/h, and the emodin was easily collected in the range of 2–6 BV.

## 2.7. Optimal Reaction Time for Conversion of Questin to Emodin

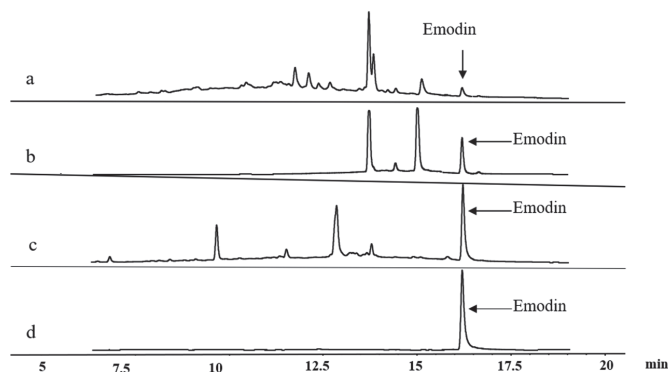
Questin is a derivative of emodin, and both have similar physicochemical properties. The two compounds could not be separated through adsorption on the XAD-16 resin and subsequent desorption, which reduced the purity of emodin in the desorption solution. Previous experiments have shown that questin can be easily and efficiently converted to emodin via a one-step chemical reaction [17]. As shown in Figure 8, when the reaction lasted for 5 h, questin in the eluate had been essentially converted to emodin.

## 2.8. Purification of Emodin

As shown in Figure 9, after enrichment using XAD-16 resin, the percentage of emodin increased from 1.16% to 11.48% with a recovery of 75.53%, which was an approximately ten-fold increase. The questin content increased from 3.70% to 18.43% with the recovery of 58.45%, representing an approximately five-fold increase. After chemical transformation, the emodin content increased to 25.75%, with a recovery of 50.32%. A total of 32.5 mg of emodin crystals was obtained with a purity of 94.4% through successive resin enrichment, chemical conversion, separation, and purification on a silica gel column and reversed-phase column. The  $^1\text{H}$  NMR and HRESIMS data of the purified emodin were detailed in the Supporting Information (Figures S1 and S2).



**Figure 8.** The optimal reaction time for the conversion of questin to emodin. Results are the mean of three determinations.



**Figure 9.** HPLC chromatograms of samples (a: Initial; b: Resin enrichment; c: Reaction conversion; d: Further purification).

### 3. Discussion

In summary, XAD-16 resin was selected for the enrichment of emodin from the fermentation broth of *A. flavipes* HN4-13. The static and dynamic parameters were optimized using the kinetic and isothermal models. High-purity emodin (94.4%), with a recovery of 75.53%, was obtained under the optimized conditions. The percentage of emodin in the *A. flavipes* HN4-13 extract reached 29.91% after enrichment with XAD-16 resin and chemical transformation, representing a more than 25-fold increase. Meanwhile, the majority of complex unknown components were removed, which was conducive to further study on the activity of emodin. Hence, the XAD-16 resin was shown as an effective and promising tool for the large-scale separation of emodin due to its high adsorption and recovery characteristics. In addition, the regeneration and stability of the adsorbent are two of the important parameters in evaluating solid-phase efficiency for adsorption studies [38]. In previous studies, Liu et al. have evaluated the reusability of XAD-16 resin and demonstrated its advantages of easy regeneration [27]. Therefore, a separation method with high separation efficiency, simple operation, and low cost for the enrichment of emodin from *A. flavipes* HN4-13 fermentation broth was successfully established, which may provide a theoretical basis for the industrial-scale production of emodin.

## 4. Materials and Methods

### 4.1. Materials and Reagents

The chemical reagents of analytical grade were purchased from Shanghai Titan Technology Co., Ltd. (Shanghai, China). Standard emodin and questin were isolated from the laboratory.

The macroporous resins D101, HP-10, HP-20, X-5, XAD-16, DM130, AB-8, YWD, ADS-17, ADS-7m, and S-8 were purchased from Nankai Hecheng Technology Co., Ltd. (Tianjin, China). The resins were pretreated with 95% ethanol for 24 h, then sequentially treated with 5% HCl, 5% NaOH, and deionized water, and finally dried at 50 °C to a constant weight. Prior to the experiments, the resins were kept in 95% ethanol for 24 h to activate and then were rinsed with deionized water thoroughly. The main physical properties of these resins are summarized in Table 1.

### 4.2. Preparation of Sample Solution

The fermentation medium used for *A. flavipes* HN4-13 was soluble starch, yeast extract, sea salt,  $\text{KH}_2\text{PO}_4$ ,  $\text{MgSO}_4 \cdot 7\text{H}_2\text{O}$ , and  $\text{FeSO}_4 \cdot 7\text{H}_2\text{O}$ , which was consistent with the emodin fermentation process reported previously [17]. The fermentation broth was concentrated by filtration, and the concentrate was extracted three times with an equal volume of ethyl acetate (EtOAc). The EtOAc extract was subjected to rotary evaporation under vacuum conditions (−0.08 MPa, 45 °C) to remove EtOAc and obtain the crude extract of the mycelia. We dissolved the crude extract completely with a suitable amount of methanol and filtered out the impurities. Methanol was then removed by a vacuum rotary evaporator to obtain the final extract. The content of emodin in the extracted sample was 1.16%, which was determined by HPLC. The sample solution used in the resin adsorption experiment was prepared by adding 40% aqueous ethanol to the extract.

### 4.3. Static Adsorption and Desorption Experiments

#### 4.3.1. Resin Screening

Different pretreated resins (each 1 g) were separately added to 250 mL flasks containing 50 mL of the sample solution (emodin concentration of 0.390 mg/mL). The flasks were shaken (120 rpm) in a constant temperature incubator for 12 h at a room temperature of 25 °C. Once the adsorption equilibrium was reached, the resins were collected by filtration and rinsed with deionized water to remove the residual sample solution. Then, for desorption, the resins were transferred to 50 mL of 95% (*v/v*) ethanol and shaken (120 rpm) for 12 h at 25 °C. The content of emodin in the solutions before and after desorption was analyzed by HPLC. The adsorption capacity ( $Q_e$ , Equation (1)), desorption capacity ( $Q_d$ , Equation (2)) and the desorption rate ( $D$ , Equation (3)) were calculated by the following equations:

$$Q_e = \frac{(C_0 - C_e)V_i}{W} \quad (1)$$

$$Q_d = \frac{C_d V_d}{W} \quad (2)$$

$$D = \frac{C_d V_d}{(C_0 - C_e)V_i} \times 100\% \quad (3)$$

where  $Q_e$  (mg/g) and  $Q_d$  (mg/g) are the equilibrium adsorption capacity and desorption capacity, respectively;  $C_0$  and  $C_e$  (mg/mL) are the initial concentration and equilibrium concentration of emodin in the solution, respectively;  $V_i$  and  $V_d$  (mL) represent the initial sample solution volume and desorption solution volume, respectively;  $W$  (g) is the dry weight of the resin;  $C_d$  represents the concentration of emodin in the desorption solution;  $D$  (%) is the desorption ratio.

#### 4.3.2. Effect of pH on Adsorption Capacity

Pretreated resins (each 1 g; wet weight) were added to 250 mL flasks containing 50 mL of the sample solution (emodin concentration 0.390 mg/mL), and the pH of the solution was adjusted with hydrochloric acid and sodium hydroxide (initial pH values were 2, 3, 4, 5, 6, 7, 8, 9, and 10, respectively). Then, the flasks were shaken (120 rpm) for 12 h at 25 °C, and the content of emodin in the solutions was analyzed by HPLC when the adsorption process reached equilibrium.

#### 4.3.3. Adsorption Kinetics Experiments

Pretreated resins (each 1 g; wet weight) were added to 250 mL flasks containing 50 mL of the sample solution (emodin concentration 0.390 mg/mL). Then, the flasks were shaken (120 rpm) for 12 h at 25 °C, and the content of emodin in the solutions during the adsorption process was analyzed by HPLC at regular intervals (30, 60, 90, 120, 150, 180, 210, and 240 min). The pseudo-first-order model (4) and pseudo-second-order model (5) were used to describe the adsorption process. The linear forms of them can be given as:

$$\log(Q_e - Q_t) = \log Q_e - \frac{k_1}{2.303}t, \quad (4)$$

$$\frac{t}{Q_t} = \frac{1}{k_2 Q_e^2} + \frac{t}{Q_e}, \quad (5)$$

where  $Q_e$  (mg/g) is the equilibrium adsorption capacity,  $Q_t$  (mg/g) is the adsorption capacity at different times;  $k_1$  ( $\text{min}^{-1}$ ) and  $k_2$  [ $\text{g}/(\text{mg}\cdot\text{min})$ ] are the adsorption rate constants of the two models, respectively.

The Weber Morris intra-particle diffusion model (6) was used to analyze the control steps in the adsorption process, which can be given as:

$$Q_t = k_t t^{1/2} + C, \quad (6)$$

where  $Q_t$  has the same meaning as above;  $k_t$  [ $\text{mg}/(\text{g}\cdot\text{min}^{1/2})$ ] is the diffusion rate constant;  $C$  (mg/g) is the constant related to the boundary layer and thickness; and  $t$  (min) represents the time.

#### 4.3.4. Adsorption Isotherms and Thermodynamics Experiments

One gram of pretreated resin (wet weight) was added to 250 mL flasks containing 50 mL of the sample solution (the  $C_0$  of emodin were 0.024, 0.048, 0.112, 0.195, 0.293, and 0.439 mg/mL, respectively). The flasks were shaken continuously (120 rpm) for 12 h at 298 K, 303 K, and 308 K, respectively. The emodin concentration in the solutions was analyzed by HPLC when the adsorption process reached equilibrium. The Langmuir model (7) and Freundlich model (8) were used to investigate the adsorption characteristics:

$$Q_e = \frac{Q_m K_L C_e}{1 - K_L C_e^{1/n}} \quad (7)$$

$$Q_e = K_F C_e^{1/n} \quad (8)$$

where  $Q_e$  (mg/g) and  $C_e$  (mg/mL) have the same meanings as above;  $Q_m$  (mg/g) is the maximum adsorption capacity;  $K_L$  (L/mg) represents the Langmuir constant;  $K_F$  ( $[(\text{mg/g}) (\text{L/mg})^{1/n}]$ ) represents the Freundlich constant, which will decrease with the increase of temperature; and  $1/n$  is an empirical constant related to the adsorption strength.

#### 4.4. Dynamic Adsorption and Desorption Experiments

These glass columns (1.5 cm × 30 cm) filled with 12 g of pretreated wet resin (1 BV = 20 mL) were utilized to perform dynamic adsorption and desorption experiments. The resin columns were washed with deionized water to remove the bubbles. The sample solution (emodin concentration 0.112 mg/mL) passed through the resin columns at different flow

rates (1.5, 2.0, and 2.5 BV/h). The concentration values of emodin in the desorption solutions were continuously recorded, and the optimal adsorption flow rate was selected based on the maximum adsorption capacity of emodin on the resin column. After adsorption reached equilibrium, the resin columns were rinsed with 6 BV deionized water followed by desorption with different concentrations of ethanol (40%, 50%, 60%, 70%, 80%, and 95%) at a flow rate of 2 BV/h. The eluents were collected and analyzed by HPLC to investigate the effect of ethanol concentration on the desorption process. To select the optimal elution flow rate, the resin columns were successively rinsed with 6 BV deionized water and 6 BV 50% ethanol after the adsorption reached equilibrium. Emodin was then eluted with 10 BV 80% ethanol at flow rates of 1.5, 2.0, 2.5, and 3.0 BV/h, and the desorption solutions were analyzed by HPLC.

#### 4.5. Demethylation of Questin

In order to obtain emodin with a higher content, questin in the desorption solution was demethylated and converted into emodin under acidic conditions [15]. The reaction was carried out as follows: 100 mg of the dried eluate was dissolved in 60 mL of glacial acetic acid, and 25 mL of HBr was added. The reaction was heated in a water bath at 85 °C. The concentrations of emodin during the reaction process were analyzed at regular intervals (1, 2, 3, 4, 5, and 6 h).

#### 4.6. HPLC Analysis of Emodin and Questin

The HPLC condition for emodin analysis was as follows: The stationary phase was Agilent ZORBAX Eclipse XDB-C18 column (4.6 × 250 mm, 5 µm); the detector was a DAD G1315B UV detector; the detection wavelength was 310 nm; the column temperature was 30 °C; the flow rate was 0.8 mL/min; the mobile phases were methanol with 0.1% formic acid (*v/v*); and the injection volume was 5 µL.

**Supplementary Materials:** The following supporting information can be downloaded at: <https://www.mdpi.com/article/10.3390/md20040231/s1>, Figures S1 and S2: <sup>1</sup>H NMR and HRESIMS spectra of the purified emodin.

**Author Contributions:** Conceptualization, L.G. and X.Q.; methodology, L.G. and Y.W.; formal analysis and data curation, L.G.; writing—original draft preparation, L.G.; writing—review and editing, X.X., F.A. and M.G.; funding acquisition, M.G. and F.A. All authors have read and agreed to the published version of the manuscript.

**Funding:** This work was funded by the National Key R&D Program of China (2018YFC1706206), the National Natural Science Foundation of China (41876189), and the Open Research Fund Program of Key Laboratory of Cosmetic (Beijing Technology and Business University), China National Light Industry (KLC-2019-ZD2).

**Institutional Review Board Statement:** Not applicable.

**Informed Consent Statement:** Not applicable.

**Data Availability Statement:** Not applicable.

**Acknowledgments:** This work was also supported by State Key Laboratory of Bioreactor Engineering and the Open Research Fund Program of Institute of regulatory science.

**Conflicts of Interest:** The authors declare no conflict of interest.

## References

1. Fang, L.; Zhao, F.; Iwanowycz, S.; Wang, J.F.; Yin, S.; Wang, Y.Z.; Fan, D.P. Anticancer activity of emodin is associated with downregulation of CD155. *Int. Immunopharmacol.* **2019**, *75*, 105763. [[CrossRef](#)] [[PubMed](#)]
2. Xia, S.; Ni, Y.; Zhou, Q.; Liu, H.; Xiang, H.; Sui, H.; Shang, D. Emodin Attenuates Severe Acute Pancreatitis via Antioxidant and Anti-inflammatory Activity. *Inflammation* **2019**, *42*, 2129–2138. [[CrossRef](#)]
3. Zhang, H.M.; Ge, X.P.; Liu, B.; Teng, T.; Zhou, Q.L.; Sun, C.X.; Song, C.Y. Comparative transcriptomic and proteomic analysis of the antibacterial activity of emodin on *Aeromonas hydrophila*. *Aquaculture* **2020**, *529*, 735589. [[CrossRef](#)]

4. Xue, J.F.; Ding, W.J.; Liu, Y. Anti-diabetic effects of emodin involved in the activation of PPARgamma on high-fat diet-fed and low dose of streptozotocin-induced diabetic mice. *Fitoroterapia* **2010**, *81*, 173–177. [[CrossRef](#)]
5. Song, Y.D.; Li, X.Z.; Wu, Y.X.; Shen, Y.; Liu, F.F.; Gao, P.P.; Sun, L.; Qian, F. Emodin alleviates alternatively activated macrophage and asthmatic airway inflammation in a murine asthma model. *Acta Pharmacol. Sin.* **2018**, *39*, 1317–1325. [[CrossRef](#)] [[PubMed](#)]
6. Ding, Q.H.; Ye, C.Y.; Chen, E.M.; Zhang, W.; Wang, X.H. Emodin ameliorates cartilage degradation in osteoarthritis by inhibiting NF-kappaB and Wnt/beta-catenin signaling in-vitro and in-vivo. *Int. Immunopharmacol.* **2018**, *61*, 222–230. [[CrossRef](#)] [[PubMed](#)]
7. Wang, L.; Liu, S.T.; Xu, J.Q.; Watanabe, N.; Mayo, K.H.; Li, J.; Li, X.M. Emodin inhibits aggregation of amyloid-beta peptide 1-42 and improves cognitive deficits in Alzheimer's disease transgenic mice. *J. Neurochem.* **2020**, *157*, 1992–2007. [[CrossRef](#)] [[PubMed](#)]
8. Hu, N.H.; Liu, J.; Xue, X.Y.; Li, Y.X. The effect of emodin on liver disease—Comprehensive advances in molecular mechanisms. *Eur. J. Pharmacol.* **2020**, *882*, 173269. [[CrossRef](#)] [[PubMed](#)]
9. Zhang, N.; Wang, J.W.; Sheng, A.M.; Huang, S.; Tang, Y.Y.; Ma, S.T.; Hong, G. Emodin Inhibits the Proliferation of MCF-7 Human Breast Cancer Cells Through Activation of Aryl Hydrocarbon Receptor (AhR). *Front. Pharmacol.* **2020**, *11*, 622046. [[CrossRef](#)]
10. Liu, Q.; Hodge, J.; Wang, J.F.; Wang, Y.Z.; Wang, L.M.; Singh, U.P.; Li, Y.; Yao, Y.Z.; Wang, D.W.; Ai, W.; et al. Emodin reduces Breast Cancer Lung Metastasis by suppressing Macrophage-induced Breast Cancer Cell Epithelial-mesenchymal transition and Cancer Stem Cell formation. *Theranostics* **2020**, *10*, 8365–8381. [[CrossRef](#)]
11. Dai, G.L.; Ding, K.; Cao, Q.Y.; Xu, T.; He, F.; Liu, S.J.; Ju, W.Z. Emodin suppresses growth and invasion of colorectal cancer cells by inhibiting VEGFR2. *Eur. J. Pharmacol.* **2019**, *859*, 172525. [[CrossRef](#)] [[PubMed](#)]
12. Tong, S.; Yan, J. Large-scale separation of hydroxyanthraquinones from *Rheum palmatum* L. by pH-zone-refining counter-current chromatography. *J. Chromatogr. A* **2007**, *1176*, 163–168. [[CrossRef](#)]
13. Guo, L.; Wang, C. Optimized production and isolation of antibacterial agent from marine *Aspergillus flavipes* against *Vibrio harveyi*. *3 Biotech* **2017**, *7*, 383. [[CrossRef](#)] [[PubMed](#)]
14. Dong, X.X.; Fu, J.; Yin, X.B.; Cao, S.L.; Li, X.C.; Lin, L.F.; Huyiligeqi; Ni, J. Emodin: A review of its pharmacology, toxicity and pharmacokinetics. *Phytother. Res.* **2016**, *30*, 1207–1218. [[CrossRef](#)] [[PubMed](#)]
15. Chalothorn, T.; Rukachaisirikul, V.; Phongpaichit, S.; Pannara, S.; Tansakul, C. Synthesis and antibacterial activity of emodin and its derivatives against methicillin-resistant *Staphylococcus aureus*. *Tetrahedron Lett.* **2019**, *60*, 151004. [[CrossRef](#)]
16. Wang, P.L.; Li, D.-Y.; Xie, L.-R.; Wu, X.; Hua, H.-M.; Li, Z.-L. Two new compounds from a marine-derived fungus *Penicillium oxalicum*. *Nat. Prod. Res.* **2014**, *28*, 290–293. [[CrossRef](#)]
17. Qiu, X.H.; Gong, L.Z.; Xin, X.J.; An, F.L. Enhancement of Emodin Production by Medium Optimization and KH<sub>2</sub>PO<sub>4</sub> Supplementation in Submerged Fermentation of Marine-Derived *Aspergillus flavipes* HN4-13. *Mar. Drugs* **2021**, *19*, 421. [[CrossRef](#)] [[PubMed](#)]
18. Jiang, H.; Li, J.; Chen, L.; Wang, Z. Adsorption and desorption of chlorogenic acid by macroporous adsorbent resins during extraction of *Eucommia ulmoides* leaves. *Ind. Crops Prod.* **2020**, *149*, 112336. [[CrossRef](#)]
19. Wu, X.Y.; Tang, Y.; Sun, Y.X.; Xiang, D.B.; Wan, Y.; Wu, Q.; Zhao, G. Extraction of flavonoids and kinetics of purification by macroporous resins from quinoa. *J. Nanopart. Res.* **2020**, *22*, 181.
20. Zhuang, M.Y.; Zhao, M.M.; Lin, L.Z.; Dong, Y.; Chen, H.P.; Feng, M.Y.; Sun-Waterhouse, D.X.; Su, G.W. Macroporous resin purification of peptides with umami taste from soy sauce. *Food Chem.* **2016**, *190*, 338–344. [[CrossRef](#)]
21. Daignault, S.A.; Noot, D.K.; Williams, D.T.; Huck, P.M. A review of the use of XAD resins to concentrate organic compounds in water. *Water Res.* **1988**, *22*, 803–813. [[CrossRef](#)]
22. Lepane, V. Comparison of XAD resins for the isolation of humic substances from seawater. *J. Chromatogr.* **1999**, *845*, 329–335. [[CrossRef](#)]
23. Kiwaan, H.A.; Atwee, T.M.; Azab, E.A.; El-Bindary, A.A. Efficient photocatalytic degradation of Acid Red 57 using synthesized ZnO nanowires. *J. Chin. Chem. Soc.* **2019**, *66*, 89–98. [[CrossRef](#)]
24. Elwakeel, K.Z.; El-Bindary, A.A.; Kouta, E.Y. Retention of copper, cadmium and lead from water by Na-Y-Zeolite confined in methyl methacrylate shell. *J. Environ. Chem. Eng.* **2017**, *5*, 3698–3710. [[CrossRef](#)]
25. Buran, T.J.; Sandhu, A.K.; Li, Z.; Rock, C.R.; Yang, W.W.; Gu, L.W. Adsorption/desorption characteristics and separation of anthocyanins and polyphenols from blueberries using macroporous adsorbent resins. *J. Food Eng.* **2014**, *128*, 167–173. [[CrossRef](#)]
26. Hou, M.Y.; Hu, W.Z.; Xiu, Z.L.; Shi, Y.S.; Hao, K.X.; Cao, D.; Guan, Y.G.; Yin, H.L. Efficient enrichment of total flavonoids from *Pteris ensiformis* Burm. extracts by macroporous adsorption resins and *in vitro* evaluation of antioxidant and antiproliferative activities. *J. Chromatogr. B* **2020**, *1138*, 121960. [[CrossRef](#)]
27. Liu, C.Q.; Jiao, R.H.; Yao, L.Y.; Zhang, Y.P.; Lu, Y.H.; Tan, R.X. Adsorption characteristics and preparative separation of chaetominine from *Aspergillus fumigatus* mycelia by macroporous resin. *J. Chromatogr. B* **2016**, *1015*, 135–141. [[CrossRef](#)]
28. Tang, L.; Wei, X.C.; An, F.L.; Lu, Y.H. Preparative separation of TL1-1 from *Daldinia eschscholzii* extract by macroporous resin and evaluation of its antimicrobial activities. *J. Chromatogr. B* **2017**, *1060*, 22–29. [[CrossRef](#)] [[PubMed](#)]
29. Zhu, L.L.; Deng, Y.F.; Zhang, J.P.; Chen, J. Adsorption of phenol from water by *N*-butylimidazolium functionalized strongly basic anion exchange resin. *J. Colloid Interface Sci.* **2011**, *364*, 462–468. [[CrossRef](#)]
30. Wang, T.; Lu, S.M.; Xia, Q.L.; Fang, Z.X.; Johnson, S. Separation and purification of amygdalin from thinned bayberry kernels by macroporous adsorption resins. *J. Chromatogr. B* **2015**, *975*, 52–58. [[CrossRef](#)] [[PubMed](#)]
31. Pan, J.L.; Yang, Y.; Zhang, R.; Yao, H.W.; Ge, K.K.; Zhang, M.Y.; Ma, L. Enrichment of chelidonine from *Chelidonium majus* L. using macroporous resin and its antifungal activity. *J. Chromatogr. B* **2017**, *1070*, 7–14. [[CrossRef](#)]

32. Rajabi, M.; Barfi, B.; Asghari, A.; Najafi, F.; Aran, R. Hybrid Amine-Functionalized Titania/Silica Nanoparticles for Solid-Phase Extraction of Lead, Copper, and Zinc from Food and Water Samples: Kinetics and Equilibrium Studies. *Food Anal. Methods* **2014**, *8*, 815–824. [[CrossRef](#)]
33. Wu, Y.F.; Zhang, L.; JianWei, M.; ShiWang, L.; Jun, H.; Ru, Y.Y.; He, M.L. Kinetic and thermodynamic studies of sulforaphane adsorption on macroporous resin. *J. Chromatogr. B* **2016**, *1028*, 231–236.
34. Gao, Z.P.; Yu, Z.F.; Yue, T.L.; Quek, S.Y. Adsorption isotherm, thermodynamics and kinetics studies of polyphenols separation from kiwifruit juice using adsorbent resin. *J. Food Eng.* **2013**, *116*, 195–201. [[CrossRef](#)]
35. Ding, L.; Deng, H.P.; Wu, C.; Han, X. Affecting factors, equilibrium, kinetics and thermodynamics of bromide removal from aqueous solutions by MIEX resin. *Chem. Eng. J.* **2012**, *181–182*, 360–370. [[CrossRef](#)]
36. Lin, L.Z.; Zhao, H.F.; Dong, Y.; Yang, B.; Zhao, M.M. Macroporous resin purification behavior of phenolics and rosmarinic acid from *Rabdosia serra* (MAXIM.) HARA leaf. *Food Chem.* **2012**, *130*, 417–424. [[CrossRef](#)]
37. Gökmen, V.; Serpen, A. Equilibrium and kinetic studies on the adsorption of dark colored compounds from apple juice using adsorbent resin. *J. Food Eng.* **2002**, *53*, 221–227. [[CrossRef](#)]
38. Kiwaan, H.A.; El-Mowafy, A.S.; El-Bindary, A.A. Synthesis, spectral characterization, DNA binding, catalytic and in vitro cytotoxicity of some metal complexes. *J. Mol. Liq.* **2021**, *326*. [[CrossRef](#)]





## Article

# New 3-Acyl Tetramic Acid Derivatives from the Deep-Sea-Derived Fungus *Lecanicillium fuisporum*

Xinya Xu <sup>1,†</sup>, Yanhui Tan <sup>2,†</sup>, Chenghai Gao <sup>1</sup>, Kai Liu <sup>1</sup>, Zhenzhou Tang <sup>1</sup>, Chunju Lu <sup>1</sup>, Haiyan Li <sup>1</sup>, Xiaoyong Zhang <sup>3,\*</sup> and Yonghong Liu <sup>1,\*</sup>

<sup>1</sup> Institute of Marine Drugs, Guangxi University of Chinese Medicine, Nanning 530200, China; xyxu@gxctmu.edu.cn (X.X.); gaoch@gxctmu.edu.cn (C.G.); liuk@gxctmu.edu.cn (K.L.); tangzz@gxctmu.edu.cn (Z.T.); luchunjv@stu.gxctmu.edu.cn (C.L.); lihaiyan12368@163.com (H.L.)

<sup>2</sup> State Key Laboratory for the Chemistry and Molecular Engineering of Medicinal Resources, School of Chemistry and Pharmaceutical Science, Guangxi Normal University, Guilin 541004, China; tyh533@smu.edu.cn

<sup>3</sup> College of Marine Sciences, South China Agricultural University, Guangzhou 510642, China

\* Correspondence: zhangxiaoyong@scau.edu.cn (X.Z.); yonghongliu@scsio.ac.cn (Y.L.)

† These authors contributed equally to this work.

**Abstract:** Seven rare C3-C6 reduced 3-acyl tetramic acid derivatives, lecanicilliumins A–G (1–7), along with the known analogue cladosporiumin D (8), were obtained from the extract of the deep-sea-derived fungus *Lecanicillium fuisporum* GXIMD00542 within the family Clavicipitaceae. Their structures were elucidated by extensive spectroscopic data analysis, quantum chemistry calculations and chemical reaction. Compounds 1, 2, 5–7 exhibited moderate anti-inflammatory activity against NF- $\kappa$ B production using lipopolysaccharide (LPS) induced RAW264.7 cells with EC<sub>50</sub> values range of 18.49–30.19  $\mu$ M.

**Keywords:** tetramic acid derivatives; deep-sea fungus; clavicipitaceae; *Lecanicillium fuisporum*; anti-inflammatory activity

**Citation:** Xu, X.; Tan, Y.; Gao, C.; Liu, K.; Tang, Z.; Lu, C.; Li, H.; Zhang, X.; Liu, Y. New 3-Acyl Tetramic Acid Derivatives from the Deep-Sea-Derived Fungus *Lecanicillium fuisporum*. *Mar. Drugs* **2022**, *20*, 255. <https://doi.org/10.3390/md20040255>

Academic Editor: Ipek Kurtboke

Received: 11 March 2022

Accepted: 4 April 2022

Published: 6 April 2022

**Publisher's Note:** MDPI stays neutral with regard to jurisdictional claims in published maps and institutional affiliations.



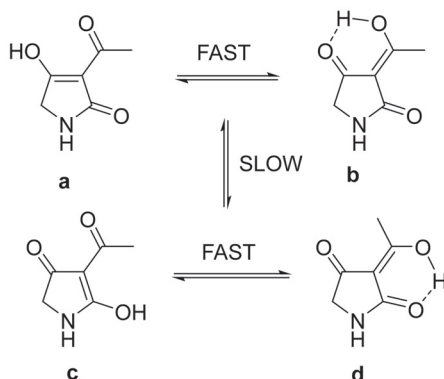
**Copyright:** © 2022 by the authors. Licensee MDPI, Basel, Switzerland. This article is an open access article distributed under the terms and conditions of the Creative Commons Attribution (CC BY) license (<https://creativecommons.org/licenses/by/4.0/>).

## 1. Introduction

Tetramic acid (2,4-pyrrolidinedione) derivatives have been isolated from many terrestrial and marine organisms, including bacteria, fungi and sponges [1]. They have attracted considerable attention from chemists, biologists and physicians for their diverse chemical structures and broad range of potent biological activities such as antimicrobial, antitumoral, antiprotozoal, protease-inhibitory and anti-inflammatory effects [2–4]. Among these tetramate derivatives, the 3-acyl tetramic acids, which contain an acyl substituent at C-3, are the most common ones found in nature [4]. The 3-acyl tetramic acids have two sets of rapidly interconverting internal tautomers **a/b** and **c/d** in solution (Figure 1). Distribution calculation of these four tautomers indicated the *exo*-enol **d** with C3-C6 olefinic bond, is the main tautomeric form and commonly reported [5–7]. The C3-C6 reduced 3-acyl tetramic acid derivatives are rarely found [8].

The fungal genus *Lecanicillium*, which once was placed in the genus *Verticillium* [9], belongs to the family Clavicipitaceae. *Lecanicillium* spp. such as *L. fuisporum*, *L. psalliotae* and *L. lecanii* are well known as entomopathogenic species and used for biological control of insect pests [10–12]. However, the secondary metabolisms of these fungi are rarely reported. Ishidoh et al. has isolated two new cyclic lipodepsipeptides verlamelins A and B from *Lecanicillium* sp. HF627 [13]. Huang et al. reported one new alkaloid lecasporinoid from marine fungal strain *L. fuisporum* [14]. Unfortunately, these compounds did not show identified biological activities. During our continuing search on bioactive compounds from marine fungi, the deep-sea-derived fungal strain GXIMD00542 has been isolated from Mariana Trench sediment (141°57' E, 10°51' N, 5467 m depth) and identified as

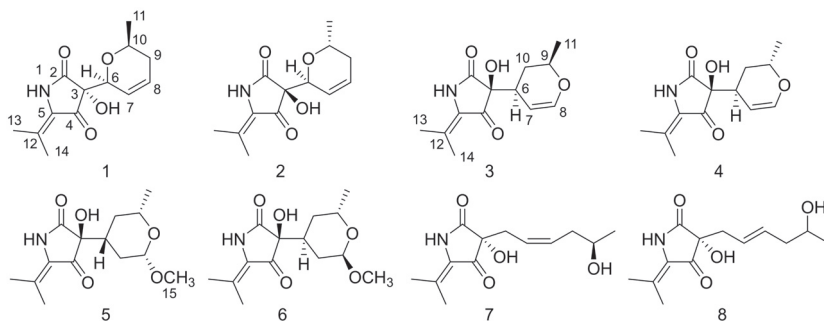
*L. fusisporum* by ITS rDNA sequence homology. Further chemical study led to the isolation of eight 3-acyl tetramic acid derivatives including seven new compounds and one known analogue cladosporiumin D (8) [8]. This is the first report of tetramic acid derivatives obtained from the genus *Lecanicillium*. Some of them exhibited moderate anti-inflammatory activity against NF- $\kappa$ B production using LPS-induced RAW264.7 cells. Herein, we report the isolation, structural elucidation and the biological determination of these compounds.



**Figure 1.** The interconverting internal tautomers of 3-acyl tetramic acid [5].

## 2. Results and Discussion

The deep-sea-derived fungal strain GXIMD00542 was inoculated and fermented using liquid medium in standing situation for 30 days at 25 °C. The HPLC-UV guided isolation of the extract led to compounds 1–8 (Figure 2).



**Figure 2.** The chemical structures of compounds 1–8.

Compound 1 was obtained as light brown orthorhombic crystal. The molecular formula of  $C_{13}H_{17}NO_4$  was established by HRTOFESIMS quasi-molecular ion at  $m/z$  274.1063  $[M + Na]^+$  (calcd. 274.1055) (Figure S8), which had six degrees of unsaturation. The 1D NMR and HSQC spectral signals revealed the presence of three methyl groups, one methylene, four methines including two oxygenated methines and one double bond, and four quaternary carbons including one amide carbonyl and one  $\alpha$ ,  $\beta$ -unsaturated ketone moiety (Tables 1 and 2). The HMBC correlations from NH-1 to C-2, C-3, C-4, C-12, and from  $CH_3$ -13/ $CH_3$ -14 to C-5, C-12 indicated the existence of the 5-isobutenyl-2,4-pyrrolidinedione moiety, which is structural core of tetramic acid derivative (Figure 3) [8].  $^1H$ - $^1H$  COSY correlations of H-6/H-7/H-8/H-9/H-10/ $CH_3$ -11, and HMBC correlations from H-6 to C-7, C-8, from H-9 to C-7, C-8, C-10, from  $CH_3$ -11 to C-9, C-10, and an extra degree of unsaturation indicated the presence of a 2-methyl-3,6-dihydro-2H-pyran moiety. HMBC correlations from H-6 to C-3 and C-4, from OH-3 to C-6 declared the 2-methyl-3,6-dihydro-2H-pyran moiety attached to the C-3 of the 5-isobutenyl-2,4-pyrrolidinedione

moiety. The NOESY correlations between H-6 and H-9 $\alpha$ , between H-9 $\alpha$  and H-10 indicated H-6 and H-10 on the same side of the 2-methyl-3,6-dihydro-2H-pyran moiety. The absolute configuration of **1** was further determined as (3R,6S,10S) by Cu K $\alpha$  radiation X-ray crystal analysis, which was obtained as orthorhombic crystal in methanol (crystal size:  $0.16 \times 0.08 \times 0.08$  mm<sup>3</sup>, Flack parameter: 0.03) (Figure 4).

**Table 1.** <sup>1</sup>H NMR data (600 MHz) for compounds **1**, **2** and **7** in DMSO-*d*<sub>6</sub> ( $\delta$  in ppm, *J* in Hz).

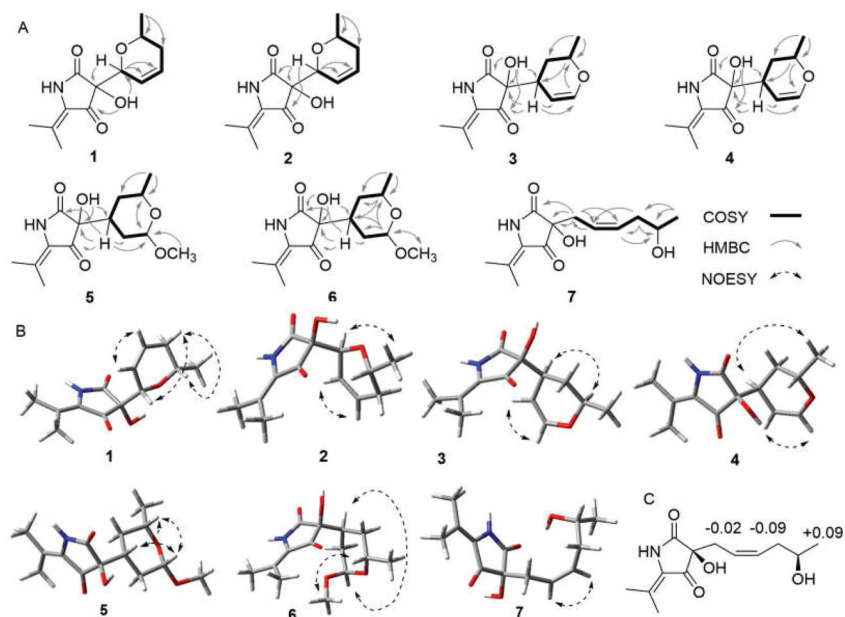
| No.   | 1   | 2                                   | 7                     |
|-------|---|-------------------------------------|-----------------------|
| 6     | 4.30, br s                                    | 4.23, m                             | 2.41, dd, (14.1, 7.5) |
| 7     | 5.97, d, (10.4)                               | 5.95, m                             | 5.17, dt, (10.9, 7.3) |
| 8     | 5.82, dtd, (10.2, 2.1, 5.7)                   | 5.79, dtd, (9.9, 4.3, 1.9)          | 5.49, dt, (10.9, 7.3) |
| 9     | 1.90, m, H-9 $\alpha$<br>1.65, m, H-9 $\beta$ | 1.93, m,<br>1.74, ovp. <sup>a</sup> | 1.94–2.04, ovp.       |
| 10    | 3.52, ddd, (15.6, 6.1, 4.6)                   | 3.52, dtd, (12.3, 6.1, 3.5)         | 3.52, m               |
| 11    | 0.99, d, (6.1)                                | 0.99, d, (6.1)                      | 0.98, d, (6.2)        |
| 13    | 1.77, s                                       | 1.77, s                             | 1.78, s               |
| 14    | 2.02, s                                       | 2.07, s                             | 2.06, s               |
| NH-1  | 10.33, br s                                   | 10.19, br s                         | 10.34, br s           |
| OH-3  | 6.32, br s                                    | 6.35, br s                          | 6.14, br s            |
| OH-13 | -   | -                                   | 4.44, d, (4.5)        |

<sup>a</sup> overlapped.

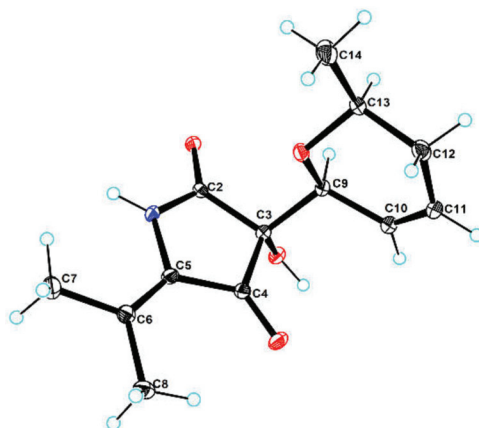
**Table 2.** <sup>13</sup>C NMR data (150 MHz) for compounds **1–7** in DMSO-*d*<sub>6</sub> ( $\delta$  in ppm).

| No. | 1                      | 2                      | 3                      | 4                      | 5                      | 6                      | 7                      |
|-----|------------------------|------------------------|------------------------|------------------------|------------------------|------------------------|------------------------|
| 2   | 171.45, C              | 169.7, C               | 171.35, C              | 171.89, C              | 171.51, C              | 171.53, C              | 171.91, C              |
| 3   | 74.31, C               | 74.22, C               | 75.14, C               | 75.85, C               | 75.29, C               | 75.55, C               | 73.96, C               |
| 4   | 197.12, C              | 199.36, C              | 199.04, C              | 199.64, C              | 199.59, C              | 199.65, C              | 199.38, C              |
| 5   | 120.24, C              | 120.52, C              | 122.3, C               | 122.07, C              | 122.44, C              | 122.28, C              | 122.47, C              |
| 6   | 76.97, CH              | 77.68, CH              | 37.73, CH              | 34.26, CH              | 39.6, CH               | 35.23, CH              | 33.46, CH <sub>2</sub> |
| 7   | 125.37, CH             | 125.44, CH             | 97.81, CH              | 96.65, CH              | 30.31, CH <sub>2</sub> | 28.86, CH <sub>2</sub> | 121.66, CH             |
| 8   | 124.85, CH             | 124.85, CH             | 145.33, CH             | 145.25, CH             | 101.66, CH             | 97.05, CH              | 130.96, CH             |
| 9   | 32.02, CH <sub>2</sub> | 32.02, CH <sub>2</sub> | 71.2, CH               | 68.28, CH              | 69.93, CH              | 63.82, CH              | 36.74, CH <sub>2</sub> |
| 10  | 69.62, CH              | 69.73, CH              | 29.7, CH <sub>2</sub>  | 27.95, CH <sub>2</sub> | 31.72, CH <sub>2</sub> | 31.85, CH <sub>2</sub> | 65.81, CH              |
| 11  | 21.4, CH <sub>3</sub>  | 21.35, CH <sub>3</sub> | 21.17, CH <sub>3</sub> | 20.63, CH <sub>3</sub> | 21.45, CH <sub>3</sub> | 21.6, CH <sub>3</sub>  | 23.11, CH <sub>3</sub> |
| 12  | 128.96, C              | 129.13, C              | 128.57, C              | 128.6, C               | 128.5, C               | 128.44, C              | 128.41, C              |
| 13  | 20.57, CH <sub>3</sub> | 20.57, CH <sub>3</sub> | 20.71, CH <sub>3</sub> | 19.91, CH <sub>3</sub> | 20.69, CH <sub>3</sub> | 20.66, CH <sub>3</sub> | 20.69, CH <sub>3</sub> |
| 14  | 18.39, CH <sub>3</sub> | 18.39, CH <sub>3</sub> | 18.49, CH <sub>3</sub> | 18.44, CH <sub>3</sub> | 18.46, CH <sub>3</sub> | 18.43, CH <sub>3</sub> | 18.46, CH <sub>3</sub> |
| 15  | -                      | -                      | -                      | -                      | 55.32, CH <sub>3</sub> | 53.67, CH <sub>3</sub> | -                      |

Compound **2** was yielded as light brown powder, with the molecular formula C<sub>13</sub>H<sub>17</sub>NO<sub>4</sub>, based on the HRTOFESIMS spectrum (*m/z* 274.1059 [M + Na]<sup>+</sup>) (Figure S15). The same molecular formula and detailed analysis of the NMR data disclosed that **2** had same plane structure with **1**. The relative configurations of 2-methyl-3,6-dihydro-2H-pyran moiety of **2** were elucidated by the NOESY correlations between H-6 and CH<sub>3</sub>-10. Based on the comparison of ECD cotton effects with **1** and similar known compound **8** [8], the absolute configuration of C-3 was assigned as 3S, in which (3S)-5-isobutenyl-2,4-pyrrolidinedione showed negative cotton effects around 210 nm and positive cotton effects around 230 nm, whereas (3R)-5-isobutenyl-2,4-pyrrolidinedione exhibited opposite cotton effects at the same wavelength. The further ECD calculation of the optimized conformations of (3S,6S,10R)-**2a** and (3S,6R,10S)-**2b** were conducted at the M062X/defTZVP level. Accordingly, the absolute configurations of **2** were assigned as (3S,6S,10R)-**2** by the comparison of calculated ECD curves with experimental ECD spectrum (Figure 5).



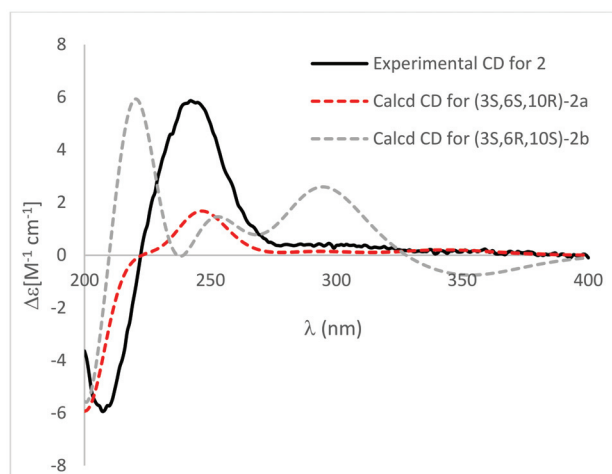
**Figure 3.** (A) Key  $^1\text{H}$ - $^1\text{H}$  COSY and HMBC correlations for compounds 1–7. (B) Key NOESY correlations for compounds 1–7. (C) The  $\Delta\delta$  ( $\delta_S - \delta_R$ ) values for MTPA esters of 7.



**Figure 4.** X-ray ORTEP drawing of compound 1. The crystal structure was deposited at the Cambridge Crystallographic Data Centre with number of CCDC 2092073.

Compound 3 was white amorphous powder with the same molecular formula as 1 and 2 by the HRTOFESIMS spectrum ( $m/z$  252.1241 [ $M + H$ ] $^+$ ) (Figure S22). The  $^1\text{H}$  NMR and  $^{13}\text{C}$  NMR data revealed 3 had high structural similarities to 1 and 2 (Tables 2 and 3) except for the chemical shift of the dihydro-2*H*-pyran moiety. The  $^1\text{H}$ - $^1\text{H}$  COSY correlations H-8/H-7/H-6/H-10/H-9/ $\text{CH}_3$ -11 and HMBC correlations from H-6 to C-7, C-8, C-10, from H-8 to C-6, C-7, C-9 and from H-9 to C-6, C-10, C-11 deduced the presence of 2-methyl-3,4-dihydro-2*H*-pyran moiety. The HMBC correlations from H-6 to C-2, C-3, and C-4 indicated that the 5-isobutenyl-2,4-pyrrolidinedione moiety was attached to  $\gamma$ -position of the 2-methyl-3,4-dihydro-2*H*-pyran moiety. The NOESY correlations between H-6 and H-9 indicated they were on the same plane of the pyran moiety. The absolute configuration of

C-3 was assigned as 3*S* on the basis of the same ECD cotton effects around 210 nm and 230 nm as compound **2**. The two candidate isomers (3*S*,6*S*,9*R*)-**3a** and (3*S*,6*R*,9*S*)-**3b** were further calculated by the quantum chemical calculations of the NMR data (qccNMR) at the B97-2/pcSseg-1 level. DP4+ analysis identified (3*S*,6*S*,9*R*)-**3** as the most probable structure with 89.66% DP4+ probability [15,16].



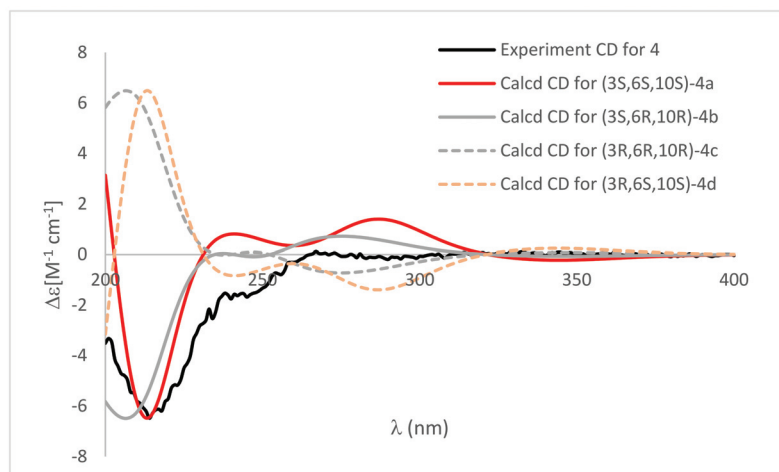
**Figure 5.** Comparison of calculated ECD spectra of (3*S*,6*S*,10*R*)-**2a** (red), (3*S*,6*R*,10*S*)-**2b** (gray) in MeOH and experimental CD (black).  $\sigma = 0.3$  eV, UV shift = 7 nm.

**Table 3.**  $^1\text{H}$  NMR data (600 MHz) for compounds **3–6** in DMSO- $d_6$  ( $\delta$  in ppm,  $J$  in Hz).

| No.  | 3                           | 4                           | 5                           | 6                           |
|------|-----------------------------|-----------------------------|-----------------------------|-----------------------------|
| 6    | 2.64, ddt, (11.4, 5.8, 2.0) | 2.45, ddd, (10.5, 4.7, 2.4) | 1.98, tt, (12.5, 3.7)       | 2.17, tt, (12.8, 3.5)       |
| 7    | 4.51, d, (6.4)              | 4.44, dd, (6.4, 3.4)        | 1.59, dt, (12.5, 2.1)       | 1.56, ovp.                  |
| 8    | 6.35, dd, (6.4, 2.3)        | 6.38, dd, (6.4, 2.2)        | 1.05, td, (12.5, 9.5)       | 1.05, ovp.                  |
| 9    | 3.85, dqd, (12.6, 6.3, 1.7) | 3.91, ddd, (11.5, 6.3, 3.2) | 4.23, dd, (9.5, 2.1)        | 4.66, d, 2.6                |
| 10   | 1.78, ovp. <sup>a</sup>     | 2.12, ddd, 1(4.2, 7.0, 3.5) | 3.41, dqd, (12.3, 6.1, 1.9) | 3.63, dqd, (12.2, 6.3, 2.1) |
|      | 1.53, dt, (13.2, 11.4)      | 1.45, ddd, (14.2, 7.0, 3.5) | 1.52, m                     | 1.56, ovp.                  |
| 11   | 1.18, d, (6.3)              | 1.13, d, (6.3)              | 0.97, td, (12.7, 11.0)      | 1.05, ovp.                  |
| 13   | 1.81, s                     | 1.78, s                     | 1.11, d, (6.1)              | 1.05, d, (6.3)              |
| 14   | 2.09, s                     | 1.78, s                     | 1.80 s                      | 1.79, s                     |
| 15   | -                           | 2.05, s                     | 2.08, s                     | 2.07, s                     |
| NH-1 | 10.37, br s                 | -                           | 3.30, s                     | 3.19, s                     |
| OH-3 | 6.09, br s                  | 10.41, br s                 | 6.04, br s                  | 10.37, br s                 |
|      |                             | 6.07, br s                  |                             | 5.97, br s                  |

<sup>a</sup> overlapped.

Compound **4** shared the same plane structure as **3** on the basis of HRTOFESIMS data ( $m/z$  252.1235  $[\text{M} + \text{H}]^+$ ) and 1D NMR data (Tables 2 and 3). The NOESY correlation between H-6 and  $\text{CH}_3$ -11 disclosed they were on the same plane of the 5-isobutenyl-2,4-pyrrolidinedione moiety. The absolute configuration of C-3 was assigned as 3*S* based on the negative cotton effect around 210 nm and the ECD calculation of (3*S*,6*S*,9*S*)-**4a**, (3*S*,6*R*,9*R*)-**4b**, (3*R*,6*R*,9*R*)-**4c** and (3*R*,6*S*,9*S*)-**4d** at the M062X/def2TZVP level (Figure 6). Further, the qccNMR calculation and the DP4+ analysis of (3*S*,6*S*,9*S*)-**4a** and (3*S*,6*R*,9*R*)-**4b** at the B97-2/pcSseg-1 level identified (3*S*,6*S*,9*S*)-**4** as the most probable structure with 91.53% DP4+ probability [15,16].



**Figure 6.** Comparison of calculated ECD spectra of (3S,6S,9S)-**4a** (red), (3S,6R,9R)-**4b** (gray), (3R,6R,9R)-**4c** (dashed gray) and (3R,6S,9S)-**4d** (dashed orange) and experimental CD (black).  $\sigma = 0.3$  eV; UV shift = 7 nm.

The molecular formula  $C_{14}H_{21}NO_5$  of **5** was deduced from the HRTOFESIMS data ( $m/z$  306.1319  $[M + Na]^+$ ). The 1D NMR data showed that **5** had 5-isobutenyl-2,4-pyrrolidinedione moiety (Tables 2 and 3). The  $^1H$ - $^1H$  COSY correlations of H-8/H-7/H-6/H-10/H-9/ $CH_3$ -11, and HMBC correlations from H-8 to C-6, C-7, C-9, C-15, from H-9 to C-8 and from  $OCH_3$ -15 to C-8 disclosed the presence of 2-methoxy-6-methyltetrahydro-2H-pyran moiety. HMBC correlations from H-6 to C-2, C-3, C-4 and from OH-3 to C-6 indicated the 5-isobutenyl-2,4-pyrrolidinedione moiety was linked to the 2-methoxy-6-methyltetrahydro-2H-pyran moiety at C-6. The relative configurations of **5** was elucidated by the NOESY spectra and 1D selective NOESY spectra. NOESY correlations between H-6 and H-9, and 1D selective NOESY correlations between H-6 and H-8, H-9, between H-8 and H-6, H-9 exhibited that H-6, H-8 and H-9 were at the same plane of the 2-methoxy-6-methyltetrahydro-2H-pyran moiety. The absolute configuration of C-3 was assigned as *S* according to the similar cotton effects tendency as compounds 2–4. The qccNMR calculation and the DP4+ analysis of (3S,6R,8S,9S)-**5a** and (3S,6S,8R,9R)-**5b** at the B97-2/pcSseg-1 level showed (3S,6R,8S,9S)-**5** as the most probable structure with 86.42% DP4+ probability [15,16].

Compound **6** had the same plane structure as **5** according to the identical HRTOFESIMS data ( $m/z$  306.1319  $[M + Na]^+$ ) and similar 1D NMR data. The observed NMR chemical shift difference between **6** and **5** of H-6, H-8, and C-6, C-8 and C-9 indicated they were diastereoisomers. NOESY correlations between H-6 and H-8, between H-9 and  $OCH_3$ -15 disclosed H-6, H-8, and  $CH_3$ -11 were on the same plane of the 2-methoxy-6-methyltetrahydro-2H-pyran moiety, while H-9 and  $OCH_3$ -15 were on the other side. The absolute configuration of C-3 was also assigned as *S* because of the similar cotton effects tendency as compounds 2–5. The qccNMR calculation and the DP4+ analysis of (3S,6S,8R,9S)-**6a** and (3S,6R,8S,9R)-**6b** at the B97-2/pcSseg-1 level showed (3S,6S,8R,9S)-**6** as the most probable structure with 86.61% DP4+ probability [15,16].

Compound **7** was obtained as light-yellow powder. The HRTOFESIMS ion signal at  $m/z$  276.1203  $[M + Na]^+$  disclosed the molecular formula  $C_{13}H_{19}NO_4$ . The 1D NMR data showed that **7** was tetramic acid derivative too. The  $^1H$ - $^1H$  COSY correlations of H-6/H-7/H-8/H-9/H-10/ $CH_3$ -11, and HMBC correlations from H-6 to C-7, C-8, from H-9 to C-7, C-8, C-10, from  $CH_3$ -11 to C-9, C-10 indicated **7** had the same plane structure as known compound **8**. The double bond  $Z$ - $\Delta^{7,8}$  configuration of **7** was assigned by the coupling constant value  $J_{H-7,8} = 10.9$  Hz instead of  $J_{H-7,8} = 15.0$  Hz in **8** ( $E$ - $\Delta^{7,8}$ ) [8].

The configuration of C-3 and C-10 were assigned as (3S,10R) based on the comparison of ECD cotton effect with 1–6 and the chemical shift values analysis of Mosher ester derivatives of 7, respectively (Figure 3C).

To access the anti-inflammatory effects of these C3–C6 reduced 3-acyl tetramic acid derivatives, all the compounds were evaluated for their inhibition of NF- $\kappa$ B production using LPS induced RAW264.7 cells. Compounds 1, 2, 5–7 exhibited moderate effect with EC<sub>50</sub> values of  $18.49 \pm 1.21$ ,  $25.81 \pm 1.30$ ,  $23.10 \pm 1.26$ ,  $24.70 \pm 1.19$ , and  $26.52 \pm 1.12$   $\mu$ M, respectively. Meanwhile, the positive control BAY11-7082 (NF- $\kappa$ B inhibitor) had the EC<sub>50</sub> values of  $1.5 \pm 1.4$   $\mu$ M.

The anti-inflammatory effects of tetramic acid derivatives have been reported. Vermelhotin, pseurotin A3 and pseurotin G showed anti-inflammatory effect for the inhibition of NO production in LPS-induced RAW264.7 cells with EC<sub>50</sub> values of 5.35  $\mu$ M, 34.5  $\mu$ M and 57.0  $\mu$ M, respectively [17,18].

Their cytotoxicity was also determined towards hepatocytes cell line LO2 and hepatoma cells line Bel-7402 and RAW264.7. No definite inhibitory effects were observed at the concentration of 30  $\mu$ M.

### 3. Materials and Methods

#### 3.1. General Experimental Procedure

Circular dichroism and optical rotations were measured with JASCO J-1500 circular dichroism spectrophotometer (JASCO, Easton, PA, USA). <sup>1</sup>H NMR, <sup>13</sup>C NMR and 2D NMR spectra were recorded on a Bruker AVANCE III HD600 spectrometer (Bruker, Billerica, MA, USA) with TMS as reference. The suitable crystal was analyzed on a Bruker Smart Apex II single crystal X-Ray diffractometer (Bruker, Billerica, MA, USA). High-resolution TOFESIMS was performed on a WATERS Xevo G2-S Qtof Quadrupole Time-of-Flight Mass Spectrometry (Waters, Milford, MA, USA). Analysis and semi-preparative reversed-phase HPLC was performed on a Shimadzu LC-2030 liquid chromatography (Shimadzu, Kyoto, Japan) with YMC-Pack ODS-A column 250  $\times$  10 mm i.d., S-5  $\mu$ m  $\times$  12 nm, and 250  $\times$  20 mm i.d., S-5  $\mu$ m  $\times$  12 nm. Column chromatography (CC) was performed on silica gel (200–300 mesh, Jianguo Silica Gel Co., Ltd., Yantai, China) or CHROMATOREX C18 silica (Fuji Silysia Chemical Ltd., Kozoji-cho, Kasugai Aichi, Japan).

#### 3.2. Fungal Material

The fungal strain GXIMD00542 was isolated from Mariana Trench sediment (141°57' E, 10°51' N, 5467 m depth), and identified as *Lecanicillium fusisporum* by ITS rDNA sequence homology (97.57% similarity with *L. fusisporum*) (GenBank accession number ON005314, Figure S1). The strain was deposited in the Guangdong Microbial Culture Collection Center (GDMCC) with the accession number 62091.

#### 3.3. Fermentation and Extraction

Spores of the fungal strain were inoculated into 1000 mL Erlenmeyer flasks each containing 300 mL of liquid medium (glucose 1%, maltose 2%, monosodium glutamate 1%, KH<sub>2</sub>PO<sub>4</sub> 0.05%, MgSO<sub>4</sub> 7H<sub>2</sub>O 0.003%, yeast extract 0.3%, dissolved in artificial sea water. After 30 days of stationary cultivation at 25 °C, the whole broths (30 L) were filtered through cheesecloth. Sterilized XAD-16 resin (20 g/L) was added to the liquor and shaken at low speed for 30 min to absorb the organic products. The resin was washed with distilled water to remove medium residue then eluted with methanol. The methanol solvent was removed under vacuum to yield a brown residue (42 g). The mycelium portion was smashed and extracted twice with 80% acetone/H<sub>2</sub>O. The acetone soluble fraction was dried in vacuo to yield 18 g of residue. The residues of liquor and mycelium extracts were combined together according to TLC chromatography detecting.



### 3.4. Isolation and Purification

The combined extract (60 g) was subjected to silica gel column (1000 g) and eluted with  $\text{CH}_2\text{Cl}_2/\text{acetone}$  (100:0–60:40, *v/v*) to yield 15 fractions (Fractions 1–15). Fraction 9 (0.41 g) was separated by C18 silica column and eluted with  $\text{CH}_3\text{CN}/\text{H}_2\text{O}$  (10:90–40:60, *v/v*) to give 20 sub-fractions (Fr. 9-1–9-20). Sub-fraction 9-11 was subjected to semi-preparation HPLC ( $\text{CH}_3\text{CN}/\text{H}_2\text{O}$ , 18:82) at the flow rate of 3 mL/min to obtain **5** ( $t_{\text{R}}$  30.3 min, 8 mg). Sub-fraction 9-13 was purified with semi-preparation HPLC ( $\text{MeOH}/\text{H}_2\text{O}$ , 40:60) at the flow rate of 3 mL/min to yield **6** ( $t_{\text{R}}$  28.9 min, 11 mg). Sub-fraction 9-14 was purified with semi-preparation HPLC ( $\text{MeOH}/\text{H}_2\text{O}$ , 40:60) at the flow rate of 3 mL/min to yield **3** ( $t_{\text{R}}$  28.9 min, 40 mg) and **4** ( $t_{\text{R}}$  33.6, 14 mg). Sub-fraction 9-15 was purified with semi-preparation HPLC ( $\text{CH}_3\text{CN}/\text{H}_2\text{O}$ , 22:78) at the flow rate of 3 mL/min to yield **2** ( $t_{\text{R}}$  35.8 min, 8 mg) and **1** ( $t_{\text{R}}$  38.2 min, 5 mg). Fraction 13 (2.0 g) was isolated with C18 silica column eluting with  $\text{CH}_3\text{CN}/\text{H}_2\text{O}$  (10:90–40:60) to obtain 17 sub-fractions (Fractions 13-1–13-17). Sub-fraction 13-11 was purified by preparatory HPLC ( $\text{MeOH}/\text{H}_2\text{O}$ , 30:70) at the flow rate of 5 mL/min to yield **8** ( $t_{\text{R}}$  96.5 min, 22 mg) and **7** ( $t_{\text{R}}$  106.1 min, 10 mg).

Lecanicilliumin A (**1**): light brown orthorhombic crystal;  $[\alpha]_{\text{D}}^{25} -34.7$  (*c* 0.09, MeOH); UV (MeOH)  $\lambda_{\text{max}}$  ( $\log \epsilon$ ) 235 (3.75), 294 (3.28) nm; CD (MeOH)  $\lambda_{\text{max}}$  ( $\Delta\epsilon$ ) 233 (−4.05), 266 (−0.21), 280 (−0.40), 347 (+0.71);  $^1\text{H}$  and  $^{13}\text{C}$  NMR data, see Tables 1 and 2; HRESIMS  $m/z$  274.1063  $[\text{M} + \text{Na}]^+$  (calcd. for 274.1055).

Lecanicilliumin B (**2**): light brown powder;  $[\alpha]_{\text{D}}^{25} +14.4$  (*c* 0.80, MeOH); UV (MeOH)  $\lambda_{\text{max}}$  ( $\log \epsilon$ ) 236 (3.78), 296 (3.31) nm; CD (MeOH)  $\lambda_{\text{max}}$  ( $\Delta\epsilon$ ) 207 (−5.93), 242 (+5.87), 297 (+0.44);  $^1\text{H}$  and  $^{13}\text{C}$  NMR data, see Tables 1 and 2; HRESIMS  $m/z$  274.1059  $[\text{M} + \text{Na}]^+$  (calcd. for 274.1055).

Lecanicilliumin C (**3**): white amorphous powder;  $[\alpha]_{\text{D}}^{25} +43.2$  (*c* 0.94, MeOH); UV (MeOH)  $\lambda_{\text{max}}$  ( $\log \epsilon$ ) 233 (4.06), 296 (3.66) nm; CD (MeOH)  $\lambda_{\text{max}}$  ( $\Delta\epsilon$ ) 216 (−3.94), 240 (+6.53), 281 (+1.84);  $^1\text{H}$  and  $^{13}\text{C}$  NMR data, see Tables 2 and 3; HRESIMS  $m/z$  252.1241  $[\text{M} + \text{H}]^+$  (calcd. for 252.1236).

Lecanicilliumin D (**4**): white amorphous powder;  $[\alpha]_{\text{D}}^{25} -18.9$  (*c* 0.41, MeOH); UV (MeOH)  $\lambda_{\text{max}}$  ( $\log \epsilon$ ) 234 (3.98), 296 (3.60) nm; CD (MeOH)  $\lambda_{\text{max}}$  ( $\Delta\epsilon$ ) 214 (−6.48), 239 (−1.60), 245 (−1.68), 269 (+0.03);  $^1\text{H}$  and  $^{13}\text{C}$  NMR data, see Tables 2 and 3; HRESIMS  $m/z$  252.1235  $[\text{M} + \text{H}]^+$  (calcd. for 252.1236).

Lecanicilliumin E (**5**): colorless solid;  $[\alpha]_{\text{D}}^{25} +12.0$  (*c* 0.27, MeOH); UV (MeOH)  $\lambda_{\text{max}}$  ( $\log \epsilon$ ) 233 (3.89), 296 (3.50) nm; CD (MeOH)  $\lambda_{\text{max}}$  ( $\Delta\epsilon$ ) 207 (−6.95), 234 (+1.80), 256 (+0.05), 303 (+0.95);  $^1\text{H}$  and  $^{13}\text{C}$  NMR data, see Tables 2 and 3; HRESIMS  $m/z$  306.1319  $[\text{M} + \text{Na}]^+$  (calcd. for 306.1317).

Lecanicilliumin F (**6**): colorless solid;  $[\alpha]_{\text{D}}^{25} -65.9$  (*c* 0.23, MeOH); UV (MeOH)  $\lambda_{\text{max}}$  ( $\log \epsilon$ ) 233 (3.99), 296 (3.60) nm; CD (MeOH)  $\lambda_{\text{max}}$  ( $\Delta\epsilon$ ) 206 (−8.38), 233 (+1.44), 251 (−0.20), 300 (+1.14);  $^1\text{H}$  and  $^{13}\text{C}$  NMR data, see Tables 2 and 3; HRESIMS  $m/z$  306.1319  $[\text{M} + \text{Na}]^+$  (calcd. for 306.1317).

Lecanicilliumin G (**7**): light yellow solid;  $[\alpha]_{\text{D}}^{25} -4.5$  (*c* 0.90, MeOH); UV (MeOH)  $\lambda_{\text{max}}$  ( $\log \epsilon$ ) no obvious absorption peak in the 200–400 range; CD (MeOH)  $\lambda_{\text{max}}$  ( $\Delta\epsilon$ ) 207 (−1.60), 234 (+2.18), 331 (−0.37);  $^1\text{H}$  and  $^{13}\text{C}$  NMR data, see Tables 1 and 2; HRESIMS  $m/z$  276.1203  $[\text{M} + \text{Na}]^+$  (calcd. for 276.1212).

### 3.5. Mosher's Ester Reaction

The Mosher's ester reaction of **7** was performed as described in the literature [19]. Briefly, 1 mg of dried **7** was dissolved in 0.5 mL anhydrous dichloromethane. Then, 10  $\mu\text{L}$  of triethylamine, 0.1 mg of 4-dimethyl aminopyridine (DMAP) and 10  $\mu\text{L}$  (*R*)-(-) or (*S*)-(+)-methoxy- $\alpha$ -(trifluoromethyl)phenylacetyl chloride (MTPA-Cl) were added, respectively. The mixtures were stirred at room temperature overnight and quenched by adding water to give the (*S*)- and (*R*)-MTPA ester derivatives of **7**.

### 3.6. X-ray Crystal Structure Analysis

Compound **1** was obtained as light brown orthorhombic crystal from MeOH with molecular formula of  $C_{26}H_{36}N_2O_9$ . The suitable crystal was selected and analyzed on a CCD area detector diffractometer (Bruker Smart Apex II) using Cu  $K\alpha$  radiation. The crystallographic data for **1** (CCDC 2092073) was deposited in the Cambridge Crystallographic Data Centre.

Crystal data for lecanicilliumin A (**1**):  $C_{26}H_{36}N_2O_9$  ( $M = 520.57$ ), orthorhombic, space group  $P2_12_12_1$ ,  $a = 11.32560(10)$  Å,  $b = 12.19970(10)$  Å,  $c = 18.5233(2)$  Å,  $\alpha = 90^\circ$ ,  $\beta = 90^\circ$ ,  $\gamma = 90^\circ$ ,  $V = 2559.34(4)$  Å<sup>3</sup>,  $Z = 4$ ,  $\rho_{\text{calc}} = 1.351$  g/cm<sup>3</sup>,  $\mu$  (Cu  $K\alpha$ ) =  $0.851$  mm<sup>-1</sup>, crystal size:  $0.16 \times 0.08 \times 0.08$  mm<sup>3</sup>, 14,388 reflections measured ( $8.678^\circ \leq \theta \leq 148.214^\circ$ ), 5046 unique ( $R_{\text{int}} = 0.0182$ ,  $R_{\text{sigma}} = 0.0192$ ). The final  $R_1$  was 0.0266 ( $I > 2\sigma(I)$ ) and  $\omega R_2$  was 0.0702, flack = 0.03 (4).

### 3.7. Computational Methods

Molecular Merck force field (MMFF) and DFT/TDDFT calculations were performed with Spartan'14 software package (Wavefunction Inc., Irvine, CA, USA) [20] and Gaussian16 program package (Gaussian Inc., Wallingford, CT, USA) [21], respectively, using default grids and convergence criteria. MMFF conformational search generated low-energy conformers within a 10 kcal/mol energy window were subjected to geometry optimization using the B3LYP/6-31G(d,p) method. Frequency calculations were performed with the same method to verify each optimized conformer was a true minimum and to estimate their relative thermal free energies ( $\Delta G$ ) at 298.15 K. Energies of the low-energy conformers in MeOH were calculated at the M062X/def2-TZVP level. Solvent effects were taken into account by using a polarizable continuum model (PCM). The TDDFT calculations were performed using the M062X functions with basis set def2-TZVP. The number of excited states per each molecule was 32. The ECD spectra were generated by the program SpecDis [22] using a Gaussian band shape from dipole-length dipolar and rotational strengths. Equilibrium population of each conformer at 298.15 K was calculated from its relative free energies using Boltzmann statistics. The calculated spectra were generated from the low-energy conformers according to the Boltzmann weighting of each conformer in a MeOH solution.

The B3LYP/6-31G(d) optimized geometries of **3–6** were adopted for further NMR computation. Gauge-Independent Atomic Orbital (GIAO) calculations of the <sup>13</sup>C NMR chemical shifts were accomplished by DFT at the B97-2/pcSseg-1 level in DMSO with PCM. The calculated <sup>13</sup>C NMR spectroscopic data were averaged according to the Boltzmann distribution by the program Multiwfn 3.7 [23]. The <sup>13</sup>C NMR chemical shifts for TMS were calculated by the same procedure and used as the reference.

### 3.8. Cytotoxicity Assay

Cytotoxicities of **1–8** were evaluated against LO2, Bel-7402 and RAW264.7 cell lines using MTT method. The detailed methodologies for cytotoxic testing have been described in previous report [24].

### 3.9. NF- $\kappa$ B Luciferase Assay

The effects of **1–8** on LPS-induced NF- $\kappa$ B luciferase activity were detected by luciferase reporter gene assay as described earlier. Briefly, RAW264.7 cells, stably transfected with a NF- $\kappa$ B luciferase reporter construct, were treated with **1–8** (30  $\mu$ M) and BAY11-7082 (NF- $\kappa$ B inhibitor, 5  $\mu$ M) for 4 h, followed by stimulation with LPS (100 ng/mL<sup>-1</sup>) for 6 h. The luciferase activity was determined using the luciferase assay system (Promega, Madison, WI, USA) [24]. The dose-dependent effects of **1–8** and BAY11-7082 on LPS induced NF- $\kappa$ B luciferase activity were detected by the same assay.

## 4. Conclusions

In conclusion, a series of rare C3-C6 reduced 3-acyl tetramic acid derivatives, lecanicilliumins A-G (**1–7**), along with the known analogue cladosporiumin D (**8**), were obtained

from the extract of the deep-sea-derived fungus *Lecanicillium fusisporum* GXIMD00542. Compounds **1**, **2**, **5**–**7** exhibited moderate anti-inflammatory activity against NF- $\kappa$ B production using LPS induced RAW264.7 cells with EC<sub>50</sub> values range of 18.49–30.19  $\mu$ M. This finding expanded the chemical diversity of 3-acyl tetramic acid derivatives, and also enriched the secondary metabolites in deep-sea-derived fungus.

**Supplementary Materials:** The following supporting information can be downloaded at: <https://www.mdpi.com/article/10.3390/md20040255/s1>, Figure S1: The colonies and the ITS rRNA sequences data of deep-sea-derived fungus *Lecanicillium fusisporum* GXIMD00542; Figures S2–S52: The 1D and 2D NMR spectra, HRTOFESIMS spectra of compound **1**–**7**; Table S1: Crystal data and structure refinement for compound **1**. Figure S53: <sup>1</sup>H NMR spectrum of (*R*)-MTPA ester of **7**; Figure S54: <sup>1</sup>H NMR spectrum of (*S*)-MTPA ester of **7**; Tables S2–S13: Relative free energies and equilibrium populations of conformers for **2**–**6**; Figures S55 and S56: The optimized structures and the calculated CD spectra of conformers for **2** in MeOH at M06-2X/def2TZVP level; Figures S57–S74: The optimized structure of conformers, correlation plots of experimental <sup>13</sup>C NMR chemical shifts versus the corresponding calculated data and DP4+ probabilities (%) for conformers of **3**–**6**. File S1: Crystallographic Data of compound **1**. References [2,25] are cited in the Supplementary Materials

**Author Contributions:** The contributions of the respective authors are as follows. X.X. drafted the work and performed the isolation and the structural elucidation. Y.T. and Z.T. performed the biological evaluations. C.L. and H.L. contributed to the fermentation and extraction. C.G. contributed to checking and confirming all isolation procedures and identification. K.L. contributed to computational sections. X.Z. contributed to the isolation and identification of the fungus strain. Y.L. designed the study, supervised the laboratory work, and contributed to the critical reading of the manuscript. All authors have read and agreed to the published version of the manuscript.

**Funding:** This research was funded by Guangxi Natural Science Foundation (AD19245116, 2020GXNS-FGA297002, 2021GXNSFDA075010), National Natural Science Foundation of China (42066006, 41606186, U20A20101), Special Fund for Bagui Scholars of Guangxi (05019055); The Scientific Research Foundation of GXUCM (2018BS039, 2018ZD005); Development Program of High level Talent Team under Qihuang Project of Guangxi University of Chinese Medicine (2018006), Guangdong Key Laboratory of Marine Materia Medica Foundation (LMM2021-3); Guangxi First-class Discipline: Chinese Materia Medica (Scientific Research of Guangxi Education Department [2018] No. 12).

**Institutional Review Board Statement:** Not applicable.

**Informed Consent Statement:** Not applicable.

**Data Availability Statement:** Data are contained within the article.

**Acknowledgments:** We thank Xuan Luo, College of Chemistry and Chemical Engineering, Guangxi University, for help with the NMR spectra measurements. We also thank Xuan Ma of the South China Sea Institute of Oceanology for help with determination of the X-ray structure of **1**.

**Conflicts of Interest:** The authors declare no conflict of interest.

## References

- Pang, X.; Chen, W.; Wang, X.; Zhou, X.; Yang, B.; Tian, X.; Wang, J.; Xu, S.; Liu, Y. New tetramic acid derivatives from the deep-sea-derived fungus *Penicillium* sp. SCSIO06868 with SARS-CoV-2 M(pro) inhibitory activity evaluation. *Front. Microbiol.* **2021**, *12*, 730807. [[CrossRef](#)] [[PubMed](#)]
- Mo, X.; Gulder, T. Biosynthetic strategies for tetramic acid formation. *Nat. Prod. Rep.* **2021**, *38*, 1555–1566. [[CrossRef](#)]
- Ghisalberti, E.L. Bioactive Tetramic Acid Metabolites. In *Studies in Natural Products Chemistry*; Rahman, A., Ed.; Elsevier: Amsterdam, The Netherlands, 2003; Volume 28, pp. 109–163. [[CrossRef](#)]
- Jiang, M.; Chen, S.; Li, J.; Liu, L. The biological and chemical diversity of tetramic acid compounds from marine-derived microorganisms. *Mar. Drugs* **2020**, *18*, 114. [[CrossRef](#)]
- Royles, B.J.L. Naturally Occurring Tetramic Acids: Structure, Isolation, and Synthesis. *Chem. Rev.* **1995**, *95*, 1981–2001. [[CrossRef](#)]
- Schobert, R.; Schlenk, A. Tetramic and tetronic acids: An update on new derivatives and biological aspects. *Bioorg. Med. Chem.* **2008**, *16*, 4203–4221. [[CrossRef](#)] [[PubMed](#)]
- Mo, X.; Li, Q.; Ju, J. Naturally occurring tetramic acid products: Isolation, structure elucidation and biological activity. *RSC Adv.* **2014**, *4*, 50566–50593. [[CrossRef](#)]

8. Huang, Z.; Nong, X.; Liang, X.; Qi, S. New tetramic acid derivatives from the deep-sea-derived fungus *Cladosporium* sp. SCSIO z0025. *Tetrahedron* **2018**, *74*, 2620–2626. [[CrossRef](#)]
9. Zare, R.; Gams, W. A revision of *Verticillium* section *Prostrata*. IV. The genera *Lecanicillium* and *Simplicillium* gen. nov. *Nova Hedwigia* **2001**, *73*, 1–50. [[CrossRef](#)]
10. Steenberg, T.; Humber, R.A. Entomopathogenic potential of *Verticillium* and *Acremonium* species (Deuteromycotina: Hyphomycetes). *J. Invertebr. Pathol.* **1999**, *73*, 309–314. [[CrossRef](#)]
11. Ekblom, B.S.; Ahman, I. The fungus *Verticillium fusisporum* as an insect pathogen. *J. Invertebr. Pathol.* **1980**, *36*, 136–138. [[CrossRef](#)]
12. Miller, L.K.; Lingg, A.J.; Bulla, L.A., Jr. Bacterial, viral, and fungal insecticides. *Science* **1983**, *219*, 715–721. [[CrossRef](#)]
13. Ishidoh, K.; Kinoshita, H.; Igarashi, Y.; Ihara, F.; Nihira, T. Cyclic lipodepsipeptides verlamelin A and B, isolated from entomopathogenic fungus *Lecanicillium* sp. *J. Antibiot.* **2014**, *67*, 459–463. [[CrossRef](#)] [[PubMed](#)]
14. Huang, Q.; Li, H.J.; Huang, C.B.; Wang, Z.H.; Lan, W.J.; Wang, L.Y. Alkaloids from the marine fungus *Lecanicillium fusisporum* using an amino acid-directed strategy. *Nat. Prod. Commun.* **2021**, *16*, 1–6. [[CrossRef](#)]
15. Zanardi, M.M.; Sarotti, A.M. Sensitivity analysis of DP4+ with the probability distribution terms: Development of a universal and customizable method. *J. Org. Chem.* **2021**, *86*, 8544–8548. [[CrossRef](#)]
16. Grimblat, N.; Zanardi, M.M.; Sarotti, A.M. Beyond DP4: An improved probability for the stereochemical assignment of isomeric compounds using quantum chemical calculations of NMR shifts. *J. Org. Chem.* **2015**, *80*, 12–34. [[CrossRef](#)]
17. Pansanit, A.; Park, E.J.; Kondratyuk, T.P.; Pezzuto, J.M.; Lirdprapamongkol, K.; Kittakoop, P. Vermelhotin, an anti-inflammatory agent, suppresses nitric oxide production in RAW 264.7 cells via p38 inhibition. *J. Nat. Prod.* **2013**, *76*, 1824–1827. [[CrossRef](#)] [[PubMed](#)]
18. Lee, M.; Wang, S.; Wang, G.; Pang, K.; Lee, C.; Kuo, Y.; Cha, H.; Lin, R.; Lee, T. Angiogenesis inhibitors and anti-inflammatory agents from *Phoma* sp. NT04195. *J. Nat. Prod.* **2016**, *79*, 2983–2990. [[CrossRef](#)]
19. Xu, X.; Tsang, S.W.; Guan, Y.; Liu, K.; Pan, W.; Lam, C.S.; Lee, K.M.; Xia, Y.; Xie, W.; Wong, W.Y.; et al. In vitro and in vivo antitumor effects of plant-derived miliusanones and their induction of cellular senescence. *J. Med. Chem.* **2019**, *62*, 1541–1561. [[CrossRef](#)]
20. *Spartan'14*; Wavefunction Inc.: Irvine, CA, USA, 2013.
21. Frisch, M.J.; Trucks, G.W.; Schlegel, H.B.; Scuseria, G.E.; Robb, M.A.; Cheeseman, J.R.; Scalmani, G.; Barone, V.; Petersson, G.A.; Nakatsuji, H.; et al. *Gaussian 16, Rev. B.01*; Gaussian Inc.: Wallingford, CT, USA, 2016.
22. Bruhn, T.; Schaumlöffel, A.; Hemberger, Y.; Bringmann, G. SpecDis: Quantifying the comparison of calculated and experimental electronic circular dichroism spectra. *Chirality* **2013**, *25*, 243–249. [[CrossRef](#)]
23. Lu, T.; Chen, F. Multiwfn: A multifunctional wavefunction analyzer. *J. Comput. Chem.* **2012**, *33*, 580–592. [[CrossRef](#)] [[PubMed](#)]
24. Tan, Y.; Deng, W.; Zhang, Y.; Ke, M.; Zou, B.; Luo, X.; Su, J.; Wang, Y.; Xu, J.; Nandakumar, K.S.; et al. A marine fungus-derived nitrobenzoyl sesquiterpenoid suppresses receptor activator of NF- $\kappa$ B ligand-induced osteoclastogenesis and inflammatory bone destruction. *Br. J. Pharmacol.* **2020**, *177*, 4242–4260. [[CrossRef](#)]
25. Rischer, M.; Lee, S.R.; Eom, H.J.; Park, H.B.; Vollmer, J.; Kaster, A.K.; Shin, Y.H.; Oh, D.C.; Kim, K.H.; Beemelmans, C. Spirocyclic cladosporicin A and cladosporiumins I and J from a Hydractinia-associated *Cladosporium sphaerospermum* SW67. *Org. Chem. Front.* **2019**, *6*, 1084–1093. [[CrossRef](#)]





## Article

# The Emerging Evidence for a Protective Role of Fucoidan from *Laminaria japonica* in Chronic Kidney Disease-Triggered Cognitive Dysfunction

Zhihui Ma <sup>1,†</sup>, Zhiyou Yang <sup>1,2,\*,†</sup>, Xinyue Feng <sup>1</sup>, Jiahang Deng <sup>1</sup>, Chuantong He <sup>1</sup>, Rui Li <sup>1</sup>, Yuntao Zhao <sup>1</sup>, Yuewei Ge <sup>3</sup>, Yongping Zhang <sup>1</sup>, Cai Song <sup>1</sup> and Saiyi Zhong <sup>1,2</sup>

- <sup>1</sup> Guangdong Provincial Key Laboratory of Aquatic Product Processing and Safety, Guangdong Province Engineering Laboratory for Marine Biological Products, Guangdong Provincial Engineering Technology Research Center of Seafood, Key Laboratory of Advanced Processing of Aquatic Product of Guangdong Higher Education Institution, College of Food Science and Technology, Guangdong Ocean University, Zhanjiang 524088, China; mazhihui@stu.gdou.edu.cn (Z.M.); 2112003030@stu.gdou.edu.cn (X.F.); 2112003070@stu.gdou.edu.cn (J.D.); 2112103046@stu.gdou.edu.cn (C.H.); lirui@gdou.edu.cn (R.L.); zhaoyt@gdou.edu.cn (Y.Z.); zhangyp@gdou.edu.cn (Y.Z.); cai.song@dal.ca (C.S.); zhongsy@gdou.edu.cn (S.Z.)
- <sup>2</sup> Collaborative Innovation Center of Seafood Deep Processing, Dalian Polytechnic University, Dalian 116034, China
- <sup>3</sup> Key Laboratory of Digital Quality Evaluation of Chinese Materia Medica of State Administration of TCM, Guangdong Pharmaceutical University, Guangzhou 510006, China; geyuewei@gdpu.edu.cn
- \* Correspondence: zyyang@gdou.edu.cn; Tel.: +86-759-2396046
- † These authors contributed equally to this work.

**Citation:** Ma, Z.; Yang, Z.; Feng, X.; Deng, J.; He, C.; Li, R.; Zhao, Y.; Ge, Y.; Zhang, Y.; Song, C.; et al. The Emerging Evidence for a Protective Role of Fucoidan from *Laminaria japonica* in Chronic Kidney Disease-Triggered Cognitive Dysfunction. *Mar. Drugs* **2022**, *20*, 258. <https://doi.org/10.3390/md20040258>

Academic Editors: Yonghong Liu and Xuefeng Zhou

Received: 13 March 2022

Accepted: 5 April 2022

Published: 7 April 2022

**Publisher's Note:** MDPI stays neutral with regard to jurisdictional claims in published maps and institutional affiliations.



**Copyright:** © 2022 by the authors. Licensee MDPI, Basel, Switzerland. This article is an open access article distributed under the terms and conditions of the Creative Commons Attribution (CC BY) license (<https://creativecommons.org/licenses/by/4.0/>).

**Abstract:** This study aimed to explore the mechanism of fucoidan in chronic kidney disease (CKD)-triggered cognitive dysfunction. The adenine-induced ICR strain CKD mice model was applied, and RNA-Seq was performed for differential gene analysis between aged-CKD and normal mice. As a result, fucoidan (100 and 200 mg kg<sup>-1</sup>) significantly reversed adenine-induced high expression of urea, uric acid in urine, and creatinine in serum, as well as the novel object recognition memory and spatial memory deficits. RNA sequencing analysis indicated that oxidative and inflammatory signaling were involved in adenine-induced kidney injury and cognitive dysfunction; furthermore, fucoidan inhibited oxidative stress via GSK3β-Nrf2-HO-1 signaling and ameliorated inflammatory response through regulation of microglia/macrophage polarization in the kidney and hippocampus of CKD mice. Additionally, we clarified six hallmarks in the hippocampus and four in the kidney, which were correlated with CKD-triggered cognitive dysfunction. This study provides a theoretical basis for the application of fucoidan in the treatment of CKD-triggered memory deficits.

**Keywords:** chronic kidney disease; fucoidan; cognitive dysfunction; neuroinflammation; oxidative stress; GSK3β-Nrf2-HO-1 signaling; microglial polarization

## 1. Introduction

Chronic kidney disease (CKD) is a chronic renal structural and functional deficit caused by multiple factors. Over the past 10 years, CKD blossomed into an important cause of morbidity and mortality worldwide with a cumulative mortality rate of 20.6% [1]. Currently, approximately 8–16% of the global adult population suffer from CKD, while the prevalence rate of CKD increases continuously along with aging and mainly by the presence of other risk factors, such as diabetes mellitus, obesity, metabolic syndrome, arterial hypertension, and indiscriminate use of nephrotoxic drugs [2]. Recently, cognitive impairment in patients, accompanied with CKD progressing, has attracted more and more attention. Cognitive dysfunction occurs not only in patients with end-stage renal disease, but also in early stage I–II CKD patients [3]. An epidemiological study demonstrated that kidney dysfunction and albuminuria are independent risk factors for the development of

dementia [4]. Reports evidenced that the incidence of cognitive impairment in children and adults with CKD is higher than that in normal people, and the subjects with kidney dysfunction are always accompanied with less cortical thickness and smaller hippocampal volume and gray matter volume than those with normal renal function [5,6]. Once cognitive impairment occurs, the resulting low medication compliance of CKD patients affects their clinical treatment efficacy and increases the risk of death [7]. However, the molecular mechanism of CKD-induced cognitive deficits remains to be elucidated, and additionally, medications are urgently needed to improve CKD-induced cognitive impairment.

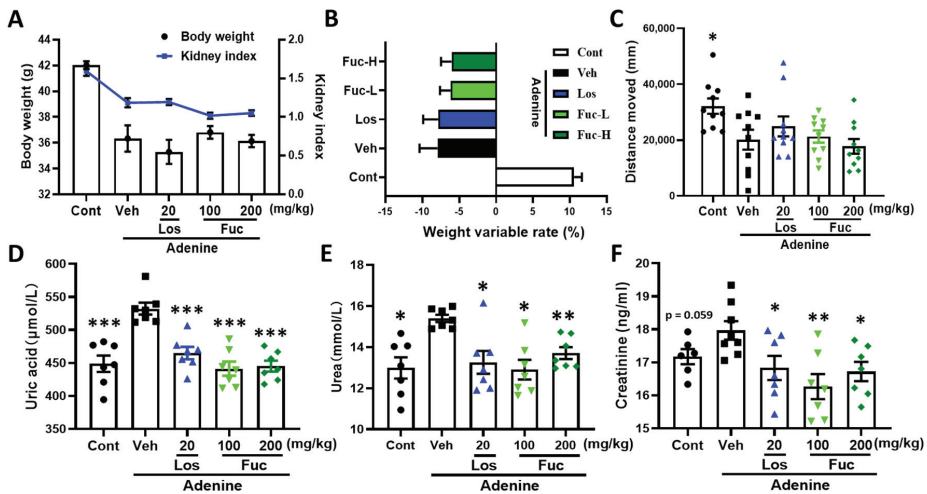
A variety of bioactive molecules, including polyunsaturated fatty acids (PUFA), polysaccharides, minerals, vitamins, antioxidants, enzymes, and peptides, are derived from marine organisms [8]. Marine algae, as a new source of bioactive substances, has attracted extensive attention [9]. Currently, worldwide different kinds of algae have been focused on and developed into functional diet and health products [10]. Fucoidan, sulfated polysaccharides from brown algae, are rich in fucose and sulfate groups, along with small proportions of mannose, glucuronic acid, glucose, xylose, arabinose, and rhamnose. The fucoidan extracted from *Fucus vesiculosus* contains a backbone of alternating (1 → 3)-linked  $\alpha$ -l-fucopyranose and (1 → 4)-linked  $\alpha$ -l-fucopyranose residues, the presence of sulfate groups mainly at O-2 and at a lesser extent at O-3 [11]. Reports have shown that fucoidan exerts multiple biological functions, such as neuroprotection, anti-tumor, anti-inflammatory, anti-virus, antioxidation, anticoagulant, hypolipidemic, and antithrombotic activity, as well as effects against hepatic, renal, and uropathic disorders [12,13]. Fucoidan ameliorated adenine-induced renal dysfunction and renal tubulointerstitial damage through regulating the FGF23–Klotho signaling axis and ERK1/2-SGK1-NHERF-1-NaPi-2a pathway in chronic kidney disease [14]. In addition, the low molecular weight fucoidan protected kidneys from dysfunction and fibrogenesis by inhibiting the TGF- $\beta$  pathway in a diabetic nephropathy (DN) rat model [15]. Nevertheless, whether fucoidan ameliorated memory deficits in adenine-induced CKD remains to be elucidated.

In the current study, we investigated the differential genes between aging-related CKD and normal young mice using RNA-Seq analysis, and oxidative and inflammatory signaling pathways involved in CKD were clarified based on GO analysis. Furthermore, the effects of fucoidan on adenine-induced memory deficits and possible signaling pathways were determined. The experimental results indicated that fucoidan could ameliorate memory deficits in CKD, which indicates that fucoidan is a likely candidate drug for CKD intervention.

## 2. Results

### 2.1. Fucoidan Ameliorated Renal Function in Adenine-Induced CKD Mice

We previously investigated the effects of fucoidan on SH-SY5Y neuronal cells, and the dosage less than 1 mg mL<sup>-1</sup> did not significantly affect the neuronal viability [12]. We orally co-administered fucoidan (Fuc) and adenine to mice (male, 8-week-old) for 33 days; the selected doses referred to previous published research [16]. The mice were immediately sacrificed after the behavioral test, and kidney, serum, and urine were collected. On day 33, the mice body weight, kidney index (ratio of kidney to body weight), and weight variable rate (the percentage of body changed within Fuc treatment) in the vehicle group were significantly decreased compared with control group (Figure 1A). The body weight and kidney index were not reversed by the low (Fuc-L, 100 mg kg<sup>-1</sup> d<sup>-1</sup>) and high (Fuc-H, 200 mg kg<sup>-1</sup> d<sup>-1</sup>) dose of Fuc treatment, or by the losartan (Los, positive control, 20 mg kg<sup>-1</sup> d<sup>-1</sup>) (Figure 1A). The weight variable rate showed an increased trend after Fuc-H treatment (Figure 1B).



**Figure 1.** Effects of fucoidan on body and renal indexes in adenine-induced CKD mice. ICR mice (male, 8-week-old) were orally co-administered with fucoidan (Fuc), losartan (Los) or vehicle (saline), and adenine (0.25% contained diets) for 33 days. (A) Body weight and kidney index (kidney weight/body weight) among five groups. (B) Body weight variable rate (the increased body weight ratio between last and first drug treatment). (C) Total distance moved (within 8 min) in the open field test. The expression levels of uric acid (D), urea (E), and creatinine (F) were determined by ELISA kits. The data are expressed as mean  $\pm$  SEM ( $n = 10$ ). \*  $p < 0.05$ , \*\*  $p < 0.01$ , and \*\*\*  $p < 0.001$  vs. vehicle group (Veh), one-way ANOVA post hoc Dunnett's test.

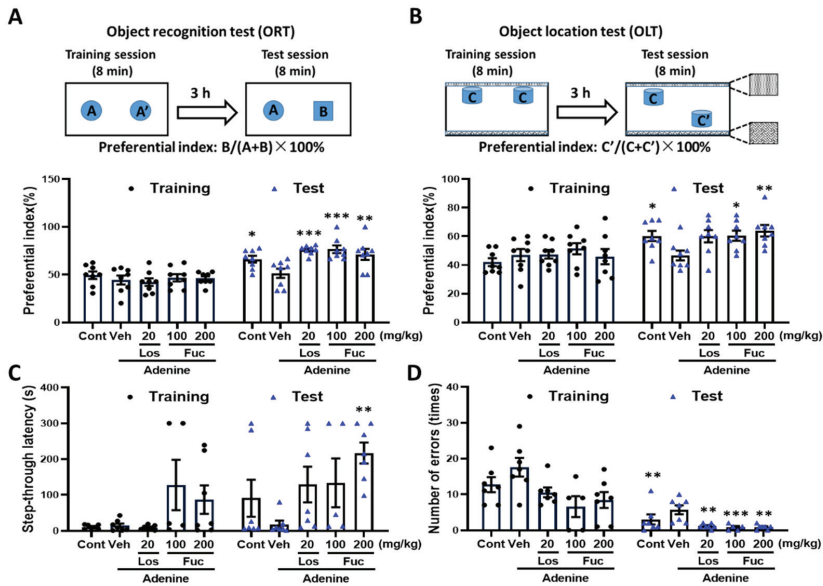
In the locomotion test, adenine treatment dramatically decreased the moved distance compared with control mice, while the drug-treated groups failed to reverse it (Figure 1C). No significant locomotor differences were detected in the distances moved between fucoidan- and vehicle-treated groups. The mice body weights were recorded during the drug administration, with no significant changes observed in fucoidan-treated groups compared with the vehicle group (Supplementary Figure S1). The results indicated that fucoidan treatment did not significantly affect the general health and behavior of the mice. The high expressed levels of uric acid and urea are important indicators for evaluation of renal failure [17]. Creatinine, a nitrogenous end product of protein metabolism, is a valuable marker for renal function [18]. CKD triggered profound histological changes, including glomeruli damages, tubular necrosis, and infiltration of inflammatory cells in kidneys, which was accompanied with a loss of renal functions indicated by the increase of urea, creatinine, and uric acid levels [19]. Thus, we determined the expressed levels of uric acid, urea, and creatinine. Compared with the control group, the uric acid and urea levels in urine were remarkably increased in adenine-treated vehicle mice, and creatinine in serum showed an increased trend, while both fucoidan (100 and 200 mg kg<sup>-1</sup> d<sup>-1</sup>) and losartan treatment dramatically decreased the levels of uric acid, urea, and creatinine (Figure 1D–F). In addition, we investigated the relatively low dose (10 mg kg<sup>-1</sup> d<sup>-1</sup>) of fucoidan on adenine-triggered chronic kidney disease and memory deficits and found that the renal as well as memory function were also significantly improved (data not shown).

## 2.2. Fucoidan Ameliorated Cognitive Deficits in Adenine-Induced CKD Mice

To explore the effects of fucoidan on CKD-triggered recognition memory deficits, we performed a novel object recognition test, object location test, and passive avoidance memory test, as described previously [20]. In the novel object recognition memory test, the mice equally explored the identical objects A and A' (preferential index approximately



50%). However, in the test session, compared with vehicle mice, fucoidan and losartan treatment significantly increased the exploration times towards novel object B, which was also observed in the control group, and indicated the recognition memory was enhanced (Figure 2A).



**Figure 2.** Effects of fucoidan on memory function in adenine-induced CKD mice. (A) Object recognition test (ORT). The preferential indexes for the training and test sessions are shown.  $p = 0.017$ , drug  $\times$  time interaction was analyzed using repeated measures two-way ANOVA,  $F(4, 28) = 3.64$ . \*  $p < 0.05$ , \*\*  $p < 0.01$ , and \*\*\*  $p < 0.001$  vs. vehicle-treated CKD mice, post hoc Dunnett’s test. (B) Object location test (OLT). The preferential indexes for the training and test sessions are shown.  $p = 0.0998$ , drug  $\times$  time interaction was analyzed using repeated measures two-way ANOVA,  $F(4, 56) = 2.05$ . \*  $p < 0.05$ , \*\*  $p < 0.01$  vs. vehicle-treated CKD mice, post hoc Dunnett’s test. (C) The step-through latency entering the darkroom in passive avoidance memory test.  $p = 0.288$ , drug  $\times$  time interaction was analyzed using repeated measures two-way ANOVA,  $F(4, 56) = 1.28$ . \*\*  $p < 0.01$  vs. vehicle-treated CKD mice, post hoc Dunnett’s test. (D) The number of errors into the darkroom were measured.  $p = 0.482$ , drug  $\times$  time interaction was analyzed using repeated measures two-way ANOVA,  $F(4, 44) = 0.88$ . \*\*  $p < 0.01$ , \*\*\*  $p < 0.001$  vs. vehicle-treated CKD mice, post hoc Dunnett’s test. The data are expressed as mean  $\pm$  SEM ( $n = 8$ ).

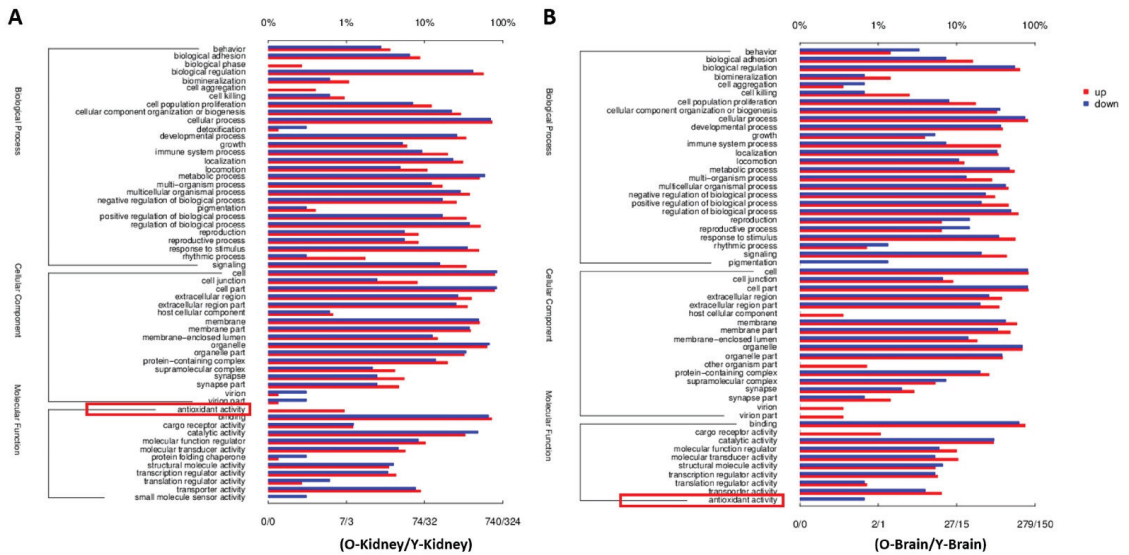
To test whether spatial memory is improved by fucoidan, we performed the object location memory test. The preferential index was approximately 50% among groups in the training session (Figure 2B). In the test session, compared with control group, the object location memory was remarkably decreased in CKD mice, which was completely reversed after fucoidan and losartan treatment (Figure 2B). In the passive avoidance memory test, the step-through latency of mice entering the darkroom in the vehicle group was shortened and the number of errors into the darkroom was significantly increased compared with normal control mice (Figure 2C,D). After treatment with fucoidan and losartan, the step-through latency was elongated, while the number of errors were dramatically decreased (Figure 2C,D).

Collectively, these results indicated that fucoidan rescues cognitive deficits when orally administered to adenine-induced CKD mice.

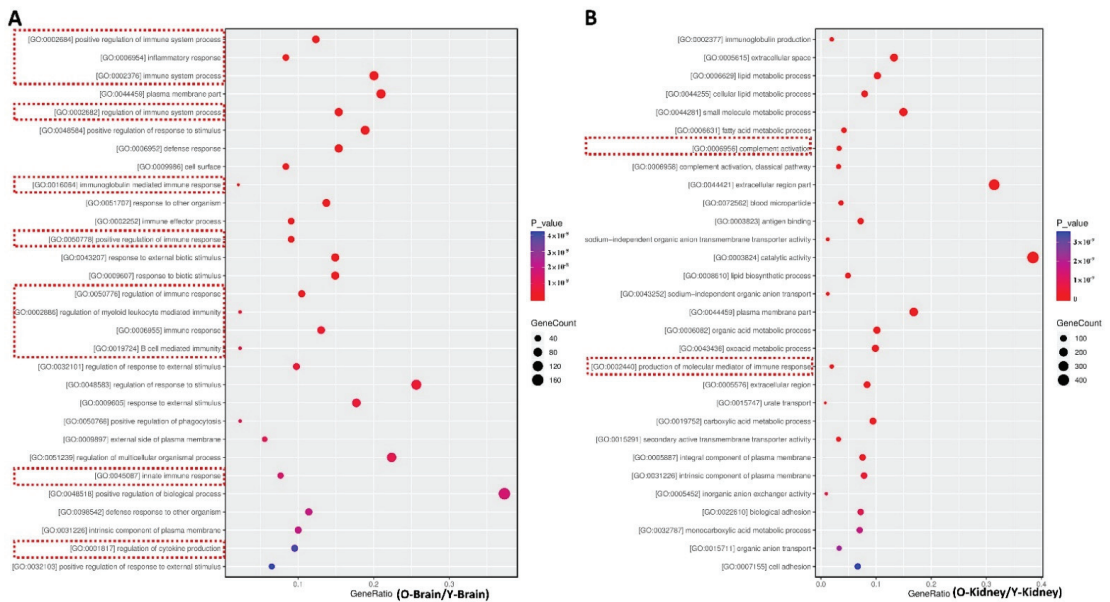
### 2.3. Fucoïdan Regulated Brain and Kidney Genes in Aging Renal Failure Mice

To investigate the key factors involved in CKD-triggered memory deficits, we performed RNA-Seq analysis using aging-induced CKD mice (male, 24-month-old) to mimic CKD conditions in human beings. As evidenced by ELISA analysis of uric acid and urea, the aging mice showed significant increased expression compared with young mice (Supplementary Figure S2). The differential genes were determined with log2Fold change <math><-1</math> or <math>>1</math>, and FDR <math>< 0.05</math> means significant difference. Compared with normal young mice (male, 3-month-old), 307 genes were upregulated and 189 genes were downregulated in the brain (Supplementary Figure S3A), while 835 genes were upregulated and 403 genes were downregulated in the kidney (Supplementary Figure S3B).

We performed GO annotation and enrichment analysis to explore the signaling pathways involved in the brain–kidney axis, which contributed to CKD-triggered memory deficits. The obtained differential genes between aged-CKD mice and normal young mice were used for GO enrichment analysis through the DAVID database. In GO annotation analysis, the regulated molecular functions include antioxidant activity, binding, cargo receptor activity, catalytic activity, and others, in kidneys (Figure 3A) as well as in the brain (Figure 3B). The GO enrichment analysis results indicated that 30 top biological processes are mainly involved, and among them inflammation-related signaling, such as immune system response, inflammatory response, B-cell-mediated immunity, innate immune response, and regulation of cytokine production, are widely regulated in naturally aging renal failure mice brain and kidneys (Figure 4A,B). Thus, we focused on the oxidative and inflammatory changes in CKD mice.



**Figure 3.** Column chart of GO annotation in the brain and kidney of CKD mice. GO analysis in the kidney (A) and brain (B) between aged-CKD and young mice was performed. The data are expressed as mean  $\pm$  SEM ( $n = 3$ ).

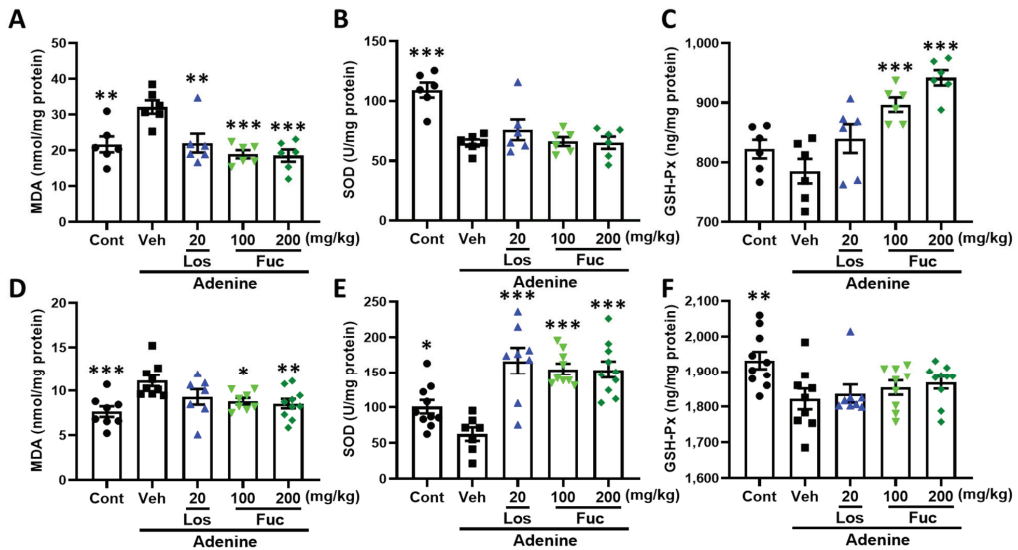


**Figure 4.** Bubble diagram of GO enrichment analysis of differential genes in the brain (A) and kidney (B) between aged-CKD and young mice was performed. The data are expressed as mean ± SEM (n = 3).

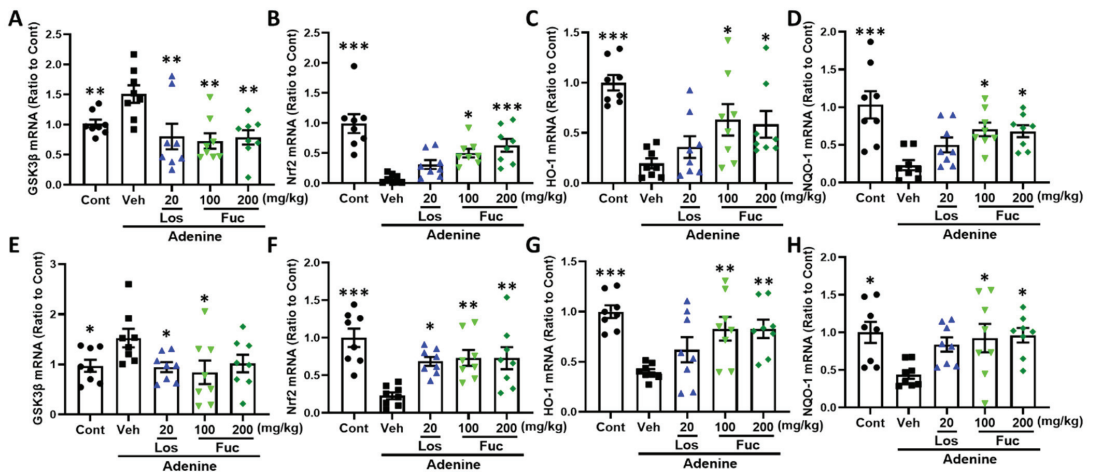
**2.4. Fucoidan Ameliorated Oxidative Stress Via Nrf2-HO-1 Signaling Pathway in Adenine-Induced CKD Mice**

Oxidative stress is harmful to cells due to excessive generation and accumulation of reactive oxygens (ROS), free radicals, and nitrogen. The kidney, a highly metabolic organ, is rich in oxidation reactions in mitochondria. Thus, the kidney is fragile and can be damaged by oxidative stress, and reports have shown that oxidative stress accelerates the progression of CKD [21]. Molecules targeting Nrf2-HO-1 signaling showed potential protective effects against oxidative stress and inflammation in CKD [22]. Cytokine-induced damage and oxidative stress play critical roles in the kidney–brain crosstalk during acute and chronic kidney injury [23]. MDA, the end product of lipid oxidation, was dramatically increased in CKD mice brain hippocampus and kidney compared with control mice. After fucoidan treatment as well as losartan intervention, the expression level of MDA was significantly reversed (Figure 5A,D). Activation of GSH-Px and SOD, the main antioxidant enzymes, is an important therapeutic strategy for the treatment of diseases characterized by elevated oxidative stress [24]. The activities of GSH-Px and SOD in CKD mice hippocampus and kidney were remarkably downregulated, while they were attenuated in mice hippocampus and kidney, respectively (Figure 5B,C,E,F).

We tested whether the GSK3β-Nrf2-HO-1 signaling pathway is involved in fucoidan-mediated antioxidative effects. Compared with control group, the expressions of GSK3β mRNA both in hippocampus and kidney were significantly increased in the vehicle group, which was ameliorated after fucoidan and losartan treatment (Figure 6A,E). Nuclear factor-E2 related factor 2 (Nrf2), a redox sensitive transcription factor, has been considered as a downstream target of GSK-3β [25]. Nrf2 can bind to antioxidant response elements (Are) in the nucleus and activate the expression of antioxidant genes, such as heme oxygenase-1 (HO-1) and NADPH quinone oxidoreductase 1 (NQO1) [26,27]. Compared with control group, the mRNA expressions of Nrf2 (Figure 6B,F), HO-1 (Figure 6C,G), and NQO1 (Figure 6D,H) in hippocampus and kidney were significantly decreased in the vehicle group, which were reversed by fucoidan treatment.



**Figure 5.** Effects of fucoidan on oxidative indexes in adenine-induced CKD mice. (A–C) The expression level of MDA and activities of SOD and GSH-Px were measured in mice hippocampus. (D–F) The expression level of MDA and activities of SOD and GSH-Px were measured in mice kidney. The data are expressed as mean  $\pm$  SEM ( $n = 6-10$ ). \*  $p < 0.05$ , \*\*  $p < 0.01$ , and \*\*\*  $p < 0.001$  vs. vehicle group (Veh), one-way ANOVA post hoc Dunnett’s test.

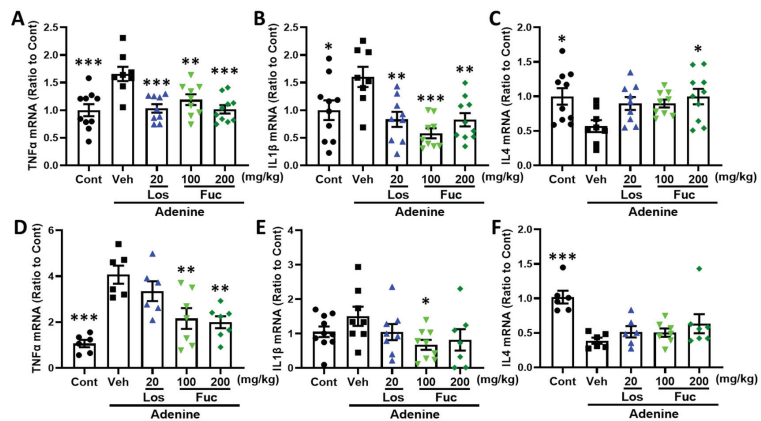


**Figure 6.** Fucoidan regulated GSK3 $\beta$ -Nrf2-HO-1 signaling pathway in hippocampus and kidney of adenine-induced CKD mice ( $n = 8$ ). (A–D) The mRNA expression of GSK3 $\beta$ , Nrf2, HO-1, and NQO-1 in the hippocampus. (E–H) The mRNA expression of GSK3 $\beta$ , Nrf2, HO-1, and NQO-1 in the kidney. \*  $p < 0.05$ , \*\*  $p < 0.01$ , and \*\*\*  $p < 0.001$  vs. vehicle group (Veh), one-way ANOVA post hoc Dunnett’s test.

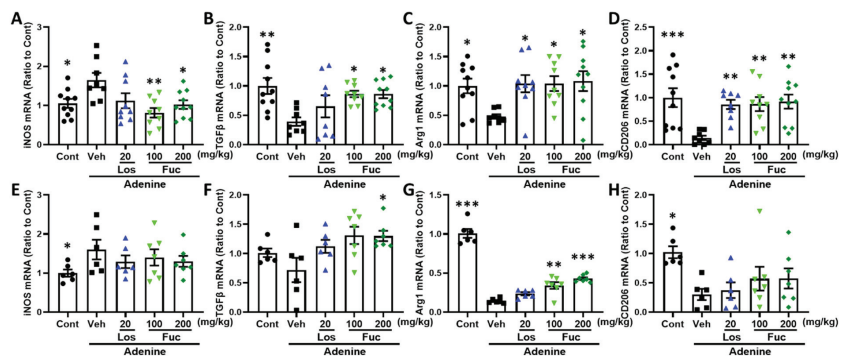
### 2.5. Fucoidan Inhibited Inflammatory Response in Adenine-Induced CKD Mice

We investigated whether fucoidan regulated the release of pro-inflammatory cytokines. As a result, fucoidan significantly inhibited the mRNA expression of TNF- $\alpha$

(Figure 7A,D) and IL-1 $\beta$  (Figure 7B,E) and promoted the mRNA expression of anti-inflammatory cytokine IL4 (Figure 7C,F) in the hippocampus and kidney of adenine-induced CKD mice. Reports have shown that the pro-inflammatory cytokines were regulated via microglial/macrophage polarization [28]. CD11b and inducible nitric oxide synthase (iNOS) are mainly expressed markers in M1 microglia/macrophage, while arginase 1, TGF $\beta$ , and CD206 are expressed in M2 microglia/macrophage [29]. The results convinced that fucoidan downregulated M1 microglia/macrophage-related mRNA expression of iNOS (Figure 8A,E), and on the contrary, fucoidan upregulated M2 microglia/macrophage-related mRNA expression of TGF $\beta$  (Figure 8B,F), Arg1 (Figure 8C,G), and CD206 (Figure 8D,H) in the hippocampus and kidney, respectively.



**Figure 7.** Effects of fucoidan on inflammatory factors in hippocampus and kidney of adenine-induced CKD mice ( $n = 6-10$ ). (A–C) TNF $\alpha$ , IL-1 $\beta$ , and IL-4 mRNA expression in the hippocampus; (D–F) TNF $\alpha$ , IL-1 $\beta$ , and IL-4 mRNA expression in the kidney. \*  $p < 0.05$ , \*\*  $p < 0.01$ , and \*\*\*  $p < 0.001$  vs. vehicle group (Veh), one-way ANOVA post hoc Dunnett’s test.

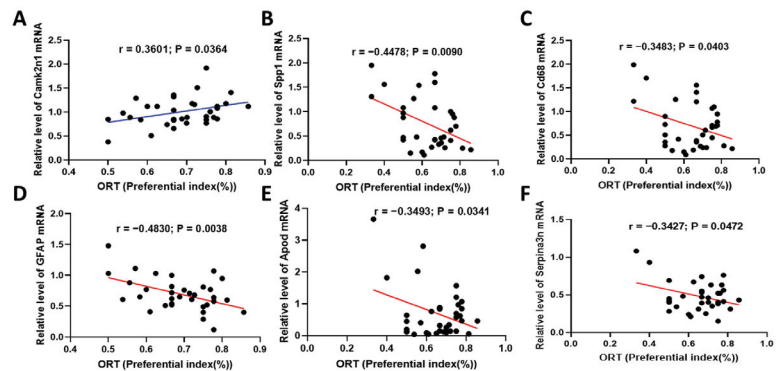


**Figure 8.** Effects of fucoidan on M1/M2 microglia or macrophage polarization in hippocampus and kidney of adenine-induced CKD mice ( $n = 6-10$ ). (A–D) iNOS, TGF $\beta$ , Arg1, and CD206 mRNA expression in the hippocampus; (E–H) iNOS, TGF $\beta$ , Arg1, and CD206 mRNA expression in the kidney. \*  $p < 0.05$ , \*\*  $p < 0.01$ , and \*\*\*  $p < 0.001$  vs. vehicle group (Veh), one-way ANOVA post hoc Dunnett’s test.

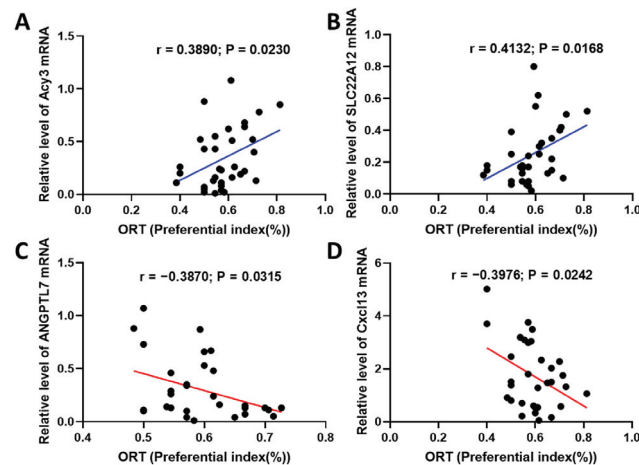
The results indicated that fucoidan exerts anti-inflammatory effects via inhibiting M1 microglial/macrophage polarization and promoting M2 microglial/macrophage polarization.

## 2.6. Fucoïdan Attenuated Cognitive-Behavior-Related Hallmarks in Adenine-Induced CKD Mice

To clarify the hallmarks involved in CKD-triggered memory deficits, we reanalyzed the differential genes between aged-CKD mice and young wild mice. In the brain, Alzheimer's disease and memory-related genes (Camk2n1, Apod, and Serpina3n), and immune-response-related genes (Spp1, CD68, GFAP, Mpeg, Ddx3y, Lyz2, CTSZ, Tyrobp, C4b, and C1qa), were selected for mRNA qPCR analysis in adenine-induced CKD mice. In the kidney, catalysis and metabolic-function-related genes (Acy3 and Angptl7), ion transporters (Slc22a12, Slco1a1, and Slc7a13), and immune-response-related genes (Cxcl13, Chd9, and Spp1) were investigated. The results were shown in Supplementary Figures S4 and S5, and the Pearson correlation analysis between gene expression and novel object recognition memory was performed. We found that the Camk2n1 gene in the hippocampus exerts obvious positive correlation with cognitive behavior (Figure 9), and SPP1, Cd68, GFAP, Apod, and Serpina3 exert negative correlation (Figure 9B–F). Additionally, Acy3 and Slc22a12 in the kidney showed positive correlation with cognitive behavior (Figure 10A,B), while Angptl7 and Cxcl13 presented negative correlation (Figure 10C,D). The other genes in the hippocampus and kidney were not correlated with cognitive memory (Supplementary Figures S6 and S7).



**Figure 9.** Pearson correlation analysis between hippocampus gene expression and cognitive behavior. The mRNA qPCR analysis of Camk2n1 (A), SPP1 (B), Cd68 (C), GFAP (D), Apod (E), and Serpina3 (F) were performed.



**Figure 10.** Pearson correlation analysis between kidney gene expression and cognitive behavior. The mRNA qPCR analysis of Acy3 (A), Slc22a12 (B), Angptl7 (C), and Cxcl13 (D) were performed.

### 3. Discussion

According to glomerular filtration rate (GFR), CKD is divided into five stages, among which end-stage renal disease (ESRD) appears directly associated with the risk of dementia [23,30]. Investigations suggested that uremic neurotoxins play crucial roles in CKD-associated mild cognitive impairment, uremic neurotoxins are harmful to the brain monoaminergic system, and that this system is involved in the altered sleep pattern commonly observed in patients with CKD [31]. Uremic neurotoxins enter the brain via the blood–brain barrier and cause oxidative stress and inflammation, as well as deteriorate neuronal cell damage. In addition, uremic neurotoxins amplify the dysregulation of sodium, potassium, and water channels in the kidney, accelerating their own accumulation and blood circulation [23]. The current therapies targeting cognitive improvement in CKD mainly include dialysis treatments and neuroinflammatory and nutritional interventions. Unfortunately, the partial clearance of blood toxins with hemodialysis, as well as the limited effects of nutritional intervention, seem unlikely to prevent or slow the progression of MCI to dementia, [31]. Fucoidan is a natural sulfated polysaccharide and has been proven to exert multiple functions, especially for renal protection. We found that fucoidan attenuates adenine-induced high expression of urea, uric acid, and serum creatinine, as reported by other groups. Nevertheless, it was the first report that fucoidan ameliorates CKD-triggered recognition memory and spatial memory deficits.

In the current study, a relatively high concentration of fucoidan was adopted; thus, the toxicity has become an issue that cannot be ignored. An acute toxic study of fucoidan from *Sargassum Wightii* grevillea in Wistar rats showed that a 2000 mg kg<sup>-1</sup> dose of fucoidan did not induce any remarkable toxic signs or mortality, while in the subacute toxicity study, except for a reduction of serum glucose and cholesterol, no significant changes of biochemical, hematological parameters, or toxic signs at organ levels were observed after daily oral administration of 100–400 mg kg<sup>-1</sup> fucoidan for 28 days [32]. The 28-day oral administration of low molecular weight of fucoidan (<667 Da) from *Laminaria japonica* up to 2000 mg kg<sup>-1</sup> caused no toxicological indications in Sprague–Dawley rats [33]. However, the 6-month treatment of fucoidan from *Laminaria japonica* at doses of 900 and 2500 mg kg<sup>-1</sup> significantly prolonged the clotting time [34]; the same phenomenon was observed after gavage of fucoidan from *Cladosiphon okamuranus* over 1200 mg kg<sup>-1</sup> for 3 months [35]. The aforementioned differential results indicate that the potential toxicity of fucoidan depends on the originated sources and doses, as well as the molecular weights. The safety of fucoidan was also evaluated in humans, and no changes in the liver and kidney parameters were observed after oral ingestion of 4.05 g per day of mozuku fucoidan derived from *Cladosiphon okamuranus* [36]. Our results indicated that 33-day oral administration of fucoidan (200 mg kg<sup>-1</sup>) did not affect the body weights and locomotor activity compared with the adenine-treated vehicle group. Nevertheless, the acute and subacute toxicity should be investigated in a future study. Losartan, an angiotensin II type 1 (AT1) receptor antagonist, was approved by the FDA in 1995 for hypertension and renal disease. Recently, losartan has been demonstrated to exert neurogenesis, astrocyte motility, and memory improvement effects in APP/PS1 AD model mice [37]. Losartan significantly improved memory function in 75–89-year-old elderly hypertensive patients [38]. Intriguingly, 30-day treatment of losartan led to a hypotension model in rats, and promoted dendritic spine loss, tau hyperphosphorylation, and memory deficits [39], indicating blood pressure as a considerable factor when taking losartan. Our study demonstrated that losartan (20 mg kg<sup>-1</sup>) treatment reversed adenine-induced memory deficits. Although a low dose of fucoidan (10 mg kg<sup>-1</sup>) in our parallel study showed memory attenuation in adenine-induced CKD mice (data not shown), a further investigation should be performed to compare the effect of fucoidan and losartan on cognitive function.

RNA sequencing analysis is an efficient way to explore possible signaling pathways. The GO annotation and enrichment analysis of significantly differential genes in naturally aging renal failure mice indicated that oxidation and inflammation were widely involved in both brain and kidney functional processes. Thus, oxidation and inflammation might

contribute to CKD-triggered cognitive deficits. Under the condition of continuous adenine treatment, the kidney defense system is disrupted, resulting in the decline of activities of a variety of antioxidant enzymes, such as SOD and GSH-Px. The low molecular weight fucoidan could enhance the activity of antioxidant enzymes and promote the decrease of lipid peroxidation, thus alleviating the symptom of CKD [40]. Nrf2 is released by oxidant stimulation and translocated into the nucleus, interacting with antioxidant response elements and inducing the transcription of downstream SOD, MDA, GSH, and other antioxidant enzyme genes to regulate the expression of antioxidant enzymes. Furthermore, Nrf2 regulated oxidative stress via activating downstream antioxidant proteins, such as HO-1 and NQO1 [41]. Reports have shown that fucoidan attenuated oxidative stress by regulating the gene expression of HO-1 and SOD-1 via the Nrf2 signaling pathway in HaCaT cells [42]. In the current study, we found that fucoidan can improve the activities of SOD and GSH-Px in the kidney and hippocampus and reduce the content of MDA. In addition, our results suggested that fucoidan protected tissue against adenine-induced injury through downregulation of GSK-3 $\beta$  and activation of the Nrf2-HO-1 signaling-pathway-mediated antioxidant responses. Another report evidenced that the possible anti-inflammatory mechanism of fucoidan is the downregulation of MAPK and NF- $\kappa$ B signaling pathways and the following reduction of pro-inflammatory cytokines [43]. Our results indicated that fucoidan significantly inhibited M1 microglia-related mRNA expression of TNF- $\alpha$ , IL-1 $\beta$ , and iNOS, and on the contrary, fucoidan upregulated M2 microglia-related mRNA expression of IL4, CD206, Arg1, and TGF $\beta$ . Therefore, we concluded that fucoidan exerts anti-inflammatory effects probably by via inhibiting M1 and promoting M2 microglial polarization.

Reports have shown that the antioxidant and anti-inflammatory activity of fucoidan is dependent on its composition and molecular weight. The higher the content of sulfated polysaccharides and phenolics, the more increased the activity of radical scavenging and antioxidation was observed [44]. In addition, ROS is difficult to be scavenged by fucose, but easy to react with galactose, mannose, and uronic acid, cleave glycosidic bonds, and oxidize uronic acid. Thus, fucoidan removes ROS possibly via reduction reaction [45]. The effect of fucoidan molecular weight on antioxidant activity is controversial. Qi et al. investigated the antioxidant function of fucoidan with different molecular weights (151.7, 64.5, 58.0, and 28.2 kDa) derived from *Ulva pertusa* Kjellm, and found that low molecular weight fucoidan showed significant inhibition on O<sub>2</sub><sup>-</sup> and OH [46]. Another study indicated that the relationship between fucoidan molecular weights and their antioxidant activities is not simply linear. The fucoidans with 3.8 kDa, 1.0 kDa, and >8.3 kDa have better hydroxyl radical scavenging activity and antioxidant activity [47]. The anti-inflammatory effects of fucoidan were dramatically increased with a corresponding decrease in molecular mass and increase of the sulfate content [48]. The fucoidan with 5–30 kDa from *Macrocystis pyrifera* showed a highly effective cytokine (TNF- $\alpha$ , IL-1 $\beta$ , and IL-6) inhibition at lower concentrations in LPS-stimulated PBMCs and human THP-1 cells [49]. The antioxidant and anti-inflammatory effects of fucoidan in this study are probably due to the high contents of sulfates and mannose.

In order to explore the hallmarks of memory impairment induced by renal injury, we reanalyzed the genes with large differences in the transcriptome analysis for qPCR analysis, and Pearson correlation with behavior was performed. Camk2n1 and Camk2n2 are endogenous inhibitors of calcium/calmodulin-dependent protein kinase II (CaMKII), a key synaptic signaling molecule for learning and memory [50], which is positively correlated with learning and memory ability. Pro-inflammatory phenotype microglia were polarized via Apod-mediated NLR4 inflammasome activation, and targeting microglial Apod promoted neural stem cell self-renewal and inhibited neuronal apoptosis [51]. The expression levels of Cd68 and Atp5b were significantly correlated with the neurofibrillary tangle burden in the AD brain and with cognitive ability [52]. Astrocyte-secreted GFAP is regarded as a marker of astrocytosis in neurodegeneration associated with neurological disorders [53,54]. Histological studies showed that activated astrocytes were located in



neuroinflammatory amyloid plaques, and a large number of astrocytes were observed near neurofibrillary tangles in autopsy specimens of AD patients [55]. Serpina3 is a serine protease inhibitor and an acute phase protein commonly associated with amyloid deposits in AD brains [56]. Osteopontin (SPP1) is a multifunctional matricellular glycoprotein, and it is notably upregulated during the inflammation associated with Alzheimer's disease and other neurodegenerative conditions [57]. In the Person correlation analysis, the aforementioned genes *Apod*, *Cd68*, *GFAP*, *Serpina3*, and *SPP1* were negatively correlated with cognitive behavior.

The differential genes in kidneys between normal mice and CKD mice were also analyzed by Person correlation analysis with cognition. *Cxcl13* is a ligand of *CXCR5*, and it is significantly secreted under inflammatory conditions [58]. Reports have indicated that the autocrine and paracrine activities of the *ANGPTL* protein family are associated with angiogenesis and inflammation; one of the members, *Angpt7*, promotes inflammation by regulating the expression of genes encoding inflammation-associated factors cyclooxygenase-2 (*COX-2*), inducible nitric oxide synthase (*iNOS*), tumor necrosis factor alpha (*TNF- $\alpha$* ), interleukin-1 beta (*IL-1 $\beta$* ), *IL-6*, and transforming growth factor beta 1 (*TGF- $\beta$ 1*) in macrophages [59]. We found that the expressions of *Angpt7* and *Cxcl13* in the kidney were negatively correlated with cognitive behavior, while the genes expressed in the kidney, such as *Slc22a12* and *Acy3*, are positively correlated with behavior. *hURAT1* (*Slc22a12*) is a transporter responsible for renal urate reabsorption; renal hypouricemia will occur in patients with abnormalities in the *hURAT1* gene [60]. In kidney proximal tubules, aminoacylase III (*Acy3*) plays an important role in deacetylating mercapturic acids, and the predominant cytoplasmic localization of *Acy3* may explain the greater sensitivity of the proximal straight tubule to the nephrotoxicity of mercapturic acids [61].

## 4. Materials and Methods

### 4.1. Materials

Fucoidan from *Laminaria japonica* with an average molecular weight of 242 kDa was purchased from Yuanye Biotech Co., Ltd., (Shanghai, China). The carbohydrates of fucoidan were composed of L-fucose (85.4 mol%), D-mannose (2.3 mol%), D-glucuronic acid (3.3 mol%), D-glucose (1.3 mol%), D-xylose (5.8 mol%), and L-Rhamnose (1.9 mol%), as evidenced by high-performance liquid chromatography (HPLC). The content of total sugar was determined as  $86.9 \pm 2.7\%$ , and  $38.9 \pm 0.4\%$  of sulfate residues were contained; the detected methods referred to previous report [44]. Adenine (Sigma-A8626) was purchased from Sigma-Aldrich, and losartan potassium tablets were produced from Merck Sharp & Dohme Limited (U.K.). Fucoidan and losartan were dissolved in saline and stored at concentrations of 10, 20, and 2 mg ml<sup>-1</sup>, respectively.

### 4.2. Animals and Experimental Procedure

All animal care and experimental schemes were carried out in accordance with the guidelines of Animal Experiment Committee of Guangdong Ocean University (SYXK2020-0021). ICR mice (male,  $34 \pm 2$  g, 8 weeks old) were purchased from Guangdong Zhiyuan Biomedical Technology Co., Ltd. (Guangzhou, China). The animals were placed in a specific environment (with 12 h of light/dark cycle starting at 7:00 a.m., temperature  $22 \pm 1$  °C, and humidity  $55\% \pm 10\%$ ). During the experiment, the animals were fed with powdered SPF grade maintenance rat feed (purchased from Guangdong Medical Experimental Animal Center) and purified water.

The mice were maintained for 7 days before experiment to adapt to the environment, and were randomly divided into 5 groups ( $n = 15$  per group), including a control group (saline), vehicle group (saline), low dose of fucoidan group ( $100 \text{ mg kg}^{-1} \text{ d}^{-1}$ , dissolved in saline), high dose of fucoidan group ( $200 \text{ mg kg}^{-1} \text{ d}^{-1}$ , dissolved in saline), and losartan group (Los, positive control,  $20 \text{ mg kg}^{-1} \text{ d}^{-1}$ , dissolved in saline). Mice in the control group were gavaged with saline and a common feed for 33 days, while mice in vehicle group were oral administered with saline and a diet containing 0.25% adenine. The drug-treated

groups were simultaneously gavaged with fucoidan (100 and 200 mg kg<sup>-1</sup> d<sup>-1</sup>) or losartan (20 mg kg<sup>-1</sup> d<sup>-1</sup>) and a diet containing 0.25% adenine. The dose of adenine was selected on the basis of previous reports in the literature [62]. To determine the administered doses of fucoidan, we investigated a large number of published literatures, and the dosages ranged from 10 to 500 mg kg<sup>-1</sup> d<sup>-1</sup>. The dosage of fucoidan in the current study was determined based on a previous report [40]. After a 4-week treatment, the behavioral experiments were performed (continual intragastric administration of the drugs during the behavioral experiment) in the following order: open field experiment, object recognition test, object location test, and passive avoidance test, on day 27, 28, 30, 32, respectively. After the behavioral test, the animals were anesthetized with chloral hydrate, the urine and serum of mice were collected, kidneys (drained and weighed) and hippocampus were taken and stored at −80 °C for subsequent experiments.

#### 4.3. Behavioral Test

The open field test is used for evaluating the autonomous behavior, exploratory behavior, and anxiety of experimental animals in novel environments. The experimental method referred to a previous method with minor modification [20]. The object recognition test and object location test were established according to the principle that an animal possesses an innate tendency to explore new objects or novel located objects. The experiments were performed as described previously with minor modification [20]. In the passive avoidance test, the box was divided into a light and dark zone. In the training trial, each mouse was allowed to move freely between the two zones for 1 min and received an electric shock (0.5 mA, 3 s) as soon as it entered the dark zone. The test trial was performed with a 24 h interval, the time of the first electric shock (step-through latency) and the number of electric shocks (number of errors) were recorded within 300 s. The experimental method referred to a previous report with partially modification [63].

#### 4.4. Measurement of Urea, Uric Acid, and Creatinine

The blood was naturally coagulated at room temperature for 10–20 min, and the urine was collected with sterile tube, the samples were centrifuged for 20 min (1000 g), and the supernatant was carefully collected. Creatinine (Cr), urea, and uric acid (UA) were quantified using ELISA kit (MEIMIAN, Jiangsu, China) according to manufacturer's instructions. The absorbances were measured using an ELISA microplate reader (Biotek, Winooski, VT, USA).

#### 4.5. RNA-Seq Analysis

The total mRNA was extracted from kidney and hippocampus using the RNA-easy Isolation Reagent following the manufacturer's protocol. The integrity of RNA samples and DNA contamination and the purity of RNA were determined by agarose gel electrophoresis, NanoPhotometer spectrophotometer, and Agilent 2100 bioanalyzer, respectively, to ensure the sequencing of qualified samples. The gene expression difference was analyzed by software ( $p < 0.05$ ). In order to explore the mechanism of fucoidan in improving memory impairment caused by renal injury, transcriptomic analysis was carried out in brain and kidney tissues of naturally aging model mice (male, 24-month-old) and young mice (male, 3-month-old). DAVID software was used for GO (Gene Ontology) functional annotation and enrichment analysis of significantly different genes obtained by transcriptome analysis.

#### 4.6. ELISA Analysis of MDA, SOD, and GSH-Px

After the behavioral experiment, the hippocampus and kidney were made into 10% homogenate with cold saline, and the supernatant after centrifugation was collected to determine the content of MDA, SOD, and GSH-Px activity. The levels of SOD and MDA were evaluated using commercial kits (Nanjing Jiancheng Bioengineering Institute, Nanjing, China) and the GSH-Px was measured by ELISA kits (MEIMIAN, YanCheng, China)

according to the manufacturer's instructions. Finally, the absorbance was measured at 450 nm using a microplate spectrophotometer (Biotek, Winooski, VT, USA).

#### 4.7. RNA Isolation and RT-qPCR Analysis

The total mRNA was extracted from kidney and hippocampus using the RNA-easy Isolation Reagent following the manufacturer's protocol. cDNA was synthesized from 1 µg total RNA using a HiScript II Q Select RT SuperMix for qPCR (+gDNA wiper) kit. PCR amplifications were performed on a CFX96Touch™ Real-Time PCR Detection System using ChamQ Universal SYBR qPCR Master Mix kit at conditions of initial activation at 95 °C for 30 s, followed by 40 cycles of amplification (95 °C for 5 s, 60 °C for 30 s). Gene expression levels were normalized to the RNA expression of housekeeping gene  $\beta$ -Actin. Fold change was calculated using the  $2^{-\Delta\Delta C_t}$  method. The amplification primers for genes are summarized in Supplementary Table S1.

#### 4.8. Statistical Analysis

All data are presented as mean  $\pm$  SEM. Statistical analysis was performed using Graph-Pad Prism 9. Statistical comparisons were performed using one- or two-way analysis of variance (ANOVA).  $p < 0.05$  was considered as statistically significant. In addition, Pearson correlation analysis was used to analyze the relationship between kidney/hippocampus gene levels and object recognition memory. All correlation statistical analyses were performed by SPSS 22.0.

### 5. Conclusions

The present study first clarified that fucoidan alleviated CKD-triggered memory deficits. GSK3 $\beta$ -Nrf2-HO-1 mediated oxidative signaling and the microglial/macrophage polarization-related inflammatory pathway are likely involved in adenine-induced kidney injury and memory deficits, and are reversed by fucoidan treatment. Additionally, four kidney genes, *Acy3*, *Slc22a12*, *Angpt7*, and *Cxcl13*, are clarified as hallmarks involved in CKD-triggered memory deficits. This work contributes to reveal the mechanism and new treatment direction of cognitive impairment in patients with CKD and provide an experimental basis for the development of fucoidan as a regulator of CKD-triggered memory deficits.

**Supplementary Materials:** The following supporting information can be downloaded at: <https://www.mdpi.com/article/10.3390/md20040258/s1>, Figure S1: Volcano map of differential genes in the brain and kidney of CKD mice; Figure S2: Effects of fucoidan (Fuc) on adenine-induced mRNA expression of differential genes in hippocampus; Figure S3: Effects of fucoidan (Fuc) on adenine-induced mRNA expression of differential genes in kidney; Figure S4: Pearson correlation analysis between hippocampus gene expression and cognitive behavior; Figure S5: Pearson correlation analysis between kidney gene expression and cognitive behavior; Table S1: Design of amplification primers for genes related to oxidative damage and inflammatory factors in epigenetic kidney and hippocampus.

**Author Contributions:** Conceptualization, Z.Y. and Z.M.; methodology, Z.Y. and C.S.; software, Z.M. and Y.Z. (Yongping Zhang); validation, X.F., J.D. and C.H.; formal analysis, Z.M. and Y.Z. (Yongping Zhang); investigation, Z.Y., Y.Z. (Yuntao Zhao), Y.G. and Z.M.; resources, R.L.; data curation, Z.M.; writing—original draft preparation, Z.M. and Z.Y.; writing—review and editing, Z.Y.; visualization, Z.M. and Z.Y.; supervision, Z.Y.; project administration, Z.Y.; funding acquisition, Z.Y. and S.Z. All authors have read and agreed to the published version of the manuscript.

**Funding:** This research was funded by the National Natural Science Foundation of China (grant number 81803753), Special Funds for Science and Technology Development of Zhanjiang City (grant number 2018A01046), Natural Science Foundation of Guangdong Province of China (grant number 2020A1515010779), Scientific Research Foundation of Guangdong Ocean University (grant number R19035), and The Innovative Team Program of High Education of Guangdong Province (2021KCXTD021).

**Institutional Review Board Statement:** The animal study protocol was approved by the Ethics Committee of Guangdong Ocean University (protocol code SYXK20200021 and date of approval 2020-01-15).

**Informed Consent Statement:** Not applicable.

**Data Availability Statement:** Not applicable.

**Conflicts of Interest:** The authors declare no conflict of interest.

## References

- Couser, W.G.; Remuzzi, G.; Mendis, S.; Tonelli, M. The contribution of chronic kidney disease to the global burden of major noncommunicable diseases. *Kidney Int.* **2012**, *80*, 1258–1270. [[CrossRef](#)] [[PubMed](#)]
- Zhang, L.; Wang, F.; Wang, L.; Wang, W.; Liu, B.; Liu, J.; Chen, M.; He, Q.; Liao, Y.; Yu, X.; et al. Prevalence of chronic kidney disease in China: A cross-sectional survey. *Lancet* **2012**, *379*, 815–822. [[CrossRef](#)]
- McQuillan, R.; Jassal, S.V. Neuropsychiatric complications of chronic kidney disease. *Nat. Rev. Nephrol.* **2010**, *6*, 471–479. [[CrossRef](#)] [[PubMed](#)]
- Chang, C.Y.; Lin, C.C.; Tsai, C.F.; Yang, W.C.; Wang, S.J.; Lin, F.H.; Fuh, J.L. Cognitive impairment and hippocampal atrophy in chronic kidney disease. *Acta Neurol. Scand.* **2017**, *136*, 477–485. [[CrossRef](#)]
- Hooper, S.R.; Gerson, A.C.; Butler, R.W.; Gipson, D.S.; Mendley, S.R.; Lande, M.B.; Shinnar, S.; Wentz, A.; Matheson, M.; Cox, C. Neurocognitive functioning of children and adolescents with mild-to-moderate chronic kidney disease. *Clin. J. Am. Soc. Nephrol.* **2011**, *6*, 1824–1830. [[CrossRef](#)]
- Elias, M.F.; Elias, P.K.; Seliger, S.L.; Narsipur, S.S.; Dore, G.A.; Robbins, M.A. Chronic kidney disease, creatinine and cognitive functioning. *Nephrol. Dial. Transplant.* **2009**, *24*, 2446–2452. [[CrossRef](#)]
- Seliger, S.L.; Weiner, D.E. Cognitive impairment in dialysis patients: Focus on the blood vessels? *Am. J. Kidney Dis.* **2013**, *61*, 187–190. [[CrossRef](#)]
- Kim, S.K.; Wijesekara, I. Development and biological activities of marine-derived bioactive peptides: A review. *J. Funct. Foods.* **2010**, *2*, 1–9. [[CrossRef](#)]
- Davis, T.A.; Volesky, B.; Mucci, A. A review of the biochemistry of heavy metal biosorption by brown algae. *Water Res.* **2003**, *37*, 4311–4330. [[CrossRef](#)]
- Souza, B.; Cerqueira, M.A.; Bourbon, A.I.; Pinheiro, A.C.; Martins, J.T.; Teixeira, J.A.; Coimbra, M.A.; Vicente, A.A. Chemical characterization and antioxidant activity of sulfated polysaccharide from the red seaweed *Gracilaria birdiae*. *Food Hydrocoll.* **2012**, *27*, 287–292. [[CrossRef](#)]
- Van Weelden, G.; Bobiński, M.; Okła, K.; van Weelden, W.J.; Romano, A.; Pijnenborg, J.M.A. Fucoidan structure and activity in relation to anti-cancer mechanisms. *Mar. Drugs* **2019**, *17*, 32. [[CrossRef](#)] [[PubMed](#)]
- Yang, Z.; Ma, Z.; Zhang, Y.; Song, C.; Hu, X. Protective effect of fucoidan on A $\beta$ 25–35-induced neuronal injury and neurite atrophy. *J. Guangdong Ocean. U.* **2021**, *41*, 77–83.
- Zhang, D.; Liu, H.; Luo, P.; Li, Y. Production inhibition and excretion promotion of urate by fucoidan from *Laminaria japonica* in adenine-induced hyperuricemic mice. *Mar. Drugs* **2018**, *16*, 472. [[CrossRef](#)] [[PubMed](#)]
- Liu, B.H.; Chong, F.L.; Yuan, C.C.; Liu, Y.L.; Yang, H.M.; Wang, W.W.; Fang, Q.J.; Wu, W.; Wang, M.Z.; Tu, Y.; et al. Fucoidan ameliorates renal injury-related calcium-phosphorus metabolic disorder and bone abnormality in the CKD-MBD model rats by targeting FGF23-klotho signaling axis. *Front. Pharmacol.* **2021**, *11*, 586725. [[CrossRef](#)] [[PubMed](#)]
- Chen, J.; Cui, W.; Zhang, Q.; Jia, Y.; Sun, Y.; Weng, L.; Luo, D.; Zhou, H.; Yang, B. Low molecular weight fucoidan ameliorates diabetic nephropathy via inhibiting epithelial-mesenchymal transition and fibrotic processes. *Am. J. Transl. Res.* **2015**, *7*, 1553–1563. [[PubMed](#)]
- Wang, J.; Liu, H.; Li, N.; Zhang, Q.; Zhang, H. The protective effect of fucoidan in rats with streptozotocin-induced diabetic nephropathy. *Mar. Drugs* **2014**, *12*, 3292–3306. [[CrossRef](#)]
- Jia, T.; Olason, H.; Lindberg, K.; Amin, R.; Edvardsson, K.; Lindholm, B.; Andersson, G.; Wernerson, A.; Sabbagh, Y.; Schiavi, S.; et al. A novel model of adenine-induced tubulointerstitial nephropathy in mice. *BMC Nephrol.* **2013**, *14*, 116. [[CrossRef](#)]
- Han, B.; Gong, M.; Li, Z.; Qiu, Y.; Zou, Z. NMR-based metabolomic study reveals intervention effects of polydatin on potassium oxonate-induced hyperuricemia in rats. *Oxid. Med. Cell Longev.* **2020**, *2020*, 6943860. [[CrossRef](#)]
- Huang, Z.; He, L.; Huang, D.; Lei, S.; Gao, J. Icaritin protects rats against 5/6 nephrectomy-induced chronic kidney failure by increasing the number of renal stem cells. *BMC Complement. Altern. Med.* **2015**, *15*, 378. [[CrossRef](#)]
- Yang, Z.Y.; Zhang, C.; Li, X.H.; Ma, Z.H.; Ge, Y.W.; Qian, Z.J.; Song, C. Heterophyllin B, a cyclopeptide from *Pseudostellaria heterophylla*, enhances cognitive function via neurite outgrowth and synaptic plasticity. *Phytother. Res.* **2021**, *35*, 5318–5329. [[CrossRef](#)]
- Daenen, K.; Andries, A.; Mekahli, D.; Van Schepdael, A.; Jouret, F.; Bammens, B. Oxidative stress in chronic kidney disease. *Pediatr. Nephrol.* **2019**, *34*, 975–991. [[CrossRef](#)] [[PubMed](#)]
- Uddin, M.J.; Kim, E.H.; Hannan, M.A.; Ha, H. Pharmacotherapy against oxidative stress in chronic kidney disease: Promising small molecule natural products targeting Nrf2-HO-1 signaling. *Antioxidants* **2021**, *10*, 258. [[CrossRef](#)] [[PubMed](#)]

23. Lu, R.; Kiernan, M.C.; Murray, A.; Rosner, M.H.; Ronco, C. Kidney-brain crosstalk in the acute and chronic setting. *Nat. Rev. Nephrol.* **2015**, *11*, 707–719. [[CrossRef](#)] [[PubMed](#)]
24. Sagoo, M.K.; Gnudi, L. Diabetic nephropathy: Is there a role for oxidative stress? *Free Radic. Biol. Med.* **2018**, *116*, 50–63. [[CrossRef](#)] [[PubMed](#)]
25. Cuadrado, A. Structural and functional characterization of Nrf2 degradation by glycogen synthase kinase 3 $\beta$ /TrCP. *Free Radic. Biol. Med.* **2015**, *88*, 147–157. [[CrossRef](#)] [[PubMed](#)]
26. Satoh, T.; Okamoto, S.I.; Cui, J.; Watanabe, Y.; Furuta, K.; Suzuki, M.; Tohyama, K.; Lipton, S.A. Activation of the Keap1/Nrf2 pathway for neuroprotection by electrophilic [correction of electrophillic] phase II inducers. *Proc. Natl. Acad. Sci. USA* **2006**, *103*, 768–773. [[CrossRef](#)]
27. Duan, Q.; Sun, W.; Yuan, H.; Mu, X. MicroRNA-135b-5p prevents oxygen-glucose deprivation and reoxygenation-induced neuronal injury through regulation of the GSK-3 $\beta$ /Nrf2/ARE signaling pathway. *Arch. Med. Sci.* **2018**, *14*, 735–744. [[CrossRef](#)]
28. Yang, Z.; Kuboyama, T.; Tohda, C. Naringenin promotes microglial M2 polarization and A $\beta$  degradation enzyme expression. *Phytother. Res.* **2019**, *33*, 1114–1121. [[CrossRef](#)]
29. Chen, L.; Deng, H.; Cui, H.; Fang, J.; Zuo, Z.; Deng, J.; Li, Y.; Wang, X.; Zhao, L. Inflammatory responses and inflammation-associated diseases in organs. *Oncotarget* **2018**, *9*, 7204–7218. [[CrossRef](#)]
30. Kuo, Y.T.; Li, C.Y.; Sung, J.M.; Chang, C.C.; Wang, J.D.; Sun, C.Y.; Wu, J.L.; Chang, Y.T. Risk of dementia in patients with end-stage renal disease under maintenance dialysis—a nationwide population-based study with consideration of competing risk of mortality. *Alzheimers Res. Ther.* **2019**, *11*, 31. [[CrossRef](#)]
31. Viggiano, D.; Wagner, C.A.; Martino, G.; Nedergaard, M.; Zoccali, C.; Unwin, R.; Capasso, G. Mechanisms of cognitive dysfunction in CKD. *Nat. Rev. Nephrol.* **2020**, *16*, 452–469. [[CrossRef](#)] [[PubMed](#)]
32. Ramu, S.; Murali, A.; Narasimhaiah, G.; Jayaraman, A. Toxicological evaluation of *Sargassum Wightii* greville derived fucoidan in wistar rats: Haematological, biochemical and histopathological evidences. *Toxicol. Rep.* **2020**, *7*, 874–882. [[CrossRef](#)] [[PubMed](#)]
33. Hwang, P.A.; Yan, M.D.; Lin, H.T.; Li, K.L.; Lin, Y.C. Toxicological evaluation of low molecular weight fucoidan in vitro and in vivo. *Mar. Drugs* **2016**, *14*, 121. [[CrossRef](#)] [[PubMed](#)]
34. Li, N.; Zhang, Q.; Song, J. Toxicological evaluation of fucoidan extracted from *Laminaria japonica* in Wistar rats. *Food Chem. Toxicol.* **2005**, *43*, 421–426. [[CrossRef](#)] [[PubMed](#)]
35. Gideon, T.P.; Rengasamy, R. Toxicological evaluation of fucoidan from *Cladosiphon okamuranus*. *J. Med. Food* **2008**, *11*, 638–642. [[CrossRef](#)]
36. Citkowska, A.; Szekalska, M.; Winnicka, K. Possibilities of fucoidan utilization in the development of pharmaceutical dosage forms. *Mar. Drugs* **2019**, *17*, 458. [[CrossRef](#)]
37. Drews, H.J.; Klein, R.; Lourhmati, A.; Buadze, M.; Schaeffeler, E.; Lang, T.; Seferyan, T.; Hanson, L.R.; Frey, W.H.; de Vries, T.C.G.M.; et al. Losartan improves memory, neurogenesis and cell motility in transgenic Alzheimer's mice. *Pharmaceuticals* **2021**, *14*, 166. [[CrossRef](#)]
38. Fogari, R.; Mugellini, A.; Zoppi, A.; Derosa, G.; Pasotti, C.; Fogari, E.; Preti, P. Influence of losartan and atenolol on memory function in very elderly hypertensive patients. *J. Hum. Hypertens.* **2003**, *17*, 781–785. [[CrossRef](#)]
39. Liu, X.; Wang, Z.; Xia, Y.; Yu, G.; Zeng, K.; Luo, H.; Hu, J.; Gong, C.X.; Wang, J.Z.; Zhou, X.W.; et al. Losartan-induced hypotension leads to tau hyperphosphorylation and memory deficit. *J. Alzheimers Dis.* **2014**, *40*, 419–427. [[CrossRef](#)]
40. Wang, J.; Zhang, Q.B.; Jin, W.H.; Niu, X.Z.; Zhang, H. Effects and mechanism of low molecular weight fucoidan in mitigating the peroxidative and renal damage induced by adenine. *Carbohydr. Polym.* **2011**, *84*, 417–423. [[CrossRef](#)]
41. Dong, H.; Xue, T.; Liu, Y.; He, S.; Yi, Y.; Zhang, B.; Xin, J.; Wang, Z.; Li, X. Low molecular weight fucoidan inhibits pulmonary fibrosis in vivo and in vitro via antioxidant activity. *Oxid. Med. Cell Longev.* **2022**, *2022*, 7038834. [[CrossRef](#)] [[PubMed](#)]
42. Ryu, M.J.; Chung, H.S. Fucoidan reduces oxidative stress by regulating the gene expression of HO-1 and SOD-1 through the Nrf2/ERK signaling pathway in HaCaT cells. *Mol. Med. Rep.* **2016**, *14*, 3255–3260. [[CrossRef](#)] [[PubMed](#)]
43. Apostolova, E.; Lukova, P.; Baldzhieva, A.; Katsarov, P.; Nikolova, M.; Iliev, I.; Peychev, L.; Trica, B.; Oancea, F.; Delattre, C.; et al. Immunomodulatory and Anti-inflammatory effects of fucoidan: A review. *Polymers* **2020**, *12*, 2338. [[CrossRef](#)] [[PubMed](#)]
44. Pozharitskaya, O.N.; Obluchinskaya, E.D.; Shikov, A.N. Mechanisms of bioactivities of Fucoidan from the brown seaweed *Fucus vesiculosus* L. of the barents sea. *Mar. Drugs* **2020**, *18*, 275. [[CrossRef](#)] [[PubMed](#)]
45. Zhao, X.; Xue, C.H.; Li, B.F. Study of antioxidant activities of sulfated polysaccharides from *Laminaria japonica*. *J. Appl. Phycol.* **2008**, *20*, 431–436. [[CrossRef](#)]
46. Qi, H.M.; Zhao, T.T.; Zhang, Q.B.; Li, Z.E.; Zhao, Z.Q.; Xing, R.E. Antioxidant activity of different molecular weight sulfated polysaccharides from *Ulva pertusa kjellm* (chlorophyta). *J. Appl. Phycol.* **2005**, *17*, 527–534. [[CrossRef](#)]
47. Hou, X.; Wang, J.; Jin, W.H.; Zhang, H.; Zhang, Q.B. Degradation of *Laminaria japonica* fucoidan by hydrogen peroxide and antioxidant activities of the degradation products of different molecular weights. *Carbohydr. Polym.* **2012**, *87*, 153–159. [[CrossRef](#)]
48. Chen, C.Y.; Wang, S.H.; Huang, C.Y.; Dong, C.D.; Huang, C.Y.; Chang, C.C.; Chang, J.S. Effect of molecular mass and sulfate content of fucoidan from *Sargassum siliquosum* on antioxidant, anti-lipogenesis, and anti-inflammatory activity. *J. Biosci. Bioeng.* **2021**, *132*, 359–364. [[CrossRef](#)]
49. Ahmad, T.; Eapen, M.S.; Ishaq, M.; Park, A.Y.; Karpiniec, S.S.; Stringer, D.N.; Sohal, S.S.; Fitton, J.H.; Guven, N.; Caruso, V.; et al. Anti-inflammatory activity of fucoidan extracts in vitro. *Mar. Drugs* **2021**, *19*, 702. [[CrossRef](#)]

50. Vigil, F.A.; Mizuno, K.; Lucchesi, W.; Valls-Comamala, V.; Giese, K.P. Prevention of long-term memory loss after retrieval by an endogenous CaMKII inhibitor. *Sci. Rep.* **2017**, *7*, 4040. [[CrossRef](#)]
51. Yu, Y.L.; Lv, J.Z.; Ma, D.; Han, Y.; Wang, Z.T. Microglial ApoD induced NLRP4 inflammasome activation promotes Alzheimer's disease progression. *Res. Sq.* **2021**. *Preprint*.
52. Wang, E.; Zhu, H.; Wang, X.; Gower, A.C.; Wallack, M.; Blusztajn, J.K.; Kowall, N.; Qiu, W.Q. Amylin treatment reduces neuroinflammation and ameliorates abnormal patterns of gene expression in the cerebral cortex of an Alzheimer's disease mouse model. *J. Alzheimers Dis.* **2017**, *56*, 47–61. [[CrossRef](#)] [[PubMed](#)]
53. Ishiki, A.; Kamada, M.; Kawamura, Y.; Terao, C.; Shimoda, F.; Tomita, N.; Arai, H.; Furukawa, K. Glial fibrillar acidic protein in the cerebrospinal fluid of Alzheimer's disease, dementia with Lewy bodies, and frontotemporal lobar degeneration. *J. Neurochem.* **2016**, *136*, 258–261. [[CrossRef](#)] [[PubMed](#)]
54. Oeckl, P.; Halbgebauer, S.; Anderl-Straub, S.; Steinacker, P.; Huss, A.M.; Neugebauer, H.; von Arnim, C.A.F.; Diehl-Schmid, J.; Grimmer, T.; Kornhuber, J. Glial fibrillary acidic protein in serum is increased in Alzheimer's disease and correlates with cognitive impairment. *J. Alzheimers Dis.* **2019**, *67*, 481–488. [[CrossRef](#)] [[PubMed](#)]
55. Colangelo, A.M.; Alberghina, L.; Papa, M. Astrogliosis as a therapeutic target for neurodegenerative diseases. *Neurosci. Lett.* **2014**, *565*, 59–64. [[CrossRef](#)]
56. Licastro, F.; Chiappelli, M.; Grimaldi, L.M.; Morgan, K.; Kalsheker, N.; Calabrese, E.; Ritchie, A.; Porcellini, E.; Salani, G.; Franceschi, M.; et al. A new promoter polymorphism in the alpha-1-antichymotrypsin gene is a disease modifier of Alzheimer's disease. *Neurobiol. Aging* **2005**, *26*, 449–453. [[CrossRef](#)]
57. Rentsendorj, A.; Sheyn, J.; Fuchs, D.T.; Daley, D.; Salumbides, B.C.; Schubloom, H.E.; Hart, N.J.; Li, S.; Hayden, E.Y.; Teplow, D.B.; et al. A novel role for osteopontin in macrophage-mediated amyloid- $\beta$  clearance in Alzheimer's models. *Brain Behav. Immun.* **2018**, *67*, 163–180. [[CrossRef](#)]
58. Lisignoli, G.; Toneguzzi, S.; Piacentini, A.; Cristino, S.; Grassi, F.; Cavallo, C.; Facchini, A. CXCL12 (SDF-1) and CXCL13 (BCA-1) chemokines significantly induce proliferation and collagen type I expression in osteoblasts from osteoarthritis patients. *J. Cell. Physiol.* **2006**, *206*, 78–85. [[CrossRef](#)]
59. Qian, T.; Wang, K.; Cui, J.S.; He, Y.D.; Yang, Z.Q. Angiotensin-like protein 7 promotes an inflammatory phenotype in RAW264.7 macrophages through the P38 MAPK signaling pathway. *Inflammation* **2016**, *39*, 974–985. [[CrossRef](#)]
60. Hosoyamada, M.; Ichida, K.; Enomoto, A.; Hosoya, T.; Endou, H. Function and localization of urate transporter 1 in mouse kidney. *J. Am. Soc. Nephrol.* **2004**, *15*, 261–268. [[CrossRef](#)]
61. Pushkin, A.; Carpenito, G.; Abuladze, N.; Newman, D.; Tsuprun, V.; Ryazantsev, S.; Motemoturu, S.; Sassani, P.; Solovieva, N.; Dukkupati, R.; et al. Structural characterization, tissue distribution, and functional expression of murine aminoacylase III. *Am. J. Physiol. Cell Physiol.* **2004**, *286*, 848–856. [[CrossRef](#)] [[PubMed](#)]
62. Nemmar, A.; Karaca, T.; Beegam, S.; Yuvaraju, P.; Yasin, J.; Ali, B.H. Lung oxidative stress, DNA damage, apoptosis, and fibrosis in adenine-induced chronic kidney disease in mice. *Front. Physiol.* **2017**, *8*, 896. [[CrossRef](#)] [[PubMed](#)]
63. Park, S.K.; Kang, J.Y.; Kim, J.M.; Yoo, S.K.; Han, H.J.; Chung, D.H.; Kim, D.O.; Kim, G.H.; Heo, H.J. Fucooidan-rich substances from *Ecklonia cava* improve trimethyltin-induced cognitive dysfunction via down-regulation of amyloid  $\beta$  production/Tau hyperphosphorylation. *Mar. Drugs* **2019**, *17*, 591. [[CrossRef](#)] [[PubMed](#)]



## Article

# Aromatic Acids and Leucine Derivatives Produced from the Deep-Sea Actinomycetes *Streptomyces chumphonensis* SCSIO15079 with Antihyperlipidemic Activities

Ziqi Su <sup>1</sup>, Kunlong Li <sup>2,3</sup>, Xiaowei Luo <sup>4</sup>, Yongyan Zhu <sup>1</sup>, Shao-Yu Mai <sup>1</sup>, Quanhong Zhu <sup>1</sup>, Bin Yang <sup>2,3</sup>, Xuefeng Zhou <sup>2,3,\*</sup> and Huaming Tao <sup>1,\*</sup>

- <sup>1</sup> Guangdong Provincial Key Laboratory of Chinese Medicine Pharmaceutics, School of Traditional Chinese Medicine, Southern Medical University, Guangzhou 510515, China; ziqisl@163.com (Z.S.); yongyanzhu0521@163.com (Y.Z.); shaoyumai@smu.edu.cn (S.-Y.M.); zqh@smu.edu.cn (Q.Z.)
- <sup>2</sup> CAS Key Laboratory of Tropical Marine Bio-Resources and Ecology, Guangdong Key Laboratory of Marine Materia Medica, South China Sea Institute of Oceanology, Chinese Academy of Sciences, Guangzhou 510301, China; likunlong16@mailsucas.ac.cn (K.L.); yangbin@scsio.ac.cn (B.Y.)
- <sup>3</sup> Southern Marine Science and Engineering Guangdong Laboratory (Guangzhou), Guangzhou 511458, China
- <sup>4</sup> Institute of Marine Drugs, Guangxi University of Chinese Medicine, Nanning 530200, China; luoxiaowei1991@126.com
- \* Correspondence: xfzhou@scsio.ac.cn (X.Z.); taohm@smu.edu.cn (H.T.); Tel.: +86-61648770 (H.T.)

**Abstract:** Six new aromatic acids (1–6) and three new leucine derivatives containing an unusual oxime moiety (7–9) were isolated and identified from the deep-sea-derived actinomycetes strain *Streptomyces chumphonensis* SCSIO15079, together with two known compounds (10–11). The structures of 1–9 including absolute configurations were determined by detailed NMR, MS, and experimental and calculated electronic circular dichroism spectroscopic analyses. Compounds 1–9 were evaluated for their antimicrobial and cytotoxicity activities, as well as their effects on intracellular lipid accumulation in HepG2 cells. Compounds 3 and 4, with the most potent inhibitory activity on intracellular lipid accumulation at 10  $\mu$ M, were revealed with potential antihyperlipidemic effects, although the mechanism needs to be further studied.

**Keywords:** deep-sea actinomycetes; aromatic acids; oximes; antihyperlipidemic

**Citation:** Su, Z.; Li, K.; Luo, X.; Zhu, Y.; Mai, S.-Y.; Zhu, Q.; Yang, B.; Zhou, X.; Tao, H. Aromatic Acids and Leucine Derivatives Produced from the Deep-Sea Actinomycetes *Streptomyces chumphonensis* SCSIO15079 with Antihyperlipidemic Activities. *Mar. Drugs* **2022**, *20*, 259. <https://doi.org/10.3390/md20040259>

Academic Editor: Vassilios Roussis

Received: 9 March 2022

Accepted: 5 April 2022

Published: 7 April 2022

**Publisher's Note:** MDPI stays neutral with regard to jurisdictional claims in published maps and institutional affiliations.



**Copyright:** © 2022 by the authors. Licensee MDPI, Basel, Switzerland. This article is an open access article distributed under the terms and conditions of the Creative Commons Attribution (CC BY) license (<https://creativecommons.org/licenses/by/4.0/>).

## 1. Introduction

Hyperlipidemia, defined as an increase in the blood lipids levels, is a risk factor for cardiovascular diseases, including coronary atherosclerosis, cardiovascular diseases, Heart failure, and other metabolic diseases. Hyperlipidemia is also known as an aggravation of several pathological conditions such as hypothyroidism and chronic renal failure. Globally, approximately 12 million people die each year due to hyperlipidemia [1–4]. At present, drugs used to reduce the level of blood lipids mainly include statins (atorvastatin, lovastatin, etc.), fibrates (bezafibrate, lifibrate, etc.), and resin (cholestyramine, colestipol, etc.). Nevertheless, these synthetic medicines are often associated with some serious side effects such as diarrhea, nausea, gallstones, myositis, and abnormal liver function [5–7]. Therefore, it is urgent to discover new lipid-lowering agents with more therapeutic value and less tolerable side effects from natural products.

For the past several decades, many marine-derived active ingredients have been tested and proven with lipid-lowering or antihyperlipidemic effects, such as the seaweed polysaccharide [8], marine algal polyphenols [9], polyunsaturated fatty acids from oily fish [10,11], and fish protein [12]. Marine-derived microorganisms have shown promising potential to produce a great number of active substances including antibacterial, antiviral, antioxidant, as well as cytotoxic compounds [13–18]. Marine extremophilic microorganisms



tend to produce fascinating novel types of bioactive secondary metabolites; therefore deep-sea-derived microorganisms seem to be significant sources for discovering lead compounds in drug discovery [19,20].

In our search, six new aromatic acids (1–6), three new leucine derivatives containing an unusual oxime moiety (7–9), and two known compounds (10, 11) were obtained from the actinomycetes strain *Streptomyces chumphonensis* SCSIO15079, isolated from a sediment sample of Indian Ocean, with a depth of 3386 m (Figure 1). In order to study the potential antihyperlipidemic effects of these compounds, their effects on intracellular lipid accumulation in HepG2 cells were evaluated. Herein, we describe the fermentation, isolation, structural determination, and biological activity of these compounds.

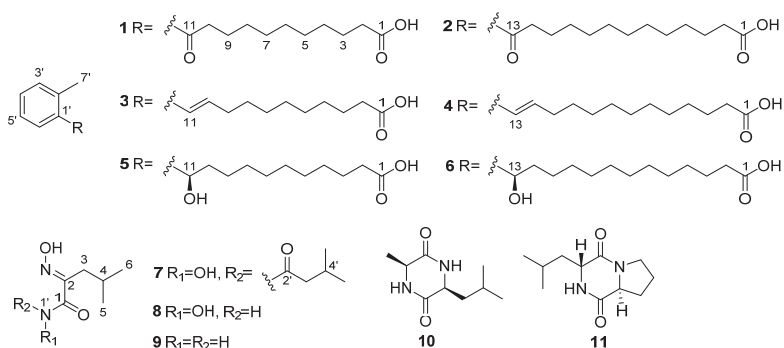


Figure 1. Structures of compounds 1–11.

## 2. Results and Discussion

### 2.1. Structure Elucidation

Compound 1 was isolated as a yellowish solid. Its molecular formula of  $C_{18}H_{26}O_3$  was determined by HRESIMS ( $m/z$  289.1809 [ $M - H$ ] $^-$ , calcd for, 289.3950), which required 6 degrees of unsaturation. The  $^1H$  NMR spectrum displayed an ABCD aromatic spin system resonated at  $\delta_H$  7.67 (1H, d,  $J = 7.6$  Hz, H-6'), 7.38 (1H, m, H-3'), 7.27 (2H, m, H-4',5') for an aromatic ring with vicinal substitution. The  $^1H-^1H$  COSY correlations established that C-2 to C-10 were a long-chain alkanes system (Figure 2). The  $^{13}C$  NMR spectrum, in combination with DEPT and HSQC spectra, revealed the presence of 18 carbons, including a methyl (C-7'), six aromatic carbons (C-1' to C-6'), nine methylenes (C-2 to C-10), and two carbonyl carbons (C-1 and C-11). The HMBC correlations from H-5' ( $\delta_H$  7.27) and H-6' ( $\delta_H$  7.67) to C-11 ( $\delta_C$  207.4) and C-9 ( $\delta_C$  26.2), respectively, established the connection of the conjugated chain to an aromatic ring. The position of the methyl group in the aromatic ring was determined by HMBC correlations observed from H-7' ( $\delta_H$  2.42) to C-2' ( $\delta_C$  138.6) and C-1' ( $\delta_C$  139.7), which indicated a methylbenzene moiety. As only H-6 showed an HMBC correlation with the ketone signal, it was deduced that the ketone C-11 ( $\delta_C$  207.4, s) must be attached directly to the benzene ring (Figure 2). Thus, the structure of 1 was identified, as shown in Figure 1, and named 11-oxo-11-(o-tolyl) undecanoic acid (1).

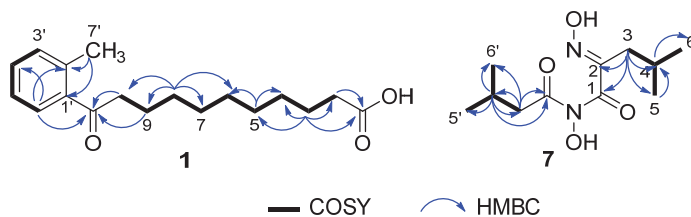


Figure 2. Key COSY and HMBC correlations in 1 and 7.

Compound **2** was isolated as a yellowish solid. Its molecular formula of  $C_{20}H_{30}O_3$  was determined by the HRESIMS ( $m/z$  319.2268  $[M - H]^-$ , calcd for, 319.2273), which required 6 degrees of unsaturation. Its  $^1H$  and  $^{13}C$  NMR data (Tables 1 and 2) revealed that the aromatic ring with vicinal substitution of **2** was the same as **1**. Compared to **1**, the only difference of **2** was two more methylene groups in the fatty acid chains, the  $^1H$  NMR data of which showed 11 methylene groups at  $\delta_H$  1.25–1.36. Thus, the structure of **2** was identified as shown in Figure 1 and named 13-oxo-13-(*o*-tolyl) tridecanoic acid (**2**).

**Table 1.**  $^1H$  NMR (600 MHz) data of compounds 1–6 in  $CD_3OD$  ( $\delta$  in ppm).

| Position | 1 (J in Hz)   | 2 (J in Hz)   | 3 (J in Hz)           | 4 (J in Hz)          | 5 (J in Hz)   | 6 (J in Hz)         |
|----------|---------------|---------------|-----------------------|----------------------|---------------|---------------------|
| 2        | 2.26 (t, 7.1) | 2.27 (t, 7.3) | 2.24 m                | 2.25 m               | 2.27 m        | 2.25 m              |
| 3        | 1.59 m        | 1.58 m        | 1.59 m                | 1.58 m               | 1.58 m        | 1.58 m              |
| 4        |               |               |                       |                      |               |                     |
| 5        |               |               |                       |                      |               |                     |
| 6        | 1.28~1.34 m   |               | 1.27~1.33 m           |                      | 1.27~1.35 m   |                     |
| 7        |               | 1.25~1.36 m   |                       | 1.28~1.31 m          |               | 1.23~1.34 m         |
| 8        |               |               |                       |                      |               |                     |
| 9        | 1.66 m        |               | 2.24 m                |                      | 1.45 m        |                     |
| 10       | 2.91 (t, 7.3) |               | 6.06 (dt, 7.02, 15.6) |                      | 1.70 m        |                     |
| 11       |               | 1.65 m        | 6.57 (d, 15.6)        | 2.24 m               | 4.86 m        | 1.46 m              |
| 12       |               | 2.90 (t, 7.3) |                       | 6.07 (dt, 7.0, 15.7) |               | 1.67 m              |
| 13       |               |               |                       | 6.57 (d, 15.7)       |               | 4.86 (dd, 4.3, 7.6) |
| 1'       |               |               |                       |                      |               |                     |
| 2'       |               |               |                       |                      |               |                     |
| 3'       | 7.38 m        | 7.37 m        |                       |                      | 7.17 m        | 7.16 m              |
| 4'       | 7.27 m        | 7.27 m        | 7.07 m                | 7.07 m               | 7.10 (d, 4.1) | 7.10 (d, 4.3)       |
| 5'       |               |               |                       |                      |               |                     |
| 6'       | 7.67 (d, 7.6) | 7.66 (d, 7.7) | 7.35 (d, 7.3)         | 7.35 (d, 7.3)        | 7.41 (d, 7.7) | 7.40 (d, 7.6)       |
| 7'       | 2.42 s        | 2.42 s        | 2.28 s                | 2.28 s               | 2.32 s        | 2.31 s              |

**Table 2.**  $^{13}C$  NMR (150 MHz) data of compounds 1–6 in  $CD_3OD$  ( $\delta$  in ppm).

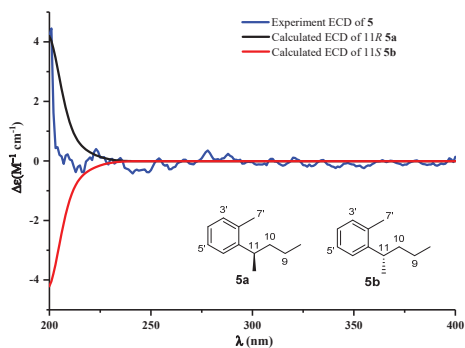
| Position | 1                    | 2                    | 3                    | 4                     | 5                    | 6                    |
|----------|----------------------|----------------------|----------------------|-----------------------|----------------------|----------------------|
| 1        | 178.2 C              | 178.1 C              | 178.6 C              | 177.9 C               | 177.9 C              | 177.9 C              |
| 2        | 35.3 CH <sub>2</sub> | 35.2 CH <sub>2</sub> | 34.3 CH <sub>2</sub> | 34.4 CH <sub>2</sub>  | 35.0 CH <sub>2</sub> | 35.0 CH <sub>2</sub> |
| 3        | 25.6 CH <sub>2</sub> | 25.6 CH <sub>2</sub> | 26.3 CH <sub>2</sub> | 26.1 CH <sub>2</sub>  | 26.1 CH <sub>2</sub> | 26.0 CH <sub>2</sub> |
| 4        | 30.3 CH <sub>2</sub> | 30.3 CH <sub>2</sub> | 30.3 CH <sub>2</sub> | 30.3 CH <sub>2</sub>  | 30.4 CH <sub>2</sub> | 30.2 CH <sub>2</sub> |
| 5        | 30.2 CH <sub>2</sub> | 30.2 CH <sub>2</sub> | 30.2 CH <sub>2</sub> | 30.2 CH <sub>2</sub>  | 30.2 CH <sub>2</sub> | 30.1 CH <sub>2</sub> |
| 6        | 30.3 CH <sub>2</sub> | 30.4 CH <sub>2</sub> | 30.4 CH <sub>2</sub> | 30.4 CH <sub>2</sub>  | 30.5 CH <sub>2</sub> | 30.4 CH <sub>2</sub> |
| 7        | 30.4 CH <sub>2</sub> | 30.4 CH <sub>2</sub> | 30.5 CH <sub>2</sub> | 30.5 CH <sub>2</sub>  | 30.6 CH <sub>2</sub> | 30.5 CH <sub>2</sub> |
| 8        | 30.5 CH <sub>2</sub> | 30.5 CH <sub>2</sub> | 30.6 CH <sub>2</sub> | 30.7 CH <sub>2</sub>  | 30.6 CH <sub>2</sub> | 30.5 CH <sub>2</sub> |
| 9        | 26.2 CH <sub>2</sub> | 30.6 CH <sub>2</sub> | 34.3 CH <sub>2</sub> | 30.8 CH <sub>2</sub>  | 27.0 CH <sub>2</sub> | 30.5 CH <sub>2</sub> |
| 10       | 42.6 CH <sub>2</sub> | 30.6 CH <sub>2</sub> | 133.2 CH             | 30.8 CH <sub>2</sub>  | 39.3 CH <sub>2</sub> | 30.5 CH <sub>2</sub> |
| 11       | 207.4 C              | 26.2 CH <sub>2</sub> | 129.0 CH             | 35.09 CH <sub>2</sub> | 71.1 CH              | 26.9 CH <sub>2</sub> |
| 12       |                      | 42.6 CH <sub>2</sub> |                      | 133.2 CH              |                      | 39.2 CH <sub>2</sub> |
| 13       |                      | 207.5 C              |                      | 129.0 CH              |                      | 71.0 CH              |
| 1'       | 139.7 C              | 139.7 C              | 138.2 C              | 138.2 C               | 144.6 C              | 144.4 C              |
| 2'       | 138.6 C              | 138.6 C              | 135.8 C              | 135.8 C               | 135.5 C              | 135.3 C              |
| 3'       | 132.8 CH             | 132.8 CH             | 127.0 CH             | 127.0 CH              | 127.1 CH             | 126.8 CH             |
| 4'       | 126.9 CH             | 126.9 CH             | 131.0 CH             | 131.1 CH              | 131.2 CH             | 131.0 CH             |
| 5'       | 132.3 CH             | 132.3 CH             | 127.8 CH             | 127.8 CH              | 127.8 CH             | 127.7 CH             |
| 6'       | 129.5 CH             | 129.5 CH             | 126.4 CH             | 126.5 CH              | 126.4 CH             | 126.3 CH             |
| 7'       | 21.1 CH <sub>3</sub> | 21.2 CH <sub>3</sub> | 19.9 CH <sub>3</sub> | 19.9 CH <sub>3</sub>  | 19.3 CH <sub>3</sub> | 19.2 CH <sub>3</sub> |

Compound **3** was isolated as a yellowish solid. Its molecular formula of  $C_{18}H_{26}O_2$  was determined by the HRESIMS ( $m/z$  297.1825  $[M + Na]^+$ , calcd for, 297.1830), which required 6 degrees of unsaturation. It was determined as a 10,11-unsaturated analogue of **1** based on the presence of the  $^1H$ - $^1H$  COSY spectrum correlated two olefinic protons

at  $\delta_{\text{H}}$  6.06 (1H, dt,  $J = 15.6, 7.0$  Hz, H-10) and 6.57 (1H, d,  $J = 15.6$  Hz, H-11), indicating an *E*-disubstituted double bond, which replaced the ketone signal at C-11 of **1**, as evident from the 2D NMR data in association with the HRESIMS data. Thus, the structure of **3** was identified (*E*)-11-(*o*-tolyl) undec-10-enoic acid (**3**).

Compound **4** was determined to be  $\text{C}_{20}\text{H}_{30}\text{O}_2$  by the HRESIMS ( $m/z$  325.2138 [ $\text{M} + \text{Na}$ ] $^+$ ) data, requiring 6 degrees of unsaturation. A comparison of the NMR data between **4** and **3** (Tables 1 and 2) revealed that the side chain of **4** possessed two methylene groups, whereas the remaining NMR data of both compounds were closely similar. Thus, the structure of **4** was identified as (*E*)-13-(*o*-tolyl) undec-12-enoic acid (**4**).

Compound **5** was isolated as a yellowish solid. Its molecular formula of  $\text{C}_{18}\text{H}_{28}\text{O}_3$  was determined by the HRESIMS ( $m/z$  291.1969 [ $\text{M} - \text{H}$ ] $^-$ , calcd for, 291.1960), which required 5 degrees of unsaturation.  $^1\text{H}$  and  $^{13}\text{C}$  NMR data (Tables 1 and 2) of **5** closely resembled those of **1**. The only difference between them was that the ketone at the 11-position in **1** was replaced by an oxygenated methine group ( $\delta_{\text{H}}$  4.86/ $\delta_{\text{C}}$  71.1) in **5**, which was corroborated by the HMBC correlation from H-11 to C-1' ( $\delta_{\text{C}}$  144.6), 2' ( $\delta_{\text{C}}$  135.5), and 6' ( $\delta_{\text{C}}$  126.4). The absolute configuration of **5** was established based on a comparison of its experimental electronic of the 11*R*-**5a** model and the 11*S*-**5b** model at the B3LYP/6-31G (d,p) level in Gaussian 03, and the former was showed relatively good agreement with the experimental one (Figure 3). Thus, the absolute structure of **5** was defined as 11*R*. We also tried employing Mosher's method to determine the absolute configuration of C-11 in **5**. The treatment of **5** with (*R*)- and (*S*)-MTPA-Cl yielded (*S*)- and (*R*)-MTPA ester derivatives, respectively. However, the values in the  $^1\text{H}$ -NMR spectrum of the mono-(*S*)- and -(*R*)-MTPA esters in **5** had no significant differences. This might be a result from the aliphatic chain being too long to flip. Thus, the structure of **5** was identified to be (*R*)-11-hydroxy-11-(*o*-tolyl) undecanoic acid (**5**).



**Figure 3.** Experimental ECD spectra of **5**, and the calculated ECD spectra of truncated models **5a/5b**.

Compound **6** showed the molecular formula of  $\text{C}_{20}\text{H}_{32}\text{O}_3$  by HRESIMS ( $m/z$  319.2279 [ $\text{M} - \text{H}$ ] $^-$ ) data, which pointed to an analogue of **5**. The  $^1\text{H}$  and  $^{13}\text{C}$  NMR spectrum was indeed similar to that of **5** (Tables 1 and 2), and as expected, the  $^{13}\text{C}$  NMR data indicated clearly two additional methylene groups (Table 2). Compound **6** was indicated to be *R*-configuration at C-13, and its optical rotation was ( $[\alpha]_{\text{D}}^{25} +2.6$  (c 0.10, MeOH)), compared with compound **5** ( $[\alpha]_{\text{D}}^{25} +4.0$  (c 0.10, MeOH)). Thus, the structure of **6** was identified to be (*R*)-11-hydroxy-11-(*o*-tolyl) undecanoic acid (**6**).

Compound **7** was afforded as a yellowish powder. Its molecular formula of  $\text{C}_{11}\text{H}_{20}\text{N}_2\text{O}_4$  was inferred from HRESIMS ( $m/z$  245.1496 [ $\text{M} + \text{H}$ ] $^+$ , calcd for, 245.2990) spectrum. Its NMR data were similar to aspergilliamide [21], which had been obtained previously. The  $^1\text{H}$  NMR data (Table 3) showed signals for two methylene groups at  $\delta_{\text{H}}$  2.49 (2H, d,  $J = 7.3$  Hz, H-3') and 2.37 (2H, d,  $J = 7.1$  Hz, H-3); two methine groups at  $\delta_{\text{H}}$  2.13 (1H, m, H-4') and 2.03 (1H, m, H-4); and four methyl groups at  $\delta_{\text{H}}$  1.04 (6H, d,  $J = 6.7$  Hz, H-5', 6'), 0.94 (6H, d,  $J = 6.7$  Hz, H-5, 6), and  $^{13}\text{C}$  NMR data at  $\delta_{\text{C}}$  41.2 (C-3'), 33.1 (C-3), 26.9 (C-4'), 27.5 (C-4),

22.6 (C-5',6'), 23.0 (C-5,6) suggested that **7** contained two isobutyl groups. In the HMBC spectrum (Figure 2), correlations from H-3' to C-2' ( $\delta_C$  172.0)/C-4'/C-5'/C-6' suggested the existence of 3-methylbutanamide unit. This deduction was further verified by HMBC correlations from H-3 to C-1 ( $\delta_C$  164.5)/C-2 ( $\delta_C$  153.4) /C-4/C-5/C-6. The hydrolysis of **7** to give N-hydroxy-2-(hydroxyimino)-4-methylpentanamide (**8**) suggested the presence of **8** unit in **7** [21]. Based on the above data, the structure of **7** was deduced as N-hydroxy-2-(hydroxyimino)-4-methyl-N-(3-methylbutanoyl) pentanamide (**7**).

**Table 3.**  $^1\text{H}$  and  $^{13}\text{C}$  NMR data (600/150 MHz) of compounds **7–9** ( $\delta$  in ppm).

| Position | <b>7</b> <sup>a</sup> |                      | <b>8</b> <sup>b</sup> |                      | <b>9</b> <sup>a</sup> |                      |
|----------|-----------------------|----------------------|-----------------------|----------------------|-----------------------|----------------------|
|          | $\delta_C$            | $\delta_H$ (J in Hz) | $\delta_C$            | $\delta_H$ (J in Hz) | $\delta_C$            | $\delta_H$ (J in Hz) |
| 1        | 164.5 C               |                      | 162.0 C               |                      | 168.9 C               |                      |
| 2=N-OH   | 153.4 C               |                      | 153.1 C               | 11.4 s               | 154.3 C               |                      |
| 3        | 33.1 CH <sub>2</sub>  | 2.37 (d, 7.1)        | 32.3 CH <sub>2</sub>  | 2.37 (d, 7.3)        | 32.6 CH <sub>2</sub>  | 2.48 (d,7.3)         |
| 4        | 27.5 CH               | 2.03 m               | 25.7 CH               | 1.90 m               | 27.6 CH               | 2.01 m               |
| 5        | 23.0 CH <sub>3</sub>  | 0.94 (d, 6.7)        | 22.6 CH <sub>3</sub>  | 0.85 (d, 6.7)        | 23.1 CH <sub>3</sub>  | 0.92 (d, 6.7)        |
| 6        | 23.0 CH <sub>3</sub>  | 0.94 (d, 6.7)        | 22.6 CH <sub>3</sub>  | 0.85 (d, 6.7)        | 23.1 CH <sub>3</sub>  | 0.92 (d, 6.7)        |
| 1'-H     |                       |                      |                       | 8.9 br.s             |                       |                      |
| 1'-OH    |                       |                      |                       | 10.7 br.s            |                       |                      |
| 2'       | 172.0 C               |                      |                       |                      |                       |                      |
| 3'       | 41.2 CH <sub>2</sub>  | 2.49 (d, 7.3)        |                       |                      |                       |                      |
| 4'       | 26.9 CH               | 2.13 m               |                       |                      |                       |                      |
| 5'       | 22.6 CH <sub>3</sub>  | 1.04 (d, 6.7)        |                       |                      |                       |                      |
| 6'       | 22.6 CH <sub>3</sub>  | 1.04 (d, 6.7)        |                       |                      |                       |                      |

<sup>a</sup> Data measured in CD<sub>3</sub>OD; <sup>b</sup> data measured in DMSO-*d*<sub>6</sub>.

Compound **8** as yellowish powder was determined as an alkaline hydrolysate of **7**. The HRESIMS peak of  $[\text{M} - \text{H}]^-$  at  $m/z$  159.0782 and NMR spectra of **8** confirmed its molecular formula as C<sub>6</sub>H<sub>11</sub>N<sub>2</sub>O<sub>3</sub>. The  $^1\text{H}$  NMR data (Table 3) showed signals for three exchangeable protons at  $\delta_H$  11.44 (1H, s, 2=N-OH), 10.68 (1H, brs, 1'-OH) and 8.90 (1H, brs, 1'-H)m and the remainder of the nine protons at  $\delta_H$  2.37 (2H, d,  $J = 7.3$  Hz, H-3), 1.90 (1H, m, H-4), 0.85 (6H, d,  $J = 6.7$  Hz, H-5, 6) were similar to those of **7** and  $^{13}\text{C}$  NMR data (Table 3) at  $\delta_C$  32.3 (C-3), 25.7 (C-4), 22.6 (C-5,6), which were suggested to also contain the isobutyl group. In the HMBC spectrum, correlations from H-3 to C-1 ( $\delta_C$  162.0)/C-2 ( $\delta_C$  153.1)/C-4/C-5/C-6 suggested the existence of 3-methylbutanamide unit. This deduction was further confirmed by HMBC correlations from H-1' ( $\delta_H$  11.4, s) to C-2. Thus, the structure of **8** was identified N-hydroxy-2-(hydroxyimino)-4-methylpentanamide (**8**), which is suggested to be a hydrolytic product of **7**.

Compound **9** was obtained as a white powder, which had the molecular formula of C<sub>6</sub>H<sub>12</sub>N<sub>2</sub>O<sub>2</sub> as inferred from HRESIMS ( $m/z$  167.0791  $[\text{M} + \text{Na}]^+$ ) and NMR data (Table 3). It had been afforded previously as a synthetic compound by the alkaline hydrolysis of aspergilliamide [21], and spectroscopic data were not reported. Thus, compound **9** was identified as (*E*)-2-(hydroxyimino)-4-methylpentanamide (**9**), and it is reported as a new natural product.

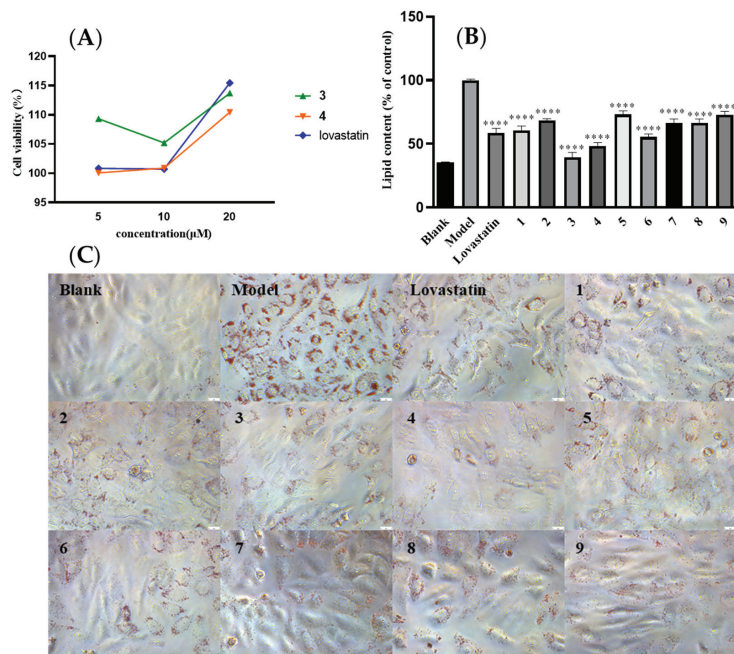
Compounds **10** and **11** were identified as Cyclo-(Ala-Leu) [22] and Cyclo-(Pro-Leu) [23] by comparing spectroscopic data with those reported in the literature.

## 2.2. Bioassays

As a conventional activity screening, compounds **1–9** were tested for their antibacterial (against *Acinetobacter baumannii*, *Staphylococcus aureus*, *Enterococcus faecalis*, *Klebsiella pneumoniae*, *S. aureus* subsp. *aureus* Rosenbach, methicillin-resistant *S. aureus*, and methicillin-resistant *S. epidermidis*) and cytotoxic (against human cancer cell lines HeLa, HCT-116, and A549) activities. However, none of them displayed obvious antibacterial or cytotoxicity activities.

The aromatic analogues containing a linear chain were reported with lowering lipid effects [24]. For example, 2-methyl-8-hydroxybenzeneheptanoic acid, an aromatic analogue obtained from a marine-derived *Streptomyces* strain, remarkably decreased lipid levels including total cholesterol (TC) and triglycerides (TG) in HepG2 cells [24]. Moreover, it is revealed that the aromatic analogue containing a linear chain with seven carbons showed stronger inhibition in comparison with those bearing a linear chain with five carbons [24]. In this study, several aromatic analogues containing a linear chain with eleven or thirteen carbons have been obtained, but their lipid-lowering effect remains unknown. Thus, the obtained new compounds, including the aromatic analogues, were evaluated with their effects on intracellular lipid accumulation in HepG2 cells by oil-red O staining, together with their brief SAR discussion.

The compounds 1–9 and the positive control lovastatin were tested for cytotoxic effects toward HepG2 cells by using the MTT (Sigma Aldrich) assay, together with oleic acid (OA). The results showed there is no obvious toxicity with these compounds. HepG2 cells were incubated with OA (500  $\mu$ M) and DMEM for 24 h and then treated with 10  $\mu$ M of indicated compounds or lovastatin for an additional 24 h. The effects of compounds 1–9 on oleic acid-elicited intracellular lipid accumulation were showed in Figure 4. All compounds tested showed a reduction in intracellular lipid accumulation, while 3 and 4 displayed stronger inhibition than the others. As for the results, there is no clear conclusion about the difference in activities in comparison with those aromatic analogues with eleven and thirteen carbons of the linear chain in the structures. However, it was speculated that the conjugated double bond in linear chain (such as in 3 or 4) is beneficial for the intracellular lipid-lowering effect than carbonyl or hydroxyl groups in this position (Figure 4). The hypolipidemic mechanism of them needs further study.



**Figure 4.** Effects of 1–9 on oleic acid-elicited intracellular lipid accumulation. (A) Cell viability of 3, 4, and lovastatin in HepG2 cells; (B) HepG2 cells were treated with isopropanol and intracellular lipid levels were measured using the absorbance at OD 510 nm; (C) Oil Red O staining showed lipid accumulation that was observed with a microscope (scale bar = 1 mm). Data were represented as the mean  $\pm$  SEM of three in dependent experiments. \*\*\*\*  $p < 0.001$ , test group vs. model group.

### 3. Materials and Methods

#### 3.1. General Experimental Procedures

Semipreparative HPLC (Agilent Technologies, 1260 Infinity II series) was performed using an ODS column (YMC-pack ODS-A, 10 mm × 250 mm, 5 µm). Column chromatography (CC) was performed over silica gel (200–300 mesh; Qingdao Marine Chemical Group Co., Qingdao, China) and Sephadex LH-20 (Amersham Biosciences Inc., Piscataway, NJ, USA) and octadecylsilyl silica gel (YMC Co., Ltd., Kyoto, Japan; 50 µm), respectively. Spots were detected on TLC (Qingdao Marine Chemical Factory, Qingdao, China) under 254 nm UV light. The NMR spectra were obtained on a Bruker Avance-600 MHz spectrometer (Bruker, Billerica, MA, USA) with tetramethylsilane as an internal standard. HR-ESI-MS spectra were recorded on a Bruker miXis TOF-QII mass spectrometer (Bruker, Billerica, MA, USA). Optical rotations were determined with a Perkin Elmer MPC 500 (Waltham, MA, USA) polarimeter. The UV, IR, and ECD spectra were recorded on a Shimadzu UV-2600 PC spectrometer (Shimadzu, Kyoto, Japan), an IR Affinity-1 spectrometer (Shimadzu, Kyoto, Japan), and a Chirascan circular dichroism spectrometer (Applied Photophysics, Leatherhead Surrey, UK), respectively. The artificial sea salt was a commercial product (Guangzhou Haili Aquarium Technology Company, Guangzhou, China). Cells were disrupted using a high pressure homogenizer NanoGenizer (Genizer LLC, Irvine, CA, USA).

#### 3.2. Strain Material

The strain SCSIO15079 used in this investigation was isolated from the deep-sea sediment sample of the Indian Ocean (Lat: 10.00371667° N, long: 88.72803333° E) at a depth of 3386 m in 2013. It was identified as a *S. chumphonensis* species by 16S rRNA gene sequence analysis (Supplementary Material). The strain SCSIO15079 is preserved at the CAS Key Laboratory of Tropical Marine Bio-Resources and Ecology, South China Sea Institute of Oceanology, Chinese Academy of Sciences.

#### 3.3. Cultivation and Extraction

A few loops of cells of the strain were inoculated into a 500 mL Erlenmeyer flask containing 150 mL of seed medium (malt extract 1%, yeast extract 0.4%, glucose 0.4%, pH 7.2) and then cultivated on a rotary shaker at 180 rpm, 28 °C for 48 h as seed culture. Then, 2 L of seed culture was inoculated into a 65 L fermenter containing 40 L medium (soybean meal 1%, corn steep liquor 0.5%, glucose 0.5%, yeast extract 0.1%, glycerol 2%, meat extract 0.2%, CaCO<sub>3</sub> 0.2%, MgSO<sub>4</sub> 0.01%, pH 7.2). After cultivation at 180 rpm and 28 °C for 80 h, the bacterial culture broth was centrifuged at 4000 rpm. Then, the mycelium and supernatant were broken using an ultrasonic treatment apparatus for 15 min and extracted three times with an equal volume of ethyl acetate, respectively. The organic extract was then concentrated under a vacuum to provide the crude extract. EtOAc was concentrated in vacuo to yield an organic extract (about 51 g).

#### 3.4. Isolation and Purification

The EtOAc crude extract (51 g) was subjected to silica gel vacuum liquid chromatography using a step gradient elution of petroleum ether (PE)–EtOA (0–100%, V/V), EtOAc–MeOH (0–100%, V/V) to yield nine fractions according to TLC profiles (Fr.1–Fr.8). Fr. 2 (1.2 g) was separated into four subfractions (Fr. 2.1–2.4) by silica gel chromatography eluting with CH<sub>2</sub>Cl<sub>2</sub>/MeOH (0–100%, V/V), and Fr. 2.2 was directly separated by semipreparative HPLC (85% MeCN/H<sub>2</sub>O, 4 mL/min, 210 nm) to yield 1 (6.5 mg, t<sub>R</sub> 26.7 min) and 2 (21.3 mg, t<sub>R</sub> 36.2 min). From Fr. 3 (2.3 g), 3 (11.6 mg, t<sub>R</sub> 29.0 min) and 4 (41.0 mg, t<sub>R</sub> 58.3 min) were repurified through a silica gel CC with PE/EtOA (10–100%, V/V) and semipreparative HPLC (73% MeCN/H<sub>2</sub>O, 3 mL/min, 254 nm). The subsequent purification of Fr. 6 (1.5 g) using Sephadex LH-20 with MeOH and semipreparative HPLC (70% MeOH/H<sub>2</sub>O, 3 mL/min, 210 nm) afforded 5 (39 mg, t<sub>R</sub> 23.5 min) and 6 (9.2 mg, t<sub>R</sub> 34 min). Fr. 5 (1.6 g) was eluted with MeOH–H<sub>2</sub>O (1:9 to 1:0) on ODS CC and further purified on HPLC with MeOH–H<sub>2</sub>O gradient (5:95 to 100:0, 3 mL/min, total 40 min, 210 nm) to

give 7 (10.2 mg,  $t_R$  24.5 min) and 8 (8.0 mg,  $t_R$  32.3 min). Fr. 4 (3.6 g) was further separated to seven subfractions (Fr. 4.1–4.8) by ODS silica gel CC eluted with MeOH–H<sub>2</sub>O gradient (1:9 to 1:0). Fr. 4.3 (563 mg) was subjected to CC on Sephadex LH-20 eluting with MeOH and then further purified by semi-preparative HPLC (MeOH–H<sub>2</sub>O 3:7, 3 mL/min, 210 nm) to afford 9 ( $t_R$  = 8.6 mg, 30.2 min). Fr. 4.7 (135 mg) was further purified on semipreparative HPLC (20% MeCN/H<sub>2</sub>O, 3 mL/min, 210 nm) to obtain 10 (3.4 mg,  $t_R$  24.0 min) and 11 (5.2 mg,  $t_R$  33.2 min).

11-Oxo-11-(*o*-tolyl) undecanoic acid (1): yellowish solid; UV (MeOH)  $\lambda_{max}$  (log  $\epsilon$ ) 206 (2.30), 241 (2.37), 279 (2.43) and 323 (2.50) nm; IR (film)  $\nu_{max}$  2926, 2852, 1732, 1681, 1506, 1465 1226, 1183, 966, 742, 653 cm<sup>-1</sup>; <sup>1</sup>H and <sup>13</sup>C NMR (see Tables 1 and 2); and HR-ESIMS  $m/z$  289.1809, [M – H]<sup>-</sup> (calculated for C<sub>18</sub>H<sub>25</sub>O<sub>3</sub> 289.1804).

13-Oxo-13-(*o*-tolyl) tridecanoic acid (2): yellowish solid; UV (MeOH)  $\lambda_{max}$  (log  $\epsilon$ ) 206 (2.34), 241 (2.41) and 283 (2.47) nm; IR (film)  $\nu_{max}$  2920, 2852, 1705, 1681, 1543, 1319 1219, 1182, 962, 759, 655 cm<sup>-1</sup>; <sup>1</sup>H and <sup>13</sup>C NMR (see Tables 1 and 2); and HR-ESIMS  $m/z$  319.2268, [M + H]<sup>+</sup> (calculated for C<sub>20</sub>H<sub>31</sub>O<sub>3</sub> 319.2273).

(*E*)-11-(*o*-tolyl) Undec-10-enoic acid (3): pale yellow oil; UV (MeOH)  $\lambda_{max}$  (log  $\epsilon$ ) 209 (2.31), 249 (2.38), 287 (2.44), 298 (2.46) and 323 (2.50) nm; IR (film)  $\nu_{max}$  2920, 2860, 1738, 1680, 1553, 1450, 1281, 1183, 968, 760 cm<sup>-1</sup>; <sup>1</sup>H and <sup>13</sup>C NMR (see Tables 1 and 2); and HR-ESIMS  $m/z$  297.1825, [M+Na]<sup>+</sup> (calculated for C<sub>18</sub>H<sub>26</sub>O<sub>2</sub>Na 297.1830).

(*E*)-13-(*o*-tolyl) Tridec-12-enoic acid (4): pale yellow solid; UV (MeOH)  $\lambda_{max}$  (log  $\epsilon$ ) 210 (2.35), 248 (2.42), 286 (2.48), 298 (2.50) and 323 (2.54) nm; IR (film)  $\nu_{max}$  2923, 2855, 1736, 1683, 1554, 1452, 1281, 1184, 966, 761 cm<sup>-1</sup>; <sup>1</sup>H and <sup>13</sup>C NMR (see Tables 1 and 2); and HR-ESIMS  $m/z$  325.2139, [M + Na]<sup>+</sup> (calculated for C<sub>20</sub>H<sub>30</sub>O<sub>2</sub>Na 325.2147).

(*R*)-11-Hydroxy-11-(*o*-tolyl) undecanoic acid (5): yellow oil; [ $\alpha$ ]<sub>D</sub><sup>25</sup> +4.0 (c 0.10, MeOH); UV (MeOH)  $\lambda_{max}$  (log  $\epsilon$ ) 210 (2.31), 264 (2.41), 323 (2.50) and 371 (2.56) nm; IR (film)  $\nu_{max}$  2926, 2854, 1734, 1676, 1541, 1456, 1280, 1182, 966, 761 cm<sup>-1</sup>; CD (0.25 mg/mL, MeOH)  $\lambda_{max}$  ( $\Delta\epsilon$ ) 210 (+0.051), 264 (−0.044), 323 (+0.025) and 370 (−0.042) nm; <sup>1</sup>H and <sup>13</sup>C NMR (see Tables 1 and 2); and HR-ESIMS  $m/z$  291.1969, [M – H]<sup>-</sup> (calculated for C<sub>18</sub>H<sub>27</sub>O<sub>3</sub> 291.1960).

(*R*)-13-Hydroxy-13-(*o*-tolyl) tridecanoic acid (6): pale yellow solid; [ $\alpha$ ]<sub>D</sub><sup>25</sup> +2.6 (c 0.10, MeOH); UV (MeOH)  $\lambda_{max}$  (log  $\epsilon$ ) 210 (2.35), 262 (2.44), 323 (2.54) and 370 (2.60) nm; IR (film)  $\nu_{max}$  2920, 2852, 1732, 1677, 1543, 1458 1281, 1183, 964, 760 cm<sup>-1</sup>; <sup>1</sup>H and <sup>13</sup>C NMR (see Tables 1 and 2); and HR-ESIMS  $m/z$  319.2279, [M – H]<sup>-</sup> (calculated for C<sub>20</sub>H<sub>31</sub>O<sub>3</sub> 319.2273).

N-Hydroxy-2-(hydroxyimino)-4-methyl-N-(3-methylbutanoyl) pentanamide (7): yellowish powder; UV (MeOH)  $\lambda_{max}$  (log  $\epsilon$ ) 207 (2.23) and 323 (2.42) nm; IR (film)  $\nu_{max}$  3915, 2927, 2872, 1653, 1554, 1095, 1002, 896, 724 cm<sup>-1</sup>; <sup>1</sup>H and <sup>13</sup>C NMR (see Table 3); and HR-ESIMS  $m/z$  245.1496, [M + H]<sup>+</sup> (calculated for C<sub>11</sub>H<sub>21</sub>O<sub>4</sub>N<sub>2</sub> 245.1501).

N-Hydroxy-2-(hydroxyimino)-4-methylpentanamide (8): yellowish powder; UV (MeOH)  $\lambda_{max}$  (log  $\epsilon$ ) 209 (2.05) and 323 (2.24) nm; IR (film)  $\nu_{max}$  3315, 2956, 2872, 1653, 1456 1095, 1002, 898, 725 cm<sup>-1</sup>; <sup>1</sup>H and <sup>13</sup>C NMR (see Table 3); and HR-ESIMS  $m/z$  159.0775, [M – H]<sup>-</sup> (calculated for C<sub>6</sub>H<sub>11</sub>O<sub>3</sub>N<sub>2</sub> 159.0770).

2-(Hydroxyimino)-4-methylpentanamide (9): white powder; UV (MeOH)  $\lambda_{max}$  (log  $\epsilon$ ) 213 (2.01) and 323 (2.19) nm; IR (film)  $\nu_{max}$  3325, 1635, 1016, 667, 555 cm<sup>-1</sup>; <sup>1</sup>H and <sup>13</sup>C NMR (see Table 3); and HR-ESIMS  $m/z$  67.0791, [M + Na]<sup>+</sup> (calculated for C<sub>6</sub>H<sub>12</sub>O<sub>2</sub>N<sub>2</sub>Na 167.0796).

### 3.5. ECD Calculation

Conformational searches were performed by employing the “systematic” procedure in the Spartan’14 software using a Molecular Merck force field. The stable conformers were further chosen for ECD calculations by TD-DFT methodology via the Gaussian 16 program [25], which were calculated at the B3LYP/6-311+G (d, p)/B3LYP/6-31+G (d) level by adopting the polarizable continuum model and 30 excited states. The calculated ECD spectra were generated by the program SpecD 1.71 using Gaussian band shapes from dipole length rotational strengths according to Boltzmann distributions.

### 3.6. Mono-MTPA Esters of 5

Compounds **5** (1.3 mg) was dissolved in freshly distilled dry pyridine (200  $\mu$ L) with dry crystals of dimethylaminopyridine (DMAP, 0.5 mg). The treatment with (*R*)-MTPA-Cl at 28  $^{\circ}$ C yielded the *S*-MTPA ester after 18 h. The reaction mixture was purified by semipreparative HPLC (70%  $\text{CH}_3\text{CN}$  in  $\text{H}_2\text{O}$ ) to produce the *S*-MTPA ester after 30 min. The *R*-MTPA ester was prepared with *S*-MTPA-Cl in the same manner. The  $\Delta\delta$  *S*–*R* values for the mono-*S*- and *R*-MTPA esters of compounds **5** were recorded in ppm in  $\text{CD}_3\text{OD}$ .

### 3.7. Antihyperlipidemic Effects

#### 3.7.1. Cell Culture and Determination of Oleic Acid Concentration

HepG2 cells were cultured in Dulbecco's modified Eagle's medium containing 10% fetal bovine serum and 1% penicillin–streptomycin in a humidified incubator with 5%  $\text{CO}_2$  at 37  $^{\circ}$ C, and cells in the logarithmic phase were taken for the experiments [26]. The oleic acid (OA) was prepared with 10% bovine serum albumin (BSA) and added to the culture medium at a final concentration of 1%, as previously described. Blank control cells were treated with 1% BSA. After reaching 70% confluence, HepG2 cells were serum-starved for 18 h and exposed to 0.5  $\mu\text{M}$  OA, with or without compound/positive, for 24 h [27].

#### 3.7.2. Cell Viability Assay

Cell viability was measured by an MTT assay. In brief, HepG2 cells were plated at a density of  $2 \times 10^4$  cells/well in 96-well plates. After the cells were attached to the plate, they were treated with the OA (0.25, 0.5, 1 mM) or compounds/lovastatin (5, 10, 20  $\mu\text{M}$ ). After 24 h, 20  $\mu\text{L}$  of an MTT solution (5 mg/mL) was added to each well, followed by incubation for 4 h. The medium was removed, and the formazan crystals formed in living cells were dissolved in 150  $\mu\text{L}$  of DMSO. Cell viability was measured at 490 nm using an iMak microplate reader (Molecular Devices, Bio-Rad, Hercules, CA, USA). Each treatment was performed in triplicate.

#### 3.7.3. Oil Red O Staining

Cells were fixed with 4% paraformaldehyde, and Oil Red O staining was performed [24]. Oil droplets were observed using microscopy (Olympus, Tokyo, Japan). Next, cells were treated with isopropanol and lipid accumulation were measured using a microplate reader and recording the absorbance at 510 nm [28].

### 3.8. Antimicrobial Assay

Compounds **1–9** were tested for antibacterial activities against seven bacterial strains: *Acinetobacter baumannii* (ATCC 19606), *Staphylococcus aureus* (ATCC 29213), *Enterococcus faecalis* (ATCC 29212), *Klebsiella pneumoniae* (ATCC 13883), *S. aureus* subsp. *aureus* Rosenbach (ATCC 43300), methicillin-resistant *S. aureus* (MRSA, clinical strain), and methicillin-resistant *S. epidermidis* (MRSE, clinical strain), respectively; they were evaluated in 96-well plates using a modification of the broth microdilution method [29].

### 3.9. Cell Culture and Cytotoxic Bioassay

Human cancer cell lines, HeLa, HCT-116, and A549, were purchased from ATCC. The HCT-116 cells were grown and maintained in a RPMI-1640 medium with 10% FBS, while the other cells were grown in a DMEM medium with 10% FBS. The cell viability was determined using a MTT assay with 50  $\mu\text{M}$  of compounds **1–9**.

## 4. Conclusions

In this study, nine new compounds, including six aromatic analogues (**1–6**) and three leucine derivatives containing an unusual oxime moiety (**7–9**), were obtained from the deep-sea-derived actinomycete strain *Streptomyces chumphonensis* SCSIO15079. The new structures including absolute configurations were determined by spectroscopic methods coupled with experimental and calculated ECD. All of those new compounds showed



inhibitory activities with intracellular lipid accumulation in HepG2 cells, while compound **3** and **4**, with a conjugated double bond in linear chain, displayed stronger inhibition than others. It will provide a new type of potential lead compounds for the development of antihyperlipidemic therapeutics.

**Supplementary Materials:** The following supporting information can be downloaded at: <https://www.mdpi.com/article/10.3390/md20040259/s1>, 16S rRNA Sequence of the Strain SCSIO15079; Figures S1–S67: <sup>1</sup>H NMR, <sup>13</sup>C NMR, DEPT, HSQC, HMBC, COSY, NOESY, HRESIMS, IR, and UV spectra of compounds 1–9; Figure S68. Hydrolysis reaction of **7**; Table S1. Cell viability of HepG2 treated with compounds.

**Author Contributions:** Funding acquisition, X.Z. and H.T.; investigation, Z.S., K.L., X.L., Y.Z., S.-Y.M. and Q.Z.; methodology, Z.S.; project administration, X.Z. and H.T.; resources, B.Y.; supervision, X.Z. and H.T.; writing—original draft, Z.S.; writing—review and editing, X.Z. and H.T. All authors have read and agreed to the published version of the manuscript.

**Funding:** This work was supported by the Special Funds for Promoting Economic Development (Marine Economic Development) of Guangdong Province (GDOE [2019] A28, GDNRC2021052), Natural Science Foundation of Guangdong Province (2021A1515011711), Key Special Project for Introduced Talents Team of Southern Marine Science and Engineering Guangdong Laboratory (Guangzhou) (GML2019ZD0406), National Natural Science Foundation of China (U20A20101, 31900286, 81973235), Administration of Traditional Chinese Medicine of Guangdong Province (20212143), and Guangdong Local Innovation Team Program (2019BT02Y262).

**Institutional Review Board Statement:** Not applicable.

**Acknowledgments:** We would like to thank Y. Gao for fermentation equipment, and we are grateful to the analytical facilities (Z. Xiao, A. Sun, and Y. Zhang et al.) at SCSIO.

**Conflicts of Interest:** The authors declare no conflict of interest.

## References

1. Yokozawa, T.; Ishida, A.; Cho, E.J.; Nakagawa, T. The effects of coptidis rhizoma extract on a hypercholesterolemic animal model. *Phytomedicine* **2003**, *10*, 17–22. [[CrossRef](#)] [[PubMed](#)]
2. Sunil, C.; Ignacimuthu, S.; Kumarappan, C. Hypolipidemic activity of *Symplocos cochinchinensis* S. Moore leaves in hyperlipidemic rats. *J. Nat. Med.* **2012**, *66*, 32–38. [[CrossRef](#)] [[PubMed](#)]
3. Saghir, S.A.M.; Revadigar, V.; Murugaiyah, V. Natural lipid-lowering agents and their effects: An update. *Eur. Food Res. Technol.* **2014**, *238*, 705–725. [[CrossRef](#)]
4. Kuzmich, N.; Andresyuk, E.; Porozov, Y.; Tarasov, V.; Samsonov, M.; Preferanskaya, N.; Veselov, V.; Alyautdin, R. PCSK9 as a target for development of a new generation of hypolipidemic drugs. *Molecules* **2022**, *27*, 434. [[CrossRef](#)]
5. Andrade, S.E.; Saperia, G.M.; Berger, M.L.; Platt, R. Effectiveness of antihyperlipidemic drug management in clinical practice. *Clin. Ther.* **1999**, *21*, 1973–1987. [[CrossRef](#)]
6. Momtazi-Borojeni, A.A.; Katsiki, N.; Pirro, M.; Banach, M.; Rasadi, K.A.; Sahebkar, A. Dietary natural products as emerging lipoprotein(a)-lowering agents. *J. Cell. Physiol.* **2019**, *234*, 12581–12594. [[CrossRef](#)] [[PubMed](#)]
7. Serban, M.C.; Colantonio, L.D.; Manthripragada, A.D.; Monda, K.L.; Bittner, V.A.; Banach, M.; Chen, L.; Huang, L.; Dent, R.; Kent, S.T.; et al. Statin intolerance and risk of coronary heart events and all-cause mortality following myocardial infarction. *J. Am. Coll. Cardiol.* **2017**, *69*, 1386–1395. [[CrossRef](#)] [[PubMed](#)]
8. Mao, W.; Li, B.; Gu, Q.; Fang, Y.; Xing, H.; Ang Jr, P.O. Preliminary studies on the chemical characterization and antihyperlipidemic activity of polysaccharide from the brown alga *Sargassum fusiforme*. *Hydrobiologia* **2004**, *512*, 263–266. [[CrossRef](#)]
9. Murray, M.; Dordevic, A.L.; Bonham, M.P.; Ryan, L. Do marine algal polyphenols have antidiabetic, antihyperlipidemic or anti-inflammatory effects in humans? A systematic review. *Crit. Rev. Food Sci.* **2018**, *58*, 2039–2054. [[CrossRef](#)]
10. Kromhout, D.; Bosschieter, E.B.; de Lezenne Coulander, C. The inverse relation between fish consumption and 20-year mortality from coronary heart disease. *N. Engl. J. Med.* **1985**, *312*, 1205–1209. [[CrossRef](#)]
11. Paoli, A.; Moro, T.; Bosco, G.; Bianco, A.; Grimaldi, K.; Camporesi, E.; Mangar, D. Effects of n-3 polyunsaturated fatty acids ( $\omega$ -3) supplementation on some cardiovascular risk factors with a ketogenic mediterranean diet. *Mar. Drugs* **2015**, *13*, 996–1009. [[CrossRef](#)]
12. Hosomi, R.; Fukunaga, K.; Arai, H.; Kanda, S.; Nishiyama, T.; Yoshida, M. Fish protein decreases serum cholesterol in rats by inhibition of cholesterol and bile acid absorption. *J. Food Sci.* **2011**, *76*, H116–H121. [[CrossRef](#)]
13. Gao, X.; Lu, Y.; Xing, Y.; Ma, Y.; Lu, J.; Bao, W.; Wang, Y.; Xi, T. A novel anticancer and antifungus phenazine derivative from a marine actinomycete BM-17. *Microbiol. Res.* **2012**, *167*, 616–622. [[CrossRef](#)]

14. El-Gendy, M.M.A.; EL-Bondkly, A.M.A. Production and genetic improvement of a novel antimycotic agent, Saadamycin, against dermatophytes and other clinical fungi from endophytic *Streptomyces* sp. Hedaya48. *J. Ind. Microbiol. Biotechnol.* **2010**, *37*, 831–841. [[CrossRef](#)]
15. Lee, J.; Yoo, I.; Kim, W. Differential antiviral activity of benzastatin C and its dechlorinated derivative from *Streptomyces nitrosporeus*. *Biol. Pharm. Bull.* **2007**, *30*, 795–797. [[CrossRef](#)]
16. Shang, N.; Zhang, Z.; Huang, J.; Wang, L.; Luo, J.; Yang, J.; Peng, T.; Yan, Y.; Ma, Y.; Huang, S. Glycosylated piericidins from an endophytic *streptomyces* with cytotoxicity and antimicrobial activity. *J. Antibiot.* **2018**, *71*, 672–676. [[CrossRef](#)]
17. Shin, H.J.; Lee, H.; Lee, J.S.; Shin, J.; Lee, M.A.; Lee, H.; Lee, Y.; Yun, J.; Kang, J.S. Violapyrones H and I, New Cytotoxic compounds isolated from *Streptomyces* sp. associated with the marine starfish *Acanthaster planci*. *Mar. Drugs* **2014**, *12*, 3283–3291. [[CrossRef](#)]
18. Oh, D.; Strangman, W.K.; Kauffman, C.A.; Jensen, P.R.; Fenical, W. Thalassospiramides A and B, immunosuppressive peptides from the marine bacterium *Thalassospira* sp. *Org. Lett.* **2007**, *9*, 1525–1528. [[CrossRef](#)]
19. Pang, X.; Zhou, X.; Lin, X.; Yang, B.; Tian, X.; Wang, J.; Xu, S.; Liu, Y. Structurally various sorbicillinoids from the deep-sea sediment derived fungus *Penicillium* sp. SCSIO06871. *Bioorg. Chem.* **2021**, *107*, 104600. [[CrossRef](#)]
20. Chen, W.; Zhang, J.; Qi, X.; Zhao, K.; Pang, X.; Lin, X.; Liao, S.; Yang, B.; Zhou, X.; Liu, S.; et al. p-Terphenyls as anti-HSV-1/2 agents from a deep-sea-derived *Penicillium* sp. *J. Nat. Prod.* **2021**, *84*, 2822–2831. [[CrossRef](#)]
21. Xu, X.; He, F.; Zhang, X.; Bao, J.; Qi, S. New mycotoxins from marine-derived fungus *Aspergillus* sp. SCSGAF0093. *Food Chem. Toxicol.* **2013**, *53*, 46–51. [[CrossRef](#)]
22. Ding, Z.G.; Zhao, J.Y.; Yang, P.W.; Li, M.G.; Wen, M.L. <sup>1</sup>H and <sup>13</sup>C NMR assignments of eight nitrogen containing compounds from *Nocardia alba* sp.nov (YIM 30243T). *Magn. Reson. Chem.* **2010**, *47*, 366–370. [[CrossRef](#)]
23. Yang, B.; Dong, J.; Zhou, X.; Yang, X.; Lee, K.; Wang, L.; Zhang, S.; Liu, Y. Proline-containing dipeptides from a marine sponge of a *Callyspongia* species. *Helv. Chim. Acta* **2009**, *92*, 1112–1117. [[CrossRef](#)]
24. Liu, D.; Yang, A.; Wu, C.; Guo, P.; Proksch, P.; Lin, W. Lipid-lowering effects of farnesylquinone and related analogues from the marine-derived *Streptomyces nitrosporeus*. *Bioorg. Med. Chem. Lett.* **2014**, *24*, 5288–5293. [[CrossRef](#)]
25. Luo, X.; Lin, X.; Tao, H.; Wang, J.; Li, J.; Yang, B.; Zhou, X.; Liu, Y. Isochromophilones A-F, Cytotoxic chloroazaphilones from the marine mangrove endophytic fungus *Diaporthe* sp. SCSIO 41011. *J. Nat. Prod.* **2018**, *81*, 934–941. [[CrossRef](#)]
26. Li, Y.; Sheng, Y.; Lu, X.; Guo, X.; Xu, G.; Han, X.; An, L.; Du, P. Isolation and purification of acidic polysaccharides from *Agaricus blazei* Murill and evaluation of their lipid-lowering mechanism. *Int. J. Biol. Macromol.* **2020**, *157*, 276–287. [[CrossRef](#)]
27. Lee, M.R.; Yang, H.J.; Park, K.I.; Ma, J.Y. *Lycopus lucidus* Turcz. ex Benth. Attenuates free fatty acid-induced steatosis in HepG2 cells and non-alcoholic fatty liver disease in high-fat diet-induced obese mice. *Phytomedicine* **2019**, *55*, 14–22. [[CrossRef](#)]
28. Mi, Y.; Tan, D.; He, Y.; Zhou, X.; Zhou, Q.; Ji, S. Melatonin modulates lipid metabolism in HepG2 Cells cultured in high concentrations of oleic acid: AMPK pathway activation may play an important role. *Cell Biochem. Biophys.* **2018**, *76*, 463–470. [[CrossRef](#)]
29. Pang, X.; Lin, X.; Yang, J.; Zhou, X.; Yang, B.; Wang, J.; Liu, Y. Spiro-phthalides and isocoumarins isolated from the marine-sponge-derived fungus *Setosphaeria* sp. SCSIO41009. *J. Nat. Prod.* **2018**, *81*, 1860–1868. [[CrossRef](#)]



## Article

# Phycocyanin Ameliorates Colitis-Associated Colorectal Cancer by Regulating the Gut Microbiota and the IL-17 Signaling Pathway

Dongjin Pan <sup>†</sup>, Bingyao Huang <sup>†</sup>, Yuman Gan, Chenghai Gao, Yonghong Liu <sup>\*</sup> and Zhenzhou Tang <sup>\*</sup>

Institute of Marine Drugs, Guangxi University of Chinese Medicine, Nanning 530200, China; 15177636866@163.com (D.P.); hby03502@126.com (B.H.); gan\_ym2018@163.com (Y.G.); gaoch@gxctmu.edu.cn (C.G.)

<sup>\*</sup> Correspondence: yonghongliu@scsio.ac.cn (Y.L.); trcstrive2015@126.com (Z.T.)

<sup>†</sup> These authors contributed equally to this work.

**Abstract:** Phycocyanin (PC) is a pigment-protein complex. It has been reported that PC exerts anti-colorectal cancer activities, although the underlying mechanism has not been fully elucidated. In the present study, azoxymethane (AOM)/dextran sulfate sodium (DSS)-induced mice were orally administrated with PC, followed by microbiota and transcriptomic analyses to investigate the effects of PC on colitis-associated cancer (CAC). Our results indicated that PC ameliorated AOM/DSS induced inflammation. PC treatment significantly reduced the number of colorectal tumors and inhibited proliferation of epithelial cell in CAC mice. Moreover, PC reduced the relative abundance of Firmicutes, Deferribacteres, Proteobacteria and Epsilonbacteraeota at phylum level. Transcriptomic analysis showed that the expression of genes involved in the intestinal barrier were altered upon PC administration, Kyoto Encyclopedia of Genes and Genomes (KEGG) pathway analysis revealed the IL-17 signaling pathway was affected by PC treatment. The study demonstrated the protective therapeutic action of PC on CAC.

**Citation:** Pan, D.; Huang, B.; Gan, Y.; Gao, C.; Liu, Y.; Tang, Z. Phycocyanin Ameliorates Colitis-Associated Colorectal Cancer by Regulating the Gut Microbiota and the IL-17 Signaling Pathway. *Mar. Drugs* **2022**, *20*, 260. <https://doi.org/10.3390/md20040260>

Academic Editor: Marc Diederich

Received: 15 March 2022

Accepted: 7 April 2022

Published: 9 April 2022

**Publisher's Note:** MDPI stays neutral with regard to jurisdictional claims in published maps and institutional affiliations.



**Copyright:** © 2022 by the authors. Licensee MDPI, Basel, Switzerland. This article is an open access article distributed under the terms and conditions of the Creative Commons Attribution (CC BY) license (<https://creativecommons.org/licenses/by/4.0/>).

**Keywords:** phycocyanin; colorectal cancer; microbiota; transcriptome; IL-17 pathway

## 1. Introduction

Colorectal cancer (CRC) is one of the most commonly diagnosed malignancies and a leading cause of cancer-related death worldwide, the majority of CRC cases are caused by multiple risk factors including chronic inflammation, dietary style, and specific intestinal commensals [1].

Among these risk factors, chronic inflammation is a prominent factor for CRC development. Patients who suffer from inflammatory bowel diseases (IBD), such as ulcerative colitis (UC) and Crohn's disease (CD), have a significantly higher risk of developing colitis-associated cancer (CAC) and have a higher mortality rate compared to other CRC patients [2]. Although there are many studies supporting the relevance of CAC to intestinal inflammation, the underlying mechanism has not been fully elucidated.

The mammalian gut microbiota is highly complex and, in a dynamic equilibrium, has a profound influence on human physiology and nutrition. The gut microbiota interacting with epithelial and stromal intestinal cells prevents pathogenic infestation and regulates barrier functions, mucosal immune homeostasis, metabolism of indigestible dietary fiber, and synthesis of essential nutrients for the human body [3]. Disturbances in the composition of the gut microbiota can cause chronic inflammatory lesions and produce carcinogenic metabolites, leading to neoplasia.

In recent years, increasing evidence has shown that changes in microbial abundance and diversity are associated with the occurrence and progression of CAC. Gagniere et al. summarized studies on gut microbiota composition of general population and CRC patients,

they found clear differences in gut microbiota diversity in abundance between healthy individuals and CRC patients, characterized by an increased abundance of Proteobacteria and decreased Firmicutes. As such, *Bacteroides fragilis* has been shown to be enriched in CRC patients. [4] The enterotoxigenic *B. fragilis* produces fragylisin, which lyses E-cadherin on colon cells, affects epithelial permeability and causes intestinal inflammation [5]. *Fusobacterium nucleatum* can trigger a local inflammatory response and suppress the anti-tumor immune response, which is associated with a higher risk of recurrence and shorter survival times in CRC patients [6]. Studies in CAC mouse models have also revealed significant changes in microbiota composition in chemically-induced chronic intestinal inflammation [7]. These findings suggest that the gut microbiota may be a key mediator of CAC progression. CAC is a progressive process from inflammation to cancer, so preventing or alleviating inflammation is one of the strategies for CAC intervention. Currently, drugs for IBD treatments often increase patient susceptibility to infection and even lead to adverse reactions [8]. New therapeutic strategies and drugs are urgently needed.

Phycocyanin (PC) is a pigment protein complex isolated from cyanobacteria, rhodophytes, cryptophytes and Glaucophyta [9]. In the past, PC was usually extracted from open pond cultures of cyanobacterium *Arthrospira platensis* (*Spirulina platensis*) as a result of the availability. Presently, improved productivities of photoautotrophic *A. platensis* cultures have been obtained in various enclosed photobioreactors [10]. The isolation of PC involves many steps, including cell disruption, primary isolation, purification, drying and characterization of the end products. The purity of PC is evaluated based on the ratio of  $A_{620}/A_{280}$ . PC preparations with  $A_{620}/A_{280}$  greater than 0.7 are considered as food grade, while those with  $A_{620}/A_{280}$  of 3.9 are reactive grade and greater than 4.0 are analytical grade [11]. Due to its good biocompatibility and bright color, PC has been widely used in food, pharmaceutical industries, cosmetics and other fields [10]. Numerous studies have shown that phycocyanin has a variety of biological activities, such as anti-inflammation [12], antioxidation, hypoglycemic and lipid-lowering and immune regulation [13–15]. PC also has excellent anti-tumor activity. Studies have shown that PC has anti-proliferative and pro-apoptotic effects on cancer cell lines in vitro, and has no obvious toxicity to normal cells [16,17]. Indeed, the role of PC in CRC cancer has been studied and PC can induce apoptosis and inhibit migration of colorectal cancer cells [17]. PC has a preventive effect on DMH-induced CRC via possible cell cycle arrest [18], down-regulation of inflammatory factors [19], up-regulation of the apoptotic proteins [20], changes in mitochondrial membrane potential, etc. [21]. PC can regulate the gut microbiota to maintain the gut barrier [22]. However, the complex interplay between gut microbiota and anti-inflammatory and antitumor activity during CAC is not fully understood.

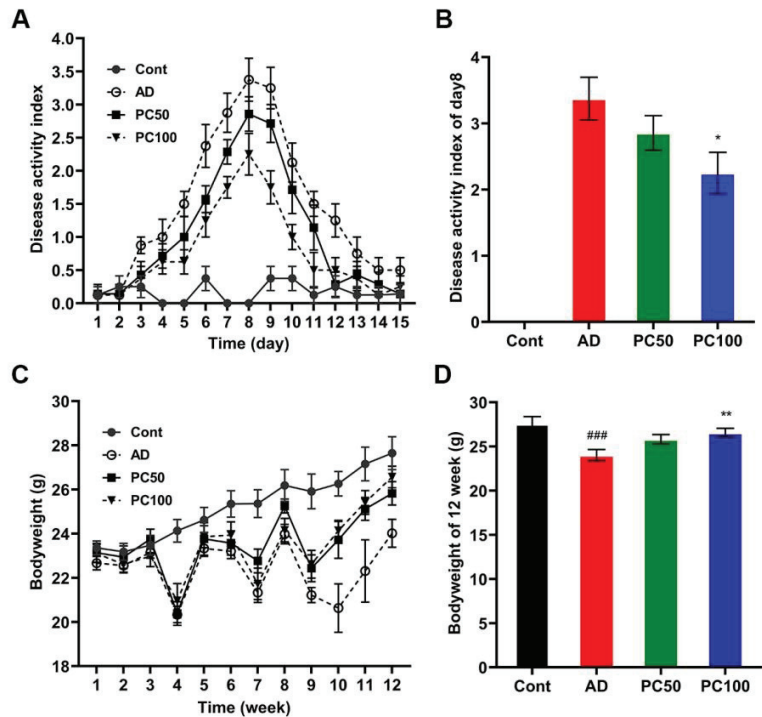
PC may not have a specific target [23]. There is a lack of knowledge about its impact on the microflora composition of CAC mice. Hence, we employed multi-omics techniques to better understand the CAC-preventing effects of PC. In this work, we aim to disclose the role of PC in CAC using microbiota and transcriptome analyses and to explore the possible crosstalk mechanism between the gut microbiota and the gene expression profile of the colon.

## 2. Results

### 2.1. PC Inhibited Azoxymethane/Dextran Sulfate Sodium (AOM/DSS)-Induced Tumorigenesis

#### 2.1.1. PC Suppressed AOM/DSS Induced Inflammation and Body Weight Loss

We first established the CAC model by injecting mice with AOM (10 mg/kg Body-weight) followed by three rounds of 2.5% DSS exposure. Disease activity index (DAI) analysis indicated that mice of AOM/DSS (AD) groups had higher DAI scores than the normal control (Cont) group on day eight, suggesting the induction of severe colitis (Figure 1A,B). The PC high-dose group (100 mg/kg, PC100) had a significantly lower DAI score than that of the AD group on day eight, the PC low-dose group (50 mg/kg, PC50) also had a lower DAI score compared with the AD group, although the difference was not significant (Figure 1A,B).



**Figure 1.** PC alleviated mice colitis symptom: (A) PC decreased the DAI score of AD mice; (B) DAI score of day eight; (C) Body weight change of mice during the study; (D) Mice body weight at 12th week. Data were expressed as mean ± SEM ( $n \geq 8$  per group). ###  $p < 0.001$  vs. Cont group; \*  $p < 0.05$ ; \*\*  $p < 0.01$  vs. AD group.

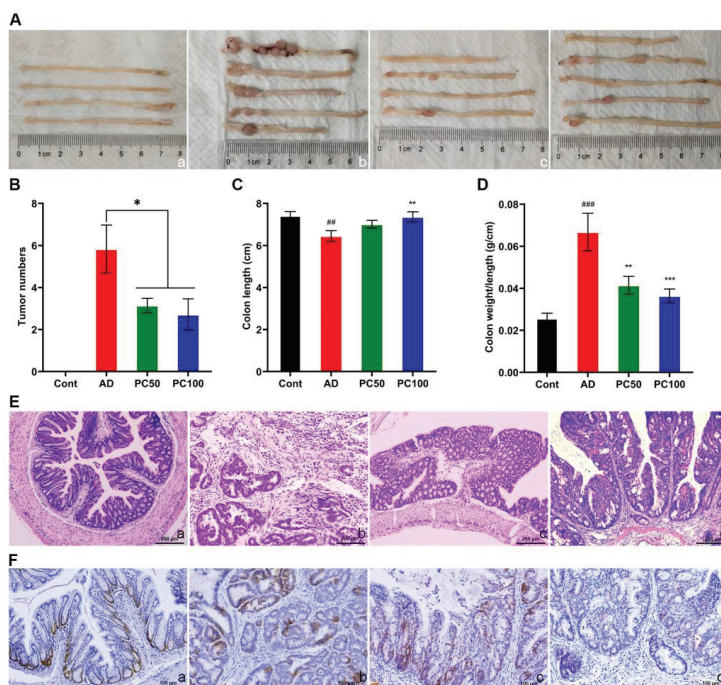
The average weight of mice belonging to the Cont group was higher than that of all other groups. AD mice exhibited a significant body weight loss when compared to the Cont group. PC treatment reversed the body weight loss induced by AOM/DSS (Figure 1C,D).

2.1.2. PC Attenuates AOM/DSS Induced Tumorigenesis

After dissection, we found different numbers and sizes of tumors at the distal part of the colon of AD mice, tumor numbers were significantly reduced in PC50 and PC100 groups, yet there was no significant difference between PC50 and PC100 groups (Figure 2A,B).

The length of the mouse colon and the ratio of colon weight to length are considered to be one of the markers of the degree of intestinal inflammation [24]. The AD mice had significantly shortened colonic length (Figure 2C), and the colon weight/length ratio was significantly increased, which was markedly reversed after high dose PC treatment (Figure 2D).

The colon mucosal histological studies also revealed that damaged epithelial integrity, and abnormal glands were partially restored in PC treated groups (Figure 2E). In addition, immunohistochemical analysis showed a significant reduction in proliferating cell nuclear antigen (PCNA) positive cells in tumor tissues of mice treated with a high dose of PC (Figure 2F). These findings indicate the anti-tumorigenic effects of PC in the AOM/DSS mice.



**Figure 2.** PC suppressed the tumorigenesis induced by AOM/DSS. Gross morphology of colon (A), tumor number (B), colon length (C) and colon weight/length ratio (D) were studied. (E) Histological observation of mice colon. Scale bars 200  $\mu$ m. (F) PC treatment decreased the number of PCNA-positive cells in the colon. Scale bars 100  $\mu$ m. a, Cont group; b, AD group; c, PC50 group; d, PC100 group. Data were presented as means  $\pm$  SEM ( $n = 6$  for AD group and  $n \geq 7$  for the other groups). ##  $p < 0.01$ ; ###  $p < 0.001$  vs. Cont group; \*  $p < 0.05$ ; \*\*  $p < 0.01$ ; \*\*\*  $p < 0.001$  vs. AD group.

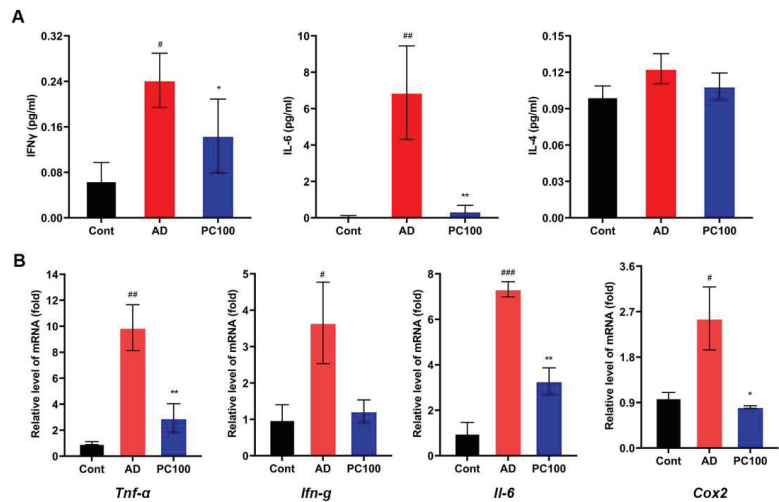
### 2.1.3. PC Reduces the Level of Proinflammatory Cytokines in CAC Mice

Some inflammatory cytokines such as IL-1, IL-6, IFN $\gamma$  and TNF $\alpha$  play an important role during the development of CAC. Studies showed an increased level of these cytokines in AOM/DSS induced mice serum or colon [25–28].

We found that PC significantly reduced the levels of IL-6 and IFN $\gamma$  in mice serum (Figure 3A). Similar results were obtained from the qPCR experiment (Figure 3B). IL-4 is considered as an anti-inflammatory cytokine [29,30] however, PC treatment did not show an obvious effect on the IL-4 level. The expression level of *clooxygenase-2* (*Cox2*), a major proinflammatory enzyme [31], was also inhibited by PC. Collectively, these results demonstrated the anti-inflammatory effect of PC.

### 2.2. PC Treatment Affected CAC Mice Gut Microbiota

Numerous research studies have shown the important role of gut microbiota in the development of colorectal cancer. To further investigate whether PC attenuated AOM/DSS induced CAC is related to gut microbiota, we performed 16S rRNA sequence analysis on feces samples collected from mice. The microbial  $\alpha$ -diversity indices (Chao, Ace, Shannon and Simpson index) were slightly declined in the AD group without significance. PC treatment significantly decreased the diversity indices (Shannon and Simpson indexes) and the richness indices Ace, indicating that PC can affect the microbial community (Supplementary Figure S1 and Table S1). PCA analysis on OTU level indicated that the microbial community changed among three groups (Figure 4A–C).



**Figure 3.** Effect of PC supplementation on proinflammatory mediators and cytokines. (A) Concentrations of IFN $\gamma$ , IL-6 and IL-4 in sera from the Cont, AD and PC100 mice. (B) qPCR evaluation of the expression of *Tnf- $\alpha$* , *Ifn- $\gamma$* , *Il-6* and *Cox2* relative to that of *Gapdh*. Data were expressed as mean  $\pm$  SEM ( $n \geq 5$  per group). #  $p < 0.05$ ; ##  $p < 0.01$ ; ###  $p < 0.001$  vs. Cont group; \*  $p < 0.05$ ; \*\*  $p < 0.01$  vs. AD group.

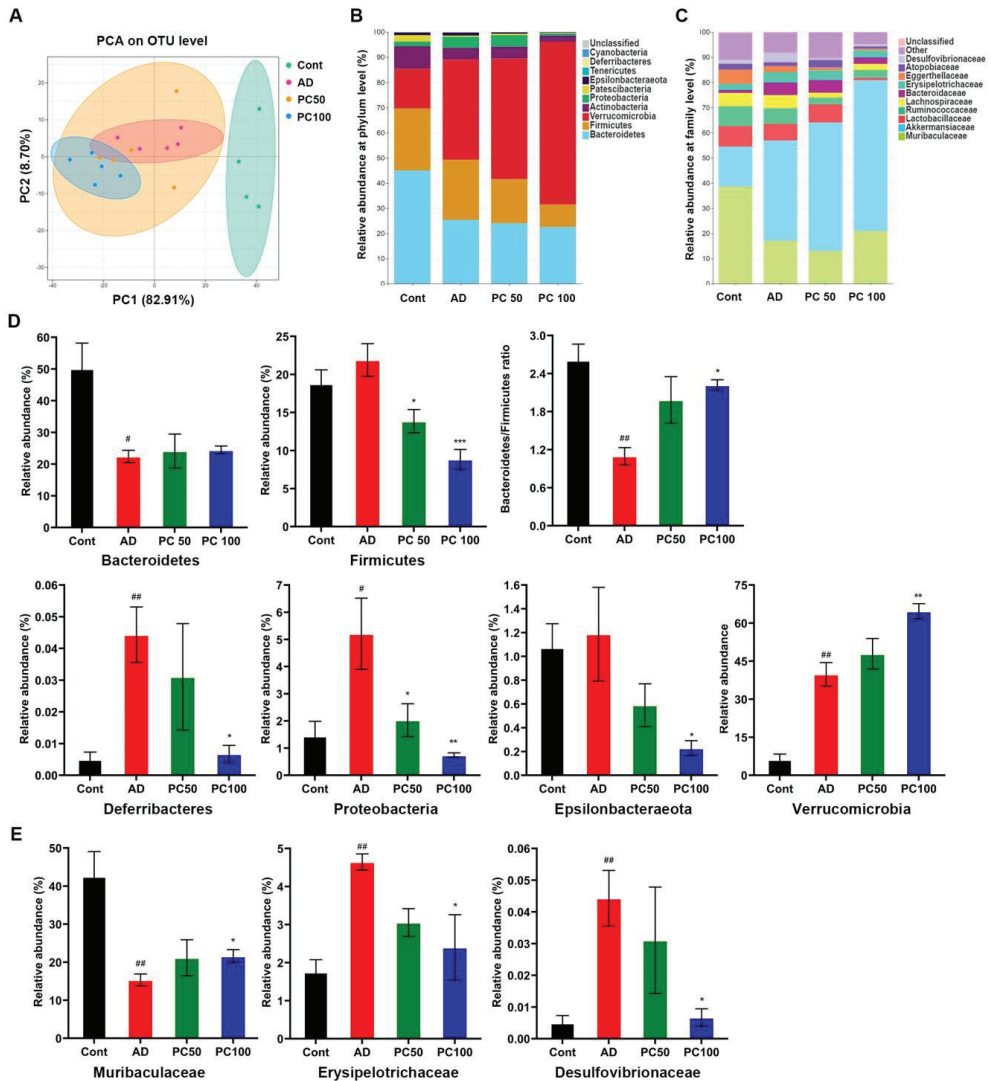
We further carried out the relative abundance analysis, at the phylum level, Verrucomicrobia, Bacteroidetes, Firmicutes, Actinobacteria and Proteobacteria were the major phyla in the three groups. Compared to the Cont group, the relative abundance of Firmicutes, Proteobacteria and Deferribacteres were significantly increased in the AD group, while the relative abundance of Bacteroidetes was dramatically decreased (Figure 4D). PC significantly decreased the abundance of Firmicutes, Proteobacteria, Deferribacteres and Epsilonbacteraeota. Interestingly, PC markedly increased the Verrucomicrobia level and the Bacteroidetes/Firmicutes ratio. At the family level, we found a significant decrease in Muribaculaceae and increase in Erysipelotrichaceae and Desulfovibrionaceae in the AD group compared to that of the Cont group, and PC treatment (100 mg/kg) significantly reversed the changes (Figure 4E).

### 2.3. Transcriptome Analysis of Genes Expressed in CAC Mice

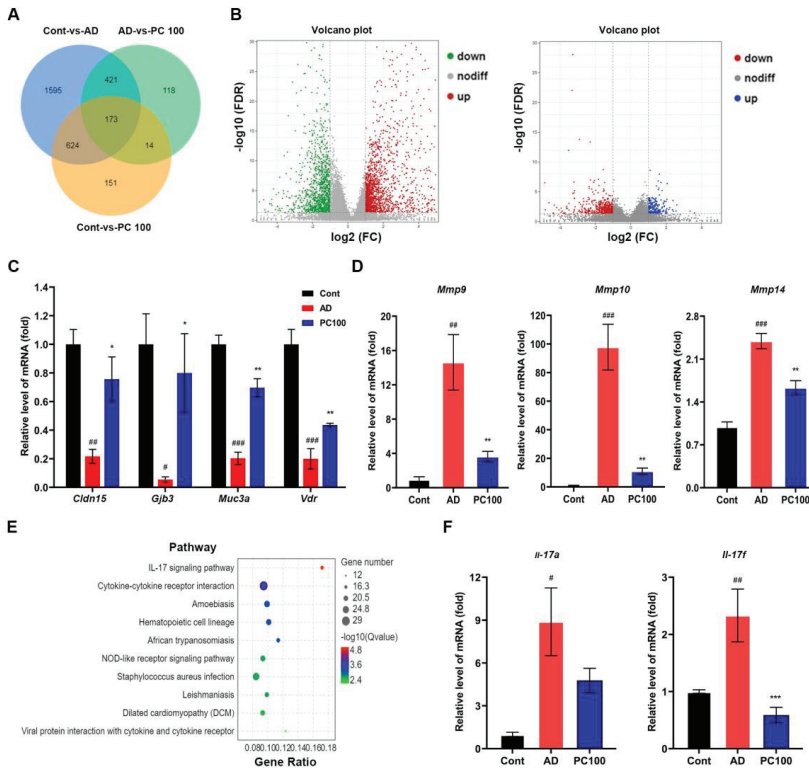
Transcriptome analysis provides an efficient way for the systematic analysis of genes that may be involved in CAC development. We therefore identified the differentially expressed genes (DEGs) between AD mice and PC100 group mice following the cutoff criteria fold-change  $|\log_2FC| \geq 1$  and  $p$ -value  $< 0.05$ . A library with size-normalized count for the specimen was generated by making volcano plots for the DEGs as described elsewhere (Figure 5A,B) [32].

Comparison of the AD group and the PC100 group identified 726 DEGs, among which 218 were upregulated and 508 were down-regulated (Supplementary Table S2). These upregulated DEGs included *Muc3a*, *Vdr*, *Cldn15* and *Gjb3*, whereas the downregulated DEGs included *Mmp9*, *Mmp10* and *Mmp14*, our qPCR study further confirmed the results (Figure 5C,D).





**Figure 4.** Effects of PC on gut microbiota in AOM/DSS induced CAC mice. PCA analysis on OTU level (A) and microbial relative abundance at phylum level (B) and family level (C) were shown. (D) At phylum level, the relative abundance of Bacteroidetes, Firmicutes, Bacteroidetes/Firmicutes ratio, Deferribacteres, Proteobacteria, Epsilonbacteraeota and Verrucomicrobia were affected by PC treatment. (E) Comparison of the relative abundance of Muribaculaceae, Erysipelotrichaceae and Desulfovibrionaceae in different groups. Data were expressed as mean  $\pm$  SEM ( $n \geq 4$  per group). #  $p < 0.01$ ; ##  $p < 0.01$  vs. Cont group; \*  $p < 0.05$ ; \*\*  $p < 0.01$ ; \*\*\*  $p < 0.001$  vs. AD group.



**Figure 5.** RNA-Seq analysis of DEGs in colon of the Cont, AD and PC100 group mice: (A) Venn diagram of DEGs; (B) volcano plot of DEGs, left, Cont vs. AD, right, AD vs. PC100; (C) Up-regulated DEGs; (D) Down-regulated DEGs in PC100 group mice were selected and validated by qPCR analysis; (E) KEGG enrichment analysis of DEGs identified from AD vs. PC100; (F) qPCR evaluation of the expression of IL-17 pathway members *Il-17a* and *Il-17f* relative to that of *Gapdh*. Three replicates were carried out in the qPCR analysis ( $n = 3$ ). #  $p < 0.01$ ; ##  $p < 0.01$ ; ###  $p < 0.001$  vs. Cont group; \*  $p < 0.05$ ; \*\*  $p < 0.01$ ; \*\*\*  $p < 0.001$  vs. AD group.

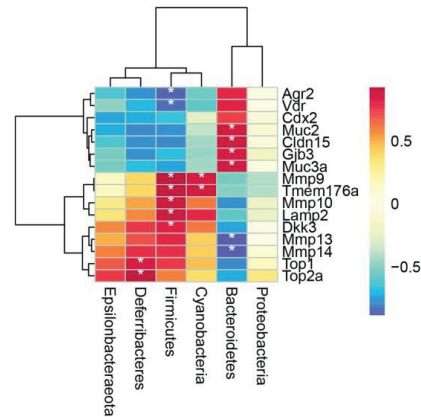
Gene ontology (GO) analysis showed that the upregulated and downregulated DEGs were significantly enriched in the cellular process, biological regulation, developmental process etc. (Supplementary Figure S2).

Kyoto Encyclopedia of Genes and Genomes (KEGG) pathway analysis showed that DEGs were mapped to numerous pathways. Figure 5E presented the top ten significantly enriched KEGG pathways of the DEGs (AD vs. PC100). The most significantly enriched pathway was the IL-17 signaling pathway. Others included pathways involved in cytokine-cytokine receptor interaction, such as Amoebiasis, Hematopoietic cell lineage and so on. To verify the KEGG enrichment results, we examined the mRNA expression level of *Il-17a* and *Il-17f* (members of the *Il-17* family). The qPCR results indicated that PC significantly inhibited *Il-17f* expression.

#### 2.4. Spearman’s Correlation Analysis of Microbiota and DEGs Regulated by PC

To further investigate the correlation between changes in gut microbiota and the expression level of DEGs, a Spearman correlation analysis between the six phyla and the selected DEGs among three groups was carried out (Figure 6, Supplementary Table S3). Bacteroides was positively correlated with *Muc2*, *Cldn15*, *Gjb3* and *Muc3a*, however, it

was negatively correlated with *Mmp13*, *Mmp14* ( $p < 0.05$ ). Firmicutes showed negative correlation with *Agr2* and *Vdr*, and showed positive correlation with *Mmp9*, *Tmem176a*, *Mmp10*, *Lamp2* and *Dkk3* ( $p < 0.05$ ). Deferribacteres was positively correlated with *Top1*, *Top2a* ( $p < 0.05$ ) and Cyanobacteria was positively correlated *Mmp1*, *Tmem176a* ( $p < 0.05$ ).



**Figure 6.** Spearman's correlation analysis of microbiota and representative DEGs. Red color denotes positive correlation, blue color denotes negative correlation. \*  $p < 0.05$ .

### 3. Discussion

CRC is one of the most common causes of cancer-related death, epidemiological reports have shown that individuals with IBD are more likely to develop colorectal cancer (CRC) than the general population [33].

CAC progression is influenced by intestinal bacteria in the mucosal layer. Many bacteria, especially *Bacteroides*, *Escherichia coli* and *Fusobacterium nucleatum*, are involved in CAC progression [6,34].

PC is a blue pigment and has multiple biological functions. It has been utilized in foods and cosmetics, biotechnology, diagnostics and medicines [10]. In vitro studies have shown the antineoplastic values of PC in different cancer cells, such as pancreatic cancer [16], lung cancer [35]. PC can inhibit cell cycle progression, induce cell apoptosis and decrease proinflammatory cytokines through regulating PI3K-Akt, Jak3-Stat3, NF- $\kappa$ b and Wnt signaling pathway [18,19,21,36]. The role of PC in modulation of the gut microbiota in CAC mice has not yet been investigated.

PC intervention increased the bacterial abundance and diversity, and reduced intestinal permeability and increased the intestinal barrier function [22], suggesting a protective role of PC in the gut.

The AOM/DSS model is a chemically induced CAC mouse model employing AOM and DSS carcinogens. When compared with the DMH induced model, the AOM/DSS-induced mouse model has higher reproducibility, mimics a form of inflammatory colorectal cancer in humans and is widely used in CAC studies [37].

In the present study, we demonstrated that orally administered PC markedly inhibited AOM/DSS induced CAC in mice, as evidenced by the tumor number and histopathological examination. PC also inhibited colorectal tumor proliferation, and alleviated colonic inflammation by decreasing the inflammatory cytokines (IFN $\gamma$  and IL-6) level. As mentioned above, the expression of proinflammatory genes (*Tnf- $\alpha$* , *Il-6* and *Cox2*) were downregulated, supporting the findings of a previous study, which showed that the application of PC resulted in the decreased protein expression of proinflammatory cytokines IL-1 $\beta$ , IFN $\gamma$  and TNF- $\alpha$  [19]. While there was a decrease in the genetic expression of *Ifn- $\gamma$*  in this study, it was not significant.

Nowadays, microbiome and transcriptome have been widely used in biological research to provide a comprehensive understanding of gene expression [32]. As such, 16S rRNA sequence analysis indicated that PC significantly changed the composition of mice gut microbiota by decreasing Firmicutes, Deferribacteres, Proteobacteria, Cyanobacteria and Epsilonbacteraeota at the phylum level. PC treatment increased the Bacteroidetes/Firmicutes ratio.

In an American patient cohort study, a notable increase in Firmicutes was observed when compared to non-adenoma subjects in adenoma biopsies [38]. The appropriate Firmicutes/Bacteroidetes ratio is accepted as a marker in maintaining normal intestinal homeostasis, and a disturbed Firmicutes/Bacteroidetes ratio is regarded as dysbiosis and has been associated with IBD [39]. Proteobacteria is enriched in intestinal pathogens, which can cause inflammation and change intestinal microbiota, and promote the development of IBD [40]. Muribaculaceae is one of the major mucin monosaccharide foragers, a recent study showed that expansion of Muribaculaceae in the gut resulted in the consumption of N-acetylglucosamine and an impeding of the colonization of pathogens such as *Clostridium perfringens*, thereby exerting a protective effect in the gut [41]. The bacterial family Erysipelotrichaceae belongs to the Firmicutes phylum. Studies have revealed the increased abundance of Erysipelotrichaceae in CRC patients and the DMH induced colon cancer animal model [28,42,43], implying that it may be involved in the occurrence and development of CRC. Few research studies have investigated the relationship between Desulfovibrionaceae and CRC, however, many studies reported that it is an endotoxin-producer [44–46], endotoxin can promote colorectal cancer cells adhesion and invasion through the regulation of the TLR4/NF- $\kappa$ B pathway [47]. The results of the present study suggest that PC has a positive effect on the gut microbiota, thus exerting a tumor preventive effect.

We also found a dramatic increase in Verrucomicrobia in both the AD and PC treated groups. A recent study showed that natural algal extracts such as ulvan and astaxanthin assist the increase in beneficial microbial populations such as Bacteroidia, Bacilli, Clostridia, and Verrucomicrobia in the gut [48]. We assumed that the increase in Verrucomicrobia might not be an adverse event.

Transcriptomic study identified that DEGs such as *Muc3a* and *Vdr* were up-regulated by PC. *Muc3a* is a very large cell surface glycoprotein present in columnar epithelial cells of the small intestine and colon [49]. Previous study suggested that *Muc3a* may inhibit pathogens attached to the intestinal epithelial cells [50]. Studies also revealed that VDR overexpression significantly reduced the sizes and numbers of tumor spheres formed by CRC stem cells [51]. We also found that PC increased the levels of the colon cell junction markers *Cldn15* and *Gjb3*, while it decreased the expression level of *Mmp9*, *Mmp10* and *Mmp14*. This result demonstrated that PC may reduce intestinal permeability and reinforce the intestinal barrier function, thus affecting AOM/DSS induced CAC progression.

KEGG enrichment analysis revealed the IL-17 signaling pathway was one of the most obvious pathways regulated by PC. The qPCR experiment validated the result. However, how PC regulated the IL-17 pathway requires further study.

There are limitations in our research, for example, although our work proposed a potential correlation between specific bacteria and the gene expression profile, we did not show any direct evidence; perhaps fecal transplantation experiments in germ-free mice would be a better way to address the question.

This study investigated the effect of PC on CAC from the perspective of microbiota modulation and can be used as a reference for researchers to further investigate the underlying mechanism of PC in CAC. PC is a promising drug for CAC prevention.

## 4. Materials and Methods

### 4.1. Reagents and Antibodies

PC (extracted from *Spirulina platensis*, Amax/A280 > 3.5) was purchased from Binmei Biotech (Taizhou, China). PC was dissolved in phosphate buffer solution (PBS) according

to the instructions. AOM (cat. no. 25843-45-2) was purchased from Sigma-Aldrich. DSS (cat. no. 160110) was purchased from MP Biomedicals, LLC (Aurora, OH, USA). Primary antibodies for PCNA (13110) were purchased from CST Company (Danvers, MA, USA).

#### 4.2. Animal

All animal experiments followed the guidelines for ethical procedures and scientific care given by the Animal Care and Use Committee of the Guangxi University of Chinese Medicine. Wild-type C57BL/6J mice were purchased from Hunan SJA Laboratory Animal Co., Ltd. (Changsha, China). All animals were housed in plastic cages under a 12 h light/dark cycle with free access to water and food. To establish the CAC mice model, the male mice were injected with AOM (10 mg/kg i.p.), exposed to drinking water containing 2% DSS for one week, and then left to drink normal water for two weeks. This treatment was repeated for three cycles.

#### 4.3. Histology

At the end of the study, mice were sacrificed by cervical dislocation. The colon was dissected, hematoxylin and eosin (H and E) staining and immunohistochemistry (IHC) analysis was performed. Briefly, the tissues were collected and fixed in 4% paraformaldehyde (PFA) overnight. Then, the tissues were embedded in paraffin wax. The paraffin-embedded tissues were sectioned serially at 5  $\mu$ m thick. The sections were dewaxed, hydrated, and stained with H and E. For immunohistochemistry, the dewaxed sections were microwaved in the antigen unmasking solution, incubated in 3% hydrogen peroxide, blocked with bovine serum albumin (dissolved in PBS), and incubated with primary antibodies at 4 °C overnight. Finally, the signals were detected by incubating the sections with horseradish peroxidase (HRP)-conjugated secondary antibodies and then 3,3'-diaminobenzidine (DAB) staining colorimetric reagent was used. All images were processed with Adobe Photoshop CS6.

#### 4.4. Serum Cytokines Detection

The concentration of IFN $\gamma$ , IL-6 and IL-4 in serum were determined follow the instructions of the commercial kits (BIORAD, cat NO. 12002798) bought from Shanghai Univ-Biotechnology Co., Ltd. (Shanghai, China). All procedures were performed according to manuals instructions.

#### 4.5. RNA Extraction, Gene Microarray and Real-Time PCR

Total RNA was isolated from testes tissues or cells using a TRIzol solution (Invitrogen). For the microarray, the RNA was labeled and hybridized to Affymetrix chips as previously described [52]. One microgram of total RNA from each sample was reverse-transcribed to cDNA in a 20  $\mu$ L reaction volume. The real-time PCR was performed using a Roche LC480 PCR system, and the mRNA expression level was normalized to *Gapdh* mRNA and analyzed using the comparative cycle threshold method. The primers employed in these experiments are listed in Supplemental Table S4.

#### 4.6. Statistical Analysis

All statistical analyses were conducted using SPSS 20.0 analysis software (SPSS Inc., Chicago, IL, USA). Data were analyzed by one-way ANOVA followed by the Tukey's post hoc test. Bioinformatics analysis of RNA-seq and 16S rRNA sequence, including species abundance, was performed using Omicsmart (Genedenovo Biotechnology Co. Ltd., Guangzhou, China), microbiota data were analyzed by Kruskal–Wallis one-way ANOVA followed by Wilcoxon–Mann–Whitney test (data not normally distributed). Significance was set at  $p < 0.05$  for all tests, data were expressed as Mean  $\pm$  SEM.

## 5. Conclusions

In this study, we demonstrated that PC alleviated inflammation and reduced tumorigenesis in AOM/DSS induced mice. The tumor prevention may be mediated through modulating the gut microbiota and gene expression in colonic cells. PC is a promising drug for clinical prevention and treatment of colorectal cancer.

**Supplementary Materials:** The following supporting information can be downloaded at: <https://www.mdpi.com/article/10.3390/md20040260/s1>. Figure S1. PC decreased the  $\alpha$ -diversity of the microbiota in AOM/DSS induced mice model; Figure S2. GO enrichment analysis of differentially expressed genes (DEGs) identified in the study; Table S1. Data of the  $\alpha$ -diversity index analysis; Table S2. DEGs were identified in CAC mice with or without PC treatment; Table S3. Data of Spearman's correlation analysis; Table S4. Primers list of qPCR.

**Author Contributions:** Conceptualization, D.P. and Z.T.; Data curation, B.H.; Formal analysis, Y.L.; Funding acquisition, Y.L. and Z.T.; Investigation, C.G.; Methodology, D.P., B.H. and Z.T.; Project administration, Y.L. and Z.T.; Software, Y.G.; Supervision, C.G., Y.L. and Z.T.; Validation, Y.G. and Z.T.; Writing—original draft, D.P. and Z.T.; Writing—review and editing, D.P. and B.H. All authors have read and agreed to the published version of the manuscript.

**Funding:** This study was supported by Guangxi Science and Technology Plan Project (NO. AD19110112, AD19110013), the Initial Scientific Research Foundation of Introduced Doctors in 2018 of Guangxi University of Chinese Medicine (NO. 2018BS046), the Special Fund for Bagui Scholars of Guangxi (05019055).

**Institutional Review Board Statement:** The animal study protocol was approved by the Institutional Animal Care and Ethical Committee, Guangxi University of Traditional Chinese Medicine, Nanning, China (Protocol number 20190723, approved: 12 July 2019).

**Data Availability Statement:** All data supporting the conclusions of this article are included in this article.

**Acknowledgments:** The authors acknowledge lab members for critical discussions and technical support.

**Conflicts of Interest:** The authors declare no conflict of interest.

## References

- Morrison, I.J.; Zhang, J.; Lin, J.; Murray, J.E.; Porter, R.; Langat, M.K.; Sadgrove, N.J.; Barker, J.; Zhang, G.; Delgoda, R. Potential chemopreventive, anticancer and anti-inflammatory properties of a refined artocarpin-rich wood extract of *Artocarpus heterophyllus* Lam. *Sci. Rep.* **2021**, *11*, 6854. [[CrossRef](#)] [[PubMed](#)]
- Feagins, L.A.; Souza, R.F.; Spechler, S.J. Carcinogenesis in IBD: Potential targets for the prevention of colorectal cancer. *Nat. Rev. Gastroenterol. Hepatol.* **2009**, *6*, 297–305. [[CrossRef](#)] [[PubMed](#)]
- Roy, S.; Trinchieri, G. Microbiota: A key orchestrator of cancer therapy. *Nat. Rev. Cancer* **2017**, *17*, 271–285. [[CrossRef](#)] [[PubMed](#)]
- Gagniere, J.; Raisch, J.; Veziat, J.; Barnich, N.; Bonnet, R.; Buc, E.; Bringer, M.A.; Pezet, D.; Bonnet, M. Gut microbiota imbalance and colorectal cancer. *World J. Gastroenterol.* **2016**, *22*, 501–518. [[CrossRef](#)]
- Boleij, A.; Hechenbleikner, E.M.; Goodwin, A.C.; Badani, R.; Stein, E.M.; Lazarev, M.G.; Ellis, B.; Carroll, K.C.; Albesiano, E.; Wick, E.C.; et al. The *Bacteroides fragilis* toxin gene is prevalent in the colon mucosa of colorectal cancer patients. *Clin. Infect. Dis.* **2015**, *60*, 208–215. [[CrossRef](#)]
- Song, M.; Chan, A.T.; Sun, J. Influence of the gut microbiome, diet, and environment on risk of colorectal cancer. *Gastroenterology* **2020**, *158*, 322–340. [[CrossRef](#)]
- Liang, X.; Li, H.; Tian, G.; Li, S. Dynamic microbe and molecule networks in a mouse model of colitis-associated colorectal cancer. *Sci. Rep.* **2014**, *4*, 4985. [[CrossRef](#)]
- Gong, Z.; Zhao, S.; Zhou, J.; Yan, J.; Wang, L.; Du, X.; Li, H.; Chen, Y.; Cai, W.; Wu, J. Curcumin alleviates DSS-induced colitis via inhibiting NLRP3 inflammasome activation and IL-1 $\beta$  production. *Mol. Immunol.* **2018**, *104*, 11–19. [[CrossRef](#)]
- Yu, P.; Wu, Y.; Wang, G.; Jia, T.; Zhang, Y. Purification and bioactivities of phycocyanin. *Crit. Rev. Food Sci. Nutr.* **2017**, *57*, 3840–3849. [[CrossRef](#)]
- Eriksen, N.T. Production of phycocyanin—A pigment with applications in biology, biotechnology, foods and medicine. *Appl. Microbiol. Biotechnol.* **2008**, *80*, 1–14. [[CrossRef](#)]
- Kuddus, M.; Singh, P.; Thomas, G.; Al-Hazimi, A. Recent developments in production and biotechnological applications of C-phycocyanin. *Biomed. Res. Int.* **2013**, *2013*, 742859. Available online: <https://pubmed.ncbi.nlm.nih.gov/24063013/> (accessed on 6 April 2022). [[CrossRef](#)] [[PubMed](#)]

12. Jensen, G.S.; Attridge, V.L.; Beaman, J.L.; Guthrie, J.; Ehmann, A.; Benson, K.F. Antioxidant and anti-inflammatory properties of an aqueous cyanophyta extract derived from *Arthrospira platensis*: Contribution to bioactivities by the non-phycoyanin aqueous fraction. *J. Med. Food* **2015**, *18*, 535–541. [[CrossRef](#)] [[PubMed](#)]
13. Ou, Y.; Ren, Z.; Wang, J.; Yang, X. Phycocyanin ameliorates alloxan-induced diabetes mellitus in mice: Involved in insulin signaling pathway and GK expression. *Chem. Biol. Interact.* **2016**, *247*, 49–54. [[CrossRef](#)] [[PubMed](#)]
14. Seo, Y.J.; Kim, K.J.; Choi, J.; Koh, E.J.; Lee, B.Y. *Spirulina maxima* extract reduces obesity through suppression of adipogenesis and activation of browning in 3T3-L1 cells and high-fat diet-induced obese mice. *Nutrients* **2018**, *10*, 712. [[CrossRef](#)] [[PubMed](#)]
15. Nemoto-Kawamura, C.; Hirahashi, T.; Nagai, T.; Yamada, H.; Katoh, T.; Hayashi, O. Phycocyanin enhances secretory IgA antibody response and suppresses allergic IgE antibody response in mice immunized with antigen-entrapped biodegradable microparticles. *J. Nutr. Sci. Vitaminol.* **2004**, *50*, 129–136. [[CrossRef](#)] [[PubMed](#)]
16. Liao, G.; Gao, B.; Gao, Y.; Yang, X.; Cheng, X.; Ou, Y. Phycocyanin inhibits tumorigenic potential of pancreatic cancer cells: Role of apoptosis and autophagy. *Sci. Rep.* **2016**, *6*, 34564. [[CrossRef](#)]
17. Kefayat, A.; Ghahremani, F.; Safavi, A.; Hajiaghababa, A.; Moshtaghian, J. C-phycoyanin: A natural product with radiosensitizing property for enhancement of colon cancer radiation therapy efficacy through inhibition of COX-2 expression. *Sci. Rep.* **2019**, *9*, 19161. [[CrossRef](#)]
18. Saini, M.K.; Sanyal, S.N. Cell cycle regulation and apoptotic cell death in experimental colon carcinogenesis: Intervening with cyclooxygenase-2 inhibitors. *Nutr. Cancer* **2015**, *67*, 620–636. [[CrossRef](#)]
19. Saini, M.K.; Vaish, V.; Sanyal, S.N. Role of cytokines and Jak3/Stat3 signaling in the 1,2-dimethylhydrazine dihydrochloride-induced rat model of colon carcinogenesis: Early target in the anticancer strategy. *Eur. J. Cancer Prev.* **2013**, *22*, 215–228. [[CrossRef](#)]
20. Saini, M.K.; Sanyal, S.N.; Vaiphei, K. Piroxicam and C-phycoyanin mediated apoptosis in 1,2-dimethylhydrazine dihydrochloride induced colon carcinogenesis: Exploring the mitochondrial pathway. *Nutr. Cancer* **2012**, *64*, 409–418. [[CrossRef](#)]
21. Saini, M.K.; Sanyal, S.N. PTEN regulates apoptotic cell death through PI3-K/Akt/GSK3beta signaling pathway in DMH induced early colon carcinogenesis in rat. *Exp. Mol. Pathol.* **2012**, *93*, 135–146. [[CrossRef](#)] [[PubMed](#)]
22. Xie, Y.; Li, W.; Zhu, L.; Zhai, S.; Qin, S.; Du, Z. Effects of phycocyanin in modulating the intestinal microbiota of mice. *Microbiologyopen* **2019**, *8*, e00825. [[CrossRef](#)] [[PubMed](#)]
23. Fernandes, E.S.E.; Figueira, F.D.S.; Lettnin, A.P.; Carrett-Dias, M.; Filgueira, D.; Kalil, S.; Trindade, G.S.; Votto, A.P.S. C-Phycocyanin: Cellular targets, mechanisms of action and multi drug resistance in cancer. *Pharmacol. Rep.* **2018**, *70*, 75–80. [[CrossRef](#)]
24. Hammad, A.; Zheng, Z.H.; Namani, A.; Elshaer, M.; Wang, X.J.; Tang, X. Transcriptome analysis of potential candidate genes and molecular pathways in colitis-associated colorectal cancer of Mkp-1-deficient mice. *BMC Cancer* **2021**, *21*, 607. [[CrossRef](#)]
25. Song, C.H.; Kim, N.; Lee, S.M.; Nam, R.H.; Choi, S.I.; Kang, S.R.; Shin, E.; Lee, D.H.; Lee, H.N.; Surh, Y.J. Effects of 17beta-estradiol on colorectal cancer development after azoxymethane/dextran sulfate sodium treatment of ovariectomized mice. *Biochem. Pharmacol.* **2019**, *164*, 139–151. [[CrossRef](#)]
26. Wang, C.; Li, W.; Wang, H.; Ma, Y.; Zhao, X.; Zhang, X.; Yang, H.; Qian, J.; Li, J. *Saccharomyces boulardii* alleviates ulcerative colitis carcinogenesis in mice by reducing TNF-alpha and IL-6 levels and functions and by rebalancing intestinal microbiota. *BMC Microbiol.* **2019**, *19*, 246. [[CrossRef](#)]
27. Wang, C.Z.; Yu, C.; Wen, X.D.; Chen, L.; Zhang, C.F.; Calway, T.; Qiu, Y.; Wang, Y.; Zhang, Z.; Anderson, S.; et al. American ginseng attenuates colitis-associated colon carcinogenesis in mice: Impact on gut microbiota and metabolomics. *Cancer Prev. Res.* **2016**, *9*, 803–811. [[CrossRef](#)]
28. Wang, M.; Zhou, B.; Cong, W.; Zhang, M.; Li, Z.; Li, Y.; Liang, S.; Chen, K.; Yang, D.; Wu, Z. Amelioration of AOM/DSS-induced murine colitis-associated cancer by evodiamine intervention is primarily associated with gut microbiota-metabolism-inflammatory signaling axis. *Front. Pharmacol.* **2021**, *12*, 797605. [[CrossRef](#)]
29. Peluzzo, A.M.; Autieri, M.V. Challenging the paradigm: Anti-inflammatory interleukins and angiogenesis. *Cells* **2022**, *11*, 587. [[CrossRef](#)]
30. Shapouri-Moghaddam, A.; Mohammadian, S.; Vazini, H.; Taghadosi, M.; Esmaeili, S.A.; Mardani, F.; Seifi, B.; Mohammadi, A.; Afshari, J.T.; Sahebkar, A. Macrophage plasticity, polarization, and function in health and disease. *J. Cell Physiol.* **2018**, *233*, 6425–6440. [[CrossRef](#)]
31. Raafat, M.; Kamel, A.A.; Shehata, A.H.; Ahmed, A.F.; Bayoumi, A.M.A.; Moussa, R.A.; Abourehab, M.A.S.; El-Daly, M. Aescin protects against experimental benign prostatic hyperplasia and preserves prostate histomorphology in rats via suppression of inflammatory cytokines and cox-2. *Pharmaceuticals* **2022**, *15*, 130. [[CrossRef](#)] [[PubMed](#)]
32. Guo, C.; Liu, X.; Xu, Y.; Han, X.; Xie, R.; Meng, X.; Li, Y.; Chen, T.; Cheng, Z.; Fu, X. Exploring the mechanism of action of cannei formula against colorectal adenoma through multi-omics technique. *Front. Cell Dev. Biol.* **2021**, *9*, 778826. [[CrossRef](#)] [[PubMed](#)]
33. Wan, D.; Wang, S.; Xu, Z.; Zan, X.; Liu, F.; Han, Y.; Jiang, M.; Wu, A.; Zhi, Q. PRKAR2A-derived circular RNAs promote the malignant transformation of colitis and distinguish patients with colitis-associated colorectal cancer. *Clin. Transl. Med.* **2022**, *12*, e683. [[CrossRef](#)] [[PubMed](#)]
34. Clay, S.L.; Fonseca-Pereira, D.; Garrett, W.S. Colorectal cancer: The facts in the case of the microbiota. *J. Clin. Investig.* **2022**, *132*, 4. [[CrossRef](#)]
35. Hao, S.; Li, S.; Wang, J.; Zhao, L.; Yan, Y.; Wu, T.; Zhang, J.; Wang, C. C-Phycocyanin suppresses the *in vitro* proliferation and migration of non-small-cell lung cancer cells through reduction of RIPK1/NF-kappaB activity. *Mar. Drugs* **2019**, *17*, 362. [[CrossRef](#)]

36. Saini, M.K.; Sanyal, S.N. Piroxicam and c-phycocyanin prevent colon carcinogenesis by inhibition of membrane fluidity and canonical Wnt/beta-catenin signaling while up-regulating ligand dependent transcription factor PPARgamma. *Biomed. Pharmacother.* **2014**, *68*, 537–550. [[CrossRef](#)]
37. Lin, R.; Piao, M.; Song, Y.; Liu, C. Quercetin Suppresses AOM/DSS-induced colon carcinogenesis through its anti-inflammation effects in mice. *J. Immunol. Res.* **2020**, *2020*, 9242601. [[CrossRef](#)]
38. Sanapareddy, N.; Legge, R.M.; Jovov, B.; McCoy, A.; Burcal, L.; Araujo-Perez, F.; Randall, T.A.; Galanko, J.; Benson, A.; Sandler, R.S.; et al. Increased rectal microbial richness is associated with the presence of colorectal adenomas in humans. *ISME J.* **2012**, *6*, 1858–1868. [[CrossRef](#)]
39. Stojanov, S.; Berlec, A.; Strukelj, B. The Influence of probiotics on the Firmicutes/Bacteroidetes ratio in the treatment of obesity and inflammatory bowel disease. *Microorganisms* **2020**, *8*, 1715. [[CrossRef](#)]
40. Mukhopadhyay, I.; Hansen, R.; El-Omar, E.M.; Hold, G.L. IBD-what role do Proteobacteria play? *Nat. Rev. Gastroenterol. Hepatol.* **2012**, *9*, 219–230. [[CrossRef](#)]
41. Hiraishi, K.; Zhao, F.; Kurahara, L.H.; Li, X.; Yamashita, T.; Hashimoto, T.; Matsuda, Y.; Sun, Z.; Zhang, H.; Hirano, K. Lactulose modulates the structure of gut microbiota and alleviates colitis-associated tumorigenesis. *Nutrients* **2022**, *14*, 649. [[CrossRef](#)] [[PubMed](#)]
42. Chen, W.; Liu, F.; Ling, Z.; Tong, X.; Xiang, C. Human intestinal lumen and mucosa-associated microbiota in patients with colorectal cancer. *PLoS ONE* **2012**, *7*, e39743. [[CrossRef](#)] [[PubMed](#)]
43. Kaakoush, N.O. Insights into the Role of Erysipelotrichaceae in the human host. *Front. Cell Infect. Microbiol.* **2015**, *5*, 84. [[CrossRef](#)] [[PubMed](#)]
44. Liu, J.; Hao, W.; He, Z.; Kwek, E.; Zhao, Y.; Zhu, H.; Liang, N.; Ma, K.Y.; Lei, L.; He, W.S.; et al. Beneficial effects of tea water extracts on the body weight and gut microbiota in C57BL/6J mice fed with a high-fat diet. *Food Funct.* **2019**, *10*, 2847–2860. [[CrossRef](#)]
45. Wu, J.; Liu, Y.; Dou, Z.; Wu, T.; Liu, R.; Sui, W.; Jin, Y.; Zhang, M. Black garlic melanoidins prevent obesity, reduce serum LPS levels and modulate the gut microbiota composition in high-fat diet-induced obese C57BL/6J mice. *Food Funct.* **2020**, *11*, 9585–9598. [[CrossRef](#)]
46. Tian, B.; Zhao, J.; Zhang, M.; Chen, Z.; Ma, Q.; Liu, H.; Nie, C.; Zhang, Z.; An, W.; Li, J. *Lycium ruthenicum* anthocyanins attenuate high-fat diet-induced colonic barrier dysfunction and inflammation in mice by modulating the gut microbiota. *Mol. Nutr. Food Res.* **2021**, *65*, e2000745. [[CrossRef](#)]
47. Killeen, S.D.; Wang, J.H.; Andrews, E.J.; Redmond, H.P. Bacterial endotoxin enhances colorectal cancer cell adhesion and invasion through TLR-4 and NF-kappaB-dependent activation of the urokinase plasminogen activator system. *Br. J. Cancer* **2009**, *100*, 1589–1602. [[CrossRef](#)]
48. Pratap, K.; Majzoub, M.E.; Taki, A.C.; Hernandez, S.M.; Magnusson, M.; Glasson, C.R.K.; de Nys, R.; Thomas, T.; Lopata, A.L.; Kamath, S.D. The algal polysaccharide ulvan and carotenoid astaxanthin both positively modulate gut microbiota in mice. *Foods* **2022**, *11*, 565. [[CrossRef](#)]
49. Byrd, J.C.; Bresalier, R.S. Mucins and mucin binding proteins in colorectal cancer. *Cancer Metastasis Rev.* **2004**, *23*, 77–99. [[CrossRef](#)]
50. Mack, D.R.; Michail, S.; Wei, S.; McDougall, L.; Hollingsworth, M.A. Probiotics inhibit enteropathogenic *E. coli* adherence in vitro by inducing intestinal mucin gene expression. *Am. J. Physiol.* **1999**, *276*, G941–G950.
51. Hu, P.S.; Li, T.; Lin, J.F.; Qiu, M.Z.; Wang, D.S.; Liu, Z.X.; Chen, Z.H.; Yang, L.P.; Zhang, X.L.; Zhao, Q.; et al. VDR-SOX2 signaling promotes colorectal cancer stemness and malignancy in an acidic microenvironment. *Signal. Transduct. Target. Ther.* **2020**, *5*, 183. [[CrossRef](#)] [[PubMed](#)]
52. Hu, X.; Tang, Z.; Li, Y.; Liu, W.; Zhang, S.; Wang, B.; Tian, Y.; Zhao, Y.; Ran, H.; Liu, W.; et al. Deletion of the tyrosine phosphatase Shp2 in sertoli cells causes infertility in mice. *Sci. Rep.* **2015**, *5*, 12982. [[CrossRef](#)] [[PubMed](#)]





## Article

# Discovery of New Secondary Metabolites from Marine Bacteria *Hahella* Based on an Omics Strategy

Shufen He <sup>1,†</sup>, Peishan Li <sup>1,†</sup>, Jinxuan Wang <sup>1</sup>, Yan Zhu Zhang <sup>1</sup>, Hongmei Lu <sup>1</sup>, Liufei Shi <sup>1</sup>, Tao Huang <sup>2</sup>, Weiyang Zhang <sup>1</sup>, Lijian Ding <sup>1</sup>, Shan He <sup>1,3</sup> and Liwei Liu <sup>1,\*</sup>

- <sup>1</sup> Li Dak Sum Marine Biopharmaceutical Research Center, Department of Marine Pharmacy, College of Food and Pharmaceutical Sciences, Ningbo University, Ningbo 315832, China; 2011085032@nbu.edu.cn (S.H.); 196000818@nbu.edu.cn (P.L.); 2111085014@nbu.edu.cn (J.W.); 2011085092@nbu.edu.cn (Y.Z.); 2111085060@nbu.edu.cn (H.L.); liufeishi@outlook.com (L.S.); zhangweiyang@nbu.edu.cn (W.Z.); dinglijian@nbu.edu.cn (L.D.); heshan@nbu.edu.cn (S.H.)
- <sup>2</sup> Department of Food Science and Engineering, College of Food and Pharmaceutical Sciences, Ningbo University, Ningbo 315211, China; huangtao@nbu.edu.cn
- <sup>3</sup> Ningbo Institute of Marine Medicine, Peking University, Ningbo 315800, China
- \* Correspondence: liuliwei@nbu.edu.cn
- † These authors contributed equally to this work.

**Abstract:** *Hahella* is one characteristic genus under the Hahellaceae family and shows a good potential for synthesizing new natural products. In this study, we examined the distribution of the secondary metabolite biosynthetic gene cluster (SMBGC) under *Hahella* with anti-SMASH. The results derived from five genomes released 70 SMBGCs. On average, each strain contains 12 gene clusters, and the most abundant ones (45.7%) are from the family of non-ribosomal peptide synthetase (NRPS) and non-ribosomal peptide synthetase hybrid with polyketide synthase (NRPS/PKS), indicating a great potential to find bioactive compounds. The comparison of SMBGC between *H. chejuensis* and other species showed that *H. chejuensis* contained two times more gene clusters than *H. ganghuensis*. One strain, designed as NBU794, was isolated from the mangrove soil of Dongzhai Port in Haikou (China) by iChip. The 16S rRNA gene of NBU794 exhibited 99% identity to *H. chejuensis* KCTC 2396 and clustered with the *H. chejuensis* clade on the phylogenetic trees. Genome mining on strain NBU794 released 17 SMBGCs and two groups of bioactive compounds, which are chejuenolide A-C and nine prodiginines derivatives. The prodiginines derivatives include the well-known lead compound prodigiosin and two new compounds, 2-methyl-3-pentyl-4-O-methyl-prodiginine and 2-methyl-3-octyl-prodiginine, which were identified through fragmentation analysis based on LC-MS/MS. The anti-microbial activity assay showed prodigiosin and 2-methyl-3-heptyl-prodiginine exhibited the best performance in inhibiting *Escherichia coli*, *Salmonella paratyphi* B, MASA *Staphylococcus aureus*, *Bacillus subtilis*, and *Candida albicans*. Moreover, the yield of prodigiosin in *H. chejuensis* NBU794 was also evaluated, which could reach 1.40 g/L under the non-optimized condition and increase to 5.83 g/L in the modified ISP4 medium with macroporous adsorption beads added, indicating that NBU794 is a promising source of prodigiosin.

**Keywords:** *Hahella*; prodiginine; chejuenolide; genome mining; LC-MS/MS

**Citation:** He, S.; Li, P.; Wang, J.; Zhang, Y.; Lu, H.; Shi, L.; Huang, T.; Zhang, W.; Ding, L.; He, S.; et al. Discovery of New Secondary Metabolites from Marine Bacteria *Hahella* Based on an Omics Strategy. *Mar. Drugs* **2022**, *20*, 269. <https://doi.org/10.3390/md20040269>

Academic Editors: Yonghong Liu and Xuefeng Zhou

Received: 28 March 2022

Accepted: 13 April 2022

Published: 18 April 2022

**Publisher's Note:** MDPI stays neutral with regard to jurisdictional claims in published maps and institutional affiliations.



**Copyright:** © 2022 by the authors. Licensee MDPI, Basel, Switzerland. This article is an open access article distributed under the terms and conditions of the Creative Commons Attribution (CC BY) license (<https://creativecommons.org/licenses/by/4.0/>).

## 1. Introduction

The ocean covers approximately 71% of the Earth's surface. As the largest aquatic ecosystem on the earth, the ocean harbors a great number of microorganisms, which occupy more than half of the world's total prokaryotes [1]. Among the marine microorganisms, bacteria are usually considered as a rich pool for bioactive compounds. The annual report of 'Marine Natural Products' reveals that more than 200 new compounds are discovered from marine bacteria each year, and this number reached 300 in 2018, displaying an increasing

trend. The natural products produced from marine bacteria include peptides, polyketides, terpenes, alkaloids, etc., which exhibit various bioactivities, such as anti-infection, anti-cancer, and protease inhibition. However, the data show that the majority of new compounds discovered from marine bacteria are from *Streptomyces* and cyanobacteria, which account for 76% in total [2], while a small proportion of natural products are discovered from other bacteria.

*Hahella* is identified by Lee et al. (2001) as a Gram-negative, facultative anaerobic marine bacteria from the family of Hahellaceae. They are mobile by means of one single polar flagellum and only live in slightly halophilic environments (2% NaCl). Up to now, three species in this genus have been identified, including *H. ganghwensis*, *H. antarctica*, and *H. chejuensis* [3–5]. One known study showed that *H. chejuensis* could cause the red egg disease in tilapia (*Oreochromis* spp.) [6], indicating that *Hahella* might be one kind of marine pathogen. When this current study was performed, only 17 *Hahella* 16S rRNA genes and 5 genomes were documented in the NCBI database (<https://www.ncbi.nlm.nih.gov/> (accessed on 14 December 2021).), so little is known about this genus.

Even though only a few strains in *Hahella* have been uncovered, they have shown a good potential for synthesizing bioactive compounds. The prodiginine derivatives, including well-known prodigiosin, are the first type of natural product identified in *H. chejuensis* (Figure S1), which are characterized with the core structure of prodiginine including three continuous pyrrole rings [7,8]. As one star molecule in this family, prodigiosin has a wide array of biomedical and industrial applications, including algicidal, antibacterial, anticancer, antimalarial, antiprotozoal, colorants, immunosuppressive agents, and insecticides [9]. Moreover, prodigiosin has been reported to exhibit no damage to chromosomes and no acute and hereditary toxicity in Kunming mice at a dose of 10 g/kg, suggesting a good selectivity on molecular targets and biological safety [10]. Actually, prodigiosin is first identified in terrestrial bacterium *Serratia marcescens* and confirmed in many different marine bacteria later on, such as *Pseudoalteromonas*, *Streptomyces*, and *Hahella* [11], indicating a wide distribution in nature. Up to now, eight prodiginine derivatives including prodigiosin have been identified in *H. chejuensis* KCTC 2396 [8].

Chejuenolide A-C are 17-membered carbocyclic tetraenes, which are the second type of bioactive compound identified in *H. chejuensis* (Figure S1) [12,13]. Their structures are very similar to the antibiotic lankacidin C produced by *Streptomyces*, except for a  $\delta$ -lactone ring and a pyruvyl group connected to C-18 via a nitrogen atom (Figure S1). However, the minor structural differences result in totally different bioactivities. In comparison with the antibiotic lankacidin C, chejuenolides exhibit no antibiotic activity, but a strong inhibitory effect on tyrosine phosphatase 1B [12]. The biosynthesis scheme of chejuenolides has been elucidated through heterologous expression and bioinformatics analysis [14]. The gene cluster of chejuenolides consists of six genes, coding one non-ribosomal peptide synthetase (NRPS) module, five polyketide synthase (PKS) modules, and one stand-alone trans-AT domain, which could be assigned to the iterative trans-AT PKS family.

Although two type of bioactive compounds have been discovered, we still have little knowledge of the real resource of secondary metabolites in *Hahella*. We hypothesized that *Hahella* might contain more valuable secondary metabolites than previously shown. Herein, we studied the SMBGC distribution in *Hahella* with genome mining and uncovered the unbalanced distribution of SMBGCs among different species. Furthermore, we isolated one new strain (*H. chejuensis* NBU794) and discovered nine prodiginine derivatives including two new molecules and chejuenolide A-C through metabolomics.

## 2. Results

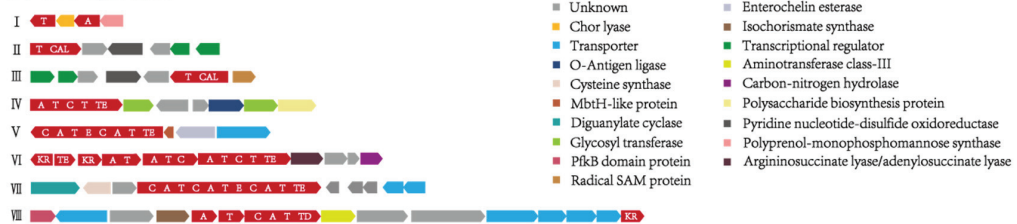
### 2.1. SMBGC Analysis in *Hahella*

Genome mining has become a key strategy to guide the discovery of new natural products [15–18]. Here, we collected five genomes from the NCBI database, including *H. ganghwensis* DSM 17,046, *H. chejuensis* KCTC 2396, *H. chejuensis* KA22, *H. chejuensis* HN01, and *Hahella* sp.CCB-MM4 (Table S1). The anti-SMASH analysis identified 70 SMBGCs,

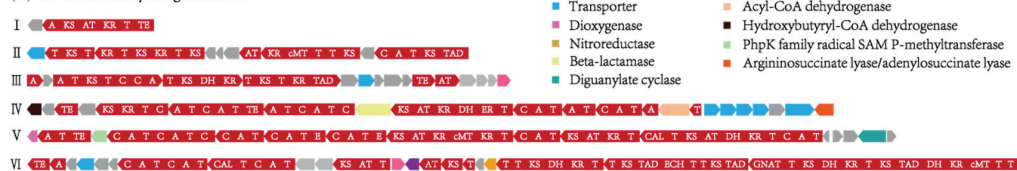
and each genome contained 12 SMBGCs on average (Table S2). It has been shown that secondary metabolites synthesized by NRPS and PKS are usually considered as a good resource for bioactive compounds [19]. Here, we found that 45.7% of SMBGCs in *Hahella* belong to the family of NRPS and NRPS/PKS hybrid (Table S2).

In total, 15 NRPS gene clusters were identified in this study and classified into eight groups based on the gene composition. Only the group I-III contained a single NRPS module, while all the others possess continuous NRPS modules, showing a good potential to find peptidic compounds with complicated structures (Figure 1A). One epimerization domain(E), which could convert the configuration of amino acid from L to D, was identified in the gene cluster of group VII (Figure 1A), indicating that the final product might contain D-amino acid. In addition, 17 NRPS/PKS hybrid gene clusters were identified and assigned to six groups based on the gene composition (Figure 1B). The group I contained one single PKS module flanked by an adenylation domain and a thiolation domain, while the others contained multiple PKS and NRPS modules, such as the groups IV, V, and VI. Moreover, a variety of modification domains, for example, KR (ketoreductase), DH (dehydratase), ECH (enoyl-CoA hydratase/isomerase), ER (enoyl-reductase), and cMT (carbon methyltransferase) (Figure 1B), were detected in the NRPS/PKS hybrid gene clusters, suggesting a great diversity in the final structures. Moreover, we also found some other types of SMBGCs, such as ectoine, NAGGN (N-acetylglutaminyglutamine amide), betalactone, PBDE (Polybrominated diphenyl ether cluster), hserlactone, CDPS (tRNA-dependent cyclodipeptide synthases), butyrolactone, prodigiosin, siderophore, and RiPPs (Ribosomally synthesized and post-translationally modified peptides) (Figures S2 and S3), indicating a great chemical diversity in *Hahella*.

#### (A) 15 NRPS gene clusters



#### (B) 17 NRPS/PKS hybrid gene clusters

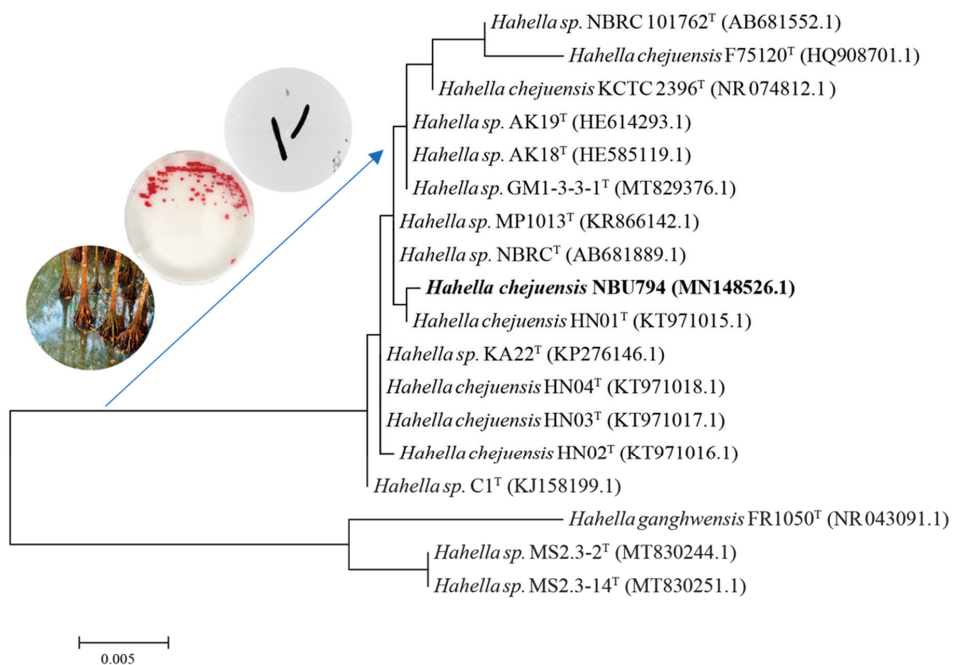


**Figure 1.** NRPS gene clusters and NRPS/PKS hybrid gene clusters are identified in *Hahella ganghwensis* DSM 17,046, *Hahella chejuensis* KCTC 2396, *Hahella chejuensis* KA22, *Hahella chejuensis* HN01, and *Hahella* sp.CCB-MM4. (A) A total of 15 NRPS gene clusters are identified and classified into eight groups based on the gene composition. (B) A total of 17 NRPS/PKS hybrid gene clusters are identified and classified into six groups based on the gene composition. The functional domains are indicated in bold letters: A, adenylation domain; AT, acyl-transferase; CAL, co-enzyme A ligase domain; C, condensation domain; cMT, carbon methyltransferase; DH, dehydratase; E, epimerization; ECH, enoyl-CoA hydratase/isomerase; ER, enoylreductase domain; GNAT, GCN5-related N-acetyltransferases domain; KR, ketoreductase; KS, ketosynthase; T, thiolation domain (peptidyl carrier protein); TAD, Trans-AT docking domain; TD, Terminal reductase domain; TE, thioesterase. The modular genes are marked with red color, while the other functional enzymes are indicated by squares with different colors.

Even though *Hahella* consists of three species, only *H. chejuensis* and *H. ganghwensis* have genome information available in the NCBI database. Therefore, we undertook a comparison of SMBGCs between *H. chejuensis* and *H. ganghwensis* and found that the SMBGCs in *H. chejuensis* were almost two times greater than *H. ganghwensis* (Table S2).

## 2.2. New Strain Isolation and Identification

By considering the high number of SMBGCs in the genome, we selected *H. chejuensis* as our target to find new bioactive compounds. The in situ culture technique (Ichip) combined with PCR screening was applied to search for new strains from mangrove soil samples collected from Dongzhai Port in Haikou, Hainan Province, China. Finally, one new strain named as NBU794 was found. It exhibited a dark red color on both the agar plate and liquid culture. We sequenced the 16S rRNA gene of NBU794 and blasted it against the NCBI database. The sequence data exhibited 99.6% similarity between NBU794 and *H. chejuensis* KCTC 2396. To study the taxonomic status of NBU794, we undertook a phylogenetic analysis of the 16S rRNA tree of NBU794 and another 17 strains in two modes, which were neighbor-joining and maximum likelihood (Figure 2 and S4). On the trees, NBU794 apparently clustered with *H. chejuensis* and was separated from *H. ganghwensis*. The cell morphology of NBU794 was examined using transmission electron microscopy. We found that NBU794 grown in M9 and 2216E medium had no flagellum and cells were long rods, which was similar to type strain *H. chejuensis* KCTC 2396 (Figure 2). The ANI value between NBU794 and type strain *H. chejuensis* KCTC 2396 was investigated, and the 88.2% value was below the thresholds (90%) recommended for species delineation [20]. Therefore, we assigned NBU794 as a new strain of *H. chejuensis* initially according to the phylogenetic analysis and morphology description.



**Figure 2.** Neighbor-joining phylogenetic tree based on 16S rRNA gene sequences showing the positions of strain NBU794 and other strains in the genus *Hahella*. Bar, 0.005 represents nucleotide substitution rate (Knuc) units. Strains *H. chejuensis* NBU794 from this study are highlighted in bold. The figures of sample collection, strain morphology on the agar plate, and transmission electron microscopy results are listed on the left top corner.

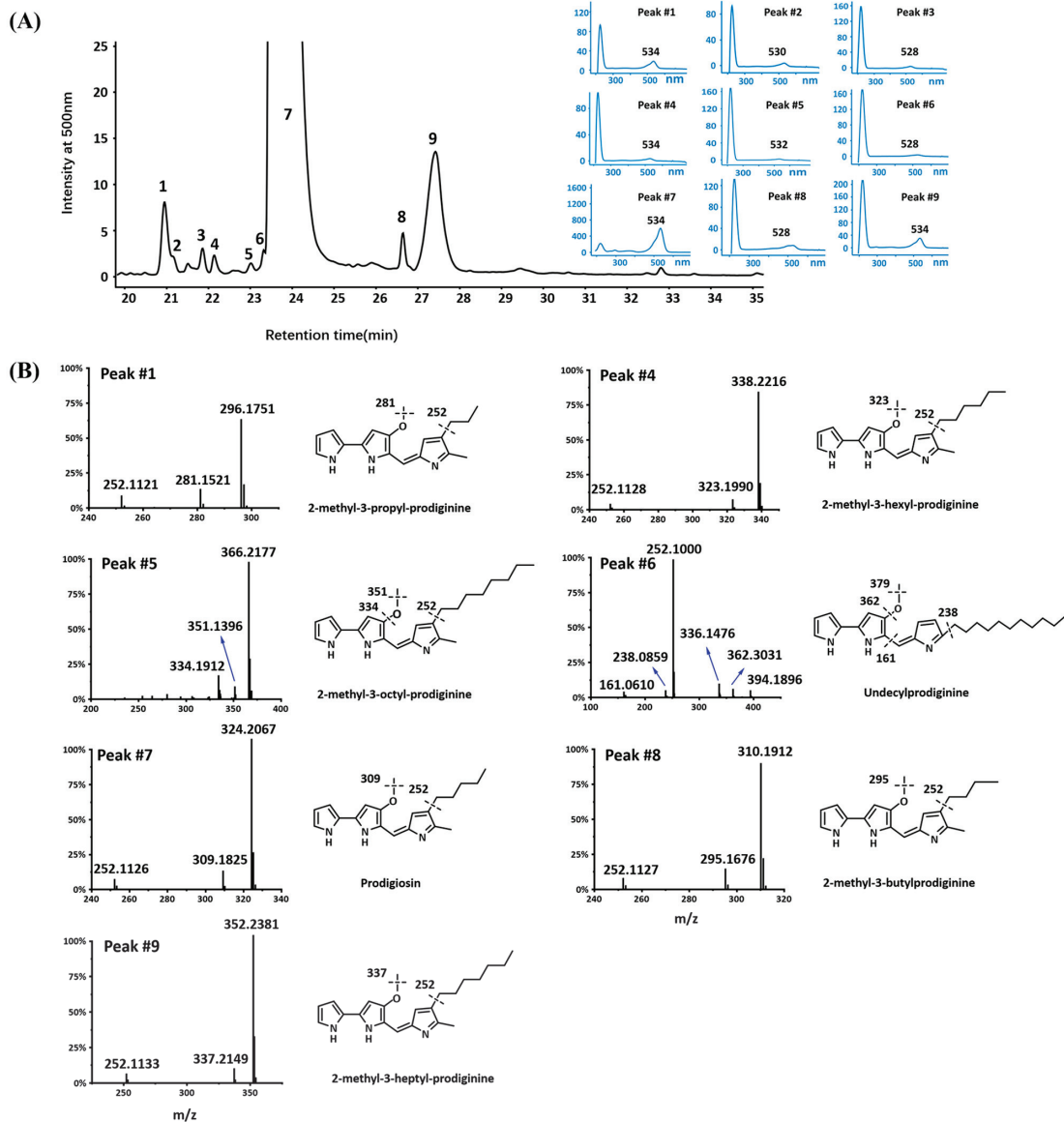
### 2.3. Genome Sequencing and SMBGCs Prediction in NBU794

The whole genome sequencing and assembly of *H. chejuensis* NBU794 were performed by using PacBio RSII/Sequel SMRT instrument and Illumina HiSeq 4000 platform at BGI company (Shenzhen, China). The full sequence data was uploaded to the web version of anti-SMASH 6.0 for the prediction of SMBGCs, and 17 SMBGCs were identified (Table S2 and Figure S5). Among the 17 detected SMBGCs, only four exhibited more than 50% similarity to the known biosynthetic gene clusters in the Minimum Information about a Biosynthetic Gene cluster database [21], while the others exhibited less than 20% similarity, indicating a good chance to find new natural products (Figure S5).

### 2.4. Prodiginines Identification

To find new natural products in the NBU794 strain, we applied the one strain many compounds (OSMAC) strategy [22]. The NBU794 strain was grown in different mediums, including M9, R2A, ISP4, and 2216E. The fermentation extracts were analyzed with LC-MS/MS-based metabolomics method. Interestingly, one prominent UV Peak (designed as Peak #7) was detected at retention time of 24 min (Figure 3A). The  $\lambda_{max}$  of the UV-Vis spectrum was 534 nm. The LC-MS analysis released a molecular ion of 324.2067 [M + H]<sup>+</sup> corresponding to a molecule formula C<sub>20</sub>H<sub>25</sub>N<sub>3</sub>O. The Global Natural Products Social Molecular Networking (GNPS) analysis showed that the compound matched with the red pigment antibiotic, prodigiosin (Figure 3B and S6). To confirm the prediction, we compared it with standard prodigiosin in *H. chejuensis* KCTC 2396, and found they shared the same retention time, UV-Vis spectrum, and high resolution mass spectrum data (Figure S7). Coincidentally, the biosynthetic gene cluster of prodigiosin was also identified in the NBU794 strain. Therefore, based on the genome data (Figure S5) and chemical analysis (Figure 3), we confirmed that the studied compound was prodigiosin.

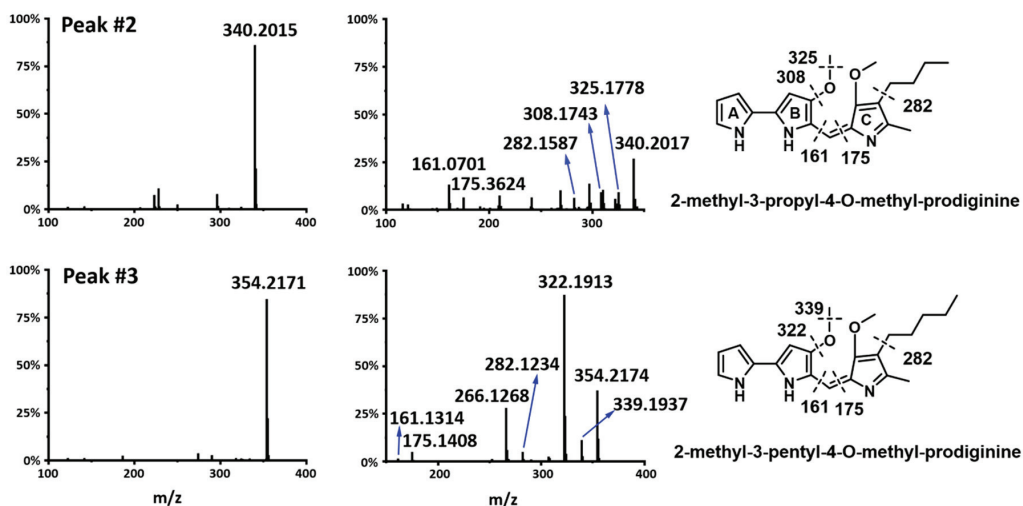
In addition to prodigiosin, we detected another eight UV peaks sharing similar UV-Vis absorption spectra, but displayed different molecular ions (Figure 3 and Table S3). The GNPS analysis showed that five ions, including prodigiosin, connected to each other on the network, while the other three ions existed independently (Figure S6). Therefore, we suspected that they were prodiginine derivatives. To confirm our prediction, we introduced the targeting LC-MS/MS experiment, which is a commonly used method to identify the structures of prodiginine derivatives. The five compounds in Peaks #1, #4, #5, #8, #9 released five molecular ions of 296.1759(C<sub>18</sub>H<sub>21</sub>N<sub>3</sub>O), 338.2216(C<sub>21</sub>H<sub>27</sub>N<sub>3</sub>O), 366.2178(C<sub>23</sub>H<sub>31</sub>N<sub>3</sub>O), 310.1909(C<sub>19</sub>H<sub>23</sub>N<sub>3</sub>O), and 352.2380(C<sub>22</sub>H<sub>29</sub>N<sub>3</sub>O) in the high resolution LC-MS (Table S3), and their fragmentation patterns were similar to prodigiosin (Figure 3B). The mass differences could be attributed to the different alkyl chains, such as propyl, butyl, hexyl, heptyl, and octyl side chains. Through the comparison of mass spectra data and UV-Vis absorption spectrum with the previous reports [8,23], we confirmed five compounds (Peak #1, #4, #5, #8, #9) as 2-methyl-3-propyl-prodiginine, 2-methyl-3-hexyl-prodiginine, 2-methyl-3-octyl-prodiginine, 2-methyl-3-butyl-prodiginine, and 2-methyl-3-heptyl-prodiginine (Figure 3B). The compound in Peak #6 released a molecular ion of 394.1896[M + H]<sup>+</sup>. Its resulting ion scan mass spectrum contained a  $m/z$  238.0859[M-156], 252.1000[M-142], 336.1476[M-58], 362.3031[M-32], which was consistent with previous data derived from undecylprodiginine [8] (Figure 3B).



**Figure 3.** LC-MS/MS analysis of prodiginine derivatives in *H. chejuensis* NBU794. **(A)** The nine UV peaks corresponding prodiginine derivatives were marked with arabic numbers, and the UV–Vis spectra of nine eluent peaks are listed on the right. **(B)** The MS/MS spectrums are listed on the left and compound structures with fragment information are listed on the right. Peak #1: 2-methyl-3-propyl-prodiginine; Peak #4: 2-methyl-3-hexyl-prodiginine; Peak #5: 2-methyl-3-octyl-prodiginine; Peak #6: Undecylprodiginine; Peak #7: prodigiosin; Peak #8: 2-methyl-3-butyl-prodiginine; Peak #9: 2-methyl-3-heptyl-prodiginine.

We also detected two new compounds in Peaks #2 and #3, which released two molecular ions  $340.2015[M + H]^+$  and  $354.2171[M + H]^+$ , respectively (Figure 4). Interestingly, they exhibited a similar UV spectrum to known prodiginine derivatives. To elucidate their

structures, we tried to isolate two compounds to run an NMR experiment, but their amount in the fermentation extract was too low, and the compounds were so sensitive to light that they kept degrading all the time, which prevented us from obtaining clean NMR data. Therefore, we introduced the LC-MS/MS method, which was a well-established and frequently used strategy for studying prodiginine derivatives. In comparison with prodigiosin (324.2067,  $[M + H]^+$ ), we predicted compound in Peak #2 to contain one more oxygen based on the molecular weight difference. To determine the location of one extra oxygen atom, we checked the MS/MS data and found the fragment 282 (Figure 4), indicating a loss of butyl alkyl chain from the parent molecule. On the contrary, prodigiosin contained a fragment of 252, suggesting a loss of pentyl alkyl chain. The 30 dalton difference between fragments 282 and 252 indicated that the new compound might contain one second O-methyl group. To our surprise, we found two characteristic fragments of 161.0702 and 175.3624, which excluded all the possibilities except for one position, 3-C on the Ring C (Figure 4). Therefore, we identified the new compound in Peak #2 as 2-methyl-3-propyl-4-O-methyl-prodiginine. Because of the 14 dalton difference between compounds in Peak #2 and Peak #3, when we replaced the butyl side chain with the pentyl side chain, the MS/MS data of the compound in Peak #3 matched with the structure of 2-methyl-3-pentyl-4-O-methyl-prodiginine.

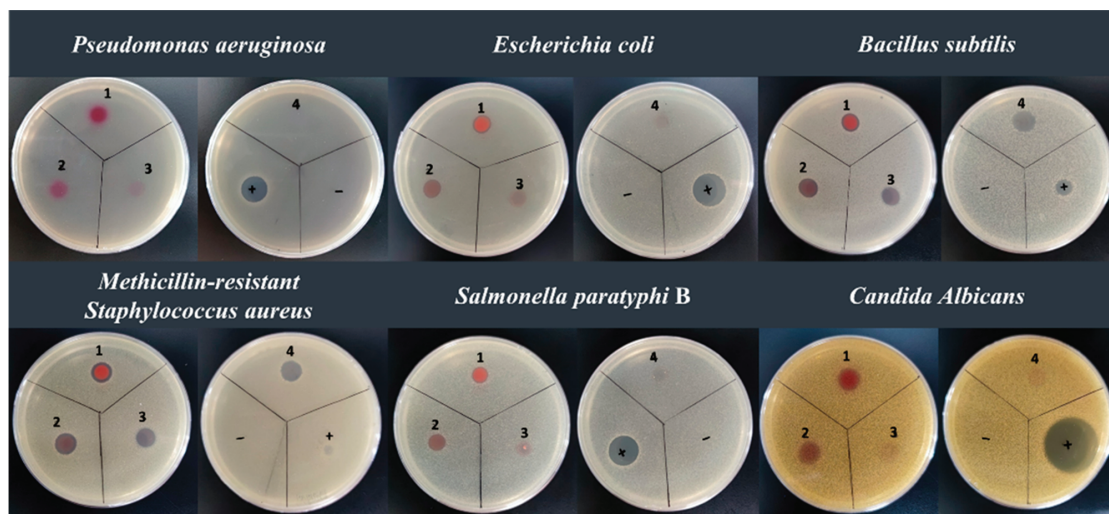


**Figure 4.** Structure elucidation of 2-methyl-3-pentyl-4-O-methyl-prodiginine, 2-methyl-3-octyl-prodiginine with LC-MS/MS. The product ion scans are listed on the left, the MS/MS spectrums are listed in the middle, and compound structures with fragment information are listed on the right.

### 2.5. Anti-Microbial Assay

Naturally occurring prodiginines are a large family of secondary metabolites, which can inhibit many different microorganisms. In this study, we grew *H. chejuensis* NBU794 in 70L M9 medium and isolated four pure prodiginine derivatives, including prodigiosin, 2-methyl-3-propyl-prodiginine, 2-methyl-3-butyl-prodiginine, and 2-methyl-3-heptyl-prodiginine. In the agar diffusion assay, we chose *S. paratyphi* B, *P. aeruginosa*, Methicillin-resistant *S. aureus*, *B. subtilis*, *E. coli*, and *C. albicans* as the indicative strains. The results showed that all four compounds could inhibit Methicillin-resistant *S. aureus* and *B. Subtilis* but failed to kill *P. aeruginosa* (Figure 5). To our surprise, the prodigiosin and 2-methyl-3-heptyl-prodiginine also gave a clear inhibition zone on the agar plate with *E. coli*, *S. paratyphi* B, and *C. albicans* (Figure 5).





**Figure 5.** Antimicrobial assay of prodigiosin (1), 2-methyl-3-heptyl-prodiginine (2), 2-methyl-3-propyl-prodiginine (3), 2-methyl-3-butyl-prodiginine (4). (–): to use DMSO as a negative control. (+): to use nystatin as a positive control in the antifungal test against *Candida albicans*; to use polymyxin as a positive control in the antibacterial test against *Salmonella paratyphi B*, *Pseudomonas aeruginosa*, Methicillin-resistant *Staphylococcus aureus*, *Bacillus subtilis*, and *Escherichia coli*.

Moreover, we also tested the  $IC_{50}$  values of isolated prodiginine derivatives. The data was included in Table 1. Both prodigiosin and 2-methyl-3-heptyl-prodiginine had the best performance against all indicative strains except *P. aeruginosa*, and their  $IC_{50}$  ranged from 1.56 to 50  $\mu\text{g/mL}$ . Regarding the other two compounds, they had a relatively higher  $IC_{50}$  against *B. subtilis* (12.5–25  $\mu\text{g/mL}$ ) and Methicillin-resistant *S. aureus* (50  $\mu\text{g/mL}$ ), but failed to inhibit *E. coli*, *S. paratyphi B*, and *C. albicans* (Table 1).

**Table 1.** Minimum inhibitory concentration of prodigiosin and three congeners.

| Compound                      | Minimum Inhibitory Concentration ( $\mu\text{g/mL}$ ) |                          |                         |                               |                         |
|-------------------------------|---|--------------------------|-------------------------|-------------------------------|-------------------------|
|                               | Methicillin-Resistant <i>Staphylococcus aureus</i>    | <i>Bacillus subtilis</i> | <i>Escherichia coli</i> | <i>Salmonella paratyphi B</i> | <i>Candida albicans</i> |
| 2-methyl-3-propyl-prodiginine | 50  | 25                       | -                       | -                             | 200                     |
| 2-methyl-3-butyl-prodiginine  | 50  | 12.5                     | -                       | -                             | -                       |
| Prodigiosin                   | 1.56  | 1.56                     | 3.12                    | 12.5                          | 1.56                    |
| 2-methyl-3-heptyl-prodiginine | 1.56  | 6.25                     | 12.5                    | 25                            | 6.25                    |

## 2.6. Production of Prodigiosin

Prodigiosin has been proved to possess various bioactivities, such as anti-bacteria, anti-cancer, algicide, and so on, showing a great potential to be developed into a lead compound. Therefore, it is very necessary to find a strain with a high yield of prodigiosin. Since the prodigiosin was the major component in *H. chejuensis* NBU794, we grew the strain under different conditions and found the production of prodigiosin in ISP4 medium was the best, which could reach 1.40 mg/mL without any optimization (Tables S4 and S5). When we added HP20 (Macroporous Adsorption Resin) in ISP4 and grew the strain at the same growth condition, the prodigiosin production increased to 3.43 g/L (Table S5). Since the different carbon sources have been proven to affect the yield of prodigiosin [24], we then introduced glucose and sucrose as the carbon source to replace starch in ISP4 and

the yield of prodiginosin in *H. chejuensis* NBU794 further increased to 3.46 and 5.83 g/L, respectively (Table S5).

### 2.7. Discovery of Chejuenolide A–C

In addition to prodiginines, we also found another three new characteristic UV peaks at a retention time of 15–18 min compared with the blank control (Figure S8). Their  $\lambda_{\text{max}}$  absorption was 210 nm, and released three molecular ions, 388.2483 (Peak A), 388.2489 (Peak B), and 388.2459 (Peak C), which corresponded to a predicted formula  $\text{C}_{23}\text{H}_{33}\text{NO}_4$ . In order to elucidate their structures, we isolated the compound in Peak A and ran it with NMR. The  $^1\text{H}$ -NMR and  $^{13}\text{C}$ -NMR data were completely the same as chejuenolid A (Table S6 and Figure S9). We further compared fermented extracts of *H. chejuensis* NBU794 with *H. chejuensis* KCTC 2396, which has been proved to produce chejuenolide A–C, and found the other two compounds in Peaks B and C had the same retention time as the chejuenolide B and C in *H. chejuensis* KCTC 2396 (Figure S10). Therefore, we confirmed that the three discovered compounds were chejuenolide A–C.

## 3. Discussion

As a good resource of natural products, marine bacteria have received a lot of attention. Even though hundreds of new compounds from marine bacteria are identified each year, most of them are from a few well-known producers, such as *Streptomyces* and cyanobacteria [2]. A previous study shows that 99% of microorganisms in nature are still uncultured [25]. Therefore, discovering natural products from marine uncultured bacteria could be a new option [26].

*Hahella* was first identified at the beginning of the 21st century. Only three new species have been identified up to now, so most of the members under this genus are still unknown. During the last two decades, several studies were performed to investigate *H. chejuensis* and a number of new bioactive compounds were found, which developed the research interests [7,8,12,13]. In this current study, we investigated *Hahella* with genome mining and found that *Hahella* contained 12 SMBGCs in each genome on average. Even though the SMBGC number in *Hahella* is not as high as the *streptomyces* and cyanobacteria, it is much higher than the average number (5) derived from 200,000 microbial genomes [27], indicating that *Hahella* is a good resource for new natural products. However, the comparison of SMBGC numbers between two different *Hahella* species showed that SMBGC in *H. chejuensis* was twice as high as in *H. ganghwensis*. The phylogenetic tree clearly showed that both species formed two separated clades, indicating they might have different evolution paths. Even though we have no idea why two *Hahella* species have a great difference in terms of SMBGCs distribution, it is widely accepted that the microorganism that contains rich secondary metabolites might have more advantages in natural selection, while the one with fewer secondary metabolites is more prone to acquiring nutrients or protection by forming a close connection with other species or a host, because this is more economical [28–31].

In order to find new natural products from *Hahella*, we applied genome mining and metabolomics to analyze a new isolated strain NBU794. Finally, two new compounds and seven known prodiginine derivatives were identified. The prodiginines are one group of microbial secondary metabolites containing one tripyrrole core structure (Figure S1) [32]. They not only exhibit good bioactivities, but also diverse structures through the modification on the third pyrrole ring, such as methylation, alkylation, and cyclization [8,33]. Our study uncovered two new compounds containing a second O-methyl group on the C-3 of the C-ring (Figure S10), indicating the existence of a new structure diversification mechanism. Kim et al. (2007) found that dipyrrolyldipyrromethene prodiginosin contains a second O-methyl group on the third pyrrole ring, but dipyrrolyldipyrromethene prodiginosin had a fourth pyrrole ring instead of one alkyl side chain (Figure S10), indicating a different biosynthesis pathway [8]. In order to provide a deep understanding of how new compounds were biosynthesized, we compared the prodiginines gene cluster within NBU794 to the homologous one in *H. chejuensis* KCTC 2396 (Figure S5). However, the almost 100%

similarity suggested that prodiginine biosynthesis enzymes might have a broad substrate specificity, which could result in new minor compounds during the biosynthesis.

In the present study, we tested four prodiginine derivatives and found that they showed a good performance against Gram positive bacteria, such as MRSA *S. aureus*, *S. paratyphi* B, and *B. subtilis*. Moreover, both prodigiosin and 2-methyl-3-heptyl-prodiginine exhibited a clear inhibition on *E. coli* with a low IC<sub>50</sub>, suggesting that they could be developed into a wide-spectrum antibiotics in the future. In contrast, the other two prodiginine derivatives (2-methyl-3-propyl-prodiginine and 2-methyl-3-butyl-prodiginine) were not effective in the anti-microbial test. Based on the anti-microbial activity and their structures, we speculated the alkyl chain is the key functional group that affects prodiginines' anti-microbial activities, and the prodiginine with a pentyl group gave the best performance in the test (Table S4 and Figure 4). The alkyl chain has been proven to be compulsory for anti-bacteria activity of many antibiotics, such as surfactins, bacillomycin L, and Pseudodesmin A [34–36]. The alkyl chain with a different length has a strong effect on the antibiotic activity. Therefore, our results not only support the previous study, but also provide a guideline for the optimization of structures and activities on prodiginine derivatives.

Considering the good bioactivity of prodigiosin, there is a great potential to develop prodigiosin into one drug lead. Therefore, it is very important to find a strain with a great yield of prodigiosin. A recent study suggested that the yield of prodigiosin in *H. chejuensis* could be increased to 2.5 g/L by using glucose as the carbon source [24]. However, our results showed that the prodigiosin in *H. chejuensis* NBU794 could reach 5.83 g/L in a modified ISP4 medium with HP20 beads (Tables S5 and S6). The HP20 beads belong to highly porous synthetic adsorbent resin. In the fermentation, HP20 could reduce the concentration of secondary metabolites in the culture due to strong binding in order to avoid feedback inhibition and promote a high production of the target molecule. Our data not only showed a high yield of prodigiosin in *H. chejuensis* NBU794, but also provided a good way to increase prodigiosin production.

Although we made some important discoveries in this study, there are still some limitations. First, the genome mining data in this study were derived from a small number of genomes. It will be more reliable to make a conclusion with more data. Therefore, more *Hahella* stains need to be studied and sequenced in the future to help us understand the real resource in the *Hahella* genus and guide the discovery of new compounds. Second, we found nine prodiginines in NBU794 strains, but only prodigiosin was abundant in the crude extract. Because of the limited production, we hardly tested anti-microbial activity of all compounds, including two new compounds, which stops us from understanding their biological functions. In addition, we also met the same problem with chejuenolides in NBU794. There are some minor peaks sharing similar UV-Vis spectra and molecular weights with chejuenolide A-C. Because of the extremely low yield, we hardly ruled out their structure with natural product chemistry techniques. Maybe the large-scale fermentation in the future could resolve the problem. Third, except for prodiginines and chejuenolides, most SMBGCs in the NBU794 strain were still silent. However, we believe that SMBGC silent problems could be bypassed in the future using the fast development of new synthetic biology techniques in *Hahella*.

## 4. Materials and Methods

### 4.1. Anti-SMASH Analysis

The genomes of *H. ganghwensis* DSM 17,046, *H. chejuensis* KCTC 2396, *H. chejuensis*. KA22, *H. chejuensis*. HN01, and *Hahella* sp.CCB-MM4 were downloaded from the NCBI database. The detailed information of five genomes is listed in Table S1. All genome sequences with Fasta format were uploaded manually to the website version anti-SMASH 6.0 for BGC prediction with default parameter settings [15].

#### 4.2. Sampling and Strain Isolation

The strain isolation was carried out with Epstein method [37]. A total of 1 g of mangrove sediment collected from Dongzhai Port in Haikou (China) was weighed and mixed with 10 mL sterilized water. The mixture was vortexed for 10 min to create a soil slurry. The slurry was left to settle for 5–10 min to allow larger particles to settle. The supernatant was diluted with sterilized water by 104 times. Then, 2.5 mL of appropriate dilution was mixed with 22.5 mL of molten ISP4 agar and vortexed for 15 s. The agar-sample mix was transferred into a sterile pipette basin and dispensed with a multichannel pipette into each well of the ichip. When the agar was solid, the ichip was sealed by sterilized polycarbonate membrane with a 0.03 µm pore size and dried in air for 30 min. The ichip devices were cultured in situ in mangrove sediments in Haikou City, Hainan Province, China for 20 days. At the end, the ichip was collected and rinsed with sterile water. After opening the ichip in a Lamina flow hood, a toothpick was used to touch the colony and streak on 50% R2A agar in order to obtain a single colony. The single colonies with great morphological differences were selected for colony PCR analysis with 16S rRNA universal primers. The primer sequences are 27F 5'-AGAGTTGATCCTGGCTCAG-3' and 1492R 5'-GGTTACCTTGTTACGACTT-3' [38]. The PCR products were sequenced and blasted against the Standard Nucleotide BLAST of National Center for Biotechnology Information (NCBI, <https://blast.ncbi.nlm.nih.gov/Blast.cgi> (accessed on 1 March 2021)).

#### 4.3. Strain Culture Condition

The NBU794 strain was grown in M9, R2A, ISP4, and 2216E liquid medium with 2% sea salt, and cultured in a 180 rpm/min shaker at 28 °C for 3–5 days. The agar plates of *S. paratyphi* B, *P. aeruginosa*, *S. aureus*, Methicillin-resistant *S. aureus*, and *B. subtilis* were grown at 37 °C for 18 h. *C. albicans* was grown on a YPD agar plate at 28 °C for 30 h. The ISP4 medium was purchased from ELITE-MEDIA (Shanghai, China), YPD and LB medium were purchased from Hopebiol (Qingdao, China), and the other reagents were purchased from Macklin (Shanghai, China).

#### 4.4. Strain Identification

The *H. chejuensis* NBU794 genomic DNA was extracted from three-day culture using the Magen HiPure Bacterial DNA Kit. The genome sequencing and assembly was performed by Shenzhen BGI company in China. The 16S rRNA gene was retrieved from the full genome data and introduced for a BLAST search against sequences in GenBank. The 16S rRNA genes from the NBU794 strain and another 17 16S rRNA gene sequences downloaded from the NCBI database were used to construct a phylogenetic tree by using the software MEGA version 7.0 after multiple alignments using CLUSTAL\_W and clustering with the neighbor-joining and maximum likelihood methods [39]. Cell morphology of the NBU794 strain was examined using transmission electron microscopy (TEM, H-7650; Hitachi) after negative staining with saturated uranyl acetate. The ANI value between strain NBU794 and *H. chejuensis* KCTC2396T was calculated by using the ANI calculator online service (<https://www.ezbiocloud.net/tools> (accessed on 1 March 2021)).

#### 4.5. Compound Purification

*H. chejuensis* NBU794 strain was inoculated in 70L M9 medium and cultured for 5 days at 28 °C with a speed of 180 rpm/min. The 70L culture were extracted with equal volume ethyl acetate twice and dried with rotating evaporator. The dried extracts were mixed with 3.25 g silica powder and dried at 70 °C for one hour and subjected to open column chromatography on silica gel (300–400 mesh, column: 7 cm [Length] × 5 cm [Diameter]). A total of five different solvents, including petroleum ether (100%), petroleum ether/ethyl acetate (7:3), petroleum ether/ethyl acetate (1:1), ethyl acetate (100%), and methanol (100%), were used to wash the silica column with three column volumes each time. Finally, we collected 36 fractions and analyzed them with HPLC. The fractions were injected into a Luna C18 column (100 × 3 mm, 2.6 µm, Phenomenex) in 50 µL batches. The column was eluted

in a gradient from 10% aqueous MeCN to 100% MeCN in 20 min at 25 °C and washed with 100% MeCN between the injections. Finally, the prodiginines were detected in NO.10–18 fractions. The NO.10–18 fractions were evaporated and suspended in 50% acetonitrile for the further semi-HPLC purification. The prodiginine extracts were injected into a Luna C18 column (250 × 10 mm, 5 µm, Phenomenex) in 400 µL batches. The column was eluted with a gradient from 42% to 60% aqueous MeCN in 55 min at 25 °C and washed with 100% MeCN between the injections. The fractions containing prodiginines were pooled and evaporated. Moreover, the fraction NO.19–27 from silica chromatography was confirmed to contain chejuenolides. We evaporated fraction NO.19–27 and suspended it in 30% MeCN. The chejuenolide samples were injected into a Luna C18 column (250 × 10 mm, 5 µm, Phenomenex) in 400 µL batches. The column was eluted isocratically with 24% aqueous MeCN at 25 °C for 43 min and washed with 100% aqueous MeCN between the injections. The fractions containing chejuenolides were pooled and evaporated. The chemical solvents were HPLC levels and purchased from Fisher Scientific.

#### 4.6. LC-MS Analysis

The LC-MS analysis was performed on an Agilent 6545 Quadrupole Time-of-Flight LC/MS. The testing samples were injected into a Luna C18(2) column (100 × 3 mm, 2.6 µm, Phenomenex) and eluted from 10% aqueous MeCN to 100% MeCN in 20 min. The flowing speed of the eluent was 0.7 mL/min with 0.1% formic acid. Mass spectra were acquired using electrospray ionization in the positive mode. Spectra were recorded using a scan range from 200 to 3200 *m/z*, and targeted MS/MS spectra were recorded as averages of three spectra. The precursors were fragmented into product ions with various CEs, including 13 eV at 250 *m/z*, 20 eV at 350 *m/z*, and 27 eV at 450 *m/z*. The DL temperature was 200 °C, the nebulizing gas flow rate was 3 L/min, the heat block temperature was 350 °C, the drying gas flow rate was 15 L/min, the column oven temperature was 30 °C, and the cooler temperature was 5 °C.

#### 4.7. Molecular Networking Analysis

The targeted LC-MS/MS data of prodiginine derivatives were converted into mzXML with MSConvert and uploaded to Global Natural Products Social Molecular Networking (GNPS, <http://gnps.ucsd.edu> (accessed on 4 June 2021).) using File Zilla Software. The molecular networking was established using the online workflow with the default parameter settings. The data was filtered by removing all MS/MS fragment ions within  $\pm 17$  Da of the precursor *m/z*. MS/MS spectra were window filtered by choosing only the top 6 fragment ions in the  $\pm 50$ Da window throughout the spectrum. The precursor ion mass tolerance was set to 2.0 Da and a MS/MS fragment ion tolerance of 0.5 Da. A network was then created where edges were filtered to have a cosine score above 0.7 and more than 6 matched peaks. Further, edges between two nodes were kept in the network if, and only if, each of the nodes appeared in each other's respective top 10 most similar nodes. Finally, the maximum size of a molecular family was set to 100, and the lowest scoring edges were removed from molecular families until the molecular family size was below this threshold. The spectra in the network were then searched against GNPS spectral libraries. The library spectra were filtered in the same manner as the input data. All matches kept between network spectra and library spectra were required to have a score above 0.7 and at least 6 matched peaks [40].

#### 4.8. NMR

NMR spectra of chejuenolide A were collected on a Varian Inova 600 NMR spectrometer and the solvent was CD<sub>3</sub>OD.

#### 4.9. Antimicrobial Activity

The anti-microbial activity of prodiginine derivatives was determined by the agar diffusion assay and MIC with a modification [41]. Compounds, including prodigiosin, 2-methyl-

3-propyl-prodiginine, 2-methyl-3-butyl-prodiginine, and 2-methyl-3-heptyl-prodiginine were used as antimicrobial agents against six pathogenic bacteria: *E. coli* ATCC 8739, *P. aeruginosa* 68 [42], Methicillin-resistant *S. aureus* ATCC6538, *S. paratyphi* B, *B. subtilis* CGMCC 1.88, and *C. albicans* ATCC 10,231. The test compounds were dissolved in DMSO with a final concentration of 5 mg/mL. For the agar diffusion assay, the indicating strains were grown in liquid medium overnight. The next morning, the cultures were mixed with 55 °C LB or YPD agar by 0.1% and poured on plastic plate. When the agar plates were solid, 5 µL (25 µg) of testing compounds were dipped. The LB agar plates were kept in the incubator at 37 °C for 16 h and the YPD agar plates were kept at 28 °C for 30 h. The MIC test was performed as below. The indicating strains were grown overnight. The next morning, the cell density (OD<sub>625</sub>) was recorded and diluted to 0.08–0.13. The diluted culture was inoculated in fresh medium by 1% and transferred to a 96-well plate with 100 µL of culture in each well. The first well of each row on the 96-well plate contained test compounds with a concentration of 400 µg/mL. After diluting each well from the left to the right by two times, the 96-well plates were kept at 28 or 37 °C overnight. The next morning, the 96-well plates were collected and checked with the naked eye.

#### 4.10. Fermentation of Prodigiosin

One single colony of *H. chejuensis* NBU794 was inoculated in 3 mL of 50% R2A liquid medium and grown at 28 °C at a speed of 180 rpm/min overnight. On the second day, the culture was used as the seed to inoculate by 1% into four different liquid mediums (50 mL), including standard ISP4, standard ISP4 with 1 g HP20 beads, modified ISP4 (starch is replaced with equal amount of glucose) with 1 g HP20 beads added, and modified ISP4 (starch is replaced with an equal amount of sucrose) with 1 g HP20 beads. The fermentation was performed at 28 °C with a speed of 180 rpm/min for three days. When the fermentation ceased, the culture without HP20 was extracted with ethyl acetate, evaporated, and suspended in MeOH for HPLC analysis. Regarding the culture with HP20 beads, the beads were filtered first, cleaned with water, and then washed with MeOH. The eluted extracts were evaporated and suspended in MeOH for HPLC analysis. The extract samples were injected into a Luna C18 column (250 × 4.6 mm, 5 µm, Phenomenex) in 10 µL batches. The column was eluted in a gradient from 30% aqueous MeCN to 65% MeCN in 18 min (LiChrosolv, Merck) at 25 °C and washed with 100% MeCN between the injections. The standard curve of prodigiosin was created based on different concentrations of prodigiosin and their corresponding peak integration areas from HPLC analysis at UV 530 nm (Table S5).

## 5. Conclusions

Herein, the genome mining of the *Hahella* genus revealed that each genome contains up to 12 SMBGCs on average, which is much more than the average number (5) derived from the analysis of 200,000 microbial genomes, indicating that *Hahella* is a good resource for finding new natural products. The omics-based analysis uncovered a number of prodiginine derivatives, including two new compounds, 2-methyl-3-propyl-4-O-methyl-prodiginine and 2-methyl-3-pentyl-4-O-methyl-prodiginine, and chejuenolide A-C from a new isolate strain *H. chejuensis* NBU794, which enriched the chemical diversity in *Hahella*.

**Supplementary Materials:** The following supporting information can be downloaded at: <https://www.mdpi.com/article/10.3390/md20040269/s1>, Figures S1–S11; Tables S1–S6.

**Author Contributions:** Conceptualization, S.H. (Shufen He), P.L. and L.L.; funding acquisition, S.H. (Shan He) and L.L.; investigation, data curation, formal analysis, visualization, S.H. (Shufen He), P.L., J.W., Y.Z., H.L., L.S., T.H., W.Z., L.D., S.H. (Shan He) and L.L.; supervision, project administration, writing—original draft preparation, L.L.; writing—review and editing, S.H. (Shufen He) and L.L. All authors have read and agreed to the published version of the manuscript.

**Funding:** This research was funded by Startup Foundation of Ningbo University (422010882, 422110473), the State Key Laboratory of Natural and Biomimetic Drugs (K202006), General scientific research projects of Zhejiang Provincial Education Department (Y202043824), National Natural Science Foundation of China (41776168), the National 111 Project of China (D16013), the Li Dak Sum Yip Yio Chin Kenneth Li Marine Biopharmaceutical Development Fund of Ningbo University(432100611), Ningbo Key Science and Technology Development Program (2021Z046) and Ningbo Natural Science Foundation (2021S129).

**Institutional Review Board Statement:** Not applicable.

**Informed Consent Statement:** Not applicable.

**Data Availability Statement:** Not applicable.

**Conflicts of Interest:** The authors declare no conflict of interest.

## References

- Casillo, A.; Lanzetta, R.; Parrilli, M.; Corsaro, M.M. Exopolysaccharides from marine and marine extremophilic bacteria: Structures, properties, ecological roles and applications. *Mar. Drugs* **2018**, *16*, 69. [[CrossRef](#)] [[PubMed](#)]
- Carroll, A.R.; Copp, B.R.; Davis, R.A.; Keyzers, R.A.; Prinsep, M.R. Marine natural products. *Nat. Prod. Rep.* **2020**, *37*, 175–223. [[CrossRef](#)] [[PubMed](#)]
- Baik, K.S.; Seong, C.N.; Kim, E.M.; Yi, H.; Bae, K.S.; Chun, J. *Hahella ganhwensis* sp. nov., isolated from tidal flat sediment. *Int. J. Syst. Evol. Microbiol.* **2005**, *55 Pt 2*, 681–684. [[CrossRef](#)] [[PubMed](#)]
- Lee, H.K.; Chun, J.; Moon, E.Y.; Ko, S.H.; Lee, D.S.; Lee, H.S.; Bae, K.S. *Hahella chejuensis* gen. nov., sp. nov., an extracellular-polysaccharide-producing marine bacterium. *Int. J. Syst. Evol. Microbiol.* **2001**, *51 Pt 2*, 661–666. [[CrossRef](#)] [[PubMed](#)]
- Lee, K.; Lee, H.K.; Cho, J.C. *Hahella antarctica* sp. nov., isolated from Antarctic seawater. *Int. J. Syst. Evol. Microbiol.* **2008**, *58 Pt 2*, 353–356. [[CrossRef](#)]
- Senapin, S.; Dong, H.T.; Meemetta, W.; Siriphongphaew, A.; Charoensapsri, W.; Santimanawong, W.; Turner, W.A.; Rodkhum, C.; Withyachumnarnkul, B.; Vanichviriyakit, R. *Hahella chejuensis* is the etiological agent of a novel red egg disease in tilapia (*Oreochromis* spp.) hatcheries in Thailand. *Aquaculture* **2016**, *454*, 1–7. [[CrossRef](#)]
- Jeong, H.; Yim, J.H.; Lee, C.; Choi, S.H.; Park, Y.K.; Yoon, S.H.; Hur, C.G.; Kang, H.Y.; Kim, D.; Lee, H.H.; et al. Genomic blueprint of *Hahella chejuensis*, a marine microbe producing an algicidal agent. *Nucl. Acids Res.* **2005**, *33*, 7066–7073. [[CrossRef](#)]
- Kim, D.; Lee, J.S.; Park, Y.K.; Kim, J.F.; Jeong, H.; Oh, T.K.; Kim, B.S.; Lee, C.H. Biosynthesis of antibiotic prodiginines in the marine bacterium *Hahella chejuensis* KCTC 2396. *J. Appl. Microbiol.* **2007**, *102*, 937–944. [[CrossRef](#)]
- Sakai-Kawada, F.E.; Ip, C.G.; Hagiwara, K.A.; Awaya, J.D. Biosynthesis and Bioactivity of Prodiginine Analogs in Marine Bacteria, *Pseudoalteromonas*: A Mini Review. *Front. Microbiol.* **2019**, *10*, 1715. [[CrossRef](#)]
- Chen, X.Y.; Yang, P.Z.; Jiang, S.T.; Zheng, G.; Cao, L.L.; Cao, X.M.; Zhu, X.X.; Zhang, D.F.; Liu, G.Q. Experimental study of acute oral toxicity and genetic toxicity of natural red pigment prodigiosin. *Food Sci.* **2017**, *38*, 224–228.
- Lin, S.R.; Chen, Y.H.; Tseng, F.J.; Weng, C.F. The production and bioactivity of prodigiosin: Quo vadis? *Drug Discov. Today* **2020**, *25*, 828–836. [[CrossRef](#)] [[PubMed](#)]
- Choi, Y.H.; Sohn, J.H.; Lee, D.; Kim, J.K.; Kong, I.S.; Ahn, S.C.; Oh, H. Chejuenolides A and B, new macrocyclic tetraenes from the marine bacterium *Hahella chejuensis*. *Tetrahedron Lett.* **2008**, *49*, 7128–7131. [[CrossRef](#)]
- Seo, C.; Oh, H. Chejuenolide C: A new macrocyclic metabolite from the marine bacterium *Hahella chejuensis*. *B Korean Chem. Soc.* **2009**, *30*, 1181–1183.
- Ng, B.G.; Han, J.W.; Lee, D.W.; Choi, G.J.; Kim, B.S. The chejuenolide biosynthetic gene cluster harboring an iterative trans-AT PKS system in *Hahella chejuensis* strain MB-1084. *J. Antibiot.* **2018**, *71*, 495–505. [[CrossRef](#)] [[PubMed](#)]
- Blin, K.; Shaw, S.; Kloosterman, A.M.; Charlop-Powers, Z.; van Wezel, G.P.; Medema, M.H.; Weber, T. antiSMASH 6.0: Improving cluster detection and comparison capabilities. *Nucl. Acids Res.* **2021**, *49*, W29–W35. [[CrossRef](#)] [[PubMed](#)]
- Medema, M.H. The year 2020 in natural product bioinformatics: An overview of the latest tools and databases. *Nat. Prod. Rep.* **2021**, *38*, 301–306. [[CrossRef](#)] [[PubMed](#)]
- Skininder, M.A.; Johnston, C.W.; Gunabalasingam, M.; Merwin, N.J.; Kieliszek, A.M.; MacLellan, R.J.; Li, H.; Ranieri, M.R.M.; Webster, A.L.H.; Cao, M.P.T.; et al. Comprehensive prediction of secondary metabolite structure and biological activity from microbial genome sequences. *Nat. Commun.* **2020**, *11*, 6058. [[CrossRef](#)]
- Ziemert, N.; Alanjary, M.; Weber, T. The evolution of genome mining in microbes—A review. *Nat. Prod. Rep.* **2016**, *33*, 988–1005. [[CrossRef](#)]
- Walsh, C.T. The chemical versatility of natural-product assembly lines. *Acc. Chem. Res.* **2008**, *41*, 4–10. [[CrossRef](#)]
- Konstantinidis, K.T.; Tiedje, J.M. Genomic insights that advance the species definition for prokaryotes. *Proc. Natl. Acad. Sci. USA* **2005**, *102*, 2567–2572. [[CrossRef](#)]
- Kautsar, S.A.; Blin, K.; Shaw, S.; Navarro-Munoz, J.C.; Terlouw, B.R.; van der Hoof, J.J.J.; van Santen, J.A.; Tracanna, V.; Suarez Duran, H.G.; Pascal Andreu, V.; et al. MIBiG 2.0: A repository for biosynthetic gene clusters of known function. *Nucl. Acids Res.* **2020**, *48*, D454–D458. [[CrossRef](#)] [[PubMed](#)]

22. Romano, S.; Jackson, S.A.; Patry, S.; Dobson, A.D.W. Extending the “One Strain Many Compounds” (OSMAC) principle to marine microorganisms. *Mar. Drugs* **2018**, *16*, 244. [[CrossRef](#)] [[PubMed](#)]
23. Lee, J.S.; Kim, Y.S.; Park, S.; Kim, J.; Kang, S.J.; Lee, M.H.; Ryu, S.; Choi, J.M.; Oh, T.K.; Yoon, J.H. Exceptional production of both prodigiosin and cycloprodigiosin as major metabolic constituents by a novel marine bacterium, *Zooshikella rubidus* S1-1. *Appl. Environ. Microbiol.* **2011**, *77*, 4967–4973. [[CrossRef](#)] [[PubMed](#)]
24. Jeong, Y.; Kim, H.J.; Kim, S.; Park, S.Y.; Kim, H.; Jeong, S.; Lee, S.J.; Lee, M.S. Enhanced large-scale production of *Hahella chejuensis*-derived prodigiosin and evaluation of its bioactivity. *J. Microbiol. Biotechnol.* **2021**, *31*, 1624–1631. [[CrossRef](#)]
25. Wang, F.P.; Li, M.; Huang, L.; Zhang, X.H. Cultivation of uncultured marine microorganisms. *Mar. Life Sci. Technol.* **2021**, *3*, 117–120. [[CrossRef](#)]
26. Pye, C.R.; Bertin, M.J.; Lokey, R.S.; Gerwick, W.H.; Lington, R.G. Retrospective analysis of natural products provides insights for future discovery trends. *Proc. Natl. Acad. Sci. USA* **2017**, *114*, 5601–5606. [[CrossRef](#)]
27. Kautsar, S.A.; van der Hooft, J.J.J.; de Ridder, D.; Medema, M.H. BiG-SLiCE: A highly scalable tool maps the diversity of 1.2 million biosynthetic gene clusters. *GigaScience* **2021**, *10*, g1154. [[CrossRef](#)]
28. Moran, N.A. Accelerated evolution and Muller’s ratchet in endosymbiotic bacteria. *Proc. Natl. Acad. Sci. USA* **1996**, *93*, 2873–2878. [[CrossRef](#)]
29. O’Fallon, B. Population structure, levels of selection, and the evolution of intracellular symbionts. *Evolution* **2008**, *62*, 361–373. [[CrossRef](#)]
30. Pettersson, M.E.; Berg, O.G. Muller’s ratchet in symbiont populations. *Genetica* **2007**, *130*, 199–211. [[CrossRef](#)]
31. Wernegreen, J.J.; Richardson, A.O.; Moran, N.A. Parallel acceleration of evolutionary rates in symbiont genes underlying host nutrition. *Mol. Phylogenet. Evol.* **2001**, *19*, 479–485. [[CrossRef](#)] [[PubMed](#)]
32. Williamson, N.R.; Fineran, P.C.; Leeper, F.J.; Salmond, G.P. The biosynthesis and regulation of bacterial prodiginines. *Nat. Rev. Microbiol.* **2006**, *4*, 887–899. [[CrossRef](#)] [[PubMed](#)]
33. Hu, D.X.; Withall, D.M.; Challis, G.L.; Thomson, R.J. Structure, chemical synthesis, and biosynthesis of prodiginine natural products. *Chem. Rev.* **2016**, *116*, 7818–7853. [[CrossRef](#)] [[PubMed](#)]
34. Henry, G.; Deleu, M.; Jourdan, E.; Thonart, P.; Ongena, M. The bacterial lipopeptide surfactin targets the lipid fraction of the plant plasma membrane to trigger immune-related defence responses. *Cell Microbiol.* **2011**, *13*, 1824–1837. [[CrossRef](#)]
35. Steigenberger, J.; Verleysen, Y.; Geudens, N.; Martins, J.C.; Heerklotz, H. The optimal lipid chain length of a membrane-permeabilizing lipopeptide results from the balance of membrane partitioning and local damage. *Front. Microbiol.* **2021**, *12*, 669709. [[CrossRef](#)]
36. Tabbene, O.; Kalai, L.; Ben Slimene, I.; Karkouch, I.; Elkahoui, S.; Gharbi, A.; Cosette, P.; Mangoni, M.L.; Jouenne, T.; Limam, F. Anti-candida effect of bacillomycin D-like lipopeptides from *Bacillus subtilis* B38. *FEMS Microbiol. Lett.* **2011**, *316*, 108–114. [[CrossRef](#)]
37. Berdy, B.; Spoering, A.L.; Ling, L.L.; Epstein, S.S. In situ cultivation of previously uncultivable microorganisms using the ichip. *Nat. Protoc.* **2017**, *12*, 2232–2242. [[CrossRef](#)]
38. Heuer, H.; Krsek, M.; Baker, P.; Smalla, K.; Wellington, E.M. Analysis of actinomycete communities by specific amplification of genes encoding 16S rRNA and gel-electrophoretic separation in denaturing gradients. *Appl. Environ. Microbiol.* **1997**, *63*, 3233–3241. [[CrossRef](#)]
39. Kumar, S.; Stecher, G.; Tamura, K. MEGA7: Molecular evolutionary genetics analysis version 7.0 for bigger datasets. *Mol. Biol. Evol.* **2016**, *33*, 1870–1874. [[CrossRef](#)]
40. Wang, M.; Carver, J.J.; Phelan, V.V.; Sanchez, L.M.; Garg, N.; Peng, Y.; Nguyen, D.D.; Watrous, J.; Kaponov, C.A.; Luzzatto-Knaan, T.; et al. Sharing and community curation of mass spectrometry data with Global Natural Products Social Molecular Networking. *Nat. Biotechnol.* **2016**, *34*, 828–837. [[CrossRef](#)]
41. Wiegand, I.; Hilpert, K.; Hancock, R.E. Agar and broth dilution methods to determine the minimal inhibitory concentration (MIC) of antimicrobial substances. *Nat. Protoc.* **2008**, *3*, 163–175. [[CrossRef](#)] [[PubMed](#)]
42. Shan, Z.Y.; Xu, H.J.; Shi, X.Q.; Nie, Z.; Yu, Y.; Zhang, X.M.; Bai, Y.L.; Qiao, M.Q.; Gao, C.C. The study of optimal conditions of electroporation in *Pseudomonas aeruginosa*. *Yi Chuan Xue Bao* **2004**, *31*, 311–316. [[PubMed](#)]





## Article

# The Inhibitors of CDK4/6 from a Library of Marine Compound Database: A Pharmacophore, ADMET, Molecular Docking and Molecular Dynamics Study

Lianxiang Luo <sup>1,2,3,\*</sup>, Qu Wang <sup>4,†</sup> and Yinglin Liao <sup>4</sup><sup>1</sup> The Marine Biomedical Research Institute, Guangdong Medical University, Zhanjiang 524023, China<sup>2</sup> The Marine Biomedical Research Institute of Guangdong Zhanjiang, Zhanjiang 524023, China<sup>3</sup> Southern Marine Science and Engineering Guangdong Laboratory (Zhanjiang), Zhanjiang 524023, China<sup>4</sup> The First Clinical College, Guangdong Medical University, Zhanjiang 524023, China; wangqu0503@gdmu.edu.cn (Q.W.); ly1212608@gdmu.edu.cn (Y.L.)

\* Correspondence: luolianxiang321@gdmu.edu.cn

† These authors contributed equally to this work.

**Abstract:** Background: CDK4/6 (Cyclin-dependent kinases 4/6) are the key promoters of cell cycle transition from G1 phase to S phase. Thus, selective inhibition of CDK4/6 is a promising cancer treatment. Methods: A total of 52,765 marine natural products were screened for CDK4/6. To screen out better natural compounds, pharmacophore models were first generated, then the absorption, distribution, metabolism, elimination, and toxicity (ADMET) were tested, followed by molecular docking. Finally, molecular dynamics simulation was carried out to verify the binding characteristics of the selected compounds. Results: Eighty-seven marine small molecules were screened based on the pharmacophore model. Then, compounds **41369** and **50843** were selected according to the ADMET and molecular docking score for further kinetic simulation evaluation. Finally, through molecular dynamics analysis, it was confirmed that compound **50843** maintained a stable conformation with the target protein, so it has the opportunity to become an inhibitor of CDK4/6. Conclusion: Through structure-based pharmacophore modeling, ADMET, the molecular docking method and molecular dynamics (MD) simulation, marine natural compound **50843** was proposed as a promising marine inhibitor of CDK4/6.

**Keywords:** CDK4/6; marine compounds; pharmacophore construction; ADMET; molecular docking; molecular dynamics; mm-pbsa

**Citation:** Luo, L.; Wang, Q.; Liao, Y. The Inhibitors of CDK4/6 from a Library of Marine Compound Database: A Pharmacophore, ADMET, Molecular Docking and Molecular Dynamics Study. *Mar. Drugs* **2022**, *20*, 319. <https://doi.org/10.3390/md20050319>

Academic Editor: Rosa Maria Vitale

Received: 17 March 2022

Accepted: 8 May 2022

Published: 12 May 2022

**Publisher's Note:** MDPI stays neutral with regard to jurisdictional claims in published maps and institutional affiliations.



**Copyright:** © 2022 by the authors. Licensee MDPI, Basel, Switzerland. This article is an open access article distributed under the terms and conditions of the Creative Commons Attribution (CC BY) license (<https://creativecommons.org/licenses/by/4.0/>).

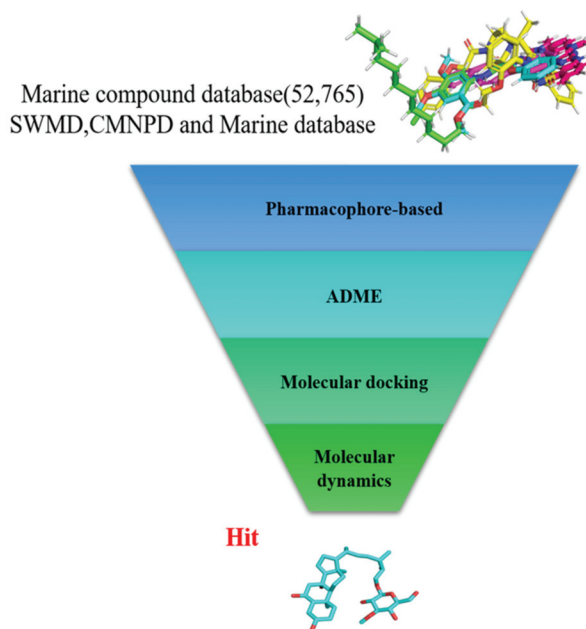
## 1. Introduction

The uncontrolled cyclin D-CDK4/6-INK4-RB (Cyclin-dependent kinases 4/6-retinoblastoma protein) signaling pathway is usually associated with the abnormal proliferation of tumor cells [1]. Furthermore, in the G1 to S phases of the cell cycle, the uncontrolled signal pathway leads to the over phosphorylation of RB and the excessive separation of E2F transcription factors, which eventually leads to the uncontrollable proliferation of cells [2–5]. In addition, breast cancer is closely related to the anomalous expression of this pathway [6]. Therefore, inhibiting the expression of CDK4/6 can play a key role in the treatment of tumors [7,8]. Moreover, CDKs are a conserved kinase family [9]. Amino acid sequence analysis showed that CDK4 and CDK6 proteins have 71% similar sequences, which leads to their similar functions [10]. The crystal structures of CDK4/6 selected in this study and the Ramachandran plot are shown in Supplementary Figure S1. It is worth mentioning that the Ramachandran plot reflects the rationality of the selected CDK4 and CDK6 structures to a certain extent. The key amino acids at the active site of CDK4/6 ATP include His-95, Val-96, Asp-97 and Thr-102, and His-100, Val101, Asp-102 and Thr-107, respectively [11,12]. The confirmation of the above crystal structure and the key amino acids at the active site provides a structural basis for the discovery of CDK4/6 inhibitors.

At present, some achievements have been made in the development of CDK4/6 inhibitors, resulting in the emergence of many selective inhibitors: Palbociclib, Abemaciclib, Ribociclib, Trilaciclib and so on [13–16]. Clinical trials of these drugs in the treatment of cancer have also been carried out worldwide. Most clinical trials are the combination of CDK4/6 inhibitors and other drugs (such as tyrosine kinase inhibitors, HER2, EGFR inhibitors, PI3K kinase inhibitors, etc.) [17]. In addition, the latest generation of CDK inhibitors can selectively inhibit CDK4/6 while having little effect on other CDKs and maintain good anticancer effects while obtaining acceptable toxicity. However, drug resistance to approved CDK4/6 inhibitors has emerged and gradually increased [18].

Due to the vast marine environment, marine organisms are regarded as the most abundant source of bioactive natural products, and the compounds obtained from them reflect their biological diversity [19]. In the past few years, with the full exploitation of other resources, the marine environment has generated a new research field, and many drugs from marine natural products have entered clinical trials [20]. Recent studies have pointed out that 170 marine natural products and their synthetic analogues have strong anticancer biological activities [21]. In addition to anticancer activities, marine natural products have structural characteristics different from other environmental natural products and have a variety of biological activities, such as antibacterial, antiviral and antiinflammatory [22]. Therefore, marine natural products have received an increasing amount of attention from scientists. Natural products are the best choice for the source of new drugs [23,24]. We collected three marine natural product databases. The Seaweed Metabolite Database (SWMD), Comprehensive Marine Natural Product Database (CMNPD) and Marine Natural Product Database (MNPDB) [25–27], and screened two small molecules of marine origin with CDK4/6 inhibitory potential from the databases by a series of computer-assisted methods.

In the present study, we found two new chemical inhibitors with CDK4/6 inhibitory properties by pharmacophore modeling, ADMET property prediction, molecular docking and molecular dynamics (MD) simulation methods [28] (Figure 1).

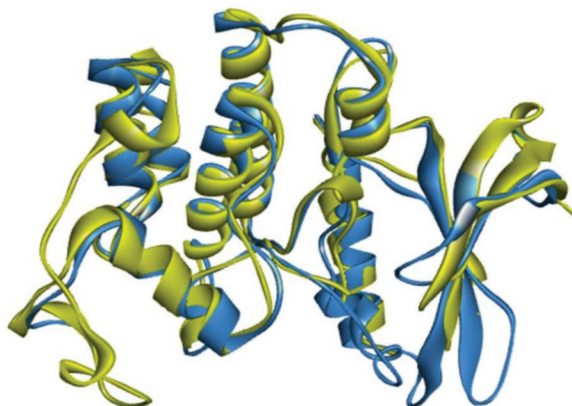


**Figure 1.** Workflow of this study: marine compound database construction, a pharmacophore, ADMET, molecular docking, and molecular dynamics.

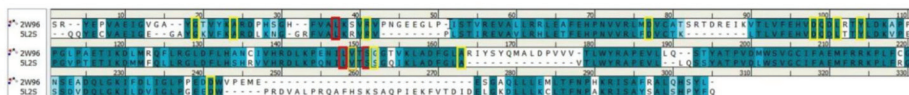
Considering that CDK4 is a dimer and that the active residues of both proteins are mainly in the A-chain, we only compared the stacked A-chain structures of CDK4 and CDK6. The Alignment C- $\alpha$  distance cutoff was set as 2.5, and length cutoff was set as 50. The RMSD (in angstrom) for the two protein structures was 1.1380. It is generally accepted that a smaller RMSD value means a higher overlap in protein spatial structure, and an RMSD value of less than 2 Å is good [29].

Figure 2 shows a comparison of the A-chain sequences of CDK4 and CDK6. The PDB structure-defining active site boundary residues of CDK4 are highlighted in red and the PDB structure-defining active site boundary residues of CDK6 are highlighted in yellow. The darker cyan residue pairs represent that they are identical, the lighter the blue the greater the difference between the residue pairs and the white residue pairs represent that they are completely different in origin. It is easy to see that the active site boundary residues of both structural A-chains are almost always highly homologous. It is worth noting that we are studying here the protein structure active residues published by PDB.

A



B



**Figure 2.** Comparison of CDK4/6 protein structures and key residues. **(A)** Schematic representation of the superimposed CDK4 and CDK6 structures. The CDK4 (PDB: 2W96) structure is shown in blue and the CDK6 (PDB: 5L2S) structure is shown in yellow. **(B)** Comparison of the amino acid sequences of CDK4 (PDB: 2W96) and CDK6 (PDB: 5L2S). Residues defining the active site boundary are highlighted in red for the PDB structure of CDK4 and in yellow for the PDB structure of CDK6.

In addition, we calculated evolutionary conserved scores for residues using the ConSurf-DB online tool for two selected CDK protein structures (CDK4: 2W96; CDK6: 5L2S). Consecutive conserved scores were divided into discrete classes of nine levels, with level 1 indicating the most variable residues and level 9 indicating the most conserved position. Figure 3 shows the conservativeness of the sequences of residues in the A-chain of the CDK4 and CDK6 proteins. Key residues in the ATP-binding pocket of the CDK4/6 proteins [11,12] are all considered to have a moderate (class 5) or higher conservativeness score. In summary, it is known that the active binding site residues of CDK4/6 are highly homologous and conserved, and thus do not affect the binding of any ligands to the protein.

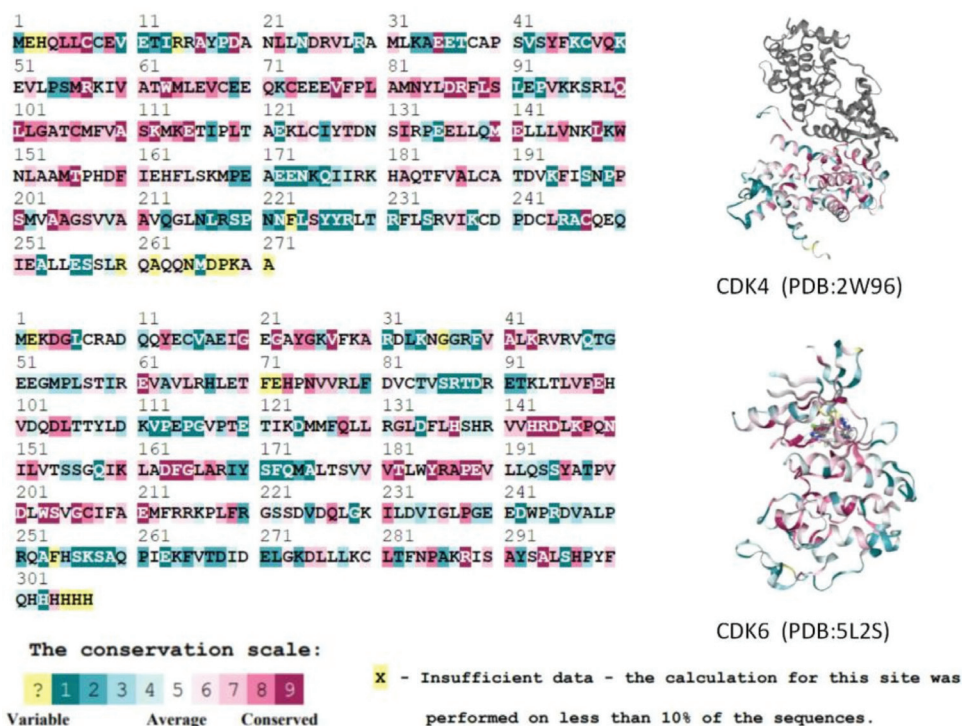
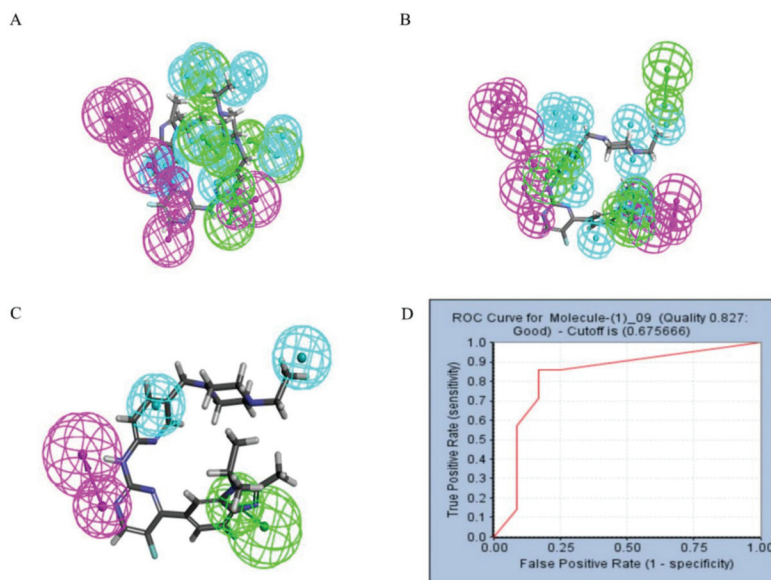


Figure 3. Comparison of CDK4 and CDK6 protein A-chain residue sequences and conservativeness. Higher scoring levels indicate higher conservativeness of residues. In this case, the yellow residues (which do not contain the active residues of the proteins) could not be classified by the conservativeness grade due to their low frequency of occurrence in the database.

## 2. Results

### 2.1. Pharmacophore Models: Construction, Selection and Application

Pharmacophore models can be used to simulate the active conformation of ligand molecules through conformational search and molecular superimposition and can be used to infer and interpret possible interaction patterns between receptor and ligand molecules. Ten common feature pharmacophore models were built with the Discovery Studio platform. The results show that all 10 pharmacophore models have good active/inactive molecule recognition. Figure 4a shows the models 01–05 and Figure 4b illustrates the pharmacophore models 06–10. As shown in Table 1, the pharmacophore model Phar09 (HHDA) had the lowest false positive and false negative error rates and the highest sensitivity for the test set molecules. In addition, the area under the curve (AUC) for Phar09 was 0.827, confirming the model's ability to identify positive molecules well (Figure 4d). The superimposed effect of Abemaciclib with Phar09 can be seen in Figure 4c. A library of 50,000 molecules of marine compounds was screened with the model Phar09. All molecules were pretreated with the Prepare Ligand program. The marine drug library was screened using Pharmacophore 09, and 87 molecules with a fit value greater than 3.50 were selected for further study.



**Figure 4.** The pharmacophore model and receiver operating characteristic (ROC) curve validation. Hydrophobic group features are shown as blue spheres, hydrogen bond acceptor features are shown as purple spheres and hydrogen bond donor features are shown as green spheres. (A) Pharmacophore model 01–05. (B) Pharmacophore model 06–10. (C) Coincidence effect drawing of Abemaciclib and pharmacophore 09. (D) ROC curve.

**Table 1.** The characteristic composition, the number of true/false positive and negative molecules, and the sensitivity of 10 pharmacophore models were constructed. Feature “H” stands for hydrophobic group, while feature “A”, “D” stand for hydrogen bond acceptor and hydrogen bond donor, respectively.

| Pharmacophore | Features | Ranking Score | True Positives | True Negatives | False Positives | False Negatives | Sensitivity |
|---------------|----------|---------------|----------------|----------------|-----------------|-----------------|-------------|
| Phar01        | HHHDA    | 55.473        | 3              | 8              | 4               | 4               | 0.42857     |
| Phar02        | HHHDA    | 55.280        | 4              | 8              | 4               | 3               | 0.57143     |
| Phar03        | HHDA     | 51.607        | 4              | 11             | 1               | 3               | 0.57143     |
| Phar04        | HHHD     | 50.761        | 4              | 10             | 2               | 3               | 0.57143     |
| Phar05        | HHDA     | 50.129        | 5              | 10             | 2               | 2               | 0.71429     |
| Phar06        | HHHD     | 49.714        | 4              | 10             | 2               | 3               | 0.57143     |
| Phar07        | HHDA     | 48.862        | 3              | 8              | 4               | 4               | 0.42857     |
| Phar08        | HHDA     | 48.828        | 2              | 9              | 3               | 5               | 0.28571     |
| Phar09        | HHDA     | 48.726        | 6              | 10             | 2               | 1               | 0.85714     |
| Phar10        | HHDA     | 48.442        | 6              | 9              | 3               | 1               | 0.85714     |

## 2.2. Absorption, Distribution, Metabolism, Excretion, and Toxicity (ADMET) Analysis

The pharmacokinetic method of ADMET (drug absorption, distribution, metabolism, excretion, and toxicity) is important in drug design and drug screening. We built a prediction process in Discovery Studio. We analyzed the ADMET descriptors of 87 marine molecules selected by pharmacophore. This research was carried out through the Calculate Molecular Properties function of the Discovery Studio platform. The blood–brain barrier permeability (BBB), water solubility, intestinal absorbance, hepatotoxicity and CYP2D6 enzyme inhibition descriptors of the drug were predicted. The blood–brain barrier permeability of all compounds was predicted to be “undefined”, indicating that the blood–brain

barrier permeability of all 20 compounds was outside of the 99% confidence ellipse [30]. Except for the blood–brain barrier permeability of the drug not being successfully predicted, the rest of the properties were described in a numerical or hierarchical manner. To efficiently select the molecules with better medicinal properties, we removed all the compounds with hepatotoxicity and CYP2D6 inhibition, and the water solubility, intestinal absorbance, hepatotoxicity and CYP2D6 inhibition values of the remaining 20 molecules are shown in Table 2. Among them, the range of water solubility grade is 1–5. The higher the grade goes, the better solubility the water has. The intestinal absorption rate is also divided into 1–5 grades. For hepatotoxicity and CYP2D6 enzyme inhibition, the negative value of the compound is inversely proportional to the cytochrome enzyme inhibition activity. Twenty compounds were predicted to have moderate water solubility and intestinal absorption; their hepatotoxicity and cytochrome enzyme inhibition was low, suggesting that they have good proprietary medicine properties.

**Table 2.** Twenty molecules’ water solubility, intestinal absorption, hepatotoxicity and CYP2D6 enzyme inhibition descriptor properties.

| Name          | Solubility | Absorption Level | Hepatotoxic | CYP2D6 Inhibit |
|---------------|------------|------------------|-------------|----------------|
| Molecule17227 | 3          | 3                | −9.93282    | −10.6775       |
| Molecule35962 | 3          | 2                | −10.2467    | −9.79215       |
| Molecule35945 | 3          | 2                | −10.3996    | −9.79215       |
| Molecule50853 | 3          | 3                | −9.27768    | −11.7400       |
| Molecule5999  | 3          | 3                | −12.0390    | −11.4830       |
| Molecule20551 | 4          | 2                | −7.04826    | −5.29830       |
| Molecule7211  | 3          | 3                | −11.8022    | −10.2513       |
| Molecule5996  | 3          | 3                | −12.0390    | −11.4830       |
| Molecule23671 | 3          | 3                | −4.67926    | −11.4629       |
| Molecule9567  | 3          | 3                | −27.0804    | −9.75238       |
| Molecule41369 | 3          | 1                | −13.8276    | −0.02226       |
| Molecule6045  | 3          | 3                | −19.2113    | −10.6996       |
| Molecule33567 | 3          | 1                | −9.88709    | −4.57087       |
| Molecule50843 | 4          | 3                | −13.7281    | −8.90702       |
| Molecule6049  | 3          | 3                | −19.2113    | −10.6996       |
| Molecule36157 | 3          | 1                | −4.28935    | −4.45112       |
| Molecule6028  | 3          | 3                | −19.2113    | −10.6996       |
| Molecule22564 | 3          | 2                | −7.74774    | −7.53197       |
| Molecule18748 | 3          | 3                | −5.33843    | −8.68489       |
| Molecule6243  | 3          | 3                | −11.4714    | −9.68009       |

### 2.3. Molecular Docking

Molecular docking can be used to explore the optimal binding mode between compounds and targets. Therefore, to further screen the compounds with good target inhibitory activity, we used CDK4 and CDK6 protein structures as targets for Libdock [31] molecular docking, and their Libdock scores and pharmacophore-screened Fit Values are listed in Table 3. The active sites of CDK4 (PDB ID:2W96) were Asp-99, Asp-140, Lys-142, Tyr-17 and Thr-172. The docking radius was set to 17. CDK6 (PDB ID:5L2S) took the original ligand as the center and set the sphere with a docking radius of 10 as the active site. The structure of the protein was optimized and hydrogenated by the Clean Protein program in advance. Docking preference was set as high quality, the number of spatial hotspots was set to 100 and the ligand conformation generation method was BEST to perform operations. To distinguish and determine which molecules had the better target binding activity, we selected the positive molecule Abemaciclib for the molecular docking study, and compounds with docking scores higher than Abemaciclib were considered valuable for further studies. The results, as shown in Table 3, indicate that all 20 molecules and CDK6 structures had higher Libdock scores, and seven of them had better scores than positive controls; but, generally speaking, there was no significant difference in docking scores between these 20 molecules and Abemaciclib. However, only three molecules bound to the active residues of the CDK4

structure, which were molecules 20551, 50843 and 41369. The docking scores of the latter two were higher than those of the positive control Abemaciclib, and they also had better docking scores with the CDK6 structure. Therefore, we chose the two molecules to dock with the two targets with higher precision CDOCKER and analyzed the interaction force between them in detail.

**Table 3.** Libdock scores of 20 selected molecules and positive control Abemaciclib with CDK4/6.

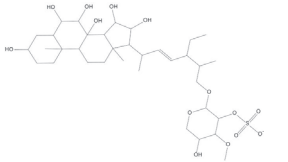
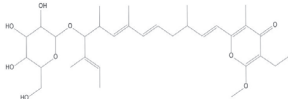
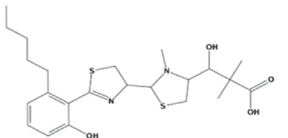
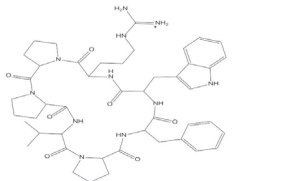
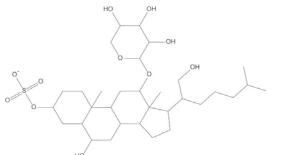
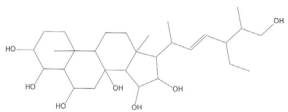
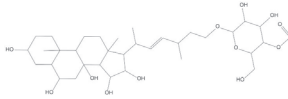
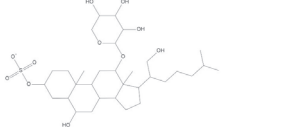
| Molecules     | 2D Structure  | Libdock Score (CDK4) | Libdock Score (CDK6) | Fit Value |
|---------------|---|----------------------|----------------------|-----------|
| Molecule17227 |    | 128.538              | 161.778              | 3.76592   |
| Molecule35962 |    | 165.215              | 149.821              | 3.74528   |
| Molecule35945 |    | 130.659              | 126.980              | 3.72383   |
| Molecule50853 |   | 144.891              | 139.235              | 3.71061   |
| Molecule5999  |  | 128.538              | 142.101              | 3.63037   |
| Molecule20551 |  | 81.8508              | 124.975              | 3.62799   |
| Molecule7211  |  | 131.753              | 154.228              | 3.60959   |
| Molecule5996  |  | 137.638              | 144.891              | 3.60816   |



Table 3. Cont.

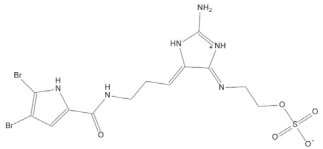
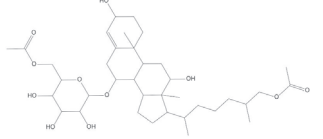
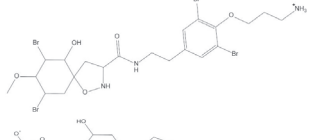
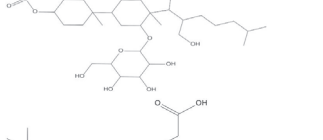
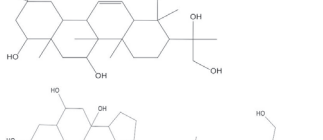

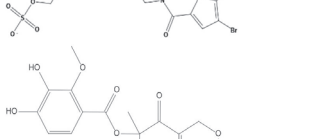
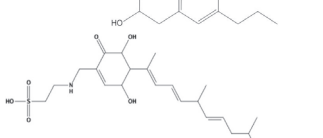
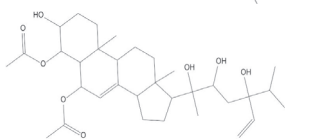

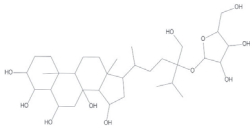
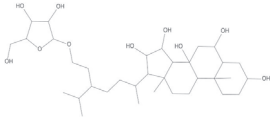
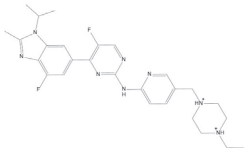
| Molecules     | 2D Structure  | Libdock Score (CDK4) | Libdock Score (CDK6) | Fit Value |
|---------------|---|----------------------|----------------------|-----------|
| Molecule23671 |    | 158.406              | 128.538              | 3.60593   |
| Molecule9567  |    | 142.101-             | 165.215              | 3.58841   |
| Molecule41369 |    | 114.793              | 130.659              | 3.57953   |
| Molecule6045  |    | 161.778              | 153.688              | 3.56692   |
| Molecule33567 |   | 149.821              | 121.223              | 3.56079   |
| Molecule50843 |  | 137.62               | 157.048              | 3.54233   |
| Molecule6049  |  | 158.406              | 152.475              | 3.53563   |
| Molecule36157 |  | 152.076              | 114.283              | 3.52724   |
| Molecule6028  |  | 139.235              | 151.536              | 3.52680   |
| Molecule22564 |  | 142.101              | 131.753              | 3.51793   |

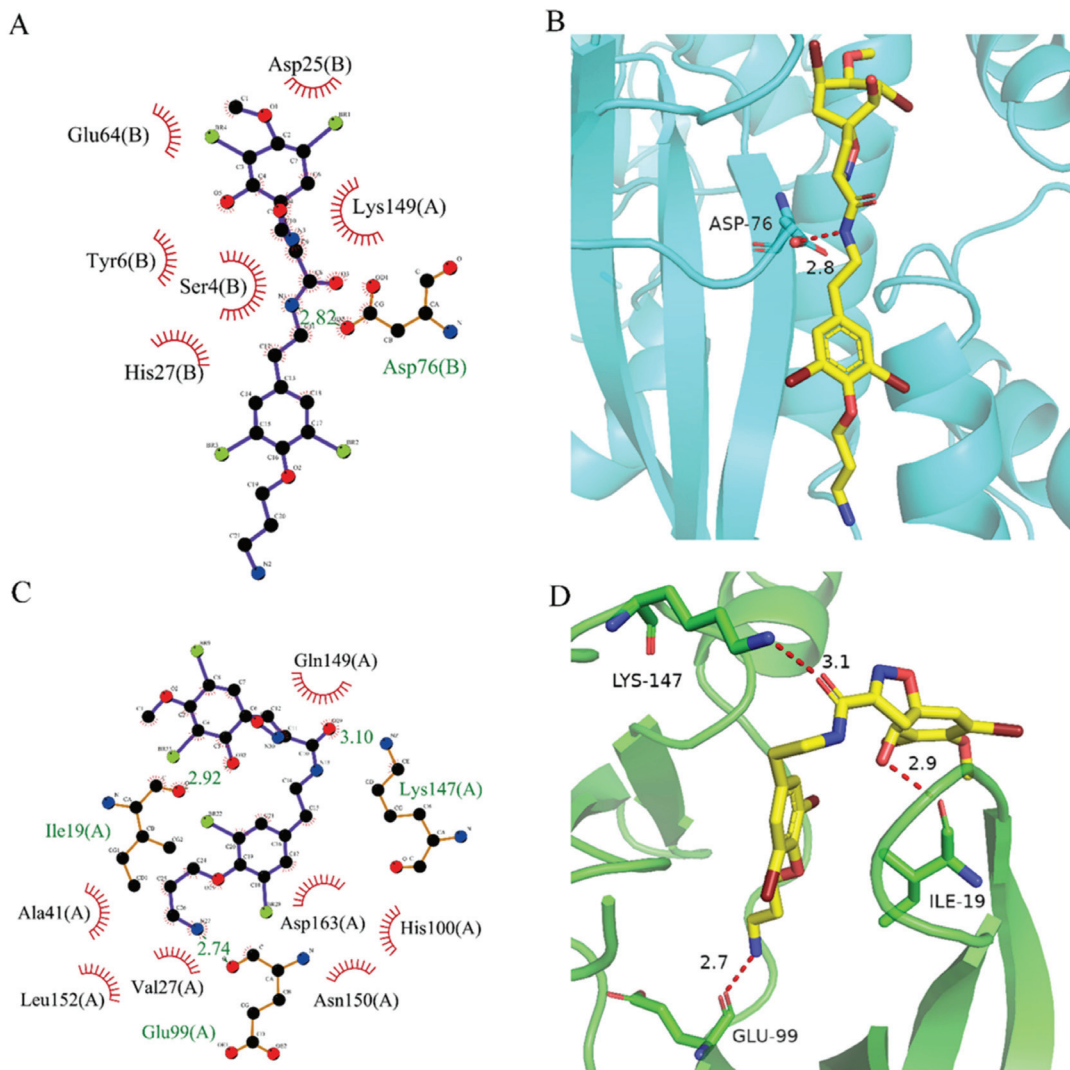
Table 3. Cont.

| Molecules     | 2D Structure  | Libdock Score (CDK4) | Libdock Score (CDK6) | Fit Value |
|---------------|---|----------------------|----------------------|-----------|
| Molecule18748 |  | 151.536              | 137.638              | 3.50622   |
| Molecule6243  |  | 131.753              | 158.406              | 3.50202   |
| Abemaciclib   |  | 97.7336              | 152.076              | 3.46079   |

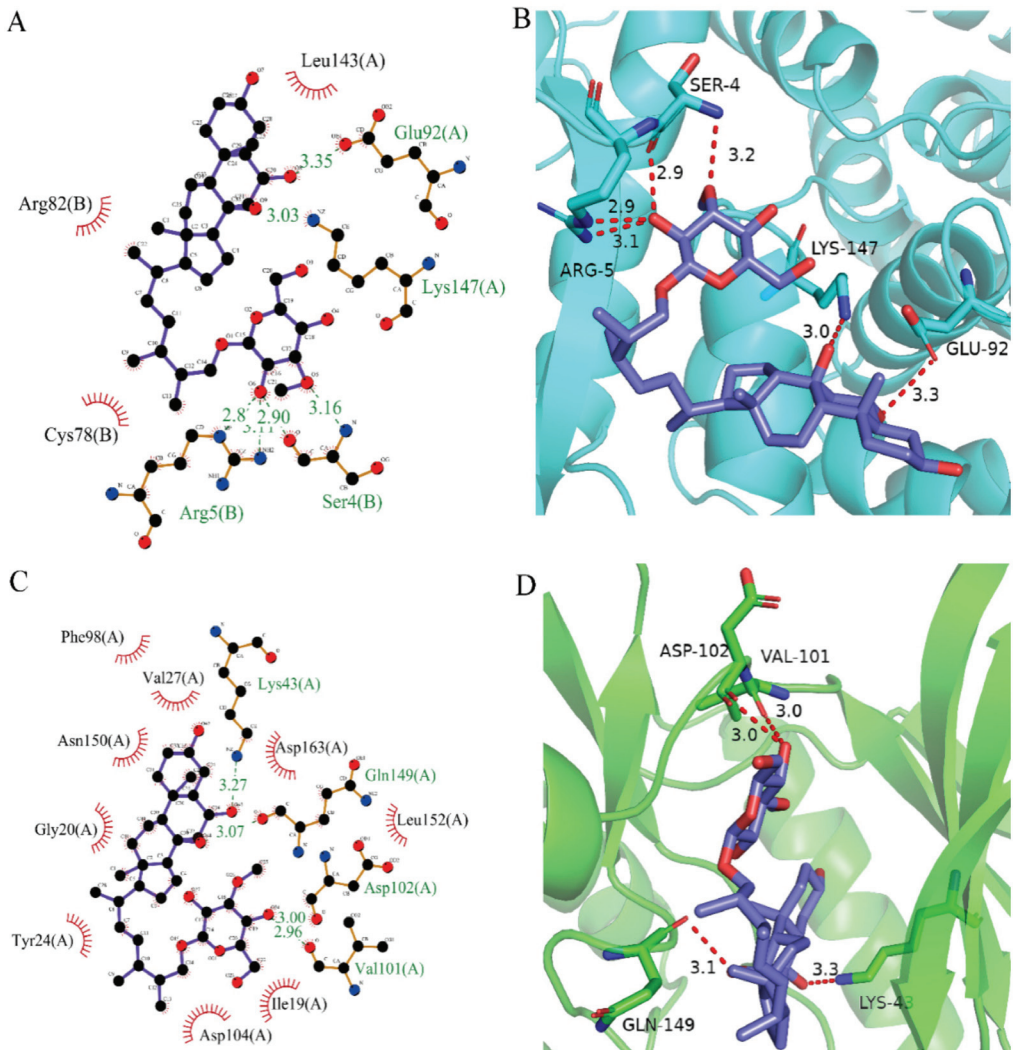
After analyzing and comparing the docking scores (Table 3), we selected the first two molecules with the highest sum of docking scores with the two targets and used the CDOCKER program to study their interaction with the receptors. The two molecules were finely docked. In the CDOCKER docking program, we used the charmM force field to deal with the protein structure and ligands. Finally, the docking results of compounds **41369** and **50843** with CDK4/6 are shown in Figures 5 and 6. The interaction diagram (Figure 5a) and three-dimensional binding pattern diagram (Figure 5b) of compound **41369** with CDK4 shows that the compound formed hydrogen bonding interactions with the side chain of protein B-chain residue Asp-76. For CDK6, compound **41369** formed hydrogen bonding interactions with the side chain of residue Lys-147 of the A-chain, the backbone of residues Ile-19 and Glu-99 (Figure 5c). Furthermore, the three-dimensional docking pattern of CDK6 with compound **41369** is shown in Figure 5d. The hydrogen bonding interaction between N and O on more residues indicates that compound **41369** and CDK4/6 had some interaction force. Furthermore, as seen in Figure 6a, compound **50843** formed hydrogen bonding interactions with residues Lys-147, Glu-92, Ser-4 and Arg-5 of CDK4, indicating tight binding (Figure 6b). For CDK6, compound **50843** formed hydrogen bonds with the side chain of A-chain residue Lys-43, and the backbone of residues Gln-149, Asp-102 and Val-101 (Figure 6c). Similarly, the three-dimensional docking pattern of CDK6 with compound **50843** is also shown in Figure 6d. Combined with the reported results, the A-chain residue Val-101 is necessary for the binding of CDK6 to the inhibitor, which could also provide guidance for future chemical optimization of this compound.

#### 2.4. RMSD and RMSF Analysis

The RMSD between two protein structures was used to describe the differences in their atomic positions, which can reflect the stability of the whole system. As shown in Figure 7, the complexes were more stable than their own receptor in the 100 ns simulation, while CDK4 and compound **50843** ended up stable at 0.15 nm and the simulation process did not fluctuate too much, and the same compound **41369** finally stabilized at 0.17 nm (Figure 7a). For CDK6, we found that the **41369** complex fluctuated at the beginning of 57 ns and finally stabilized at 62 ns with the RMSD value being 0.25 nm. Interestingly, the RMSD value of the **50843** complex did not fluctuate too much in the process of the 100 ns simulation and the RMSD value was 0.2 nm. The last four systems were able to reach a stable state in the simulation process. For the RMSD values of ligands in the system, compounds **41369** and **50843** remained stable in the simulation process of 100 ns and finally balanced in an appropriate range (Figure 7b).



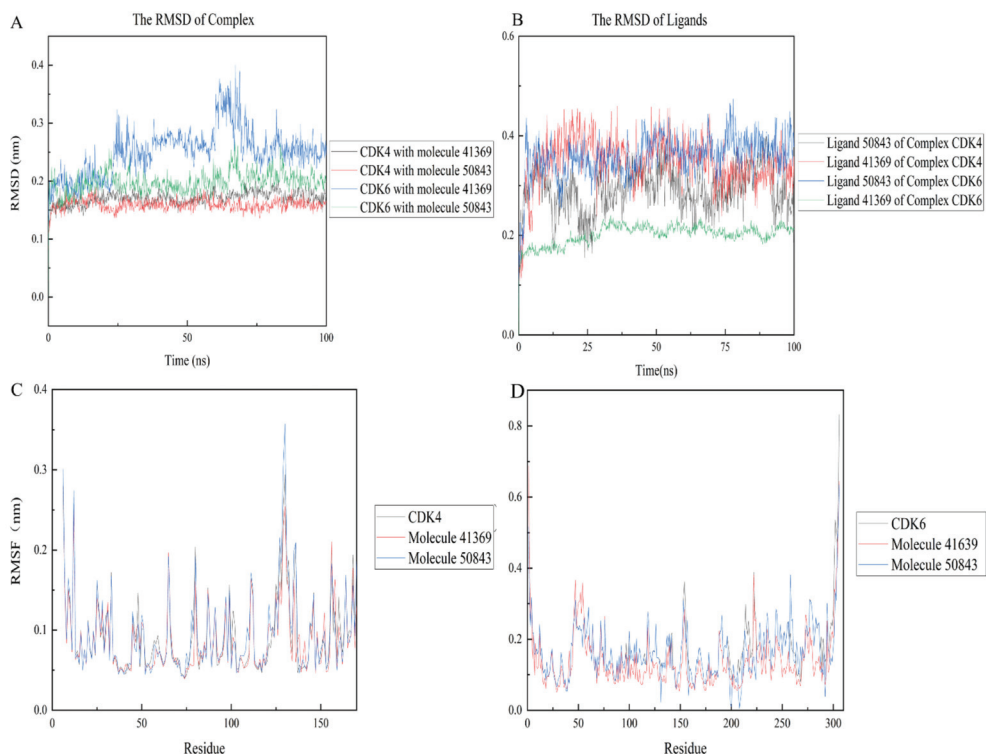
**Figure 5.** Analysis of binding mode between compound **41369** and CDK4/6. (A) A 2D interaction schematic of compound **41369** with CDK4. Hydrogen bonds are shown as green dashed lines, hydrophobicity is in red lines. (B) A 3D binding mode of compound **41369** with CDK4. Hydrogen bonds are shown as red dashed lines, while compound **41369** is shown in golden yellow. (C) A 2D interaction schematic of compound **41369** with CDK6. Hydrogen bonds are shown as green dashed lines, hydrophobicity is in red lines. (D) A 3D binding mode of compound **41369** with CDK6. Hydrogen bonds are shown as red dashed lines, while compound **50843** is shown in golden yellow.



**Figure 6.** Analysis of binding mode between compound 50843 and CDK4/6. (A) A 2D interaction schematic of compound 50843 with CDK4. Hydrogen bonds are shown as green dashed lines, hydrophobicity is in red lines. (B) A 3D binding mode of compound 50843 with CDK4. Hydrogen bonds are shown as red dashed lines, while compound 50843 is shown in blue. (C) A 2D interaction schematic of compound 50843 with CDK6. Hydrogen bonds are shown as green dashed lines, hydrophobicity is in red lines. (D) A 3D binding mode of compound 50843 with CDK6. Hydrogen bonds are shown as red dashed lines, while compound 50843 is shown in blue.

The RMSF refers to the root mean square displacement of each amino acid of a certain frame conformation compared with the average conformation, which is used to determine the flexibility of a region of a protein. Firstly, it can be seen from Figure 7c that the three systems all show high RMSF values near the binding pocket, which to a certain extent indicates that the pocket is more flexible. In contrast, compound 50843 increases the flexibility of the pocket slightly, but the RMSF value of the pocket is within an acceptable range; for CDK6 we focus on residue Val-101, compound 50843 has a hydrogen

bond with Val-101 of CDK6. It was found that the RMSF value of val-101 decreases (Figure 7d). In terms of flexibility, the four complex systems exhibited minor fluctuation, and the comprehensive RMSD and RMSF compounds **41369** and **50843** could stably bind to CDK4/6.

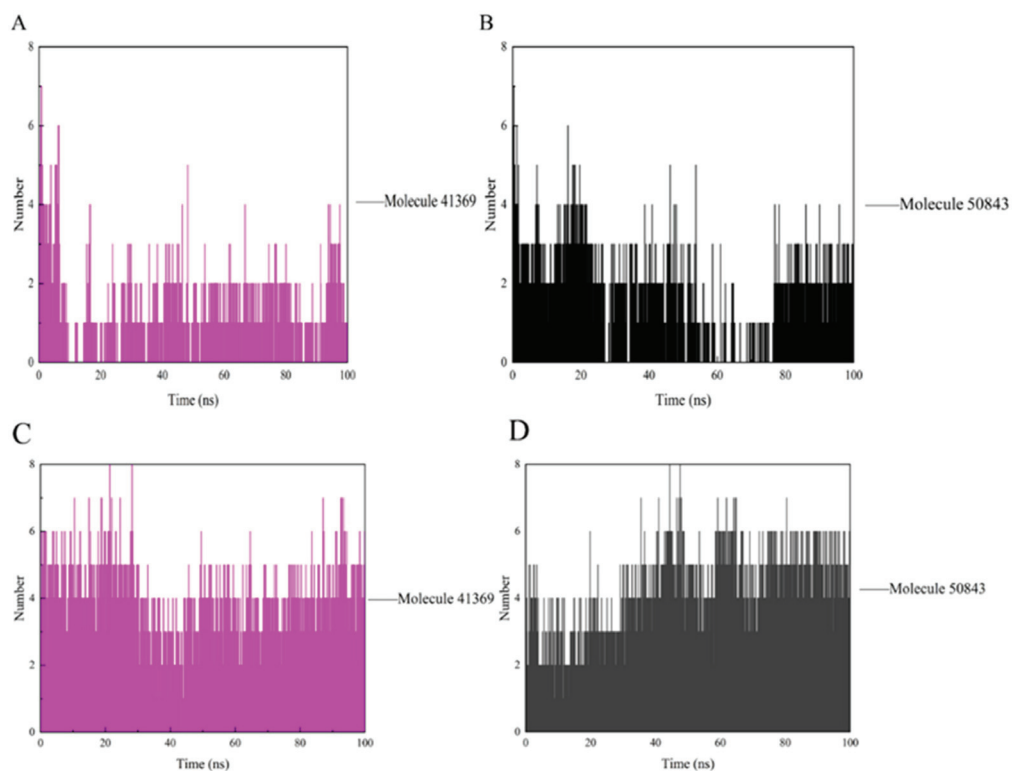


**Figure 7.** RMSD and RMSF plots of compound **50843** and **41369** with CDK4/6. (A) The RMSD of complexes. CDK4 and compound **41369** is shown as black lines, CDK4 and compound **50843** is in the red line, CDK6 and compound **41369** is shown as blue lines, CDK6 and compound **50843** is in the green line. (B) The RMSD of ligands. Ligand **50843** of complex CDK4 is shown as black lines, Ligand **41369** of complex CDK4 is shown as red lines, Ligand **50843** of complex CDK6 is shown as blue lines, Ligand **41369** of complex CDK6 is shown as green lines. (C) The RMSF of complexes and CDK4. CDK4 is shown as black lines, compound **41369** is in the red line and compound **50843** is in the blue line. (D) The RMSF of complexes and CDK6. CDK6 is shown as black lines, compound **41369** is in the red line and compound **50843** is in the blue line.

### 2.5. The Hydrogen Bond Analysis

During the simulation, the ligand formed a certain number of hydrogen bonds with the protein, and the number and survival time of these hydrogen bonds also reflected the binding degree of the ligand to the protein. In Figure 8a, compound **41369** had too few hydrogen bonds for a period of time in the simulation, while compound **50843** formed more hydrogen bonds with CDK4 overall and survived longer (Figure 8b). As for CDK6, there was always hydrogen bond interaction during the complex system in the 100 ns simulation process. The hydrogen bond formed by compound **41369** and CDK6 fluctuated at the simulated 40 ns (Figure 8c). In Figure 8d, it is shown that CDK6 and compound **50843** fluctuated in the early stages of the simulation, and the hydrogen bond fluctuated in the simulation process. It is able to be seen from these figures that compounds **41369**

and **50843** formed hydrogen bonds with the CDK4/6 simulation process and survived for a long time.

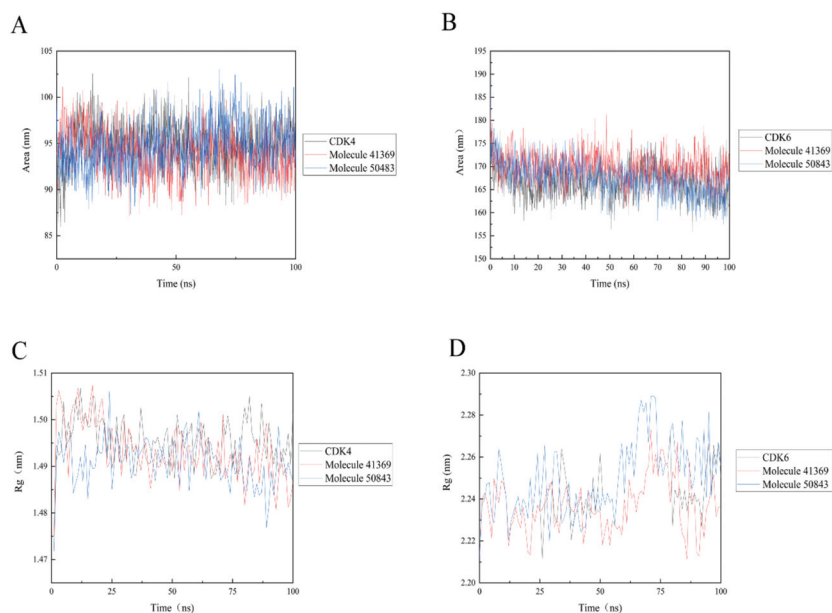


**Figure 8.** The hydrogen bond of CDK4/6 with compound **41369** and **50843**. (A) Compound **41369** (magenta) with CDK4. (B) Compound **50843** (black) with CDK4. (C) Compound **41369** (magenta) with CDK6. (D) Compound **50843** (black) with CDK6.

## 2.6. Solvent Accessible Surface Area and Radius of Gyration Analysis

Solvent accessible surface area (SASA) analysis can be used to indicate the solvent accessible surface area of the entire complex. The final simulation results show that the SASA values of the protein complexes (see Figure 9) are relatively stable during the trajectory; in Figure 9a, the complex systems all show lower SASA values. The complex system of CDK6 shows a higher SASA value, indicating that the complex system of compounds **41369** and **50843** with CDK6 found it easier to approach the solvent (Figure 9b).

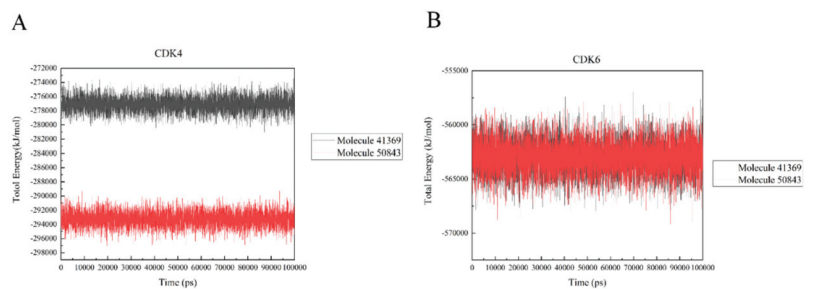
The radius of gyration (Rg) indicates the firmness of the protein structure. As shown in Figure 9, the average Rg values of CDK4 with compounds **50843** and **41369** were lower than 2.3 nm (Figure 9c), while a similar pattern was shown in the systems complexed with CDK6, and the average Rg values of these systems were lower than 1.5 nanometer; it is worth mentioning that the Rg value of compound **50843** with the CDK6 system was lower (Figure 9d). The results show that the compactness of the complex was maintained during the simulation.



**Figure 9.** Solvent accessible surface area (SASA) and radius of gyration (Rg) of 100 ns simulation process. (A) SASA plots of compound **50843** (blue) and **41369** (red) with CDK4 (black). (B) SASA plots of compound **50843** (blue) and **41369** (red) with CDK6 (black). (C) Rg plots of compound **50843** (blue) and **41369** (red) with CDK4 (black). (D) Rg plots of compound **50843** (blue) and **41369** (red) with CDK6 (black).

### 2.7. Protein–Ligand Interaction Energy Analysis

In a bid to quantify the interaction strength between the ligand and receptor, the non-bonding interaction energy between the two needs to be calculated; we used the `gmx_energy` program to calculate the energy change of the ligand and protein during the simulation. It is vital to note that the values here are not free energies or binding energies. Figure 10a shows that the estimated total energy value between compound **41369** and CDK4 is  $-277,000$  kJ/mol, while the total energy value of compound **50843** is  $-293,000$  kJ/mol; CDK6 and compounds **41369** and **50843** are both  $-562,000$  kJ/mol (Figure 10b). The results show that the interaction of compound **50843** with CDK4/6 is stronger in this energy numerical calculation.



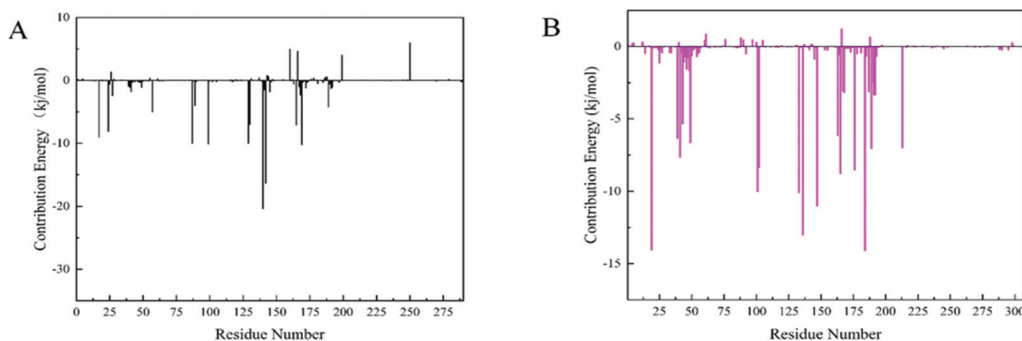
**Figure 10.** The total energy of CDK4/6 with molecule **41369** and **50843**. (A) The total energy of compound **41369** (black) and **50843** (red) with CDK4. (B) The total energy of compound **41369** (black) and **50843** (red) with CDK6.

### 2.8. MM-PBSA Analysis

The Molecular mechanics Poisson Boltzmann surface area (MM-PBSA) method is prevalent in the estimation of the free binding energy between CDK4 and CDK6 with compound **50843**. From the aspects of structural stability and flexibility and the simulation results of quantitative interaction, we finally selected compound **50843** for MM-PBSA calculation. The binding free energy component of each complex with compound **50843** was calculated in a time step of 1 ns in a molecular dynamics simulation of 100 ns. It can be seen from Table 4 that the binding free energies of compound **50843** and CDK4/6 are  $-154.655$  kJ/mol and  $-212.082$  kJ/mol respectively, which are also contributed to by van der Waals force to a great extent. Therefore, according to the energy calculation of MM-PBSA, a stronger binding interaction with protein was established. To further analyze the interaction between compound **50843** and protein, we decomposed the binding free energy of MM-PBSA into the energy contribution of each protein residue to evaluate the key binding residues; that is, the residues with higher energy contribution to the binding free energy. It can be seen from Figure 11a that the key residues in compound **50843** and CDK4 are Arg-5, Ser-4, Met-17, Arg-87, Asp-129, Asn-130, Leu-142 and Pro-169. Interestingly, the residues forming the hydrogen bond interaction in molecular docking appear in it. For Cdk6 and compound **50843**, their key residues include Ile-19, Ala-41, Val-101, Leu-133, Leu-136, Lys-147, Asp-163, Gly-165 and Glu-189. It is worth mentioning that the binding energy contributed by residue val-101 is  $-10.0042$  kJ/mol (Figure 11b). The results show that MM-PBSA not only verified the results of molecular docking but also further quantified the binding energy between compound **50843** and CDK4/6.

**Table 4.** Binding energy of binding for the compound **50843** complexed with CDK4/6.

| Pharmacophore                   | Features              | Ranking Score         |
|---------------------------------|-----------------------|-----------------------|
| Van der Waal energy (kJ/mol)    | $-192.855 \pm 90.101$ | $-254.799 \pm 51.499$ |
| Electrostatic energy (kJ/mol)   | $-84.560 \pm 49.773$  | $-59.732 \pm 23.528$  |
| Polar solvation energy (kJ/mol) | $139.559 \pm 111.556$ | $121.507 \pm 47.040$  |
| SASA energy (kJ/mol)            | $-16.800 \pm 9.461$   | $-19.058 \pm 4.394$   |
| Binding energy(kJ/mol)          | $-154.655 \pm 39.178$ | $-212.082 \pm 42.561$ |



**Figure 11.** Residue decomposition diagram of binding energy. (A) Compound **50843** with CDK4 (black). (B) Compound **50843** with CDK6 (magenta).

### 2.9. Analysis of Synthetic Accessibility Score Parameters

To explore the further synthetic and application potential of these two compounds, the SA scores of the compounds calculated using ADMETlab were used to assess the synthesizability of the two alternative compounds. As shown in Table 5, the SA scores for compound **41369** and compound **50843** were 5.226 and 5.517, respectively. Lower SA scores tend to imply better synthesizability. Although not as good as the positive control,



the two compounds we selected still had good SA scores, suggesting their potential to be synthesized as new drugs.

**Table 5.** Synthetic accessibility score parameters (SA score) for molecule **41369** and molecule **50843**.

| Molecule     | SA Score |
|--------------|----------|
| <b>41369</b> | 5.226    |
| <b>50843</b> | 5.517    |
| Abemaciclib  | 3.415    |

### 2.10. Prediction of Inhibitory Activity of Tumor Cell Lines

To predict the potential inhibitory activity of two candidate compounds against tumor cell lines, the way2durg online tool was applied. Both Pi and Pa of the two compounds were predicted. The results showed that both compounds exhibited inhibitory activity against MDA-MB-231 and HL-60 cell lines, respectively (Table 6).

**Table 6.** Predicted inhibitory activity of two alternative compounds against tumor cell lines.

| Compound     | Pa    | Pi    | Cell Line  | Tissue                            | Tumor Type     |
|--------------|-------|-------|------------|-----------------------------------|----------------|
| <b>41369</b> | 0.498 | 0.028 | MDA-MB-231 | Breast                            | Adenocarcinoma |
| <b>50843</b> | 0.625 | 0.014 | HL-60      | Hematopoietic and lymphoid tissue | Leukemia       |
| Abemaciclib  | 0.750 | 0.004 | LoVo       | Colon                             | Adenocarcinoma |

## 3. Discussion

In recent years, CDK4/6 inhibitors have continued to be applied to the clinical trials of various malignant tumors. However, these inhibitors have some disadvantages, such as gastrointestinal toxicity and drug resistance, which lead to the decline in their efficacy. At present, drug research and development are also taking more heed of the existing natural products in nature, and marine natural products have been of interest to the scientific community for their unique ecological advantages. Therefore, our study aims to screen CDK4/6 compounds using marine natural products.

In this study, we collected some listed CDK4/6 inhibitors by reading the literature, constructed a structure-based pharmacophore model using Discovery Studio and selected model 09 with the highest selection score; in addition, we verified the model. AUC under the ROC curve reflects the discrimination ability of the model. It is worth mentioning that some studies also use the QSAR model to screen a marine natural product, and our pharmacophore modeling was based on the selected known inhibitors, instead of structured modeling on the complex. The marine natural product compounds obtained from the pharmacophore model generated by this method can be more appropriate to the known CDK4/6 inhibitors in terms of conformation [32,33]. Then we carried out the ADMET test, and finally obtained 20 compounds that showed good ADMET characteristics.

In the molecular docking study, compound Abemaciclib was selected as the positive control, and then docking was carried out by the Libdock program. Finally, compounds **41369** and **50843** were selected according to the comprehensive scoring performance of compounds and CDK4/6, and their binding modes were further analyzed by a more precise CDOCKER program. It was found that compound **50843** could form a hydrogen bond with val-101 of CDK6, this residue has an important relationship with CDK6, and compound **41369** also formed a close interaction with CDK4/6 [34].

Molecular dynamics is of great significance to confirm the stability of binding between compounds and proteins. After the 100 ns simulation, we collected the RMSD and RMSF data of the trajectory to confirm the stability and flexibility of the binding between the compound and protein. In addition, we also analyzed the stability of the whole complex system in terms of the hydrogen bond, SASA and Rg. Distinct from some previous studies,

we analyzed the stability from many aspects. For the interaction and free binding energy between compounds and proteins, we first used the total energy of the system to quantify the interaction between compounds **41369** and **50843** and CDK4/6. Interestingly, compound **50843** performed much better in the comparison of interaction strength [35]. Finally, we selected the trajectories of compound **50843** and CDK4/6 for MM-PBSA calculation. In the residue energy contribution, we found some key residues not mentioned in previous studies, such as Arg-5, Ser-4 and Pro-169 of CDK4 and Asp-163, Gly-165 and Glu-189 of CDK6. Of course, Val-101 of CDK6 contributes a very high negative binding energy, further indicating the important relationship of compound **50843** for CDK6.

Finally, we carried out some studies on the synthesis and cytotoxicity of compounds **50843** and **41369**. In terms of results, SA score shows that compounds **50843** and **41369** can be synthesized, and their toxicity is also within an acceptable range, which also provides some reference data for subsequent experimental verification.

Briefly, marine natural products have made an immense contribution to the pharmacy domain owing to its ample resources. Through the method of computer-aided drug design, CDK4/6 inhibitors were quickly found from 52,765 marine natural products. In addition, compound **50843** can be optimized as a crucial lead compound to become a better CDK4/6 inhibitor.

#### 4. Materials and Methods

##### 4.1. Database Construction and Molecular Preparation

Seaweed Metabolite Database (<http://www.swmd.co.in>, accessed on 1 April 2021), Comprehensive Marine Natural Products Database (<https://www.cmnpd.org>, accessed on 1 April 2021) and Marine Database (<http://docking.umh.es/>, accessed on 1 April 2021) were integrated into one database. The database, which included 50,000 marine compounds, was saved in mol format in advance and imported into the Discovery Studio platform. The internal database of the platform was constructed with the help of the function of constructing a 3D database. Compounds with erroneous valence states were removed and 3D coordinates were generated for the rest of the molecules. The resulting database contained all the molecules of the three databases. Finally, the structure of the compound in the database was repaired by the Prepare Ligand tool in Discovery Studio. ConSurf-DB online tool [36] was used to calculate the evolutionary conserved scores of CDK4/6 structures.

##### 4.2. Pharmacophore Construction

Using the Discovery Studio platform, five CDK4/6 inhibitors that have entered clinical studies [13–16] (Supplementary Figure S2) were superimposed and 10 pharmacophore hypotheses were generated based on their molecular common features. For each generated hypothesis, we set the features it could contain to be hydrogen bond acceptors(A), hydrogen bond donors(D) and hydrophobic features(H), and each pharmacophore hypothesis contained up to five of the same feature. The minimum distance between pharmacophore features within the model was set at 2.97 Å and the best conformation method was applied to generate potential conformations for the positive compounds.

In addition, seven newly published inhibitors from Li et al. were selected as active molecules for testing [37], and 12 inactive decoy molecules were generated using the DUD-E online tool for all inhibitors (five marketed and seven newly published structures, shown in Supplementary Figure S2 and Supplementary Table S1). The DUD-E online decoy generation tool preserved the backbone structure of the positive inhibitors better, allowing the generated inactive molecules to maintain maximum structural similarity to the positive inhibitor [38]. The discriminatory ability and sensitivity of the pharmacophore model was characterized by subject operating characteristic (ROC) curves. The X-axis of the horizontal coordinate of the curve plot is 1-specificity, i.e., the false positive rate. The closer the X-axis is to zero, the higher the accuracy; the Y-axis of the vertical coordinate is called sensitivity, also known as the true positive rate (sensitivity), and the larger the

Y-axis is, the higher the accuracy, as reflected by the area under the ROC curve (AUC) being closer to 1 [39]. The pharmacophore ranking score given by the platform was also considered, and the pharmacophore with both the optimal ranking score and the area under the ROC curve (AUC) value was selected as the next step in the virtual screening [30]. The structures of all inhibitor and decoy molecules are shown in Figure S2 and Table S1 of the Supplementary Material.

#### 4.3. Absorption, Distribution, Metabolism, Elimination, and Toxicity (ADMET)

Pharmacokinetics and toxicity (ADMET) assessment is helpful to screen and eliminate molecules with poor proprietary properties from a large number of compounds. Using Discovery Studio's Calculate Molecule Properties tool, we calculated the ADME properties of 87 compounds. Four pharmacokinetic parameters, including intestinal absorption (HIA), hepatotoxicity (hepatotoxic), cytochrome CYP2D6 inhibitory activity and water solubility at 25 °C, were predicted. CYP2D6 plays an important role in the degradation of drugs in vivo. Better intestinal absorbance and CYP2D6 inhibitory activity can prolong the action time of drugs in the human body to the greatest extent. We removed the compounds with poor water solubility, intestinal absorbance and CYP2D6 inhibition, and selected the remaining compounds for further study.

#### 4.4. Molecular Docking

The molecular docking program consists of two parts. First of all, to quickly select the molecules with good target binding activity, 20 molecules selected by ADMET were docked with CDK4 and CDK6, respectively. Among them, the binding site of CDK4 (PDB:5L2S) was determined by the original ligand, the residue of the binding site of CDK6 (PDB:2W96) was identified as Asp-99, Asp-140, Lys-142 and Tyr-17, the central coordinate of the docking site was 24.870297, 18.922378 and 10.713189, and the radius of the two receptor structures was determined to be 15. Then, we used the CDOCKER program to fine dock two molecules with good Libdock scores with the two targets and analyze the interaction between them and the target. Pose Cluster Radius was set to 0.1, and the number of conformations randomly generated by ligands was 10, to achieve the purpose of ligand–receptor semi-flexible docking.

#### 4.5. Molecular Dynamics

After docking, the 100 ns molecular dynamics simulation was used to simulate the complex model of CDK4 and CDK6 with compound **50843** and compound **41369** to test the stability and flexibility of the complex. In this study, the GROMACS2018.1 software package, AMBER99SB-ILDN force field, and SPC216 water model were used for molecular dynamics simulation [40,41]. To ensure the total charge neutrality of the simulation system, a corresponding number of sodium ions were added to the system to replace water molecules to form a solvent box of appropriate size. Then the periodic boundary condition (PBC) was applied to three directions of the system. Using the AMBER99SB-ILDN force field, the force field parameters of the compound were obtained from the ACPYPE website (<https://www.bio2byte.be/acpype/>, accessed on 3 May 2021) [42]. Initially, the energy of 50,000 steps of the whole system was minimized (EM) at 300 K. After energy minimization, in order to maintain the pressure and temperature of the system, the two minimized systems were balanced by position constrained MD simulation at 300 K for 100 ps. After balancing, the four systems all carried out the final production operation of 100 ns MD simulation at 300 K. The Berendsen coupling algorithm was used to apply periodic boundary conditions under isothermal and isobaric conditions, and the pressure was set to 1 atm. In these four systems, Lin CS algorithm was used to constrain hydrogen bonds. The electrostatic interaction was analyzed by particle grid Ewald method. The calculation of van der Waals Coulomb interaction took 1.3 nm as the cutoff point. The whole MD track was recorded every 100 picoseconds (PS) [43–45]. Finally, the root means square deviation (RMSD) of the system and the root mean square fluctuation of atomic position

(RMSF) were analyzed. In addition, the radius of gyration (Rg), the solvent accessible surface area (SASA), the total potential energy change curve and the number of hydrogen bonds of each system were also collected [46].

#### 4.6. MM-PBSA

MM/PBSA method is widely used in the calculation of free energy of receptor–ligand binding. This method is called Molecular Mechanics/Poisson Boltzmann (Generalized Born) Surface Area [47]. The basic principle is to calculate the difference between the bound and unbound free energies of two solvated molecules or to compare the free energies of different solvated conformations of the same molecule. We extracted a stable 10 ns from the trajectory for calculation. The following Equation (1) below describes the binding free energy, and the resulting output formula is related to the calculated energies of the ligand and receptor.

$$G_{\text{binding}} = G_{\text{protein}} - (G_{\text{complex}} + G_{\text{ligand}}) \quad (1)$$

The free energy of the protein–ligand complex is expressed by  $G_{\text{Complex}}$ ,  $G_{\text{protein}}$  represents the free energy of the protein in the solvent and  $G_{\text{ligand}}$  represents the free energy of the ligand in the solvent.

#### 4.7. Analysis of Synthetic Accessibility Score Parameters

The SA score was calculated for the two best compounds using the ADMETlab 2.0 (public by Guoli Xiong et al., Xiangya School of Pharmaceutical Sciences, Central South University, Changsha Hunan, China) online platform [48], considering that the two compounds we selected were not existing available molecules. The SA Score is based on the “complexity” of the molecule, weighting the frequencies of the ECFP4 fingerprints of 1 million compounds obtained from PubChem and summing them to obtain a fragment Score, assuming that “frequently occurring substructures are easy to synthesize”. Meanwhile, the “Complexity Penalty” takes into account the molecular weight and complexity of the compound and normalizes the value from 1 (easy) to 10 (difficult), as is shown in Equation (2). A lower SA score implying that the compound is easier to synthesize.

$$SA \text{ score} = \text{fragment score} - \text{complexity Penalty} \quad (2)$$

#### 4.8. Prediction of Inhibitory Activity of Tumor Cell Lines

We used the way2drug online tool to predict the inhibitory activity of two alternative compounds against tumor cell lines. This analysis was performed by using the CLC-Pred web facility [48]. The activity assessment of both compounds was performed based on QSAR models built on the Prediction of Substance Activity Spectra (PASS) tool (<http://www.way2drug.com/PASSonline>, accessed on 14 April 2022) and a training dataset based on ChEMBLdb cytotoxicity data.

## 5. Conclusions

In conclusion, in this study, compound **50843** was screened from marine natural products as a CDK4/6 inhibitor by means of a structure-based pharmacophore model, molecular docking, ADMET analysis and kinetic simulation; Preliminary analysis indicated that compound **50843** is a potential small-molecule inhibitor that helps inhibit CDK4/6. Subsequent analysis can further evaluate small molecules through structural modification and experimental techniques to help determine the activity of compounds, thereby providing new drug-like leads for CDK4/6.

**Supplementary Materials:** The following supporting information can be downloaded at: <https://www.mdpi.com/article/10.3390/md20050319/s1>, Figure S1: The Crystal structure and Ramachandran plot of CDK4/6.; Figure S2: Five marketed and seven newly published inhibitor structures used to construct/test the pharmacophore; Table S1: The 12 inactive decoy molecule’s smile formula in the test set.

**Author Contributions:** L.L. conceived and designed the study; Q.W. and Y.L. contributed to the acquisition, analysis and interpretation of data. L.L. and Q.W. wrote the manuscript; L.L. reviewed the paper and provided comments. All authors have read and agreed to the published version of the manuscript.

**Funding:** This project was supported by the Basic and Applied Basic Research Program of Guangdong Province (2019A15110201); Program of Department of Natural Resources of Guangdong Province ([2021]53); Discipline Construction Project of Guangdong Medical University (4SG21004G); The Science and technology program of Guangdong Province (2019B090905011).

**Institutional Review Board Statement:** Not applicable.

**Informed Consent Statement:** Not applicable.

**Data Availability Statement:** The data used to support the findings of this study are included within the article.

**Acknowledgments:** We thank the Public Service Platform of South China Sea for R&D Marine Biomedicine Resources for support.

**Conflicts of Interest:** The authors declare that they have no known competing financial interests or personal relationships that could have appeared to influence the work reported in this paper.

## References

1. Malumbres, M.; Barbacid, M. Cell cycle, CDKs and cancer: A changing paradigm. *Nat. Rev. Cancer* **2009**, *9*, 153–166. [[CrossRef](#)] [[PubMed](#)]
2. Hiebert, S.; Chellappan, S.; Horowitz, J.; Nevins, J. The interaction of RB with E2F coincides with an inhibition of the transcriptional activity of E2F. *Genes Dev.* **1992**, *6*, 177–185. [[CrossRef](#)] [[PubMed](#)]
3. Talluri, S.; Isaac, C.E.; Ahmad, M.; Henley, S.A.; Francis, S.M.; Martens, A.L.; Bremner, R.; Dick, F.A. A G1 checkpoint mediated by the retinoblastoma protein that is dispensable in terminal differentiation but essential for senescence. *Mol. Cell Biol.* **2010**, *30*, 948–960. [[CrossRef](#)]
4. Weintraub, S.J.; Chow, K.N.; Luo, R.X.; Zhang, S.H.; He, S.; Dean, D.C. Mechanism of active transcriptional repression by the retinoblastoma protein. *Nature* **1995**, *375*, 812–816. [[CrossRef](#)] [[PubMed](#)]
5. Harbour, J.W.; Luo, R.X.; Dei Santi, A.; Postigo, A.A.; Dean, D.C. Cdk phosphorylation triggers sequential intramolecular interactions that progressively block Rb functions as cells move through G1. *Cell* **1999**, *98*, 859–869. [[CrossRef](#)]
6. Pandey, K.; An, H.J.; Kim, S.K.; Lee, S.A.; Kim, S.; Lim, S.M.; Kim, G.M.; Sohn, J.; Moon, Y.W. Molecular mechanisms of resistance to CDK4/6 inhibitors in breast cancer: A review. *Int. J. Cancer* **2019**, *145*, 1179–1188. [[CrossRef](#)]
7. Chen, P.; Xu, Y.; Li, X.; Yao, H.; Lin, K. Development and strategies of CDK4/6 inhibitors. *Future Med. Chem.* **2020**, *12*, 127–145. [[CrossRef](#)]
8. Goel, S.; DeCristo, M.J.; McAllister, S.S.; Zhao, J.J. CDK4/6 inhibition in cancer: Beyond cell cycle arrest. *Trends Cell Biol.* **2018**, *28*, 911–925. [[CrossRef](#)]
9. Wood, D.J.; Endicott, J.A. Structural insights into the functional diversity of the CDK–cyclin family. *Open Biol.* **2018**, *8*, 180112. [[CrossRef](#)]
10. Kaltheuner, I.H.; Anand, K.; Moecking, J.; Düster, R.; Wang, J.; Gray, N.S.; Geyer, M. Abemaciclib is a potent inhibitor of DYRK1A and HIP kinases involved in transcriptional regulation. *Nat. Commun.* **2021**, *12*, 1–15. [[CrossRef](#)]
11. Day, P.J.; Cleasby, A.; Tickle, I.J.; O'Reilly, M.; Coyle, J.E.; Holding, F.P.; McMenamin, R.L.; Yon, J.; Chopra, R.; Lengauer, C.; et al. Crystal structure of human CDK4 in complex with a D-type cyclin. *Proc. Natl. Acad. Sci. USA* **2009**, *106*, 4166–4170. [[CrossRef](#)] [[PubMed](#)]
12. Chen, P.; Lee, N.V.; Hu, W.; Xu, M.; Ferre, R.A.; Lam, H.; Bergqvist, S.; Solowiej, J.; Diehl, W.; He, Y.-A.; et al. Spectrum and Degree of CDK Drug Interactions Predicts Clinical Performance. *Mol. Cancer Ther.* **2016**, *15*, 2273–2281. [[CrossRef](#)] [[PubMed](#)]
13. Liu, C.; Huang, Y.; Qin, T.; You, L.; Lu, F.; Hu, D.; Xiao, R.; Qin, X.; Guo, E.; Yang, B.; et al. AZD5153 reverses palbociclib resistance in ovarian cancer by inhibiting cell cycle-related proteins and the MAPK/PI3K-AKT pathway. *Cancer Lett.* **2022**, *528*, 31–44. [[CrossRef](#)]
14. Braal, C.L.; Jongbloed, E.M.; Wilting, S.M.; Mathijssen, R.H.J.; Koolen, S.L.W.; Jager, A. Inhibiting CDK4/6 in Breast Cancer with Palbociclib, Ribociclib, and Abemaciclib: Similarities and Differences. *Drugs* **2020**, *81*, 317–331. [[CrossRef](#)] [[PubMed](#)]
15. Weiss, J.M.; Csoszi, T.; Maglakelidze, M.; Hoyer, R.J.; Beck, J.T.; Gomez, M.D.; Lowczak, A.; Aljumaily, R.; Lima, C.M.R.; Boccia, R.V.; et al. Myelopreservation with the CDK4/6 inhibitor trilaciclib in patients with small-cell lung cancer receiving first-line chemotherapy: A phase Ib/randomized phase II trial. *Ann. Oncol.* **2019**, *30*, 1613–1621. [[CrossRef](#)] [[PubMed](#)]
16. Limagne, E.; Nuttin, L.; Thibaudin, M.; Jacquin, E.; Aucagne, R.; Bon, M.; Revy, S.; Barnestein, R.; Ballot, E.; Truntzer, C.; et al. MEK inhibition overcomes chemioimmunotherapy resistance by inducing CXCL10 in cancer cells. *Cancer Cell* **2022**, *40*, 136–152.e12. [[CrossRef](#)]

17. Meric-Bernstam, F. Combining neratinib with CDK4/6, mTOR and MEK inhibitors in models of HER2-positive cancer. *Clin. Cancer Res.* **2021**, *27*, 1681–1694.
18. Yang, C.; Li, Z.; Bhatt, T.; Dickler, M.; Giri, D.; Scaltriti, M.; Baselga, J.; Rosen, N.; Chandarlapaty, S. Acquired CDK6 amplification promotes breast cancer resistance to CDK4/6 inhibitors and loss of ER signaling and dependence. *Oncogene* **2016**, *36*, 2255–2264. [[CrossRef](#)]
19. Molinski, T.F.; Dalisay, D.S.; Lievens, S.L.; Saludes, J.P. Drug development from marine natural products. *Nat. Rev. Drug Discov.* **2009**, *8*, 69–85. [[CrossRef](#)]
20. Song, C.; Yang, J.; Zhang, M.; Ding, G.; Jia, C.; Qin, J.; Guo, L. Marine Natural Products: The Important Resource of Biological Insecticide. *Chem. Biodivers.* **2021**, *18*, e2001020. [[CrossRef](#)]
21. Matulija, D.; Wittine, K.; Malatesti, N.; Laclef, S.; Turks, M.; Markovic, M.K.; Ambrožić, G.; Marković, D. Marine natural products with high anticancer activities. *Curr. Med. Chem.* **2020**, *27*, 1243–1307. [[CrossRef](#)] [[PubMed](#)]
22. Villa, F.A.; Gerwick, L. Marine natural product drug discovery: Leads for treatment of inflammation, cancer, infections, and neurological disorders. *Immunopharmacol. Immunotoxicol.* **2010**, *32*, 228–237. [[CrossRef](#)] [[PubMed](#)]
23. Jiménez, C. Marine Natural Products in Medicinal Chemistry. *ACS Med. Chem. Lett.* **2018**, *9*, 959–961. [[CrossRef](#)] [[PubMed](#)]
24. Bauer, R.A.; Wurst, J.M.; Tan, D.S. Expanding the range of ‘druggable’ targets with natural product-based libraries: An academic perspective. *Curr. Opin. Chem. Biol.* **2010**, *14*, 308–314. [[CrossRef](#)] [[PubMed](#)]
25. Lyu, C.; Chen, T.; Qiang, B.; Liu, N.; Wang, H.; Zhang, L.; Liu, Z. CMNPD: A comprehensive marine natural products database towards facilitating drug discovery from the ocean. *Nucleic Acids Res.* **2021**, *49*, D509–D515. [[CrossRef](#)] [[PubMed](#)]
26. Blunt, J.W.; Copp, B.R.; Munro, M.H.G.; Northcote, P.T.; Prinsep, M.R. Marine natural products. *Nat. Prod. Rep.* **2010**, *27*. [[CrossRef](#)]
27. Davis, G.D.J.; Vasanthi, A.H.R. Seaweed metabolite database (SWMD): A database of natural compounds from marine algae. *Bioinformatics* **2011**, *5*, 361–364. [[CrossRef](#)]
28. Alnabulsi, S.M.; Al-shar’i, N.A. Hit identification of SMYD3 enzyme inhibitors using structure-based pharmacophore modeling. *Future Med. Chem.* **2019**, *11*, 1107–1117. [[CrossRef](#)]
29. Damm, K.L.; Carlson, H.A. Gaussian-weighted RMSD superposition of proteins: A structural comparison for flexible proteins and predicted protein structures. *Biophys. J.* **2006**, *90*, 4558–4573. [[CrossRef](#)]
30. Liu, N.; Wang, X.; Wu, H.; Lv, X.; Xie, H.; Guo, Z.; Wang, J.; Dou, G.; Zhang, C.; Sun, M. Computational study of effective matrix metalloproteinase 9 (MMP9) targeting natural inhibitors. *Aging* **2021**, *13*, 22867–22882. [[CrossRef](#)]
31. Rao, S.N.; Head, M.S.; Kulkarni, A.; Kulkarni, A.; LaLonde, J.M. Validation studies of the site-directed docking program LibDock. *J. Chem. Inf. Model.* **2007**, *47*, 2159–2171. [[CrossRef](#)] [[PubMed](#)]
32. Yuan, K.; Min, W.; Wang, X.; Li, J.; Kuang, W.; Zhang, F.; Xie, S.; Yang, P. Discovery of novel and selective CDK4/6 inhibitors by pharmacophore and structure-based virtual screening. *Future Med. Chem.* **2020**, *12*, 1121–1136. [[CrossRef](#)] [[PubMed](#)]
33. Luo, L.; Zhong, A.; Wang, Q.; Zheng, T. Structure-Based Pharmacophore Modeling, Virtual Screening, Molecular Docking, ADMET, and Molecular Dynamics (MD) Simulation of Potential Inhibitors of PD-L1 from the Library of Marine Natural Products. *Mar. Drugs* **2022**, *20*, 29. [[CrossRef](#)] [[PubMed](#)]
34. O’leary, B.; Finn, R.S.; Turner, N.C. Treating cancer with selective CDK4/6 inhibitors. *Nat. Rev. Clin. Oncol.* **2016**, *13*, 417–430. [[CrossRef](#)]
35. Cruz, J.V.; Giuliatti, S.; Alves, L.B.; Silva, R.C.; Ferreira, E.F.; Kimani, N.M.; Silva, C.H.; de Souza, J.S.; Espejo-Román, J.M.; Santos, C.B.R. Identification of novel potential cyclooxygenase-2 inhibitors using ligand-and structure-based virtual screening approaches. *J. Biomol. Struct. Dyn.* **2021**, 1–23. [[CrossRef](#)]
36. Goldenberg, O.; Erez, E.; Nimrod, G.; Ben-Tal, N. The ConSurf-DB: Pre-calculated evolutionary conservation profiles of protein structures. *Nucleic Acids Res.* **2009**, *37*, D323–D327. [[CrossRef](#)]
37. Li, Q.; Chen, L.; Ma, Y.F.; Jian, X.E.; Ji, J.H.; You, W.W.; Zhao, P.L. Development of pteridin-7(8H)-one analogues as highly potent cyclin-dependent kinase 4/6 inhibitors: Synthesis, structure-activity relationship, and biological activity. *Bioorganic Chem.* **2021**, *116*, 105324. [[CrossRef](#)]
38. Mysinger, M.M.; Carchia, M.; Irwin, J.J.; Shoichet, B.K. Directory of useful decoys, enhanced (DUD-E): Better ligands and decoys for better benchmarking. *J. Med. Chem.* **2012**, *55*, 6582–6594. [[CrossRef](#)]
39. Abraham, M.J.; Murtola, T.; Schulz, R.; Páll, S.; Smith, J.C.; Hess, B.; Lindahl, E.J.S. GROMACS: High performance molecular simulations through multi-level parallelism from laptops to supercomputers. *SoftwareX* **2015**, *1*, 19–25. [[CrossRef](#)]
40. Mark, P.; Nilsson, L. Structure and dynamics of the TIP3P, SPC, and SPC/E water models at 298 K. *J. Phys. Chem. A* **2001**, *105*, 9954–9960. [[CrossRef](#)]
41. da Silva, A.W.S.; Vranken, W.F. ACPYPE-Antechamber python parser interface. *BMC Res. Notes* **2012**, *5*, 367. [[CrossRef](#)] [[PubMed](#)]
42. Miller, A.; Carchman, R.; Long, R.; Denslow, S.A. La Crosse viral infection in hospitalized pediatric patients in Western North Carolina. *Hosp. Pediatr.* **2012**, *2*, 235–242. [[CrossRef](#)] [[PubMed](#)]
43. Linse, B.; Linse, P. Tuning the smooth particle mesh Ewald sum: Application on ionic solutions and dipolar fluids. *J. Chem. Phys.* **2014**, *141*, 184114. [[CrossRef](#)] [[PubMed](#)]
44. Hess, B. P-LINCS: A parallel linear constraint solver for molecular simulation. *J. Chem. Theory Comput.* **2008**, *4*, 116–122. [[CrossRef](#)] [[PubMed](#)]

45. Beckstein, O.; Denning, E.J.; Perilla, J.R.; Woolf, T.B. Zipping and unzipping of adenylate kinase: Atomistic insights into the ensemble of open $\leftrightarrow$  closed transitions. *J. Mol. Biol.* **2009**, *394*, 160–176. [[CrossRef](#)]
46. Kumari, R.; Kumar, R.; Open Source Drug Discovery Consortium; Lynn, A. g\_mmpbsa A GROMACS tool for high-throughput MM-PBSA calculations. *J. Chem. Inf. Modeling* **2014**, *54*, 1951–1962. [[CrossRef](#)]
47. Xiong, G.; Wu, Z.; Yi, J.; Fu, L.; Yang, Z.; Hsieh, C.; Yin, M.; Zeng, X.; Wu, C.; Lu, A.; et al. ADMETlab 2.0: An integrated online platform for accurate and comprehensive predictions of ADMET properties. *Nucleic Acids Res.* **2021**, *49*, W5–W14. [[CrossRef](#)]
48. Lagunin, A.A.-O.; Dubovskaja, V.I.; Rudik, A.V.; Pogodin, P.V.; Druzhilovskiy, D.S.; Glorizova, T.A.; Filimonov, D.A.; Sastry, N.G.; Poroikov, V.V. CLC-Pred: A freely available web-service for in silico prediction of human cell line cytotoxicity for drug-like compounds. *PLoS ONE* **2018**, *13*, e0191838. [[CrossRef](#)]

MDPI  
St. Alban-Anlage 66  
4052 Basel  
Switzerland  
Tel. +41 61 683 77 34  
Fax +41 61 302 89 18  
[www.mdpi.com](http://www.mdpi.com)

*Marine Drugs* Editorial Office  
E-mail: [marinedrugs@mdpi.com](mailto:marinedrugs@mdpi.com)  
[www.mdpi.com/journal/marinedrugs](http://www.mdpi.com/journal/marinedrugs)







MDPI  
St. Alban-Anlage 66  
4052 Basel  
Switzerland

Tel: +41 61 683 77 34

[www.mdpi.com](http://www.mdpi.com)



ISBN 978-3-0365-4570-7